NANOSTRUCTURES:
PHYSICS AND TECHNOLOGY

9th International Symposium

St Petersburg, Russia, June 18–22, 2001

Co-Chairs

Zh. Alferov
L. Esaki

P R O C E E D I N G S

Ioffe Institute
St Petersburg, 2001

Published by
Ioffe Physico-Technical Institute
26 Politekhnicheskaya, St Petersburg 194021, Russia
http://www.ioffe.rssi.ru/

Publishing license ΛP No 040971 of June 16, 1999.

ISBN 5-93634-005-8

The International Symposium "Nanostructures: Physics and Technology" is held annually since 1993. The first Symposium was initiated by Prof. Zh. Alferov and Prof. L. Esaki who are its permanent co-chairs. More detailed information on the Symposium is presented on the World Wide Web **http://www.ioffe.rssi.ru/NANO2001/**

The Proceedings include extended abstracts of invited talks and contributed papers to be presented at the Symposium. By tradition this book is published before the beginning of the meeting.

The volume was composed at the Information Services and Publishing Department of the Ioffe Institute from electronic files submitted by the authors. When necessary these files were converted into the Symposium LaTeX 2_ε style without any text revisions. Only minor technical corrections were made by the composers.

Design and layout: N. Vsesvetskii
Desk editor: L. Solovyova

Information Services and Publishing Department
Ioffe Physico-Technical Institute
26 Politekhnicheskaya, St Petersburg 194021, Russia
Phones: (812) 247 2617, 247 9932
Fax: (812) 247 1017
E-mail: vgrig@eo.ioffe.rssi.ru

Printed in Russian Federation

The Symposium is held under the auspices of
the Russian Academy of Sciences

Organizers

Ioffe Physico-Technical Institute

Scientific Engineering Center for Microelectronics at the Ioffe Institute

in association with

Research Council for the Project "Physics of Solid State Nanostructures" at the Ministry of Industry, Science and Technologies of Russian Federation

and

the institutions of the Russian Academy of Sciences

Division of General Physics and Astronomy

St Petersburg Scientific Center

Acknowledgments

The Organizers gratefully acknowledge the following for their contribution to the success of the Symposium:

Ministry of Industry, Science and Technologies of Russian Federation

Russian Foundation for Basic Research

AIXTRON AG, Germany

Office of Naval Research International Field Office

European Office of Aerospace Research and Development, United Kingdom

Location and Date

The Symposium is held at St Petersburg's recreation area Repino on June 18–22, 2001.

Advisory Committee

Zh. Alferov (*Russia*)
Y. Arakawa (*Japan*)
A. Aseev (*Russia*)
D. Bimberg (*Germany*)
L. Esaki (*Japan*)
S. Gaponov (*Russia*)
E. Gornik (*Austria*)
Yu. Gulyaev (*Russia*)
N. Holonyak Jr. (*USA*)
L. Keldysh (*Russia*)
G. Landwehr (*Germany*)
J. Merz (*USA*)
L. Molenkamp (*Germany*)
M. Shur (*USA*)
M. Skolnick (*United Kingdom*)
B. Zakharchenya (*Russia*)

Programme Committee

R. Suris, Chair (*St Petersburg*)
V. Evtikhiev, Secretary (*St Petersburg*)

A. Andronov (*Nizhny Novgorod*)
N. Bert (*St Petersburg*)
A. Chaplik (*Novosibirsk*)
V. Dneprovskii (*Moscow*)
B. Egorov (*St Petersburg*)
A. Gippius (*Moscow*)
S. Gurevich (*St Petersburg*)
Yu. Kopaev (*Moscow*)
P. Kop'ev (*St Petersburg*)
Z. Krasil'nik (*Nizhny Novgorod*)
V. Kulakovskii (*Chernogolovka*)
M. Kupriyanov (*Moscow*)
I. Merkulov (*St Petersburg*)
V. Panov (*Moscow*)
E. Poltoratskii (*Moscow*)
N. Sibel'din (*Moscow*)
V. Timofeev (*Chernogolovka*)
V. Volkov (*Moscow*)
L. Vorobjev (*St Petersburg*)

Organizing Committee

M. Mizerov, Chair (*Center for Microelectronics*)
V. Grigor'yants, Vice-Chair (*Ioffe Institute*)
B. Egorov, Secretary (*Ioffe Institute*)
D. Donskoy (*St Petersburg Scientific Center*)
P. Kop'ev (*Ioffe Institute*)
G. Mikhailov (*St Petersburg*)
N. Sibel'din (*Lebedev Physical Institute*)
E. Solov'eva (*Ioffe Institute*)
V. Zayats (*Division of General Physics and Astronomy*)

Award Committee

Zh. Alferov, Chair (*Russia*)
L. Esaki (*Japan*)
M. Heuken (*Germany*)
L. Keldysh (*Russia*)
R. Suris (*Russia*)
V. Timofeev (*Russia*)
R. Tsu (*USA*)
M. Willander (*Sweden*)

Contents

Nanostructure Technology

Silicon Based Nanostructures

Infrared Phenomena in Nanostructures

Wide Band Gap Nanostructures

Microcavity and Photonic Cristal

Nanostructure Characterization and Novel Atomic-Scale Probing Techniques

Quantum Wells and Superlattices

Quantum Wires and Quantum Dots

Tunnelling Phenomena

General Properties of Low Dimensional Structures

Spin Related Phenomena in Nanostructures

Quantum Computing

Ordered Arrays and Nanoparticles

Nanostructure Devices

Transport in Nanostructures

Lasers and Optoelectronic Devices

Excitons in Nanostructures

2D Electron Gas

Closing Session

Unprinted Papers

The papers listed below are included in the Symposium Programme, but not printed in the Proceedings, as the authors had not submitted electronic files in due time.

OS.01i *Zh. Alferov*
Quantum dots heterostructures and lasers

OS.02i *F. Capasso*
Micro- and nano Electro Mechanical Systems (MEMS and NEMS) based on vacuum fluctuation forces: a new frontier of nanotechnology

NT.02i *O. Pchelyakov*
State of the art and perspectives of molecular beam epitaxy development

SBNS.01i *K. Tanaka*
Advanced silicon nanotechnology at JRCAT

NC.02i *M. Kovalchuk*
X-ray standing wave technique structure-sensitive spectroscopy for nanoscale-samples. New perspectives with Synchrotron radiation

LOED.05p *G. G. Zegrya*, V. P. Evtikhiev, E. Yu. Kotelnikov, I. V. Kudryashov and A. S. Shkolnik
Basic physical processes which influence on the maximal optical power of semiconductor laser

CS.01i *L. Keldysh*
Dynamic Stark effect for excitons

CS.02i *R. Suris* and I. A. Dmitriev
Bloch oscillations in 2D and 3D quantum dot superlattices

AIXTRON Young Scientist Award

In 1999, the Symposium Programme Committee and the Board of AIXTRON AG (Germany) established a special award to honour a young scientist who will present at the Symposium the best paper in the field of solid state nanostructures. The award comprises a diploma and a $500 reward sponsored by AIXTRON.

The AIXTRON Young Scientist Award recipients are:
1999 **Alexey R. Kovsh**, Ioffe Institute, Russia.
2000 **Thomas Gruber**, Physikalisches Institut Universität Würzburg Am Hubland, Würzburg, Germany.

Mr. Thomas Gruber
became the recipient of AIXTRON Award for the presentation of the paper:

Semimagnetic resonant tunneling diodes for electron spin manipulation

Co-authors: *M. Keim, R. Fiederling, G. Reuscher, A. Waag, W. Ossau, G. Schmidt and L. Molenkamp*.

Thomas Gruber was born in Braunschweig, Germany in 1974. He graduated from high school as best of his class in 1993. He studied general physics at the University of Würzburg and got first involved in experimental research in 1998. In a 3-months project he investigated the general characteristics of BeTe-ZnSe resonant tunneling diodes, including temperature- and magneto-dependent measurements.

He continued the studies in his diploma thesis “Spin Manipulation with semimagnetic BeTe-ZnMnSe Resonant Tunneling Diodes” (1999–2000) as a member of the semiconductor research group of Prof. Waag. The work consisted both of growing the structures by molecular beam epitaxy and characterising them by optical and electrical measurements. The main objective was to develop a semiconductor device that made it possible to manipulate and eventually reverse the spin polarization of an electron current injected into the widely used semiconductor material GaAs. This would be a further step towards the development of active spintronic devices.

The paper “Semimagnetic resonant tunneling diodes for electron spin manipulation” presented at the NANO 2000 conference portrayed the main results of that work. It demonstrates that not only an efficient injection of spin-polarized electrons into GaAs can be achieved using semimagnetic resonant tunneling diodes, but also a manipulation of the spin polarization to a certain degree via an external voltage applied to the device. Further work, however, is needed to accomplish a complete reversal of the spin polarization.

Having started his PhD studies at the Department of Semiconductor Physics, University of Ulm, Thomas Gruber’s principal area of research interest is now the development of wide band-gap ZnO-based semiconductor structures. Again the research work includes both the investigation of the epitaxial growth conditions and their effects on structural, electrical and optical properties of the devices. An MOCVD method is now being used for the epitaxy, though.

9th Int. Symp. "Nanostructures: Physics and Technology"
St Petersburg, Russia, June 18–22, 2001

Molecular beam epitaxy (MBE) of quantum devices

A. Y. Cho, D. L. Sivco, H. M. Ng, C. Gmachl, A. Tredicucci,
R. Colombelli and F. Capasso
Bell Laboratories, Lucent Technologies 600 Mountain Avenue,
Murray Hill, NJ 07974 USA

Molecular beam epitaxy (MBE) is a thin film process for the growth of single crystalline semiconductor, metal, and insulator materials. A unique feature of MBE is the ability to prepare layers with atomic precision. The film grows atomic layer by atomic layer. This allows us to achieve "band structure engineering" and it is the basis of many high-performance semiconductor devices such as high-speed electronic circuits, lasers, and detectors.

One illustration of the demanding structures grown by MBE is the Quantum Cascade (QC) Laser. This laser is fundamentally different from conventional lasers in that it can be tailored to emit light at a specific wavelength by simply varying the quantum well width using the same combination of semiconducting materials. The quantum wells may be as thin as 10 Angstroms and the whole QC laser may be composed of over five hundred precise layers. This can only be achieved by computer controlled MBE. With InGaAs for the well and InAlAs for the barrier, we have demonstrated emission wavelengths from 3.5 μm to 24 μm. The highest peak optical power we have obtained is 2 W pulsed and 0.5 W cw. The highest operating temperature was demonstrated at 425 K for an 8.4 μm laser with an output power of 17 mW.

Most of the QC lasers made today are with InGaAs/InAlAs and GaAs/AlGaAs systems. In order to achieve shorter wavelength, intersubband transitions useful for the fiber communication wavelength, we have to extend the material system to GaN/AlGaN, which has a maximum conduction band offset of 2 eV. Preliminary studies of that system will also be discussed.

MBE is now a high volume production technology for microwave and photonic quantum devices. Multi-wafer, computer controlled high throughput MBE systems can automatically grow as many as seven 6″ or fifteen 4″ wafers on each platen with uniformity and reproducibility within 1%.

9th Int. Symp. "Nanostructures: Physics and Technology"
St Petersburg, Russia, June 18–22, 2001

X-ray diffraction study of CdSe/BeTe nanostructures grown by MBE with stressor-controlled interfaces

R. N. Kyutt†⋆, T. V. Shubina‡, S. V. Sorokin‡⋆, S. V. Ivanov‡⋆, P. S. Kop'ev‡, A. Waag‡, G. Landwehr⋆ and M. Willander⋆⋆

† Ioffe Physico-Technical Institute, St Petersburg, Russia
‡ Abteilung Halbleiterphysik, Universität Ulm, 89081 Ulm, Germany
⋆Physikalisches Institute der Universität Würzburg, D-97074 Würzburg, Germany
⋆⋆Physical Electronics and Photonics, Dept of Microelectronics and Nanoscience, Chalmers University of Technology and Göteborg University, S-412 96 Göteborg, Sweden

Self-formation of quantum-confined nanostructures of wide gap II-VI compounds (e.g. CdSe/ZnSe) is characterised by enhanced broadening (up to 10 monolayers (ML)) of the deposited strained insertions even when they are in a sub-monolayer thickness range [1, 2]. This results in smoothing a carrier localisation potential, preventing fabrication of real quantum dots (QDs) optically active up to the room temperature. Therefore, looking for a novel approach to the 0D-nanostructure fabrication, differing from the conventional Stranski–Krastanov growth mode, is of great importance. Recently, a stimulating effect of an intentionally-introduced super-strained fractional monolayer (FM) of BeSe — "stressor" — on the self-formation of CdSe QDs in ZnSe has been observed [3]. The stressor-assisted growth appears to be most effective for the Be-containing compounds with strong chemical bonds resulting in sharp nanostructure interfaces [4]. Novel CdSe/BeTe nanostructures grown using CdTe FM as a stressor [5] have demonstrated a possibility of CdSe nano-island (< 10 nm) ordering and an interface-induced linear optical anisotropy due to using two binary compounds with no-common atoms [6].

In the paper we report on x-ray diffraction (XRD) study of the CdSe/BeTe nanostructures, intended to elucidate chemical composition of interfaces, playing a role of natural stressors, and process of their formation during molecular beam epitaxial (MBE) growth.

The study has been performed on CdSe/BeTe superlattice (SL) structures grown on GaAs(100) substrates at 300°C in a Riber 2300 MBE setup. RHEED specular spot intensity (SSI) oscillations were monitored to control the interface formation with a high accuracy [5]. Three sets of the structures were investigated. Two sets involve CdSe/BeTe SLs with CdTe interfaces intentionally formed by CdTe FMs (< 0.3 ML) deposited prior the growth of each CdSe and BeTe layers. For the first set of the SL structures, CdTe growth at the first BeTe-CdSe interface was interrupted at a local RHEED SSI maximum and for the second SL set – at the SSI minimum [5]. In both sets the second interfaces are grown at the SSI maximum. SL samples of the third set contain only the CdTe FM insertions in BeTe, deposited till either the SSI minimum or the SSI maximum for the reference. The intended SL period is between 5–6 nm, a nominal thickness of the CdSe insertion is varied in the $0.4-1.5$ ML range for different samples. The parameters of the samples are listed in Table 1. XRD measurement were performed on a Philips X-Pert Diffractometer using the symmetrical Bragg reflections 002 and 004. The double crystal diffraction (DCD) rocking curves (RCs) and triple crystal scans were recorded using $CuK_{\alpha 1}$ radiation.

The XRD curves measured demonstrate periodical intensity distribution with SL-satellites and well-resolved thickness fringes for most of the samples. We present here only 002 reflection RCs containing more details and having the more distinct satellites and fringes as compared to 004 ones, which is due to the larger value of the BeTe structural factor than those of CdTe and CdSe.

The accurate theoretical simulation of the RCs of CdTe/BeTe SLs (the samples of the third set) (see Fig. 1(a)) allowed us to determine the CdTe nominal thicknesses corresponding to both the

Table 1. Parameters of the samples used in the study.

Sample No	CdSe width (ML)	CdTe interface deposition	SL period thickness (Å)	SL(0) position (arc. sec)	$\Delta\Theta$ deviation (arc. sec)	BeSe (ML)
1480	—	min SSI (0.08 ML)	39.3	433	—	—
1481	—	max SSI (0.2 ML)	44.9	205	—	—
1484	0.4	Max–max	45.9	147	229	0.45
1487	0.7	Max–max	50.8	25	229	0.48
1483	1.0	Max–max	56	310	716	1.12
1489	1.5	Max–max	57–66	−173	383	0.77
1502	0.7	Min–max	51	51	641	1.04
1505	1.0	Min–max	29.4	1610	2500	0.45
1503	1.5	Min–max	54	54	973	1.59

SSI maximum and minimum. The values were further employed in processing XRD data of other samples. One should stress that 004 RCs of the samples of the both first and second sets have a similar shape, while the 002 curves differ considerably by the satellite intensity. Samples of the first set exhibit a more strong SL(+1) satellite peak, whereas the SL(−1) one almost disappears (Fig. 1(b)). For samples of the second set RCs have a more symmetrical character (Fig. 1(c)). The values of the SL-period determined from simulation these RCs are also given in Table 1.

Comparison of the experimental SL(0) peak positions with those expected from the measured

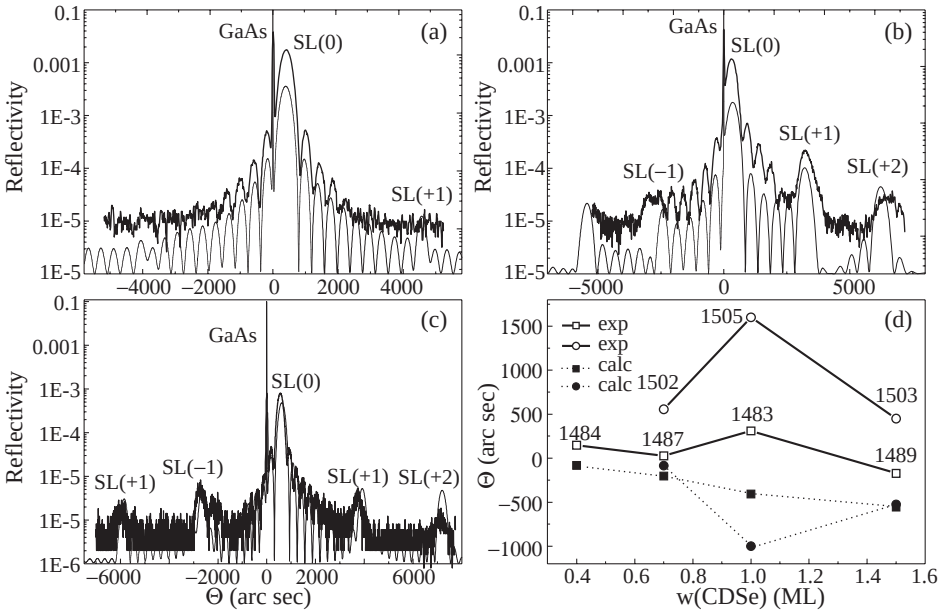

Fig. 1. Experimental (thick line) and simulated (thin line) DCD (002) rocking curves for (a) CdTe/BeTe SL (#1480); (b) CdSe/BeTe SL with the max-max CdTe interfaces (#1483); (c) CdSe/BeTe SL with the min-max CdTe interfaces (#1502). Angular position of the SL(0) peak at 002-rocking curves for the samples of the first set (squares) and the second set (circles) as a function of CdSe nominal thickness is presented in (d).

SL period and intended composition (CdSe and CdTe contents) shows that the experimental values are strongly deviated to the positive angles. The dependence of the angular deviation on the CdSe-content (Fig. 1(d), Table 1) has a non-monotonic character: an abrupt shift of the SL(0) peak position for samples #1483 and #1505 with $w \sim 1.0$ ML is observed as compared to others in each set following a monotonically decreasing dependence. The deviation is obviously larger for the second set samples, reaching for #1505 the value which gives the SL(0) position at the angle higher than that corresponding to a pure BeTe layer.

These facts make us suppose that there exists an additional component with the lattice parameter smaller than that of BeTe in the SLs studied, which can be BeSe only. Be-Se interface bonds can arise at the BeTe surface free from the intentionally deposited CdTe islands due to exchange reactions between Se atoms impinging onto the surface with the BeTe lattice. These reactions are strongly shifted to the BeSe formation owing to its much higher binding energy. Obviously, the SLs of the second set with the smaller CdTe coverage (SSI minimum) of BeTe surface should display higher contribution of BeSe interface bonds. To explain the maximum of BeSe-bond contribution at w(CdSe)$\sim$ 1 ML one should take into account that CdSe is deposited in MBE mode under strong Se-rich conditions. The excessive Se atoms may interact with the free BeTe surface, resulting in the BeSe bonds formation, faster than a CdSe deposition rate. However, this process comes to saturation soon, while CdSe amount continuously increases.

Simulation including BeSe contribution provides more satisfactory coincidence of the experimental and calculated RCs (Fig. 1(b) and (c)), although does not reproduce all the details of the experimental curves, particularly the shape of the satellite peaks. Probably, there are some additional peculiarities of the interface structure, like e.g. lateral composition distribution, which influence the diffraction intensity distribution.

In conclusion, we perform a detail XRD study of the novel type-II CdSe/BeTe nanostructures formed by stressor-assisted self-formation. High sensitivity of the diffraction curves to interface types is revealed. The model developed for a simulation of rocking curves includes spontaneous formation of BeSe-enriched interface formation when the smaller amount of CdTe FM stressor as compared to that corresponding to a maximum RHEED SSI is intentionally deposited.

Acknowledgements

This work is partly supported by the Program of the Ministry of Sciences of RF "Physics of Solid State Nanostructures", RFBR and INTAS Grants ##97-31907, 99-00015.

References

[1] R. N. Kyutt, A. A. Toropov, S. V. Sorokin, T. V. Shubina, S. V. Ivanov, M. Karlsteen and M. Willander, *Appl. Phys. Lett.* **75**, 373 (1999).

[2] N. Peranio, A. Rosenauer, D. Gerthsen, S. V. Sorokin, I. V. Sedova and S. V. Ivanov, *Phys. Rev. B* **61 (23)**, 16015 (2000).

[3] M. Keim, M. Korn, F. Bensing, A. Waag, G. Landwehr, L. W. Molenkamp, S. V. Ivanov, S. V. Sorokin, A. A Toropov, T. V. Shubina, P. S. Kop'ev, J. Seufert, R. Weigand, G. Bacher and A. Forchel, *J. Cryst. Growth*, **214/215**, 684 (2000).

[4] Th. Walter, A. Rosenauer, D. Gerthsen, F. Fischer, R. Gall, Th. Litz, A. Waag and G. Landwehr, *Microscopy of Semiconducting Materials*, UK: Institute of Physics Publishing, Oxford, 1997, p. 315.

[5] S. V. Ivanov, G. Reuscher, T. Gruber, T. Muck, V. Wagner, J. Geurts, A. Waag, G. Landwehr, T. V. Shubina, N. A. Sadchikov, A. A. Toropov and P. S. Kop'ev, *Proc. 8^{th} Int. Symposium "Nanostructures: Physics and Technology"*, St Peterburg, 2000, p. 98.

[6] T. V. Shubina, A. A. Toropov, S. V. Sorokin, A. V. Lebedev, S. V. Ivanov, A. Waag, G. Landwehr and L. W. Molenkamp, *Abstracts of 25^{th} Int. Conf. on the Physics of Semiconductors*, Ocaka, Japan, 2000, p. 219.

9th Int. Symp. "Nanostructures: Physics and Technology"
St Petersburg, Russia, June 18–22, 2001

Novel GaAs/GaSb heterostructures emitting at 2 μm wavelength

V. A. Solov'ev†, A. A. Toropov†, B. Ya. Mel'tser†, Ya. V. Terent'ev†, R. N. Kyutt†, A. A. Sitnikova†, A. N. Semenov†‡, S. V. Ivanov†, Motlan§, E. M. Goldys§ and P. S. Kop'ev†

† Ioffe Physico-Technical Institute, St Petersburg, Russia
‡ St Petersburg Electrotechnical University, St Petersburg, Russia
§Division of Information and Communication Sciences, Macquarie University, North Ryde, NSW 2109, Australia

Abstract. We report on growth as well as optical, transmission electron microscopy and X-ray diffraction studies of a new type of a GaAs/GaSb heterostructure, with 1 to 3 monolayer thick GaAs layers embedded within unstrained GaSb. In such structures the GaAs layer is under tensile stress, in contrast to the situation in which self-organized growth of quantum dots is commonly observed. The structure emits light in the 2 μm wavelength range.

Quantum dots (QDs) have recently attracted considerable interest due to their rich physics and optoelectronic applications, especially in prospective lasers [1]. Up to date, a number of the lattice mismatched semiconductor systems including InAs/GaAs [2], (Ga,In,Al)Sb/GaAs [3, 4], InAs/InP [5] and InP/InGaP [6] were found to form self-organized QDs under appropriate conditions. Most of the papers concern the situation when a thin strained layer is inserted in a matrix of an unstrained wider band-gap semiconductor with a smaller lattice constant. The quantum well (QW) and QD structures with different types of band offsets have been studied, including both type I [2, 5, 6] and type II [3, 4] band line-ups. The common feature of all these heterostructures is that the narrow band-gap material is under compressive strain. Furthermore, the surrounding matrix material is usually a relatively wide-gap compound such as GaAs or InP. As a result, the possible operating wavelength of such QD lasers is shorter than 1.55 μm. The potential advantage of type II QDs for the suppression of the Auger recombination channels make them particularly promising for light emission in the near- and mid-IR regions, particularly above 2 μm, where conventional types of semiconductor lasers meet severe problems due to Auger processes [7]. Thus, it is important to be able to extend the emission wavelength range of type II QD heterostructures beyond 2 μm.

In this paper we demonstrate a new type of a lattice-mismatched heterostructure characterized by intense photoluminescence (PL) in the spectral range of 1.7–2.3 μm at low temperatures. The samples contain ultrathin GaAs layers grown pseudomorphically in a GaSb matrix. The GaAs thickness was varied between 1 and 3 monolayers (MLs), i.e. within a typical range for the formation of self-organized QDs driven by a 7% lattice mismatch between GaAs and GaSb [3]. In contrast to the systems studied previously, the GaAs layer inserted into GaSb is under tensile stress and it can serve as a model for experimental studies of such systems, particularly that in the reversed structures (GaSb in GaAs) the self-organised QD formation is reasonably well documented [3, 4]. To the best of our knowledge, the only work concerned with the emission properties of comparable structures was reported recently by Glaser et al. [8], who observed a strong emission from AlAs monolayers in AlSb.

Both single GaAs/GaSb structures and a superlattice (SL) were grown by molecular beam epitaxy (MBE) on GaSb(001) substrates at a constant temperature of 520°C. Conventional solid source effusion cells were used to produce Ga, Al and As_4 fluxes, whereas Sb_2 flux was supplied from a RB-075-Sb cracking cell. The single structures contain a 0.5 μm thick GaSb buffer layer followed by a 0.3 μm GaSb layer with an ultrathin GaAs layer of varying thickness inserted in the center and confined by 30 nm $Al_{0.5}Ga_{0.5}As$ barriers on both sides. The GaAs layer is grown under (2×4)As-stabilized conditions with a 10 s growth interruption before and after to avoid As and Sb flux intermixing. The growth time of GaAs was varied between 2" and 5" in different samples, or between 1.2 and 3 MLs. Several samples were grown without substrate rotation to ensure a uniform variation of the GaAs thickness across the substrate surface. A ten-period 1.2 ML-GaAs/4 nm-GaSb SL sample was grown under the same conditions. The PL experiments were performed in a closed-cycle He cryostat or a liquid nitrogen cryostat, in the temperature range from 8 K to 300 K. CW laser diodes emitting either at 0.8 μm or at 1.3 μm were used for the PL excitation.

The SL structure was characterized by X-ray diffraction (XRD). Figure 1 shows a (004) $\theta - 2\theta$ XRD rocking curve measured in the SL sample. Both a zero-order SL reflection and higher-order satellites are prominent, providing an estimate of the SL period of 4.3 nm and nominal thickness of GaAs layers within the SL of 1.2 ML, in good agreement with design specifications. The simulations of the SL XRD rocking curves (Fig. 1) yield an estimate of the average broadening of the layers along the growth direction, resulting e.g. from the effects of inter-diffusion and Sb segregation during MBE growth [9]. This effect is observed through a fast decrease of the relative intensities of the SL satellites with the satellite order. The broadening of the GaAs layers in our sample is 4–5 ML. In such case the formation of ideal abrupt GaAs quantum wells can be ruled out, as well as the formation of a dense array of thick 3-dimensional (3D) QDs. Rather, the XRD data describe a SL built from GaAsSb layers, with spatial nonuniformities due to the nanoscale alloy composition or thickness fluctuations.

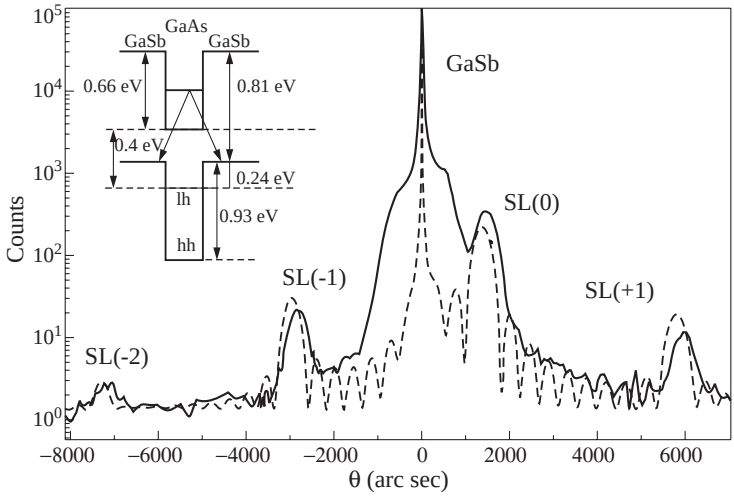

Fig. 1. XRD $\theta-2\theta$ rocking curves for the SL sample: experimental (solid curve) and simulated using with a Gaussian-like broadened distribution of As atoms up to 4.5 ML FWHM (dashed curve). The inset shows the schematic diagram of band line-ups and optical transitions for tensile strained GaAs in unstrained GaSb.

A set of the samples was studied by transmission electron microscopy (TEM) in cross-section geometry using a Philips EM-420 microscope at 100 kV. It is well known that (200) reflections are chemically-sensitive for face-centered cubic materials and can be used to detect the composition variation [10]. Figure 2 demonstrates the dark field (DF) images of single GaAs/GaSb samples with different GaAs thickness. All the images were obtained at the same conditions. It should be noted that GaAs insertions in all the images are seen as thin dark stripes, which are not continuous. The image of the 0.8 ML GaAs layer looks like a dotted line and consists of the dots with lateral sizes of about 1 nm (Fig. 2(a)). By raising the nominal thickness of GaAs, the TEM image shows dash line contrast and reveals the extended islands having noticeable strain field (Fig. 2(b)). These islands do not interlock themselves with the further increase in the GaAs thickness. But their sizes raise in the growth direction, that is seen in Fig. 2(c) as enlargement of dark haloes near the islands. In Fig. 2(d) one can see the extended defects near some islands, that demonstrates the starting of relaxation process in the structure with a 2 ML GaAs insertion.

The structures with thin GaAs layers exhibit PL at low temperatures. Figure 3 displays the PL spectra measured at 80 K at low excitation conditions (1 W/cm^2) in the single layer samples with varying GaAs thickness. All the spectra show a peak at $\sim$0.8 eV due to the band-to-band transitions in bulk GaSb, accompanied by a 0.775 eV peak attributed to donor - deep native acceptor recombination, and another peak, with the peak energy related to the GaAs thickness as deduced from the XRD measurements and extrapolating the GaAs deposition time. As the thickness increases from 1.2 to about 3.5 ML the peak shifts from 1.7 μm to 2.3 μm. Simultaneously, the peak undergoes some broadening, and its maximum intensity progressively decreases. The integrated intensity remains almost constant up to the nominal thickness of about 2.5–3 ML, and then it abruptly decreases in thicker layers. The emission wavelength of the GaAs/GaSb structures remains well below the GaSb band gap due to the type II band line-up. The inset in Fig. 1 demonstrates the expected band offsets and the scheme of optical transitions, as estimated using the van der

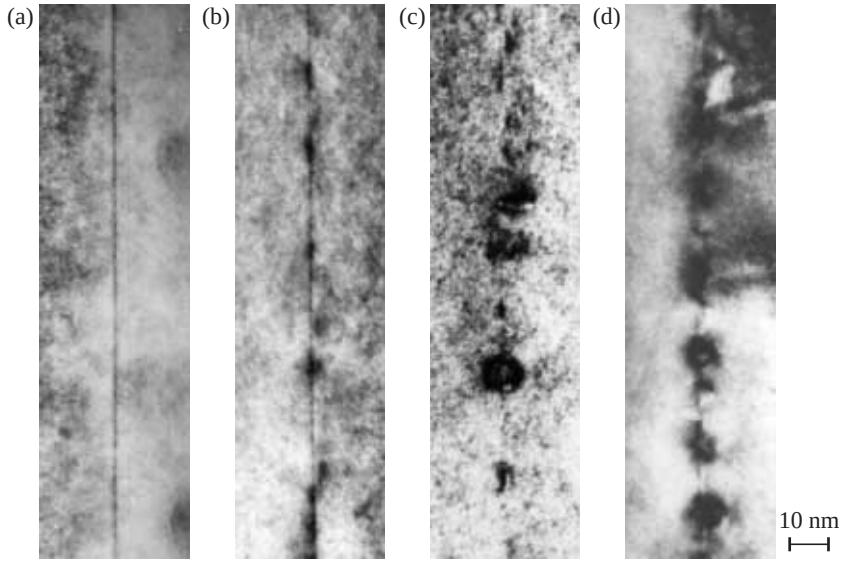

Fig. 2. Cross-section g[002] DF TEM images of the single-layer GaAs/GaSb samples with different nominal thicknesses of a GaAs layer: (a) 0.8 ML, (b) 1.2 ML, (c) 1.5 ML and (d) 2.0 ML.

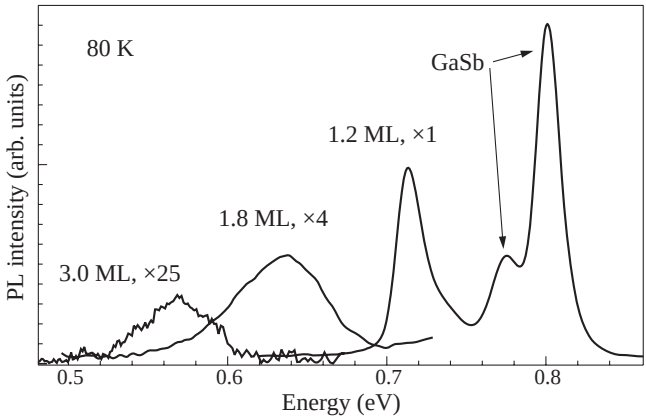

Fig. 3. Low excitation PL spectra of single-layer GaAs/GaSb samples with different GaAs nominal thicknesses.

Walle approach [11]. A strong biaxial stress induced by the 7% lattice mismatch results in a shrinkage of the GaAs band gap down to about 0.4 eV, making it noticeably smaller than the equilibrium band gap of the surrounding bulk GaSb. Nevertheless, the resulting band line-ups are of type II with electrons confined in GaAs and holes in GaSb.

In conclusion, we have presented an optical, TEM and XRD studies of a new type of heterostructure combining a thin layer of GaAs in GaSb, where GaAs is under tensile strain. The structure is characterized by a type II band offset and it emits bright PL in the spectral range of 1.7–2.3 μm, depending on the nominal thickness of the GaAs layers.

Acknowledgements

This work was supported in part by RFBR Grant 01-02-17933, the Program of the Ministry of Sciences of RF "Physics of Solid State Nanostructures" and CRDF Grant No RP1-2265.

References

[1] Y. Arakawa, H. Sakaki, *Appl. Phys. Lett.* **40**, 939 (1982).
[2] A. Madhukar, Q. Xie, P. Chen, A. Konkar, *Appl. Phys.Lett.* **64**, 2727 (1994).
[3] F. Hatami, N. N. Ledentsov, M. Grundmann, J. Bhrer, F. Heinrichsdorff, M. Beer, D. Bimberg, S. S. Ruvimov, P. Werner, U. Gsele, J. Heydenreich, U. Richter, S. V. Ivanov, B. Ya. Meltser, P. S. Kop'ev, Zh. I. Alferov, *Appl. Phys. Lett.* **67**, 656 (1995).
[4] E. R. Glaser, B. R. Bennett, B. V. Shanabrook, R. Magno, *Appl. Phys. Lett.* **68**, 3614 (1996).
[5] H. Marchand, P. Desjardins, S. Guillon, J. -E. Paultre, Z. Bougrioua, R. Y. -F. Yip, R. A. Masut, *Appl. Phys. Lett.* **71**, 527 (1997).
[6] N. Carlsson, W. Seifert, A. Petersson, P. Castrillo, M. E. Pistol, L. Samuelson, *Appl. Phys. Lett.* **65**, 3093 (1994).
[7] G. G. Zegrya, A. D. Andreev, *Appl. Phys. Lett.* **67**, 2681 (1995).
[8] E. R. Glaser, T. A. Kennedy, B. R. Bennett, B. V. Shanabrook, *Phys. Rev.* **B 59**, 2240 (1999).
[9] R. N. Kyutt, A. A. Toropov, S. V. Sorokin, T. V. Shubina, S. V. Ivanov, M. Karlsteen, M. Willander, *Appl. Phys. Lett.* **75**, 373 (1999).
[10] E. Bithnel, W. Stobbs, *Phil. Mag.* **A 60**, 39 (1989).
[11] C. G. van der Walle, *Phys. Rev.* **B 39**, 1871 (1989).

9th Int. Symp. "Nanostructures: Physics and Technology"
St Petersburg, Russia, June 18–22, 2001

Evolution of RHEED intensity in the simulated homoepitaxial growth of GaAs(001)

*M. Itoh**† and T. Ohno‡
* Department of Physics, Graduate School of Science, Osaka University,
Toyonaka, Osaka 560-0043 Japan; Electronic address
† Computer Center, Gakushuin University,
1-5-1, Mejiro, Toshima-ku, Tokyo 171-8588 Japan
‡ National Research Institute for Metals,
1-2-1, Sengen, Tsukuba, Ibaraki 305-0047, Japan

Abstract. The influence of surface reconstruction on the homoepitaxial growth of GaAs(001) has been studied by the Monte Carlo simulations. In the model, both Ga and As species are deposited onto a GaAs(001)-$\beta 2(2\times 4)$ reconstructed surface simultaneously at $T \simeq 580^{\circ}$C as this corresponds to the ordinary growth condition of molecular beam epitaxy. The growth mechanism of the $\beta 2(2\times 4)$ structure has been identified; also studied are the step-flow growth modes on vicinal surfaces of various misorientations.

Introduction

Molecular beam epitaxy (MBE) and reflection high-energy electron diffraction (RHEED) have been the useful tools in developing semiconductor devices by controlling growth at the accuracy of atomic layers. This is based on the fact that the oscillation period of a RHEED intensity during steady state growth mode corresponds to the growth of one atomic layer. The conventional use of these techniques relies on the claim that the evolution of the specular intensity of RHEED in MBE can be well accounted for by that of the density of atomic steps [1, 2, 3]. However, by carrying out kinetic Monte Carlo (KMC) simulations of the homoepitaxial growth on a GaAs(001)-$\beta 2(2\times 4)$ reconstructed surface with the growth condition of the ordinary MBE, we found that the calculated density of double As dimers which characterizes the $\beta 2(2\times 4)$ reconstruction, and not that of atomic steps, evolves synchronously with an observed RHEED intensity. We also found that the growth of an atomic step is strongly affected by the diffusion anisotropy of Ga adatoms as well as the relative phase of the $\beta 2(2\times 4)$ structures between an upper and a lower terraces.

1. The model

Experimentally, it is well known that the $\beta 2(2\times 4)$ reconstruction is kept stable in the homoepitaxial MBE growth of GaAs(001) when the substrate temperature is kept at $T = 580^{\circ}\text{C} \pm 20^{\circ}\text{C}$, both Ga and As species are supplied onto the substrate simultaneously, and the V/III flux ratio is sufficiently high. To simulate this, we use Ga atoms and As_2 molecules for the deposition sources of the MBE growth. The substrate is constructed on the zinc-blende structure, on which the $\beta 2(2\times 4)$ reconstruction is realized by the Coulomb repulsion between surface As atoms located at the in-plane next nearest neighbor sites in the [110] direction [5].

For the atomistic kinetics, the diffusion of a Ga adatom is realized by the random walk. Moreover, we introduce the reservoir of As_2 species to approximate the chemisorbed as

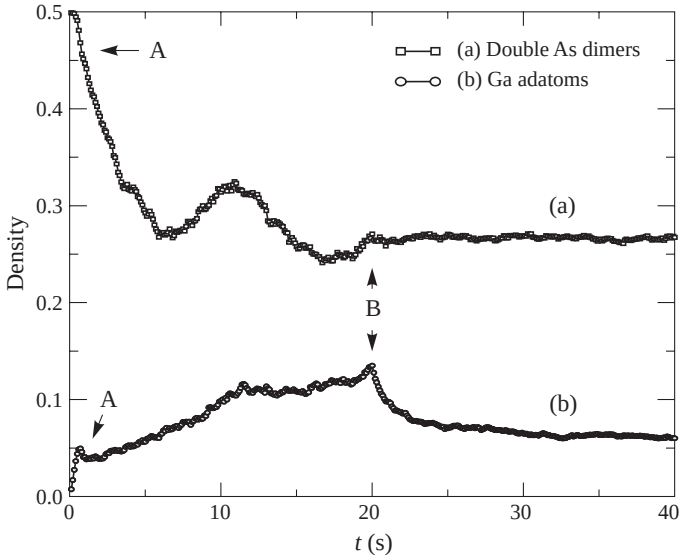

Fig. 1. (a) The density of double As dimers and (b) the density of Ga adatoms plotted as functions of growth time. The growth simulations were carried out on the $120a_s \times 120a_s$ lattice. The symbols A and B indicate the occurrence of the structural transformation and the growth interruption, respectively. The decay constant of (b) after the growth interruption is about 2.5 s.

well as physisorbed states of this species [6] in a mean-field manner. Then, when As_2 molecule is deposited from its source, it is once stored at the reservoir, from where it is either supplied onto a surface or desorbs into vacuum. It is actually the introduction of this state that makes possible the growth simulations under the realistic range of V/III flux ratio, i.e., ≥ 6 [7]. In the growth simulations which follow, the deposition fluxes are fixed to be 0.1 and 0.4 monolayers (ML)/s for Ga atoms and As_2 molecules, respectively.

Furthermore, to examine the effect of the diffusion anisotropy of a Ga adatom, we introduce the parameter G to denote the enhanced ratio of its random walk between parallel and perpendicular to the As dimer row.

2. Island growth mode

With this model, we found that the nucleation of an island occurs on top of the double As dimer row of the $\beta 2(2 \times 4)$ structure. However, the initial island thus appeared does not take the $\beta 2(2 \times 4)$ structure. Instead, an island adopts this reconstruction after it becomes wide enough in the [110] direction to split into two parts. By calculating the density of double As dimers during growth simulation and after its interruption, we found that this density, and not the density of atomic steps, evolves synchronously with an observed RHEED intensity, as seen in Figs. 1(a) and 1(b) [4]. The growth simulations were carried out on the $120a_s \times 120a_s$ lattice, where $a_s = 4.0$ Å denotes the surface lattice constant.

Moreover, we found that the structural transformation of initial growing islands can be identified *in situ* by observing RHEED. When combined with our discovery that this structural transformation is particularly prominent when the deposition coverage of Ga atoms is at around 0.1 ML, this result means that it is appropriate to interrupt growth before the oscillation of a RHEED intensity reaches its maximum by about 10% of an

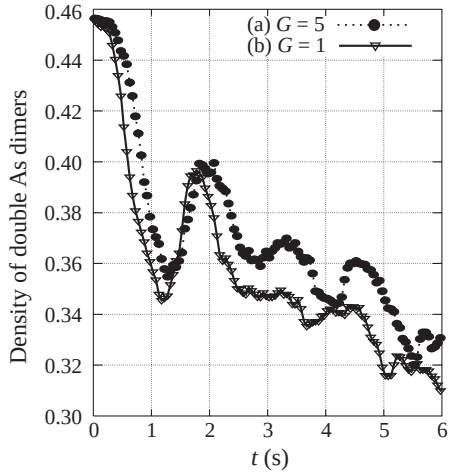

Fig. 2. Evolution of the density of double As dimers on the A surface. The simulations were carried out on a $120a_s \times 120a_s$ lattice, on which the $80a_s \times 120a_s$ strip and the $40a_s \times 120a_s$ strip are stacked consecutively. The deposition fluxes of Ga atoms and As_2 molecules are chosen to be 0.1 ML/s and 0.4 ML/s, respectively. (a) $G = 5$ and (b) $G = 1$.

oscillation period. This is contrasted with the conventional use of RHEED in which growth is interrupted when its intensity arrives exactly at its maximum of the oscillation because the evolution of a RHEED intensity has been supposed to correspond to that of surface step density.

3. Step-flow growth mode

Typical step-flow growth directions which have been studied hitherto are for the vicinal surfaces misoriented from (001) toward the [110] direction, the $[\bar{1}10]$ direction, and the $\langle 010 \rangle$ directions, which are called the A, B and C surfaces, respectively [3]. For these surfaces, it was found that the RHEED intensity evolves completely differently between A and B or C surfaces. According to our simulations, this difference is caused by the diffusion anisotropy of Ga adatoms which is enhanced parallel to the As dimer row direction than to the perpendicular direction. Due to this anisotropy, once a Ga adatom is deposited onto a surface, it hardly reaches a step edge when it is running parallel to the As dimer row. Following the previous case, we calculated the density of double As dimers in the initial stage of the simulated growth with such step edges. To this end, we constructed the three-bilayer structure consisting of the stacking of the first and second strips of $80a_s \times 120a_s$ and $40a_s \times 120a_s$ in their sizes on top of the $120a_s \times 120a_s$ lattice used as the substrate. By these simulations, we found that the density of double As dimers exhibits a rapid oscillation of only one period, followed by its gradual decrease, as seen in Fig. 2 [8]. Note that, in this particular configuration, a small value of G induces the nucleation and growth of islands, whereas on a real A surface, a large value of G does this task.

In contrast, this diffusion anisotropy makes a Ga adatom to reach a step edge more easily on the B and C surfaces and, hence, it is naturally expected that the growth proceeds similarly on these surfaces. Therefore, the RHEED experiment on the A, B and C surfaces are qualitatively accounted for by these simulations.

4. Summary

By carrying out KMC simulations with the use of the realistic two-species model, we showed that the evolution of a specular intensity of RHEED is well accounted for by that of the density of double As dimers which characterize the $\beta 2(2 \times 4)$ reconstruction. On a singular surface, the structural transformation associated with the growth of the GaAs(001)-$\beta 2(2 \times 4)$ surface is found to shift the origin of the growth time by the coverage of approximately 0.1 ML. Our result suggests that one should take account of this effect in determining the time to interrupt growth in the fabrication of heterostructures. On the A surface, the similar calculation showed again that the density of double As dimers accounts for the evolution of the observed specular RHEED intensity. Thus we conclude that the qualitative difference in the evolution of a RHEED intensity between A and B or C surfaces is due to the diffusion anisotropy of Ga adatoms.

Acknowledgements

M.I. was supported by the 'Research for the Future' program of the Japan Society for the Promotion of Science (JSPS-RFTF97P00201).

References

[1] J. H. Neave, B. A. Joyce, P. J. Dobson and N. Norton, *Appl. Phys. A* **31**, 1 (1983).
[2] J. Sudijono, M. D. Johnson, C. W. Snyder, M. B. Elowitz and B. G. Orr, *Phys. Rev. Lett.* **69**, 2811 (1992).
[3] T. Shitara, D. D. Vvedensky, M. R. Wilby, J. Zhang, J. H. Neave and B. A. Joyce, *Phys. Rev. B* **46**, 6815; 6825 (1992).
[4] M. Itoh and T. Ohno, *Phys. Rev. B* **62**, 7219 (2000).
[5] J. E. Northrup and S. Froyen, *Phys. Rev. B* **50**, 2015 (1994).
[6] C. G. Morgan, P. Kratzer and M. Scheffler, *Phys. Rev. Lett.* **82**, 4886 (1999).
[7] M. Itoh, G. R. Bell, A. R. Avery, T. S. Jones, B. A. Joyce and D. D. Vvedensky, *Phys. Rev. Lett.* **81**, 633 (1998).
[8] M. Itoh and T. Ohno, *Phys. Rev. B* **63**, (2001), to appear.

9th Int. Symp. "Nanostructures: Physics and Technology"
St Petersburg, Russia, June 18–22, 2001

A new technique for fabricating three-dimensional micro- and nanostructures of various shapes

V. Ya. Prinz, *D. Grützmacher*, A. Beyer, C. David, B. Ketterer and E. Deccard
Laboratory for Micro- and Nanotechnology, Paul Scherer Institute,
CH-5232 Villigen PSI, Switzerland

Abstract. We have shown that complex 3-dimensional micro- and nanostructures (shells) can be formed by directional rolling up of strained thin heterofilms debonded from the substrate. A technique for controlling the shape and lacation of the structures is proposed and realized.

Introduction

Nanometer-range structures are of great interest since they hold much promise as building blocks for future electronic and mechanical nanodevices. In nanotechnology, molecular-beam epitaxy offers wide possibilities for precise nanostructuring in the growth direction. However, structuring with similar precision in the remaining two dimensions has not yet been achieved: in this respect, capabilities of traditional lithographic methods remain restricted to some tenth parts of nanometer.

Recently, a breakthrough in this direction was made in [1, 2]. The possibilities were shown i) of detaching from substrate atomically smooth heterolayers of nanometer-range thicknesses (by selective etching of sacrificial underlayers contained in the initial structure) and ii) of fabricating from the strained heterofilms thus obtained nanotubes and other nano-objects of cylindrical geometry. It was shown that using self-scrolling process of detached heterofilms it is possible to obtain nanotubes with almost any desired diameter (from 100 μm to 2 nm for InGaAs/GaAs films [1, 2], and to 10 nm for SiGe/Si films [3, 4]).

The present work is aimed to solving another, more difficult problem, namely, the problem of giving a freed atomically smooth nanometer-thick film a more complicated desired shape. In this study, more intricate objects were obtained from Si/GeSi films.

1. Fabrication technique

Figure 1 depicts the self-scrolling process by the example of a strained GeSi/Si heterostructure heavily doped with boron. In this case, the undoped sacrificial layer can be selectively removed by dissolving it in a 3.7% NH_4OH:H_2O solution, the heavily Boron doped Si and GeSi layers remaining nearly intact due to high selectivity of the etching process between heavily and lightly doped layers [3, 4]. Due to high elastic strain in the GeSi/Si system, the freed film starts rolling thus forming a tube, a spiral or a ring.

To transform a plane figure in a three-dimensional shell of a desired shape, it is required to develop a method that would provide a possibility to roll the plain figure, in a controllable manner, in preset directions. Although, to do this, several approaches can be used, on imposing an additional requirement, i.e., applicability of the method to fabricating nanometer-size objects, too evolved variants (such as, e.g., two-level lithography) should be rejected.

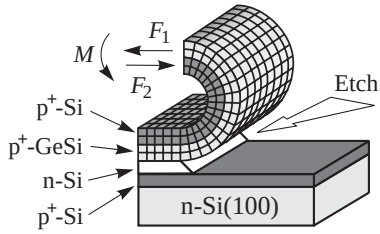

Fig. 1. Schematic view of the self-scrolling mechanism. p^+-Si/GeSi is strained bilayer, n-Si is sacrificial layer. The elastic forces F_1 and F_2 give rise to a moment M of forces which tends to bend the bilayer.

Below, we extend the previously developed nanotube formation technology to fabrication of more complicated three-dimensional objects using a merely geometric approach. The essence of the approach is the following. Obviously, the geometry of the initial plane area determines the sites at which the rolling process is initiated and terminated; this predetermines the rolling directions suitable for rolling more complicated objects. Figure 2 schematically shows initial lithographically obtained plane figures that were used in this study. Apparently, during isotropic lateral selective etching of the underlying sacrificial layer, the acute angles will detach from substrate first, Then, the mechanism of enhanced (by a factor of 1000) etching of the sacrificial layer in the places where the film bends off the substrate starts operating. As the films rolls, access for the etchant to still intact parts of the sacrificial layer opens. This mechanism of enhancement determines directions along which the freed parts of the film roll. The rapid rolling results in formation, in a simplest case, of a ring. On reaching the end of the strip, the rolling processes slows down, thus determining the final position of the resultant three-dimensional shell on the substrate.

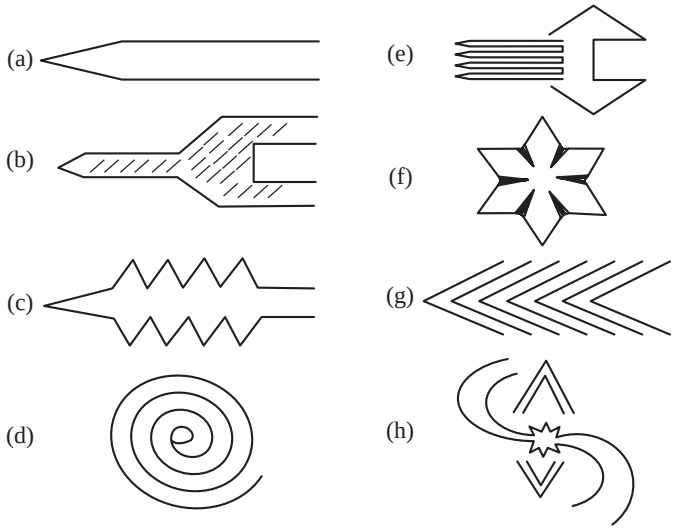

Fig. 2. Simplest patterns formed on strained Si/SiGe heterostructures.

2. Results

Figure 2 shows some examples of simplest patterns that were formed with the help of electron-beam lithography on strained Si/SiGe heterostructures. Regions exposed to the

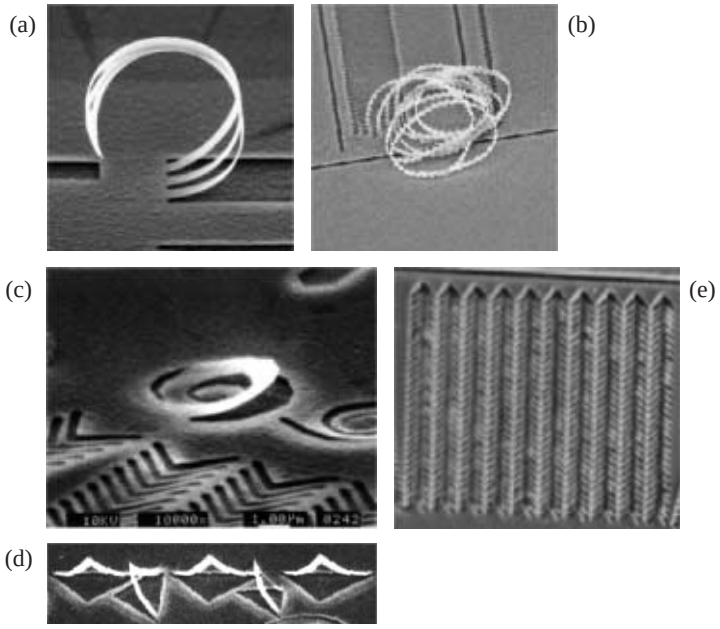

Fig. 3. Open shells formed from bilayer strips of length $L \approx R$, $R = 2\,\mu$m and thickness $d = 35$ nm.

electron beam (seen in the figure as dark parts) were removed by dry etching to locally disclose the undoped-Si sacrificial layer. The experiments were carried out on Si/SiGe heterostructures with the total thickness of bilayer $d = 35$ nm (the equilibrium curvature radius of the relaxed bilayer $R = 2\ \mu$m and also on structures with $d = 6$ nm and $R = 300$ nm. Using these patterns and the above-described directional self-rolling process of the Si/GeSi bilayer, we have fabricated shells of various shapes. Some of these shells are shown in Figs. 3 and 4. Among them are open shells formed from bilayer strips of length $L \approx R$ (Fig. 3), and also closed shells formed from strips with $L \gg R$ (Fig. 4).

Below, open shells are listed which were obtained from the patterns shown in Figs. 2(a)-(h), respectively: (a) strips-needles bent off the surface or directed toward it with their sharp ends (as shown in Fig. 3(a)); (b) a strip-needle bent-off from the substrate upward and aside, which is a result of artificially introduced anisotropy of mechanical properties of the strip (perforation); (c) a sawing (as shown in Fig. 3(b)); (d) a spiral-like strip (Fig. 3(c)).

From pattern shown in Fig. 2(e)-(h) we fabricate shells interacting between themselves: (e) strips-needles directed one toward another; (f) a ball-shaped shell formed by six "petals"; (g) tips (Fig. 3(d)) and an ordered array of needles (which may be used in fabrication of "cold" cathodes) (Fig. 3(e)); (h) a small ball-shaped shell suspended on "pedicles", with two needles attached to it (a useful construction for nanomechanics).

For the case $L \gg R$, the following shells were obtained using the patterns Figs. 2(a)-(f): (a) rings (Fig. 4(a),(b)), a helix (Fig. 4(c)) or tube (Fig. 4(d)); (b) a spiral smoothly passing into a tube at the place where the strip was widening; (c) a tube with modulated wall thickness; (d) rings attached to a tube; (f) six rings (tubes) attached to each other; (g) an array of double (left and right) spirals fixed to substrate with their ends (Fig. 4(e)) (a basic structure for nanomechanics and nanoelectronics devices).

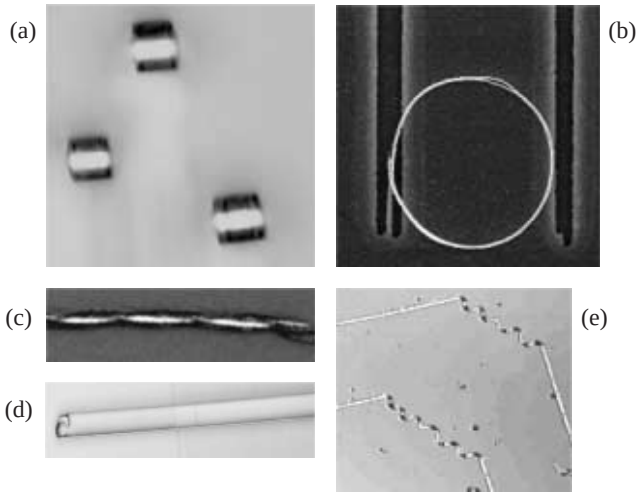

Fig. 4. Shells formed from bilayer strips of length $L \gg R$, $R = 2$ mm and thickness $d = 35$ nm (a,b,d,e), $R = 300$ nm, $d = 6$ nm (c).

3. Conclusion

In conclusion a rich variety of shapes that can be obtained with the above-described technology is noteworthy. In fact, a wide set of plane geometric figures may be transformed into a wide set of three-dimensional shells of various shapes. The simplicity of the method, its applicability to a broad class of materials and, finally, its compatibility with the mature integrated-circuit technology allows us to anticipate its wide practical applications in the future. It is extremely important that, just changing the dimensions of the plane figure to be rolled up in a shell, locally thinning it (by etching) or introducing artificial anisotropy of its mechanical properties, one can obtain a multitude of various shells from identical patterns on one and the same heterostructure. Assembling shells of various shapes into arrays and filling or overgrowing them with various materials, one can fabricate complex architectures the industry requires today.

References

[1] V. Ya. Prinz, V. A. Seleznev and A. K. Gutakovsky, *Proc. ICPS-24 (Jerusalem 1998)*, World Scientific, 1999.
[2] V. Ya. Prinz, V. A. Seleznev, A. K. Gutakovsky, A. V. Chehovskiy, V. V. Preobrazhenskii, M. A. Putyato and T. A. Gavrilova, *Physica E* **6**, 828 (2000).
[3] V. Ya. Prinz, S. V. Golod, V. I. MashanovV and A. K. Gutakovsky, *Inst. Phys. Conf. Ser.* **166**, 203 (2000).
[4] S. V. Golod, V. Ya. Prinz, V. I. MashanovV and A. K. Gutakovsky, *Semicond. Sci. Technol.* **16**, 181 (2001).

9th Int. Symp. "Nanostructures: Physics and Technology"
St Petersburg, Russia, June 18–22, 2001

Initial stages of growth and formation of CaF_2 nanostructures on Si (001)

L. Pasquali†, S. D'Addato†, S. Nannarone†, N. S. Sokolov‡, S. M. Suturin‡ and H. Zogg§
† INFM and Department of Physics, University of Modena, Italy
‡ Ioffe Physico-Technical Institute, St. Petersburg, Russia
§ Swiss Federal Institute of Technology, Zurich, Switzerland

Introduction

Stimulated by a number of potential applications [1], growth of fluorite (CaF_2) on Si(111) has been extensively studied [2]. Only a few attempts have been undertaken, however, to investigate the initial stages of CaF_2 growth on a technologically important Si(001) surface [3, 4], where anisotropic CaF_2 growth accompanied by the formation of the quasi-one-dimensional islands was observed using TEM and STM techniques. Such islands with nanometer scale width could be attractive for nanolithography. In this work we studied the initial stages of the fluorite growth and the formation of nanometer-scale islands on Si(001) using electron diffraction (RHEED and LEED), atomic force microscopy (AFM), ultra-violet photoemission spectroscopy (UPS) and metastable atom deexcitation spectroscopy (MDS).

1. Experimental

Calcium fluoride nanostructures have been grown in the UHV conditions by evaporation of CaF_2 small pieces in an amorphous carbon crucible onto a thermally cleaned at 1250°C Si(001) surface. The temperature of the substrate during the fluorite deposition was in 400−750°C range, the deposition rate was 2–3 nm/min. Electron energies in RHEED and LEED measurements were 15 keV and 70 eV respectively. The surface morphology of the CaF_2/Si(001) structures was measured *ex-situ* in the tapping mode of a P4-SPM atomic force microscope produced by NT-MDT (Zelenograd, Russia). The typical lateral resolution of the AFM measurements was 10–20 nm, depending on the sharpness of the cantilever tip. In the UPS experiments a He windowless differentially pumped discharge lamp emitting He I (21.2 eV) photons and a hemispherical electron analyzer have been used. In the MDS a differentially pumped discharge nozzle-skimmer source was used.

2. Results and discussion

Before the fluorite deposition, electron diffraction patterns clearly showed 2×1 and 1×2 domains (see for example inset in Fig. 1). Atomic force microscopy showed 100–200 nm width terraces separated by steps of 1 to 8 monolayers (ML) height (Fig. 1). Depositing a few CaF_2 monolayers (typically 1–6 ML) at this surface, we found that the surface morphology drastically changed with the temperature of the Si(001) substrate.

After the growth at 450°C, an array of more or less uniformly distributed CaF_2 islands with characteristic size of 10–20 nm (Fig. 2(a)) could be seen on the surface. The islands were 3–8 nm in height and most of them were elongated in the [110] or [$1\bar{1}0$] directions. The transmission spots on the RHEED patterns taken along these directions (inset in Fig. 2(a)) showed that the lattice orientation in the silicon substrate coincided with that of the fluorite islands. It is noteworthy that during the CaF_2 growth the Si(001) 2×1 superstructure

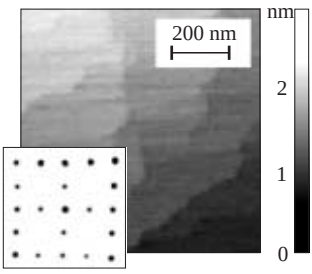

Fig. 1. AFM topography image of Si(001) substrate before CaF_2 deposition. Inset — LEED pattern of the surface taken at 70 eV.

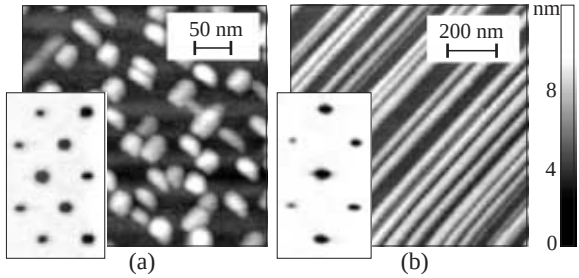

Fig. 2. AFM topography images after deposition of one CaF_2 monolayer at 450°C (a) and 6 ML at 650°C. Insets — corresponding RHEED patterns.

disappeared gradually: it could be distinguished in the pattern even after 2–3 ML of CaF_2 were deposited.

Increasing the deposition temperature above 700°C, a different type of nanostructures was obtained. The fluorite forms an array of very narrow parallel stripes of several microns length (Fig. 2(b)), running along either the [110] or [$1\bar{1}0$] directions, depending on which direction was closer to the surface steps on Si. At intermediate temperature, however, structures with two perpendicular arrays could be observed. The width of the stripes was 15–20 nm, measured by AFM, and their height was 3–8 nm. Since the earlier stages of deposition, the RHEED pattern taken with the e-beam perpendicular to the stripes (inset in Fig. 2(b)) showed distinct transmission spots which were different from the low-temperature case (see inset in Fig. 2(a)). The pattern indicated that CaF_2 [110] axis was normal to the substrate plane while the CaF_2 [$1\bar{1}0$] axis coincided with Si [$1\bar{1}0$]. The RHEED pattern taken with the e-beam parallel to the stripes showed the 3×1 reconstruction, reported earlier [5] for CaF_2 growth on the Si(110) surface. This fact was another evidence for the unusual (110) orientation of the CaF_2 lattice.

A detailed analysis of the RHEED pattern evolution during the high-temperature growth has shown that the stripes form after the deposition of a single CaF_2 monolayer. Unlike thicker structures, the first CaF_2 monolayer covered the substrate uniformly, acting as a wetting layer (Fig. 3). During the formation of the wetting layer the surface remained flat. However, a drastic change of the surface step pattern took place. Instead of the ill-defined shape of the step edges on the initial silicon surface, the step edges of the wetting layer were aligned along the [110] or [$1\bar{1}0$] directions. During the wetting layer formation, in the direction where the stripes were expected to develop at higher CaF_2 coverage, one could observe a 3×1 superstructure in the RHEED pattern (inset in Fig. 3).

MDS and Photoemission measurements with He I photons allowed us to monitor the formation of new bonds at the interface. Figure 4 (curves a and b) shows that the intensity of the Si surface state peak after the deposition at low temperature (450°C) practically has not change, indicating that the most part of the surface keeps the silicon superstructure. This correlates with the observation of the Si(001) 2×1 superstructure in the RHEED patterns even after the deposition of 2–3 ML of CaF_2. These findings allowed us to conclude that the area between the CaF_2 dots (see Fig. 2(a)) was bare silicon surface. However, after the deposition of one CaF_2 monolayer at high temperature (700°C) the silicon surface state peak disappeared (Fig. 4(c)). This correlates with the formation of the wetting layer uniformly covering the silicon surface. It is believed that the wetting layer results from the

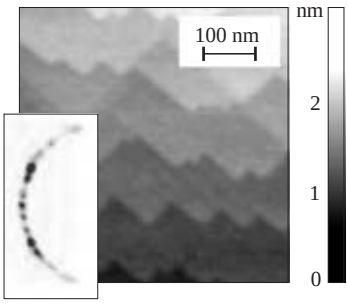

Fig. 3. AFM topography image of the wetting layer formed after fluorite deposition at 750°C. Inset — RHEED pattern.

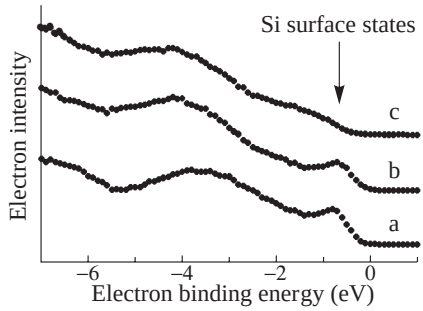

Fig. 4. Ultraviolet photoemission spectra in Si valence band region: (a) bare Si(001) 2 × 1 surface; the same surface covered with 1 ML of CaF_2: (b) at 450°C; (c) at 700°C.

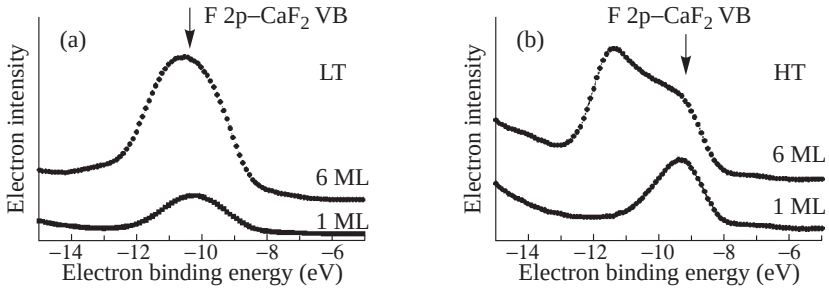

Fig. 5. Ultraviolet photoemission spectra in CaF_2 valence band region after CaF_2 deposition at 450°C (a) and 700°C (b).

chemical reaction at the interface with the creation of strong chemical bonds and change in calcium ion charge, somewhat similar to what is observed in CaF_2/Si(111) [2].

Also from MDS measurements it was evident that a part of the substrate remained unreacted when deposition occured at low temperature, since contributions from Auger neutralization [6] from clean Si were observed on the experimental spectrum. On the other hand, after the completion of 1 ML at high temperature, MDS showed the formation of a distinct low binding energy band that could be associated to the Ca 4*s* states. In this case no contributions from the substrate were observed.

UPS spectra at increasing CaF_2 coverage (Fig. 5) were drastically different for low-temperature and high-temperature growths. At low temperature deposition (Fig. 5(a)) the position of F2*p* line was almost independent on the CaF_2 coverage: this could be explained in terms of the 3D growth mode observed in RHEED from the initial stages of deposition. The slight shift to the higher binding electron energy and the broadening of the peak could be associated to an increase of the average size of the CaF_2 dots.

As was mentioned above, at high temperatures and submonolayer coverage, the formation of reacted fluoride wetting layer took place. The considerable shift (∼1 eV) to the lower binding energies of the fluorine peak (Fig. 5(b), lower curve) could be associated to the different from the bulk fluorine environment in this layer. Drastic transformations of the photoemission spectra at larger coverage and high deposition temperature (Fig. 5(b), upper curve) could be naturally related with the formation of a bulk-like valence band in the fluoride stripes observed in RHEED and AFM (see Fig. 2(b)). A similar effect was

observed in the CaF_2/Si(111) system after the deposition of a CaF_2 layer as thin as 2.5 ML.

One of the puzzling phenomena observed in our experiments was the formation of the single array of the parallel fluorite stripes on the initially two-domain 2×1 and 1×2 surface. The well-pronounced two-fold anisotropy of the RHEED patterns taken from the wetting layer provided a strong evidence for the transformation of the surface symmetry from four- to two-fold during the formation of the wetting layer. We found that several CaF_2 MLs deposited on the wetting layer at low temperature resulted in the formation of the stripes rather than dots. The RHEED pattern taken in the azimuth across these stripes obtained at low temperature showed that the CaF_2 lattice was oriented in the same way as in the high-temperature stripes, i.e. with the CaF_2 axis normal to the substrate. This was an additional evidence of the key role played by the wetting layer in the formation of the fluoride stripes.

Another attractive issue was clarifying the driving forces for the formation of so narrow and long fluorite stripes. Taking into account that in the fluorite structure (111)-surface has the minimum energy [1], one could expect that both CaF_2 islands and stripes were formed by (111) facets. Though the resolution of the AFM was not sufficient to confirm this, in the RHEED patterns, at certain diffraction conditions, inclined streaks expected for such facets were clearly seen. From the RHEED data one could conclude that a good lattice matching existed only along the stripes, but across the stripes a mismatch as high as 45% was expected. This is one of the possible reasons for the observed growth anisotropy. Another probable reason of the long fluorite stripes formation could be due to the diffusion anisotropy of the CaF_2 molecules on the surface of the wetting layer. One more reason of the anisotropy in CaF_2 growth could be related to the fact that the ends of the stripes are formed by the vertical (111) facets. The molecules, which attach the stripes in the base of these facets, form a larger number of bonds than the molecules at the base of the inclined facets. This would also favor the preferential growth along the stripes.

Acknowledgements

This study was partially supported by Russian Ministry of Sciences, INTAS (Grant No 97-10528) and Swiss National Science Foundation (Grant No 7SUPJ062359).

References

[1] L. J. Schowalter and R. W. Fathauer, *J. Vac. Sci. Technol.* **A4**, 1026 (1986).
[2] M. A. Olmstead, review
[3] D. Loretto, F. M. Ross and C. A. Lucas, *Appl. Phys. Lett.* **68**, 2363 (1996).
[4] T. Sumiya, T. Miura, H. Fujinuma and S. Tanaka, *Surf. Sci.* **376**, 192 (1996).
[5] W. K. Liu, X. M. Fang and P. J. McCann, *Appl. Phys. Lett.* **67**, 1695 (1995).
[6] S. Nannarone and L. Pasquali, *Nuclear Instruments and Methods B*, in press.

9th Int. Symp. "Nanostructures: Physics and Technology" **NT.08**
St Petersburg, Russia, June 18–22, 2001

Structure and optical properties of periodic submonolayer insertions of Ge in Si grown by MBE

N. D. Zakharov†$, G. E. Cirlin†‡§, P. Werner†, U. Gösele†, G. Gerth†,
B. V. Volovik‡, N. N. Ledentsov‡ and V. M. Ustinov‡

† Max-Planck Institute of Microstructure Physics, Halle/Saale, Germany
‡ Ioffe Physico-Technical Institute, St Petersburg, Russia
§ Institute for Analytical Instrumentation, St Petersburg, Russia
$ Institute of Crystallography, Moscow, Russia

Introduction

Silicon is the basis of almost the entire market of microelectronic devices, but it can practically not be used in light-emitting devices because of the indirect nature of its bandgap, which drastically limits the luminescence efficiency of this material. As silicon integration with optical interconnects is an urgent task of the industry, different ideas are under discussion to overcome this significant disadvantage. We propose to incorporate dense arrays of submonolayer (SML) narrow gap Ge insertions into a Si matrix. The incorporation of SML insertions in other material systens was previously demonstrated in resulting in very small islands having a very high density (for a review see *e.g.* [1]). In the case of Si–Ge structures SML islands, or quantum dots (QDs) can, on the one side, provide a partial lifting of the k-selection rule for radiative recombination. On the other side, electron attraction to the confined holes may result in confined excitons, assuming that the potential spike in the conduction band due to Ge SML is small. This, taken together with potentially very high density of SML QDs, the resulting efficiency of luminescence and gain may be , probably, sufficient for optical applications. Photoluminescence from SML Ge embedded in silicon was investigated by Sunamura *et al.* [2]. The PL energy was shown to decrease with increasing Ge coverage. The effect was explained by quantum confinement caused by the formation of quantum wires at surface steps and the emission was attributed to a biexciton process. At the same time no structural characterization of these features has been performed.

More traditionally SiGe QDs are fabricated by relatively thick SiGe deposits, resulting in transition to Stranski–Krastanow (SK) growth (see *e.g.* [3]). In [3] SK QDs were grown by low-pressure chemical vapor deposition and their PL properties were investigated. The authors observed that the localization of excitons in the dots leads to an increase of the luminescence efficiency as compared to the smooth SiGe layers. The disadvantage of SK QDs is the low in-plane density and the relatively large size, which defines only weak lifting of the k selection rule on one side, and a small e–h wavefunction overlap due to the type-II band alignment on the other.

The goal of this work is to study structural and optical properties submonolayer Ge insertions in a Si matrix with an aim of developing a better approach for QDs in this system.

Experiment

To investigate the influence of the nominal Ge thickness matrix on the structural properties, two samples with were grown by MBE (Fig. 1(a)). Both structures were grown using

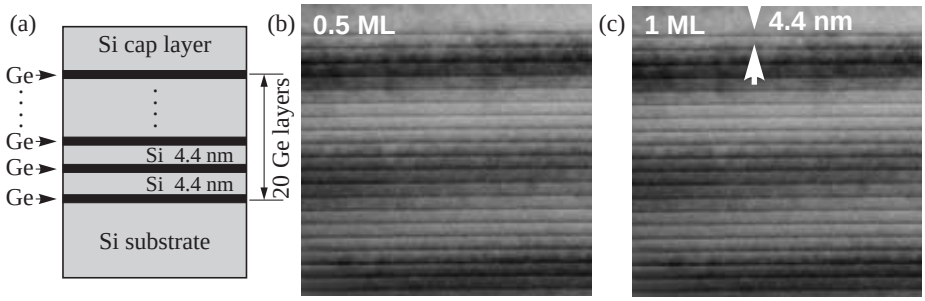

Fig. 1. (a) Sequence of the layers in the grown structures. The thickness of the Ge layers was 0.5 ML (0.07 nm) or 1 ML (0.14 nm) in two different samples. Cross section diffraction contrast images of specimen with 0.5 ML Ge (b) and 1 ML Ge (c). The periodicity in the [001] direction is equal to 4.4 nm in both cases.

Riber SIVA 45 setup on a Si(100) n-type substrates (conductivity 3Ω cm). Five-inch Si substrates (OKMETIC) were used. After chemical treatment the substrates were transferred to the MBE setup. During the growth process the rotation of the samples was used, the temperature inhomogenity along sample was about ∼5%. Structures consist of a 100 nm-thick Si buffer layer, Ge(0.7 Å or 1.4 Å)/Si(44 Å) superlattice (20 pairs) and a 20 nm-thick Si cap layer. The substrate temperature was 750°C for the superlattice growth. For all other layers it was 600°C. The growth rates for Si and Ge were 0.5 Å/s and 0.05 Å/s, respectively.

The growth rates were controlled by 2 mass-spectrometers with feedback, the spectrometers were set to 28 (Si) and 74 (Ge) masses. The total gas pressure during the growth was better than $5 \cdot 10^{-9}$ Torr. The surface was *in situ* controlled using reflection high-energy electron diffraction.

Photoluminescence (PL) was excited by Ar^+-laser $\lambda = 514.5$ nm, maximal excitation density ∼500 W/cm^2. PL was detected by Ge cooled photodiode. The samples were investigated by different electron microscopic techniques and Selected Area Electron Diffraction (SAED).

Results

The cross section images of the grown structures taken in a diffraction contrast mode at relatively low resolution are shown in Fig. 1(b,c). The periodicity in growth [001] direction is 4.4 nm in both cases. It should be noticed that the images of both structures A and B look almost identical at these imaging conditions. However diffraction patterns show a distinct

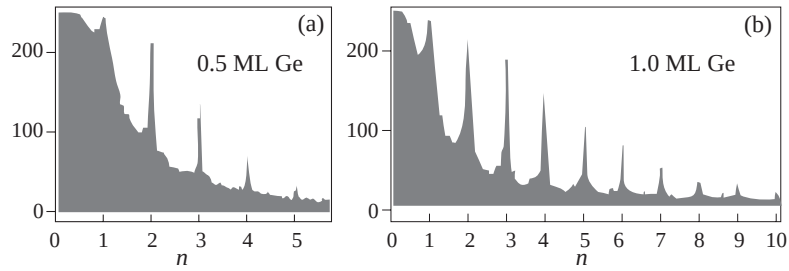

Fig. 2. Line scans in [001] growth direction of zero beam spot in diffraction patterns from multilayer structures A (a) and B (b). In the case of sample B the number of satellites n is twice as large as in sample A.

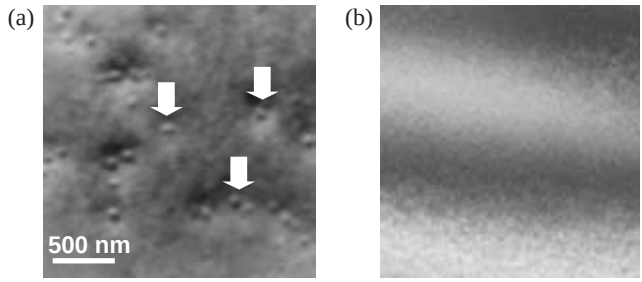

Fig. 3. Plan view images of sample A (a) and B (b). The compositional fluctuations can be clearly seen in sample with 0.5 ML Ge, while the sample B (1 ML Ge) is very homogeneous.

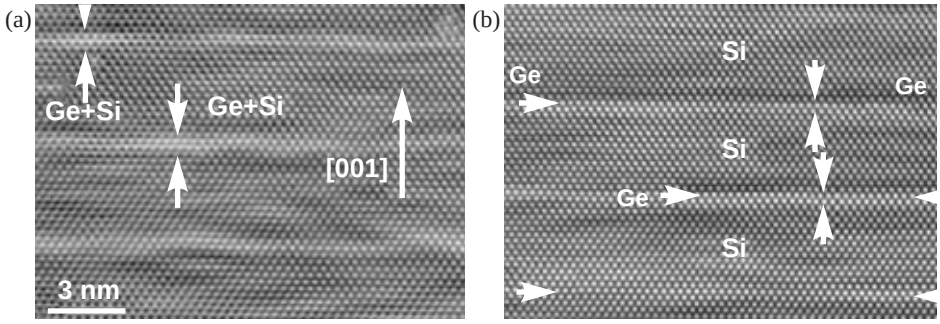

Fig. 4. HRTEM cross-section images of samples A (a) and B (b). The thickness of compositional fluctuations measured along [001] growth direction are marked. It is equal about ∼1 nm and ∼0.27 nm in specimens A and B respectively.

difference (Fig. 2(a,b)). In the diffraction pattern from super lattice formed by 0.5 ML Ge layers (specimen A) the number of Fourier harmonic n is twice less than in the case of 1 ML one (specimen B). This means that the thickness of the incorporated Ge layers in the second case is practically one or/and two mono atomic layers while in the first case it amounts to several mono layers.

Compositional nonuniformities of different contrast and very high density are clearly resolved in plan-view TEM image (Fig. 3(a)) of the SML sample, as opposite to the smooth TEM image of the 1ML structure.

The single layers of Ge are clearly seen in high resolution cross-section image (Fig. 4(b)) taken from very thin crystal region ($t \approx 20$ nm) where the kinematical approximation still works well enough. According to this approximation concentration of Ge $x = (k - 1)/(f_{\mathrm{Ge}}/f_{\mathrm{Si}} - 1)$, where f_{Ge}, f_{Si} — atomic scattering amplitudes for Ge and Si respectively,

$$k = \frac{I_x}{I_{\mathrm{Si}}} = \frac{I_{x,\max} - I_{x,\min}}{I_{\mathrm{Si},\max} - I_{\mathrm{Si},\min}}.$$

It gives $x = 0.9 \pm 0.1$ what indicates that these layers are practically pure Ge. In the case of sample A (Ge submonolayers) the compositional fluctuations are observed in (Fig. 4(a)). The thickness of these fluctuations in the growth direction [001] is about 0.8 nm being in a good agreement with the diffraction data in Fig. 2(a). Besides, in the plane view images of sample A one can observe larger domains ($N = 1.7 \times 10^{10}\,1/\mathrm{cm}^2$) which look like very small quantum dots. They are completely absent in the sample B (Fig. 3(a,b)). The lateral size and the width of these QD estimated in cross-section HRTEM image (Fig. 5)

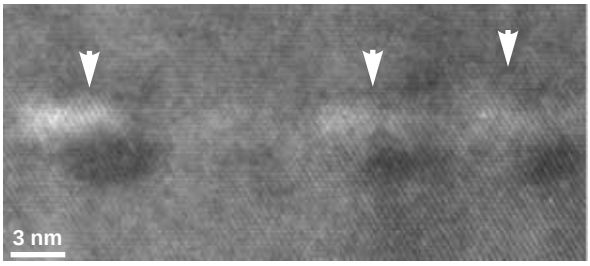

Fig. 5. Cross-section HRTEM image of the Ge-rich domains in sample A. The lateral size and the thickness of the domains are about 7 nm and 3.5 nm respectively.

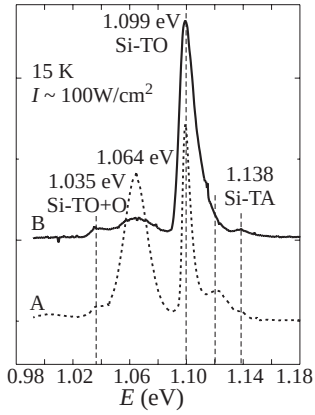

Fig. 6. PL spectra from samples A and B (0.5 and 1 ML Ge respectively).

are equal 7 nm and 3.5 nm respectively. These larger Ge domains may be responsible for high-contrast features revealed in the plan-view image, while the weaker contrast plan-view perculiarities may be associated with flatter islands revealed in Fig. 4(a). PL spectra from specimens A and B are shown in Fig. 6. One can notice an appearance of a peak at 1.064 eV in sample A. At the same time, the Ge-related emission in this range is very weak in sample B with 1 Ge ML due to small localization energy of carriers in the 1 ML sample [4].

Discussion

One should point out that the appearance of intense PL peak at 1.064 eV in the SML sample is related to the Ge compositional fluctuations. These fluctuations appear only in sample A with 0.5 ML insertion. Sample B with 1 ML shows rather uniform distribution of Ge in the layer plane. Almost no intermixing in perpendicular direction is revealed. This is a strong indication of morphological stability of one monolayer structure. Strong compositional fluctuations in sample A (Figs. 3(a), 5) can be treated as QDs which can result in the charge carriers localization. In the case of SML QDs the ir size (< 8 nm — in-plane, < 3.5 nm-thickness) is much smaller than for SK QDs [2] ($\sim$150 nm-diameter, $\sim$9 nm thickness). This is possibly a reason for shift of PL peak at approximately 100 meV into high energy region. It occurs due to increasing confinement energy with decreasing QDs thickness. In the case of sample B the thickness of Ge insertions is too small (1–2 ML) for charge carrier localization.

Acknowledgements

The authors would like to acknowledge P. Laveant and A. Frommfeld for their help during the MBE growth experiments.

References

[1] N. N. Ledentsov *et al. Thin Solid Films* **367**, 40 (2000).
[2] R. Apetz, L. Vescan, A. Hartmann, C. Dieker and H. Lüth, *Appl. Phys. Lett.* **66**, 445 (1995).
[3] H. Sunamura, Y. Shiraki and S. Fukatsu, *Solid-State Electron.* **40**, 693 (2000).
[4] L. P. Rokhinson *et al.*, *Appl. Phys. Lett.* **75**, 2413 (1999).

9th Int. Symp. "Nanostructures: Physics and Technology"
St Petersburg, Russia, June 18–22, 2001

Epitaxial stabilization of a-PbO_2 structure in MnF_2 layers on Si and GaP

A. G. Banshchikov, O. V. Anisimov, N. F. Kartenko, M. M. Moisseeva, N. S. Sokolov and V. P. Ulin
Ioffe Physico-Technical Institute, St Petersburg, Russia

1. Introduction

In recent years, the search for new materials for magnetic storage systems has motivated a number of studies on magnetic multilayers. This interest has been stimulated by the discovery of a giant magnetoresistance effect [1], followed by the design of spin valves [2, 3] with antiferromagnetic films playing an important role. It is well known that manganese fluoride (MnF_2) is a classical antiferromagnetic material, whose magnetic and optical properties are well understood. It was also established that it undergoes polymorphic transitions between the stable rutile-type phase in normal conditions and metastable phases having fluorite or $\alpha-PbO_2$ structures at high pressures and temperatures [4, 5]. Studies of physical properties of these metastable phases are attractive from both academic and applied points of view. While earlier studies concentrated on bulk polycrystalline systems, our efforts have been focused on MnF_2 thin films. In this connection, it is noteworthy that we have demonstrated the growth of ultrathin MnF_2 layers with the inherited cubic structure of fluorite (CaF_2) buffer on a silicon substrate [6]. In this work, we studied MBE growth and structural properties of relatively thick manganese fluoride layers on different heteroepitaxial substrates.

2. Experimental

Manganese fluoride layers were grown on Si(111), Si(001) and GaP(001) in a custom MBE system. CaF_2 or CdF_2 buffer layers were deposited before the MnF_2 growth. At high growth temperatures [7], we used CaF_2 layers to prevent a chemical interaction between MnF_2 and a Si substrate. As was found for GaP(001) substrates, CdF_2 provided the growth of large surface areas of atomic scale smooth. After standard chemical treatment [8], the silicon substrates were loaded into the growth chamber and cleaned thermally at 1250°C in an ultrahigh vacuum. This procedure produces atomically clean Si(111) surfaces with the 7×7 superstructure. The GaP(001) substrates were polished by a Br_2-isobutyl alcohol solution and washed in chloroform and acetone. Before the epitaxy, the substrates were dipped in a HF solution and fixed on Si platelets with InGa eutectic. The crystalline quality of the substrates and the growth of the buffer layers and MnF_2 films were monitored *in situ* by reflection high-energy electron diffraction (RHEED) at electron energy of 15 keV. We used a recrystallization annealing (RA) in the 550–700°C range to improve the MnF_2 film quality of some epitaxial structures grown at lower temperatures. The MnF_2 films were covered with a few CaF_2 monolayers in order to protect the grown structures from ambient humidity. X-ray diffraction measurements were carried out on a conventional DRON system with CuK_α (Ni-filter) radiation. The $\theta - 2\theta$ curves were measured in symmetrical Bragg geometry in the 2θ (6–126°) range. Side reflections were measured in a manual regime. The surface morphology measurements have been carried out in the tapping mode using a P4-SPM-MDT atomic force microscope manufactured by NT-MDT (Zelenograd, Russia).

3. Results and discussion

It was found in our previous study [9] that the surface of thick MnF_2 films grown on CaF_2/Si(111) at 400°C was relatively rough. Weak and diffused X-ray diffraction peaks prevent the identification of the film structure. In this work, we explored a low-temperature growth followed by recrystallization annealing.

The inset in Fig. 1(a) shows the RHEED pattern of a 30 nm MnF_2 film grown at 100°C and annealed at 550°C. Well-pronounced streaks indicate the single crystallinity of the film and relatively smooth surface. The AFM topography (Fig. 1(a)) demonstrates less than 10 nm of height difference on the 1×1 μm^2 square surface. There are irregular shape grains with an average size of about 100 nm. In the AFM and RHEED patterns (Fig. 1(b)), the surface roughening was observed during the further 400°C film growth on the RA surface. One can see that the height difference increases up to 60 nm with the total MnF_2 film thickness of about 100 nm. To reduce the roughness, the film growth time was divided into several stages in such a way that the growth of each 30 nm MnF_2 film at 100°C was followed by RA (at 550°C for 3 seconds). This procedure enabled growing 120–350 nm thick MnF_2 single-crystal films with a relatively smooth surface (Fig. 1(c)).

The X-ray diffraction measurements of the $\theta - 2\theta$ curves have shown the first- and second-order film peaks corresponding to $d = 0.309$ nm interplanar spacing near the intense 111 and 222 Si(111) substrate peaks. To specify the film structure, we additionally measured 19 side reflections, which unambiguously indicated that the film had 6 domains with the $\alpha-PbO_2$ structure [10]. According to [11], MnF_2 polycrystals with a metastable $\alpha-PbO_2$ phase were revealed under normal conditions just after the high-pressure drop. Following the MnF_2 film growth with RA, the MnF_2(111) planes of each domain were parallel to the Si(111) substrate, though in some cases they were rotated by $\approx 1^\circ$ off the substrate surface, whose misorientation relative to the exact crystallographic plane did not exceed 15–20 arcmin. It was found that the lattice constants of the orthorhombic ($\alpha-PbO_2$) unit in a MnF_2 layer were $a = 0.4953$ nm, $b = 0.5798$ nm and $c = 0.5362$ nm. They are very close to the lattice constants ($a = 0.4960$ nm, $b = 0.5800$ nm, $c = 0.5359$ nm) of polycrystalline MnF_2 measured in [5]. The structural $\alpha-PbO_2$ type, like the rutile one, possesses the octahedral coordination of each Mn ion with fluorine, though the octahedron positions in the rutile and $\alpha-PbO_2$ structures are quite different. The octahedra are arranged into linear chains in the former case and into zigzag chain pattern in the latter chain [12]. The X-ray data analysis shows the following epitaxial relations: $(111)_{Si} \| (111)_{MnF_2}$, and $[2\overline{1}\overline{1}]_{Si} \| [2\overline{1}\overline{1}]_{MnF_2}$. Since conjugation of the low-symmetry ($\alpha-PbO_2$) MnF_2 phase with

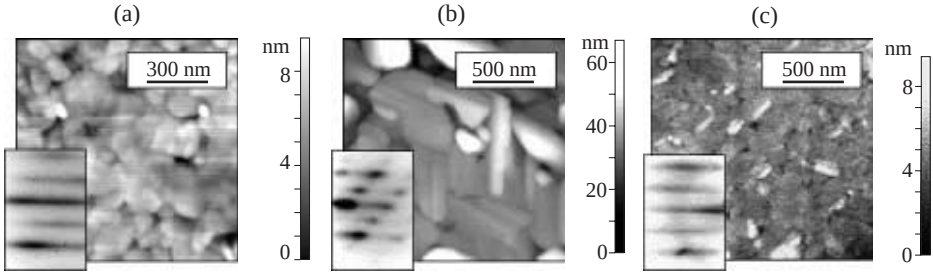

Fig. 1. AFM images and RHEED patterns (insets) of MnF_2 layers grown on Si(111) with CaF_2 buffer layer: (a) 30 nm, 20°C, RA at 550°C; (b) 85 nm, 400°C; (c) 25 nm, RA at 550°C.

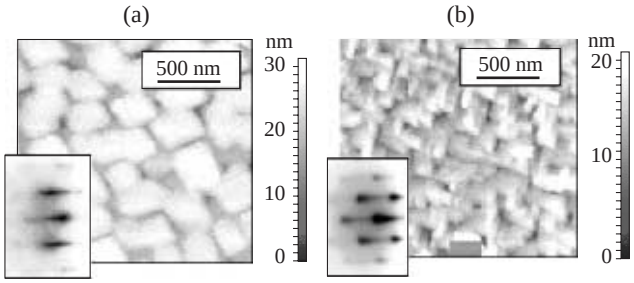

Fig. 2. AFM images and RHEED patterns (insets) of (a) 100 ml CdF_2 buffer layer on GaP(001); (b) 100 ml MnF_2, 300°C.

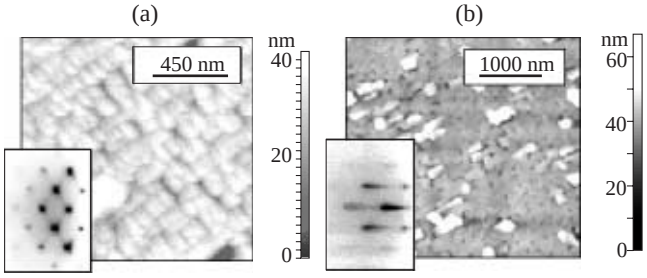

Fig. 3. AFM images and RHEED patterns (insets) of (a) 180 nm CaF_2 buffer layer on Si(001); (b) 100 nm MnF_2, 300°C, RA at 580°C.

the Si substrate takes place along high (3 m) symmetry (111) surface, it is not unexpected that the layer is formed by 120°-domains observed in the topographic images of the surface (Fig. 1(b)).

The growth of MnF_2 epitaxial films has also been studied on Si(001) and GaP(001) substrates. A smooth 100 monolayer epitaxial layer was obtained by room temperature MnF_2 deposition on a thin CaF_2 wetting layer on Si(001) [13], followed by a rapid thermal annealing at 700°C. Three well-pronounced diffraction orders of $MnF_2(010)$ ($b = 0.580$ nm) could be seen in the $\theta - 2\theta$ curve taken from this structure in the symmetrical geometry. These peaks correspond to 020, 040 and 060 reflections in the $\alpha-PbO_2$ structure. Thus, the [010] direction in this film was parallel to the Si[001]. A similar epitaxial relation was found for the film grown on GaP(001) with a CdF_2 buffer layer having a large area of atomically flat (001) surface (Fig. 2(a)).

A RHEED pattern taken from the MnF_2 film grown on such a buffer is shown in the inset to Fig. 2(b). X-ray diffractometry shows that the film was mainly monocrystalline with interlayer spacing $d = 0.291$ nm. One could see (Fig. 2(b)) well-pronounced orthogonal elongated crystallites on the film, which was not unexpected for orthorhombic structure of the layer. The growth of MnF_2 layers on a relatively thick CaF_2 buffer layer on Si(001) at 300–600°C provided a facetted surface. Bright spots at intersections of inclined streaks in the RHEED pattern (inset to Fig. 3(a))were due to the fluorite islands with {111} facets (Fig. 3(a)). After the beginning of the MnF_2 growth, diffused spots appeared. Further growth resulted in their elongation normal to the surface, indicating the surface flattening. Annealing of the grown structure at 580°C improved its crystallinity and planarity

(Fig. 3(b)). The X-ray diffraction $\theta - 2\theta$ curve taken from this film showed only 200 and 400 reflections of the orthorhombic structure. This indicates that the [100] film direction was aligned with the [001] substrate direction.

4. Summary

Epitaxial MnF_2 films as thick as 350 nm have been grown on Si and GaP substrates. X-ray diffractometry revealed that the MnF_2 films have the $\alpha-PbO_2$-type orthorhombic structure with the lattice parameters $a = 0.4953$ nm, $b = 0.5798$ nm, $c = 0.5362$ nm. It was found that the films grown on Si(111) have $(111)_{Si} \| [2\overline{11}]_{MnF_2}$ and $[2\overline{11}]_{Si} \| [2\overline{11}]_{MnF_2}$ orientations. These epitaxial relations agree with three crystallite orientations observed by AFM. Manganese fluoride films grown on Si(001) had the same orthorhombic structure, however $[010]_{MnF_2}$ or $[100]_{MnF_2}$ were directed along the surface normal, depending on the surface morphology of the buffer layer. Optical and magnetic measurements of the MnF_2 layers are underway.

Acknowledgements

This work was supported by grants of Russian Ministry of Sciences (No 99-2043) and Swiss National Science foundation (No 7SUPJ062359).

References

[1] M. N. Baibich, J. M. Broto, et al, *Phys. Rev. Lett.* **61**, 2472 (1988).
[2] B. Dieny, V. S. Speriosu, S. S. P. Parkin, et al, *Phys. Rev.* **B43**, 1297 (1991).
[3] J. Nogues, Ivan K. Schuller, *J. Magn. Magn. Mat.* **192**, 203 (1999).
[4] L. M. Lityagina, M. F. Kachan, S. S. Kabalkina and L. F. Vereshchagin, *Dokl. Chem. Proc. Acad. Sci. USSR* **214/219**, 424 (1974).
[5] L. M. Azzaria and Frank Dachille, *J. Phys. Chem.* **65**, 889 (1961).
[6] N. L. Yakovlev, A. G. Banshchikov, M. M. Moisseeva, N. S. Sokolov, J. L. Beeby and P. A. Maksym, *Surf. & Interf. Analysis* **28**, 264 (1999).
[7] O. V. Anisimov, A. G. Banshchikov, A. V. Krupin, M. M. Moisseeva, N. S. Sokolov, et al., *Probe Microscopy-2000* Niznii Novgorod **70** (2000).
[8] A. Ishizaka and Y. Shiraki, *J. Electrochem. Soc.* **133**, 666 (1986).
[9] O. V. Anisimov, A. G. Banshchikov, A. V. Krupin, M. M. Moisseeva, N. S. Sokolov, V. P. Ulin and N. L. Yakovlev, *Thin Solid Films* **367**, 199 (2000).
[10] A. I. Zaslavskii, Yu. D. Kondrashov and S. S. Tolkachev, *Dokl. Akad. Nauk SSSR* **75**, 559 (1950).
[11] L. F. Vereshchagin, S. S. Kabalkina and A. A. Kotilevets, *Sov. Phys.-JETP* **22**, (1965).
[12] S. S. Kabalkina and S. V. Popova, *Sov. Phys.-Dokl.* **8**, 1141 (1963).
[13] N. S. Sokolov and S. M. Suturin, *Appl. Surf. Sci.* (2001).

9th Int. Symp. "Nanostructures: Physics and Technology"
St Petersburg, Russia, June 18–22, 2001

Pulsed ion-beam synthesis of β-$FeSi_2$ layers on Si implanted by Fe^+ ions

R. I. Batalov†, R. M. Bayazitov†, I. B. Khaibullin†, E. I. Terukov‡
and *V. Kh. Kudoyarova*‡
† Kazan Physical-Technical Institute of RAS,
Sibirsky trakt 10/7, 420029 Kazan, Russia
‡ Ioffe Physico-Technical Institute, St Petersburg, Russia

Abstract. Synthesis of β-$FeSi_2$ layers on Si was performed by high-dose Fe^+ implantation in Si at 300 K with subsequent pulsed ion treatment (PIT) on implanted layers by powerful ion beams (PIB) of nanosecond duration. It was shown that the layer consists of the grains (presipitates) β-$FeSi_2$ with size approximately 30–40 nm. The results of the optical absorption indicate the formation of direct-band gap structures with an optical gap $E_g \sim 0.82-0.83$ eV. It is shown that the pulsed ion-beam synthesized sample is able to emit at the $\lambda \sim 1.56\,\mu$m up to temperature of 210 K.

Introduction

Recently the formation of Si-based structures emitting in the visible and near infrared (IR) spectral region attracts essential interest. There are two main approaches to the fabrication of structures emitting in the wavelength $\lambda \sim 1.55\,\mu$m: formation of Si:Er and β-$FeSi_2$ layers. β-disilicide is a direct-band material with an optical gap $E_g = 0.8-0.9$ eV [1]. This gap value corresponds to the optical wavelength $\lambda \sim 1.45\,\mu$m which is close to the technologically important $\lambda \sim 1.55\,\mu$m corresponding to the absorption minimum of the silica optical fibers. This fact allows one to create optoelectronic devices in the near IR region integrated in the silicon microelectronic technology.

One of the main approaches for the formation of buried layers of low-defect, emitting β-$FeSi_2$ is an ion-beam synthesis (IBS) i.e. high-dose Fe^+ implantation in Si with subsequent high-temperature and long-duration annealing ($T = 800-900^\circ$C, $t \sim 20$ h) [2, 3].

In this work an influence of pulsed ion treatment (PIT) by powerful ion beams (PIB) on the implanted Si layers in order to synthesize β-$FeSi_2$ is investigated.

1. Experimental

Single-crystalline n-type Si wafers with (100) orientation were implanted by Fe^+ ions at room temperature (RT) with energy of 40 keV and dose of $1.8\cdot10^{17}$ cm^{-2} (ion current density of 5 $\mu A/cm^2$). One part of implanted samples was subjected to PIT on a TEMP accelerator (C^+, H^+, $E = 300$ keV, $\tau = 50$ ns, $j \sim 50$ A/cm^2) and the other part was thermally annealed (TA) in N_2 ambient (800°C, 2.5 h) to compare the results.

Crystallographic structure of implanted and annealed layers was studied by glancing x-ray diffraction technique (XRD) on a diffractometer with an iron anode ($\lambda = 1.93$ A). IR spectroscopy in the reflection and transmission mode was employed to determine the band gap energy. In photoluminescence (PL) measurements optical excitation was provided by an Ar^+ laser ($\lambda = 514.5$ nm) with an average excitation power of 50 mW. PL signal was registered with a liquid nitrogen-cooled Ge photodiode (North Coast).

2. Results and discussion

X-ray characterization. After ion implantation no reflections are present in XRD pattern (not shown) indicating that complete amorphization of the implanted layer takes place. Figure 1 shows XRD patterns of the samples subjected to various treatment regimes after ion implantation. From Fig. 1(a) one can see that after PIT mixing of two phases takes place: the metallic FeSi and semiconducting β-$FeSi_2$. The most intensive peak in the spectrum belongs to the β-$FeSi_2$ phase with indistinguishable reflections (220)/(202) due to proximity of their positions.

In order to remove the lattice strain and to transform the residual amount of FeSi phase into β-$FeSi_2$ a short-time TA (800°C, 20 min) in N_2 atmosphere was performed. XRD pattern after additional TA is shown in Fig. 1(b). From this figure one can see the essential increase of (220)/(202) β-$FeSi_2$ peak intensity. In the inset of Fig. 1(b) is shown an azimuth dependence of (220) peak indicating the presence of the [110] texture in the silicide layer. To compare results Fig. 1(c) shows the XRD pattern of the implanted sample after long-time TA (800°C, 2.5 h). In this case the formation of β-$FeSi_2$ with unstrained lattice and [110] texture (inset of Fig. 1(c)) The XRD patterns were evaluated by using the MAUD program. It was obtained that these layers consist of the grains (presipitates) with the size 30–40 nm.

Optical characterization. Since the dependence of the absorption coefficient (α) on the photon energy (E) for the direct interband transitions it is given by [4]: $\alpha = A(E - E_g)^{1/2}$, where A is a constant that is associated with specific features of the band structure and E_g is the magnitude of the direct band gap, then drawing up the dependence of the absorption exponent $(\alpha d)^2$ on E (d is the silicide thickness) according to the equation $\alpha d = \ln(1 - R)/T$, one can determine the E_g value extrapolating the straight line up to the intersection with the E axis (Fig. 2). E_g values (~0.82 eV for the sample only after

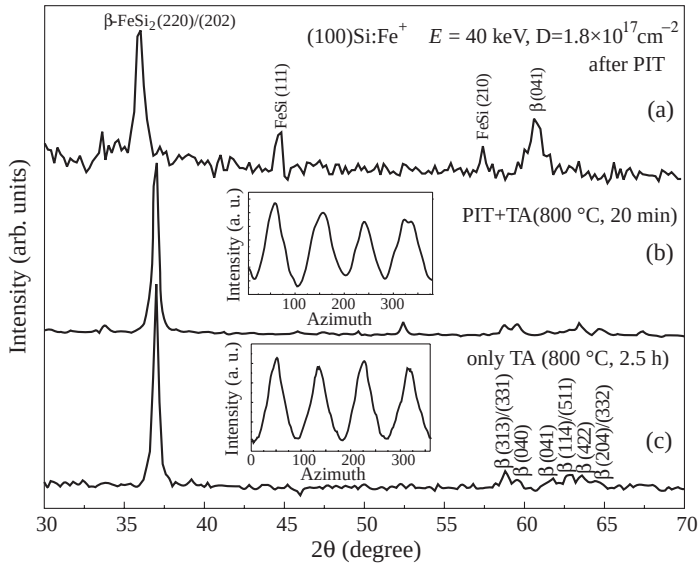

Fig. 1. XRD patterns of the implanted sample ($E = 40$ keV, $D = 1.8 \times 10^{17}$ Fe^+/cm^{-2}) after PIT (C^+, H^+, $E = 300$ keV, $\tau = 50$ ns, $j \sim 50$ A/cm^2) (a), after PIT with additional TA (800°C, 20 min) (b), only after TA (800°C, 2.5 h) (c). In the insets are shown an azimuth dependencies of β-$FeSi_2$ (220)/(202) peak intensity.

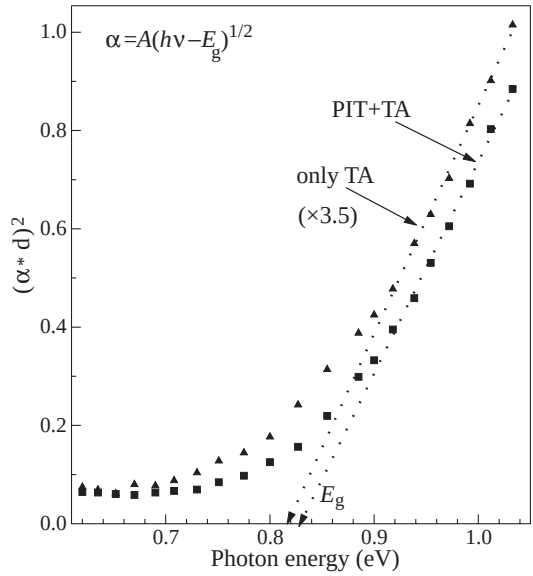

Fig. 2. Square of absorption exponent vs photon energy for the implanted sample after PIT with short-time TA and only after long-time TA.

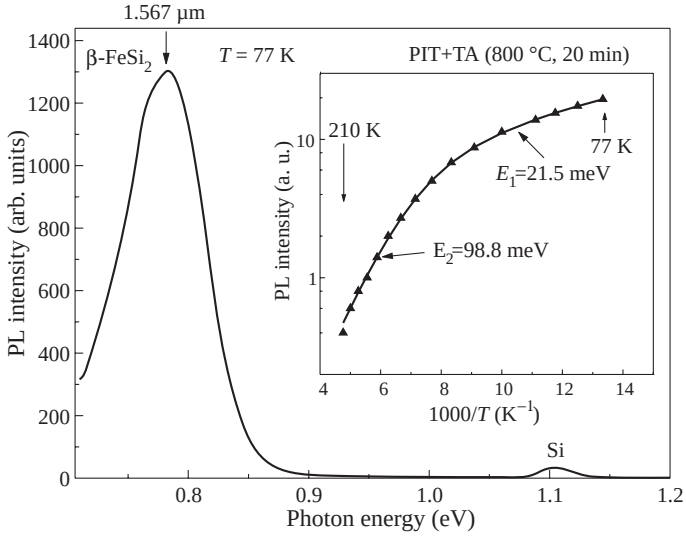

Fig. 3. PL spectra of the implanted sample after PIT with short-time TA. Inset shows a temperature dependence of PL intensity (solid circles) and the theoretical data fitting by Eq. (1).

TA and ∼0.83 eV after PIT and TA) correspond to the E_g values of β-$FeSi_2$ given in the literature [3].

Figure 3 shows the PL spectrum measured at 77 K in the implanted sample after PIT and additional TA (800°C, 20 min). One can see two emission bands corresponding to the PL signal from the Si substrate ($E \sim 1.10$ eV) and from β-$FeSi_2$ ($E \sim 0.785$ eV - $\lambda \sim 1.567\,\mu$m). The PL signal is observed up to $T = 210$ K by about 40–50 K exceeding

the maximum temperature which is reached by other authors on the samples prepared by the traditional IBS method [3]. In the inset of Fig. 3 the temperature dependence of the PL intensity of the sample after PIT and TA is shown. The equation describing a PL quenching curve has a two-exponential form [5]:

$$I(T) = \frac{I_0}{1 + C_1 \exp[-(E_1/kT)] + C_2 \exp[-(E_2/kT)]}, \quad (1)$$

where I_0 is the saturated PL intensity at very low temperature, C_1 and C_2 are the coupling coefficients, E_1 and E_2 are the thermal annealing energies. E_1 and E_2 are values at which Eq. (1) most satisfactorily describes the experimental data and they were determined to be 21.5 and 98.8 meV, respectively.

The origin of the PL signal is one of the problems associated with the light emission in the region of $\lambda \sim 1.55\,\mu$m. It is known that when a dislocation network and β-$FeSi_2$ phase are simultaneously present in a sample it is necessary to disentangle the contribution of β-$FeSi_2$ and dislocations to the $1.55\,\mu$m luminescence [6]. Thermal quenching energy values for the registered PL signal differ from those for the D1 dislocation center ($\sim 7-12$ meV) [7] whose energetic position ($E \sim 0.81$ eV) is very close to the PL maximum position ($E \sim 0.785$ eV). Because of this we conclude that the origin of the PL signal at the $\lambda \sim 1.56\,\mu$m is not connected with the dislocation-related emission and is caused due to the direct interband transitions in a β-$FeSi_2$ optical gap.

3. Conclusions

We have shown that the PIT of Fe^+-implanted layer leads to the mixing of two phases (FeSi and β-$FeSi_2$) with a strained state of the crystal lattice. Subsequent short-time TA (800°C, 20 min) results in the complete transformation of FeSi phase into β-$FeSi_2$ with the production of a highly textured layer. It was shown that these layers consist of the grains with size 30–40 nm. The results of the optical absorption indicate the formation of direct-band gap structures with an optical gap $E_g \sim 0.82-0.83$ eV in both cases. It is shown that the pulsed ion-beam synthesized sample is able to emit at the $\lambda \sim 1.56\,\mu$m up to temperature of 210 K. From the results of PL signal temperature dependence the light emission at the $\lambda \sim 1.56\,\mu$m was attributed to the direct interband transitions in the β-$FeSi_2$ optical gap with thermal quenching energies of 21.5 and 98.8 meV.

The result demonstrates the potential of β-$FeSi_2$ as an important candidate for a silicon-based optoelectronic technology.

Acknowledgments. This work was supported by NIOKR Foundation of Tatarstan Republic, Russian Federation (grant No 16-03). The authors would like to thank V. A. Shustov for his experimental support in X-ray measurements.

References

[1] C. A. Dimitriadis, J. H. Werner, S. Logothetidis et al., *J. Appl. Phys.* **68**, 1726 (1990).
[2] Z. Yang, K. P. Homewood, M. S. Finney, et al., *J. Appl. Phys.* **78**, 1958 (1995).
[3] H. Katsumata, Y. Makita, N. Kobayashi et al., *J. Appl. Phys.* **80**, 5955 (1996).
[4] J. J. Pankov, *Optical Process in Semiconductors* (Dover, New York, 1971), p. 34
[5] F. Priolo and G. Franzo, *J. Appl. Phys.* **78**, 3874 (1995).
[6] N. A. Drozdov and A. A. Patrin, *Pisma Zh. Eksp. Teor. Fiz.* **23**, 651 (1976).
[7] M. Suezawa and Y. Sasaki, *Phys. Status Solidi* **A79**, 173 (1983).

9th Int. Symp. "Nanostructures: Physics and Technology"
St Petersburg, Russia, June 18–22, 2001

Schwoebel barrires as the reason for 3D-island formation during heteroepitaxy

D. V. Brunev, I. G. Neizvestny, *N. L. Shwartz* and Z. Sh. Yanovitskaya
Institute of Semiconductor Physics, RAS SB,
13 pr. Lavrenteva, Novosibirsk, 630090, Russia

Abstract. Self-assembled 3D-islands formation during heteroepitaxial growth was investigated by Monte Carlo simulation. Shwoebel barriers for explanation of 3D growth kinetic were suggested. Island size equalization during growth process was observed. Necessity of atomic flux from island edge to the upper layers for 3D island formation was demonstrated.

Heteroepitaxial growth have been utilized for the generation of strongly strained coherent 3D islands, named quantum dots (QDs) [1, 2]. The elastic energy of the initially planar strained layer increases during heteroepitaxial growth. The system can lower its free energy by atom transitions from the island edge to the upper layer as that leads to decrease of contact area between substrate and new layer [1, 3–6]. Kinetic of such process could be described taking into consideration diffusion peculiarities when an atom crosses island edges. Additional energy barriers for atoms crossing monoatomic step (Schwoebel barriers) are suggested to be responsible for QD formation [7, 8]. Kinetic problems of epitaxial growth with Shwoebel barriers were considered theoretically in [9]. Increase of nucleation rate of islands in the second monolayer was associated in [10] with asymmetry of Schwoebel barriers in SiGe system.

Introduction of additional energy barriers E_{st} for atom hops over monoatomic steps in the model enable us to investigate Schwoebel barriers influence on surface relief formation during epitaxy [11]. Diffusion hop probability to cross the step is changed by the factor $P = exp(-E_{st}/kT)$ as compared with diffusion hops at the same atomic level. Factor P_{up} changes probability of atom hops to the upper layers, and P_{down} — to the lower ones. Phase diagram in coordinates $P_{\text{up}} - P_{\text{down}}$ is presented in Fig. 1(a). Shaded area — Stransky-Krastanov growth mode – separates layer-by-layer regime (2D) from 3D-island growth

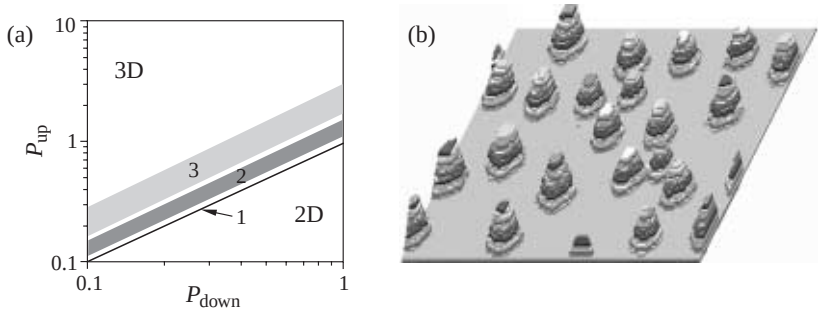

Fig. 1. (a) Phase diagram indicating conditions for 3D islands formation, shaded area — Stransky–Krastanov growth mode, 1 — line $P_{\text{up}} = P_{\text{down}}$, 2 — $\lambda = 40$ a.s., 3 — $\lambda = 20$ a.s.; (b) simulated surface after 1.5 ML deposition, $\lambda = 20$ a.s., $\chi = 10$.

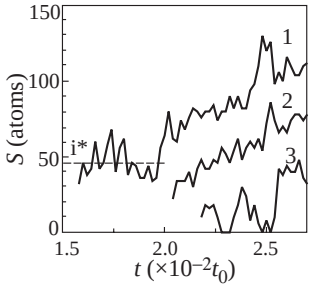

Fig. 2. Number of atoms in three successive atomic layers of 3D island formed at $\lambda = 40$ a.s. versus time for $\chi = 2$ (figure at the curve corresponds to atomic layer number), i^* — critical (2D) nucleus size (CNS).

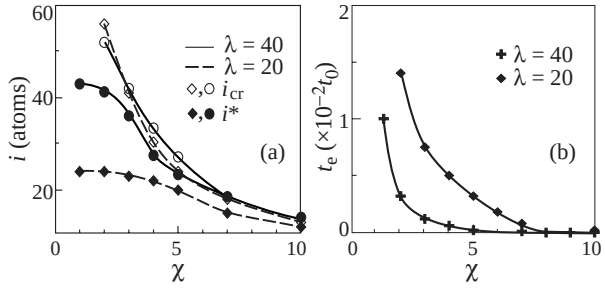

Fig. 3. (a) CNS dependence on χ; (b) expectation time t_e for appearance of the nucleus of the second monolaeyr on 2D islands versus χ.

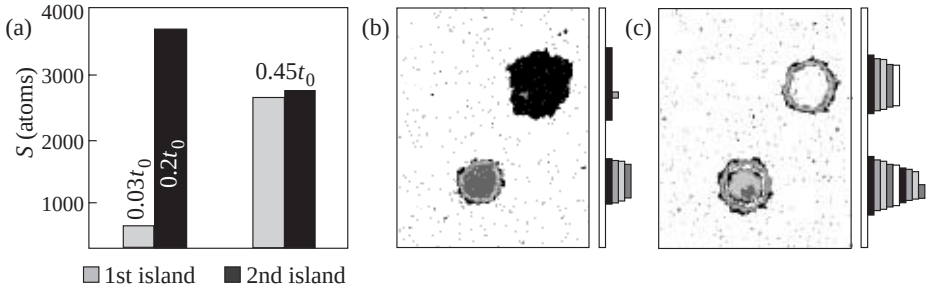

Fig. 4. Islands self-organization during growth process, $\lambda = 40$ a.s.: (a) histogram of size redistribution of two islands with time, left columns correspond to the moments of the second layer nucleus creation on 2D islands; top view of model surface (200×250 a.s.) after deposition 0.2 ML (b) and 0.45 ML (c), to the right of each surface — its profile (b-c).

mode. Shaded area is parallel to the line $P_{\text{up}} = P_{\text{down}}$ which is to say that the change-over from 2D to 3D mode (2D $\longrightarrow$ 3D) is determined only by the parameter $\chi = P_{\text{up}}/P_{\text{down}}$ and not by the absolute values P_{up}, P_{down}. Notice that for 3D island formation without wetting layer condition $\chi > 1$ is necessary. Increasing of migration adatom length $\lambda(D/V)$, (D — surface diffusion coefficient, V — deposition rate) leads to parallel shift of transition 2D $\longrightarrow$ 3D to the lower values P_{up}, under condition $\chi > 1$. Figure 1(b) represents the model surface with 3D islands.

Number of atoms in three successive atomic layers of 3D island formed on (100) surface at $\lambda = 40$ atomic sites (a.s.) versus time is shown in Fig. 2. Fig. 2 demonstrates stable 2D-island formation till 3D island growth starts. Size of this 2D island fluctuates about average value i^*, that is equal to critical nucleus size (CNS). Large CNS corresponds to active exchange between islands and equilibrium adatom gas due to small binding energy between neighboring atoms. For equilibrium conditions following relationship was obtained $i^* \sim (D/V)^{1/5}$ that means slight increase of i^* with λ increase. As one can see in Fig. 2 CNS decreases in each next atomic layer.

The critical size of island i_{cr} when nucleation of new layer starts is of interest. Dependence $i_{cr}(\chi)$ was investigated. Dependencies i^* and i_{cr} on χ for two λ are presented in

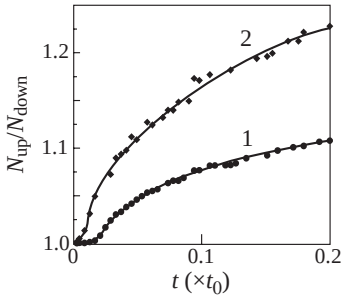

Fig. 5. $N_{\rm up}/N_{\rm down}$ (ratio of absolute number of hops to the upper layers to hops to the lower layers) dependence on time; $\lambda = 40$ a.s., $1 - \chi = 2$, $2 - \chi = 10$.

Fig. 3(a). As χ increases these sizes decrease approaching 1 for $\chi \longrightarrow \infty$. From some χ, $i^* = i_{cr}$, that means 3D nucleation from the initial phase of growth. Expectation time t_e for appearance of the nucleus of the second monolaeyr on 2D islands versus χ is represented in Fig. 3(b). This dependence is exponential one: $t_e(\chi) = \tau_0 \cdot \exp(-\alpha \cdot \chi)$. For $\lambda = 40$ a.s. — $\tau_0 = 0.017 \cdot t_0$, $\alpha = 0.8$, and for $\lambda = 20$ a.s. — $\tau_0 = 0.035 \cdot t_0$, $\alpha = 0.5$, where t_0 – time necessary of one monolayer deposition.

3D islands without wetting layer demonstrate rather sharp size distribution. That is due not only to the most synchronous 2D island nucleation in the first atomic layer. Lateral size equalization when 3D growth process starts (case of large size fluctuation of initial 2D-islands) could be seen in Fig. 4. Figure 5 demonstrate increase with time of hops up to hops down ratio $N_{\rm up}/N_{\rm down}$. Such $N_{\rm up}/N_{\rm down}$ variation is due to decrease of atoms capable to attach into descending island boundary because of their attachment to the island of upper layer.

Acknowledgements

This work were supported by the Russian Foundation for Basic Research (No. 99-02-16742) and the Federal Target-Orientated Programs “Prospective technologies and structures for micro- and nanoelectronic” and “Surface Atomic Structures”.

References

[1] V. A. Shchukin and D. Bimberg, *Rev. Modern Phys.* **71**, 1125 (1999).
[2] N. N. Ledentsov, V. M. Ustinov, V. A. Shchukin, P. S. Kopev, J. I. Alferov and D. Bimberg, *FTP* **32**, 385 (1998) (in russian).
[3] R. Kern and P. Muller, *Surf. Sci.* **392**, 103 (1997).
[4] S. A. Chaparro, Y. Zhang, J. Drucker, D. Chandrasekhar and D. J. Smith, *J. Appl. Phys.* **87**, 2245 (2000).
[5] S. A. Chaparro, Y. Zhang and J. Drucker, *Appl. Phys. Lett.* **76**, 3534 (2000).
[6] P. Sutter and M. G. Lagally, *Phys. Rev. Lett.* **84**, 4637 (2000).
[7] Th. Wiebach, M. Schmidbauer, M. Hanke, H. Raidt, R. Kohler and H. Wawra, *Phys. Rev. B* **61**, 5571 (2000).
[8] J. Rottler and P. Maass, *Phys. Rev. Lett.* **83**, 3490 (1999).
[9] V. I. Trofimov and V. G. Mokerov. *DAN* **367**, 749 (1999) (in russian).
[10] M. Kummer, B. Vogeli, T. Meyer and H. Kanel, *Phys. Rev. Lett.* **84**, 107 (2000).
[11] I. G. Neizvestny, L. N. Safronov, N. L. Shwartz, Z. Sh. Yanovitskaya and A. V. Zverev, *Proc. 8^{th} Int. Symposium Nanostructures: Physics and technology* (St.Peterburg, Russia, June 19-23) 2000, P. 129.

9th Int. Symp. "Nanostructures: Physics and Technology"
St Petersburg, Russia, June 18–22, 2001

Effect of growth conditions on optical properties of Ge submonolayer nanoiclusions in a Si matrix grown by molecular beam epitaxy

G. E. Cirlin†‡§, *V. A. Egorov*†‡, B. V. Volovik‡,
A. F. Tsatsul'nikov‡, V. M. Ustinov‡, N. N. Ledentsov‡,
N. D. Zakharov§, P. Werner§ and U. Gösele§
† Institute for Analytical Instrumentation RAS,
Rizhsky 26, 198103, St Petersburg, Russia
‡ Ioffe Physico-Technical Institute, St Petersburg, Russia
§ Max-Planck-Institut für Mikrostrukturphysik, Halle/Saale, Germany

Abstract. Optical properties of the Ge submonolayer (SML) nanoinclusions in a Si matrix grown by molecular beam epitaxy (MBE) are investigated. It is shown that at relatively high growth temperatures ($> 600^{\circ}$C) there are new features appear in a PL spectra. These features correspond to formation of the germanium nanoobjects in a silicon media.

Introduction

Nowadays silicon is the base material in a microelectronics market but it is hardly applicable in optoelectronics due to its indirect band gap nature. Nevertheless, the integration on-the-same-wafer of the well-developed silicon microelectronics technology with optical devices is one of the most actual task which attracts significant efforts. There are proposed several approaches to realise silicon–based light-emission (SBLE) devices: using of porous silicon [1], using of Ge/Si and GeSiC/Si quantum dots fabricated by MBE [2], rare-earth doping of silicon [3], insertion of InAs nanoiclusions in a Si matrix [4], etc. Despite of progress in this area these approaches doesn't find industrial applications, yet. This point stimulates us to find out other ways allowing to get SBLE. In this paper we propose to insert Ge SML in a Si matrix and investigate optical properties of these heterostructures. Our approach is based on the following assumption: Ge submonolayers may lead to the formation of the ensemble of relatively small islands (with lateral sizes less than hole Bohr radius). This can result in a partial lifting of the selection rule for radiative recombination and possibility of exciton formation (which may be stable up to room temperature) via electron and localised–hole interaction. This situation is possible if Coulomb attraction energy will be higher to localise electrons near potential barrier which is produced by Ge SML inclusions in the conductivity band. In the case of relatively large sizes of quantum dots or large widths of quantum wells this barrier also may lead to spatial separation of the electrons and holes [5]. Furthermore, for the SML in other heteroepitaxial systems [6, 7] narrow PL line leads to the increasing of the absorption (gain). The PL intensity will increase if multiple vertical stacking of the layers with Ge SML separated by Si spacers is used. Due to relatively small strain accumulation in such system a low probability of dislocations and structural defects formation is expected.

Experiment

All structures are grown by molecular beam epitaxy using Riber SIVA 45 setup on a Si(100) n–type substrates (conductivity 3 $\Omega \cdot$ cm). Substrates are 5 inches in a diameter manufactured by OKMETIC. After chemical preparation by the method described in [13]

the substrates are transferred in the MBE setup loading chamber. This method of preparation allows to remove oxide layer from silicon surface at 840°C in the growth chamber by direct radiating heating. During the growth process the rotation of the samples is used, temperature field inhomogenity across the surface is about $\sim$ 5%. In order to grow Ge SML we use submonolayer epitaxy technique, which we also used to grow SML insertions in A^3B^5 and A^2B^6 systems [8, 9, 10].

Structures consist of Si 1000 Å buffer layer, Ge(0.7–1.3 Å)/Si(44 Å) superlattice (20 pairs) and silicon 200 Å capping layer. Growth rates for Si and Ge are 0.5 Å/s and 0.05 Å/s, respectively. The growth rates is controlled by 2 mass-spectrometers with feedback which are set to 28 (Si) and 74 (Ge) masses. The substrate temperatures are varied from 600°C to 750°C. Total pressure during growth is better than $5 \cdot 10^{-9}$ Torr. Surface is monitored *in situ* by the reflection high–energy electron diffraction (RHEED).

Photoluminescence (PL) is excited by an Ar^+–laser ($\lambda = 514.5$ nm, maximal excitation density is $\sim$ 500W/cm^2). PL is detected by Ge cooled photodiode. During the growth process the RHEED patterns show independent behaviour on the growth temperature in comparison with initial surface reconstruction (2×2). Thus, even on the upper layers of the superlattice the surface remains atomically smooth and 3D–structure formation due to strain relaxation doesn't occur.

Results and discussion

As it was shown in [13] there is a new set of PL lines appear if the structure with SML Ge inclusions (structure consisted of 99 pairs of 0.7 Å Ge SML separated with 35 Å Si spacers) was grown at relatively high temperature (> 750°C). These PL lines exist both at high and low levels of excitation density and correspond to emission from excitons localised at germanium islands in the SML superlattice. We have found that there are no such lines (marked in following as SL lines) in PL spectra if the growth temperature is below 600°C and above $\sim$ 800°C (due to effective silicon and germanium intermixing and formation of the solid solution). Increase in growth temperature leads to narrowing of SL PL line. A maximal PL intensity from SL is observed for the substrate temperature of 650°C (for active region) at other equal growth conditions.

For the set of the samples investigated in a frame of this work we have found that integral intensity ratio between SL–TO line and Si–TO line critically depends on the excitation density. In Fig. 1(a) are shown PL spectra taken at different excitation density for the sample with 20 layers of 1 ML of Ge separated by 44 Å Si spacers (growth temperature for the active region is 750°C). There is steady increasing of the integral intensity ratio of Si–TO/SL–TO lines with the increasing of excitation density, but even at very high excitation levels the integral intensity ratio of these lines is comparable. At low excitation levels SL–TO line dominates in spectra. Full width at half maximum is about 15 meV. There is SL–TO line shifting towards long–wavelengths with the increasing of the excitation density.

In Fig. 1(b) are shown PL spectra for the same sample taken at different temperatures and constant excitation density of $\sim$ 500 W/cm^2. There is significant intensity decreasing of the SL–TO line, which accompanies with blueshifting. Opposite situation (large redshift in compare with shift of band PL) was observed, for example, in InAs/GaAs heteroepitaxial system [12] and it is explained by both bandgap shifting and evaporation of carriers from small QDs having lower localization energy. In our case the observed phenomena cannot be explained in a frame of this simple model. and, indeed, is due to occupation of excited states on the islands with increase in temperature or redistribution of carriers between islands having different sizes.

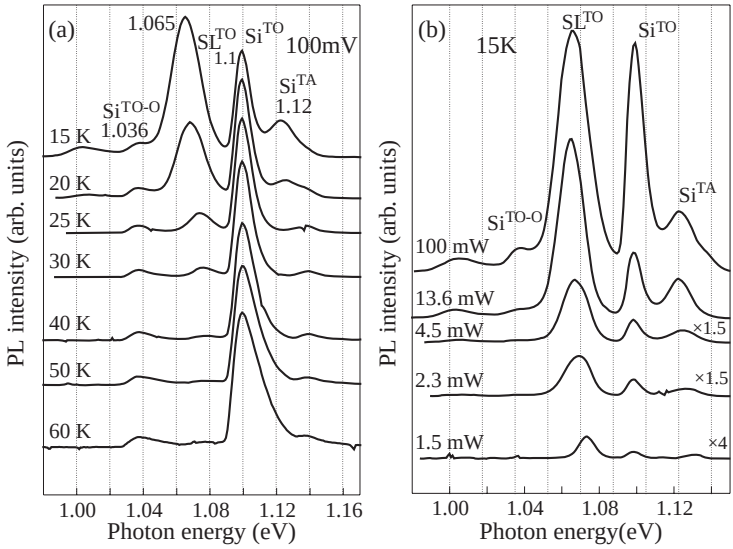

Fig. 1. PL spectra for the Ge/Si SML structure grown at 750°C taken at (a) different temperature and (b) different excitation density.

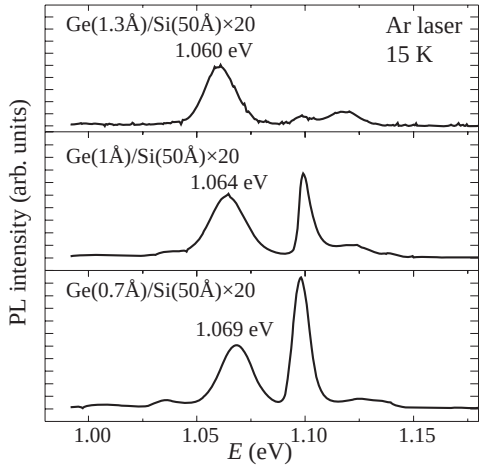

Fig. 2. Effect of the influence of Ge amount in each layer on PL peak position.

The SL–TO line exhibits shift towards long-wavelengths with increasing of the quantity of Ge in each layer of the SL. In Fig. 2 are shown PL spectra for the samples with 0.7 Å, 1.0 Å and 1.3 Å of Ge in each layer of the SL. This shift is explained by the increasing of the Ge islands lateral sizes. However, if Ge nanoislands become higher in size than the respective hole Bohr radius then holes delocalise in direction perpendicular to the growth direction and efficiency of corresponding lines in the PL spectra can be decreased. High-resolution transmission electron microscopy study shows that for the case of lower germanium amount deposited there are well pronounced Ge nanoinclusions with 7 nm in lateral size and 3.5 nm in height clearly seen [14]. For higher Ge amount (1 ML) single monolayer of Ge is observed.

In conclusion, we have investigated optical properties of the Ge SML nanoinclusions

in a Si matrix. We have shown that under certain growth conditions there are new lines in the PL spectra appear. These lines correspond to formation of the Ge nanoislands with sizes lower than respective hole Bohr radius. If their sizes are higher there are no such PL lines. The investigated system may be considered as the one the possible way for the SBLE devices creating.

Acknowledgement

This work is partially supported by DFG.

References

[1] A. G. Cullis, L. T. Canham and P. D. J. Calcott, *J. Appl. Phys.* **82**, 909 (1997).

[2] K. Eberl, K. Brunner and W. Winter, *Thin Solid Films* **294**, 98 (1997).

[3] S. Coffa, G. Franzo and F. Priolo, *MRS Bulletin* **23(4)**, 25 (1998).

[4] G. E. Cirlin *et al*., *Semicond. Sci. Technol.* **13**, 1262 (1998).

[5] N. N. Ledentsov, J. Bohrer, M. Beer, F. Heinrichsdorff, M. Grundmann, D. Bimberg, S. V. Ivanov, B. Ya. Meltser, I. N. Yassievich, N. N. Faleev, P. S. Kop'ev and Zh. I. Alferov, *Phys. Rev. B* **52**, 14058 (1995).

[6] N. N. Ledentsov, I. L. Krestnikov, M. V. Maximov, S. V. Ivanov, S. L. Sorokin, P. S. Kop'ev, Zh. I. Alferov, D. Bimberg and C. M. Sotomayor Torres, *Appl. Phys. Lett.* **69**, 1343 (1996).

[7] M. V. Belousov, N. N. Ledentsov, M. V. Maximov, P. D. Wang, I. N. Yassievich, N. N. Faleev, I. A. Kozin, V. M. Ustinov, P. S. Kop'ev and Zh. I. Alferov, *Phys. Rev. B* **51**, 14346 (1995).

[8] P. D. Wang, N. N. Ledentsov, C. M. Sotomayor Torres, P. S. Kop'ev and V. M. Ustinov, *Appl. Phys. Lett.*, **64**, 1526 (1994).

[9] G. E. Cirlin, A. O. Golubok, S. Ya. Tipissev, N. N. Ledenstov and G. M. Guryanov, *Phys. Tekn. Poluprovodn.* **29**, 1697 (1995).

[10] G. E. Cirlin, V. N. Petrov, A. O. Golubok, S. Ya. Tipissev, V. G. Dubrovskii, G. M. Guryanov, N. N. Ledentsov and D. Bimberg, *Surf. Sci.* **377–379**, 895 (1997).

[11] H. Sunamara, N. Usami, Y. Shiraki and S. Fukatsu, *Appl. Phys. Lett.* **68**, 1847 (1996).

[12] R. Heitz, N. N. Ledentsov, D. Bimberg, A. Yu. Egorov, M. V. Maximov, V. M. Ustinov, A. E. Zhukov, Zh. I. Alferov, G. E. Cirlin, I. P. Soshnikov, N. D. Zakharov, P. Werner and U. Gösele, *Appl. Phys. Lett.* **74**, 1701 (1999).

[13] G. E. Cirlin,P. Werner, U. Gösele, B. V. Volovik, V. M. Ustinov and N. N. Ledentsov, *Tech. Phys. Lett.* **27**, 14 (2001).

[14] N. D. Zakharov *et al*., this volume, p. 21.

9th Int. Symp. "Nanostructures: Physics and Technology"
St Petersburg, Russia, June 18–22, 2001

Interface reconstruction in GaAs/AlAs ultrathin superlattices grown on (311) and (001) surfaces

M. D. Efremov†, V. A. Volodin†, V. A. Sachcov‡, V. V. Preobrazhenski†, B. R. Semyagin†, V. V. Bolotov‡, E. A. Galaktionov§ and A. V. Kretinin§
† Institute of Semiconductor Physics SB RAS,
pr. Lavrentjeva 13, Novosibirsk 630090, Russia
‡ Institute of Sensor Microelectronics SB RAS, pr.Mira 55a, Omsk 644077, Russia
§ Novosibirsk State University, 630090, Pirogova 2, Novosibirsk, Russia

$A^{III}B^{V}$ semiconductor superlattices (SLs) are widely used for electronic and optoelectronics devices. The properties of the SLs depend on the interface structure. For atomic scale studies of the interfaces and the quantum objects the scanning tunnelling microscopy (STM) and high resolution electronic microscopy (HREM) are usually used. Raman spectroscopy is non-destructive technique for studies of the SLs [1]. In recent time the SLs grown on not only traditional (001), but on high-index surfaces are widely studied [2]. One of the interesting problem is how the surface reconstruction affects on atomic structures of the quantum objects. For instance, in some growth conditions, the GaAs (001) surface appeared to be (2×4) reconstructed [3], and (311)A surface appeared to be corrugated [2] or (1×8) reconstructed [4]. Recently, it was observed, that after deposition of GaAs submonolayer cover on (001)-(2×4) reconstructed GaAs surface, the GaAs islands, containing 6 or less Ga dimers, are formed [5]. The $GaAs_nAlAs_m$ superlattices (SLs) grown on (311)A, (311)B and (001)-(2×4) surfaces was studied using Raman spectroscopy, $12 \geq n \geq 1$, $m = 8$ monolayers (mls) in (311) direction. The phonon spectra were studied using the Raman spectroscopy technique. The Raman spectra were registered at room temperature in quasi-backscattering geometry using the Ar laser.

The Raman spectra of SLs grown on (311)B and faceted (311)A surfaces are shown in Fig. 1(a,b). Due to symmetry selection rules, the TO_y and TO_x modes (atoms vibrate along the crystallographic directions Y and X, along and transverse to GaAs quantum wires) are observed in polarisation geometries $Z(YY)\bar{Z}$ and $Z(YX)\bar{Z}$ respectively. In Fig. 1(a), one can see the splitting of confined TO modes of first order $TO1_y$ and $TO1_x$. The splitting increases with decreasing of average thickness of GaAs layers. The Raman spectra of (311)B SLs grown in the same conditions and have the same thickness of layers as in the case of the (311)A surface are swown in Fig. 1(b). It is seen, that in this case the effect of splitting of TO modes is negligible. In the case of (311)A SLs the splitting sharply increases when the average thickness of GaAs layers is equal or less than the height of facets in one of the model of (311)A surface reconstruction (6 monolayers) [2]. This fact can be an indirect evidence of the quantum wire-like growth model [2]. And indeed, the cross section HREM data of (311)A SLs confirms this model, the modulation of GaAs and AlAs layers in (01-1) direction with period about 3.0 nm was observed [6].

The experimental Raman spectrum of GaAs/AlAs SL grown on (2×4) reconstructed surface is presented in Fig. 2. The thickness of GaAs layers was 0.6 ml, the full period was 6 mls, the SLs contains 400 periods. As one can see, peak associated with the scattering on GaAs-type localized LO phonons has distinguishable triplet structure. The observed structure of Raman spectra did not change when the probing laser beam was scanned the SL

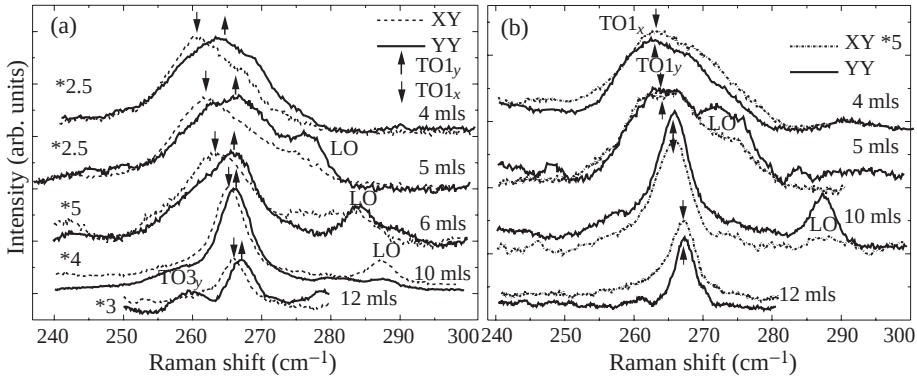

Fig. 1. Raman spectra of GaAs/AlAs SL with various thickness of GaAs layers grown on: (a) (311)A faceted surface, (b) (311)B surface.

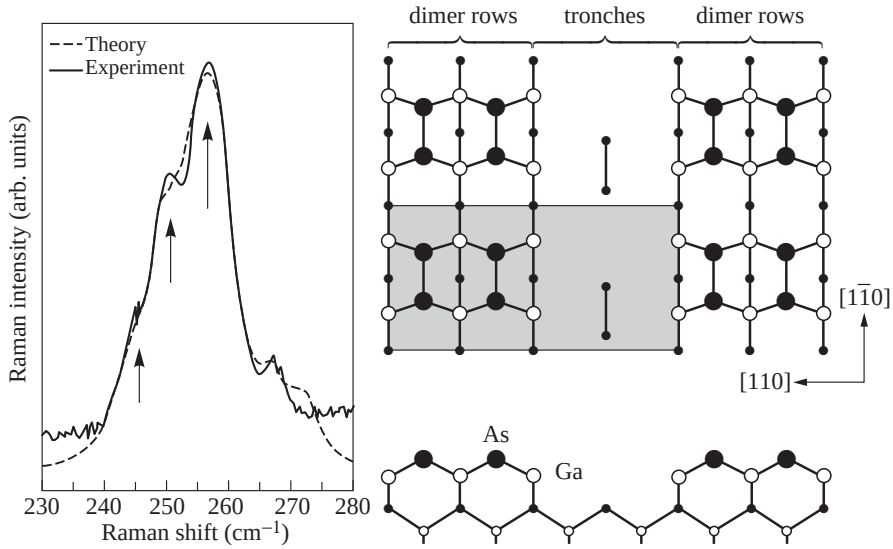

Fig. 2. The experimental ($\lambda_{exc} = 488$ nm, SL $GaAs_{0.6}/AlAs_5$) and the calculated Raman spectra of GaAs islands (left) grown on (2×4) reconstructed (001) AlAs surface [5] (right).

surface. To find the shapes of the GaAs islands formed on (001)-(2×4) reconstructed AlAs surface, the calculations of the phonon spectra of the islands of various shapes were carried out. The calculations of the phonon frequencies and the vectors of atomic displacements had been made within the Born approximation. The consideration of the long-range Coulomb interaction had been carried out in dipole approximation within model of "rigid ions". The Raman spectra were calculated using the bond polarisability model of Wolkenstein. The GaAs islands shapes were chosen on a basis of a known model of the island nucleation on (2×4) reconstructed (001) surface [5, 7]. The phonon spectra and the Raman spectra in $Z(XY)\bar{Z}$ geometry of the islands of various shapes were calculated. According to the calculations, the lateral localization of LO-like phonons in GaAs quantum islands leads to appearance of new Raman active modes. The calculations of Raman spectrum of the real $GaAs_{0.6}/AlAs_5$ SL, grown in (001)-(2×4) reconstructed surface and containing GaAs

islands, were carried out with account of scattering from GaAs islands of 10 various shapes.

The contribution of the islands with a specific shape in the total calculated Raman spectrum was determined in approximation of the theoretical spectrum to the experimental one. As one can see in Fig. 2 the calculated spectrum is in remarkable agreement with the experimental one. That is very surprising, but the average GaAs cover calculated from the contribution of the islands of all shapes is occurs to be equal to the experimental one (0.6 ML) with the very good accuracy, although this parameter was not fitted specially. According to the result of the approximation, about 70% of GaAs islands contains less than 18 Ga atoms. This result is in good correlation with the STM data [5, 7] according to which the small islands are the most stable. So, the non-destructive and informative technique for analysis of shapes of subnanometer quantum objects, using Raman spectroscopy and localized phonon spectrum calculations is developed. The lateral localization of optic phonons in GaAs quantum islands and quantum wires was observed using Raman spectroscopy. The lateral localization takes place when the GaAs islands are separated by AlAs barriers thicker than 2 interatomic dimensions.

Acknowledgements

This work is supported by the Russian Foundation for Basic Research (grant No 99-02-16668). One of the authors (V. A. Volodin) is grateful to the Scientific Council of the Institute of Semiconductor Physics SB RAS for the Stipend for Young Scientists.

References

[1] M. Cardona and G. Gunterodt, *Light Scattering in Solids V. Superlattices and Other Microstructures*, (Springer-Verlag, Berlin) 1989.
[2] R. Notzel, N. Ledentsov, K. Ploog, et. al., *Phys. Rev. B* **45**, No 7, 3507 (1992).
[3] A. R. Avery, C. M. Goringe, D. M. Holmes, J. L. Sidijono and T. S. Jones, *Phys. Rev. Lett.* **76**, No 18, 3344 (1996).
[4] L. Geelhaar, J. Marquez and K. Jacobi, *Phys. Rev. B* **60**, No 23, 15890 (1999).
[5] M. Itoh, G. R. Bell, A. R. Avery, T. S. Jones, B. A. Joyce and D. D. Vvedensky, *Phys. Rev. Lett.* **81**, No.3, 633 (1998).
[6] N. N. Ledentsov, D. Litvinov, A. Rosenauer, D. Gerthsen, I. P. Soshnikov, V. A. Shchukin, V. M. Ustinov, A. Yu. Egorov, A. E. Zukov, V. A. Volodin, M. D. Efremov, V. V. Preobrazhenskii, B. P. Semyagin, D. Bimberg and Zh. I. Alferov, *J. Electron. Materials* **30 (5)**, in print (2001).
[7] G. R. Bell, M. Itoh, T. S. Jones, B. A. Joyse, *Surface Science* **423**, L280 (1999).

9th Int. Symp. "Nanostructures: Physics and Technology"
St Petersburg, Russia, June 18–22, 2001

Effect of the surface relaxation on spinodal decomposition of semiconductor epitaxial films

I. P. Ipatova, S. G. Konnikov, M. B. Lifchits and A. Yu. Maslov
Ioffe Physico-Technical Institute, St Petersburg, Russia

Abstract. Semiconductor alloys are unstable at critical temperatures because of the positive enthalpy of alloy formation. The critical temperature of decomposition is the function of elastic parameters which differ due to structure relaxation of epitaxial film. It opens the new way to vary the critical temperature and the phase diagram.

There are numerous experimental data [1] which show that in the process of semiconductor alloy epitaxial growth there exist some temperature and composition intervals where semiconductor alloy is unstable, and decompose into periodic structures with composition modulations. The formation of such structures is possible due to the high value of surface diffusion coefficient (with respect to semiconductor bulk diffusion coefficient).

To explain the similar effect in the metal alloys Cahn [2] and Khachaturyan [3] suggested the theory of spinodal decomposition. Ipatova et al [4] have studied the spinodal decomposition of the thin epitaxial films of semiconductor alloys. It is showed that formation of periodic structures is defined by both the chemical energy and the elastic energy of semiconductor alloy caused by the composition fluctuations. However the phenomena of surface relaxation and reconstruction which change the crystal lattice structure near the growing surface have not been taken into account.

This paper deals with the effect of the surface relaxation on the critical temperature of spinodal decomposition. The surface relaxation means [5] that the surface crystalline plane atoms shift to the new equilibrium positions in a way that crystalline plane shifts as a whole in the direction normal to the surface. It leads to specific change of the lattice parameter in the direction of the normal. The surface crystalline planes of different orientation could relax either inward or outward. Some surface crystalline planes do not relax at all.

The semiconductor alloys are unstable at some temperatures because they have the positive enthalpy of formation. It means that at $T = 0$ K the composition modulated alloy corresponds to smaller Helmholtz free energy than homogeneous alloy.

Semiconductor alloys are disordered systems with composition fluctuations at each point

$$c(\mathbf{r}) = \overline{c} + \delta c(\mathbf{r}). \tag{1}$$

According to the Vegard's law, the lattice parameter fluctuated with composition (1). Coherent conjugation of regions with different lattice parameters requires elastic strains and results in specific elastic energy

$$\delta F_{\text{elastic}} = \frac{1}{2} \int dxdy \int_{-\infty}^{h} dz \lambda_{ijlm} \Big(\varepsilon_{ij}(\mathbf{r}) - \varepsilon^0_{ij}(\mathbf{r})\Big)\Big(\varepsilon_{lm}(\mathbf{r}) - \varepsilon^0_{lm}(\mathbf{r})\Big) \tag{2}$$

where $\varepsilon^0_{ij}(\mathbf{r})$ is the static intrinsic strains, λ_{ijlm} is the tensor of elastic moduli.

The elastic stress is equal by definition to

$$\sigma_{ij}(\mathbf{r}) = \frac{\partial f_{\text{elastic}}}{\partial \varepsilon_{ij}(\mathbf{r})} = \lambda_{ijlm}\Big(\varepsilon_{lm}(\mathbf{r}) - \varepsilon^0_{lm}(\mathbf{r})\Big). \tag{3}$$

It follows from Eq. (3) that the stress–free state corresponds to the strained state of the medium, $\varepsilon_{lm}(\mathbf{r}) = \varepsilon^0_{lm}(\mathbf{r}) \neq 0$. The local intrinsic strain is a linear function of composition fluctuations

$$\varepsilon^0_{ij}(\mathbf{r}) = \varepsilon^0_{ij}\delta c(\mathbf{r}), \qquad \varepsilon^0_{ij} = \begin{bmatrix} \varepsilon_\parallel & 0 & 0 \\ 0 & \varepsilon_\parallel & 0 \\ 0 & 0 & \varepsilon_\perp \end{bmatrix} \tag{4}$$

where ε^0_{ij} reflects the influence of relaxation on the symmetry of intrinsic strains. Disregarding surface relaxation: $\varepsilon^0_{ij} = \varepsilon_0\delta_{ij}$.

Semiconductor alloys consist of binary compounds of similar chemical nature. The mixture components have close chemical energies. As a result, the change of the chemical energy in semiconductor alloy is the same order of magnitude as the elastic energy (2). The total Helmholtz free energy equals

$$\delta F = F_{\text{inhom}} - F_{hom} = \delta F_{\text{elastic}} + \delta F_{\text{chem}}. \tag{5}$$

The requirement of total elastic energy minimum yields equilibrium equations of the theory of elasticity, such as the absence of external forces in the bulk and the boundary conditions of the absence of external stresses at the free surface. It is convenient to express the solution of these equilibrium equations in terms of the Green's tensor of the semi–infinite cubic elastic medium $G_{\alpha\beta}(\mathbf{r}, \mathbf{r}') = G_{\alpha\beta}(x - x', y - y', z, z')$. This Green's tensor was found by Portz and Maradudin [6]. Finally we obtain the elastic free energy in the form:

$$\delta F_{\text{elastic}} = \frac{1}{2}\int d^3r d^3r' \delta c(\mathbf{r})\Big[\varepsilon^0_{\alpha\alpha}\lambda_{\alpha\alpha\beta\beta}\varepsilon^0_{\beta\beta}\delta(\mathbf{r}-\mathbf{r}') - A_{\alpha\beta}\frac{d}{dr_\alpha}\frac{d}{dr_\beta}G_{\alpha\beta}(\mathbf{r}, \mathbf{r}')\Big]\delta c(\mathbf{r}') \tag{6}$$

where, considering the surface relaxation:

$$A_{\alpha\beta} = (c_{11}-c_{12})^2\varepsilon^0_{\alpha\alpha}\varepsilon^0_{\beta\beta} + c_{12}(c_{11}-c_{12})\Big(\sum_j \varepsilon^0_{jj}\Big)\big(\varepsilon^0_{\alpha\alpha}+\varepsilon^0_{\beta\beta}\big) + c_{12}^2\Big(\sum_{ij}\varepsilon^0_{ii}\varepsilon^0_{jj}\Big)\delta_{\alpha\alpha}\delta_{\beta\beta}, \tag{7}$$

(c_{11}, c_{12}, c_{44} being the elastic moduli in the Voigt notation). Disregarding surface relaxation: $A_{\alpha\beta} = (c_{11} - c_{12})^2\varepsilon_0^2\delta_{\alpha\alpha}$.

Since elastic properties of semi–infinite medium are homogeneous in the x- and y-directions in the substrate plain, it is convenient to use Fourier transformation in x and y and express the composition fluctuations as a linear combinations of static concentration waves with different $\mathbf{k}_\parallel = (k_x, k_y)$,

$$\delta c(\mathbf{r}) = \int \frac{d^2k_\parallel}{(2\pi)^2}\delta\tilde{c}(\mathbf{k}_\parallel, z)\exp\big(i(k_x x + k_y y)\big). \tag{8}$$

Substitution (8) into (6) results in

$$\delta F_{\text{elastic}} = \frac{S}{2}\int \frac{d^2k_\parallel}{(2\pi)^2} dz dz' \delta\tilde{c}(\mathbf{k}_\parallel, z) B_{\text{elastic}}(\mathbf{k}_\parallel, z, z')\delta\tilde{c}(\mathbf{k}_\parallel, z') \tag{9}$$

where S is the substrate area, the operator $\hat{B}_{\text{elastic}}(\mathbf{k}_\parallel, z, z')$ is equal to

$$B_{\text{elastic}}(\mathbf{k}_\parallel, z, z') = B_0\delta(z-z') + \sum_{s=1}^{3} C_s(\Theta)k_\parallel \exp\left[-\alpha_s k_\parallel \mid z-z' \mid\right] + \\ + \sum_{s'=1}^{3}\sum_{s=1}^{3} D_{ss'}(\Theta)k_\parallel \exp\left[-\alpha_s k_\parallel (h-z)\right]\exp\left[-\alpha_{s'} k_\parallel (h-z')\right]. \qquad (10)$$

The first and the second terms on the right–hand–side of Eq. (10) correspond to the operator $\hat{B}^{\infty}_{\text{elastic}}$ for an infinite cubic medium. The third term is the surface contribution to $\hat{B}_{\text{elastic}}$. The angel Θ is the angel between the direction of the wave vector $\mathbf{k}_\parallel$ and [100]–direction on the surface. The three dimensionless parameters α_s ($s = 1, 2, 3$) describe the spatial attenuation of three static analogues of Rayleigh waves generated by static fluctuations of alloy composition. These parameters are defined in [6]. The coefficients B_0, C_s, $D_{ss'}$ are obtained here considering the surface relaxation, and they differ from the ones corresponding to surface relaxation disregarding in [4].

To derive the criterion of absolute instability it is convenient to present the variation of the Helmholtz free energy δF which is quadratic functional in $\delta c(\mathbf{k}_\parallel, z)$, in the diagonal form. Thereto we define the orthonormal eigenfunctions $\varphi_p(\mathbf{k}_\parallel, z)$ and eigenvalues $\lambda_p(\mathbf{k}_\parallel)$ of operator $\hat{B}_{\text{elastic}}$ by the following equation:

$$\int_0^h B_{\text{elastic}}(\mathbf{k}_\parallel, z, z')\varphi_p(\mathbf{k}_\parallel, z')dz' = \lambda_p(\mathbf{k}_\parallel)\varphi_p(\mathbf{k}_\parallel, z) \qquad (11)$$

Expanding an arbitrary composition fluctuation $\delta c(\mathbf{r})$ in eigenfunctions $\varphi_p(\mathbf{k}_\parallel, z)$, one obtains the variation δF of the total Helmholtz free energy of the system in the diagonal form:

$$\delta F = \frac{S}{2}\int \frac{d^2k_\parallel}{(2\pi)^2}\sum_{p=0}^{\infty}\left[\left(\frac{\partial^2 f}{\partial c^2}\right)+\lambda_p(\mathbf{k}_\parallel)\right] \mid a_p(\mathbf{k}_\parallel) \mid^2, \qquad (12)$$

$a_p(\mathbf{k}_\parallel)$ being coefficients in expansion of $\delta\tilde{c}(\mathbf{k}_\parallel, z)$ in eigenfunctions $\varphi_p(\mathbf{k}_\parallel, z)$.

It follows from Eq. (2) that the operator $\hat{B}_{\text{elastic}}$ yields always a positive contribution to the variation of free energy. It means that all eigenvalues λ_p of the operator $\hat{B}_{\text{elastic}}$ are positive.

Due to mixing entropy at sufficiently high temperatures both bulk ternary III–V alloys and epitaxial films of alloys are stable, i.e. $\left(\partial^2 f/\partial c^2\right) > 0$, and the chemical free energy contribution to δF is positive. However the positive formation enthalpies of those alloys results in the fact that at sufficiently low temperatures $\left(\partial^2 f/\partial c^2\right) < 0$, and the chemical free energy decreases due to composition fluctuations. As a result, infinitesimal fluctuations of composition in the epitaxial film may lead to the decrease of the total Helmholtz energy, i.e. to $\delta F < 0$. This means the spinodal instability in the epitaxial film. The negative contribution of chemical free energy, $\left(\partial^2 f/\partial c^2\right) < 0$ to δF in Eq. (12) competes with the minimum of all positive eigenvalues of operator $\hat{B}_{\text{elastic}}$ denoted as λ_0^{min}. Then the

thermodynamic criterion of the spinodal instability is as follows,

$$\frac{\partial^2 f}{\partial c^2} + \lambda_0^{min} = 0. \tag{13}$$

Equation (13) determines the critical temperature of spinodal instability T_c, the critical alloy composition and the wave vector $\mathbf{k}_{\|}^0$ of the "soft mode" responsible for the decomposition. The profile of composition fluctuations in this mode is described by the corresponding eigenfunction $\varphi_0(\mathbf{k}_{\|}^0, z)$.

The minimum eigenvalue $\lambda_0^{\min}$ of $\hat{B}_{\text{elastic}}$ defining the critical temperature T_c became different as we consider the surface relaxation. It is shown that the outward relaxation conforms the elastic energy decrease thus the critical temperature of spinodal decomposition T_c is getting higher; on the contrary the inward relaxation increase the elastic energy and makes the critical temperature lower.

Since the effect of relaxation on the critical temperature of spinodal decomposition is different for different surfaces, it allows to operate the miscibility gaps and temperature T_c.

Acknowledgements

The work was supported, in different parts, by the Russian Federal Programs of Ministry of Industry, Science and Technology “Solid State Nanostructures”, project 97-2014 and “Surface Atomic Structures”, project 3.6.99.

References

[1] A. Zunger and S. Mahajan, *Handbook on Semiconductors* ed. T. S. Moss. Elsevier, Amsterdam, vol. 3, p. 1399, 1994.
[2] J. W. Cahn, *Trans. Met. Soc.* **242**, 166 (1968).
[3] A. G. Khachaturyan, *Theory of structural transformations in solids* John Wiley and Sons, New York, 1983.
[4] I. P. Ipatova, V. G. Malyshkin and V. A. Shchukin, *J. Appl. Phys.* **74**, 7198 (1993).
[5] A. Zangwill, *Physic of Surfaces* Cambridge University Press, Cambridge, 1988.
[6] K. Portz and A. A. Maradudin, *Phys. Rev. B* **16**, 3535 (1977).

9th Int. Symp. "Nanostructures: Physics and Technology"
St Petersburg, Russia, June 18–22, 2001

Surface segregation in epitaxy of III–V compounds

S. Yu. Karpov† and Yu. N. Makarov‡
† Soft-Impact, Ltd., P.O.Box 33, St Petersburg, 194156 Russia
‡ Semiconductor Technology Research, Inc.
1610 Swinton Lane, Richmond VA, 23233 USA

Abstract. Surface segregation in III–V compound heterostructures grown by Molecular Beam Epitaxy (MBE) and Metal-Organic Vapor Phase Epitaxy (MOVPE) is studied theoretically. The suggested model treats segregation as a transient process resulting in a delayed highly-volatile species incorporation into the crystal accompanied by its accumulation on the growth surface. Specific features of In segregation in InGaAs and InGaN are discussed with respect to control of the composition profile and efficiency of In incorporation into the crystal.

Introduction

Nowadays, principles of band gap engineering are widely employed for designing most advanced semiconductor devices. This requires to control heterostructure layer thicknesses, composition and doping profiles on the atomic scale. The growth techniques like MOVPE and MBE provide potential facilities for such a control. However, researchers are frequently face with natural physical limitations on abrupt interfaces, composition and dopant distributions. Among the limitation factors, surface segregation is one of the most important phenomena because of considerable effect on the composition profile in the grown III–V ternary compounds.

The earlier MBE studies revealed two principal experimental manifestations of segregation: (i) delayed incorporation of a highly-volatile species into the crystal at the epilayer growth onset, and (ii) penetration of the species into the cap layer after the species supply to the growth surface was terminated. A short review of the experimental observations is given in [1, 2]. The segregation depended significantly on temperature and, to a smaller extent, on the V/III ratio in the incident fluxes. Elastic strain in the epilayer due to lattice constant mismatch was found to be a crucial factor significantly enhancing segregation effects.

Recently we suggested a rate-equation model of surface segregation on ternary III–V compounds, providing excellent fitting of the literature data on MBE of InGaAs without any adjustable parameters [1, 2]. In this paper we apply the model to InGaN growth both by plasma enhanced MBE and ammonia MBE. The results are compared with those obtained for InGaAs. The segregation effect on In incorporation efficiency in MOVPE of InGaN is also discussed.

1. Control of composition profile in MBE of InGaAs

Detailed theoretical study of In segregation in MBE of InGaAs was reported in [1, 2]. Here we consider the ways to control the interface abruptness in a GaAs/InGaAs/GaAs heterostructure. The interface control utilizes the idea that In in the adsorption layer is nearly in equilibrium with the InGaAs crystal bulk, see, for instance, [2]. Indeed, Fig. 1 shows a nearly linear relationship between the In surface coverage (θ_{In}) and InGaAs composition

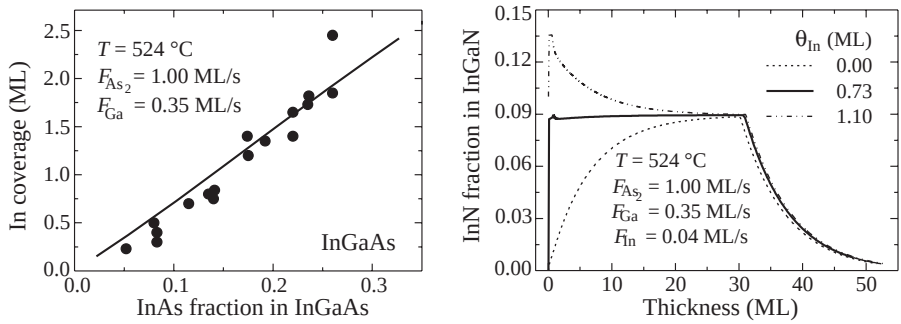

Fig. 1. In surface coverage against InGaAs composition measured in [3]; circles are experimental data, line is theoretical curve (left). InGaAs composition profile for the quantum wells grown with In pre-deposited on the growth surface (right).

(x) with a temperature-dependent slope, as measured in [3]. This enables one to introduce the segregation coefficient $\mathcal{S}(T) = \theta_{\mathrm{In}}/x$, which is an evidence for the adsorption layer – crystal bulk near-equilibrium.

Normally, direct InGaAs/GaAs growth results in a delayed In incorporation into solid, see dashed line in Fig. 1 (right). Pre-deposition of In on the GaAs surface without As_4 flux produces In in the adsorption layer. If the In coverage is equal to an equilibrium value, no transient effect at the growth onset is observed [4, 5], see solid line in Fig. 1 (right). As a result, a perfectly abrupt front interface is formed. If the In coverage exceeds the equilibrium value, then inverse profiling of solid composition can be obtained, see dash-dotted line in Fig. 1 (right).

The back GaAs/InGaAs interface can be controlled by evaporation of In from the growth surface after the InGaAs epilayer has been grown. It must be done with the As_4 flux switched off to prevent growth surface from InAs island formation. Duration of this stage depends on the temperature-dependent rate of In desorption.

2. Indium segregation in MBE of InGaN

Specific feature of InGaN MBE is a relatively high growth temperature. This decreases the segregation length characterizing the transition layer thickness at the InGaN/GaN interface, see Fig. 2. However, the strain effect on surface segregation is rather strong due to a considerable lattice mismatch between the InGaN and underlying GaN. Therefore, In

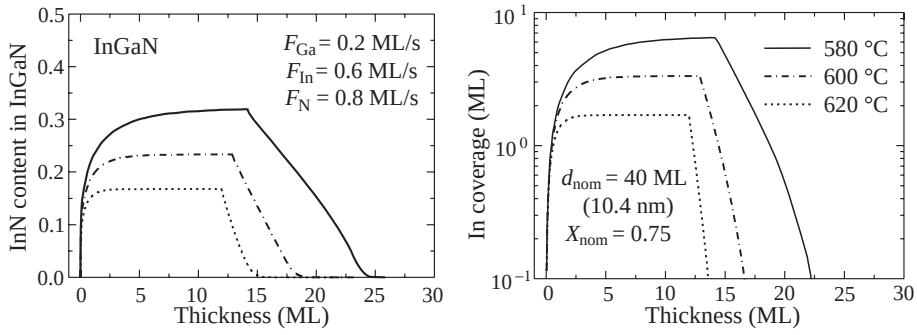

Fig. 2. InGaN composition profile (left) and In coverage (right) as a function of quantum well thickness computed for different temperatures of plasma-enhanced MBE.

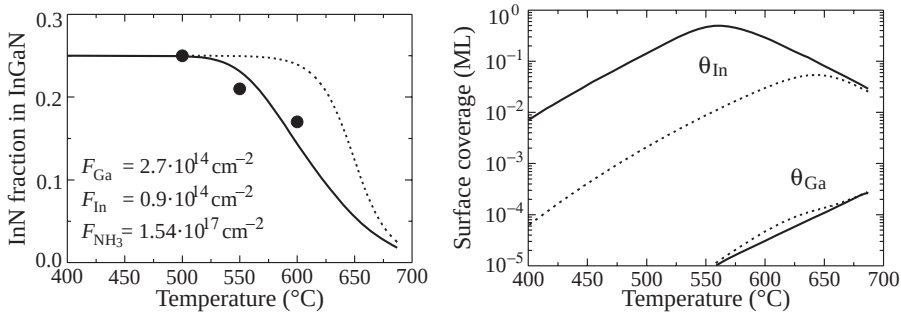

Fig. 3. Temperature dependence of InGaN composition (left) and In surface coverage (right) computed for ammonia MBE reported in [6].

accumulation on the growth surface is extremely high for InGaN growth (Fig. 2).

The effect of In accumulation is especially important for ammonia gas-source MBE. Figure 3 shows temperature dependence of the composition profile and In surface coverage calculated for the strained and relaxed InGaN/GaN heterostructures. The computations were carried out for the growth conditions reported in [6]. Comparison with the data [6] shows the theoretical predictions for the strained epilayers to be in good agreement with the observations. Up to 0.6 ML In is predicted to accumulate on the growth surface under the conditions used in [6].

It was found earlier that Ga accumulation on GaN(0001) surface resulted in NH_3 adsorption site blocking [7] and consequent growth rate reduction. If In behaves similarly to Ga, we can expect the termination of InGaN growth when In coverage exceeds unity. This occurs in a temperature gap with the width primarily dependent on the incident In flux. Normally, high growth temperatures are beneficial for InGaN improving their optical characteristics. However, In incorporation into the crystal is limited in the high-temperature range due to intensive In desorption. Computations show the InN content to be limited by 15–20% in that case.

3. Surface segregation in MOVPE of InGaN

Accumulation of surface In is also responsible for limited In incorporation efficiency in MOVPE of InGaN. Figure 4 displays the In coverage as a function of InGaN composition computed for MOVPE in a vertical rotating-disk reactor using N_2 as a carrier gas. One can see that the composition of the strained InGaN is limited by 30%. Use of H_2 as a carrier

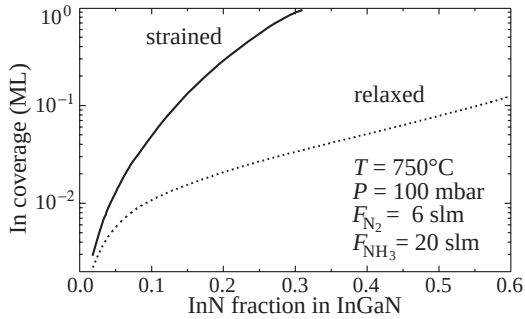

Fig. 4. In coverage as a function of InGaN composition computed for MOVPE in a vertical rotating-disk reactor.

gas results in enhancement of In segregation, especially at low temperatures. This is due to high reactivity of hydrogen on the nitride surface. In the case of the relaxed InGaN epilayers, no segregation effect on In incorporation is found.

Conclusions

In this paper various aspects of surface segregation have been discussed with the focus on InGaN growth by MBE and MOVPE. The segregation effects are found to be much more pronounced for InGaN/GaN structures than for InGaAs grown on GaAs. Modification of a heterostructure composition profile due to segregation is important for band-gap engineering of advanced semiconductor devices. The methods of interface control include pre-deposition of equilibrium amount of highly-volatile species on the growth surface before growth and evaporation of the species excess after the epilayer is formed.

References

[1] S. Yu. Karpov and Yu. N. Makarov, *Mat. Res. Soc. Symp. Proc.* (2001) to be published .
[2] S. Yu. Karpov and Yu. N. Makarov, *Thin Solid Films* **380**, 71 (2001).
[3] A. Jackson, P. Pinsukanjana, L. Coldren and A. Gossard *J. Cryst. Growth* **175/176**, 244 (1997).
[4] J.-M. Gerard and C. d'Anterroches, *J. Cryst. Growth* **150**, 467 (1995).
[5] R. Kaspi and K. R. Evans, *Appl. Phys. Lett.* **67**, 219 (1995).
[6] N. Grandjean and J. Massies, *Appl. Phys. Lett.* **72**, 1078 (1998).
[7] D. Crawford, R. Held, A. M. Johnston, A. M. Dabiran and P. I. Cohen, *MRS Internet J. Nitride Semicond. Res.* **1**, No 12 (1996).

9th Int. Symp. "Nanostructures: Physics and Technology"
St Petersburg, Russia, June 18–22, 2001

Morphology and photoelectronic properties of the InAs/GaAs surface quantum dots grown by vapor phase epitaxy

I. A. Karpovich, N. V. Baidus, B. N. Zvonkov, S. V. Morozov,
D. O. Filatov and A. V. Zdoroveishev
University of Nizhny Novgorod, Nizhny Novgorod 603 950, Russia

Abstract. A comparative study of the surface morphology, photoluminescence and photoelectric properties of the heterostructures with InAs/GaAs quantum dots (QDs) grown on the surface and uncovered by etching away the GaAs cladding layer has been carried out. The red shift of the ground transition energy in the surface QDs compared to the QDs embedded into the GaAs matrix has been shown to be related not only to relaxation of the elastic strain but also to the differences in the size and shape of the nanoclusters.

Investigation of the surface quantum dots (SQDs) are interesting because of possibility to establish a direct correlation between their photoelectronic properties and morphology determined by Scanning Probe Microscopy. SQDs differ from the QDs built in a wider gap semiconductor matrix (buried QDs or BQDs) by different field of the elastic strain and another shape of the potential well that effect on their energy spectrum essentially. Surface location of the SQDs allows to apply various processings (oxidation, etching, chemical modification, etc.). On the other hand, the photoelectronic properties of the SQDs are difficult for investigation due to a number of reasons, so far they are much less investigated to date than the BQDs [1, 2]. In the present work the morphology, photoluminescence (PL), and photovoltage spectra at the semiconductor/electrolyte interface (PSE) of the InAs/GaAs SQDs and BQDs grown by Atmospheric Pressure Metal-Organic Vapor Phase Epitaxy (AP-MOVPE) [3, 4] have been studied. It is known that deposition of a cladding layer may influence on the QDs formation essentially especially during vapor-phase epitaxy [5]. Using preferential chemical etching for removing the cladding layer [3] one can turn the BQDs into SQDs (further referred to as etched SQDs or ESQDs in order to distinguish between ones and as-grown SQDs). In this work the morphology of the ESQDs was also studied.

In Figures 1(a) and 1(b) the Atomic Force Microscopy (AFM) images of the SQDs and ESQDs respectively are shown. The typical lateral base size of the SQDs was $\approx$ 40 nm and height $\approx$ 6 nm. The ESQDs usually have less height ($\approx$ 4 nm) but larger base size ($\approx$ 50 nm). Their surface density was as a rule 1.5–2 times higher than the one of the SQDs

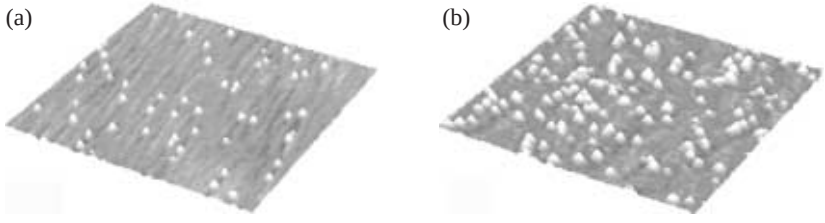

Fig. 1. AFM images of the SQDs (a) and ESQDs (b). Frame size: 1000×1000 nm; vertical scale: 6 nm.

($(4-9) \times 10^9$ cm^{-2}) that was attributed to suppression of coalescence of the nanoclusters by deposition of the cladding layer.

The difference in sizes between the SQDs and the ESQDs can be explained as follows. In [3] we have suggested formation of a graded composition $In_xGa_{1-x}As$ transition layer at the QD's heterointerface because of diffusion intermixing of In and Ga during overgrowth of the BQDs by GaAs cladding layer. This effect should increase the volume where the In atoms are distributed around a BQD as compared to the volume of a SQD. Since the etchant used for removing the cladding layer has high selectivity, the layer where In fraction exceeds some threshold value x should be a stop-layer for etching process (the more selectivity, the lover the threshold x). So far, as the surface $x = \text{const}$ determines the topography of the ESQDs, the latter should be larger in size than the SQDs. Otherwise, if no In redistribution during overgrowth takes place the etched surface should represent a sharp InAs/GaAs heterointerface.

PL measurements in the (E)SQDs are rather, more difficult because of a channel of the surface non-radiative recombination which decreases the PL intensity in 3–4 orders of magnitude as compared to the BQDs PL. While the latter can be observed easily even at room temperature the PL from the (E)SQDs can be observed at 77 K only. Typical PL spectra (77 K) from the SQDs and BQDs obtained at the same growth conditions are presented in Fig. 2. The PL peak from the SQDs is shifted by 350–400 meV to lower energies (curves 1 and 5), the lowest peak maximum position observed was 0.72 eV, which corresponds to the emission wavelength 1.72 μm. The fact that this peak is from the SQDs was proven by etching away the surface oxide layer in HF. After formation and etching of the oxide has been observed a blue shift of the PL peak from the SQDs by 80 meV (curves 1–3) which was explained by decreasing of the volume of the SQDs. The spectral position of the higher energy shoulder of the peak at 0.85 eV remains the same. This shoulder should be obviously attributed rather to some deep levels in the epilayer than to the SQDs.

The red shift of the PL peak takes place also at formation of the ESQDs but its value is much less ($\approx$ 150 meV) that in the SQD heterostructures (curves 4 and 5). This indicates that the change in the field of the elastic strain is not the only cause for the shift of the transition energies. The differences between the SQDs and BQDs in size, in shape, and in the chemical composition arising during overgrowth probably also introduce comparable

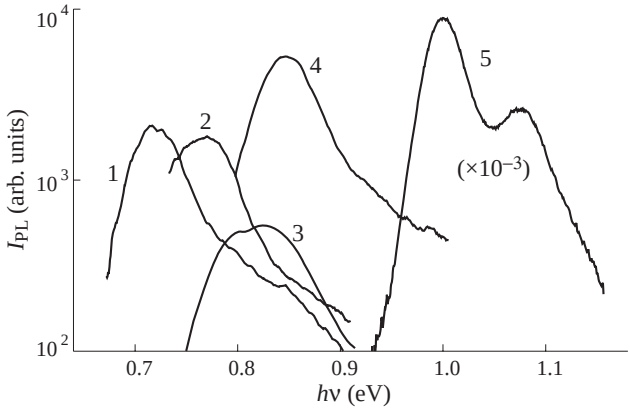

Fig. 2. Photoluminescence spectra of the quantum dots: SQDs (1–3), ESQDs (4), and BQDs (5). Curves 2 and 3 were obtained after first and second removing of the oxide layer in HF respectively.

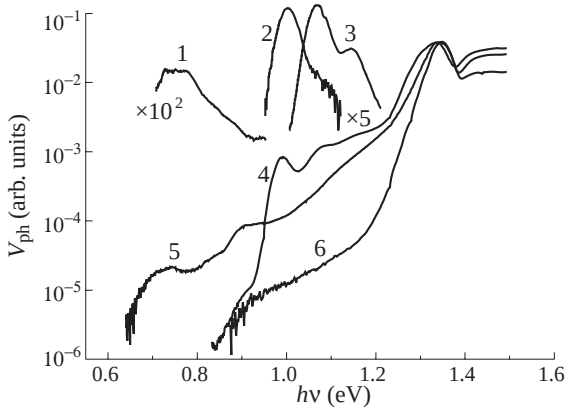

Fig. 3. PL (1–3) and PSE (4–6) spectra of the QD heterostructures: 2–4 — BQDs; 1, 5 — SQDs; 6 — GaAs. 2, 4–6 — 300 K; 1, 3 — 77 K.

contributions in the red shift.

In difference from the PL measurements the main problem in the photoelectric measurements in the SQDs is related not to the surface recombination but to low values of the ground transition energy in the SQDs. Increasing of the barrier height decreases the probability both of direct and thermally activated tunneling emission of the electrons from the SQDs into the matrix and, in turn, the photosensitivity. High sensitivity of the PSE method allowed to measure the photoelectric spectra from the SQDs at its surface density $\sim 10^{10}$ cm^{-2}.

In Figure 3 the PSE spectra of the 3 structures grown at the same conditions: BQDs (curve 4), SQDs (curve 5), and a homogeneous GaAs layer similar to the buffer in the QD structures (curve 6) are presented. A broad and weak peak of the SQDs photosensitivity at ≈ 0.7 eV is shifted to lower energies by ≈ 0.3 eV from the BQDs peak and is approximately in 2 orders of magnitude weaker than the latter at close values of the QD surface density, in correlation with the PL spectra of these samples (curves 1, 3). This peak crowns the wide band of approximately exponential decay of the photosensitivity within the band 0.75–1.2 eV which was attributed to the surface states (SSs) below the Fermi level at the surface having quasi-continuous energy distribution. Similar band can be observed in the photosensitivity spectra of the GaAs homogenous epilayers (curve 6) and bulk single crystals as well. It is interesting that on the GaAs surface covered by InAs wetting layer, which is obviously oxidized fully beetween the SQD clusters, the SS density is much higher (curve 5) than on the surface covered by a natural oxide in the BQD structure and in the homogeneous layer.

In the photoelectric spectra of all GaAs based structures, homogeneous GaAs layers and GaAs single crystals a more or less expressed photosensitivity edge at ≈ 0.9 eV has been observed (Fig. 3) which can be related to some single-level surface states in the native oxide on the GaAs surface. The density of these states also increases on the surface covered by a SQD layer.

Acknowledgements

This work was supported by the Russian Foundation for Basic Research (00-02-17598), by Russian Ministry of Science (015.06.0.19), by NATO (SfP-973799), by "Physics of the Solid State Nanostructures" Program (99-1141), and especially by a joint Russian-

American Basic Research and Higher Education (BRHE) Program sponsored jointly by Russian Ministry of Education and by US Civilian Research and Development Foundation (CRDF) (Award No. REC-001).

References

[1] H. Saito, K. Nishi and S. Sugou, *Appl. Phys. Lett.* **73**, 2742 (1998).
[2] J. Z. Wang, Z .Yang and C. L. Yang, *Appl. Phys. Lett.* **77**, 2837 (2000).
[3] B. N. Zvonkov, I. A. Karpovich, N. V. Baidus, D. O. Filatov and S. V. Morozov, *Semiconductors* **35**, 93 (2001)
[4] I. A. Karpovich, A. P. Gorshkov, S. B. Levichev, S. V. Morozov, B. N. Zvonkov and D. O. Filatov, *Fiz. Tekh. Poluprovod.* **35**, 564 (2001) (*in Russian*).
[5] N. V. Baidus, B. N. Zvonkov, D. O. Filatov, Yu. Yu .Gushina, I. A. Karpovich and A. V. Zdoroveishev, *Poverkhnost' (Surface)* **7**, 75 (2001) (*in Russian*) .

9th Int. Symp. "Nanostructures: Physics and Technology"
St Petersburg, Russia, June 18–22, 2001

MBE growth of high quality GaAsN bulk layers

A. R. Kovsh†‡, J. Y. Chi†, J. S. Wang†, L. Wei†, Y. T. Wu†, C. H. Chen§, B. V. Volovik‡, A. F. Tsatsul'nikov‡ and V. M. Ustinov‡
† Industrial Technology Research Institute, Hsinchu 310, Taiwan, R.O.C.
‡ Ioffe Physico-Technical Institute, St Petersburg, Russia
§ National Taiwan University, Taipei 104, Taiwan, R.O.C.

Abstract. In the present work we have carefully optimized the operation of plasma source and the growth parameters of GaAsN layers. We have demonstrated the possibility of incorporation about 1.5% of N into GaAs without decreasing the photoluminescence intensity.

1. Introduction

Presently one of the main directions of III–V compound epitaxy is the development of long-wavelength GaAs-based structures. 1.3 μm VCSEL pseudomorphically grown on GaAs substrate can realize the low-cost light source required for optical local area network. First demonstrations of the 1.3 μm GaAs-VCSELs based on InAs QDs and InGaAsN QWs were presented in [1] and [2], respectively. The most outstanding results for edge emitting lasers were achieved by MBE grown InGaAsN QWs using RF (radio-frequency) plasma nitrogen source [3]. So far the same team has presented the best characteristics of 1.3 μm VCSEL [4].

However, in spite of extensive investigation of the growth condition and post-growth annealing, there is a wide dispersion of the published characteristics of InGaAsN QW lasers. This variation indicates that the technology of InGaAsN-based lasers is still immature compared with the InGaAs-based counterparts. Presumably this situation can be attributed to different nitrogen sources and plasma conditions, which are used to grow (In)GaAsN. Nevertheless, little attention is paid to the study of the effect of plasma condition on (In)GaAsN quality. Defects from ion damage, impurities coming from the plasma source, and non-radiative recombination fundamental to the band structure are some of the accepted reasons to explain the decreasing efficiency of the radiative recombination even in the case when N content is less than 1–2%. However, in the present work we have achieved highly efficient radiative recombination in GaAsN layers by optimizing the RF plasma nitrogen source operation, growth regimes, and post-growth annealing.

2. Experiment

In our experiments we used Riber Epineat apparatus equipped with conventional effusion cells for group III elements and arsenic. UNI Bulb RF Plasma Source produced by Applied EPI was used to generate active species of N. Samples under investigation were grown on n^+-(001) GaAs substrate. A special structure design with the layer to be studied sandwiched between short period AlGaAs/GaAs superlattice (SL) was used for PL studies. We varied the growth temperature and growth rate of the core layer whereas substrate temperature of the rest of the structure was set at 600 °C.

The crystal quality of the samples was evaluated by x-ray diffraction measured with incident beam in the [004] and [511] azimuths. PL measurements were carried out using a doubled frequency YAG:Nd solid state laser ($\sim$40 W/cm^2) and CCD a (Charge Couple Device) spectrometer.

To clarify the effect of plasma source operation we chose the simpler GaAsN composition rather than the highly strained InGaAsN QW. Effects related to 2D–3D growth mode transition and the presence of high strain could complicate our study.

2.1. Effect of aperture design

The first set of GaAsN layers was grown at 470 °C using different aperture design. In a simple way, ignition of plasma in N_2 gas flow leads to formation of N atomic species as well as excited molecules and ions of N_2. The former incorporate into growing film whereas the latter lead to non-radiative defect formation. Thus, the quality of the layer is expected to be dependent on plasma composition, which can be affected by the aperture layout. Three apertures with different conductance (ø 200 μm, number of holes, h = 25, 50, 66) were used. The intensity of plasma can be controlled by the RF power and the flow rate of N_2. Figure 1(a) shows the dependence of nitrogen content, y, in $GaAs_{1-y}N_y$ layers on plasma light intensity as measured by a photodetector voltage, V_{OPT}. In Figure 1(b) we showed N content versus parameter C_{SOURCE}, which is definite as $h \times V_{OPT}/R_{GaAs}$, where R_{GaAs} is the growth rate. It is clearly seen that the dependence of y on C_{SOURCE} is linear. Thus, C_{SOURCE} is an universal parameter responsible for N content in the growing film.

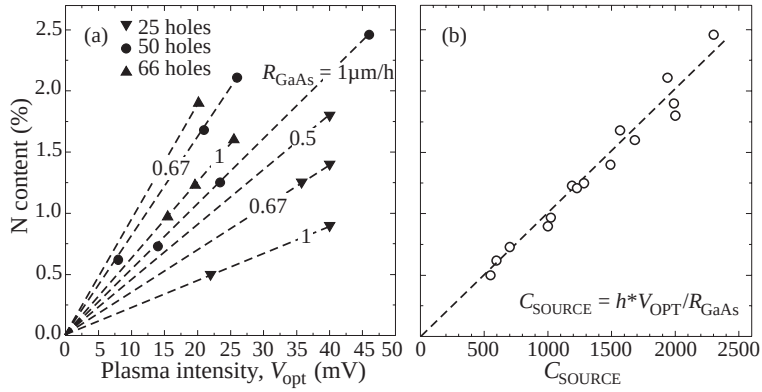

Fig. 1. Dependence of N composition of GaAsN layers on plasma conditions. (a) N content vs plasma light intensity at different GaAs growth rate and different aperture layouts, (b) N content vs parameter C_{SOURCE}.

Figure 2 shows the dependence of PL intensity of 0.2 μm-thick GaAsN layers on the PL peak position and nitrogen composition. All samples were grown under the same growth conditions. N_2 flow rate was tuned to get the lowest RF power at a given plasma intensity. One can see that we can obtain the required nitrogen composition for any aperture. However, the optical quality of the samples is quite different. Using the 50-hole aperture allowed us to improve several folds the PL intensity of GaAsN layers. All following growth experiments were done using the 50-hole aperture.

2.2. Effect of growth temperature and growth rate

We found that in our case the sticking coefficient of nitrogen is temperature independent from 430 to 550 °C and decreases at higher temperatures. GaAsN (1.3%) samples grown within the 520–540 °C temperature range demonstrated the brightest and narrowest PL spectra. At temperatures below 540 °C the 2×4 reconstruction of RHEED pattern was similar to the case of the GaAs growth. However, we observed 3×1 reconstruction when substrate temperature was higher than 550 °C. This fact is presumably due to N segregation

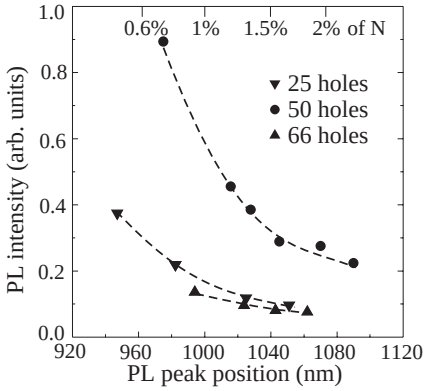

Fig. 2. Dependence of the PL intensity of GaAsN layers on wavelength for different aperture layouts.

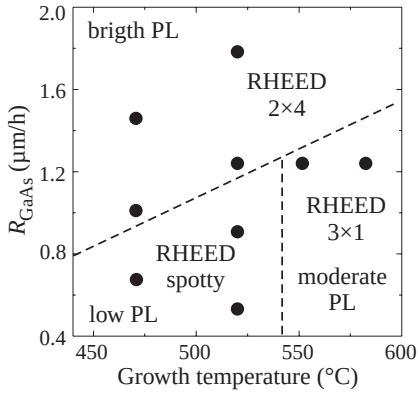

Fig. 3. "Growth temperature/growth rate" diagram of RHEED pattern. Points indicates samples grown at given growth rate and temperature.

on the growing surface [5]. This is in good agreement with PL and XRD measurements, which showed the presence of N-rich regions in grown films.

We did not find strong dependence of GaAsN quality on V/III ratio within typical range.

We observed the strong dependence of GaAsN properties on growth rate. When growth rate became lower than a certain value, the growth mode changes from 2D to 3D and N-rich clusters are formed. This minimum growth rate depends on temperature. Figure 3 showed "temperature-rate" phase diagram of RHEED pattern during the growth of GaAsN layers with N content about 1.3%. The upper region corresponds to normal GaAs-like growth mode and bright PL intensity. Both of the bottom regions correspond to the growth modes leading to fluctuation of N content in layers and lower PL intensity. So, we can conclude that there is some region of high "growth rate/growth temperature" that is free of the effects related to phase separation during the growth of GaAsN.

2.3. Effect of plasma operation condition

As we mentioned above one can tune the flow rate of nitrogen gas to get the lowest RF power at a required plasma intensity. However, we found that the plasma operation with lower nitrogen flow rate and therefore higher RF power is preferable to achieve brighter PL intensity. We also developed a "pre-operation" procedure to further enhance PL intensity. This procedure is the operation of plasma source at high flow rate and high power before growth run.

2.4. Comparison of GaAsN with GaAs layers

Figure 4 shows PL spectra of GaAsN(1%), and GaAsN(1.3%) grown using optimized conditions. The spectrum of GaAs grown at the same conditions is presented for comparison. Using AlGaAs/GaAs SLs allowed us to avoid leakage of non-equilibrium carriers into the substrate and surface and thereby obtain equal effective pumping of GaAs and GaAsN layers. The growth temperature was set at 520 °C and V/III ratio was about three. Adding N leads to strong red shift and broadening of PL line whereas integrated PL intensity remains almost the same.

2.5. Effect of annealing

We have also investigated the effect of in situ annealing on our GaAsN layers. We found that the maximum improvement in intensity for a given sample varied from 3 to 100 times

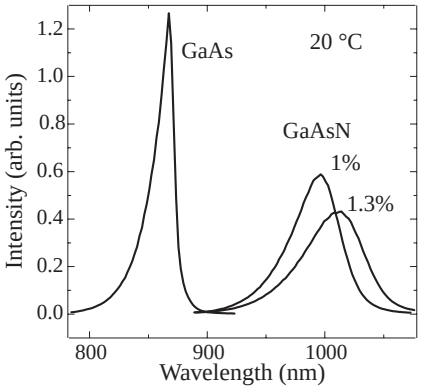

Fig. 4. PL spectra of GaAs and GaAsN layers.

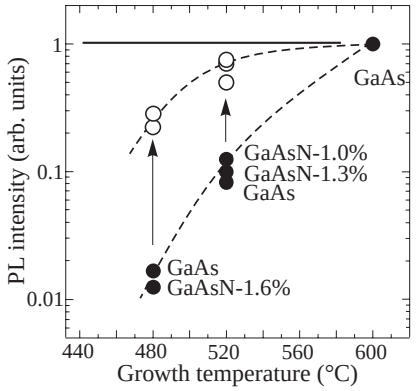

Fig. 5. Growth temperature dependence of integrated PL intensity of GaAs and GaAsN layers as grown (solid circles) and after annealing (open circles).

depending on its initial quality. Figure 5 shows dependence of integrated PL intensity of the GaAsN and GaAs layers grown at different growth temperatures. The solid horizontal line shows intensity of GaAs grown at 600 °C, which is an optimal growth temperature for GaAs. One can see that PL intensity depends on growth temperature but not on the presence of N in the layers. The point defects related to low temperature growth can be removed by annealing. The PL intensity of samples after annealing is shown as open circles. For samples grown at 520 °C and annealed for 2 hours at 750 °C under arsenic overpressure we achieved almost the same level of PL intensity as GaAs grown at 600 °C.

3. Conclusion

The quality of GaAsN layers is very sensitive to the plasma source operation conditions and growth temperature and growth rate. Detailed optimization of these parameters and annealing regime allowed us to achieve very high optical quality GaAsN layers with N composition about 1.5%.

Acknowledgements

The work was supported by the Ioffe-ITRI Joint Scientific Program. The work in Ioffe Institute was also partly supported by the NATO Science for Peace Program (grant SfP-972484).

References

[1] J. A. Lott, N. N. Ledentsov, V. M. Ustinov, N. A. Maleev, A. E. Zhukov, A. R. Kovsh, M. V. Maximov, B. V. Volovik, Zh. I. Alferov and D. Bimberg, *Electron. Lett.* **36**, 1384–1385 (2000).

[2] K. D. Choquette, J. F. Klem, A. J. Fischer, O. Blum, A. A. Allerman, I. J. Fritz, S. R. Kurtz, W. G. Breiland, R. Sieg, K. M. Geib, J. W. Scottand and R. L. Naone, *Electron. Lett.* **36**, (2000).

[3] B. Borchert, A. Yu. Egorov, S. Illek, M. Komainda and H. Riechert, *Electron. Lett.* **35** (25) (1999)

[4] H. Riechert, A. Yu. Egorov and G. Steinle, *11th European Workshop on MBE*, Hinterzarten, 4–7 February, 2001.

[5] R. J. Hauenstein, D. A. Collins, X. P. Cai, M. L. O'Steen and T. C. McGill, *Appl. Phys. Lett.* **66** (21) (1995).

9th Int. Symp. "Nanostructures: Physics and Technology"
St Petersburg, Russia, June 18–22, 2001

E-beam irradiation effect on CdSe/ZnSe QDs formation by MBE

V. I. Kozlovsky, *Yu. G. Sadofyev* and Ya. K. Skasyrsky
P. N. Lebedev Physical Institute RAS, 117924, 53 Leninsky pr., Moscow, Russia

Abstract. The strong influence of the RHEED e-beam irradiation on formation of CdSe QDs by MBE has been found. Large difference in CL spectra between inside the e-beam trace and outside it was observed. Probably, the e-beam stimulates the adatoms diffusion along the growth surface and/or plays role of a catalyst of chemical reaction between Cd and Se.

1. Introduction

Self-assembling quantum dot structures (QDs) are promising active medium for semiconductor lasers [1], in particular for e-beam longitudinally pumped lasers [2]. CdSe/ZnSe system is interesting for visual spectral range. Process of self-assembled QD layers depends strongly on growth procedure, temperature, layer thickness and other growth conditions [3–7]. So *in-situ* control of QD formation is very important. The reflective high-energy electron diffraction (RHEED) is usually used as a control during molecular beam epitaxy (MBE). At the formation of zero-dimensional entities, the RHEED pattern undergoes typically a sharp transition from streaky to spotty [8]. However, only small area of a wafer is monitored in such a way. We have observed that the other area of the wafer has very different emission spectrum. It proves that RHEED e-beam has an influence on the QD formation during MBE.

2. Experiment

Studied structures were grown on GaAs(100) by MBE and contained single or 15 CdSe layers separated by ZnSe barriers. The thickness of each CdSe layer was in 3–5 monolayer (ML) range. In the multiple CdSe/ZnSe layer structures the thickness of ZnSe was 50 or 200 nm. This was large enough to reject any influence of the CdSe layers on each other. Such a design was taken for future investigation of stimulated emission under e-beam pumping.

Growth of the ZnSe buffer was carried out at $T = 280^\circ$C and a VI/II flux ratio of 3:1. The CdSe layer was deposited at smaller temperature $T = 230^\circ$C. After deposition of each CdSe layer, the Cd beam was blocked and the structure was heated up to $T = 340^\circ$C and then cooled to $T = 280^\circ$C under Se flux. Time duration of temperature increase and decrease was 4 and 5 minutes respectively. After such procedure, next ZnSe barrier or top layer was grown. The RHEED e-beam was switched on before the CdSe deposition and switched off before the following ZnSe growth. Its parameters were the following: 0.2 mA current, 12 keV electron energy, 0.5 mm e-beam diameter near the growth surface and 3° angle between the e-beam and the growth surface.

3. Results and discussion

Typical changes of the RHEED patterns during the CdSe deposition followed by the heating procedure were presented in Fig. 1. Before the CdSe deposition (Fig.1a) the RHEED pattern was streaky. This proves that the ZnSe surface was flat enough. During the CdSe

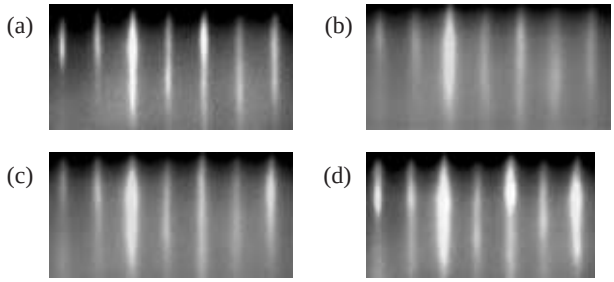

Fig. 1. The RHEED patterns at different time moments of the growth: before (a) and after (b) 3 ML CdSe deposition at $T = 230^{\circ}$C, and after heating to 340°C (c) and after cooling to $T = 230^{\circ}$C (d) under Se flux.

Fig. 2. CL image of the RHEED e-beam track on the structure with 15 CdSe layers and 50 nm thick ZnSe barriers. Oval spot is an area excited by CL e-beam of 5 mm in diameter. The white stripe inside the spot emits in yellow spectral range while the other part of the spot emits in blue-green spectral range.

deposition (Fig. 1(b)) the reflex width increased and a contrast of the diffraction reflexes became smaller. However, there weren't any features of 3-dimensional growth at this stage. The spotty pattern appeared more clearly only at a cooling stage (Fig. 1(d)).

Cathodoluminescence (CL) measurements at electron energy of 10–30 keV, current density up to 1 mA/cm^2, e-beam diameter from 10 to 0.1 mm and $T = 300$ and 14 K were carried out. The CL image of a small area of the structure with 15 CdSe layers and 50 nm thick ZnSe barriers is shown in Fig. 2 at room temperature. Oval spot on the image is the area excited by the e-beam of 5 mm in diameter. The e-beam drops on the sample surface at 45° angle. Most of the spot area emits in green-blue spectral range while an 0.5 mm thick stripe inside the spot emits in yellow spectral range (lighter stripe). It should be noted that total intensity of the stripe emission was higher (about 2.5 times for this structure) than that from the other area. This stripe is the RHEED e-beam track. Such a difference may be due to strong influence of the RHEED e-beam on the CdSe QDs formation.

In Fig. 3 the comparison of CL spectra of the RHEED e-beam trace and outside the trace is shown for different structures at RT. The CL spectrum of the structure with one CdSe layer outside the RHEED e-beam trace contains a wide emission band with maximum at 610 nm. This band is probably caused by deep level defects. Besides, there are two lines with maximum at 461 and 478 nm (Fig. 3(a)). The first is an emission line due to the ZnSe buffer layer and the second may be an emission of thin wet CdSe (or ZnCdSe) layer. The CL spectrum of the RHEED e-beam trace contains an intense line with maximum at 518 nm instead of the 478 nm line and more weak emission from the ZnSe barrier and deep levels

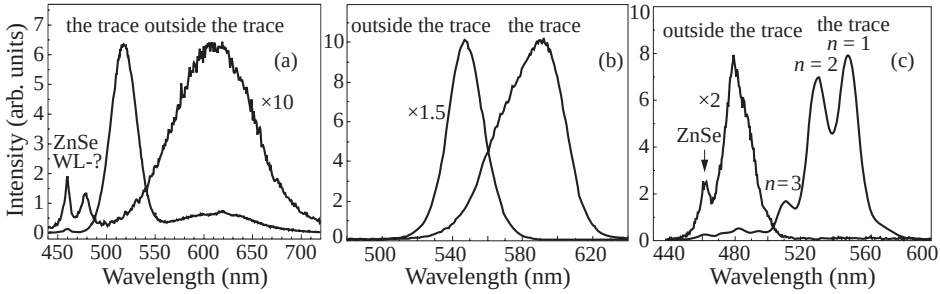

Fig. 3. Comparison of CL spectra from the RHEED e-beam track and an area outside the trace for three different structures contained 1 CdSe layer (a) or 15 CdSe layers separated by 50 nm (b) and 200 nm (c) thick ZnSe barriers, at RT, 1 mA/cm^2 current density and 10 keV electron energy.

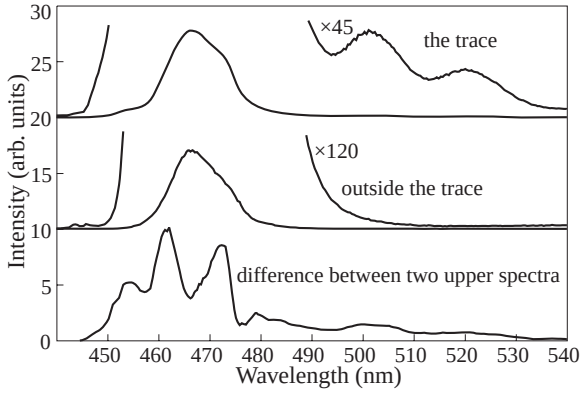

Fig. 4. The 14 K temperature CL spectra of the structure with 15 CdSe layers and 200 nm ZnSe barriers from the RHEEDe-beam trace (upper spectra) and outside the trace (middle spectra) and difference of these spectra (lower spectrum).

defects. In this case the e-beam irradiation essentially improves efficiency of CdSe related emission. The structures with 15 CdSe layers (Fig. 3(a), 3(b)) show more intense CdSe related emission even outside the RHEED e-beam track. Nevertheless the total intensity of the emission from the trace is higher again. Besides, the wavelength maximum of the CdSe related emission shifts to long-wavelength side from 547 nm to 590 nm and from 480 nm to 549 nm for the structure with 50 nm (Fig. 3(b)) and 200 nm (Fig. 3(c)) thick ZnSe barrier layers respectively. Moreover for last structure the CdSe related emission spectrum from the trace consists of several lines with maximum at 549, 531 and 510 nm. At 10 keV excitation only one CdSe layer of this structure is in the excitation area. Indeed the electron penetration depth is 250 nm at 10 keV but the total thickness of the 100 nm thick ZnSe top layer and the 200 nm ZnSe barrier layer separating the first CdSe layer from the next is 300 nm. It means that the different lines are not due to different CdSe layers. However, even at 30 keV (the penetration depth is about 2.3 μm), CL spectrum is practically the same. Such a spectrum is very close to the one observed for InAs/GaAs QDs [9, 10]. By analogy with InAs QDs we suppose that the observed spectrum is related to emission from not only ground level in QDs (line with 549 nm maximum) but also from excited levels $n = 2$ and 3 (lines with $\lambda_{\max} = 531$ and 510 nm). Then the full width at haft maximum (FWHM) of the lines is small enough and equal to 66 meV. In Fig. 4, similar CL spectra for the 15 CdSe layer structure with 200 nm ZnSe barriers are presented

at $T = 14$ K. At low temperature the CL spectra from the track and outside it are more close than at RT. Nevertheless some differences in the form of spectral lines especially on the low-wavelength tail are observed. For clearness, a calculated spectrum difference is presented in Fig. 4 by the lower curve. There are several lines on this spectrum. The lines with $\lambda_{max} = 481$, 501 and 520 nm are likely to correspond to the lines with $\lambda_{max} = 510$, 531 and 549 nm at RT (Fig. 3(c)). The other lines with $\lambda_{max} = 454$, 462 and 472 nm may also have some analogues in the 465–500 nm spectral range at RT. However, it is difficult to do such a comparison because of other intense line with $\lambda_{max} = 465$ nm in this spectral range. To explain the observed spectral features we suppose that the CdSe layer outside the RHEED e-beam trace constitutes the layer with nonuniform thickness. This nonuniformity leads to very strong localization of excitons at low temperature. This localization should not be presented as formation of QDs with regular form. However, such formation is likely to occur under the e-beam irradiation. In this case some CdSe material stays in the layer form. Such CdSe layer is likely to be responsible for intense emission line with $\lambda_{max} = 465$ nm at $T = 14$ K. At low temperature the transport of excitons to the CdSe QDs is difficult because of the strong localization in the CdSe-related layer. At RT the transport is easier and the CdSe QD emission becomes predominant in the spectrum.

Mechanism of the e-beam influence on CdSe QDs formation is not clear yet. Probably, the e-beam stimulates the adatoms diffusion along the growth surface and/or plays role of a catalyst of chemical reaction. However, it is clear that rejection of such an effect may lead to mistake in interpretation of RHEED and optical measurements carried out on samples cut from different parts of a structure. On the other hand the observed effect may be used for purposeful improvement of QD formation procedure.

4. Conclusion

In conclusion the strong influence of the RHEED e-beam irradiation on CdSe QDs formation has been found. Large difference in CL spectra from the e-beam track and outside the track was observed. The emission spectrum of the CdSe QDs formed under e-beam has a set of lines due to excited levels in the QDs.

The work was partially supported by Russian Foundation for Basic Researches, grant No. 00-15-96624.

References

[1] Zh. I. Alferov, *Semiconductors* **32**, 3 (1998).
[2] N. G. Basov, E. M. Dianov, V. I. Kozlovsky, A. B. Krysa, A. S. Nasibov, Yu. M. Popov, A. M. Prokhorov, P. A. Trubenko and E. A. Shcherbakov, *Laser Physics* **6**, 608 (1996).
[3] K. Leonardi, H. Heinke, K. Ohkawa, D. Hommel, H. Selke, F. Gindele and U. Woggon, *Appl. Phys. Lett.* **71**, 1510 (1997).
[4] H. Kirmse, R. Schneider, M. Rabe, W. Neumann and F. Henneberger, *Appl. Phys. Lett.* **72**, 1329 (1998).
[5] C. S. Kim, M. Kim, S. Lee, J. K. Furdyna, M. Dobrowolska, H. Rho, L. M. Smith, H. E. Jackson and J. L. Merz, *J. Cryst. Growth* **214/215**, 761 (2000).
[6] S. V. Ivanov, A. A. Toropov, T. V. Shubina, S. V. Sorokin, A. V. Lebedev, I. V. Sedova, P. S. Kop'ev, G. R. Pozina, J. P. Bergman and B. Monemar, *J. Appl. Phys.* **83**, 3168 (1998).
[7] P. A. Trubenko, V. I. Kozlovsky and V. V. Roddatis, *J. Cryst. Growth* **214/215**, 671 (2000).
[8] K. Arai, T. Hanada and T. Yao, *J. Cryst. Growth* **214/215**, 703 (2000).
[9] J. J. Dudowski, C. Ni Allen and S. Fafard, *Appl. Phys. Lett.* **77**, 3583 (2000).
[10] Z. R. Wasilewski, S. Fafard and J. P. McCaffrey, *J. Cryst. Growth* **201/202**, 1131 (1999).

9th Int. Symp. "Nanostructures: Physics and Technology"
St Petersburg, Russia, June 18–22, 2001

Indium distribution in pseudomorphic InGaAs/(Al)GaAs quantum wells grown by MOCVD

A. A. Marmalyuk†, O. I. Govorkov‡, A. V. Petrovsky†, D. B. Nikitin†,
A. A. Padalitsa†, P. V. Bulaev†, I. V. Budkin† and I. D. Zalevsky†
† Sigm Plus, Moscow, Russia
‡ RDI Polyus, Moscow, Russia

Abstract. Indium atom distribution in InGaAs/(Al)GaAs quantum wells (QWs) grown by metal organic chemical vapor deposition (MOCVD) was systematically studied. High resolution grazing sputter angle Auger electron spectroscopy was used as a method of indium depth profile investigation. Broadening and shift to the surface of indium concentration profile in single QW, the increase of indium content in upper quantum well for close spaced QWs were found. It was observed that the use of AlGaAs barriers between QWs reduces indium surface segregation.

Introduction

In last decades InGaAs/AlGaAs quantum well heterostructures are widely used in optoelectronic and microwave applications. Fabrication of high quality devices demands flat and abrupt QW interfaces. Surface segregation of indium atoms during growth process causes indium enrichment of upper layer and broadened QW interfaces. These phenomena have been observed using second ion mass spectroscopy [1], Auger electron spectroscopy (AES) [2], reflection mass spectrometry [3], reflection high-energy electron diffraction [2, 4], ultraviolet photoemission spectroscopy [2, 5], transmission electron microscopy [6], X-ray diffraction [6, 7], photoluminescence [1], electrolyte electroreflectance [8]. Special growth procedures to improve interface abruptness are required. The main part of indium surface segregation investigation were carried out on molecular beam epitaxy grown InGaAs QW heterostructures. At the same time for device manufacturing the metal organic chemical vapour deposition large-scale production is necessary. In this work we study indium distribution in InGaAs/(Al)GaAs QWs grown by MOCVD. High depth resolution AES was chosen as an indium profile investigation method.

1. Experiments

The InGaAs/(Al)GaAs QW heterostructures were grown on n^+-GaAs substrates by low pressure MOCVD at Sigm Plus Co. The patented design homemade rectangular quartz tube horizontal reactor "SIGMOC-130" with gas flow rotation of susceptor was used. TEGa, TMAl and TMIn were used as group-III sources and arsine as a group-V source. Growth was performed at temperature 720 °C and pressure 60 torr on (001) with 0.5° misorientation toward the [110] GaAs substrates.

Five types of InGaAs/(Al)GaAs QW heterostructures were investigated. Sample A consisted of single InGaAs quantum well sandwiched between GaAs spacer layers and AlGaAs barrier layers (inset to Fig. 1(a)). Sample B consisted of two InGaAs quantum wells separated by GaAs barrier. QWs were sandwiched between GaAs spacer layers and

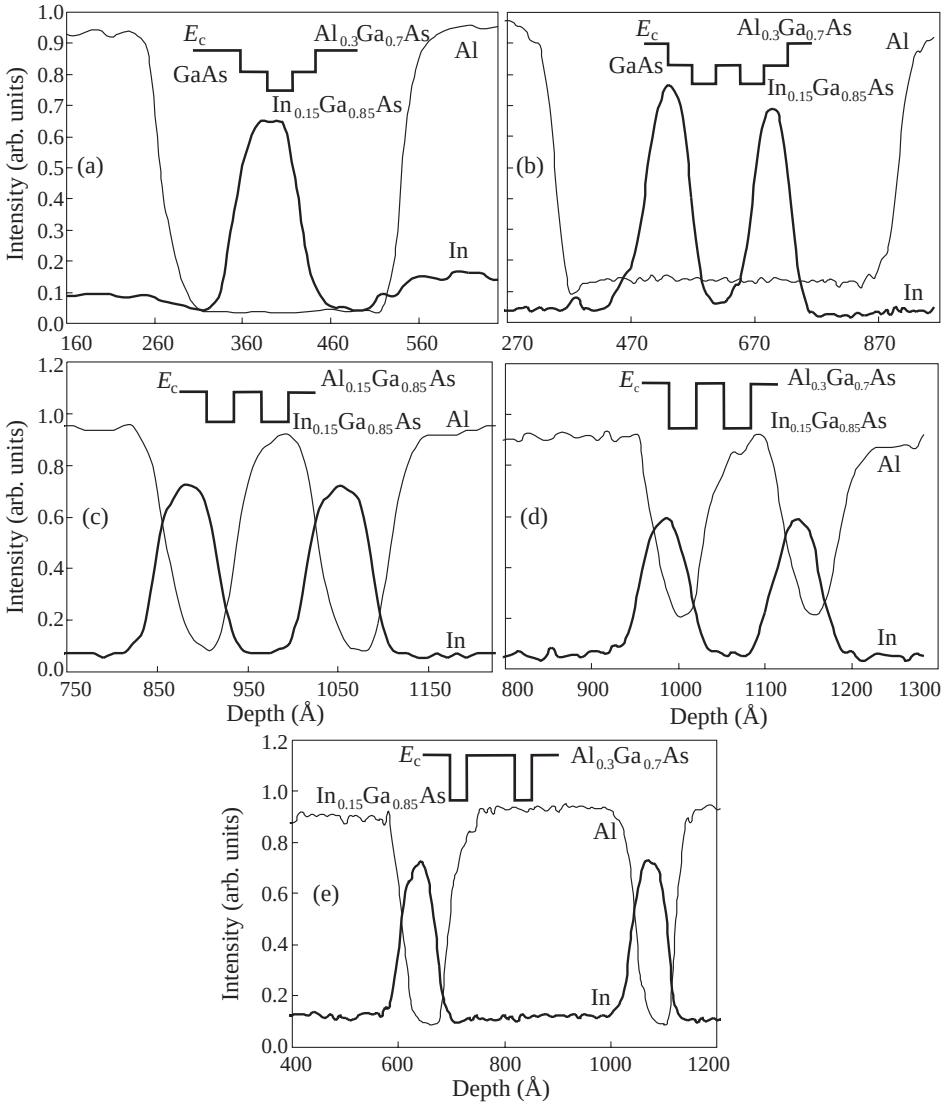

Fig. 1. AES depth profiles of: (a) sample A; (b) sample B; (c) sample C; (d) sample D; (e) sample E. The insets show conduction band edge of samples.

AlGaAs barrier layers (inset to Fig. 1(b)). Sample C was identical to sample B but GaAs layers were replaced by $Al_{0.15}Ga_{0.85}As$ layers (inset to Fig. 1(c)). Sample D was identical to sample C but $Al_{0.15}Ga_{0.85}As$ layers were replaced by $Al_{0.30}Ga_{0.70}As$ layers (inset to Fig. 1(d)). Sample E consisted of several periods of InGaAs/$Al_{0.30}Ga_{0.70}As$ superlattice (inset to Fig. 1(e)).

The InGaAs/(Al)GaAs QW heterostructures were investigated by AES. The AES depth profiling was performed at Scanning Auger Spectrometer PHI-560. In order to improve the depth resolution low energy Ar^+ ions (1 keV) and a grazing sputter angle profiling (80° with respect to surface normal) was used.

2. Results and discussion

AES depth profile of sample A demonstrates broadening of upper QW interface via indium surface segregation effect (Fig. 1(a)). During epitaxial growth indium atoms tend to move to upper layer [1, 2]. Therefore the peak of indium distribution is shifted toward growing surface in relation to GaAs/AlGaAs interfaces. Indium segregation length (λ) determined as $1/e$ decay length of In from AES profile is 42 Å. The segregation probability (R) of In atoms from topmost layer determined as $R = \exp(-d/\lambda)$ [1] is 0.93. Here d is half the lattice constant of GaAs. Surface segregation effect leads to narrowing of upper GaAs spacer layer. The thickness of upper spacer has a great influence on the threshold current of laser diodes based on InGaAs/AlGaAs QW heterostructures. Therefore the growth process must be corrected to obtain optimal thickness of spacers [9].

If indium segregation probability is rather high and distance between QWs is small the indium atoms from deeper QW can reach upper QW and increase indium content in it. This situation is illustrated by sample B AES profile (Fig. 1(b)). Distance between QWs is 100 Å and indium segregation length is 45 Å, $R = 0.94$. In this case two different phenomena occur. As in case of sample A the indium peak shift to growth direction is observed. Moreover upper QW is enriched with indium atoms segregated from deeper QW during growth process. The ratio of upper QW indium peak intensity to deeper QW indium peak intensity (I_{DQW}) is 1.15. This phenomenon may result in appearing of particularities in emission spectrum of laser diodes (especially for single mode devices) [10].

It was observed that the replacement of GaAs barriers and spacers by AlGaAs barriers (sample C and D) decreases indium segregation in QWs. Figure 1(c) shows that indium peak shift for is less than that one for sample B. AlGaAs barriers decrease indium carry over into upper layer. Hence indium segregation length and probability ($\lambda = 33$ Å, $R = 0.92$) decrease and both QWs have approximately the same indium content ($I_{\mathrm{DQW}} = 1.03$). The substitution of $Al_{0.15}Ga_{0.85}As$ (sample C) on $Al_{0.30}Ga_{0.70}As$ (sample D) lead to further decrease of both indium peak shift ($\lambda = 29$ Å, $R = 0.91$) and difference of indium content in QWs ($I_{\mathrm{DQW}} = 1.01$) (Fig. 1(d)).

However if distance between QWs is considerable as in case of sample E ($Al_{0.30}Ga_{0.70}As$ barrier thickness 350 Å) QWs have an identical indium content (Fig. 1(e)). The indium peak shift toward upper InGaAs/$Al_{0.30}Ga_{0.70}As$ interface still remains ($\lambda = 32$ Å, $R = 0.91$).

For receiving of identical InGaAs/(Al)GaAs QWs with sharp interfaces by MOCVD it is necessary to use rather thick AlGaAs barriers with high AlAs mole fraction. Developing InGaAs based heterostructures the indium surface segregation effect leading to observed phenomena should be taken into account.

Summary

In summary indium atoms distribution in InGaAs/(Al)GaAs QWs grown by MOCVD were systematically studied using grazing sputter angle AES. The shift of indium concentration profile toward the surface in single QWs and relative shift of composition in close spaced multiple QWs were found.

The influence of barrier materials on indium distribution in QWs was investigated. The increase of AlAs mole fraction in AlGaAs barrier resulted in the decrease of indium surface segregation.

References

[1] K. Muraki et al., *Appl. Phys. Lett.*, **61** 557 (1992).

[2] J. M. Moison et al., *J. Cryst. Growth*, **111** 141 (1991).
[3] Y. C. Kao et al., *J. Vac. Sci. Technol.*, **11** 1023 (1993).
[4] H. Toyoshima et al., *J. Appl. Phys.*, **75** 3908 (1994).
[5] R. Kaspi et al., *Appl. Phys. Lett.*, **67** 819 (1995).
[6] C. Frigeri et al., *Mater. Sci. Eng*, **28** 346 (1994).
[7] S. Fujimoto et al., *Jpn. J. Appl. Phys.*, **38** 1872 (1999).
[8] K. Chattopadhyay et al., *J. Appl. Phys.*, **81** 3601 (1997).
[9] P. V. Bulaev et al., *Abstracts of VIII European Conference on Applications of Surface and Interface Analysis (ECASIA'99), 4-8 October, 1999, Sevilla, Spain.* p. 478.
[10] I. D. Zalevsky et al., *Abstracts of X Intetnational Conference on Laser Optics 2000 (LO'2000). St. Petersburg, Russia, June 26-30.* p. 62.

9th Int. Symp. "Nanostructures: Physics and Technology"
St Petersburg, Russia, June 18–22, 2001

Thickness-roughness phase diagram of multilayer ferromagnet-antiferromagnet nanostructures and their hysteresis loops

A. I. Morozov†, A. S. Sigov† and A. V. Bobyl‡
† Moscow Institute of Radioengineering, Electronics, and Automation
78, Av. Vernadsky, Moscow 117454, Russia
‡ Ioffe Physico-Technical Institute, St Petersburg, Russia

Abstract. For a three-layer system consisting of two ferromagnetic layers separated by an antiferromagnetic interlayer it is shown that the stability region of single-domain ferromagnetic layers is technologically dependent on the ratio between the width of interface atomic steps and the thickness of layers. The thickness-roughness phase diagram has three regions: a collinear orientation of the magnetizations of ferromagnetic layers (1), oriented to each other at 90° (2), and a multidomain structure of ferromagnetic layers (3). The proposed approach can be compared with experiment by studying magnetic hysteresis loops against nanostructure layer thicknesses and their roughnesses owing to atomic steps on interfaces.

Introduction

The discovery of giant magnetoresistance [1] has stimulated interest in sandwiches consisting of alternating thin ferromagnetic (Fe, Co) and nonmagnetic (Cr, Cu) metallic layers.

An antiparallel or parallel orientation of adjacent ferromagnetic layer magnetization is energetically favorable when the number of atomic planes in the antiferromagnetic spacer is even or odd, as in Fig. 1(a) and 1(b) respectively. In the latter case an external magnetic field changes the antiparallel orientation of magnetization to parallel one. It is accompained by a drop in the electric resistance up to tens of percent.

An example of such a layered antiferromagnet is a chromium film with the thickness 32 Å $< d <$ 150 Å, in which at low temperature there appears a commensurate transverse spin-density wave [2]. A similar structure occurs when the iron impurities with the concentration exceeding 2% are introduced into chromium [3].

The roughness of the interfaces owing to atomic steps on them can make the uniform order parameter distribution energetically unfavourable, because the spin orientations of adjacent atoms on the step are opposite (Fig. 2). If the characteristic distance R between atomic steps exceeds some critical value, it is energetically favourable to break up the layers into domains with parallel and antiparallel orientation of magnetization [4].

In this paper we report a phase diagram of multilayer ferromagnet–antiferromagnet nanostructures with arbitrary ratios between the exchange interactions as well as between the layer thickness and the characteristic separation of steps at interfaces. The proposed approach can be used in the experiments studying the forms of magnetic hysteresis loops.

1. Description of the model

We shall investigate the disrtibution of order parameters in layers in the mean-field approximation [5, 6]. The parameters can be introduced for each layer as follows: the magnetization vector for ferromagnetic layers and the antiferromagnetism vector, equal the difference in

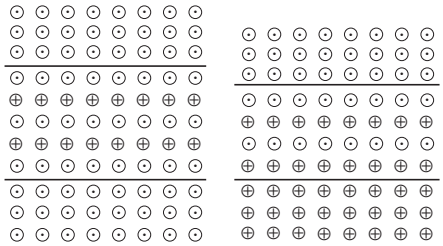

Fig. 1. Orientation of spins in a three-layer system consisting of two ferromagnetic layers and an antiferromagnetic interlayer in the case of smooth interfaces and odd (a) and even (b) number of atomic planes in the interlayer.

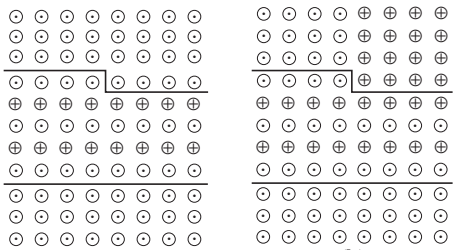

Fig. 2. Orientation of spins near the step at the interface for homogeneous distribution of the order parameters (a) and in the presence of a domain wall (b).

the magnetizations of sublattices, for antiferromagnetic layers. In case of sufficiently thin layers, the spins of atoms lie in the plane and, therefore, the orientation of the vector order parameter can be given by the angle θ that it forms with the x axis, which lies in the plane of the layer.

Far from Curie and Neel temperature, the exchange energy W_i caused by the interaction inside the ith layer can be written as

$$W_i = \frac{A_i}{2} \int (\nabla \theta_i)^2 \, \mathrm{d}V, \tag{1}$$

where the integral is taken over the volume of the layer, and A_i is the corresponding exchange constant. In the order of magnitude, $A_i \sim J_i S_i^2 / b$, where J_i is the exchange integral between adjacent atoms, b is the interatomic distance, and S_i is a mean spin of an atom.

The energy of the exchange interaction between adjacent layers with numbers i and $i + 1$ can be written

$$W_{i,i+1} = \pm B \int \cos(\theta_i - \theta_{i+1}) \mathrm{d}S, \tag{2}$$

where integration is performed over the layer interface, $B \sim J_{f,af} S_i S_{i+1} / b^2$, $J_{f,af}$ is the exchange integral between adjacent atoms belonging to different layers, and the sign " + " is opposite for different sides of an atomic step at the interface of the layers.

We divide all distances by b, assuming it to be virtually identical in both sorts of layers and divide all energies by the constant A_{af} for an antiferromagnetic layer. We introduce dimensionless parameters

$$\alpha = \frac{J_{f,af} S_f}{J_{af} S_{af}} \text{ and } \gamma = \frac{J_f S_f^2}{J_{af} S_{af}^2}, \tag{3}$$

where the subscripts f and af correspond to a ferro- and antiferromagnet.

By varying the parameters θ_i in (1), we obtain a differential equation that describes the distribution of the order parameter in a layer

$$\Delta \theta_i = 0. \tag{4}$$

A more careful procedure is needed to obtain correct conditions at the interface of layers. The energies of intra- and interlayer interactions must be varied in a discrete model, and then we must go to a continuum limit. As a result we get

$$\widetilde{\Delta}\theta_i - \frac{\partial\theta_i}{\partial n} = \mp\frac{B}{A_i b}\sin(\theta_i - \theta_{i+1}), \tag{5}$$

where $\widetilde{\Delta}$ is a two-dimensional Laplacian in the plane of a layer, $\partial/\partial n$ is the derivative in the direction of an outer normal to the boundary of the layer, and upper and lower signs in (5) correspond to those in (2).

Thus, to find the distribution of order parameters in a multilayer nanostructure, it is necessary to solve the system of linear differential equations (4) with non-linear boundary conditions (5). The distribution will depend on the values of α and γ, on the thickness of layers, as well as on the characteristic distance R between the steps at the interface of layers.

2. Phase diagram of a three-layer system

The results of model calculations can be shortly displayed on the phase diagram (Fig. 3). Phase 1 is characterized by the presence of static vortices at the interfaces and a collinear orientation of magnetization of ferromagnetic layers. In phase 2, the magnetizations of the ferromagnetic layers are homogeneous and, in the absence of an external magnetic field, are oriented to each other at 90°. Phase 3 corresponds to a multidomain structure of ferromagnetic layers.

The phase diagram can be compared with experimental data by studying the state of ferromagnetic layers using a magnetic-force microscope with various ratios between R and a and different temperatures, because α and γ are temperature-dependent.

3. Effect of a magnetic field: hysteresis loops

The magnetic flux reversal of ferromagnetic layers in phase 1 occurs virtually independently, and the hysteresis loops must coincide with those in a two-layer system consisting of one ferromagnetic and one antiferromagnetic layer. Here and below we assume that the maximum magnetic field is much less than the exchange field in the antiferromagnet. Therefore, the magnetization of antiferromagnetic layers can be neglected.

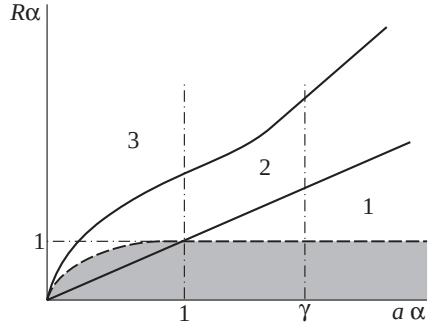

Fig. 3. Thickness-roughness phase diagram for a three-layer system consisting of layers of identical thickness. The region of weak distortion of order parameters is hatched.

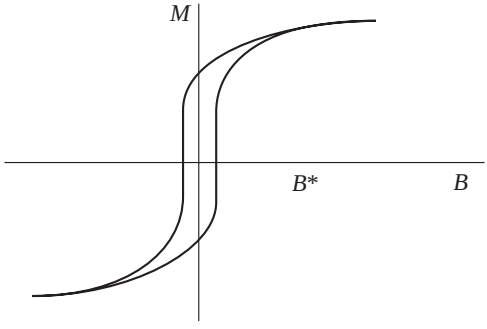

Fig. 4. Hysteresis loops of a three-layer nanostructure consisting of two ferromagnetic layers separated by an antiferromagnetic interlayer with identical thickness.

In phase 2, in a weak magnetic field that exceeds the anisotropy field in the plane of ferromagnetic layers, the magnetizations of ferromagnetic layers are oriented at 45° to the field while remaining virtually perpendicular to each other. In this case, the magnetization of the system is $M_{\max}/\sqrt{2}$, where $M_{\max}$ is the maximum magnetization of ferromagnetic layers. Its further evolution can be studied by minimizing the sum of the energies of ferromagnetic layer interaction with each other and with the magnetic field. The energy of a ferromagnetic layer in the magnetic field with inductance B is given by

$$W_f = -2\mu l B \cos\frac{\Psi}{2}, \tag{6}$$

where μ is the magnetic moment of an atom of a ferromagnet. For the angle Ψ between the magnetization of layers we have a transcendental equation

$$\frac{J_{af} S_{af}^2}{a}\left(\frac{\pi}{2}\Psi\right) = \mu l B \cos\frac{\Psi}{2}. \tag{7}$$

The characteristic field B^* (Fig. 4) at which there occurs a substantial magnetization change is

$$B^* \approx \frac{J_{af} S_{af}^2}{\mu a l}. \tag{8}$$

In phase 3, in a weak magnetic field, the domains with parallel orientation of the magnetization of layers are oriented along the field. In this case the system magnetization is $M_{max}/2$. The magnetizations of ferromagnetic layers in domains with antiparallel orientation in a zero field behave similarly to the magnetizations of the sublattices in the volume of an antiferromagnet. They are oriented virtually perpendicular to the external field.

As B increases, the angle Ψ between them decreases. The characteristic value of induction B^* of the external magnetic field in which the angle varies substantially, is found by the method similar to that for phase 2 and is given in order of magnitude by (8). Therefore, the form of the hysteresis loops in phases 2 and 3 differs only in the magnitude of magnetization in weak fields.

References

[1] M. N. Baibich, J. M. Broto, A. Fert, Nguyen van Dau, F. Petroff, P. Etienne, G. Creuzet, A. Friederich, J. Chazelas. *Phys. Rev. Lett.* **61**, 1472 (1988).
[2] A. Schreyer, C. F. Majkrzak, Th. Zeidler, T. Schmitte, P. Bodeker, K. Theis-Brohl, A. Abromeit, J. A. Dura, T. Watanabe, *Phys. Rev. Lett.* **79**, 4914 (1997).
[3] E. Fawcett, H. L. Albert, V. Yugalkin, D. R. Noakos, J. V. Yakhmi, *Rev. Mod. Phys.* **66**, 25 (1994).
[4] A. Berger and H. Hopster, *Phys. Rev. Lett.* **73**, 193 (1994).
[5] A. I. Morosov and A. S. Sigov, *JETP Lett.* **61**, 911 (1995).
[6] V. D. Levchenko, A. I. Morosov, A. S. Sigov and Yu. S. Sigov, *JETP* **87**, 985 (1998).

9th Int. Symp. "Nanostructures: Physics and Technology"
St Petersburg, Russia, June 18–22, 2001

Thermodynamic analysis of MBE growth of quarternary InGaAsN compounds

V. A. Odnoblyudov, A. Yu. Egorov, A. R. Kovsh, A. E. Zhukov,
N. A. Maleev and V. M. Ustinov
Ioffe Physico-Technical Institute, St Petersburg, Russia

InGaAsN has recently been proposed as a novel material for near-infrared lasers [1]. The merits of this material are due to the strong bowing in the bandgap of the GaAs-GaN alloy system, which offers the extension of the light emission range from GaAs-based structures to 1.3 μm and longer. At the same time, the band-offsets between InGaAsN and GaAs are larger than in the conventionally used InGaAsP system, which should greatly improve high-temperature performance of 1.3 μm lasers. The combination with the presently available GaAs/AlAs distributed Bragg reflector (DBR) technology could also lead to novel vertical cavity lasers for the long wavelength region.

Up to now the best results on GaInAsN QW laser structure were demonstrated by using the MBE as a growth technique [2–5]. However, there is a wide dispersion of the published characteristics of lasers based InGaAsN quantum wells. A little attention was paid to theoretical modelling and interpretation of the growth processes of the nitride-arsenide compound. The kinetic models of growth of GaInAsN quarternary alloys were developed in Ref. [6]. However, this approach did not predict a relationship between the growth parameters and the element composition of the growing film. And the question is still actual, how incorporation of indium into GaAsN compound affects the sticking coefficient of the nitrogen.

It has been shown recently that molecular beam epitaxy can be considered in the framework of thermodynamic description under assumption that equilibrium between the gas and solid phases is established on the surface of the crystal at the substrate temperature [7, 8]. In this work we present the thermodynamic analysis of the growth of nitrogen containing ternary and quaternary Ga(In)AsN compounds. The used model allows us to predict the nitrogen mole fraction in the grown alloys as a function of external growth parameters (III- and V-group element fluxes and growth temperature).

We use the thermodynamic model developed in [9] for the analysis of the MBE growth of the quaternary (ternary) nitrogen containing compounds. The acting mass law describes the equilibrium between the gas and solid phases. The substrate temperature is taken as the system temperature. The properties of quaternary compounds are described within the model of regular solution [10]. Nitrogen atoms are assumed to be the active species.

This model predicts that dependence of the nitrogen sticking coefficient on the substrate in the case of GaAsN growth has the range of constant value which is very close to unity, i.e. complete nitrogen incorporation into the growing film (Fig. 1). In the substrate temperature range of 480–550°C strong decrease of η with increasing T was observed. The dependence of the nitrogen mole fraction on the substrate temperature demonstrates the same behaviour as the dependence of the nitrogen sticking coefficient vs substrate temperature (Fig. 2), theoretical predictions are confirmed by the experimental data with the very good precision, which is of the order of accuracy of detecting the substrate temperature. The dependence of the nitrogen fraction in the GaAsN and in the InGaAsN layers on the

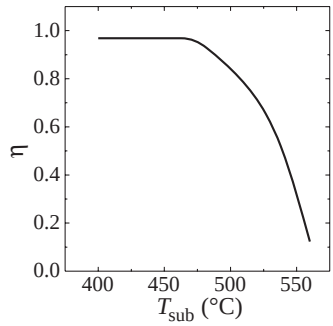

Fig. 1. The dependence of the nitrogen sticking coefficient, η, on the substrate temperature, T, for the growth of GaAsN. ($V = 1$ ML/sec, $F^0_{As2} = 1.5 \cdot 10^{15}$ cm^{-2}s^{-1}, $F^0_N = 1.2 \cdot 10^{13}$ cm^{-2}s^{-1}).

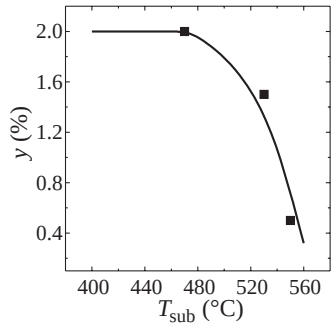

Fig. 2. The temperature dependence of the nitrogen mole fraction, y, for the growth of GaAsN. ($V = 1$ ML/sec, $F^0_{As2} = 1.5 \cdot 10^{15}$ cm^{-2}s^{-1}, $F^0_N = 1.2 \cdot 10^{13}$ cm^{-2}s^{-1}).

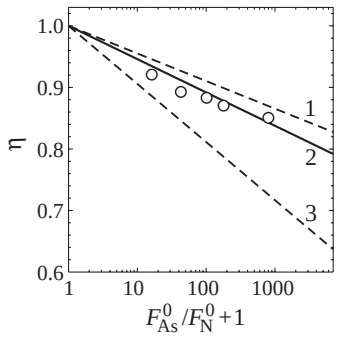

Fig. 3. The calculated sticking coefficient of the nitrogen, η, for GaAsN growth under varied flux of As and constant fluxes of N ($F^0_N = 1.2 \cdot 10^{13}$ cm^{-2}s^{-1}) and Ga ($V = 1$ ML/s), and fixed growth temperatures (curve 1 $T = 440^\circ$C, curve 3 $T = 490^\circ$C). Experimental data for $T = 440^\circ$C are shown as symbols and fitting curve 2.

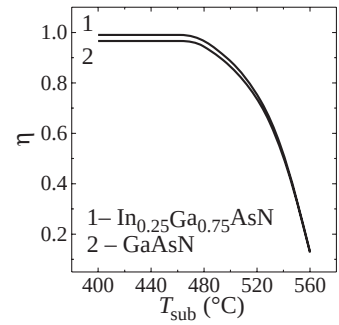

Fig. 4. The sticking coefficient of nitrogen, η, versus the growth temperature, T. ($V = 1$ ML/sec, $F^0_{As2} = 1.5 \cdot 10^{15}$ cm^{-2}s-1, $F^0_N = 1.2 \cdot 10^{13}$ cm^{-2}s^{-1}). Curve 1 illustrates the case of $In_{0.25}$GaAsN growth, curve 2 does the case of GaAsN growth.

growth rate was investigated (Fig. 3). In the range of high growth rates ($V > 1$ ML/s) nitrogen sticking coefficient is close to unity and nitrogen may be considered as a dopant element, i.e. $y(V)$ directly proportional to $1/V$ function. In the range of lower growth rates the nitrogen sticking coefficient becomes less than unity and $y(V)$ dependence deflects from the inverse proportionality. It should be taken into account in the case of the growth of In(Ga)AsN quantum dots because of typically small V in this case. It was found that the nitrogen sticking coefficient depends on the ratio of the V group elements fluxes (Fig. 4) and independent of the absolute values of those parameters in the range of typical atomic nitrogen fluxes. Thus, good agreement of the theoretical predictions and the experimental data was demonstrated. Moreover, it was shown that the nitrogen sticking coefficient is determined by the total group III elements flux, i.e. adding indium (keeping the constant

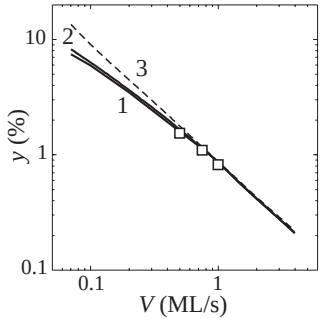

Fig. 5. The calculated dependencies of the nitrogen alloy content, y, versus growth rate, V, for the cases of growth of GaAsN (curve 1) and $In_{0.25}GaAsN$ (curve 2) with fixed $T = 450^{\circ}C$, $F^0_{As2} = 1.5 \cdot 10^{15}$ cm^{-2}s^{-1} and $F^0_N = 1.2 \cdot 10^{13}$ cm^{-2}s^{-1}. Curve 3 illustrates dependence which is directly proportional to the ratio of the atomic nitrogen external flux, F^0_N, to the total III-group element external flux (which is equivalent to the V).

total growth rate) does not change significantly nitrogen incorporation into the growing film (Fig. 5).

Acknowledgements

This work was supported by the Nato Science for Peace program (grant SfP-972484), CRDF (grant RE1-2221), and the Program of the Ministry of Science of Russia "Physics of Solid State Nanostructures" (grant 99-2034).

References

[1] M. Kondow, T. Kitatani, S. Nakatsuka, M. C. Larson, K. Nakahara, Y. Yazawa and K. Uomi, *IEEE J. Sel. Topics Quantum Electron.* **3**, 719–730 (1997).
[2] F. Huhnsdorf, J. Koch, S. Leu, W. Stolz, B. Borchert and M. Druminski, *Electron. Lett.* **35**, 571–572 (1999).
[3] D. Livshits, A. Yu. Egorov and H. Riechert, *Electron. Lett.* bf 36, 1381–1382 (2000).
[4] A. Yu. Egorov, D. Bernklau, D. Livshits, V. Ustinov, Zh. I. Alferov and H. Riechert, *Inst.Phys. Ser.* No.166: Chapter 6, pp. 359–362, paper presented at 26th Int. Symp. on Compound Semiconductors, Berlin, Germany, 22–26 August, 1999.
[5] V. M. Ustinov and A. E. Zhukov, *Semicond. Sci. Technol.* **15**, R41-R54 (2000).
[6] Z. Pan, L. H. Li, W. Zhang, Y. W. Lin and R. H. Wu, *Appl. Phys. Lett.* **77**, 214 (2000).
[7] P. S. Kop'ev and N. N. Ledentsov, *Semiconductors* **22**, 1729 (1988).
[8] A. Yu. Egorov, A. R. Kovsh, A. E. Zhukov, V. M. Ustinov and P. S. Kop'ev, *Semiconductors* **31**, 1153 (1997).
[9] V. A. Odnoblyudov, A. R. Kovsh, A. E. Zhukov, N. A. Maleev, E. S. Semenova and V. M. Ustinov, *Semiconductors* to be published (2001)
[10] A. S. Jordan and M. Ilegems, *J. Phys. Chem. Sol.* **36**, 329 (1975).

9th Int. Symp. "Nanostructures: Physics and Technology"
St Petersburg, Russia, June 18–22, 2001

A technique for fabricating InGaAs/GaAs nanotubes of precisely controlled length

V. Ya. Prinz, *A. V. Chehovskiy*, V. V. Preobrazenski, B. R. Semyagin and A. K. Gutakovsky
Institute of Semiconductor Physics, Lavrent'eva 13, 630090, Novosibirsk, Russia

Abstract. Single-crystal nanotubes of precisely controlled length were produced on a (110) cleaved facet of heterostructure. The selective MBE growth of a strained InGaAs/GaAs strip and its subsequent self-rolling were used. The proposed technique is capable of ensuring good reproducibility of all sizes and exact positioning of nanotubes.

Introduction

Achieving good reproducibility of sizes in nanotechnology, although being a problem of great significance, has not yet found a satisfactory solution. For instance, the electrical capacitance of a single-electron transistor Coulomb island, a key part of one of the most remarkable nonoelectronic devices, depends on the dimensions of this island and should be precisely controlled. In spite of a considerable number of advantageous properties of nanoobjects obtainable nowadays, the use of these objects in nanotechnology remains difficult. For instance, carbon nanotubes have poorly reproducible lengths, semiconductor mesostructures have rather irregular edges, etc. In this work we propose a technique which enables fabricating nanoobjects of precisely controllable dimensions. The method employs the possibility of self-rolling of a highly strained InGaAs/GaAs heterolayer in a tube-shaped scroll as the heterolayer detaches from substrate during selective etching of an AlAs sacrificial layer underlying it (Fig. 1). The diameter of the tube thus formed depends on the thickness of the heterolayer and on the mismatch of lattice parameters in it; hence, this diameter can be precisely controlled [1]. Recently, this possibility was used to obtain InGaAs/GaAs tubes with tube diameters as small as 2 nm and lengths as large as 1 mm. For successive use of such tubes in nanotechnology, it is required that their lengths be highly reproducible in the nanometer-size range. As evident from Fig. 1, in order the length L

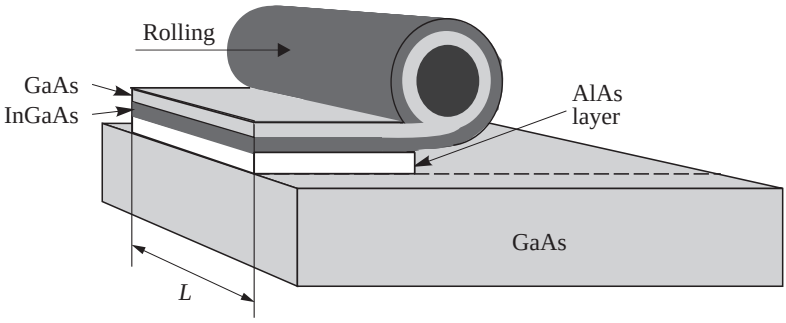

Fig. 1. A tube of length L is rolled from an InGaAs/GaAs heterolayer.

of an InGaAs/GaAs nanotube be controlled, it suffices that the nanotube be rolled from a plane InGaAs/GaAs bilayer of a precisely controlled width L.

Experemental

In this work, for the first time a InGaAs/GaAs bilayer of precise width to be rolled up in a tube was grown on a cleaved facet of a heterostructure using selective growth [2]. To grow such a bilayer, first, a heterostructure having a GaAs layer sandwiched between AlGaAs layers was cleaved to obtain a flat cleaved facet (see Fig. 2). The GaAs strip on the cleaved facet (edge of the GaAs layer in the initial heterostructure) has a precise preset width because the GaAs layer was grown by MBE (Fig. 2(a)). Second, an InGaAs/GaAs/AlAs heterolayer was selectively grown on that GaAs strip. No growth occurred on adjacent AlGaAs strips because they were oxidized. For preparetion of desired samples, the cleaved surface of the initial heterostructure was oxidized and then annealed at 620 °C to selectively remove oxide from the GaAs strip, the oxide on the AlGaAs strips remained intact (Fig. 2(b)).

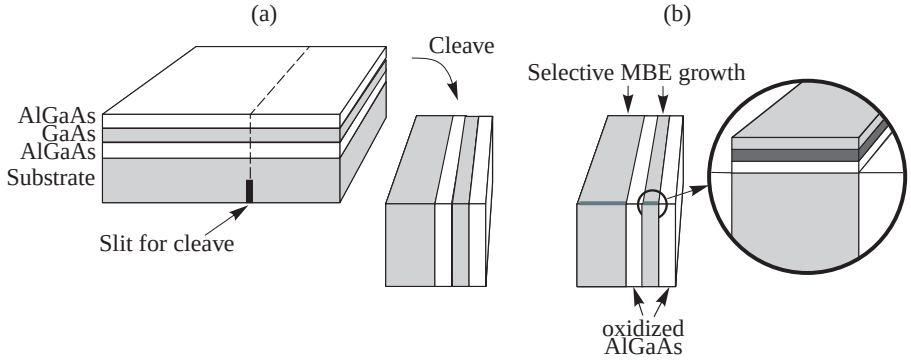

Fig. 2. (a) An initial herostructure has a GaAs layer sandwiched between two AlGaAs layers. The heterostructure is cleaved along a (110) cleavage plane, shown by the dashed line. (b) The cleaved facet thus obtained is subjected to oxidation followed by an anneal for evaporating oxide from the GaAs strip. Afterwords, a strained InGaAs/GaAs/AlAs heterolayer was selective grown on the GaAs strip.

Some experimental details are the following:

1. In order to obtain a desired facet of the heterostructure slits were prepared at desired places of the substrate with the help of optical lithography and liquid etching. Along these slits, cleavage was afterwards initiated.
2. To oxidize the cleaved facet it was exposed to atmospheric air or heated in wet nitrogen.
3. The heterostructures to be rolled were $In_{0.5}Ga_{0.5}As/GaAs$ heterolayer of various thicknesses were grown on the GaAs strip at 400 °C. The GaAs buffer layer of thickness 20 nm was grown before growth the sacrificial AlAs later.
4. The AlAs sacrificial layer was subjected to selective liquid etching in an HF-based solution. As a result of this etching, the InGaAs/GaAs heterolayer of a precise width rolled in a tube of precise length as shown in Fig. 1.

Results and discussion

In this manner, tubes with preset lengths ranging from 200 to 500 nm and with diameters ranging from 80 to 200 nm were obtained. Figure 3 shows an SEM photograph of an $In_{0.5}Ga_{0.5}As/GaAs$ (8 ML/4 ML) tube of length 400 nm and diameter 80 nm. Additional windows were preliminary made in the $In_{0.5}Ga_{0.5}As/GaAs$ heterolayer to open access for the etchant to the sacrificial layer. Therefore, this bilayer was rolling along to the longitudinal axis of the $In_{0.5}Ga_{0.5}As/GaAs$ strip.

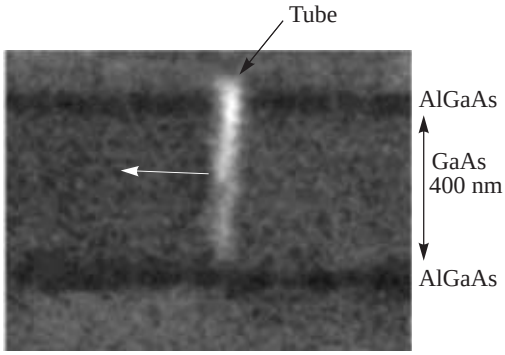

Fig. 3. An InGaAs/GaAs (8 ML/4 ML) tube of length 400 nm and diameter 80 nm prepared using the proposed technique.

In those cases in which no additional windows were made in the bilayer, this bilayer was rolling in the direction normal to its longitudinal axis. Figure 4 shows an SEM photograph of two such $In_{0.5}Ga_{0.5}As/GaAs$ tubes, 200 nm in diameter, occupying a final position of the center of the GaAs strip. As described above, these tubes were rolled up from different parts of a single 1 mm-wide InGaAs/GaAs heterolayer. As they were rolling during etching of the sacrificial layer, they moved one toward the other till they finally stopped. On their stoppage, the etch rate of the sacrificial layer beneath the tubes was drastically diminished because the access for the etchant to the AlAs layer was hampered. As a result, the tubes remained fixed to the GaAs cleaved edge approximately at its center. Thus, tubes prepared in this manner can be composed of a preset number of coils (one, in the case shown in Fig. 4), their final position being predetermined with good accuracy as well.

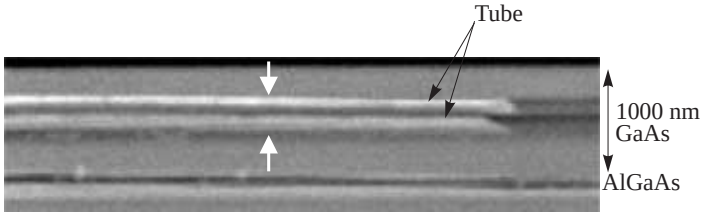

Fig. 4. Two coupled InGaAs/GaAs tubes 200 nm in diameter self-positioned in the center of the GaAs cleaved facet. White arrows show direction of the rolling.

If such nanotubes are composed of severals coils of a heterolayer, the surface atoms in adjacent coils appear to be in such a close proximity that they readily interact with one another. An HRTEM image shown in Fig. 5 shows that the wall of a two-coil tube prepared

by rolling an $In_{0.5}Ga_{0.5}As/GaAs$ (10 ML/5 ML) heterolayer grown on an (110) cleaved facet of a heterostructure is indeed a single-crystal one. The coils have stuck together quite perfectly, and no oxide was observed at the interface between them. On the other hand, the photographs revealed dislocations at the interface between coils caused by slight misorientation between crystallographic directions in them (chirality).

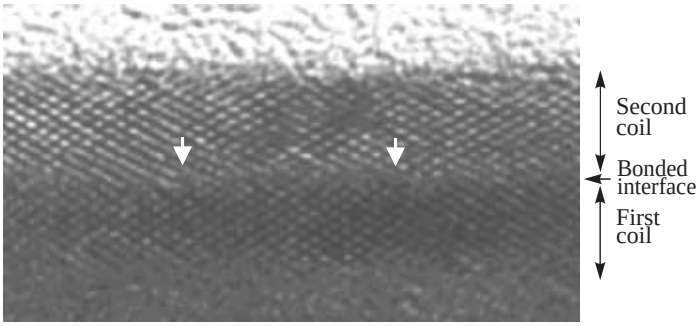

Fig. 5. An HRTEM cross-sectional image of the wall of a two-coil tube prepared by rolling an $In_{0.5}Ga_{0.5}As/GaAs$ (14 ML/5 ML) heterolayer grown on a (110) GaAs cleaved facet. The photograph confirms that the wall is indeed a single-crystal one. The coils stick together quite perfectly, no oxide being observed at the interface between them. The white arrows show dislocations at the bounded interface.

In conclusion, it may be argued that, using narrow GaAs strip, one can prepare even shorter nanotubes than those described in this work. Nanospirals and some other objects can be also obtained by selective growth of heterolayers on cleaved facets of other orientations, and also, for example, on the surfaces of V-shaped mesastructures.

Acknowledgements

This work was supported by the Russian Foundation for Fundamental Research (Grant 00-02-16764) and the Russian National Program “Physics of Solid State Nanostructures”.

References

[1] V. Ya. Prinz,V. A. Seleznev, A. K. Gutakovsky, A. V. Chehovskiy, V. V. Preobrazenskii, M. A. Putyato and T. A. Gavrilova, *J. Phys. E* **6**, 829 (2000).

[2] M .Natomi, Y. Kadota and T. Tamamura, *Jpn. J. Appl. Phys.* **34**, 1451 (1995).

9th Int. Symp. "Nanostructures: Physics and Technology"
St Petersburg, Russia, June 18–22, 2001

Anion incorporation in AlGaAsSb alloys grown by MBE

A. N. Semenov†‡, *V. A. Solov'ev*†, B. Ya. Mel'tser†, V. S. Sorokin‡,
S. V. Ivanov† and P. S. Kop'ev†
† Ioffe Physico-Technical Institute, St Petersburg, Russia
‡St Petersburg Electrotechnical University, St Petersburg, Russia

Abstract. An influence of MBE growth parameters (substrate temperature, total group V flux, and As/Sb flux ratio) on a composition of $Al_xGa_{1-x}As_ySb_{1-y}$ alloys ($x = 0.5$) as well as their structural quality have been studied in details. Using these data, As and Sb incorporation coefficients have been calculated in two different ways. An effect of the unintentional Sb incorporation in InAs layers is also discussed.

AlGaAsSb alloys are widely used as cladding layers of laser diodes emitting in mid-infrared spectral range [1]. Such lasers are of great importance for a large variety of applications, including remote trace-gas sensing, pollution monitoring, molecular spectroscopy [2] and optical communications using fluoride glass fibers [3].

One of the general problems in molecular beam epitaxy (MBE) growth, that has not been completely solved so far, is a compositional control of the multicomponent alloys with two volatile elements, in particular, the AlGaAsSb alloys involving As and Sb [4–6]. The available theoretical models of the MBE growth do not allow an unambiguous quantitative description of the composition dependence on growth parameters. An adequate thermodynamic model of anion-mixed alloy MBE growth is still questionable. The difficulties in composition control of the anion-mixed alloys are due to non-unity incorporation coefficients of the volatile elements. Most of the previous papers on MBE of III-(Sb, As) alloys consider situations when both antimony and arsenic cracking cells [4, 5] or the arsenic cracking cell in combination with a conventional antimony cell [6] are used as molecular beam sources. This paper reports on MBE growth of AlGaAsSb alloys using conventional arsenic and cracking antimony cells.

Three series of samples were grown on a RIBER 32P setup equipped with the antimony cracking cell RB-075-Sb providing mostly Sb_2 flux. Both InAs and GaSb substrates were used. The structures contain a 0.2 μm-thick InAs or GaSb buffer layer followed by a (0.5–1) μm-thick $Al_{0.5}Ga_{0.5}As_ySb_{1-y}$ layer. The samples of series A were grown at different As fluxes and other equal growth conditions. In the samples of series B and C the varying parameters were the Sb flux and the substrate temperature, respectively, while the As flux was kept constant and high enough to provide As/III > 1 conditions.

The AlGaAsSb composition was measured by electron probe microanalysis (EPMA) and verified through the simulation of high resolution X-ray diffraction (XRD) rocking curves using the EPMA data on Al and Ga content. Additionally, the compositional profiles of the structures were obtained by SIMS.

Figure 1 presents XRD rocking curves of one of the InAs/AlGaAsSb structures. Three main peaks are clearly resolved in both curves. Besides a dominating InAs substrate peak, there is an intensive peak located at ~100 arcsec, which is attributed to the AlGaAsSb layer nearly lattice-matched to InAs ($\Delta a/a < 5 \times 10^{-4}$). The small difference in FWHM values of the corresponding peaks for both $\omega-$ and $\theta - 2\theta$ rocking curves as well as an

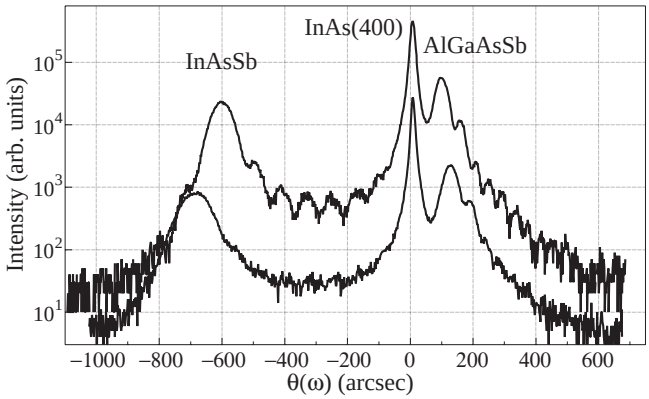

Fig. 1. The (004) ω- (bottom) and $\theta-2\theta$ (upper) XRD rocking curves of the InAs/$Al_{0.5}Ga_{0.5}As_{0.13}Sb_{0.87}$ structure.

existence of clearly visible interference fringes confirm the high structural quality and plain morphology of this layer. The third weaker peak at $\sim$(620−680) arcsec, that is absent in the samples grown on GaSb substrates as well as grown using conventional Sb cell, seems to be attributed to the InAs buffer layer contaminated with Sb. The layer thickness estimated from the period of the third $\theta-2\theta$ peak fringes is consistent well with that of the buffer layer. The presence of Sb in the buffer layers was confirmed by SIMS measurements. An estimation of the $InAs_{1-y}Sb_y$ alloy composition from the XRD peak position gives $y \sim 0.05$. The similar effect of the uncontrolled As incorporation into Sb-based compounds was observed earlier [7]. In our case, the main reason of the unintentionally Sb incorporation into As-based layers is probably a significantly increased reactivity of Sb_2 dimer molecules as compared to Sb_4 ones.

It was found from EPMA studying of the samples of series A, that As flux variation within a wide range does not affect the composition of AlGaAsSb, provided that it is grown at the Sb_2 flux large enough to keep V-stabilized growth conditions. The results of EPMA measurements of the samples of series B and C are summarized in Fig. 2 and Fig. 3, respectively. One should note that the samples grown at high growth temperature ($T_S \sim 520^\circ$C) and high V/III ratio (high As flux) demonstrate much worse morphology and structural quality. The minimum beam equivalent pressure (BEP) of Sb flux corresponding to Sb-stabilized growth of $Al_{0.5}Ga_{0.5}Sb$ was 1.7×10^{-6} and 2.2×10^{-6} Torr at T_S of 480°C and 520°C, respectively, as shown by vertical dashed lines in Fig. 2.

Some of the $Al_{0.5}Ga_{0.5}As_ySb_{1-y}$ layers were grown with the composition inside a thermodynamic miscibility gap ($y = 0.3$ and 0.5). The possibility of MBE growth of $Al_xGa_{1-x}As_ySb_{1-y}$ alloys lattice-matched to InP (also inside the thermodynamic instability region) with good structural and optical properties has been recently demonstrated [4]. On the other hand, the authors of Ref. [5] could not penetrate deep in the miscibility gap and assumed that the Al(As,Sb) miscibility gap manifests itself in a shift in As composition due to a rejection of excess As, rather than in phase separation. Therefore, the reliability of our data for $y \succ 0.3$ does not seem to be high.

In contrast to thermodynamic predictions, the experimental data demonstrate the dominant Sb incorporation in AlGaAsSb layers even at rather low Sb fluxes. Such incorporation behavior of the volatile elements can be explained by a strong difference in kinetically controlled As and Sb incorporation coefficients, defined as a ratio of a number of atoms incorporated into the grown layer to a total number of incident atoms. Thus, to be correct any

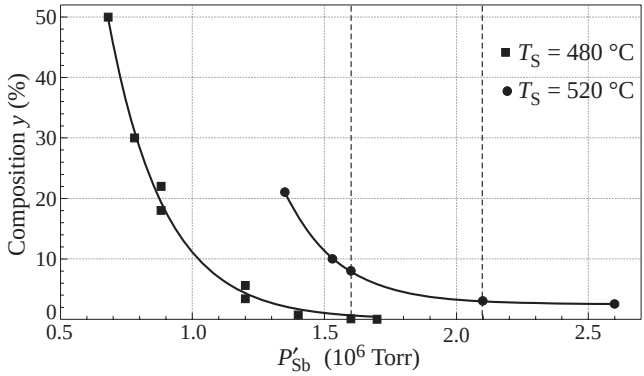

Fig. 2. As content as a function of Sb BEP at two different growth temperatures.

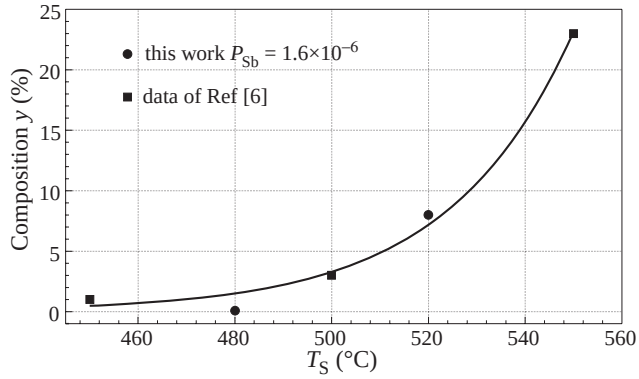

Fig. 3. As content as a function of the growth temperature.

thermodynamic model of MBE should take into account the kinetics processes on growth surfaces.

The analysis of the AlGaAsSb composition dependencies was carried out within the framework of kinetic conception only, using expression for the As and Sb incorporation coefficients as the main parameters affecting the alloy composition.

The dependence of composition on a flux ratio, taking into account the incorporation coefficients of the elements, can be written as follows

$$y = \left[1 + \frac{1}{2\alpha^N_{\mathrm{As}}} \frac{\eta_{\mathrm{As_4}}}{\eta_{\mathrm{Sb_2}}} \left(\frac{P'_{\mathrm{Sb_2}}}{P'_{\mathrm{As_4}}}\right)\right]^{-1} \tag{1}$$

where $\alpha^N_{\mathrm{As}} = \alpha_{\mathrm{As}}/\alpha_{\mathrm{Sb}}$ is a relative As incorporation coefficient, P'_i is a BEP of the respective molecular fluxe and η_i is a sensitivity coefficient of the Bayard–Alpert ion gauge [8].

To calculate the absolute incorporation coefficients of the elements, the well-known expression for the fluxes condensed on a substrate has been used [9]. Then the As and Sb incorporation coefficients can be expressed as

$$\alpha_{\mathrm{As}} = \frac{y v_g \pi r^2 \sqrt{2\pi R M_{\mathrm{As_4}} T_{\mathrm{As}}}}{a^3 S^{ev}_{\mathrm{As}} P_{\mathrm{As_4}} S_S \cos(\varphi) \sin(\Theta) N_A}, \alpha_{\mathrm{As}} = \frac{2(1-y) v_g \pi r^2 \sqrt{2\pi R M_{\mathrm{Sb_2}} T_{\mathrm{Sb}}}}{a^3 S^{ev}_{rmSb} P_{\mathrm{Sb_2}} S_S \cos(\varphi) \sin(\Theta) N_A} \tag{2}$$

where r is a distance between substrate and cell orifice, φ is an angle between the direction of molecular beam and the normal to cell aperture, Θ is an incident angle; N_A is the

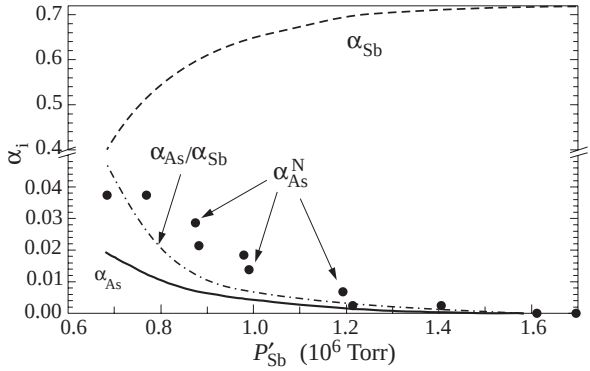

Fig. 4. As and Sb absolute and relative incorporation coefficients versus Sb BEP.

Avogadro number, M_i is molar mass of evaporated element, S_i^{ev} and S_s are areas of a cell orifice and a substrate, P_i is an equilibrium pressure in the cell, v_g is the alloy layer growth rate and a is a lattice constant.

As a result the calculated dependencies of As and Sb incorporation coefficients on Sb BEP are presented in Fig. 4. As shown in Fig. 4, the dependencies of relative As incorporation coefficient on Sb BEP calculated by two different ways, using expression (1) and expressions (2), are in good agreement. A small discrepancy appears to be due to some inaccuracy in estimation of equilibrium pressures and in cell temperature measurements using a thermocouple. The absolute values of As and Sb incorporation coefficients have been found to be much smaller than unity, with the α_{As}/α_{Sb} ratio exceeding 10.

In summary, both the experimental data and theoretical calculations demonstrate strong dependencies of AlGaAsSb alloy composition on growth temperature and Sb flux. The alloy composition has been found to be efficiently controlled by varying only the Sb BEP with Al, Ga, As BEPs and growth temperature kept constant.

Acknowledgements

This work was supported in part by RFBR Grants 01-02-17933, 00-02-17047, 00-02-17043, ISTC Grant No 007036, CRDF Grants No RP1-2270 and No RP1-2265. The authors acknowledge to Dr M. Baidakova for XRD and Dr. B. Ber for SIMS measurements.

References

[1] P. S. Dutta, H. L. Bhat and Vikram Kumar, *Appl. Phys* **81**, 5821 (1997).
[2] P. Werle, R. Mucke, F. D'Amato, L. Lancia, *J. Appl. Phys.* **B 67**, 307 (1998).
[3] J. Lucas, *Infrared Phys*, **25**, 277, (1985).
[4] G. Almuneau, E. Hall, S. Mathis, L. A. Coldren, *J. Cryst. Growth*, **208**, 113 (2000).
[5] H. R. Blank, S. Mathis, E. Hall, S. Bhargava, A. Behres, M. Heuken, H. Kroemer, V. Narayanamurti, *J. Cryst. Growth* **187**, 18 (1998).
[6] A. Bosacchi, S. Franchi, P. Allegri, V. Avanzini, A. Baraldi, R. Magnanini, M. Berti, D. De Salvador, S. K. Sinha, *J. Cryst. Growth*, **201/202**, 858 (1999).
[7] M. Yano, M. Ashida, A. Kawaguchi, Y. Iwai and M. Inoue, *J. Vac. Sci. Technol.*, **B 7**, 199 (1989).
[8] V. V. Preobrazhenskii, M. A. Putyato, O. P. Pchelyakov, B. R. Semyagin, *J. Cryst. Growth* **201/202**, 170 (1999).
[9] L. Massel, R. Glang, *Thin Film Technology (in Russian)*, 1977 (Soviet Radio, Moscow).

9th Int. Symp. "Nanostructures: Physics and Technology"
St Petersburg, Russia, June 18–22, 2001

Nitrogen-activated phase separation in InGaAsN/GaAs heterostructures grown by MBE

I. P. Soshnikov[1], N. N. Ledentsov[1], B. V. Volovik[1], A. Kovsh[1], N. A. Maleev[1], S. S. Mikhrin[1], O. M. Gorbenko[6], W. Passenberg[2], H. Kuenzel[2], N. Grote[2], V. M. Ustinov[1], H. Kirmse[3], W. Neuman[3], P. Werner[4], N. D. Zakharov[4], D. Bimberg[5] and Zh. I. Alferov[1]

[1] Ioffe Physico-Technical Institute, St Petersburg, Russia
[2] Heinrich-Hertz-Institut für Nachrichtentechnik, Berlin, Germany,
[3] Humboldt Universität Berlin, Insitut für Physik, 10115 Berlin, Germany
[4] Max-Plank-Institut für Mikrostrkturphysik, 06120 Halle, Germany
[5] Institut für Festkörperphysik, TU Berlin, 10623 Berlin, Germany
[6] Institute for Analytical Instrumentation, St Petersburg, 198103 Russia

Abstract. InGaAsN insertions in a GaAs matrix grown by molecular beam epitaxy (MBE) demonstrate a pronounced effect of phase separation even at relatively low indium and nitrogen concentrations. Cross-section high-resolution transmission electron microscopy (TEM) images, processed using a specially-developed software, demonstrated an effect of nitrogen decoration of InAs-rich regions in the structures studied. Formation of ordered structures of compositional domains has been revealed in plan-view TEM images.

Introduction

We report on studies of InGaAsN insertions in a GaAs matrix using transmission electron microscopy (TEM), high-resolution TEM (HRTEM) and HRTEM image processing. InGaAsN-based structures recently attracted much attention due to the possibility to cover the long wavelength spectral range (1.3 and 1.55 μm) using GaAs substrates [1]. Several groups have reported on the fabrication of InGaAsN/GaAs based devices using molecular beam epitaxy (MBE) [2–7] or MOCVD [8, 9] growth techniques. At the same time the main growth mechanisms and the internal structure of these insertions is still not well understood.

1. Experimental

In this work we study 6 nm-thick InGaAsN insertions in a GaAs matrix grown by MBE using RIBER 32 machine with RF nitrogen source on (100)-oriented GaAs substrates. We used a special pneumatic separator between the vacuum chamber and the nitrogen source. This allowed us to control plasma-assisted epitaxy on a very short time scale (around 1 s), which is much shorter than the transient processes in the RF plasma itself. Changing the power of the RF plasma source varied nitrogen content. RHEED was used for in situ characterization of the surface morphology. The samples' descriptions are listed in Table 1.

Specimens for TEM study were prepared by standard methods using 4 keV Ar^+ ion beam etching. HREM images were processed using the image-processing technique [10] based on the evaluation of the local lattice parameter. Photoluminescence was excited using a 514.5 nm line of Ar^+ laser at 300 K and detected with a cooled Ge photodiode.

Table 1. Nominal parameters of the structures studied.

Sample	In-content	Power of the nitrogen	Size of the lateral	RHEED	PL peak energy (eV)
1	0.25	0	Not observed	streaky	1.214
2	0.25	75 W	Not observed	streaky	1.130
3	0.25	160 W	∼35 nm	dashed	1.020
4	0.30	75 W	∼30 nm	dashed	1.133
5	0.30	115 W	∼25 nm	spotty	1.068
6	0.35	0	—	spotty	—
7	0.35	75 W	∼25 nm	spotty	1.06
8	0.40	75 W	∼30 nm	spotty	1.080

2. Results and discussion

The results of TEM studies indicate that the samples can be roughly divided in two main groups. The samples with low indium ($x \sim 0.25$) and/or nitrogen ($y \sim 75$ W or less) contents emitting at and below 1 μm at room temperature demonstrate layer-like contrast in TEM with uniform interfaces. HRTEM image of such a structure is shown in Fig. 1(a). The image processing of the HREM image (Fig. 1(b)) shows nevertheless the modulations of the local interplane distance a_{200}, which is defined by an expression

$$-0.03 \leq \delta a_{\mathrm{InGaAsN}}/a_{\mathrm{GaAs}} \leq 0.05 \tag{1}$$

where $\delta a_{\mathrm{InGaAsN}} = a_{\mathrm{InGaAsN}} - a_{\mathrm{GaAs}}$ is different of local interplane distances of InGaAsN and of matrix.

The range of values of the local lattice parameter fits to the whole range of the lattice parameters of the InAs-GaAs system, pointing to severe InAs local accumulation effect also

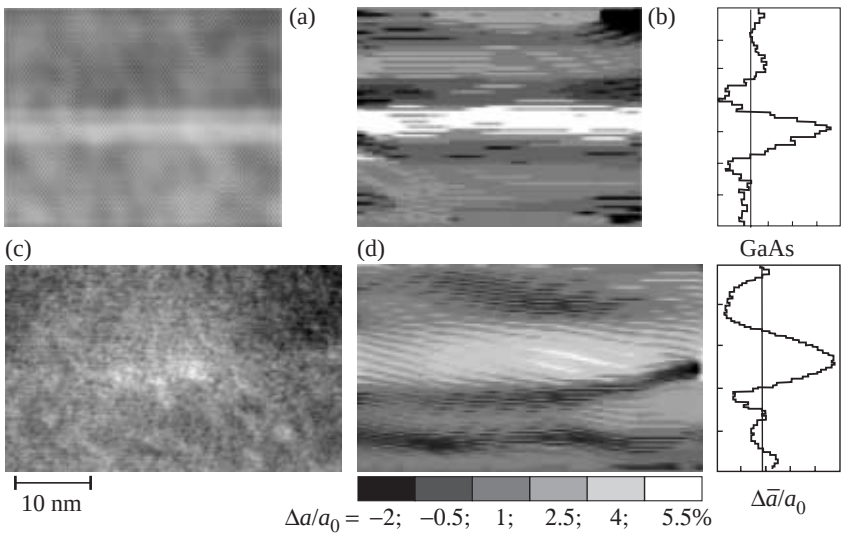

Fig. 1. HREM images of $In_{0.25}Ga_{0.75}As_{0.994}N_{0.006}/GaAs$ (a) and $In_{0.30}Ga_{0.70}As_{0.99}N_{0.01}/GaAs$ (b) insertions and their tone-coded maps of local interplane distance in vertical direction (c, d, respectively).

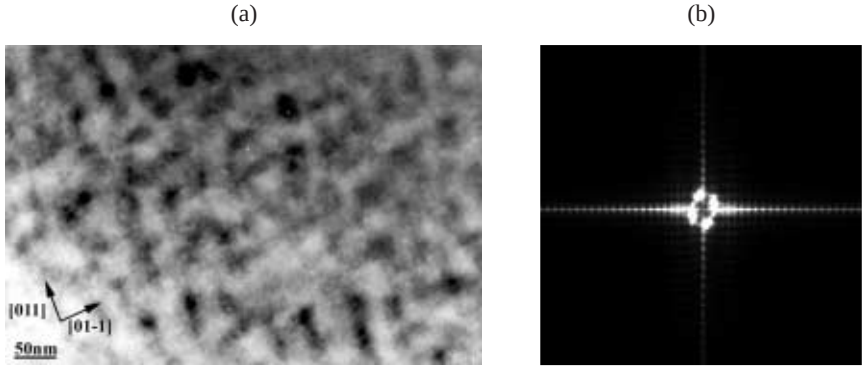

Fig. 2. Plan view TEM image of $In_{0.25}Ga_{0.75}As_{0.99}N_{0.01}/GaAs$ (a) structure and its Fourier transformation image (b).

in the case of planar layers ($-0.005 \leq \delta a_{\mathrm{InGaAsN}}/a_{\mathrm{GaAs}} \leq 0.08$). Even more interesting, negative negative values of $\delta a_{\mathrm{InGaAsN}}$ are found, as opposite to the InGaAs-GaAs quantum well or quantum dot case. These regions are accumulated around the InAs-rich region. One may speculate that the effect originates either from perculiarities of growth (switching on or off of the nitrogen plasma source prior to the InGaAsN growth, or after it) or form the self-organized strain compensation effect related to the phase separation of InAs and GaN phases. In the small-composition case the N-rich regions are formed near the top and bottom interfaces. We note that in-plane compositional nonuniformities (2% modulation of the lattice parameter in vertical direction) are revealed in the InGaAsN layers with low indium content and nominally lower average lattice mismatch with the substrate, as compared to the stable InGaAs quantum wells with similar indium composition. This indicates the nitrogen-activated phase separation process occurs despite of the small average lattice mismatch with the substrate. In the group of the samples, emitting at and beyond 1.1 μm at 300 K, in addition to compositional modulations, a very pronounced modulation of the layer thickness was observed [2, 3]. The group includes samples with composition of $x = 0.3$ and composition $x = 0.25$ and $y \sim 75$ W. A HREM image a the map of local interplane distance are demonstrated in Fig. 1(c),(d). One can see that the effective height of the contrast Is greatly increased as compared to the nominal well width. This is typical for self-organized InGaAs quantum dot structures. A typical size of the modulation is given in Table 1 and is equal about 30 nm. Processed maps of local interplane distance indicate also regions with a small value of lattice parameter ($\delta a_{\mathrm{InGaAsN}}/a_{\mathrm{GaAs}} \sim -0.03$). This again indicates nitrogen decoration. The nitrogen-rich region decorates In-rich quantum dot forming a curved shell-like arrangement. Increase in the nitrogen content for the same indium concentration causes stronger effect of phase separation. Plan view TEM image and its Fourier transformation of an indium-rich InGaAsN insertion are given in Fig. 2. One can see that the structure is composed of nanodomains with a typical size about 20–30 nm. The results agree well with the TEM data in cross-section geometry. The density of the nanodomains is about $p \sim 10^{10}$ cm^{-3}. Fourier transform images contain ordered spots indicating partial ordering of the domain size and their orientation.

PL spectra of the structures studied are given in Fig. 3. The spectra contain an InGaAsN-related line at 1.0–1.2 eV. The width of the PL peak of samples with the interface modulation (80–90 meV) is increased as compared to that in layer-like samples, as expected from the nanodomain formation [11].

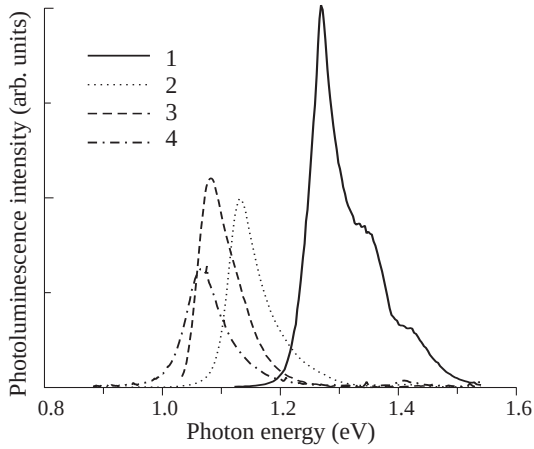

Fig. 3. PL spectra of InGaAsN/GaAs structures. 1—$x = 0.25$, $y \sim 0$ W, 2—$x = 0.25$, $y \sim 75$ W, 3—$x = 0.30$, $y \sim 160$ W, 4—$x = 0.4$, $y \sim 75$ W.

3. Conclusions

InGaAsN/GaAs insertions grown by MBE growth have been investigated. In addition to the transition to laterally-corrugated growth we found an effect of nitroden decoration of the In-rich regions.

Acknowledgments

Authors are greatly Dr. I. Haehnert and D. Lucht for help to TEM specimen preparation. Parts of this work are supported by NATO SfP programme, CRDF and the Russian Foundation for Basic Research.

References

[1] G. Steine, H. Riechert and A. Yu. Egorov, *Electr. Lett.* **37**, 93 (2001).
[2] B. V. Volovik, A. R. Kovsh, W. Passenberg, H. Kuenzel, N. N. Ledentsov and V. M. Ustinov, *Tech. Phys. Lett.* **26**, 443 (2000).
[3] B. V. Volovik, A. R. Kovsh, W. Passenberg, H. Kuenzel, N. Grote, N. A. Cherkashin, Yu. G. Musikhin, N. N. Ledentsov, D. Bimberg and V. M. Ustinov, *Semicond. Sci. Techn.* **16**, (2001), in print.
[4] T. Miyamoto, K. Takeuchi, T. Kageyama, F. Koyama and K. Iga, *J. Cryst. Growth* **197**, 67 (1999).
[5] S. Francoeur, G. Sivaraman, Y. Qiu, S. Nikishin and H. Temkin, *Appl. Phys. Lett.* **72**, 1857 (1998).
[6] A. Yu. Egorov, A. E. Zhukov, A. R. Kovsh, V. M. Ustinov, V. V. Mamutin, S. V. Ivanov, V. N. Zhmerik, A. F. Tsatsul'nikov, D. A. Bedarev and P. S. Kop'ev, *Tech. Phys. Lett.* **24**, 942 (1998).
[7] S. R. Kurtz, A. A. Alleman, E. D. Jones, J. M. Gee, J. Banas, *Appl. Phys. Lett.* **74**, 729 (1999).
[8] Z. Pan, T. Miyamoto, D. Schlenker, S. Sato, F. Koyama, Kiga, *J. Appl. Phys.* **84**, 6409 (1998).
[9] S. Sato and S. Satoh, *J. Cryst. Growth* **192**, 381 (1998).
[10] I. P. Soshnikov, O. M. Gorbenko, A. O. Golubok and N. N. Ledentsov, *Semiconductors* **35**, 347 (2001) .
[11] D. Bimberg M. Grundmann and N. N. Ledentsov, *Quantum Dot Heterostructures*, J. Wiley, 1999.

9th Int. Symp. "Nanostructures: Physics and Technology"
St Petersburg, Russia, June 18–22, 2001

Effect of species-dependent surface atomic mobility on pattern selection during alloy growth

A. N. Starodubtsev[1] and V. A. Shchukin[1,2]
[1] Ioffe Physico-Technical Institute, St Petersburg, Russia
[2] Technische Universität Berlin, 10623, Germany

Spontaneous formation of nanometer-scale composition-modulated structures is a common phenomenon for III–V and II–VI semiconductor alloys [1]. These structures are mostly formed in open systems during the epitaxial growth. It is typical for semiconductor epitaxial growth that bulk diffusivity of atoms is negligibly small compared to the surface diffusivity. For an alloy growth, composition modulation in every atomic layer is being formed at the surface during the growth of this layer and persists when this layer is buried by the subsequent layers. Modulations of composition from the entire thickness of the epitaxial film affect, via long-range strain field, the surface migration of atoms [2, 3, 4].

For alloys grown on a (001)-substrate, most of observed composition-modulated structures are 2D ones modulated in both [100] and [010] directions. The possible directions of modulation can be explained by the linear stability analysis of the homogeneous alloy growth. If the elastic anisotropy is the dominant effect compared to the surface diffusion anisotropy [4], the instability occurs for the first time in elastically soft directions [100] and [010]. Then, however, the linear stability analysis does not address the question of the selection between 1D and 2D structures. To describe the final modulated structure, a non-linear theory is needed.

In our earlier papers [5] we considered the effect of non-linear coupling between compositional and morphological instabilities on steady-state structures formed during epitaxial growth. It was shown that at sufficiently low growth velocities 2D steady-state structures form, modulated in both [100] and [010] directions. This effect is similar to that for strained islands in lattice-mismatched systems where 2D structures such as an array of pyramids provide more efficient elastic relaxation than 1D structures such as an array of prisms [6]. However, for lattice-matched systems this effect is important only for sufficiently large periods of the resulting structures, $d > 700$ Å. This is beyond typical scales where modulated structures could serve as quantum dots.

Among other non-linear effects which may lead to the formation of 2D structures the effect of species-dependent atomic mobility [7] is the most plausible. The Arrhenius-type behavior of the diffusion coefficient, $D(T) = D_0 \exp(-E_a/T)$, together with the dependence of the activation energy on composition $E_a = E_a(c)$ results in very strong dependence of diffusion coefficient on composition. In the present paper we consider the effect of this dependence on steady-state structures. This effect is purely kinetic and has no analogs in thermodynamics.

We consider the growth of an alloy $A_{1-c}B_cC$ by molecular beam epitaxy on an atomically rough surface. The alloy is *lattice-matched on average* to the (001)-substrate. The growth proceeds via deposition of atoms on the surface, surface migration of atoms in a stress- and composition-dependent chemical potential, and incorporation of atoms into the growing crystal, desorption being neglected. Let the composition be equal to $c(\mathbf{r}) = \bar{c} + \phi(\mathbf{r})$, the average composition being $\bar{c} = 1/2$, and, for simplicity, the surface profile be taken to be flat $h(x, y) = vt$, where v is the average growth velocity controlled

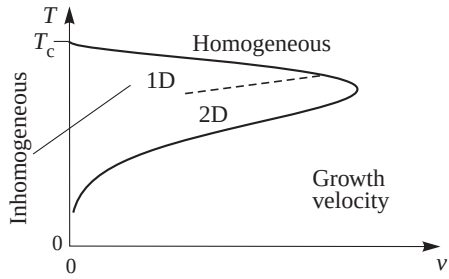

Fig. 1. Steady-state diagram containing the regions of homogeneous growth, of the growth of a 1D structure, and of the growth of a 2D structure.

by the deposition flux. The kinetic equation describes the evolution of composition fluctuations $\phi(\mathbf{r})$ at the advancing surface

$$\frac{\partial \phi}{\partial t} = \nabla_i \left[\frac{D(\phi)}{T} \nabla_i \frac{\delta F}{\delta \phi} \right] - \frac{v}{a} \phi \,. \tag{1}$$

Here $F = F_{\text{chem}} + F_{\text{grad}} + F_{\text{elast}}$ is the total Helmholtz free energy, where $F_{\text{chem}} \sim \int f_{\text{chem}}(c) dV$ is a chemical free energy of the alloy depending locally on the alloy composition, F_{grad} is a gradient energy, $\sim \kappa \int (\nabla \phi)^2 dV$, and F_{elast} is the elastic energy induced by composition fluctuations. The composition-dependent diffusion coefficient $D(\phi)$ is related to the substitutional diffusion of alloy components on the surface which is taken into account up to the second order in ϕ, $D(\phi) = D_0 + D_1\phi + D_2\phi^2$ and a is the lattice parameter.

The linear stability analysis [3, 5] showed that, for a given growth velocity v, the instability occurs in a certain temperature interval. The positive formation enthalpy of the alloy and the elastic interaction energy between the adatoms and the "buried" composition modulation in the entire thickness of the epitaxial film are the two driving forces of the decomposition. At high temperatures, the entropy contribution to the alloy free energy hinders the driving forces to decomposition and stabilizes the growth of a homogeneous alloy. At low temperatures, the surface diffusion is "freezed" out and does not provide formation of a modulated structure. The solid line in Fig. 1 depicts the boundary of the instability region found in [5]. The homogeneous growth is unstable at $v < v_c(T) = [4D_0(T_c - T)]/(a^2\kappa)$, where T_c is the critical temperature in the slow deposition limit [2].

In the present paper we seek the steady-state solution to kinetic equation (1) in the weak segregation regime close to the boundary of the instability region, i. e. at $v/v_c = 1 - \eta^2$, where $\eta \ll 1$. In this regime there is only one unstable mode for each elastically soft direction, and composition fluctuations can be written in the form $\phi(x, y) = 2\eta \left[(T_c - T)/a^3 \right]^{1/2} \left[\psi_x \cos(k_0 x) + \psi_y \cos(k_0 y) \right] +$ stable modes, where $k_0 = \sqrt{2(T_c - T)/(a^3\kappa)}$. The reaction of stable modes, such as those with $\mathbf{k} = (2k_0, 0)$ and $\mathbf{k} = (k_0, k_0)$, on unstable modes can be taken into account in the adiabatic approximation.

To illustrate this reaction, we consider a composition fluctuation with the wave vector $\mathbf{k} = (k_0, 0)$ (Fig. 2(a)). This fluctuation is unstable and its amplification implies the surface flux of atoms B from A-rich domains to B-rich domains, Fig. 2(b). Assume that A-rich domains have larger atomic mobility than B-rich domains, $D(\phi < 0) > D(\phi > 0)$,

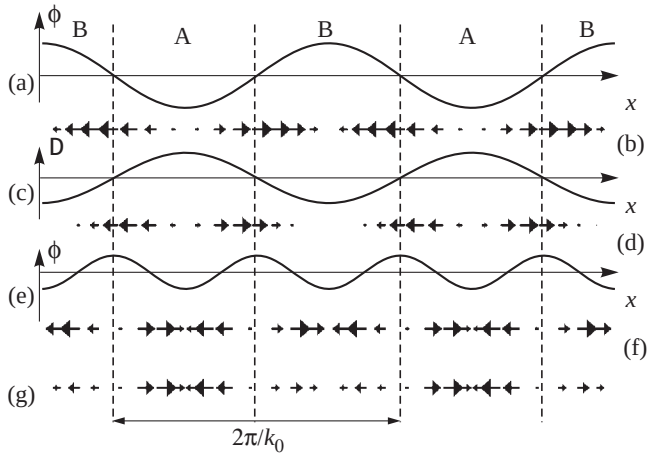

Fig. 2. Stabilizing effect due to the dependence of surface atomic mobility on composition in 1D system. (a): Unstable composition fluctuation. (b): Surface flux forming composition fluctuations of Fig. 2(a). (c): Surface atomic mobility. (d): Surface flux of Fig. 2(b) in case of varied atomic mobility (c). (e): Second harmonic of composition fluctuations due to modulated surface flux (d). (f): Surface flux induced by the second harmonic (e). (g): The first harmonic of the surface flux in case of varied atomic mobility (c).

Fig. 2(c). In this case the flux of atoms B from A-rich domains towards domain boundaries is larger than the flux from domain boundaries to B-rich domains Fig. 2(d). This results in the accumulation of atoms B at domain boundaries, i.e. in formation of a composition fluctuation with the wave vector $\mathbf{k} = (2k_0, 0)$, Fig. 2(e). Such a fluctuation is energetically not favorable and decays via surface flux out of domain boundaries, Fig. 2(f). Due to composition dependence of atomic mobility this flux is also deformed in a way that most of atoms B move towards A-rich domains, Fig. 2(g). As a result, there appears non-linear stabilizing effect. This is the action of the composition fluctuation along x-direction on itself by means of the second harmonic. There is a similar action of the composition fluctuation in the x- direction on fluctuations in the y-direction and vise versa due to the appearance of composition fluctuations with wave vectors like $\mathbf{k} = (k_0, k_0)$.

The resulting kinetic equations in the weak segregation regime have the following form, very similar to that of Ref. [5]:

$$\begin{aligned} \frac{\partial \psi_x}{\partial \tau} &= \eta^2 \left[\psi_x - a_L \psi_x^3 - a_T \psi_x \psi_y^2 \right] + O(\eta^4) \\ \frac{\partial \psi_y}{\partial \tau} &= \eta^2 \left[\psi_y - a_L \psi_y^3 - a_T \psi_y \psi_x^2 \right] + O(\eta^4) , \end{aligned} \tag{2}$$

where

$$\begin{aligned} a_L &= 3 - \frac{D_2}{D_0} \times \frac{(T_c - T)}{A_4 a^3} + \frac{D_1^2}{D_0^2} \times \frac{10(T_c - T)}{9 A_4 a^3} \\ a_T &= 6 - \frac{D_2}{D_0} \times \frac{2(T_c - T)}{A_4 a^3} + \frac{D_1^2}{D_0^2} \times \frac{2}{A_4 a^3} \times \frac{(T_c - T)\varepsilon_0^2 R a^3}{\varepsilon_0^2 R a^3 + (T_c - T)} \end{aligned} \tag{3}$$

Here ε_0 is the lattice mismatch between pure binary constituents of the alloy, AC and BC, R is a certain combination of elastic moduli, for GaAs $R = 0.2\text{eV}/\text{Å}^3$, and A_4 is related to the fourth-order contribution to the chemical energy, ($A_4 = 6\left(\partial^4 f_{\text{chem}}/\partial^4 c\right)$ at $c = 1/2$). If $a_L < a_T$, the steady state structure is 1D and, if $a_L > a_T$, the steady state structure is 2D. It follows from Eqs. (3) that at temperatures close to T_c the final structure is one-dimensional and at lower temperatures $(T_c - T) > \varepsilon_0^2 R a^3$, the final structure is 2D.

This transition can be explained as follows. The species dependent atomic mobility results in "effective barriers" hindering surface atoms from migration across domain boundaries. These barriers are unavoidable for a surface flux in case of 1D structure (Fig. 2), while in case of 2D structure there is a possibility for a surface flux to go around these barriers, e.g. along $<110>$-directions. Therefore, the effect of species-dependent atomic mobility favors 2D structures. The dependence of atomic mobility on composition enhances as the growth temperature decreases. As a result, below a certain temperature the steady-state structure is 2D.

This effect is in a way complementary to the effect of surface corrugation. While the effect of surface corrugation is important in case of a large mismatch ε_0 between two binary constituents of the alloy and at a large spatial scale, the effect of species-dependent atomic mobility is stronger for moderate ε_0 and is essential at small scales. E.g. for $\varepsilon_0 = 0.08$ the final structure is 2D at periods 50 Å and smaller, and for $\varepsilon_0 = 0.02$ the final structure is 2D at $d < 200$ Å.

To conclude, the steady state phase diagram of Fig. 1 applies to any alloy. We show a possibility to form 2D structures with arbitrary small wavelength and explain commonly observed 2D structures modulated in [100] and [010] directions (see, e. g. [8]). Kinetic phase transition between the growth of 1D structure and the growth of 2D structure provides a possibility to tune the structure between 1D and 2D ones at arbitrary scale by varying temperature and/or growth velocity.

Acknowledgments

The work was supported by Russian Foundation for Basic Research (grant 98-02-18304), and by Russian Federal Programs "Solid State Nanostructures" (grant 97-2014), "Leading Research Schools" (grant 00-15-96812), and "Surface atomic structures" (grant 1.207). V.A. Sh. is grateful to the Alexander von Humboldt Foundation.

References

[1] A. Zunger and S. Mahajan, in *Handbook on Semiconductors*, ed T. S. Moss, vol. 3, ed S. Mahajan, (Elsevier, Amsterdam, 1994), p. 1399.
[2] V. G. Malyshkin and V. A. Shchukin, *Semiconductors* **32**, 1062 (1993).
[3] J. E. Guyer and P. W. Voorhees, *Phys. Rev. Lett.* **74**, 4031 (1995).
[4] I. P. Ipatova, *et al. Proc. 23rd Int. Symp. on Compound Semiconductors*, 1996 (American Inst. Phys. Conf. Ser. **155**, 617); *Phys. Rev. B* **57**, 12968 (1998).
[5] V. A. Shchukin and A. N. Starodubtsev, *Proc. 7th Int. Symp. "Nanostructures: Physics and Technology"*, St. Petersburg 1999, p. 497; *Mat. Res. Soc. Symp. Proc.* **583**, 327 (2000).
[6] V. A. Shchukin, *et al.*, *Phys. Rev. Lett.* **75**, 2968 (1995).
[7] B. J. Spencer, *et al.*, *Appl. Phys. Lett.* **71**, 3022 (2000).
[8] T. L. McDevitt, *et al.*, *Phys. Rev. B* **45**, 6614 (1992).

9th Int. Symp. "Nanostructures: Physics and Technology"
St Petersburg, Russia, June 18–22, 2001

Thin epitaxial Al and Cu films grown on CaF_2/Si(111)

N. L. Yakovlev†, Y. V. Shusterman‡ and L. J. Schowalter‡
† Ioffe Physico-Technical Institute, St Petersburg, Russia
‡ Department of Physics, Rensselaer Polytechnic Institute, Troy, NY 12180, USA

Abstract. Molecular beam epitaxy was used to grow single crystal CaF_2, Al and Cu films on Si(111). Reflection high energy electron diffraction indicated that Al film was epitaxial when it was grown on CaF_2/Si, and that epitaxial Cu film can be grown on Al/CaF_2/Si heteroepitaxial substrates. Room temperature measurements of resistivity of Al films 10 to 300 nm thick agree with the Fuchs-Sondheimer model, in which only diffuse scattering of conduction electrons occurs at the film interfaces. For 50 to 1000 nm thick Cu films, the resistivity size effect is greater than the prediction of this model.

Introduction

In the next decade, the width of some metal lines inside integrated circuits will decrease to approximately 50 nm, which is comparable to the mean free path of conduction electrons in both Al and Cu at room temperature. At those small dimensions, electron scattering from metal surfaces will play an important role in electron transport. The well-established way to characterize surface scattering is to study the electrical properties of thin metal films. Most previous work related to Al and Cu has been done on polycrystalline films deposited on SiO_2 [1, 2]. However, in such cases, the scattering at grain boundaries may be dominant. To avoid this masking effect, it is desirable to work with single-crystal films.

The epitaxial CaF_2 on Si is a convenient choice for a single-crystal insulating substrate [3]. Epitaxy has been reported previously for both Al and Cu on CaF_2(111) [4, 5], but the initial stages of their growth have not been addressed. In this work, we have studied thin Al and Cu films grown on CaF_2/Si(111) by molecular beam epitaxy (MBE). The samples were characterized by reflection high-energy electron diffraction (RHEED), scanning tunnelling microscopy (STM) and atomic force microscopy (AFM). We have also measured the resistivity dependence on film thickness for both Al and Cu, fitted these data to the Fuchs-Sondheimer size effect model, and discussed the relationship between resistivity and structural properties.

Growth

The films studied in this work were grown in a commercial VG90S MBE apparatus with a base pressure of 3×10^{-8} Pa. Molecular beam of CaF_2 was produced by sublimation of the fluoride from boron nitride crucible. The Al and Cu were deposited from electron beam evaporators. The RHEED patterns were obtained at electron energy of 13 keV and beam incidence angle of 2.5°. The STM work was performed on a locally designed instrument coupled to the MBE chamber. The AFM images were obtained by a Digital Instruments "Dimension 3100" microscope in the tapping mode with a tip having the apex radius below 30 nm.

When Al is deposited on traditional SiO_2, the film starts growing as isolated clusters, Fig. 1(a). RHEED showed that their crystallographic orientation is random. At room

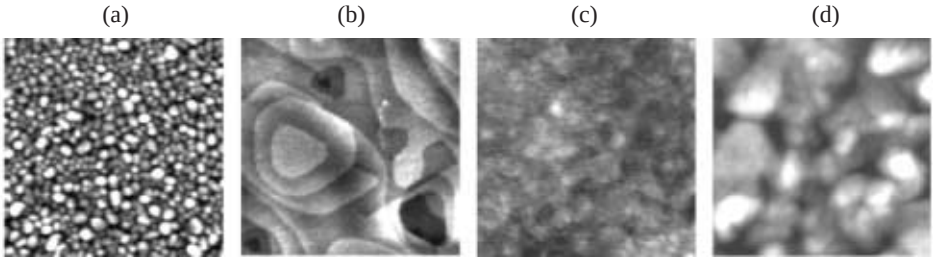

Fig. 1. AFM images of (a) 10 nm of Al on SiO_2, (b) 50 nm of CaF_2 on Si(111), (c) 10 nm of Al on CaF_2, (d) 130nm of Cu on Al seed layer. Scan size is 500 nm, grey scale is 8 nm in (a), 2 nm in (b) and (c), 5 nm in (d). Root-mean-square roughness is 5 nm in (a), 0.5 nm in (b), 0.3 nm in (c), 3.5 nm in (d).

temperature and relatively high deposition rate of 1 nm/s, a continuous film can be obtained when average thickness of Al is around 10 nm.

Epitaxial films were grown on hydrogen-terminated Si(111) substrates prepared by wet etching in 40% NH_4F. One molecular layer (ML) of CaF_2 was deposited on the surface at 250°C, then heated to 770°C and the CaF_2 deposition was continued. In this way, we obtained a well-reacted CaF_2/Si(111) interface without long exposure of the bare Si surface to an imperfect vacuum (the pressure rose to 10^{-6} Pa when the substrate was at high temperature). The surface of 50 nm thick layer had atomically flat terraces 50 nm wide, as shown in Fig. 1(b).

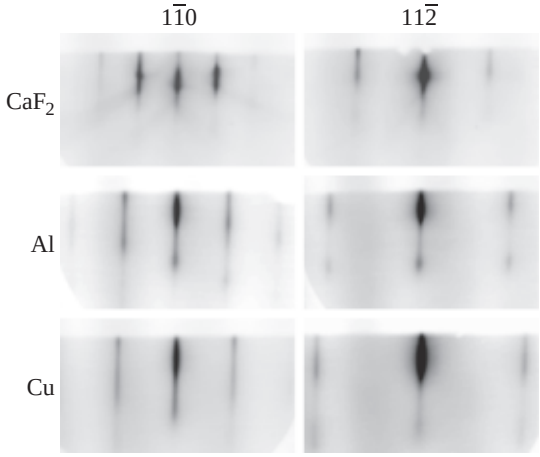

Fig. 2. RHEED patterns showing epitaxy of Cu on Al on CaF_2(111).

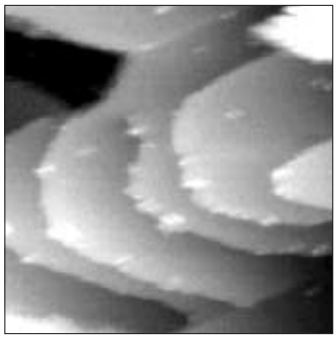

Fig. 3. STM image of 10 nm Al on CaF_2; scan 20 nm, grey scale 0.8 nm.

Al film grown on this surface was epitaxial, as shown by RHEED images in Fig. 2. The streak pattern was consistent with that from (111) face of bulk Al. To improve continuity of very thin films, we increased nucleation density as follows. Additional 1.5 ML of CaF_2 was grown at room temperature, as suggested in Ref. [6], this created high concentration of atomic steps on the CaF_2 surface. The metal layer was grown also at room temperature at high deposition rates above 1 nm/s. The resulting rms roughness was below 0.3 nm on a 500 nm AFM scan, Fig. 1(c). On STM images of this surface shown in Fig. 3, one can see individual monolayer steps; some of them originate at outlets of screw dislocations.

They are due to large lattice mismatch between Al and CaF_2 (the ratio of lattice constants is 1.36), and their density was estimated to be $5 \times 10^{11}/cm^2$.

For Cu deposition on CaF_2, RHEED showed the formation of a polycrystalline film. However, we succeeded in growing epitaxial Cu by depositing it on a 1 nm-thick Al seed layer grown on CaF_2. Only Cu(111) streaks were visible in RHEED, with a spacing indicative of the bulk Cu lattice spacing, as shown Fig. 2. This result is consistent with the report of Cu epitaxy on the (111) surface of bulk Al [7]. During the growth at room temperature, Cu surface became rough quickly, so after the growth of 50 nm, the temperature was increased to 100°C and the films were grown up to intended thickness. The rms roughness of the final surface was below 5% of the average film thickness, Fig. 1(d).

Resistivity measurements

The insulator covered the substrate uniformly. The metals were deposited onto it through a shadow mask designed to measure sheet resistance ex-situ by a linear 4-point probe, as described in ref. [8]. Precision of the resistance measurements was better than 0.1%. For films thicker than 50 nm, the thickness was measured with precision of ±2 nm using Tencor Alpha-Step 200 profilometer. For thinner films, the thickness was obtained with a precision of ±0.5 nm from AFM scan at the metal shadow edge. Oxidation of Al films was taken into account like it was done in ref. [8].

The thin-film resistivity data for epitaxial Al and Cu on CaF_2 are presented in Fig. 4, along with the fit by the Fuchs-Sondheimer model [9], which treats additional contribution to the resistivity arising from diffuse scattering of electrons at the film surfaces. Even though this model is very crude and has been refined several times (see ref. [10] for review), it is still customarily used for analysis. It expresses the resistivity as

$$\rho(h) = \rho_\infty \left(1 + \frac{C}{h}\right) \quad \text{with} \quad C = \frac{3}{8}\lambda(1-p),$$

where ρ is the resistivity of the film, ρ_∞ is that of the bulk, h is the metal thickness, λ is the bulk electron mean free path, p is the probability of a specular surface scattering event. We cast the equation into such a form because C is what is actually determined from the fit to the experimental data; thus we obtained $C = 6.4 \pm 0.6$ nm for Al and $C = 26 \pm 2$ nm for Cu.

For the surface scattering contribution, it is expected that $p > 0$ and hence $C < 3\lambda/8$. Here, λ is the product of Fermi velocity and relaxation time. Taking those from ref. [11],

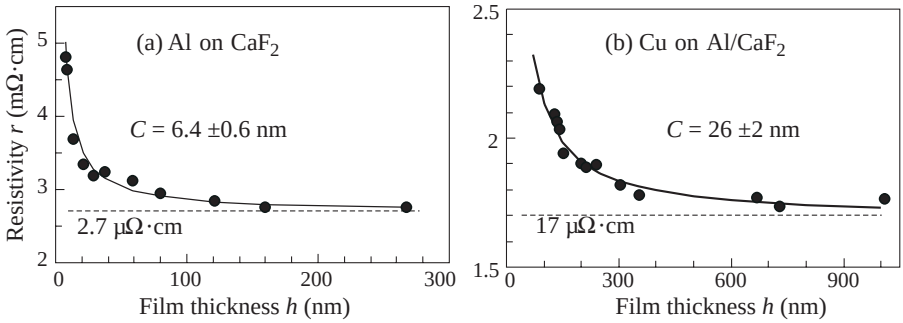

Fig. 4. Resistivity size effect for (a) Al and (b) Cu epitaxial films on CaF_2. The dotted line is the bulk resistivity $2.7\mu\Omega \cdot$ cm for Al and $1.7\mu\Omega \cdot$ cm for Cu.

we obtain $\lambda = 16$ nm for Al and $\lambda = 42$ nm for Cu. With these values, $3\lambda/8 = 6$ nm for Al, so we can say that $C \approx 3\lambda/8$ within the experimental precision and that $p \approx 0$, i.e. almost all of the surface scattering events are diffuse. This is not surprising since both Al interfaces with CaF_2 and the oxide are expected to be atomically rough and hence should efficiently scatter conduction electrons whose Fermi wavelength is comparable with the lattice constant.

However for Cu, $3\lambda/8 \approx 16$ nm and $C > 3\lambda/8$. So we conclude that in addition to diffuse surface scattering, another contribution to the resistivity size effect must be present which is also inversely proportional to the thickness. Analysis of RHEED images with variation of electron beam azimuth showed that there are domains with small in-plane misorientation $\pm 10^\circ$. Scattering at their boundaries can cause additional resistivity of thin films. In thicker films, these domains are overgrown by exactly epitaxial Cu, so relative contribution of this effect is smaller.

To conclude, thin epitaxial Al films on $CaF_2(111)$ can be grown very smooth. Their crystal quality is good enough to perform meaningful studies of the resistivity size effect due to surface scattering of electrons, without the masking effect of grain boundary scattering. These Al films can also be used as a template to grow other metals epitaxially, notably Cu.

Acknowledgements

This work was supported by the NYS Science and Technology Foundation, DARPA, Sematech, and the New York Interconnect Focus Research Center.

References

[1] J. Gogl, J. Vancea and H. Hoffmann, *J. Phys.: Condens. Matter* **2**, 1795 (1990).
[2] E. Dobierzewska-Mozrzymas, F. Warkusz, *Thin Solid Films* **43**, 267 (1977).
[3] L. J. Schowalter and R. Fathauer, *CRC Crit. Rev. Sol. St. Mat. Sci.* **15**, 367 (1989).
[4] C.-C. Cho, H.-Y. Liu and H.-L. Tsai, *Appl. Phys. Lett.* **61**, 270 (1992).
[5] N. Mattoso, D. H. Mosca, I. Mazzaro, S. R. Teixeira and W. H. Schreiner, *J. Appl. Phys.* **77**, 2831 (1995).
[6] K. Kawasaki and K. Tsutsui, *Appl. Surf. Sci.* **130-132**, 464 (1998).
[7] C. J. Barnes, H. Asonen, A. Salokatve and M. Pessa, *Surface Science* **184**, 163 (1987).
[8] Y. V. Shusterman, N. L. Yakovlev and L. J. Schowalter, *Appl. Surf. Sci.* to be published in proceedings of the ICSFS-10, Princeton NJ, July 2000.
[9] E. H. Sondheimer, *Adv. Phys.* **1**, 1 (1952).
[10] F. Warkusz, *Progress in Surf. Sci.* **10**, 287 (1980).
[11] N. W. Ashcroft and N. D. Mermin, *Solid State Physics* ch. 2, Harcourt College Publishers.

9th Int. Symp. "Nanostructures: Physics and Technology"
St Petersburg, Russia, June 18–22, 2001

Spatially indirect excitons in self-assembled Ge/Si quantum dots

A. I. Yakimov, A. V. Dvurechenskii, N. P. Stepina, A. V. Nenashev and A. I. Nikiforov
Institute of Semiconductor Physics, 630090 Novosibirsk, Russia

Abstract. Using electron-filling modulation absorption spectroscopy, we study the effect of quantum dot charging on the interband excitonic transitions in type-II Ge/Si heterostructures containing pyramidal Ge nanocrystals. In contrast to type-I systems, the ground state absorption is found to be blueshifted when exciton-hole and exciton-exciton complexes are formed. For a positively charged dot, we argue that this is the consequence of dominance of the hole-hole and electron-electron interactions compared to the electron-hole interaction due to the spatial separation of the electron and hole. When two excitons are excited in the dot, the electrons are found to be spatially separated and have different single-particle quantization energies. This is the reason why the biexciton absorption is blushifted as compared to a single exciton.

The study of the excitonic properties in quantum-dot (QD) structures has drawn considerable interest in recent years. Most of the work has been reported in the type-I QD structures, where an electron and a hole are confined spatially in the same quantum well. Ge/Si(001) quantum dots exhibit a type-II band lineup. The large ($\sim$ 0.7 eV) valence-band offset characteristic of this heterojunction leads to an effective localization of holes in Ge regions, which represent potential barriers for electrons. When an electron-hole pair is photoexcited, the hole is captured by the Ge dot and creates a Coulomb potential resulting in a binding of an electron in the vicinity of the Ge dot. The spatially separated interacting electron and hole are usually referred to as 'spatially indirect exciton' [1].

In this paper, we use electron-filling modulation absorption spectroscopy (EFA) to study effect of dot charging on the interband transitions in 10-nm-scale Ge/Si QDs. Ge dots are embedded into a n^+-p-p^+ Si diode, in which the number of holes in the QDs can be finely tuned by an external applied bias. When a state is occupied by a hole, no interband transition from this state is possible. When the hole is evacuated from the level, the interband transition is allowed. Modulating the holes in and out of the state by applying an ac bias voltage therefore induces corresponding changes in the infrared absorption. Thus the absorption signal measured under different bias conditions reflects directly properties of excitons at charged quantum dots.

The sample was grown by molecular beam epitaxy on a (001) oriented 4.5 Ω cm boron doped Si substrate. The Ge quantum dot layer with a nominal thickness of 10 ML was symmetrically embedded into a 1-μm thick p-Si region (B, 5×10^{16} cm^{-3}) at 300 °C. A buried back contact is formed by 50-nm B-doped p^+-Si (2×10^{18} cm^{-3}). The structure was finally capped with a 50 nm n^+-Si front contact (Sb, 1×10^{19} cm^{-3}). The dots are pyramidal with base orientation along [100] and [010] directions. The area density of the dots was estimated to be 3×10^{11} cm^{-2}. The average size of the dot base length was found to be about 15 nm, the height about 1.5 nm, and the dot uniformity approximately $\pm$20%.

To reveal the charge state of the dots we measure the capacitance-voltage characteristics. The dots are charged with holes at zero bias. The holes begin to escape at $V > 0.5$ V and the dots become totally depleted at $V > 8.5$ V. In the discussion that follows, we modulate

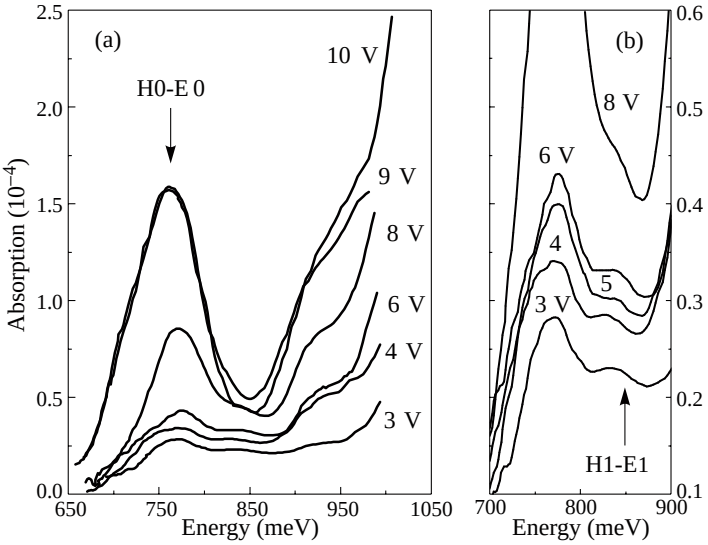

Fig. 1. (a) Room-temperature electron-filling absorption spectra at different reverse bias. (b) Expanded view of the spectra at low bias.

the reverse bias voltage between $V = 0$ V and $V = 2$–10 V with a frequency of 700 Hz. Differential aborption was measured at the voltage modulation frequency with the lock-in technique.

Figure 1 shows the EFA signal measured at different values of the bias V. Below the energy gap of Si, at energies 650–850 meV, we observe an absorption maximum with a broadening of $\sim$ 50–70 meV. An expanded view shows that this maximum can be well described by a sum of two Gaussian peaks. Symmetric line shape of the two peaks is characteristic of a bound-to-bound transition. We interpret the first absorption peak as an excitonic transition between the hole ground state (H0) in the Ge dots and the electron ground state (E0) confined in Si near the heterojunction. A second maxima at $\approx$ 860 meV is assigned to the excited-state excitonic transition (the H1–E1 transition). We assume that the broadening of the interband transitions is mainly due to the dispersion of the carrier confinement energies of dots with different sizes.

To obtain evidence to support the proposed origin of the EFA peak, we have studied the effect of additional interband optical excitation of the sample by a tungsten halogen lamp with a bandpass filter as source. When the sample is illuminated, nonequilibrium electrons and holes are photogenerated. The holes are captured by the dots while the electrons are accumulated near the dots forming the indirect excitons. At high pump intensities, the hole and electron ground states become fully occupied and the Pauli exclusion principle forbids the H0-E0 transition. We find that the experimental EFA signal is actually suppressed by the optical pumping.

One of the main results is that the excitonic transitions show a substantial stepwise blueshift with decreasing reverse bias. A qualitatively similar effect is seen with increasing the pump excitation density at fixed V. This result differs drastically from what has been observed for direct excitons, in which case charging leads to a redshift of the excitonic transition [2]. From the oscillator strength (0.5) obtained in [1] and the measured integrated absorption we calculate the number of holes per dot, N, at different biases in the dark and at different pump intensities. The energetic position of the excitonic transitions is shown in

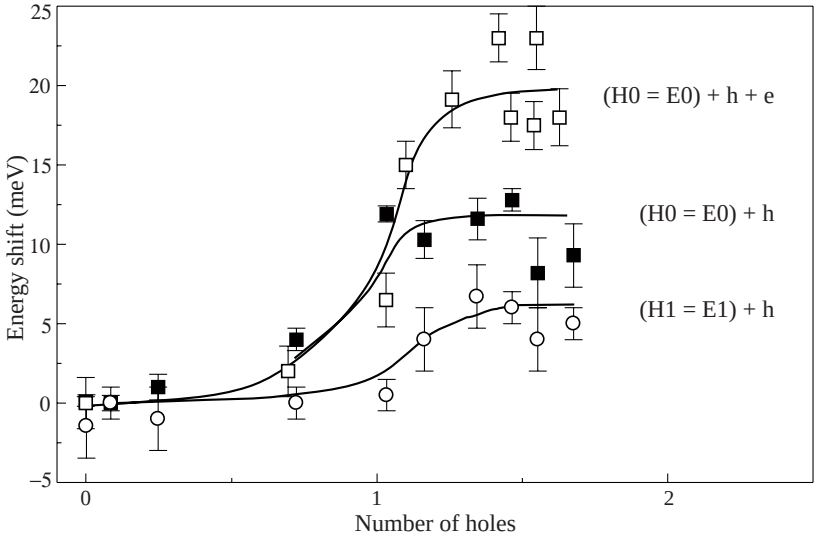

Fig. 2. Shift of the H0–E0 (solid squares) and H1–E1 (open circles) transitions as a function of the hole occupation per dot. The open squares show the shift of the ground state transition at different pump intensities at fixed bias voltage ($V = 9$ V).

figure 2 as a function of N. It should be noted that the transition energy increases sharply when the first hole enters the ground state and then is approximately insensitive to further increase in the hole concentration.

When a H0–E0 exciton is created in a positively charged dot, an exciton-hole complex is formed consisting of two holes in the dot and an electron confined near the dot. There are two additional contributions to the energy of the exciton-hole complex as compared to e-h excitation in a neutral dot. The first is a positive Coulomb energy due to correlation between the two holes in the dot, $E_{\rm hh}$, and the second is a negative contribution from the Coulomb attraction between the excited electron in the nearby silicon and the second hole on the dot, $E_{\rm eh}$. Here we neglect the exchange interaction between the two holes since they have antiparallel spin orientation. For spatially direct excitons, the electron-hole interaction dominates and the resulting shift $\Delta E_{\rm h-ex} = E_{\rm hh} - E_{\rm eh}$ is negative [2]. Hence the expected reduction of the overlap factor for type-II excitons as compared with type-I systems yields a smaller magnitude of the electron-hole interaction energy $E_{\rm eh}$. As a result, the energy of the exciton-hole interaction referenced to a neutral exciton energy can be positive. Taking the experimentally observed shift of 11 meV and $E_{\rm hh} = 36$ meV [3], the ground state exciton binding energy is estimated to be $E_{\rm eh} = 25$ meV. Similar estimate gives $E_{\rm eh} \approx 15$ meV for the exciton in excited state.

As can be seen from Fig. 2, optical pumping affects the transition energy more strongly than the bias voltage. This stems from the fact that illumination creates both holes and electrons while the field effect only induces holes in the dots. Under illumination we have two interacting excitons in the dot: the first is generated by the pump illumination, the second is excited by the infrared probing light. As compared to a single exciton, the transition energy now increases by $\Delta E_{\rm ex-ex} = E_{ee} + E_{hh} - 2E_{eh}$, where E_{ee} is the energy of repulsive interaction between two electrons confined near the dot. For $\Delta E_{\rm ex-ex} = 20$ meV, $E_{hh} = 36$ meV and $E_{eh} = 25$ meV, we obtain a suprising result $E_{ee} = 34$ meV. It is quite

improbable that E_{ee} could be so close to E_{hh} in a system where the hole states are more localized than the electron states. To resolve this problem we make self-consisitent calculations of the expected electronic structure [1]. The calculations show that the two electrons in the exciton-exciton complex are *spatially separated*. Electron-electron repulsion causes the second electron to localize below the dot base. As a result, the e-e interaction energy turns out to be only 19 meV, i.e., about two times less than the energy of the h-h interaction. Moreover, the single-particle energy of the second electron is larger than that for the first one, and the resulting shift of the absorption $E_{\mathrm{ex-ex}}$ turns out to be positive and equals to 10.2 meV.

Acknowledgements

This work was financially supported by the Russian Foundation for Basic Research and the State Foundation of Natural Sciences of China under Grant No. 99-02-39051GFEN-a.

References

[1] A. I. Yakimov, N. P. Stepina, A. V. Dvurechenskii, A. I. Nikiforov and A. V. Nenashev, *Phys. Rev. B* **63**, 45 312 (2001).

[2] R. J. Warburton, C. S. Dürr, K. Karrai, J. P. Kotthaus, G. Medeiros-Ribeiro and P. M. Petroff, *Phys. Rev. Lett.* **79** 5282 (1997).

[3] A. I. Yakimov, A. V. Dvurechenskii, A. I. Nikiforov and O. P. Pchelykov, *JETP Lett.* **68** 135 (1998).

9th Int. Symp. "Nanostructures: Physics and Technology"
St Petersburg, Russia, June 18–22, 2001

Impurity potential fluctuations for selectively doped p-Ge/$Ge_{1-x}Si_x$ heterostructures in the quantum Hall regime

Yu. G. Arapov†, O. A. Kuznetsov‡, V. N. Neverov†, G. I. Harus†,
N. G. Shelushinina† and M. V. Yakunin†

† Institute of Metal Physics RAS Ural branch, Ekaterinburg GSP-170, 620219 Russia
‡ Scientific Research Institute at Nizhnii Novgorod State University, Russia

Abstract. Two models for random impurity potential (the model with randomly distributed charged centers located within a layer and the model of the system with spacer) are used for the estimation the impurity potential fluctuation parameter's values: random potential amplitude, the nonlinear screening length in vicinity of integer filling factors $\nu = 1$ and $\nu = 2$, the background density of state (DOS). The described models are suitable for the explanation of unusual high value of DOS at $\nu = 1$ and $\nu = 2$ in contrast to short-range impurity potential models.

The nature of quantum Hall effect (QHE) is closely linked with a phenomenon of electron localization in a two-dimensional (2D) disorder system in quantizing magnetic field (B) [1, 2]. The appearance of quantum plateaux in the $\rho_{xy}(B)$ dependences with vanishing values of ρ_{xx} is now commonly accepted to be caused by the existence of disorder-induced mobility gaps in the density of states (DOS) of a 2D-system. When the Fermi level is settled down in the gap the thermally activated behavior of ρ_{xx} (or σ_{xx}) is observed due to the excitation of electrons to the very narrow bands of extended states centered at Landau level (LL) energies E_N. The determination of the DOS in the mobility gaps is possible from the data on activation energy E_A as a function of the LL filling factor $\nu = n/n_B$ (n is the electron density, $n_B = eB/hc$) [3–6]. The filling factor can be tuned by the change of either the carrier density [3] or the magnetic field [4–6].

We have used the method of activated magnetoresistivity for the reconstruction of 2D-hole gas (2DHG) spectrum in quantizing magnetic fields for p-Ge/$Ge_{1-x}Si_x$ systems with complex valence band structure [7]. The measurements of longitudinal ρ_{xx} and Hall ρ_{xy} resistivities are carried out for multilayer p-Ge/$Ge_{1-x}Si_x$ ($x = 0.07$) heterostructures with hole concentration $p = (2.4 \div 2.6) \cdot 10^{11}$ cm^{-2} and mobilities $\mu_p = (1.1 \div 1.7) \cdot 10^4$ cm^2/Vs in magnetic fields up to 12 T at $T = (1.6 \div 15)$ K.

The heterostructures are consisting of a 20-nm Ge and $Ge_{1-x}Si_x$ layers repeated $15 \div 30$ times. The 2DHG forms just inside the undoped Ge layer. The regions of $Ge_{1-x}Si_x$ barriers doped with boron are separated from the Ge layers by 5-nm undoped $Ge_{1-x}Si_x$ spacer layers (d_s) (Fig. 1).

The following results for the mobility gap DOS as a function of energy $g(\varepsilon)$ have been obtained. Even in the middle of a gap when the filling factor is close to an integer the density of localized states is found to have a value comparable with or even higher than the DOS of 2DHG without magnetic field ($g_0 \cong 4.5 \cdot 10^{10}$ cm^{-2} meV^{-1}). Moreover, $g(\varepsilon)$ remains almost constant in the overwhelming part of the energy intervals between adjacent LL: $g(\varepsilon) \cong g_c = (5 \div 7) \cdot 10^{10}$ cm^{-2} meV^{-1} for $\nu = 1$ and $\nu = 2$ (Fig. 2). This result is consistent qualitatively with data for the structures with n-type conductivity [3–6]. As for our value of g_c, it is roughly an order of magnitude higher than those for InGaAs/InP [5]

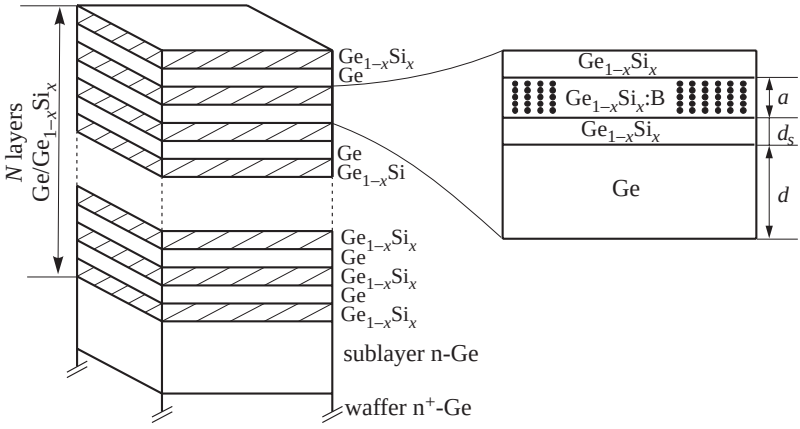

Fig. 1.

and for high-mobility AlGaAs/GaAs [4] heterostructures but comparable with those for Si-MOSFET [3] and for intermediate-mobility AlGaAs/GaAs heterostructures [6].

As all short-range impurity potential models lead to an exponential drop in DOS between Landau levels, the clear picture for the DOS in QHE regime may be presented only in terms of the long-range potential fluctuations in combination with the oscillation dependence of DOS on the filling factor. Such an idea has been advanced in early work of Shklovskii and Efros [8] and then developed in series of works of Efros with collaborations (see [9, 10] and references therein). In selectively doped heterostructures the smooth random potential is formed by fluctuations in concentration of remote impurities.

For a random potential $V(r)$ smooth on the scale of magnetic length l_B the localization in QHE regime can be discussed in terms of semiclassical quantization and percolation [11]. In the quasiclassical limit the electron energy in quantizing magnetic field may be presented as

$$E_N(r_0) = \hbar\omega_c \left(N + \frac{1}{2}\right) + V(r_0) \tag{1}$$

with r_0 being the oscillator center coordinate. Thus the smooth potential removes the degeneracy on r_0 and makes the LL energy dependent on spatial coordinates.

We report here an order of magnitude estimation of spatial scale and amplitude of random potential in p-Ge/$Ge_{1-x}Si_x$ heterostructures in QHE regime obtained from an analysis of the mobility gap DOS. Two models for random impurity potential are used.

(i) The model with randomly distributed charged centers located within a thick layer (of a width b) close to the 2D electron (hole) gas [8]. For the fluctuation amplitude F of a scale L it is obtained [8]

$$F(L) = \beta \frac{e^2\sqrt{NL}}{\kappa}, \tag{2}$$

where β is a numerical coefficient ($\beta \cong 0.1$ [9]), N – the density of charged impurities (per volume) and κ – the dielectric constant.

(ii) The model of the system with spacer: a condenser with 2D electron (hole) gas as one plate and randomly distributed charged centers as the other plate, separated by a

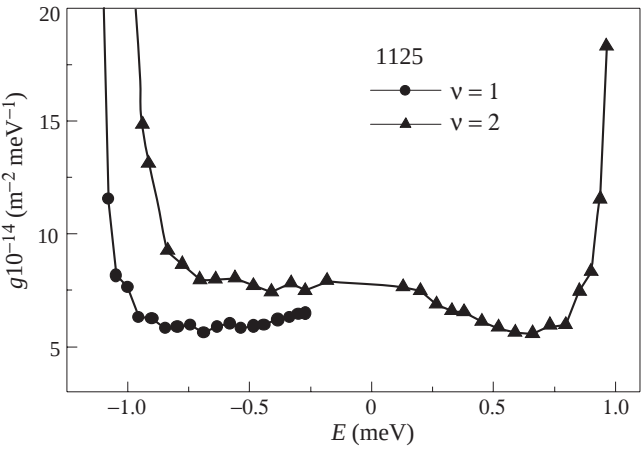

Fig. 2.

distance d_s [9, 10]. In this case:

$$F(L) = 2\pi \frac{e^2\sqrt{C}}{\kappa}\sqrt{ln\frac{L}{2d_s}}, \tag{3}$$

where C is average impurity density (per area).

It is seen from Eqs. (2) and (3) that without screening the amplitude F diverges at large L. When filling factor is close to integer (i) very small concentration of electrons $\delta n \ll n_B$ can be redistributed in space and thus one occurs in conditions of so called nonlinear screening [8–10] ("threshold" screening in terms of [12]). For $\nu = i$ exactly the screening is realized only due to electrons (and holes) induced by an overlap of adjacent fluctuating Landau levels, and so the amplitude of random potential is of the order of corresponding LL gap.

For the investigated heterostructures $N \cong 10^{17}\,\mathrm{cm}^{-3}$ ($C = Na \cong 10^{11}\,\mathrm{cm}^{-2}$) and the mean distance between impurities ($N^{1/3} \cong 200$ Å) is comparable both with the width of 2D Ge layer ($d \cong 200$ Å) and the width of doped part of the sample ($a \cong 100$ Å).

Thus the described models are not valid precisely but they are suitable to obtain a range of random potential parameter values.

In nonlinear screening regime for the DOS in the middle of mobility gap of width W ($\cong 2$ meV) we have [8–10]:

(i)

$$g\left(\frac{W}{2}\right) = \frac{4\beta e^2 N}{\kappa W^2} \cong 7.5 \cdot 10^{10}\mathrm{cm}^{-2}\mathrm{meV}^{-1}, \tag{4}$$

(ii)

$$g\left(\frac{W}{2}\right) = \frac{2\sqrt{C}}{7Wd_s} \cong 9 \cdot 10^{10}\mathrm{cm}^{-2}\mathrm{meV}^{-1}. \tag{5}$$

Thus without any fitting parameter we obtain a rather resonable estimation of background DOS, and the two models give values close to each other. For random potential

amplitude comparable to the mobility gap, $F \cong W$, we obtain an estimation of the nonlinear screening length L_c (the scale of optimal fluctuation): $L_c \cong 1000$ Å for model (i) (see Eq. (2)) and $L_c \cong 400$ Å for model (ii) (see Eq. (3)). As seen in both cases the spatial scale of fluctuations is essentially larger than the magnetic length ($l_B \cong 80$ Å at $B = 10$ T) and the random potential may be really regarded as the smooth one.

Thus an order of magnitude estimates of random impurity potential parameters for the p-Ge/$Ge_{1-x}Si_x$ heterostructures shows that in vicinity of integer filling factors $\nu = 1$ and $\nu = 2$ (i.e. in the regions of plateaux in QHE regime) a sharp broadening of LL takes place. It is reputed that for the filling factors close to half integer (the regions of plateau to plateau transition) the potential fluctuations will be small due to effective (linear) electron screening [8–10].

Acknowledgements

This work is supported in part by RFBR, projects No 99-02-16256 and No 01-02-17685.

References

[1] R. B. Laughlin, *Phys.Rev.B* **23**, 5632 (1981).
[2] B. I. Halperin, *Phys.Rev.B* **25**, 2185 (1982).
[3] M. G. Gavrilov, I. V. Kukushkin, *Pis'ma v ZhETF* **43**, 79 (1986).
[4] D. Weiss et al., *Surf. Sci.*, **170** 285 (1986).
[5] H. P. Wei et al., *Phys.Rev.B* **32** 7016 (1985).
[6] P. Svoboda et al., *cond-mat* / 9612053.
[7] Yu. G. Arapov et al., *Nanotechnology* **11**, 351 (2000).
[8] B. I. Shklovskii, A. L. Efros, *Pis'ma v ZhETF* **44**, 520 (1986).
[9] A. L. Efros, *Sol. St. Commun.* **70**, 253 (1989).
[10] A. L. Efros, F. G. Pikus, V. G. Burnett, *Phys.Rev.B* **47**, 2233 (1993).
[11] B. Huckestein, *Rev. Mod. Phys.* **67**, 357 (1995).
[12] I. V. Kukushkin, S. V. Meshkov and V. B. Timofeev, *Usp. Fiz. Nauk* **155**, 219 (1988).

9th Int. Symp. "Nanostructures: Physics and Technology"
St Petersburg, Russia, June 18–22, 2001

Size-selective Raman scattering in self-assembled Ge/Si quantum dot superlattices

A. G. Milekhin†, A. I. Nikiforov†, O. P. Pchelyakov†, S. Schulze‡ and D. R. T. Zahn‡

† Institute of Semiconductor Physics, RAS, 630090 Novosibirsk, Russia
‡ Institut für Physik, Technische Universität Chemnitz, D-09107 Chemnitz, Germany

Abstract. Self-organised Ge quantum dot (QD) superlattices having properties of two- and zero-dimensional structures were investigated by Raman spectroscopy. Longitudinal optical Ge (LO) and Ge-Si (L) phonons and folded acoustic (LA) phonons superimposed with a strong continuous emission were studied under resonant conditions. The measured phonon frequencies of folded LA phonons up to 15^{th} order are in a good agreement with those calculated using the Rytov model. The low frequency continuous emission can be explained in terms of a breakdown of crystal momentum conservation for resonant Raman processes involving acoustic phonons. A frequency enlargement of continuous emission band and a downward shift of LO Ge phonons with increasing excitation energy (2.54–2.71 eV) are attributed to electron and phonon size-confinement in the small Ge QDs resonantly contributing to the scattering process.

Introduction

Recently, Raman spectroscopy was applied for characterisation of vibrational modes in self-assembled Ge QDs superlattices [1, 2]. It was found, that these structures behave very similar compared to the planar superlattices exhibiting folded acoustical phonons and LO and TO phonons in the Raman spectra [2, 3]. However, a weakening of selection rules in Ge QD superlattices due to the non-conserving momentum transfer is expected. Very recently, Cazayous *et al.* [4] has reported on observation of continuous emission even from the single layer with the large-size Ge QDs (dot base size of 170 nm) attributed to the breakdown of the wave vector conservation law due to the loss of translational invariance. Nevertheless, no detailed study of Ge QD superlattices, containing small-size QDs where three-dimensional confinement is especially important has been performed yet.

In this paper we report on size-selective Raman scattering in self-organised Ge/Si superlattices with small-size Ge QDs performed under resonant conditions.

1. Experimental

Samples were grown by molecular beam epitaxy of Ge and Si layers utilising Stranski-Krastanov growth mode on Si(001) substrates. The growth temperature of the silicon layers was 800 and 500°C before and after deposition of Ge layer, respectively. The Ge quantum dot layers were grown at 300°C. The set of samples under investigation consists of Ge and Si layers with nominal thickness of 1.4 nm and 30 nm, respectively. The samples were delta-doped with boron atoms ($N_b = 6 \times 10^{11}$ cm^{-2}) and ($N_b = 1.5 \times 10^{11}$ cm^{-2}) in the middle of Si layers for samples A and B, respectively. However, no noticeable influence of the doping on the Raman spectra was found.

A dot base size of 15 nm, a QD height of 1.5 nm and period of the structure of 38.5±1.0 nm were found using a cross-sectional high-resolution transmission electron microscopy (HRTEM).

The Raman scattering experiments were performed using lines of an Ar^+, Kr^+ and HeNe lasers in the range of 1.83–2.71 eV. The scattering geometries employed were z(xx)-z and z(xy)-z, where the labels x, y, z refer to [100], [010], [001] directions, respectively. Raman spectra were measured in Stokes and anti-Stokes region.

2. Low frequency region

According to the selection rules for Raman scattering in planar Ge/Si superlattices grown on Si(001) the LO phonons can be seen in z(yx)-z scattering geometry while the LA phonons can be observed in z(xx)-z geometry. As in the case of the planar Ge/Si superlattices, the experimental Raman spectra of Ge QD superlattices (sample A) measured in z(xx)-z geometry and shown in Fig. 1 reveal the a number of periodic oscillations (up to 15^{th} order) assigned to folded LA phonons in the Ge dot superlattice. The doublets of the folded phonons are not resolved because of the small splitting value (of about 1 cm^{-1}). These oscillations are superimposed with a broad continuous emission with a maximum at about 40 cm^{-1}.

The folded acoustical phonons observed can be well described using the Rytov model [5]. The calculated acoustic phonon dispersion curve is shown in the inset to Fig. 1. The horizontal line corresponds to the scattering wave vector used in experiment. It can be seen, that the agreement with the Rytov model is excellent and no adjusting of parameters is required. The period of structures deduced from the calculation is found to be 37.9 nm that corresponds very well to the average value evaluated from the HRTEM images.

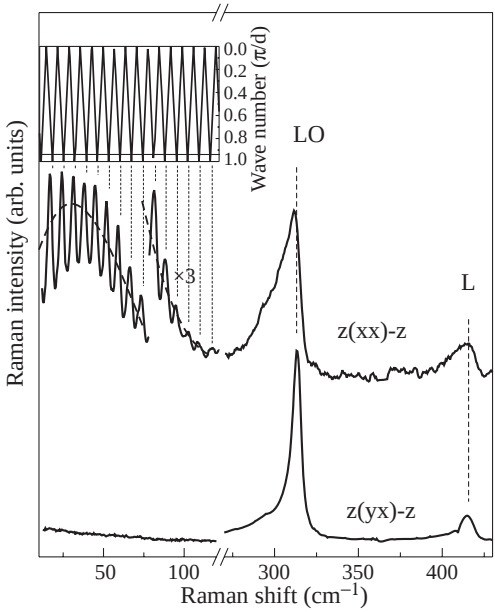

Fig. 1. Raman spectra of the sample A taken at $E_i = 2.41$ eV. The inset shows the calculated dispersion of LA phonons for the planar Ge/Si superlattice. Calculated Raman spectra are shown by dashed lines.

The Raman spectra were measured in Stokes and anti-Stokes regions with various excitation energies. The continuous emission and the scattering efficiency of the folded acoustic phonons is strongly enhanced for an excitation energy of 2.34 eV. Moreover, the observed emission band shifts toward higher free value of 25 cm^{-1} for excitation energy of 2.61 eV. The origin of the continuous emission observed can be understood using a model based on interaction between bulk-like acoustic phonons and confined electronic states. The electronic (or hole) confinement causes a breaking up of translational invariance and leads to Raman scattering by phonons originating from the whole acoustic dispersion branch [6, 7]. Following to Mlayah *et al.* [7] the scattering intensity under resonant conditions is calculated. Due to the particular shape and size of QDs (the dot base size is about one order of magnitude larger than the QD height) only the confinement along the growth axis can be considered. Coupling between Ge layers is neglected. The calculated Raman spectrum with an average value of Ge dot height of 1.2 nm is shown in Fig. 1 by a dashed line. The maximum and the spectral shape of the calculated emission band is consistent with those observed in experiment. The frequency enlargement of continuous emission observed at excitation energy of 2.61 eV corresponds to the Raman response from the QDs of the smaller size (0.8 nm). Indeed, the frequency position of continuous emission band is a measure (Fourier transform) of electronic confinement. Thus, strong electronic confinement in the small-size Ge QDs is very likely responsible for the frequency enlargement of continuous emission band resonantly enhanced at higher excitation energies.

3. Optical spectral region

In optical spectral range, the experimental Raman spectra of Ge QD superlattices (sample A) shown in Fig. 1 reveal the LO phonons in Ge QDs at 315 cm^{-1} in the z(yx)-z scattering geometry. The appearence of LO phonons in the "prohibited" z(xx)-z geometry manifests the lifting of the Raman selection rules for the planar superlattices due to QD formation. Frequency position of LO phonons corresponds to fully strained Ge QD layers where the biaxial compressive strain of Ge bonds is $\sim$ 4% [2]. Weaker feature at 417 cm^{-1} (labelled as L) was attributed to the longitudinal Ge-Si vibrational modes.

While the experimental facts considered above can be satisfactorily explained using various two-dimensional models, behaviour of optical phonons in Ge QD superlattices probed with different laser excitation lines can be understood only in terms of the zero-dimensional confinement. Figure 2 shows the Raman efficiencies and the frequency positions for the

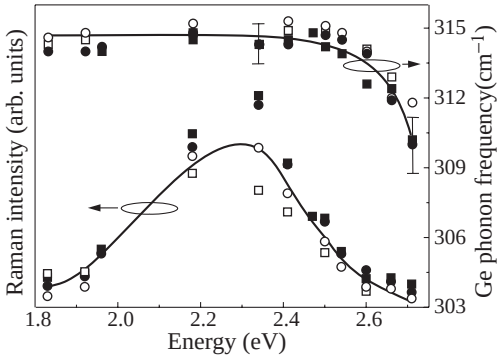

Fig. 2. Raman intensity and frequency positions of LO Ge phonons for the samples A (squares) and B (circles) measured in z(xy)-z (open) and z(xx)-z (solid) geometry.

LO Ge phonons displayed as a function of excitation energy. The resonance peak at about 2.34 eV that is very similar to the resonance observed in Ref. [1] is attributed to the E_1 exciton in Ge quantum dots. The position of the LO phonons localised in Ge QDs shifts towards lower frequency with the excitation energy (from 2.5 to 2.7 eV). This shift amounts to 4–5 cm^{-1} and indicates the presence of a QD size distribution in Ge dot superlattices. Raman scattering from smaller Ge QDs for which the E_1 exciton is at the higher energies, is size-selectively enhanced by the resonance of the exciting laser energy and the confined excitonic states. The size-confinement effect of optical phonons in Ge QDs which is stronger for the QDs with a small size, gives rise to a shift of optical phonons towards lower frequencies due to a negative dispersion of optical phonons in Ge.

The interdiffusion at Ge-Si interface in the structures under investigation was found to be very small [2] and cannot be responsible for this effect. A good agreement of calculated and experimental Ge phonon frequency positions as well as a small broadening of Ge optical phonons ($\sim 6\ cm^{-1}$) suggests that the fluctuation of strain for different QDs is small. Thus, in our samples, the atom intermixing and strain variation can be neglected.

In conclusion, we have carried out a detailed analysis of the Raman spectra of Ge QD superlattices. The folded LA phonons seen in the spectra can be very well described by Rytov theory usually applied for conventional superlattices. The weakening of selection rules due to non-conservation of crystal momentum gives rise to the low frequency continuous emission. The confined electron-hole transitions which lead to an increase of the E_1 exciton energy with decreasing Ge QD size allow size-selective Raman scattering under resonance conditions. Strong electronic confinement in small size Ge QDs is very likely responsible for frequency enlargement of continuous emission.

References

[1] S. H. Kwok, P. Y. Yu, C. H. Tung, Y. H. Zhang, M. F. Li, C. S. Peng and J. M. Zhou, *Phys. Rev. B* **59**, 4980 (1999).
[2] A. Milekhin, N. Stepina, A. Yakimov, A. Nikiforov, S. Schulze and D. R. T. Zahn, *Eur. Phys. J. B* **16**, 355 (2000).
[3] A. Milekhin, N. Stepina, A. Yakimov, A. Nikiforov, S. Schulze, T.Kampen and D. R. T. Zahn, *to published in Poceedings of ICPS-10, Osaka, Japan, sept. 2000*, (2001).
[4] M. Cazayous, J. R. Huntzinger, J. Groenen, A. Mlayah, S. Christiansen, H. P. Strunk, O. G. Schmidt and K. Eberl, *Phys. Rev. B* **62**, 7243 (2000).
[5] S. M. Rytov, *Akoust. Zh.* **2**, 71 (1956).
[6] T. Ruf, V. I. Belitsky, J. Spitzer, V. F. Sapega, M. Cardona and K. Ploog, *Phys. Rev. Lett.* **71**, 3035 (1993).
[7] A. Mlayah, A. Sayari, R. Grac, A. Zwick, R. Carles, M. A. Maaref and R. Planel, *Phys. Rev. B* **56**, 1486 (1997).
[8] F. Cerdeira, C. J. Buchenauer, F. H. Pollak and M. Cardona, *Phys. Rev. B* **5**, 580 (1972).

9th Int. Symp. "Nanostructures: Physics and Technology"
St Petersburg, Russia, June 18–22, 2001

Near and mid infrared spectroscopy of InGaAs/GaAs quantum dot structures

V. A. Shalygin†, L. E. Vorobjev†, A. V. Glukhovskoy†, S. N. Danilov†, V. Yu. Panevin†, D. A. Firsov†, B. V. Volovik‡, N. N. Ledentsov‡, D. A. Livshits‡, V. M. Ustinov‡, Yu. M. Shernyakov‡, A. F. Tsatsul'nikov‡, A. Weber§ and M. Grundmann§♯

† St Petersburg State Technical University, 195251, St Petersburg, Russia
‡ Ioffe Physico-Technical Institute, St Petersburg, Russia
§ Institut für Festkörperphysik, TU Berlin, D-10623 Berlin, Germany
♯ present address: Universität Leipzig, Institut für Experimentelle Physik II, D-04103 Leipzig, Germany

Abstract. Results of a photo- and electroluminescence study of vertically coupled $In_{0.5}Ga_{0.5}As$/GaAs quantum dot structures with extended waveguide (1.24 μm thick) are presented. Spectra of spontaneous and stimulated near-infrared ($\lambda \simeq 1$ μm) emission as well as spectra of spontaneous mid-infrared ($\lambda \simeq 12$ μm) emission are obtained under optical and electrical pumping. It is shown that the observed mid-infrared emission is connected with intraband electron optical transitions in the quantum dot structures.

Introduction

The use of intraband (intersubband or intersublevel) optical transitions in quantum wells and quantum dots (QDs) allows to extend the emission spectrum of semiconductor lasers into the mid-infrared range (10–20 μm). QD structures attracted particular interest because of the high electron lifetimes on excited states (phonon bottleneck effect). The feasibility of bipolar mid-infrared (MIR) lasers based on electron intersublevel transitions in QD structures during near-infrared (NIR) interband lasing has been theoretically considered in [1, 2, 3]. The first experimental studies of MIR spontaneous emission accompanying NIR stimulated emission were performed with edge-emitting QD lasers under current injection [3, 4, 5].

Here we report on a study of spectra of interband spontaneous and stimulated emission as well as spectra of intraband (intersublevel) spontaneous emision from QD structures with extended waveguide. Optical and current pumping were used for electron-hole pair injection.

1. Samples and techniques

Quantum dot structures were grown by solid source MBE system on (001) GaAs substrates. The 0.24 μm active layer of the structures consisted of six periods of $In_{0.5}Ga_{0.5}As$/GaAs vertically coupled quantum dots embedded in a waveguide between doped cladding layers. The extended NIR waveguide was formed with two 0.5 μm low-doped graded $Al_xGa_{1-x}As$ layers. For studies of NIR stimulated interband emission the cavity length was chosen between 0.15 and 2.5 mm.

Optical pumping was provided by means of a 3 W Ar laser. A step-scan Fourier spectrometer with MCT detector (cut-off energy is 54 meV) was used for obtaining emission

spectra. For the measurements of MIR spectra, the NIR radiation was blocked by an InAs filter. The emission under optical pumping was collected from the surface of the sample. In this case a part of the Be-doped top layers was removed with chemical etching. All measurements were carried out at 77 K.

2. Spontaneous and stimulated NIR emission

The aim of these studies was to find the electron energy structure in our samples. Spectra of spontaneous and stimulated interband NIR emission obtained under optical pumping are shown in Fig. 1. Investigations under optical pumping were carried out for different thicknesses of etched top layer and for different cavity lengths. These factors are responsible for the actual value of the optical losses in the waveguide. The results are shown in Fig. 1(a) (low losses) and 1(b) (high losses). The increase of excitation power in both cases leads to the blue shift of PL line position (curves 7–4). This can be explained by the presence of miniband-like electron energy spectra in QDs caused by vertical coupling. Spectra of spontaneous emission consist of two peaks probably connected with e-h transitions between ground and excited electron and hole states in QDs. Lasing appears at 1263 meV and at 1307 meV for samples with low and high losses, respectively. We connect these spectral features with laser emission through the ground and first excited states, respectively.

Electroluminescence (EL) spectra are presented in Fig. 2. In these spectra lines connected with ground state (near 1260 meV), first excited state (near 1310 meV) and a peak at 1400 meV probably connected with EL from wetting layer appear. The cavity length was 2.5 mm: thus lasing occurs through the ground state.

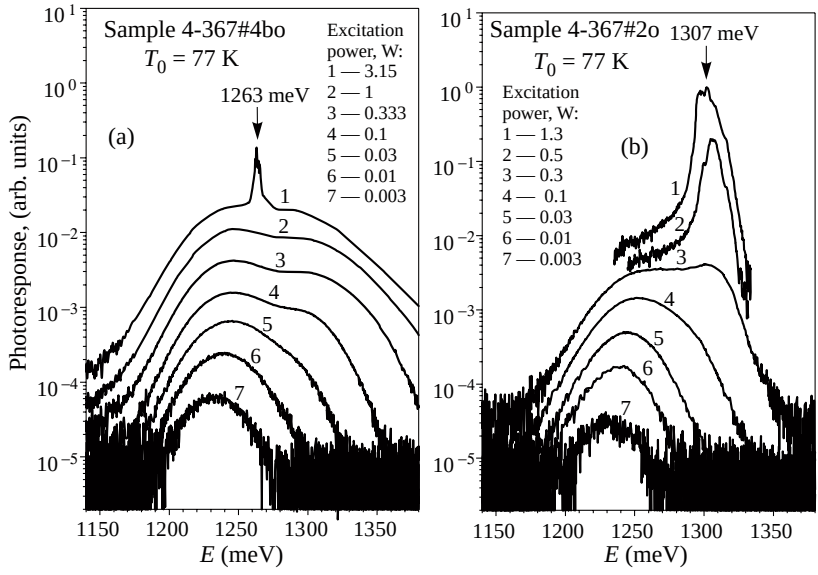

Fig. 1. NIR PL spectra under different pumping power: (a) for samples with low optical losses (etching time is more than 25 s, cavity length is 2.2 mm); (b) for samples with high optical losses (etching time is 25 s, cavity length is 1.1 mm).

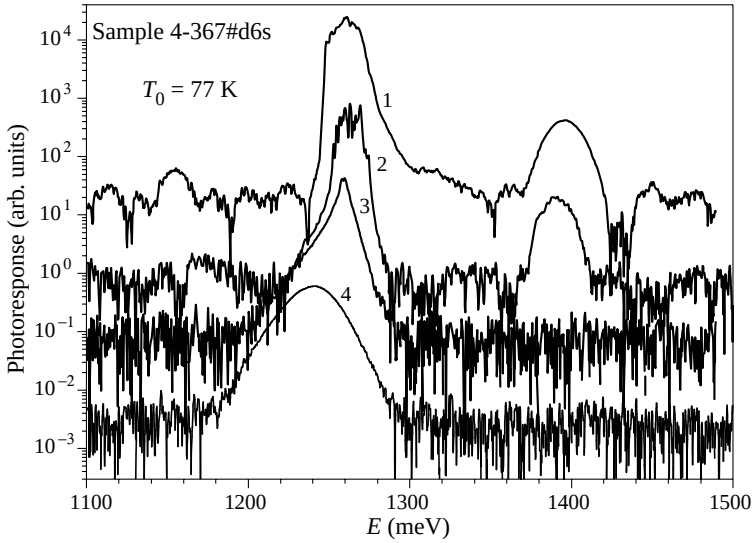

Fig. 2. NIR spectra of electroluminescence. Injection current (A) is: 4 (curve 1), 0.2 (curve 2), 0.08 (curve 3), 0.02 (curve 4). Cavity length is 2.5 mm, strip width is 100 μm.

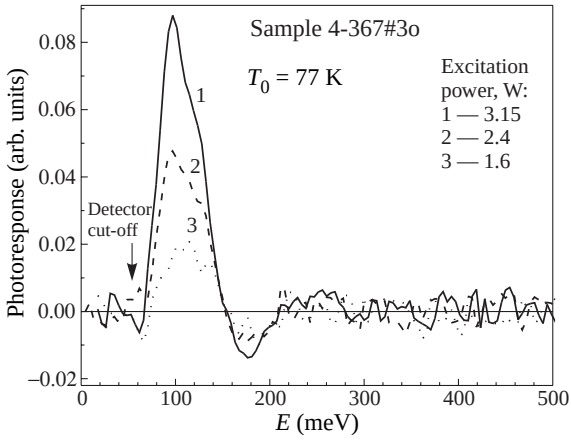

Fig. 3. The spectra of MIR photoresponse for different intensities of optical pumping. Cavity length is 1 mm, etching time is 15 s, excitation area is 0.0037 cm^2.

3. Spontaneous MIR emission

The MIR emission under optical pumping was studied for a set of samples, which were made from the same QD laser structure. They had different thicknesses of the top layer after etching. Measured spectra resulted from a superposition of MIR emission from the sample as well as photorefraction and photoinduced absorption of blackbody-like background radiation. The MIR photoresponse spectra for one of the samples, where the contributions of pumping induced absorption and refraction are the smallest, are presented in Fig. 3. For this sample approximately 1 μm top layer was removed by etching. The spectral position of

the MIR emission line (about 100 meV) corresponds to the NIR emission spectra, namely it can be connected with electron transitions from the wetting layer states to the ground state of the QDs. We could not observe MIR emission connected with electron transitions from excited to ground QD states (all the more so for similar transitions for holes) because such transition energies are smaller then the present detector cut-off energy.

Conclusion

NIR and MIR emission from vertically coupled InGaAs/GaAs QDs under optical and electrical pumping were observed. The peculiarities of spectra of NIR stimulated and spontaneous emission are associated with e-h transitions between ground, excited and wetting layer states of electrons and holes. The wide peak of MIR ($\lambda \simeq 12\ \mu$m) spontaneous emission can be connected with electron transitions between wetting layer or second excited states and ground states of QDs. The next step should be to study MIR emission from QD structures with MIR waveguide in a spectral range extended to longer wavelengths as well as a comparison of these results with calculated electron and hole energy spectra in QDs.

Acknowledgements

This work was supported by the DFG (Gr 1011/7 and 436 RNS 17/36/00), INTAS (97-751), RFBR, Russian Program “Integration”, Russian Ministry of Industry, Science and Technology (program PSNS) and Russian Ministry of Education.

References

[1] J. Singh, *IEEE Photonics Technol. Lett.* **8**, 488 (1996).
[2] L. E. Vorobjev, *JETP Lett.* **68** 417 (1998).
[3] M. Grundmann, A. Weber, K. Goede, V. M. Ustinov, A. E. Zhukov, N. N. Ledentsov, P. S. Kop’ev and Zh. I. Alferov, *Appl. Phys. Lett.* **77** 4 (2000).
[4] L. E. Vorobjev, D. A. Firsov, V. A. Shalygin, V. N. Tulupenko, Yu. M. Shernyakov, N. N. Ledentsov, V. M. Ustinov and Zh. I. Alferov, *JETP Lett.* **67** 275 (1998).
[5] S. Krishna, Q. Qasaimeh, P. Bhattacharya, P. J. McCann and K. Namjou, *Appl. Phys. Lett.* **76** 3355 (2000).

9th Int. Symp. "Nanostructures: Physics and Technology"
St Petersburg, Russia, June 18–22, 2001

Resonant parametric generation of infrared radiation on intersubband transitions in low-dimensional semiconductor heterostructures

A. A. Belyanin†, F. Capasso‡, V. V. Kocharovsky†, Vl. V. Kocharovsky† and M. O. Scully§

† Institute of Applied Physics RAS, 46 Ulyanov Str., 603600 Nizhny Novgorod, Russia
‡ Bell Laboratories, Lucent Technologies,
600 Mountain Avenue, Murray Hill, NJ07974, USA
§ Physics Department and Center for Theoretical Physics,
Texas A&M University, College Station, TX 77843-4242

Abstract. A new scheme for generation of coherent radiation on the intersubband transition without population inversion between subbands is presented. The scheme is based on the resonant nonlinear mixing of the optical laser fields on the two interband transitions which are generated in the same active region and serve as a coherent drive for the infrared field. This mechanism for frequency self-conversion can work efficiently at room temperature and with injection current pumping. Due to the parametric nature of infrared generation, the proposed inversionless scheme is especially promising for long-wavelength (far-infrared) operation.

Introduction

Lasing on the intraband transitions between levels of dimensional quantization in quantum-well (QW) and quantum-dot heterostructures is a promising way towards injection-pumped laser generating in the mid- and far-infrared range (denoted below as IR for brevity). There are however two major problems. The first one is strong non-resonant losses of the IR field due to free-carrier absorption and diffraction, which become increasingly important at longer far-IR wavelengths. Second, due to very short lifetime of excited states it is difficult to maintain a large enough population inversion and high gain at the intersubband transitions, necessary to overcome losses. There were many suggestions to solve this problem by rapid depletion of the lower lasing state using, e.g., the resonant tunneling to adjacent semiconductor layers or transition to yet lower subbands due to phonon emission [1], or even stimulated interband recombination [2]. The successful culmination of these studies is the realization of quantum cascade lasers [3], in which the lower lasing state is depopulated either by tunneling in the superlattice or due to transition to lower-lying levels separated from the lasing state by nearly the energy of a LO-phonon.

We put forward another possibility [4], allowing us to achieve IR generation without population inversion at the intraband transition. This becomes possible with the aid of laser fields simultaneously generated at the *interband* transitions (called optical fields for brevity), which serve as the coherent drive for the frequency down-conversion to the IR. Employing self-generated optical lasing fields provides the possibility of injection current pumping and also removes the problems associated with external drive (beam overlap, drive absorption, spatial inhomogeneity), which were inherent in previous works on parametric down-conversion in semiconductors.

1. Generic three-level scheme

As the simplest case, consider the situation when only three levels of dimensional quantization are involved in generation: one (lowest-lying) heavy-hole level, and two electron

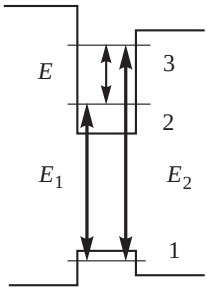

Fig. 1. Generic level scheme for three-color generation in an asymmetric quantum well: two strong fields E_1 and E_2 lasing at adjacent interband transitions $2 \rightarrow 1$ and $3 \rightarrow 1$ generate coherent IR radiation E at the beat frequency.

levels; see Fig. 1. Of course, this scheme also describes the situation when there are two hole levels and one electron level involved.

We need all three transitions to be allowed by selection rules. In a QW this will generally require using asymmetric structures, e.g. rectangular well with different barrier heights. Our calculations for asymmetric AlGaAs/GaAs structures based on the Kane model show that it is relatively easy to obtain the ratio of dipole moments of $e1 - hh1$ and $e2 - hh1$ transitions close to 3 for a wide range of parameters. Symmetric QWs can also be employed, e.g., under a strong DC field bias or in the case of a strong coupling between different subbands of heavy and light holes. In quantum dots the three-level scheme can be easily realized with all three transitions allowed.

When the injection current density reaches the threshold value $j_{\rm th}$, optical generation starts between ground electron and hole states. Upon increasing the pumping current, optical generation can start also from excited states and the laser can be completely switched to lasing from the excited state which has higher maximum gain due to a larger density of states. The effect of excited-state lasing was studied both in QW and QD lasers [5–7]. It was found that with optimized laser parameters the region of simultaneous ground-state and excited-state lasing can be around $j \sim 2j_{\rm th}$ [5, 6].

The presence of one or two strong optical driving fields in the cavity gives rise to a rich variety of *resonant* coupling mechanisms by which the IR field can be produced. Here we will concentrate on one such scheme in which the two coherent optical fields having frequencies ω_1 and ω_2 excite the induced electronic oscillations at the difference frequency $\omega = \omega_2 - \omega_1$. It is important to note that the coherent IR polarization is parametrically excited independently on the sign of population difference at the IR transition.

To maximize the IR output, the phase matching condition must be satisfied. This requires special waveguide design since refractive indices of bulk semiconductor materials for optical and IR frequencies are different. This issue is discussed elsewhere. Basically, one needs separate confinement layers of the IR and optical modes. For far-IR generation, there is more flexibility due to more efficient manipulation of the refractive index by doping.

2. Efficiency of IR generation

To quantify the above ideas, we have calculated the excited IR polarization and field by solving the coupled electronic density-matrix equations and electromagnetic Maxwell equations for the three fields, assuming steady-state generation.

In the case of homogeneous broadening, one can obtain analytic expression for the IR intensity $|\mathcal{E}|^2$:

$$|\mathcal{E}|^2 \simeq |\mathcal{E}_1|^2 \frac{|\mathcal{E}_2|^2}{|\mathcal{E}_2|_s^2} \left(\frac{d}{d_1} \frac{\omega}{\omega_1} \frac{\kappa_1}{G_1} \frac{G}{\kappa} \right)^2 + |\mathcal{E}_2|^2 \frac{|\mathcal{E}_1|^2}{|\mathcal{E}_1|_s^2} \left(\frac{d}{d_2} \frac{\omega}{\omega_2} \frac{\kappa_2}{G_2} \frac{G}{\kappa} \right)^2, \qquad (1)$$

Here the quantities without indices and with indices 1,2 correspond to the intersubband transition and to the interband transitions, respectively; d's are the dipole moments of the transitions; κ's and G's are the material losses and optical confinement factors of the waveguide modes; $|\mathcal{E}_{1,2}|_s^2$ are the saturation intensities.

At a given wavelength, the crucial parameter in the above equation which governs the efficiency of down-conversion, is $\eta = (\kappa_{1,2}/G_{1,2})(G/\kappa)$. The main source of IR losses is free-carrier absorption in the active region and doped cladding layers. Our detailed calculations for the GaAs-based structure with separate confinement of IR ($\lambda = 8\ \mu$m) and optical modes ($\lambda = 0.73$ and $0.8\ \mu$m) yield the value of η around 0.5–0.8.

In the opposite limiting case of very large inhomogeneous broadening, we will assume that the inhomogeneous widths u_{ik} of all transitions are much larger than all homogeneous bandwidths γ_{ik}. In this case the precise shape of the inhomogeneous line is not important and explicit analytic formulas can be obtained for two different situations: when the optical field intensities are much smaller or much greater than the saturation values. Detailed analysis [4] shows that the IR intensity grows rapidly as the product of optical intensities generated on the interband transitions,

$$|\mathcal{E}|^2 \simeq |\mathcal{E}_1|^2 \frac{|\mathcal{E}_2|^2}{|\mathcal{E}_2|_s^2} \left(\frac{2\gamma_{32}}{(\gamma_{32}+\gamma_{21})} \frac{d}{d_1} \frac{\omega}{\omega_1} \frac{u_{21}}{u_{32}} \frac{\kappa_1}{G_1} \frac{G}{\kappa} \right)^2, \tag{2}$$

until it reaches the saturation value. Above this value, the IR field begins to deplete the electron populations, and its growth becomes nonlinearly saturated. In the optimal case, the maximum internal efficiency of the down-conversion can reach the limiting quantum value corresponding to one IR photon per one optical photon.

For the mid-IR range $5-10\ \mu$m the maximum IR power is of order 10 mW if we have the value of 100 cm^{-1} for IR losses, and the optical field intensities inside the cavity are of the order of saturation values. Here we assumed $\eta \sim 0.1$. Beyond the reststrahlen region of strong phonon dispersion ($\lambda \geq 50\ \mu$m for AlGaAs/GaAs structure) the expected IR power is ≤ 1 mW due to rapidly growing losses.

3. Conclusions

Our calculations demonstrate the generation of coherent IR emission at intersubband transitions due to nonlinear wave mixing in standard multiple QW or QD laser diodes. The prerequisite for this is simultaneous lasing at two optical wavelengths which provide the necessary drive fields. This mechanism does not require population inversion at the IR transition, and its threshold current is determined by the minimum injection current necessary for the interband lasing from higher (excited) carrier states of dimensional quantization.

References

[1] R. F. Kazarinov and R. A. Suris, *Sov. Phys. Semicond.* **5**, 707 (1971).
[2] J. Singh, *IEEE Photon Techn. Lett.* **8**, 488 (1996).
[3] J. Faist, F. Capasso, D. L. Sivco et al., *Science* **264**, 553 (1994).
[4] A. A. Belyanin, F. Capasso, V. V. Kocharovsky, Vl. V. Kocharovsky and M. O. Scully, *Phys. Rev. A*, submitted.
[5] Y. Tokuda, N. Tsukada, K. Fujiwara et al., *Appl. Phys. Lett.* **49**, 1629 (1986).
[6] T. R. Chen, Y. Zhuang, Y. J. Xu et al., *Appl. Phys. Lett.* **60**, 2954 (1992).
[7] D. Bimberg, M. Grundmann and N. N. Ledentsov, *Quantum Dot Heterostructures*, J. Wiley & Sons, New York, 1998.

9th Int. Symp. "Nanostructures: Physics and Technology"
St Petersburg, Russia, June 18–22, 2001

Time constant of far IR response of quantum Hall device

I. V. Erofeeva†, *V. I. Gavrilenko*†, O. Astafiev, Y. Kawano‡ and S. Komiyama‡
† Institute for Physics of Microstructures, RAS,
603600, Nizhny Novgorod, GSP-105, Russia
‡ Department of Basic Science, University of Tokyo,
Komaba 3-8-1, Meguro-ku, Tokyo 153-8902, Japan

Abstract. The characteristic time of far IR response of quantum Hall effect detector in GaA/AlGaAs has been investigated versus the magnetic field. The response time is shown to increase dramatically with the field due to the spatial separation of photoexcited electrons and holes captured by localized states formed by the disordered potential.

Introduction

Quantum Hall effect (QHE) device is known to be a sensitive detector of far infrared (FIR) radiation [1–5]. At QHE the Hall resistance is quantized and the longitudinal resistance R_{xx} vanishes. The finite R_{xx} emerges when electrons and holes are excited by FIR radiation at cyclotron resonance (CR) in the delocalized (extended) states near the Landau level centers above and below the Fermi level E_F. A thorough investigation of the photoresponse has been undertaken recently [5]. The results obtained revealed the key role of the random potential in the mechanism of FIR-photoresponse. The present paper deals with the magnetic field dependence of the response time that has been shown to be consistent with the response mechanism proposed in [5].

1. Experimental

Samples under study were Hall bars fabricated on selectively doped heterostructure GaAs/$Al_{0.3}Ga_{0.7}As$ with two-dimensional electron gas (2DEG) ($\mu_{4.2\,\mathrm{K}} = 8 \times 10^5$ cm$^2 \cdot$s, $n_s = 2.8 \times 10^{11}$ cm^{-2}). They have a long 2DEG channel 50 μm $\times$170 mm in size patterned in a zigzag shape and fitted into an area of 4×4 mm^2 [1, 5]. The sample placed in the liquid helium in the center of a superconducting solenoid was biased by a d.c. current of 3 μA. As a broad band FIR emitter we used bulk p-Ge crystal ($N_A - N_D = 2 \times 10^{13}$ cm^{-3}) of $8 \times 4 \times 0.5$ mm^3 in size, ohmic contacts being deposited onto 8×0.5 mm^2 opposite faces. The emitter was excited with a voltage pulses of 16 V and 200 μs in duration with a repetition rate 8 Hz. The emitter was placed in the same cryostat, the emitter radiation being guided to the sample through a metallic light pipe of 7 mm in diameter and 30 cm long. The pulsed response from the detector was analyzed using either digital oscilloscope or boxcar integrator. To provide a possibility of the detector tuning the 2DEG concentration was successively increased by the detector band-gap illumination using a GaAs light emitting diode. The increased 2DEG concentration persisted up to the heat recycling of the sample.

2. Results and discussion

Typical magnetic field dependences of R_{xx} and photoresponse are shown in Figures 1(a-c) for three different values of 2DEG concentration. It is clearly seen that the response

occurs near the $R_{xx}(H)$ minimums at the even values of the filling factor $\nu = 4$ and $\nu = 2$. In Figure 1(a) the photoresponse at both the $\nu = 4$ and $\nu = 2$ consists of two prominent peaks that is a general trend observed if QHE plateaus are well developed [5]. It is clearly seen in Figures 1(b-c) that after a band-gap-illumination the depths of R_{xx} minima decrease (probably due to nonuniform increase of 2DEG concentration) thus resulting in a single peak structure of the response. Figures 1(d-f) give examples of the response oscilloscope traces recorded either in the 'right' peak maxima (Fig. 1(d)) or in maxima of single peak structures Figures 1(e,f). Some data on $\tau(H)$ dependence ate summarized in Fig. 2. It is clearly seen that within a single series of measurements the response time exponentially increases with the magnetic field that is consistent with the mechanism of FIR-response of QHE device proposed in [5]. It is known that there is a

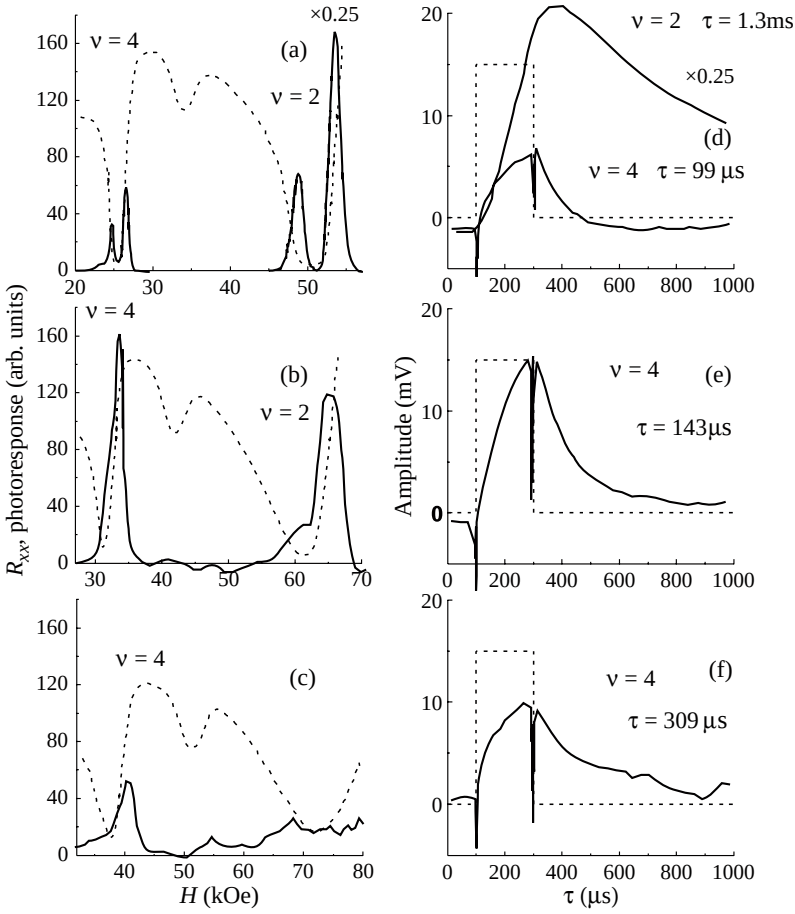

Fig. 1. Longitudinal resistance R_{xx} (brouken curves) and photoresponse of QHE detector (solid curves) versus the magnetic field before (a) and after (b),(c) band-gap illumination, $T = 2.2$ K. Solidcurves in plots (d)-(f): examples of the response oscillograms measured at $\nu = 4$, $H = 25.9$ kOe and $\nu = 2$, $H = 52.9$ kOe (d), $\nu = 4$, $H = 31.7$ kOe (e) and $\nu = 4$, $H = 39.4$ kOe (f), brouken curves: oscillograms of the voltage pulses applied to the emitter.

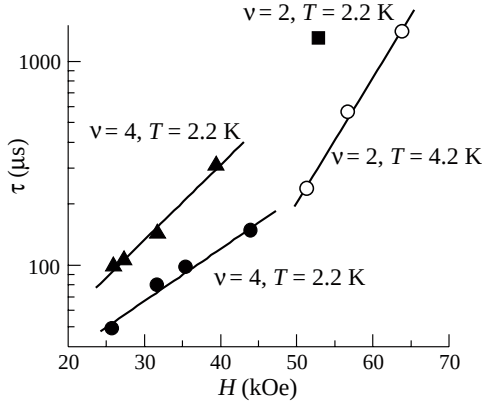

Fig. 2. Time constant of QHE detector photoresponse versus the msgnetic field measured at the successive increase of 2DEG concentration produced by band-gap illumination of the sample. Two different series of $\tau(H)$ data at $\nu = 4$, $T = 2.2$ K were obtaned one after another after heating the sample up to the room temperature and subsequent cooling down. To the author's opinion this testify a nonreproducibility of 2DEG in one in the same GaAs/AlGaAs sample (from one cooling to another one).

long-range random potential in 2DEG systems at high magnetic field, the amplitude of the fluctuation potential reaching the order of $\hbar\omega_c$ in the close vicinity of QHE state [6]. When an electron and a hole are photoexcited at CR in Landau levels above and below E_F, respectively, the excited electron (hole) will rapidly (within 10 ns) fall into a local minimum (maximum) energy (i.e. into a localized state). This spatial separation prevents the excited carriers from quickly recombining. The localized electron (hole) can be excited occasionally to a delocalized state formed around the Landau level center. Once delocalized, the nonequilibrium electron (hole) participates in the longitudinal conductivity thus giving rise to the photoresponse, recaptured by localized states etc. At low enough both the lattice temperature and the excitation level the time constant of FIR response is closely related to the recombination lifetime of localized carriers separated by the characteristic distance ΔY. In strong magnetic fields in high mobility samples ΔY could exceed significantly the magnetic length $l_B = (\hbar c/eH)^{1/2}$ that is the extension of a carrier wavefunction. Thus the recombination may be strongly suppressed due to the small overlapping between the electron and hole wavefunctions [5]:

$$\tau = A \exp[(\Delta Y/l_B)^2] = A \exp[(\Delta Y)^2 eH/\hbar c] = A \exp(H/H^*). \qquad (1)$$

From the slope of $\lg \tau(H)$ dependences (Fig. 2) one can determine the characteristic magnetic fields H^* and obtain the following data for $\Delta Y = (\hbar c/eH^*)^{1/2}$:

$\nu = 4$, $T = 2.2$ K (closed circles): $H^* = 17.0$ kOe, $\Delta Y = 200$ Å;
$\nu = 4$, $T = 2.2$ K (triangles): $H^* = 11.8$ kOe, $\Delta Y = 235$ Å;
$\nu = 2$, $T = 4.2$ K (open circles): $H^* = 7.1$ kOe, $\Delta Y = 300$ Å.

The figures obtained are noticeably less than those obtained recently in a similar 2DEG system using a scanning probe technique with a spatial resolution of 900 Å: ($\Delta Y = 900 - 2000$ Å) [7]. However it should be noted that in the present work we have determined the

smallest characteristic length of the disordered potential which is responsible for the shortest lifetime of the photoexcited carriers. In general, if measured with sufficient accuracy, there is long-lived components in the response decay [5] that is a signature of relaxation kinetics in disordered systems.

Acknowledgements

This work was financially supported by RFBR (No 00-02-16568, No 00-02-81022) and the Russian Scientific Programs: "Physics of Solid State Nanostructures" (No 99-1128), "Fundamental Spectroscopy" (No 8/02.08), "Physics of Microwaves" (No 4.5), "Leading Scientific Schools" (No 00-15-96618), "Integration" (540, 41).

References

[1] S. Komiyama, Y. Kawano and Y. Hisanaga, *Proc. 21st Int.Conf. on IR&MM Waves (Berlin 1996)*, p. BT2.
[2] Y. Kawano and S. Komiyama, *Phys. Rev. B* **61**, 2931 (2000).
[3] A. V. Antonov, I. V. Erofeeva, V. I. Gavrilenko *et al., 1999 Compound Semiconductors (Inst. Phys. Conf. Ser. 162)*, IOP Publishing, p. 111.
[4] B. A. Andreev, I. V. Erofeeva, V. I. Gavrilenko *et al., Semicond. Sci. Technol.* **16**, (2001) (to be published).
[5] Y. Kawano, Y. Hisanaga, H. Takenouchi and S. Komiyama, *Journ. Appl. Phys.* (2001) (to be published).
[6] D. B. Chklovskii, B. I. Shklovskii and L. I. Glasman, *Phys. Rev. B* **46**, 4026 (1992).
[7] S. H. Tessmer, P. I. Glicofridis, R. C. Ashoori *et al., Nature* **392**, 51 (1998).

9th Int. Symp. "Nanostructures: Physics and Technology"
St Petersburg, Russia, June 18–22, 2001

Nonlinear generation of mid-infrared radiation in quantum well laser

A. A. Afonenko†, *V. Ya. Aleshkin*‡ and N. B. Zvonkov§
† Byelorussian State University, Minsk, Byelorussia
‡ Institute for Physics of Microstructures of RAS, Nizhny Novgorod, Russia
§ Physical-Technical Institute of Nizhny Novgorod State University, Russia

Abstract. A possibility of mid-infrared radiation generation due to lattice nonlinearity in a quantum well laser based on InGaP/GaAs/InGaAs heterostructure is discussed. It is shown that this mechanism can provide radiation power of about 10 mW in the 10 μm wavelength region in a laser which generates two 10 W modes in the 1 μm wavelength range.

Introduction

A semiconductor laser based on GaAs is a promising device in terms of nonlinear optical effects. Indeed, there is an extremely high light intensity inside the laser. Besides, the second order optical nonlinear coefficient of GaAs is six times larger than that of the popular nonlinear crystal $LiNbO_3$. This nonlinearity is responsible for the frequently observed weak green light emission near cleavages in lasers generating 1 μm radiation which is the second harmonic generation. To date the second harmonic generation has been observed in the vertical cavity lasers [1, 2], too. A possibility of the difference mode generation in a quantum well laser emitting two short wavelength modes was discussed in [3]. However, the authors of [3] suggested using the electron nonlinearity of a quantum well containing three electron levels. Probably, this generation is not effective due to the smallness of mode overlapping in the nonlinear region and due to the difficulty in providing the phase matching condition.

In this work we discuss a possibility of the difference mode generation due to the lattice nonlinearity of GaAs in a semiconductor quantum well laser based on InGaP/GaAs/$In_xGa_{1-x}As$ heterostructure, which simultaneously generates two modes in the 1 μm wavelength range. We have suggested a special laser construction able to generate these two modes and to satisfy the phase matching condition which is necessary for effective generation of the difference mode. It has been shown that, if the phase matching condition is satisfied, the difference mode power can be of the order of 10 mW for a 10 μm wavelength region in a laser generating two short-wavelength modes with power 10 W.

1. Laser design

Consider the difference mode generation in a InGaP/GaAs/$In_xGa_{1-x}As$ quantum well laser. In ordinary lasers the waveguide consists of three layers. The central GaAs layer containing one or more quantum wells has a larger refractive index than the neighboring InGaP layers. As a rule, quantum wells generating radiation are situated near the GaAs layer centre. Due to this arrangement and the selection rules for radiative electron transition this laser generates the fundamental TE mode. The phase velocity of this mode is close to the light velocity in GaAs. Such a laser construction is not suitable for difference mode generation, since the dispersion of the refractive index in GaAs prevents phase matching. Indeed, the

phase velocity of the difference mode in this case is greater than the phase velocity of the polarization wave corresponding to the difference frequency ($\omega = \omega_1 - \omega_2$) which appears due to nonlinearity.

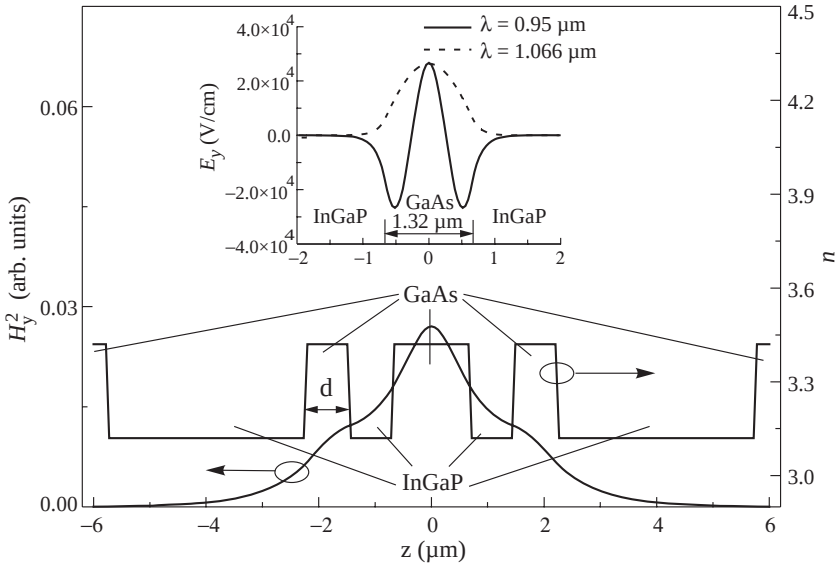

Fig. 1. Dependencies of the real part of refractive index and the square of magnetic field on coordinate for the difference mode. The widths of the lateral GaAs layers equal 0.81 μm and correspond to the power peak in Fig. 2. The value of the imaginary part of refractive index equals 10^{-3}. The dependencies of the electric field on coordinate for two high-frequency modes are shown in the insert. The powers of both high-frequency modes equal 10 W.

To satisfy the phase matching condition, we suggest using the second order mode for the highest frequency (ω_1) generation and the fundamental mode of the waveguide for other high frequency (ω_2) generation. The excited mode phase velocity is greater than the fundamental mode one, if the mode frequencies are equal. Using this peculiarity it is possible to compensate the dispersion of the refractive index and to satisfy the phase matching condition. Besides, in this case it is possible to avoid high absorption of mode with frequency ω_1 in the quantum wells generating mode ω_2, if the latter are situated in the places where the second order mode amplitude is near zero. The electric field distributions across the waveguide for the fundamental mode ($\lambda = 1.067$ μm) and the second order mode($\lambda = 0.95$ μm) are shown in the insert to Fig. 1.

How to excite simultaneously the second order mode for frequency ω_1 and the fundamental mode for frequency ω_2? To this effect we suggest that quantum wells generating frequencies ω_1 and ω_2 should be placed in the centre of the middle GaAs layer and at zero point of the second order mode, respectively. In this case for frequency ω_1 the second order mode has the smallest losses and, therefore, just this mode will be excited. The fundamental and the first order modes for this frequency have substantial losses due to absorption in the quantum wells generating frequency ω_2. For the frequency ω_2 the generation of the fundamental mode is preferable since this mode has the smallest losses and the greatest optical restriction coefficient.

The proposed laser waveguide construction is shown in Fig. 1. Additional lateral GaAs

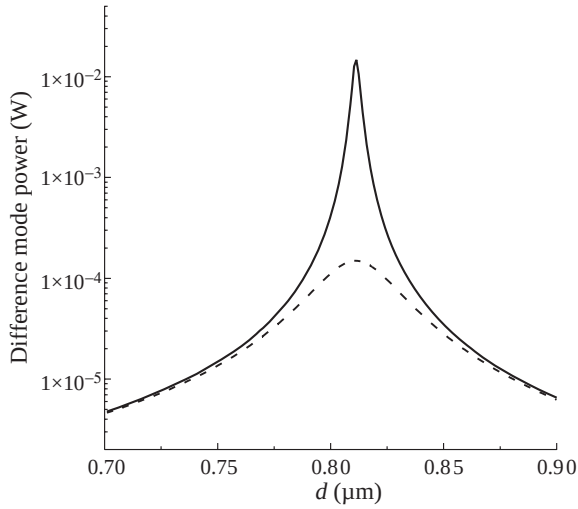

Fig. 2. Calculated dependency of the difference mode power on the width of the lateral GaAs layers. Imaginary part of refractive index equals 10^{-4} (solid line) and 10^{-3} (dash line). Wavelength of the difference mode is 8.66 μm and the ones for high-frequency modes are 0.95 and 1.067 μm. Calculations were carried out for the high-frequency mode powers 10 W and the waveguide width of 100 μm.

layers are necessary to provide low leakage losses of the difference mode. The width of these layers d we will consider as a parameter to satisfy the phase matching condition. Further we will assume that both GaAs lateral layers are of equal width d.

We also assume that a laser structure is grown on the (001) plane and the mirrors are the facets (110) or $(1\bar{1}0)$. In zinc blend-type crystals the optical second-order nonlinear tensor has equal nonzero elements only when three indexes are different $\varepsilon^{(2)}_{xyz}$. The axes x, y, z are directed along [100], [010] and [001], respectively. The electric field vectors of the high frequency modes have nonzero x- and y-components. Therefore, the electrical induction vector for the difference frequency is directed along z and the difference mode is a TM mode. The calculated dependence of the magnetic field squared on the coordinate for the excited TM difference mode is shown in Fig. 1. It is clear from the figure that the fundamental difference mode is excited.

2. Difference mode power

The calculated dependencies of the difference mode power on the width of lateral GaAs layers are shown in Fig. 2. We assume the powers of both short wavelength modes equal to 10 W and the waveguide width equal to 100 μm. The solid line corresponds to the free carrier concentration 10^{17} cm^{-3}. In this case we set the imaginary part of the refractive index for the difference mode ($\lambda = 8.66$ μm) to be $n' = 10^{-4}$ [4]. The real part of the refractive index equals 3.42 in GaAs [4] and 3.12 in InGaP. The dashed line corresponds to free carrier concentration 10^{18} cm^{-3}, in this case we set $n' = 10^{-3}$ [4]. From Fig. 2 it is clear that there are peaks of power when $d = 0.81$ μm. These peaks correspond to the phase matching. With an increase in losses the peak decreases and grows in width. For the considered parameters the maximal power of the difference mode is of order 10 mW

for $n' = 10^{-4}$ and 100 μW for $n' = 10^{-3}$. To ensure low leakage losses the widths of the external InGaP layers should be more than 5 μm and 3.5 μm in the first and the second cases, respectively.

Thus the proposed laser is able to generate power of order of ten mW in a 10 μm wavelength range. Note that to decrease the threshold current and improve efficiency it is possible to increase the reflection of mirrors for the short wavelength modes by using of multi-layer dielectric coatings.

Acknowledgements

This work was financially supported by the grants from RFBR-BRBR (00-02-81022), Russian scientific programs "Physics of Solid Nanostructures" (99-1128), "Fundamental spectroscopy" (8/02.08), "Leading scientific schools" (00-15-96618), Russian-Ukrainian program "Nanophysics and nanoelectronics" (2000-3F), NWO 047.006.014.

References

[1] Y. Kaneko, S. Nakagava, Y. Ichimura, N. Yamada, D. E. Mars and T. Tekeuchi, *J. Appl. Phys.* **87**, 1597 (2000).

[2] D. Vakhshoori, R. J. Fischer, M. Hong, D. L. Sivko, G. J. Zydzik, G. N. S. Chu and A. Y. Cho, *Appl. Phys. Lett.* **59**, 896 (1991).

[3] A. A. Belyanin, F. Capasso, V. V. Kocharovsky, Vl. V. Kocharovsky and M. O. Scully, *Phys. Rev. A* (in press) (2000)

[4] *Handbook of Optical Constants of Solids*, ed E. D. Palik, Academic, Orlando, FL, 1985.

9th Int. Symp. "Nanostructures: Physics and Technology"
St Petersburg, Russia, June 18–22, 2001

Configuration interaction applied to resonant states in semiconductors and semiconductor nanostructures

A. A. Prokofiev†, I. N. Yassievich†, A. Blom‡, M. A. Odnoblyudov‡ and K.-A. Chao‡
† Ioffe Physico-Technical Institute, St Petersburg, Russia
‡ Fasta tillståndets teori, Sölvegatan 14 A, S-223 62 Lund, Sweden

Abstract. A new approach for calculation of resonant state parameters is developed. The method proposed allows to solve different scattering problems, such as scattering and capture probability as well as calculations of shifts and widths of energy levels. It has been applied to the problem of resonant states induced by impurities in the barrier of quantum wells and by strain in uniaxially stressed germanium.

Introduction

Quasistationary (or resonant) states have been studied in atomic physics very well. Semiconductors are other systems where resonant states play a significant role in physical processes. Such states appear, for example, in gapless semiconductors when doped by shallow acceptors. The system of special interest is uniaxially strained germanium where the generation of THz radiation has been achieved [1, 2].

Here we suggest a new method for calculating the parameters of resonant states and the probability of resonant scattering, capture and emission of carriers. The approuch is based on the configuration interaction method which was first introduced by Fano [3] in the problem of autoionization of He. The main idea is to choose two different hamiltonians for the initial approximation one for continuum states and the other for localized states. The method is applied to resonant states induced (i) by impurities in the barrier of quantum wells and (ii) by shallow acceptors in Ge under stress.

1. Resonant states induced by localized states in barriers

We will demonstrate the general idea by applying it to the system consisting of a quantum well (QW) and one impurity in the barrier. The full hamiltonian is given by

$$\hat{H} = -\frac{\hbar^2}{2m}\Delta + V(z) + V_d(\mathbf{r} - \mathbf{r}_0), \tag{1}$$

where the potential of the QW $V(z)$ is shown in Fig. 1, V_d is the defect potential and $\mathbf{r}_0 = (0, 0, z_0)$ is the position of defect.

As an initial approximation for the wave function of the localized state induced by the impurity we use the solution of the equation:

$$\left[-\frac{\hbar^2}{2m}\Delta + V_d(\mathbf{r} - \mathbf{r}_0)\right]\varphi(\mathbf{r} - \mathbf{r}_0) = E_0\varphi(\mathbf{r} - \mathbf{r}_0). \tag{2}$$

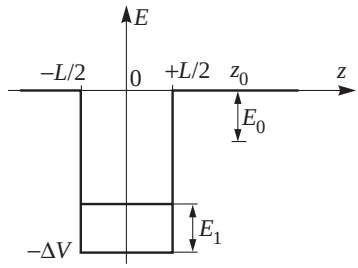

Fig. 1. The parameters of the well and impurity.

The wave functions of continuum states $\psi_{\mathbf{k}}(\mathbf{r})$ satisfy the following equation:

$$\left[-\frac{\hbar^2}{2m}\Delta + V(z)\right]\psi_{\mathbf{k}}(\mathbf{r}) = E_k\psi_{\mathbf{k}}(\mathbf{r}). \tag{3}$$

We are considering a QW with one energy level only, so that

$$E_k = -\Delta V + E_1 + \varepsilon_k, \tag{4}$$

where E_1 is the space quantization level and $\varepsilon_k = \hbar^2k^2/2m$ is kinetic energy of the 2D motion. So we can write for $\psi_{\mathbf{k}}(\mathbf{r})$:

$$\psi_{\mathbf{k}}(\mathbf{r}) = \frac{1}{\sqrt{S}}\phi(z)e^{i\mathbf{k}\rho}, \tag{5}$$

where S is a normalizing square.

Now we consider the problem of scattering of the in-plane moving carrier by the impurity in the barrier. Following Dirac, we construct the wave function in terms of scattering theory in the following form:

$$\Psi_{\mathbf{k}}(\mathbf{r}) = \psi_{\mathbf{k}}(\mathbf{r}) + a_{\mathbf{k}}\varphi(\mathbf{r}-\mathbf{r}_0) + \sum_{\mathbf{k}'}\frac{t_{\mathbf{k}\mathbf{k}'}}{\varepsilon_k - \varepsilon_{k'} + i\gamma}\psi_{\mathbf{k}'}(\mathbf{r}), \quad \gamma \to 0. \tag{6}$$

As the presence of one impurity does not perturb the continuum spectrum significantly, $\Psi_{\mathbf{k}}(\mathbf{r})$ should correspond to the energy E_k. Solving the Schrödinger equation with the full hamiltonian (1) for $\Psi_{\mathbf{k}}(\mathbf{r})$ one obtains the following expressions for $a_{\mathbf{k}}$ and $t_{\mathbf{k}\mathbf{k}'}$:

$$a_{\mathbf{k}} = \frac{1}{\sqrt{S}}\frac{V_{\mathbf{k}}}{E_k - (E_0 + \Delta E) + i\Gamma/2}, \quad t_{\mathbf{k}\mathbf{k}'} = \frac{1}{S}\frac{V_{\mathbf{k}}Z^*_{\mathbf{k}'}}{E_k - (E_0 + \Delta E) + i\Gamma/2} \tag{7}$$

The energy shift ΔE and the width $\Gamma/2$ of the resonant level are given by:

$$\Delta E = \delta - \frac{1}{(2\pi)^2}\int d^2k' Z^*_{\mathbf{k}'}W_{\mathbf{k}'} + \frac{1}{(2\pi)^2}P\int d^2k'\frac{Z^*_{\mathbf{k}'}V_{\mathbf{k}'}}{E_k - E_{k'}}, \tag{8}$$

$$\frac{\Gamma}{2} = \frac{1}{4\pi}\int d^2k' Z^*_{\mathbf{k}'}V_{\mathbf{k}'}\delta(E_k - E_{k'}). \tag{9}$$

Here the matrix elements

$$V_{\mathbf{k}} = \sqrt{S}\langle\varphi|V_d|\psi_{\mathbf{k}}\rangle,\ W_{\mathbf{k}} = \sqrt{S}\langle\varphi|\psi_{\mathbf{k}}\rangle,\ \delta = \langle\varphi|V(z)|\varphi\rangle,\ Z_{\mathbf{k}} = \sqrt{S}\langle\varphi|V(z)|\psi_{\mathbf{k}}\rangle, \tag{10}$$

are introduced.

The probability of resonant elastic scattering $W_{\mathbf{k}\mathbf{k}'}$ of 2D carriers and the capture probability $W_{\mathbf{k}r}$ are given by:

$$W_{\mathbf{k}\mathbf{k}'} = \frac{2\pi}{\hbar}|t_{\mathbf{k}\mathbf{k}'}|^2\delta(\varepsilon_k - \varepsilon_{k'}), \qquad W_{\mathbf{k}r} = |a_{\mathbf{k}}|^2, \tag{11}$$

respectively. Both probabilities contain the same resonant denominator.

The resonant scattering should be introduced into the kinetic equation when one solves the problem of the 2D carriers distribution function under an electric field applied in plane of the quantum well. This scattering affects the distribution function $f_{\mathbf{k}}$ of hot carriers, which is connected with the population of impurities in the barrier f_r [4]:

$$f_r = \sum_{\mathbf{k}} W_{\mathbf{k}r} f_{\mathbf{k}}. \tag{12}$$

2. Resonant acceptor states in uniaxially strained germanium

Tetraherally coordinated semiconductors (eg. GaAs, Ge, Si) have a fourfold degenerate top of the valence band. When strained, the top of valence band is split into two doubly degenerate states. The ground state of an acceptor shows the same behavior under uniaxial stress. At some critical value of the stress — when the splitting is larger than the acceptor binding energy — one of the split levels is shifted into the continuous spectrum of the other valence subband and becomes resonant. An effective optical transitions between resonant and localized states of the same impurities can take place. If the electric field is strong enough an electric impurity breackdown occurs and practically all localized impurity states become depopulated. Now capture and emission processes lead to an effective population of resonant states. This may cause an intracenter population inversion that is the basis for THz generation [1, 2].

Resonant acceptor states were considered in [4] by using the Dirac approach, which requires choosing an initial approximation hamiltonian giving localized states overlapping with the continuous spectrum. The approach in [4] applies for large stresses and for small quasimomenta but it fails for the region of the spectrum where resonant states are present.

Using our new approach we will consider the ground resonant state induced by shallow acceptors in uniaxially strained p-Ge along [001] direction.

As the initial approximation for localized states we choose the diagonal part of the Luttinger hamiltonian and the Coulomb potential of an acceptor. For continuum states we use the eigenfunctions $\psi_{\mathbf{k}}^{\pm 1/2}(\mathbf{r})$ of the full Luttinger hamiltonian for free holes in cylindrical approximation. Following the procedure from the first section we are looking for wave functions in the form:

$$\begin{aligned}\Psi_{\mathbf{k}}^{\pm 1/2} = \psi_{\mathbf{k}}^{\pm 1/2} + a_{\mathbf{k}}^{\pm 1/2,+3/2}\varphi^{+3/2}(\mathbf{r}) + a_{\mathbf{k}}^{\pm 1/2,-3/2}\varphi^{-3/2}(\mathbf{r}) \\ + \sum_{\mathbf{k}'} \frac{t_{\mathbf{k}\mathbf{k}'}^{\pm 1/2,+1/2}}{\varepsilon_{\mathbf{k}} - \varepsilon_{\mathbf{k}'} + i\gamma}\psi_{\mathbf{k}'}^{+1/2} + \sum_{\mathbf{k}'} \frac{t_{\mathbf{k}\mathbf{k}'}^{\pm 1/2,-1/2}}{\varepsilon_{\mathbf{k}} - \varepsilon_{\mathbf{k}'} + i\gamma}\psi_{\mathbf{k}'}^{-1/2}.\end{aligned} \tag{13}$$

We carried out calculations taking into account non-resonant scattering by the Coulomb potential in first order only. The probability of capturing holes with momentum projection $+1/2$ $W_{\mathbf{k}r}$ and the probability of elastic resonant scattering $W_{\mathbf{k}\mathbf{k}'}$ are defined now by

$$W_{\mathbf{k}r} = \left|a_{\mathbf{k}}^{+1/2,+3/2}\right|^2 + \left|a_{\mathbf{k}}^{+1/2,-3/2}\right|^2. \tag{14}$$

$$W_{\mathbf{k}\mathbf{k}'} = \frac{2\pi}{\hbar}\left(\left|t_{\mathbf{k}\mathbf{k}'}^{+1/2,+1/2}\right|^2 + \left|t_{\mathbf{k}\mathbf{k}'}^{+1/2,-1/2}\right|^2\right)\delta(\varepsilon_{\mathbf{k}} - \varepsilon_{\mathbf{k}'}) \tag{15}$$

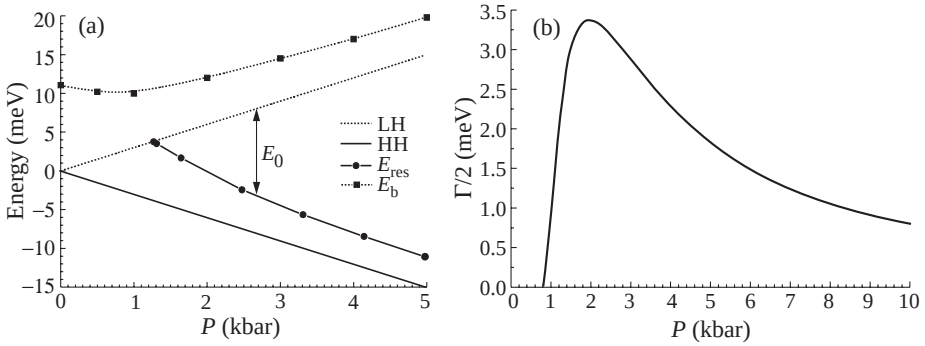

Fig. 2. The position (a) and width (b) of resonant state as a function of stress applied in [001] direction.

The expressions for the case of momentum projection $-1/2$ are similar. The results of calculations of the resonant level shift and level width are given in Fig. 2.

Acknowledgements

This work has been partially supported by the RFBR, The Swedish Foundation for International Cooperation in Research and Higher Education (contract 99/527 (00)) and NorFA Grant. A. A. Prokofiev thanks also Swedish Institute for Visby Programme Grant.

References

[1] I. V. Altukhov, E. G. Chirkova, M. S. Kagan, K. A. Korolev, V. P. Sinis, M. A. Odnoblyudov and I. N. Yassievich, *JETPh*, **88**, 51 (1999).

[2] Yu. P. Gousev, I. V. Altukhov, K. A. Korolev, V. P. Sinis, M. S. Kagan, E. E. Haller, M. A. Odnoblyudov, I. N. Yassievich and K.-A. Chao, *Appl. Phys. Lett.* **75**, 757 (1999).

[3] U. Fano, *Phys. Rev.* **124**, 1866 (1961).

[4] M. A. Odnoblyudov, I. N. Yassievich, V. M. Chistyakov and K.-A. Chao, *Phys. Rev. B* **62**, 2486 (2000).

9th Int. Symp. "Nanostructures: Physics and Technology"
St Petersburg, Russia, June 18–22, 2001

Dynamics of electrons at intersubband excitation in asymmetric tunnel-coupled quantum well structure

E. A. Zibik†, L. E. Vorobjev†, S. R. Schmidt‡, A. Seilmeier‡, D. A. Firsov†, V. L. Zerova† and E. Towe§

† St Petersburg State Technical University, St Petersburg 195251, Russia
‡ Institute of Physics, University of Bayreuth, D-95440 Bayreuth, Germany
§ University of Virginia, Thornton Hall, Charlottesville, VA 22903-2442, USA

Abstract. We present investigations of the intersubband electron dynamics in asymmetric tunnel-coupled GaAs/AlGaAs quantum wells. The study is performed by time resolved pump and probe experiments. Temporal evolution of the bleaching signals has biexponential behaviour. In addition to the time of the relaxation into the ground state with LO-phonon emission a second long decay time depending on transition energy and temperature is observed. We associate the second recovery time with transitions between confined Γ-state of quantum wells and states in the barriers including X_Z-states which appear due to high content of Al. The influence of the transitions between subbands with energy separation less than optical phonon energy on the relaxation processes is also discussed.

Introduction

The asymmetric tunnel-coupled quantum well (ATCQW) structures attracted considerable attention because of possibility of lasing [1] and modulation of MIR radiation [2] due to intersubband transitions. The knowledge of the electron dynamics is very essential to improve the properties of these devices. In the double quantum well structures the electron dynamics is very complicated due to a large number of the levels. There are a lot of methods for measurement of electron relaxation time, for example intersubband saturation method [3] or excited-state induced absorption spectroscopy technique [4]. However, these methods have the some limitations, as it is necessary to know the homogeneous broadening of the absorption line. Generally the intersubband line has an inhomogeneous broadening [5]. The investigations by pump and probe techniques allow us to measure directly the temporal evolution of the transmission spectra after excitation, and to determine the respective relaxation time. In this work we study the relaxation processes in ATCQW structure by the time and frequency resolved pump and probe spectroscopy.

1. Sample structure and experimental method

The studied modulated doped structure was grown by MBE on semiinsulated GaAs (100) substrate. The widths of the first GaAs quantum well (QW) and the second $Al_{0.1}Ga_{0.9}As$ well are 5 nm and 8.3 nm respectively. The width of the tunnel-transparent $Al_{0.42}Ga_{0.58}As$ barrier between them is 2 nm. The width of $Al_{0.42}Ga_{0.58}As$ barrier between pairs of QWs is 25 nm. The center of 25 nm barrier was doped by Si. The surface electron concentrations is $N_S = 5 \times 10^{11}$ cm^{-2}.

The sample is prepared in a prism geometry with one reflection at 65° at the plane of QW layers to get strong absorption signals.

The relaxation measurements are performed by a Nd:glass laser system of 8 Hz repetition rate with two travelling wave IR dye lasers and two difference frequency mixing stages.

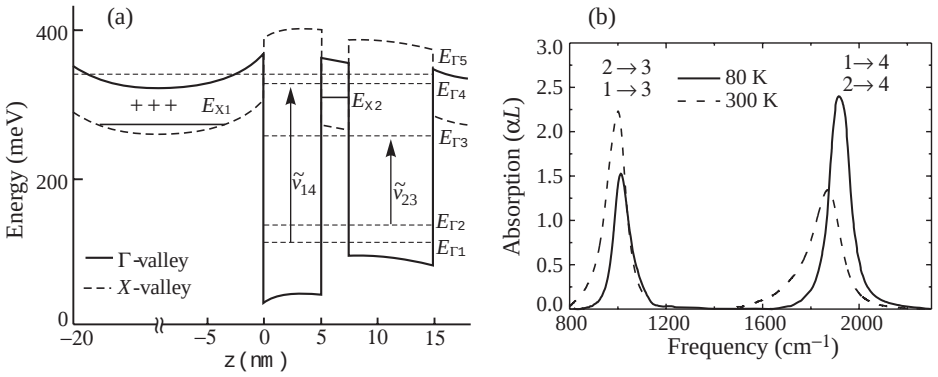

Fig. 1. (a) The potential profile of the structure and calculated energy levels; (b) equilibrium intersubband absorption spectra at different temperatures.

The system generates two light pulses of 2 ps duration with a spectral width of 10 cm^{-1} independently tunable between 800 cm^{-1} and 2500 cm^{-1}. One of the two infrared pulses excites electrons at a good defined pump frequency $\tilde{\nu}_{\text{pump}}$ from the lower states to the excited subbands. The subsequent time resolved change of the intersubband absorption is measured by the second weaker infrared pulse at any probe frequency $\tilde{\nu}_{\text{probe}}$.

2. Results and discussion

Due to high contents of Al in the barriers it is necessary to consider the effect of $\Gamma - X$ mixing [6]. The potential profile of Γ and X valleys and energy levels in the structure are presented in Fig. 1(a). The states with the energy $E_{\Gamma1}$, $E_{\Gamma4}$ and $E_{\Gamma2}$, $E_{\Gamma3}$ are generated by the narrow and wide wells respectively. It leads in particular to the different localization of wave functions. Wave functions Ψ_1 and Ψ_2 are localized mainly within the first and the second well respectively. Moreover, optical dipole matrix elements strongly differ: $Z_{14} = 1.13$ nm, $Z_{24} = 0.7$ nm and $Z_{13} = 0.4$ nm, $Z_{23} = 2.27$ nm. The greatest contribution to intersubband absorption is made by transitions between levels originated from the same well. One more state $E_{\Gamma5}$ can appear in QW, which is formed in wide barrier due to space charge effect.

The $Al_{0.42}Ga_{0.58}As$ layers are quantum wells for X-electrons, the thin barrier contains one confined E_{X2}-state. There are also quantum-confined states for X-electrons in thick barrier dividing the pairs of QWs.

The absorption spectra measured with a BRUKER FTIR spectrometer contain two absorption bands (Fig. 1(b)) having at liquid nitrogen temperature the peak frequencies of 1010 cm^{-1} and 1915 cm^{-1}. With increase of temperature the typical redshift and broadening of absorption lines are observed. At room temperature the peak frequencies are 1000 cm^{-1} and 1870 cm^{-1} respectively.

The investigation of the temporal evolution of the transmission spectra at different pump and probe frequencies in resonance of transitions at 300 K are presented in Fig.2. The results were also obtained at other temperatures. Pump and probe measurements at the same pump and probe frequencies show the biexponential behaviour of carrier relaxation. The fast relaxation time (1.2 ps) is almost independent of pump frequencies and temperature, whereas the long term decay strongly depends on these factors. Besides when pump and probe frequencies are located in the center of the different absorption bands mainly the long relaxation time can be observed. We connect the fast relaxation processes with scattering

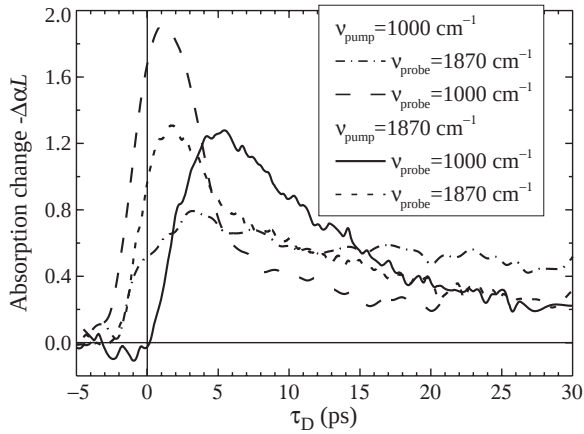

Fig. 2. Time resolved absorption change at 300 K after excitation at different pump frequencies.

of the electrons into the ground state due to LO-phonon emission. The nature of the slow component will be discussed below. We can assume that the pump pulse excites the carriers only within the one well, because the transitions between levels originated from the same well give the main contribution to the intersubband absorption. However, one can see, that when the pump frequency lies in maximum of long-wavelength absorption band there is also the bleaching of the short-wavelength absorption band and vice versa. This bleaching comes from the electron redistribution among the first and second subbands. In spite of small distance between $E_{\Gamma 1}$ and $E_{\Gamma 2}$ ($\sim$10 meV) such redistribution becames possible due to LO-phonon scattering at room temperature with time less than 1 ps. This time (5 ps) is longer at 80 K. At this temperature LO-phonon scattering is suppressed and a scattering on impurities and acoustic phonons can play a key role.

In order to understand the strong dependence of long recovery time on pump frequencies let us consider the potential structure of ATCQW. The high contents of Al in barrier leads to appearing the QWs for X-electrons and to coupling the Γ- and X-states. It makes possible a scattering between Γ- and X-states. An intervalley $\Gamma - X$ scattering time is directly proportional to the overlap integral of wave functions [7] and is about 1 ps. Excitation at $\tilde{\nu}_{14}$ or $\tilde{\nu}_{23}$ leads to filling of these states that are mixed with the X-states of tunnel-transparent barrier and barriers between pairs. An intervalley scattering into the X-states takes place. Electrons return from X-valley to ground subband with the large back scattering time (40 ps) because the density of states in Γ-valley is lower compared to the one in X-valley. At excitation between $E_{\Gamma 1}$ and $E_{\Gamma 4}$ levels the real space transfer into confined barrier states can play the main role. This can determine a long decay time (15–20 ps). Similar mechanism was considered in [8].

3. Conclusion

The dynamics of intersubband transitions in asymmetric tunnel-coupled quantum well structure is investigated by time resolved pump and probe experiments. The biexponential behaviour of absortpion recovery is found. The fast time is responsible for intersubband relaxation of the electrons due to emission of LO-phonons. The long term decay time comes from the intervalley $\Gamma - X$ scattering and real space transfer in confined barrier states. The effect of interwell transitions on intersubband relaxation is also considered.

Acknowledgements

This work was supported by RFBR and programme “Physics of Solid State Nanostructures”.

References

[1] O. Gauthier-Lafaye, P. Boucaud, F. H. Julien, S. Sauvage, S. Cabaret, J.-M. Lourtioz, V. Thierry-Mieg and R. Planel, *Appl. Phys. Lett.* **71** 619, (1997).
[2] E. Dupont and D. Delacourt, *Appl. Phys. Lett.* **62** 1907, (1993).
[3] M. Helm, T. Fromherz, B. N. Murdin, C. R. Pidgeon, K. K. Geerinck, N. J. Hovenyer, W. Th. Wenckebach, A. F. G. van der Meer and P. W. Amersfoort, *Appl. Phys. Lett.* **63** 3315, (1993).
[4] J. Faist, C. Sirtori, F. Capasso, L. Pfeiffer and K. W. West, *Appl. Phys. Lett.* **64**, 872 (1994).
[5] G. Beadie, W. S. Rabinovich, D. S. Katzer and M. Goldenberg, *Phys. Rev. B* **55**, 9731 (1997).
[6] Yan-Ten Lu and L. J. Sham, *Phys. Rev. B* **40**, 5567 (1989).
[7] J. Feldmann, J. Nunnenkamp, G. Peter, E. Göbel, J. Kuhl, K. Ploog, P. Dawson and C. T. Foxon, *Phys. Rev. B* **42**, 5809 (1990).
[8] J. Baier, I. M. Bayanov, U. Plödereder and A. Seilmeier, *Superlatt. Microstruct.* **19**, 9 (1996).

9th Int. Symp. "Nanostructures: Physics and Technology"
St Petersburg, Russia, June 18–22, 2001

Excitons in nitride-based low dimensional systems

Bernard Gil
Université de Montpellier II-Groupe d'Etude des Semiconducteurs Case Courrier 074-34095 Montpellier Cedex 5 - France

The exciton binding energy is large (25–27 meV) in bulk GaN. The coupling with the electromagnetic is large too. Together with my friend Alexey Kavokin, I predicted a Rabbi oscillation splitting of some 45 meV in GaN based microcavities.

Cubic GaN-AlGaN quantum wells can theoretically lead to an improvement of the optical response compared to the case of bulk c-GaN due to the know well known physics of the 2D confinement in type I quantum wells. This is not systematic for quantum wells based on wurtzite GaN and AlGaN due to difference of the spontaneous polarization of the two materials which together with piezoelectric field effect produce an efficient Quantum Confined Stark Effect. Consequently the optical transition can be boosted either toward shorter wavelength than the one of bulk GaN or can be boosted in the realm of long wavelength radiations, depending on well width, at the first order.

I first show using cw spectroscopy arguments, and samples grown by molecular beam epitaxy, that the magnitude of the internal electric field depends on the aluminum composition, and of the ratio between the width of the well layers relatively to the width of the barriers. In particular for aluminum compositions ranging up to 27 percents, it is measured that for well width larger than 12 monolayers (3 nm) the photoluminescence energy is lower than the bandgap of bulk GaN. Comparing cw photoluminescence and reflectance spectra reveals a stokes-shift of the photoluminescence compared to the reflectance at low temperature as an evidence of a localized nature of the excitons that are observed in photoluminescence, at low temperatures. Increasing the temperature gives an excess of kinetic energy, that can facilitate the exciton detrapping. The relative ratio of free to bound excitons promotes the free exciton population so that, at high temperature, photoluminescence is dominated by free exciton recombination. The internal electric field localizes electrons and holes at different interfaces. Envelope function calculations indicate that, when the well-width increases, this drastically reduces the overlap between their wavefunctions and increases the radiative decay time, but has poorer influence at the scale of the exciton binding energy (long range interaction). Simple envelope function calculation also indicates that the in-plane extension of the hole and electron wavefunctions is comparable in size with the average aluminum-aluminum separation for alloy compositions ranging up to at least 30 percents. The interfacial exciton localization results of the comparable values of the Bohr radii and of the characteristics length of the alloy disorder.

Time resolved spectroscopy measurements are performed which permitt to extract both the radiative and non-radiative contributions to the photoluminescence decays. These experiments were achieved on single quantum wells, assymetric multiple quantum wells and superlattices. It could then be possible to discriminate between the different contributions that rule the non-radiative recombinations mechanisms. The strength of the coupling with the LO phon is reported to increase when increasing the well width. This we compare to what is observed for GaInN-GaN quantum wells. For that semiconductors combination, the structural disorder occurs in the confining material: GaInN, and the localization

phenomena are more crucial than for GaN-AlGaN. By comparing photoluminescence and photoreflectance spectra taken on a series of InGaN-GaN quantum wells grown under identical conditions except the growth time of the InGaN layers, the Quantum Confined Stark Effect (QCSE) could be monitored without changing the nanotexture of the alloy layers. The results indicates that, for quantum wells which radiate in the red, the contribution of the QCSE superimposes to an intrinsic localization phenomena of the carriers in the InGaN alloy, and is larger by one order of magnitude. I show that the interpretation of data for samples that emit from the blue to the red can provide only partial conclusions if both localization effects and (QCSE) are not taken into consideration. This is further comfirmed by similar experiments performed on Stranski–Krastanov GaInN-GaN quantum boxes. The net result is that the localization of the exciton is occurs in alloy regions very small, smaller than 1 nanometer, in fairly nice agreement with the ideas that are defended by Kevin O'Donnell. Although heuristic effective mass calculations are helpfull for interpreting optical properties of GaN-AlGaN quantum wells one has to be more cautious if using them for GaInN-GaN quantum wells. Indeed, slightly changing the growth temperature but not the well width alters the colour of the light emitted by the samples which indicates that the nanotexture of the alloy is changed.

Acknowledgments

I wish to thank Alexey Kavokin, Nicolas Grandjean, Jean Massies, Pierre Bigenwald, Tomasz Ochalski, Kevin Peter O'Donnell, Hadis Morkoc, Pierre Lefebvre, Thierry Taliercio, Jacques Allegre, Aurelien Morel, Mathieu Gallart and many others that I hope it, will not feel upset if they do not see their name in the list above.

9th Int. Symp. "Nanostructures: Physics and Technology"
St Petersburg, Russia, June 18–22, 2001

Optical properties of CdS nanostructures crystallized in the pores of insulating template

V. Dneprovskii, S. Gavrilov†, E. Muljarov‡, A. Syrnicov and E. Zhukov
Moscow St. University, Dept. of Physics, 119899 Moscow, Russia
† Moscow Institute of Electronics, 103498 Moscow, Russia
‡ Institute of General Physics, 117942 Moscow, Russia

Abstract. The characteristic features of the luminescence spectra obtained at different polarization of the exciting light beam and time-resolved luminescence spectra of CdS nanocrystals crystallized in 8–10 nm diameter hollow channels of a dielectric Al_2O_3 template have been explained in terms of exciton transitions in semiconductor-dielectric quantum wires. In these structures the dielectric confinement effect leads to a considerable increase of the exciton binding energy — the Coulomb attraction between electron and hole is considerably enhanced as a result of the difference between the permittivities of the semiconductor and insulator.

In semiconductor quantum wires (QWRs) — nanostructures in which carriers and excitons move freely in one direction but are localized in two others, the electron-hole attraction is intensified and excitonic transitions dominate in the absorption and luminescence spectra. Quantum confinement results in prominent exciton features such as large binding energies and oscillator strengths. The binding energy and oscillator strength of an exciton transition can be substantially increased by replacing the semiconductor barriers with insulators having much lower permittivities than the semiconductor [1, 2, 3].

For semiconductor-dielectric (S–D) QWRs the enhancement of exciton binding energy (dielectric confinement), predicted in Ref. [4], can be explained by the fact that although electron and hole are located in the thin semiconductor filament, the Coulomb interaction energy is concentrated in the insulator because of the large difference of the permittivities. The electric field lines connecting electron and hole partially or, for thin wires mainly, pass through the dielectric. The binding energy and oscillator strength of excitons in S–D QWRs can be varied over wide limits (the binding energy may exceed 100 meV) by choosing semiconductor and dielectric with different permittivities — realizing "Coulomb interaction engineering" [3].

We report the results of optical properties' investigation of CdS nanostructures crystallized in the pores of Al_2O_3 insulating template. We show that in these nanostructures the role of dielectric confinement effect is of paramount importance that leads to large values of the exciton binding energies (> 100 meV). Large oscillator strengths of exciton transitions make it possible to observe different physical processes determined by excitons in the samples with substantial size (diameter) dispersion of QWRs.

CdS nanostructures have been made by crystallization of the semiconductor in insulating template [5] prepared by anodic oxidation of an aluminum substrate. CdS was formed in the resulting pores of about 8–10 nm in diameter (the atomic force microscope have been used to measure the diameters of pores) and several microns long by cathodic electrodeposition. The formation of CdS nanocrystals was confirmed by their phonon spectra (IR Fourier spectroscopy method have been used) measured by A. I. and L. I. Belogorokhov.

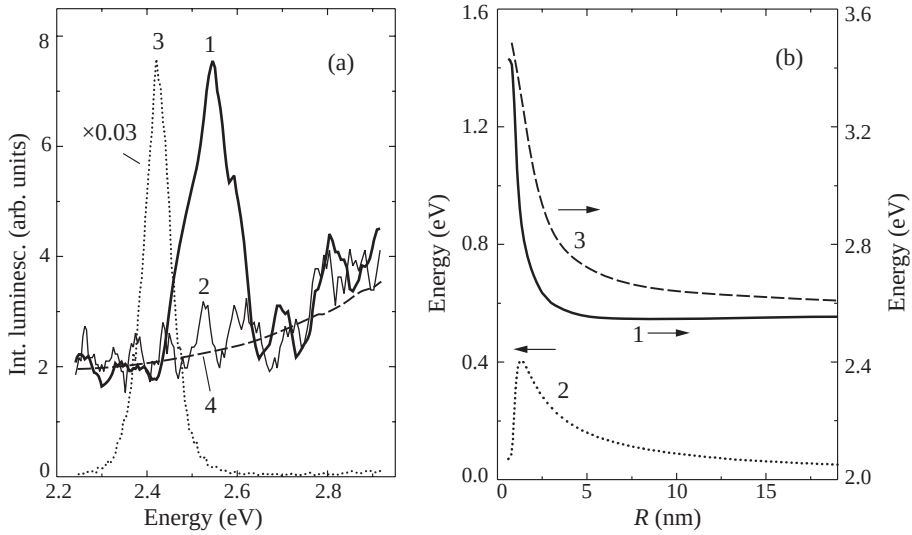

Fig. 1. (a) PL spectra of CdS nanocrystals crystallized in hollow channels of insulating matrix measured with pumping beam polarized at angles 45 (1) and 90 (2) degrees with respect to the direction of the channels of the matrix, as well as the spectra of bulk CdS (3) and matrix (4). (b) Theoretically computed exciton transition energy (1), exciton binding energy (2), renormalized band gap (3) as a function of radius of a cylindrical quantum wire surrounded by Al_2O_3.

Figure 1(a) shows the photoluminescence (PL) spectra of the sample A containing CdS nanocrystals ($T = 300$ K) for different polarization of the exciting light of a Hg-lamp. For comparison, the luminescence spectra of bulk CdS (a single crystal grown from the vapour phase) and of the insulating Al_2O_3 matrix are presented in the same figure. Comparing the spectra, we can conclude that the luminescence band with maximum at 2.54 eV and a half-width of about 150 meV arises due to CdS nanocrystals. It can be attributed either to the lowest electron–hole transition in quantum dots (QDs), or to excitonic transitions in QWRs, or to transitions in nanostructures of both types. However, the well-expressed luminescence band of CdS nanocrystals arises only if the excitation radiation contains a field component parallel to the axis of the channels. This allows us to suggest that nanostructures have been crystallized primarily as QWRs. Inside thin nanometer size parallel wires surrounded by an insulator the field component of the exciting radiation perpendicular to the axis of the wire is substantially weakened as a result of the boundary conditions, which decreases the absorption (and the luminescence intensity) of light with such polarization [6]. Thus, we attribute the characteristic features of the spectra of CdS structures to the dominant luminescence of excitons in S–D QWRs.

The theoretically computed exciton transition energy, the renormalized band gap and the exciton binding energy of CdS S–D QWRs as a function of the wire radius are presented in Fig. 1(b). Comparing the experimentally determined exciton transition energy 2.54 eV with the computed values (Fig. 1), we find that the QWR radius can lie in the range from 5 nm to 15 nm. In this region (Fig. 1(b)) the changes in the energy of a free transition are compensated by the changes in the binding energy. As a result, the exciton transition energy is independent of the wire's radius over a wide range of its values that largely suppresses the

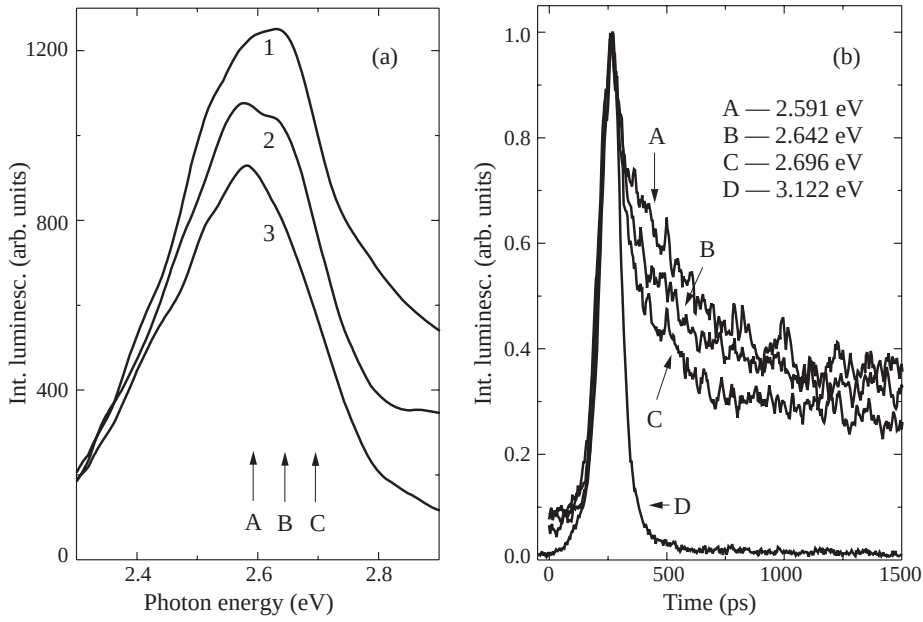

Fig. 2. (a) PL spectra registered at different delays after excitation: 100 ps (1), 200 ps (2), 300 ps (3); (b) The kinetics of PL for different parts of the spectrum are shown by arrows in Fig. 2(a). (D) is the kinetic of matrix PL.

inhomogeneous broadening of the exciton absorption and luminescence bands in samples with large QWR's size variance.

The time-resolved PL spectra were registered using a Ritsu MC-12N polychromator and Hamamatsu C1587 synchroscan streak camera with a two-dimensional detector. The focused beam ($0.2\,\mu$J/cm^2) of the second harmonic of the Argon–ion laser pumped Ti–sapphire laser ($\hbar\omega = 3.3$ eV, pulse duration 1.5 ps, repetition rate 82 MHz) was used for excitation of nanostructures. The time resolution was less than 50 ps and the spectral resolution about 1 meV. The time-resolved luminescence spectra of sample B ($T = 2$ K) are presented in Fig. 2(a). The maxima of the broad luminescence spectra (we assume that the inhomogeneous broadening arises due to the size dispersion of QWRs) are shifted with time to the low energy side. It may be explained by the difference in relaxation of excitons in QWRs with different lateral dimensions. In the inhomogeneously broadened spectrum the high energy part (it belongs to the wires of lesser diameter) decays faster than that of the low energy part. The latter is confirmed by the kinetic profiles of the different parts of the spectrum (Fig. 2(b)). The relaxation time may be associated with the nonradiative recombination. In the wires of lesser diameter it is more effective probably due to the more essential role of surface states.

In summary, the peculiarities of the luminescence and time-resolved luminescece spectra of CdS nanostructures crystallized in hollow channels of Al_2O_3 dielectric matrix show that exciton transitions dominate in quantum wires of approximately 10 nm in diameter. The great binding energies of excitons (about 170 meV) arise both due to quantum and dielectric confinement.

Acknowledgments

The research described in this publication was made possible in part by Grant 99-02-18327 from the Russian Foundation for Basic Research and by the Grant 97-1083 of the "Physics of Nanostructures" program.

References

[1] E. A. Muljarov and S. G. Tikhodeev, *JETP* **8**, 151 (1977).
[2] V. S. Dneprovskii, E. A. Zhukov, E. A. Muljarov and S. G. Tikhodeev, *JETP* **87**, 382 (1998).
[3] L. V. Keldysh, *phys. stat. sol (a)* **164**, 3 (1997).
[4] N. S. Rytova, *Dokl. Akad. Nauk SSSR* **163**, 1118 (1965).
[5] S. A. Gavrilov, V. V. Gusev, V. S. Dneprovskii, E. A. Zhukov, A. N. Syrnikov and I. V. Yaminskii, *JETP Lett.* **70**, 216 (1999).
[6] P. Ils, C. H. Greus, A. Forchel, V. D. Kulakovskii, N. A. Gippius and S. G. Tichodeev, *Phys. Rev. B* **51**, 4272 (1995).

9th Int. Symp. "Nanostructures: Physics and Technology"
St Petersburg, Russia, June 18–22, 2001

Planetary® production type MOCVD reactors for blue laser applications in the GaInN material system

O. Schoen†, H. Protzmann†, M. Luenenbuerger†, B. Schineller†, M. Dauelsberg†, G. P. Yablonskii‡, E. V. Lutsenko‡, A. V. Mudryi‡ and *M. Heuken*†

† AIXTRON AG, 52072 Aachen, Germany
‡ Stepanov Institute of Physics, National Academy of Sciences of Belarus, 220072 Minsk, Belarus

Abstract. Growth parameters for the growth of heterostructures in the GaN/GaInN material system are studied through numerical simulation of thermal, fluid dynamical and kinetical behavior of the AIX 2000 G3 HT Planetary® reactor. Good on wafer, wafer to wafer and run to run uniformity over the whole spectral range are demonstrated. Lasing at wavelengths up to 470 nm of such structures is achieved by optical pumping at 300 K, proving high optical quality of the obtained layers and good control of the formation of quantum dot or disk like organization of In-rich clusters in the QW material.

Introduction

By now heterostructures in the material system GaInN/GaN are widely used for display and lighting applications in the green to blue/UV spectral range. Furthermore, nitride based lasers operating at 390 to 420 nm emission wavelength have become availabe recently [1]. GaInN-based LDs visible in the blue-violet (near 450 nm) have also been reported in the last year [2]. The metal organic vapor phase epitaxy (MOVPE) has established itself as the layer growth method of choice for these (and other) semiconductor materials. AIXTRON's AIX 2000 G3 HT system family was developed to meet the needs of modern production facilities by low overall running costs and low cost of ownership while maintaining high standards for layer quality and uniformity on wafer and wafer to wafer.

1. Experimental and results

Growth runs were performed in an AIX 2000 G3 HT reactor in the 6×2" configuration using triethylgallium (TEGa), trimethylgallium (TMGa), trimethylindium (TMIn), ammonia (NH_3), silane (SiH_4) and biscyclopentadienylmagnesium (CP_2Mg) as precursors and H_2 and N_2 as carrier gases. Structures were grown on c-plane sapphire using a conventional low temperature GaN nucleation layer with subsequent anneal step prior to a high temperature buffer layer. The active region contained 5 and 10 period MQW structures with QW thicknesses in the range of 2 to 3 nm.

To optimize on wafer deposition uniformity and to establish easily reproducible deposition processes critical steps in the growth procedure are analyzed through numerical simulation of heat transfer and fluid field interaction including species diffusion and a simplified reaction chain model. In figure 1 the conditions for the growth of GaInN at 200 mbar and 800 °C are examined. A homogenous depletion of both NH_3 and TEGa have

Fig. 1. Concentration profiles of TEGa (upper) and NH_3 (lower) mass flows inside the reactor chamber for $T_D = 800\,^{\circ}\mathrm{C}$, $P_{tot} = 200$ mbar and $Q_{tot} = 28$ slm from numerical simulations – symmetry axis of the reactor chamber and the inlet are on the left hand side, direction of gas flow is left to right.

been achieved at these conditions, guaranteeing good on wafer layer uniformity through gas foil rotation of the substrates.

Figure 2 combines wafer to wafer comparison data for several runs. On the left the variation of average layer thickness for a single GaN buffer layer run is displayed (thickness on radius, angular position corresponds to load position in the reactor), showing a wafer to wafer standard deviation of 0.7%. On the right the average photoluminescence (PL) peak emission wavelength of wafers from several runs is compared in a similar way, showing 4.0 nm standard deviation at 441.5 nm, 6.7 nm at 470.7 nm, 6.4 nm at 499.3 nm, 3.0 nm at 529.0 nm and 1.9 nm at 579.8 nm. The PL spectra were recorded at $T = 300$ K under low intensity cw excitation. Clearly, material around the center of the GaInN miscibility gap (emitting at 470 to 500 nm) is most sensitive to the process conditions and thus exhibits the largest spread. Nevertheless these results evidence good control of process conditions between wafers as well as on wafer (as has been published earlier).

To further assess the quality of the layers thus grown PL and stimulated emission spectra were studied as a function of excitation intensity at low (4.2 K) and room temperature. Figure 3 shows both PL and PLE (photoluminescence excitation) spectra measured under

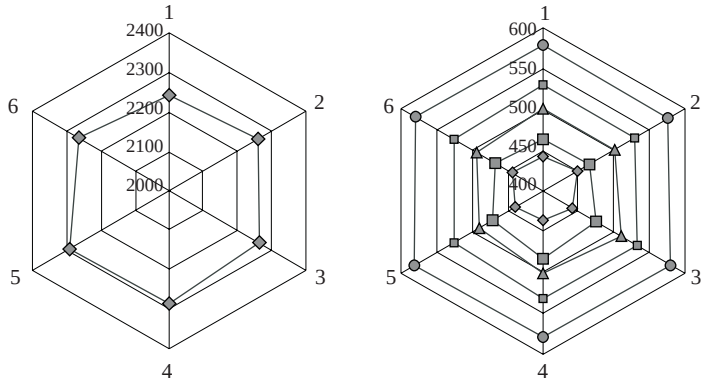

Fig. 2. Overviews for wafer to wafer reproducibility for total thickness (left) and peak emission wavelength (right) at various process conditions – the azimuthal position indicates the load position of the wafer.

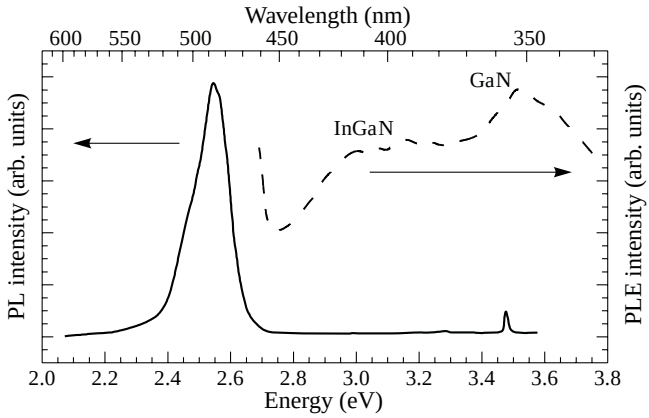

Fig. 3. Normalized PL (solid) and PLE (dashed) spectra of GaN/GaInN quantum well structures at $T = 4.2$ K.

illumination of quasi-monochromatic light dispersed from a xenon lamp by a monochromator. The PL spectrum consists of a line of low intensity near 3.5 eV, belonging to emission from the GaN barrier layers, and an intensive band from the active layers located at roughly 2.5 eV. The PLE spectrum reveals a UV band due to the light absorption in the GaN barrier and a low energy band near the mobility edge of the active layer. The high Stokes shift between the PL and PLE response of the QWs indicates that the radiative recombination at low excitation density is due to In-rich clusters inside the QW layers such as quantum dots or discs. A high efficiency in direct excitation of carriers near the mobility edge of the GaInN evidences a good quality of the active layer.

Photoluminescence and laser spectra were also taken at higher excitation densities afforded by pulsed nitrogen laser irradiation at low (78 K) and room temperature ($h\nu = 3.68$ eV, $f = 1000$ Hz, $t = 8$ ns, $I_{ex} = [0.01, 1]$ MW cm^{-2}). Figure 4 illustrates the influence of increasing I_{ex} on the PL response of the sample examined above: a shoulder is formed on the higher energy side of the peak with increasing I_{ex}, evidencing a small extension of the emission band there, modulated by the thickness interference pattern in the buffer layer. Stimulated emission bands appear at relatively low excitation, but lasing requires higher intensities than other samples studied in comparison [3, 4] due to a reduced layer thickness and thus lower optical confinement factor in the samples studied here.

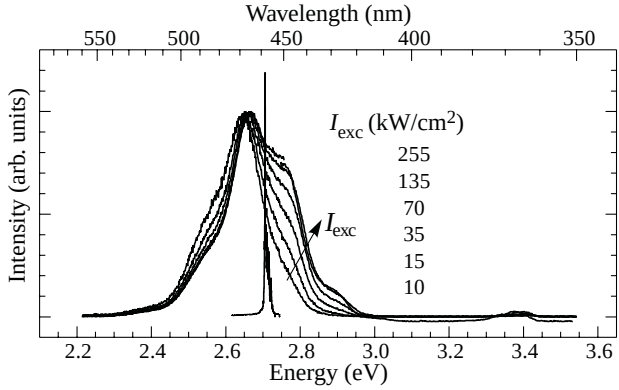

Fig. 4. Room temperature PL spectra at different excitation densities and laser spectrum (narrow).

Generally, the optical characteristics demonstrated prove excellent material quality.

2. Summary and conclusion

Investigation of growth parameters through numerical simulation of thermal, fluid dynamical and kinetical behavior of the AIX 2000 G3 HT Planetary® and experimental optimization led to good on wafer, wafer to wafer and run to run uniformity over the whole spectral range accessible via the material system GaInN. Lasing was achieved at wavelengths up to 470 nm by optical pumping at room temperature, proving high optical quality of the obtained layers and good control of the formation of quantum dot or disk like organization of In-rich clusters in the QW material. We conclude that the AIX 2000 G3 HT MOCVD system is an excellent tool for the mass production of laser structures.

Acknowledgements

We thank I. P. Marko, V. N. Pavlovskii and V. V. Zubjalevich for their assistance. The work was partly supported by the ISTC project B-176.

References

[1] S. Nakamura, M. Senoh, S. Nagahama, T. Matsushita, H. Kiyoku, Y. Sugimoto, T. Kozaki, H. Umemoto, M. Sano and T. Mukai, *Japan. J. Appl. Phys., part 2-letters* **38**, L226-L229 (1999).

[2] S. Nakamura, M. Senoh, S. Nagahama, N. Iwasa, T. Matsushita and T. Mukai, *Appl. Phys. Lett.* **76**, 22-24 (2000).

[3] I. P. Marko, E. V. Lutsenko, V. N. Pavlovskii, G. P. Yablonskii, O. Schoen, H. Protzmann, M. Luenenbuerger, B. Schineller and K. Heime, *Phys. Stat. Sol. (b)* **216**, 491-494 (1999).

[4] G. P. Yablonskii, E. V. Lutsenko, I. P. Marko, V. N. Pavlovskii, A. V. Mudryi, A. I. Stognii, O. Schoen, H. Protzmann, M. Luenenbuerger, B. Schineller, M. Heuken and K. Heime, *Phys. Stat. Sol. (a)* **180**, 149-155 (2000).

9th Int. Symp. "Nanostructures: Physics and Technology"
St Petersburg, Russia, June 18–22, 2001

Correlation of mosaic structure peculiarities with electric characteristics and surface multifractal parameters for GaN epitaxial layers

A. G. Kolmakov†, *N. M. Shmidt*‡, V. V. Emtsev‡, A. D. Kryzhanovsky‡, W. V. Lundin‡, D. S. Poloskin‡, V. V. Ratnikov‡, A. N. Titkov‡, A. S. Usikov‡ and E. E. Zavarin‡

† Institute of Metallurgy, Moscow 117911, Russia

‡ Ioffe Physico-Technical Institute, St Petersburg, Russia

Abstract. The first successful results of multifractal analysis application to a quantitative description of mosaic structure peculiarities, which are typical of GaN epitaxial layer with hexagonal modification grown on (0001) sapphire substrates, have been obtained. Characteristic size of the mosaic structure has been measured to be 200–800 nm. The direct dependence of mobility on the multifractal parameters (the Renyi dimension and the degree of the order index) of the surface topology of the mosaic structure has been observed for all GaN layers investigated.

Introduction

GaN epitaxial layers are a basis of light-emitting devices and photodetectors operating over the short wavelength region. It well known, a high density (10^8-10^{10} cm^{-2}) of dislocations, which form the mosaic (columnar) structure of the epitaxial layers with the domain size of 200–800 nm, is typical of hexagonal III-nitrides. The results concerning with the dislocation density effect on electrical characteristics of the layers are quite contradictory, while the data on the mosaic structure effect on these characteristics are a few in number.

Our first investigations [1, 2] of the GaN epitaxial layers demonstrated at a qualitative level that the mosaic structure peculiarities played an important role in the electrical properties of the layer and device parameters, including the Schottky barrier height, leakage current, and persistent photoconductivity. In this connection a quantitative characterization of the mosaic structure is required to investigate an influence of its peculiarities on the electrical properties of the layers.

However, the traditional characterization techniques do not allow the peculiarities of the mosaic structure to be described in detail. For instance, the average domain size along with the basic axes is evaluated be the X-ray diffraction analysis. The diagnostics of the GaN surface topology with a use of atomic-force microscope gives only quality characteristics of the mosaic structure. It has been known that the multifractal analysis of a surface structure can be used to compare the mosaic structure peculiarities of a complex system quantitatively. This method has been not applied for semiconductors [3]. In contrast with conventional techniques, the multifractal analysis allows the structure peculiarities to be characterized as a whole. As a result, the quantitative correlation between individual elements of the complex structure could be obtained using multifractal parameters.

In the present paper the potentialities of the multifractal parameterization method have been evaluated for the quantitative description of the structure peculiarities of the GaN epitaxial layers grown on sapphire substrates as well as for establishing the interrelation between the multifractal characteristics of the GaN surface structure and the GaN electrophysical properties.

1. Experiment

GaN epitaxial layers with a specular surface, which were grown by metal-organic chemical vapor deposition on (0001) sapphire substrates at pressure of 200 mbar, were investigated. The layers were of n-type conductivity with the concentration of $(1-2)\times 10^{17}$ cm^{-3}. They differed both in the buffer layer growth conditions and in carrier mobility from 20 to 600 cm^{2}V^{-1}s^{-1} (see Table 1). The mobility was determined by the Van-der-Pauw technique in the temperature range 78–300 K with a use of Ti/Al ohmic contacts. The dislocation density was about 10^9 cm^{-2} for all layers but the layer #598 had the dislocation density of one order of magnitude less.

The structural peculiarities of the mosaic structure (the domain size, the domain tilt and twist angles) were investigated by X-ray diffractometry [4]. An additional information on the mosaic structure (roughness and a lateral size of surface domains) was obtained with a use of an atomic force microscopy (AFM).

The approximated images of the topographic surface structure (TSS) for the layers investigated by AFM are presented in Fig. 1. The images were used to obtain multifractal parameters of TSS. For this purpose the original method based on generation of rough partitioning measures was applied using the computer program MFRDrom developed by G.B. Vstovskii [5]. According to previous theoretical and experimental studies [3], the multifractal parameters, like the Renyi dimension (D_q) and the degree of the order index (Δ_{100}), are reasonable for quantitative parameterization. The value of D_q carries the information on thermodynamic conditions for the structure formation and hence it can be used for recognition of material structures, which are slightly distinguished by conventional techniques.

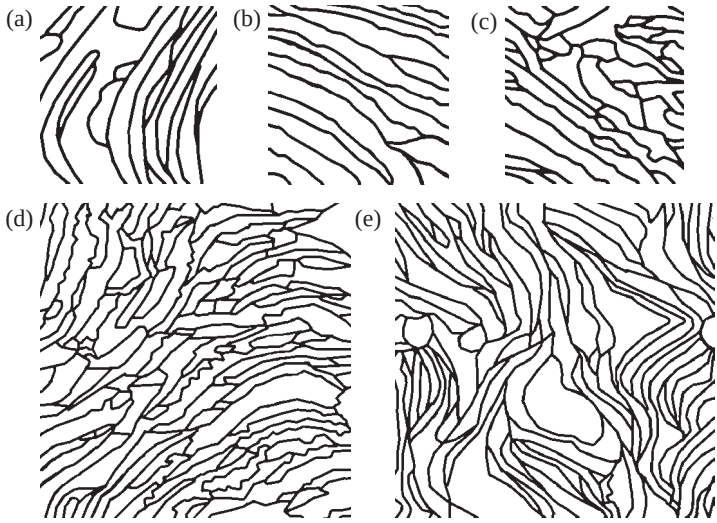

Fig. 1. The approximated images of the topographic surface structure for the GaN epitaxial layers: (*a*) #413, (*b*) #598, (*c*) #646, (*d*) #644, and (*e*) #776.

2. Results and discussion

The layers #413 and #598 differ dramatically in the mosaic structure peculiarities (see Table 1 and Fig. 1) as well as in the mobility (μ) and in a form of the temperature dependencies of μ and conductivity (σ) (see Fig. 2, curves 1 and 2). The other layers are not too distinct

Table 1. Basic characteristics of the GaN epitaxial layers.

	Epitaxial layer				
	#413	#598	#646	#644	#776
X-ray data					
Domain twist angle	20′	6′	18′	20′	25′
Average domain size, nm	2000	480	500	800	800
AFM data					
Surface domain size, nm	500–1500	200–300	200–500	200–500	300–1500
Roughness, nm	2.0	0.4	0.6	0.6	1.0
Electron mobility at room temperature, $cm^2V^{-1}s^{-1}$	55	600	400	30	50
Renyi dimension (D_q)	1.62	1.49	1.55	1.63	1.64

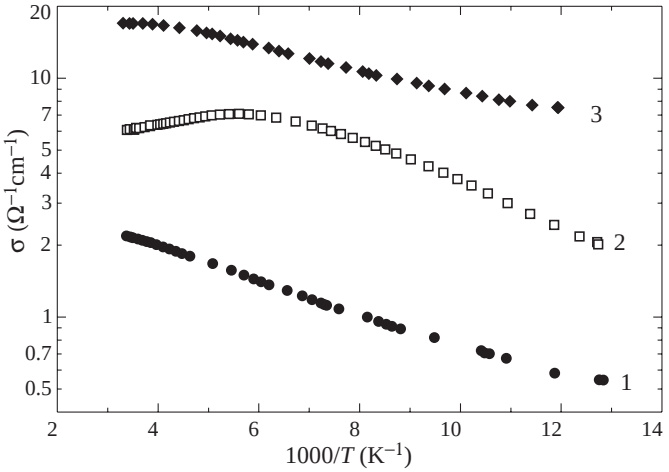

Fig. 2. Temperature dependence of conductivity for the GaN layers: (1) #413, (2) #598, and (3) #646.

in the mosaic structure peculiarities determined by the conventional techniques (AFM and X-ray diffractometry) as well as in the dislocation density.

These layers differ in the mobility, while their temperature dependence of conductivity points to unconventional carrier transport, that is typical both of the materials with localized charge defects and of low-dimensional structures.

The multifractal parameters of TSS allowed the GaN layers to be clearly distinguished. The direct dependence of μ on D_q and Δ_{100} was observed for all layers (see Fig. 3). That correlation was reasonable, because the carrier transport mechanism was unconventional and it depended on probability of the current channel formation. The values of D_q was the least for the most perfection layer #598. That was indicative of the more uniform conditions for the layer growth.

Therefore, the TSS multifractal parameters carry the information on the self-organization of the epitaxial layer mosaic structure. They allow the mosaic structure peculiarities to be quantitatively classified as a whole using the degree of the order index and the Renyi dimension. Moreover, the structure-properties correlation could be established, while the conventional techniques commonly manipulating the dislocation density and the averaged mosaic structure characteristics fail to do it.

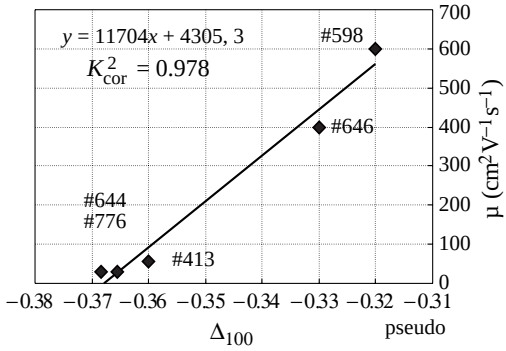

Fig. 3. Correlation between the degree of the order index (Δ_{100}) and the mobility (μ) at room temperature obtained from pseudo-multifractal computation. Correlation coefficient is 0.989.

The first successful results are indicative of great promise of the multifractal analysis to investigate III-nitrides.

References

[1] N. Shmidt, V. Emtsev, A. Kryzhanovsky, R. Kyutt, W. Lundin, D. Poloskin, V. Ratnikov, A. Titkov, A. Usikov and P. Girard, *Phys. Stat. Sol. (b)* **216** 581 (1999).
[2] N. M. Shmidt, W. V. Lundin, A. V. Sakharov, A. S. Usikov, E. E. Zavarin, A. V. Govorkov, A. Ya. Polyakov and N. B. Smirnov, *Proc. SPIE* (to be published).
[3] A. G. Kolmakov, V. N. Geminov, G. V. Vstovsky, V. F. Terent'ev, V. T. Zabolotny and E. E. Starostin, *Surf. Coat. Technol.* **72** 43 (1995).
[4] R. N. Kyutt, V. V. Ratnikov, G. N. Mosina and M. P. Shcheglov, *Phys. Solid State* **41** 25 (1999).
[5] A. G. Kolmakov and G. V. Vstovsky, *Mater. Sci. Technol.* **15** 705 (1999).

9th Int. Symp. "Nanostructures: Physics and Technology"
St Petersburg, Russia, June 18–22, 2001

The Bloch oscillations and mobile electrical domains in 6H-SiC natural superlattice

V. I. Sankin and P. P. Shkrebiy
Ioffe Physico-Technical Institute, St Petersburg, Russia

Introduction

The threshold field of the Bloch oscillation (BO) is:

$$F = 2\pi\hbar/e\tau d. \tag{1}$$

Here τ is the scattering time, d is a period of superlattice (SL). The BO in static regime is expressed as a negative differential conductivity (NDC). It should be noted that for realization the BO regime in crystal the following condition should be performed:

$$eF\ell = E_1, \tag{2}$$

where ℓ — the mean free path, E_1 — the first band width. Therefore to operate with not very large threshold fields semiconductors with relatively narrow band are to construct. In [1] it was shown that in narrow band (miniband) one more effect connected with a zone curvature namely with negative effective mass region is possible. It is difficult to distinguish what one of two effects is observed experimentally because for correct estimations the scattering time at strong fields is necessary.

The 6H-SiC polytype has a natural SL which is created at crystal growth automatically. Therefore such SL should be ideal from structurally quality point of view. The problem is only one of necessary miniband parameters. Our investigation [2] allowed to show a presence the miniband structure in electron band only. The experimental method for investigation I–V characteristics at the fields more than 100 kV/cm was described in [3, 4].

1. I–V characteristics of SiC polytypes in static regime. Experimental observation of the Bloch oscillation

I–V characteristics of tree terminal bipolar experimental structure on the base of 4H-, 6H-, 8H-SiC is shown in Fig. 1. All three curves is characterized by sufficiently extensive NDC region. The threshold fields are different. In accordance with Eq. (2) such situation is possible if E_1 or ℓ different. Indeed the miniband width are different: the most wide for 4H-SiC and the narrowest for 8H-SiC. It correlates with the set of the curves maxima in Fig. 1. We carried out the measurements of drift velocities and the time scattering τ at strong fields were received from Eq. (3). The time scattering for three polytypes were approximately identical: $\tau = 5 \cdot 10^{-13}$ s.

$$V_d = A \cdot \frac{F}{B} \cdot \frac{1}{1 + \left(\frac{F}{B}\right)^2}, \tag{3}$$

where $A = dE_1/2\hbar$, $B = \hbar/ed\tau$, d is the SL period. The experimental values of the threshold fields much nearer to BO Eq. (1).

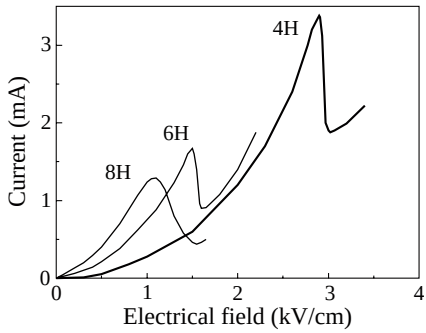

Fig. 1. I–V characteristics of SiC polytypes superlattice.

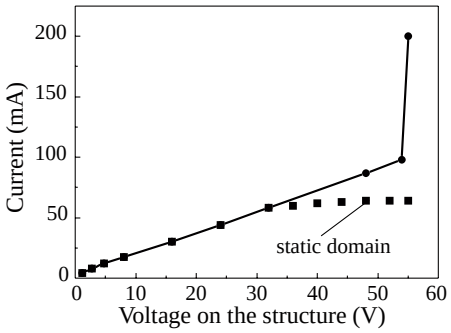

Fig. 2. I–V characteristic of 6H-SiC $n^+-n^--n^+$ diode structures.

2. The investigation of regime BO in 6H-SiC $n^+-n^--n^+$ diode structures

The above mentioned three terminal bipolar experimental structure is not available as working sample for UHF measurements because of its long time parameters. To operate in this frequency range the 6H-SiC $n^+-n^--n^+$ diode structures were developed. The structure consisted of an 3–5 microns base n^--layer doped to $(2-5)\cdot(10^{15}-10^{16})$ cm^{-3}, 0.15 microns upper n^+-layer doped to 10^{20} cm^{-3} and substrate doped to $2\cdot 10^{18}$ cm^{-3}. In fabrication of structure reactive ion etching was used for creation of mesa isolation 25–40 microns in diameter. Ni sintered by thermal annealing was used as ohmic contacts to n^+-layers. The I–V characteristic of such structure is shown in Fig. 2. It consists of the linear almost ohmic region and the region of the sharp current change. The latter is followed by a light radiation. The spectrum of this radiation is identical to a breakdown radiation in 6H-SiC. Consequently, this region is result from breakdown. But the field in the breakdown point (Fig. 2) do not exceed 150–170 kV/cm. It is less than 15 times of the breakdown field in 6H-SiC (the mean value $F_b = (2-3)$ MV/cm [5]), but it is approximately equal to $F_t = 150$ kV/cm of BO and NDC regime in 6H-SiC (Fig. 1).

As known the NDC state stimulates a generation of the field domain where the field exceeds one in the neighborhood and can achieve the breakdown field. There are some evidences that it is a mobile domain. In a case of static domain the I–V characteristic would be as shown in Fig. 2 by single points. Besides an instability of the domain in initial phase and very low differential resistance (10–20 Ω) of the breakdown region are additional evidences of mobile domain. In case of static domain it would be more than 200 Ω.

3. The investigation of regime BO in 6H-SiC $n^+-n^--n^+$ triode structures

To obtain more convincing evidences a SiC transistor with static induction have been created for the first time. The channel size was equal to $40\times 2\times 3$ μm^3, (Fig. 3).

The idea is the following: if the domain exists in channel the cross field of the gate $p-n$ junction subjecting to the domain will set into its destroying. It do occurred at the field approximately equal to 600 kV/cm resulting in the sharp amplitude reduction of breakdown region on I–V characteristic, Fig. 4 (curve 4).

Therewith the cross field influences on linear region in a usual manner as in field transistor only. The point where spread the cross field is placed so far from cathode that only mobile domain can come up to there. Thus in the channel with 6H-SiC natural superlattice the mobile domain was discovered. It oscillates there with UH frequency and

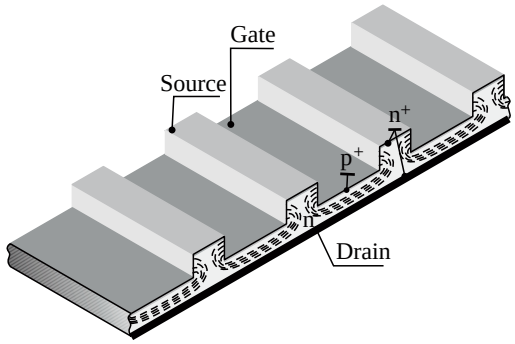

Fig. 3. The common view of ststic induction transistor structure.

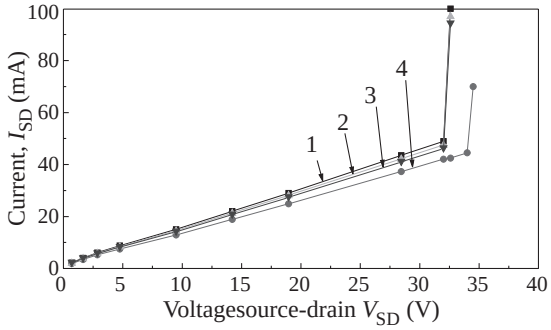

Fig. 4. I–V characteristic of 6H-SiC $n^+ - n^- - n^+$ triode structure.

it is the transformed Bloch oscillations which intrinsic frequency is approximately equal to $3 \cdot 10^{12}$ Hz. Unfortunately the sample degrades in this breakdown regime very rapidly. Therefore a direct discovering of UHF oscillations have been as yet impossible. It appears to be because of low quality of the using n-material. It is necessary to repeat the same experiment on 6H-SiC of another technology fabrication.

4. Conclusion

The discovering of NDC and mobile domain due to Bloch oscillations are the more important results in study the strong field transport in SiC superlattice. The presence of unusual mobile domain creating the breakdown avalanche is evidence oscillations possibly with terra Hz frequency.

Acknowledgements

The partial financial support of Russian Foundation for Basic Research project 00-02-16943 and Russian Science Program “Physics of Solid State Nanostructures” project 97-1038 is gratefully acknowledged

References

[1] L. Esaki and R. Tsu, *IBM J. Res. Develop.* **14**, 61 (1970).
[2] V. Sankin and I. Stolichnov, *JETF Letters* **64**, 114 (1994).
[3] V. Sankin, A. Naumov, A. Volfson et al., *Pis’ma Zh. Tekh. Fiz.* **15**, 43 (1989).
[4] V. Sankin and A. Naumov, *Superlattices and Microsructures* **10**, 353 (1991).
[5] V. I. Sankin, Yu. A. Vodakov and D. P. Litvin, *Sov. Phys. Semicond.* **18**, 2146 (1984).

9th Int. Symp. "Nanostructures: Physics and Technology"
St Petersburg, Russia, June 18–22, 2001

Dissimilarity between cleaved edge and surface regions of GaN (0001) epitaxial layers studied by spatially-resolved photoluminescence and reflectivity

T. V. Shubina†, *M. G. Tkachman*†, A. A. Toropov†, A. I. Karlik†, S. V. Ivanov†, P. S. Kop'ev†, T. Paskova‡ and B. Monemar‡

† Ioffe Physico-Technical Institute, St Petersburg, Russia

‡ Department of Physics and Measurement Technology, Linköping University, S-581 83 Linköping, Sweden

Optical properties of GaN, the perspective material for modern optoelectronics, have been intensively studied during last three decades. Generally, three exciton transitions A ($\Gamma_7 \times \Gamma_9$), B ($\Gamma_7 \times \Gamma_7$), C ($\Gamma_7 \times \Gamma_7$) observed in GaN with $C_{6\nu}$ symmetry originate from crystal-field and spin-orbit splitting. Exchange interaction removes the degeneracy of the fourfold degenerate exciton series and splits the A ($n = 1$) level into an allowed Γ_5 and a forbidden Γ_6 component. Both ground B and C levels split into three levels: Γ_5, Γ_1 and Γ_2. The allowed optical transitions involve the Γ_1 state in an $\mathbf{E} \parallel \mathbf{c}$ polarization and the Γ_2 state in $\mathbf{E} \perp \mathbf{c}$ [1].

Most of the GaN optical studies have been performed from the surface of epitaxial layers in the so-called α-polarization, when the wave vector $\mathbf{k}$ is parallel to the crystal axis $\mathbf{c}$ and the electric field vector $\mathbf{E}$ is normal to it. Very few papers concern investigation from a cleaved edge (facet) of the epitaxial layers, although such a study performed by Dingle *et al.* for $\pi-$ ($\mathbf{k} \perp \mathbf{c}, \mathbf{E} \parallel \mathbf{c}$) and $\sigma-$ ($\mathbf{k} \parallel \mathbf{c}, \mathbf{E} \parallel \mathbf{c}$) polarizations permitted one to check selection rules and determine experimentally the principal parameters of GaN valence bands [2]. During the edge study some dissimilarity between $\alpha-$ and $\sigma-$polarized reflectance spectra was observed, which is not explained in the classical model and was not discussed in detail. Moreover, to the best of our knowledge, the edge reflectance measurements have not been repeated since that time due to obvious difficulties in preparation of high quality cleaved facets.

In this paper we present results of comparative studies of the edge and the surface optical properties of GaN epilayers done, using micro-photoluminescence (μ-PL) and reflectance (R) spectroscopies. The results undoubtedly demonstrate inequality in exciton transitions taking place in the internal and near surface regions of the epilayers, which is presumably controlled by anisotropic strain and defect density.

The study was performed using a typical $\sim$25 μm-thick sample grown by HVPE as described previously [3]. Detailed structural characterization by x-ray diffractometry (XRD) and transmission electron microscopy demonstrates a good quality of the sample, especially in the top near surface regions where the dislocation density is less then 10^8 cm^{-2}. At room temperature the layer experiences a biaxial compressive strain ($\sim$0.2 Gpa).

Measurements of μ-PL were carried out in a He continuous flow cryostat at 4 K under cw excitation by a 266 nm laser line of a solid-state diode-pumped frequency-doubled Nd:Vanadate cw laser followed by a MDB-266 frequency doubler unit. The beam impinging normally onto a surface or a cleaved edge facet of the sample was focused using a reflective objective creating an excitation spot of $\sim$1.5 μm in diameter. The same objective collects

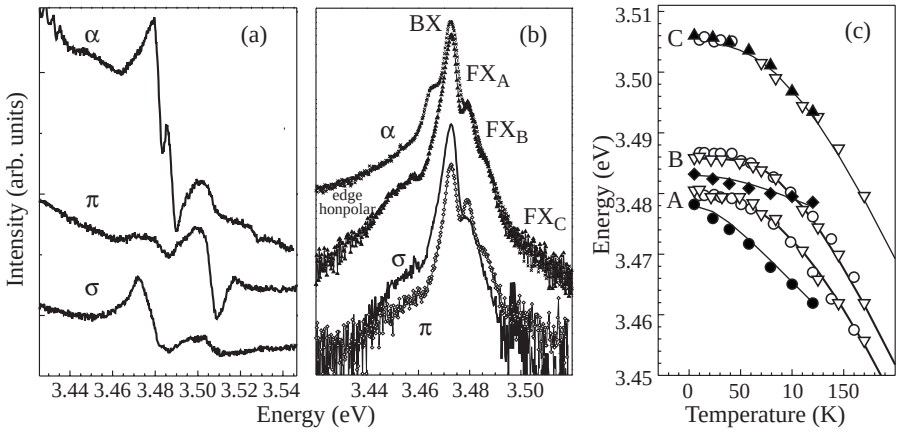

Fig. 1. Reflectance (a) and μ-PL (b) spectra measured at 5 K in a GaN epitaxial layer in different polarizations: α ($\mathbf{k} \parallel \mathbf{c}$, $\mathbf{E} \perp \mathbf{c}$), σ ($\mathbf{k} \perp \mathbf{c}$, $\mathbf{E} \perp \mathbf{c}$) and π ($\mathbf{k} \perp \mathbf{c}, \mathbf{E} \parallel \mathbf{c}$). Non-polarized facet μ-PL spectrum is shown by triangles. (c) Temperature dependencies of exciton energies obtained from polarized reflectance (σ solid circles, π solid diamonds (B) and triangles (C), and α open circles) and μ-PL (open triangles).

the PL signal and the sample image which is monitored by a charge coupled detector (CCD). The PL is relayed to the slits of an asymmetrical Czerny-Turner type monochromator and then to the nitrogen cooled CCD. The spectral resolution of the system is estimated as $\sim$0.6 meV. The R measurements were performed in the same set-up, using a tungsten lamp as an excitation source. At the same focusing conditions the R spatial resolution is estimated as $\sim$10 μm. A linear polarizer (followed by a depolarizer) was mounted before monochromator slits to analyze the PL and R polarization.

The comparison of R and μ-PL data presented in Fig. 1(a) and (b) permits us to assign the most intense peak to a bound A exciton which appears to be generally σ-polarized. The ordering and peak energy of free A, B and C excitonic transitions (marked as FX_A, FX_B and FX_C, respectively) are consistent with published data for weakly strained GaN on sapphire [4]. The μ-PL spectra are characterized by the distinctiveness of the excitonic features, whose width is about 3 meV at low power. The μ-PL measurements across the layer edge permit us to attribute a distinguished shoulder in the α-polarized μ-PL spectrum as reemission from relaxed bottom-interface regions, whereas temperature- and power-dependent studies show that an enhanced π-polarized component in the vicinity of a free A exciton peak FX_A is related to joint contribution of bound excitons of the B band and scattered states of the A bands.

The reflectance spectra (Fig. 1(a)) satisfy generally the selection rules and the expected intensity relationship of the exciton transitions [2]. At the $\alpha-$ and σ-polarizations the $FX_A(\Gamma_5)$ and $FX_B(\Gamma_5)$ exciton resonances are well pronounced, while the $FX_C(\Gamma_5)$ one is rather weak. Contrary, in the π-polarization, the $FX_C(\Gamma_1)$ resonance dominates with a well-distinguished $FX_B(\Gamma_1)$ feature and negligible FX_A. However, the $\alpha-$ and σ-polarized R spectra are appreciably different - the α-polarized spectrum is shifted to higher energies as compared to the σ-polarized one. Exciton resonances in the facet spectra are wider, likely, due to the edge region imperfection.

The difference between the $\alpha-$ and σ-polarized R becomes more pronounced with the temperature variation. Figure 1(c) presents exciton energies which are deduced from the R

spectra using a three oscillator model of the dielectric constant [5]. The exciton resonances, belonging to the same band, shift differently in the facet and surface spectra, although the energy gap between Γ_5 and Γ_1 states is expected to be less than 2 meV [6]. Only the C-band exciton transitions, shifted in energy due to spin-orbit splitting, coincide at all temperatures.

We have performed fitting of the facet R and μ-PL temperature dependencies of the exciton energies using an analytical four-parameter model proposed by R. Pässler [7]

$$E(T) = E(0) - \frac{\alpha_p \Theta_p}{2} \times \left[\frac{\rho}{2} \left(\sqrt[4]{1 + \frac{\pi^2}{6}\left(\frac{4T}{\Theta_p}\right)^2 + \left(\frac{4T}{\Theta_p}\right)^4} - 1 \right) + (1-\rho)\left(\coth\left(\frac{\Theta_p}{2T}\right) - 1 \right) \right]$$

where $E(0)$ is a zero-temperature transition energy; α_p is a high-temperature slope of the dependence; the parameter $0 \le \rho \le 1$ determines relative weights of long-wavelength acoustical phonons (ρ) and a combination of optical and short-wavelength acoustical phonons ($1-\rho$); Θ_p is defined via the Debye temperature Θ_D as $\Theta_p \cong (2/3)\Theta_D/(1-1/2\rho)$.

The fit of the μ-PL data has been performed using $E = 3.4810$, 3.4858, 3.5053 eV; $\Theta_p = 420$, 400, 420 K; $\rho = 0.4$, 0.3, 0.42 for $FX_A(\sigma)$, $FX_B(\pi)$, $FX_C(\pi)$, respectively, with the same $\alpha = 0.42$. The parameters are close to those found for perfect homoepitaxial GaN films [8]. It appears that the α-polarized R data can be successfully described by the parameters obtained from the edge μ-PL fitting. The coincidence of the μ-PL and the α-polarized R dependencies (Fig. 1(c)) means that the main part of the polarized μ-PL is provided by internal regions and is not a characteristic of the outer surface of the edge.

The edge reflectance data are fitted with $E = 3.4780$, 3.4830, 3.5053 eV; $\Theta_p = 100$, 200, 420 K; $\rho = 0.9, 0.85, 0.4$ for $FX_A(\sigma)$, $FX_B(\pi)$, $FX_C(\pi)$, respectively. The parameters are hardly meaningful in the model. It is worth to note that the energy gaps between the exciton energies taken as a function of the A exciton line, assumed frequently as a measure of stress in GaN [6], vary differently in the edge and internal regions. Reflectance edge data demonstrate the anti-correlated variation between bands, while similar energy gaps found from μ-PL and surface R are almost constant. Thus, the facet R dependencies seem to reflect a strong anisotropic strain near the facet surface [9].

The data on the band separations in the edge and internal regions are used to estimate spin-orbit Δ_{SO} and crystal-field Δ_{CR} parameters in the Hopfield's quasicubic model [10]. The obtained values at 5 K are: $\Delta_{CR} = 9.5$ meV and $\Delta_{SO} = 22$ meV – for edge regions; $\Delta_{CR} = 10.4$ meV and $\Delta_{SO} = 20.3$ meV – for internal regions. The set is generally consistent with that previously reported for surface measurements [6]. Particularly, the edge parameters are close to those found in facet studies [2], but with opposite assignment of Δ_{CR} and Δ_{SO}, which is possible because the Hopfield's model is symmetrical with respect to these parameters.

In conclusion, polarized photoluminescence and reflectance spectroscopy with high spatial resolution are employed to show the different optical properties of cleaved edges with respect to internal regions of thick GaN epitaxial layers. The values of spin-orbit and crystal-field parameters are determined separately for these areas. The obtained data indicate that an absorption edge of the material within the cleaved edge regions is below the energy of emission from internal regions (see Fig. 1(c)), which can be disadvantageous for the operation of edge-emitting devices, such as LED and lasers.

Acknowledgements

This work is partly supported by the Program of the Ministry of Sciences of RF "Physics of Solid State Nanostructures" and RFBR Grants (No. 99-02-17103 and No. 00-02-17022).

References

[1] E. L. Ivchenko and G. E. Pikus, *in Superlattices and Other Heterostructures, Springer Series in Solid-State Sciences*, 1997.
[2] R. Dingle, D. D. Sell, S. E. Stokowski and M. Ilegems, *Phys. Rev. B.* **4**, 1211 (1971).
[3] V. Ratnikov, R. Kyutt, T. Shubina, T. Paskova, E. Valcheva and B. Monemar, *J. Appl. Phys.* **88**, 6252 (2000).
[4] B. Monemar, J. P. Bergman, I. A. Buyanova, W. Li, H. Amano and I. Akasaki, *MRS Internet Journal of Nitride Semiconductor Research (MIJ-NSR)* **1**, article 2 (1997).
[5] J. J. Hopfield and D. J. Thomas, *Phys. Rev.* **132**, 563 (1963).
[6] B. Gil, *Strain Effect on Optical Properties, in Gallium Nitride II*, Vol 57. Eds J. I. Pankove and T. D. Moustakas, Academic Press, 1999, p. 209.
[7] R. Pässler, *J. App. Phys.* **83**, 3356 (1998).
[8] K. Thonke, K. Kornitzer, M. Grehl, R. Sauer, C. Kirchner, V. Schwegler, M. Kamp, M. Leszczynski, I. Grzegory and S. Porowski, *IPAP Conf. Series 1: IWN2000*, p. 587 (2000).
[9] K. Domen, H. Horino, A. Karamata and T. Tanahashi, *Appl. Phys. Lett.* **70**, 987 (1997).
[10] J. J. Hopfield, *J. Phys. Chem. Solids* **15**, 97 (1960).

9th Int. Symp. "Nanostructures: Physics and Technology"
St Petersburg, Russia, June 18–22, 2001

Modeling of band offsets in GaN based heterostructures

H. Ünlü
Istanbul Technical University, Department of Physics
Maslak 80626 Istanbul, Turkey

Abstract. We present a tight binding modeling of the band offsets of GaN based heterostructures. The model considers the nonorthogonality of the sp^3 set of orbitals of adjacent atoms and spin-orbit coupling and uses the Hartre–Fock atomic energies and interacting matrix element, obtained by fitting existing band structures for bulk materials, to determine the valence band energies at 0 K and 1 Bar, which are screened by the optical dielectric constants of bulk materials at any temperature, pressure, strain, and composition. The model compares very well with experiment for the valence and conduction band offsets of GaN based and many other heterostructures.

Introduction

The band offsets appearing at heterointerfaces dominate various device properties such as injection efficiency in heterojunction bipolar transistors (HBT) and the carrier confinement in modulation doped FETs (MODFETs) [1]. The need for precise and reliable prediction of band offsets has received the considerable attention of the solid state device scientists and engineers over the years (see Ref. [2] for a detailed discussion). In this article, the band offsets at GaN based heterointerfaces are determined using the extended tight binding model [3]. The presented model includes the overlapping of hybrids at neighboring bonds and anti-bonds such that it cannot simply be absorbed into a re-scaling of other parameters to find the valence band energies which are screened by the optical dielectric constants of constituents which are temperature, pressure, interface strain, and alloy composition dependent.

1. Extended tight binding modeling of band offsets

Consider the formation of bonding and antibonding states for a binary semiconductor from isolated c-cation and a-anion atoms. One uses the linear combination of bond orbitals sp^3 hybrids of the s-and p-states to write a bond orbital wave function as $|\phi_{\rm hac}>= {\rm u_c}|\phi_{\rm ha}> +{\rm u_c}|\phi_{\rm hc}>$ [3]. Here $|\phi_{\rm h}>= \frac{1}{2}(|{\rm s}> +\sqrt{3}|{\rm p}>)$ is the wavefunction of the sp^3 hybrid which has the expectation value of $\epsilon_{\rm h} =<\phi_{\rm h}|{\rm H}|\phi_{\rm h}>= (\epsilon_{\rm s}+3\epsilon_{\rm p})/4$ and $\rm u_c$ and $\rm u_a$ are the coefficients. $\epsilon_s =<\phi_s|H|\phi_s>$ and $\epsilon_p =<\phi_p|H|\phi_p>= \epsilon_{op}+\Delta/3$ are Hartree-Fock free atomic term values, where $\Delta/3$ is the crystal field splitting energy of p-states [4] and $\epsilon_{\rm op}$ is the value of $\epsilon_{\rm p}$ without the splitting. By using the variational principle the bond and antibond orbital energies can be obtained and minimizing the expectation value E with respect to coefficients $\rm u_c$ and $\rm u_a$ ($\partial {\rm E}/\partial {\rm u_c}=0$ and $\partial {\rm E}/\partial {\rm u_a}=0$) one obtains a set of two linear equations for $\rm u_c$ and $\rm u_a$. The solutions of this set of equations are the energies of antibonding and bonding hybrids, obtained from : $\sum_{\rm i,j=1}^{2}({\rm H_{ij}}-{\rm ES_{ij}})=0$. Here ${\rm H}_{11}=\epsilon_{\rm hc}$ and ${\rm H}_{22}=\epsilon_{\rm ha}$ are the hybrid energies, ${\rm H}_{12}={\rm H}_{21}^{*}={\rm V}_{sp^3}$ is the interaction matrix and ${\rm S}_{12}={\rm S}_{21}^{*}={\rm S}_{sp^3}$ and ${\rm S}_{11}={\rm S}_{22}=1$ are the overlap integrals between orbitals on adjacent anion and cation and on the same cation or anion. The interaction between the hybrids on

the same anion and cation, or between the bond and neighboring antibonds will broaden the hybrid energies into valence and conduction bands at k=0, and for the valence band energy is written as [3]:

$$E_v(\Gamma_{8v}) = E_b - E_{mv} = \frac{\epsilon_{hc} + \epsilon_{ha}}{2\left(1 - S_{sp^3}^2\right)} - \frac{V_{sp^3} S_{sp^3}}{\left(1 - S_{sp^3}^2\right)} - \Delta E_h - E_{mv} \quad (1)$$

$$\Delta E_h = \frac{1}{2\left(1 - S_{sp^3}^2\right)} \left[(\epsilon_{hc} - \epsilon_{ha})^2 - 4\left(\epsilon_{ha} + \epsilon_{ha}\right) S_{sp^3} V_{sp^3} + 4\epsilon_{hc}\epsilon_{ha} S_{sp^3}^2 + 4V_{sp^3}^2 \right]^{1/2} \quad (2)$$

where ΔE_h is the hybrid bonding gap. Minimizing ΔE_h relative to lattice constant a ($(\partial \Delta E_h)/(\partial V_{sp^3}) = 0$) one obtains the overlap integral: $S_{sp^3} = 2V_{sp^3}(\epsilon_{hA} + \epsilon_{hB})$, where $V_{sp^3} = k/a^2$, with coefficient $k \approx 107$ obtained from the fitting to band structure of bulk semiconductors. The metallization contribution to the broadening of bonding energy E_b into valence band energy E_v is [4]: $E_{mv} = (1/2)[(1+\alpha_p)V_{1c} + (1-\alpha_p)V_{1a}] + 2\alpha_c V_1^x$, where $V_1 = (\epsilon_p - \epsilon_s)/4$ characterizes the s-p splitting in the free atom. $V_1^x = -\frac{1}{4}(V_{ss} + 2V_{sp}/\sqrt{3} - V_{pp})$ is the additional contribution to the matrix elements between nearest neighbor bonds. Since the u_c/u_c ratio defines ionic character of hybrid, the polarity α_p and covalencey α_c of hybrid bond are defined as [3]: $\alpha_p = u_c/(u_c^2 + u_a^2)^{1/2}$ and $\alpha_c = (1 - \alpha_p^2)^{1/2}$. Demanding that $|\phi_{hac}>$ is normalized, $< \phi_{hac}|\phi_{hca} >= u_c^2 + u_a^2 + 2u_c u_c S_{sp^3} = 1$, coefficients u_c and u_c can be obtained by solving the secular equations using the bonding energy $E = E_b$ giving u_c and u_c for the bonding hybrid:

$$u_c = \frac{\left(V_{sp^3} - S_{sp^3} E\right)}{U_{sp^3}}, \qquad u_a = \frac{(E - \epsilon_{hc})}{U_{sp^3}} \quad (3)$$

$$U_{sp^3} = \left[\left(V_{sp^3} - S_{sp^3} E\right)^2 + (\epsilon_{hc} - E)^2 - 2S_{sp^3}\left(E - \epsilon_{hc}\right)\left(V_{sp^3} - S_{sp^3} E\right) \right]^{1/2} \quad (4)$$

The band offset at A/B heterointerface is then found from the following equation

$$\Delta E_v = \left(\frac{E_v}{\varepsilon_\infty}\right)_B - \left(\frac{E_v}{\varepsilon_\infty}\right)_A \quad (5)$$

where ε_∞ the optical dielectric constant of the constituent semiconductors. The conduction band offsets at high symmetry points Γ_{6c}, L_{6c}, and X_{6c} can be obtained from $\Delta E_{ci} = \Delta E_{gi} - \Delta E_v$, where ΔE_{gi} ((with i=Γ, L, X)) is the bandgap difference. The conduction and valence band energies, defined as the standard state chemical potentials, at any temperature and pressure can be written as [5]:

$$E_c(T, P) = E_c(0, P_0) + C_{cP}^0 T(1 - \ln T) - \frac{a_c}{B}\left[P - \frac{P^2}{2B} - \frac{(1 + B')P^3}{6B^2}\right] \quad (6)$$

$$E_v(T, P) = E_v(0, P_0) + C_{vP}^0 T(1 - \ln T) + \frac{a_v}{B}\left[P - \frac{P^2}{2B} - \frac{(1 + B')P^3}{6B^2}\right] \quad (7)$$

where P_0=1 Bar and P is the applied pressure. $a_c = -B(\partial E_c/\partial P)$ and $a_v = B(\partial E_v/\partial P)$ are deformation potentials of E_c and E_v, with bulk modulus B and its derivative $B' = \partial B/\partial P$. $C_{cP}^0 = C_{nP}^0 - C_{0P}^0 = -C_{pP}^0 + \Delta C_P^0$ and $C_{vP}^0 = C_{pP}^0$ standard heat capacities of conduction electrons and valence holes, where $C_{iP}^0 = C_{nP}^0 = C_{pP}^0 = (5/2)k_B$ and

$C^0_{0P} = C^0_{nP} + C^0_{pP} - \Delta C^0_P$, with ΔC^0_P being the heat capacity of reaction which is obtained from fitting of the bandgap $E_{gi}(T, P) = E_{ci}(T, P) - E_v(T, P)$ to its corresponding measured value [6]. The effects of interface strain on ΔE_c and ΔE_v can be found by substituting $P = -2B_f C_f \epsilon_{f\perp}$ for heterolayer and $P = -3B_s\epsilon_s = 0$ for substrate for a (001) growth, written as [3]:

$$\Delta E_v(T, \epsilon) = \Delta E_v(T) - 2a_{vf}C_f\epsilon_{f\perp}[1 + C_f\epsilon_{f\perp}] - 2a_{vf}C_f\epsilon_{f\perp}\frac{2\left(1 + B'_f\right)}{3}C_f^2\epsilon_{f\perp}^2 \quad (8)$$

$$\Delta E_{ci}(T, \epsilon) = \Delta E_{ci}(T) + 2a_{cf}C_f\epsilon_{f\perp}[1 + C_f\epsilon_{f\perp}] - 2a_{cf}C_f\epsilon_{f\perp}\frac{2\left(1 + B'_f\right)}{3}C_f^2\epsilon_{f\perp}^2 \quad (9)$$

where $\epsilon_{f\perp} = (a_{f\perp} - a_f))/a_f$. Here $a_{f\parallel} = a_s$ and $a_{f\perp} = a_f[1 - D_f(a_{f\parallel} - a_f)/a_f]$ and $D_f = 2C_{12}/C_{11}$ with C_{11} and C_{12} the elastic constants.

The valence band offset at $A_xB_{1-x}C/BC$ heterointerface is obtained by taking anion energy as $\epsilon_{pa}(C)$ and cation energy as $\epsilon_{pc}(x) = x\epsilon_{pc}(A) + (1-x)\epsilon_{pc}(B)$ and lattice constant $a(x) = xa(AC) + (1-x)a(BC)$, in calculating $E_v(x)$ of $A_xB_{1-x}C$ ternary. The composition effects on conduction band offset $\Delta E_c(x)$ can be obtained with the use of Vegard's rule and Kane's $\mathbf{k}\cdot\mathbf{p}$ model for semiconductors [1, 7]: $(1/m_n(x)) = 1 + (P^2(x)/3)[(2/E_g(x)) + 1/(E_g(x) + \Delta(x))]$, where $m_n(x) = m_{nA}m_{nB}/(xm_{nB} + (1-x)m_{nA})$ is the ternary electron effective mass obtained from Vegard's rule [1, 7]. m_{nA} and m_{nB} are the electron effective masses of binaries A and B. $P(x) = xP_A + (1-x)P_B$ is the momentum matrix and $\Delta(x) = x\Delta_A + (1-x)\Delta_B$ is the spin-orbit energy. P_A and P_B of binaries A and B are obtained from Kane's equation with measured $m_n(x)$ and $\Delta(x)$ for x=0 and 1 [6]. Kane's equation can be rewritten in a quadratic form for bandgap $E_{g\Gamma}$, whose positive root gives [3]:

$$E_{g\Gamma}(x) = \frac{3/y(x) - \Delta(x)}{2} + \frac{1}{2}\left[(\Delta(x) - 3/y(x))^2 + 8\Delta(x)/y(x)\right]^{1/2} \quad (10)$$

where $y(x) = 3(1 - m_n(x))/m_n(x)P^2(x)$. A similar expression can be found for E_{gL} bandgap using equation (31) of Adachi [7]. The indirect gap E_{gX} is determined from $E_{gX}(x) = E_{g\Gamma}(x) + (E_{gXA} - E_{g\Gamma A})x + (E_{gXB} - E_{g\Gamma B})(1-x)$. Here E_{gXA}, E_{gXB}, $E_{g\Gamma A}$, and $E_{g\Gamma B}$ are the indirect and direct bandgaps of binaries A and B.

Results and discussion

The valence band offsets at AlN/GaN, GaN/InN and AlN/InN and GaN/GaP heterointerfaces are obtained from Eq. (5) using the Hartree–Fock free term values [4], measured bandgaps, and the spin orbit splitting energies [4, 6]. Predictions of this work (ETB1) are given in Table I, compared with those of p-p extended tight binding model (ETB1) [8], self consistent tight binding model (SCTB) [9], linear mufin thin orbital model (LMTO) [10], and the first principles electronic structure model (FPES) [11] against the experiment [12, 13]. The model predictions are compatible with those of quantum mechanical models, which are based on the elaborate band structure calculations of heterojunction components.

The model was also applied to III-Nitride based ternary/binary heterostructures to determine the composition effects on band gaps and band offsets. The parameters used for AlGaN/GaN heterostructure are: m_n/m_0=015 and 0.25, m_p/m_0=0.40 and 0.70, Δ_s/meV=11 and 19, and $E_{g\Gamma}$/eV=6.20 and 3.39 for GaN and AlN, respectively [14, 15]. Although there is no data available for ΔE_v at $Al_xGa_{1-x}N/GaN$ heterointerface, prediction of Eq. (10) for the direct bandgap $E_{g\Gamma}$ of $Al_xGa_{1-x}N$, is found to be in good agreement with experiment[14].

Table 1. Comparison of this work (ETB1) with those of p-p extended tight binding (ETB2) model [8], self consistent tight binding model (SCTB) [9], linear mufin thin orbital model (LMTO) [10], and first principles electronic structure model (FPES) [11], against the measured valence band offsets [12, 13]. (All values are in eV.)

System	ETB1	ETB2	SCTB	FPES	LMTO	Experiment
AlN/GaN	0.26	0.33	0.17	0.84	0.85	0.57 ± 0.22 [12]
AlN/InN	1.52	1.66	0.13	1.04	1.09	1.81 ± 0.20[12]
GaN/InN	1.27	1.33	-0.04	0.26	0.51	1.05 ± 0.25[12]
GaN/GaP	1.84	1.74	1.89	1.72	—	2.30 ± 0.6 [13]

Acknowledgements

This work was supported by the Research Foundation of Istanbul Technical University and by the Scientific and Technical Research Council of Turkey (TÜBİTAK).

References

[1] H. Morkoç , H. Ünlü and G. Ji, *Principles and Technology of MODFETs*, vol 1, 2 (John Wiley & Sons, 1991).
[2] E. T. Yu, J. O. McCaldin and T. C. McGill, *Solid State Physics*, **46**, 1, (1992).
[3] H. Ünlü, *Phys. Stat. Sol. (B)* **223**, 95 (2001).
[4] W. A. Harrison, *Electronic Structure and the Properties of Solids*, Freeman (1980).
[5] H. Ünlü, *Solid State Electron.* **35**, 1343 (1992).
[6] O. Madelung, *Numerical Data and Functional Relationships in Science and Technology*, Part a, vol. 17, Springer (1982).
[7] S. Adachi, *J. Appl. Phys*. **58** R1 (1985).
[8] H. Ünlü, *Phys. Stat. Sol. (B)* **216**, 107 (1999).
[9] W. A. Harrison and J. Tersoff, *J. Vac. Sci. Technolog.* **B5**, 1068 (1986).
[10] W. R. Lambrecht and B. Segall, *Phys. Rev. B* **41**, 2832 (1990).
[11] S. H. Wei and A. Zunger, *Appl. Phys. Lett.* **72**, 2011 (1998).
[12] H. Morkoç , F. Handani, and A. Salvador, *Semiconductors and Semimetals* vol. 50, p. 193, Academic (1998).
[13] H. Sato et al., *Solid State Electron.* **41**, 205 (1997).
[14] Y. Koide et al., *J. Appl. Phys.* **61**, 4540 (1987).
[15] S. K. Pugh et al., *J. Appl. Phys.* **86**, 3768 (1999).

9th Int. Symp. "Nanostructures: Physics and Technology"
St Petersburg, Russia, June 18–22, 2001

Raman studies of acoustical phonons in strained hexagonal GaN/AlGaN superlattices

V. Yu. Davydov†, A. A. Klochikhin†‡, I. E. Kozin§, I. N. Goncharuk†, A. N. Smirnov†, R. N. Kyutt†, M. P. Scheglov†, A. V. Sakharov†, V. V. Tretyakov†, A. V. Ankudinov†, M. S. Dunaevskii†, W. V. Lundin†, E. E. Zavarin† and A. S. Usikov†

† Ioffe Physico-Technical Institute, St Petersburg, Russia

‡ Petersburg Nuclear Physics Institute, Russian Academy of Sciences, Gatchina, 188350 St Petersburg, Russia

§ Institute of Physics, St Petersburg State University, 198904 St Petersburg, Russia

Abstract. We report the first experimental observation of folded acoustical modes in strained hexagonal GaN/$Al_xGa_{1-x}N$ superlattices by Raman scattering. The dispersion of LA phonon branch was determined by using different scattering configurations. It was found that the zone-center gap of folded phonon branch is beyond the instrumental resolution ($\approx 0.5\,cm^{-1}$). The sound velocity for GaN/$Al_xGa_{1-x}N$ SL with Al content $x = 0.28$ was found to be 8410 m/s.

1. Introduction

GaN, AlN and $Al_xGa_{1-x}N$ alloys are promising materials for realization of optoelectronic devices operating in blue and green spectral region. During last few years GaN/AlN and GaN/$Al_xGa_{1-x}N$ short-period superlattices (SLs) were under intensive investigation, but only a few reports were devoted to studies of lattice dynamics in SLs. The available experimental data are mainly concerned with the long wave optical lattice vibrations in these structures [1, 2]. To our knowledge, no data on Raman scattering in the region of acoustical phonons in GaN based SLs have been published. The formation of SL induces a folding of the Brillouin zone in the growth direction, which result in appearance of new Raman active phonon modes. The investigation of folded acoustical modes can provide information on the SL parameters, sound velocity for average compound of SL, and dispersion of acoustical phonons [3]. The goal of this work is to study the Raman scattering in the region of folded acoustical modes in strained hexagonal GaN/$Al_xGa_{1-x}N$ SLs.

2. Sample characterization

The structures were grown by MOCVD and consisted of 500–1000 nm GaN or $Al_xGa_{1-x}N$ buffer layer grown directly on sapphire substrate followed by SL. The period of SLs was varied from 5 nm to 40 nm. The GaN well and $Al_xGa_{1-x}N$ barrier thickness were equal and the total thickness of all SLs was close to 3 μm. The SLs have been characterized by X-ray diffraction, electron probe microanalysis and atomic force microscopy (AFM). X-ray diffraction rocking curves for (0002) reflection measured in $\Theta - 2\Theta$ scan mode demonstrate well resolved satellite pattern indicating a well defined period d_p (Fig. 1(a)). By fitting of simulating rocking curves to the experimental ones the SL period, Al content in the alloy and the strain of the alternative layers were obtained.

We have obtained image of SL layers by using AFM P4-Solver (produced by NT-MDT, Russia) operating in local elasticity mode (Fig. 1(b)). The contrast in this picture arises

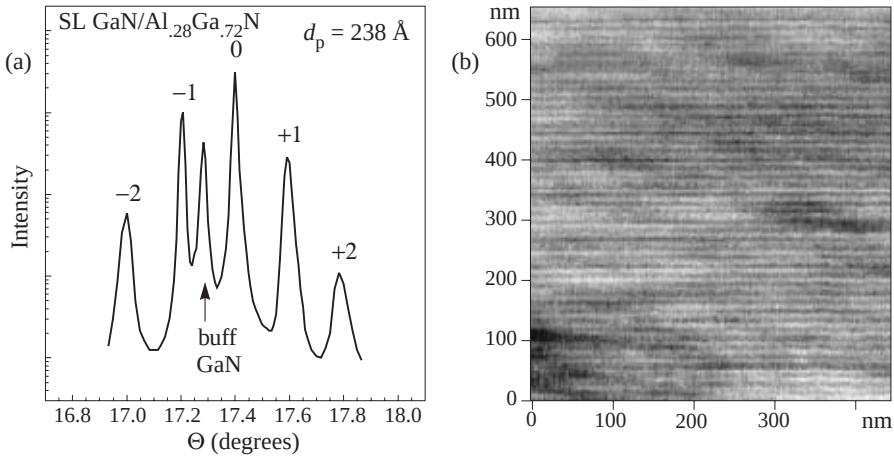

Fig. 1. (a) $\Theta - 2\Theta$ diffraction curve of (0002) reflection for SL with the period $d_p = 238$ Å; (b) AFM-image of cleavage surface relief obtained from GaN/Al_xGa_{1-x}N SL ($d_p = 128$ Å).

from extremely small variations of relief due to the different sign of strain in the SL layers. SLs parameters obtained from X-ray and AFM measurements agree well with growth calibrations.

3. Experimental results and discussion

Raman spectra of GaN/Al_xGa_{1-x}N SLs were measured in backscattering and 90-degree configurations at room temperature and at 100 K, with an Ar^+ laser ($\lambda = 488$ nm) excitation. Figure 2(a) shows Raman spectra in the acoustical frequency range, obtained for some of the samples in $z(xx)\bar{z}$ configuration. Here, the Porto's notation is used for scattering geometries with z to be parallel to the wurtzite c axis, and x and y to be mutually orthogonal and oriented in arbitrary manner in the substrate plane. The Raman spectra of all samples contain the doublets of narrow lines. The shift of doublets toward the exciting line with

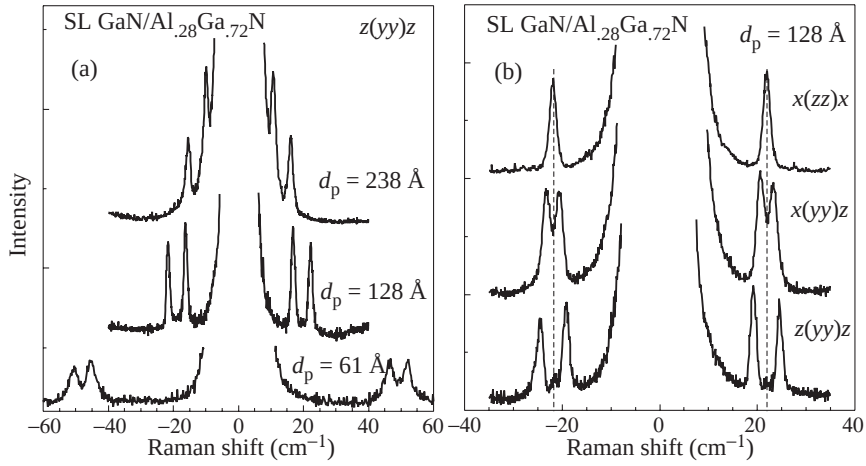

Fig. 2. (a) Raman spectra of SLs with different periods at $T = 300$ K; (b) Raman spectra of GaN/Al_xGa_{1-x}N SL obtained in different scattering configurations at $T = 300$ K.

the increase of SL-period is inherent for the folded acoustical phonons. The Raman shift $\Delta\omega^{\pm}_{n,q_z}$ of the doublet lines is given by

$$\Delta\omega^{\pm}_{n,q_z} = \omega_{n,0} \pm q_z\, s. \tag{1}$$

Here $\omega_{n,0} = 2\pi ns/d_p$ is a frequency of the folded zone center LA-phonon, q_z is the phonon wave vector projection in the folding direction, s the LA sound velocity for averaged compound of SL, and $n = 0, 1, 2\ldots$. The value of s is different for SL's with abrupt interface [4] and structures with smooth modulation [5].

We have evaluated the sound velocity from the Raman data presented in Fig. 2(a). The data for different SLs are close and the averaged velocity is equal to 8410 m/s for $x = 0.28$. Experiments performed in different configurations allowed us to vary the phonon wave-vector from its maximum value in backscattering geometry along c-axis to almost zero for the in-plane scattering and thus to determine the dispersion curves of LA-phonon branch in SLs. We used three scattering configurations (Fig. 2(b)). The backscattering configuration provides the wave vector equal to $2k_{\text{photon}}$. The 90-degree configuration $z(xx)y$ reduces the z-projection of phonon wave vector to $q_z = k_{\text{photon}}$. The further decrease of phonon wave vector is reached for the in-plane backscattering configuration $x(zz)\bar{x}$ which leads to vanishing q_z. Doublets with the line spacing depending on the value of q_z were found in Raman spectra for $z(xx)\bar{z}$ and $z(xx)y$ configurations. However, in $x(zz)\bar{x}$ geometry only the single line at the position corresponding to the center of the doublets was observed. Since the first observation of folded acoustical phonons in Raman scattering [6] the behavior of modes at vanishing q_z was a subject of high interest. The zone center gap between folded acoustical branches provides an information about the SL parameters [3, 5]. Our results show that the zone-center gap of folded phonon branch for GaN/Al_xGa_{1-x}N SLs is beyond the instrumental resolution (≈ 0.5 cm^{-1}), which suggests the smooth modulation of SLs studied.

4. Summary

The Raman scattering from folded acoustical modes have been studied in strained hexagonal GaN/Al_xGa_{1-x}N SLs for the first time. The dispersion of LA phonon branch along the c-axis was determined by using different scattering configurations. It was found that the zone-center gap of folded phonon branch is beyond the instrumental resolution (≈ 0.5 cm^{-1}). The sound velocity for GaN/Al_xGa_{1-x}N SL with Al content $x = 0.28$ was estimated from Raman data. Study of dependence of LA sound velocity on Al content in GaN/Al_xGa_{1-x}N SL is in progress.

Acknowledgments. This work was partly supported by Program "Physics of Solid State Nanostructures" and Russian Foundation for Basic Research (projects No. 99-02-18318 and No. 01-02-18011).

References

[1] J. Gleize, et al., *Appl. Phys. Lett.* **74**, 703 (1999).
[2] V. Yu. Davydov, et al., *Proc. Int. Workshop on Nitride Semiconductors*, IPAP Conference Series 1, 665 (2000).
[3] B. Jusserand and M. Cardona, *Light Scattering in Solids V*, Ed. by M. Cardona and G. Gunterherodt, Springer-Verlag, Berlin, p. 49 (1988) (and references therein).
[4] S. M. Rytov, *Akust. Zh.* **2**, 71 (1956) [Sov. Phys. — Acoust. **2**, 68 (1956)].
[5] B. Jusserand, D. Paquet, F. Mollot, F. Alexandre and G. Le Roux, *Phys. Rev.* **B35**,2808 (1987).
[6] C. Colvard, R. Merlin, M. V. Klein and A. C. Cossard, *Phys. Rev. Lett.* **43**, 298 (1980).

9th Int. Symp. "Nanostructures: Physics and Technology"
St Petersburg, Russia, June 18–22, 2001

Nonlinear effects in dense two-dimensional exciton–polariton system

V. D. Kulakovskii[1], A. I. Tartakovskii[1], D. N. Krizhanovskii[1],
N. A. Gippius[2] and M. S. Skolnick[3]

[1] Institute of Solid State Physics, Chernogolovka, 142432, Russia
[2] Institute of General Physics, Moscow, Russia
[3] University of Sheffield, Sheffield, UK

Abstract. Angle resolved emission spectra of MCs with quantum wells embedded in the active layer have been investigated under conditions of resonant excitation into the lower polariton (LP) branch. The conditions have been found at which macroscopic filling at the LP branch bottom is reached in the strong coupling regime. Under these conditions strong nonlinear effects in the intensity and the degree of polarisation of polariton emission have been observed and investigated. The experimental dispersion of renormalized cavity mode and its strong narrowing have been explained using an interacting polariton model predicting that the coupling between the LP mode $E_{\mathrm{LP}}(k)$ and the mode $E^*(k) = 2\hbar\omega - E_{\mathrm{LP}}(k + 2k_{\mathrm{excitation}})$ is qualitatively different from that of exciton and photon.

Semiconductor microcavities (MCs) with planar Bragg mirrors change substantially the properties of excitons in quantum wells located at the antinodes of electric field [1–3]. In high quality MCs where the interaction between photon (C) and exciton (X) modes in a quantum well exceeds broadening of the modes, these interacting photons and excitons are considered as MC exciton polaritons revealing a number of peculiar features. The exciton polaritons in bulk semiconductors are stable three-dimensional quasi-particles, their energy tends to zero (at low polariton branch (LPB)) as the wave vector k decreases. In planar MC the polaritons are quasi-two-dimensional and their annihilation does not require conservation of the momentum in the direction perpendicular to the MC plane. As a result, (i) the life time of MC polaritons is finite and is of the order of picoseconds in MCs with a finesse about several thousands; (ii) their energy is finite at $k = 0$. In such a system a strong two-dimensional (2D) confinement of light makes accessible very high densities of the photonic field which may result in a different type of nonlinear effects [4, 5]. Another intriguing property is connected to the boson nature of the mixed exciton-photon states in MCs, 2D polaritons, characterized by an extremely small ($< 10^{-4} m_0$, m_0 being the free electron mass) in-plane effective mass. The low density of polariton states makes possible the high filling at the LP band bottom to be achieved at relatively low densities when the influence of the fermion nature of electron and hole in exciton compound is yet negligible. In this case, the bosonic nature of polaritons can favor stimulated scattering [5, 6] and allow Bose condensation. Experimental observation of these, presumably, nonlinear effects in the strong coupling regime is usually prevented by a slow relaxation of photoexcited polaritons into the LP band bottom [7, 8]. Only recently the stimulated character of polariton relaxation has been demonstrated using resonant excitation into the lower or upper polariton branch [9, 10].

In this work we discuss the properties of dense polariton system generated with the use of resonant excitations by circularly and elliptically polarised light. We succeeded (i) in generation of polaritons at the LPB bottom with a high degree of polarisation that

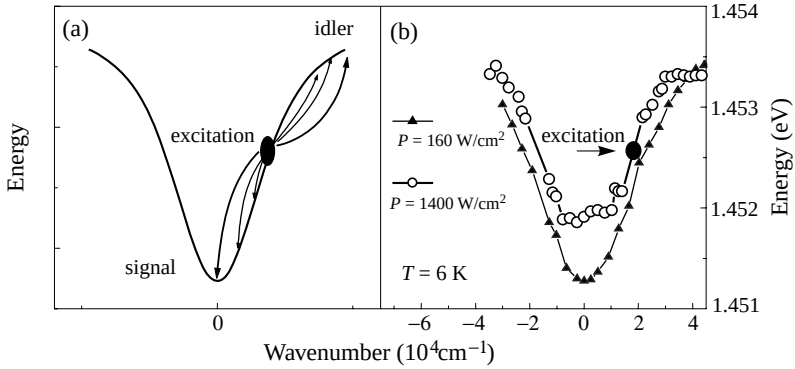

Fig. 1. (a) Polariton dispersion, measured at low and high excitation densities at $\Phi = 16^\circ$. (b) Schematic diagram of two-photon scattering.

under particular conditions exceeds markedly that of the exciting light and (ii) in observing nonlinear effects both in the emission intensity and in the circular polarisation degree.

A GaAs/AlAs MC containing 6 InGaAs quantum wells in the active layer (Rabi splitting, Ω of 6–7 meV) have been studied under the conditions of resonance between the photon and the exciton modes, when polaritons at $k = 0$ have half-exciton-half-photon character. We used a tunable Ti-Sapphire laser to excite luminescence in the MC. A sample was mounted in a cryostat at temperature $T = 1.8{-}20$ K.

Figure 1 displays the dispersion dependence for polaritons, that was measured at low excitation density. The excitation with the energy lower than the energy E_X of free excitons near the LPB bottom close to the inflection point of the dispersion curve, is the most promising for achieving high density of polaritons without filling of exciton states with large k. However experimental realisation of the idea is problematic because the time of acoustic phonon-mediated scattering into polaritons with $k < 10^4$ cm^{-1} is comparable to the life time of $k = 0$ polaritons. For this reason the k-distribution of polaritons is not in thermodynamic equilibrium. This situation is illustrated in Fig. 2, where LP emission spectra recorded with high angular resolution ($< 1^\circ$) at $T = 2$ K and low density of resonant excitation at $\Phi = 16^\circ$ ($k \sim 2 \cdot 10^4$ cm^{-1}) are displayed. It is seen that the LP emission intensity and, hence, their population decreases as k reduces, while thermodynamically equilibrium system should have demonstrated a sharp increase of LP concentration at the LPB bottom at so low temperature (2 K).

Thus, the phonon mechanism does not provide any effective relaxation of the energy of photoexcited polaritons. The problem can be solved in the case when the exciting light scatters directly into polariton states at the LPB bottom. Following the dispersion law (Fig. 1), that is possible at resonant excitation near the inflection point ($k_{\rm ex} \sim 1.8 \cdot 10^4$ cm^{-1}, or $\Phi \sim 16^\circ$), when a direct two-photon scattering into polariton states at $k = 0$ and $2k_{\rm ex}$ can occur with the conservation of the energy and the momentum.

Figure 2 displays experimental spectra of polariton emission recorded for two circular polarisations at $\Phi = 0^\circ$ and $T = 2$ Š under the conditions of circularly (σ^+) polarised excitation at $\Phi \sim 16^\circ$. In the spectrum there is a single line corresponding to the LP emission at $k = 0$. The fine structure of the line is related to the light interference in the sample (the sample thickness is 0.5 mm) and is not considered below. For the σ^+ polarisation the emission intensity at low density of excitation (the LP$^+$ peak) is slightly stronger than that for the σ^- polarisation (LP$^-$ peak), which implies that the spin relaxation time is larger than the lifetime. With increasing P the LP$^+$ peak at $k = 0$ shifts slightly

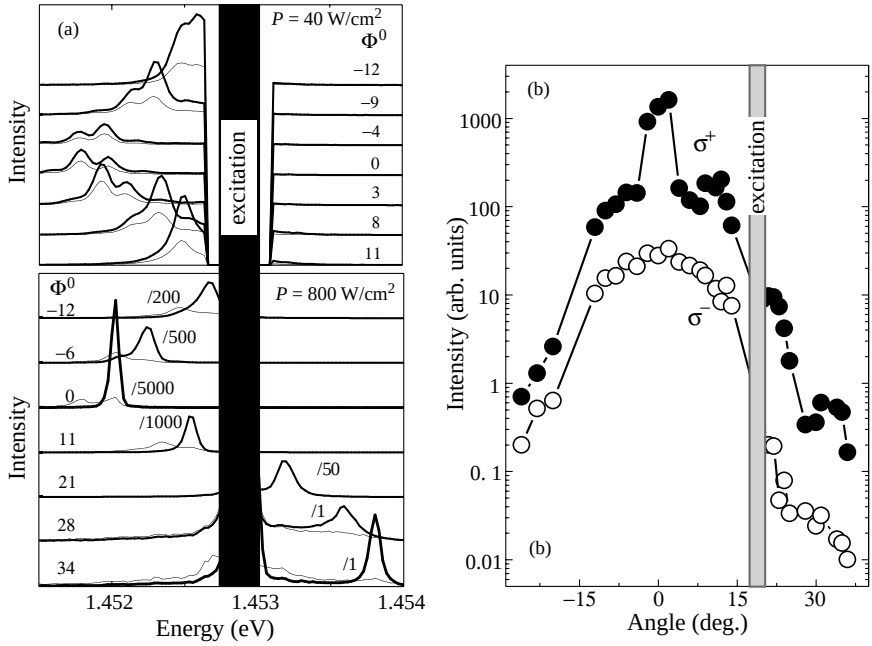

Fig. 2. (a) Polarized σ^+ (thick lines) and σ^- (thin lines) emission spectra of MC recorded for various detection angles under σ^+ polarized excitation into the LPB at angle $\Phi = 16^\circ$ at low and high excitation densities. (b) Angle dependence of the intensity of the LP^+ and LP^- lines.

to higher energies, increases superlinearly, and becomes narrow. The LP^- peak, on the contrary, increases linearly with P and its energy does not notably shift. As a result, at high P, the degree of circular polarisation of the LP line reaches 95%. Note that even at the highest P the shift of the LP^+ peak is much smaller than the Rabi splitting, which suggests that nonlinear emission effects are related to mixed exciton-photon system.

The dependences of the LP line intensity I_{LP} and polarisation degree ρ_{LP} on the density of excitation at $k = 0$ are plotted in Figs.3(a) and 3(b). There are four regions of the density, revealing qualitatively different behaviour. In the first region ($P < 150$ W/cm^2) $I_{LP}+$ and $I_{LP}-$ are nearly linear in P whereas $\rho_{LP}(P)$ changes rather weakly (between 30 and 40%). In this range the light excites mainly localised excitons, and the quantum yield of LP emission does not exceed 0.1%.

In the second range ($P = 150-200$ W/cm^2) the dependence $I_{LP} + (P)$ is replaced by the squared one, while $I_{LP} - (P)$ remains close to linear and hence ρ_{LP} starts increasing. In this region the most effective mechanism of filling of polariton states near $k = 0$ is direct two-photon scattering: $2\hbar\omega(k_{ex}) = E(k = 0) + E(k = 2k_{ex})$, which increases the quantum yield of the polariton emission at $k = 0$. A strong narrow line arising in the MC emission spectrum at the detection angles $\Phi = 30-34^\circ$ exactly corresponding to $k = 2k_{ex}$ is a direct proof of the process. Figure 1 shows as well that this line has the energy $\hbar\omega = 2\hbar\omega(k_{ex}) - E_{LP}(k = 0)$ and the same polarisation as the LP line at $k = 0$.

As the excitation density rises above 450 W/cm^2 the squared dependence of $I_{LP}+(k = 0)$ first changes to steep function close to the exponential one, and then saturates at $P >$ 650 W/cm^2. Since the increase in $I_{LP}-$ continues to be sublinear, the degree of circular polarisation of the LP line at $k = 0$ and $k = 2k_{ex}$ increases highly and approaches unity. The quantum yield of the emission at the $LP^+(k = 0)$ mode at $P = 1000$ W/cm^2 approaches

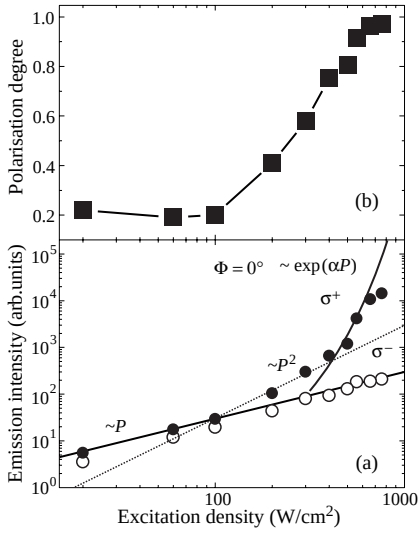

Fig. 3. (a) Dependence of σ^+ and σ^- emission intensity at $\Phi = 0^\circ$ on the density of σ^+ excitation into the LPB at $\Phi = 16^\circ$. (b) Degree of polarisation of polariton emission at $\Phi = 0^\circ$.

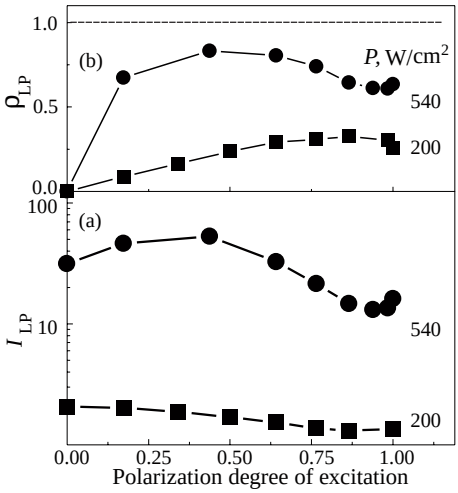

Fig. 4. Dependencies of degree of circular polarisation $\rho_{\rm LP}$ (b) and intensity of the LP line $I_{\rm LP} = I_{\rm LP^+} + I_{\rm LP^-}$ (a) on the degree of circular polarisation of the excitation at $P = 200$ and 540 W/cm^2.

10%.

The change from the squared dependence of $I_{\rm LP} + (P)$ to the near-exponential suggests the initiation of the stimulated two-photon scattering, and is related to the bosonic nature of polaritons. An additional argument in favour of the stimulated origin of the process is nearly 100% polarisation of the LP line at $k = 0$. The stimulated process develops at increased LP filling factors $\nu_{\rm LP}(k = 0)$. The exponential growth of $I_{\rm LP} + (k = 0)$ is caused not only by increased efficiency of the direct two-photon scattering shown in Fig. 1 but also by stimulated scattering of photoexcited localised excitons and polaritons with $k > 0$. Scattering of localised excitons occurs with emission of acoustic phonons and becomes effective at $\nu_{\rm LP}(E) > \nu_{\rm ph}(E)$, where $\nu_{\rm ph}(E)$ is the filling factor of the phonon mode at the energy E counted from the LPB bottom.

As seen from Fig. 1(b), under the excitation into the inflection point $k_{\rm inf}$ there is no way to obtain effective two-photon scattering into the LP states outside the range $0 < k < 2k_{\rm inf}$. However inside this range the scattering is possible for a wide range of k due to a small difference between $E_{\rm LP}(k)$ and $E^*(k) = 2\hbar\omega(k_{\rm inf}) - E_{\rm LP}(k)$. As a result, one can expect the LP emission under high excitation densities to depend not only on the energy but also on the k direction. Thereby we have measured LP emission spectra in a wide range of angles from -35 to $+35^\circ$. Experimental results are shown in Fig. 2(a) and (b). In the range of $k < 0$ the emission intensity decreases while the PL peaks width becomes broad with increasing $|k|$. In contrast, at positive k the LP line is very strong and relatively narrow in the whole range of $k < 2k_{\rm inf}$, especially at $k = 0$, $2k_{\rm inf}$, and near $k_{\rm inf}$.

So far we have discussed the behaviour of polaritons excited by circularly polarised light and found them to result in a well pronounced polariton-polariton scattering despite the absence of any absorption resonance near the two photon energy. Note, however, that $2\hbar\omega_{\rm ex}$ is close (lower by about 1 meV) to the energy of the ground biexciton state in the

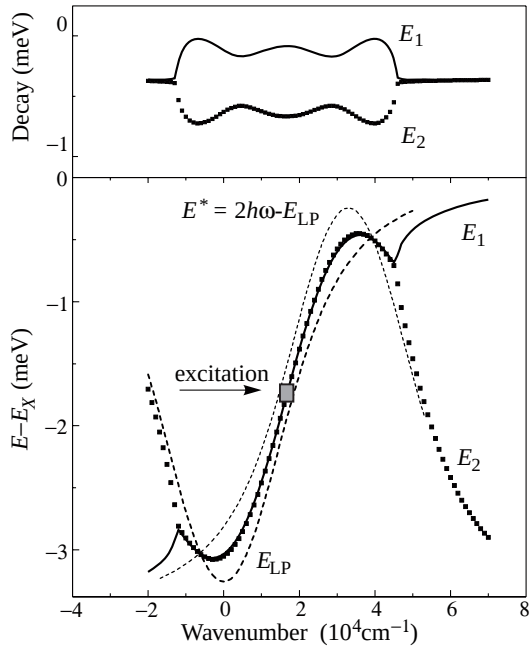

Fig. 5. Calculated dependences of the real (a) and imaginary parts (b) for the polariton modes in the highly excited MC. Dash lines show the dispersion of the modes $E_{\rm LP}$ and $E^*(k) = 2\hbar\omega - E_{\rm LP}(2k_{\rm ex} - k)$ in the weakly excited MC. The parameters used in the calculations are $\Omega = 6.3$ meV, $\Delta_{XC} = 0.09$ meV and the decay of exciton and cavity modes was taken as 0.3 meV, Renormalization of polariton energy due to exciton-exciton interaction is neglected.

quantum well. The biexciton state being a spin singlet is expected to result in an additional resonant contribution in the two-photon scattering only for not completely polarised light, the contribution being increased with decreasing degree of the circular polarisation of exciting light $\rho_{\rm ex}$ from 1 to 0. Thus, the two-photon scattering is expected to increase markedly with decreasing $\rho_{\rm ex}$.

Figure 5 displays the dependences of $\rho_{\rm LP}$ and total intensity of the LP line $I_{\rm LP} = I_{\rm LP}++I_{\rm LP}-$ on $\rho_{\rm ex}$ at two excitation densities. As seen, $I_{\rm LP}$ increases when the circularly polarised light is replaced by the linearly polarised one. At low excitation density (i.e. under the conditions of spontaneous two-photon scattering) the degree of circular polarisation of the LP emission at $k = 0$ $\rho_{\rm LP}(0)$ monotonically decreases with depolarization of the exciting light. In contrast, at high P the magnitude of $\rho_{\rm LP}$ first grows considerably up to $\rho_{\rm ex} \sim 0.6$ where it even exceeds the degree of polarisation of exciting light. Only at $\rho_{\rm ex} < 0.4$ the value $\rho_{\rm LP}$ decreases rapidly down to zero. Such a behaviour of $I_{\rm LP}$ and $\rho_{\rm LP}$ is an additional strong evidence in favour of (i) that the two- photon scattering process is highly enhanced due to the resonance of the two-photon energy to the biexciton one and (ii) that the process acquires the stimulated character at high P.

The experimental results can be partly explained using an interacting polariton model. The coupling between photon and exciton which give rise to the polaritons results in the repulsion of cavity and exciton modes whereas their imaginary parts become averaging. In MCs highly excited into the LP branch, the wave mixing results in the appearance of an additional branch $E^*(k)$ with the dispersion $E^*(k) = 2\hbar\omega - E_{\rm LP}(2k_{\rm ex} - k)$. Calculations

have shown that the coupling between the waves $E_{\mathrm{LP}}(k)$ and $E^*(k)$ is qualitatively different from that of exciton and photon. In case of the polariton formation the cavity mode transforms to exciton and vice versa, in case of four wave mixing the coupling occurs between pairs of the modes $E_{\mathrm{LP}}(k)$, $E_{\mathrm{LP}}(2k_{\mathrm{ex}}-k)$, and the two quanta of the pump. When the pump is strong enough the LP modes start to grow up. In the frequency domain it manifests in the attracting of the levels $E_{\mathrm{LP}}(k)$ and $E^*(k)$ whereas their imaginary parts repel with one of the level exhibiting gain (when the imaginary part of the mode energy becomes positive) and the other mode becoming overdamped. Figure 5 displays the calculated dependence of the real and imaginary parts for the "gain" mode in the MC highly excited under $\Phi = 14^\circ$. The figure shows that the calculated mode dispersion $ReE(k)$ is very similar to the experimental one. In a qualitative agreement with the experiment the calculations show as well the strong line narrowing in the whole range $0 < k < 2k_{\mathrm{ex}}$. However the more detailed comparison shows that the calculations predict the appearance of the gain first at the points of the crossing of $E^*(k)$ and $E_{\mathrm{LP}}(k)$ whereas the experiment shows that this occurs just at $k \sim 0$. It seems that exciton localisation effects as well as relaxation processes have to be taken into account in order to fit the experimental k-dependence of decay of the renormalized polariton mode. Thus, investigating angle resolved emission spectra of MCs with quantum wells embedded in the active layer we have found the conditions at which macroscopic filling is reached at the LPB bottom. Under these conditions we observed and studied strong nonlinear effects in the intensity and the degree of polarisation of polariton emission, and demonstrated that these nonlinearities occur in the strong coupling regime. The experimental dispersion of renormalized cavity mode and its strong narrowing have been explained using an interacting polariton model predicting that the coupling between the modes $E_{\mathrm{LP}}(k)$ and $E^*(k)$ is qualitatively different from that of exciton and photon.

Acknowledgements

We wish to thank M. Bayer, L. V. Keldysh, V. B. Timofeev and S. G. Tikhodeev for fruitful discussions. The work was supported by the RFBR and the Program 'Nanostructures'.

References

[1] C. Weisbush *et al.*, *Phys. Rev. Lett.* **69**, 3314 (1992).
[2] M. S. Skolnick, *et al.*, *Semicond. Sci. Technol.* **13**, 645 (1998).
[3] G. Khitrova, *et al.*, *Rev. Mod. Phys.* **71**, 1591 (1999).
[4] D. M. Whittaker *et al.*, *Phys. Rev. Lett.* **77**, 4792 (1996);
V. Savona *et al.*, *Phys. Rev. Lett.* **78**, 4470 (1997);
R. Houdre *et al.*, *Phys. Rev. Lett.* **73**, 2043 (1994).
[5] A. Imamoglu *et al.*, *Phys. Rev. A* **53**, 4250 (1996).
[6] S. Pau, *et al.*, *Phys. Rev. A* **54**, 1789 (1996).
[7] F. Tassone *et al.*, *Phys. Rev. B* **56**, 7554 (1997).
[8] A. I. Tartakovskii, *et al.*, *Phys.Rev. B* **61**, R2283 (2000).
[9] A. I. Tartakovskii, *et al.*, *Phys. Rev. B* **60**, R11293 (1999).
[10] P. N. Savvidis *et al.*, *Phys. Rev. Lett.* **84**, 1547 (2000);

9th Int. Symp. "Nanostructures: Physics and Technology"
St Petersburg, Russia, June 18–22, 2001

Development of 1300 nm GaAs-based microcavity light-emitting diodes

C. Möller, N. A. Maleev†, W. Passenberg, J. Böttcher, H. Künzel,
A. V. Sakharov†, A. E. Zhukov†, A. F. Tsatsul'nikov† and V. M. Ustinov†
Heinrich-Hertz-Institut für Nachrichtentechnik Berlin GmbH,
Einsteinufer 37, D-10587 Berlin, Germany
† Ioffe Institute, St Petersburg, Russia

Abstract. The present status of basic development steps towards AlGaAs/GaAs microcavity devices emitting at 1.3 μm is presented. An emission wavelength of the active medium of 1.3 μm was achieved by the implementation of self-organized InAs/GaInAs quantum dots. To match the wavelength tight control of the microcavity parameters was ensured by an improved layer thickness calibration procedure. Incorporation of a reverse-biased Si/Be-doped GaAs tunnel junction with record low junction resistance is expected to improve the lateral carrier distribution for intra-cavity contacted devices.

1. Introduction

An attractive way to fabricate vertical-cavity surface emitting lasers (VCSEL) and microcavity light-emitting diodes (MC-LED) for short-to-medium-haul fiber optical links is to combine Al(Ga)As/GaAs distributed Bragg reflectors (DBR) with a GaAs-based 1.3 μm emitting active medium in a single epitaxial growth run [1].

Self-organized In(Ga)As quantum dot (QD) heterostructures grown by molecular beam epitaxy (MBE) are promising candidates as an active region for GaAs-based 1.3 μm light emitting devices. Ground state emission at 1.3 μm was demonstrated using sub-monolayer deposition, low-rate growth, InGaAs barrier layers and InGaAs overgrowth [2].

For the successful growth of microcavity devices extremely precise control of the layer thicknesses is very crucial and thus requires extensive calibration procedures. We present a simple calibration technique for MBE systems which are not equipped with in-situ thickness control. In this contribution we demonstrate that QD microcavity devices for long-wavelength applications can be successfully grown using an optimised growth procedure of the active region combined with a relatively simple preliminary calibration technique.

2. MBE growth of multiple stacked InAs/InGaAs QDs

In this contribution we apply the MBE technique for the fabrication of Al(Ga)As/GaAs based microcavity structures which incorporate InAs/InGaAs QDs as active region. Recently, we have shown that improved MBE growth conditions for InAs QDs covered by InGaAs cladding layers allow the fabrication of structures which exhibit intense and narrow 300 K photoluminescence (PL) in the 1.3 μm wavelength range [3]. The most important advantages of this approach is that a QD density in each layer may be as high as $(3-5) \times 10^{10}$ cm^{-2}. To overcome the general problem of gain saturation, the QD planes may be successfully stacked by using relatively thick GaAs spacer layers (15–30 nm) without degradation of PL properties [4]. For samples with different numbers of QD planes the integrated PL efficiency at 300 K as a function of excitation power density (Ar^+ ion laser, 514.5 nm, 0.5–500 W/cm^2) was close to linear for all test samples. The onset of saturation of PL efficiency was observed only for the highest excitation power.

3. Layer thickness calibration

For MBE systems that are not equipped with in-situ thickness control we have developed a preliminary alternative calibration procedure for the layer thickness based on reference layers. A specific test structure for the DBR calibration consists of six pairs of AlGaAs/GaAs with a nominal layer thickness equal to one quarter of the operation wavelength ($\lambda/4n_i$, where n_i are the refractive indices of AlGaAs and GaAs) followed by the GaAs cavity of a nominal thickness of $\lambda/2n_i$. Two reflection spectra of each sample were measured consecutively, firstly the as-grown structure and secondly after selectively etching off the GaAs cavity layer and potentially one or several of the AlGaAs/GaAs DBR pairs. Comparing experimental and simulated reflection spectra delivers the individual real layer thicknesses. Thus, using this procedure only one test structure is necessary for growth rate calibration of GaAs and AlGaAs.

4. QD-based microcavity structures and MC-LEDs

The calibration procedure described was verified using several microcavity structures, containing also InAs/InGaAs QD active regions. As an example the experimental reflectivity spectrum for a structure containing a bottom 12-pair $Al_{0.85}Ga_{0.15}As$/GaAs DBR and a top GaAs(cavity layer)/air surface is presented in Fig. 1 and is labelled 'as grown'. Additionally depicted is a reflectivity spectrum measured after ion beam sputter-deposition of an additional 2-pair dielectric SiO_2/TiO_2 top mirror. The experimental 300 K PL spectra of both microcavity structures are additionally compared in Fig. 1 with a reference sample composed of the same active region without any optical resonator. The experimental reflection spectra and PL intensity ratios are close to the corresponding simulation results.

QD MC-LED samples were fabricated in intra-cavity contact geometry using proton implanted current apertures [4]. As shown in Fig. 2 the emission peaks of all devices investigated are centered in the projected wavelength range and exhibit a FWHM of approximately 13–26 nm depending on the active layer/top mirror parameters and have a circular output beam with a low divergence of less than 17° for the complete wavelength range and less than 10° for the resonant wavelength (angles measured at $1/e^2$ of the maximum intensity). The light output versus current characteristic is linear at low current values and saturates at current densities of about 100–200 A/cm^2. At 10 mA drive current the total top-side optical power emitted from a 40 μm diameter MC-LED was 5–7 μW. The corresponding power density is several times higher than previously published values [5].

5. Tunnel junctions in MCLEDs

High-quality tunnel junctions (TJ) open new possibilities for the design of MC-light sources, since they serve as an electron-hole converter. For intra-cavity contacted microcavity structures with oxidised current apertures, a tunnel junction (positioned at a node of the optical longitudinal field to minimise absorption) may be used as a high electron mobility layer to spread the carriers across the nearby aperture, ensuring improved lateral uniform current flow through the oxide-defined cavity.

The basic requirements for a TJ in a VCSEL are low resistivity, good thermal conductivity, temperature stability and long-term reliability.

To develop TJs, test samples were grown by MBE. The layer sequence consisted of a 400 nm low doped GaAs:Si buffer layer grown at 600°C on GaAs:Si substrate, followed by the tunnel region consisting of 100 nm n^{++} GaAs:Si and 100 nm p^{++} GaAs:Be, both layers homogenious doped and grown at reduced temperature (400°C). This reduces diffusion of

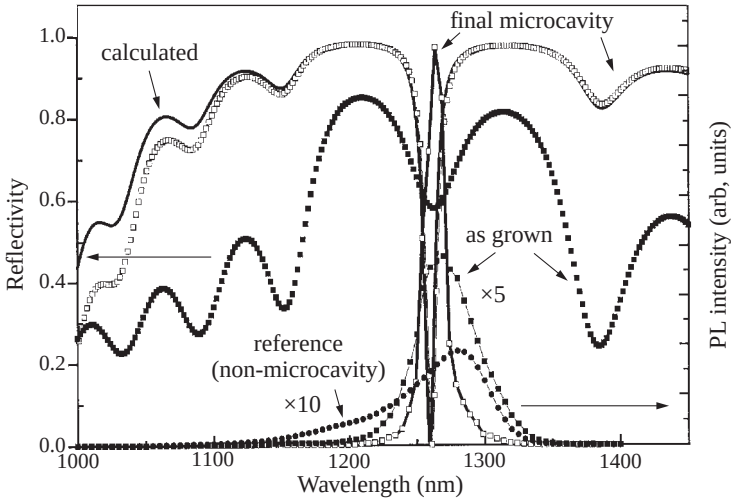

Fig. 1. Reflectivity and 300 K PL spectra taken at different stages during MC-LED layer deposition: as-grown MBE microcavity structure (black square) and after deposition of top SiO_2/TiO_2 DBR (square). For comparison, the 300 K PL spectrum of a reference active region without optical resonator (black circle) and the simulated reflectivity spectrum for the completed MC structure (solid line) are included.

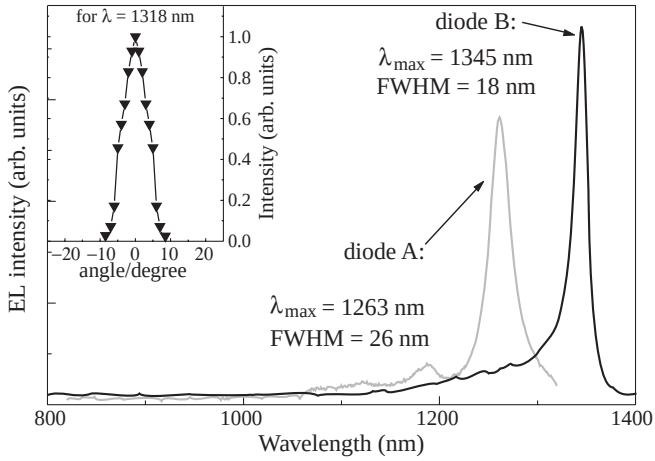

Fig. 2. 300 K CW-EL spectra of two 40 μm diameter MC-LEDs with InAs/InGaAs QD active layer emitting in the 1300 nm range (on-wafer measurement at a drive current of 10 mA). The insert shows a representative far field pattern for a mounted device (circular symmetry).

the dopants to achieve very abrupt junctions. The measured net carrier concentrations are 1.8×10^{19} cm^{-3} for silicon and 2×10^{20} cm^{-3} for beryllium. When the Si concentration is further increased, the dopant begins to substitute on the acceptor sites which results in self compensation, limiting practical net electron concentrations to 2×10^{19} cm^{-3}. On top we evaporated standard non-alloyed Ti/Pt/Au contacts, which we used as an etch mask to form 30×30 μm mesa. The back-side contact was fabricated by evaporating and alloying (400°C, 20 s) AuGe/Ni/Au.

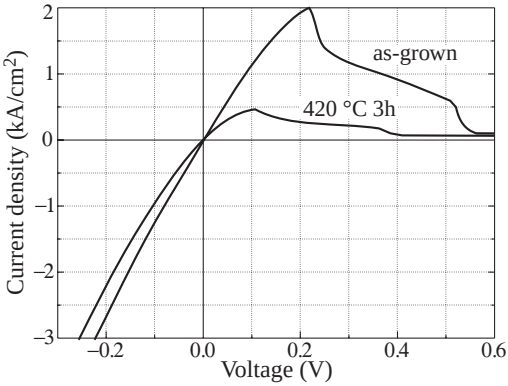

Fig. 3. Current-voltage characteristic of a 30×30 μm tunnel junction taken at room temperature, with and without tempering at 420°C for 3 hours.

The experimental I–V curves for the GaAs tunnel junction are shown in Fig. 3. The as-grown tunnel diode shows a zero-bias specific resistance of less than 7×10^{-5} W/cm^2, a peak current density of 1900 A/cm^2 and a peak-to-valley current ratio of ∼19:1. To the authors knowledge this is the highest peak current density and lowest specific resistance ever reported for a GaAs tunnel diode. The results are in good agreement with calculated values.

By heat treatment of the sample at 420°C for 3 hours we simulated oxidisation process. The decrease of the peak voltage and the peak-to-valley current ratio (∼6:1) is attributed to be directly related to the diffusion of the dopants. The junction is no longer abrupt, but the reverse current is still acceptably high. Under reverse-biased continuous current (cw) conditions both diodes are stable up to 15 kA/cm^2.

Summary

AlGaAs/GaAs microcavity structures incorporating self-organized InAs/InGaAs QD as active medium emitting at 1.3 μm were successfully grown by molecular beam epitaxy on GaAs substrates without the need to rely on any in-situ calibration technique. Fabricated intra-cavity contacted MC-LEDs demonstrate narrow electroluminescence spectra (FWHM $<$ 15 nm) accompanied by a circular output beam divergence of down to 10°. Thus, MBE-growth combined with intra-cavity design and top tunnel junction contact open new possibilities to design high-performance 1.3 μm microcavity light emitters.

Acknowledgements

Part of the work was sponsored by the Bundesministerium für Bildung und Forschung, BMBF, within the NanOp program, and by the Russian Foundation of Basic Research.

References

[1] *Vertical-Cavity Surface-Emitting Lasers*, Ed. C. W. Wilmsen, H. Temkin and L. A. Coldren, Cambridge Univ. Press, 1999.
[2] V. M. Ustinov and A. E. Zhukov, *Semicon. Sci. Technol.* **15**, R41 (2000).
[3] V. M. Ustinov, N. A. Maleev, A. E. Zhukov, et al., *Appl. Phys. Lett.* **74**, 1815 (1999).
[4] N. A. Maleev, A. V. Sakharov, C. Möller, et al., *J. Cryst. Growth*, accepted (2001).
[5] J. W. Gray, D. Childs, S. Malik, P. Siverns, C. Roberts, P. N. Stavrinou, M. Whitehead, R. Murray and G. Parry, *Electron. Lett.* **35**, 242 (1999).

9th Int. Symp. "Nanostructures: Physics and Technology"
St Petersburg, Russia, June 18–22, 2001

1.5 μm Fabry–Perot microcavities based on hydrogenated silicon and related materials

A. A. Dukin†, N. A. Feoktistov†, V. G. Golubev†, A. V. Medvedev†,
A. B. Pevtsov† and *A. V. Sel'kin*†‡
† Ioffe Physico-Technical Institute, RAS, 194021 St. Petersburg, Russia
‡ CIDS-ICBUAP, APDO. POSTAL 1651 Puebla, Pue, 72000, Mexico

Abstract. Fabry–Perot a-Si:H/a-Si:O:H microcavities with Er-doped a-Si:H active region were fabricated by plasma-enhanced chemical vapour deposition technique. A metalorganic compound was used to incorporate erbium into the active a-Si:H layer. The room temperature transmission, reflection and spontaneous emission spectra of the microcavities with 2 and 3 pairs of layers in distributed Bragg reflectors are measured. An intensity enhancement by two order of magnitude and selective narrowing of the 1.54 μm erbium emission line was observed as compared to the case of a single a-Si(Er):H film deposed on a quartz substrate. A theoretical analysis of the experimental data presented is given.

Introduction

Hydrogenated amorphous silicon doped with erbium, a-Si(Er):H, is known to exhibit at 1.54 μm (the wavelength of the $^4I_{13/2} \rightarrow {}^4I_{15/2}$ optical transition in Er^{3+}-ions) stronger room temperature photoluminescence (PL), smaller temperature quenching and shorter radiative lifetime of Er^{3+}-ions than its crystalline counterpart [1]. On the other hand, the 1.54 μm band coincides with the minimum-loss spectral range in optical-fiber-based telecommunications. For this reason, a-Si(Er):H can be considered as a promising optical material for optical communication systems, in particular, for amplifiers, light-emitting and lasing devices operating at 1.54 μm at room temperature. In our work, the transmission, reflection and emission characteristics of a-Si:H/a-Si:O:H Fabry-Perot microcavities (MCs) with a-Si(Er):H active region tuned around 1.54 μm are studied both experimentally and theoretically. Special emphasis is given to an analysis of the PL spectra. Preliminary results of our work were published in Ref. [2].

1. Results and discussion

Figure 1(a) shows schematically the layer sequence in the MC. The distributed Bragg reflectors (DBRs) and active layer of the MC were fabricated by plasma-enhanced chemical vapour deposition (PECVD) in a single technological cycle without exposure to air between the intermediate operations. The active a-Si:H layer was doped with Er during deposition by making use of the metalorganic fluorine containing compound [3]. The top (A) and bottom (B) DBRs consisted of three a-Si:H/a-Si:O:H quarter-wave layer pairs ($\lambda_1/4 \approx 110$ nm for a-Si:H and $\lambda_2/4 \approx 260$ nm for a-Si:O:H, the corresponding refractive indices at 1.54 μm are $n_1 = 3.46$ and $n_2 = 1.46$), the $\lambda_c/2$ a-Si(Er):H active region thickness being around 220 nm.

The transmittance spectrum of the MC is shown in Fig. 1(b). The long-wave cut-off of the spectrum is limited by sensitivity of InGaAs photodiode. A sharp 1.54 μm peak corresponds to a resonant mode of the MC.

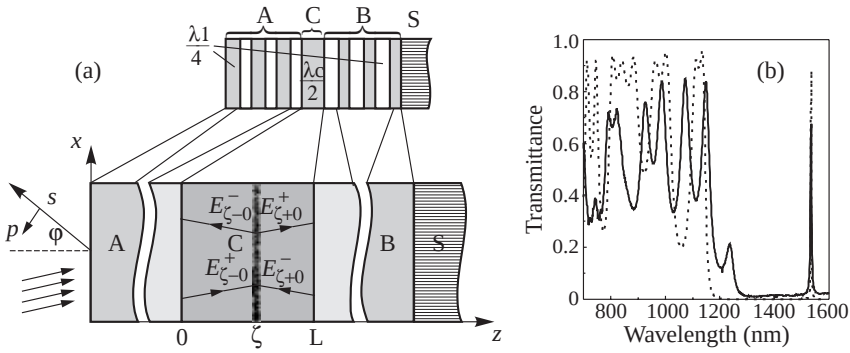

Fig. 1. (a) Schematic diagram of an a-Si:H/a-Si:O:H microcavity consisting of the A- and B-$\lambda/4$ DBRs with the $\lambda/2$ active layer C incide, S being the substrate. Also is shown an elementary emitting layer centered at z=ζ. (b) Experimental (solid) and theoretical (dashed) transmittance spectra of the microcavity structure shown in Fig. 1(a).

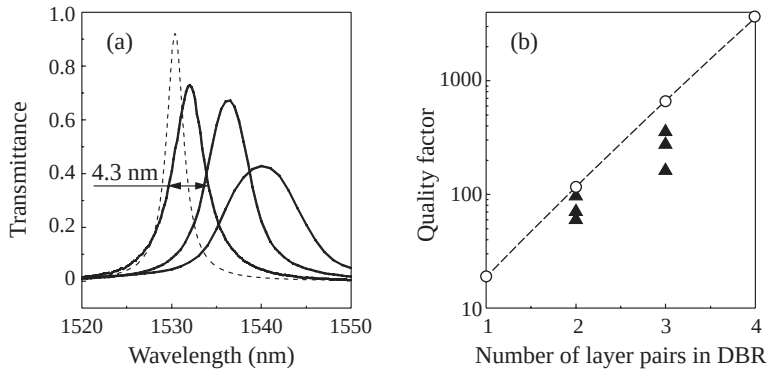

Fig. 2. (a) Experimental (solid) and theoretical (dashed) resonant contours for various microcavities with DBRs consisting of three pairs of layers. (b) Theoretical (circles) and experimental (triangles) values of the quality factor.

Figure 2(a) shows resonant transmission peaks for MCs with DBRs consisting of three pairs of layers. The full width at half maximum (FWHM) of the resonant peak as low as $\Delta\lambda$=4.3 nm is achieved. Corresponding cavity quality factor, $Q=\lambda_{res}/\Delta\lambda$, was estimated from the transmission resonance line width as 350. In Figure 2(b), a comparison of the experimental (triangles) and theoretical (circles) values of the Q for two types of MCs with DBRs consisting of 2 and 3 pairs of layers are given. The experimental values approach to the theoretical ones.

The theoretical spectrum of transmittance plotted in Fig. 2(a) as dashed line shows a difference as compared to measured ones. To our opinion, such a difference is due to deviations of the cavity thickness within the illuminated area.

Figure 3 shows the room temperature PL spectrum (curve 1) of the MC (Fig. 1(a)) measured for light propagation along the normal to the surface. For comparison, the PL spectrum (curve 2) of a 220 nm thick a-Si(Er):H film deposed on a quartz substrate (without DBRs) is plotted. The PL peak intensity in the MC structure is seen to be two

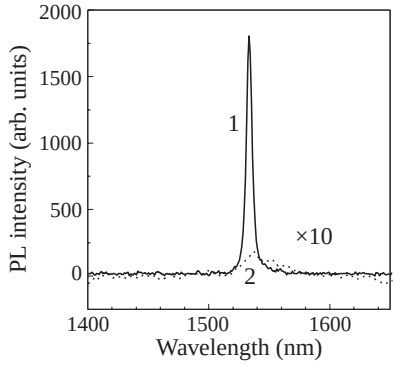

Fig. 3. Room temperature PL spectra: 1 — a-Si:H/a-Si:O:H microcavity structure; 2 — a-Si(Er):H single film without a cavity.

orders of magnitude higher, the PL line FWHM being reduced from 20 nm to 4.3 nm. The enhancement and narrowing of the PL peak are entirely due to the frequency of electronic transitions being resonant with the optical mode of the MC.

The emission problem was considered in terms of field amplitudes generated by stochastic excitation sources [4]. Figure 1*a* shows schematically the emission process from a MC structure. An elementary layer located at z=ζ inside the MC, $0<z<L$, emits two plane outgoing waves with the amplitudes $E^{-}_{\zeta-0}$ and $E^{+}_{\zeta+0}$ which are related to the amplitudes $E^{+}_{\zeta-0}$ and $E^{-}_{\zeta+0}$ of the incoming (reflected from the DBRs) waves by the boundary conditions. Direct solution of Maxwell's equations allows one to express field amplitudes at the outer boundary of the top DBR in terms of the induced singular polarization currents. After integrating bilinear combinations of the amplitudes over the thickness of the MC and statistical averaging the result over the ensemble of random-current realizations we obtain the following expression for the outer radiation intensity I in *p*-polarization of light:

$$I \propto I_0(\omega)\left|\frac{\tilde{t}_{AA}\Phi}{D\,\varepsilon\cos\varphi}\right|^2\left\{\left(|n_z|^2+n_x^2\right)\left(I_1+|r_B|^2\,I_2\right)+2\left(|n_z|^2-n_x^2\right)|r_B|\,I_3\right\} \qquad (1)$$

where $I_0(\omega)$ is the intrinsic spectral density of emission inside the infinite medium of the dielectric constant ε of the cavity, $D=1-\tilde{r}_A r_B\Phi^2$, $\Phi=\exp(ik_0 n_z L)$, $I_1=\left[\exp(\kappa L)-1\right]/\kappa$, $I_2=\left[1-\exp(-\kappa L)\right]/\kappa$, $I_3=\left[\sin(qL+\Delta_B)-\sin\Delta_B\right]/q$, $\Delta_B=\arg r_B$, $\kappa=2k_0\,\mathrm{Im}(n_z)$, $q=2k_0\,\mathrm{Re}(n_z)$, $k_0=\omega/c$; $\tilde{r}_A$ and r_B are the reflection coefficients on A- and B- DBRs, respectively, for light propagating from the inside of the cavity, $\tilde{t}_{AA}$ is the transmission coefficient for light passing through the A - DBR to outer medium, $n_z=\sqrt{\varepsilon-n_x^2}$, $n_x=\sqrt{\varepsilon_{\mathrm{v}}}\sin\varphi$; φ is the emission angle, ε_{v} is the dielectric constant of the outer medium.

The transmittance T for the whole structure can be written in the form

$$T=|t_{AA}t_{BB}\Phi/D|^2 \qquad (2)$$

where t_{AA} and t_{BB} are the transmission coefficients for the A- and B- DBRs, respectively, for the light incident from the left outer space. It should be noted that the above expressions for transmittance (2) and luminescence intensity (1) contain the same resonant denominator $|D|^2$ which mainly governs the spectral shape of both transmission and emission lines. The shapes of the PL and transmission spectra are found to be close to each other in agreement with our theoretical analysis.

2. Conclusions

In summary, by making use of the plasma-enhanced chemical vapour deposition technique we have fabricated a-Si:H/a-Si:O:H microcavities with Er-doped a-Si:H active region. A drastic enhancement of the erbium photoluminescence in a microcavity, by two orders of magnitude as compared to a single a-Si(Er):H film, was observed. The cavity quality factor as high as 350 was achieved in the microcavity with only 3 pairs of layers in distributed Bragg reflectors.

Acknowledgements

The work was supported by the network TIMOC under Grant ERB IC15 CT98 0819 and the RFBR under Grant 98-02-17350.

References

[1] M. S. Bresler, O. B. Gusev, V. Kh. Kudoyarova, A. N. Kuznetsov, P. E. Pak, E. I. Terukov, I. N. Yassievich, B. P. Zakharchenya, W. Fuhs and A. Sturm, *Appl. Phys. Lett.* **67**, 3599 (1995).

[2] A. A. Dukin, N. A. Feoktistov, V. G. Golubev, A. V. Medvedev, A. B. Pevtsov and A. V. Sel'kin, *Appl. Phys. Lett.* **77**, 3009 (2000).

[3] N. A. Feoktistov, V. G. Golubev, A. V. Medvedev and A. B. Pevtsov, *Amorphous and Microcrystalline Silicon Technology-1998, Mat. Res. Soc. Symp. Proc.* (Materials Research Society, Warrendale 1998) **507**, 255.

[4] V. G. Golubev, A. V. Medvedev, A. B. Pevtsov, A. V. Sel'kin and N. A. Feoktistov, *Phys. Solid State* **41**, 137 (1999).

9th Int. Symp. "Nanostructures: Physics and Technology"
St Petersburg, Russia, June 18–22, 2001

InGaAs resonant cavity light emitting diodes (RC LEDs)

J. Muszalski, T. Ochalski, E. Kowalczyk, A. Wojcik, H. Wrzesinska,
B. Mroziewicz and M. Bugajski
Institute of Electron Technology, Al. Lotników 32/46, 02 668 Warsaw, Poland

Abstract. We have developed technology of resonant-cavity light emitting diodes (RC LED) with very good emission characteristics. RC LED spectrum is determined mainly by the cavity resonance and is concentrated into a narrow line with 1.3 nm halfwidth. The directionality of RC LED emission depends on the tuning between QW emission and cavity resonance.

Introduction

In recent years a number of optoelectronic devices employing microcavity structures were proposed. Such devices benefit from utilization of specific effects resulting from placing the active structure inside the Fabry–Perot type microcavity. The most notable examples of such devices are Resonant Cavity Light Emitting Diodes (RC LED) realized in the early nineties [1]. The main advantages of resonant cavity LEDs over conventional devices are higher emission intensities, higher spectral purity and more directional emission patterns. In conventional LEDs it is difficult to achieve high quantum efficiencies. High difference between the refractive index of GaAs and the air results in low critical angle and extraction efficiency of the order of 2% for isotropic light source. On the other hand in RC LED external quantum efficiencies in excess of 20% have been reported [2]. All above mentioned features make RC LEDs attractive alternative for lasers in many applications.

1. RC LED design and technology

The RC LED cavity is constructed normal to the substrate plane by stacking multilayer films including an active region, spacer and two dielectric mirrors. Such a structure forms a one-dimensional Fabry–Perot cavity resonator. A dielectric mirror is formed with a periodic stack of quarter wavelength thick layers of alternating high and low refractive index material and is referred to as a distributed Bragg reflector (DBR). The active region consists of a spacer layer of the thickness equal to integer multiple of the half wavelength and of one or several quantum wells (QWs). The quantum wells are situated at the antinodes of the standing wave pattern. Such configuration of the microcavity offers possibility of controlling the spontaneous emission in the structure, and in particular allows for enhanced coupling of the spontaneous emission into the cavity mode [3, 4].

The optimisation of the microcavity requires proper tuning of the wavelength of radiation emitted from the active region, the peak reflectivity of the DBRs, and the cavity resonance. This is the reason why the structure performance is very sensitive to the variations in thickness of the layers and their composition. The wavelength of radiation from the QW depends on both the composition and thickness. The spectral shape of the reflectivity of DBRs in the case of GaAs/AlAs reflectors depends on the layer thickness in the mirrors. Similarly, the position of the cavity resonance depends on the thickness of the spacer layers between the mirrors and the QW region and the phase of the reflection from the mirrors. Thus, the optimum performance of the structure requires simultaneous alignment

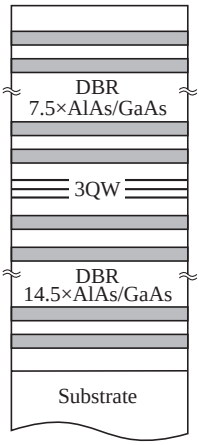

Fig. 1. Schematic RC LED structure with InGaAs 3 QW active region, designed for operation at 1000 nm.

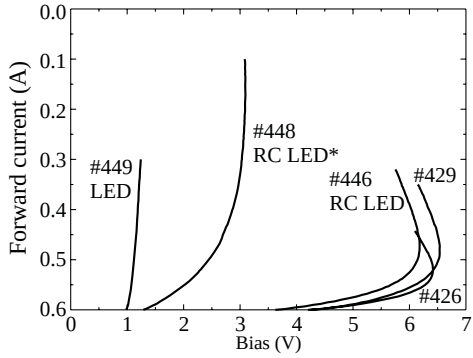

Fig. 2. I–V characteristics of RC LED structures with different DBR reflector design.

of all three features [5]. The goal in growing the mirrors for RC LED is to get the layers each approximately a quarter wavelength thick and to get the reflection band centered at the right wavelength range. The position of the cavity resonance determines the diode emission wavelength. The RC LED operation relays on enhanced spontaneous emission occuring in microcavity structures.

The RC LED structures studied in this work were fabricated by MBE. The schematic view of a typical structure is shown in Fig. 1. The active region consists of λ-type cavity with either 1 or 3 InGaAs QWs, each 80 Å thick, separated by 100 Å GaAs barriers. The devices were designed for the emission at $\lambda = 1000$ nm. The structure #426 is a high Q (quality factor) microcavity with single quantum well. The structures #446, #448 have lower number pairs of quarter-wavelength layers in the reflectors and consequently lower Q. They also have 3 QW active region. The structures #426, #446 have abrupt GaAs/AlAs interfaces in DBR reflectors, whereas in the case of the structure #448, 20 nm thick $Al_{0.5}Ga_{0.5}As$ layers were inserted in between GaAs and AlAs layers to lower DBR resistivity. The reference structure #449 of conventional LED without DBR reflectors has been grown for the sake of comparison. After MBE growth wafers were tested by photoluminescence mapping and reflectivity, in order to select material meeting device requirements before further processing.

The diodes were fabricated by conventional photolitography and metalization process. The light from the diode is extracted through the openings in the upper Cr-Pt contact. The bottom Au-Ge contact (to the n-type substrate) formed a solid circle. The diodes were electrically tested at probe tester and good ones were assembled in high frequency microwave type cases. Generally we have found very good correlation between the results of optical tests on as grown wafers and probe tests on final devices.

2. RC LED characteristics

The assembled diodes were subjected to electrical and optical tests. The I–V characteristics of the diodes are shown in Fig. 2. The series resistance of the diodes fabricated from

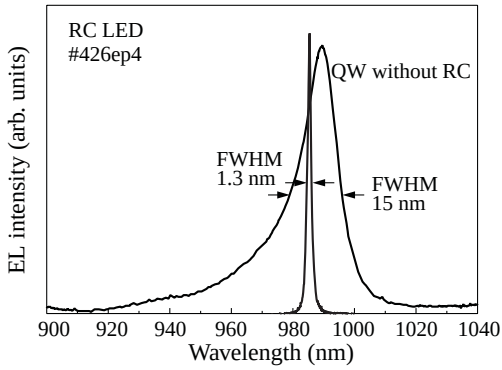

Fig. 3. Emission spectrum of RC LED compared to conventional LED.

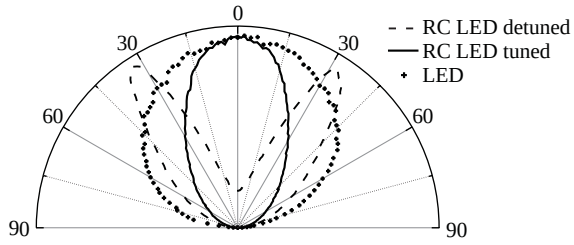

Fig. 4. Angular spectrum of RC LED compared to conventional LED.

wafer #448, although still higher than the one for reference diode without microcavity is acceptable. The diodes made of wafers #426, #446 with abrupt DBRs show up to 3 times higher resistance and roll-over of I–V characteristics due to the heating. We have found that DBR profile even stronger influences diode resistivity than does the number of pairs of the layers.

The emission properties of RC LED and conventional LED are shown in Fig. 3. In both cases the spectra have been collected from the small solid angle and sent by an optical fiber to the spectrometer. Comparing to classical LED the spectrum of RC LED is concentrated into a narrow line with 1.3 nm halfwidth. The shape of LED spectrum reflects thermal distribution of electrons and holes in the conduction and valence bands. On the other hand the RC LED spectrum is determined mainly by the cavity resonance; its width decreases with the increase of the cavity finess Q and the intensity increase reflects the on-axis cavity enhancement. The figure of merit of LED used in optical fiber communication systems is the photon flux density emitted from the diode at a given current, for a given wavelength. Since the optical power coupled into a fiber is directly proportional to the photon flux density the RC LEDs are particularly suitable for fiber link applications. The higher spectral purity of RC LED reduces also chromatic dispersion in optical fiber communications. Additional, favorable RC LED property is its emission characteristic directionality which depends on the tuning between QW emission and cavity resonance. The angular characteristics of RC LED emission for perfectly tuned and substantially detuned diodes are shown in Fig. 4. Also included is the angular characteristic of conventional LED. The frequency of the cavity resonance depends on the angle of observation, which means that emission line shifts to shorter wavelengths with increasing angle between the direction of observation and the normal to the surface. Nevertheless at any angle this is a narrow line in contrast to conventional LED. That is we have spectral concentration in all directions. The RC LEDs

can indeed be very bright. In principle the enhancement of the spontaneous emission inside the cavity and emission through one of the mirrors out of the cavity can be very different. For very high finesse cavities, which are typical for VCSELs the overall emission out of the cavity can decrease (in the limit of very high reflectivity $R = 100\%$ the emission out of the cavity becomes zero). At moderate values of the Q factor, which are characteristic for RC LEDs the spontaneous emission both inside and out of the cavity can be enhanced even by more than an order of magnitude [6].

3. Conclusions

We have demonstrated reproducible growth of microcavities and in particular we have developed technology of resonant-cavity light emitting diodes (RC LED) with very good emission charactristics. RC LEDs proved to be more tolerant to the epitaxial growth parameters and device fabrication procedures than VCSELs. As relatively robust devices they are less sensitive to typical for VCSEL manufacturing challenges and seem to have great potential for commercialization. The problems which are still to be solved, before the technology can be regarded as fully mature are wafer uniformity, yield and reliability of the devices. Nevertheless even at the moment there is no doubt that resonant cavity enhanced devices will have a profound impact on optoelectronic systems.

Acknowledgements

This work has been supported by the State Committee for Scientific Research (Poland) under Contract No. 8T11B 020 18. The authors would like to acknowledge collaboration of number of colleagues from the Institute of Electron Technology, who contributed to the research described in this paper: J. Kubica, P. Sajewicz, T. Piwonski, K. Goszczynski, A. Jachymek, M. Gorska, M. Nikodem, M. Szymanski.

References

[1] M. S. Unlu and S. Strite, *J. Appl. Phys.* **78**, 607 (1995).
[2] H. Benisty, H. De Neve and C. Weisbuch, *IEEE J. Quantum. Electron.* **34**, 1612 (1998).
[3] T. Baba, T. Hamano,F. Koyama and K. Iga, *IEEE J. Quantum. Electron.* **27**, 1347 (1991).
[4] T. J. Ochalski, J. Muszalski, M. Zbroszczyk, J. Kubica, K. Reginski, J. Katcki and M. Bugajski, *NATO Science Series, 3. High Technology, Optical Properties of Semiconductor Nanostructures, M. L. Sadowski et al. (eds.)* **81**, 201 (2000).
[5] K. Reginski, J. Muszalski, M. Bugajski, T. Ochalski, J. M. Kubica, M. Zbroszczyk, J. Katcki and J. Ratajczak, *Thin Solid Films* **367**, 290 (2000).
[6] N. Hunt, E. F. Schubert, R. A. Logan and G. J. Zydzik, *Appl. Phys. Lett.* **60**, 921 (1992).

9th Int. Symp. "Nanostructures: Physics and Technology"
St Petersburg, Russia, June 18–22, 2001

Polariton effect in a photonic crystal slab

A. L. Yablonskii†‡, E. A. Muljarov†, N. A. Gippius†, *S. G. Tikhodeev*†, Tohru Fujita§ and Teruya Ishihara‡

† General Physics Institute, Russian Academy of Sciences, 117942 Moscow, Russia
‡ Frontier Research System, RIKEN, Wako, Japan
§ Department of Physical Electronics, Hiroshima University, Higashi-Hiroshima,Japan

Abstract. We have investigated theoretically and experimentally the transmission of light through a photonic crystal of finite thickness, a distributed feed-back (DFB) microcavity with one dimensionally (1D) arranged semiconducting wires. To describe this system theoretically we have developed a numerical method, based on scattering matrix formalism, which takes into account the polaritonic effect via the exciton poles in dielectric susceptibility of the semiconducting wires. Theoretical results reproduce and explain the characteristic measured features of the transmission spectra such as anticrossing behavior of transmission dips in vicinity of the excitonic resonance and strong polarization dependence of their position and depth.

The optical properties of photonic crystals have been the subject of intensive studies during the past decade. As the next phase, it is interesting and meaningful to introduce an optically active semiconducting material into such systems to provide a strong interaction of excitons with Bloch-like photonic modes. This interaction can considerably change the optical response of the whole system, which opens a way for designing new high-performance optical devices such as ultralow-threshold lasers. Among the most well studied realizations of these periodic semiconductor structures we should point out so called Bragg superlattices, i.e., the systems of multiple quantum wells [1, 2, 3] or quantum wires [4] coupled via resonant photons.

In the present work we study the optical properties of another realization of such a system, namely, a distributed feedback (DFB) microcavity [5]. In this DFB microcavity a rectangular mesoscopic wires of self-organized PbI-based layered organic-inorganic semiconductor were arranged periodically on a quartz substrate. Owing to the effect of dielectric enhancement, the excitons in this material have large binding energies and oscillator strengths [6], which leads to a strong polaritonic effect.

The structure of the DFB microcavity is schematically shown in Fig. 1(a). The cavity consists of quartz grating substrate, semiconducting (active) layer, and polystyrene overcoating film. The grating was fabricated on a quartz substrate by means of the electron-beam lithography and dry etching techniques. Typical grating pitch (Λ), depth (h), line-to-space ratio, and area are, respectively, 0.7, 0.4 μm, 1:4, and 1.5×1.5 mm. The thickness of active and overcoating layers are estimated in our work as 18 nm and 50 nm, respectively. The active material used is $(C_6H_5C_2H_4NH_3)_2PbI_4$, [bis-(phenethylammonium) tetraiodoplumbate] (PEPI) which is one of the PbI_4-based layered perovskite-type semiconductors consisting of self-organized multiple-quantum-well structure with $[PbI_6]^{4-}$ layers as wells and organic alkylammonium layers as barriers. Excitons in the quantum wells are strongly enhanced due to a large difference in dielectric constants between the wells ($\varepsilon_{\text{well}} = 6.41$), and the barriers ($\varepsilon_{\text{bar}} = 2.34$). The exciton binding energy, oscillator

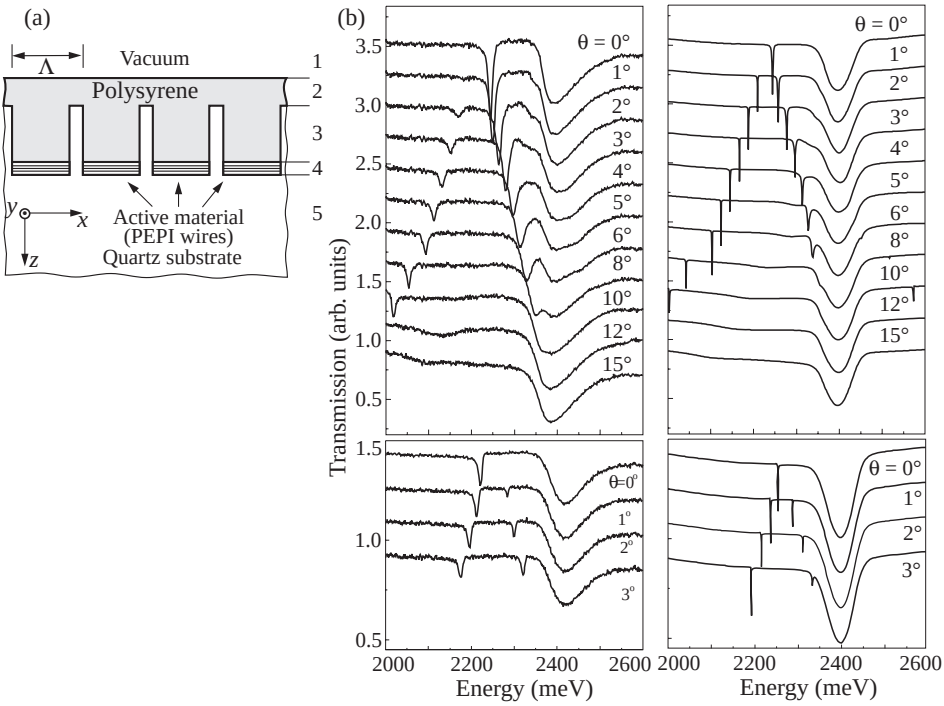

Fig. 1. (a) Schematic structure of DFB microcavity. (b) Measured (left) and calculated (right) transmission spectra of DFB microcavity for different incidence angles θ, in S- (top) and P-polarizations (bottom).

strength, and longitudinal-transverse (LT) splitting in PEPI are extremely large: 220 meV, 0.5 per formula unit, and 50 meV, respectively. Six gratings were made on a quartz substrate with grating pitch Λ_x ranging from 0.62 to 0.72 μm every 20 nm, so that it was possible to compare their transmission spectra under the same conditions. Transmitted intensity of a light through the sample was measured in Ref. [5] as a function of the photon energy for different gratings and for different angles of incidence.

The optics of infinite polaritonic crystal with full allowance for nonlocal effects has been recently studied in Ref. [7]. It turns out, however, that the main characteristic features of the optical response of DFB microcavities can be satisfactorily modeled within a local polariton response theory, because the wavelength of light is much larger than all characteristic exciton lengths. Much more important is to take into consideration the finite thickness of the polaritonic crystal, and to analyze the optical response of the system for arbitrary polarization and angle of incidence.

To describe the system theoretically we have built up a numerical scheme, which utilizes and develops approaches of Refs. [8] and [9]. The scheme was proved to work for arbitrary number of layers, arbitrary angle of incidence and polarization state of incoming light, the case of 2D patterning of DFB microcavity layers can be included as well. Moreover, we have focused our interest on polaritonic effects in transmission properties of periodic multilayer structure, which is principally new.

The theoretical procedure [10] can be divided into three logical steps.

(i) We split the whole structure into layers, either homogeneous or periodical in xy-plane, to define tensors of the dielectric susceptibilities in each layer. The model structure, shown on Fig. 1(a) consists of five layers with layers 3 and 4 periodically patterned.

(ii) We find a general solution of the Maxwell's equations in each layer. To do so, we use the plane waves decomposition of the electric and magnetic fields expanding it into Fourier series in x-direction (the axis of periodicity). The local piecewise-constant dielectric susceptibility is also Fourier transformed, and the most important point here is its frequency dependence which appears due to the inclusion of the exciton pole in semiconductor. Then the Maxwell's equation is converted into infinite-matrix eigenproblem for x, y-amplitudes of the electric field serving as an eigenvector and the z-projection of the wavevector as an eigenvalue. In numerical calculations the infinite matrix problem is trancated in a way to hold all important Fourier harmonics (Bragg reflections). The general solution becomes a superposition of these basic eigenvectors corresponding to along- and counter-propagating partial waves.

(iii) Using the Maxwell's boundary conditions we generate a transfer matrix, which connects the amplitudes of partial waves in different layers throughout the whole system, and then apply the scattering matrix formalism [9]. It's essential to note that the scattering matrix method allows us to avoid numerical instability caused by appearance of evanescent waves. Finally we calculate the coefficients of reflection, transmission, and absorption of the whole system.

The experimentally measured and calculated within our theoretical model transmission spectra of DFB structure with $\Lambda = 0.72\,\mu$m are shown in Fig. 1(b) (left and right panels, respectively), for S- and P-polarization (top and bottom, respectively) and different angle of incidence θ. A broad absorption band near 2.4 eV which is clearly seen in all plots of Fig. 1(b) corresponds to the lowest ($1S$) exciton transition in the PEPI material. Sharp dips to the left of the exciton-like mode are the DFB cavity modes. The lower (upper) line originates from the top of the fourth (bottom of the fifth) photonic band. In case of S-polarization the eigenmode of the fourth band appears to be anti-symmetric in the center of the first Brillouin zone (BZ), and the eigenmode of the fifth band appears to be symmetric. Vice versa, in case of P-polarization the eigenmode of the fourth band is symmetric in the center of the first BZ, and the eigenmode of the fifth band is anti-symmetric. Thus, for $\theta = 0$, which corresponds to the center of the first BZ, only the upper line is seen for S-polarization, and only the lower one is seen for P-polarization, because anti-symmetric modes do not interact with symmetric field of incoming light at normal incidence. When moving away from the center of Brillouin zone (θ increases), both the symmetric and anti-symmetric modes become visible and the upper lines show a strong polariton mixing with excitonic mode.

In conclusion, we have investigated the optical properties of 1D patterned distributed feedback microcavities with strong exciton-photon coupling. We have developed a theoretical model of calculation of the optical response of such a layered system for arbitrary geometry of the incident beam. This model quantitatively reproduces the experimental behaviour of the DFB microresonator transmission.

Acknowledgements

This work was supported in part by CREST, Japan Science and Technology Foundation Corporation, Grant-in-Aid for Scientific Research from the Ministry of Education, Science and Culture of Japan, Russian Foundation for Basic Research and Russian Ministry of Science program "Nanostructures".

References

[1] E. L. Ivchenko, *Sov. Phys. Solid State* **33**, 1344 (1991).
[2] E. L. Ivchenko, V. P. Kochereshko, A. V. Platonov, D. R. Yakovlev, A. Waag, W. Ossau and G. Landwehr, *Sov. Phys. Solid State* **39**, 1852 (1997).
[3] J. P. Prineas, C. Ell, E. S. Lee, G. Khitrova, H. M. Gibbs and S. W. Koch, *Phys. Rev. B* **61**, 13 863 (2000).
[4] E. L. Ivchenko and A. V. Kavokin, *Sov. Phys. Solid State* **34**, 968 (1992).
[5] T. Fujita, Y. Sato, T. Kuitani and T. Ishihara, *Phys. Rev. B* **57**, 12 428 (1998).
[6] E. A. Muljarov, S. G. Tikhodeev, N. A. Gippius and Teruya Ishihara, *Phys. Rev. B* **51**, 14 370 (1995).
[7] S. Nojima, *Phys. Rev. B* **59**, 5662 (1999).
[8] L. Pilozzi, A. D' Andrea and R. Del Sole, *Phys. Rev. B* **54**, 10 751 (1996).
[9] D. M. Whittaker and I. S. Culshaw, *Phys. Rev. B* **60**, 2610 (1999).
[10] A. L. Yablonskii, E. A. Muljarov, N. A. Gippius, S. G. Tikhodeev, T. Fujita and T. Ishihara, *J. Phys. Soc. Jpn* **70**, n.4 (2001).

9th Int. Symp. "Nanostructures: Physics and Technology"
St Petersburg, Russia, June 18–22, 2001

The coupling of zero-dimensional exciton and photon states: a quantum dot in a spherical microcavity

R. A. Abram†, S. Brand†, M. A. Kaliteevski¶, A. V. Kavokin#, V. V. Nikolaev‡, M. V. Maximov‡ and C. M. Sotomayor Torres§

‡ Ioffe Physico-Technical Institute, St Petersburg, Russia
† Department of Physics, University of Durham, South Road, Durham, UK
§ Institute Material Science, University of Wuppertal, Wuppertal, Germany
# Universite Blaise Pascal-Clermont-Ferrand II,63177 Aubiere Cedex, France
¶ Groupe d'Etude des Semiconducteurs, Université de Montpellier II CC074, Place Eugene Bataillon, 34095 Montpellier Cedex 05, France

Abstract. Exciton-light coupling in spherical microcavities containing a quantum dot has been treated by means of classical electrodynamics within the non-local dielectric response model. Typical anticrossing behavior of zero dimensional exciton–polariton modes has been obtained, as well as the weak coupling — strong coupling threshold.

Introduction

Since the first report of the strong coupling in quantum microcavities by Weisbuch et al [1], a huge number of papers devoted to exciton–polaritons in planar microcavities have appeared. Strong enhancement of the light-matter coupling strength in these structures has been demonstrated, both experimentally and theoretically. Recent progress [2] in photonic crystal fabrication gives hope that the four-decade long progression to lower dimensionality in exciton–polariton systems will soon achieve its logical conclusion with the appearance of a photonic dot with an embedded electronic quantum dot (QD). In particular, technological advances in the fabrication of spherical objects by the techniques of colloidal chemistry [3] will hopefully provide a means for the practical fabrication of multilayered structures of spherical symmetry in due course. A rigorous theoretical analysis of an ideal system that exhibits coupling of zero-dimensional photons and excitons seems timely. We consider a spherical QD embedded in a spherical microcavity (SMC), as shown in Fig. 1(a).

1. Basic equations

A spherical electromagnetic wave can be represented as a superposition of two waves with decoupled polarizations [4]: a TE wave with components H_r, E_θ, E_ϕ, H_θ, H_ϕ, and a TM wave with components E_r, E_θ, E_ϕ, H_θ, H_ϕ. The spatial dependence of the electric and magnetic fields in a spherical wave can be expressed in terms of spherical harmonics characterized by a positive integer l, and an integer m, in the interval from $-l$ to l, which are related to the angular orbital momentum and its projection.

Only in the case of TM mode with $l = 1$, is the electric field of the eigenmode not equal to zero at the centre of the SMC. The electric field of TM mode with $l = 1$, $m = 0$ near the centre of the SMC is spatially uniform and is directed along the z-axis, as illustrated in Fig. 1(b). Hence, only with this mode is there significant interaction with a (nonmagnetic) quantum dot placed at the centre of the microcavity. For all other cavity modes the electric

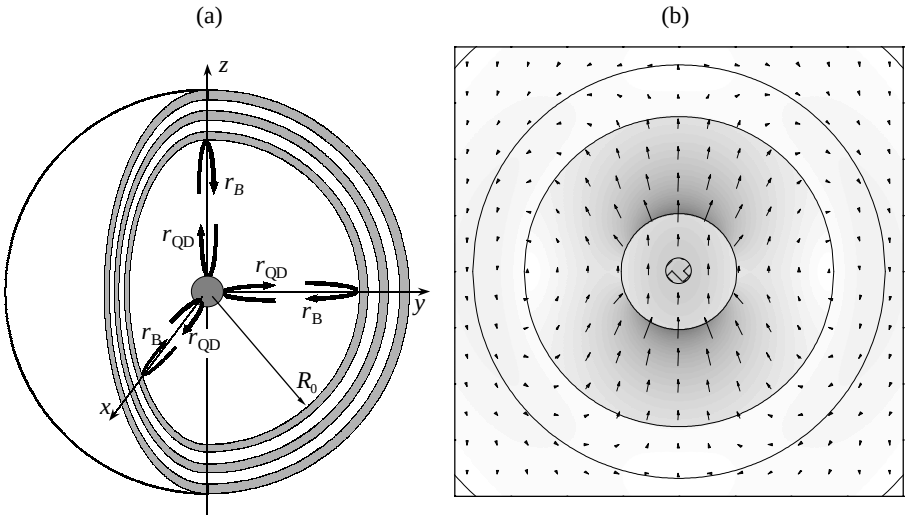

Fig. 1. (a) A schematic diagram of a spherical microcavity with a quantum dot at its centre. A central core of radius R_0 with the refractive index n_0 is surrounded by a spherical Bragg reflector, constructed from alternative layers of refractive indices n_1 and n_2. (b) The distribution of the electric field in a cross-section of the spherical microcavity for the TM mode with $l = 1$, $m = 0$.

field at the centre of the SMC vanishes, and there is negligible interaction with a QD placed there.

The electromagnetic field in the vicinity of a QD is described by Maxwell's equations with the excitonic contribution to the polarization $\vec{P}(\vec{r})$ taken into account:

$$\nabla \times \nabla \times \vec{E} - \varepsilon k_0^2 \vec{E} = 4\pi k_0^2 \vec{P}(\vec{r}). \tag{1}$$

where $k_0 = \omega/c$ and the polarization $\vec{P}(\vec{r})$ is coupled to the non-local excitonic susceptibility $\tilde{\chi}$ by $\vec{P}(\vec{r}) = \int \tilde{\chi}(\omega, \vec{r}, \vec{r'}) \vec{E}(\vec{r})\, d\vec{r'}$.

Further, using a Green function approach [5] we can obtain an amplitude reflection coefficient for the TM wave with $l = 1$ incident to the quantum dot in the form

$$r_{QD} = 1 + \frac{2i\Gamma_0}{\omega_{\text{ex}} - \omega - i\,(\Gamma + \Gamma_0)}. \tag{2}$$

where the radiative damping factor Γ_0 is defined by the geometry of the exciton wave function, transverse-longitudinal splitting and the excitonic Bohr radius.

Connecting the electromagnetic field near the quantun dot and at the boundary of the central core by the transfer matrix method we can obtain an equation for the frequencies of the eigenmodes of the SMC with an embedded quantum dot:

$$h_1^{(2)}(kR_0) = r_{BR} r_{QD} h_1^{(1)}(kR_0). \tag{3}$$

where $h_1^{(1,2)}$ are the spherical Bessel function. When the central core radius exceed the wavelength of the light the spherical function and the phase of the reflection coefficient of the Bragg reflector can be approximated by their asymptotic values [6] that allows us to rewrite equation (41) in the simplified form

$$(\omega - \omega_N)\,(\omega - \omega_{\text{ex}}) = (\Delta/2)^2 \tag{4}$$

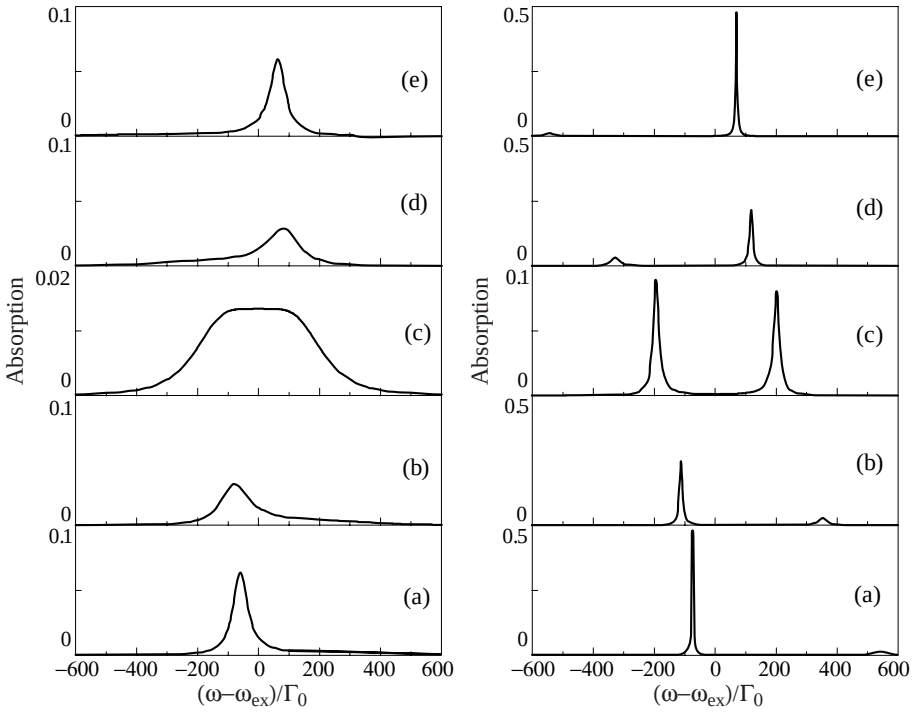

Fig. 2. Absorption spectra of a spherical microcavity with a 5-period thick Bragg reflector (weak coupling regime, left picture) and 7-period thick Bragg reflector (strong coupling regime, right picture) The five spectra relate to different values of the central core radius R_0; (a) $R_0\omega_{ex}/2\pi c = 0.10265$; (b) $R_0\omega_{ex}/2\pi c = 0.1028$; (c) $R_0\omega_{ex}/2\pi c = 0.102955$; (d) $R_0\omega_{ex}/2\pi c = 0.1031$; (e) $R_0\omega_{ex}/2\pi c = 0.10325$.

where the value of the Rabi splitting is $\Delta = 2\sqrt{2\Gamma_0\omega_b/\left(b + 2\frac{R_0}{c}\sqrt{\varepsilon}\omega_b\right)}$ and $b = \pi n_1 n_2/\sqrt{\varepsilon}(n_2 - n_1)$.

2. Results and discussions

The interaction between localized exciton and photon modes has two different regimes; namely the strong coupling regime that holds when the splitting of the modes exceeds the half-sum of their damping parameters, and two peaks can be distinguished in the absorption spectrum, and the weak coupling regime that holds when the half-sum of the damping parameters exceed the splitting and the two peaks in the absorption spectra merge into one. In the case of a realistic quantum well or quantum wire exciton, the non-radiative damping of the exciton is usually much larger than the radiative term. In contrast, due to a discrete energy spectrum, the non-radiative damping of a quantum dot exciton is very small, and comparable with the radiative damping [7]. Therefore the lifetime of the zero-dimensional polariton in this case is governed by the quality factor (Q-factor) of the spherical Bragg microcavity.

Figure 2 shows the absorption spectra, calculated using the transfer matrix method, of the two SMC with Bragg reflectors with thicknesses: 5-period (left picture) and 7 periods (right picture). The refractive index of the central core is 2.7 while the refractive indices

of the layers forming the Bragg reflector are 1.45 and 2.7 and correspond to the materials ZnTe and SiO_2, which are materials whose layers can be deposited by means of colloidal chemistry. The parameters of the QD are chosen to be similar to those for realistic QDs based on a II-VI semiconductor compound: $\Gamma_0 = 2 \times 10^{-6}\omega_{\text{ex}}$, $\Gamma = 10^{-6}\omega_{\text{ex}}$. For the the cavity with a 5 period Bragg relector the width of the cavity mode exceed the Rabi splitting Δ and the weak coupling occurs which manifests itself as the one peak in the absorption spectra (left). The shape of the peak in absorption becomes symmetric in the case of the precise tuning of the exciton and cavity modes. Increasing the thickness of the Bragg reflector we deacrease the width of the cavity mode and for the SMC with a 7-period Bragg reflector one can see the two separated peaks in the absorption spectra as it should be in the case of the strong coupling regime.

3. Conclusions

The interaction of zero-dimensional excitons and photons has been analyzed theoretically using the theory of non-local dielectric response and the transfer matrix method. Light absorption by a single quantum dot has been analyzed and it is shown that the resonant excitonic absorption of the $l = 1$ TM spherical wave incident on the quantum dot is total when the non-radiative and radiative damping factors of the exciton are equal. An equation for the eigenenergies and an expression for the value of the vacuum Rabi-splitting for the zero-dimensional polariton have also been obtained. Absorption spectra for a specific type of structure have been obtained and the transition between the strong and weak coupling regime has been illustrated.

References

[1] C. Weisbuch et al, *Phys. Rev. Lett.* **69**, 3314 (1992).
[2] L. C. Andreani, G. Panzarini and J. M. Gerard, *Phys. Rev. B* **60**, 13 276 (1999).
[3] M. V. Artemyev and U. Woggon, *Appl. Phys. Lett.* **76**(11) 1353-5 (2000).
[4] M. A. Kaliteevski et al., *Phys. Stat. Solidi A* **183**(1), 183–7 (2001).
[5] E. L. Ivchenko and A. V. Kavokin, *Sov. Phys. Solid State* **34**, 1815 (1992).
[6] M. A. Kaliteevski et al, *Phys. Rev. B* **61**(20), 13 791–7, (2000).
[7] M. Grundmann et al., *Phys. Rev. Lett.* **74**(20), 4043–6 (1995).

9th Int. Symp. "Nanostructures: Physics and Technology"
St Petersburg, Russia, June 18–22, 2001

Photonic crystals with tunable band gap based on infilled and inverted opal-silicon composites

V. G. Golubev†, *V. A. Kosobukin*†, D. A. Kurdyukov†, A. V. Medvedev†, A. B. Pevtsov†, S. M. Samoilovich‡ and L. M. Sorokin†
† Ioffe Physico-Technical Institute, St Petersburg, Russia
‡ Almaztechnocrystal Ltd., Aleksandrov, Russia

Abstract. Three-dimensional opal-Si composites with both direct (a variable extent of filling of opal voids with Si) and inverted structures have been synthesized. A structural analysis of these fabricated systems is performed. Reflectance spectra from the surface (111) of the composites are measured. Observed spectral features are interpreted as a manifestation of the direction [111] photonic band gap that is tunable in position and width in the visible and near-infrared spectral ranges.

Introduction

Photonic crystals are structures in which the dielectric constant is modulated with a period comparable to wavelength of light and a photonic band gap (PBG) occurs in the electromagnetic spectrum as a result of Bragg diffraction at the edge of Brillouin zone [1]. If there exist a complete PBG, light propagation is inhibited in any direction inside the crystal within the spectral range of the PBG. This effect is believed to be crucial for potential applications of photonic crystals in optical communication, laser physics and quantum computing.

Artificial opals are considered as promising materials with photonic-crystal properties. The opals have a structure with the fcc lattice formed by close-packed amorphous silica spheres with diameters 150 to 1000 nm. Voids between the spheres may occupy up to 26% of total volume. This allows to change the material parameter $\eta = \sqrt{\varepsilon_v/\varepsilon_s}$ by introducing various fillings into the voids. (Hereafter, ε_s and ε_v designate dielectric constants of bulk materials, respectively, inside and outside of the space that were occupied in bare opal by silica spheres, $\eta = \max\left(\sqrt{\varepsilon_v/\varepsilon_s}, \sqrt{\varepsilon_s/\varepsilon_v}\right)$ being referred to as optical contrast when ε_v and ε_s are real values [1]). According to a theoretical estimation the complete PBG may open up at $\eta \geq 2.8$ [2].

This work is aimed at synthesizing opal-Si composites with direct (infilled with Si) and inverted (SiO_2 spheres are removed from original opal-Si composite) opal structures and investigating their optical properties. This study is expected to conclude about the possibility of designing opal-Si composite based photonic crystals with a PBG whose position and width are tunable in a wide wavelength range, the tuning being provided by the variation of ε_v and ε_s. To verify these suggestions reflectance spectra from the synthesized composites were measured, and specific spectral features are found. Theoretically, the observed features were interpreted as a manifestation of the PBG for "one-dimensional" propagation of light waves in high-symmetry directions [111] of the periodic fcc dielectric structure.

1. Experimental

Opals with the sphere diameter of 230 nm are used as original matrices to synthesize opal-Si composites. Preliminary analysis by SEM shows that silica spheres are tangent (Fig. 1*a*).

Silicon was embedded in the opal voids by thermal decomposition of 5% SiH_4-Ar gas mixture [3]. This results in formation of uniformly thick silicon layer covering the surface of silica spheres (Fig. 1*b*). Developed technique allows us to change the fill factor of the opal voids by silicon gradually. The fill factor of the voids could be varied from 0 to 100% depending on deposition conditions. Thickness of a sample with 100% filling of voids reaches 0.4 mm. As-prepared samples are subjected to annealing at $T = 800^{\circ}$C and pressure 1 Torr in ambient atmosphere. SEM image of the inverted structure (the (111) surface) is shown in Fig. 1*c*. The inverted structure was obtained by etching out substance of an opal matrix (SiO_2) in an aqueous solution of HF. The samples selected for further investigations were about $5\times5\times0.4$ mm in size. For the inverted structures the ratio η is estimated to be approximately 3.5.

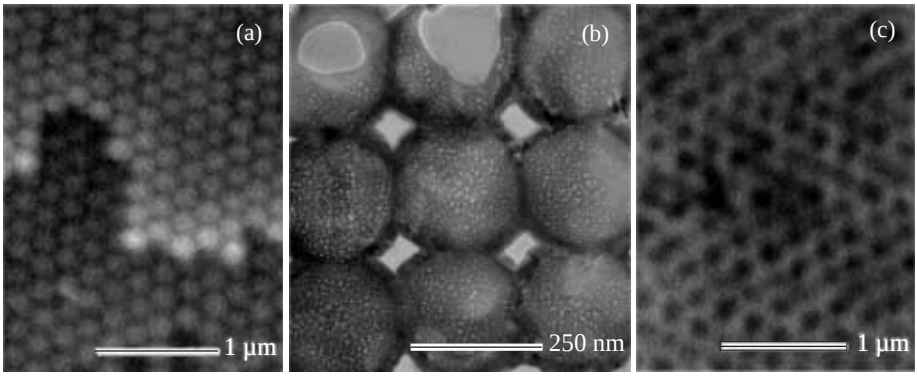

Fig. 1. SEM images of the (111) facet of bare opal (a), TEM image of the (100) plane of opal-Si composite (b), an inverted structure fabricated by selective etching out silica spheres from an opal-silicon composite (c).

2. Results and discussion

The problem of normal reflection of light from a photonic crystal may be considered as one-dimensional one based on the model of one-dimensional dielectric superlattice. Like in the light transmission problem [4], we describe the properties of opal-based structures using an "in-plane-averaged" dielectric constant

$$\varepsilon(z) = \varepsilon_s \cdot S(z) + \varepsilon_v \cdot [1 - S(z)].$$

Here, the coordinate z is measured along the normal vector to the (111) surface of a sample. Geometry of the structure is defined by the fcc lattice and the radius of spheres r. The function $S(z)$ is equal to the partial square belonging to the spheres in the cross-section with the coordinate z, therefore in our experiments $S(z)$ is periodic in the direction [111] with the period $d = r\sqrt{8/3}$. After calculating the function $S(z)$ for opal-based composites one-dimensional photonic bands as well as reflectance and transmittance spectra are calculated by transfer matrix technique within a model of periodically alternating ε-uniform layers [5].

Within the model [5] we have analyzed theoretically the effect of bulk refraction indices $\sqrt{\varepsilon_v}$ and $\sqrt{\varepsilon_s}$ on the reflectance spectra (Fig. 2*a*), the position and width of the stop bands (Fig. 2*b*). Used in these calculations are known complex values of silicon refraction index $\sqrt{\varepsilon_{Si}}$ taking into account optical dispersion and absorption. The refraction index $\sqrt{\varepsilon_s}$ of SiO_2 spheres was taken to be 1.37. Figure 2*b* presents theoretical estimations

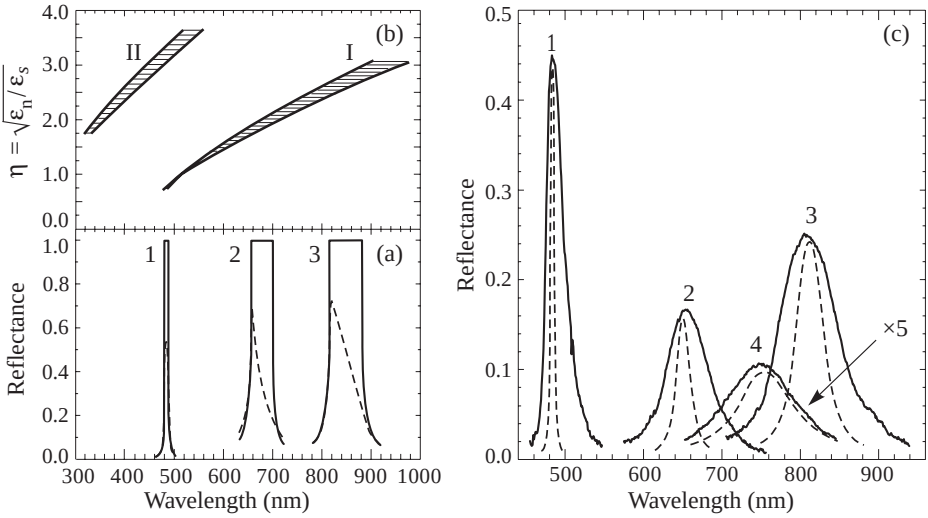

Fig. 2. Theoretical estimations of $\eta-$dependent (*a*) reflectance spectra from the (111) facet of opal-based composites at normal light incidence and (*b*) position and width of the two lower one-dimensional photonic band gaps (I and II). Solid curves are calculated in the absence of optical absorption, and dashed curves in making allowance for absorption. Curves 1 correspond to bare opal, 2 to opal partially filled with Si ($\sqrt{\varepsilon_{Si}}$=3.7), and 3 to opal completely filled with Si ($\sqrt{\varepsilon_{Si}}$=3.5). (*c*) Experimental (solid) and calculated (dashed) reflectance spectra at normal light incidence onto the (111) facet of various opaline composites specified in the text.

of one-dimensional stop bands. Widths and positions of the two lowest stop bands are shown as a function of η when optical absorption is neglected. Theoretical reflectance spectra corresponding to normal incidence of light onto the (111) surface (Fig. 2*a*) evidence existence of the stop bands (only data for the first stop band). Solid curves display total reflection resulted from existence of a stop band when optical absorption is neglected. In the presence of light absorption the shape of spectra changes, however, positions and widths of the spectral features stay approximately within the range of corresponding stop bands.

To verify the theoretical estimations we have measured the specular reflectance spectra from the (111) surface of synthesized composites. Additional light scattering resulted from the polydomain structure of opal samples was eliminated by applying optical microscope technique. Experimental reflectance spectra are shown by solid curves in Fig. 2*c* for the following samples: 1) bare opal, 2) opal partially filled with Si, 3) opal completely filled with Si, 4) silicon inverted opal. The spectra in Si-filled opals are found to shift to the long wavelength range and broaden as the parameter η increases. The observed peculiarities are confirmed by calculations (dashed curves in Fig. 2*c*) fitted to experimental data by small variation of the imaginary part of dielectric permittivity. This fitting procedure may be interpreted as introducing an extinction effect attributed to light scattering in the directions other than [111] inside the photonic crystal.

3. Conclusions

We have synthesized opal-Si composites with direct and inverse structure and studied, both experimentally and theoretically, their reflection spectra in a wide spectral range. Comparison of the experimental results with a theory, that predicts occurence of one-dimensional stop bands, has evidenced unambiguously that maxima in the observed reflection spectra are

due to Bragg diffraction of Bloch-type electromagnetic waves caused by one-dimensional periodic dielectric structure of investigated samples. Since the designed CVD technique enables us to control the fill factor of opal voids precisely it opens up an opportunity to create tunable Si-based photonic crystals with the prescribed position and width of the PBG.

Acknowledgements

This work was supported by the RFBR (Grant No 00-02-16924), the Russian R&D Program "Nanostructures" (Grant No 97-2016) and the Inco-Copernicus program (Grant "TIMOC" No ICI5 ST98 0819).

References

[1] *Photonic Band Gap Materials*, ed. by C. M. Soukoulis. Advanced Studies Institute of NATO, Ser. E, vol. 315 (Kluwer, Dordrecht, 1996).

[2] K. Bush and S. John, *Phys. Rev. E* **58**, 3896 (1998); A. Blanco, E. Chomski, S. Grabtcak, M. Ibisate, S. John, S. W. Leonard, C. Lopez, F. Mesequer, H. Miguez, J. P. Mondia, G. A. Ozin, O. Toader and H. M. van Driel, *Nature* **405**, 437 (2000).

[3] V. N. Bogomolov, V. G. Golubev, N. F. Kartenko, D. A. Kurdyukov, A. B. Pevtsov, A. V. Prokofiev, V. V. Ratnikov, N. A. Feoktistov, and N. V. Sharenkova, *Tech. Phys. Lett.* **24**, 326 (1998).

[4] Yu. A. Vlasov, V. N. Astratov, O. Z. Karimov, A. A. Kaplyanskii, V.N.Bogomolov and A.V.Prokofiev, *Phys. Rev. B* **55**, R13357 (1997); Yu. A. Vlasov, M. A. Kalitievskii and V. V. Nikolaev, *Phys. Rev. B* **60**, 1555 (1999).

[5] V. G. Golubev, V. A. Kosobukin, D. A. Kurdyukov, A. V. Medvedev and A. B. Pevtsov, *Semiconductors* **35**, (2001) (in press).

9th Int. Symp. "Nanostructures: Physics and Technology"
St Petersburg, Russia, June 18–22, 2001

Multiple polariton scattering in semiconductor microcavities

D. N. Krizhanovskii[1], A. I. Tartakovskii[2,1], V. D. Kulakovskii[1], M. S. Skolnick[2] and J. S. Roberts[3]

[1] Institute of Solid State Physics, Chernogolovka, 142432, Russia
[2] Department of Physics and Astronomy, University of Sheffield, Sheffield S3 7RH, UK
[3]Department of Electronic and Electrical Engineering, University of Sheffield, Sheffield S1 3JD, UK

In semiconductor microcavities (MCs) with embedded quantum wells a strong two-dimensional (2D) confinement of light makes accessible very high densities of photonic field which may result in the realization of a new type of nonlinear effects. Another intriguing property is connected to the boson nature of the mixed exciton–photon states in MCs, 2D polaritons. Due to a very small in-plane mass the density of polariton states is strongly reduced relative to that of excitons. This makes it possible to achieve high filling factors of the polariton states, which in turn may lead to the stimulation of scattering processes. Indeed, recent studies demonstrated that scattering involving two polaritons photocreated with particular momentum k to final states with $2k$ and $k = 0$ is stimulated above a particular threshold density by a high population of the $k = 0$ polaritons [1]. Theory predicts that as a result of polariton–polariton interaction the low polariton (LP) dispersion curve shifts to higher energy [2]. Both the magnitude of such shift and the threshold density for occurrence of polariton–polariton scattering is proportional to LP homogeneous linewidth γ.

Here we present the detailed investigations of the LP properties in the regime of polariton–polariton scattering in a wide range of temperature 2 K $< T <$ 30 K. Firstly, it was observed that both the amplitude of renormalisation of polariton energy and threshold density increase with growing temperature, which is accompanied by increasing of γ. The changes of γ is assumed to be connected to free excitons the density of which increases with T. Such growth of high k exciton population should lead to a significant polariton–exciton interaction and, consequently, larger γ.

Most surprisingly in addition to previous observations of strong nonlinearities in polariton emission at $k = 0$ (energy E_S) and $2k$ (E_I) at resonant excitation at k (E_L) we have also observed a novel feature in the emission pattern at $3k$. The linewidth (0.1 meV) and polarization degree (> 0.95) of the new peak is very similar to those of the peaks at $k = 0$ and $2k$. The energy of this line (E_M) with very high accuracy satisfies the condition for higher order polariton scattering process (in which k-vector is also conserved), namely, $3E_L = 2E_S + E_M$. Also it satisfies the condition $2E_I = E_L + E_M$. We thus clearly demonstrate that the higher order multiple polariton scattering processes should be taken into account for full description of the observed nonlinearities.

References

[1] A. I. Taratkovskii et al., *Phys. Rev. B* **62**, R13298 (2000).
[2] Ciuti et al., *Phys. Rev. B* **62**, R4825 (2000).

9th Int. Symp. "Nanostructures: Physics and Technology"
St Petersburg, Russia, June 18–22, 2001

Guided plasmon–polaritons in a planar Bragg microresonator with two-dimesional electron system

V. V. Popov, G. M. Tsymbalov and T. V. Teperik
Institute of Radio Engineering and Electronics (Saratov Division),
RAS, 410019 Saratov, Russia

Abstract. We present the results of theoretical investigation of the plasmon–polaritons formed due to the interaction of two-dimensional plasmons in a planar Bragg microresonator with guided modes of dielectric substrate slab. A conclusion is made that guided plasmon–polaritons may be taken up for the development of controllable guided wave THz frequency filters and modulators.

Introduction

Recently, the interaction of dipole electron excitations in two-dimensional (2D) electron systems with electromagnetic (EM) cavity modes have been extensively studied. Particularly, the exciton–phonon coupling in cavity-embedded quantum wells has received the bulk of attention. The exciton–phonon coupling results in the anticrossing between excitonic states and the resonator confined photon modes which gives birth to the cavity-polaritons [1–4]. The cited papers are devoted to radiative exciton–polaritons. Radiative exciton–polariton dispersion has been measured from angle-resolved photoluminescence experiments [3, 4].

Plasma oscillations in 2D electron systems (2D plasmons) are nonradiative electron dipole excitations [5]. Hence they can not couple to EM radiation through one-phonon absorption or emission processes. To couple 2D plasmons to EM wave a lateral diffraction grating with periodicity $L \ll \lambda$, where λ is the EM wavelength, is formed on the top surface of the structure [5]. The grating couples transverse EM wave to longitudinal plasma oscillations with in-plane wavevectors $k_{\|} = 2\pi m/L$ ($m = 1, 2, 3\ldots$). In fact, such a grating makes up an open Bragg resonator for 2D plasma oscillations. The theory of EM emission from 2D plasmons in semiconductor heterostructure with planar metal grating was developed in [6–8].

In a plane-parallel dielectric substrate slab the EM field confinement takes place for guided modes with in-plane wavevectors from the interval $\omega/c < k_{\|} < \omega\sqrt{\varepsilon_s}/c$, where c is the light velocity, ω is the angular frequency of EM wave, ε_s is the dielectric constant of the substrate medium. In this paper we present a theoretical investigation of the polaritons formed due to the interaction of 2D plasmons in a planar Bragg resonator with EM guided modes of dielectric substrate slab.

1. Guided plasmon–polariton dispersion

The structure under consideration involves a plane-parallel dielectric slab of thickness d (semi-insulating GaAs in actual semiconductor heterostructures) with 2D electron system on one of its faces. Planar grating with periodicity L consists of perfectly conducting strips of width w and it is separated from 2D electron system by dielectric interlayer of thickness δ

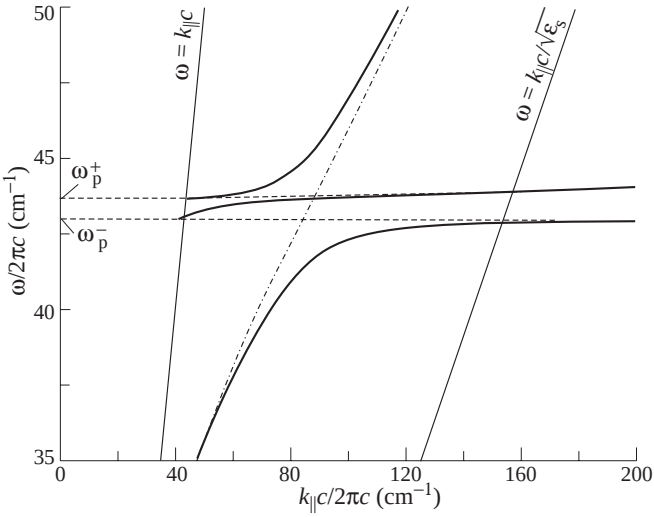

Fig. 1. Guided plasmon-polariton dispersion in the structure with parameters $N_{2D} = 6.7 \times 10^{11}$ cm^{-2}, $\varepsilon_s = 12.8$, $d = 3.5 \times 10^{-3}$ cm, $\delta = 8 \times 10^{-6}$ cm, $L = 8.7 \times 10^{-5}$ cm, and $w/L = 0.9$ in the case of $1/\tau = 0$.

(wide band gap semiconductor AlGaAs). The in-plane wavevector of polariton excitations studied in this paper is aligned with the direction of the grating periodicity.

The theoretical results given below are obtained through a straightforward extension of our previously published theory [8] to the case of finite thickness of the structure substrate. Similarly to [6–8], 2D electron plasma is described by the areal conductivity σ_{2D} in a local approximation (the Drude model) with the areal density of electrons N_{2D} and a phenomenological electron relaxation time τ. The parameters used in the calculations are typical of that for 2D electron systems in GaAs/AlGaAs heterostructures. We assume that the substrate dielectric constant ε_s is equal to that of the interlayer.

Figure 1 shows the region of interaction of the fundamental (lowest in the frequency) 2D plasma oscillations with the fundamental EM guided TM-mode of the dielectric substrate slab for the case where there is no electron scattering in the 2D system ($1/\tau = 0$). Dispersion of the fundamental TM-mode is given in Fig. 1 by dash-dotted line. Dashed lines in Fig. 1 mark dispersions of the fundamental 2D plasma eigen-oscillations in a planar Bragg resonator on a semi-infinite substrate. It is known [8] that 2D plasma eigen-oscillations with wavevector $k_{\|} = 0$, which corresponds to the center of the first Brillouin zone in the reduced band scheme of the Bragg resonator, split up into doublets. One mode in a doublet is radiative while the other is nonradiative. The frequencies of the fundamental nonradiative and rediative modes are denoted in Fig. 1 as ω_p^+ and ω_p^- respectively. The electric fields of different plasma oscillations in the doublet have symmetry of different parities in relation to the centers of the grating slits. The nonradiative mode possesses nodes of the longitudinal electric field at the centers of the grating slits while the radiative one exhibits antinodes of that there.

For $k_{\|} \neq 0$ a plasmon electric field amplitude distribution does not possess the symmetry with a definite parity in relation to the centers of the grating slits. Therefore, strictly speaking, the both plasma oscillations in the doublet experience radiative damping when their wavevector values fall into the interval $0 < k_{\|} < \omega/c$. However, the radiative

damping of "nonradiative" mode remains several orders of magnitude weaker than that of the "radiative" one since the inequality $\omega/c \ll 2\pi/L$ (i.e. $L \ll \lambda$) is fulfilled. For the same reason, the plasma modes practically conserve definite parities of the symmetry of the electric field amplitude distributions in the interval of $k_\parallel$ shown in Fig. 1.

All modes become nonradiative in the region of the dispersion plane to the right from the light line $\omega = k_\parallel c$ in Fig. 1. In the sector between the light lines $\omega = k_\parallel c$ and $\omega = k_\parallel c/\sqrt{\varepsilon_s}$, the confinement of polariton fields in the transverse direction arises from the total internal reflection of EM wave in the plane-parallel dielectric substrate slab. The electric fields of the guided modes decay with distance from the structure faces whereas inside the substrate a transverse standing wave is formed. When $k_\parallel > \omega\sqrt{\varepsilon_s}/c$, there are only nonradiative 2D plasma oscillations with the electric fields decaying from 2D electron system survive in the structure.

One can see from Fig. 1 that well away from the interaction region the polariton dispersion merges into the dispersion of an uncoupled plasma or EM mode. In the interaction region the EM guided mode demonstrates the anticrossing with the plasmon doublet. As the wavevector increases the lowermost polariton mode transforms from photonlike mode into plasmonlike one. On the contrary, the uppermost polariton mode transforms from plasmonlike mode into photonlike one. The third mode retains its plasmon character at any wavevector value. But the parity of symmetry of the electric field distribution for this mode is reversed with increasing $k_\parallel$.

2. Guided plasmon–polariton resonance

Dispersion and attenuation of guided plasmon–polaritons in the vicinity of the fundamental plasmon doublet at finite electron relaxation in 2D system are shown in Fig. 2 which represent a typical single-resonance behaviour of the system with a full width at half maximum of the attenuation resonance curves of $\Delta\omega = 1/\tau$ in spite of the fact that there

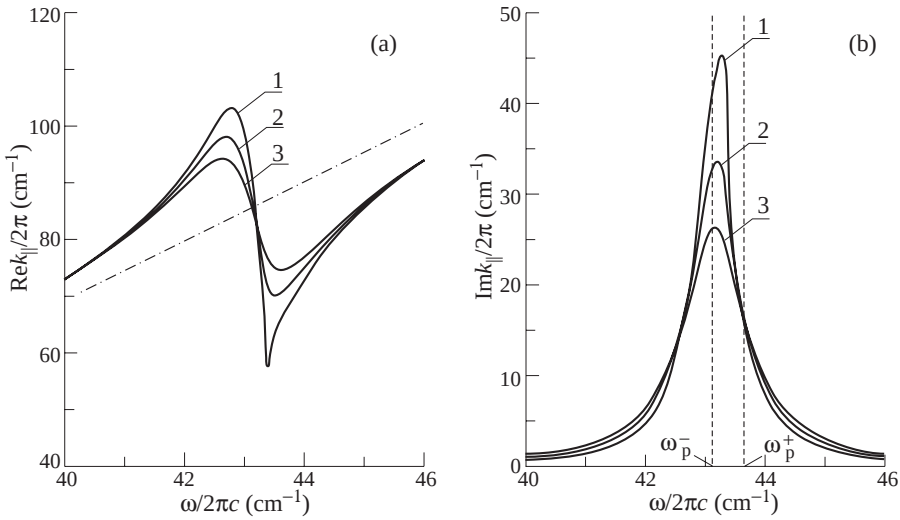

Fig. 2. Dispersion (a) and attenuation (b) of guided plasmon–polaritons for various values of 2D electron relaxation time $\tau = 6.5$ (10^{-12} s) (curves 1), $\tau = 5$ (curves 2) and $\tau = 4$ (curves 3). The other parameters of the structure are the same as in Fig. 1. Dashed-dotted line in Fig. 2(a) marks the dispersion of the fundamental TM-mode of the substrate slab.

are two plasmon eigen-modes with different frequencies in the plasmon doublet. The point here is that the upper plasmon mode in the doublet does not virtually couple to a long-wavelength EM substrate quided mode due to its peculiar electric field distribution parity mentioned above. Hence this mode does not essentially affect the plasmon–polariton resonance curve shape.

The frequency of the fundamental guided plasmon–polariton resonance practically coincides with the frequency ω_p^- of the lower fundamental 2D plasmon mode in the doublet. Clearly this frequency varies with the areal electron density in the 2D system. Culculations show that guided plasmon–polariton attenuation at the resonance may be as great as 50 dB/λ while it is under 0.5 dB/λ away from the resonance. This offers possibilities for the development of controllable guided wave THz frequency filters and modulators.

Acknowledgements

This work was supported by the Russian Foundation for Basic Research through grant 00-02-16440.

References

[1] V. Savona, Z. Hradil, A. Quattropani and P. Schwendimann, *Phys. Rev. B* **49**, 8774 (1994).
[2] S. Jorda, *Phys. Rev. B* **51**, 10185 (1995).
[3] R. Houdre, J. L. Gibernon, P. Pelladini et al., *Phys. Rev. B* **52**, 7810 (1995).
[4] A. I. Tartakovskii, V. D. Kulakovskii, A. Forchel and J. P. Reithmaier, *Phys. Rev. B* **57**, 6807 (1998).
[5] A. V. Chaplik, *Surface Sci. Rep.* **5**, 289 (1985).
[6] O. R. Matov, O. V. Polischuk and V. V. Popov, *Pis'ma v Zh. Tekh. Fiz.* **18**, No.16, 86 (1992) [*Sov. Tech. Phys. Lett.* **18**, 646].
[7] C. D. Ager, R. J. Wilkinson and H. P. Hughes, *J. Appl. Phys.* **71** 1322 (1992).
[8] O. R. Matov, O. V. Polischuk and V. V. Popov, *Int. J. Infrared and Millimeter Waves* **14**, 1445 (1993).

9th Int. Symp. "Nanostructures: Physics and Technology"
St Petersburg, Russia, June 18–22, 2001

Comparison of dye photoluminescence spectra in direct and inverted opaline films

S. G. Romanov[1,2], T. Maka[2], C. M. Sotomayor Torres[2],
M. Müller[3] and R. Zentel[3]

[1] Ioffe Physico-Technical Institute, St Petersburg, Russia
[2] Institute of Materials Science and Dept. of Electrical & Information Engineering, University of Wuppertal, Gauss-str. 20, 42097 Wuppertal, Germany
[3] Institute for Organic Chemistry, Department of Chemistry and Pharmacy University of Mainz, Duesbergweg 10-14, 55099 Mainz, Germany

Abstract. Changes introduced by a photonic bandgap environment in an emission spectrum of a light source have been compared for direct and inverted opals and a qualitative difference has been revealed.

Introduction

3-dimensional light emitting photonic bandgap (PBG) structures are periodical spatial ensembles of scatterers integrated with light sources, moreover the emission band of the latter has to be tuned with the PBG frequency range in order to realise the emission-to-structure feedback. Studied so far 3-dimensional photonic crystal light sources for the visible are based on opals. The closest approach to the complete PBG has been achieved with TiO_2 (refractive index (RI) contrast up to 2.7 to 1) [1] and SnS_2 (RI contrast up to 3.4 to 1) inverted opals [2]. These structures are incomplete due to an insufficient volume fraction of the dielectric, which is 10–13 vol.% instead of $\sim$30% necessary for maximising the gap. Nevertheless, the scattering strength of these opaline structures is high enough to provide the strong interaction between the emitter and the emitted photon and thus to alter parameters of the spontaneous emission. In what follows we discuss the qualitative difference between emission spectra of organic dyes embedded in direct opal and in its SnS_2 replica.

1. Experimental details

Opaline films have been used in this work as those advance structurally over bulky opals [3]. PMMA opaline films were formed from beads possessing a small amount of fluorescent dye (Coumarin 6) [4] by casting the bead suspension on hydrophilized microscope slides. These thin film polymeric crystals consist of ca. 30–50 monolayers and possess domains extending over 100 s of micrometers. Dye molecules are distributed homogeneously in beads. The RI contrast as 1.5 to 1 and the filling fraction of 74% are characteristics of this photonic crystal. These films were used as templates to prepare inverted opals by synthesising SnS_2 in interstitials and subsequent dissolving of PMMA beads. As a light source the Perylene dye deposited on the inner surface of the inverted opal was used. The effective RI contrast in studied samples was about 2.1 to 1 and the SnS_2 filling fraction was about 13%. The plain Coumarin-loaded PMMA film and the unstructured SnS_2 film with Perylene coating, both on glass substrates, have been prepared as reference samples.

Photoluminescence (PL) spectra of Coumarin/PMMA opaline films have been collected within the $\sim 5^\circ$ fraction of the solid angle along the direction of the stop-band appearance.

The emission intensity of Coumarin in the opal is suppressed in the stop-band frequency range as compared with the reference sample (Fig. 1(a)). To demonstrate the relative changes in the number of photonic states in the PBG region, PL spectra are shown normalised to the PL spectrum on unstructured Coumarin-PMMA film (Fig. 1(c)). Stop-bands obtained from the emission are compared with transmission spectra of the PMMA opaline film (Fig. 1(b)). The stop-band related minimum appears at the same frequency and shows the similar depth in both transmission and emission spectra, moreover, the similarity of their angular dispersions is obvious.

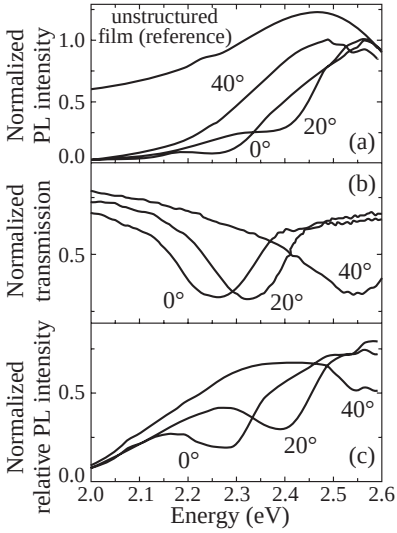

Fig. 1. Angle resolved PL spectra (panel a), transmission spectra (b) and relative PL spectra (c) of Coumarun/PMMA opaline film for angles of 0, 20, and 40 degrees. The reference PL spectrum is shown in the top panel.

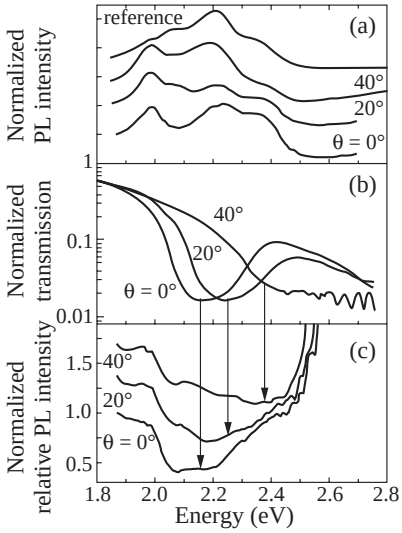

Fig. 2. The same as Fig. 1 for the Perylene/SnS_2 inverted opaline film.

PL spectra of SnS_2 inverted opal (Fig. 2(a)) have been measured under similar conditions as PMMA opals. Comparing them with the PL spectrum of the reference sample one can see the additional 1.98 eV band. Stop-band spectra extracted from the PL of Perylene in SnS_2 inverted opal (Fig. 2(c)) show a factor of 10 shallower minimum as compared with the stop-band in transmission (Fig. 2(b)). The stop-band angular dispersions are shown for both relative PL and transmission spectra.

2. Discussion

The crucial question to be addressed with regard to a PBG light source is physical mechanisms responsible for changes in the emission as compared with the free space case. To illustrate the role of the PBG incompleteness, the reconstruction of the PL spectra has been made by multiplying the PL spectrum of the reference sample with the transmission spectra of opaline films measured at certain angles. In the case of PMMA opal the reconstructed PL spectra (Fig. 3) correlate well with those observed for specified angles. As well, fitting of the reconstructed PL spectrum with the observed one for the Perylene/SnS_2 opaline film can be achieved under certain circumstances for angles close to [111] direction. However,

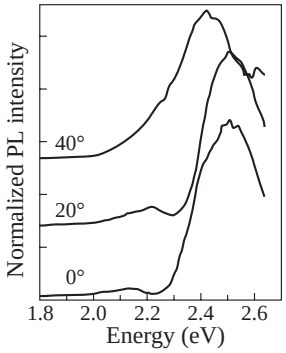

Fig. 3. Reconstructed PL spectra of Coumarun/PMMA opaline film for angles of 0, 20, and 40 degrees.

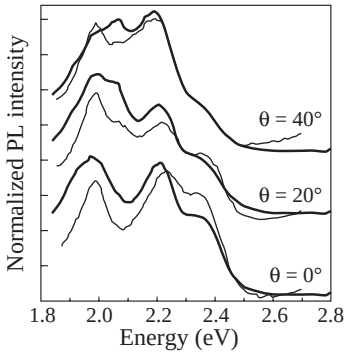

Fig. 4. The same as Fig. 3 for the Perylene/SnS_2 inverted opaline film. Bold and thin lines represent reconstructed and experimental spectra, respectively.

with further deviation from this direction the reconstructed spectra do not reproduce the 1.98 eV emission band (Fig. 4).

There are two scenarios can be followed. The first one is realised in the PMMA opaline film, whose PBG does not affect the spontaneous emission but simply changes the angular distribution of the emission flow in accord with the transmission function. The angular dispersion of this band-pass filtering relates to the incompleteness of the PBG. Certainly, with the broadening of the stop-band and squeezing of its dispersion occurring in SnS_2 inverted opaline films, a more intimate relation between the emission and the PBG structure can be expected. The physical reason is the development of the dip in the density of the photon state profile, which is an integral of state numbers over the whole solid angle (see e.g. [5]). The corresponding spectral redistribution of the emission flow acquires the angular independence, to which feature the angular independent 1.98 eV PL band is tentatively ascribed.

In summary, we have studied the emission of organic dyes from direct and inverted opaline films. The suppression of the emission intensity in direct opals can be referred as its angular redistribution due to the decrease of the number of photon states in a given direction. The enhancement of the PBG in inverted opals results in the co-existence of effects related to both the density and the number of photon states, which appears as the persistent spectral redistribution of the emission out of the PBG frequency range as well as the angular redistribution of the emission flow.

References

[1] H. P. Schriemer, H. M. van Driel, A. F. Koenderink and W. L. Vos, *Phys. Rev. A* **63**, 11801(R) (2001).
[2] M. Müller, R. Zentel, T. Maka, S. G. Romanov and C. M. Sotomayor Torres, *Adv. Materials* **12**, 1499 (2000).
[3] Y. Xia, B. Gates, Y. Yin and Y. Lu, *Adv. Mater.* **12**, 693 (2000).
[4] M. Müller, R. Zentel, T. Maka, S. G. Romanov and C. M. Sotomayor Torres, *Chemistry of Materials* **12**, 2508-2512 (2000).
[5] K. Busch and S. John, *Phys. Rev. E* **58**, 3896 –3908, (1998).

9th Int. Symp. "Nanostructures: Physics and Technology"
St Petersburg, Russia, June 18–22, 2001

Electrostatic Force Microscopy, principles and applications to semiconductor materials and devices

Paul Girard

Laboratoire d'Analyse des Interfaces et de Nanophysique (LAIN), UMR CNRS 5011, CC 082, Universite de Montpellier II, Place Eugene Bataillon, 34095 Montpellier Cedex 5, FRANCE

Issued on Scanning Probe Microscopy, the Electrostatic Force Microscopy (EFM) [1] appears as a new and attractive method to explore local electrical properties and bring useful informations, particularly to semiconductor technologists. The aim of this paper is to examine the principles of operation, discuss the observations, illustrate the capabilities of this method in the domain of semiconductors and foresee some future developments.

Generally, Atomic Force Microscopy surface profiles [2] and EFM data can be simultaneously and independently obtained, because the electric effects on the mechanical oscillations are at the second order. The principle of EFM operation is as follows. The SFM like sensor, that must be conducting on the surface facing the examined material, behaves like the mobile plate of a capacitor, the other being the sample. If a voltage difference V is existing between the two plates, an electrostatic force F appears and it is written: $F = 1/2\mathrm{d}C/\mathrm{d}zV^2$. Besides, if a dc surface charge is electrostatically coupled with the sensor, the Coulomb law gives an attractive force too. These attractive forces induce effects in two ways: they bend the sensor and they change the resonance frequency of the vibrating sensor. Then ω_0 is reduced from $\omega_0 = (k/m)1/2$ to $\omega_0' = (k/m - \mathrm{Grad}F/m)^{1/2}$ [3]. So, when scanning the object, it becomes possible to obtain data about charges [4] and voltages [1]. Since voltage measurements can be reached (nano Kelvin), we shall concentrate mainly on voltage observations. But, now, three questions arise and they concern: the EFM performances, the interpretation of the results and the implementation of EFM.

Since the electrostatic force is a long range interaction and the sensor configuration is complex, the first question is: how to obtain local electrical data and which are the expected performances? The force can be described using numerical simulations [5]. It is shown that a suitable shape of the sensor is required to localise the electrostatic interaction at the extreme end of the sensor — i.e. the tip apex — [6] and that the tip sample distance is a critical parameter which allows to localise the electrostatic interaction on the sample too. Under these conditions, the spatial resolution expected on voltage observations can be deduced [7], then the nanometer scale is related to a tip sample distance lying in the nanometer range. Besides, there is an improvement when detecting the force gradient instead of the force. But, since the force operation is now well established, we shall interest mainly with it.

The second question is the interpretation of the electrical images, or in other terms, the physical significance of the contrasts we can get and how to discriminate between them. For example, if a tip sample voltage V exists and $V = (V_{\mathrm{dc\,applied}} + V_{\mathrm{surface}}) + V_{\mathrm{ac}} \sin \Omega t$,

two types of informations are resulting, depending on the observation frequency. First of all, $F_\Omega = \mathrm{d}C/\mathrm{d}z(V_{\mathrm{dc\,applied}} + V_{\mathrm{surface}})V_{\mathrm{ac}} \sin \Omega t$ is depending on both the capacitive coupling $\mathrm{d}C/\mathrm{d}z$ and the surface potential V_{surface}. Secondly, $F_{2\Omega} = -1/4\mathrm{d}C/\mathrm{d}z V_{\mathrm{ac}}^2$ is only related to the capacitive coupling $\mathrm{d}C/\mathrm{d}z$. Basing on experimental cases, we can show how to explain the EFM observations.

The third question is the implementation of EFM. Generally, EFM is working under ambient conditions, but up to ultra high vacuum conditions remain possible. Some configurations are examined, it is shown that: (i) we can simultaneously obtain the morphology in the so called "tapping mode" and the EFM data, or (ii) we can use the double pass method on the same line or area. In that case, the tip is retracted from the sample for the electrical observations. The interest of the two methods have to be discussed. In addition, the nanokelvin operation allows to obtain surface voltage variations when making F_Ω equal to zero, using a supplementary loop to inject a voltage such as $(V_{\mathrm{dc\,applied}} + V_{\mathrm{surface}}) = 0$.

Then we can enter into the applications, especially in the case of semiconductors. First of all, the detection of the electrical homogeneity in semiconductor material is to be expected, lateral control can be performed using observations on F_Ω pictures [8]. Secondly, examination of nano-islands brings useful informations using nanokelvin voltage and force gradient measurements [9], it allows to situate the EFM performances too. Thirdly, observations on structures easily gives the localisation of doped and undoped areas [10]. On semiconductors, the so called capacitive coupling $\mathrm{d}C/\mathrm{d}z$ is sensitive to the surface bulk capacitor, changing from accumulation to depletion areas is observed. Recent experiments on working LASER structures give access to the control of internal field distributions [11]. Besides, such results are a particularly striking example of coupling three simultaneous observations. They concern: morphology, capacitive coupling and voltage measurements, all things that are important for development of semiconductor technology and for control of modern devices.

We could foresee some directions for future developments of electrical SPM observations. For example, they concern the performance improvements, extension of EFM use and the development of SPM. Based on force gradient detection, the improvement of spatial resolution is under development at our laboratory, first experimental results confirm the expected predictions [6]. At that time, we deal mainly with ambient working conditions but low temperature opens new fields for fundamental physics investigations. Coupling EFM with other electrical methods is also promising. Parallel sensors working simultaneously [12] — like a millipede — open the increase of speed operation and some generalisation of these methods.

In summary, we have shown the principles on which is based the Electrostatic Force Microscopy and the expected performances. Basing on experimental data, we have seen how to interpret the contrasts observed in the experiments. Then we have shown typical observations on semiconductors. We can say that the EFM is now an established method to explore local properties of semiconductor materials, structures and devices, but the field can be widened by new developments.

Acknowledgements

I would like to particularly acknowledge colleagues from Montpellier University: G. Leveque, S. Belaidi, M. Ramonda, Cl. Alibert and from Ioffe Institute: A. N. Titkov, A. N. Usikov, W. Lundin who participated to the works or provided useful and demonstrative samples.

References

[1] M. Nonnemmacher, M. O'Boyle and H. K. Wrickramasinghe, *Appl; Phys. Lett.* **58**(25), 292 (1991).
[2] G. Binnig, Ch. Gerber and C. F. Quate, *Europhys. Lett.* **3**, 1281 (1987).
[3] Y. Martin, C. C. Williams and H. K. Wickramasinghe, *J. Appl. Phys.* **61**(10), 4723 (1997).
[4] B. D. Terris, J. E. Stern, D. Rugar and H. Mamin, *J. Vac. Sc. And Tech. A* **8**(1), 374 (1990).
[5] S. Belaidi, P. Girard and G. Leveque, *J. Appl. Phys.* **81**(3), 1023 (1997).
[6] S. Belaidi, P. Girard and G. Leveque, *Microel. and Rel.* **37**(11), 1627, Elsevier ed (1997).
[7] S. Belaidi, F. Lebon, P. Girard, G. Leveque and S. Pagano, *Appl. Phys. A* **66**, S239 (1998).
[8] N. Shmidt, V. V. Emtsev, A. S. Kryzhanovsky, R. N. Kyutt, W. V. Lundin, D. S. Poloskin, V. V. Ratnikov, A. V. Sakharov, A. N. Titkov, A. S. Usikov and P. Girard, *Phys. Stat. Sol.(b)*, **216**, 581 (1999).
[9] A. N. Titkov, P. Girard, V. P. Evtikhiev, M. Ramonda, V. E. Tokranov and V. P. Ulin, *NC-AFM 99 Conference Proceedings*, Sept. 99, Pontresina, Switzeland
[10] A. H. Kenning, T. Hochwitz, J. Slinnkman, J. Never, S. Hoffmann, P. Kaszuba and C. Daghlian, *J. Appl. Phys.* **77**(5), 1888 (1995).
[11] G. Leveque, P. Girard, E. Skouri and D. Yareka, *Appl. Surf. Science* **157**, 251 (2000).
[12] P. Wettiger, *STM'99 Conference Seoul*, July 1999.

9th Int. Symp. "Nanostructures: Physics and Technology"
St Petersburg, Russia, June 18–22, 2001

Electrostatic force microscopy study of the electric field distribution in semiconductor laser diodes under applied biases

A. Ankudinov†, A. Titkov†, V. Evtikhiev†, E. Kotelnikov†, D. Livshiz†, I. Tarasov†, A. Egorov†, H. Riechert‡, H. Huhtinen§ and R. Laiho§
† Ioffe Physico-Technical Institute, St Petersburg, Russia
‡ Infineon Technologies AG, Corporate Research, D-81730, München, Germany
§ Wihuru Physical Laboratory, Turku University, Turku, FIN20014, Finland

In the semiconductor laser diodes the inner electric field distribution is the characteristic of significant interest in device design and failure analysis. In the modern lasers the applied voltage usually drops within the narrow layers of submicron range, and the precise information on the electric field distribution must be extracted by means of methods having nanometer spatial resolution. The electrostatic force microscopy (EFM [1] is the excellent candidate to solve this problem. This technique presents the development of the atomic force microscopy (AFM [2] which allows direct measuring of the electrostatic force acting between the nanometer-size probe and the surface. The electrostatic force in such system depends on the capacitance and the potential difference between the probe and the surface. These two contributions into the force can be separated in EFM, thus providing a way for high resolution surface potential and capacitance mapping. Until now only a few EFM studies were performed to probe electric characteristics of semiconductor light emitting devices [3–5]. The potential profiles in the devices under applied bias were measured for AlGaSb/GaSb based lasers [4] and for GaP based light emitting diodes [3]. Robin *et.al.* [5] investigated the potential and the corresponding electric field profiles in InP/InGaAsP p-i-n laser diode without external bias.

In this work we applied the EFM method to investigate AlGaAs/GaAs and InGaP/GaAs based p-i-n laser diodes and have found the main features of the electric field and capacitance distributions on the cross-sections of the devices under the applied forward and backward biases. The fine structure of the electric field distribution presented by two spikes localized at the n-emitter/i-waveguide and p-emitter/i-waveguide interfaces is analyzed. Our study shows that at the low level of the injection current the inner electric field induced by the applied bias is concentrated in the vicinity of the n-emitter/i-waveguide interface, while at the high level of injection it is redistributed in favor of the p-emitter/i-waveguide interface. With increasing forward bias the growth and broadening of the capacitance signal at the undoped waveguide region is also observed, that may reflect the injected carriers distribution.

We have used the EFM method in which an alternative bias at the frequency ω is applied to the AFM probe inducing it's mechanical oscillations due to electrostatic force variations. The first and the second harmonics ($H(\omega)$, $H(2\omega)$) of oscillations, which are two main EFM signals, can be detected by lock-in technique. $H(\omega)$ depends mainly on the probe-surface potential difference, $H(2\omega)$ is proportional to the corresponding capacitance. The AFM operates in tapping mode and in addition to the EFM signals the topography data are measured.

The microscope used for the measurements is an air-AFM system (Autoprobe CP Research, ThermoMicroscopes). Alternative voltage is applied to the highly doped Si probe

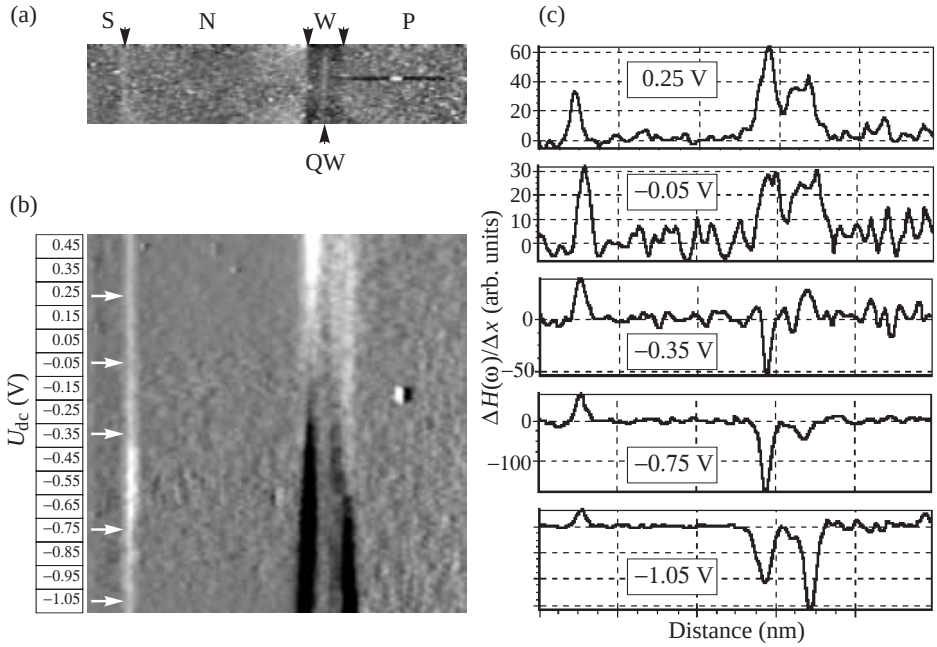

Fig. 1.

at a typical frequency of around 50 KHz and a voltage amplitude of 0.7 V. The EFM signals are analyzed through a Stanford Lock-in Amplifier 8230. The studied lasers are biased by the constant voltage source built in the microscope.

Figure 1(a) shows an AFM tapping mode topography image of the cleaved surface of one of the p-i-n laser diodes studied in this work. The structure was grown by the molecular beam epitaxy and consists of an n-doped GaAs substrate (S), an n-doped (Si) 2 μm-thick AlGaAs emitter (N), an undoped 0.4 μm-thick GaAs waveguide (W) centered with 9 nm InGaAs quantum well (QW), a p-doped (Be) 2 μm-thick AlGaAs emitter (P) followed by heavily doped p-GaAs contact layer. All the main layers of the structure can be identified in the image, in which the darker contrast corresponds to the depression of the surface relief. The waveguide region of the structure is several angstroms lower then n- and p-emitters due to known difference in oxide layer thickness on GaAs and AlGaAs [6]. The bright line in the middle of the waveguide corresponds to the compressed InGaAs QW. As it was shown earlier, thin compressed layers can noticeably extrude out on the cleavage [7].

In Figure 1(b) the variations of the $\delta H(\omega)/\delta x$ magnitude over the studied surface area are presented. The data were obtained as follows. First, simultaneously with the topography data acquisition, the $H(\omega)$ signal was measured as a function of the dc bias applied to the N-contact of the laser; the bias is decreased by the steps of 0.1 V every 1/16-th of the image height from 0.45 V (top of image) to -1.05 V (bottom of image). Then, the first derivative $\delta H(\omega)/\delta x$ was calculated numerically along the direction x perpendicular to the interfaces. Figure 1(c) shows the profiles of $\delta H(\omega)/\delta x$ taken under different applied bias (the white arrows in Fig. 1(b) indicate the lines in image along which the profiles are taken). The meaning of the $\delta H(\omega)/\delta x$ signal is the electric field at the surface in the direction perpendicular to the interfaces. Variations of this field should reflect variations

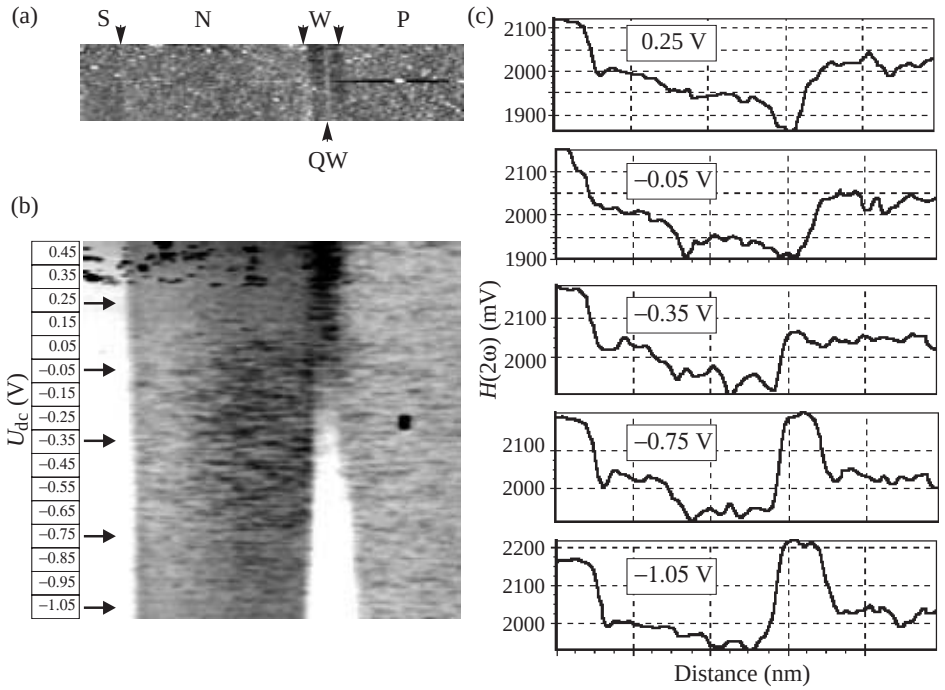

Fig. 2.

of the inner electrical field in laser diodes in the same direction. Without bias (a profile taken at -0.05 V) the distribution of the electric field is symmetric and formed by the two spikes whose extremums are localized near the waveguide interfaces. For the low level of injection current, the inner electric field is concentrated at the n-emitter/i-waveguide interface (the left spike in the profiles taken at 0.25 V, -0.35 V and -0.75 V is mainly changed). However, under the high level of injection, the redistribution of the inner electric field in favor of the p-emitter/i-waveguide interface is observed (the right spike in the profile taken at -1.05 V is deeper than the left one). It is interesting to note considerable reduction of the electric field at the waveguide center.

The variations of the $H(2\omega)$ signal (capacitance) are shown in Fig. 2(b) (the applied bias is changed in the same manner as in Fig. 1(b)) and in Fig. 2(c) with the profiles of $H(2\omega)$ along the lines marked by the black arrows in Fig. 2(b). The white band in the left part of the image in Fig. 2(b) is attributed to the n-GaAs substrate, see also the topography image in Fig. 2(a). An increase of the capacitance at the n-GaAs substrate compared to the n- and p-AlGaAs emitters is related to the thinner native oxide on GaAs [6]. The capacitance at the substrate and the emitter layers does not depend on the applied bias. However, the applied bias affects strongly the capacitance at the waveguide region. For the backward biases, the signal has low magnitude. Under the forward bias of approximately -0.35 V, there appear at the middle of the waveguide the spike in the $H(2\omega)$ signal which amplitude is higher than the signal level at the surrounding emitters. The spike grows in height and broadens with increasing forward bias, and at -1.05 V (see Fig. 2(c)) it's top is formed by the wide $\sim 0.4\,\mu$m plateau that coincides well with the position of the waveguide.

In conclusion, we present a new and direct electrostatic force microscopy method to resolve the electric field and capacitance distributions in laser diodes. Using this method we have investigated the fine structure of the electric field in AlGaAs/GaAs and InGaP/GaAs p-i-n based laser diodes under forward and backward biases. We have also found a strong increase in the capacitance at the waveguide under forward biases. We believe that this effect is related to the carriers injection into the waveguide and can be used to study the injected carriers distribution.

The presented method can be also used to study the electric fields in the other semiconductor devices.

Acknowledgements

The work was partly funded by RFBR (grant No 00-02-16948). A.A. and A.T. are grateful to the Wihury foundation for the support.

References

[1] M. Nonemacher, M. P. O'Boyle and H. K. Wickramasinghe, *Appl. Phys. Lett.* **58**, 2091 (1991).
[2] G. Binig, Ch. Gerber, E. Stell and T. R. Quake, *Europhys. Lett.* **3**, 1281 (1987).
[3] R. Shikler, T. Meoded, N. Fried and Y. Roesenwaks, *Appl. Phys. Lett.***74**, 2972 (1999).
[4] G. Leveque, P. Girard, E. Skouri and D. Yarekha, *Appl. Surf. Sci.* **157**, 251 (2000).
[5] F. Robin, H. Jacobs, O. Homan, A. Stemmer and W. Bächtold, *Appl. Phys. Lett.* **76**, 2907 (2000).
[6] A. V. Ankudinov, V. P. Evtikhiev, V. E. Tokranov, V. P. Ulin and A. N. Titkov *Semiconductors* **33**, 555 (1999).
[7] A. V. Ankudinov, A. N. Titkov, T. V. Shubina, S. V. Ivanov, P. S. Kop'ev, H. -J. Lugauer, G. Reusher, M. Keim, A. Waag and G. Landwehr, *Appl. Phys. Lett.* **75**, 2626 (1999).

9th Int. Symp. "Nanostructures: Physics and Technology"
St Petersburg, Russia, June 18–22, 2001

Scanning Joule expansion microscopy as a tool for studying local heating phenomena

M. Cannaerts†, R. J. M. Vullers‡ and Chris Van Haesendonck†
† Laboratorium voor Vaste-Stoffysica en Magnetisme, Katholieke Universiteit Leuven, Celestijnenlaan 200 D, B-3001 Leuven, Belgium
‡ Philips Research Laboratories, Prof. Holstlaan 4, NL-5656 AA Eindhoven, The Netherlands

Abstract. Scanning Joule expansion microscopy (SJEM) is a powerful technique enabling the generation of temperature maps of nanostructured samples [1]. It operates by examining in detail the thermal expansion of a current-carrying structure with an atomic force microscope (AFM). The thermal expansion varies proportional to the temperature, making it possible to simultaneously generate topographical maps as well as thermal maps of samples. The lateral resolution of the SJEM technique (estimated to be 20 nm or better) is considerably better than that of other comparable techniques (e.g. scanning thermal microscopy, with a typical resolution of 100 nm). Previously we implemented and optimized a SJEM in an existing AFM system [2]. Using the SJEM technique it is possible to identify 'hot spots', and to examine in detail the temperature profile in nanostructured materials. Here, we investigate the reliability of this technique for microelectronics related applications.

Introduction

The ever decreasing dimensions of microelectronic structures has made it necessary for engineers and physicists to look for new and better characterization tools. Scanning probe microscopes have proven to be valuable and versatile tools for quality control of samples with submicrometer dimensions. Recently, new lithography techniques (based on extreme ultraviolet light with a wavelength of 13.4 nm) have been announced, making it possible to fabricate 30 nm sized transistors. Chips generated with this technique could consist of 400 million transistors, making 10 GHz operating speeds attainable in the near future [3]. One of the major issues linked to this continuing downscaling of features, is the problem of local heat generation and dissipation.

An atomic force microscope (AFM) can be adapted to map local variations of the temperature. This technique is referred to as 'scanning thermal microscopy' (SThM), and relies on the use of a microfabricated thermocouple or a small resistor as the local probe [4, 5]. The SThM technique makes it possible to generate temperature maps of a sample surface or plots of the thermal conductivity. While the resolution of SThM is much better than that of other techniques (for example infrared imaging), the resolution is still limited to 100 nm for typical commercially available setups. A 25 nm spatial resolution was obtained using thin film technology coupled with electron beam lithography [6]. This seems to be the realistic limit for the SThM technique under ambient conditions because of the nature of the tip-sample thermal contact. For more detailed information on SThM we refer the reader to a recent review article [7].

1. Experimental setup

An alternative powerful and versatile technique to map local temperature variations of surfaces was recently presented [1]. An atomic force microscope, operating with a silicon cantilever, scans the surface of a current-carrying structure. By examining in detail the thermal expansion (due to Joule heating) of the structure at a given point (which is proportional to the temperature at that point), it is possible to infer the local temperature. This technique is called 'scanning Joule expansion microscopy' (SJEM). The signal to noise level is considerably improved by working with ac currents and a lock-in detection technique. The details of our experimental setup can be found elsewhere [2].

The advantage of the SJEM technique is that no complicated miniature thermocouple fabrication is required. Another advantage is the nature of the temperature detection: SThM operates because of heat extending into the microfabricated thermocouple. Therefore, the nature of the thermal contact between tip and sample strongly affects the resolution and the interpretation of data. On the other hand, SJEM infers the temperature from the thermal expansion of the sample. In principle, this implies a resolution comparable to that of regular AFM. The disadvantage is that only conducting structures can be thermally examined with the SJEM technique.

Our SJEM is based on a commercially available AFM setup (Park Scientific Instruments M5 autoprobe), using commercial cantilevers (type PSI *Ultralever*, with a spring constant of typically 1 to 10 N/m). Measurements were performed in the contact mode, with setpoint forces of typically 50 nN. Using the relatively stiff cantilevers in the contact mode minimizes the contribution of electrostatic forces to the expansion signal [2].

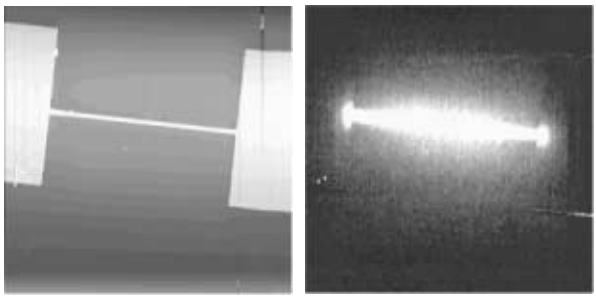

(a) (b)

Fig. 1. (a) Topographical AFM image of a 37 nm thick gold line on an oxidized silicon surface (length 52 micron, width 700 nm). (b) Thermal expansion (i.e. temperature map) of the line obtained with an alternating current with an amplitude of 21 mA and a frequency of 20 kHz. Black regions in the expansion map correspond to regions with a small expansion amplitude (lower temperatures), white regions have a higher expansion signal (higher temperatures).

2. Heat distribution in narrow gold lines

Using electron beam lithography combined with lift-off techniques, narrow gold lines were fabricated on oxidized silicon wafers. Figure 1(a) shows a typical topographical AFM picture of a gold structure. An alternating current of 21 mA at 20 kHz causes a thermal expansion of the gold line at 40 kHz, which is at too high a frequency for the AFM feedback to react. Therefore, the error signal will contain this high frequency component, which can be measured with a lock-in amplifier (Stanford Research, SR830). The dc output of the

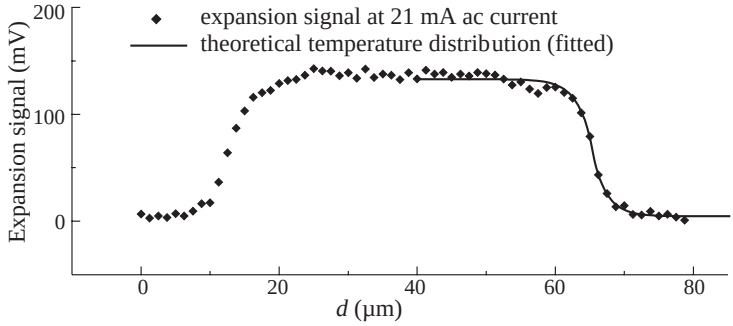

Fig. 2. Experimental expansion signal measured along the gold wire, which has been fitted to the theoretical temperature distribution in the wire.

lock-in amplifier gives the oscillation amplitude of the thermal expansion, and can be plotted simultaneously with the sample topography. This expansion map is visible in Fig. 1(b).

In order to prove that the measured expansion signal varies indeed proportional to temperature (and is not, e.g., strongly influenced by electrostatic force interactions between the cantilever and the sample), the measured expansion profile has been compared to the theoretical temperature profile in a small gold line (for more details, see reference [2]). Figure 2 shows the measured expansion signal which has been fitted with the theoretical temperature profile in the gold line.

3. Applications of SJEM

We have applied our SJEM technique to identify the 'hot spots' in copper coils. These copper coils are to be used for future magneto-optical recording systems, featuring laser-pulsed magnetic field modulation [8]. The studied copper coil is embedded in an oxide layer, and has an inner diameter of 90 μm.

Figure 3(a) shows an optical micrograph of a copper coil. Within the region marked by a square, an expansion map was generated. The three-dimensional expansion map is shown in Fig. 3(b).

Since the material in which the copper coil is embedded also expands, it is difficult to quantitatively compare the temperature on top of the copper wires to the temperature at the center of the coil. In the near future, we will try to link the expansion maps of the coils to thermal maps generated with infrared imaging techniques in order to perform a quantitative

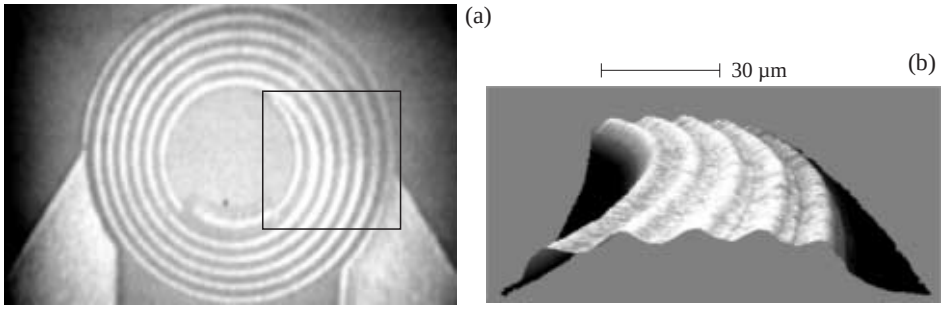

Fig. 3. (a) Light microscopy picture of the copper coil. (b) Thermal expansion map for the square area indicated in (a).

temperature calibration, and to check in more detail the applicability of SJEM as a quick thermal characterization tool.

Acknowledgements

The authors would like to thank Dieter Buntinx for sample preparation. This work has been supported by the Fund for Scientific Research Flanders (FWO) as well as by the Flemish Concerted Action (GOA) and the Belgian Inter-University Attraction Poles (IUAP) research programs.

References

[1] J. Varesi and A. Majumdar, *Appl. Phys. Lett.* **72** 37 (1998).
[2] M. Cannaerts, G. Rens, A. Volodin and C. Van Haesendonck, *Appl. Surf. Sci.* **157** 308 (2000).
[3] http://www.newscientist.com.
[4] M. Nonnenmacher and H. K. Wickramasinghe, *Appl. Phys. Lett.* **61** 168 (1992).
[5] A. Majumdar, J. P. Carrejo and J. Lai, *Apl. Phys. Lett.* **62** 2501 (1993).
[6] K. Luo, Z. Shi, J. Varesi and A. Majumdar, *J. Vac. Sci. Technol. B* **15** 349 (1997).
[7] A. Majumdar, *Annu. Rev. Mater. Sci.* **29** 505 (1999).
[8] F. C. Penning, H. W. Van Kesteren, M. A. H. Van der Aa, Y. V. Martynov and R. J. M. Vullers, *accepted for publication in Jap. J. Appl. Phys., vol. 40* (2001).

9th Int. Symp. "Nanostructures: Physics and Technology"
St Petersburg, Russia, June 18–22, 2001

Magneto-tunnelling spectroscopy of localised and extended states in a quantum well containing quantum dots

Yu. V. Dubrovskii[1], A. Patane[2], P. N. Brounkov[3], E. E. Vdovin[1], I. A. Larkin[1,4], L Eaves[2], P. C. Main[2], D. K. Maude[5], J.-C. Portal[5,7,8], *D. Yu. Ivanov*[1], Yu. N. Khanin[1], V. V. Sirotkin[1], A. Levin[2], M. Henini[2] and G. Hill[6]

[1] Institute of Microelectronics Technology RAS, 142432 Chernogolovka, Russia
[2] The School of Physics and Astronomy, University of Nottingham, Nottingham NG7 2RD, UK
[3] Ioffe Physico-Technical Institute, St Petersburg, Russia
[4] The School of Physics and Astronomy, University of Sheffield, Sheffield S3 3JD, UK
[5] Grenoble High Magnetic Field Laboratory, MPI-CNRS, BP166 38042 Grenoble Cedex 9, France
[6] Dept of Physics, University of Sheffield, Sheffield S3 3JD, UK
[7] Institut Universitaire de France, France
[8] INSA, F31077 Toulouse Cedex 4, France

Abstract. We investigate resonant tunnelling in GaAs/(AlGa)As double-barrier resonant-tunnelling diodes (RTDs) in which a single layer of InAs self-assembled quantum dots (SAQDs) is embedded in the centre of the GaAs quantum well. The dots provide a well-defined and controllable source of disorder in the well and we use resonant tunnelling for studying the effect of disorder on the electronic properties of the well.

A thin pseudomorphic InAs layer (wetting layer-WL) incorporated in the central plane of an (AlGa)As/GaAs/(AlGa)As quantum well (QW) leads to a significant lowering of the energy of the quasi-two dimensional (2D) ground state subband of the QW [1]. Above a critical wetting layer thickness, self-assembled InAs quantum dots (SAQDs) are formed. This modifies further the electronic states of the system: firstly, the dots give rise to discrete zero-dimensional bound states and, secondly, they create a considerable amount of disorder, which influences the properties of the continuum of wetting layer subband states. The disorder is a consequence of the fluctuating random potential arising from local strains and charging of the quantum dots. Within a single-electron picture, it could change the localisation length of the 2D states.

In this work, we investigate resonant tunnelling in MBE-grown GaAs/(AlGa)As double-barrier resonant-tunnelling diodes (RTDs) in which a single layer of InAs SAQDs is embedded in the centre of the GaAs QW. These RTDs form a flexible "quantum laboratory" for investigating a variety of phenomena, including the dynamics of carrier tunnelling, capture and recombination [1] and the spatial distribution of the probability density of the electron wave function in the dots [2]. Here we use resonant tunnelling spectroscopy to demonstrate that the random potential in the well due the presence of dots strongly influences the electronic properties of the disordered ground state two-dimensional subband in the QW.

Three different structures were investigated: Sample *qd* comprised (in the order of growth) a lightly Si-doped, 300-nm-thick GaAs layer ($N_d = 3 \cdot 10^{18}\,\mathrm{cm}^{-3}$); a 50.4-nm-thick GaAs layer ($N_d = 2 \cdot 10^{18}\,\mathrm{cm}^{-3}$); a 50.4-nm-thick undoped GaAs spacer layer; a 8.3-nm-thick $Al_{0.4}Ga_{0.6}As$ barrier layer; a 5.6 nm undoped GaAs layer; a 1.8 monolayer

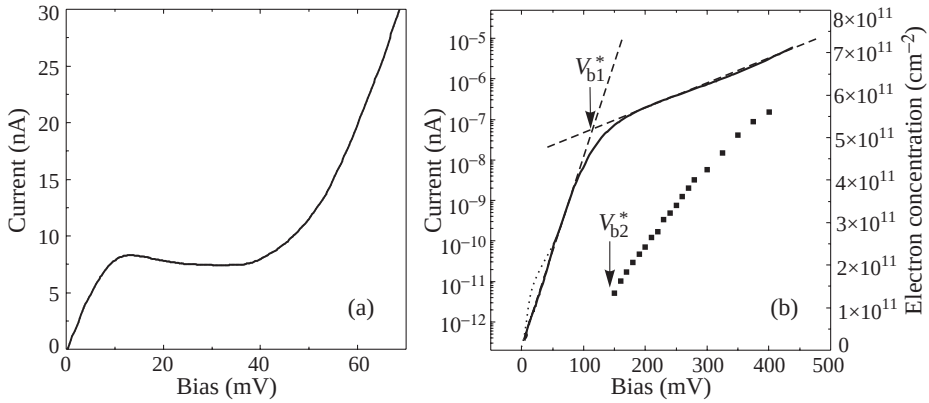

Fig. 1. (a) Low bias I–V curve of the sample with only wetting layer. (b) Logarithmic plot of the current versus voltage dependence of the tunnelling current for the sample with embedded in the well quantum dots (solid line, left scale). Dotted line shows extra current which appears only at positive bias. V_{b1^*} and V_{b2^*} are described in the text. Squares show concentration of electrons in the accumulation layer versus bias (right scale).

(ML) InAs with growth rate 0.13 ML/s to form InAs QD; a 5.6-nm-thick undoped GaAs layer; a 8.3-nm-thick $Al_{0.4}Ga_{0.6}As$ barrier; a 50.4 nm undoped GaAs; a 50.4-nm-thick GaAs layer ($N_d = 2 \cdot 10^{18}\,\mathrm{cm}^{-3}$); and a 300-nm-thick GaAs layer ($N_d = 3 \cdot 10^{18}\,\mathrm{cm}^{-3}$) cap-layer. Two control samples were also grown. One had only an InAs wetting layer (sample *wl*) in place of the QDs and the other had no InAs layer at all.

The presence of the narrow InAs WL modifies the electronic structure of the QW lowering ground state down bellow the GaAs conduction band edge whereas the excited QW subbands are relatively uneffected. Simple self-consistent calculations of Schrödinger and Poisson equations show that ground state in the sample with wetting layer only is located about 50 mV bellow the GaAs conduction band edge and filled with electrons from contact layers. The ground state is in resonance with 3D electrons in contacts at zero bias. This is illustrated in Figure 1(a). The resonance feature is observed at $V_b = 0$ and NDC corresponding to the exit from resonance is around 30 mV. The control sample without the InAs wetting layer shows resonant tunnelling features in I(V) due to the tunnelling through the umperturbed ground state in the well at higher bias voltage, $V_b = 0.1$ V.

For the sample in which the dots are formed (sample *qd*), a wetting layer is still present and the overall effect on the energy spectrum is to add zero- dimensional bound states below the ground state level. The negative charging of the dots by electrons from the contacts could only shifts up the ground state relatively to the equilibrium Fermi level in the RTD. This means that the resonance condition between the 3D electrons in the doped contact layers and ground state subband remains at zero bias, or shifts to higher bias, depending on the QD density in the layer. Therefore, for the QD sample, we would also expect to see a resonant tunnelling feature in I(V) associated with the ground state subband.

In contrast to this expectation, the I–V curve of the sample *qd* shows only exponential increase of the current with bias voltage (Fig. 1(b)). Nevertheless there are two distinct features in the curve. First, the exponential current onset changes exponent at around $V_{b1^*} \approx 110$ mV. Secondly, there is a shoulder in the current bellow 50 mV appeared only at positive bias (shown by dotted line). We associate the shoulder with tunnelling through excited states in the quantum dots and will discuss it in detail elsewhere. Here we focus on the two exponents in the I–V curves.

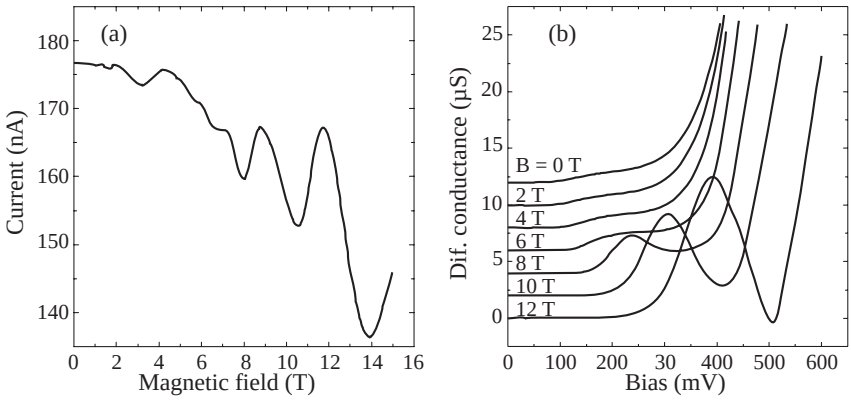

Fig. 2. (a) Variation of the tunnelling current with normal magnetic field at 300 mV bias voltage. (b) Differential conductance of the sample with quantum dots versus bias voltage in different in-plane magnetic fields.

In order to understand the absence of any resonant current features related to the ground state in the sample *qd*, we need to take into account that the layer of charged dots is a source of strong potential fluctuations. This leads to a non-uniform broadening of the ground state level in the well and strong localisation of the corresponding two-dimensional electron states. Then, if the localisation length of the final states is comparable with the Fermi wavelength of the electron tunnelling from the emitter, momentum conservation is destroyed and only energy conservation is important for the tunnelling process. In the sequential resonant tunnelling model, it is the conservation of the in-plane momentum that leads to the current peaks and the NDC regions in the I(V) curves [3]. Thus we argue that the exponential increase of the current at low bias simply reflects tunnelling through strongly localised two-dimensional states in the well with no momentum conservation.

In tunnelling experiments the exponential I–V dependences arise since the tunnelling current exponentially depends on the barrier height and/or effective barrier thickness. At low bias electrons in the 3D contacts tunnel to the states in the well across the complex barrier involving the spacer layer and the main AlGaAs barrier. At higher bias voltage above some critical value V_{b1^*} when the 2D accumulation layer is formed near the main barrier only the last one determines tunnel exponent. It is easy to show that for these two cases we should have different exponents.

Magnetotunnelling data obtained in the field normal to the layers confirm the formation of the accumulation layer above V_{b1^*}. Figure 2(a) shows variation of tunnel current versus magnetic field at $V_b = 300$ mV. There are two distinct series of oscillations each periodic in 1/B. It follows from analysis of the data that low magnetic field oscillations (below 4 T) are due to the electron concentration variation in the accumulation layer with magnetic field. Oscillations in a high magnetic field reflect the tunnelling through empty Landau states in the quantum well. In the field higher then 4 T only ground Landau level in the accumulation layer emitter is occupied and all tunnelling electrons have approximately the same energy. Consequently magnetotunnelling spectra measured at constant bias reflects the variation of the density of state at some fixed energy in the well with magnetic field. Electron concentration in the accumulation layer versus voltage bias determined from the low magnetic field oscillations is shown in Fig. 1(b) by squares. The electron concentration comes to zero just at V_{b1^*}.

It should be noted that both sets of magneto-oscillations appear simultaneously at bias voltage $V_{b2^*} \approx 140$ mV. Below this bias no any oscillations have been resolved in the sample containing QD. In the wetting layer sample tunnelling through Landau states in the well was observable at all voltages. If appearance of low field oscillations is as usual related with formation of the accumulation layer continues along barrier, the appearance of high field oscillations one should relate with formation of Landau states in the presence of random potential only above some energy E^* in the well. This apparent (seeming) threshold between localised and delocalised states can simply be explained in terms of random potential screening by electrons in the accumulation layer after its formation. Estimations based on the theory developed by Davies [4] show that for our structure dispersion of the random potential in the well is reduced about ten times after the accumulation layer formation.

This model explains also surprising from the first glance appearance of the negative differential conductance in the I–V curves in magnetic field perpendicular to the tunnel current (Fig. 2(b)). In common RTDs the resonant peak is shifted to higher biases with in-plane magnetic field [5]. It happens because Lorentz force change the in plane momentum of tunnelling electron shifting bias voltage where both momentum and energy conservation conditons are satisfied to higher value. In in-plane magnetic field in resonance electrons tunnel to the states with higher energy in the well relative to the case B=0. Since, if there is threshold energy E^* in our structure, one could expect appearance of negative differential conductance region in I–V curves in in-plane magnetic field when electrons start to tunnel into the states above E^* with momentum and energy conservation.

In conclusion, we have studied details of resonant tunnelling through AlGaAs/GaAs/AlGaAs double barrier heterostructures (DBHS) with InAs self-assembled quantum dots embedded in the well region. The I–V curves show only exponential increase of the current with bias voltage without any features reminding resonant tunnelling through the ground state in the well, e.g. current peaks or negative differential conductance regions. This is related with tunnelling through the tails of strongly localised two dimensional states in the well with only energy conservation. The strong localisation of the states is due to the random potential originated from local strains in the InAs layer and charging of the quantum dots. At high enough bias voltage the 2D accumulation layer formed near the main barrier reduces dispersion of the random potential in the well by screening. As the result the formation of Landau states above some energy E^* in the well have been observed. The tunnelling into the states above E^* with momentum conservation have been also found in the in-plane magnetic field.

Acknowledgements

We are grateful to V. A. Volkov, V. G. Popov and S. V. Morozov for helpful discussions. This work was supported by INTAS (97-11475), RFBR (98-02-22008, 00-01-00656, 00-02-17903, 01-02-17844, 01-02-97020), PICS (628), Ministry of Science (FTNS-97-1057), and EPSRC (UK).

References

[1] A. Patane, *et al.*, *Phys. Rev. B* **62**, 13595 (2000).
[2] E. E. Vdovin, *et al.*, *Science* **290**, 122 (2000).
[3] S. Luryi, *Appl. Phys. Let.* **47**, 490 (1985).
[4] J. H. Davies and G. Timp, *Heterostructures and Quantum Devices*, vol 24, eds N. G. Einspruch and W. R. Frensley, pp 385–418, San Diego, Academic Press, 1994.
[5] R.K. Hayden, *et al.*, *Phys. Rev. Let.* **66**, 1749 (1991).

9th Int. Symp. "Nanostructures: Physics and Technology"
St Petersburg, Russia, June 18–22, 2001

Spatial mapping of the electron eigenfunctions in InAs self-assembled quantum dots by magnetotunneling

E. E. Vdovin†, A. Levin‡, A. Patanè‡, L. Eaves‡, P. C. Main‡,
Yu. N. Khanin†, Yu. V. Dubrovskii†, M. Henini‡ and G. Hill§
† Institute of Microelectronics Technology RAS, Chernogolovka, Russia
‡ School of Physics and Astronomy, University of Nottingham,
Nottingham NG7 2RD, UK
§ Dept. of Electronic and Electrical Engineering, University of Sheffield, UK

Abstract. We use magnetotunnelling spectroscopy as a non-invasive probe to produce two-dimensional spatial images of the probability density of an electron confined in a self-assembled semiconductor quantum dot. The images reveal clearly the elliptical symmetry of the ground state and the characteristic lobes of the higher energy states.

Self-assembled quantum dots (QDs) are nanometer-sized clusters, that are formed spontaneously in strained semiconductor heterostructures. They can confine the motion of an electron in all three spatial dimensions [1]. The strong confinement in the QD gives rise to a set of discrete and narrow electronic energy levels similar to those in atomic physics. Experimentally, the quantized energy levels of a given potential can be probed using various spectroscopic techniques. The corresponding wave functions are much more difficult to measure. We report an experimental study of the spatial distribution of the wavefunction probability density of electron states in InAs/GaAs self-assembled quantum dots (QDs) by magnetotunnelling spectroscopy.

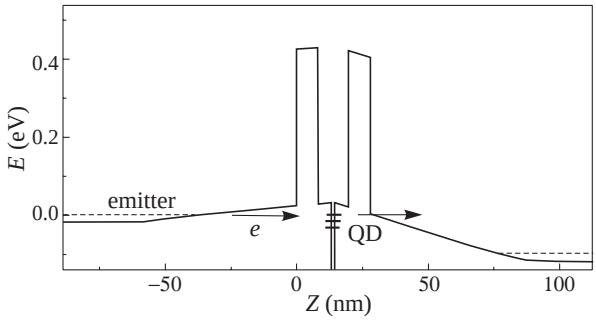

Fig. 1. Schematic conduction band profile under an applied bias of an n-i-n GaAs/(AlGa)As double barrier resonant tunneling diode incorporating InAs self-assembled quantum dots (QDs).

The InAs QDs are embedded in a n-i-n, resonant tunnelling diode. The samples were grown by molecular beam epitaxy on a GaAs substrate with the orientation (311)B. Figure 1 shows a schematic energy band diagram for our device under bias voltage. We observe series of resonant peaks in the low-temperature ($T = 1.5$ K) current–voltage characteristics, I(V), of the diode, corresponding to carrier tunnelling into the dot states . Pronounced current features appear at biases as low bias as 55 mV. They are superimposed on a rising background

current and cannot be resolved for $V > 200$ mV. The amplitude of each resonance exhibits a strong dependence on the intensity of B, applied parallel to the growth plane. In particular, with increasing B, the low-voltage resonances decrease steadily in amplitude, whereas the others have a non-monotonous magnetic field dependence.

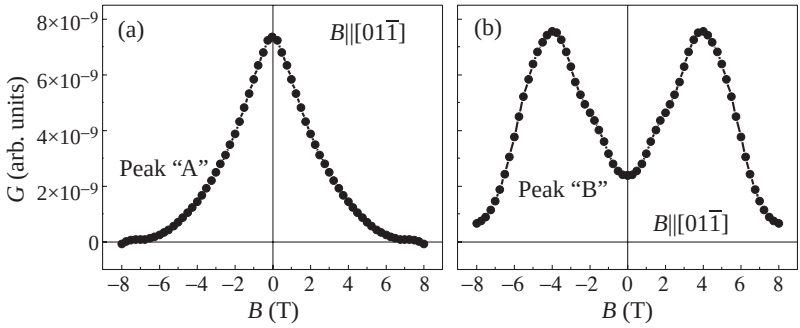

Fig. 2. Dependence of G on magnetic field for B parallel and antiparallel to [01$\bar{1}$] for the different QDs states.

Figure 2 shows clearly two characteristic types of magnetic field dependence: type "A" shows a maximum on $G(B)$ at $B = 0$ T followed by a steady decay to zero at around 8 T; type "B" shows a broad maximum at ~ 4.5 T, followed by a gradual decay to zero.

Figure 3(a) shows the I(V) characteristics in an in-plaine magnetic field of 4.5 T. The first curve (cicles) is for $B \parallel [01\bar{1}]$; the second curve (triangeles) is for $B \parallel [\bar{2}33]$. We have also determined angular dependense of the peaks current. The results are plotted in Fig. 3(b) for the peaks "A " and "B". The main effect to be noted from Fig. 4 is the dependence of the current as a function of the in-plane magnetic field orientation.

We can understand the magnetic field dependence of the features in terms of the effect of B on a tunnelling electron. In the experiment, carriers tunnel through a barrier into the dots in the presence of a magnetic field, **B**, perpendicular to the current, **I**. If x and z indicate the directions of **B** and **I**, respectively, then when carriers move from the emitter into the dot, they acquire an in-plane momentum

$$\Delta k_y = eB\Delta s/\hbar \tag{1}$$

from the action of the Lorentz force, where Δs is the effective distance tunnelled along z [2, 3]. This has pronounced effects on the tunnelling process. In particular, the intensity of the current resonances is modified with B and we relate these variations to the square of the Fourier transform, $|\Phi_{\rm QD}(\underline{k})|^2$, of the electron probability density. The $G(B)$ plots provide a means of probing the characteristic form of the wavefunction probability density of the electron confined in the dot as a function of and hence of the corresponding spatial coordinate, y. Thus by plotting $G(B)$ for a *particular* direction of B we can measure the dependence of $|\Phi_{\rm QD}(\underline{k})|^2$ along the $\underline{k}$-direction perpendicular to B. Then, by rotating B in the plane *(X, Y)* and making a series of measurements of I(B) with **B** set at regular intervals ($\Delta\theta \sim 5^\circ$) of the rotation angle θ, we obtain a full spatial profile of $|\Psi_{\rm QD}(k_x, k_y)|^2$. This represents the projection in $\underline{k}$-space of the probability density of a given electronic state confined in the QD.

The model provides a simple explanation of the magnetic field dependence of the resonant current features "A"–"C". In particular, the *forbidden* nature of the tunnelling transition

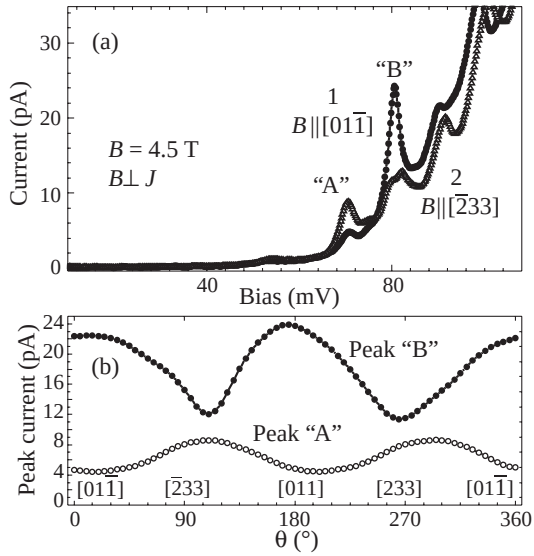

Fig. 3. (a) I(V) characteristics in an in-plaine magnetic field of 4.5 T. The first curve (cicles) is for $B\|[01\bar{1}]$; the second curve (triangeles) is for $B \parallel [\bar{2}33]$
(b) angular dependense of the peaks current.

associated with "B" (see Fig. 2(b)) at $B = 0$ T is due to the odd parity of the final state wavefunction, which corresponds to the first excited state of a QD. The applied magnetic field (i.e. the Lorentz force) effectively breaks the mirror symmetry at $B = 0$ and thus makes the transition *allowed*.

Figure 4 shows the spatial form of $G(B) \sim |\Psi_{\mathrm{QD}}(k_x, k_y)|^2$, in the plane for the two representative QD states corresponding to the labelled features in Fig. 2. The $\underline{k}$-values are estimated from relation (1), Δs assuming has nominal value of 63 nm consistent with the doping profile and composition of the device. The contour plots reveal clearly the characteristic form of the probability density distribution of a ground state orbital and the characteristic lobes of the higher energy states of the QD. The electron wavefunctions have

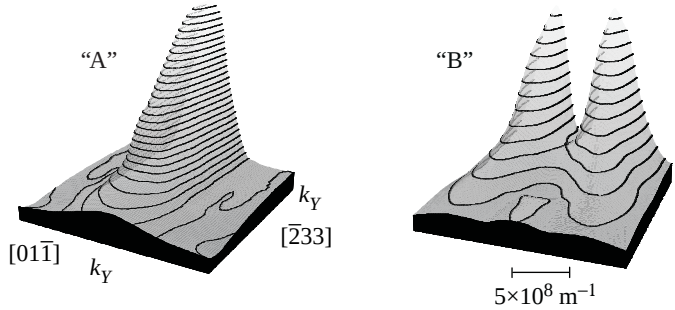

Fig. 4. Dependence of G on magnetic field for B parallel and antiparallel to $[01\bar{1}]$ for the different QDs states.

a biaxial symmetry in the growth plane, with axes corresponding quite closely (within measurement error of 15°) to the main crystallographic directions $X-$ and $Y-$ for (311)B-substrate orientation.

We have shown that magnetotunnelling spectroscopy provides us with a new means of probing the spatial form of the wavefunctions of electrons confined in zero-dimensional quantum dots. The technique exploits the effect of the classical Lorentz force on the motion of a tunnelling electron and can be regarded as the momentum $\underline{k}$-space analogue of STM imaging. The technique is both non-invasive and non-destructive and allows to spatial probe quantum states that are buried hundreds of nanometers below the surface.

Acknowledgements

The work is supported by Russian Foundation for Basic Research (00-02-17903) and (01-02-17844) and APS 3.11.99. EEV gratefully acknowledge supports from the Royal Society. We are grateful to V. V. Belov and A. Veretennikov for technical assistance.

References

[1] D. Bimberg, M. Grundmann and N. N. Ledentsov, *Quantum Dot Heterostructures* (John Wiley & Sons, New York, 1999).
[2] R. K. Hayden et al., *Phys. Rev. Lett.* **66**, 1749 (1991).
[3] P. H. Beton et al., *Phys. Rev. Lett.* **75**, 1996 (1995).

9th Int. Symp. "Nanostructures: Physics and Technology"
St Petersburg, Russia, June 18–22, 2001

A study of semiconductor quantum structures by microwave modulated photolumenescence

R. Gulyamov†, *E. Lifshitz*†, E. Cohen‡, A. Ron† and H. Shtrikman§
† Department of Chemistry and Solid State Institute, Technion, Haifa, 32000, Israel
‡ Department of Physics and Solid State Institute, Technion, Haifa, 32000, Israel
§ Department of Condensed Matter Physics, The Weizmann Institute of Science, Rehovot, Israel

Abstract. Mixed types I–type II multiple quantum wells structures consist of alternating narrow- and wide GaAs wells (WW and NW), separated by AlAs barriers. Transfer of electrons from the narrow- to the wide well results in the formation of two-dimensional electron and hole gases (2DEG and 2DHG) at the WW and NW, respectively. The present study investigated the influence of the 2DEG and the 2DHG on the optical properties of the materials. The study utilized two modulations techniques: double beam photoluminescence and microwave modulated PL, offering high-resolution spectroscopy, control of the density of the gases and their kinetic energy. The results showed that the existence of the low density 2DEG in the wide well cause the formation of trions or plasma-like recombination. In addition, electrons transfer through the barrier leads to a barrier-NW indirect recombination emission. The latter is influenced by an electrostatic potential induced by the two-dimensional gases.

1. Introduction

The optical properties of quantum well (QW) structures, containing a two-dimensional electron and hole gases (2DEG and 2DHG), have a scientific and technological importance [1, 2]. The influence of those gases are studied in mixed type I–type II quantum wells (MTQW) structure, enabling the control of the electron-density (n_e) between $10^{10}-10^{11}$ carriers/cm^2 by optical pumping [4–7].

The present study utilized MTQW's structure that is drawn schematically in Fig. 1(a). This structure consists of a sequence of alternating narrow- and wide GaAs wells, separated by AlAs barriers [1]. Furthermore, it is designed in such a way that the lowest Γ state of the GaAs narrow well (NW) is higher in energy than the lowest X state of the adjacent AlAs layer, leading to type II alignment. However, the last X state is energetically higher than the Γ state of the wide GaAs well (WW), creating type I alignment. Then, photocreated electron–hole pairs become spatially separated by a rapid ($\sim$30 ps). $\Gamma - X - \Gamma$ electron transfer from the NW to the WW. Conversely, the hole tunneling through the barrier occurs in the millisecond range, thus leading to a temporary accumulation of the 2DEG in the WW. The present study describes our attempts to follow the interactions of the 2DEG and 2DHG with other photogenerated species. The results revealed the existence of the following events: (a) attachment of an excess electron to an existing exciton in the WW, to form a negatively charged specie, named a trion [4, 5]; (b) direct recombination of an ensemble of free electrons with an existing hole within the WW, forming a plasma-like emission band [5, 7]; (c) indirect recombination between electron in the barrier X state and the 2DHG in the NW. The present study utilized double beam photoluminescence (PL) and microwave modulated PL (MMPL) for the study of the aforementioned processes.

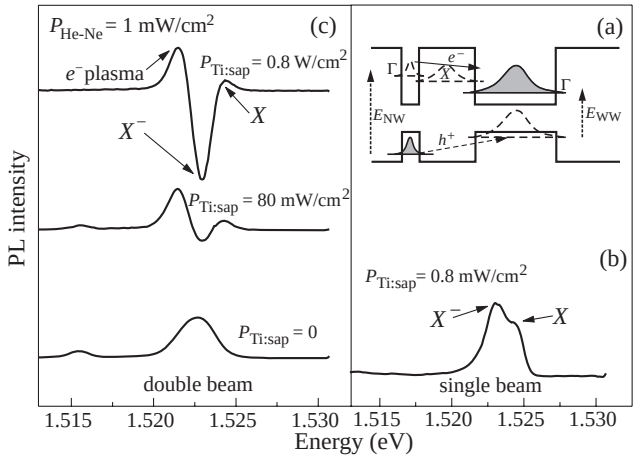

Fig. 1. Schematic energy band diagram of MTQW structure (a), PL spectrum under Ti: sapphire laser excitation (b), and PL spectra under double beam excitation with modulation of the He-Ne laser (c).

2. Experiment

A MTQW structure, consisting of 30 periods of alternating, wide (198 Å) and narrow (26 Å) GaAs wells, separated by 102 Å width AlAs barriers, have been used in the present research. The sample was placed in a microwave (mw) resonance cavity (operating at 10.755 GHz), which by itself was mounted in the liquid-He dewar with a superconductive magnet (up to 3 T). The mw power dissipation within the cavity at 0-dB attenuation was about 55 mW, however only 2% of it was absorbed by the sample.

The electron–hole pairs in the NW were generated by nearly resonance excitation with $E_{\text{L1}} = 1.96$ eV, by a He–Ne laser. The excitons in the WW were generated by nearly resonance excitation with E_{WW}, by a Ti sapphire (1.62 eV) laser. Accumulation of electrons in the barrier was formed by excitation with an Ar^+ (2.41 eV) laser. The single beam, double beam and mw modulated PL spectra, were all recorded at 1.4 K. In addition, in the double beam experiment, both lasers impinged on the same spot of the sample.

3. Results and discussion

A representative PL spectrum of the MTQW structure, excited at $E_{\text{L1}} = 1.96$ eV, is shown in Fig. 1(b). It consists of exciton (X) and trion (X^-) bands, centered at 1.524 eV and separated by 1.7 meV. A PL spectrum of the MTQW structure, excited at E_{NW}, is shown in Fig. 1(c) (bottom curve). It is dominated by a broad and featureless band, associated with the recombination between large density of 2DEG (generated with E_{NW}) and holes in the WW. It should be noted that this plasma-like band extends to lower energy than the corresponding exciton and trion, due to the re-normalization of the conduction band, occurring at large n_{e} [7]. The weak band at 1.515 eV corresponds to a bulk GaAs substrate and will not be discussed any further.

The double beam PL spectra, recorded at two different excitation powers ($E_{\text{L1}} = 1.96$ eV and $E_{\text{L2}} = 1.62$ eV) are shown in the middle and top curves of Fig. 1(c). It is seen that a modulation of n_{e} leads to difference spectra resolving the exciton (high energy and positive), trion (negative) and distinct plasma (low energy and positive) bands. The quenching of the trions population corresponds to their dissociation under intense flux of n_{e} and their conversion into excitons and plasma species [7].

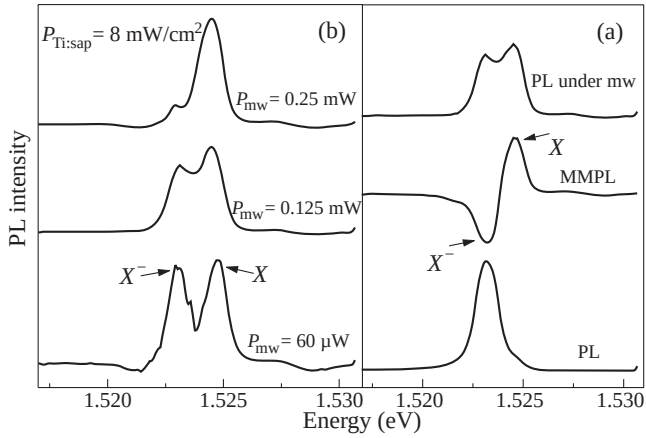

Fig. 2. The MMPL spectrum evolution as indicated in the text (a), PL spectra excited by Ti: sapphire laser under mw radiation at different mw powers (b).

The evolution of a MMPL spectrum is shown in Fig. 2(a). The bottom curve corresponds to a conventional PL spectrum, excited at E_{WW} with 8 mW/cm^2. A trion band dominates it, while the exciton emission is hardly resolved at this excitation power. The PL spectrum recorded under the influence of a mw radiation is shown at the top curve of Fig. 2(a), while the difference spectrum, labeled as MMPL, is shown in the middle curve. One can see that mw absorption causes a decrease of X^- with simultaneous increase of the X band. This is due to the induced collisions between mw-heated 2DEG with the trions that consequently lead to the dissociation of X^-. An absorption of 60 μW of mw power by the sample, still equalize population of excitons and trions in the WW (Fig. 2(b), bottom curve), however above this power, most of the trions dissociated and thus, the spectrum is dominated by the X band (middle and top curve in Fig. 2(b)). It should be noted that n_e is relatively small under E_{WW} excitation and therefore, the plasma band is not pronounced under the MMPL experimental conditions.

As indicated at the introduction, the electron transfer via the $\Gamma-X-\Gamma$ cascade of states results in a pause of 30 ps at the barrier. At this time, electrons make indirect recombination with the 2DHG in the N. Representative PL spectra of those indirect transitions are shown in Fig. 3. The spectra contain two groups, each consists of two bands, as labeled in the figure.

Recording the indirect transitions at various laser excitation powers (Fig. 3(a)) or strength of an external magnetic field (Fig. 3(b)) showed a minor influence on group II and pronounced change of group I. Group II was assigned to recombination processes at interface defects and will not be discussed any further. While group I corresponds to the recombination between the barrier X_{xy} (centered 1.752 eV) and the X_z (centered at 1.756 eV) with the 2DHG in the NW. Figure 3 suggests a blue shift of the X state-NW transitions and increase in their intensity with an increase in the laser or magnetic field strength. Our calculations [8] show that the blue shift is associated with an electrostatic potential induced by the 2DHG and 2DEG on both sides of the barrier. The latter leads to a blue shift of the X_{xy} and the X_z states (when the X_{xy} state exhibit a larger shift due to a smaller effective mass).

The MMPL spectra of the indirect transitions are shown in Fig. 4(a). Quenching of the entire spectrum suggests enhancement of the barrier electrons into the WW and reduction of their lifetime at the barrier, thus reducing the probability of recombination with the 2DHG

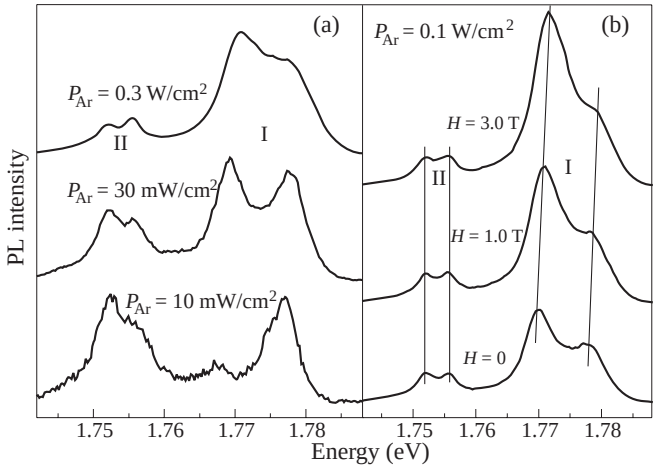

Fig. 3. PL spectra at the barrier energy range at different levels of Ar^+ laser excitation (a), and different magnetic fields (b)

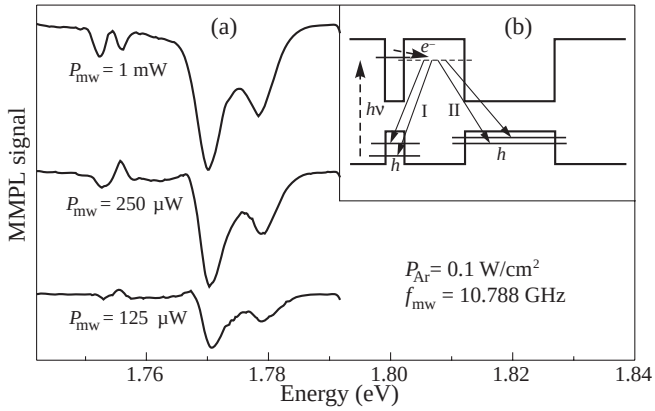

Fig. 4. MMPL spectra at the barrier energy range at different mw powers (a), recombination scheme, associated with the barrier (b).

in the NW, as shown schematically in Fig. 4(b).

Acknowledgements

The Project was supported by the Israel Ministry of Scinece and was conducted at the Technion Barbara and Norman Seiden Advanced Optoelectronics Research Center.

References

[1] I. Galbraith, P. Dawson and C. T. Foxon, *Phys. Rev. B* **45** (23), 13499 (1992).
[2] G. Finkelstein, H. Shtrikman and I. Bar-Joseph, *Phys. Rev. B* **56** (16), 10326 (1997).
[3] A. Manassen, et al., *Phys. Rev. B* **54**(15), 10609 (1996).
[4] Arza Ron, et al., *Solid State Commun.* **97** (9), 741 (1996).
[5] R. Harel, et al., *Phys. Rev. B* **53** (12), 7868 (1996).
[6] A. Manassen, et al., *Superl.& Microstr.* **15** (2), 175 (1994).
[7] A. Manassen, et al., *Surf. Sci.* **361/362**, 443 (1996).
[8] R. Guliemov, E. Lifsthiz, E. Cohen, A. Ron and L. Pfeiffer, *Phys. Rev. B* (2001) in press.

9th Int. Symp. "Nanostructures: Physics and Technology"
St Petersburg, Russia, June 18–22, 2001

Stoichiometry and atomic concentration depth profiles in InAs/Si quantum dot systems by Rutherford backscattering spectroscopy and secondary ion mass spectroscopy

H. Karl†, A. Wenzel†, B. Stritzker†, R. Claessen†, V. N. Strocov†,
G. E. Cirlin‡§, V. A. Egorov‡§, N. K. Polyakov‡§, V. N. Petrov‡§,
V. M. Ustinov§, N. N. Ledentsov§, Zh. I. Alferov§
† Universitat Augsburg, D-86135 Augsburg, Germany
‡ Institute for Analytical Instrumentation RAS, 198903 St. Petersburg, Russia
§ Ioffe Physico-Technical Institute, St Petersburg, Russia

Abstract. Stoichiometry and atomic concentration distributions for MBE grown systems of InAs quantum dots buried in a Si matrix has been studied using Rutherford Backscattering spectroscopy and Secondary Ion Mass Spectroscopy depth profiling. We have found a significant excess of As atoms which under elevated temperatures diffuse into the Si matrix despite of a larger ionic radius. This may affect the band alignment on the QD/matrix interface. Our findings suggest improvements of the MBE growth process for InAs/Si and similar systems.

Si based devices predominate modern microelectronics. This material can however not be immediately used for light-emitting devices due to its indirect band gap, which limits the luminescence efficiency. Several approaches are under development to incorporate optoelectronics into the widespread Si technology. One of them is to embed semiconductor nanocrystals having a narrow direct band gap into a Si matrix. Accumulation of the electrons and holes in the nanocrystals requires a proper band alignment relative to the matrix, which in many cases is critically influenced by a strain imposed by a lattice mismatch [1]. It is anticipated, that the luminescence efficiency can be increased, if an atomlike discrete electronic spectrum is formed by the confining potential in the nanocrystals - quantum dots (QDs).

Characterization of QD nanocrystals is a challenging task, because they are normally buried under a capping layer having a thickness of some tens of nanometers. Usually Transmission Electron Microscopy (TEM) is used, but it is less sensitive to the stoichiometry and atomic concentration distributions, including point defects (e.g. interstitial inclusions). Here we report on studies of these aspects of InAs/Si QD systems using Rutherford Backscattering Spectroscopy (RBS) and Secondary Ion Mass Spectroscopy (SIMS). The first method is able to reach buried atomic layers non-destructively and to quantitatively determine their atomic content.

We report on RBS and SIMS measurements on a system of InAs nanocrystals grown by MBE in a Si matrix [1]. This system is particularly interesting, because a strain induced by the lattice mismatch between InAs and Si is presumably crucial for formation of the band alignment required for the carrier accumulation in the QDs. The obtained results on stoichiometry and atomic concentrations are helpful for further optimization of the growth process for these and similar systems.

The InAs/Si samples were grown on highly-oriented Si(100) substrates using an EP1203 (Russia) MBE machine. Thermal desorption of native silicon oxide before growth was achieved by heating the substrate up to 830°C-870°C for 15 min. After that well resolved

(2×1) or mixed (1×2) and (2×1) surface reconstructions, typical for cleaved Si(100) surfaces, were observed. The substrate was then cooled down to the required growth temperature, and deposition of InAs was initiated. The InAs deposition rate was typically 0.1 monolayers (ML) per second. Calibration of the growth rate, the As-to-In flux ratio, and monitoring of the surface morphology during growth was performed using Reflection High-Energy Electron Diffraction (RHEED). The as-grown InAs nanocrystals, as revealed by STM [2], are pyramids with lateral dimensions of $\sim$ 12 × 20 nm and a heights of $\sim$4 nm. They are placed randomly and occupy $\sim$50% of the substrate area. Just after the InAs deposition, a 10–20 nm thick Si capping layer was grown at the same substrate temperature. The growth was followed by annealing at 650–700°C lasting 10 min. Then an additional 20–40 nm thick Si capping layer was grown at the same temperature. It was followed by annealing at 700–800°C for 10 min in order to activate migration of the surface atoms and smoothen the resulting Si surface. The grown samples were characterized by photoluminescence (PL) spectroscopy, which revealed spectral peaks originated from the InAs QDs [3].

The RBS measurements were performed on a few InAs/Si samples with a nominal InAs layer thickness of 2 and 2.5 monolayers, respectively, and a Si capping layer thickness of $\sim$15 nm. He^+ ions with the energy of 1.5 MeV were used in the primary beam, which allowed to probe to depths much larger than the thickness of the capping layer. A typical RBS spectrum is shown in Fig. 1. It is taken for a representative sample containing a 2.5 ML thick InAs layer grown at 400°C, which was capped by a 16 nm thick Si layer grown at approximately the same temperature and annealed at 780°C for 10 min. The spectrum reveals the depth distribution and the amount of material of the different atomic species. The measured spectra shows well-separated peaks of As and In (see the main pane of Fig. 1) and a steep increase in the backscattering yield at lower energies due to the Si matrix (insert). The ratio of the areas below the As and In peaks, weighted with the corresponding backscattering cross-sections proportional to Z^2, directly gives the ratio of the number of the As to In atoms incorporated.

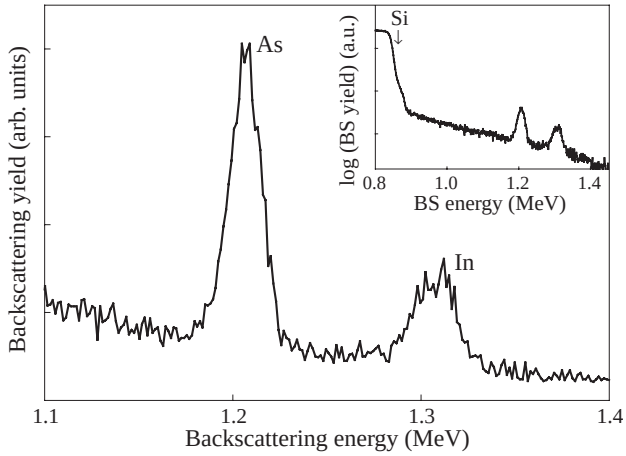

Fig. 1. A portion of the RBS spectrum taken on a representative InAs/Si sample, showing the signals of As and In. The insert shows the entire energy range. The steep increase in backscattering yield below 0.9 MeV is due to the Si matrix.

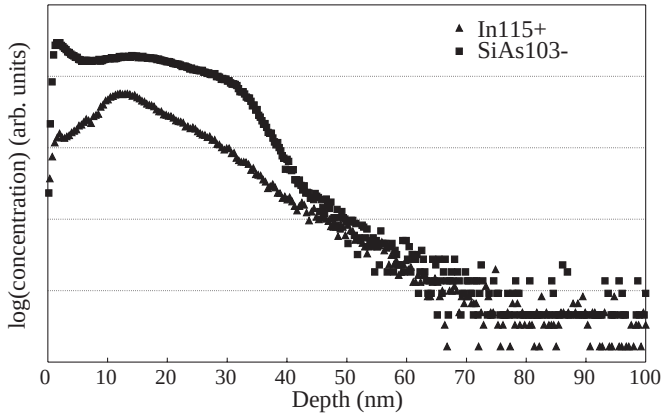

Fig. 2. SIMS depth profiles of $^{115}In^{+}$ measured by O^{2+} sputtering and $^{103}SiAs^{+}$ measured by Cs^{+} sputtering. In both cases the ion beam energy was 3 keV. The sample is the same as in Fig. 1. A clear change in the slope of the As profile indicates diffusion of excess As atoms into the Si substrate.

The In-to-As ratio N_{As}/N_{In} was determined within the accuracy of about 1%. Surprisingly, we have found that there was ∼5 times more As than In and even more, depending on the preparation condition. As the nanocrystalline InAs in the QDs have nevertheless the ideal stoichiometry, as indicated by high-resolution TEM [4], the excess As atoms must be diluted in the surrounding epitaxially grown Si capping layer and substrate without affecting the properties of the QDs. Apart from possible small excess of As during growth of the InAs layer, these As atoms were apparently built in during MBE growth of the capping layers, as the partial pressure of As_4 after closing the shutter of the source decreases rather slowly. Due to elevated temperatures during the growth and annealing steps the As atoms could then diffuse over the capping layer and even into the substrate.

The elemental depth distributions could also be extracted from the RBS spectra using a fitting procedure. We however used for this purpose dynamic SIMS depth profiling which has a higher depth resolution. The area density of As and In, evaluated from a fit to the RBS-spectra, was used to calibrate the SIMS depth profiles in absolute In and As concentrations allowing thus their direct comparison. The depth scale was calibrated using stylus profiler measurements of the sputtered crater depths. Typical SIMS-spectra of In and As are shown in Fig. 2.

The SIMS-profiles within a depth region of ∼5 nm from the surface are distorted by surface effects due to non-stationary sputtering conditions and a layer of native silicon oxide formed during storage in air. Upon passing of the InAs layer the In and SiAs signals do not drop abruptly, because a certain amount of sputtered material remains on the surface and is driven into the surface by knock-on collisions. However, a distinct peculiarity of the As spectrum is that it decays to larger depths with two different rates. While the background decay can be explained by the knock-on collisions, the slower decay next to the maximum indicates diffusion of As atoms into the substrate. This finding is particularly interesting in view of the As atomic radius being larger than the Si one. It hints to an anomalous diffusion mechanism of As in Si. This effect, previously neglected, should be taken into account in the MBE growth. For example, a pause after the InAs growth followed by flashing off the adsorbed As atoms could be introduced before deposition of the Si capping layer. The excess As atoms can act as additional dopants in the Si matrix around the QDs and thus

influence the band alignment.

Summarizing, we have determined the stoichiometry and atomic concentration distributions in the MBE grown samples of InAs QDs buried in a Si matrix using non-destructive RBS measurements and SIMS depth profiling. A significant excess of As atoms built in during the growth of the capping layers has been found. Under elevated growth and annealing temperatures the As atoms diffuse into the Si matrix despite of their larger ionic radius. These findings can help to optimize the MBE growth process for InAs/Si and similar systems.

References

[1] G. E. Cirlin, V. N. Petrov, V. G. Dubrovskii, S. A. Masalov, A. O. Golubok, N. I. Komyak, N. N. Ledentsov, Zh. I. Alferov and D. Bimberg, *Tech. Phys. Lett.* **24**, 290 (1998).

[2] G. E. Cirlin, V. G. Dubrovskii, V. N. Petrov, N. K. Polyakov, N. P. Korneeva, V. N. Demidov, A. O. Golubok, S. A. Masalov, D. V. Kurochkin, O. M. Gorbenko, N. I. Komyak, V. M. Ustinov, A. Yu. Egorov, A. R. Kovsh, M. V. Maximov, A. F. Tsatsul'nikov, B. V. Volovik, A. E. Zhukov, P. S. Kop'ev, Zh. I. Alferov, N. N. Ledentsov, M. Grundmann and D. Bimberg, *Semicond. Sci. Technol.* **13**, 1262 (1998).

[3] R. Heitz, N. N. Ledentsov, D. Bimberg, A. Yu. Egorov, M. V. Maximov, V. M. Ustinov, A. E. Zhukov, Zh. I. Alferov, G. E. Cirlin, I. P. Soshnikov, N. D. Zakharov, P. Werner and U. Gösele, *Appl. Phys. Lett.* **74**, 1701 (1999).

[4] N. D. Zakharov, P. Werner, U. Gösele, R. Heitz, D. Bimberg, N. N. Ledentsov, V. M. Ustinov, B. V. Volovik, Zh. I. Alferov, N. K. Polyakov, V. N. Petrov, V. A. Egorov and G. E. Cirlin, *Appl. Phys. Lett.* **76**, 2677 (2000).

9th Int. Symp. "Nanostructures: Physics and Technology"
St Petersburg, Russia, June 18–22, 2001

Scanning tunneling spectroscopy study of three-dimensional nanoscale silicon and platinum assemblies in an opal matrix

C. Díaz-Guerra†, V. G. Golubev‡, *D. A. Kurdyukov*‡, A. B. Pevtsov‡, J. Piqueras† and M. V. Zamoryanskaya‡

† Departamento de Fisica de Materiales, Facultad de Fisicas, Universidad Complutense, E-28040 Madrid, Spain

‡ Ioffe Physico-Technical Institute, St Petersburg, Russia

Abstract. Regular systems of Si and Pt nanoclusters have been fabricated in a void sublattice of artificial opal. To incorporate Si into opal voids the thermal CVD technique is used. The samples are filled with Pt from a solution of $PtCl_4$ in ethanol to fabricate metal contacts to silicon. STM and STS are used to investigate the local electronic behavior of Pt-Si nanostructures. It is shown that Si and Pt are regularly distributed inside the opal voids and form nanoscale metal-semiconductor-metal junctions.

Introduction

Synthetic opals, which are composed of ordered amorphous SiO_2 spheres, have attracted interest in the past years because of potential applications of these systems in optoelectronics. Some applications relate to the photonic band gap phenomenon [1]. On the other hand, synthetic opal has a regular sublattice of submicron channels and voids permitting us to obtain three-dimensional (3D) assemblies of Si nanostructures in opal matrices which can be used as the basis of objects for microelectronics, e.g., solid state devices with p-n junctions or Schottky diodes. For the fabrication of opal-based Si solid-state electronic devices it is necessary to deposit a homogeneous layer on the internal surface of the voids and to create metallic contacts. Feoktistov et al [2] have formed Pt-Si contacts by coating the silica spheres with a Pt layer before embedding in Si and demonstrated the possibility of creating 3D multilayer semiconductor structures (p-n junctions or Schottky barriers) on the inner surface of the opal voids. These authors [2, 3] obtained 3D cluster systems with cluster sizes ranging from 1 to 100 nm and a density of elements as high as 10^{14} cm^{-3}. In the present work we use scanning tunneling microscopy (STM) and a spatially resolved scanning tunneling spectroscopy (STS) technique, namely current imaging tunneling spectroscopy (CITS) [4], to investigate the local electronic properties of the opal-Pt-Si samples used in Refs. [2, 3].

1. Experimental details

The opals used in this work consist of SiO_2 spheres of about 250-nm-diameter forming a fcc lattice. The sizes of the octahedral and tetrahedral voids in this lattice are of about 100 and 50 nm, respectively. For the preparation of the opal-Pt-Si samples, the opals were embedded first with Pt and then with Si following the procedure described in Ref. [2]. The fill factors of Si and Pt evaluated from electron probe microanalysis results were 65% and 25%, respectively. Transmission electron microscopy (TEM) has shown [2] that on the surface of the silica spheres different distributions of Pt may result. In some cases,

Pt particles in the range of several nanometers and in different stages of coalescence are observed, while it is also possible to obtain a uniform Pt layer of 5–6 nm thickness. In the samples used in this work the spheres have a discontinuous Pt distribution on their surface.

The samples were observed in the secondary electron mode of a Leica 440 scanning electron microscope (SEM). The STM used was a small size instrument fixed in the chamber of the SEM. The main features of this instrument are similar to the one previously described in [5]. The STM was operated in the constant-current and CITS modes using electrochemically etched or mechanically sharpened Pt-Ir wires as probe tips. CITS provides real space imaging of surface electronic states by recording I–V curves at fixed tip-sample separation at every pixel within an image. In addition to the I–V curves, current images can be formed by plotting the measured current at any voltage. Details of the CITS procedure used here have been described elsewhere [6]. In order to analyze the I–V data of the different points of an image, the normalized differential conductance $(\mathrm{d}I/\mathrm{d}V)/(I/V)$ spectra were used. This quantity removes most of the exponential dependence of tunneling current on tip-sample separation [7] and is proportional to the surface density of states [8, 9].

2. Results and discussion

Figure 1(a) is the STM image, obtained under an applied bias of 0.9 V and 0.3 nA tunneling current, of the contact region of three spheres. The $(\mathrm{d}I/\mathrm{d}V)/(I/V)$ curves recorded on the free surface of the spheres, like the region marked as 1 in Fig. 1(a), show a conduction behavior that depends on the point considered (Fig. 1(b), curves 1, 2). Two different kinds of curves are obtained; one represents a metallic conduction [curve (1)] and is related to the existence of Pt clusters. The other one, in which a surface band gap of about 1 eV is observed, indicates the presence of Si [curve (2)]. In the contact region of the spheres (labeled as 2 in Fig. 1(a)) a more complex behavior has been observed. In addition to the curves attributed to Pt and Si, other curves reveal the existence of surface band gaps in the range 0.5–0.8 eV. An example of this behavior is shown in Fig. 1(b), curve 3. We tentatively explain this result by considering the different species detected in these regions by TEM [2], where the experimentally measured interplanar distances on high-resolution images demonstrated the presence of Pt and Si, but interplanar distances which could not be related to these elements were measured as well. By comparison of the unidentified interplanar distances with those of Pt-Si compounds, close matchings were observed with the $Pt_{12}Si_5$ tetragonal phase and the PtSi hexagonal phase. The formation of the $Pt_{12}Si_5$ phase can take place during the thermal treatment of filled opal fabrication at temperatures at which this phase is formed from Pt deposited on Si wafers [10]. The band gaps in the range 0.5–0.8 eV, measured by tunneling spectroscopy in the area of contact between spheres, could be related to the presence of Pt silicides. This suggestion is also supported by theoretical calculations on the electronic structure of silicides, in which band gaps narrower than that corresponding to Si were predicted [11].

Another specific feature of the conductance measurements performed in these regions is the appearance in some of the curves ($\sim$ 20% of the total analyzed) of negative differential conductance around $+2.2$ V applied bias voltage (Fig. 2(a)). This effect has been previously reported in tunneling spectroscopy investigations of ultrathin oxide films on Si [12].

The differences in the electronic properties of different regions of the sample, revealed in the $(\mathrm{d}I/\mathrm{d}V)/(I/V)$ curves, are also appreciated in the CITS images. Figure 2(b) shows a CITS image of an opal sample in which an enhanced contrast at the periphery of the spheres, related to local conductance variations, can be clearly observed. In those areas like that marked as 3 in Fig. 1(a) the differential conductance curves show frequently the

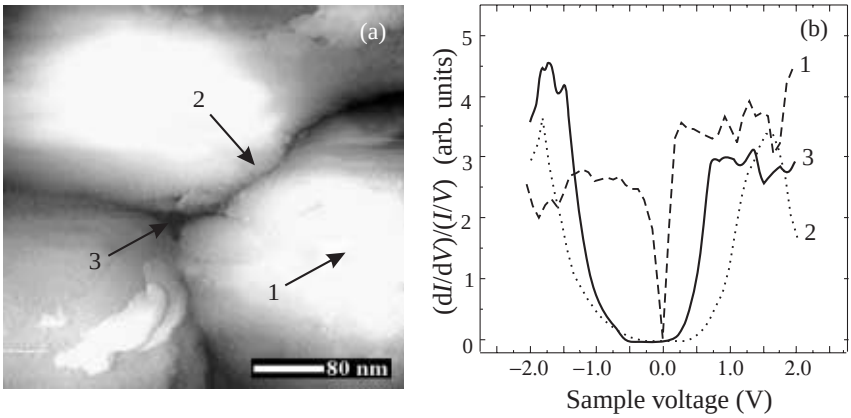

Fig. 1. (a) Constant current STM image showing the contact region of three spheres of an opal. (b) The $(\mathrm{d}I/\mathrm{d}V)/(I/V)$ spectra recorded at regions marked in Fig. 1(a). Curves 1 and 2 are usually obtained at regions marked as 1 in the image. Curve 3 is usually recorded at regions labeled 2 in the figure. Spectra obtained at regions labeled as 3 are similar to curve 1.

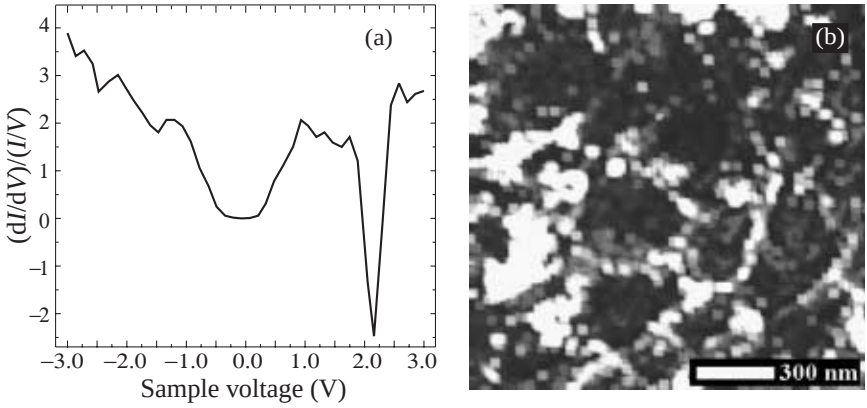

Fig. 2. (a) The $(\mathrm{d}I/\mathrm{d}V)/(I/V)$ curve, showing negative differential conductance at about +2.2 V sample voltage, recorded at the contact region of two spheres of a sample. (b) CITS image acquired at −1.75 V sample voltage in one of the opals. Gray scale range is 2.9 nA.

same metallic behavior shown in Fig. 1(b) (curve 1). This result agrees with the presence of bigger Pt particles observed by TEM in these regions.

3. Conclusions

A 3D regular lattice of Pt-Si nanostructures fabricated using an opal matrix has been characterized by STS. The conductance behavior of the structure has been analyzed with high spatial resolution to determine the presence of Pt and Si in the different regions of the sample. Using STM and spatially resolved STS technique the local electronic properties of opal-Pt-Si composites have been investigated. CITS measurements allowed us to study the I–V behavior and the band gaps in different places of the structure and to observe nanoscale active semiconductor elements.

Acknowledgements

This work was supported by DGES (Project No. PB96-0639) and the Russian R&D program "Nanostructures" (Grant No. 97-2016).

References

[1] Photonic Band Gap Materials, ed. by C. M. Soukoulis. Advanced Studies Institute of NATO, Ser. E, vol. 315 (Kluwer, Dordrecht, 1996).
[2] N. A. Feoktistov, V. G. Golubev, J. L. Hutchison, D. A. Kurdyukov, A. B. Pevtsov, R. Schwarz, J. Sloan and L. M. Sorokin, *Abstr. Mater. Res. Soc. Spring Meeting*, A24.4.1 (2000).
[3] V. N. Bogomolov, N. A. Feoktistov, V. G. Golubev, J. L. Hutchison, D. A. Kurdyukov, A. B. Pevtsov, R. Schwarz, J. Sloan and L. M. Sorokin, *J. Non-Cryst. Solids* **266-269**, 1021 (2000).
[4] R. J. Hamers, R. M. Tromp and J. E. Demuth, *Phys. Rev. Lett.* **56**, 1972 (1986).
[5] A. Asenjo, A. Buendía, J. M. Gómez-Rodríguez and A. Baró , *J.Vac.Sci. Technol. B* **12**, 1658 (1994).
[6] G. Panin, C. Díaz-Guerra and J. Piqueras, *Appl. Phys. Lett.* **72**, 2129 (1998).
[7] J. A. Stroscio, R. M. Feenstra and A. P. Fein, *Phys. Rev. Lett.* **57**, 2579 (1986).
[8] N. D. Lang, *Phys. Rev. B* **34**, 5947 (1986).
[9] R. M. Feenstra, J. A. Stroscio and A. P. Fein, *Surf. Sci.* **181**, 295 (1987).
[10] B. Tsui and M. Chen, *J. Appl. Phys.* **68**, 6246 (1990).
[11] O. Bisi and C. Calandra, *J. Phys. C* **14**, 5479 (1981).
[12] H. Watanabe, K. Fujita and M. Ichikawa, *Appl. Phys. Lett.* **72**, 1987 (1998).

9th Int. Symp. "Nanostructures: Physics and Technology"
St Petersburg, Russia, June 18–22, 2001

Theory of electrostatic probe microscopy: a simple perturbative approach

S. Gómez-Moñivas†, L. S. Froufe†, *J. J. Sáenz*†, R. Carminati‡ and J. J. Greffet‡

† Departamento de Física de la Materia Condensada and Instituto de Ciencia de Materiales "Nicolás Cabrera", Universidad Autónoma de Madrid, Cantoblanco, 28049 Madrid, Spain

‡ Laboratoire d'Energétique Moléculaire et Macroscopique, Combustion; Ecole Centrale Paris, Centre National de la Recherche Scientifique, 92295 Châtenay-Malabry Cedex, France

Abstract. A theoretical approach to electrostatic scanning probe microscopy is presented. We show that a simple perturbation formula, originally derived in the context of scattering theory of electromagnetic waves, can be used to obtain the capacitance and the electrostatic force between a metallic tip and an inhomogeneous dielectric sample. For inhomogeneous thin dielectric films, the scanning probe signal is shown to be proportional to the convolution between an effective surface profile and a response function of the microscope. This provides a rigorous framework to address the resolution issue and the inverse problem.

Introduction

Since the development of Scanning Tunneling Microscopy and Atomic Force Microscopy in the early eighties various techniques of Scanning Probe Microscopy (SPM) have been proposed [1], based on different local interactions between a sharp tip and the sample under study. The long range nature of electrostatic interactions makes them specially suitable to perform noncontact SPM imaging of both conducting and insulating materials. By applying a voltage between a force microscope tip and a sample, electrostatic force microscopy (EFM) has been used to study capacitance , surface potential , charge or dopant distribution, topography and dielectric properties of metallic and insulating surfaces . . . [2].

As in other SPM techniques, the interpretation of the EFM images is not always evident. Since EFM is a nonlocal technique due to the long range nature of the electrostatic interaction, the detailed shape and dimensions of the tip must then be taken into account for a precise calculation of both force and capacitance [3]. Most of the theoretical work on EFM has been focused on a better understanding of tip shape effects on the electric field, force and capacitance [4, 5]. Although the influence of the tip shape is now more or less well understood for flat and homogeneous samples, there is no simple way to directly relate the electrostatic image with the dielectric and topographic properties of the sample. In this work, we propose a theoretical approach to electrostatic probe microscopy that represents a first step to fill this gap [2]. In analogy with previous theoretical work on scanning near-field optical microscopy (SNOM) [6], we will show that the EFM image is related to both the topography and dielectric inhomogeneities of the sample through a response function which describes all the instrument properties. In the important case of imaging of thin dielectric films deposited on metallic substrates, we show that the force (or capacitance)

signal closely follows an *equivalent surface profile*. This equivalent surface profile connects the film topography with the dielectric inhomogeneities, providing a simple physical picture of the contrast mechanism in EFM.

1. Perturbative approach

We consider a three-dimensional sample with both topographic and dielectric constant inhomogeneities (see Fig. 1). This sample is a finite layer of profile $Z(x, y) = Z(\mathbf{r}_{||})$ and dielectric constant $\epsilon(\mathbf{r})$ on top of a reference sample. For simplicity, we will take a semiinfinite homogeneous ($z > 0$) substrate of dielectric constant ϵ_s as the reference sample. Our approach would equally apply to any reference sample surface with known dielectric response, however.

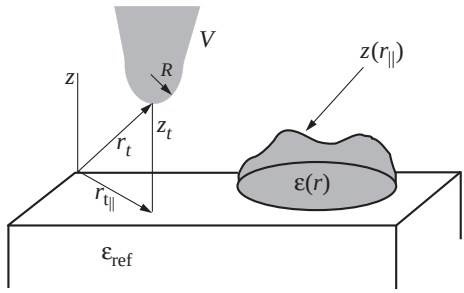

Fig. 1. Schematic configuration of an EFM.

Under a constant tip-sample bias V, the electrostatic energy of the reference system (i.e. in the homogeneous case), is given by:

$$U_0 = \frac{1}{2}\int \epsilon_0 \mathbf{E_0}^2 d^3\mathbf{r} = \frac{1}{2} C_0 V^2 \tag{1}$$

where $\mathbf{E_0}$ is the electric field and C_0 is the capacitance. The electrostatic force (normal to the sample surface) F_{0z} can be written as the energy gradient:

$$F_{0z} = -\frac{\partial}{\partial z} U_0 = -\frac{1}{2} V^2 \frac{\partial}{\partial z} C_0 \tag{2}$$

The presence of surface or volume inhomogeneities induces a change in the electrostatic energy (with respect to the reference sample),

$$\Delta U = -\frac{1}{2}\int_{\mathcal{V}} \mathbf{P} \cdot \mathbf{E_0} d^3\mathbf{r} \tag{3}$$

where $\mathbf{E_0}$ is the reference field and $\mathbf{P} = \epsilon_0(\epsilon(\mathbf{r}) - 1)\mathbf{E}$, being $\mathbf{E}$ the total field. In practice, computing the electrostatic energy (i.e. the force or/and the capacitance) from Eq. 3 requires the knowledge of the total selfconsistent field in the gap region. These are solutions of a difficult Laplace problem in an open geometry, which can only be solved numerically. In order to handle this problem we will make use of a simple perturbative approach which was shown to be useful in scattering from rough surfaces [7].

Following a simple Born-like approach one could replace the total field $\mathbf{E}$ in Eq. 3 by the nonperturbed field $\mathbf{E_0}$. However, this simple approach is known to give wrong results

in scattering from rough surfaces [7] One way to improve this approximation is to take into account the discontinuity of the normal component of the field at the boundaries [7]

$$\Delta U = -\frac{1}{2}\epsilon_0 \int_{\mathcal{V}_0} (\epsilon(\mathbf{r}) - 1) \left[\frac{E_{0z}^2}{\epsilon(\mathbf{r})} + \mathbf{E}_{0||}^2 \right] d^3\mathbf{r}. \tag{4}$$

The force signal (or the capacitance) is directly obtained from ΔU through $\Delta F = \partial \Delta U / \partial z_t$ (or $\Delta C = V^2 \Delta U/2$). Although, in general, it is only a perturbative result, it is worth noticing that this equation gives the exact result for a parallel plate capacitor.

2. Equivalent surface profile

In order to get a deeper understanding on the nature of the image contrast, let us consider a common experimental situation in which a dielectric soft sample is on a substrate with metallic character (i.e. $\epsilon_s \to \infty$). In this case, the electric field parallel to the substrate surface will be close to zero and the main contribution to the signal will come from the normal electric field. If the dielectric thickness is small compared with a typical field gradient length scale, i.e. $E_{0z}(\mathbf{r}_{t||} - \mathbf{r}_{||}, z_t - z) \approx E_{0z}(\mathbf{r}_{t||} - \mathbf{r}_{||}, z_t)$, the energy will take the simple form of

$$\Delta U \approx \frac{1}{2}\epsilon_0 \int_{\mathcal{S}_r} \left\{ Z_{eff}(\mathbf{r}_{||}) \cdot E_{0z}^2(\mathbf{r}_{t||} - \mathbf{r}_{||}, z_t) \right\} d^2\mathbf{r}_{||}, \tag{5}$$

where

$$Z_{eff}(\mathbf{r}_{||}) \equiv \int_0^{Z(\mathbf{r}_{||})} \frac{\epsilon(\mathbf{r}) - 1}{\epsilon(\mathbf{r})} dz \tag{6}$$

is an *equivalent surface profile* connecting the dielectric constant variation and the topography of the sample. The signal $\Delta F = \partial \Delta U / \partial z_t$ (or $\Delta C = V^2 \Delta U/2$) will then be a simple two-dimensional convolution between the equivalent surface profile Z_{eff} and the *response function of the microscope* $\mathcal{F}(\mathbf{r}_{||}) = \partial |E_{0z}(\mathbf{r}_{||}, z_t)|^2 / \partial z_t$. Notice that the actual image would give information about Z_{eff}. For a homogeneous sample, Z_{eff} is directly proportional to the true topographic profile, while for a flat surface it reflects an average of the dielectric constant along the normal to the surface.

3. Summary

In summary, we have presented a formalism for electrostatic force microscopy based on a modified first order perturbation theory. We have checked and illustrated our theory with exact numerical results for a model system. Our model describes how the topographic and dielectric constant variations of the sample influences the observed image in EFM. This is a very important point in EFM, were the purely dielectric properties of the sample are of great interest. In analogy with SNOM imaging, we have introduced the concept of equivalent surface profile as the physical measured quantity in force microscopy. We believe that the results in this Letter should find broad applications in the analysis of electrostatic imaging with scanning probe methods.

Acknowledgment

This work was supported by the french-spanish Integrated Program PICASSO and INTAS (Project No 97-10528).

References

[1] C. J. Chen, *Introduction to Scanning Tunneling Microscopy* (Oxford University Press, Oxford, 1993);
R. Wiesendanger, *Scanning Probe Microscopy and Spectroscopy: Methods and Applications* (Cambridge Univ. Press, Cambridge, 1994);
Scanning Tunneling Microscopy and Scanning Force Microscopy of Biological Samples, O. Marti and M. Amrein, eds (Academic Press, New York, 1993).

[2] S. Gómez-Moñivas, J.J. Sáenz, R. Carminati and J. J. Greffet, *Appl. Phys. Lett.* **76**, 2955 (2000) and references therein.

[3] H. W. Hao, A. M. Baró and J. J. Sáenz, *J. Vac. Sci. Technol B* **9**, 1323 (1991);
S. Watanabe, K. Hane, T. Ohye, M. Ito and T. Goto, *J. Vac. Sci. Technol. B* **11**, 1774 (1993);
S. Belaidi, P. Girard and G. Leveque, *J. Appl. Phys.* **81**, 1023 (1997);
S. Hudlet, M. Saint Jean, C. Guthmann and J. Berger, *Eur. Phys. J.* **2**, 5 (1998).

[4] G. Mesa, E. Dobado-Fuentes and J. J. Sáenz, *J. Appl. Phys.* **79**, 39 (1996);
G. Mesa and J. J. Sáenz, *Appl. Phys. Lett.* **69**, 1169 (1996).

[5] R. Carminati and J.-J. Greffet, *J. Opt. Soc. Am. A* **12**, 2716 (1995);
Ultramicroscopy **61**, 11 (1995);
J.-J. Greffet and R. Carminati, *Prog. Surf. Sci.* **56**, 133 (1997).

[6] G. S. Agarwal, *Phys. Rev. B* **14**, 846 (1976).

9th Int. Symp. "Nanostructures: Physics and Technology"
St Petersburg, Russia, June 18–22, 2001

Computational and experimental studies on strain induced effects in InGaAs/GaAs HFET structure using C–V profiling

M. F. Kokorev†, N. A. Maleev‡, D. V. Pakhnin†, A. E. Zhukov‡
and V. M. Ustinov‡

† Radioengineering and Electronics Department,
State Electrotechnical University, 197376 St Petersburg, Russia
‡ Ioffe Physico-Technical Institute, St Petersburg, Russia

Abstract. We analyze strain induced effects on the capacitance-voltage (C–V) profile for MBE grown GaAs/$In_{0.1}Ga_{0.9}As$/GaAs HFET structure. The calculations of C–V profile were made using a small-signal approach developed for the quantum well (QW) structures. The self-consistent numerical simulations and results of measurements show that strain causes significant changes in the electron distribution of the QW structure and its C–V profile.

1. Introduction

Capacitance-voltage (C–V) profiling is on of the methods for the investigation and design of heterostructures quantum-well (QW) electronic and optoelectronic devices [1–5]. This technique is used for determining band offsets at the heterointerface. In the case of the psedomorphic structures, in particular, the GaAs/$In_{0.1}Ga_{0.9}As$/GaAs system, with sufficiently thin central layer the lattice constant mismatch is accommodated by internal strains rather than by formation of misfit dislocations. The strains lead to two consequences: the shifts of the conduction and valence bands in the well for the structures grown in [100] direction [6] and the built-in piezoelectric field for the structures grown in [111] direction [7]. However, with the exception of the Ref. [2], the calculations of band offsets from C–V experimental data were made without the strain effect. At the same time, the strain is sufficient large and produces the important changes in interband optical transitions [6]. The purpose of this work is to study the strain effect in GaAs/$In_{0.1}Ga_{0.9}As$/GaAs quantum-well HFET structure using the self-consistent numerical simulations and to compare the theoretical results with the measured C–V profile. The new simulation technique of the C–V characteristics for QW structures based on the small-signal approach [8] is developed.

2. Experiment

Experimental sample was grown by molecular beam epitaxy using a Riber32P system. Undoped GaAs layer with thickness 0.5 mm was used as a buffer. The conductive channel consists of n-GaAs (10 nm) followed by n-InGaAs (25 nm) and n-GaAs (75 nm) layers. Structure was capped by n-GaAs contact layer. The channel composition was optimized to obtain high linearity of the static and dynamic HFET characteristics. The process sequence for device fabrication is listed bellow:

1. Source and drain AuGa/Ni/Au contacts formation;
2. Device isolation by mesa etching and following proton implantation;
3. Gate electrode formation (E-beam lithography, gate recess and Ti/Pt/Au metallization);
4. Device passivation and contact pads metallization.

C–V profile for Schottky diode test structures (100 mm in diameter) was obtained from capacitance-voltage measurements at 1 MHz.

3. Theoretical model

The C–V (or apparent) profile N_{ap} (W) is given as usual by:

$$N_{ap} = -\frac{C^3(V)}{e\varepsilon(dC/dV)}, W(V) = \frac{\varepsilon}{C(V)}\,, \tag{1}$$

where e is the electron charge, ε is the semiconductor permittivity, and V is the reverse bias voltage applied to the Schottky barrier. Capacitance $C(V)$ can be calculated as [8]:

$$C(V) = \frac{\varepsilon}{W(V)} = \varepsilon\left(\frac{\int_0^L z\Delta n(z,V)dz}{\int_0^L \Delta n(z,V)dz}\right)^{-1} = \varepsilon\left(\int_0^L z\rho(z,V)dz\right)^{-1}, \tag{2}$$

where z is the space coordinate, L is the total structure thickness, and $\Delta n(z, V)$ is the perturbation of electron concentration due to the small voltage variation ΔV, ρ is the distribution function for the perturbed space charge density. Usually the perturbation $\Delta n(z, V)$ is calculated as the difference beetwen two static states $n(z, V + \Delta V)$ and $n(z, V)$ [3, 4]. Such approach demands the high accuracy and, consequently, the considerable computer resources. Recently we reported about very effective simulation technique of the barrier capacitance for the classical structures based on the small-signal approximation [8]. Now we applied this technique to the QW structure. In this case the electron concentration distribution $n(z, V)$ must be determined as the sum of the 3D and 2D concentrations, this later is obtained by following expression:

$$n_{2D}(z,V) = \sum_{i=1}^{m} |\Psi_i(z,V)|^2 n_i(V)\,, \tag{3}$$

where m is number of bound states in QW, n_i is the electron occupation of state with eigenenergy E_i and wavefunction Ψ_i. The static 2D electron distribution is determined from the Schrödinger's equation. The Hamiltonian H in the effective-mass approximation for the conduction band can be written as [2]:

$$H = -\frac{\hbar^2}{2a(z)}\frac{d}{dz}\frac{a^2(z)}{m(z)}\frac{d}{dz}\frac{1}{a(z)} + V_{ef}(z)\,, \tag{4}$$

were $a(z)$ and $m(z)$ are the position-dependent lattice constant and effective mass. The effective potential energy V_{ef} includes four terms:

$$V_{ef}(z) = E_c(z) + 2a_c\left(1 - \frac{C_{12}}{C_{11}}\right)\varepsilon_{xx} + eU(z) + V_{xc}(z), \tag{5}$$

were $E_c(z)$ is the conduction-band-edge energy, a_c is the hydrostatic deformation potential, C_{11} and C_{12} are the elastic stiffness constants, $\varepsilon_{xx} = \varepsilon_{yy}$ is the strain in the plane of the epitaxial growth [001], $V_{xc}(z)$ is the exchange-correlation energy. The Hartree electrostatic potential $U(z)$ is determined using the one-dimensional Boltzmann–Poisson equation. So, the calculation of the static electron distribution includes the quantum effects. After this, the barrier capacitance and apparent profile are simulated in the classical small-signal approximation [8]. The comparison of such "semi-classical" technique with the usual quasistatic approach gives that capacitance error is bellow 0.2%.

4. Results and discussion

In Fig.1 are presented the simulated 3D and 3D+2D electron distributions at the reverse bias $V = 0$ V. One cane see that the quantum effect changes the electron profile in the QW of HFET.

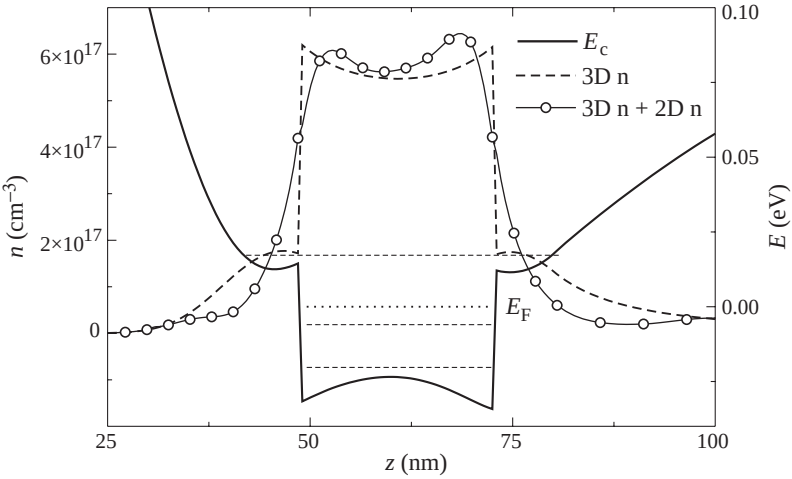

Fig. 1. Conduction-band-edge energy, lowest three sub-bands and electron distributions in QW.

Next Fig. 2 shows the results of C–V profiling and simulated apparent profiles for three cases: (i) unstrained QW; (ii) strained QW, the static electron distributions are calculated in classical approach; (iii) strained QW, the self-consistent simulation of the static electron distributions. On can conclude that strain effect makes the considerable influence to the apparent profile by the shift of conduction-band-edge energy in the QW. At the same time, the inclusion of the size effects produces the lesser influence for the given structure. The some discrepancy between the right slope of the simulated apparent profile and the experimental data cane be explicated by the effects of the edge capacitance and increasing

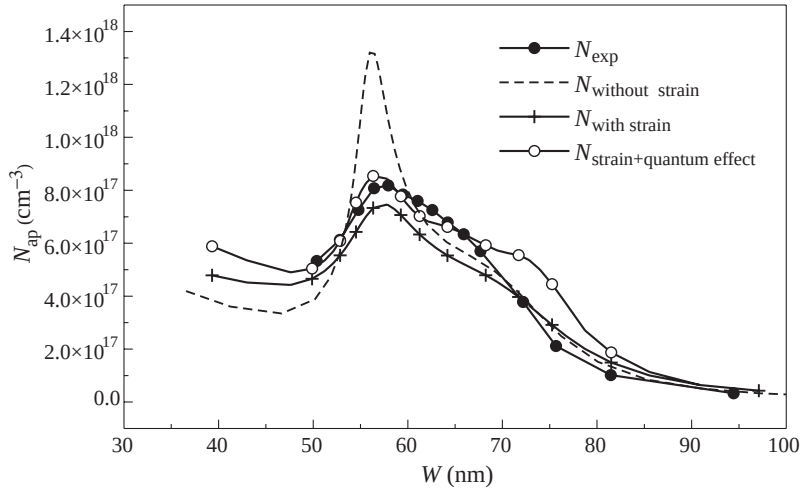

Fig. 2. Experimental and simulated apparent profiles.

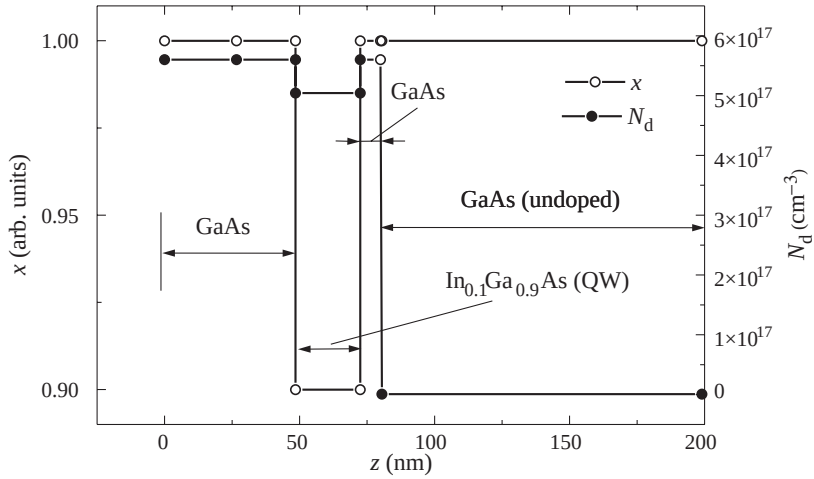

Fig. 3. Extracted mole fraction and doping profiles.

of the channel resistance. The extracted mole fraction and doping profiles are presented in Fig. 3.

The obtained thicknesses of the first GaAs n-layer is 48.5 nm and the second n-layer is 9 nm, the thickness of the QW is 24 nm. The doping level of the GaAs n-layers is $5.6 \cdot 10^{17}\,\mathrm{cm}^{-3}$. This results demonstrate the validity of the proposed "semi-classical" small-signal technique for the C–V profiling simulation of the real QW structures including strain effects.

Acknowledgments

The authors wish to thank the Russian Ministry of Education for the financial support.

References

[1] D. I. Babic, and H. Kroemer, *Solid-State Electron.* **28**, 1015 (1985).
[2] J. E. Manzoli, M. A. Romero and O. Hipolito, *Superlattices and Microstructures* **25**, 289 (1999).
[3] C. R. Moon, B.-D. Choe, S. D. Kwon and H. Lim, *Appl. Phys. Lett.* **72**, 1196 (1998).
[4] C. R. Moon, B.-D. Choe, S. D. Kwon, H. K. Shin and H. Lim, *J. Appl. Phys.* **84**, 2673 (1998).
[5] L. Lu, J. Wang, Y. Wang, W. Ge, G. Yang and Z. Wang, *J. Appl. Phys.* **83**, 2093 (1998).
[6] J. Minch, S. H. Park, T. Keating and S. L. Chuang, *IEEE J. Quantum Electron.* **35**, 771 (1999).
[7] B. W. Kim, *J. Appl. Phys.* **89**, 1197 (2001).
[8] M. F. Kokorev, N. A. Maleev, *et al*., *Semicond. Sci. Technol.* **15**, 301 (2000).

9th Int. Symp. "Nanostructures: Physics and Technology"
St Petersburg, Russia, June 18–22, 2001

Polarized elecrton photoemission studies of spin relaxation in thin GaAs epitaxial films

Yuri A. Mamaev†, Yuri P. Yashin†, Arsen V. Subashiev‡, Anton N. Ambrajei† and *Alexander V. Rochansky*†

† Laboratory of Spin-Polarized Electron Spectroscopy, State Technical University, 195251, St Petersburg, Russia

‡State Technical University, 195251, St Petersburg, Russia

Abstract. The results of systematic study of polarized electron emission from unstrained GaAs thin epitaxial layers with varying thickness are presented. Excitation spectra of the polarized photoemission reflect the optical spin orientation of the electrons produced by the circularly polarized light excitation and spin relaxation kinetics. The interpretation of the spectra and their temperature dependencies shows the importance of valence band wrapping and correlation between the spin and the momentum of an electron. For thin overlayers the residual polarization losses occur in the band-bending region.

Optical spin orientation in GaAs in known to give information on the spin relaxation mechanisms and the electron kinetics. With the aim to clarify the mechanisms of photoelectron polarization losses, we have performed a set of the polarized electron emission experiments with unstrained GaAs epitaxial thin films.

The GaAs overlayers with the thickness 70, 100, 150, 500, 1000 and 1500 nm were MBE-grown at the top of n-doped GaAs wafer. An advantage of n-doped GaAs wafer is the elimination of the back scattering of photoexcited electrons from the overlayer/wafer interface, which leads to the lowering of an effective lifetime of electrons prior the emission. At the same time the study of electron emission from the overlayers with various thickness allowed us to investigate the emission of electrons as a function of the electron extraction time from the GaAs film.

In the modulation doped GaAs overlayers the main part of a layer was low p-doped (5×10^{17} cm^{-3}), which should help to suppress Bir–Aronov–Pikus (BAP) spin relaxation mechanism, while the top 10 nm were heavily p-doped (5×10^{19} cm^{-3}) with the aim to achieve high quantum yield at the NEA surface. The working GaAs overlayer was capped with As to prevent the layer pollution by the air. With the aim to study temperature dependence of electron spin dynamics, the electron polarization and yield spectral dependencies were measured at the temperatures 300 and 130 K for freshly activated samples and in the course of the photocathode surface degradation.

All measurements have been performed at the computer-controlled set-up [2] at the residual pressure $1-2\times10^{-10}$ Torr, circularly polarized light monochromaticity being equal $\Delta\lambda = 2$ nm. Thermal cleaning procedure (at the pressure not exceeding $3-5 \times 10^{-9}$ Torr) consisted of the sample heating with gradual increase of temperature up to 560–580 degrees centigrade, one hour exposition at 560–580 degrees centigrade and than cooling for one hour till room temperature. NEA has been achieved by cesium and oxygen deposition. During the course of experiments Mini–Mott detector was calibrated both with the energy — loss extrapolation procedure [3] and with GaAs/AlGaAs derivative standard for polarimeter calibration [4].

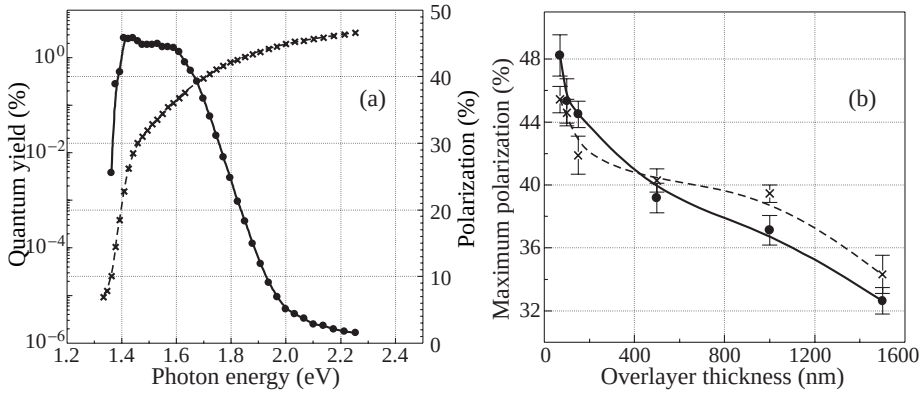

Fig. 1. Electron spin polarization (circles) and quantum yield (crosses) as a function of excitation energy for the GaAs unstrained sample (overlayer thickness 100 nm) at room temperature (a) and maximum polarization values at various GaAs overlayer thickness for freshly activated cathodes (b). Solid line and circles — room temperature; dash line and crosses — $T = 130$ K.

Figure 1(a) shows the electron spin polarization $P(h\nu)$ and quantum yield $Y(h\nu)$ as a function of excitation energy for the GaAs unstrained sample with overlayer thickness 100 nm at room temperature. The typical features of $P(h\nu)$ and $Y(h\nu)$ curves are clearly seen, i.e. high spin polarization P near the photothreshold, then rather wide plateau, followed by decreasing of P when $h\nu$ is close to $E_g + \Delta$, where spin-orbit splitting $\Delta = 0.3$ eV. The maximum value of P is about 46% for 100 nm films.

In general, the polarization of the optically oriented electrons can be lost [1]:

(i) at the electrons creation under circular light excitation; (ii) during the thermalisation; (iii) in course of electrons transport to the band-bending region (BBR); (iv) in the BBR; (v) during the escape to vacuum through the NEA surface barrier. The processes at different stages of the photoemission have strongly different time scales, and are essentially independent, so that the polarization P of the emitted electrons can be expressed as a product of the factors reflecting each step of the emission process [6],

$$P(h\nu) = P_0(h\nu) R_{\text{th}} R_{\text{tr}} R_{\text{BBR}} R_{\text{emi}}, \tag{1}$$

where $P_0(h\nu)$ is the electron polarization in the conduction band at the excitation moment, the factors R_{th}, R_{tr}, R_{BBR}, and R_{emi} describe spin relaxation during each of the subsequent stages of emission as listed above.

The wide plateau is a sequence of a suppression of the BAP spin relaxation mechanism due to low doping at the main part of the GaAs overlayer. It also a manifest of negligible polarization losses at the step (ii) of the photoemission.

The dependence of the polarization in the polarization maximum on the layer thickness d is presented in Fig. 1(b). As it is evident from Fig. 1(b), the maximum polarization value grows upon the reduction of GaAs overlayer thickness and for the most thin overlayer practically reaches 50%, which is the theoretical maximum value of P_{max} in equilibrium. This dependence can be used to evaluate the polarization losses in the step (iii) and to estimate the spin relaxation time in the layer.

At the small layer thickness $d \ll l$ (l is the diffusion length) the corresponding depolarization factor can be written as

$$R_{\text{tr}} = \frac{\tau_s}{\tau_{\text{esc}} + \tau_s}, \tag{2}$$

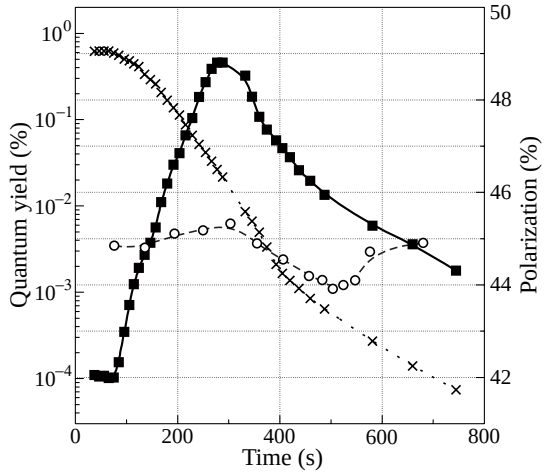

Fig. 2. Polarization (circles and squares) and Quantum Yield (crosses) evolution upon the degradation of the GaAs sample surface at $T = 130$ K for the near-threshold (open circles) excitation ($\Delta = h\nu\ E_g = 15$ meV) and excitation at 190 meV above the energy gap (solid squares).

where τ_s is the spin relaxation time in the active layer. The escape time from the active layer equals $\tau_{\text{esc}} = d/S$, S being the surface recombination velocity. The comparison with the experiment gives the estimate for the spin relaxation time $\tau_s \approx 50$ ps in line with the luminescence data, while the temperature dependence is found to be slower than that for the D'yakonov and Perel' (DP) mechanism.

One can see that at the thickness less than 400 nm $P_{\max}(300\,\text{K}) > \text{P}_{\max}$ (130 K). This observation can be explained by more effective spin relaxation in BBR at 130 K, since at low temperature the BBR quantum well is deeper, than at $T = 300$ K [5] and DP mechanism becomes more effective at the step (iv) [6].

At the thickness d more than 400 nm the value of $P_{\max}$ for cool cathode exceeds one at room temperature. This feature is typical as well for the bulk cathodes and is explained by faster spin relaxation in the working layer (in the step (iii)) prior the emission into vacuum.

Data of Fig. 1(b) were obtained for freshly activated cathodes, i.e. $P(h\nu)$ and $Y(h\nu)$ curves were measured just after activation of NEA surface. The increase of the work function, which occurs upon the degradation of the sample surface, leads to the cut-off the photoelectrons which are captured in the BBR and thermalised at the bottom of the conduction band.

Hence, the only "hot" electrons, which have not yet undergo spin relaxation due to steps (ii)–(iv), can escape into vacuum. This experiment enables us to evaluate the polarization losses in these steps. Figure 2 shows that in the case of photoexcitation at about 200 meV above the photo-threshold polarization is growing up upon the surface degradation, which is explained by the higher polarization of hot electrons. The GaAs valence band wrapping effect and the relationship between the spin and the momentum of an electron just after excitation can lead to the electron polarization of up to 67% [7]. It was first time illustrated by Mirlin [7], who measured the hot photoluminescence circular polarization of up to 35%. High polarization was achieved with specially designed and modified GaAs sample. Valence band wrapping and the relationship between the spin and the momentum of an electron are essential for high-polarization photoemission. High polarization obseved in

this case suggests that for thin overlayers the residual depolarization occurs due to spin relaxation in the band bending region.

The presented analysis of the polarization losses in the photoemission processes in the unstrained GaAs thin layers shows the perspectives for the polarization increase in the highly polarized electron sources based on the strained GaAs layer and the short-period semiconductor superlattices [1]. Since the losses in BBR and in the emission in vacuum are not enhanced for these cases the limiting factors are found to be associated with the polarization losses in the excitation and in the electron extraction in BBR.

Acknowledgments

This work was supported by the Russian State Program "Physics of Solid State Nanosr-tuctures" under grant 97-1091, Russian Foundation for Basic Research under grant 00-02-16775, INTAS under grant 99-00125 and SNSF under grant 7IP 062585.

References

[1] A. V. Subashiev, Yu. A. Mamaev, Yu. P. Yashin and J. E. Clendenin, *Phys. Low-Dim. Structures* **1/2**, 1 (1999).

[2] Yu. P. Yashin, A. N. Ambrajei and Yu. A. Mamaev *Instruments for Experimental Techniques* **43** (2), 245 (2000).

[3] T. J. Gay, M. A. Khakoo, J. A. Brand, J. E. Furst, W. V. Meyer, W. M. K. P. Wijayaratna and F.B. Dunning, *Rev. Sci. Instrum.* **63** (1), 114 (1992).

[4] G. Mulhollan et al., *Proceedings of the 16th IEEE Particle Accelerator Conference (PAC 95) and International Conference on High-energy Accelerators (IUPAP)*, Dallas, Texas, 1995, p. 1043.

[5] C. Herman, H.-J. Drouhin and G. Lampel, *Spectroscopy of Nonequilibrium Electrons and Phonons* ed C. V. Shank and B. P. Zakharchenya, Elseiver Science, B.V., 1992, Ch. 9.

[6] A. V. Subashiev and J. E. Clendenin, *Journ. Modern Physics* **A 15** (1), 2519 (2000).

[7] D. N. Mirlin, *Optical Orientation*, ed F. Meier and B. P. Zakharchenya, North-Holland, Amsterdam, 1984, Ch. 4.

9th Int. Symp. "Nanostructures: Physics and Technology"
St Petersburg, Russia, June 18–22, 2001

Vibrational study of nitrogen incorporation in InGaAsN alloys

A. M. Mintairov†‡, P. A. Blagnov†, J. L. Merz‡, V. M. Ustinov† and A. S. Vlasov†

† Ioffe Physico-Technical Institute, St Petersburg, Russia
‡ Dept. of Electrical Engineering, University of Notre Dame, Notre Dame, IN 46556, USA

Abstract. We present an infra-red (IR) reflectivity and Raman study of $In_xGa_{1-x}As_{1-y}N_y$ ($x = 0$ and $\sim$0.08, $y \sim 0.03$) alloys grown by molecular beam epitaxy. We observed: — strong diagonal Raman components of GaAs-type phonons, indicating a local trigonal distortion of the alloy lattice induced by nitrogen ordering; — indium induced splitting of the Ga-N type vibration, indicating a formation of different local nitrogen atomic arrangements; — a sharp (halfwidth $\sim$1 cm^{-1}) IR mode at 360 cm^{-1}, of unknown origin.

Introduction

The InGaAsN alloys have recently attracted considerable attention as promising materials for laser diodes in the 1.3–1.5 μm range as well as more efficient solar cells. These applications exploit the unusual electronic property — a "giant bowing", which arises from the large elecrtonegativity and very small ion radii of the nitrogen [1, 2], together with the possibility of perfect lattice matching to GaAs substrates. Up to now little is known about the micro/nanostructure, i.e. possible atomic ordering and phase separation, of these alloys, which can dramatically alter their electronic and transport properties important for device applications. In our previous paper [3] using Raman spectra we revealed local trigonal distortion of coherently strained $GaAs_{1-x}N_x$ ($x \sim 0.02$) alloys, indicating the existence of [111] GaAs/GaN ordering. In present paper using Raman and IR vibrational spectroscopy we study of the properties of N incorporation into InGaAsN alloys lattice matched to GaAs.

1. Experiment

Coherently strained $GaAs_{1-y}N_y$ and lattice matched $In_xGa_{1-x}As_{1-y}N_y$ ($x \sim 0.08$, $y \sim 0.03$) layers with thickness $\sim$0.2 μm were grown by solid source MBE on (001) semi-insulating GaAs substrates at temperature 450°C. An RF-plasma source was used to generate atomic nitrogen from N2. The composition was determined by calibration growths of GaAsN and InGaAs along with x-ray diffraction. The layers have strong photoluminescence at room temperature at 1.05–1.15 eV.

We also used MOCVD grown reference samples of $In_xGa_{1-x}As$ ($x \sim 0.1$) and $GaAs_{1-y}N_y$ ($y \sim 0.03$) studied by us previously in [3].

Polarized room temperature IR spectra were taken at oblique incidence (45°) with a Bruker IFS-66V spectrometer.

The Raman spectra (RS) were measured in the backscattering geometry using a double monochromator DFS-52 and excited with a 488 nm Ar^+-ion laser at room temperature. The xy and xx (where the $x \parallel [100]$ and $y \parallel [010]$) components of RS excited from the (001) growth plane were analyzed. According to Raman selection rules of zinc blende structure

only optical phonons with longitudinal (LO) polarization are allowed in xy configuration, while all optical modes are forbidden in the xx one.

2. Results and discussion

The results of our IR and Raman measurements are presented in Figs. 1–4. As can be seen from Fig. 1, the IR spectra of $In_{0.07}Ga_{0.93}As_{0.97}N_{0.03}$ alloys have a main intense restrahl band 270–290 cm^{-1} due to the GaAs-type phonons, a very sharp peak A at 360 cm^{-1}, and several weak bands in the range 400–550 cm^{-1}, corresponding to second order spectra of GaAs-type. The Ga-N type phonon TO_2 also observed at 470 cm^{-1}.

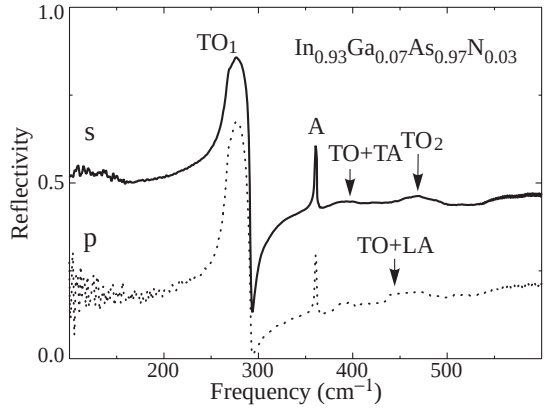

Fig. 1. Polarized (s — solid, p —- dashed curves) IR reflection spectra of $In_{0.07}Ga_{0.93}As_{0.97}N_{0.03}$ alloys.

The A peak has unusually small halfwidth 1.5 cm^{-1}, which is much smaller then the typical phonon damping parameter of binary III–V compounds ($\sim$3 cm^{-1}). We observed this IR peak in all GaAsN and InGaAsN layers grown by MBE, but it was absent in the IR spectra of the MOCVD grown GaAsN layers. On the other hand, our Raman measurements did not reveal any band at 360 cm^{-1}, what makes the origin of this peak at the moment unclear.

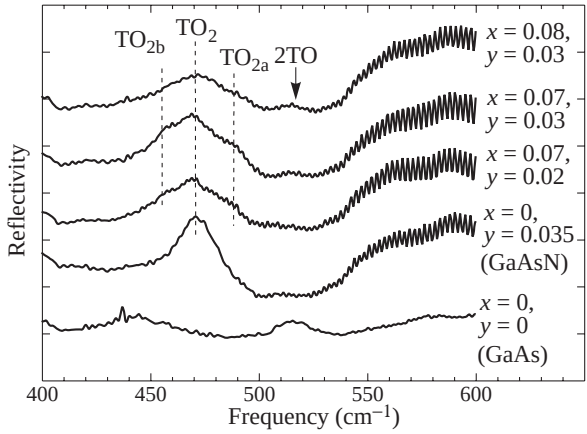

Fig. 2. s-polarized IR reflection spectra of $GaAs_{1-y}N_y$, $In_xGa_{1-x}As_{1-y}N_y$ alloys and GaAs substrate in 400–600 cm^{-1} frequency range.

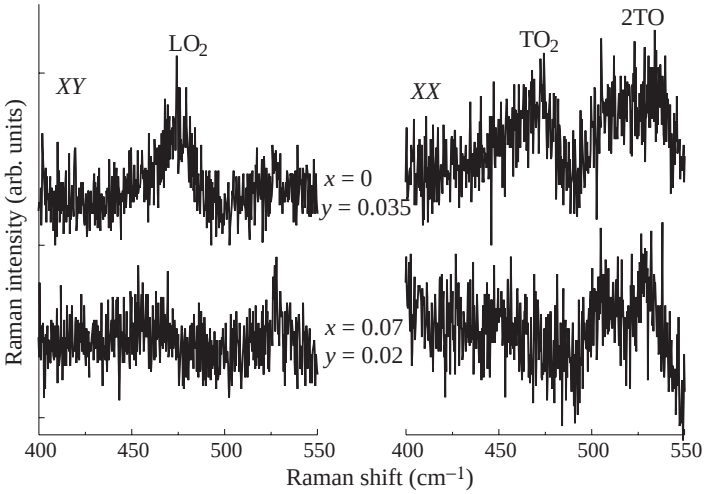

Fig. 3. xy (left) and xx (right) Raman components of Ga-N type mode of $In_{0.07}Ga_{0.93}As_{0.02}N_{0.98}$ and $GaAs_{0.965}N_{0.035}$.

In the IR spectra we observed the GaN-type vibration (TO_2) in both InGaAsN and GaAsN, as can be seen from Fig. 2, where we compare the spectra of three $In_xGa_{1-x}As_{1-y}N_y$ ($x \sim 0.08$, $y \sim 0.03$) and one $GaAs_{1-y}N_y$ ($y \sim 0.035$) layers with the spectra of GaAs. It can bee seen that in InGaAsN the TO_2 band is much broader. It reveals a fine structure consisting of a low — TO_{2b} and a high — TO_{2a} frequency shoulder split by $\sim$15 cm^{-1} from the central TO_2 peak. The splitting clearly indicates that there are three different local atomic arrangements of nitrogen in the lattice of InGaAsN, which is induced by the presence of indium.

In the Raman spectra the Ga-N type mode was observed only in GaAsN (see Fig. 3). As in our previous study [3] it appears in both zinc blende allowed — xy and forbidden — xx configurations, which is due to a strong local trigonal distortion of the GaAsN lattice

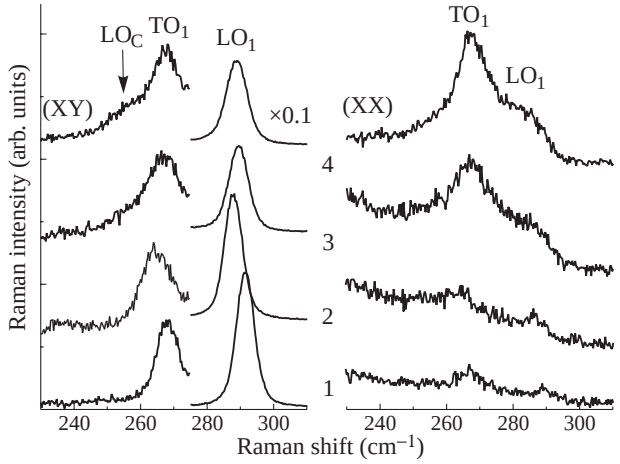

Fig. 4. xy (left) and xx (right) Raman components of GaAs-type modes of GaAs (1), $In_{0.14}Ga_{0.86}As$ (2), $In_{0.07}Ga_{0.93}As_{0.02}N_{0.98}$ (3) and $GaAs_{0.965}N_{0.035}$ (4) alloys.

caused by the bond relaxation and ordering of GaN_3As microclusters ([111] GaN/GaAs ordering).

While we did not detect the GaN-type mode in InGaAsN we did get evidence that the GaN_3As microcluster ordering is preserved in the presence of In. This is seen in Fig. 4, where the strong enhancement (compared with GaAs and InGaAs) of the forbidden xx scattering of the GaAs-type TO_1 phonon is observed for both GaAsN and InGaAsN.

The appearance of the strong zinc blende forbidden Raman components, indicating [111] GaN/GaAs ordering, is an anomalous property of InGaAsN, which was not observed in conventional III–V alloys. The results presented show that it does not depend on the macroscopic strain due to lattice mismatch between epi layer and substrate. The driving force for the ordering can be strong local strains (bond relaxation) caused by the small nitrogen radii.

Acknowledgments

The authors wish to acknowledge the NATO Science for Piece Program (grant SFP-972484).

References

[1] S. Sakai, Y. Ueta and Y. Terauchi, *Jpn. J. Appl. Phys.* **32**, p. 4413 (1993).
[2] S.-H. Wei and A. Zunger, *Phys. Rev. Lett.* **76**, 664 (1996).
[3] A. M. Mintairov, P. A. Blagnov, V. G. Melehin, N. N. Faleev, J. L. Merz, Y. Qiu, S. A. Nikishin and H. Temkin, *Phys. Rev. B* **56**, 15836 (1997).

9th Int. Symp. "Nanostructures: Physics and Technology"
St Petersburg, Russia, June 18–22, 2001

HRXRD and TEM studies of cluster formation in LT GaAs.

D. A. Vasukov†, V. V. Chaldyshev†, A. A. Suvorova†,
V. V. Preobrazhenskii‡, M. A. Putyato‡ and B. R. Semyagin‡
† Ioffe Physico-Technical Institute, St Petersburg, Russia
‡ Institute of Semiconductor Physics, Siberian Division of Russian Academy of Science, 630090, Novosibirsk, Russia

GaAs films grown by molecular beam epitaxy (MBE) at low temperature (LT GaAs) have attracted much attention due to high electrical resistivity and short carrier lifetime. Distinctive feature of this material is a large quantity of As antisites (As_{Ga}). The arsenic excess can be varied in a wide range by the growth temperature and As/Ga flux ratio, and also enhanced by isovalent indium impurity doping or reduced by doping with Be acceptors and Si donors. Upon annealing, the excess As segregates in clusters, size and concentration of which can be varied by annealing conditions. It should be noted that formation of As clusters does not deteriorate the crystallinity of the LT GaAs matrices either undoped or doped with In, Be, or Si [1–3].

In this paper we employ high resolution x-ray diffractometry (HRXRD) and transmission electron microscopy (TEM) to study structural transformations in LT GaAs films doped with isovalent Sb impurity.

The LT GaAs film doped with Sb ($\sim$ 1 at.%) as well as conventional (Sb-free) sample were grown by MBE at (200°C) on 2-inch GaAs(001) substrates. Both samples were divided into ten parts, one of which was kept as grown, the others were annealed in the MBE setup under arsenic overpressure at 500–880°C.

The HRXRD measurements of as-grown conventional LT GaAs showed lattice mismatch between the layer and substrate to be as high as $\Delta a/a = 8.4 \cdot 10^{-4}$. This value was in excellent agreement with As_{Ga} concentration of $7 \cdot 10^{19}$ cm^{-3}, witch was determined from the near-infra-red optical absorption study using Martin's calibration [4 ,5]. Multiple interference fringes at the x-ray rocking curve proved a high crystalline quality of the film. Reduced $\Delta a/a$ values were measured after anneals. That was the signature of transformation of As antisite defects to nanoscale As clusters. After anneal at 600°C, $\Delta a/a$ was close to zero. A system of nanoscale As clusters built in crystalline dislocation-free GaAs matrix was observed in the annealed samples by TEM.

The HRXRD measurements of as-grown Sb-doped LT GaAs showed multiple interference fringes and evidenced high crystalline quality of the film that was characterized by $\Delta a/a = 3.6 \cdot 10^{-3}$. After anneals at the temperatures of 500–700°C, the lattice mismatch decreased to $2 \cdot 10^{-3}$. The relaxation was much higher than what could be expected for the antisite defect concentration determined from optical measurements. We suggest that such a strong relaxation could be due to segregation of isovalent Sb impurity into the As clusters.

Another structural transformation was detected by HRXRD when the Sb-doped samples were annealed at the temperature higher than 700°C. It manifested itself by a strong broadening of the diffraction maximum related to the LT GaAs:Sb layer. The TEM study showed that the high temperature anneals result in formation of dislocation loops attached to the big As clusters. Thus, a new phenomenon was found, which originates from Sb doping of LT GaAs films. We may suggest that the break of crystallinity is due to incorporation of

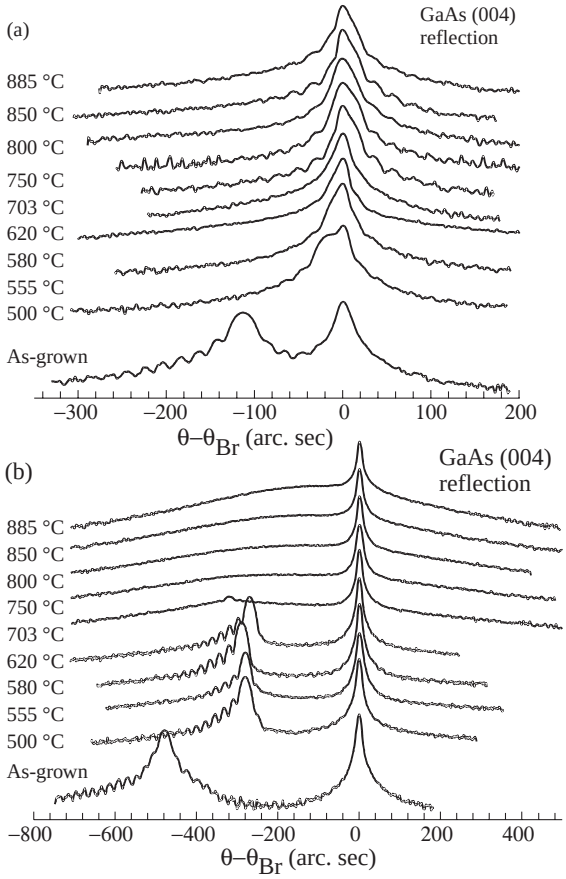

Fig. 1. X-ray rocking curves for conventional Sb-free (a) and Sb-doped (b) LT GaAs films annealed at various temperatures. The annealing temperatures are shown on the curves.

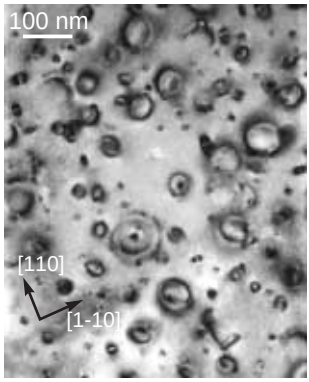

Fig. 2. Bright-field TEM image along [001] direction for Sb-doped LT GaAs film annealed at 703°C.

Sb in As clusters, so that big clusters induce fairly strong strains in the surrounding matrix.

References

[1] N. A. Bert, V. V. Chaldyshev, A. E. Kunitsyn, Yu. G. Musikhin, N. N. Faleev, V. V. Tretyakov, V. V. Preobrazhenskii, M. A. Putyato and B. R. Semyagin, *Appl. Phys. Lett.* **70**, 3146-3148 (1997).

[2] V. V. Chaldyshev, A. E. Kunitsyn, V. V. Tretyakov, N. N. Faleev, V. V. Preobrazhenskii, M. A. Putyato and B. R. Semyagin, *Semiconductors* **32**, 692-695 (1998).

[3] N. N. Faleev, V. V. Chaldyshev, A. E. Kunitsyn, V. V. Preobrazhenskii, M. A. Putyato, B. R. Semyagin and V. V. Tretyakov, *Semiconductors* **32**, 19-25 (1998).

[4] G. M. Martin, *Appl. Phys. Lett.* **39**, 747 (1981).

[5] X. Liu, A. Prasad, J. Nishio, E. R. Weber, Z. Liliental-Weber and W. Walukievich, *Appl. Phys. Lett.* **67**, 279-281 (1995).

9th Int. Symp. "Nanostructures: Physics and Technology"
St Petersburg, Russia, June 18–22, 2001

Direct observation of two-level electronic emission from QDs InAs/GaAs by means of C–V and admittance spectroscopy

V. I. Zubkov and A. V. Solomonov
St Petersburg State Electrotechnical University, 197376 St Petersburg, Russia

Abstract. The emission of electrons from ground and first excited energy levels of InAs self-organized quantum dots grown by MOCVD has been registered by means of steady-state capacitance vs. voltage technique and admittance spectroscopy. We found a fine structure of carrier concentration profile in the area of QDs. The dependence of activation energy of the levels in the QDs on applied bias also has been obtained.

Introduction

There has been considerable interest at present in studying of electronic properties of quantum dot (QD) heterostructures InAs/GaAs, suitable for fabricating laser diodes emitting at 1.3 μm [1, 2]. Optical methods (PL, PLE) have been commonly used for getting information about the optical transients between energy levels inside the quantum dots [1, 3], but these methods do involves both electron and hole subsystems, so one can not obtain the absolute values of quantized energy levels.

Capacitance spectroscopy (and admittance spectroscopy as its modification) makes it possible to test separately either electron or hole emission mechanism, as well as the precise obtaining of concentration, geometric parameters and energy band discontinuities have became possible. In this work we present the results of admittance and capacitance measurements of p-n- heterostructures InAs/GaAs with self-organized quantum dots, which directly indicate the emission from ground and first excited electron levels.

Experimental results and discussion

The structures were grown by MOCVD (metal-organic chemical vapor deposition) on highly n^+-doped GaAs substrate, followed by Si-doped buffer layer. The array of quantum dots consisted of three sheets of vertically coupled InAs QDs was spaced with 2.8-nm undoped GaAs layers. The structures were capped with 448-nm GaAs layer, and then 650-nm thick p-GaAs layer was deposited to create p-n junction (Fig. 1). Details of growth and device fabrication see in Ref. [4].

The measurements were performed using HP4284A RLC meter in the range of frequencies 1 kHz. . . 1 MHz and temperatures 10–300 K. The amplitude of measuring signal was 10 or 50 mV.

The C–V-characteristics of the sample have an inherent for quantum wells and QDs plateau in the range of reverse biases $-1.0 \div -3.0$ V (Fig. 2). The width of the plateau increases permanently when the temperature goes down to 10 K.

This behavior indicates the growth of electron charge inside the QDs with temperature lowering due to enhancement of energy barriers. We didn't observe the suppressing of the plateau for temperatures below 80 K, as was reported in [3, 5] for Shottky barriers with InAs quantum dots, but grown by molecular beam epitaxy (MBE).

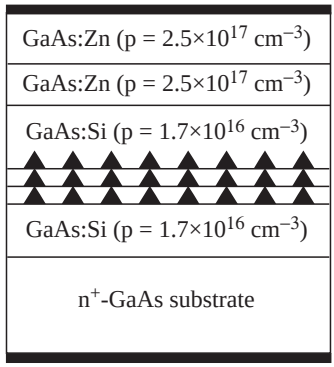

Fig. 1. Layer sequence of p-n structure with self-organized InAs quantum dots [4].

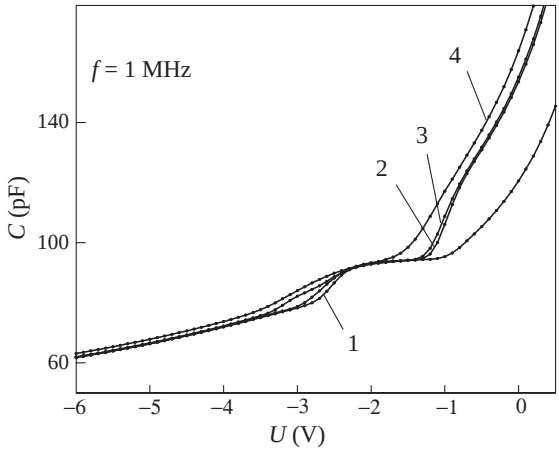

Fig. 2. C–V characteristics of the structure with InAs QDs at the temperatures: 1—10 K; 2—45 K; 3—80 K; 4—200 K.

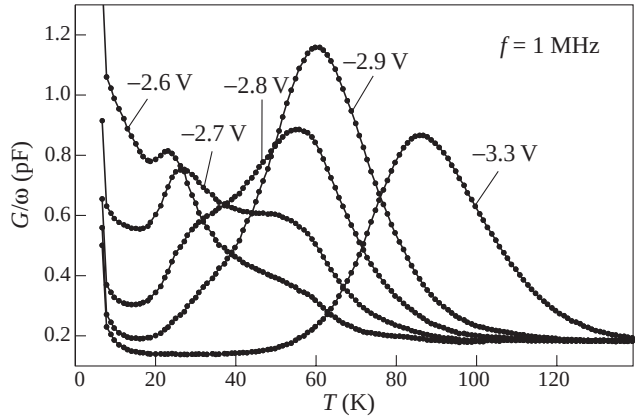

Fig. 3. The admittance spectra of the structure as a function of applied reverse bias.

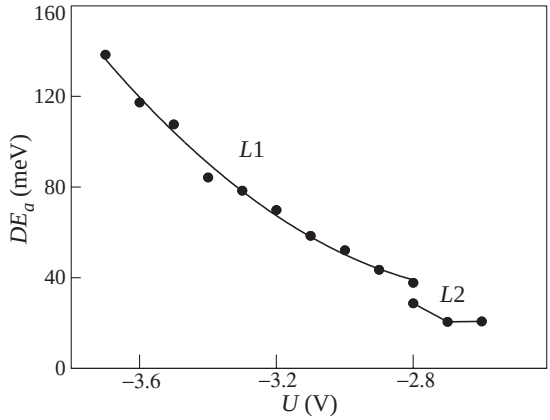

Fig. 4. Dependence of "apparent" activation energy of ground (L1) and first excited (L2) levels in the QD on reverse bias.

After ending the plateau (approximately at $|U| > 2.2$ V) a step in C–V characteristics was observed. This step corresponds to the strong energy bands bending in applied electric field when the conditions for thermionic emission of electrons from the QDs fulfill. It may be registered with the help of admittance spectroscopy. The spectra of admittance spectroscopy have been measured at frequencies from 1 kHz up to 1 MHz. We detected the QDs response in the range of reverse biases $-2.2 \ldots -3.7$ V. A set of spectra for different applied biases is shown in Fig. 3. At high electric fields ($|U| > 3$ V) there was a single peak in admittance spectra. It's amplitude and temperature maximum had strong dependencies on frequency and bias. With reducing of reverse bias a second, additional, peak was appeared at the low temperature side of the spectra, which, in turn, had his own frequency and bias behaviors. We attribute these peaks to the emission of carriers from the ground and first excited levels in the QD. At $U = -2.7$ V the two peaks are about equal to each other.

Determined from Arrenius plot the "apparent" ionization energy of the levels L1 and L2 depended considerably on U_{rev} (Fig. 4). The energy of L1 level changed 3 times. This phenomenon is well known for DLTS and admittance measurements of structures with quantum wells and quantum dots. The reason of it is the changing of the electrostatic potential at different applied biases and following modification of electron energy spectrum inside the QD.

The second reason, as was pointed by D. V. Lang [6], may be the competing mechanisms of thermal activation and thermally independent tunneling from the level. Actually the tunneling mechanism dominated in DLTS spectra of the same samples at low temperatures in Ref. [4, 7].

When calculating the apparent concentration profile $n = f(w)$ using conventional differentiation of C–V characteristics we found a fine structure of concentration peak in vicinity of the QDs layer, Fig. 5(a). (The plots were built in coordinates $n - U$, which is more convenient in this case due to nonlinear dependence $w = f(U)$). The fine structure was detected only at low frequencies in the range of temperatures 40–80 K (In contrast see Fig. 5(b), where no fine structure is observed). We guess this fine structure was created by the symmetrical and asymmetrical wave functions of the ground (L1) and first excited (L2) energy levels of electrons in the QD. This suggestion is in agreement with the results of admittance spectroscopy.

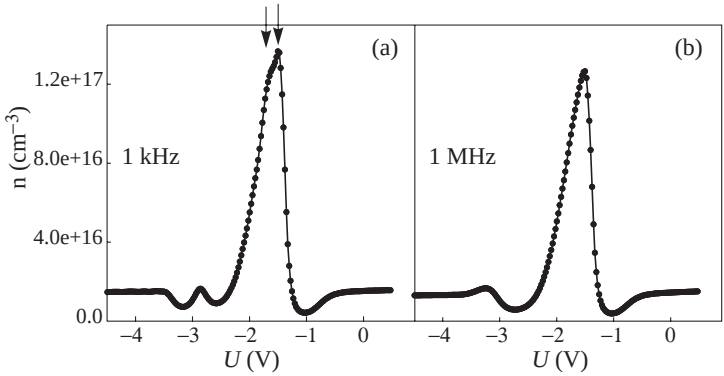

Fig. 5. N-U characteristics of the structure with the QDs at different frequencies. $T = 45$ K.

There also noticed another small peak (positioned at $U = -2.8$ V) in the low frequency concentration profile (Fig. 5(a)). One may explain its origin following [5] as due to modulation by testing AC signal the charge at the edge of the space charge region far from the QDs location.

Acknowledgements

This work was performed in part in Institut für Festkörperphysik, Technische Universität Berlin. The authors wish great thanks to Prof. D. Bimberg, the Director of the Institute, for granting the possibility to work on the equipment of the Institute.

References

[1] D. Bimberg, M. Grundmann and N. N. Ledentsov, *Quantum Dot Heterostructures*, Wiley: Chichester, 1998.
[2] D. Bimberg, M. Grundmann, F. Heinrichsdorff, N. N. Ledentsov, V. M. Ustinov, A. E. Zhukov, A. R. Kovsh, M. V. Maximov, Y. M. Shernyakov, B. V. Volovik, A. F. Tsatsul'nikov, P. S. Kop'ev and Zh. I. Alferov, *Thin Solid Films* **367** 235 (2000).
[3] P. N. Brunkov, A. R. Kovsh, V. M. Ustinov, et al., *J. Electron. Mater.* **28** 486 (1999).
[4] C. M. A. Kapteyn, F. Heinrichsdorff, O. Stier, R. Heitz, M. Grundmann, N. D. Zakharov, D. Bimberg and P. Werner, *Phys. Rev. B.* **60** 14265 (1999).
[5] P. N. Brunkov, A. A. Suvorova, M. V. Maximov, et al., *Proc. Int. Symp. 'Nanostructures: Physics and Technology' (St Petersburg 1997)* 236 (1997).
[6] D. V. Lang, *Heterojunction Band Discontinuites: Physics and Device Applications* Elsevier Science Publishers B.V. (1987).
[7] C. M. A. Kapteyn, M. Lion, R. Heitz, D. Bimberg, P. N. Brunkov, B. V. Volovik, S. G. Konnikov, A. R. Kovsh and V. M. Ustinov, *Appl. Phys. Letters* **76** 1573 (2000).

9th Int. Symp. "Nanostructures: Physics and Technology"
St Petersburg, Russia, June 18–22, 2001

Theory of magnetophonon resonance in quantum wells. Tilted magnetic field

V. V. Afonin†, *V. L. Gurevich*† and R. Laiho§
† Ioffe Physico-Technical Institute, St Petersburg, Russia
§ Wihuri Physical Laboratory, Department of Physics, University of Turku, FIN-20014 Turku, Finland

Abstract. We develope a theory of magnetophonon resonance (MPR) in quantum wells in a tilted magnetic field. We explain the existence of two peaks of MPR in its angular dependence that may be very sharp. A relation between the MPR amplitude in the perpendicular magnetic field and its θ-dependence in a tilted field is discussed. We come to conclusion that the θ-dependence of MPR can give valuable information concerning the optic phonon damping and the electron-phonon interaction in quantum wells.

Magnetophonon resonance (MPR) is the first *internal* resonance in solids that has been predicted theoretically and subsequently observed experimentally (see the review paper [1]). The resonant condition is met every time when the limiting frequency of an optical phonon equals the cyclotron frequency of an electron, $\omega_B = eB/mc$, times some small integer, $\mathcal{N}$. Since its theoretical prediction and subsequent experimental discovery MPR has become a powerful tool to investigate the electron spectra in semiconductors. The magnetophonon resonance in quantum wells has been investigated since the pioneering paper by Tsui *et al.*. The most detailed experimental investigation of the phenomenon has been done by Nicholas with co-workers (see the review paper [2] and the references therein).

There are two main groups of such experiments. The first group deals with the MPR in the perpendicular (to the plane of 2DEG) magnetic field. The main features of this case are (*i*) the fact that the resonance is determined by the transverse optic frequency ω_t (rather than the longitudinal frequency ω_l) and (*ii*) a rather narrow interval of electron concentrations where the MPR is observable. The second group concerns with the experiments in magnetic field tilted at an angle θ to the perpendicular. For small values of θ the MPR is determined by ω_t. For slightly larger values its amplitude sharply goes down within a narrow angular interval of the order of 10°. For even bigger values of θ there is another maximum, this time determined by ω_l [2].

In our paper [3] we give interpretation of the first group of experiments. Here we offer interpretation of the second group and show that the angular and concentration dependencies of the MPR amplitudes are deeply interrelated.

We assume that the well is so narrow that only one electron band of spatial quantization is filled. The magnetic field **B** is assumed to be in the (y, z)-plane, the z-axis being perpendicular to the 2DEG, while the external electric field is oriented along the y-axis.

We choose the following gauge for the vector potential $\mathbf{A} = (-By\cos\theta + Bz\sin\theta, 0, 0)$ and assume a parabolic confining potential $m\omega_0^2 z^2/2$ where m is the effective mass. It is also assumed that $\hbar\omega_0 \gg \hbar\Omega, k_{\mathrm{B}}T$ (where $\Omega = eB/mc$ while T is the temperature). This assumption permits to consider only the lowest miniband. This means that our problem differs from that in perpendicular magnetic field by replacement $B \to B\cos\theta$.

Using the method developed by Kubo *et al.* and applying the method of Ref. [3] one can get for the conductance averaged over cross section of the sample

$$\sigma_{xx} = \frac{1}{2k_{\rm B}T}\left(\frac{c}{B\cos\theta}\right)^2 \int\limits_{-\infty}^{\infty} \frac{d\omega}{2\pi} \int \frac{d^2q}{(2\pi)^2} \int dz \int dz' \frac{q_y^2 N(\omega)}{1-\exp(-\hbar\omega/k_{\rm B}T)} \times [D_R(\mathbf{q},-\omega) - \mathbf{D_A}(\mathbf{q},-\omega)][\Pi_{\mathbf{R}}(\mathbf{q},\omega;\mathbf{z}',\mathbf{z}) - \Pi_{\mathbf{A}}(\mathbf{q},\omega;\mathbf{z}',\mathbf{z})]. \quad (1)$$

Here $D_{R,A}$ is the full polarization optic phonon propagator while $\Pi_{R,A}$ is the electron polarization operator.

$$\Pi_R^{(2)} = -2n_s \exp\left[-\frac{(qa_B)^2\coth\alpha}{2\cos\theta}\right] \sum_{\mathcal{N}=-\infty}^{\infty} \frac{\sinh\mathcal{N}\alpha}{\omega - \mathcal{N}\Omega\cos\theta + i\delta} I_{\mathcal{N}}\left(\frac{q^2a_B^2}{2\cos\theta\sinh\alpha}\right). \quad (2)$$

Here $I_{\mathcal{N}}$ is the modified Bessel function, $\alpha = \hbar\Omega\cos\theta/2k_{\rm B}T$, $a_B^2 = c\hbar/eB$, n_s is the 2D electron concentration. The polarization operator of Eq. (1) differs from $\Pi_R^{(2)}$ by the factor $\psi(z)\psi(z')$ due to the electron propagation along the z-axis. Here $\psi(z)$ is the wave function of the lowest level of the transverse quantization.

The zeroth-order phonon propagator (including the Frölich electron-phonon interaction) is

$$D_R^{(0)}(\omega,\mathbf{q}) = \frac{4\pi\mathbf{e}^2}{\mathbf{q}^2\varepsilon(\omega+\mathbf{i}\Gamma)}, \quad \varepsilon(\omega) = \varepsilon_\infty\frac{\omega_{\mathbf{l}}^2-\omega^2}{\omega_{\mathbf{t}}^2-\omega^2} \quad (3)$$

where ε_∞ is the lattice dielectric susceptibility at $\omega\to\infty$ while Γ is the phonon damping. As in Ref. [3], we assume that it is determined by the lattice anharmonicity. Further on we assume that one can neglect the difference between the lattice properties within and outside the well. Both these assumptions should not affect the qualitative results of the theory.

Eq. (2) shows that the electron-phonon interaction cannot be treated within the perturbation theory. The point is that the higher orders of the perturbation theory (without regard of the electron damping Γ_e) give powers of an extra factor $1/(\omega-\mathcal{N}\omega_B\cos\theta+i\delta)$. Therefore, as is shown in Ref. [3], the phonon Green function includes a sum of chains of loop diagrams. Physically this means taking into account the screening of the phonon polarization potential by the conduction electrons. Thus in 2D case in a resonance the screening can be very important.

One should observe the following essential point exploited in Ref. [3]. Both ends of the chain *should be ordinary phonon lines without addition of any Coulomb interaction lines.* This is due to the fact that the electron-electron (e-e) interaction conserves the electron quasimomentum.

Thus the oscillatory part of σ_{xx} near the $\mathcal{N}$th MPR (without regard of the electron damping) is given by

$$\Delta\sigma_{xx} = \frac{2n_sc^2\hbar^2\mathcal{J}_{\mathcal{N}}}{\varepsilon_\infty^2 k_{\rm B}TB^2\cos^2\theta}\frac{N(\omega_t)\sinh(\hbar\omega_t/2k_{\rm B}T)}{1-\exp(-\hbar\omega_t/k_{\rm B}T)}\,\mathrm{Im}\,\varepsilon_R\Big|_{\omega=\mathcal{N}\Omega\cos\theta+i\Gamma} \quad (4)$$

where

$$\mathcal{J}_{\mathcal{N}} = 2\pi e^2\int\frac{d^2q\,q}{(2\pi)^2}I_{\mathcal{N}}\left(\frac{a_B^2q^2}{2\cos\theta\sinh\alpha}\right)\exp\left(-\frac{a_B^2q^2\coth\alpha}{2\cos\theta}\right). \quad (5)$$

As $\mathrm{Im}\,\varepsilon$ has a singularity at $\omega = \omega_t$, $\Delta\sigma_{xx}$ exhibits the MPR's at $\mathcal{N}\Omega\cos\theta = \omega_t$. Physically this is due to the fact that the e-e interaction without regard of the damping is infinitely strong in the resonance.

Further on we will treat the case $\hbar\Omega \ll k_\mathrm{B}T$ that corresponds to a most usual experimental situation. Then

$$\mathcal{J}_\mathcal{N} \approx \frac{2}{\sqrt{\pi}}\frac{e^2}{a_B^3}\sqrt{\frac{k_\mathrm{B}T}{\hbar\Omega}}\cos\theta. \tag{6}$$

One can see that the integral (4) $\mathcal{J}_\mathcal{N}$ is dominated by $q \approx q_T = \sqrt{2mk_\mathrm{B}T}/\hbar$.

In order to explain the sharp angular dependence of the MPR's one should take into account the electron damping. As a result, for small electron concentrations [3] (or, for large values of θ) one can neglect the e-e interaction at the frequencies ω near ω_t and the MPR at this phonon frequency disappears. This is why we take into account the electron damping Γ_e. The characteristic angle θ_t of the sharpest angular dependence of the MPR maximum can be determined experimentally as a minimum of the derivative of the MPR amplitude over θ.

We assume that $\Gamma_e \ll \Omega\cos\theta$. The electron Green function in magnetic field has been investigated by Ando and Uemura for Γ_e determined by the elastic scattering. They have shown that the electron Green function has a non-Lorentzian form with the characteristic width Γ_e given by $\Gamma_e^2 = \Omega\cos\theta/2\pi\tau$ where τ is the relaxation time for $B = 0$ obtained by assuming the same scatterers as for finite B.

For the order-of-magnitude estimates it will be sufficient to use the Lorentzian form of $\Pi^{(2)}(\omega, \mathbf{q})$. Moreover, in the resonance approximation one should retain only the resonant term of all the series for $\Pi_R^{(2)}(\omega, \mathbf{q})$

$$\Pi_R^{(2)}(\omega, \mathbf{q}) = -\frac{\mathcal{R}_\mathcal{N}(\omega, \mathbf{q})}{\omega - \mathcal{N}\Omega\cos\theta + i\Gamma_e}. \tag{7}$$

where $\mathcal{R}_\mathcal{N}$ is the residue at the pole $\omega = \mathcal{N}\Omega\cos\theta - i\Gamma_e$. Calculating $\Delta\sigma_{xx}$ one can evaluate the integral over frequency taking the residues in the poles $\omega = \mathcal{N}\Omega\cos\theta \pm i\Gamma_e$. This results in replacement of $\mathrm{Im}\,\varepsilon_R$ under the integral by

$$\Delta \equiv \frac{1}{\pi}\frac{\mathrm{Im}\,\varepsilon_A^{-1} + 2\gamma}{(2\gamma + \mathrm{Im}\,\varepsilon_A^{-1})^2 + (\mathrm{Re}\,\varepsilon_A^{-1})^2} \tag{8}$$

where $\gamma = \Gamma_e/\overline{\omega}$; $\overline{\omega} = 2\pi e^2/q\mathcal{R}_\mathcal{N}(\mathcal{N}\Omega\cos\theta, \mathbf{q})$ while ε_A is calculated at $\omega = \mathcal{N}\Omega\cos\theta + i(\Gamma + \Gamma_e)$. The angle θ_t is given by the condition $2\gamma = \varepsilon_A^{-1}$. As the integral in (4) is dominated by $q = q_T$ this condition should be fulfilled for $q = q_T$ and has the form

$$\frac{1}{1 + \Gamma/\Gamma_e(\theta_t)} = \frac{n_s}{n_1}\cos\theta_t. \tag{9}$$

Here and henceforth we assume that $\Gamma, \Gamma_e \ll \omega_l - \omega_t \ll \omega_l$ while

$$\frac{1}{n_1} = \frac{e^2\Omega^{1/2}\omega_t}{\varepsilon_\infty\hbar a_B q_T^2 T^{3/2}(\omega_l - \omega_t)}. \tag{10}$$

Eq. (9) establishes a correspondence between the low concentration dependence of the MPR amplitude for perpendicular $\mathbf{B}$ [3] and its angular dependence in a tilted field $\mathbf{B}$ for a fixed concentration. Indeed, the sharpest dependence of MPR amplitude on n_s as well

as on θ comes from the resonant factor Eq. (8). In particular, for $\Gamma/\Gamma_e \ll 1$ the MPR amplitude is determined by the effective concentration $n_s \cos\theta$. Thus according to Eq. (9) the decrease of the MPR amplitude for $\theta = 0$ when n_s goes down and its decrease when θ goes up are interrelated.

For further enhancement of the angle θ the resonance at $\mathcal{N}\Omega\cos\theta = \omega_t$ disappears. As soon as the condition $2\gamma = \varepsilon_A^{-1}$ is satisfied for $\omega = \omega_l + i\Gamma + i\Gamma_e$ direct application of the perturbation theory is permissible [3] as the screening ceases to play any role. Then we have a resonance at $\mathcal{N}\Omega\cos\theta = \omega_l$. The angle corresponding to the amplitude maximum will be denoted by θ_l. Due to the strong dispersion of $\varepsilon(\omega)$ the angles θ_t and θ_l can be discerned on experiment. Thus the equation $2\gamma = \varepsilon_A^{-1}$ for calculation of θ_t and θ_l has the same form for frequencies ω_t and ω_l respectively. As a result, we have

$$\sqrt{\frac{\cos\theta_l}{\cos\theta_t}} = \frac{\operatorname{Im}\varepsilon^{-1}(\omega_t + i\Gamma + i\Gamma_e, \theta_t)}{\operatorname{Im}\varepsilon^{-1}(\omega_l + i\Gamma + i\Gamma_e, \theta_l)}. \tag{11}$$

The dependence of ε^{-1} on θ is due to the θ-dependence of Γ_e. We find a reasonable correspondence between the experiment and this theory.

To summarize, we stress that the interpretation of behavior of the MPR in a tilted magnetic field has been a long-standing problem [2]. Two types of resonant maxima have been discovered on experiment. They may be called the ω_t- and ω_l-resonances as their positions are determined by the frequencies ω_t and ω_l respectively. We have determined the angular intervals where both types of resonance exist. We have found that sharp decrease of the ω_t-resonance amplitudes is due to the sharp angular dependence of the screening. The ω_l-resonance is analogous to the 3D MPR as there the screening plays no role. Therefore this resonance is suitable for investigation of the electron spectrum in the quantum wells. We wish to emphasize that its experimental investigation in the perpendicular magnetic field should be very difficult as it would demand very low electron concentrations [3]. For bigger electron concentrations one can expect an enhancement of the MPR amplitudes for large values of θ.

Acknowledgements

V.V.A. and V.L.G. are grateful to the Wihuri Foundation as well as to the Russian Foundation for Basic Research, grant No 00-15-96748 for financial support.

References

[1] Yu. A. Firsov, V. L. Gurevich, R. V. Parfeniev and I. M. Tsidil'kovskii, *Magnetophonon Resonance*. In: *Landau Level Spectroscopy*, ed. G. Landwehr and E. I. Rashba, Elsevier, 1991.

[2] R. J. Nicholas, *Two-dimensional Magnetophonon Effect*. In: *Landau Level Spectroscopy*, ed. G. Landwehr and E. I. Rashba, Elsevier, 1991, p. 778.

[3] V. V. Afonin, V. L. Gurevich and R. Laiho, *Phys. Rev. B* **62**, 15913 (2000).

9th Int. Symp. "Nanostructures: Physics and Technology"
St Petersburg, Russia, June 18–22, 2001

Magnetic field induced circular photogalvanic effect in InAs quantum wells

S. D. Ganichev†‡, *V. V. Bel'kov*‡, E. L. Ivchenko‡, S. A. Tarasenko‡,
M. Sollinger†, F.-P. Kalz†, D. Weiss†, J. Eroms† and W. Prettl†
† Institut für Experimentelle und Angewandte Physik,
Universität Regensburg, D-93040 Regensburg, Germany
‡ Ioffe Physico-Technical Institute, St Petersburg, Russia

We report on the first observation of a magnetic field induced circular photogalvanic effect (CPGE) in quantum wells (QWs). The experiments were carried out on (001)-MBE-grown n-InAs/AlGaSb QW structures with a 15 nm single InAs channel at 4.2 K. For optical excitation we used the $\lambda = 148$ μm of a high power far-infrared pulsed NH_3 laser optically pumped by a TEA-CO_2. The peak power of a single laser pulse was about 40 kW. The helicity $P_{\rm circ}$ of the incident light varied from -1 (left handed circular, σ_-) to $+1$ (right handed circular, σ_+) according to $P_{\rm circ} = \sin 2\varphi$ were φ is the angle between the initial polarization plane and the optical axis of the $\lambda/4$ plate.

In the absence of a magnetic field, $\mathbf{B} = 0$, the irradiation of these semicontuctor structures by far-infrared laser radiation results in a photocurrent, $\mathbf{j} \propto P_{\rm circ}$, which reverses its sign by switching the helicity of radiation from left handed to right handed [1]. Due to the point-group symmetry C_{2v} of the studied QWs, the photogalvanic current at $\mathbf{B} = 0$ is only observed under oblique incidence. Here we demonstrate that the application of an external magnetic field, $\mathbf{B}$, in the interface plane induces a helicity-dependent current even at normal incidence. The current is proportional to B (up to 5 T) and inverts its direction with the reversal of the magnetic field. For the sake of brevity we refer to the effect under consideration as to the magneto-CPGE. For bulk materials this effect was theoretically treated in [2, 3] and observed in p-GaAs [4].

Phenomenologically, the magneto-CPGE is described by a third-rank tensor as

$$j_\alpha = \mu_{\alpha\beta\gamma} B_\beta i \left(\mathbf{E} \times \mathbf{E}^*\right)_\gamma = \mu_{\alpha\beta\gamma} E^2 B_\beta \hat{e}_\gamma P_{\rm circ}, \tag{1}$$

where $\mathbf{E}$ is the amplitude of the electric field of the radiation, $E = |\mathbf{E}|$, and $\hat{\mathbf{e}}$ is a unit vector pointing in the direction radiation propagaion.

In bulk crystals of the class T_d, the tensor $\mu_{\alpha\beta\gamma}$ has only one independent component $\mu \equiv \mu_{xyz}$, $\mu_{\alpha\beta\gamma} = \mu$ if $\alpha \neq \beta \neq \gamma$ and $\mu_{\alpha\beta\gamma} = 0$ otherwise. Hereafter we use the coordinate systems $x \parallel [100]$, $y \parallel [010]$, $z \parallel [001]$ and $x' \parallel [1\bar{1}0]$, $y' \parallel [110]$, $z \parallel [001]$. In a (001)-grown zinc-blende-lattice QW with non-equivalent normal and inverted interfaces, the point-group symmetry is reduced to C_{2v}. Under normal incidence of the light and for the magnetic field lying in the interface plane, the magneto-CPGE is described by two independent constants and, in the coordinate system (x', y', z), can be presented as

$$\begin{aligned} \delta j_{x'} &= (\mu' + \mu) E^2 B_{x'} \hat{e}_z P_{\rm circ}, \\ \delta j_{y'} &= (\mu' - \mu) E^2 B_{y'} \hat{e}_z P_{\rm circ}. \end{aligned} \tag{2}$$

The photocurrent induced in the same geometry, $\hat{\mathbf{e}} \parallel z$, $\mathbf{B} \perp z$, in a bulk T_d-symmetry crystal or in a D_{2d}-symmetry QW with symmetrical interfaces is described by Eqs. (2)

assuming $\mu \neq 0$, $\mu' = 0$. In this case the directions of the vectors **j** and **B** are interconnected by the mirror reflection in the plane (110) if $\mu > 0$ or the plane $(1\bar{1}0)$ if $\mu < 0$. In particular, **j** and **B** are parallel (or antiparallel) when the magnetic field is applied along x' or y' and perpendicular when $\mathbf{B} \parallel x$ or $\mathbf{B} \parallel y$.

Another limiting case $\mu = 0$, $\mu' \neq 0$ is allowed not only by the C_{2v} symmetry but also by the polar uniaxial symmetry $C_{\infty v}$. The latter corresponds to the symmetry of a QW structure which is grown as if from isotropic compositional materials and has non-equivalent left- and right-hand-side interfaces. Note that if $\mu = 0$ then Eqs. (2) can be rewritten in the following two-dimensional vector form

$$\mathbf{j} = \mu' E^2 \mathbf{B} \hat{e}_z P_{\mathrm{circ}}, \tag{3}$$

i.e. the vectors **j** and **B** are parallel irrespective to the in-plane orientation of **B**.

The present experimental results are well described by Eq. (3) indicating that the symmetry of the investigated QW is $C_{\infty v}$. This is supported by the investigaton of the circular photocurrent in the same structure under oblique incidence at $\mathbf{B} = 0$ for different geometries.

Acknowledgements

We thank for support the DFG, the RFBR and the NATO (Linkage Grant).

References

[1] S. D. Ganichev, E. L. Ivchenko, S. N. Danilov, J. Eroms, W. Wegscheider, D. Weiss and W. Prettl, submitted to PRL.
[2] E. L. Ivchenko and G. E. Pikus, *Problems in Modern Physics*, Nauka, Leningrad, 1980, p. 275.
[3] E. L. Ivchenko, Yu. B. Lyanda-Geller and G. E. Pikus, *Sov. Phys. Solid State* **30**, 575 (1988).
[4] A. V. Andrianov and I. D. Yaroshetskii, *Pis'ma Zh. Eksp. Teor. Fiz.* **40**, 131 (1984).

9th Int. Symp. "Nanostructures: Physics and Technology"
St Petersburg, Russia, June 18–22, 2001

Resonant Γ–X-transfer in GaAs/AlAs quantum-well structures

S. R. Schmidt†, A. Seilmeier†, E. A. Zibik‡, L. E. Vorobjev‡,
A. E. Zhukov§ and V. M. Ustinov§
† Institute of Physics, University of Bayreuth, D-95440 Bayreuth, Germany
‡ St. Petersburg State Technical University, St Petersburg 195251, Russia
§ Ioffe Physico-Technical Institute, St Petersburg, Russia

Abstract. We investigate the Γ_2–X_{z1} intersubband dynamics in GaAs/AlAs quantum-well structures by time-resolved infrared pump and probe experiments. In the studied structure, the second Γ-level in GaAs is nearly resonant to the first X_z-level in AlAs. We observe a biexponential decay of the bleaching signal with a fast time constant in the order of 1 ps and a second slower time constant of about 7 ps at 10 K and 4 ps at 300 K, respectively. The long term decay represents the X_z–Γ_2 transfer by elastic Γ–X scattering at low temperatures. At 300 K electron-LO-phonon-scattering accelerates the Γ–X transfer.

Introduction

Investigation of intersubband carrier dynamics is very important for application of quantum well structures as infrared devices. In particular, GaAs/AlAs structures are promising candidates for infrared photodetectors (QWIPs) [1] and quantum cascade lasers (QCLs) [2]. As these structures have extreme deep quantum wells ($\sim$ 1 eV) the dark current in QWIPs is strongly reduced and the operating temperature in QCLs is increased. However, in GaAs/AlAs quantum well structures intersubband dynamics not only occurs in the Γ-valley of the GaAs layers but also the AlAs barriers, which are the quantum wells for X-electrons, have to be considered. At the heterointerface Γ–X-mixing takes place, that significantly influences the intraband carrier dynamics [3]. Recently, a laser scheme with strong population inversion between mixed Γ and X states in GaAs/AlAs-structures has been proposed in [4].

1. Sample structure and experimental method

The investigated GaAs/AlAs quantum well structure consists of 100 layers with 10 nm wide GaAs quantum wells embedded in between 2.5 nm thick AlAs layers. The central 5 nm of the wells are doped by silicon with a concentration of 6×10^{17} cm^{-3}. The structure is grown by MBE on a semiinsulated GaAs (100) substrate. According to our band structure calculations the first excited Γ-state in GaAs is nearly in resonance with the ground X_z state in AlAs and Γ–X-mixing occurs (see Fig. 1(a)), corresponding to an overlap integral $S_{\Gamma X} = | < \psi_{\Gamma 2} \mid \psi_{X1} > |^2 = 0.03$.

The relaxation measurements are performed by a Nd:glass laser system of 8 Hz repetition rate with two travelling wave IR dye lasers and two difference frequency mixing stages [5]. The system generates two pulses of 2 ps duration and a spectral width of 10 cm^{-1} independently tunable between 800 cm^{-1} and 2500 cm^{-1}. One of the two infrared pulses excites electrons at a well defined pump frequency $\tilde{\nu}_{\text{pump}}$ from the ground subband to the excited subbands. The subsequent change of the intersubband absorption is measured time-resolved by the second weaker infrared pulse at $\tilde{\nu}_{\text{probe}}$.

2. Results and discussion

The absorption spectra shown in Fig. 1(b) represent the transition between the Γ_1- and the Γ_2-state which has a strong Γ-character at small k [see Fig. 1(a)]. At 10 K the peak frequency is located at 915 cm^{-1}. At higher temperatures the typical redshift and broadening of the absorption lines from 50 cm^{-1} at 10 K to 73 cm^{-1} at 300 K are observed. The absorption $\alpha L = -\ln T$ decreases from 2.5 at 10 K to 1.5 at 300 K.

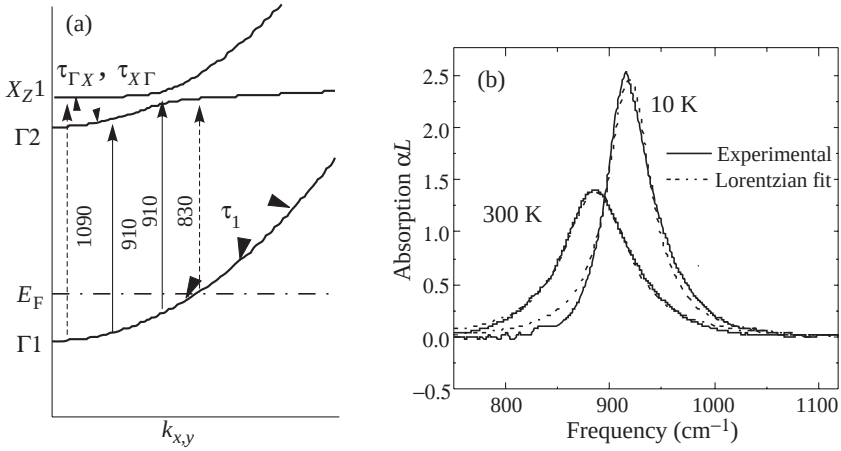

Fig. 1. (a) Schematic conduction band dispersion for the GaAs/AlAs QW structure in the presence of Γ–X-mixing. Arrows indicate the possible transitions at $T = 10$ K. (b) Intersubband absorption spectra.

Pump and probe measurements at different pump frequencies with a probe frequency at the Γ_1–Γ_2 resonance are compared for $T = 10$ K [6] and $T = 300$ K. For $T = 10$ K the transmission changes at $\tilde{\nu}_{\text{probe}} = 910$ cm^{-1} are plotted in Fig. 2 after excitation at

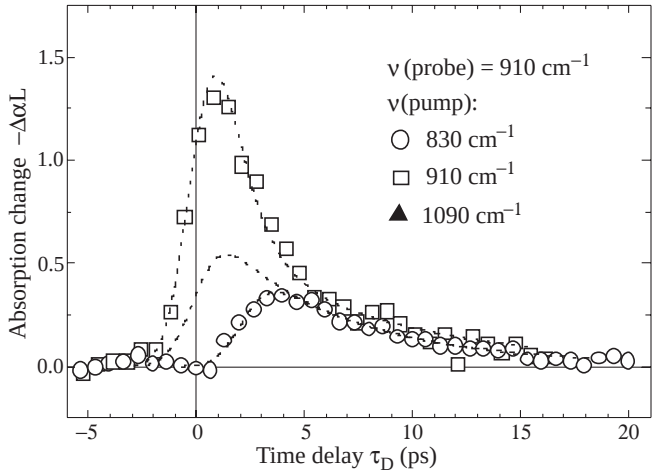

Fig. 2. Time resolved absorption change at $T = 10$ K after excitation at different pump frequencies. Dashed lines are fits of the experimental data by solving rate equations.

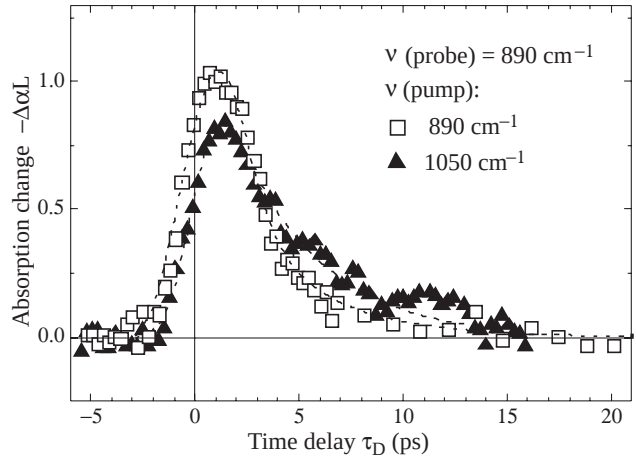

Fig. 3. Time resolved absorption change at $T = 300$ K after excitation at different pump frequencies. Dashed lines are fits of the experimental data by solving rate equations.

$\tilde{\nu}_{\text{pump}} = 830$, 910 and 1090 cm^{-1}. Excitation in the center of the intersubband absorption line at 910 cm^{-1} occupates Γ and X_z states [see Fig. 1(a)] and leads to a biexponential behavior of the relaxation signal with a fast relaxation time $\tau_1 = 1.2$ ps and a long term decay $\tau_2 = 7.0$ ps. In contrast, pumping at 830 and 1090 cm^{-1} excites states with strong X_z character and a decay dominated by the long relaxation time τ_2 is found. This observation can be explained by a rapid $\Gamma_2 \rightarrow \Gamma_1$ recovery time τ_1 together with long term carrier scattering processes between the nearly resonant Γ_2- and X_{z1}-valleys, which are strongly coupled [3]. For $T = 300$ K the transmission changes at $\tilde{\nu}_{\text{probe}} = 890$ cm^{-1} are shown in Fig. 3 after excitation at $\tilde{\nu}_{\text{pump}} = 890$ and 1050 cm^{-1}. Similar to the measurements at low temperature two relaxation times are observed. Pumping in the center of the absorption band we obtain two time constants, 1 ps for the fast decay and about 4 ps for the long term decay. The curve for the pump frequency of 1050 cm^{-1} only shows the long relaxation time.

For a detailed interpretation of the results the energy dispersion diagram of the studied structure is considered [Fig. 1(a)]. Under excitation, the electrons fill the Γ–X-mixed subbands. Due to the Γ–X interaction at the heterointerface direct transitions to the X_{z1}-subbands become possible. Absorption of light due to Γ_1–X_z transitions was already detected in GaAs/AlAs quantum-well structures previously [1]. Thus for intense excitation in and around the absorption peak, both Γ_1–Γ_2 and Γ_1–X_{z1} optical transitions take place. As the energy dispersions for Γ and X electrons are strongly different, the absorption band for intervalley transitions must be broader than that for Γ–Γ transitions. Consequently, in spite of the weak oscillator strength of the Γ_1–X_{z1} transition, it dominates the absorption change at pump frequencies at the feet of the absorption line, where the absorption coefficient for the Γ_1–Γ_2 transition is negligibly small. On the other hand, intervalley scattering processes play a key role in carrier relaxation. After excitation, electrons are redistributed among the second Γ-subband and the X_z-subband and vice versa. Electron-LO-phonon scattering and elastic electron scattering due to the interface mixing potential (Γ–X_z mixing) are relevant mechanisms for the Γ–X transfer in GaAs/AlAs type II superlattices [3, 7]. In our sample electron-LO-phonon scattering is believed to be of minor importance at low temperature, because the separation of the coupled Γ_2- and X_{z1}-subbands (about 15 meV)

is below the optical phonon energy. Therefore, the elastic electron scattering due to the interface mixing potential is expected to dominate the transfer process between the Γ_2 and X_{z1}-states of the AlAs barrier at 10 K [8]. At 300 K also electron-LO-phonon-scattering becomes possible due to the increased phonon occupation probability and a shorter time constant τ_2 is observed.

Electrons return from AlAs to GaAs mainly via the Γ_2-subband, as transitions into the Γ_1-subband are suppressed because of the smaller overlap integral. The X_1–Γ_2 relaxation time $\tau_{X\Gamma}$ can be determined for pump frequencies at the feet of the absorption line, when electrons are directly excited into subband states with strong X_{z1} character. Due to the lower density of states in the Γ-valley compared to the X-valley X–Γ scattering times $\tau_{X\Gamma}$ are longer than Γ–X scattering times $\tau_{\Gamma X}$.

Modell calculations using rate equations show the best fit with $\tau_1 = 0.8\,\text{ps}$, $\tau_{\Gamma X} = 2.5\,\text{ps}$ and $\tau_{X\Gamma} = 4.5\,\text{ps}$ for $T = 10\,\text{K}$ and $\tau_1 = 0.6\,\text{ps}$, $\tau_{\Gamma X} = 2.0\,\text{ps}$, $\tau_{X\Gamma} = 2.5\,\text{ps}$ for $T = 300\,\text{K}$, respectively [6].

3. Conclusion

We have directly observed the influence of Γ–X mixing on intersubband relaxation in a GaAs/AlAs quantum-well structure. The resonant intersubband carrier transfer from the Γ valley in GaAs to the X_z valley in AlAs and vice versa, has been observed at 10 K. At room temperature an additional electron-LO-phonon-scattering channel enhances the transfer rates.

References

[1] H. C. Liu, P. H. Wilson, M. Lamm, A. G. Steele, Z. R. Wasilewski, Janmeng Li, M. Buchanan and J. G. Simmons, *Appl. Phys. Lett.* **64**, 475 (1994).
[2] C. Becker, C. Sirtori, H. Page, G. Glastre, V. Ortiz, X. Marcadet, M. Stellmacher and J. Nagle, *Appl. Phys. Lett.* **77**, 463 (2000).
[3] H. C. Liu, *Appl. Phys. Lett.* **51**, 1019 (1987).
[4] V. Y. Aleshkin and A. A. Andronov, *JETP Lett.* **68**, 79 (1998).
[5] I. M. Bayanov, R. Danielius, P. Heinz and A. Seilmeier, *Optics Commun.* **113**, 99 (1994)
[6] S. R. Schmidt, E. A. Zibik, A. Seilmeier, L. E. Vorobjev, A. E. Zhukov and U. M. Ustinov, *Appl. Phys. Lett.* **78**, (2001) to be published
[7] J. Feldmann, J. Nunnenkamp, G. Peter, E. Göbel, J. Kuhl, K. Ploog, P. Dawson and C. T. Foxon, *Phys. Rev. B* **42**, 5809 (1990).
[8] O. E. Raichev, *Phys. Rev. B* **49**, 5448 (1994).

9th Int. Symp. "Nanostructures: Physics and Technology"
St Petersburg, Russia, June 18–22, 2001

Linearly-polarized photoluminescence from type II ZnSe/BeTe quantum wells with atomically-flat interfaces

A. A. Toropov†‡, *S. V. Sorokin*†§, S. V. Ivanov†§, N. Hori‡, M. Ichida‡, A. Nakamura‡, A. Waag¶ and G. Landwehr§

† Ioffe Physico-Technical Institute, St Petersburg, Russia
‡Nagoya University, Chikusa-ku, Nagoya 464-8603, Japan
¶Abteilung Halbleiterphysik, Universität Ulm, 89081 Ulm, Germany
§Physikalisches Institut der Universität Würzburg, D-97074 Würzburg, Germany

ZnSe/BeTe multiple quantum well (MQW) heterostructures have recently attracted attention due to the unique electronic and optical properties [1]. Since the hetero-interface between ZnSe and BeTe is of a strong type II, electrons are localized in ZnSe layers and holes in BeTe. Both electron- and hole-band offsets are extremely high (∼2 eV for electrons and ∼1 eV for holes). As a result, the photoluminescence (PL) of the MQW samples originates in spatially indirect transitions. Usually, one or two emission bands are observed in a 1.9–2.2 eV region, depending on a thickness of the constituent layers and experimental conditions [2, 3]. The higher-energy PL peak originates from band-to-band, spatially indirect transitions, whereas the lowest-energy one has been attributed to emission of carriers localized by fluctuations of the QW thickness or some other interface imperfections [3]. The reported spectral width of the peaks was rather large (10–100 meV), which prevented accurate identification of the lowest-energy peak origin. Another specific feature of the PL bands in such samples is frequently observed strong linear polarization of the emission with respect to [110] and $[1\bar{1}0]$ in-plane crystal axes. The polarization has been explained by breaking down the QW roto-inversion symmetry due to either application of external electric field (the quantum confined Pockels effect [2]) or occurrence of chemically non-equivalent left- and right-QW interfaces [3].

In this paper we report on molecular beam epitaxy (MBE) growth and PL studies of ZnSe/BeTe MQW samples with improved quality of interfaces. Narrow linearly polarized lines have been observed in cw PL spectra, which has been attributed to recombination of carriers localized by mono-layer (either *mono-molecular* or *mono-atomic*) fluctuations of the QW thickness.

A typical sample studied was grown by MBE in a Riber 2300 two-chamber system on a GaAs(001) substrate. A GaAs epitaxial buffer was used to improve the quality of the GaAs surfaces. Elemental Be, Te, and Zn effusion cells as well as a Se valve cracking cell were used as molecular beam sources. The substrate temperature was kept constant at T_S of 300°C. The ZnSe and BeTe layers were grown in a group VI-rich regime as confirmed by the (2×1)Se and (2×1)Te RHEED reconstructions at Se/Zn∼1.5 and Te/Be∼2 ($P_{Te}/P_{Be} \sim 20$) flux ratios, respectively. One should stress that for these experiments the Te/Be flux ratio has been lowered by 1.5 times as compared to that used for growth of the structures studied in [1–3], which has been found to result in much smoother layer-by-layer BeTe growth characterized by long lasting RHEED oscillations at T_S of 300°C. This agrees well with recent independent findings of the optimum MBE growth conditions of flat surface and high structural quality BeTe films [4].

The structure contains a 20-period ZnSe(5 nm)/BeTe(1.8 nm) MQW sandwiched between two thick $Zn_{1-x}Be_xSe$ layers nearly lattice-matched to a GaAs substrate ($x \sim$

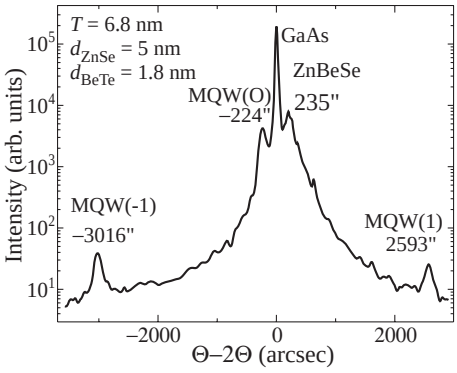

Fig. 1. (004) Θ−2Θ XRD rocking curve of the structure.

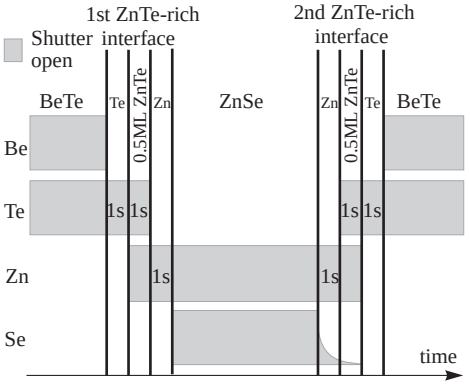

Fig. 2. Shutter sequence applied for obtaining ZnTe-rich interfaces.

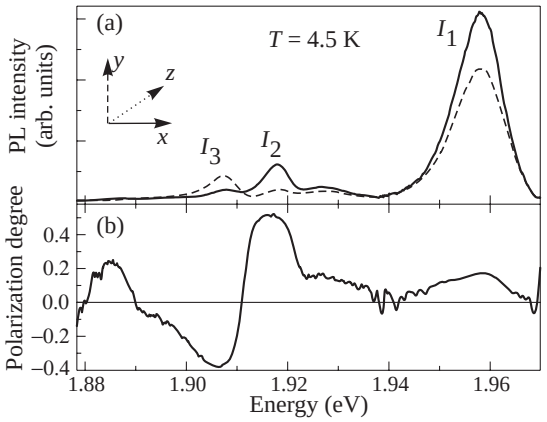

Fig. 3. (a) Photoluminescence spectra measured for two orthogonal linear polarizations along [110] and [1$\bar{1}$0] in-plane crystal axes (x and y directions); (b) the spectrum of the degree of linear polarization with respect to the [110] and [1$\bar{1}$0] axis.

0.03−0.04). Figure 1 shows an X-ray diffraction (XRD) rocking curve measured in the sample near a (004) reflection. Besides the peak originating from the GaAs substrate (at 0 arcsec), there are three narrow peaks attributed to 0-, +1-, and −1-order satellite reflections from the MQW structure and a peak at 235" relevant to the ZnBeSe claddings. Small width of the peaks as well as close to GaAs symmetrical arrangement of the 0-order MQW satellite and the peak related to the claddings indicate perfect structural quality and pseudomorphic nature of the structure.

The BeTe/ZnSe interfaces were grown as containing predominantly ZnTe bonds with a shutter sequence shown in Fig. 2. The first interface of the ZnSe QW (epitaxy of ZnSe on BeTe) was fabricated by a deposition of 0.5 ML ZnTe in MBE mode under Te-stabilized growth conditions on a Te-terminated surface of BeTe. Then the Te shutter was closed, providing a 1 s exposure of the surface to the Zn flux, which corresponds to deposition of the rest ∼0.5 ML of Zn atoms, assuming the ZnSe growth rate to be 0.6 ML/s as measured by a RHEED oscillation technique. Although this Zn coverage can be slightly less than 0.5 ML due to some expected reduction of a Zn incorporation coefficient at the absence of

the Se flux, by analogy with the case of CdSe growth [5], it is expected that the additional Zn atoms mostly occupy ZnTe-free sites on the BeTe surface to complete the ZnTe ML. The deposition of BeTe on ZnSe was done by the opposite shutter sequence. A 1 s exposure of ZnSe surface to the Zn flux was followed by a 0.5 ML ZnTe deposition. Then the Zn shutter was closed for 1 s and BeTe growth was initiated on a Te-terminated surface of ZnTe. However, formation of the second ZnTe interface was done at a relatively high Se background pressure due to a finite time of Se valve closing (about 2 s). The latter growth peculiarity is expected to result in essential chemical bond type fluctuations (BeSe instead of ZnTe) at the second interface of ZnSe QWs (or at the first interface of BeTe QW), especially when taking into account the higher binding energy of ZnSe as compared to ZnTe. The latter is additionally reduced by a strain induced Gibbs free energy due to ~7% lattice-mismatch of ZnTe with respect to GaAs and the higher Be incorporation coefficient in comparison with that of Zn. Nevertheless, the roughness of the consequent interfaces of the MQW structure does not increase, as follows from a nearly constant RHEED specular spot intensity observed during the whole growth run, which is probably due to a strong surface smoothing effect of the BeTe growth under the growth conditions used.

Photoluminescence (PL) spectra were measured at 4.5 K in a bath He cryostat in a back-scattering geometry. A 325 nm laser line of a He-Cd laser was used for the PL excitation. The excitation spot size was about 0.5 mm, whereas the excitation power was kept below 1 mW. So the excitation power density in these experiments was below 0.4 W/cm^2. The spectra were measured for two orthogonal linear polarizations along [110] and [1$\bar{1}$0] in-plane crystal axes. Figure 3(a) demonstrates the two spectra of linearly polarized PL. There are three main peaks in the spectra, labeled as I_1, I_2 and I_3.

The peak intensities clearly depend on the detected light polarization, which is illustrated by the spectrum of linear polarization degree shown in Fig. 3(b). The degree of polarization P is defined as

$$P = \frac{I_{[100]} - I_{[1\bar{1}0]}}{I_{[100]} + I_{[1\bar{1}0]}},$$

where $I_{[110]}$ and $I_{[1\bar{1}0]}$ are the PL intensities measured using a linear polarizer oriented along [110] and [1$\bar{1}$0] directions, respectively. The polarization of I_1 peak is rather small (in the range 12–25%, depending on the experimental conditions), whereas I_2 and I_3 emission bands are linearly polarized in opposite directions at the maximum degree in the range of 40–60%. Note that FWHM value of the I_2 and I_3 peaks is as small as 3–5 meV. To our knowledge, this is the smallest value ever reported for PL peaks in ZnSe/BeTe samples, which confirms an extraordinary quality of the sample.

The observed peaks are located in the range of 1.9–2.0 eV, which is usual for observation of the PL related to spatially indirect excitons [1–3]. Keeping in mind that all interfaces in the sample are expected to be almost equivalent (ZnTe-like) one can anticipate relatively small in-plane linear polarization anisotropy of the excitonic emission [3]. From this point of view, it seems natural to attribute the most intensive, in spite of its higher energy position, smaller polarized peak I_1 to emission of indirect excitons in the sample regions with almost equivalent ZnTe-like interfaces.

To explain the two narrow oppositely polarized peaks I_2 and I_3 we assume occurrence of discrete mono-layer fluctuations of the QW thickness, by analogy with the well-known explanation of multiple PL peaks in GaAs/Al(Ga)As multiple QWs. The principle difference is that a ZnSe/BeTe multiple QW structure consists of binary materials which share neither common cations nor anions. For such structures there is a possibility of a mono-atomic (or half-mono-molecular) fluctuation of the QW effective thickness as well. This

imperfection can be regarded as a replacement of one atomic layer (either cation or anion) at the hetero-boundary between the two binary compounds with no common atoms, which results in a single-atomic shift of the interface, accompanied by a change of the interface chemical bond.

The energy gap between I_1 and I_2 is comparable with the carrier confinement energy corresponding to a mono-molecular fluctuation of the hole (BeTe) QW thickness. The respective energy is $\sim 35-40$ meV for heavy holes, as estimated within the effective mass approximation. For electrons this energy is much smaller (4–8 meV) because of a larger thickness of the ZnSe electron QWs. Therefore we attribute the two peaks (I_2 and I_3) to recombination of holes, localized in plane of the BeTe QW by a mono-layer thickness fluctuation, with electrons in left and right ZnSe layers. This interpretation also explains the opposite polarizations of I_2 and I_3 bands in agreement with the orthogonal polarizations of the interface bonds at the direct and inverted interfaces of an ideal QW with atomically abrupt interfaces [2]. The splitting between the two transitions can result from the inherent difference in the structure of the "left" and "right" interfaces of the BeTe layer, which is in agreement with the above sample growth analysis. In particular, only mono-molecular terraces are expected at the "left" (direct) ZnTe-like interface, whereas mono-atomic terraces can take place at the "right" (inverted) interface of the BeTe QW. The former terraces do not change the chemical type of the interface bond. The latter ones induce the change of the interface bond type and presumably the energy of the transition.

In conclusion, we have reported on improvements in the MBE growth of ZnSe/BeTe QW heterostructures with ZnTe-like interfaces, resulting in observation of two narrow oppositely polarized PL peaks. The peaks are attributed to recombination of holes localized by mono-layer fluctuations of the BeTe QW thickness with electrons from either left or right ZnSe layer. This interpretation is in qualitative agreement with the estimation of the carries confinement energies, performed within the effective mass approximation for a mono-molecular QW thickness fluctuation, as well as with the symmetry analysis of the QW interface bonds. On the other hand, accurate quantitative description of the energy splitting between the peaks and their degree of linear polarization require additional studies.

Acknowledgements

The authors are thankful to E. L. Ivchenko for useful discussions. This work was supported in part by RFBR Grants, the Program of the Ministry of Sciences of RF "Physics of Solid State Nanostructures", Volkswagen Stiftung and INTAS Grants No 97-31907 and No 00-02-16997a.

References

[1] A. Waag, *et alJ. Appl. Phys*, **80**, 792 (1996).
[2] A. V. Platonov, *et alPhys. Rev. Lett.*, **83**, 3546 (1999).
[3] D. R. Yakovlev, *et alPhys. Rev. B* **61**, 2421 (2000).
[4] M. W. Cho, *et alJ. Vac. Scie. Technol. A* **18(2)**, 457 (2000).
[5] S. V. Sorokin, *et alJ. Cryst.Growth* **201/202**, 461 (1999).
[6] Th. Walter, *et alMicroscopy of Semiconducting Materials*, UK: Institute of Physics Publishing, Oxford, 315 (1997).

9th Int. Symp. "Nanostructures: Physics and Technology"
St Petersburg, Russia, June 18–22, 2001

Unconventional Landau states in the quantum well with embedded self-arranged quantum dots

Yu. V. Dubrovskii[1], *V.A. Volkov*[2], E. E. Vdovin[1], L. Eaves[3], P. C. Main[3], D. K. Maude[4], J.-C. Portal[4,7,8], A. Neumann[3], M. Henini[3], J. C. Maan[5] and G. Hill[6]

[1] Institute of Microelectronics Technology RAS, 142432 Chernogolovka, Russia
[2] Institute of Electronics and Radioengineering RAS, Moscow, Russia
[3] The School of Physics and Astronomy, University of Nottingham, Nottingham NG7 2RD, UK
[4] Grenoble High Magnetic Field Laboratory, MPI-CNRS, BP166 38042 Grenoble Cedex 9, France
[5] High Field Magnet Laboratory, Research Institute for Materials, University of Nijmegen, 6525 ED Nijmegen, The Netherlands
[6] Department of Physics, University of Sheffield, Sheffield S3 3JD, UK
[7] Institut Universitaire de France 8 INSA, F31077 Toulouse Cedex 4, France

Abstract. It have been found that that the presence of InA self-arranged quantum dots strongly modify the structure of Landau levels in a host GaAs quantum well.

It was shown recently that the presence of InA self-arranged quantum dots (QD) in a host GaAs quantum well containing a two-dimensional electron gas strongly effects the electron transport [1], dramatically modifies the cyclotron resonance [2], and even more in the presence of quantum dots electron system exhibits metal-insulator transition in zero magnetic field otherwise not observable [3]. In this work we demonstrate with the help of the tunneling spectroscopy that QD also modify the structure of Landau level states in the quantum well.

The structure for the present studies was the same double barrier AlGaAs/GaAs/AlGaAs heterostructure as used before [4] containing layer of InAs QD in the center of the well, which was confirmed by photoluminescence spectroscopy. In equilibrium the dots is normally charged with electrons from contact layers.

After application of the high enough voltage bias to the structure the accumulation layer adjacent to the barrier is formed which serves as two dimensional emitter. In normal to the barriers magnetic field electrons tunnel into empty Landau level states in the well. If all tunneling electrons have the same energy, which happens if only ground Landau level is occupied in the two-dimensional emitter, the tunneling spectra measured at different biases give direct mapping of the density of states in the quantum well. The energy of the states is related with bias voltage by approximately linear dependence.

Figure 1 shows tunneling current versus magnetic field at different biases obtained when only ground Landau level is occupied in the emitter. Peaks correspond to the tunneling into Landau states in the well. The oscillations is periodic in reverse magnetic field and it is easy by simple analysis to determine the relation between peak on the curve and the number of the corresponding Landau level. The most interesting feature of the data is that some of the peaks (for example one indicated by arrow) are transformed from the well defined peak into the shoulder and then again to the peak with bias voltage.

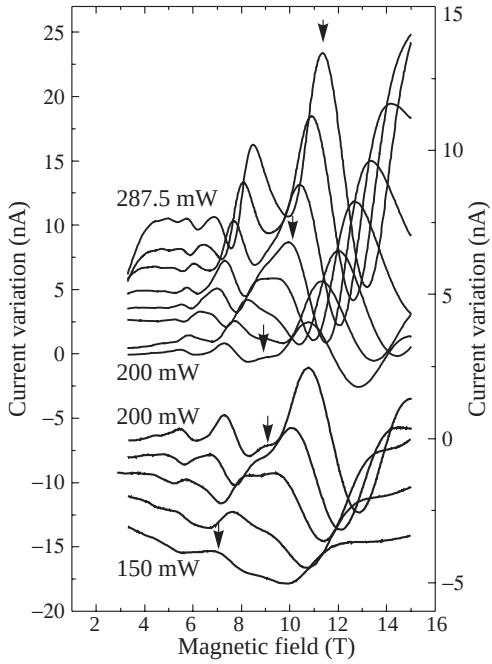

Fig. 1. Tunneling current variation with magnetic field at different voltage biases V_b. Curves are shifted arbitrary in vertical direction. The lower set of the curves for bias voltage range from 150 mV to 200 mV (right scale). The upper set for the range from 200 mV to 287.5 mV (left scale). Bias voltage step between curves is 12.5 mV for both sets. Arrows indicate the peak which transformation with magnetic field is discussed in the text.

Figure 2 shows the fan diagram of the observed peaks, that is the dependence of the peak position on the voltage scale versus magnetic field. The solid circles indicate position of the well defined peaks when the open circles indicate position of the shoulders. It is obvious that in magnetic fields defined as B_1^* and B_2^* unusual perturbation with Landau levels take place. In these magnetic field the area of the ground Landau level state in the well is approximately equal to $2S$ and $3S$, where $S = 12\,\text{nm} \times 12\,\text{nm}$ is the average area of the quantum dots known from the electron microscopy studies.

At the moment we do not have exact model of the observed influence of the quantum dots on Landau levels. We could propose that in the bias voltage region where the features were found the dots is still charged by electrons and in fact arrange in the well layer of

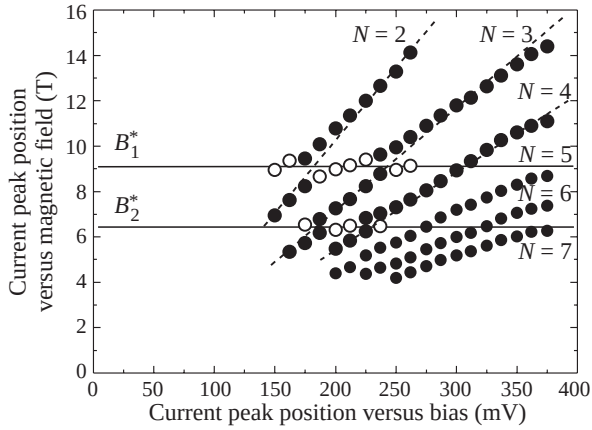

Fig. 2. Fan diagram of the Landau levels in the well. N is the Landau level number. Other details in the text.

the approximately equal size randomly located antidots. There also must exist clusters of 2, 3 and more antidots. Evidently that one should expect some kind of interaction in the structure when the area of clusters becomes commensurate with the area of cyclotron orbits. It should be expected also that some features will appear in tunneling spectra when area of ground state Landau level becomes equal to S which happens in magnetic field about 18 T. This value was out of magnetic field range used in our studies.

In conclusion, we demonstrate with the help of the tunneling spectroscopy that that the presence of InA self-arranged quantum dots modify the structure of Landau levels in a host GaAs quantum well. It could be proposed that some new commensurate type effect have been found in our studies.

Acknowledgements

This work was supported by INTAS (97-11475), RFBR (98-02-22008, 99-02-17592, 00-02-17903, 01-02-17844, 01-02-97020), PICS (628), Ministry of Science (FTNS-97-1057, 99-1124), and EPSRC (UK).

References

[1] G.H. Kim, *et al.*, *Appl. Phys. Let.* **73**, 2468 (1998).
[2] S. Cina, *et al.*, *Phys. Rev.* **B60**, 7780 (1999).
[3] E. Ribeiro, *et al.*, *Phys. Rev. Let.* **82**, 996 (1999).
[4] A. Patane, *et al.*, *J. Appl. Phys.* **88**, 2005 (2000).

9th Int. Symp. "Nanostructures: Physics and Technology"
St Petersburg, Russia, June 18–22, 2001

Shalow acceptors in strained MQW heterostructures in strong magnetic fields

V. Ya. Aleshkin, V. I. Gavrilenko and *D. B. Veksler*
Institute for Physics of Microstructures of Russian Academy of Sciences, GSP-105, Nizhny Novgorod, 603600, Russia.

Abstract. A new nonvariational theoretical technique allowing to calculate both ground and exited states of shallow impurity in a quantum well in the presence of strong magnetic field has been developed. The method has been applied to study the acceptor states in $Ge/Ge_{1-x}Si_x$ MQW heterostructures. The results obtained allow to explain the measured far IR photoconductivity spectra of the heterostructures and to identify the observed spectral lines.

Introduction

The problem of shallow impurities in multiple quantum wells (MQW) heterostructures in strong magnetic fields have been attracting the interest of researches during the last decade (see, for example, [1] and reference therein). As usual various variational methods are used for the interpretation of the experimental data. However in the most studies variational calculations are limited to consideration of the ground (1s) and the lowest exited states only because it is necessary to use trial functions with a large number of variational parameters for a satisfactory description of higher states. Sometimes it appears insufficiently for an explanation of all observed lines in the spectra of impurity absorption/photoconductivity. The technique developed in the present work is similar to that used in [2] for the calculation of the acceptor states in quantum wells structures without a magnetic field. The acceptor envelope function was expanded in the basis of Landau level wavefunctions of free holes (without the Coulomb potential) in the quantum well. By diagonalization of the acceptor Hamiltonian in this basis the series of acceptor state energies and wavefunctions was obtained, thus allowing to calculate the energies and the matrix elements of the optical transitions. The results obtained allow to interpret the observed shallow acceptor photoconductivity spectra in the far infrared range in the magnetic fields reported in [3].

1. Theoretical formalism

A calculation of the acceptor states is a rather complicated problem due to the degeneration of the valence band in semiconductors under consideration. Let's consider the problem of a hole in the impurity center Coulomb potential in a strained MQW heterostructure in strong magnetic field. The magnetic field is parallel to the growth direction. The total Hamiltonian 4×4 (without the spin-split subband terms) consists of the Luttinger Hamiltonian in the magnetic field [4], deformation terms [5], the rectangular quantum well (QW) potential and the Coulomb potential. As a first step we calculated the basis functions $\vec{\Psi}_{i,r}^{J_z}$ (the hole wave-functions in QW in the absence of the Coulomb potential). The calculations were performed using the axial approximation thus neglecting the off-diagonal elements proportional to $\gamma_2 - \gamma_3$ in the Hamiltonian, the graduation $\vec{A} = 1/2[\vec{H} \times \vec{r}]$ being chosen. The axial symmetry results in the conservation of the total angular momentum projection

on the magnetic field direction J_z. Each Landau state in the QW is characterized by the number n ($n = r + (|M| + M)/2$, $r = 0, 1, \ldots, \infty$,$M = J_z/\hbar + 3/2$), wave-function parity p and the subband number i. The Landau states prove to be degenerated on M ($M = -\infty, \ldots, -1, 0, \ldots, n$). In the above approximation the problem of the basis functions search was reduced to the solving of the system of four differential equations [6].

2. Results and discussion

In order to test the developed technique we have calculated the donor states in the GaAs/$Al_xGa_{1-x}As$ MQW. In strong magnetic fields ($H > 2$ kOe) our approach gives the results which fit the experimental data much better [7] than those obtained by the variational method [1].

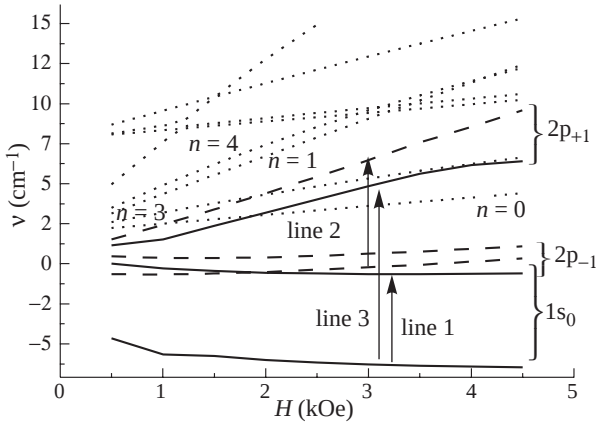

Fig. 1. Chart of calculated acceptor state energies in rectangular QW in the strained Ge/GeSi heterostructure #306 ($d_{GeSi} \approx d_{Ge} = 200$ Å, $\varepsilon = 2.1 \times 10^{-3}$, $x = 0.12$) vs the magnetic field. The solid lines correspond to the impurity states located in the center of QW. The dash lines refer to impurity states in the barrier center. Thin dotted lines — correspond Landau levels of free holes.

The calculation results for the ground ($1s$) and two exited ($2p_{\pm1}$) states energies for the acceptors in the $Ge/Ge_{1-x}Si_x$ heterostructures located in the center of a QW (solid lines) and in the center of a barrier (dashed lines) are given in Fig. 1. The $2p_{\pm1}$ states are the lowest ones to which the dipole transitions from the ground state are allowed. The Coulomb potential splits the degenerated over the M Landau states. The ground state wavefunction in strong magnetic fields is similar to that of the lowest Landau level ($n = 0$) with $J_z = -3\hbar/2$ in the first subband. It is easy to see from Fig. 1 the $2p_{-1}$ state also originate from the zeroth Landau level, however its wavefunction corresponds to the momentum projection $J_z = -5\hbar/2$. The $2p_{+1}$ state with $J_z = -1\hbar/2$ in the limit of the strong magnetic field is 'bound' to the first Landau level ($n = 1$) in the lowest subband. As one can see from Fig. 1, the impurity placed in the barrier center results in the formation of more shallow states if compared with the acceptor in the QW center. It should be mentioned, that it proved be possible to use the above method in the magnetic fields $H > 10$ kOe only. Otherwise it is necessary to increase the dimension of the basis in weaker fields significantly. The comparison of the measured and simulated FIR photoconductivity spectra in Ge/GeSi heterostructure #306 is shown in Fig. 2. The photoconductivity spectrum calculation was produced in the approach of uniform distribution of an impurity in the structure. All exited

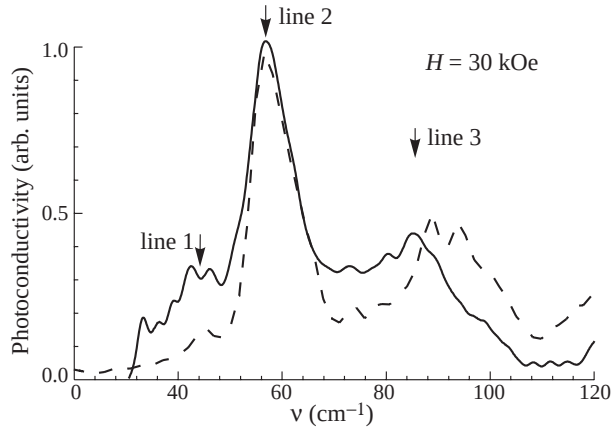

Fig. 2. Comparison of the measured and simulated FIR photoconductivity spectra in Ge/GeSi heterostructure #306. Solid line is the measured FIR photoconductivity spectra in magnetic fields. $T = 4.2$ K. Dashed curve is the simulated photoconductivity spectra for the uniform impurity distribution over the QW and the barrier.

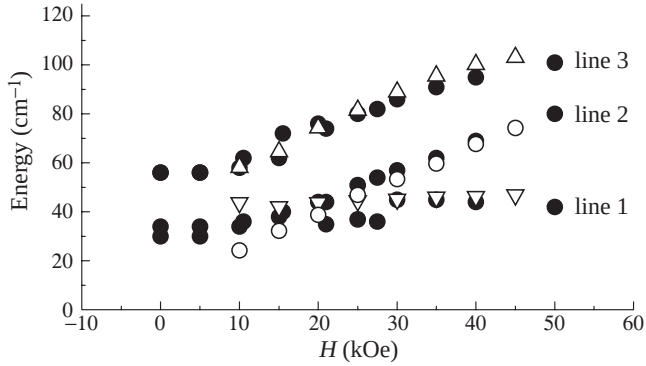

Fig. 3. Spectral positions of the measured (•) photoconductivity peaks versus the magnetic field. Signs Δ denotes $1s \rightarrow 2p_{+1}$ transition energies for well-center acceptors, O corresponds $1s \rightarrow 2p_{+1}$ transition for barrier-center acceptors, ∇ is used for $1s \rightarrow 2p_{-1}$ transition for well-center acceptors.

states, the optical transitions on which are allowed and which lay in the range up to 150 cm^{-1} were taken into account. It is necessary to note that at uniform distribution the maximal contribution to photoconductivity will be brought by transitions between states of acceptors located in the center of the quantum well and at the center of the quantum barrier. This fact is connected with the state density singularity in these places. The arrows 1, 2 and 3 in Fig. 1 indicate the optical transitions, which correspond to the observed spectral lines at the same magnetic field of 30 kOe (Fig. 2). Spectral positions of the measured photoconductivity lines on the magnetic field are shown in Fig. 3. Calculated energies of optical transitions for two acceptor positions are presented in Fig. 3 for comparison. One can easily see the good agreement between the calculated and measured data. This fact allows to unambiguously

identify these lines as the transitions $1s \rightarrow 2p_{+1}$ and $1s \rightarrow 2p_{-1}$ for the acceptor located at the center of the quantum well and $1s \rightarrow 2p_{+1}$ for the barrier-center acceptor.

Acknowledgements

This work was supported by the Russian Scientific Programs "Physics of Solid State Nanostructures" (# 99-1128, # 97-1069), "Leading Science Schools" (# 96-15-96719), "Integration" (# 540,541) and by the grant from Russian Foundation for Basic Research (# 00-02-16568).

References

[1] R. Chen, J. P. Cheng, et al., *J. Phys.: Condens. Matter*. **7**, 3577 (1995).

[2] V. Ya. Aleshkin, V. I. Gavrilenko, et al., *Fiz. Tekh. Poluprovod. (Semiconductors)* **34**, 563 (2000).

[3] V. I. Gavrilenko, I. V. Erofeeva, A. L. Korotkov, et al., *JETP Lett*. **65**, 209 (1997).

[4] R. Winnkler, M. Merkler, T. Darnhofer and U. Rössler, *Phys. Rev. B* **53**, 16, 10 858 (19??).

[5] G. L. Bir and G. E. Pikus, *Symmetry and Strain-Induced Effects in Semiconductors*, New York: Wiley, 1974.

[6] V. Ya. Aleshkin, V. I. Gavrilenko et al. *Proc. of Workshop 'Nanophotonika'*, Nizhny Novgorod, IPM RAS, 1999, p. 114

[7] V. Ya. Aleshkin, D. B. Veksler and V. I. Gavrilenko, *Proc. of Workshop 'Nanophotonika'*, Nizhny Novgorod, IPM RAS, 2000, p. 88

9th Int. Symp. "Nanostructures: Physics and Technology"
St Petersburg, Russia, June 18–22, 2001

Electron optical orientation in strained superlattices

A. D. Andreev† and *A. V. Subashiev*‡
† Ioffe Physico-Technical Institute, St Petersburg, Russia
‡ State Technical University, 195251, St Petersburg, Russia

Abstract. Optical spin orientation in the strained short-period semiconductor superlattices is investigated theoretically using 8-band effective mass Hamiltonian. We demonstrate that the strong features in the spin-polarization dependence on the electron energy are associated with Van-Hove singularities in absorption spectra and can be observed both for large and small barriers for the electrons. Calculated polarization spectra are close to the experimental spectra of polarized electron emission.

Introduction

Optical orientation in semiconductor structures has been extensively studied in recent years (see e.g. [1]). In quantum well (QW) and superlattice (SL) structures the 4-fold degenerate Γ_8 valence band state is splitted into only 2-fold spin-degenerate states Γ_6 (heavy-hole subband) and Γ_7 (light hole subband), the heavy-hole band being moved up. The splitting is enlarged with compressive layer strain. Therefore when the electrons are excited by circularly polarized light at the absorption edge from the heavy-hole subband the polarization of the excited electron is $P = 1$.

At higher energies the light holes contribute to the absorption, and smaller polarization is obtained, since the direction of the spin orientation is opposite for the electrons excited from the edge of heavy-hole and light-hole bands.

The electron optical orientation is widely used for the studies of the spin relaxation processes in the heterostructures (see e.g [2]). In addition, high electronic polarization have made strained GaAs-based superlattices (SLs) very promising as photoemitters of highly polarized electrons [3]. They have proven to provide reproducibly the emitted electron polarization as high as 86% with sufficiently high quantum efficiency at the polarization maximum [4].

In this paper, we report the first theoretical studies of the optical orientation of the electrons in the strained InGaAs-AlGaAs and GaAs-AlInGaAs superlattices studied experimentally (see [3, 4]) by the polarized electron emission spectroscopy with high energy resolution. The interpretation of the observed features in the spectrum is obtained.

Model, absorption and polarization spectra

We have calculated the miniband spectrum, optical absorption and spin polarization spectra of strained superlattices using the envelope-function approximation, in the framework of the Kane model including the conduction band Γ_6, the states of light and heavy holes of the valence band Γ_8 and also the states of the spin-orbit splitted band Γ_7 [5]. The miniband spectrum as a function of wave vector in the layer plane $k_\parallel$ and along the growth direction, k_z parallel to [100] axis is presented in Fig. 1(a), for a strained $GaAs - Al_{0.18}In_{0.16}Ga_{0.66}As$ SL with well and barrier thicknesses $d_w = d_b = 4$ nm. The positions of the band edges

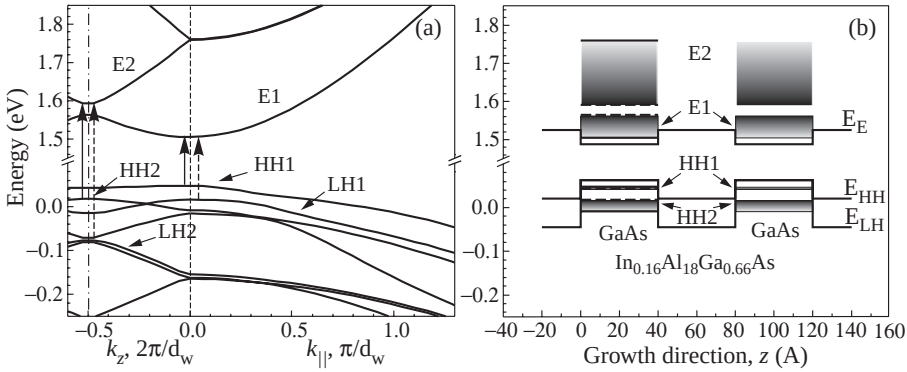

Fig. 1. (a) Miniband spectrum of GaAs-AlInGaAs superalttice and the major optical transitions (shown by vertical arrows) contributing to the absorption spectrum, and (b) the positions of the band edges.

are illustrated in Fig. 1(b). The composition of the SL layers in this SL is aimed to get large enough valence band splitting in addition to a small conduction band offset to provide high polarization and high mobility of the excited electrons. In Fig. 1 the small conduction band offset shows itself in a very small splitting between the 2-d and the 3-d electronic minibands at the center of the Brilluin zone. Still noticeable splitting between the first and the second electronic minibands remains at $k_z = \pi/d$, $d = d_w + d_b$.

For the circularly polarized light absorption the spin polarization of electrons excited in all minibands of the conduction band at the excitation moment was calculated as

$$P = \frac{\sum_n (K_\uparrow^n - K_\downarrow^n)}{\sum_n (K_\uparrow^n + K_\downarrow^n)} \tag{1}$$

Here $K_\uparrow^n$ ($K_\downarrow^n$) is the absorption coefficient for the excitation in the n electronic miniband state with spin up (spin down) from all the hole minibands. According to Eq. (1), the resulting electron polarization depends on the relative contribution of the light- and heavy-hole bands, the singularities in the polarization being originated from the Van-Hove singularities in the absorption spectra.

The transition rate for the electrons excited by the circularly polarized light from the minibands of the valence band states in the n-th conduction miniband state with spin up (↑) and spin down (↓) is proportional to the squared dipole matrix element and the interband density of states. The squared matrix elements $|M|^2_{i,k}$ for the main optical transitions in two electron spin states (↑ and ↓) are depicted in Fig. 2. Note that the dependence of $|M|^2_{i,k}$ on the lateral wave vector $k_\parallel$ is qualitatively similar to that calculated previously for the infinitely large band offsets (infinitely deep QW model) [6]. Then, the dependence of the matrix element on the momentum k_z along the SL axis is rather weak. Finally, the absolute value of the hh2 → e2 matrix element is found to be close to that for the hh1 → e1 transition even in the case of small conduction band offset.

In Fig. 3 calculated spectra of the electron polarization at the excitation as a function of the excitation energy for GaAs–$Al_{018}In_{0.16}Ga_{0.66}As$ superlattice are presented. The dependence of the polarization and absorption spectra on excitation energy reproduces the sequence of the miniband transitions. The polarization in the first maximum is found to

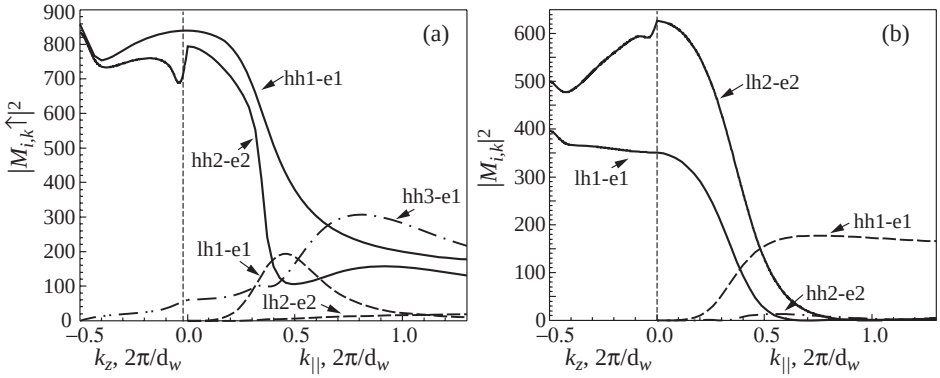

Fig. 2. Matrix elements for the interband optical transitions induced by circularly polarized light to the final state with spin up (a) and spin down (b) as a function of excitation energy for the GaAs-AlInGaAs strained superlattice.

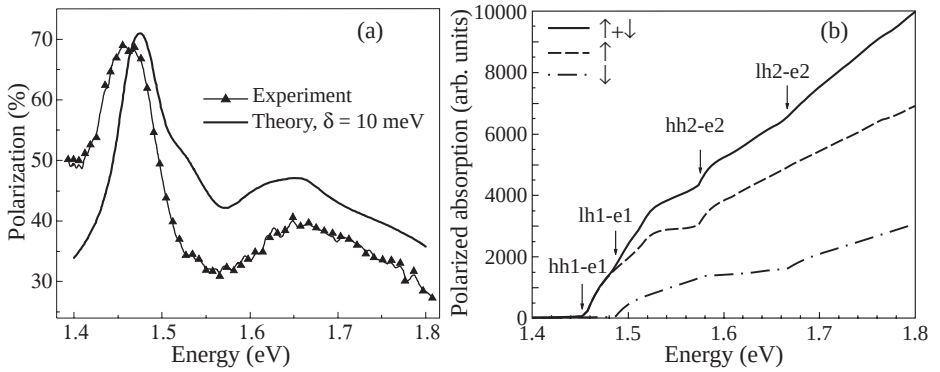

Fig. 3. (a) Polarization of the excited electrons (solid line) for the circularly polarized excitation of GaAs/AlInGaAs superlatice structure and the experimentally observed spectra of polarized photoemission from Ref. [4] (shown by triangles), $T = 300$ K; (b) absorption coefficients for two final electronic states and resulting sum as a function of excitation energy, $\delta = 1$ meV.

be very sensitive to the smearing of the absorption edge by the electron and the hole scattering processes, as well as the band edge fluctuations. In our calculations this factor is parametrized by a Lorentzian broadening of the interband transitions with the half width δ. While the minimum in the polarization spectra is definitely associated with lh1→e1 transitions, the second maximum in the polarization spectra is found to be due to the transitions at $k_z = \pi/d$ of the miniband edge. For both considered superlattices it corresponds to electronic states with the energy above the barriers in the conduction band. Therefore the structure of the maximum and its contribution to polarization is sensitive to the barrier height (i.e. conduction band offset). The maximum polarization in this peak is found to exceed 50%. Taking into account the electron spin relaxation, the calculated spectra are in very good agreement with the observed excitation spectra of polarized electron photoemission both for AlGaAs-InGaAs and GaAs-AlInGaAs strained superlattices.

Conclusions

Thus, we have preformed the optical orientation calculations within 8-band Kane model for the strained superlattices. Three features originating from hh1→e1, lh1→e1 at $k_z = 0$ and hh2→e2 at $k_z = \pi/d$ are shown to dominate in the polarization spectra. This result is in line with the experimental data on the polarized electron emission. The last feature is sensitive to the band offset in the conduction band and can be used for the band offset evaluation and fine tailoring of the band structure.

Acknowledgments

This work was supported by the Russian State Program "Physics of Solid State Nanosrtuctures" under grant 97-1091, Russian Foundation for Basic Research under grant 00-02-16775, INTAS under grant 99-00125 and SNSF under grant 7IP 062585.

References

[1] D. N. Mirlin and V. I. Perel,' *Semicond. Sci. Technol.* **7**, 1221 (1992).
[2] Y. Ohno, R. Terauchi, T. Adachi et al. *Phys. Rev. Let.* **83**, 4196 (1999).
[3] A. V. Subashiev, Yu. A. Mamaev, Yu. P. Yashin and J. E. Clendenin, *Phys. Low-Dim. Struct.* **1/2**, 1 (1999).
[4] A. V. Subashiev et al., *Proc. 24-th Int. Conf. on Phys. of Semicond.* (ICPS-24), Jerusalem 1998, (also SLAC-Pub-7922, 1998).
[5] G. L. Bir and G. E. Pikus, *Symmetry and Strain-Induced Effects in Semiconductors*, New York: Wiley, 1974.
[6] I. A. Merkulov, V. I. Perel' and M. E. Portnoi, *JETP* **72**, 669 (1991).

9th Int. Symp. "Nanostructures: Physics and Technology"
St Petersburg, Russia, June 18–22, 2001

Polariton local states in periodic Bragg multiple quantum well structures

Lev Deych†, Alexey Yamilov‡ and Alexander Lisyansky‡
† Seton Hall University, South Orange, NJ 07079, USA
‡ Department of Physics, Queens College of CUNY, Flushing, NY 11367, USA

Abstract. Defect polariton states in Bragg multiple-quantum-well structures are studied along with defect induced changes in transmission and reflection spectra. Analytical results for eigen frequencies of the local states and for respective transmission coefficients are obtained. It is shown that the local polaritons result in resonance tunneling of light through the stop band of MQW structure, but unlike other types of local states, the transmission resonance frequencies are always shifted with respect to eigen frequencies of the local modes. Exciton homogeneous broadening is taken into account phenomenologically and recommendations regarding the experimental observation of the predicted effects are given.

Introduction

Optical properties of multiple quantum wells (MQW) have attracted a great deal of interest recently [1–8]. The exciton–photon coupling results in MQW polaritons — coherently coupled quazi-stationary excitations of quantum well (QW) excitons and transverse electromagnetic field. So called Bragg structures, in which interwell spacing, a, is tuned to the exciton resonance frequency Ω_0 ($a = \lambda_0/2$, where λ_0 is the wavelength of the light at the exciton frequency Ω_0) attracted special attention [2, 5, 7, 8]. A well-pronounced polariton gap was observed in recent experiments [8] with GaInAs/GaAs Bragg structures with the number of wells up to 100. These experiments convincingly demonstrated that despite homogeneous and inhomogeneous broadening the coherent exciton–photon coupling in long MQW is experimentally feasible. Polariton effects arising as a result of this coupling open up new opportunities for manipulating optical properties of quantum heterostructures.

One of such opportunities is associated with introducing defects in MQW structures. These defects can be either QW's of different compositions replacing one or several "host" wells, or locally altered spacing between elements of the structure. This idea was first applied to MQW by Citrin [9], where it was shown that different defects can give rise to local exciton–polariton modes in infinite MQW. Unlike regular interface modes in superlattices, local modes in a defect MQW structure exists at $k_\parallel = 0$ and can be excited at normal incidence. In this paper we present results of detailed studies of local polariton modes (LPM's) produced by two different types of individual defects in Bragg MQW structures. We consider LPM's with zero in-plane wave vector only. Such modes are excited by light incident in the growth direction of the structure, and can result in resonance transmission of light through the polariton gap of the host structure. Using parameters of a realistic InGaAs/GaAs system studied experimentally in Ref. [8], we give recommendation on the experimental observation of the LPM's.

1. Eigen frequencies of local polaritons in defect MQW's

We describe optical properties of MQW's using polarization density of the form: $\mathbf{P}(\mathbf{r}, z) = \mathbf{P}_n(\mathbf{r})\delta(z - z_n)$, where $\mathbf{r}$ is an in-plane position vector, z_n represents a coordinate of the

n-th well, and $\mathbf{P}_n$ is a surface polarization density of the respective well. The latter is determined by the exciton dynamics, described in the considered situation by the equation $\left(\Omega_n^2 - \omega^2\right) P_n = \frac{1}{\pi} c\Gamma_n E(z_n)$, where Ω_n and Γ_n are exciton frequency and exciton-light coupling of the n-th QW, respectively. In an infinite pure system, all $\Gamma_n = \Gamma_0,\ \Omega_n = \Omega_0,\ z_n = na$, where $a = \lambda_0/2$ is the Bragg's interwell separation.

The spectrum of ideal periodic MQW's has been studied in many papers [1, 3, 10, 11, 12]. In the specific case of Bragg structures, the exciton resonance frequency, Ω_0, is at the center of the bandgap determined by the inequality $\omega_l < \omega < \omega_u$, where $\omega_l = \Omega_0\left(1 - \sqrt{2\Gamma_0/\pi\Omega_0}\right)$ and $\omega_u = \Omega_0\left(1 + \sqrt{2\Gamma_0/\pi\Omega_0}\right)$ [10]. This bandgap is the frequency region where we will look for new local states associated with the defects. Two types of defect are of the greatest interest. One is associated with replacing an original QW with a QW with different exciton frequency (Ω-defect), and the other one results from perturbation of an interwell spacing between two wells. The dispersion equation for Ω-defect has, in the case of the Bragg structures, two solutions, one below Ω_0 and one above. One solution demonstrates a radiative shift from the defect frequency Ω_1,

$$\omega_{\text{def}}^{(1)} = \Omega_1 - \Gamma_0 \frac{\Omega_1 - \Omega_0}{\sqrt{(\omega_u - \Omega_1)(\Omega_1 - \omega_l)}}, \tag{1}$$

while the second solution splits off the upper or lower boundary depending upon the sign of $\Omega_1 - \Omega_0$:

$$\omega_{\text{def}}^{(2)} = \omega_{u,l} \pm \frac{1}{2}(\omega_u - \omega_l)\left(\frac{\pi}{2}\frac{\Omega_1 - \Omega_0}{\Omega_0}\right)^2, \tag{2}$$

where one chooses ω_u and "$-$" for $\Omega_1 > \Omega_0$, and ω_l and "$+$" in the opposite case. It can be seen that the shift of $\omega_{\text{def}}^{(1)}$ from the defect exciton frequency Ω_1 is negative for $\Omega_1 > \Omega_0$ and positive for $\Omega_1 < \Omega_0$.

The a-defect is actually a cavity, whith QW's playing the role of the mirrors. Unlike regular cavities, however, the "mirrors" in our case are themselves optically active, and this fact is responsible for significant peculiarities of the case under consideration. Eigen frequencies for this situation can be found using transfer matrix approach. Solutions of the respective dispersion equation can be approximated as

$$\omega_{\text{def}}^{(1)} = \Omega_0 - \frac{\omega_u - \omega_l}{2} \frac{(-1)^{\left[\frac{\xi+1}{2}\right]} \sin(\pi\xi/2)}{1 + \frac{\omega_u - \omega_l}{2\Omega_0}\xi(-1)^{\left[\frac{\xi+1}{2}\right]}\cos(\pi\xi/2)}, \tag{3}$$

$$\omega_{\text{def}}^{(2)} = \Omega_0 + \frac{\omega_u - \omega_l}{2} \frac{(-1)^{\left[\frac{\xi+1}{2}\right]} \cos(\pi\xi/2)}{1 - \frac{\omega_u - \omega_l}{2\Omega_0}\xi(-1)^{\left[\frac{\xi+1}{2}\right]}\sin(\pi\xi/2)}, \tag{4}$$

where $\xi = b/a$, and [...] denotes an integer part. Therefore, for $\Gamma_0 \ll \Omega_0$ and not very large ξ, $\xi \ll \Omega_0/\Gamma_0 \simeq 10^4$, both solutions are almost periodic functions of b/a with the period of 1. These solutions oscillate between respective boundaries of the gap (ω_u or ω_l) and the exciton frequency Ω_0.

2. Defect local polariton modes and transmittance and reflectance experiments

Resonance transmission in the case of Ω-defect is described by

$$T = \frac{4\gamma_\Omega^2}{Q^2}\frac{(\omega-\omega_T+Q)^2}{(\omega-\omega_T)^2+4\gamma^2}, \tag{5}$$

where $Q = \omega_T - \Omega_1$, and parameter γ_Ω is given by

$$\gamma_\Omega = \pi\Omega_0\left(\frac{\omega_{def}-\Omega_0}{\Omega_0}\right)^2 e^{-\kappa Na}. \tag{6}$$

The transmission spectrum Eq. (5) has a shape known as Fano resonance where ω_T is the resonance frequency, at which transmission turns unity, parameters γ_Ω and Q describe the width and the assymetry of the resonance respectively. The resonance transmission in the case of a-defect is described by the standard Breit–Wigner shape with the half-width, γ_a, proprtional to $\sqrt{\Gamma_0\Omega_0}e^{-\kappa Na}$.

In general, the transmission resonance frequency in both cases is shifted with respect to the frequency of the local mode. The shift, though exponentially small for long systems considered here, is of the same order of magnitude as the width of the resonance, and is, therefore, significant.

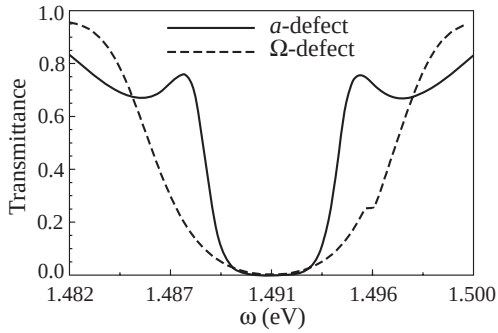

Fig. 1. Numerically generated transmission spectra of GaInAs/GaAs MQW's with Ω- (dashed line) and a—(solid line) defects. Input parameters were chosen from Ref. [8]: $\Omega_0 = 1.491$ eV, $\Gamma_0 = 27\,\mu$eV, and exciton relaxation parameter $\gamma_{hom} = 0.28$ meV. The length of the system is $N = 200$.

Reaction of the transmission resonance to the presence of a homogeneous broadening in the case of Ω-defect is determined by interplay between the width of the resonance and the assymetry parameter Q. The later is rather small, and, therefore, in practically important cases, is responsible for the survival of the resonance. For InGaAs/GaAs MQW's of Ref. [8] homogeneous broadening is rather large, and instead of a full fledged Fano resonance one will observe in such systems only a small spike (see Fig. 1). It does not preclude, however, an opportunity to observe such a resonance in other systems with an increased exciton-photon coupling. For a-defect the situation is completely different (Fig. 1). The large prefactor in the resonance width parameter γ makes this defect quite stable with respect to absorption. The resonance transmission with two nice maximums can, therefore, be observed in the systems with lengths ranging between 100 and 400 wells in the case of InGaAs/GaAs systems.

References

[1] D. S. Citrin, *Solid State Commun.* **89**, 139 (1994).
[2] E. L. Ivchenko, A. I. Nesvizhskii and S. Jorda, *Phys. Solid State* **36**, 1156 (1994).
[3] L. C. Andreani, *Phys. Lett. A* **192**, 99 (1994); *Phys. Status Solidi B* **188**, 29 (1995).
[4] G. Björk, S. Pau, J.M. Jakobson, H. Cao and Y. Yamamoto, *Phys. Rev. B* **52**, 17 310 (1995).
[5] M. Hübner, J. Kuhl, T. Stroucken, A. Knorr, S. W. Koch, R. Hey and K. Ploog, *Phys. Rev. Lett.* **76**, 4199 (1996).
[6] T. Stroucken, A. Knorr, P. Thomas and S. W. Koch, *Phys. Rev. B* **53**, 2026 (1996).
[7] M. P. Vladimirova, E. L. Ivchenko and A. V. Kavokin, *Semiconductors* **32**, 90 (1998).
[8] M. Hübner, J. P. Prineas, C. Ell, P. Brick, E. S. Lee, G. Khitrova, H. M. Gibbs and S. W. Koch, *Phys. Rev. Lett.* **83**, 2841 (1999).
[9] D. S. Citrin, *Appl. Phys. Lett.* **66**, 994 (1995).
[10] L. I. Deych and A. A. Lisyansky, *Phys. Rev. B* **60**, 4242 (2000).
[11] L. V. Keldysh, *Superlattices and Microstructure* **4**, 637 (1988).
[12] E. L. Ivchenko, *Phys. Solid State* **33**, 1344 (1991).

9th Int. Symp. "Nanostructures: Physics and Technology"
St Petersburg, Russia, June 18–22, 2001

Spin sensitive bleaching of absorption in p-type GaAs/AlGaAs QWs

S. D. Ganichev†‡, *S. N. Danilov*§, V. V. Bel'kov‡, E. L. Ivchenko‡,
L. E. Vorobjev§, W. Wegscheider†, M. Bichler¶ and W. Prettl†
† Institut für Experimentelle und Angewandte Physik,
Universität Regensburg, D-93040 Regensburg, Germany
‡ Ioffe Physico-Technical Institute, St Petersburg, Russia
§ St Petersburg State Technical University, 195251, St Petersburg, Russia
¶ Walter Schottky Institut, TU München, 85748, Garching, Germany

We report on the first observation of the spin sensitive bleaching of heavy hole — light hole absorption in p-doped quantum-well (QW) structures. Due to selection rules as well energy and momentum conservation direct intersubband transitions induced by circularly polarized light depopulate and populate selectively spin states at certain energies in the valence band causing a monopolar spin orientation. Since the transition rate is proportional to the difference of populations in the initial and final states, the increasing selective population tends to equalize the differing transition rates and, hence, leads to a sublinear dependence of the absorption on the intensity. The bleaching is controlled by both the hole spin relaxation and the energy relaxation of photoexcited carriers. In contrast to circularly polarized light, optical transitions induced by the linearly polarized light are not spin selective and the saturation is controlled by energy relaxation of photoexcited carriers only. The experimentally observed difference between absorption saturation of circularly and linearly polarized radiation gives evidence for spin controlled relaxation and allows to distinguish between energy and spin relaxation.

The experiments have been carried out on p-GaAs/AlGaAs (311)-MBE-grown single QW and 20 QWs of 15 nm width as well as MOCVD-grown p-GaAs/AlGaAs multiple QWs with 300 or 400 wells of 20 nm width on vicinal (001)-substrates. The growth direction of the latter structures was tilted by an angle of 50 with respect to the [001]-crystallographic axis as has been verified by X-ray diffraction. Samples with free-carrier densities between 10^{11} cm^{-2} and $2 \cdot 10^{12}$ cm^{-2} were studied in the range from liquid helium to room temperature. As a terahertz radiation source a high power pulsed far-infrared molecular laser optically pumped by a TEA-CO_2 laser has been used delivering 100 ns pulses with intensity up to 1 MW/cm^2 at wavelengths $\lambda = 35$ μm, 76 μm, 90 μm, and 148 μm.

The nonlinear behavior of the absorption of intense terahertz radiation in the wavelength range between 35 and 148 μm has been investigated by application of the recently observed circular and linear photogalvanic effects [1]. The photocurrent has been measured in unbiased samples at two contacts placed along $[1\bar{1}0]$-crystallographic directions. Absorption of circularly and linearly polarized radiation results in a direct motion of free carriers in the plane of a quantum well perpendicular to the direction of light propagation. The photocurrent j is proportional to the light intensity at low power levels and gradually saturates with increasing intensity I as $j \propto (I/(1 + I/I_s)$ due to the absorption saturation. I_s is the saturation intensity which allows to determine relaxation times. Saturation intensities have been measured for a wide range of temperatures between 4.2 K and 300 K, hole densities, and photon energies, corresponding to different initial and final energy levels of holes. The

experimentally obtained values varies from 30 kW/cm^2 to non-measurably large values at room temperatures. The magnitude I_s for the circular photogalvanic effect is generally smaller than for the linear photogalvanic effect. It varies with the radiation wavelength and increases with increasing temperature and doping density.

Acknowledgements

This work was financially supported by the Deutsche Forschungsgemeinschaft, the Russian Foundation for Basic Research and NATO Linkage Grant.

References

[1] S. D. Ganichev, E. L. Ivchenko, H. Ketterl, W. Prettl and L.E. Vorobjev, *Appl. Phys. Lett.* **77**, 3146 (2000).

9th Int. Symp. "Nanostructures: Physics and Technology"
St Petersburg, Russia, June 18–22, 2001

Spin-orbit interaction in AlGaAs/GaAs p-type quantum wells — a possible explanation of the 'metal-insulator' transition observed in two-dimensional hole systems

L. E. Golub† and S. Pedersen‡

† Ioffe Physico-Technical Institute, St Petersburg, Russia

‡ Microtechnology Center at Chalmers MC2, Department of Microelectronics and Nanoscience, Chalmers University of Technology and Göteborg University, S-412 96, Göteborg, Sweden

Abstract. We have performed a calculation of the temperature dependence of the weak-localization correction to resistance in a AlGaAs/GaAs p-type quantum well. In such systems, where the spin-orbit coupling by far dominates the energy dispersion, we find that the spin relaxation time becomes comparable with the estimated value of the phase coherence time at sufficiently low temperatures and low hole densities. We wish to suggest this crossover between these different relaxation times as a possible explanation of the experimentally observed 'metal-insulator' transition in two-dimensional hole systems.

In a series of recent experiments an anomalous temperature dependence of the resistivity has been observed in a wide range of two-dimensional systems — for an extensive overview see [1] and references therein. These results have been interpreted as evidence for the existence of a so-called metal-insulator transition in two-dimensional systems | a conclusion considered by far the most as controversial.

In this work we theoretically address one specific system | namely the 200 Å wide AlGaAs/GaAs p-type quantum well which has been experimentally studied in [2, 3]. Several other similar studies has been reported in the literature [4, 5, 6, 7], but for clarity we will primarily focus on the work done by Simmons and co-workers.

The results of these experiments can be summarized as follows: A transition between an isolating phase at low hole densities and a metallic phase at high hole densities is observed at a critically hole density $p_c \approx 5 \times 10^{14}\,\mathrm{m}^{-2}$ | by isolating (metallic) phase is meant that the resistivity increases (decreases) with decreasing temperature. Furthermore the investigation of the magnetoresistance lead to the following observations: (1) The phase coherence time τ_φ extracted from weak localization measurement agrees well with the theoretical estimates [8], (2) The effect of hole-hole interacting on the resistivity was found to be of the same size as the weak localization correction, and in agreement with the theory for weak hole-hole interaction [9], and (3) No weak anti-localization was observed. Observation (1) and (2) was independent on which side of 'metal-isolator' transition the measurement was performed and hence lead to the surprising conclusion that the hole-hole interactions properly not are responsible for the observed transition even though $r_s > 1$.

In this letter we take the above conclusion as starting point for our examination, hence we neglect hole-hole interaction and try to explain the observed behavior within weak-localization theory, which is reasonable to assume valid since the experiment where performed in the regime where $\tau_\varphi > \tau_{\mathrm{tr}}$; τ_{tr} being the transport relaxation time.

The reason why no weak anti-localization was observed is most likely, that in these structures the weak anti-localization is expected to be very small since $k_F a/\pi \ll 1$ [10] (k_F is the Fermi wavevector, a is the quantum well width), and furthermore in the performed

experiment the magnetic field was stepped with an increment of ~ 50 Gauss which would be much to gross to resolve the effect (In a similar hole system the whole weak anti-localization regime was found within ± 30 Gauss [11]).

Contrary to what is commonly believed, a metallic phase can in principle occur in two dimensions. Such a 'metal-insulator' transition is as a fact expected to occur in non-interacting systems with strong spin-orbit coupling [12, 13]. In real systems this so-called anti-localization is expected to be suppressed due to hole-hole interaction, which is supposed to dominate if interactions are present. However for the system in question, one of the surprising experimental findings were, that the effect of hole-hole interaction was comparable with the interference effects even though $r_s > 1$.

For a non-interacting two-dimensional system where $\tau_\varphi \sim \tau_s > \tau_{tr}$; τ_s being the spin relaxation time, the weak localization approximation is valid and the temperature dependence of the conductivity is given by [12]

$$\sigma(T) - \sigma_0 = \begin{cases} \frac{e^2}{\pi h} \ln(\tau_\varphi/\tau_s), & \tau_s/\tau_\varphi < 1 \\ -\frac{e^2}{\pi h} \ln(\tau_\varphi/\tau_{tr}), & \tau_s/\tau_\varphi > 1, \end{cases} \tag{1}$$

where $\sigma_0 = pe^2\tau_{tr}/m$ is the temperature independent Drude conductivity (m is the effective mass in the bottom of the first size-quantized hole subband). Hence the sign of the weak-localization correction is given by the ratio between the strength of the spin coherence and the phase coherence τ_s/τ_φ. If the spin relaxation is strong $\tau_s/\tau_\varphi < 1$ the plus sign is valid. On the other hand if the spin relaxation is weak the minus sign is valid and the well known weak-localization result is retained [8]. Hence we see that by changing the ratio τ_s/τ_φ it is possible to induce a transition like the one observed in the experiments.

Spin relaxation of holes is caused by spin-orbit interaction, therefore it is governed by the hole density, p. Changing p, one can transfer the system from one to the other case (1). In real p-type two-dimensional systems, hole spin relaxation is anisotropic and, hence, it is described by two characteristic times, $\tau_\parallel$ and $\tau_\perp$. The conductivity correction has the form [10]

$$\sigma(T) - \sigma_0 = \frac{e^2}{\pi h}\left[2\ln\left(\frac{\tau_{tr}}{\tau_\varphi} + \frac{\tau_{tr}}{\tau_\parallel}\right) + \ln\left(\frac{\tau_{tr}}{\tau_\varphi} + \frac{\tau_{tr}}{\tau_\perp}\right) - \ln\left(\frac{\tau_{tr}}{\tau_\varphi}\right)\right]. \tag{2}$$

In the lowest order in pa^2, we obtained [10]

$$\frac{\tau_{tr}}{\tau_\parallel} = L_\parallel\,(pa^2)^2\,, \qquad \frac{\tau_{tr}}{\tau_\perp} = L_\perp\,(pa^2)^3\,. \tag{3}$$

For a GaAs/AlGaAs quantum well, $L_\parallel = 2.7 \cdot 10^{-4}$, $L_\perp = 0.12$ [14].

The phase coherence time τ_φ is assumed to be caused by hole-hole interaction and, hence, it is determined by both temperature, T, and density:

$$\frac{\tau_{tr}}{\tau_\varphi} = \frac{mk_B T}{2\pi\hbar^2 p}\ln\left(\frac{2\pi\hbar p\tau_{tr}}{m}\right). \tag{4}$$

The system is insulating at high temperatures and low densities, when $\tau_\varphi < \tau_\parallel, \tau_\perp$, and it is metallic in the opposite case of low T and high p, when spin-orbit interaction is more effective than dephasing.

The transition between these two states of matter, the 'metal-insulator' transition (MIT) takes place at $\partial\Delta\sigma/\partial T = 0$. From (2) follows that the curve $\sigma(T)$ has zero slope at

$$\frac{1}{\tau_\varphi} = \sqrt{\frac{1}{(4\tau_\perp)^2} + \frac{1}{2\tau_\parallel\tau_\perp}} - \frac{1}{4\tau_\perp}\,. \tag{5}$$

This condition defines the dependence of the critical density, p_c, on temperature or, vice versa, the MIT-temperature, T_c, as a function of p. From (3) follows that $1/\tau_\parallel \gg 1/\tau_\perp$ at $pa^2 \ll L_\parallel/L_\perp$. Therefore according to (5) the MIT occurs at $\tau_{tr}/\tau_\varphi \approx \tau_{tr}/\sqrt{2\tau_\parallel\tau_\perp}$, i.e.

$$T_c(p) = \frac{2\pi\hbar^2}{mk_B \ln(2\pi\hbar p\tau_{tr}/m)}\sqrt{\frac{L_\parallel L_\perp}{2}}p^{7/2}a^5\,, \qquad pa^2 \ll L_\parallel/L_\perp\,. \tag{6}$$

For $pa^2 \gg L_\parallel/L_\perp$, $1/\tau_\parallel \ll 1/\tau_\perp$ and the p-dependence of T_c is given by $1/\tau_\varphi \approx 1/\tau_\parallel$, i.e.

$$T_c(p) = \frac{2\pi\hbar^2}{mk_B \ln(2\pi\hbar p\tau_{tr}/m)}L_\parallel p^3 a^4\,, \qquad pa^2 \gg L_\parallel/L_\perp\,. \tag{7}$$

The expressions (6,7) give $T_c \sim 10^{-2}$ K for the structure parameters of the experiments [2, 3] ($a = 200$ Å, $m = 0.3m_0$). This is about an order of magnitude smaller than the experimental temperature of MIT. This discrepance could be due to under-estimation of the spin-orbit interaction strength in the lowest-order calculations leading to very small values of $L_\perp$ and, especially, $L_\parallel$. Besides, the higher degrees of p could be important in the expressions for the spin relaxation rates (3). The corresponding calculation is performed taking into account heavy-light hole mixing in a quantum well in all orders in wavevector and will be published elsewhere.

Acknowledgements

L.E.G. acknowledges the Russian Foundation of Basic Research, projects 00-02-17011 and 00-02-16894, and the Russian State Programme "Physics of Solid State Nanostructures" for financial support.

References

[1] E. Abrahams, S. V. Kravchenko and M. P. Sarachik, cond-mat/0006055.
[2] M. Y. Simmons, A. R. Hamiliton, M. Pepper, E. H. Linfield, P. D. Rose and D. A. Ritchie, *Phys. Rev. Lett.* **84**, 2489 (2000).
[3] M. Y. Simmons, A. R. Hamiliton, M. Pepper, E. H. Linfield, P. D. Rose, D. A. Ritchie, A. K. Savchenko and T. G. Griffiths, *Phys. Rev. Lett.* **80**, 1292 (1998).
[4] A. P. Mills,Jr., A. P. Ramirez, L. N. Pfeiffer and K. W. West, *Phys. Rev. Lett.* **83**, 2805 (1999).
[5] V. Senz, T. Heinzel, T. Ihn, K. Ensslin, G. Dehlinger, D. Grützmacher and U. Gennser, *Phys. Rev. B* **61**, R5082 (2000).
[6] Y. Hanein, U. Meirav, D. Shahar, C. C. Li, D. C. Tsui and H. Shtrikman, *Phys. Rev. Lett.* **80**, 1288 (1998).
[7] J. Yoon, C. C. Li, D. Shahar, D. C. Tsui and M. Shayegan, *Phys. Rev. Lett.* **82**, 1744 (1999).
[8] B. L. Altschuler, A. G. Aronov and D. E. Khmel'nitskii, *J. Phys. C* **15**, 7367 (1982).
[9] B. L. Altschuler, A. G. Aronov and P. A. Lee, *Phys. Rev. Lett.* **44**, 1288 (1980).
[10] N. S. Avierkiev, L. E. Golub and G. E. Pikus, *JETP* **86**, 780 (1998).
[11] S. Pedersen, C. B. Sørensen, A. K. Kristensen, P. E. Lindelof, L. E. Golub and N. S. Averkiev, *Phys. Rev. B* **60**, 4880 (1999).
[12] B. L. Altschuler, A. G. Aronov, D. E. Khmelnitskii and A. I. Larkin, *Quantum Theory of Solids*, ed I. M. Lifshits (MIR Publishers, Moscow, 1983).
[13] B. L. Altschuler, D. L. Maslov and V. M. Pudalov, cond-mat/0003032.
[14] N. S. Averkiev, L. E. Golub and G. E. Pikus. *Solid State Commun.* **107** 757 (1998).

9th Int. Symp. "Nanostructures: Physics and Technology"
St Petersburg, Russia, June 18–22, 2001

Natural in-plane optical anisotropy of ZnSe/BeTe superlattices with no-common atom at the interfaces

A. S Gurevich†, V. P. Kochereshko†, A. V. Platonov†‡, D. R. Yakovlev‡†, W. Ossau‡, A. Waag‡[] and G. Landwehr‡
† Ioffe Physico-Technical Institute, St Petersburg, Russia
‡ Physikalisches Institut der Universität Würzburg, 97074, Würzburg, Germany

Abstract. Reflectivity and ellipsometry methods were applied to study optical properties of type-II ZnSe/BeTe superlattices. Natural in-plane optical anisotropy of the refractive and absorption indices has been found in the spectral range of direct excitonic transitions. The observed effects are interpreted in a model of optical anisotropy of heterostructures with no-common atom at the interfaces.

Recently it was found that in type-II ZnSe/BeTe superlattices with no-common atom at the interfaces photoluminescence signal is linearly polarized along a $[1\bar{1}0]$ direction with a polarization degree of 80%, in a spectral range of spatially indirect exciton transitions [1]. This effect is attributed to the low local symmetry of the single interface between two different zinc-blend type materials. Such an interface has C_{2v} symmetry instead of D_{2d} symmetry in the bulk that allows the observation of an anisotropy of the optical constants in the structure plane [2]. The lowering of the interface symmetry leads to a mixing of light-hole and heavy-hole states [3], which results in polarized photoluminescence of spatially indirect excitonic transitions, which are strongly localized near the interface. Polarized photoluminescence of spatially indirect excitonic transitions display intrinsic properties of the interface with no-common atom and can give no information about optical properties such as reflection and transition of the whole heterostructure.

One of the most common methods to study optical properties of heterostructures is reflection spectroscopy. However, this method is not sensitive enough to measure a small optical anisotropy in heterostructures with a low number of interfaces. In the present paper we use ellipsometry [4] to measure an optical anisotropy of ZnSe/BeTe superlattices with no- common atom at the interfaces. This method is extremely sensitive to the optical thickness of thin layers. It makes use of changes in the polarization of incident light when it is reflected from the surface of the sample.

The samples were grown by MBE on (100)-oriented GaAs substrates. During the growth procedure both interfaces were fabricated with a ZnTe transition layer. ZnSe/BeTe superlattice has type-II band alignment where electrons and holes are separated spatially in the subsequent layers. The period of the heterostructures was 150 Å and the width of the quantum wells was 50 Å. All studied heterostructures contained 20 periods. The band offset for holes is 0.9 eV and for electrons it is 2.3 eV. The period of the investigated structures (150 Å) is much less than the thickness of the whole superlattice (3000 Å). Therefore, we can describe the optical properties of this superlattice using an effective complex dielectric function $\varepsilon(\omega)$ [5].

By using the ellipsometry we have measured a spectral dependence of the complex dielectric function (refractive and absorption parts) of the superlattice in a spectral range

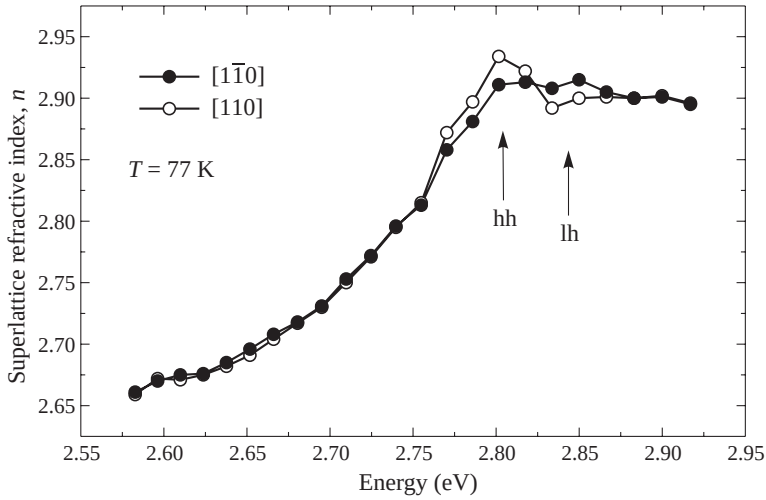

Fig. 1. Spectral dependence of the superlattice refractive index $n(\omega)$. Solid circles present the refractive index for the [1$\bar{1}$0] crystallographic direction. Open circles present it for the [110] crystallographic direction.

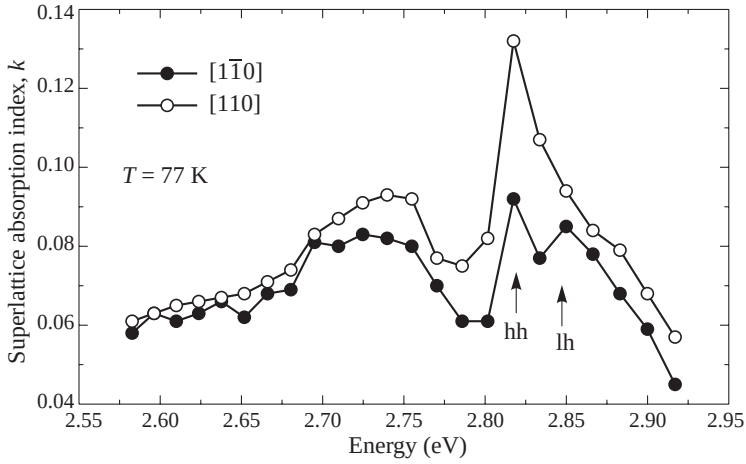

Fig. 2. Spectral dependence of the superlattice absorption index $k(\omega)$. Solid circles present the absorption index for the [1$\bar{1}$0] crystallographic direction. Open circles present it for the [110] crystallographic direction.

of spatially direct exitonic transitions. These measurements were performed at oblique incidence at 55.05° at temperature 77 K

Spectral dependencies of the refractive index $n(\omega)$ and absorption index $k(\omega)$ for [110] and [1$\bar{1}$0] crystallographic axis are presented at Fig. 1 and Fig. 2. In Fig. 1 one can see that the superlattice refractive index $n(\omega)$ is anisotropic in the spectral range from 2.755 to 2.833 eV and that this anisotropy has a resonant character with a maximum at 2.82 eV. The anisotropy of the superlattice absorption index $k(\omega)$ has also resonant character (Fig. 2).

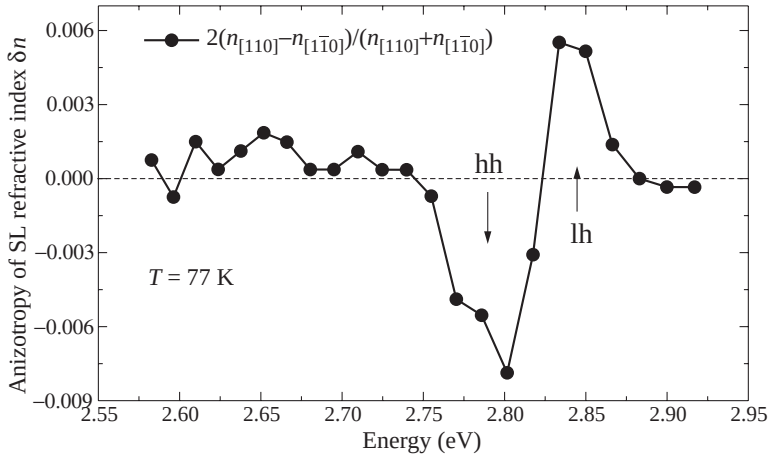

Fig. 3. Spectral dependence of the superlattice refractive index anisotropy. Sign of this anisotropy is different for heavy hole and light hole states.

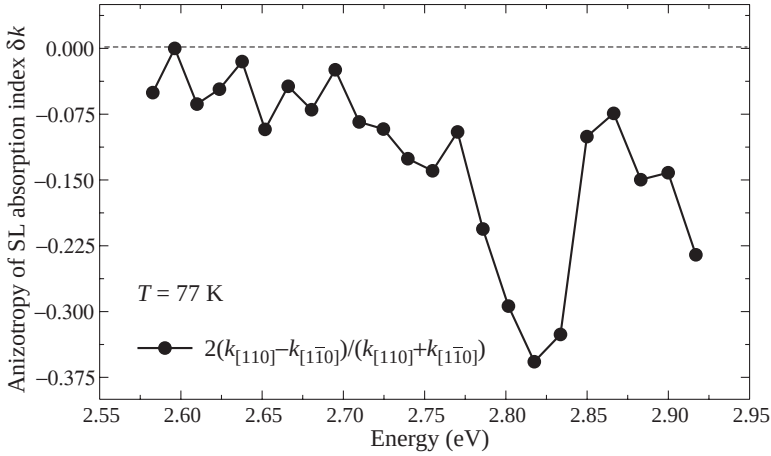

Fig. 4. Spectral dependence of the superlattice absorption index anisotropy. In this case sign of absorption index anisotropy is independed of the photon energy.

In Fig. 3 and Fig. 4 the anisotropy of the optical constants is presented. The sign of the anisotropy of the superlattice refractive index is different for heavy hole and light hole excitons (see Fig. 3). But for the absorption index (Fig. 4) the sign is independent of the photon energy. The maximum absolute value of measured refractive index anisotropy is 0.079 and for the absorption index is 0.357.

The obtained results allow us to conclude that the main part of the superlattice optical anisotropy corresponds with absorption index of the superlattice in the spectral range of the spatially direct excitonic transition.

Acknowledgements

The work was supported in part by Russian Foundation for Basic Research grant No. 01-02-17758, and INTAS grant No. 9900015 and the program Nanostructures. Authors are very thankful to E. L. Ivchenko for fruitful discussions.

References

[1] A. V. Platonov et al., *6th Int. Symp. Nanostructures: Physics and Technology*, St Petersburg, 1998.
A. V. Platonov et al., *Phys. Rev. Lett.* **83**, 3546, (1999).
D. R. Yakovlev et al., *Phys. Rev.* **B61**, R2421, (2000).
[2] O. Krebs and P. Voisin, *Phus. Rev. Lett.* **77**, 1829, (1996).
[3] E. L. Ivchenko and A. A. Toropov, *Phys. Solid State* **40**, 1925 (1998).
[4] R. M. Azzam and N. H. Bashara, *Ellipsometry and Polarised Light*: North Holland publishing company, 1974.
[5] E. L. Ivchenko and G. E. Pikus, *Superlattices and other Heterostructures. Symmetry and Optical Phenomena*: Springer-Verlag, 1995.

9th Int. Symp. "Nanostructures: Physics and Technology"
St Petersburg, Russia, June 18–22, 2001

Persistent 2D states of δ-layer quantum well and resonant polaron in δ-GaAs/Al structures

I. N. Kotel'nikov and S. E. Dizhur
Institute of Radioengineering and Electronics, RAS, 101999 Moscow, Russia

Abstract. The effect of time illumination by radiation $\hbar\omega > Eg$ on conductance between 2DEG and Al-electrode was investigated in tunnel structures Al/δ-GaAs at $T = 4.2$ K. Persistent tunneling photoconductivity (PTPC) and "thickening" 2D levels E_i to the ground state E_0 direction in the quantum well (QW) of the δ-layer was discovered. Subband energies were calculated from the tunneling spectra. PTPC achieved saturation as a function of illumination time t. The change of the tunneling conductivity $\Delta\sigma_S$ of the structures reaches 10%. There was a weak dependence E_0 on t, and its change at the saturation corresponded to 10–15% increase of 2D electron concentration. Shift of the energies E_i of the empty subbands of the QW amounts to 10–50 meV which leads to noticeable decrease of the intersubband energies. Persistent states' behaviour in the 2D-subband spectrum and the value of $\Delta\sigma_S$ indicates on broadening of the QW at fixed potential barrier between δ-layer and Al. It was observed that one of the terms $E_i(t)$ manifested the anticrossing and pinning to other one $E_j(t) + \hbar\omega_{\mathrm{LO}}$ ($\hbar\omega_{\mathrm{LO}}$ is LO-phonon energy in GaAs). These singularities could be associated with resonant intersubband polaron.

Introduction

Recently the intersubband resonant polaron in tunnel structure Al/δ-GaAs has been observed [1, 2]. In these experiments the diamagnetic shift of the 2D-subbunds was used. Subband energy positions in the δ-layer must also change due to persistent photoconductivity (PPC) effect. It is well known for "deep" δ-layers and filled subbands (see review [3] or more recent works [4, 5]). Models of increase of 2DEG concentration in the δ-structures due to the PPC (DX-centers [6], interface states [4], etc.) are still being discussed [5]. However, as far as we know, the spectra of the unoccupied subbands of the δ-layers in PPC regime have not been studied. Magnetotransport measurements allow to analyze only filled subbands of the 2DEG. The 2D subband features in the tunnel spectra (TS) of the junctions emerge irrespective to occupation of the 2D levels. Therefore the tunneling spectroscopy allow us to investigate experimentally the changes of the energy levels in the PPC regime for the near-surface δ-layers. It has been demonstrated first time in [7]. Moreover, we have the possibility to investigate resonant manybody effects by tuning the subband (or intersubband) energies by the PPC.

1. Samples and experiment

The tunnel structures Al/δ-GaAs were prepared in IRE RAS on semi-insulating (100) GaAs substrates by the method of molecular beam epitaxy (MBE) [2]. The δ-doped layer with the density of Si atoms 5.2×10^{12} cm^{-2} was formed at 570 °C and the distance of $L = 20$ nm from Al/GaAs interface. Deposition of Al from the Knudsen cell took place directly in the MBE chamber. The width of a semitransparent Al film was 80–100 nm. Al/δ-GaAs tunnel junctions were photolitographically defined and etched into samples. 2DEG concentration was in the range $0.5-1.5 \times 10^{12}$ cm^{-2}. The other samples parameters and measuring

technique see in [2]. The sample illumination was performed by LED with $\hbar\omega > E_g$, mounted in the cryostat.

2. Results and discussions

Figure 1 demonstrates TS of the Al/δ-GaAs junction with $n_{2D} \simeq 1 \times 10^{12}$ cm^{-2} at the temperature $T = 4.2$ K after cooling in dark (upper curve). Strong dips in TS are related with the bottoms E_i of the two-dimensional subbands in the δ-layer.

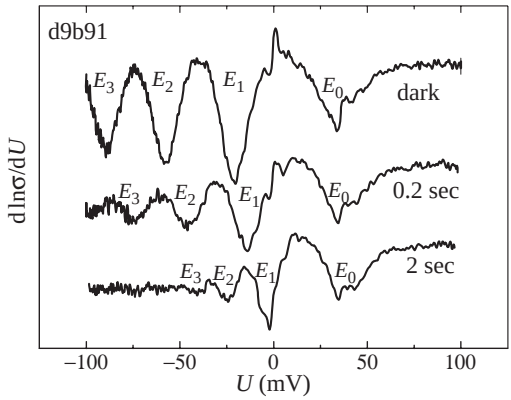

Fig. 1. Tunnel spectra at the dark (top curve) and different illuminations (bottom curves). Signs E_i show subband positions. Temperature is 4.2 K. Sample d9b91.

It is well known that the tunnel conductance in the i-subband is: $\sigma_i(U) \propto \rho_{\|i}(E_i - eU) \cdot D(E_i, E_F - eU)$, where $\rho_{\|i} = (m/\pi\hbar^2) \cdot \theta(E_i - eU)$ is the two-dimensional density of states and D is the barrier transmission. Thus the positions U_i of dips in TS $d \ln \sigma / dU$ can be used to determine the subband energies E_i in 2DEG. The dips at $U > 0$ and $U < 0$ correspond to full and empty subbands, respectively. According to Fig. 1, only one subband E_0 is occupied in this sample and the value of Fermi energy is $eU_0 = E_0 \simeq$ 40 meV. In all tested samples only E_0 subband was partially filled at the dark condition and the position U_0 in TS at different 2DEG concentrations was changed from 20 to 50 mV. Illumination of samples by LED at liquid helium temperatures in time t led to variation of the tunnel conductance and of the dips positions in TS [7]. Dips shifts are well seen in TS of Fig. 1. It is clear seen that unfilled levels "thicken"to the ground state E_0, changing their position on $\simeq 10-50$ meV. Variation of the E_0 value with t corresponds to $\simeq 10\%$ increase of 2DEG concentration. Observed PTPC and subband spectra variation reach saturation that corresponds to illumination time. Persistent state of the illuminated tunnel structure practically was not changed in several hours. Heating the sample to room temperature with following cooling in the dark returned the structures parameters to the initial (dark) values. Notice that at $T = 77$ K tunnel conductance $\Delta\sigma_S$ variation in saturation is about 1–2% (at $T = 4.2$ K $\Delta\sigma_S$ reach 10%), but all 2D subband levels shift to the bottom of conductance band of the GaAs on the same value $\simeq 1-2$ mV.

The data of the temperature dependence of $S_0 = d \ln \sigma / dU$ at $U = 0$ show (Fig. 2) the presence of two characteristic temperatures of the PTPC. At $T \simeq 40$ K main changes in S_0 vanished, and at $T \geq 120$ K curve $S_0(T)$ coincides with "dark" curve. The results obtained allow to suggest two mechanisms of PTPC in our samples. At $T = 77$ K the change of

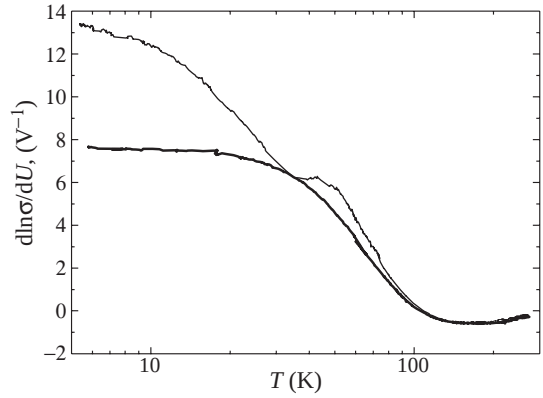

Fig. 2. $S_0 = d \ln \sigma / dU$ at $U = 0$ as a function of temperature: cooling in darkness (thick curve), reverse warming after illumination right up to saturation (thin curve). Sample d5b42.

the electrons concentration in QW occurs, possibly because of DX-centers ionization. At liquid helium temperatures, in addition, the broadening of the QW takes place. As the barrier hight at Al/GaAs interface is independent on illumination, such broadening can be associated with the change of the Fermi level position in the bulk of GaAs. This means that the photo-exited electrons are trapped in the impurity states beyond the δ-doped region.

Let's return to the persistent changes in 2D level positions at $T = 4.2$ K. In Fig. 3(a) we can see curves $E_i(t)$ obtained from TS measured for the junction with $n_{2D} \simeq 1.5 \times 10^{12}$ cm^{-2}. Displayed energies $E_i(t)$ are counted off from the GaAs Fermi level. The results seem to indicate that pinning of one of the unoccupated subband to the energy of the one of the filled subband plus LO-phonon takes place. Such pinning is typical for resonant intersubband polaron. This effect becomes more noticeable in Fig. 3(b), where levels E_1 and E_3 are in resonance with LO-phonon; moreover, an appreciable anticrossing of terms

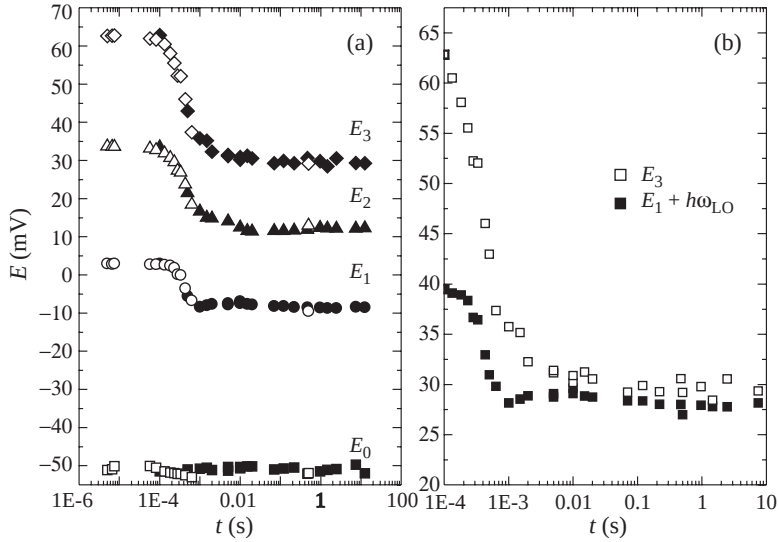

Fig. 3. Subband energies E_i of the sample d7c52 as functions of the illumination time t at $T = 4.2$ K.

occurs (see illumination time range 0.3–10 ms). Similar pinning and anticrossing effects are observed for the samples with other 2DEG concentrations, but for the other pair of terms. Note that in PTPC regime the anticrossing effect is localized by the parameter t, while in magnetic field B this effect increases with B [2].

The results obtained show that PTPC permits to provide the resonance conditions for detecting polaron effects in the QW of the near-surface δ-layer. In combination with the planned experiments being in parallel magnetic field, the PTPC effect allows to obtain new data on threshold interaction of 2D electrons with optical phonons. In our opinion, the significant value of the polaron effects in our structures is related to the self-consistent potential profile of δ-layer QW. Unfortunately, there is no theory of resonant intersubband polaron in such systems, which does not permit to compare observed effects with calculations.

Acknowledgements

We are grateful to Yu. V. Fedorov and A. V. Hook for preparation of the samples in MBE chamber, V. A. Volkov for helpful discussions and V. G. Mokerov for attention. This work was supported by INTAS (Pr. 97-11475), Russian Foundation for Basic Research and Russian Federal Program “Surface Atomic Structures”.

References

[1] I. N. Kotel’nikov and V. A. Volkov, *Proc. 7th Int. Symp. “’Nanostructures: Physisc and Technology”, St Petersburg* p 272, 1999.
[2] I. N. Kotel’nikov *et al*, *Pis’ma Zh. Eksper. Teor. Fiz.* **71**, 564 (2000).
[3] A. Ya. Shik, *Fiz. Tekh. Poluprov.* **26**, 1161 (1992).
[4] A. G. Oliveira *et al*, *J. Appl. Phys.* **78**(4), 2659 (1995).
[5] V. V. Valyaev *et al*, *Zh. Eksper. Teor. Fiz.* **113**, 693 (1998).
[6] P. M. Koenraad *et al*, *Semicond. Sci. Technol.* **6**, 143 (1991).
[7] S. E. Dizhur *et al*, *Abstr. 2nd All-Rus. Young Conf. on the Phys. of Semicond. and Semicond. Opto- and Nanoelectr. (in Russian), St. Petersburg.* p 48, 2000.

9th Int. Symp. "Nanostructures: Physics and Technology"
St Petersburg, Russia, June 18–22, 2001

Optical and transport properties of short period InAs/GaAs superlattices

V. A. Kulbachinskii†, R. A. Lunin†, A. V. Golikov†, V. A. Rogozin†,
V. G. Mokerov‡, Yu. V. Fedorov‡, A. V. Hook‡ and Yu. V. Khabarov‡
† Low Temperature Physics Department, Moscow State University,
119899, Moscow, Russia
‡ Institute of Radioengineering and Electronics, RAS, Moscow, Russia

Abstract. The photoluminescence, magnetoresistance, Shubnikov-de Haas and Hall effect have been investigated in modulation doped short period InAs/GaAs superlattices as a function of InAs layer thickness Q in the range $0.33 < Q < 2.7$ monolayer (ML). Large photoluminescence enhancement takes place when InAs layer thickness $Q = 0.33$ ML. When $Q > 2.7$ ML the quantum dots are formed. The anisotropy of resistivity and mobility of electrons depends not monotonically on the thickness Q of InAs layers.

Introduction

In recent years considerable attention has been focussed on the research of the self-organized ensembles of quantum dots, that is the quasi-zero-dimensional objects (with dimensions 5–20 nm) shaped during heteroepitaxial growth in case of misalignment of lattice parameters with a substrate [1–3]. While the mechanism of a nucleation and formation of quantum dots and optical properties of undoped structures with quantum dots have been widely studied, the optical and electrical properties of doped structures at initial stage of quantum dot formation have not been investigated enough. In the present work the investigation of a photoluminescence at the temperature 77 K, magnetoresistance and Hall effect in modulation doped shot period InAs/GaAs superlattices with very thin InAs layers in magnetic fields up to 8 T in the temperature range 0.4–4.2 K was conducted.

1. Samples

The structures were grown by MBE at 490 °C on semi-insulating (001) GaAs substrates. The samples consisted of 1 μm thick GaAs buffer layer, superlattice InAs/GaAs (with different periods and total thickness 14 nm), a 10 nm thick spacer layer $Al_{0.2}Ga_{0.8}As$, a 35 nm thick Si-doped layer $Al_{0.2}Ga_{0.8}As$ and a 6 nm thick GaAs cap layer. In investigated structures the effective thickness Q of InAs layers was changed from 0.33 ML up to 2.7 ML. The thickness of GaAs layers in superlattice was also proportionally changed to keep the mean composition of the superlattice equivalent to solid solution $In_{0.16}Ga_{0.84}As$. From the wafers double Hall bars were fabricated for anisotropy and magnetotransport experiments with the current (I) channel along [110] (pa-direction) and perpendicular (I parallel to [$\bar{1}$10], pe-direction) in the same sample. Thus the anisotropy of resistance have been measured in the samples with single current channel bended to 90 degrees. The relevant parameters of the structures are listed in Table 1.

2. Photoluminescence

In Fig. 1 the photoluminescence spectra are shown for samples with InAs layer thickness Q from 0.33 up to 2.7 ML. The photoluminescence spectra of samples with thickness less than 2 monolayers showed two peacks: a low-energy peak with a maximum at photon energy 1.356–1.375 eV and a high-energy peak with a maximum at photon energy 1.406–1.434 eV (see Table 1). These two peaks correspond to optical transitions from the two occupied electronic subbands to hole subband [4] because in the case of undoped quantum well only optical transition from lowest subband is visible in PL spectra. Always the intensity of the peak with higher energy is higher (see Fig. 1). However, when the effective thickness of InAs layers equal to or exceeds 2.7 monolayers, the photoluminescence spectrum essentially transforms. A new broad and intensive photoluminescence peak with a maximum at 1.265 eV appears in long-wavelength region of the photoluminescence spectrum (Fig. 1(8)). As shown in Ref. [1–3], such change of photoluminescence spectrum may be ascribed to the phase transition from two-dimensional layer-by-layer growth to the formation of a vertically-stacked quantum dots. The second feature of the photoluminescence spectra is not monotonous dependence of the intensity I_{PL} on the InAs layer thickness Q. Maximal intensity was observed for $Q = 0.33$ ML. The maximal electron mobility was observed in this sample (see later).

Table 1. The InAs layer thickness Q in monolayers (ML), the energy $h\nu_{\max}$ of the maximum of the photoluminescence spectra at $T = 77$ K, the Hall density n, and the Hall mobility μ, at $T = 4.2$ K for modulation doped InAs/GaAs superlattices.

Sample number	Q (ML)	$h\nu_{\max}$ (eV)	n (10^{11} cm^{-2})	μ (cm^2/Vs)
1	solid solution $In_{0.16}Ga_{0.84}As$	1.434, 1.375	8.7	8100
2	0.33	1.419, 1.367	11.5	9400
3	0.67	1.411, 1.369	5.98	2060
4	1.00	1.411, 1.370	15.2	2450
5	1.33	1.418, 1.374	8.66	4220
6	1.58	1.404, 1.368	5.60	4910
7	2.00	1.406, 1.356	10.4	7060
8	2.70	1.390, 1.265	1.52	120

3. Magnetoresistance

A negative magnetoresistance was observed at low temperatures in magnetic fields $B < 0.1$ T in all samples. In high magnetic fields the Shubnikov–de Haas effect and quantum Hall effect was observed (Fig. 2,3). The Hall electron concentration is equal to $(1.5-15) \times 10^{11}$ cm^{-2} in different samples at temperature 4.2 K and coincides with concentration determined from the Shubnikov–de Haas effect. The obtained carrier concentration n and mobility μ are listed in Table 1. The maximum value of electron mobility 9400 cm^2/Vs is observed in a sample with a InAs thickness 0.33 monolayers. When InAs thickness increases the mobility decreases down to approximately 4000 cm^2/Vs at temperature 4.2 K (Fig. 4). The relatively high mobility in sample with minimum submonolayer thickness $Q = 0.33$ ML of InAs may be explained by a small fluctuation of elastic strains and most

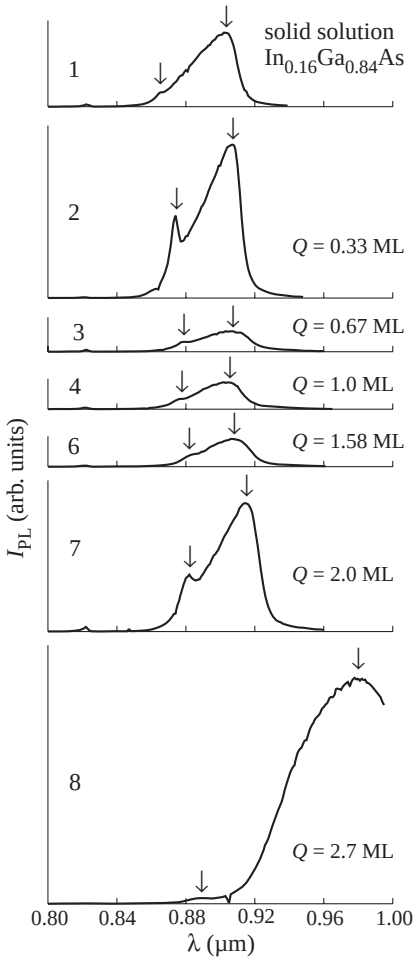

Fig. 1. Photoluminescence spectra of modulation doped InAs/GaAs superlattices with InAs layer thickness Q from 0.33 up to 2.7 monolayer and the mean composition $In_{0.16}Ga_{0.84}As$ sample.

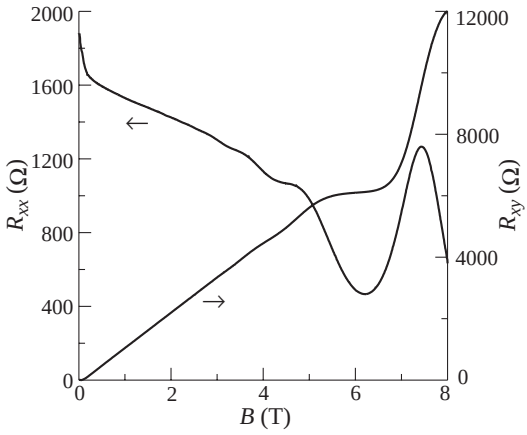

Fig. 2. Transverse magnetoresistance R_{xx} and Hall resistance R_{xy} for sample with InAs layer thickness $Q = 1.58$ ML at $T = 0.4$ K.

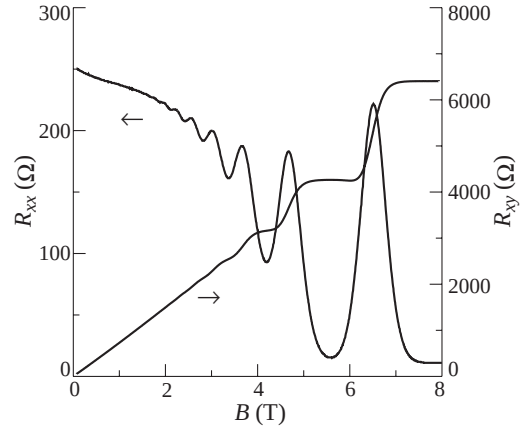

Fig. 3. Transverse magnetoresistance R_{xx} and Hall resistance R_{xy} for sample with solid solution $In_{0.16}Ga_{0.84}As$ at $T = 0.4$ K.

perfect crystal lattice as compared with solid solution $In_{0.16}Ga_{0.84}As$. In sample 8 quantum dots are formed and electron concentration is much lower than in other samples. Due to low electron concentration the electron mobility in this sample is very low.

4. Anisotropy of conductivity

In all samples except solid solution $In_{0.16}Ga_{0.84}As$ the anisotropy of conductivity is observed. The dependence of ratio of resistance R_{pe} in the $[\bar{1}10]$ direction to resistance R_{pa} in the [110] direction on thickness of InAs layers is shown in Fig. 5.

The anisotropic electron mobility correlates to the asymmetric dislocation distribution [5]. The anisotropy of resistance in 2D electron system is typical for structures with

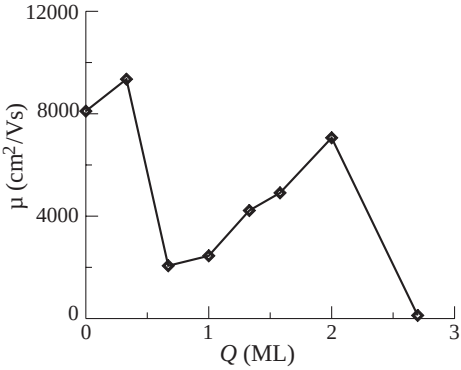

Fig. 4. Dependence of Hall mobility μ on InAs layer thickness Q for different superlattices at $T = 4.2$ K.

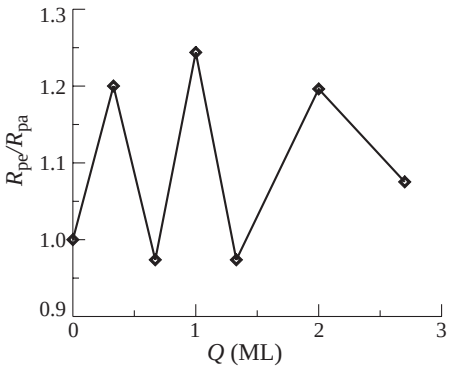

Fig. 5. Dependence of ratio of resistance R_{pe} in the [$\bar{1}$10] direction to resistance R_{pa} in the [110] direction on thickness Q (in ML) of InAs layers.

preferential growth of deposited material in one direction (see [6, 7], for example). The dependence of anisotropy on thickness of InAs layers shows that at definite ML deposition Q there are an island growth which leads to the anisotropy of resistance (see Fig. 5).

Acknowledgements

The work was supported by the RFBR (Grant N 00-02-17493).

References

[1] N. N. Ledentsov, V. M. Ustinov, V. A. Shchukin, *et al.*, *Semiconductors* **32**, 343 (1998).
[2] D. Bimberg, V. A. Shchukin, N. N. Ledentsov, *et al.*, *Appl. Surf. Sci.* **130-132**, 71 (1998).
[3] V. A. Kulbachinskii, V. G. Kytin, R. A. Lunin, *et al.*, *Semiconductors* **33**, 318 (1999).
[4] Y. K. Yuan, K. Mohammed, M. A. A. Pudensi, *et al.*, *Appl. Phys. Lett.* **45**, 739 (1984).
[5] T. Schweizer, K. Kohler, W. Rothemund, *et al.*, *Appl. Phys. Lett.* **59**, 2736 (1991).
[6] A. de Visser, V. I. Kadushkin, V. A. Kulbachinskii, *et al.*, *JETP Lett.* **59**, 364 (1994).
[7] V. A. Kulbachinskii, V. G. Kytin, V. I. Kadushkin, *et al.*, *Solid State Physics* **37**, 2693 (1995).

9th Int. Symp. "Nanostructures: Physics and Technology"
St Petersburg, Russia, June 18–22, 2001

Electron dispersion in a three-dimensional regimented quantum dot superlattice

Olga L. Lazarenkova[1] and Alexander A. Balandin
Department of Electrical Engineering, University of California-Riverside,
Riverside, CA 92521, USA

Abstract. The electron band structure in a three-dimensional *regimented* quantum dot superlattice is analyzed using an envelope function approximation. It is shown that the electron density of states, effective mass, and carrier mobility in these structures are drastically different from those in quantum well superlattices and bulk materials. By changing the size of quantum dots, inter-dot distances, barrier height and regimentation, one can effectively tune the electronic properties of the quantum dot superlattices and make them suitable for a variety of device applications.

Introduction

Quantum dot arrays or stacks of quantum dot arrays, which we refer to as quantum dot superlattices (QDS), feature very different degrees of periodicity. Quantum dots grown by molecular beam epitaxy (MBE) can be completely random in such structures, partially regimented, like in QDS with vertical dot site correlation [1], or may have very high degree of regimentation [2]. Although many types of regimented QDS have been fabricated using different self-assembly techniques [3], very little attention has been paid to a theoretical description of electron spectrum in such structures [4].

The goal of this work is to develop a model for calculating the electronic structure in QDS that can serve as a useful tool for experimentalists and materials growers. To achieve this goal, we limit ourselves to the envelope function approximation and the perturbation theory. We show that our approach can provide the accuracy comparable to other treatments such as the finite-elements method, and plain-wave expansion technique. The regimentation, e.g. long-range spatial ordering, of quantum dots along all three directions results in the formation of an artificial crystal, where quantum dots play the role of atoms. Thus, this structure can also be referred to as a *quantum dot crystal* (QDC).

It is well known that the solution of Schrödinger equation in the three-dimensional space can be greatly simplified if the potential $V(x, y, z)$ is written as a sum of three independent potential functions of coordinates x, y, and z. We use this specific form of the confining potential as a zero approximation for our solution. Then we apply the time-independent perturbation theory in order to obtain a solution for the potential of interest, which is quantum dot potential well surrounded from each side by the barriers of equal height. A particular choice of the values of the zero-approximation and perturbing potentials allows us to make the corrections to our initial solution rather small. It is interesting to note that our initial choice of spatially separable potential corresponds to the real potential profile in quantum dots induced by strain from buried stressors [5].

For this work, the numerical simulations are carried out for a QDC that consists of very small (feature size is on the order of 5–10 nm) Ge quantum dots embedded in Si. This

[1] On leave from St Petersburg State Electrotechnical University "LETI", St Petersburg, 197376, Russia.

structure is similar to multiple arrays of Ge quantum dots grown on (001) Si by solid-source MBE [1]. Approximately 90% of the band offset in such structure goes to the valence band. Due to this reason, our analysis is restricted to heavy holes in Ge/Si QDC. The light-hole states are split and located above the barrier due to the strain effects. The band offset for the heavy holes is approximately equal to 0.45 eV. In our calculations we used the following values for the effective masses $m^*_W = m^*_{\mathrm{Ge}} = 0.28m_0$ and $m^*_B = m^*_{\mathrm{Si}} = 0.49m_0$.

1. Electron dispersion

Figure 1 presents electron dispersion in a *simple cubic* QDC along the [[111]] *quasi*-crystallographic direction. Here the directions denoted with double square brackets are associated with the ordering of the quantum dots and are not related to the symmetry directions of the Si crystal itself. The energy bands are denoted by three quantum numbers $n_x n_y n_z$ with the superscript indicating the degeneracy of the band. The spin degeneracy is not counted here. Like in real crystals, the energy in QDC has the full symmetry of the reciprocal lattice. The energy bands are degenerated in the center of the *quasi*-Brillouin zone (QBZ) of the artificial crystal. The highest, sixfold, degeneracy is achieved in mini-bands of *cubic* QDC characterized by different quantum numbers $n_x n_y n_z$. If two of these three quantum numbers are equal, the degeneracy is threefold. Finally, if $n_x = n_y = n_z$

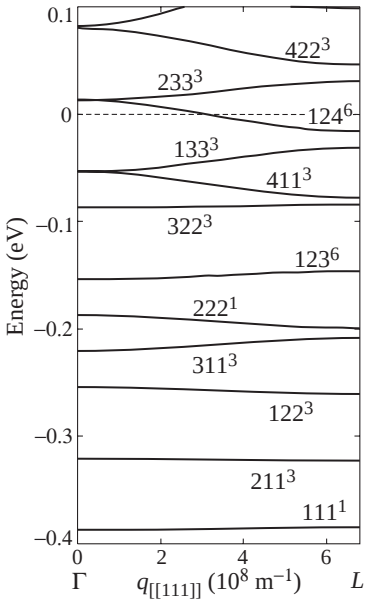

Fig. 1. Dispersion relation in a cubical quantum dot crystal shown along [[111]] quasi-crystallographic direction. The energy in units of eV is counted from the position of the potential barrier. The dot size is $L_x = L_y = L_z = 6.5$ nm and the inter-dot distance is $H_x = H_y = H_z = 1.5$ nm. Material parameters used in simulation correspond to the valence band of Ge/Si system.

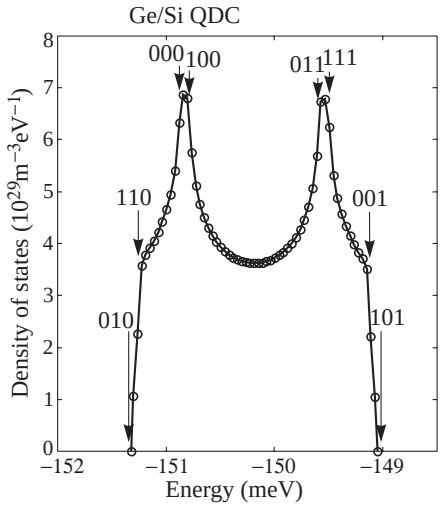

Fig. 2. Electron density of states in a cubical quantum dot crystal for 3D mini-bands defined by the following quantum numbers $n_x = 1, n_y = 2$, and $n_z = 3$. The dot size is $L_x = L_y = L_z = 6.5$ nm and the inter-dot distance is $H_x = H_y = H_z = 1.5$ nm. The arrows in this figure indicate particular quasi-crystallographic points. The energy in units of meV is counted from the position of the potential barrier.

there is no symmetry degeneracy in such a mini-band. Moving from the point of high symmetry in the center of the QBZ to a point of lower symmetry, the energy bands split. Unlike in real crystals, in artificial quantum dot crystal the degeneracy can be up to sixfold along [[111]] quasi-crystallographic direction even far from the center of QBZ. This is a result of the cubic symmetry both of the dot and the superlattice (see Fig. 1). If their symmetries are different, the twofold degeneracy will be the maximum permitted in all directions.

2. Density of states

An electron (hole) density of states (DOS) has been calculated taking into account the twofold electron spin degeneracy. The results of our numerical simulation of DOS in a cubic QDC for the most intricate case of all different quantum numbers $n_x = 1$, $n_y = 2$, and $n_z = 3$ are presented in Fig. 2. The points of high symmetry correspond to analytic critical points with van Hove singularities. The shape of DOS is defined by the quantum numbers of the corresponding mini-band. The arrows in this figure indicate particular quasi-crystallographic points. One should mention here that the areas under each DOS curve corresponded to different dispersion brunches, e.g. integral of each DOS, are all equal and defined by the density of quantum dots in a crystal. Note that the shape of DOS in the quantum dot crystal is drastically different from that in the quantum well superlattice and random quantum dot (QD) array.

3. Effective mass tensor and mobility of carriers

The simulation shows that the effective mass and the group velocity in QDC is highly anisotropic and strongly dependent on the mini-band index, e.g. quantum numbers which define the mini-band. The effective mass strongly depends on the periodicity and regimentation of the dots in the artificial crystal. It is almost always different from that one in the corresponding bulk material, and changes dramatically within a very narrow range of energy. This leads to a strong modification of the carrier mobility and conductivity in such structures.

The carrier motion perpendicular to the sides of quantum dots is completely defined by only one quantum number that describes quantization in the direction of motion. In this case a family of mini-bands is characterized by the same effective mass. Thus, along [[100]] direction, electron (hole) transport in QDC is similar to the one in conventional quantum well superlattices. The effective mass along [[110]] direction is determined by two quantum numbers, so that few mini-bands have the same value of the effective mass. Transport along [[111]] direction, e.g. cube diagonal, is more complicated and the effective mass is different for each branch. Application of electric field along this direction would initiate electron (hole) transport drastically different from that in quantum well superlattices.

4. Conclusion

The carrier band structure in a three-dimensional *regimented* quantum dot superlattice, e.g. quantum dot crystal, has been analyzed. Numerical simulations have been carried out for the valence band of a Ge/Si quantum dot crystals with the quantum dot feature size on the order of 5–10 nm. By changing the size of quantum dots, inter-dot distances, barrier height and regimentation, one can control the electronic properties of this artificial crystal, which are significantly different from those in bulk, quantum well superlattices, and random QD array.

Acknowledgement

The work was supported by the UC Energy Institute's EST program and CRDF Award MP2-2281.

References

[1] J. L. Liu, W. G. Wu, A. Balandin, G. L. Jin, Y. H. Luo, S. G. Thomas and K. L. Wang, *Appl. Phys. Lett.*,**75**, 1745 (1999).
[2] G. Springholz, V. Holy, M. Pinczolits and G. Bauer, *Science*, **282**, 734 (1998).
[3] K. L. Wang and A. Balandin, *Quantum Dots: Physics and Applications*, in *Optics of Nanostructured Materials*, ed. by V. Markel and T. George, (J. Wiley & Sons, New York, 2001) pp. 515–550.
[4] O. L. Lazarenkova and A. A. Balandin, *J. Appl. Phys.* (in review, 2001).
[5] J. H. Davies, *Appl. Phys. Lett.*, **75**, 4142 (1999).

9th Int. Symp. "Nanostructures: Physics and Technology"
St Petersburg, Russia, June 18–22, 2001

Investigation of hot electron distribution by interband transmittance in n-type InGaAs/GaAs MQW heterostructures

D. G. Revin†, V. Ya. Aleshkin†, D. M. Gaponova†, V. I. Gavrilenko†,
Z. F. Krasil'nik†, B. N. Zvonkov‡ and E. A. Uskova‡
† Institute for Physics of Microstructures, RAS, N.Novgorod, Russia
‡ Physical-Technical Institute N. Novgorod State University, Russia

Abstract. High lateral electric field effects on transmittance in selectively doped n-type MQW InGaAs/GaAs heterostructures with δ-doped barriers have been studied. The peculiarities of the transmittance modulation spectra associated with electron heating have been observed. The effective temperature of hot electrons in the quantum wells was obtained.

Introduction

In recent papers [1–3] the far IR emission, absorption as well as photoluminescence and transmittance modulation from 2D hot holes in MQW InGaAs/GaAs heterostructures at lateral transport have been investigated experimentally. The remarkable high nonequilibrium phenomena in the high electric fields were revealed under real space transfer [4] and new mechanism of the intraband population inversion and far IR lasing was put forward [3]. Due to higher mobility in the electron structures the proposed mechanism can be realized more effectively. The paper presents the first study of lateral electric field effects on the optical transmittance in n-type InGaAs/GaAs heterostructures by method suggested in previous works of authors (for example [2]). Investigation of optical transmittance near fundamental absorption edge in quantum well allow us to study directly the energy distribution function of hot electrons. This modulation method (measuring the "destruction" of Burstein-Moss effect by applied electric field) is similar to one used for bulk semiconductors [5].

1. Experimental

$In_xGa_{1-x}As/GaAs$ heterostructures ($0.1 < x < 0.15$, $d_{InGaAs} = 5$ to 7 nm, $d_{GaAs} = 60$ nm, the number of quantum wells is 10 or 20) were grown by MOCVD technique at atmospheric pressure on semi-insulating GaAs (001) substrates. Two δ-layers of Si were introduced at 10 to 20 nm from both sides of each InGaAs quantum well in GaAs barrier layers. Typical values of 2D electron concentration were 0.7 to 2×10^{11} cm^{-2}. The lateral pulse electric field (E) up to 1.5 kV/cm^2 to 10 μs in duration was applied to the structure via strip electric contacts deposited on the sample surface. The experimental details were described in [2]. In transmittance experiments the measured signal was proportional to the difference between the intensities of light passed through the sample under and without applied electric field. To determine the energy of main (e1-hh1) optical transition in quantum wells in addition to the transmittance modulation spectra the photoluminescence and transmittance at $E = 0$ were investigated also. The measurements were carried out at 4.2 K. In all experiments with pulse electric field box-car integrator was used for data acquisition.

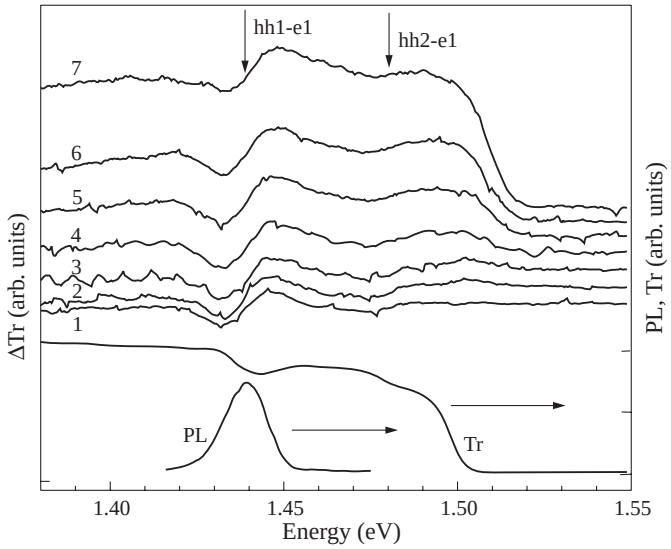

Fig. 1. Photoluminescence (PL), transmittance (Tr) and transmittance modulation (ΔTr) spectra for heterostructure with 5 nm $In_{0.15}Ga_{0.85}As/GaAs$ quantum wells. The electron concentration is 7×10^{10} cm^{-2}. Electric field (V/cm): 1—115, 2—230, 3—345, 4—460, 5—575, 6—690, 7—920. The arrows indicate the calculated positions of hh1-e1 and hh2-e1 optical transitions.

2. Results and discussion

As it follows from calculations for investigated heterostructures there are one electron and two heavy hole subbands in quantum wells. The energy of the first electron subband (e1) in the quantum wells is less than the conductivity band edge in δ-layer in GaAs and therefore the most of electrons turn to be in the quantum wells. At zero electric field the electron concentration in the quantum wells is high enough and therefore the edge of the fundamental absorption is shifted to the shortwavelength region due to Burstein–Moss effect. Electron heating results in the change of the electron distribution function and hence in the tailing of the fundamental absorption edge. This leads to both the increase of the transmittance for the optical transitions to the electron states over Fermi energy and the decrease for ones under Fermi energy.

In Figure 1 the typical transmittance modulation spectra as well as transmittance and photoluminescence spectra for one of investigated heterostructure are shown. As one can see from transmittance spectrum the energy of the main (hh1-e1) optical transition in these quantum wells is about 1.438 eV. In this energy region both the “negative” (decrease of transmittance) and “positive” (increase of transmittance) peaks were observed in the transmittance modulation spectra. This results from the electron redistribution near Fermi level due to electric field heating. In contrast to p-type structures less effective mass for electrons in comparison for holes leads to the less widths of negative and positive peaks. Transmittance modulation is observed at low electric fields. Starting from approximately 300 V/cm the amplitudes of both negative and positive peaks change weakly. Scattering on the optical phonons prevents further effective electron heating. Other peculiarity in transmittance spectra near 1.482 eV probably corresponds to the hh2-e1 optical transition. Due to weak overlapping of wave function for hh2-holes and e1-electrons this transition

has low intensity. The form of high energy peak (positive) in the transmittance modulation spectra specifies the effective temperature of hot electrons in the quantum wells that reaches approximately 100 K at electric field about 500 V/cm and changes weakly at the further electric field increase. At considerable electric fields (about 500 V/cm) broad band modulation was observed within GaAs band gap. The intensity of this modulation grows with electric field increase as a superlinear function. The nature of this phenomena is not clearly understand yet. One of the possible mechanism may be recharging of deep acceptor levels in highly doped and compensated substrate.

Thus the transmittance modulation by electric field in n-type InGaAs/GaAs heterostructures with quantum wells was studied. The hot electron effective temperature is shown to be approximately the same for hot hole one in p-type heterostructures.

Acknowledgements

This work was supported in part by the grants No. 00-02-16159, 00-02-81022 from Russian Foundation for Basic Research, 99-1128 from Russian Scientific Program "Physics of Solid State Nanostructures" and No. 99-01242 from INTAS.

References

[1] V. Ya. Aleshkin, A. A. Andronov, A. V. Antonov, N. A. Bekin, V. I. Gavrilenko, D. G. Revin, B. N. Zvonkov, E. R. Lin'kova, I. G. Malkina and E. A. Uskova *JETP Lett.* **64**, 7, 520 (1996).

[2] V. Ya. Aleshkin, A. A. Andronov, A. V. Antonov, D. M. Gaponova, V. I. Gavrilenko, D. G. Revin, B. N. Zvonkov, I. G. Malkina and E. A. Uskova, *Materials Science Forum* **297-298**, 37 (1999).

[3] V. Ya. Aleshkin, A. A. Andronov, A. V. Antonov, N. A. Bekin, V. I. Gavrilenko, A. V. Muravjev, S. G. Pavlov, V. N. Shastin, D. G. Revin, E. R. Lin'kova, I. G. Malkina, E. A.Uskova and B. N. Zvonkov, *Proc. Int. Semicond. Devica Research Symp. (USA, 1997)*, p. 263.

[4] Z. S. Gribnikov, K. Hess and G. A. Kosinovsky *J. Appl. Phys.* **77**, 1337 (1995).

[5] W. Jantsch and H. Brucker, *Phys. Rev. B* **15**, 4014, (1977).

9th Int. Symp. "Nanostructures: Physics and Technology"
St Petersburg, Russia, June 18–22, 2001

Raman study of phonon–plasmon coupling modes in tunnelling GaAs/AlAs SLs, grown on (311) and (001) surfaces

V. A. Volodin†, M. D. Efremov†, V. A. Sachcov‡, V. V. Preobrazhenski†, B. R. Semyagin†, E. A. Galaktionov§ and D. A. Orehov§

† Institute of Semiconductor Physics SB RAS, pr. Lavrentjeva 13, Novosibirsk 630090, Russia

‡ Institute of Sensor Microelectronics SB RAS, pr. Mira 55a, Omsk 644077, Russia

§ Novosibirsk State University, 630090, Pirogova 2, Novosibirsk, Russia

The undoped and doped GaAs/AlAs superlattices (SLs) grown by MBE on (100), (311)B surfaces and facet (311)A surface were studied using Raman spectroscopy. Thickness of GaAs layers of the studied SLs was varied from 1 to 10 monolayers (mls), thickness of AlAs barriers was 8 mls, the concentration of impurity (Si) in doped SLs was 2×10^{18} cm^{-3}. Parameters of the SLs are shown in Table 1. The Raman spectra were registered at room

Table 1. Specifications of the studied superlattices $GaAs_nAlAs_m$.

	Substrate			GaAs thikness,	AlAs thikness,	Periods
No	(311)A	(311)B	(001)	mls	mls	
1	1A	1B	1	10	8	100
2	2A	2B	2	6	8	100
3	3A	3B	3	4	8	200
4	4A	4B	4	2	8	300
5	5A	5B	5	1	8	400

temperature in quasibackscattering geometry in various polarization geometries. The line 514.5 nm of Ar laser was used. As one can see in Fig. 1, when the width of GaAs quantum wells decrease, the interaction of plasmons with the GaAs-like LO-phonons also decrease, but the interaction of plasmons with the AlAs-like LO phonons increase, and the intermixed mode AlAs-like LO-phonons with plasmons was observed. For relatively thick SLs (10 mls GaAs), the width of peaks for doped and undoped SL is nearly equal. In the case of doped sample the peak position shifted to higher energy region. The shift may be caused by intersubband optical plasmons interaction with optical phonons; meanwhile intrasubband contribution is negligible due to localization of electrons.

Some changes in spectra of doped and undoped SL 2 take place, but in the case of SLs 3–5, these changes are dramatic. The coupled modes (for doped SLs — marked as LP2) are shifted and broadened. Peaks resulting of scattering on TO modes in these samples are also a little broadened. The coupling modes in the case of very thin SLs are similar to coupling modes in 3D-case of doped $Ga_xAl_{(1-x)}As$ solid solutions [1]. According to simple appraising using the Kronig–Penny model in the case of SL 4 and 5 the electrons are practically delocalizated, what in good agreement in experimental data. As one can see, the coupled modes of plasmons with optical phonons of GaAs type (marked as LP1) are shifted in low energy region comparing with pure phonon modes in undoped SLs. The coupled modes are also broader. The effect of "softening" modes in the case of doping cannot be explained in frames of macroscopic approach [2]. The zeroes of dielectric constant with phonon and plasmon deposition gives the frequencies of LO-modes always

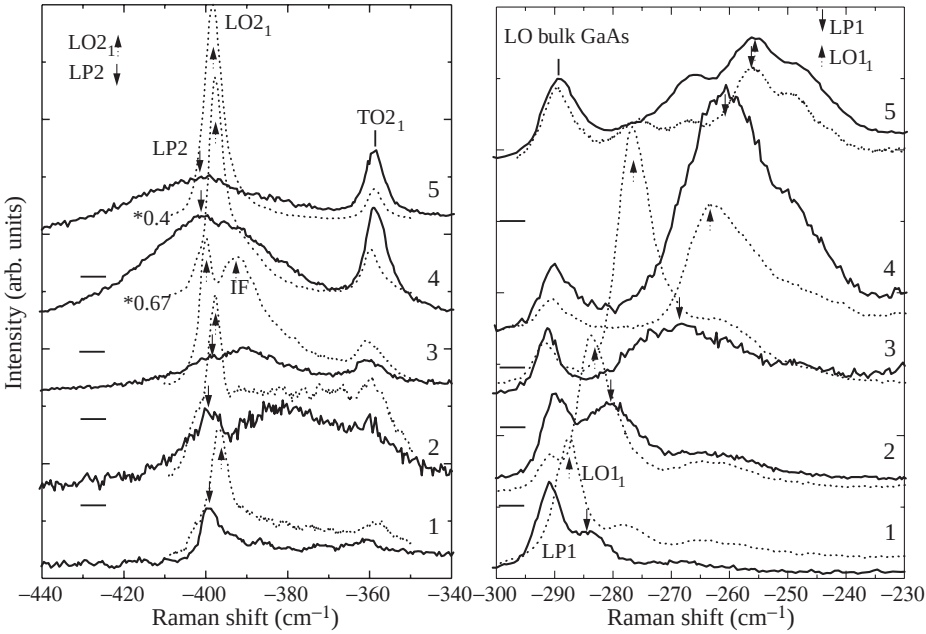

Fig. 1. Raman spectra in (XY) geometry of doped (solid lines) and undoped (dashed lines) GaAs/AlAs SLs, grown on (001) substrate in the condition of (2×4) surface reconstruction. The directions X and Y are (100) and (010) correspondingly.

bellow the frequencies of pure LO modes. So, the more accurate approach is needed to calculate the dispersion of the coupled phonon–plasmon modes in tunnelling SLs. We have advanced microscopically approach for calculations of phonon–plasmon mode dispersion. The dynamic matrix of atomic vibrations was taken in "bond-charge" model. Phonons were considered as subsystem in dielectric media, which permittivity is defined by electron gas in Lindhard–Mermin approximation [3]. Long range dynamical screening of phonons by electron gas was taken into account by self-consistent solution for the dynamic matrix. The resultant dependence of frequencies of coupled phonon–plasmons on wave vector and frequency was derived, as well as corresponded Raman spectra. Some results are presented in Fig. 2(a).

The mass of electron along GaAs layer (mL) was the volume mass of electron, and the mass along direction of SL growth (mT) was changed. As on can see, at some volumes of mT, the frequency of phonon-GaAs-type phonon mode is low energy shifted, but the frequency of phonon-AlAs-type phonon mode is high energy shifted. The similar picture we can observe in the experiment. The wave numbers of LO1 modes of undoped and LP1 and LP2 modes of doped SL 3 are shown for comparison. The difference in Raman spectra of the phonon–plasmon modes was observed for the SLs containing the GaAs quantum well wires (QWWs) grown on corrugated (311)A surface and for (311)B SLs. The example is presented in Fig. 2(b). It is known, that surface (311)A are the very periodical massive of microfacets in direction Y ($\bar{2}33$) [4]. The difference is supposed to be due to anisotropic dispersion of the phonon–plasmon modes along and across to GaAs quantum wires on faceted (311)A surface. For not-corrugated SLs grown on (311)B surface such anisotropy is absent, and its spectra are similar to spectra of (001) SLs. The anisotropy of TO phonons in (311)A corrugated SLs were observed earlier [5], the result of structural anisotropy

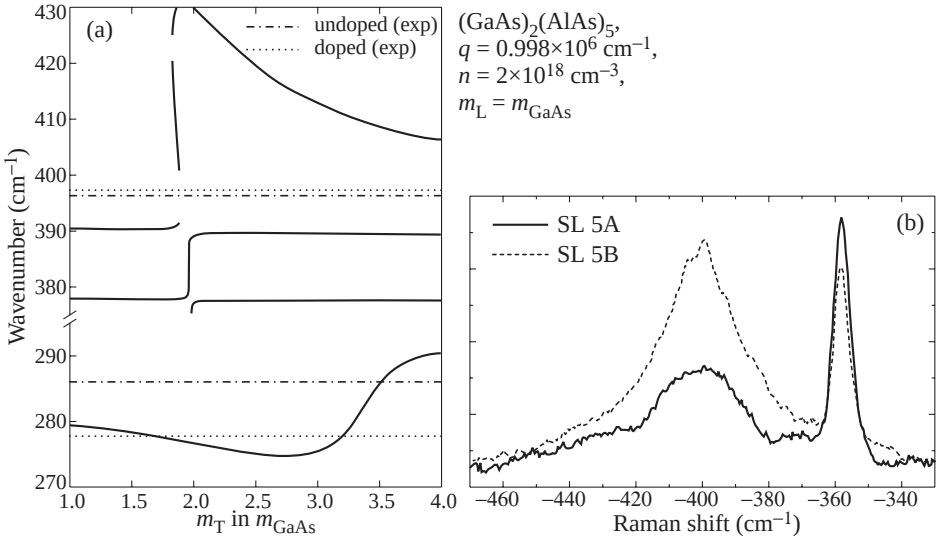

Fig. 2. (a) Calculated position of phonon–plasmons in $(GaAs)_3/(AlAs)_5$ SL. (b) The Raman spectra of doped SLs, grown on (311)A and B surfaces.

was splitting of TO phonon localized in QWWs, for modes with atom displacement along and across to QWWs. The structural anisotropy of (311)A SLs (undoped sample 5) was confirmed using HREM cross-section [6]. So, experimental and the theoretical results concerning phonon–plasmon interaction in tunnelling GaAs/AlAs SLs were obtained for the first time. The agreement between the experiment and the calculations is achieved. The difference in phonon–plasmon modes of (311)A and (311)B SLs was observed, it can be result of interface corrugation in (311)A SLs.

Acknowledgements

Russian Fund for Fundamental Research supported this work (grant No 99-02-16668). One of the authors (V. A. Volodin) is grateful to the Scientific Council of the Institute of Semiconductor Physics SB RAS for the Stipend for Young Scientists.

References

[1] A. M. Mintairov, K. E. Smekalin, V. M. Ustinov and V. P. Hvosticov, *Semiconductors* **26**, 614 (1992).
[2] V. A. Volodin, M. D. Efremov and V. V. Preobrazhenski, *JETP Lett.* **71**, 698 (2000).
[3] M. Cardona, *Light Scattering in Solids IV. (Springer-Verlag, Berlin, 1982).*
[4] R. Nötzel, N. N. Ledentsov, L. Dawerits, M. Hohenstein and K. Ploog, *Phys. Rev. Lett.* **67**, 3812 (1991).
[5] V. A. Volodin, M. D. Efremov, V. V. Preobrazhenskii, B. R. Semyagin and V. V. Bolotov, *Superlatt. Microstructures* **26**, 11 (1999).
[6] N. N. Ledentsov, D. Litvinov, A. Rosenauer, D. Gerthsen, I. P. Soshnikov, V. A. Shchukin, V. M. Ustinov, A. Yu. Egorov, A. E. Zukov, V. A. Volodin, M. D. Efremov, V. V. Preobrazhenskii, B. P. Semyagin, D. Bimberg and Zh. I. Alferov, *J. Electron. Mater.* **30 (5)**, in print (2001).

9th Int. Symp. "Nanostructures: Physics and Technology"
St Petersburg, Russia, June 18–22, 2001

Interaction in the final state of the interface luminescence with delta-doped layers

A. Yu. Silov†, N. S. Averkiev‡, P. M. Koenraad† and J. H. Wolter†
† COBRA Inter-University, Eindhoven University of Technology,
P.O. Box 513, 5600 MB Eindhoven, The Nethelands
‡ Ioffe Physico-Technical Institute, St Petersburg, Russia

Abstract. We show that Coulomb interaction within a delta-layer of donors is governed by the neighbouring two-dimensional hole gas. It has been found experimentally that the interface luminescence band displays pronounced blue shift when the two-dimensional holes recombine with delta-donors. Our analysis confirms that uniform distribution of the delta-dopants provides adequate description of the energy shift versus excitation level.

Introduction

Atomic monolayers of dopants in close proximity of the two-dimensional electronic systems have formerly been used as effective optical probes in the Quantum Hall regime. Here we reverse the situation: the Coulomb interaction within a delta-layer of donors is probed by the neighbouring two-dimensional hole gas (2DHG). The latter is mainly responsible for low-dimensional screening of the electrostatic interaction between ionised delta-dopants.

In our photoluminescence experiments, an optical excitation above the bandgap produces electron-hole pairs with the photoelectrons successively captured by the delta-donors. Once a given fraction of the delta-donors has been neutralised, valence holes from the 2DHG may radiatively recombine with the donors. We show that energy of the outcoming photon depends on Coulomb interaction between delta-donors, which we refer to as an interaction in the final state.

Model

Experimentally this interaction in the final state translates into a spectral shift of the photoluminescence band towards the higher energy side of the spectrum as the density of the optical excitation increases. Under conditions of high optical pumping, all delta-donors are neutralised and the photon energy is at a maximum. The photon energy reaches its minimum when all donors are ionised. The total value of this blue shift is given by

$$\Delta = \frac{2e^2}{\epsilon}\left[\pi\left(2z_0 + q_s^{-1}\right)N\right], \tag{1}$$

where z_0 is the distance between 2DHG and the delta-layer, q_s^{-1} is the inverse screening radii, and N is a concentration of the delta-donors. Notice that without screening, $q_s = 0$, the energy shift would be infinitely large. However, in the case of the screening radii reduced to zero, the low-dimensional screening converts to induction of the image charge at the distance of $(-z_0)$ behind the 2DHG.

Experiments

In all our samples the 2DHG was formed within the potential notch at the modulation doped $Al_xGa_{1-x}As/GaAs$ heterojunctions. The samples were grown by molecular-beam epitaxy on CrO-doped (100) substrates. We used three different types of the layer sequences:
(*i*) The first structure contains a delta-layer of Si with concentration of $N = 4 \times 10^{10}$ cm^{-2}. The delta-layer was placed in GaAs at the distance of 350 Å from the heterointerface. This active layer of GaAs (700 Å) was terminated with a 30-period GaAs/AlAs superlattice buffer layer to prevent the diffusion of photocreated electrons away from the interface.
(*ii*) The second sample was a precise replica of the first one except that the GaAs layer was nominally undoped.
(*iii*) Finally, we also used an asymmetrically doped GaAs quantum well where the GaAs thickness was reduced down to 150 Å. In all structures we found that Hall measurements yield the 2DHG concentration of about 5×10^{11} cm^{-2}. During PL measurements, the samples were mounted in a He-flow cryostat. PL was excited by 5145 Å of Ar^+ laser line. The light was dispersed and subsequently detected by a liquid-nitrogen-cooled charge-coupled device detector array. All three types of the samples display an intensive interface PL band.

Results

The spectral shift of the interface luminescence in the delta-doped samples greatly exceeds that from the samples without delta-doping: We observe up to 30 meV of energy shift when the two-dimensional holes recombine with delta-donors as opposed to only 3 meV for the recombination with free electrons in the conduction band. To account for trivial band bending, the asymmetrical quantum wells were also studied.

We show that the large value of the blue shift, much in excess of the 2DHG Fermi energy, is explained by the electrostatic repulsion between ionised delta-donors. Our analysis confirms that uniform distribution of the delta-dopants provides adequate description of both the energy shift and the full width at a half maximum of the interface PL band. Taking into consideration also the concentration fluctuations within the delta-layer accounts for less than 10% of the total effect.

Acknowledgments

This work was supported by the Nederlandse Organisatie voor Wetenschappelijk Onderzoek (NWO). Work at the Ioffe Institute was also supported by the program PSSNS of the Russian Ministry for Science.

9th Int. Symp. "Nanostructures: Physics and Technology"
St Petersburg, Russia, June 18–22, 2001

Properties of InP self-assembled quantum dots embedded in $In_{0.49}(Al_xGa_{1-x})_{0.51}P$ grown by metalorganic chemical vapor deposition

R. D. Dupuis†, J.-H. Ryou†, C. V. Reddy‡, V. Narayanamurti‡, D. T. Mathes§, R. Hull§, D. A. Kellogg¶, G. Walter¶ and N. Holonyak, Jr¶

† Microelectronics Research Center, The University of Texas at Austin, Austin, TX 78712, USA
‡ Gordon McKay Laboratory of Applied Science, Harvard University, Cambridge, MA 02138, USA
§ Department of Materials Science and Engineering, The University of Virginia, Charlottesville, VA 22906, USA
¶ Center for Compound Semiconductor Microelectronics, The University of Illinois at Urbana-Champaign, Urbana, IL 61801, USA

III-Phosphide self-assembled quantum dot (SAQD or simply QD) structures offer the potential to realize injection lasers operating in the visible spectral region with improved performance characteristics such as low threshold current density, high characteristic temperature, and high differential gain. Also, SAQD growth can overcome the limitation of lattice matching between the substrate and the epitaxial active region due to the intrinsic nature of the growth mode (i.e., strain-induced S-K growth).

InP quantum dots have been grown and characterized on direct-bandgap $In_{0.49}Ga_{0.51}P$ matrices by several research groups and on indirect-bandgap $In_{0.49}Al_{0.51}P$ matrices by these authors. As expected, the growth characteristics and optical properties are different in these cases. In this study, we report the characteristics of InP SAQDs embedded in $In_{0.49}(Al_xGa_{1-x})_{0.51}P$ grown by low-pressure metalorganic chemical vapor deposition (LP-MOCVD) to make a complete bridge between two material systems. The InP QD growth studies are done at a temperature of $\sim$650 °C by altering growth times and using various $In_{0.49}(Al_xGa_{1-x})_{0.51}P$ matrices ($x = 0.0$, 0.3, 0.6, and 1.0). The morphology changes (average sizes and densities) of the exposed SAQDs (grown without the upper cladding layer), depend on the growth time and the matrix material, and are characterized by atomic force microscopy (AFM). As the growth time increases from the "planar-layer-growth equivalent" of 7.5 MLs to 15 MLs for InP/$In_{0.49}(Al_{0.6}Ga_{0.4})_{0.51}P$ quantum dot structures, the dominant QD size increases, while the densities remain almost the same ($\sim 1-2 \times 10^8$ dots/mm^{-2}) and the dominant heights are $\sim 10-25$ nm, depending on growth time.

Photoluminescence (PL) spectra were taken at 4 K and 300 K to determine the light-emitting characteristics of the $In_{0.49}(Al_xGa_{1-x})_{0.51}P$ quantum-dot heterostructures (QDHs). 4 K PL spectra from the InP SAQDs embedded in $In_{0.49}(Al_xGa_{1-x})_{0.51}P$ cladding layers exhibit PL emission in the visible orange and red spectral regions. Emission peaks appear at higher energy for shorter growth times and higher bandgap matrices -2.10 eV, 1.90 eV, and 1.82 eV peak energies for 3.75, 7.5, and 15 ML InP/$In_{0.49}(Al_{0.6}Ga_{0.4})_{0.51}P$ QDH, while emission peaks occur at 2.06 eV, 1.92 eV, and 1.87 eV for 7.5, 11.25, and 15 ML InP/$In_{0.49}Al_{0.51}P$ QDH, respectively. Since the bandgap of the "active" InP SAQDs is modified by multi-dimensional quantum confinement, bulk material properties like the band offset do not apply in this case. We further study the InP/$In_{0.49}(Al_xGa_{1-x})_{0.51}P$ ($x = 0.6$) SAQDs using ballistic electron emission microscopy (BEEM) techniques to

determine the band structure of the dots. Also, transmission electron microscopy (TEM) is used to characterize the microscopic material quality and morphology of the individual QD and the interfaces between SAQD and cladding layers. Defect-free SAQDs are observed for the height of less than ∼30 nm. Furthermore, we have achieved 300 K lasing from InP SAQDs at the shortest wavelength yet reported for III-P QDs.

In summary, we will report on the optical, structural, and electronic properties of InP SAQDs embedded in $In_{0.49}(Al_xGa_{1-x})_{0.51}P$ layers grown on GaAs substrates by MOCVD.

9th Int. Symp. "Nanostructures: Physics and Technology"
St Petersburg, Russia, June 18–22, 2001

Random telegraph noise in InGaAs self-assembled quantum dots

M.-E. Pistol, N. Panev, V. Zwiller, L. Samuelson, W. Jiang§,
B. Xu§ and Z. Wang§
Solid State Physics, Lund University, Box 118, S-221 00 Lund Sweden
§ Laboratory of Semiconductor Materials Science, Institute of Semiconductors,
Chinese Academy of Sciences, P.O. Box 912, Beijing, 100083, China

Abstract. We have measured random telegraph noise in the photoluminescence of individual quantum dots of InGaAs in GaAs. We have observed not only two-level dots but also dots switching among three level in both systems. The experiments show that the switching InGaAs dots behave very similarly to switching InP dots in GaInP. The switching is attributed to defects and we show that the switching can be used as a monitor of the defect.

Introduction

Random telegraph noise, or blinking, has recently been observed in the photoluminescence from several quantum dot systems, such as colloidal dots of CdSe [1, 2], coherently grown dots of InP in GaInP [3], and strain-induced dots in GaAs [4]. There have also been reports of intermittencies, although not clearly displaying a telegraph signal in coherently grown II–VI dots [5]. The switching rate can be very slow, having typical timescales of seconds or even minutes. In some cases (colloidal [1, 2] and strain-induced dots [4]) the emission changes in energy and in some cases (coherently grown InP-dots [3]) only the intensity is modulated by the switching. For colloidal dots, a model based on photo-ionization has been used to explain the switching [2, 6], whereas for coherently grown dots, a model involving a mobile photo-activated defect has been proposed [3]. This defect was proposed to have two fairly longlived configurations. In one of the configurations the defect captures carriers from the dot causing a low emission intensity whereas in the other configuration the capture of carriers is less efficient and the dot is luminescing in its on-state. The defect model for coherently grown InP dots has received support by experiments in which the defect has been excited independently of the dot, causing a change in the rate of switching [7]. Interestingly, not only switching between two levels have been observed in InP dots, but also switching between three levels [2, 8]. However only one III–V system of coherently grown dots have been observed to exhibit blinking (InP dots in GaInP) and it is important to know if this effect is peculiar to this system. We will here show that GaInAs quantum dots in GaAs also exhibit switching and that the phenomenon could be quite general in III–V semiconductors. In fact the two systems behave in a very similar way, offering the hope for a unifying principle.

1. Experimental

The samples were grown by solid source molecular beam epitaxy. The substrates used were (211) A/B oriented GaAs. They were mounted side by side on the same Mo block with indium to ensure identical growth conditions. After removing the surface oxide at a temperature of 580 °C, a 30 nm GaAs buffer layer was deposited at 600 °C, followed by

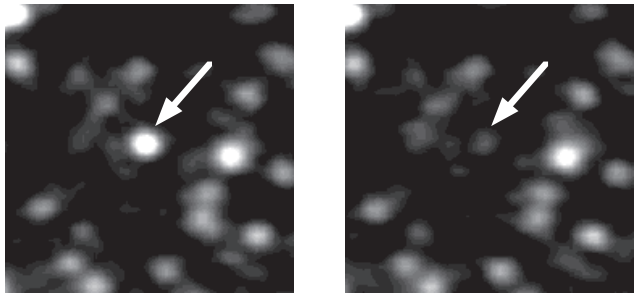

Fig. 1. Images of the sample taken at two different occasions. One dot, marked with an arrow has changed its emission intensity.

a 10 period GaAs/AlAs superlattice, and finally by a 200 nm thick layer of GaAs. The $In_{0.4}Ga_{0.6}As$ quantum dots were then grown at 500 °C via the Stranski–Krastanow growth mode. The InGaAs thickness was 9 monolayers. The quantum dots were covered by 10 nm of GaAs before increasing the temperature back to 600 °C, where a 50 nm GaAs layer was grown followed by a 30 nm of AlGaAs layer and a 40 nm layer of GaAs serving as a cap layer. The samples were not intentionally doped.

The quantum dots were usually excited with the 532 nm line from a frequency doubled YAG-laser with typical excitation power densities of 10–100 W/cm^2. The emission was collected through a microscope and detected with a video-camera, connected to a computer. In order to select a certain wavelength range we used a tunable interference filter having a bandpass of 0 nm. The measurement temperature was typically about 10 K unless temperature dependent measurements were performed. In order to change the excitation power density we used a continuously variable neutral density filter. Unless noted, every experiment has been repeated on several dots in order to find the general behaviour of the switching phenomenon. In fact two samples (with (211)A and (211)B orientation) have been measured showing essentially identical behaviour.

2. Results and discussion

In Figure 1 we show two images of a region of the sample taken at two different times. It can be seen that although the intensities of most dots is constant, there is one dot which has changed its emission intensity between the images, going from an on-state to an off-state. The images were taken through a band-pass filter centered around 1.37 eV, having a bandwidth of 15 meV. We find that for a given experiement only a few (about one in one hundred) dots are blinking. The excitation was in the GaAs barrier in this case. We have also dots directly using an energy of the excitation laser which was below the wetting layer energy, and we find that the dots are still switching. It is thus unlikely that the switching is due to variations in the capture probability.

In Figure 2 we show intensity traces of a two-level quantum dot for different excitation power densities. It can be seen that the frequency of switching increases very rapidly with increasing excitation power density. There is emission from the dot also in the off-state with an intensity of about one third of the intensity in the on-state. We have confirmed for a few dots that the emission energy do not change appreciably between the on-state and the off-state using either visual inspection of video-images after a monochromator, or by using interference filters. Unfortunately the dot density is too high to make detailed investigations.

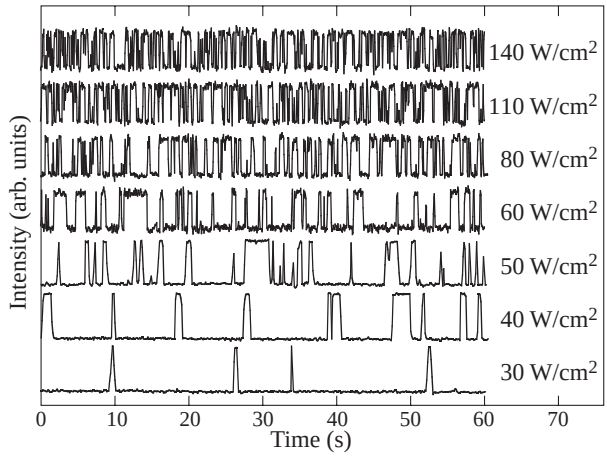

Fig. 2. Traces of the emission intensity for a two-level dot at different excitation power densities.

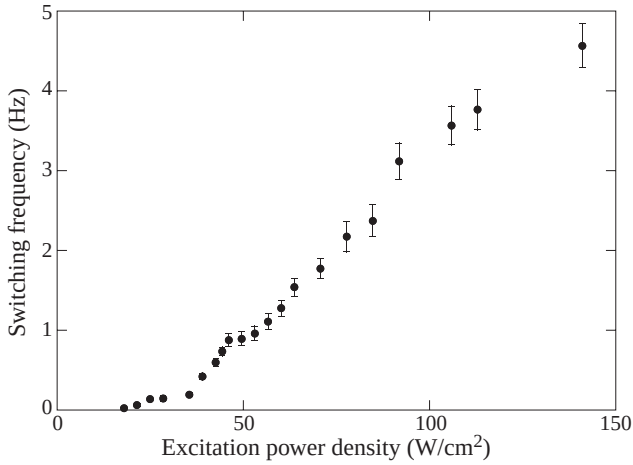

Fig. 3. A plot of the switching frequency as a function of the excitation power density.

It is interesting to notice that for sufficiently low excitation power density the dot is in an off-state which appears to be permanent. All investigated dots have been found to be in an off-state at low excitation power density. This argues against the alternative explanation that the switching frequency is too low to measure, in which case we would expect to see some dots in the on-state (although not appearing to be switching). Figure 3 shows a plot of the switching frequency as a function of excitation power density. In contrast to InP dots, which can irreversibly (and easily) be changed to a permanently on-state by increasing the excitation power density, we find that the GaInAs dots are much more robust. Many GaInAs dots have been exposed to fairly high excitation power densities (5 kW/cm^2) without changing to non-switching dots. At even higher excitation densities (50 W/cm^2) most dots do quench and then always to an on-state, exactly like InP dots. We have also observed dots switching among three levels.

If we compare the behaviour of GaInAs dots and InP dots we mostly find similarities.

Only very few dots are found to exhibit switching and there is emission also in the off-state. The rate of switching increases with excitation power density and with temperature. Dots switching between two levels and dots switching among three levels are present. In both systems about 1 percent of the switching dots are three-level dots and the rest are two-level dots.

There are, however, one significant difference between the two systems. In the InP system it is easy to quench the dots permanently to an on-state by strong illumination. In the GaInAs it is far harder to quench the emission to a permanently on state although this has been done in a few cases. We tentatively propose that this difference could due to the different stiffnesses of the matrix, with GaAs being stiffer than GaInP, leading to a reduced mobility of the defects. However more work is needed to reach a more definite conclusion.

Acknowledgement

This work was performed within the nanometer structure consortium in Lund and was supported by NFR, TFR and SSF.

References

[1] M. Nirmal, B. O. Dabbousi, M. G. Bawendi, J. J. Macklin, J. K. Trautman, T. D. Harris and L. E. Brus, *Nature* **383**, 802 (1996).
[2] S. A. Empedocles, D. J. Norris and M. G. Bawendi, *Phys. Rev. Lett.* **77**, 3873 (1996).
[3] M.-E. Pistol, P. Castrillo, D. Hessman, J. A. Prieto and L. Samuelson, *Phys. Rev. B* **59**, 10 725 (1999).
[4] D. Bertram, M. C. Hanna and A. J. Nozik, *Appl. Phys. Lett.* **74**, 2666 (1999).
[5] B. P. Zhang, Y. Q. Li, T. Yasuda, W. X. Wang, Y. Segawa, K. Edamatsu and T. Itoh, *Appl. Phys. Lett.* **73**, 1266 (1998).
[6] Al. L. Efros and M. Rosen, *Phys. Rev. Lett.* **78**, 1110 (1997).
[7] M. Sugisaki, H.-W. Ren, S. V. Nair, J.-S. Lee, S. Sugou, T. Okuno and Y. Masumoto, *J. Lumin.* **87-89**, 45 (2000).
[8] Mats-Erik Pistol, *Phys. Rev. B* (2001) (accepted).

9th Int. Symp. "Nanostructures: Physics and Technology"
St Petersburg, Russia, June 18–22, 2001

Photoluminescence decay time measurements from self-organized InAs/GaAs quantum dots grown on misoriented substrates

A. S. Shkolnik†, E. B. Dogonkin†, V. P. Evtikhiev†, E. Yu. Kotelnikov†, I. V. Kudryashov†, V. G. Talalaev‡, B. V. Novikov‡, J. W. Tomm& and G. Gobsch§

† Ioffe Physico-Technical Institute, St Petersburg, Russia
‡ Institute of Physics, St Petersburg State University, 198504 St Petersburg, Russia
& Max-Born-Institut für Nichtlineare Optik, 12489 Berlin, Germany
§ Institut für Physik, Technische Universität Ilmenau, D-98684 Ilmenau, Germany

Introduction

Lately a lot of papers were devoted to the investigations of laser heterostructures based on quantum dots (QDs). This interest is based on the fact that QDs provide a zero-dimensional system, with 3D carrier confinement resulting in atomic-like, discrete electronic eigenstates. The δ-like state density preconditions the low threshold current densities of laser diodes [1, 2] and higher values of T_0 [3] compared to existing semiconductor lasers. But the threshold current density of the "classical" QD laser diodes based on the single layer InAs heterostructures is far from predicted values [4, 5]. One of the possible obstacles to achieving the low threshold current density is low internal quantum efficiency in predicted by the theory excitation level range (10–100 A/cm^2). The laser diode, which was made during this work, has a threshold current 110 A/cm^2. The aim of this work is to study the mechanism limiting the quantum efficiency.

1. Experimental details

For our studies we have grown two samples the only one difference between them was that one was a laser diode sample and another one for the photoluminescence (PL) investigations. Samples were grown by the molecular beam epitaxy (MBE) in Stransky–Krastanow growth mode. To increase the density of QD arrays we used InAs QD single layer array grown on GaAs(001) substrate misoriented by 4° to the [010] direction [6]. Using this method in our samples we achieved a relatively high density of QDs ($\approx 10^{11}$ cm^{-2}). The interruption time between the end of QD growth and the start of the GaAs layer overgrowth was 10 s. The thickness of the InAs covering was 2.9 monolayer. The InAs QD growth temperature was 470°C and the III/V element flux ratio was 2. The InAs QD array was confined by GaAs barriers (20 nm) which were surrounded by AlAs/GaAs superlattices and by $Al_0.7Ga_0.3As$ cladding layers and practically repeats the corresponding part of the laser heterstructure reported earlier [5]. Steady-state photoluminescence (PL) spectra were obtained using Ar^+-ion laser (2.41 eV) and Ti-sapphire tunable laser. The laser beam was focused onto the sample installed in a He cryostat. The PL signal was dispersed by a 2m grating monochromator and detected by a cooled Ge photodiode.

Time-resolved PL was measured at sub-100 fs pulse excitation (repetition rate of 82 MHz) from a Ti-sapphire laser at 1.68 eV. A grating monochromator in combination with a streak camera having an infrared-enhanced photocathode allowed spectral discrimination and detection. The total system response was under 15 ps.

2. Results and discussion

Figure 1 shows the steady-state PL spectra for different excitation power densities equivalent to electron-hole pair density up to 6.7×10^{13} cm^{-3}. These densities are sufficient to cover the range of average carrier densities captured by QDs. All excitation power densities for convenience in comparison with laser diodes excitation power densities are given in current values (A/cm^2).

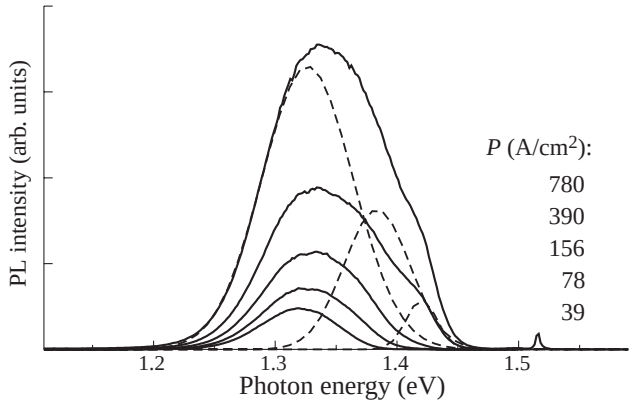

Fig. 1. Steady-state PL spectra at different excitation density of InAs QDs grown on GaAs substrate with 4 degree misorientation. $T = 5$ K.

The PL spectra recorded at the low excitation densities (Fig. 1) is described by a single gaussian with peak energy of 1.33 eV. This can be ascribed to the recombination of electron-hole pairs in ground state. As the excitation power density increases, two new gaussians appear in the high energy part of PL spectrum. Their peak energy is 1.38 and 1.42 eV (gaussians shown in Fig. 1 as dashed curves). First one (1.38 eV) is attributed to the recombination of electron-hole pairs in excited state [7] and the second one (1.42 eV) — to the recombination of electron-hole pairs in wetting layer [8].

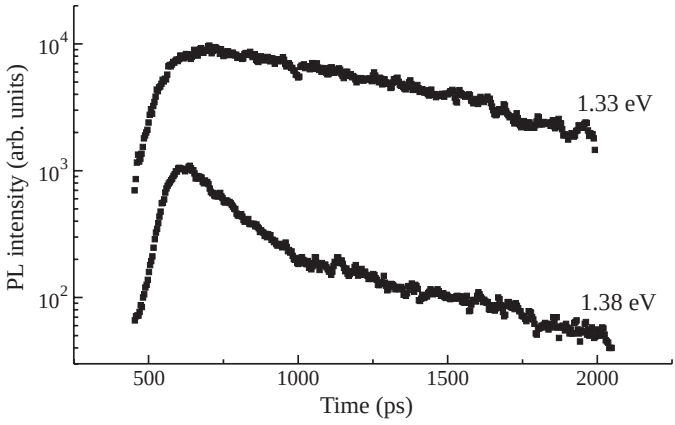

Fig. 2. Time-resolved PL from the ground state (upper curve) and first excited state (lower curve) of InAs QDs at excitation density 7.8 A/cm^2 and $T = 10$ K.

Figure 2 shows the PL time decay curves measured for the ground and first excited states of the electron-hole pair (1.33 and 1.38 eV respectively). The PL decay of the ground state is described by one exponent with characteristic time ($t \approx 3.1$ ns). The PL decay curve of the excited state is substantially different from the same of the ground state. Its shape has the biexponential feature: the initial fast component and the slower second component. Their estimated characteristic times are 210 ps and 700 ps respectively. Such kind of the behavior is explained by two processes: fast — free relaxation of the carriers into the unoccupied ground state and slow-radiative recombination from the excited state. An increase of the excitation density (Fig. 3) leads to the fast component disappearance. In accordance with [8] this behavior can be explained by the blocking of relaxation to the fully occupied ground state. As seen from Fig. 3 this effect took place at the excitation density range 20–80 A/cm^2. The full carrier relaxation scheme is very complex. It should comprise a lot of processes, such as sequential, nonsequential, multiphonon scattering and Auger recombination [9] etc. Taking this fact into account we use more simple model — we are examining only concentration of carriers on the energy levels without considering all above mentioned mechanisms. Later we will show that such approach is a sufficient approximation to explain the addressed problem.

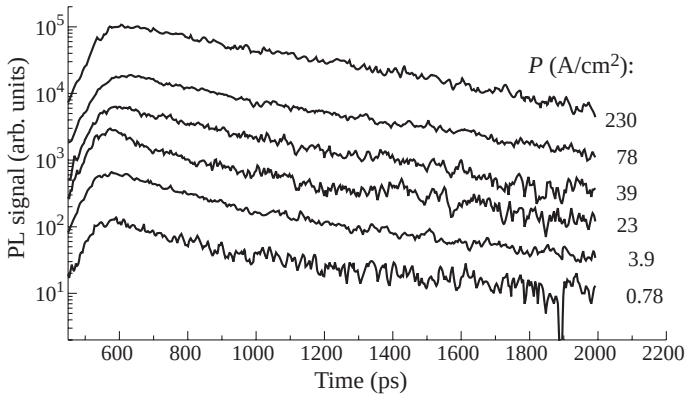

Fig. 3. Time-resolved PL from the excited state of InAs QDs at different excitation density and $T = 10$ K.

Figure 4 shows the ground state, excited state and wetting layer PL intensity divided by the excitation density ($\zeta_{G,S}$, $\zeta_{E,S}$ and $\zeta_{W,L}$ correspondingly) versus excitation density. As seen from the figure, $\zeta_{G,S}$ has three parts — the increase, saturation and decrease. $\zeta_{G,S}$ achieves the maximal value at excitation density $\approx$10 A/cm^2 and rapidly decreases after 40 A/cm^2. The value of $\zeta_{E,S}$ starts to increase after 20 A/cm^2 — directly before the decrease of $\zeta_{G,S}$. Both of these facts clearly demonstrate the filling of the ground state and the blocking of carrier free relaxation from the excited state. In this case the radiative recombination rate on the ground state is determined by the density of QDs. An increase in excitation density leads to the decrease of quantum yield of PL ground state. The estimated excitation density for the ground state filling is 20–30 A/cm^2. This value of excitation density is very close to the theoreticaly predicted threshold current of QD laser diodes diodes. In practically developing QD laser need for compensation of inevitably nascent losses can demand such values of current density at which value of quantum yield starts to decrease. It is obvious that in laser diodes everyone have to our results show that the

ground state filling effect should be taken into account in QD laser diodes design.

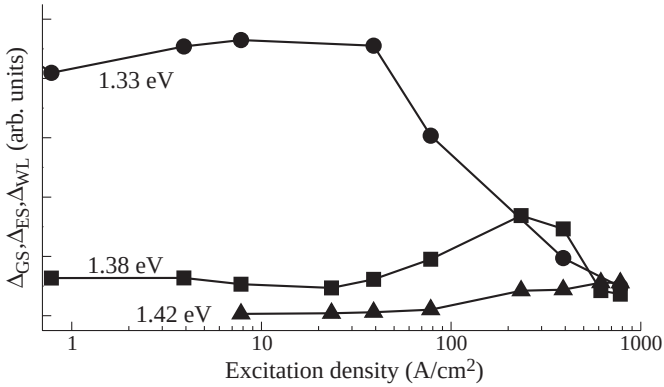

Fig. 4. PL intensity of the ground state, exited state and wetting layer divided by excitation power density versus the excitation density at $T = 10$ K.

Acknowledgements

This work was supported by Russian Foundation for Basic Research grants number 99-02-16766A and 01-02-17092A

References

[1] Y. Arakawa and H. Sakaki, *Appl. Phys. Lett.* **40**, 939 (1982).
[2] M. Asada, Y. Miyamoto and Y. Suematsu, *IEEE J. Quantum Electron.* **QE-22**, 1915 (1986).
[3] Y. Arakawa and A. Yariv, *IEEE J. Quantum Electron.* **QE-22**, 1887 (1986).
[4] V. P. Evtikhiev, I. V. Kudryashov, E. Yu. Kotel'nikov, V. E. Tokranov, A. N. Titkov, I. S. Tarasov and Zh. I. Alferov, *Semiconductures* **32**, 1323 (1998).
[5] F. Klopf, J. P. Reithmaier and A. Forchel, *Appl. Phys. Lett.* **77**, 1419 (2000).
[6] V. P. Evtikhiev, A. K. Kryganovskii, A. B. Komissarov et.al., *Inst. Phys. Conf. Ser.* **155**, 351 (1996).
[7] L. Landin, M.-E. Pistol, C. Pryor, M. Persson, L. Samuelson and M. Miller, *Phys. Rev. B* **60**, 16640 (1999).
[8] P. D. Buckle, P. Dawson, S. A. Hall, X. Chen, M. J. Steer, D. J. Mowbray, M. S. Skolnik and M. Hopkinson, *J. Appl. Phys.*, **86**, 2555 (1999).
[9] R. Heitz, M. Veit, N. N. Ledentsov, A. Hoffmann, D. Bimberg, V. M. Ustinov, P. S. Kop'ev and Zh. I. Alferov, *Phys. Rev.* **B 56**, 10435 (1997).

9th Int. Symp. "Nanostructures: Physics and Technology"
St Petersburg, Russia, June 18–22, 2001

Double injection currents in p-i-n diodes incorporating self-assembled quantum dots

A. E. Belyaev†, A. Patané†, L. Eaves†, P. C. Main†, M. Henini†
and S. V. Danylyuk§

† School of Physics and Astronomy, University of Nottingham,
Nottingham NG7 2RD, United Kingdom
§ Institute of Semiconductor Physics, NASU, Kiev 03028, Ukraine

Abstract. We study *p–i–n* diodes incorporating InAs/AlAs self-assembled quantum dots (QDs) to probe the electron and hole levels of the dots. Comparative analysis of capacitance-voltage ($C-V$), current-voltage ($I-V$) and electroluminescence (EL) measurements shows that *p–i–n* structures could be successfully used as a quantum dots spectrometer.

Introduction

Among the structures proposed as quantum dots (QDs) spectrometers, devices with Schottky contacts [1] and unipolar structures [2] (i.e. *n–i–n* or *p–i–p* diodes) are those more frequently used. In contrast, *p–i–n* diode incorporating QDs have not been deeply investigated. In contrast to the case of Schottky diodes, the potential distribution over the intrinsic region (i) of a *p–i–n* diode is almost linear. This implies a simple procedure for converting an applied voltage to the energy shift of the QD states. Also, in contrast to unipolar devices, *p–i–n* diodes offer the possibility to investigate in the same device both the electron and the hole dot states. In this work, we present a study of bipolar transport in a *p–i–n* diode incorporating InAs/AlAs QDs. This study is carried out by a comparative analysis of capacitance-voltage ($C-V$), current-voltage ($I-V$) and electroluminescence (EL) measurements.

Experimental results and discussion

In our *p–i–n* diode, the composition of the layers in order of growth on a n^+-substrate is as follows: an n^+-doped $GaAs$ buffer layer ($n^+ = 4\times10^{18}\,\mathrm{cm}^{-3}$); a 100 nm-thick n-doped GaAs layer ($n = 2\times10^{16}\,\mathrm{cm}^{-3}$); an undoped, intrinsic region (i), which consists respectively of a 100 nm-thick GaAs layer, a 10.2 nm-thick AlAs barrier and a 60 nm-thick GaAs layer. The growth was completed by a p^+-doped GaAs layer ($p^+ = 2\times10^{18}\,\mathrm{cm}^{-3}$). The QDs were grown in the middle of the AlAs barrier, by depositing 1.8 ML of InAs.

The $C-V$ and $I-V$ characteristics of the sample are shown in Fig. 1. The $C-V$ curve is characterized by two distinct regions, — low- and high-capacitance. The value of the capacitance in the first region is consistent with the value expected for a flat capacitor, with a distance between the capacitor plates equals to total base length of the structure, L. Sharp transition from the low- to the high-capacitance region occurs when the flat band regime is achieved and the electron and hole 2D layers form outside the AlAs barrier.

The formation of the 2D layers is also confirmed by the appearance of Shubnikov–de Haas-like magneto-capacitance oscillations vs. magnetic field, B, (at fixed voltage) for B applied parallel to the growth direction. The charge modulation arising in this case affects

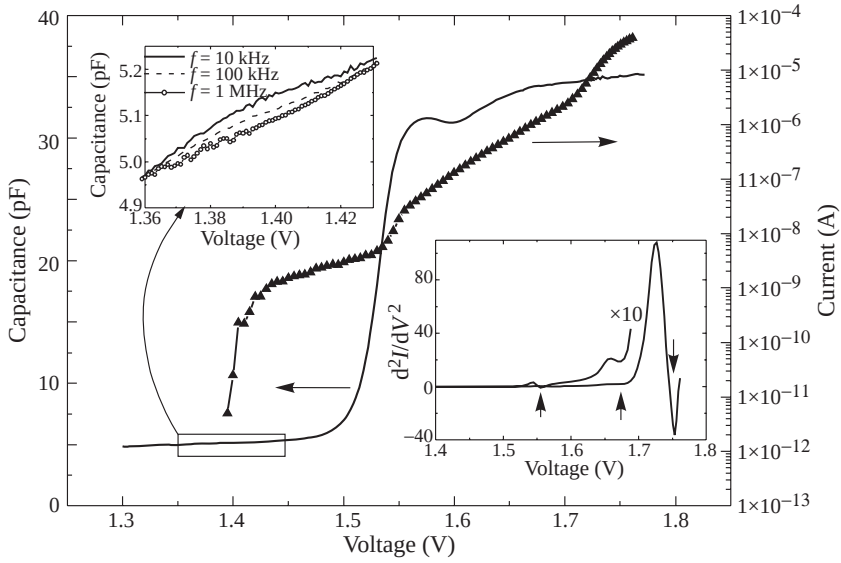

Fig. 1. Capacitance–voltage dependence measured at frequency of 10 kHz and zero magnetic field (left-bottom) and dc current–voltage characteristics (top-right) of the p-i-n diode. Upper inset: Capacitance curves near voltage 1.4 V for different frequencies of a modulating signal. Lower inset: the second derivative of current vs applied voltage.

the distribution of electric potential and screening length, and hence modulates the capacitance of the device. The fundamental field, $B_f = [\triangle(1/B)]^{-1}$, measures the electronic sheet density of 2DEG in the accumulation layer $n_s = 2eB_f/h$. Thus, extrapolation of fundamental field B_f dependence on applied voltage to zero-B_f value yields an information about voltage at which the flat band regime occurs. The obtained voltage value is close to GaAs band gap at 4.2 K – 1.512 eV.

In further, we will focus on the resonant features of the capacitance, which appear in both low- and high-capacitance regions. A wide bump is observed at 1.4 V for a frequency of 10 kHz (upper inset in Fig. 1). The current increasing is also observed in the $I-V$ curve within the same voltage region. We believe that this feature is caused by filling of impurity states located in i-region. This feature depends on the modulation frequency. With increasing frequency the amplitude of this feature becomes weaker and disappears for a frequency of about 1 MHz. This frequency dependence could be explained in the next way. Magnitude of the effect depends on number parameters — tunneling and emission rates for both electrons and holes as well as $e-h$ recombination rate. To reach equilibrium between impurity levels and emitter, a modulation signal frequency must be much lower than the thermionic emission rate. When frequency becomes considerably larger than emission rate the carriers cannot follow the measurement signal and do not modulate charge both at the edge of space charge region and at the point where the Fermi level crosses the impurity level.

The second feature appears at around 1.56 V in both the $C-V$ and $I-V$ curves. A sharp resonance at this point is clearly visible on the second current derivative presented in lower inset of Fig. 1. A wide bump followed by dip is observed on $C-V$ curve that correlates with sharp increasing of the current at the same bias voltage. We attribute these features to capture of holes onto the QDs. Assuming uniform voltage distribution, then

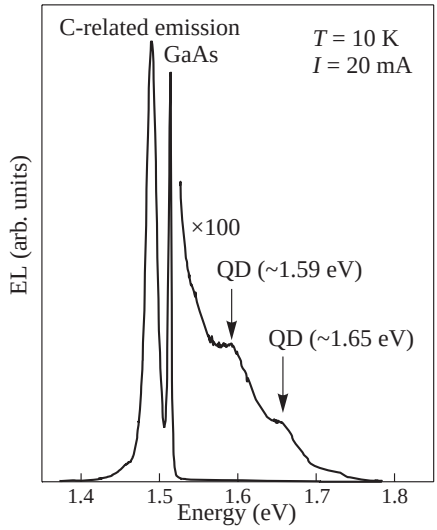

Fig. 2. EL spectrum of the QD structure measured at $T = 10$ K and $I = 20$ mA.

the leverage factor can be simply calculated for electrons (holes) as ratio $\frac{\lambda_{e(h)}+b/2}{\lambda_e+b+\lambda_h}$, where λ_e and λ_h are the quantum stand-off distances of the carriers in the accumulation layers formed to the left and right of the barrier b. The carrier sheet concentration, n_s, provides us with wavefunction stand-offs [3] ($\lambda_{e,h} \sim n_s^{-1/3}$). We obtain the leverage factor for high capacitance region equal to 0.33 and 0.67 for holes and electrons, respectively. Performing the procedure for QDs hole state, we estimate the position of ground QDs hole state at 15 meV beneath the top of $GaAs$ valence band.

Around the voltage of 1.67 V we observe a kink on $I-V$ curve that is reflected in $C-V$ dependence as increase of capacitance. The feature is more visible on the second derivative, d^2I/dV^2 and should be prescribed to the transport through the ground electron level of the QD. Using electron leverage factor for this voltage, we obtain the energy position of the ground electron state of the QD at 105 meV above GaAs band gap. Besides, there is noticeable increase of current in $I-V$ dependence at 1.71 V (Fig. 1). For that bias a probability of $\Gamma-X$ tunnelling strongly increases, that yields considerable contribution to the tunnel current.

To approve our model electroluminescence (EL) measurements were performed. Figure 2 shows the 10 K resulting EL spectrum of our device. The dot emission appears on the high energy side of the GaAs emission and it consists of two weak bands peaked at about 1.59 eV and 1.65 eV. The origin of these features should be the $e-h$ recombination via indirect exciton states that form at voltages far away the flat band condition. Really, at voltage bias exceeding 1.5 V the electron and hole 2D layers accumulate on outer sides of the barrier. The Coulomb attraction should promote the formation of spatially indirect excitons. However, the EL spectra were measured at 2 V when the $e-e$ interaction in 2DEG effectively suppresses the formation of indirect excitons. Moreover, we did not observe any manifestation of interplay between screening and exciton binding like that reported in [4], for similar device but without QD layer. If a feature in EL spectra at 1.59 eV is due the electron-hole recombination from the ground states of the dots, the energy gap between ground electron and hole QD state is 40 meV less, then value obtained from transport measurements. We assume, that in EL measurements, ground states of QD is affected by

Coulomb interaction between carriers and excitonic state forms. In this case corresponding transition energy could be considerably lower, especially with spatial 3D confinement. Thus, we obtain exciton binding energy of order of 40 meV. The next feature observed in the EL spectra 1.65 eV we attribute to the electron-hole recombination from the excited states of the QD bare exciton. The weak intensity of the dot signal is probably due to the presence of non-radiative recombination centers existing in the AlAs layers.

Conclusions

In conclusion, we have used the p-i-n diodes containing the layer of InAs quantum dots in an insulating region as spectrometer for probing electronic levels of QDs. Advantages of such devices for capacitance measurements are shown. It is shown that ground electron level of the InAs quantum dots in AlAs matrix reveals itself 105 meV above the GaAs conduction band edge, while the lowest hole level moves 15 meV downward the GaAs valence band edge.

Acknowledgements

This work is supported by EPSRC (UK) and Ukrainian Ministry of Education and Science. A.E.B. acknowledges the Royal Society for financial support.

References

[1] R. J. Luyken, A. Lorke, A. O. Govorov, J. P. Kotthaus, G. Medeiros-Ribeiro and P. M. Petroff, *Appl. Phys. Lett.* **74** 2486 (1999).
[2] P. M. Martin, A. E. Belyaev, L. Eaves, P. C. Main, F. W. Sheard, T. Ihn and M. Henini, *Solid State Electron.* **42** 1293 (1998).
[3] F. F. Fang and W. E. Howard, *Phys. Rev. Lett.* **16** 797 (1966).
[4] A. Parlangeli, P. C. Christisnen, A. K. Geim, J. C. Maan, L. Eaves, P. C. Main and M. Henini, *Phys. Rev. B.* **60** 13302 (1999).

9th Int. Symp. "Nanostructures: Physics and Technology"
St Petersburg, Russia, June 18–22, 2001

Modulation of the optical absorption in self-organized InAs/GaAs quantum dots

P. N. Brunkov†‡, A. Patane‡, A. Levin‡, L. Eaves‡, P. C. Main‡,
Yu. G. Musikhin†, B. V. Volovik†, A. E. Zhukov†, V. M. Ustinov†
and S. G. Konnikov†

† Ioffe Physico-Technical Institute, St Petersburg, Russia
‡ School of Physics and Astronomy, University of Nottingham,
NG7 2RD Nottingham, UK

Abstract. Capacitance and photocurrent spectroscopy are used to investigate a Schottky barrier structure containing a single layer of self-organized InAs/GaAs quantum dots. We show that applying a bias to the structure it is possible to change the electron occupation of the dot levels. This in turns is used for controlling the intensity of the light absorbed by the dots and proposed as a novel way for realizing optical modulators operating in the infrared (~ 1.1 μm) wavelenght range.

Introduction

Nowadays InAs/GaAs self-organized quantum dots (QDs) are of great interest because of their zero-dimensional properties, which open up wide possibilities to develop new optoelectronic devices such as low-threshold lasers, infrared detectors and high-density optical memory devices [1]. Recently it was shown that the photocurrent (PC) spectroscopy can be used to measure the absorption of QDs [2]. In this paper we show that using capacitance [3, 4] and PC spectroscopy it is possible to control the electron occupation of the dot levels and correspondingly the dot absorption.

1. Experimental details

The QDs structures were grown by molecular beam epitaxy (MBE) on n^+-GaAs (001) substrates. The formation of InAs QDs was monitored by reflection high-energy electron diffraction (RHEED) patterns, and the average thickness of InAs deposited was 4 ML at 485 °C. The InAs QDs were sandwiched between a 0.4 μm-thick GaAs cap and a 1 μm-thick GaAs buffer layer. The cap and buffer layers were uniformly doped with Si at a level of $2.0 \times 10^{16}\text{cm}^{-3}$ except for 10 nm thick undoped spacers on each side of the QD layer. The excitation source for PC measurements was a tungsten-halogen lamp dispersed by 0.25 m monochromator and the PC signal was recorded with standard lock-in technique. The C(V) characteristics of the devices were measured using an HP4275A LCR meter.

2. Results and discussion

Figure 2(a) shows C(V) characteristic of the QD structure at $T = 80$ K. The C(V) characteristic at 80 K has two plateaux with a small step between them at -2.0 V, indicating that there are two filled electron states in the QD plane [4]. At a given temperature, the charge located in the QDs is determined by the sheet concentration N_{QD} of QDs and the relative positions of the electron level in the QDs (E_{ei}) and chemical potential (μ) in the GaAs

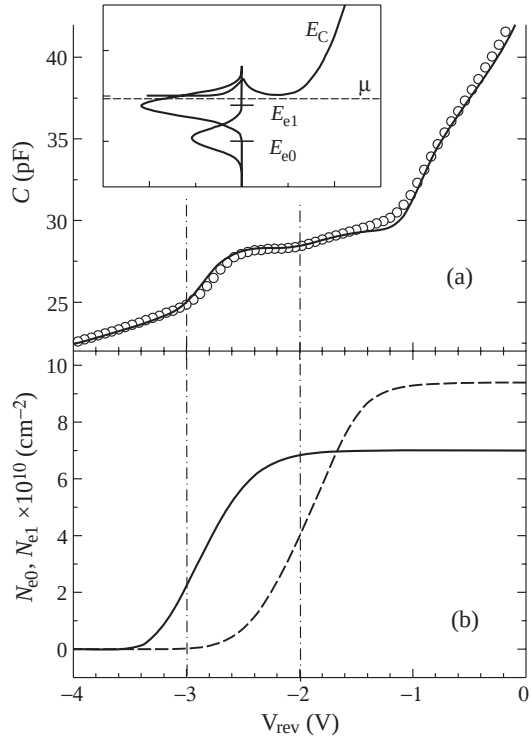

Fig. 1. (a) C–V characteristics measured at 1 kHz and 80 K and simulated with a quasi-static model. (b) Simulated occupations of the electron ground (solid line) and first excited (dashed line) states in QDs as a function of the reverse bias at $T = 80$ K. The insert shows the conduction band diagram of the QD structure. The horizontal lines represent the electron energy levels E_{ei} in the QDs, broadened by the size distribution.

matrix (see insert in the Fig. 1(a)). We use a Gaussian distribution to describe the DOS associated with the distribution of QD sizes. The density of charge $Q_{\rm QD}$ accumulated in the QD plane may be written as [3, 4]:

$$Q_{\rm QD} = q \sum_i \int \frac{g_i N_{\rm QD}}{\Delta E \sqrt{\frac{\pi}{2}}} \exp\left(\frac{-2(E - E_{ei})^2}{(\Delta E)^2}\right) \frac{1}{1 + \exp\left(\frac{E-\mu}{k_B T}\right)} dE \qquad (1)$$

where k_B is the Boltzmann constant, g_i is a spin degeneracy factor, q is electron charge, and T is temperature. Summation is provided over all i subbands.

Figure 1(a) shows the fit to the C(V) characteristic at 80 K by a quasi-static charging model [3, 4]. The numerical analysis indicates that at $V_{rev} = 0$ V there are two filled electron states in the QDs at $E_{e0} = 140$ meV and $E_{e1} = 60$ meV below the bottom of the GaAs conduction band (see insert in the Fig. 1(a)). We use a value of $\Delta E = 50$ meV as deduced from the broadening of the photoluminescence (PL) QD band. Also the value of $N_{\rm QD}$ was taken from plan-view transmission electron microscopy studies, which reveals a uniform distribution of dot sizes with mean QD diameter of 15 nm and a density $N_{\rm QD} = (3.5 \pm 0.5) \times 10^{10}{\rm cm}^{-2}$.

Figure 2(a) shows PC spectra of our sample measured at $T = 200$ K as a function of the reverse bias (positive biased substrate). At $V_{rev} = 0$ V one can see only step at 1.45 eV

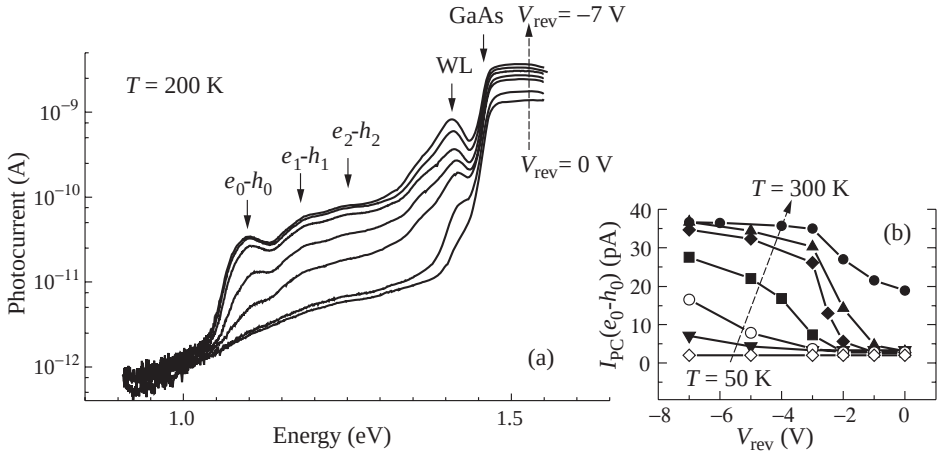

Fig. 2. (a) Photocurrent spectra of the QD structure as a function of reverse bias V_{rev} at $T = 200$ K: from the bottom to the top traces are 0, −1, −2, −2.5, −3, −5, −7 V, respectively. (b) Dependence on the temperature and the reverse bias V_{rev} intensity of the PC ground state peak $I_{PC}(e_0 - h_0)$: from the bottom to the top traces are 50, 100, 125, 150, 200, 250, 300 K, respectively.

related with the band-edge absorption of GaAs. Increasing the the reverse bias up to −7 V results in the appearance of the resonance peak at 1.41 eV related with optical absorption in InAs wetting layer and three additional features at 1.102 eV, 1.182 eV and 1.240 eV, which originate from the photon absorption in the ground and excited states of InAs QDs, respectively [2]. The position of the last three features agrees quite well with the position of the corresponding PL peaks [4].

At $T = 200$ K the PC signal from QDs monotonically grows up with increasing of the reverse bias and saturates at $|V_{rev}| > -3$ V (Fig. 2(a)). The same behaviour is observed in the temperature range from 150 K to 300 K (Fig. 2(b)). With decreasing the temperature below 150 K voltage modulation of the PC signal becomes weaker and below 100 K there is no PC signal from QDs (Fig. 2(b)).

The PC signal from QDs is proportional to the absorption coefficient of QDs. Also it depends on the recombination rate $(1/\tau_{rec})$ of carriers from the dot levels and on the escape rates $(1/\tau_{esc})$ of carriers out of the dots [2]. To a first approximation, the PC signal due to QDs can be expressed in the following form:

$$I_{PC} = G/(1 - \tau_{esc}/\tau_{rec}) \tag{2}$$

where G is the carrier generation rate in QDs.

Time-resolved PL studies revealed that the recombination time constant is about 1 ns for this type of QDs [1]. Also time-resolved capacitance spectroscopy revealed that the carrier emission from the InAs QDs to the GaAs barrier is faster then 1 ns at temperatures above 150 K [5]. Therefore suppression of the PC signal from QDs below 150 K (Fig. 2(b)) is probably due to the fast recombination of photo-generated carriers in the QDs relative to the escape time of carriers out of the dots.

Analysis of the C(V) characteristic of the QD structure showed that at $V_{rev} = 0$ V two lowest electron states are filled in the QDs (Fig. 1(b)). The increasing of the value of the reverse bias $|V_{rev}|$ from 0 V to −3 V results in successive depopulation of the levels E_{e1} and E_{e0}, respectively (Fig. 2(b)). Note that the PC signal from QDs grows up in this

voltage range (Fig. 2(b)). It is found that at $|V_{rev}| > -3$ V there are no electrons on ground state level in QDs (Fig. 1(b)). And this value of the reverse bias agrees very well with the start of saturation of the PC signal from QDs (Fig. 2(b)). Thus through the change of electron occupation in the QDs one can control photon absorption in QDs. At 300 K voltage modulation of the PC signal from QDs are weaker (Fig. 2(b)), because the concentration of electrons on electron ground state in the QDs decreases with increasing temperature [3].

3. Conclusions

In summary, we showed that through the change of electron occupation in the QDs one can control the photon absorption in QDs, thus opening a possibility for optical modulators based on QDs and operating in the infrared wavelength range.

Acknowledgements

The work is supported by the International Russian-Ukrainian project on nanoelectronics. Two authors, P.N.B. and L.E., gratefully acknowledge support from the Royal Society and EPSRC, respectively.

References

[1] D. Bimberg, M. Grundmann and N. N. Ledentsov, *Quantum Dot Heterostructures*, John Wiley and Sons Ltd., Chichester, 1998.

[2] P. W. Fry, I. E. Itskevich, D. J. Mowbray, M. S. Skolnick, J. J. Finley, J. A. Barker, E. P. O'Reilly, L. R. Wilson, I. A. Larkin, P. A. Maksym, M. Hopkinson, M. Al-Khafaji, J. P. R. David, A. G. Cullis, G. Hill and J. C. Clark *Phys. Rev. Lett.* **84**, 733 (2000).

[3] P. N. Brounkov, A. Polimeni, S. T. Stoddart, M. Henini, L. Eaves, P. C. Main, A. R. Kovsh, Y. G. Musikhin and S. G. Konnikov, *Appl. Phys. Lett.* **73**, 1092 (1998).

[4] P. N. Brunkov, A. R. Kovsh, V. M. Ustinov, Y. G. Musikhin, N. N. Ledentsov, S. G. Konnikov, A. Polimeni, A. Patane, P. C. Main, L. Eaves and C. M. A. Kapteyn, *J. Electr. Mat.* **28**, 486 (1999).

[5] C. M. A. Kapteyn, M. Lion, R. Heitz, D. Bimberg, P. N. Brunkov, B. V. Volovik, S. G. Konnikov, A. R. Kovsh and V. M. Ustinov, *Appl. Phys. Lett.* **76**, 1573 (2000).

9th Int. Symp. "Nanostructures: Physics and Technology"
St Petersburg, Russia, June 18–22, 2001

Homogeneous broadening of the zero optical phonon spectral line in semiconductor quantum dots

S. V. Goupalov†‡, R. A. Suris† and P. Lavallard§
† Ioffe Physico-Technical Institute, St Petersburg, Russia
‡ Department of Physics, Washington State University,
Pullman, Washington 99164-2814 USA
§ Groupe de Physique des Solides, Universités Paris 6 et 7, 75251 Paris, France

Introduction

In recent years semiconductor quantum dots (QDs) have been attracting much attention due to their promising advantages in optoelectronic device applications. Investigation of different mechanisms leading to homogeneous broadening of optical spectral lines in QDs, stimulated by experimental studies [1], is therefore of utmost importance. Various theoretical treatments applicable to this problem were developed more than 30 years ago for multi-phonon-assisted optical transitions of electrons localized on lattice defects (for a review see [2] and Refs. therein). In the adiabatic approximation the crystal nuclear system is treated as the slowest one. The relatively fast motion of the electron localized on a lattice defect or exciton localized in a QD is perturbed by the electron-phonon interaction which is supposed to be linear in the nuclear displacement. The perturbed energy of the localized electron (exciton) serves as an adiabatic potential for the nuclear system. The perturbation is usually considered up to the second order. As a result, parabolic adiabatic potentials for the nuclear motion corresponding to the crystal ground state and to a state, where the localized electron or exciton is excited, differ. The first-order perturbation term leads to a difference in the parabolic potentials minima positions while the second-order term leads to a difference in their frequencies. As a result, the phonon wave functions of the ground and the excited states are no longer orthogonal and multi-phonon-assisted transitions become possible.

In case of optical phonons possessing relatively high frequency several spectral lines corresponding to phonon-assisted transitions are usually experimentally resolved. In what follows we will be interested in the zero optical phonon line (ZOPL) broadening. As it was pointed out by Krivoglaz [3], the first-order perturbation term can not lead to the zero-phonon line broadening unless the phonon damping is taken into account. At the same time, the second-order term does lead to the finite zero-phonon line width [3].

On the other hand, due to a strong interaction of electrons with acoustic phonons in a QD, the latter should contribute substantially to the ZOPL width [4, 5]. Since the frequencies of acoustic phonons are much less than that of optical ones, the ZOPL broadening may be caused by multiple acoustic phonon assisted transitions governed by the first order perturbation term.

The aim of this work is to calculate the contributions to the ZOPL homogeneous broadening due to both optical and acoustic phonons making the most reasonable assumptions and to compare them for a one particular QD system. Since the available experimental data [1] were obtained for CdSe spherical nanocrystals of the radius R less than the exciton Bohr radius in a bulk material, we have chosen this system for our study.

1. Homogeneous broadening due to optical phonons

Let us consider the homogeneous broadening of the ZOPL associated with an optical transition to the ground ($1S_e1S_{h,3/2}$) state of the exciton confined in a spherical CdSe nanocrystal. In this section we will discuss the broadening governed by the second-order perturbation term [2] $\sum_{æ} B_{æ,s}\hat{a}^{+}_{æ}\,\hat{a}_{æ}$, where $\hat{a}^{+}_{æ}$ and $\hat{a}_{æ}$ are the phonon creation and annihilation operators,

$$B_{æ,s} = \sum_{s'\neq s} \frac{\left|V^{æ,e}_{ss'} + V^{æ,h}_{ss'}\right|^2}{E^0_s - E^0_{s'}}\,, \tag{1}$$

$s = 1S_e1S_{h,3/2}$, the subscript s' enumerates the upper exciton states, the index æ enumerates different phonon modes, $V^{æ,e}_{ss'}\left(V^{æ,h}_{ss'}\right)$ is the matrix element of electron(hole)-phonon interaction, E^0_s is the exciton energy in the state s. Here we will consider the Fröhlich polar electron-phonon interaction and treat optical phonons as in Ref. [6]. In this treatment the quantized polar phonon modes, characterized by the phonon total angular momentum $\mathcal{F}$, have, generally speaking, a mixed LO-TO character. However, in what follows we will consider only modes with $\mathcal{F} = 0$ which are purely longitudinal. The boundary condition of the relative sublattice displacement vanishing at the nanocrystal surface is also supposed to be applicable. Thus, the electrostatic potential induced by the polar optical phonon modes with the total angular momentum $\mathcal{F} = 0$ is given by $\Phi(x, R) = \sum_{æ}\phi_{æ}(x, R)\,\left(\hat{a}^{+}_{æ} + \hat{a}_{æ}\right)$, where the sum is hold over the phonon modes with $\mathcal{F} = 0$,

$$\phi_{æ}(x, R) = \sqrt{\frac{\hbar}{\omega_{æ}}(\varepsilon_0 - \varepsilon_\infty)}\,\frac{\omega_{TO}}{\varepsilon_\infty \nu_{æ}\sqrt{R}}\,\frac{j_0(\nu_{æ}) - j_0(\nu_{æ}x)}{|j_0(\nu_{æ})|}\,, \tag{2}$$

$x = r/R$, $j_l(x)$ is the spherical Bessel function of the l-th order, ε_0 and ε_∞ are the CdSe static and high-frequency dielectric constants, respectively, $\nu_{æ} = \sqrt{\omega^2_{LO} - \omega^2_{æ}}R/\beta_L$, $\omega_{LO}(\omega_{TO})$ is the bulk LO(TO)-phonon frequency, β_L is the LO-phonon dispersion parameter, the phonon mode frequencies are defined by equation $j_1(\nu_{æ}) = 0$. The lowest exciton state which mainly contributes to the sum in the right-hand part of Eq. (1) is the state $\tilde{s} = 1S_e2S_{h,3/2}$. The matrix element of the exciton-phonon interaction between this state and the exciton ground state is given by

$$V^{æ,e}_{s\tilde{s}} + V^{æ,h}_{s\tilde{s}} = e\int_0^1 dx\left\{-2\sin^2\pi x + x^2\left[f^s_0(x)f^{\tilde{s}}_0(x) + f^s_2(x)f^{\tilde{s}}_2(x)\right]\right\}\phi_{æ}(x, R)\,, \tag{3}$$

where e is the electron charge, $f^s_0(x)$, $f^s_2(x)$ are dimensionless functions defined in Ref. [7] and describing the radial dependence of the hole envelope wave function. If we neglect phonon damping and omit in the adiabatic phonon Hamiltonians contributions arising from the first-order perturbation term, then we will find that the cross-section of light absorption by the QD is proportional to [3]

$$\sigma_a(\Omega) \propto \exp\left[-\frac{(\Omega - \Omega_{fi})^2}{2\delta^2_{opt}}\right], \quad \delta^2_{opt} = \sum_{æ}\bar{n}_{æ}(\bar{n}_{æ} + 1)B^2_{æ}\,, \tag{4}$$

where Ω is the light frequency, $\hbar\Omega_{fi}$ is the energy difference of the electron system before and after the optical transition, $\bar{n}_{æ} = (\exp\beta_{æ} - 1)^{-1}$, $\beta_{æ} = \hbar\omega_{æ}/T$, T is the temperature in energy units. Thus, for high temperatures $\delta_{opt} \propto T$ while at $T \to 0$ it vanishes very rapidly as $\exp(-\beta_{æ}/2)$. Since the energy of confined exciton $E_s^0 \propto R^{-2}$, from Eqs. (1)–(4) it follows that $\delta_{opt} \propto R$.

2. Homogeneous broadening due to acoustic phonons

In this section we will discuss the broadening of the ZOPL due to the first order perturbation term $\sum_{æ} A_{æ}\left(\hat{a}_{æ}^{+} + \hat{a}_{æ}\right)$. In the strong coupling approximation one obtains [4, 5]

$$\sigma_a(\Omega) \propto \exp\left[-\frac{(\Omega - \Omega_{fi} + \Delta_{ac})^2}{2\delta_{ac}^2}\right], \quad \delta_{ac}^2 = \sum_{æ} \frac{A_{æ}^2}{\hbar^2} \coth\frac{\beta_{æ}}{2}, \tag{5}$$

where $\Delta_{ac} = \sum_{æ} A_{æ}^2/\hbar^2\omega_{æ}$. For high temperatures $\delta_{\mathrm{ac}} \propto \sqrt{T}$ while for $T \to 0$ it tends to a constant value.

Here we will treat acoustic phonons as in Ref. [7], where it was shown that the spectrum of the acoustic vibration modes of a semiconductor QD embedded in a glass matrix is continuous and contains maxima corresponding to the acoustic phonon resonant reflection from the QD surface. We will again restrict our consideration to the case of $\mathcal{F} = 0$ vibrational modes, which in fact play the major role in the ZOPL broadening, and treat the exciton-phonon interaction in the framework of the deformation potential approximation. Thus we obtain

$$\delta_{ac}^2 = \frac{\hbar}{4\pi^2\rho_{out}R^4 c_l^{(in)}} \int_0^{\infty} dy\, y^3 \coth\left(\frac{\hbar c_l^{(in)} y}{2RT}\right) \left(\frac{c_l^{(out)}}{c_l^{(in)}}\right)^4 \frac{y^4}{Y^2(y)} F^2(y), \tag{6}$$

where $c_l^{(\mathrm{in})}\left(c_l^{(\mathrm{out})}\right)$ is the longitudinal sound velocity inside (outside) the QD, $\rho_{\mathrm{in}}(\rho_{\mathrm{out}})$ is the mass density inside (outside) the QD, $Y(y)$ is the function given in an explicit form in Ref. [7] and dependent on $c_l^{(\mathrm{in})}$, $c_l^{(\mathrm{out})}$, ρ_{in}, ρ_{out} and the transversal sound velocities inside and outside the QD,

$$F(y) \approx \int_0^1 dx \left\{a_v x^2 \left[f_0^{s\,2}(x) + f_2^{s\,2}(x)\right] + 2a_c \sin^2\pi x\right\} j_0(xy),$$

a_c, a_v are the deformation potential constants defined as in Ref. [7].

3. Results and discussion

The calculated QD size dependencies of δ_{ac} and δ_{opt} for $T = 300K$ are shown in Fig. 1(a). For small QD radii the contribution to the ZOPL homogeneous broadening due to acoustic phonons predominates. As QD radius increases, the role of optical phonons in the ZOPL broadening increases and their contribution to the ZOPL width can exceed that of acoustic phonons. For higher temperatures the role of optical phonons becomes more important while for lower temperatures the ZOPL broadening is mainly governed by acoustic phonons. The temperature dependence of their contribution is shown in Fig. 1(b) for a 11 Å-size

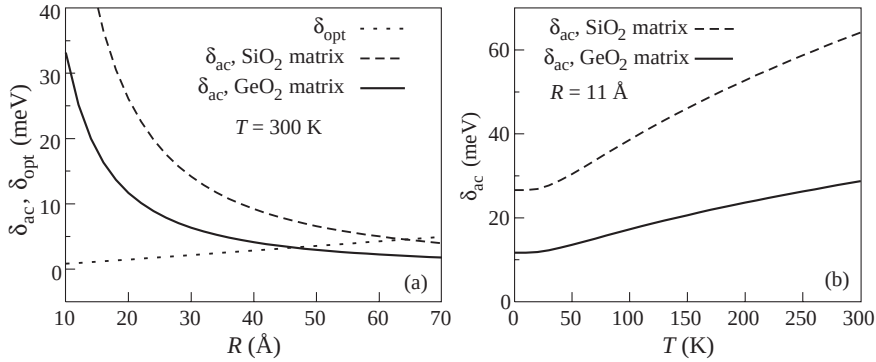

Fig. 1. (a): Dependencies of δ_{opt} (dotted line) and δ_{ac} (solid and dashed lines) on CdSe QD radius for $T = 300K$. Solid and dashed lines correspond to the GeO_2 and SiO_2 host matrices, respectively. (b): Temperature dependencies of δ_{ac} for a 11 Å-size CdSe QD embedded in a GeO_2 (solid line) and SiO_2 (dashed line) matrix.

QD embedded in different glass matrices and is in a good agreement with the ZOPL homogeneous linewidth temperature dependence obtained from experimental studies [1]. One can see from Fig. 1(a,b) that the ZOPL homogeneous broadening due to acoustic phonons is strongly dependent on the elastic properties of the host matrices.

Acknowledgements

We are grateful to D.S. Citrin for useful discussions. Support of INTAS (code 99-O-0858) is gratefully acknowledged. The work of SVG was supported in part by the Office of Naval Research and the National Science Foundation through ECS-0072986, DMR9705403, and DMR-0073364.

References

[1] R. W. Schoenlein *et al.*, *Phys. Rev. Lett.* **70**, 1014 (1993).
[2] Yu. E. Perlin, *Usp. Fiz. Nauk* **80**, 553 (1963).
[3] M. A. Krivoglaz, *Fiz. Tverd. Tela* **6**, 1707 (1964).
[4] T. Takagahara, J. Lumin. **70**, 129 (1996).
[5] X.-Q. Li and Y. Arakawa, *Phys. Rev. B* **60**, 1915 (1999).
[6] E. Roca, C. Trallero-Giner and M. Cardona, *Phys. Rev. B* **49**, 13704 (1994).
[7] S.V. Goupalov and I.A. Merkulov, Fiz. Tverd. Tela **41**, 1473 (1999).

9th Int. Symp. "Nanostructures: Physics and Technology"
St Petersburg, Russia, June 18–22, 2001

Non-equilibrium carriers in type-II quantum dots

A. Shik†, H. Ruda† and E. H. Sargent‡
† Energenius Centre for Advanced Nanotechnology,
University of Toronto, Toronto M5S 3E4, Canada
‡ Department of Electrical & Computer Engineering,
University of Toronto, Toronto M5S 3G4, Canada

Abstract. The spatial distribution and recombination of nonequilibium electrons and holes in a system of type-II quantum dots is considered theoretically. In this system, contrary to the well-known type-I quantum dots system, one type of carrier is confined to the dot whereas the other type is localized in a Coulomb potential well outside the dot. The alters the recombination processes dramatically and results in new intensity and temperature dependencies in the photoconductivity. Possible device applications of type-II quantum dots, in particular for photovoltaic structures, are discussed.

Properties of non-equilibrium carriers in quantum dots (QD) have been actively studied in recent years, especially in connection with QD lasers. These investigations concerned QDs which employed type-I heterojunctions, wherein the narrow-gap dot material presents a potential well for both electrons and holes. There exists, however, another group of semiconductor heterojunctions, so-called type-II junctions, where the band diagram has a staggered character so that the material with lower potential energy for electrons has higher energy for holes and vice versa (Fig. 1(a)). This type of band diagram is realized in Ge_xSi_{1-x} alloys, in a series of III-V-compounds, particularly, $In_{1-x}Ga_xAs_{1-y}Sb_y$, and in AlAs/GaAs nanostructures with very thin GaAs layers. The problem of type-II QDs has become especially urgent in the recent years in connection with the creation and investigation of polymer-nanocrystal composites for light-emitting and photovoltaic devices [1, 2] since conducting polymers tend to have low electron affinities and form type-II junctions with the majority of semiconductors and dielectrics.

In the present work we consider the optical generation, spatial separation and recombination of non-equilibrium carriers in a system of QDs forming type-II heterojunctions with the matrix semiconductor. We discuss the prospects of using these structures in photovoltaic and light-emitting devices.

In the system considered, Coulomb effects resulting from charge separation play a crucial role, in contradistinction with the case of type-I QDs. One type of carrier (usually electrons) is captured into the quantum well of the QD, whereas the other type is concentrated mostly outside the QD in the potential well formed by Coulomb forces (Fig. 1(b)). First, we calculate self-consistently the potential profile of the system and find its main parameters: the band bending V_0 and the QD charge Q for different electron and hole Fermi quasi-levels F_n and F_p characterizing non-equilibrium carriers. We assumed $Q/e \gg 1$ which allows us to use the quasi-classical approximation in our calculations. At a very high excitation intensity both electron and hole gases become degenerate, and the problem requires solution of the corresponding Thomas–Fermi equation.

We proceed to calculate the recombination rate in a type-II QD given Q and V_0. Since electrons and holes are spatially separated, recombination requires either tunneling or ther-

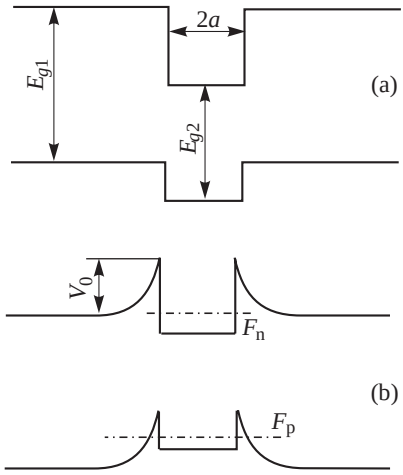

Fig. 1. Band diagram of an undoped type-II quantum dot in equilibrium (a) and under illumination (b).

mal activation. For III–V semiconductor heterosystems the main recombination mechanism at moderate temperatures is connected with the tails of electron wave functions in the matrix material. For spherical QDs, the corresponding radiative transitions occur between the states with equal angular momenta but have no selection rules in terms of the principal quantum number. This results in a broad spectrum of emitted radiation. The recombination rate depends weakly on the quasi-level positions and on the band bending V_0. In systems with a dramatic mismatch of wave functions at the QD interface (in particular, for polymer-based mixtures) tunneling effects are weak and recombination is related mostly with thermal activation. In this case the recombination rate is an exponential function of F_n, F_p and V_0. If the QD has a smaller band gap than the matrix (as in Fig. 1), F_p may cross the valence band inside the QD under high excitation. Holes will then enter the QD and recombination becomes activationless.

The calculations of recombination rate allow us to express the quasi-level energies F_n and F_p in terms of the light intensity I and, ultimately, calculate photoelectric phenomena in composite media containing type-II QDs. It is shown that the separation of non-equilibrium carriers in these systems increases the hole component of photoconductivity, decreases the electron component, and results in a substantial increase of the total photoconductivity $\Delta\sigma$ [3]. The effect is observed experimentally in a wide range of polymer-based composites with disparate inclusions [4–6]. When recombination has an activation (rather than tunnel) character, the modulation of V_0 by the light intensity results in a strongly sublinear character of the $\Delta\sigma(I)$ dependence.

In practical designing of QD-based light-emitting and photovoltaic devices the problem of optimal spatial distribution of QDs in the active region, $N(x)$, arises. In ordinary semiconductors with high carrier mobilities F_n and F_p are constant throughout the region and the profile of this distribution does not play a role. However, in polymer-nanocrystal mixtures, due to very low mobilities in conducting polymers, the processes of carrier separation and recombination are determined by their transport in the matrix and depend on the $N(x)$ profile. The complete theoretical description includes the equations connecting Q, V_0 and the recombination-generation rate with local carrier concentration, the continuity equations for electrons and holes in the matrix, and the Poisson equation describing the

electric field distribution in the active region [7]. This system was solved for a light-emitting diode and its current-voltage characteristics and quantum yield η were calculated at different $N(x)$. It was shown that to maximize η, QDs must be concentrated in a thin layer shifted towards the contact with lower injection effectiveness. The theoretical results are in agreement with the experimental data, both from literature [1, 2, 4] and obtained in our laboratory for the PPV-CdS composites.

Type-II QDs are particularly promising for use in photovoltaic devices. In type-I systems photogenerated electrons and holes are concentrated in the dot regions and their effective separation requires additional excitation into the matrix material, which may suppress the effectiveness of photovoltaic devices. In type-II systems, the interface barriers do not prevent non-equilibrium carriers from effective separation.

References

[1] M. C. Schlamp, X. Peng and A. P. Alivisatos, *J. Appl. Phys.* **82**, 5837 (1997).
[2] H. Mattoussi, L. H. Radzilowski, B. O. Dabbousi, E. L. Thomas, M. G. Bawendi and M. F. Rubner, *J. Appl. Phys.* **83**, 7965 (1998).
[3] A. Shik, H. Ruda and E. H. Sargent, *J. Appl. Phys.* **88**, 3448 (2000).
[4] N. C. Greenham, X. Peng and A. P. Alivisatos, *Phys. Rev. B* **54**, 17628 (1996).
[5] Y. Wang and N. Herron, *J. of Luminescence* **70**, 48 (1996).
[6] A. C. Arango, S. A. Carter and P. J. Brock, *Appl. Phys. Lett.* **74**, 1698 (1999).
[7] L. Bakueva, A. Shik, H. Ruda and E. H. Sargent, *J. Appl. Phys.* (in press).

9th Int. Symp. "Nanostructures: Physics and Technology"
St Petersburg, Russia, June 18–22, 2001

Effective medium approach for planar QD structures

G. Ya. Slepyan†, S. A. Maksimenko†, V. P. Kalosha†, A. Hoffmann‡ and D. Bimberg‡
† Institute for Nuclear Problems, Belarus State University, Bobruiskaya 11, 220050 Minsk, Belarus
‡ Institut für Festkörperphysik, Technische Universität Berlin, Hardenbergstr. 36, 10623 Berlin, Germany

Abstract. The effective boundary condition (EBC) method is extended to nano-scale planar mesoscopic systems. The EBCs appear as a result of the 2D-homogenization procedure and have the form of two-side anisotropic impedance boundary conditions stated on the structure surface. The EBC method supplemented with well-developed mathematical techniques of classical electrodynamics creates unified basis for solution of boundary-value problems in electrodynamics of quantum dots.

1. Introduction

The key peculiarities of quantum dot (QD) heterostructures [1] are related to spatial confinement of the charge carrier motion and intrinsic spatial inhomogeneity. Since the inhomogeneity scale is much less than the optical wavelength, QDs can be treated as *electrically small* objects and electromagnetic response of such structures can be evaluated by means of effective medium theory. Effective medium approach as applied to 3D arrays of QDs has been developed in Refs. [2, 3]. In this paper we present a general method which allows us to evaluate electromagnetic response of planar arrays of QDs and to establish correlation between properties of such systems and homogeneous 2D structures like quantum wells (QWs). This method, the effective boundary condition (EBC) method, has been originally developed for microwaves and antenna theory (see, e.g., [4]) and is modification of the effective medium theory as applied to 2D-confined structures. Its basic idea is that a smooth homogeneous surface is considered instead of the initial structure, and appropriate EBCs for the electromagnetic field are stated for this surface. These conditions are chosen in such a way that the spatial structure of the field due to an effective current, and the field of the real current in the initial structure turn out to be identical at some distance away from the surface. Material characteristics of the structure and its geometrical parameters are included in coefficients of the EBCs.

2. EBCs for planar nanostructures

Under the derivation of EBCs, the kernel problem is the diffraction of electromagnetic field by an infinite planar quadratic lattice constituted by identical QDs imbedded in a host medium those permittivity ε_h is assumed to be real–valued and dispersionless. In the strong confinement regime, when the exciton Bohr radius exceeds significantly the QD linear extention ($a_B \gg R$), the Lorentz dispersion law $\varepsilon(\omega) = \varepsilon_h + g_0/(\omega - \omega_0 + i/\tau)$ can be used as model of dispersion in a single QD in the vicinity of the exciton resonance [5]; here ω_0 is the frequency of the transition, τ is the effective exciton dephasing time in the QD, $g_0 = -4\pi\mu^2 W/\hbar V$ where μ and V are the QD dipole moment and volume, W is the level population difference ($W < 0$ in an inverted medium).

In the dipole approximation, electromagnetic field scattered from an isolated QD can be expressed in terms of Hertz potentials by

$$\mathbf{E}(\mathbf{r}) = \mathbf{E}_0(\mathbf{r}) + \sum_{l,m=-\infty}^{\infty} \left[\nabla\nabla\cdot\mathbf{\Pi}^e_{lm}(\mathbf{r}) + k_1^2\mathbf{\Pi}^e_{lm}(\mathbf{r})\right] . \tag{1}$$

Corresponding equation for the magnetic component is also presented. Here $k = \omega/c$, $k_1 = k\sqrt{\varepsilon_h}$, $\mathbf{E}_0(\mathbf{r})$ stands for the incident field; an $\exp(-i\omega t)$ time-dependence is supposed. Further the incident field is assumed to be $\mathbf{e}_x$-polarized plane wave propagating at angle θ with respect to the z axis. Hertz potentials are given by

$$\mathbf{\Pi}^e_{lm}(\mathbf{r}) = \left[\mathbf{e}_x\alpha_{xx}\mathcal{E}_x(\mathbf{R}_{lm}) + \mathbf{e}_z\alpha_{zz}\mathcal{E}_x(\mathbf{R}_{lm})\right]\frac{\exp(ik_1|\mathbf{r}-\mathbf{R}_{lm}|)}{|\mathbf{r}-\mathbf{R}_{lm}|} , \tag{2}$$

where $\mathbf{R}_{lm} = \{ld, md, 0\}$ is the radius–vector of a lattice site, d is the lattice period, α_{ii} are the components of the QD polarizability tensor $\widehat{\boldsymbol{\alpha}}$, and $\mathcal{E}(\mathbf{r})$ is the electric field inside QD. This field is related to the Hertz potentials by the equation analogous to Eqs. (1) in the limit $\mathbf{r} \to 0$ with the term $l = m = 0$ excluded. For QDs with planar configuration in the $x0y$ plane, e.g., discs, islands, flattened pyramids, etc., the QD polarizability in the z direction α_{zz} can be neglected.

The next step is the 2D–averaging of the electromagnetic field in the $z = 0$ plane. Such a procedure implies replacement of the discrete 2D elementary scatterer by a homogeneous $d \times d$ surface element; mathematically this procedure reduces summation in equations for inner and outer fields to integration. Then, one should find discontinuities of the mean field tangential components at $z = 0$ taking into account that the mean field has $\exp(ik_1 x \sin\theta)$ dependence on the x co-ordinate. Then, after some manipulations, we come to the covariant notation of the EBCs:

$$\begin{aligned} \mathbf{n}\times\mathbf{n}\times(\mathbf{H}^{\mathrm{I}} - \mathbf{H}^{\mathrm{II}}) &= -\frac{2\pi}{c}\widehat{\boldsymbol{\sigma}}\,\mathbf{n}\times(\mathbf{E}^{\mathrm{I}} + \mathbf{E}^{\mathrm{II}}) , \\ \mathbf{n}\times(\mathbf{E}^{\mathrm{I}} - \mathbf{E}^{\mathrm{II}}) &= -\xi\,\mathbf{n}\times\nabla[\mathbf{n}\cdot(\mathbf{E}^{\mathrm{I}} + \mathbf{E}^{\mathrm{II}})] \end{aligned} \tag{3}$$

where

$$\widehat{\boldsymbol{\sigma}} = \begin{pmatrix} \widehat{\boldsymbol{\sigma}}_{\parallel} & 0 \\ 0 & 0 \end{pmatrix} , \qquad \widehat{\boldsymbol{\sigma}}_{\parallel} = i\frac{\omega\varepsilon_h}{d^2}\widehat{\boldsymbol{\alpha}}_{\parallel}\left(\hat{\mathbf{I}}_{\parallel} + \frac{\delta_x}{d^2}\widehat{\boldsymbol{\alpha}}_{\parallel}\right)^{-1} , \qquad \xi = \frac{2\pi\alpha_{zz}}{d^2 + \delta_z\alpha_{zz}} . \tag{4}$$

Here, $\hat{\mathbf{I}}_{\parallel}$ is the 2×2 unit tensor and $\widehat{\boldsymbol{\alpha}}_{\parallel}$ is the surface polarizability tensor with components α_{ij} $(i, j = x, y)$; $\delta_x \approx -8/\sqrt{2}d$, $\delta_z \approx 2\pi\sqrt{\pi}/d$.

The equations (3) and (4) constitute the complete system of EBCs for electromagnetic field in planar QD structures. The technique of macroscopic averaging used under their derivation is similar to one which introduces the constitutive parameters for bulk media, but differs in that the averaging occurs in boundary conditions rather than in field equations. Thus, in electrodynamics of low-dimensional structures the EBCs play the same role as constitutive relations in electrodynamics of bulk media. The EBCs keep validity for arbitrary configuration of elementary cell and for planar layers with random distribution of QDs. The difference will manifest itself in the modified coefficients δ_i. Since EBCs (3) are local and the coefficients $\widehat{\boldsymbol{\sigma}}_{\parallel}$, ξ do not depend on the angle of incidence θ, they are applicable at arbitrary excitation in spite of that they have been obtained originally for plane waves. Moreover, the EBCs (3) are analogous to corresponding EBCs for QWs (see,

e.g., [6]) if spatial dispersion in the latter can be neglected. Thus, a planar layer comprising a 2D array of QDs can be treated as an effective QW. As a result, well-developed formalism of investigation of QWs can be extended to QD arrays by introducing of effective integral parameters of the array defined by Eqs. (4).

3. The role of nonlocality

In the weak confinement regime, the QD electromagnetic response becomes nonlocal and the medium polarization takes the form of the integral operator [7]:

$$\mathbf{P}(\mathbf{r}) = A\Phi(\mathbf{r}) \int\limits_V \Phi(\mathbf{r}')\mathbf{E}(\mathbf{r}')\, d^3\mathbf{r}' \,, \tag{5}$$

where $A \sim 1/(\omega - \omega_0 + i/\tau)$, $\Phi(\mathbf{r})$ is the envelope function of the exciton ground state. Eq. (5) defines very special type of nonlocality: the integral operator has degenerated kernel. This property makes possible analytical consideration of the nonlocality problem: integral differential equations describing electromagnetic field in QD turn out to be equivalent to the integral Fredholm equations with degenerated kernels. As a result, we obtain the polarizability tensor of an isolated QD as $\widehat{\boldsymbol{\alpha}} = AN^2(\widehat{\mathbf{I}} - 4\pi A\widehat{\boldsymbol{\Upsilon}})^{-1}$, where the 3D-tensor $\widehat{\boldsymbol{\Upsilon}}$ is given by

$$\Upsilon_{\alpha\beta} = \frac{1}{4\pi} \int\limits_V \int\limits_V \Phi(\mathbf{r})\Phi(\mathbf{r}') \frac{\partial^2}{\partial x_\alpha \partial x_\beta} \frac{1}{|\mathbf{r} - \mathbf{r}'|}\, d^3\mathbf{r} d^3\mathbf{r}' \qquad x_\alpha,\ x_\beta = x, y, z \,. \tag{6}$$

Thus, we have shown that the nonlocality changes values of the polarizability tensor components but does not change the general representation of the scattering operators as compared to the strong confinement regime. This allows us to conclude that the above introduced EBCs remain valid in the weak confinement regime as well. Note that the above result admits extension of the Maxwell Garnett approach to 3D composites constituted by QDs in weak confinement regime.

4. Radiative decay rate in planar array of QDs

Let us apply the EBC method for the investigation of exciton radiative time in 2D-array of QDs which are assumed to be spherical inclusions of the radius R. The problem of the radiative linewidth evaluation in QWs is solved by finding of the frequency poles of the reflection coefficients [6]. Real parts of these poles determine resonant frequencies while imaginary parts give the homogeneous linewidths. It can easily be shown that EBCs (3) with $\widehat{\boldsymbol{\sigma}}_\parallel = ick\eta\widehat{\mathbf{I}}_\parallel/4\pi$, $\xi = -\eta/2\varepsilon(\omega)$ and $\eta = L_{\mathrm{QW}}[\varepsilon(\omega) - \epsilon_h]$ describe a QW with L_{QW} as its thickness. Thus, the reflection coefficient for planar array of spherical QDs are given by a corresponding equation for QW after substitutions $L_{\mathrm{QW}} \to 2R$, $g_0^{\mathrm{QW}} \to g_0^{\mathrm{eff}} \approx (2\pi R^2/3d^2)g_0$ and $\omega_0 \to \tilde{\omega}_0 = \omega_0 - g_0/3\varepsilon_h$. Then, using results of Ref. [6] and above defined substitutions, we obtain the expressions $\Gamma_p = \Gamma_0/\cos\theta$, $\Gamma_s = \Gamma_0\cos\theta$, for TE and TM polaritons, correspondingly; here

$$\Gamma_0 \approx -\frac{2\pi}{3\sqrt{\varepsilon_h}} \frac{R^2}{d^2} \frac{\tilde{\omega}_0}{c} R\, g_0 \,, \tag{7}$$

Comparison of Γ_0 with the radiative decay rate of a single spherical QD γ gives us $\Gamma_0/\gamma = B \approx 3\pi/(k_1 d)^2$. In dense arrays of QDs $B \gg 1$ signaling significant enhancement of

the decay rate Analogous superradiance factor with the Bohr radius a_B instead of d was introduced also for QWs [8]. One can interpret the coefficient B in close analogy with Ref. [8]: it results from the coherent excitation of QDs located at distance d from each other.

5. Conclusion

EBCs given by Eqs. (3) state mathematical equivalence of optical properties of a 2D periodical layer of QDs and an isolated QW. It should be stressed that the mechanisms of transport processes and oscillator strengths in each case are essentially different. Nevertheless, the equivalence makes it possible to extend to QD-based planar structures with more complicated configurations (finite-sized QD layer, QD layer in microcavity, several QD layers, etc.) the well-developed mathematical formalism of investigation of QWs. Namely this equivalence provides promising potentiality of the derived EBCs for particular electrodynamical problems in QD-based structures. In particular, threshold current for QD-based lasers can be evaluated by analogy with solution of corresponding problem for the QW lasers; the EBC method allows us to analyze electromagnetic response of a QD layer (or a multilayer structure) placed in microcavity: this is very important for the design of QD-based semiconductor lasers [1].

Acknowledgments

The research is partially supported through the NATO Science for Peace Program under project SfP-972614.

References

[1] D. Bimberg, M. Grundmann and N. N. Ledentsov, *Quantum Dot Heterostructures* (John Wiley & Sons, Chichester), 1999.
[2] G. Ya. Slepyan *et al.*, *Phys. Rev. B* **59**, 1275 (1999).
[3] S. A. Maksimenko, *et al.*, *J. Electron. Materials* **29**, 494 (2000).
[4] A. S. Ilyinsky, G. Ya. Slepyan and A. Ya. Slepyan, *Propagation, Scattering and Dissipation of Electromagnetic Waves* (Peter Peregrinus, London), 1993.
[5] S. Schmitt-Rink,*et al.*, *Phys. Rev. B* **35**, 8113 (1987).
[6] R. Atanasov, *et al.*, *Phys. Rev. B* **49**, 2658 (1994).
[7] E. L. Ivchenko, *et al.*, *Sov. Phys. Solid State* **42**, 168 (2000).
[8] E. Hanamura, *Phys. Rev. B* **38**, 1228 (1988).

9th Int. Symp. "Nanostructures: Physics and Technology"
St Petersburg, Russia, June 18–22, 2001

Photoluminescense of isolated quantum dots in metastable InAs arrays

V. G. Talalaev†, B. V. Novikov†, M. A. Smirnov†, G. Gobsch‡, R. Goldhahn‡, A. Winzer‡, G. E. Cirlin§¶, N. K. Polyakov§¶, V. N. Petrov§¶, V. A. Egorov§¶ and V. M. Ustinov§

† Institute of Physics, St Petersburg State University, 198504 St Petersburg, Russia
‡ Institut für Physik, Technische Universität Ilmenau, D-98684 Ilmenau, Germany
§ Ioffe Physico-Technical Institute, St Petersburg, Russia
¶ Institite for Analytical Instrumentation RAS, 198103 St Petersburg, Russia

Abstract. Certain cases are studied, in which quantum dots showing no collective characteristics appear. It is demonstrated that isolated quantum dots are typical of the metastable arrays. The light radiated by these nanoislands has a narrower spectral band as compared to other dot arrays. This effect should be taken into account for the development of quantum dot lasers, in particular, for vertically cavity surface emitting lasers.

Introduction

It has been observed that in metastable arrays the quantum dot (QD) 0D-properties are more prominent than in case of stable QDs, which have square bases and are organized into the dense 2D square lattice [1]. This phenomenon is not explained by the available calculations [2] justifying the metastable QD existence. The narrow photoluminescence (PL) band of metastable QDs provides an advantage for device application. But structural (morphological) instability and tendency to coalescence are restrictive factors for the metastable array application, therefore they need thorough studies. Up to now, the questions remain: what are the metastability consequences on the QD array and which mechanisms are responsible for its PL spectrum?

1. Samples

The structures comprised arrays having 1, 6, 10 or 15 InAs QD layers in GaAs matrix confined on both sides by $Al_{0.25}Ga_{0.75}As$/GaAs superlattices. Singular and vicinal GaAs(100) substrates misoriented towards [001] and [010] directions with 3°, 5°, 7° angles were used. For the single-layer structures (2D arrays) the submonolayer migration enhanced epitaxy (SMEE) mode was applied. For the multi-layer structures (multiply stacked arrays) the combined MBE + SMEE technique was used. The adjacent InAs layers were separated by the GaAs spacer. In different samples it had 8, 10 or 12 nm thickness. Each SMEE InAs layer was produced by the repeated deposition cycle including 0.5 monolayer (ML). In followed by the surface exposure to As_4 flux during $\tau = 10$ s. The InAs QD layer growth temperature was 470°C, growth rate – 0.1 ML/s. QDs formed by the deposition of 1.8, 2.5 and 3.0 InAs ML were studied.

2. Isolated InAs QDs in 2D arrays on the GaAs vicinal surface

STM images reveal the morphological metastability of resulting QD arrays [3]. On the singular GaAs surface this growth mode forms the well-ordered InAs QD array with a

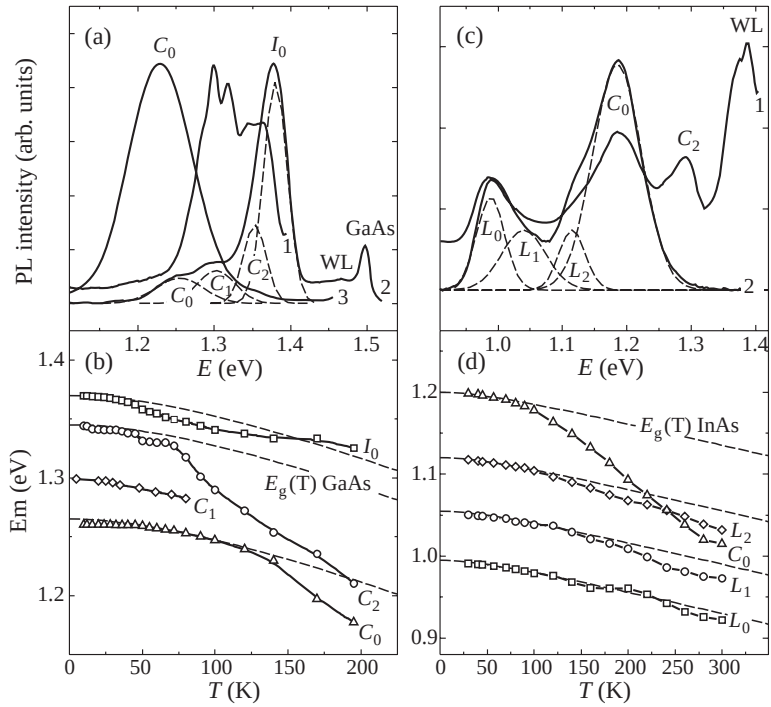

Fig. 1. PL spectra at $T = 5$ K (a,c) and PL peak energy *vs* temperature (b,d) for the 2D arrays of 1.8 ML InAs QD (a,b) and for the 10 multiply stacked arrays of 2.5 ML InAs QD (c,d) on GaAs (100) substrates: (a, curve 3), (c) and (d) — singular substrate; in other cases — 7°[001] vicinal substrate. Selective excitation: (a, c, curves 1) — WL excitation, in other cases — GaAs matrix excitation. Dashed lines in (a), (c) — deconvolution of PL spectrum (curves 2).

chain-like structure organized along the [001] direction. For the 1.8 ML InAs the linear density of QDs in the chain is 0.1 nm^{-1} and the area coverage is 0.3. The QDs have a rectangular 5×12 nm base. The vicinal surface is characterized by a strong step bunching effect. For the 7° angle the average statistical terrace size is 50 nm. The QD arrays are located on the terraces. The chain-like structure remains.

The PL studies have shown that samples with a small substrate misorientation (including singular) have one QD group radiating in the ground and excited states: C_0 and C_n bands ($n = 1, 2$ and more, depending on the excitation conditions). Full width at half maximum (FWHM) for the C_0 band is: 95 meV for a singular substrate and 80 meV for the 3° misoriented one. In the samples with a high misorientation degree (5°, 7°) the second QD group appears, which gives a more intensive I_0 band with FWHM = 35 meV in the short-wave part of the PL spectrum (Fig. 1a).

The PL spectrum *vs* the excitation energy, as well as the PL peak energy and FWHM *vs* temperature showed that these QD groups (CQD and IQD) had basically different properties.

Selective excitation showed that CQD group is connected to the wetting layer (WL), and IQD – only to the GaAs matrix (Fig. 1a). The PL excitation spectra demonstrated the absence of carrier exchange between CQD and IQD groups.

The CQD PL peak energy and FWHM *vs* temperature is the evidence of carrier redistribution from small to large QDs (Fig. 1b). As the temperature grows, the C-bands

get narrower and reveal a red shift considerably exceeding the temperature shifts of the InAs and GaAs band gaps. Presence of such temperature redistribution indicates a close vicinity of CQD (15 nm from the tunnelling length calculations). Such QDs constitute the chain-like structure (CQD — conjunct QDs).

The I_0 band evolution at increasing temperature shows the absence of carrier exchange between the IQD. Their FWHM increases and the red shift follows the GaAs band gap change (Fig. 1b). Consequently these QDs are separated not only from the CQD group but also from each other (IQD — isolated QDs). This can be caused by the WL local absence due to its ruptures at step edges for samples with a high degree of step bunching [4].

The metastable array formation can probably be caused by the combination of SMEE mode ($\tau = 10$ s), which efficiently increases the adatom migration length, and the low growth temperature, which decreases the adatom mobility on the surface. By this the conditions for the appearance of GaAs substrate elastic anisotropy are established, which is expressed as the distinct direction [001], along which QD chains are arranged. It has been previously noted [3] that at the alternate submonolayer deposition the chain formation is accompanied by the generation of WL corrugations. It can be assumed that the overlap of corrugation structures and the system of multiatomic steps can result in WL ruptures on the vicinal surface. In this way the elastic strain relaxation mechanism, which competes with QD formation, is eliminated and isolated QDs are formed.

3. Isolated QDs in multiply stacked arrays

TEM images of multiply stacked arrays [5] demonstrated large QDs (LQD) along with CQD in the upper layers. LQD had lateral sizes ranging within 20–40 nm.

PL spectrum for single-layer structures had a previously-mentioned C_0 band with a 1.2 eV peak energy and 95 meV FWHM ($T = 5$ K). In the structures with six QD layers and 8 nm thick spacer the main C_0 band developed a long-wave shoulder. When ten InAs layers were grown the main C_0 maximum was accompanied by the long-wave maximum L_0 having the 0.98 eV energy (Fig. 1c). The multiplication of 15 layers made the L_0 maximum domineer in the PL spectrum in the 0.96 eV position (FWHM = 50 meV). Under room temperature its position was at 1.4 μm.

The increase of spacer size inhibited the new L_0 band formation in the PL spectrum. It was enough to increase the spacer thickness to 12 nm to make it disappear.

In our opinion a new L_0 band appearance was caused by the formation of islands with sizes larger than those of CQD in the InAs layers. The gap between C_0 and L_0 bands reached 200 meV. A new LQD group could appear as the result of QD coalescence in the InAs upper layers [5, 6]. The SMEE method promotes the growth of metastable QDs, which coalesce readily, and it stimulates the QD coalescence. Large InAs islands appear in the upper layers, they have the lateral sizes about 30 nm and produce L_0 radiation at 1.3 μm.

The deconvolution of multiply stacked QD PL spectrum into gaussians gives 4 components (Fig. 1c), the exterior ones are the L_0 and C_0 bands, they result from the transitions between the ground states. The L_1 and L_2 transitions take place with the involvement of large QD excited states.

The studies of PL spectrum dependence on the excitation energy (Fig. 1c), as well as the PL peak energy on temperature (Fig. 1d) enabled to draw the following conclusions.

Large QDs (L_0, L_1, L_2 bands) lie on the WL, but are not connected to each other. There is no carrier redistribution within the LQD group in the whole temperature interval. Consequently the carrier exchange between LQD is either missing or impeded. Because

of this such QDs are also isolated [7]. Such isolation can be caused by the low density in the coalesced QD group. The dot–dot separation exceeds the carrier diffusion length in the WL, taking into account the carrier dissipation across the shallow CQD quantum wells.

The InAs layer multiplication on the vicinal GaAs(100) substrates results in the I_0 band (physically isolated QDs) disappearance from the PL spectrum. We suppose that IQD serve as the elastic strain relaxation mechanism in the bottom layer, therefore they do not reproduce in the upper layers.

In this way, due to the lack of carrier exchange the isolated QDs in IQD and LQD groups demonstrate only individual properties. The PL bands corresponding to them are two times narrower than the conjunct QD bands. The inhomogeneous broadening of IQD depends on the size variation only for the narrow terraces, on the edges of which the WL rupture takes place [4]. FWHM of LQD is just a part of the inhomogeneous CQD broadening, as only the largest CQD take part in the LQD group formation.

Conclusion

QD metastability causes the array separation into two subsystems. On the vicinal surface the separation results from the morphological instability (CQD and IQD); on the stack upper layers it is caused by the tendency to coalesce (CQD and LQD). Therefore we can conclude that isolated QDs accompany metastable QD arrays. The specific features of this phenomenon and the inevitable development of the isolated QD subsystem are discussed.

Acknowledgement

The work was supported by the Russian Foundation for Basic Research (grants 99-02–7780 and 00-15-96–756), by German Academic Exchange Service (DAAD) and by a grant of the Thüringian Ministry of Science, Research and Art.

References

[1] R. Leon, S. Marcinkevicius, X. Z. Liao, J. Zou, D. J. H. Cockayne and S. Fafard, *Phys. Rev. B* **60**, R8517 (1999).

[2] V. A. Shchukin, N. N. Ledentsov, P. S. Kop'ev and D. Bimberg, *Phys. Rev. Lett.* **75**, 2968 (1995).

[3] G. M. Guryanov, G. E. Cirlin, V. N. Petrov, N. K. Polyakov, A. O. Golubok, S. Ya. Tipissev, V. B. Gubanov, Yu. B. Samsonenko, N. N. Ledentsov, V. A. Shchukin, M. Grundmann, D. Bimberg and Zh. I. Alferov, *Surf. Sci.* **352-354**, 651 (1996).

[4] V. G. Talalaev, B. V. Novikov, S. Yu. Verbin, A. B. Novikov, Dinh Son Thach, I. V. Shchur, G. Gobsch, R. Goldhahn, N. Stein, A. Golombek, G. E. Cirlin, V. N. Petrov, V. M. Ustinov, A. E. Zhukov and A. Yu. Egorov, *Semiconductors* **34**, 453 (2000).

[5] B. V. Volovik, D. S. Sizov, A. F. Tsatsulnikov, Yu. G. Musikhin, N. N. Ledentsov, V. M. Ustinov, V. A. Egorov, V. N. Petrov, N. K. Polyakov and G. E. Cirlin, *Semiconductors* **34**, 1316 (2000).

[6] V. G. Talalaev, B. V. Novikov, V. V. Kachkanov, M. A. Smirnov, G. Gobsch, R. Goldhahn, A. Winzer, V.–M. Gnehr, G. E. Cirlin, V. N. Petrov and V. M. Ustinov, *Newsletter of St Petersburg University* **4**, 4, 28, (2000).

[7] C. Lobo, R. Leon, S. Marcinkevicius, W. Yang, P. C. Sercel, X. Z. Liao, J. Zou and D. J. H. Cockayne, *Phys. Rev. B* **60**, 16647 (1999).

9th Int. Symp. "Nanostructures: Physics and Technology"
St Petersburg, Russia, June 18–22, 2001

Spontaneous magnetization in single and coupled quantum dots

I. I. Yakimenko†, A. M. Bychkov‡§ and *K.-F. Berggren*†

† Department of Physics and Measurement Technology, Linköping University, S-58183 Linköping, Sweden
‡ Moscow State Engineering Physics Institute (Technical University), 115409 Moscow, Russia
§ Centre for Quantum Computation, Clarendon Laboratory, Oxford OX1 3PU, United Kingdom

Abstract. Spontaneous magnetization of single and coupled quantum dots formed by lateral confinement of a high-mobility two-dimensional electron gas is studied for a realistic semiconductor heterostructure. The modeling of the device takes into account contributions from a patterned gate, doping, surface states and mirror charges. To explore the magnetic properties we use the Kohn–Sham local spin-density formalism including the contributions from electron correlation as well as from exchange. We show, however, by explicit calulations that the exchange is the dominant mechanism driving a spontaneous magnetization of a dot. Single dots and pairs of dots with up to about 50 electrons per dot have been studied. The question of very large dots is also addressed briefly.

Introduction

The expectations to utilize quantum dots and the inherent magnetic properties in semiconductor electronics are high [1]. There is, for example, the emerging field of spin electronics, or 'spintronics', which takes advantage of electron spin rather than its charge and which may bring about new devices such as spin transistors, magnetic random access memories, and optical encoders and decoders [2]. An even more ambitious application might be in using coherent states of electron spins for quantum information processing. Semiconductor quantum dots are especially attractive for these purposes since their electronic properties can be readily engineered and spin coherence can be sustained long enough to be monitored and transported within the device [3]. Given such a motivation, it is instructive to study single and coupled quantum dots in terms of their magnetization (spin polarization), and how the latter could be controlled by external means.

In this paper we will discuss the self-consistent Kohn–Sham local spin density functional method (LSD) [4] as applied to the calculation of the capacitance and charging energies, i.e., basic parameters of quantum devices containing arrays of ultra-small dots in GaAs/$Al_xGa_{1-x}As$ heterojunction. With this approach, we thus investigate atomic-like shell structures and magnetized states. Details of our work are found in [1, 5].

1. Theoretical modeling

Quantum-dot devices may be fabricated in a semiconductor heterostructure with a patterned metallic top gate [6]. The gate is deposited everywhere on top of the structure except for ungated openings. Dots residing at the interface arise from the depletion of the two-dimensional electron gas (2DEG) under the gated regions when a negative gate voltage is

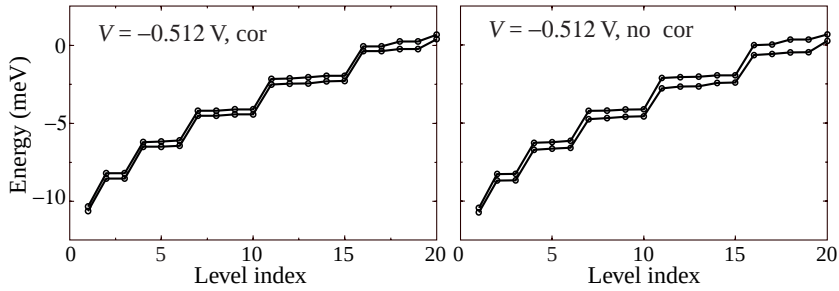

Fig. 1. Spin-split electron levels in a quantum dot at a certain gate voltage V. In the upper case both electron correlation and exhange are included in the Kohn–Sham potential U_{ex}^{σ}, while the lower one includes exchange only. The chemical potential is set to zero, hence there are 19 up-spin and 17 down-spin electrons in the upper case. The corresponding numbers for the lower case are 19 and 16.

applied. The actual size of the dots can be varied by changing the geometry of the gate, i.e. its lithography, as well as the applied gate voltage.

To find the electronic structure, number of electrons in a dot etc. we solve the Kohn–Sham equations by discretizing on a square grid:

$$-\frac{\hbar^2}{2m^*}\left(\frac{\partial^2}{\partial x^2}+\frac{\partial^2}{\partial y^2}\right)\varphi^{\sigma}(x,y)+[U(x,y)+U_{ex}^{\sigma}(x,y)]\varphi^{\sigma}(x,y)=E^{\sigma}\varphi^{\sigma}(x,y). \quad (1)$$

Here $\sigma = \pm\frac{1}{2}$ refers to the two spin directions, $U(x,y)$ represents the potential from the electrostatic confinement and the repulsive Hartree term. The important exchange-correlation potential is denoted $U_{ex}^{\sigma}(x,y)$. In the calculations we have used two form for U_{ex}^{σ}, one with both electron correlation and exchange included and one with exchange only.

2. Electronic configurations and spontaneous magnetization

The magnetization (spin polarization) of a dot is defined as the difference between the densities n^{σ} of the up and down-spin electrons

$$p = n^{\uparrow} - n^{\downarrow}. \quad (2)$$

We have simulated a single quantum associated with a symmetric square opening in the gate. At the interface the corresonding potential is in practice circular. We have searched a large gate voltage region yielding 0 to 50 electrons in the dot. The results show a rich variety of magnetizations depending on the number of electrons occupying the dot. Because of the high symmetry there is a pronounced shell structure where the lower shells are filled with both up and down-spin electrons while the uppermost shell may be only partially filled with, let us say, up-spin electrons. The corresponding states for down-spin electrons are above the Fermi level. A typical example is presented in Fig. 1 for a given gate voltage V. The upper case shows the spin-polarised levels with both electron interactions and exchange included in U_{ex}^{σ} while the lower case refers to exchange only. Although the splitting of levels is reduced with correlations included the total spin and shell-filling remain the same as for the case with only exchange. Obviously, correlation also requires slight adjustments of V to have the same number of electrons in the dot.

The overall results for the single symmetric quantum dot are presented in Fig. 2. A Coulomb staircase that is shown to the right reflects the filling of the dot with electrons

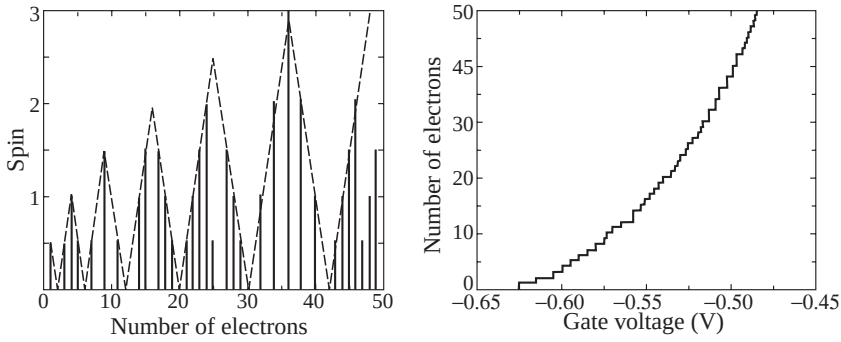

Fig. 2. (a) Coulomb staircase diagram for a single square quantum dot. (b) Variation of the total spin polarization in the square quantum dot containing N_{tot} electrons. Solid bars represent the results of the modeling. The dashed line indicates the spin configuration when Hund's rule is satisfied.

as a function of the gate voltage. The total number of electrons varies from 0 at a pinch-off voltage of -0.62 V and up to 50 electrons. Some of the steps along the vertical axis experience a jump of two electrons (such as from 12 to 14 and in the region from 30 to 42 electrons). In those cases the step of the gate voltage $\Delta V_g = 1$ mV has not been sufficiently small to distinguish between a pair of highly degenerate energy states, and a double filling has occurred.

The left part of Fig. 2 plots the total spin polarization S_z of the dot as a function of its electron content. In general, by external variations in the gate voltage one can vary the spin polarization (magnetization) of a single symmetric quantum dot in a range limited by Hund's rule. This is as long as the dot has circular symmetry. If we introduce a dent by applying different voltages to different segments of the gate the shell structure breaks down and the magnetization is removed. In the same way we find that the magnetization is stongly affected when two dots are made to interact. This gives in principle a way to control the magnetization. Presently we are extending this considerations to very large dots with up to 1000 electrons for which our methos is well suited. In this way we plan make contact with current measurements of the magnetization of dots.

References

[1] For reason of space we refer to I. I. Yakimenko, A. M. Bychkov and K.-F. Berggren, *Phys. Rev. B* (in press), for further references to this very active field.
[2] J. de Boeck and G. Borghs, *Phys. World*, April 1999, pp 27–32;
P. Ball, *Nature* **404**, 918 (2000), and references therein.
[3] J. M. Kikkawa and D. D. Awschalom, *Nature* **397**, 139 (1999).
[4] R. G. Parr and W. Yang, *Density-functional theory of atoms and molecules* (Oxford University Press, New York, 1989).
[5] A. M. Bychkov, I. I. Yakimenko and K.-F. Berggren, *Nanotechnology*, **11**, 318 (2001).
[6] J. H. Davies, *Semicond. Sci. Technol*, **3**, 995 (1988);
J. H. Davies, I. A. Larkin and E. V. Sukhorukov, *J. Appl. Phys.* **77**, 4504 (1995).
[7] M. I. Lubin, O. Heinonen and M. D. Johnson, *Phys. Rev. B* **56**, 10 373 (1997).

9th Int. Symp. "Nanostructures: Physics and Technology"
St Petersburg, Russia, June 18–22, 2001

Peculiarities in equilibrium tunneling between disordered two-dimensional electron systems: from Fermi edge singularity to linear gap in high magnetic field

Yu. V. Dubrovskii[1], R. Hill[2], V. A. Volkov[3], V. G. Popov[1], E. E. Vdovin[1], D. Yu. Ivanov[1], A. Kotel'nikov, L. Eaves[2], P. C. Main[2], D. K. Maude[4], J.-C. Portal[4,6,7], M. Henini[2], G. Hill[5] and J. C. Maan[8]

[1] Institute of Microelectronics Technology RAS, 142432 Chernogolovka, Russia
[2] The School of Physics and Astronomy, University of Nottingham, Nottingham NG7 2RD, United Kingdom
[3] Institute of Electronics and Radioengineering RAS, Moscow, Russia
[4] Grenoble High Magnetic Field Laboratory, MPI-CNRS, BP166 38042 Grenoble Cedex 9, France
[5] Dept of Electr. and Electron. Eng., University of Sheffield, Sheffield S3 3JD, UK
[6] Institut Universitaire de France
[7] INSA, F31077 Toulouse Cedex 4, France
[8] High Field Magnet Laboratory, Research Institute for Materials, University of Nijmegen, 6525 ED Nijmegen, The Netherlands

Abstract. We have investigated equilibrium tunnelling between disordered two-dimensional electron systems at temperatures below 0.3 K and in a wide range of magnetic field normal to the electron layers. Observed transformation of a narrow conductance peak of about 1 mV width at zero bias into the narrow dip with magnetic field is discussed in the frame of many-electron interaction effects in tunnel phenomena.

It was discovered recently that a high magnetic field normal to the layers suppresses equilibrium tunnelling between two-dimensional electron systems [1–3] and between 2D and 3D electron systems [4]. These studies were performed on samples with low [2–4] or very low disorder in the 2D electron gas [1]. There is general agreement that the observed suppression is related to in-plane Coulomb correlations between 2D electrons in a high magnetic field. Equilibrium tunnelling between strongly disordered electron systems has been recently studied only for the case of 3D electron systems [5], where a gap in the tunnelling density of states in zero magnetic field was reported. Earlier we reported that high magnetic field $B > 8$ T parallel to the current suppresses tunnelling between disordered two-dimensional electron systems near zero bias [6]. These studies were performed at temperatures above 2.4 K. It was found that the main features related with tunnelling gap appeared in a high magnetic field in temperature range used was similar to those found in samples with low disorder [2, 3].

In this work we present studies of tunnelling between two strongly disordered two-dimensional electron systems (2DES) at temperature lower then before ($T \leq 0.3$ K) in a magnetic field parallel to the current, that is normal to the electron layers. We have found extra equilibrium tunnel current without magnetic field which was manifested as very narrow conductance peak at zero bias. The gap in tunnel spectra appears at zero bias in magnetic field about 4 T with disappearance of the extra current features at the same time. Analysis shows that the gap has linear form, and the slope of the gap oscillate with magnetic field. It is possible also to extract from the data the gap width and depth dependences on

magnetic field. We argue that wide differential conductance maximums on both sides of the gap in the tunnel spectra measured in a high magnetic field are due to the energy relaxation of tunnelling electrons by emission of some kind quasi-particles.

To form the 2DES we used Si donors sheets (δ-doped layers) with the donor concentration corresponding to insulator behaviour in electron transport [7, 8], i.e. slightly below the metal–insulator transition at zero magnetic field. In our experiments, electron transport along the layers does not contribute to the measured current which flows perpendicular to the plane of the barrier. This allows us to measure the zero-bias conductance which is proportional to the convolution of the tunnelling density of states.

The MBE-grown sample was a single barrier $GaAs/Al_{0.4}Ga_{0.6}As/GaAs$ heterostructure with a 12 nm thick barrier. The barrier was separated from the highly-doped, bulk contact regions by 50 nm thick, undoped GaAs spacer layers. Si donors sheets with concentration of $3 \cdot 10^{11}$ cm^{-2} were located 5 nm from each side of the barrier. The tunnelling transparency of the main barrier was much lower than that of the spacer regions, so that most of the applied voltage is dropped across the barrier.

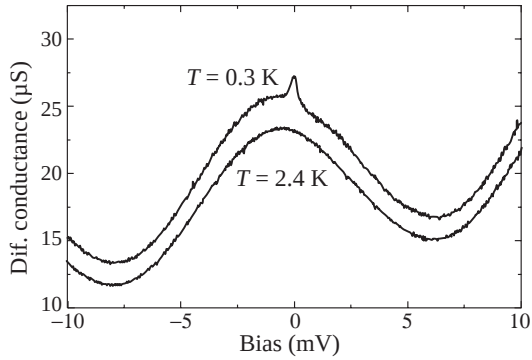

Fig. 1. Tunnelling differential conductance at 0.3 K and 2.4 K as a function of external voltage in zero magnetic field. Curves arbitrary shifted in vertical direction for clarity.

Figure 1 shows the differential tunnel conductance G, at 0.3 K and 2.6 K, measured using standard lock-in techniques, versus external voltage V_b in zero magnetic field. At 2.6 K the differential conductance has a wide peak around zero bias. We argue that peak reflects resonant tunnelling between the ground states of the 2DESs. The maximum of the peak is slightly shifted (1 mV) from zero bias since as grown concentrations in the layers is slightly different. At 0.3 K additional narrow conductance peak with maximum exactly at zero bias is perfectly resolved.

Figure 2(a) shows that this narrow conductance peak transforms into the dip with magnetic field. It happens in B between 3.5 and 4 T. Further variation of the tunnel spectra with magnetic field in B ranged from 7 T to 15 T is shown in Fig. 2(b).

In this work, we focuse on the equilibrium tunnelling processes around zero bias and start with the analysis of the dip appeared in magnetic field. The tunnelling differential conductance at low voltage reflects the joint density of states at the Fermi levels in the 2D electron layers. We found that differential conductance in a dip around zero bias has parabolic dependence on bias voltage at all magnetic fields, which is the main difference from the systems with low disorder where exponential increase of the current around the gap ("hard" gap) created by magnetic field was found [2, 3]. The parabolic form of differential conductance corresponds to the linear gap in the density of states near Fermi level in each

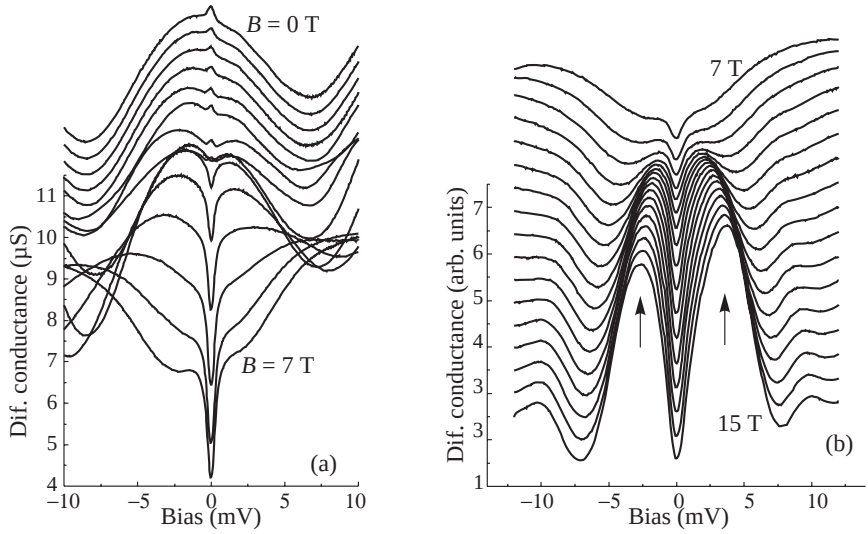

Fig. 2. (a) Tunnelling differential conductance at 0.3 K as a function of external voltage in different magnetic fields from 0 T up to 7 T with 0.5 T magnetic field step between the curves. Curves arbitrary shifted in vertical direction for clarity. (b) Tunnelling differential conductance at 0.3 K as a function of external voltage in different magnetic fields from 7 T up to 15 T with 0.5 T magnetic field step between the curves. Arrows indicate differential conductance peaks discussed in the text. Curves arbitrary shifted in vertical direction for clarity.

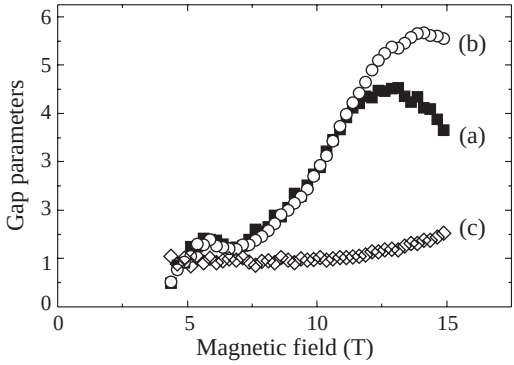

Fig. 3. (a) The slope of the linear gap in arbitrary units, (b) the depth of the linear gap in arbitrary units, (c) the width of the gap in mV, all versus magnetic field normal to the 2DES.

2DES. The existence of the "soft" linear gap in the density of states near Fermi level due to the Coulomb interaction of localised electrons was found theoretically many years ago by Efros and Shklovskii [9]. Since the localisation is increased with magnetic field it is not surprise that the dip due to the gap in the density of states appears in the tunnel spectra only in a magnetic field when most of the states along the 2DEG becomes localised. But behaviour of the gap with magnetic field is unusual and until now has not been described in the literature. The dependence of the slope of the linear gap, that is the coefficient at quadratic term describing the experimental parabolic dependence, versus magnetic field is shown in Fig. 3. The slope oscillates with B. In the same Fig. 3 the width and depth

of the gap as function of magnetic field are shown also. The width was determined in the preposition that the gap are terminated at point where dependence of the differential conductance on bias voltage becomes sublinear, and was extracted from the position of extremums on the conductance derivative plot. The depth value was obtained from the values of slope and width of the gap.

The wide peaks in the differential conductance appeared in a high magnetic fields out of the gap, shifted linear with magnetic field, and shown in Fig. 2(b) by arrows are similar to those which was found before in tunnelling between 2DES with different level of disorder [1–3, 6]. For samples with very low disorder it was proposed that wide peaks appeared out of tunnelling "hard" gap was due to the relaxation of tunnelling electron into the ground state with emission of some kind of quasiparticles [10, 11], e.g. plasmon vortexes [10], or some specific oscillations in the electron system [11].

Coming back to the narrow conductance peak at zero bias without magnetic field we argue that it is related with the tunnelling from the puddles with strongly localised states in the emitter into the puddles of 2D extended states in the collector. That is well known Fermi edge singularity and was observed before in tunnelling between 2D and zero-dimensional impurity states [12]. The donor concentration fluctuates along the 2DES in our structure. So one could find the regions with low concentration of strongly localised electrons and regions of high enough concentration with extended 2D electrons states. Since the fluctuation in the electron systems on different sides of the barrier are independent, there should exist regions where electrons tunnel from localised to extended states. Magnetic field suppresses extended states and Fermi edge singularity is disappeared from tunnel spectra.

In conclusion, we have investigated equilibrium tunnelling between disordered two-dimensional electron systems at temperatures below 0.3 K and in a wide range of magnetic field normal to electron layers. The Coulomb interaction between electrons in the layers leads to the different anomalies found in the tunnel spectra: Fermi edge singularity in zero magnetic field and linear gap in the density of states developed in magnetic field. The slope of the linear gap oscillates with magnetic field. At the moment we do not know any theoretical model describing gap behaviour with magnetic field.

Acknowledgements

This work was supported by INTAS (97-11475), RFBR (98-02-22008, 00-02-17903, 01-02-17844, 01-02-97020), PICS (628), Ministry of Science (FTNS-97-1057, 99-1124), and EPSRC (UK). Three of us YuVD, VAV, and JCP are grateful to Chateau de Beaufort whose wine helped us to carry out this work.

References

[1] J. P. Eisenstein *et al.*, *Phys. Rev. Lett.* **69**, 3804 (1992).
[2] N. Turner *et al.*, *Phys. Rev.* **B54**, 10614 (1996).
[3] Yu. V. Dubrovskii *et al.*, *JETP Letters* **69**, 255 (1999).
[4] R. C. Ashoori *et al.*, *Phys. Rev.* **B48**, 4616 (1993).
[5] M. Lee *et al.*, *Phys. Rev.* **B60**, 1582 (1999).
[6] Yu. N. Khanin *et al.*, *Physica E* **6**, 602 (2000).
[7] Qiu-Yi Ye *et al.*, *Semicond. Sci. Technol.* **4**, 500 (1989).
[8] R. J. F.Hughes *et al.*, *J. Phys.: Condens. Matter* **6**, 4763 (1994).
[9] A. L. Efros and B. I. Shklovskii, *J. Phys C: Solid State Phys* **8**, 49 (1975).
[10] I. L. Aleiner *et al.*, *Phys. Rev. Lett.* **74**, 3435 (1995).
[11] P. Johansen and J. M. Kinaret, *Phys. Rev. Lett.* **71**, 1435 (1993).
[12] A. K. Geim *et al.*, *Phys. Rev. Lett.* **72**, 2061 (1994).

9th Int. Symp. "Nanostructures: Physics and Technology"
St Petersburg, Russia, June 18–22, 2001

Non-equilibrium tunneling effects of interacting Hubbard–Anderson impurities

P. I. Arseev‡, *N. S. Maslova*† V. I. Panov† and S. V. Savinov†
† Moscow State University, 119899 Moscow, Russia
‡ Lebedev Physical Institute, 247166 Moscow, Russia

Abstract. Non-equilibrium interaction effects of Hubbard-Anderson impurities have been experimentally studied by means of STM/STS methods and theoretically analyzed using self-consistent approach based on Keldysh formalism.

In this work, the interaction of the localized impurity states formed by a pair of identical impurity Si 3 nm apart at the (110) GaAs surface are studied by scanning tunneling microscopy and spectroscopy (STM/STS). In the experimentally observed spatial distribution of the local tunneling conductivity, one can recognize a two-fold switching on and off of each of atomic *a* and *b* states upon changing the tunneling bias. After switching on, the excess tunneling conductance occurs in the vicinity of each of these atoms in a bias range about 0.75 eV, which is much greater than the level width of localized state. At the same time, the transition from one state to other occurs upon changing bias in the range of 0.15 eV, which is comparable to the energy level width of the localized state.

Such effects have not been observed for individual impurity. We suggests self-consistent theoretical analysis of local tunneling conductivity behavior in the vicinity of two interacting Anderson impurities on semiconductor surface [1].

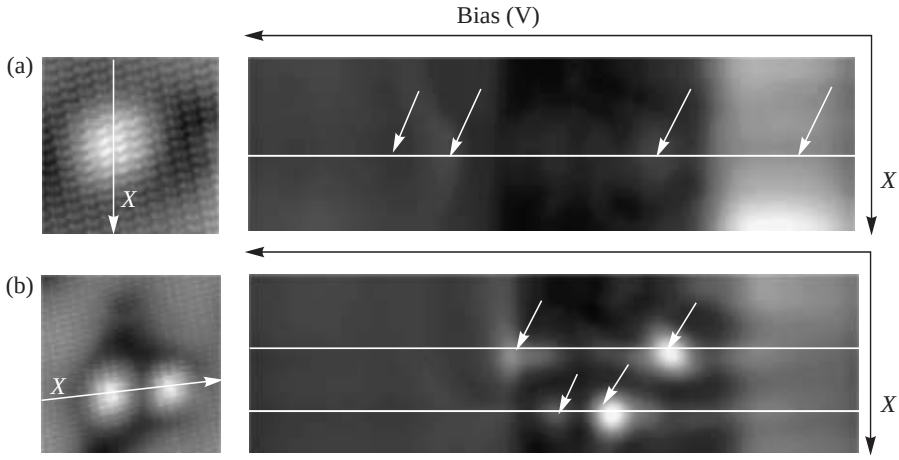

Fig. 1. STM images (right panel) and map view of normalized tunneling conductivity measured along direction depicted on STM topography images (left panel). Specific features on STS images are marked by arrows. (a) Isolated Si impurity, scan area 5.8 nm, bias range from +2.5 V to −2 V, (b) two interacting Si impuriies scan area 10 nm, bias range from +2.9 V to −2 V.

The influence of tunneling bias voltage on the impurity states energy values is taken into account. Non-equilibrium electron filling numbers on Hubbard–Anderson impurities are obtained from self-consistent system of kinetic equations based on Keldysh diagram technique. Coulomb interaction of localized electrons is treated self-consistently in mean-field approximation and is determined by these non-equilibrium filling numbers. It is shown that with increasing of tunneling bias two states with different energies for opposite spin electrons can appear on each impurity: the transition from "paramagnetic" regime to "magnetic" one can occur. The inverse transition from "magnetic" to "paramagnetic" state can also occur with further increasing of tunneling bias. We have also determined the conditions for enhancement of transition to magnetic state by increasing of interaction between two Anderson impurities. We revealed that impurity interaction results in redistribution of localized non-equilibrium charges and can lead to pinning of impurity levels near the Fermi level of each electrode and to mutual attraction of energy levels of different impurities in particular range of applied bias.

Non-equilibrium two impurity Anderson model is analyzed in mean-field approximation.

1. Mixed valence regime is considered $\varepsilon/\Gamma \geq 1$, $U \gg \varepsilon, \Gamma$.
ε, Γ are energy value and broadening of impurity state, U is on-site Coulomb interaction. Electron filling numbers n_σ and $n_{-\sigma}$ can differ from 0 and 1.

If $\Gamma \ll \varepsilon$ and the influence of tunneling interaction with the banks of the contact on impurity spectrum is neglected one obtain Coulomb blockade regime with n_σ and $n_{-\sigma}$ equal to 0 or 1 for $U \gg \varepsilon \gg \Gamma$. For Kondo regime $U \gg \varepsilon \gg \Gamma$ and the influence of tunneling interaction and electron correlation on quasi-particle spectrum in the banks of the contact and on impurity spectrum is taken into account. But in this case impurity level lies deep below E_F, n_σ and $n_{-\sigma}$ are also equal to 0 or 1.

2. Tunneling and relaxation rates $\gamma_a, \gamma_b, \gamma_k$ are not infinite, so electron filling numbers n_σ and $n_{-\sigma}$ are non-equilibrium.

3. Energy values of impurity states are treated in self-consistent mean-field approximation $\varepsilon_\sigma^a(V, n_{-\sigma}^a(V)) = \varepsilon_a + \alpha V + U\langle n_{-\sigma}^a\rangle$.

4. Enchantment of tunneling conductivity with changing of tunneling bias voltage can be observed when $|\varepsilon_a^{\pm\sigma}(V) - E_F^t| < \Gamma$ or $|\varepsilon_a^{\pm\sigma}(V) - E_F^s| < \Gamma$.

Any increasing of LDOS at energy value $E_F - eV < \varepsilon < E_F$ when changing applied bias V leads to enhancement of tunneling conductivity at eV which can differ from ε.

Self consistent analysis of suggested model allows to distinguish different regimes of tunneling conductivity behaviour in the vicinity of impurity atoms with changes of tunneling bias.

(i) If $\gamma_k \ll \gamma_a, \gamma_b$ one of impurity atoms (atom a) can be in "magnetic" state in certain range of tunneling bias. With changing of applied voltage transition from "paramagnetic" regime to "magnetic" one and vise versa can occur. This behavior leads to switching "ON" and "OFF" twice of a atom on spatially resolved local tunneling conductivity spectra.

Besides energy levels are pinned in vicinity of Fermi level of one of electrodes (tip or sample) while bias voltage changes in the range of order of U.

In non-equilibrium case, when tunneling bias in not zero interaction between atoms a and b can enhance "magnetic" state and increase difference between energy values ε_σ and $\varepsilon_{-\sigma}$ of electrons with opposite spins localized on atom a.

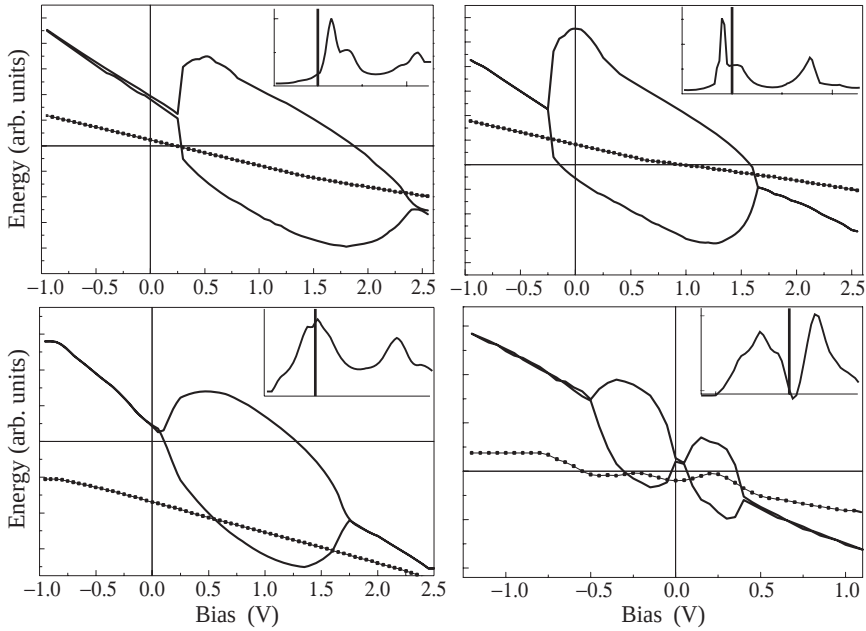

Fig. 2. Behavior of atoms a and b energy levels vs. tunneling bias for different parameters of tunneling junction. Two left graphs correspond to weak coupling to STM tip. Upper right graph corresponds to noninteracting impurity atoms, while lower one — to strong coupling to STM tip. Inserts show corresponding calculated normalized differential tunneling conductivity for the same bias range.

Detailed analysis of tunneling bias V range $|\varepsilon_a^{-\sigma}(V, n_a^{\sigma}) - E_F^s| < \Gamma$ leads to the following conclusions.

When there is no interaction between atoms (bias range $|\varepsilon_a^{-\sigma}(V, n_a^{\sigma}) - E_F^s| < \Gamma$) the state $\varepsilon_a^{-\sigma}(V, n_a^{\sigma})$ is filling and $n_a^{-\sigma}(V)$, $\varepsilon_a^{\sigma}(V)$ are increasing, consequently $n_a^{\sigma}(V)$ and $\varepsilon_a^{-\sigma}(V)$ are decreasing. Levels $\varepsilon_a^{-\sigma}(V, n_a^{\sigma})$ and $\varepsilon_a^{\sigma}(V, n_a^{-\sigma})$ become closer and sharp transition from "magnetic" to "paramagnetic" state occurs (Fig. 2(b)).

In presence of interaction filling of state $\varepsilon_a^{-\sigma}(V, n_a^{\sigma})$ is suppressed due to charge redistribution between two interacting atom a and b. Correspondingly, increasing of $\varepsilon_a^{\sigma}(V, n_a^{-\sigma})$ and decreasing of $\varepsilon_a^{-\sigma}(V, n_a^{\sigma})$ is also going slower than in non-interacting case. Thus the range of applied bias when atom a is in "magnetic" state become wider because of interatomic interaction (Fig. 2(a)). Let us stress the fact that this enhancement of "magnetic" regime is possible only in non-equilibrium case, i.e. for nonzero tunneling bias, and when energy levels $\varepsilon_{a(b)}^{\pm\sigma}(V, n_{a(b)}^{\mp\sigma})$ are close to the Fermi level of one of the electrodes.

In equilibrium case interaction with paramagnetic atom b will result in suppression of "magnetic" state on atom a (Fig. 2(a)).

Figure 2(c) depicts the dependence of tunneling conductivity on applied bias in vicinity of a atom. Two wide peaks on tunneling conductivity spectra correspond to switching "ON" of a atom at $\varepsilon_a^{\sigma}(V, n_a^{-\sigma}) = E_F^t$ and $\varepsilon_a^{-\sigma}(V, n_a^{\sigma}) = E_F^s$.

(ii) For $\gamma_k >> \gamma_a, \gamma_b$ (sufficiently strong coupling to STM tip) the situation when "magnetic" state on a atom appears twice is possible. In Fig. 2(d) the dependence of

$\varepsilon^{\pm\sigma}_{a(b)}(V, n^{\mp\sigma}_{a(b)})$ on applied bias is shown. In the range of applied bias $|\varepsilon^{\sigma}_{a}(V, n^{-\sigma}_{a}) - E^{s}_{F}| < \Gamma$ atom a is in the "magnetic" state. But with increasing of tunneling bias, filling numbers quickly decrease and "magnetic" regime is suppressed, and atom a can be found in "paramagnetic" state. However at opposite polarity of applied bias atom a can again be found in "magnetic" state when $|\varepsilon^{\sigma}_{a}(V, n^{-\sigma}_{a})$ is close to the Fermi level of the tip $|\varepsilon^{\sigma}_{a}(V, n^{-\sigma}_{a}) - E^{t}_{F}| < \Gamma$. Interaction between a and b atom can enhance this transition.

(iii) And finally, when coupling to the STM tip is comparable with coupling of impurity atom to the substrate $\gamma_k \geq \gamma_a, \gamma_b$ increasing of tunneling bias usually leads to suppression of "magnetic" state because filling numbers decrease due tunneling processes. Thus, we demonstrate the crucial rope of non-equilibrium effects in interacting bound tunneling nanostructures.

References

[1] P. I. Arseev, N. S. Maslova, S. I. Oreshkin, V. I. Panov and S. V. Savinov, *JETP Lett.* **72**, 121, 565, (2000).

9th Int. Symp. "Nanostructures: Physics and Technology"
St Petersburg, Russia, June 18–22, 2001

Resonant tunnelling via states of the X-related donors located at different atomic layer in AlAs barrier

Yu. N. Khanin, E. E. Vdovin and Yu. V. Dubrovskii
Institute of Microelectronics Technology and High Purity Material, Russian Academy of Sciences, Chernogolovka, Moscow District, 142432 Russia

Abstract. We report an electrical transport and magnetotransport study of GaAs/AlAs/GaAs single-barrier heterostructures incorporating unintentional donors in the barrier. Resonant tunnelling was observed both through the quasiconfined states in the AlAs layer originated from the X_{XY} and X_Z conduction band minima and through two distinct states of the donors bound to the X_{XY} and X_Z valleys. Furthermore we observed an additional oscillatory like fine structure of the donor resonances that we attribute to difference in binding energies of donors located at different position of the AlAs layer. Magnetic field behaviour of the fine structure demonstrated that the binding energy of X-related donors has an essential dependence on both magnetic field and donor position in the barrier.

Recent investigations of AlAs/GaAs heterostructures have demonstrated that X-valley states in AlAs have a substantial influence on their optical and electrical properties [1, 2]. For silicon donors in bulk AlAs, the central cell potential does not mix the three hydrogenic effective-mass states and its thus can be described as corresponding to independent X valleys. Therefore, the ground state of a silicon donor is threefold degenerated. However, in a thin AlAs layer this degeneracy is lifted due to confinement and strain, so that threefold degenerated state splits into a two-fold degenerate state associated with X_{XY} valleys and a non-degenerate state associated with X_Z valley [1]. The binding energies of hydrogenic-like donors bound to the X_{XY} and X_Z valleys were calculated by Gerald Weber, with both the mass anisotropy and the quantum confinement taken into account [3]. Moreover was shownthat the binding energy of the donor depends on it position in the AlAs layer and donor resonances should occur at a different voltages for impurities located at different distances from the heterointerface. Tunnelling spectroscopy allows to measure directly the donor binding energy provided that resonanses corresponding to tunnelling via both the confined state and the donor state associated with them is observed. In our previous paper we have reported the detection of two X_{XY} and X_Z-related donor resonances [4] (see Figure 1).

In this paper we report the first observation an additional oscillatory like fine structure of the donor resonances that we attribute to difference in binding energies of donors located at different position of the AlAs layer. Study of the behaviour of the fine structure with magnetic field demonstrate that the binding energy of X related donors has an essential dependence on both magnetic field and donor position in the barrier in agreement with earlier theoretical results [3, 5].

The sample studied was a single-barrier GaAs-AlAs-GaAs heterodiode, grown by molecular-beam epitaxy on (100)-oriented Si doped n-GaAs substrate. The AlAs layer was not intentionally doped but the donor impurities were present in AlAs because of diffusion from the highly doped region during the growth. Figure 2(a) displays the additional oscillatory like fine structure of the X_{XY}-related donor resonance at magnetic fields from 12.75 to 14 T and $T = 0.4$ K. Note that the fine structure exists in the absence of the magnetic

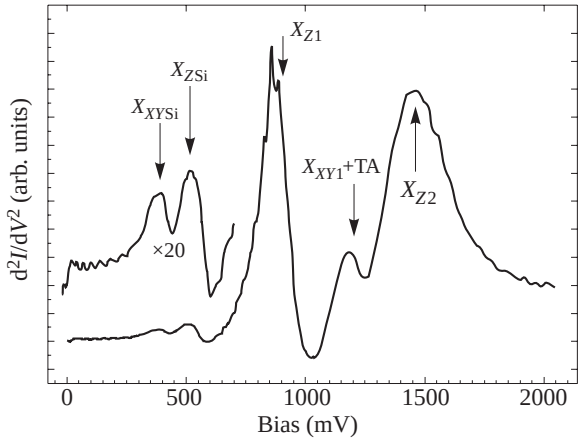

Fig. 1. The second derivative characteristic of the experimental device at 4.2 K. The calculated threshold voltages are denoted by arrows. Two lowest quasiconfined states in the X quantum well and two states of the donors linked to them are denoted by X_{XY1}, X_{Z1} and X_{XY} Si, X_Z Si.

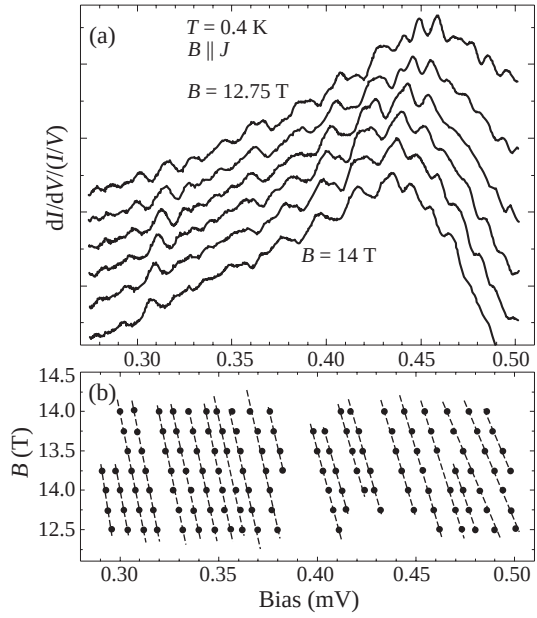

Fig. 2. (a) Normalised conductance-voltage curves for magnetic fields from 12.75 to 14 T at $T = 0.4$ K. The curves are vertically offset for clarity. (b) Fan diagram of the fine structure peak positions as function of the magnetic field.

field and intensifies with increasing magnetic field. However the conductance curve shows complex changes with the magnetic field which are partly due to Landau level quantization in the emitter and partly due to the fine structure. Therefore we studied the fine structure in a strong magnetic field when Landau level quantization leads only to monotonic moving of the resonant peaks. The structure appears to be sample specific but is exactly reproducible for a given sample even after thermal recycling. The medium period of this structure is about 15 mV that corresponds to an energy separation by approximately 1.2 meV. When

the temperature was increased up to 20 K ($kT \approx 1.25$ meV) the fine structure disappeared completely due to the thermal broadening. Resonant tunnelling via individual states of the donors located at different atomic layer leads only to an additional fine structure of the main impurity resonances [3]. On the other hand, the fine structure of resonances in devices with large lateral dimensions can be caused by interface roughness [6]. However, the binding energy of donor has stronger dependence on its position in the barrier than on the width of the barrier itself. When the thickness of the 5 nm AlAs barrier varies on 2 monolayers (it's a typically value of MBE technology interface roughness) the binding energies of the central X_Z and X_{XY} related donors varies on 2 and 4 meV respectively. The difference in binding energies of donors located at the center of the 5 nm AlAs barrier and at the heterointerface is 30 meV and 20 meV for X_Z and X_{XY} related donors respectively [10]. Thus we consider that in our experimental situation the fine structure is related to the random distribution of the donors in the barrier. In a magnetic field applied along the direction of the current, the fine structure shows a shift to lower bias with increasing field. The fan diagram of the observed peak position as a function of the magnetic field is shown in Fig. 2(b). Fine structure peaks in the voltage range from 300 to 500 mV near X_{XY}-related donor resonance move to lower bias as the magnetic field increases at a rate from 8 to 20 mV/T respectively and the rate is a monotonic increasing function of the voltage (see Fig. 2(b)). It should be noted that Landau quantization leads to equal voltage shift of the resonant peaks. On the other hand, our self-consistent Poisson-Schrodinger calculations show that over the bias range of interest (300–500 mV) the ratio of the total voltage drop in the structure to that in the barrier region (leverage factor) varies slightly from 12 to 12.7. Therefore we consider that the significant difference in shift rates of the peaks is due to binding energy of the more spread out state of the donor located at the heterointerface has a stronger dependence on magnetic field then that of the more localised state of the donor located at the centre of the barrier [3, 5]. In other words behaviour of the fine structure with magnetic field is the experimental verification of the significant dependence of the binding energies of X-related donors on its position in barrier that has been predicted theoretically [3].

To summarise we have reported a transport study of tunnelling through indirect-gap GaAs/AlAs/GaAs single-barrier structure. We have observed an additional oscillatory like fine structure of the donor resonances that we attribute to difference in binding energies of donors located at different position of the AlAs layer. Study of the behaviour of the fine structure with magnetic field demonstrated that the binding energy of X-related donors has an essential dependence on magnetic field and donor position in the barrier in agreement with earlier theoretical results [3, 5].

The authors would like to thank T.G. Adersson for the MBE growth. We are grateful to Prof. V. A. Tulin for encouragement and useful discussions and V. V. Belov for technical assistance. The work was supported by the Russian Foundation for Basic Research (00-02-17903) and (01-02-22008), APS 3.11.99 and FTNS 97-1057.

References

[1] H. W. van Kesteren, E. C. Cosman, P. Dawson *et al.*, *Phys. Rev. B* **39**, 13426 (1989).
[2] R. Teissier, J. J. Finley, M. S. Skholnic *et al.*, *Phys. Rev. B* **54**, 8329 (1996).
[3] Gerald Weber, *Appl. Phys. Lett.* **67**(10), 1447 (1995).
[4] Yu. N. Khanin, K. S. Novoselov and E. E. Vdovin, *Fiz. Tekh. Poluprovod.* **35**(2), 206 (2001).
[5] J. M. Shi, F. M. Peeters, G. Q. Hai and J. T. Devreese, *Phys. Rev. B* **44**, 5692 (1991).
[6] Y. C. Kang, M. Suhara, K. Furuya *et al.*, *Jpn. J. Appl. Phys.***34** Pt.1 , 4417 (1995).

9th Int. Symp. "Nanostructures: Physics and Technology"
St Petersburg, Russia, June 18–22, 2001

The new approach to the single-electron electrometer design

V. A. Krupenin†, A. B. Zorin§‡, D. E. Presnov‡, M. N. Savvateev†
and J. Niemeyer§

† Laboratory of Cryoelectronics, Moscow State University, 119899 Moscow, Russia
‡ Nuclear Physics Institute, Moscow State University, 119899 Moscow, Russia
§ Physikalisch-Technische Bundesanstalt, 38116 Braunschweig, Germany

Abstract. We report on new two types of single-electron tunneling (SET) transistor-electrometer. The both transistor types comprised two chains of tunnel junctions instead of two single junctions. In the first case (Type I) the role of junctions plays the shadow-evaporated chains of stack tunnel Al/AlO_x/Al junctions with an island in between. In the second case (Type II) there were two highly resistive Cr thin-film strips ($\sim$1 μm long) connecting a 1 μm-long Al island to two Al outer electrodes. Our transistor demonstrated very sharp Coulomb blockade and reproducible, deep and strictly e-periodic gate-modulation in wide ranges of bias currents I and gate voltages V_g. In the Coulomb blockade region ($|V| \leq$ about 0.5 mV) we observed strong suppression of cotunneling current enabling to measure appreciable modulation curves $V(V_g)$ at current I as low as 100 fA (Type II transistor). The noise figure of our SET transistors was found to be similar to that of typical Al/AlO_x/Al SET transistors, viz. $\delta Q_x \approx 3.5 \div 5 \times 10^{-4} e/\sqrt{\text{Hz}}$ at 10 Hz.

Introduction

The SET transistor is a system of two ultra-small metal-insulator-metal tunnel junctions attached to a small island which is capacitively coupled to a gate electrode. Due to their considerable resistance, $R \gg R_Q \equiv \hbar/4e^2 \cong 6.5$ kΩ, the tunnel junctions ensure quantization of charge on the island. On the other hand, the junctions still make possible the correlated charging and discharging of the island by individual electrons when temperature is sufficiently low, $k_B T \ll E_c$. Here $E_c = e^2/2C_\Sigma$ is the charging energy, $C_\Sigma = C_1 + C_2 + C_0 + C_g$ is the total capacitance of the island which includes the capacitances of the junctions $C_{1,2}$, self capacitance of the island C_0 and capacitance between the island and gate electrode C_g. Transport of electrons is controlled by the transistor gate polarizing the island and therefore changing the Coulomb blockade threshold. Increase of the gate voltage V_g causes a stepping increment of the number of electrons on the island and this leads to e-periodic dependence of the $I - V$ characteristic on V_g. Due to this effect the transistor provides a means for measuring the polarization charge on its island with sub-electron accuracy. This property of SET transistors was successfully exploited in many experiments on measuring and monitoring sub-electron quantities of charge in mesoscopic systems (see some examples in Refs. [1], [2, 3, 4] and [5]). Different materials and methods have been used for fabrication of SET transistors. Although substantial progress in fabrication techniques has been done, there is still a demand for devices simple in fabrication, less subject to the electrical shock destruction and with good electric parameters. In this paper we present a new type of SET transistor-electrometer having potential to meet these requirements. The idea of our work was to fabricate and characterize a metallic transistor with chains of stack tunnel Al/AlO_x/Al junctions (Type I) or with high-ohmic ($R \gg R_Q$) Cr-film microstrips (Type II) replacing the traditional (oxide) tunnel barriers between the

island and outer electrodes. The junctions of this type should, to our mind, also ensure sufficient isolation of the island leading to the correlated electron motion across the device [6]. Below we report the SET characteristics of our device.

1. Sample fabrication

The structures of both types were fabricated by the shadow evaporation through a suspended mask [7] on Si substrate buffered by AlO_x layer (about 200 nm thick). The structures of Type I were fabricated by sequential evaporation of the chain islands through the same opening in the mask. After each evaporation the angle of the evaporation was slightly changed to shift the the islands a little from each other. The oxidation were done between each evaporation. By this way we got a very compact chain (about 100 nm long) of stack tunnel junctions.
For the structures of Type II the fabrication process was carried out *in situ* by three steps to obtain reliable metallic contacts between Cr and Al films. First, the Al film 10 nm thick was deposited by e-gun at the first angle. It formed the bottom layers of the island and outer electrodes. Secondly, the Cr film of thickness $6 \div 8$ nm was evaporated at small residual pressure ($\approx 10^{-5}$ mbar) of oxygen. This evaporation was made at another angle to overlap the bottom Al layer giving rise to the electric connection of the island and outer electrodes. The nominal contact area between Al and Cr layers was 100 nm by 120 nm. Finally, the second Al layer (about 30 nm thick) was evaporated at the first angle so that the ends of Cr strips were clasped by Al electrodes from bottom and from top. The gate electrode was positioned near the island. The top view of the resulting structure is presented sketchy in Fig. 1 where the stray metal shadows are not shown for the sake of clarity.

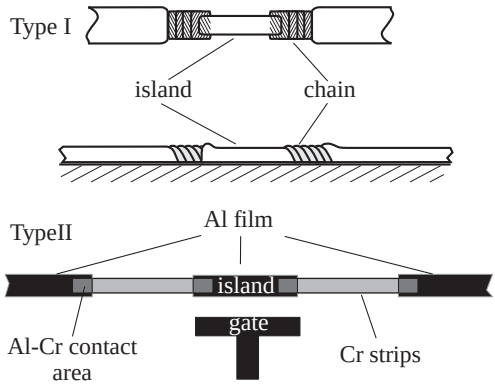

Fig. 1. The geometry of the Cr-film transistor structure. The width of the strips (about 100 nm) is shown somewhat larger for clarity.

2. Results and discussion

The transistor of the first type comprised two chains of tunnel junctions instead of two single junctions. We have studied the electrical and noise properties of the device. The transistor has shown periodical modulation curves with slowly variable amplitude depended on background charges on the islands located between junctions in the chains. The measured value of charge noise was to be closed to a typical value for a planar transistor structures: $\delta Q_x \approx 3.5 \times 10^{-4} e/\sqrt{\text{Hz}}$ at 10 Hz and mostly determined by the size of its central

island ($\sim$0.5 μm). In comparison with traditional SET transistor (two single junction structure) our devise had considerably lower cotunneling current that can be important for the transistor being used in electronic circuits as a current switch. The transistor of the second type had even more unusual design: it comprised two highly resistive Cr thin-film strips ($\sim$1.2 μm long)) connecting a 1 μm long Al island to two Al outer electrodes. These resistors replace small-area oxide tunnel junctions of traditional SET transistors. Our transistor with a total asymptotic resistance of 110 kΩ showed a very sharp Coulomb blockade and reproducible, deep and strictly e-periodic gate modulation in wide ranges of bias currents I and gate voltages V_g. In the Coulomb blockade region, we observed a strong suppression of the cotunneling current allowing us to measure appreciable modulation curves $V(V_g)$ at currents I as low as 100 fA. The noise figure of our SET was found to be similar to that of typical Al/AlO_x/Al SET transistors, viz. $\delta Q_x \approx 5 \times 10^{-4} e/\sqrt{\text{Hz}}$ at 10 Hz.

Acknowledgements

We wish to thank M.Yu. Kupriyanov for the valuable discussion. This work was supported by the German BMBF, Russian Foundation for Basic Research, Russian Program "Physics of Solid State Nanostructures" and Russian Ministry of Science.

References

[1] P. Lafarge, H. Pothier, E. R. Williams, D. Estive, C. Urbina and M. H. Devoret, *Z. Phys. B* **85**, 327 (1997).
[2] M. W. Keller, J. M. Martinis, A. H. Steinbach and N. M. Zimmerman, *IEEE Trans. on Instrum. and Meas.* **46**, 307 (1997).
[3] P. D. Dresselhaus, J. Li, S. Han, L. Ji, J. E. Lukens and K. K. Likharev, *Phys. Rev. Lett.* **72**, 3226 (1994).
[4] V. A. Krupenin, S. V. Lotkhov, D. E. Presnov, A. B. Zorin, F.-J. Ahlers, J. Niemeyer, H. Scherer, T. Weimann and H. Wolf, *Czech. J. Phys.* **46**, suppl. 4, 2283 (1996).
[5] Y. Y Wei, J. Weis, K. V. Klitzing and K. Eberl, *Appl. Phys. Lett.* **71**, 2514 (1997).
[6] The idea that the single electron effects can occur in a metallic island connected to electron reservoir by means "arbitrary scatterer" (not necessarily by a tunnel junction) was first proposed by Nazarov: Yu. V. Nazarov, *Phys. Rev. Lett.* **82**, 1245 (1999).
[7] J. Niemeyer, *PTB Mitt.* **84**, 251 (1974); G. D. Dolan, *Appl. Phys. Lett.* **31**, 337 (1977).
[8] L. S. Kuzmin, P. Delsing, T. Claeson and K. K. Likharev, *Phys. Rev. Lett.* **62**, 2539 (1989).
[9] P. Delsing, *Single Charge Tunneling*, H. Grabert and M. H. Devoret, eds, pp. 249–274, New York, Plenum, 1992.
[10] V. A. Krupenin, D. E. Presnov, A. B. Zorin and J. Niemeyer, *J. Low Temp. Phys.* **118**, Nos. 5/6, 287 (2000).
[11] L. J. Geerligs, D. V. Averin and J. E. Mooij, *Phys. Rev. Lett.* **65**, 3037 (1990).
[12] The cotunneling process in SET transistor is associated with coherent tunneling of two electrons across two junctions simultaneously, see D. V. Averin and A. A. Odintsov, *Phys. Lett. A* **140**, 251 (1989).
[13] A. B. Zorin, S. V. Lotkhov, H. Zangerle and J. Niemeyer, *J. Appl. Phys.* **88**, 2665 (2000).
[14] A. A. Odintsov, V. Bubanja and G. Schön, *Phys. Rev. B* **46**, 6875 (1992).

9th Int. Symp. "Nanostructures: Physics and Technology"
St Petersburg, Russia, June 18–22, 2001

Coulomb interaction of quasi-2D magnetoplasmons

E. E. Takhtamirov and V. A. Volkov
Institute of Radioengineering and Electronics of RAS,
Mokhovaya 11, 101999 Moscow, Russia

Abstract. Tunneling is a powerfull tool of the determination of one-electron structure of 2D systems. Recently a strong interaction of cyclotron and intersubband tunneling resonanses was observed in the case when the one-particle Landau levels of different 2D subbands do not interact. In this connection the long-wave structure of quasi-2D magnetoplasmons is calculated for the actual system of two quasi-2D layers divided by a barrier in a perpendicular magnetic field. It is shown that the Coulomb interaction of inter- and intrasubband magnetoplasmons is able to lead to their strong anticrossing. Magnetoplasmon-assisted tunneling processes will reveal themselves as anticrossing Landau levels of different 2D subbands.

Investigations of the tunneling between quasi-two-dimensional electron systems based on (001) GaAs/$Al_{0.4}Ga_{0.6}As$/GaAs in a magnetic field parallel to the current revealed a strong interaction between Landau levels of different two-dimensional subbands in GaAs which was observed as an anticrossing of the related peak positions in the tunnel current vs voltage curves as a function of magnetic field [1]. The splitting of the interacting Landau levels was of the order of 10 meV, which cannot be explained by nonparabolicity of the conduction band in GaAs. An alternative mechanism leading to the anticrossing is related to the emission of magnetoplasmons. Energy of an electron that has tunneled into the system with the completely discrete spectrum may relax by the emission of 2D magnetoplasmons (the emission of optical and acoustic phonons is forbiden in that case).

The aim of the paper is calculation of the magnetoplasmon spectrum in the above tunnel structure. The results published in the theoretical papers contain very rich resonance structure of the magnetoplasmon spectrum in several 2D systems, but the results depend very sensitively on the approximation used. Here it is shown that the Coulomb interaction of inter- and intrasubband magnetoplasmon branches leads to their strong anticrossing in qualitative agreement with the experimental data.

We consider a symmetric structure (001) GaAs/$Al_{0.4}Ga_{0.6}As$/GaAs with a single thick barrier in magnetic field $\mathbf{B}$ parallel to the growth axis Oz in the gauge of the vector potential $\mathbf{A} = (-By, 0, 0)$. The 2D electron gas (in (x, y) plane) occupy two accumulation layers (with the concentration of 2D electrons N_s in each) formed in GaAs close to both sides of the AlGaAs barrier. The single-particle electron states in both quasi-2D layers are considered independetly, so that, for instance, the states in the right-hand layer are described with the envelope function:

$$F_{nmk}(\mathbf{r}) = (2\pi)^{-1/2} f_n(z) \exp(ikx) \chi_{mk}(y), \tag{1}$$

and the proper self energy E_{nm}. Here n is the subband index, $f_n(z)$ is the z-motion function, m is the Landau level index, k is the wave number, and $\chi_{mk}(y)$ relates to the oscillator function. Following Ref. [2] we will consider the linear response of the system on the perturbation

$$\delta U = U(z) \exp(-i(qx + \omega t)). \tag{2}$$

In the random phase approximation after some algebra we will have the following equation for the perturbation ($\hbar = 1$):

$$\frac{d^2U(z)}{dz^2} - q^2U(z) = -\frac{2e^3B^2}{\epsilon c}\sum_{\substack{n,m\\n',m'}} \frac{\left(f^0_{nm} - f^0_{n'm'}\right)A^2_{mm'}(q)U_{nn'}f_n(z)f_{n'}(z)}{E_{nm} - E_{n'm'} + \omega + i\delta}. \tag{3}$$

Here e is the electron charge, $\epsilon = const$ is the dielectric constant, c is the speed of light, $f^0_{n,m}$ is the Fermi function, $U_{nn'}$ is the matrix element of $U(z)$ on the functions of z-motion, and for $A_{mm'}(q)$ we have:

$$A_{mm'}(q) = \frac{eB}{c}\int\limits_{-\infty}^{\infty} \chi_m(y)\,\chi_{m'}\left(y + \frac{cq}{eB}\right)dy. \tag{4}$$

As we are considering the electrons tunneling from the left-hand layer to the right-hand one, only anti-symmetric solutions of Eq. (3) we are interested in. So, the Green function of Eq. (3) is taken in the form

$$G(z,z') = \frac{1}{2q}\exp\left(-q\left|z+z'\right|\right) - \frac{1}{2q}\exp\left(-q\left|z-z'\right|\right), \tag{5}$$

where $z = 0$ is the coordinate of the middle of the barrier. Now Eq. (3) takes the matrix form:

$$U_{ll'} + \frac{e^3B}{\epsilon cq}\sum_{nn'}\mathcal{I}_{ll'nn'}\Pi_{nn'}U_{nn'} = 0. \tag{6}$$

where

$$\Pi_{nn'} = \sum_{mm'}\frac{\left(f^0_{nm} - f^0_{n'm'}\right)A^2_{mm'}(q)}{E_{nm} - E_{n'm'} + \omega + i\delta}, \tag{7}$$

and in the dipole approximation

$$\mathcal{I}_{ll'nn'} \approx q\int\limits_0^{+\infty}\left(\left|z-z'\right| - (z+z')\right)f_n(z')f_{n'}(z')f_l(z)f_{l'}(z)dzdz'. \tag{8}$$

In the long-wave approximation we have non-zero $A_{mm'}$:

$$A^2_{mm} \approx 1; \qquad A^2_{mm-1} = A^2_{m-1m} \approx \frac{cq^2m}{2eB}. \tag{9}$$

We take into account only the ground and first excited subbands, energy separation between which is Δ. We will have a system of three linear equations (6), determinant of which defines the spectrum of magnetoplasmons. The final dispersion equation is:

$$\begin{aligned}&\left(\omega^2 - \omega_0^2\right)\left(\omega^2 - \omega_c^2\right)\left(\omega^2 - (\Delta+\omega_c)^2\right) - \gamma q^2\left(\omega^2 - \Delta^2\right)\left(\omega^2 - \omega_c^2\right)\\ &-\alpha q^2\left(\omega^2 - \omega_0^2\right)\left(\omega^2 - (\Delta+\omega_c)^2\right) - \beta q^2\left(\omega^2 - (\Delta+\omega_c)^2\right)\\ &+q^4\left(\omega^2 - \Delta^2\right)(\alpha\gamma - \rho) = 0,\end{aligned} \tag{10}$$

where

$$\begin{aligned}&\alpha = \frac{e^2M_1 2\pi N_s}{m\epsilon}, \quad \beta = \frac{e^4M_2^2\Delta 8\pi^2N_s^2}{m\epsilon^2}, \quad \omega_0^2 = \Delta^2 + \frac{e^2M_3\Delta 4\pi N_s}{\epsilon},\\ &\gamma = \frac{e^2M_3 2\pi N_s(\Delta+\omega_c)}{m\epsilon\omega_c}, \quad \rho = \frac{e^4M_2^2 4\pi^2N_s^2(\Delta+\omega_c)}{m^2\epsilon^2\omega_c},\end{aligned} \tag{11}$$

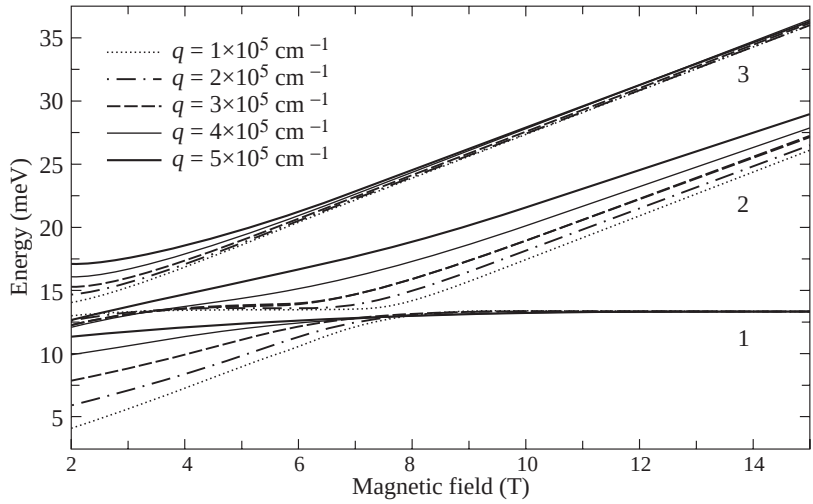

Fig. 1. Plasmon energy (three branches) vs magnetic field at various wave numbers. The branch #1 is the intrasubband plasmon, the one #2 is the intersubband plasmon, the last one #3 is the combination resonance plasmon.

m is the band edge electron effective mass, ω_c is the cyclotron energy, and the dipole matrix elements

$$M_1 = -q^{-1}\mathcal{I}_{1111} > 0, \quad M_2 = -q^{-1}\mathcal{I}_{1112}, \quad M_3 = -q^{-1}\mathcal{I}_{1212} > 0. \tag{12}$$

The result (10) may be understood as following: the intrasubband magnetoplasmons, intersubband ones and combined resonance ones mutually interact via the Coulomb energy.

The result may be presented on the plot 1. The dependence of the magnetoplasmon energy on the magnetic field at various wave numbers is shown. The performed self-consistent calculation yelds $M_1 = 270$ Å, $M_2 = 26.6$ Å, $M_3 = 20.7$ Å, and we take $N_s = 3 \times 10^{11}\,\mathrm{cm}^{-2}$. This plot demonstrates the above-mentioned effect of anticrossing. There are three magnetoplasmon branches: intrasubband branch 1, intersubband branch 2, and combined resonance branch 3, which appears due to the ($n = 0$, $N = 0$) to ($n = 1$, $N = 1$) transition, where n is the principal quantum number of the two-dimensional subband and N is the Landau level index. Only the anticrossing of branches 1 and 3 is resolved in the experiment. Magnetoplasmon-assisted tunneling processes can thus be revealed in this type of structure as an anticrossing effect in the resonances observed between different 2D subbands.

Acknowledgements

The work was supported by RFBR 99-02-17592, INTAS 97-11475, Federal Programs "Physics of Solid State Nanostructures" 99-1124 and "Surface Atomic Structures" 3.1.99.

References

[1] D. Yu. Ivanov, et al., *JETP Lett.* **72** 476 (2000).
[2] R. Z. Vitlina and A. V. Chaplik, *ZhETF* **81**, 1011 (1981).

9th Int. Symp. "Nanostructures: Physics and Technology"
St Petersburg, Russia, June 18–22, 2001

GPLDS.01p

Spin-orbit interaction of electrons on curved surface

M. V. Entin and *L. I. Magarill*
Institute of Semiconductor Physics, Siberian Branch of Russian Academy of Sciences, Novosibirsk, 630090, Russia

Abstract. Spin-orbit (SO) interaction of electrons confined near the curved semiconductor surface is studied. The curvature of surface determines the new mechanism of SO interaction which complements the known mechanisms occurring in planar systems. The specific cases of nanosphere and nanotube are considered.

Introduction

It is well known that the Hamiltonian for electrons, confined near the oriented two-dimensional system, contains linear in lateral momentum $\mathbf{p}$ terms, which describe the spin-orbit (SO) interaction [1]. The orientation of the surface may be determined by the asymmetry of the confining potential [1] as well as by the lack of the inversion symmetry of the initial crystal [2, 3] or the asymmetric orientation of the surface relative to the crystal axes of symmetry.

In the first case (the Rashba model) the SO Hamiltonian has the form [1]:

$$\bar{\mathcal{H}}_{SO} = \alpha(\hat{\boldsymbol{\sigma}}[\hat{\mathbf{p}} \times \mathbf{n}]), \tag{1}$$

where $\hat{\boldsymbol{\sigma}}$ are Pauli matrices, $\hat{\mathbf{p}}$ is the 2D electron momentum. The Hamiltonian (1) appears in the third order on the basic SO interaction. This results in relative smallness of the effective SO interaction for the conduction band electrons in semiconductors with small SO splitting of the valence band edge.

The linear terms in Hamiltonian lead to the spin-splitting of energy bands in the absence of magnetic field and to the possibility of electric-field-induced spin-flip transitions [3]. Recently SO was shown to be responsible for spin ordering by a lateral electric field [4] and a mixed spin-plasmon polaritons [5]. SO interaction of electrons on the cylindrical surface were studied in [6,7] on the basis o the Rashba model.

In the present paper we draw attention to the fact that the curvature itself marks down the surface orientation and hence causes the additional SO interaction. This curvature-induced SO interaction is proportional to the ratio of quantum well width to the radius of curvature. Most distinctly the proposed mechanism can be illustrated by the difference of the planar quantum well and a system with the spherical symmetry. In symmetric planar quantum wells the effective SO interaction is absent for free electrons. Conversely, SO interaction in a spherically symmetric system (e.g., atom) does not vanishes after averaging over radial states. This means that a spherical system has additional effective SO interaction due to curvature.

Spherical quantum well

Let us consider a potential $U(r)$ confining electrons near some radius R (spherical quantum well). The width of a well d is supposed to be much less than R. The same is assumed

concerning the characteristic size of radial states. In this limit effective SO interaction can be expressed in the form containing only the surface coordinates on the sphere.

For spherically symmetric potential the basic SO interaction has the well known form:

$$\mathcal{H}_{SO} = \alpha \frac{1}{r} \frac{dU(r)}{dr} (\hat{\boldsymbol{\sigma}} \hat{\mathbf{l}}). \tag{2}$$

Here $\hat{\mathbf{l}}$ is the orbital momentum (we set $\hbar = 1$). The coefficient of spin-orbit coupling α for free electrons is $\alpha = 1/4(m_e c)^2$, where m_e is the electron mass, c is the velocity of light. In the two-band Dirac model of semiconductor bands, $\alpha = 1/2E_g m_e$, where E_g is the width of the forbidden band and m_e is the effective electron mass.

The Hamiltonian (2) should be averaged over radial states $\psi_n(r)$ of the Hamiltonian without SO interaction. The radial states satisfy the equation

$$\frac{1}{2m_e r^2}(r^2 \psi_n'(r))' + (E - U(r) - \frac{l(l+1)}{2m_e r^2})\psi_n(r) = 0, \tag{3}$$

where E is the energy of the state, l is the angular momentum.

The averaging should be done by integrating with the measure r^2. Expressing the result via the radial wave function we have

$$\bar{\mathcal{H}}_{SO} = -\frac{2\alpha}{R}(T_n - T_t)(\hat{\boldsymbol{\sigma}} \hat{\mathbf{l}}) \tag{4}$$

Here

$$T_n = \frac{1}{2m_e} \int (\psi_n'(r))^2 r^2 dr, \qquad T_t = \frac{\hat{\mathbf{l}}^2}{2m_e R^2} \tag{5}$$

are the radial and tangential parts of electron kinetic energy, respectively. The integration in (5) is effectively run within the layer of width d near R and T_n has the order of magnitude of $1/m_e d^2$ for lowest levels.

The Eq. (4) can be rewritten in the other form, using translational momentum $\hat{\mathbf{p}} = (\hat{p}_\theta, \hat{p}_\varphi) = -i(\partial/\partial\theta, (1/\sin\theta)\partial/\partial\varphi)/R$ on the sphere surface:

$$\bar{\mathcal{H}}_{SO} = \frac{2\alpha}{R^2}(T_n - \frac{\hat{p}^2}{2m_e})([\hat{\mathbf{p}}\mathbf{n}_\mathbf{R}]\,\hat{\boldsymbol{\sigma}}) \quad \mathbf{n}_\mathbf{R} = \mathbf{R}/R. \tag{6}$$

In the form of Eq. (4) the SO Hamiltonian looks like Rashba Hamiltonian, Eq. (1), for a planar system. Really, in the small neighborhood of some point on sphere the vector $\mathbf{n}_\mathbf{R}$ is constant, the sphere can be considered as a plane, and $\hat{\mathbf{p}}$ as a usual momentum along the plane. The difference of Eq. (4) and the Rashba Hamiltonian, Eq. (1), lies in the momentum dependence of the SO coupling constant. In particular, it can change sign with the longitudinal energy $p^2/2m_e$.

Physically, the SO term, proportional to T_n, originates from the difference of electron tangential velocity on the inner and the outer well boundaries. In the frame accompanying the rotating electron the electron spin experiences a magnetic field $\mathbf{B}' = \frac{1}{c}[\mathbf{vE}]$, where $\mathbf{v}$ is the linear velocity of rotation, $\mathbf{E}$ is a confining electric field of well walls. The averaging of $\mathbf{B}'$ with respect to radial motion gives a finite result due to angular momentum conservation. The other contribution to SO interaction, proportional to T_t, originates from magnetic field, induced by the centripetal force. The difference of signs of terms in Eq. (6) is explained by

the difference in directions of dominating accelerations. For specific cases of wells with hard wall potential and a parabolic well ($U(r) = m_e\omega^2(r-R)^2/2$) we have:

$$T_n = \pi^2 n^2/2m_e d^2 \quad n \geq 1 \text{ (hard wall)};$$

$$T_n = \omega(n+1/2)/2 \quad n \geq 0 \text{ (parabolic well)}.$$

The change of SO interaction sign occurs at $p^2/2m_e = \pi^2/2m_e d^2$ and $p^2/2m_e = \omega/4$, respectively.

If the number of electrons is small enough, they occupy the bottom of the first radial subband only, $\mathbf{p}^2/2m_e \ll E_2 - E_1$, and the radial term in Eq. (7) is dominating.

Cylindrical quantum well

The case of electrons locating on a cylindrical surface can be considered analogously. Starting from the more general expression for SO interaction, $\mathcal{H}_{SO} = \alpha[\,\hat{\boldsymbol{\sigma}}\nabla U]\mathbf{p}$ and using cylindrical coordinates (ρ, φ, z) with axis z directed along the cylinder axis, one can find

$$\mathcal{H}_{SO} = \frac{2\alpha}{R}\left((\hat{T}_t - T_n)\hat{p}_\varphi\hat{\sigma}_z + \{[\mathbf{n}_\rho\,\hat{\boldsymbol{\sigma}}]_z, \hat{T}_t\}\hat{p}_z\right), \tag{7}$$

$$T_n = \frac{1}{2m_e}\int(\psi_n'(\rho))^2\rho d\rho, \qquad \hat{T}_t = \frac{\hat{p}_\varphi^2}{2m_e}, \tag{8}$$

where $\hat{p}_\varphi = -(i/R)\partial/\partial\varphi$, R is the cylinder radius; figure brackets in Eq. (7) stands for the operation of symmetrization: $\{\hat{A}, \hat{B}\} = (\hat{A}\hat{B} + \hat{B}\hat{A})/2$.

Note, that the considered SO Hamiltonians contain both the terms, caused by quick transversal motion, depending on the specific structure of transversal wave function, and pure geometrical terms, caused by centripetal acceleration.

The case of slightly curved surface can be studied exploiting the additivity of contributions from the eigenvalues of the curvature tensor. Here we restrict ourselves by the main (transversal) contribution to the SO Hamiltonian, assuming the longitudinal energy to be much less than the distance between the levels of transversal quantization.

Consider the curved surface, tangent to the plane (x, y) in the point 0, where x and y are the main axes of the curvature tensor. The SO Hamiltonian near this point reads as:

$$\mathcal{H}_{SO} = -2\alpha\left(\{\hat{p}_x, \frac{T_n}{R_x}\}\hat{\sigma}_y - \{\hat{p}_y, \frac{T_n}{R_y}\}\sigma_x\right), \tag{9}$$

where T_n is the local transversal kinetic energy (the energy level of the main state of transversal motion), $R_{x,y}$ are the main curvature radii.

We have also obtained the SO Hamiltonian in the general case of curved surface. Similar to the particular cases of sphere and cylinder this Hamiltonian contains terms due to transversal wave function structure and centripetal acceleration. This Hamiltonian can be used to find the energy states on the curved surface without and with external fields. It is also useful for calculation of responses to external fields.

Generally speaking, the obtained curvature-induced SO Hamiltonians should be added by the other (mentioned in the Introduction) terms, which are not related with the curvature. In dependence on the radius of curvature one or another mechanism will prevail. For lesser radii the curvature contribution becomes more essential.

Acknowledgements

The authors are grateful to A. V. Chaplik for useful discussions. The work was supported by the Russian Fund for Basic Researches (grants 99-02-17127 and 00-02-17658) and the State Program of Russian Federation “Physics of Solid State Nanostructures”.

References

[1] Yu. A. Bychkov and E. I. Rashba, *JETP Lett.* **39**, 78 (1984).
[2] M. I. D’yakonov and V. Yu. Kachorovskii, *Sov.Phys.- Semiconductors* **20**, 110 (1986).
[3] E. I. Rashba and V. I. Sheka, *Landau Level Spectroscopy*, eds. G. Landwehr and E. I. Rashba (Elsevier, 1991), p 178.
[4] L. I. Magarill and M. V. Entin, *JETP Lett.* **72**, 134 (2000).
[5] L. I. Magarill, A. V. Chaplik and M. V. Entin, *JETP* **92**, 151 (2001).
[6] L. I. Magarill, D. A. Romanov and A. V. Chaplik, *JETP* **86**, 771 (1998).
[7] L. I. Magarill and A. V.Chaplik, *JETP* **88**, 815 (1999).

9th Int. Symp. "Nanostructures: Physics and Technology"
St Petersburg, Russia, June 18–22, 2001

Surface and edge energy of electron gas in nanocrystals.

M. V. Entin and M. M. Mahmoodian
Institute of Semiconductor Physics, Siberian Branch of the RAS,
630090 Novosibirsk, Russia

Abstract. The energy of a many-electrons nanoparticle depends on its form via the surface and edge contributions to the thermodynamic functions. The surface energy of free electron gas is found for a semiconductor with the Dirac spectrum. The edge energy of electron gas is calculated for quadratic energy spectrum of electrons without and with anisotropy. We find also spin-orbit corrections to the surface energy, which behave like the inverse square of crystal size.

Quantum dots with the large number of electrons are intermediate objects between the quantum and the classical limits. On the one hand, their sizes are large compared with the electron wavelength. On the other hand, the transport and thermodynamic properties of the system are affected by the quantization of the electron states.

In the degenerated electron system the surface contribution to the thermodynamics of small particles is determined by the small ratio of the Fermi wavelength of the electron $1/k_F$ to the particle size L. The presence of the surface leads to the regular corrections in powers of this parameter to the chemical potential of electrons [1].

The surface contributions to the energy of the electron gas lead to the different physical effects. In particular, they affect the surface tension in small particles and, consequently, their equilibrium form. Establishment of the equilibrium between the electron gas in microparticles with different size or form is accompanied by their spontaneous charging [1]. As was shown in [2], owing to charge discreteness, the chemical potentials in microparticles are not completely equalized. As a result, the system of metal granules becomes a gapless insulator (the gapless Hubbard insulator).

Aside from the surface contribution to the energy, in facetted nanocrystals there are contributions caused by their edges and vertexes [3]. The goal of the present report is the study of surface and edge energies of three- and two-dimensional facetted nanocrystals.

Edge contribution to the energy in the free electron model

Here we consider two or three-dimensional gas of free electrons, bounded by an angle $0 < \varphi < \phi, r = \sqrt{x^2 + y^2} < R$ (the dihedral angle in 3D case). The electron wave function ψ satisfies the condition $\psi = 0$ on the angle borders. We search the corrections to the Ω potential at zero temperature, caused by presence of the edge and the boundary. The contribution to the Ω potential from the vicinity $r < r_0$ of the edge $r = 0$ is

$$\Omega = -\int_0^{L_z} dz \int_0^{r_0} r dr \int_0^{\phi} d\varphi \sum (\mu - \varepsilon_{n,m} - k_z^2/2m_e)|\psi_{n,m}(z, r, \varphi)|^2 \qquad (1)$$

Here $\varepsilon_{n,m}$ is the energy level of the electron with the main n and the magnetic m quantum numbers, k_z is the momentum along the edge, m_e is the electron effective mass, $\mu =$

$k_F^2/2m_e$ is the chemical potential. The axis z is directed along the edge and L_z is the edge length. In 2D case this variable and corresponding integration should be excluded.

When the radius R of the sector goes to infinity, Ω ceases to depend on the sector size. In the limit $k_F r_0 \gg 1$ Ω yields an asymptotic expansion (3D case):

$$\Omega = \omega_3 L_z \phi r_0^2/2 + \omega_2 L_z r_0 + \omega_1 L_z + o(1). \tag{2}$$

The wave function, satisfying boundary conditions is

$$\psi_{n,m}(z, r, \varphi) = \sqrt{\frac{2\pi k}{\phi R}} \exp(ik_z z) J_\nu(kr) \sin(\nu\varphi), \qquad \nu = \frac{\pi m}{\phi}. \tag{3}$$

Using the wave function (3) we find

$$\Omega = \frac{1}{m_e r_0^2} \frac{L_z}{\pi} \int_0^{k_F} dk_z u^4 \int_0^1 x dx [\ln x + \frac{1}{2}(1 - x^2)] \sum_{m=1}^{\infty} J^2_{\frac{\pi m}{\phi}}(ux). \tag{4}$$

Here $u = (k_F^2 - k_z^2)^{1/2} r_0$.

The expansion of (4) in the orders of r_0 at $r_0 \to \infty$ gives ω_3, ω_2 and ω_1. The term $\omega_3 = -k_F^5/15\pi^2 m_e$ is the usual Ω potential of 3D gas. The term $\omega_2 = k_F^4/32\pi m_e$ represents the surface contribution [1,2].

The edge contribution ω_1 yields

$$\omega_1(\phi) = -\frac{k_F^3}{36\pi m_e}\Big(\frac{\pi}{\phi} - \frac{\phi}{\pi}\Big). \tag{5}$$

Physically the dependence of $\omega_1(\phi)$ is explained by the same factors as the positive sign of the surface contribution to the energy. Zero boundary conditions on the crystal surface deplete the electron gas density in the boundary region. As a result, the size of occupied region decreases that raises the energy of electron gas at the unchangeable number of electrons. The volume of the depletion region grows with the angle that leads to the same change of the energy of electron gas if both crystal volume and surface area don't vary. The change of $\omega_1(\phi)$ sign at $\phi = \pi$ is caused by extracting of the surface part of energy.

Two cases are of special interest. They are the right angle, typical for the facetting of a cubic crystal and the angle $\phi = 2\pi$, corresponding to the rift in the crystal. In these cases $\omega_1(\pi/2) = -k_F^3/24\pi m_e$ and $\omega_1(2\pi) = k_F^3/24\pi m_e$.

By means of (5) the number of electrons in nanocrystal of volume V, the surface area S and edges with angles ϕ_n and lengths L_n is expressed through the chemical potential:

$$N = -\frac{\partial\Omega}{\partial\mu} = \frac{(2m_e\mu)^{\frac{3}{2}} V}{3\pi^2} - \frac{m_e \mu S}{4\pi} + \frac{(2m_e\mu)^{\frac{1}{2}}}{12\pi} \sum_n L_n \Big(\frac{\pi}{\phi_n} - \frac{\phi_n}{\pi}\Big). \tag{6}$$

The analogous formula is found for the edge energy of a 2D quantum dot with a polygonal border. The angle energy of 2D gas is

$$\omega_1(\phi) = -\frac{k_F^2}{24 m_e}\Big(\frac{\pi}{\phi} - \frac{\phi}{\pi}\Big). \tag{7}$$

Anisotropic electron energy spectrum

The expression for the edge contribution to the energy allows generalization to the case of the anisotropic quadratic-law energy spectrum $\varepsilon(k) = \sum k_i^2/2m_i$. The affine transformation $x_i' = x_i(m_i/m_e)^{1/2}$, where $m_e = (m_1 m_2 m_3)^{1/3}$, converts the Schrödinger equation to isotropic one, for which the previous consideration is valid.

If we establish the dihedral angle by means of the normal vectors $\mathbf{n_1}$ and $\mathbf{n_2}$ to the forming planes, the transformed angle between these planes, entering into previous formulas, is defined by the relation:

$$\cos\phi = \sum_{i=1}^{3} \frac{n_{1i} n_{2i}}{m_i} \left[\sum_{i=1}^{3} \frac{n_{1i}^2}{m_i} \sum_{i=1}^{3} \frac{n_{2i}^2}{m_i} \right]^{-\frac{1}{2}}, \tag{8}$$

and the edge length $L_n = \left[\sum\limits_{i=1}^{3} L_{ni}^2 \right]^{1/2}$ is changed on $\left[\sum\limits_{i=1}^{3} \frac{m_i}{m_e} L_{ni}^2 \right]^{1/2}$.

Dirac model

The Dirac model is the simplest Hamiltonian, describing the energy spectrum of a semiconductor. The most adequately it corresponds to a cubic semiconductor with a non-degenerate central main minimum of the conductivity band and maximum of the valence band. The standard Lattinger model with degenerate maximum of the valence band turns into the Dirac model, if an anisotropy of the band, heavy holes and spin-orbitally splitted band are overlooked. In comparison with the quadratic-law spectrum the Dirac model allows to take into account non-parabolicity of the electron energy spectrum.

The Dirac equation for the spinor component u and v has the form

$$(\varepsilon - m_e c^2)u - c(k\sigma)v = 0, \quad (\varepsilon + m_e c^2)v - c(k\sigma)u = 0. \tag{9}$$

Here ε is the energy of the electron, counted out from the center of the forbidden band with the width $E_g = 2m_e c^2$, σ is the Pauli spin matrix.

Each of the spinor component satisfy the Klein-Gordon equation

$$(\varepsilon^2 - (m_e c^2)^2)u - c^2 k^2 u = 0. \tag{10}$$

The equation (10) transforms into the Schrödinger equation after substitution $(\varepsilon^2 - (m_e c^2)^2) \to 2m_e c^2 E$. If we suppose zero boundary conditions for the large components of the wave function $u = 0$, the agreement with the Schrödinger equation becomes full. Hence, the previous formulae prove correct if we change $\mu = k_F^2/2m_e \to \mu \frac{\mu + E_g}{E_g}$ referring μ to the conduction band bottom.

Spin-orbit induced surface corrections

The spin-orbit interaction is relativistic and usually small effect. Nevertheless, spin-orbit interaction is known [4-5] to be amplified due to confinement by quantum wells. If the width of a well tends to infinity, while the Fermi energy keeps constant, the corrections to the electron spectrum go down inversely as the size. This give rise a new mechanism of the surface corrections to the thermodynamic functions.

Let us consider a planar sample with the width L and the normal z. The spin-orbital correction to the Hamiltonian yields

$$H_{SO} = \lambda \frac{k_z^2}{m_e L}(\sigma_x k_y - \sigma_y k_x) \quad \lambda = \chi \frac{1}{4m_e^2 c^2}. \tag{11}$$

where χ is some constant of order of unit, depending on the specific surfaces. If the surfaces are equivalent χ vanishes, but in the general case χ is finite.

The Hamiltonian (11) has the energy spectrum $\epsilon(k) = k^2/2m_e \pm \lambda \frac{k_z^2}{m_e L}\sqrt{k_x^2 + k_y^2}$. Substituting this spectrum to Ω potential we find the correction to the number of electrons in the crystal $\Delta N_{SO} = V\lambda^2 L^{-2} k_F^5/5\pi^2$. The found correction has, evidently, surface origin. So the order of such correction will be the same in a nanocrystal of any shape with the characteristic size L. This correction turns out to be weaker than the surface correction, proportional to L^{-1}, but may be comparable with the edge corrections.

The numerical calculations of the energy states in many-electron quantum dots are complicated enough problem because of the exponential increasing of the number of energy states, included in the Hamiltonian matrix, with the growing number of electrons. At the same time the considered approach, based on the expanding of thermodynamic quantities in powers of size, allows to get simple estimations without complex calculations.

Acknowledgements

This work was financially supported by the Russian Foundation for Basic Researches (grant 00-02-17658) and the State Program of Russian Federation "Physics of Solid State Nanostructures".

References

[1] E. L. Nagaev, *Usp. Fiz. Nauk* **162**, 49 (1992).
[2] E. M. Baskin and M. V. Entin, *JETP Lett.* **70**, 520 (1999).
[3] M. V. Entin and M. M. Mahmoodian, *JETP Lett.* **73**, N3 (2001).
[4] F. T. Vas'ko, *JETP Lett.* **30**, 541 (1979).
[5] Yu. A. Bychkov and E. I. Rashba, *JETP Lett.* **39**, 78 (1984).

9th Int. Symp. "Nanostructures: Physics and Technology"
St Petersburg, Russia, June 18–22, 2001

Ballistic conductance of a quantum sphere

J. Brüning†, V. A. Geyler‡, *V. A. Margulis*‡ and M. A. Pyataev‡
† Institut für Mathematik, Humboldt-Universität zu Berlin,
Unter den Linden 6, D-10099 Berlin, Germany
‡ Institute of Physics and Chemistry, Mordovian State University,
430000, Saransk, Russia

Abstract. The conductance of a quantum sphere with two one-dimensional wires attached to it is investigated. An explicit form for the conductance as a function of the chemical potential is found from the first principles. The form and positions of the resonance maxima on the plot of the conductance are studied.

Introduction

The aim of this paper is the theoretical study of the ballistic electron transport of a nanodevice consisting of a sphere and two wires attached to the sphere. We consider an idealized model in which the wires are taken to be one-dimensional. This crucial simplification is based on the possibility to describe the electron motion in nanowires only by means of longitudinal part of wave functions. To join the wave functions in the wires with those in the sphere we use boundary conditions at points of gluing the wires to the sphere. These boundary conditions are similar to those in the zero-range potential theory and lead to appearance of phenomenological parameters like the scattering length for a zero-range potential [1]. A useful mathematical formalization of the approach considered here is founded on the Krein resolvent formula from the self-adjoint operator theory and gives the scattering matrix in terms of the renormalized Green functions for the free Hamiltonians on the sphere and in the wires.

1. Boundary conditions and scattering matrix

We consider a wire $\mathbf{R}_j^+$ $(j = 1, 2)$ as the semi-axis $x \geq 0$. The wire $\mathbf{R}_j^+$ is attached to the sphere $\mathbf{S}$ ($\mathbf{S}$ has the radius R) by gluing the point 0 from $\mathbf{R}_j^+$ to a point q_j from $\mathbf{S}$. Denote by H_0 the electron Hamiltonian on $\mathbf{S}$, which coincides with $(2m^*R^2)^{-1}\mathbf{L}^2$, where $\mathbf{L}$ is the angular momentum operator and m^* is the effective mass. A wave function f of the device consists of three parts: f_0, f_1, f_2, where f_0 is a function on $\mathbf{S}$, and f_j $(j = 1, 2)$ is a function on $\mathbf{R}_j^+$. Let $r(q, q')$ be the geodesic distance between points q and q' on the sphere $\mathbf{S}$. Since we are going to use boundary conditions of the zero-range potential theory, we must consider the function f_0 having the following asymptotics near the points q_j [1]:

$$f_0(x) = a_j(f_0) \ln r(x, q_j) + b_j(f_0) + o(1), \tag{1}$$

where $a_j(f_0)$ and $b_j(f_0)$ are complex numbers; they play the role of the boundary values for the function f_0. As to the functions f_j, the role of their boundary values are played, as usual, by $f_j(0)$ and $f_j'(0)$. For reasons of space we shall consider here only the boundary

conditions of the Neumann type; the most general form of these conditions is given by the expressions

$$\begin{cases} b_j(f_0) = \sum\limits_{k=1}^{2} \left[\beta_{jk} a_k(f_0) + \alpha_{jk} f_k(0)\right], \\ f_j'(0) = \sum\limits_{k=1}^{2} \left[\bar{\alpha}_{jk} a_k(f_0) + \gamma_{jk} f_k(0)\right]. \end{cases} \tag{2}$$

Here the parameters α_{jk}, β_{jk} and γ_{jk} forms 2×2-matrices A, B, and C, respectively, such that the 4×4-matrix

$$P = \begin{bmatrix} B & A \\ A^* & C \end{bmatrix}$$

is Hermitian. Let $\widetilde{G}_0(q, q'; E)$ be the renormalized Green function of H_0, i.e., the function obtained from the Green function $G_0(q, q'; E)$ by extracting the singular term $(m^* R^2/\pi\hbar^2) \ln r(q, q',)$. Denote by $Q_0(E)$ the Krein $\mathcal{Q}$-matrix [1]; this is a matrix with the elements $Q_0^{jk}(E) = G_0(q_j, q_k; E)$, if $j \neq k$, and $Q_0^{jk}(E) = \widetilde{G}_0(q_j, q_k; E)$, if $j = k$. Using the explicit form of G_0 we can show that

$$Q_0^{11}(E) = Q_0^{22}(E) = -\frac{m^*}{\pi\hbar^2}\left[\psi\left(\frac{1}{2} + t(E)\right) - \frac{\pi}{2}\mathrm{tg}\,(\pi t(E)) - \ln(2R) + C_E\right], \tag{3}$$

where $\psi(x)$ is the logarithmic derivative of the Γ-function, C_E is the Euler constant, and $t(E) = (2\hbar)^{-1}\sqrt{\hbar^2 + 2m^* R^2 E}$. The non-diagonal elements of $Q_0(E)$ have the form

$$Q_0^{12}(E) = Q_0^{21}(E) = -\frac{m^*}{2\hbar^2}\frac{1}{\cos(\pi t(E))}\mathcal{P}_{-\frac{1}{2}+t(E)}\left(-\cos(r_{12}/R)\right), \tag{4}$$

where $\mathcal{P}_\nu(x)$ is the Legendre function and $r_{12} = r(q_1, q_2)$. The transition amplitudes $S_{jk}(E)$ from the channel $\mathbf{R}_j^+$ to $\mathbf{R}_k^+$ at the energy level E and reflection amplitudes $S_{jj}(E)$ in the channel $\mathbf{R}_j^+$ forms the scattering matrix on the sphere $S(E)$. Using the Krein resolvent formula we can find as $S(E)$:

$$S = \left[\frac{i\hbar^2}{m^*}k + C + A^*\left(Q_0(E) - B\right)^{-1} A\right]\left[\frac{i\hbar^2}{m^*}k - C - A^*\left(Q_0(E) - B\right)^{-1} A\right]^{-1} \tag{5}$$

(here $k = \sqrt{2m^* E}/\hbar$ is the electron wave vector). Eq. (5) shows that the matrix B is just a matrix of parameters for a zero-range perturbation of H_0 at the points q_j; therefore, to avoid effects of non-locality we must choose B in a diagonal form: $\beta_{jk} = \delta_{jk}\beta_j$. It is known that the diagonal element β_j is expressed in terms of the scattering length $\lambda_j^{(0)}$ on the zero-range potential at the point q_j as follows: $\beta_j = -m^* \ln(\lambda_j^{(0)})/\pi\hbar^2$. The matrix C has a similar meaning, namely, C is a matrix of parameters for a zero-range perturbation of the free Hamiltonians in the wires. Thus, we must suppose C to be diagonal with the diagonal elements $\gamma_j = -m^*\lambda_j^{(1)}/\hbar^2$ where $\lambda_j^{(1)}$ is the scattering length for the zero-range potential at the point 0 in the wire $\mathbf{R}_j^+$. As to the matrix A, it is responsible for the transmission from the wires to the sphere. Indeed, if $A = 0$, then the transition coefficient $|S_{12}|^2 = |S_{21}|^2 = 0$. Eqs. (2) show that in the case of $\alpha_{jk} \neq 0$ for $j \neq k$ there are non-trivial boundary conditions which connect the wire $\mathbf{R}_j^+$ with the point q_k; therefore, we must suppose A to be diagonal, too. Moreover, the matrix $S(E)$ is symmetric only in the case of real elements $\alpha_{jj} \equiv \alpha_j$.

It is convenient to express these elements in terms of parameters λ_j having the dimension of length: $\alpha_j^2 = (m^*)^2\lambda_j/\hbar^2$. Thus, in our model the scattering on the sphere is described by means of the six real parameters α_j, β_j, γ_j. Note, that in the case of a two-dimensional system, the zero-range perturbation vanishes in the limit $\beta_j \to \infty$; Eq. (5) shows that in this limit $S_{12}(E) \to 0$, as might be expected. We stress that the idealization of the one-dimensional wire is possible only in the case that the cross-section of the real wire is much less than the typical sizes of the system. In particular, our model works only in the case of relatively large distance r_{12}; namely, we shall suppose r_{12} is vastly larger than the Fermi wave length of an electron in the wire. Nevertheless, we can get the proper limit ($|S_{12}(E)| \to 1$ as $r_{12} \to 0$) using more general boundary conditions than those in (2).

2. Results and discussion

For reasons of symmetry we shall suppose $\gamma_1 = \gamma_2 \equiv \gamma$ and denote $\lambda_j^{(1)}$ simply by λ. In this case Eq. (5) gives the transition coefficient $T_{12}(E) = |S_{12}(E)|^2$ in the following form:

$$T_{12}(E) = \frac{(16k)^2\lambda_1\lambda_2\,|\widetilde{Q}_0^{12}|^2}{\left|4\lambda_1\lambda_2k^2 - 2ik(4-ik\lambda)(\lambda_2\widetilde{Q}_0^{11} + \lambda_1\widetilde{Q}_0^{22}) - (4-ik\lambda)^2\det\widetilde{Q}\right|^2}, \qquad (6)$$

where $\widetilde{Q}(E)$ is the dimensionless $\mathcal{Q}$-matrix: $\widetilde{Q}(E) = (\hbar^2/m^*)(Q(E) - B)$. Using Eq. (6) we can find the conductance G as a function of the chemical potential μ at temperature T. Namely, according to the Landauer–Büttiker formula

$$G(\mu, T) = \frac{2e^2}{\hbar^2}\int_0^\infty T_{12}(E)\left(-\frac{\partial f_0}{\partial E}\right)dE, \qquad (7)$$

where f_0 is the Fermi distribution function.

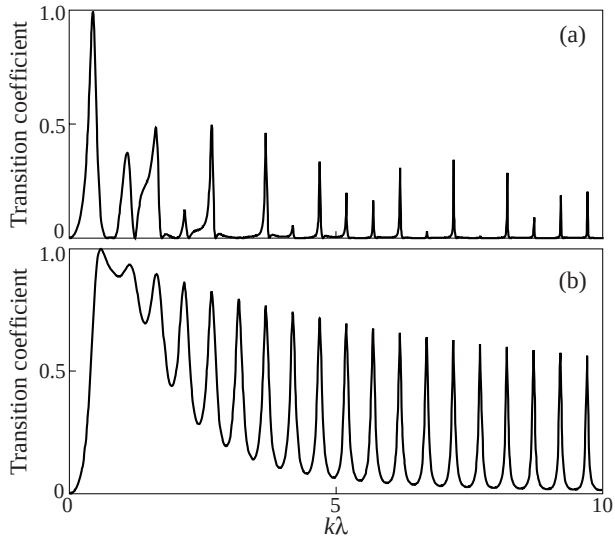

Fig. 1. Transition coefficient T_{12} as a function of $k\lambda$ ($k = \sqrt{2m^*E}/\hbar$): (a) case of a generic position for wires ($r_{12} = \sqrt{\pi}R$); (b) case of an antipodal position for wires ($r_{12} = \pi R$).

In the discussion, we restrict ourselves to the case of $\lambda_j = \lambda_j^{(0)} = \lambda$. The quantity T_{12} as a function of E has a series of sharp splash-like maxima, their positions are determined by the zeroes of $\det \widetilde{Q}(E)$, i.e., by the levels of the zero-range perturbation of H_0 with parameters β_j. On the other hand, if $r_{12} \neq \pi R$, then $\det \widetilde{Q}(E)$ has poles of the second order at the points of the spectrum of H_0, i.e., at the energy levels $E_l = \hbar^2 l(l+1)/2m^* R^2$ of an electron on the sphere **S**, and Eq. (7) shows that $T_{12}(E_l) = 0$ (see Figure 1(a)). It follows from the numerical analysis that T_{12} depends only slightly on the parameters β and γ.

If the points q_1 and q_2 are antipodal ($r_{12} = \pi R$), then the behavior of T_{12} at points E_l changes drastically. Indeed, at $E = E_l$ the numerator and the denominator in Eq. (7) have a pole of the same order, hence, $T_{12}(E_l)$ does not vanish. Therefore, the oscillation minima are not positioned on abscissa but they lay on a curve of the form $T_{12} = k(ak^2 + bk + c)^{-1}$ (Figure 1(b)). In the region $l \gg 1$ the oscillation period Δk is practically constant: $\Delta k = R^{-1}$. A numerical analysis of the conductivity at finite temperature shows that with a rise of temperature the peaks are smoothed and their amplitudes are lowered.

Acknowledgements

This work was financially supported by the DFG, SFB 288, RFBR and the Russian Ministry of Education.

References

[1] S. Albeverio, F. Gesztesy, R. Høegh-Krohn and H. Holden. *Solvable models in quantum mechanics*. Springer–Verlag: Berlin etc., 1988.

[2] V. A. Geyler, V. A. Margulis and I. I. Chuchaev. *Phys. Solid State*. **37**, 455 (1995).

9th Int. Symp. "Nanostructures: Physics and Technology"
St Petersburg, Russia, June 18–22, 2001

Spin coherence in semiconductor nanostructures

X. Marie†, A. Jbeli†, M. Paillard†, T. Amand† and J. M. Gérard‡
† Laboratoire de Physique de la Matiere Condensee, INSA-CNRS
135, Avenue de Rangueil, 31077 Toulouse cedex, France
‡ France Telecom, 196 avenue H. Ravera 92220 Bagneux, France

Abstract. We have studied the spin dynamics in self-organized InAs/GaAs quantum dots (QD) by time-resolved photoluminescence performed under strictly resonant excitation. We demonstrate that the carrier spins in these nanostructures are totally frozen on the exciton lifetime scale.

Introduction

A recent challenge in solid state physics is based on the manipulation of the electronic spin in order to build elementary quantum gates. The most important requirement for the operation of such future devices is a very long spin coherence time. Semiconductor QD appear as good candidates from this point of view. The discrete energy levels in artificial atoms like semiconductor quantum dots and the corresponding lack of energy dispersion lead indeed to a predicted modification of the spin relaxation dynamics compared to bulk or two-dimensional structures. Extensive experimental and theoretical works in the latter systems have identified the main carrier spin-flip mechanisms, which rely on exchange interaction, mixing between conduction and valence band states through spin-orbit coupling leading to motional narrowing effects in materials without inversion symmetry [1, 2]. In QD, all these processes have to be reconsidered since the wavevector k is no more a good quantum number [3, 4]. The absolute lack of energy states between QD energy levels is expected to suppress not only the elastic processes of spin relaxation but also the inelastic ones such as phonon scattering. The expected long spin relaxation time makes thus QD structures promising candidate for the implementation of spintronic and quantum information processing devices [5, 6]. Recent optical pumping experiments have indeed given good indications of a slowing down of the carrier spin relaxation processes in QD compared to bulk or quantum wells (QW) structures. The spin orientation in Wurtzite-type nanocrystals has been studied both in continuous wave (cw) and in time-resolved experiments [3, 7]. These investigations have revealed the QD size dependence of the spin polarization decay time. In naturally formed GaAs single QD, Gammon *et al.* deduced from cw photoluminescence (PL) experiments that the spin-flip scattering rate was lower than the radiative recombination rate of the ground state [8]. Similar experiments performed in self-organized InAs/GaAs QD lead to the same qualitative conclusion [9]. Recently, Gotoh *et al.* reported on an exciton spin relaxation time of about 900 ps in zero-dimensional InGaAs quantum disks, which is almost twice as long as the radiative recombination lifetime [10]. However most of these studies have been performed in non-resonant excitation conditions i.e. the QD polarization dynamics is studied when the spin-polarized carriers are photogenerated in the barrier. The observed spin polarization dynamics of the QD ground state is then the result of all the spin relaxation mechanisms which have occurred in the bulk barrier, in the QD excited state and finally in the QD ground state, including any spin flip scattering due to the energy relaxation process itself. In order to study the intrinsic spin dynamics, a time-resolved

strictly resonant excitation of the QD ground state is highly desirable [11]. Note that the free exciton radiative and the spin relaxation times in semiconductor QW have only been identified in such clear resonant excitation conditions [2, 12, 13]. We present here a detailed time-resolved investigation of the exciton optical alignment dynamics in self-organized InAs/GaAs QD performed under strictly resonant excitation. These experiments evidence a spin relaxation quenching at low temperature.

1. Samples and experimental setup

The investigated structure, grown by molecular beam epitaxy on a (001) GaAs substrate, consists of 5 InAs QD planes embedded in a GaAs λ planar cavity, inserted between two GaAs/AlAs Bragg mirror [14]. The QD layers are localized in the vicinity of the electromagnetic field antinodes into the microcavity which operates in the weak coupling regime. The QDs are obtained after a nominal deposition of 2.2 InAs monolayers and a 21 s growth interruption. These growth conditions lead to a QD density of $\sim 4 \times 10^{10}$ cm^{-2} per array, and to a QD emission centered around 1.15 eV with a Full Width at Half Maximum (FWHM) of $\sim$60 meV. A variation of the cavity thickness along the radial direction of the wafer allows us to tune the cavity resonance by moving the laser beam across the sample surface. The microcavity is designed so that the cavity mode (FWHM $\sim$3 meV) can be tuned in the energy range of the QD ground state emission. Inserting the QD in a microcavity brings two major improvements with respect to bare QD: (i) the filtering operated by the optical mode results in a reduction of the energetic inhomogeneity of the studied QD (ii) the narrowing of the radiation pattern emitted by the microcavity allows us to collect the QD emission efficiently in spite of the very small acceptance solid angle ($\sim 10^{-3}$ steradians) of the up-conversion detection set-up we have used [15].

The sample is excited by 1.5 ps pulses generated by an Optical Parametric Oscillator, synchronously pumped by a mode-locked Ti-doped sapphire laser. The time-resolved PL is then recorded by up-converting the luminescence signal in a $LiIO_3$ non-linear crystal with the picosecond pulses generated by the Ti:Sa laser [11, 15]. The time-resolution is limited by the laser pulse-width ($\sim$1.5 ps) and the spectral resolution is about 3 meV.

The linear and the circular polarization degrees of the luminescence are defined as $P_{\mathrm{Lin}} = (I^X - I^Y)/(I^X + I^Y)$ and $P_C = (I^+ - I^-)/(I^+ + I^-)$ respectively. Here I^X (I^Y) and I^+ (I^-) denote respectively the $X(Y)$ linearly polarized and the right (left) circularly polarized luminescence components (X and Y are chosen parallel to the [110] and [1$\bar{1}$0] sample directions). The experiments in section 2 and 3 have been performed at low excitation power ($\sim$7 W cm^{-2}) which corresponds to an average estimated density of photoexcited carriers less than one electron-hole pair per QD. In the following, the laser excitation energy is set to 1.137 eV; it coincides with both the cavity mode and a given QD family ground state energies. The detection energy is strictly the same as the excitation one [16].

Let us recall that in a (001)-grown type I quantum well, the relevant symmetry is D_{2d}. If the growth direction Oz is chosen as the quantization axis for the angular momentum, the conduction band is s-like, with two spin states $s_{e,z} = \pm 1/2$; the upper valence band is split into a heavy-hole band with the angular momentum projection $j_{hh,z} = \pm 3/2$ and a light-hole band with $j_{lh,z} = \pm 1/2$ at the center of the Brillouin zone. The heavy-hole exciton states can be described using the basis set $|J_z\rangle = \left|j_{hh,z}, s_{e,z}\right\rangle$, i.e.$|J_z = 1\rangle \equiv |3/2, -1/2\rangle$, $|J_z = -1\rangle \equiv |-3/2, 1/2\rangle$, $|J_z = 2\rangle \equiv |3/2, 1/2\rangle$, $|J_z = -2\rangle \equiv |-3/2, -1/2\rangle$ (J_z represents the total angular momentum projection of the exciton state on the quantization axis). This basis set is diagonal with respect to the exciton exchange interaction and the

twofold degenerate optically-active $J_z = |\pm 1\rangle$ states are split from the non-optically-active $J_z = |\pm 2\rangle$ states by the electron-hole exchange interaction energy [17].

In QD structures, the symmetry of the system is lowered and the exchange interaction is thus no longer isotropic [18]. The anisotropic exchange interaction splits the $|\pm 1\rangle$ radiative doublets into two eigenstates labeled $|X\rangle = (|1\rangle + |-1\rangle)/\sqrt{2}$ and $|Y\rangle = (|1\rangle - |-1\rangle)/(i\sqrt{2})$, linearly polarized along the [110] and [1$\bar{1}$0] directions respectively. Cw single dot spectroscopy experiments have clearly evidenced these two linearly polarized lines in self-organized InGaAs QD with an exchange splitting of $\hbar\omega \sim 150$ meV [9]. This anisotropic exchange splitting may originate from QD elongation [8] and/or interface optical anisotropy [18, 20].

2. Linear polarization dynamics at low temperature

Figure 1(a) displays the time-resolved PL intensity with polarization parallel (I^X) and perpendicular (I^Y) to the linearly polarized σ^X excitation laser ($T = 10$ K) (the initial peak on the I^X luminescence components intensity close to $t = 0$ corresponds to backscattered laser light from the sample surface). The corresponding linear polarization ($P_{\rm Lin}$) kinetics is also plotted. The PL intensity decays with a characteristic time $\tau_{rad} \sim 800$ ps. After the pulsed excitation, the QD emission exhibits a strong linear polarization ($P_{\rm Lin} \sim 0.75$) which remains strictly constant within the experimental accuracy during the exciton emission (i.e. over ~2.5 ns). This behavior differs strongly from the exciton linear polarization dynamics in bulk or type I QW structures, characterized by a linear polarization decay time of a few tens of picoseconds [1, 15]. In the latter structures, it has been demonstrated that any scattering mechanism (phonon, exchange interaction, electron and/or hole single particle spin relaxation) results in the destruction of the coherent superposition between the $|1\rangle$ and $|-1\rangle$ components of the linear exciton [15]. The experimental observation of a QD exciton linear polarization which does not decay with time is the proof that neither the electron nor the hole spin relax on the exciton lifetime scale. It shows also that the exciton spin coherence between $|1\rangle$ and $|-1\rangle$ states is maintained during the whole exciton lifetime. From our observation, we can infer that the exciton spin relaxation time is longer than 20 ns, i.e. at least 25 times larger than the radiative lifetime.

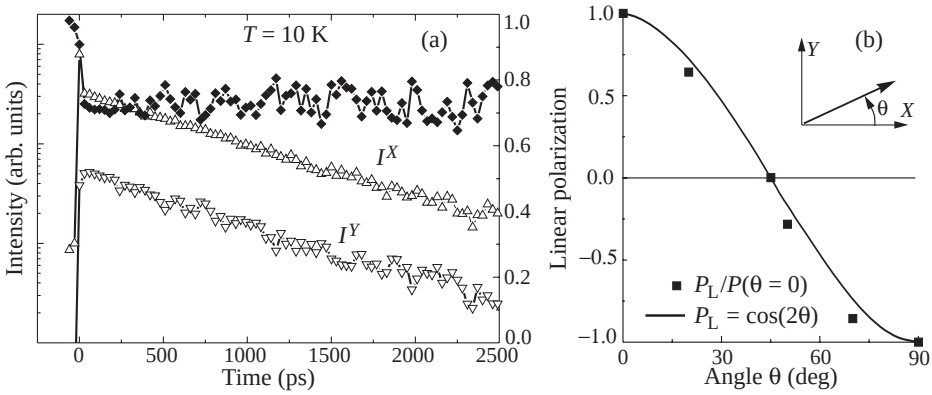

Fig. 1. (a) Time resolved PL intensity with polarization parallel I^X (Δ) and perpendicular I^Y (∇) to the linearly polarized (σ^X) excitation laser ($T = 10$ K); the time evolution of the corresponding linear polarization $P_{\rm Lin}$ is also displayed. (b) Dependence of the luminescence linear polarization on the angle of the excitation laser field with respect to the [110] direction (see text).

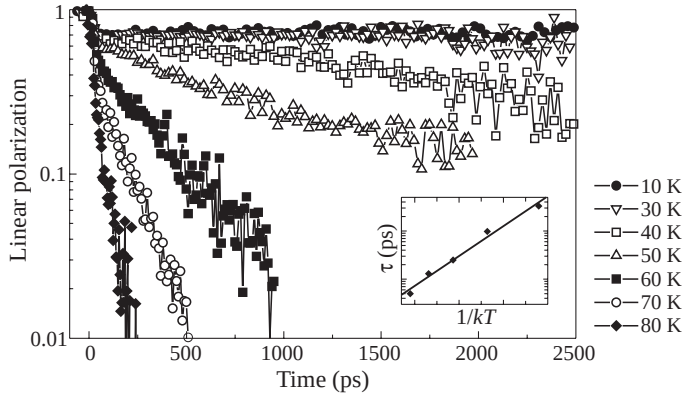

Fig. 2. Temperature dependence of the linear polarization dynamics (the excitation laser is σ^X polarized). Inset: P_{Lin} decay time as a function of $1/(K_B T)$.

Figure 2(b) displays the dependence of the luminescence linear polarization on the angle of the excitation laser field with respect to the [110] direction (see the inset).

The linearly polarized luminescence components are still detected along the [110] (X) and [1$\bar{1}$0] (Y) directions. As expected for exciton eigenstates polarized along the [110] and [1$\bar{1}$0] directions, the linear polarization follows a simple law with the angle θ given by:

$$P_{\mathrm{Lin}}(\theta) = \frac{I^X - I^Y}{I^X + I^Y} = \frac{\cos^2\theta - \sin^2\theta}{\cos^2\theta + \sin^2\theta} = \cos 2\theta.$$

A circularly polarized excitation should lead to the observation of P_{Lin} beats at the pulsation corresponding to the exchange splitting. After about 15 ps, the time required for the QD PL signal to overcome the backscattered laser light, we do not observe any linear or circular polarization and as a consequence any beat in this excitation configuration. This absence of polarization is interpreted as a consequence of the exchange splitting energy statistical fluctuations among the QD family selected by the cavity mode.

3. Temperature dependence of the linear polarization dynamics

Figure 2 presents the dependence of the exciton PL linear polarization dynamics as a function of the lattice temperature. A clear temporal decay of P_{Lin} is observed above 30 K: the linear polarization decay time drops from ~3500 ps at 40 K down to 50 ps at 80 K with an activation energy $E_a = 30 \pm 1$ meV (see the inset in Fig. 2). This very strong P_{Lin} temperature dependence can be due either to any electron, hole, exciton spin-flip scattering or any spin-conserving scattering processes which break the coherent superposition of the linearly photogenerated excitons $|X\rangle = (|1\rangle + |-1\rangle)/\sqrt{2}$ [21]. To the best of our knowledge there is no available theory on the exciton spin-flip and its temperature dependence in QD. However one can speculate that the depolarization mechanism is due to hole scattering to higher QD excited states since the measured activation energy is close to the energy splitting between the ground and first excited heavy-hole state and to the InAs LO phonon energy [22].

4. Excitation intensity dependence of the linear polarization dynamics

All the results presented up to now have been obtained at low excitation intensity (i.e. when the number of photo-generated electron-hole pairs is small compared to the num-

ber of QDs). Figure 3(a) displays the linear polarization dynamics under resonant linear polarization excitation for three excitation intensities. We note that the linear polarization never decays with time but the amplitude of this polarization decreases when the excitation intensity increases. This effect is due to the photo-generation of biexciton states. Under linearly polarized excitation, a quantum dot in which the ground state is already occupied by an exciton $|X\rangle = (|1\rangle + |-1\rangle)/\sqrt{2}$ can absorb another photon, which yields the photogeneration of a biexciton state labeled $(|XX + YY\rangle)/\sqrt{2}$. This biexciton state can emit σ^X or σ^Y photons with the same probability (the QDs occupied only by an exciton will still emit fully polarized σ^X luminescence). As a consequence, the amplitude of the measured linear polarization decays when the number of photogenerated biexciton states increases. We emphasize that the spectral resolution of our setup (∼3 meV) does not allow to resolve separately the exciton and the biexciton emission lines.

This interpretation in terms of biexciton photogeneration is confirmed by the observed dependence of the total luminescence intensity on the excitation intensity displayed in Fig. 3(b). We observe that the luminescence intensity increases linearly with the excitation intensity at low excitation ($P < 10\,\mathrm{W\,cm^{-2}}$). In this regime when the number of photogenerated electron-hole pairs is small compared to the number of QDs, the photogeneration of biexciton states is negligible and the linear polarization does not depend on the excitation intensity. At higher excitation intensities ($P > 10\,\mathrm{W\,cm^{-2}}$), we note in Fig. 3(b) a clear saturation of the luminescence intensity and a simultaneous drop of the measured linear polarization value. The non-linear dependence of the luminescence intensity comes from

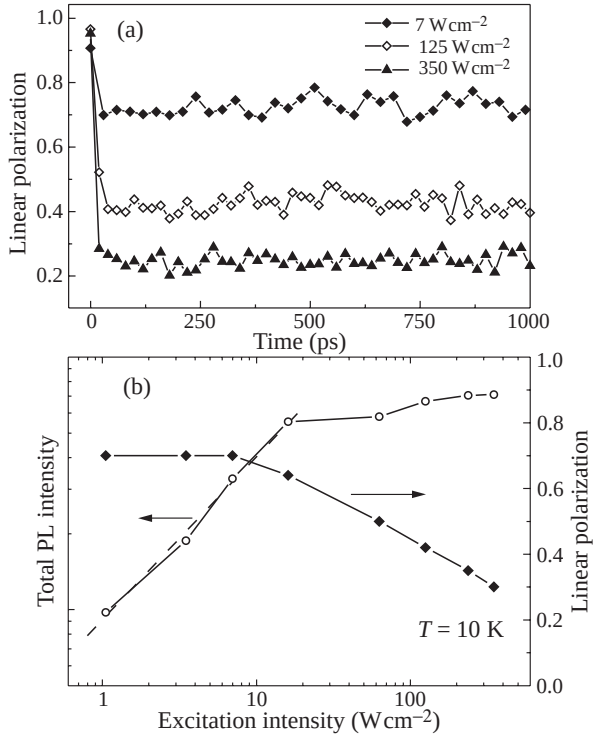

Fig. 3. (a) Linear polarization dynamics for three excitation laser powers ($T = 10$ K). (b) Total luminescence intensity and linear polarization as a function of the excitation power.

the saturation of the ground state absorption due to the photogeneration of biexciton states in most of the analysed QDs.

5. Conclusion

We have studied the linear PL polarization dynamics in self-organized QD under strictly resonant excitation. We never observe at low temperature any measurable temporal decay of the linear luminescence polarization regardless of the excitation intensity. This evidences a complete spin relaxation quenching in these zero-dimensional structures. This contrasts with the clear spin relaxation previously observed in non-resonant excitation conditions [10, 23]. The main difference between these two kinds of experiments relies on the higher energy carrier state occupation, including barrier, wetting layer and QD excited states which may induce the spin flip of the QD ground state by Coulomb exchange. The role of the carrier-carrier interaction in zero dimensional systems should be investigated theoretically to fully understand this difference.

The long spin coherence make these nanostructures an ideal candidate for the implementation of an elementary quantum gate in a solid state system.

Acknowledgments

We thank V. Thierry-Mieg for the sample growth. We are grateful to V. K. Kalevich, E. L. Ivchenko, K. V. Kavokin for fruitful discussions.

References

[1] *Optical Orientation*, eds F. Meier and B. Zakharchenya, *Modern Problems in Condensed Matter Sciences* Vol. 8 (North-Holland, Amsterdam, 1984).
[2] M. Z. Maialle et al., *Phys. Rev. B* **47**, 15 776 (1993).
[3] M. Chamaro et al., *J. of Lumin.* **70**, 222 (1996).
[4] A. V. Khaetskii et al., *Physica E* **6**, 470 (2000).
[5] R. Fiederling et al., *Nature* **402**, 787 (1999).
[6] A. Imamoglu et al, *Phys. Rev. Lett.* **83**, 4204 (1999).
[7] J. A. Gupta et al., *Phys. Rev. B* **59**, R10 421 (1999).
[8] D. Gammon et al., *Science* **273**, 87 (1996).
[9] M. Bayer et al., *Phys. Rev. Lett.* **82**, 1748 (1999).
[10] H. Gotoh et al. *Appl. Phys. Lett.* **72**, 1341 (1998).
[11] M. Paillard et al., *Appl. Phys. Lett.* **76**, 76 (2000).
[12] B. Deveaud et al., *Phys. Rev. Lett.* **67**, 2355 (1991).
[13] A. Vinattieri et al., *Phys. Rev. B* **50**, 10 868 (1994).
[14] J. M. Gerard et al., *Phys. Rev. Lett.* **81**, 1110 (1998).
[15] X. Marie et al., *Phys. Rev. Lett.* **79**, 3222 (1997).
[16] We did not notice any change in the presented effect when the excitation/detection energy was set to another value within the QD ground state energy distribution.
[17] T. Amand et al., *Phys. Rev. Lett.* **78**, 1355 (1997).
[18] E. L. Ivchenko, *Pure Appl. Chem.* **67**, 463 (1995); R. I. Dzhioev et al., *Phys. Solid State* **40**, 790 (1998).
[19] S. Hameau et al., *Phys. Rev. Lett.* **83**, 4152 (1999).
[20] R. I. Dzhioev et al., *Phys. Rev. B* **56**, 13 405 (1997); C. Gourdon et al., *Phys. Rev. B* **46**, 4644 (1992).
[21] M. Paillard et al., *Phys. Rev. Lett.* **86**, 1634 (2001).
[22] S. Sauvage et al., *Phys. Rev. B* **60**, 15 589 (1999).
[23] M. Paillard et al., *Phys. Stat. Sol.* (b) **221**, 71 (2000).

9th Int. Symp. "Nanostructures: Physics and Technology"
St Petersburg, Russia, June 18–22, 2001

Suppression of Overhauser effect in the exciton-nuclear spin system of GaAs quantum dot

V. L. Korenev†, I. A. Merkulov†, D. Gammon‡, Al. L. Efros‡,
T. A. Kennedy‡, M. Rosen‡, D. S. Katzer‡ and S. W. Brown§
† Ioffe Physico-Technical Institute, St Petersburg, Russia
‡ Naval Research Laboratory, Washington DC 20375, USA
§ NIST, Gaithersburg, USA

The spin of a single electron localized on monolayer-high fluctuation of quantum well width (quantum dot) interacts with macroscopic number ($\sim 10^5$) of nuclear spins. As a result the tight-binding electron-nuclear spin system (ENSS) develops in nanostructures [1, 2]. Due to rather long spin relaxation time the nuclear spin could be used (at least in principle) for information storage and to control the electron spin. For example, the hysteresis phenomena have been found in ENSS of quantum wells [3].

Here we show that the presence of a hole in the quantum dot (i.e. exciton instead of a single electron) strongly affects the magnetic properties of the unified exciton-nuclear spin system (ExNSS). In spite of the absence of contact interaction between hole and nuclei the hole affects the ExNSS properties via the exchange coupling with electron. The interaction splits the quartet of exciton spin levels into pair of optically allowed states (bright excitons: electron and hole spins are antiparallel) and pair of optically forbidden states (dark excitons: electron and hole spins are parallel) [4]. This splitting (δ_0) suppresses the Overhauser effect. Indeed, an amount of energy δ_0 should be compensated to satisfy the energy conservation law under mutual electron-nuclear spin flip transitions. Under these conditions the role of dipole–dipole interactions between nuclei becomes anomalously large in comparison with bulk GaAs. This interaction destroys the nuclear polarization and acts as a leakage of nuclear spin. The external magnetic field eliminates the leakage. However, as a result of suppression of Overhauser effect the characteristic field value restoring the nuclear polarization is two orders in magnitude larger than that for the bulk GaAs.

Near-field magneto-photoluminescence spectroscopy [5, 6] has been used to study the ExNSS in single GaAs quantum dot. This method allows one to measure the splitting of exciton radiative levels and its magnetic field dependence under circularly polarized excitation directly. It is found that the splitting is minimal when external field compensates the internal nuclear magnetic field $B_{\mathrm{N}} = 1.3$ T which is proportional to the nuclear polarization ($\sim$65%). This shifts the magnetic field dependence as a whole by the B_{N} value. The exception takes place in low magnetic fields $B < 1$ kG where the nuclear polarization is strongly reduced (the splitting is minimal for $B = 0$, too). The field range of the reduction is 300 times larger than that for bulk GaAs ($\sim$3 G [7]).

To explain the unexpected behavior of ExNSS we have deduced the average nuclear spin polarization determined by the balance between dynamical nuclear polarization (Overhauser effect) and depolarization (leakage). These processes are governed by fluctuations of the electron and nuclear polarization from their average values.

Polarization of the nuclear spins by optically oriented excitons arises from the "flip/flop" processes involving the simultaneous spin flip of a nucleus and electron. The electronic spin

flip causes the exciton to transform between bright and dark states and requires emission or absorption of energy ($\delta_0 \approx 100\,\mu$eV) because of the large mismatch in electronic and nuclear Zeeman energies. Therefore some additional "assisting" process is necessary to satisfy energy conservation (e.g. emission or absorption of a photon or a phonon). Transition rates for flip/flop transitions calculated in second order perturbation theory are (δ_s^2/δ_0^2) smaller than those for the assisting processes with no spin flips, where $\delta_s \propto A/\sqrt{N}$ (A is hyperfine constant, N number of nuclei in the dot) is the splitting of electron spin states in a random nuclear magnetic field. If the dark exciton lifetime (τ_d) is much longer than the bright exciton lifetime (τ_b), nuclear polarization is determined by spin–flip assisted radiative recombination of the dark excitons [8]. We calculate the nuclear spin polarization rate to be $T_e^{-1} = (\delta_s^2/15N\delta_0^2)\tau_b^{-1} \approx 2.5\,s^{-1}$ for $N \sim 10^5$ nuclei in the quantum dot [5] and $\tau_b \sim 0.1$ ns [9]. The estimation is in agreement with experiment ($T_{exp} \approx 3$ s).

Coupling of neighboring nuclear spins through the dipole–dipole interaction leads to the leakage of nuclear polarization. In a magnetic field B larger than the dipole field, $B_L \sim 1.5$ G, the energy of the nuclear dipole–dipole interaction is not enough to drive the transition between two nuclear spin sublevels split by the Zeeman energy. However, fluctuations of the z-component of the hyperfine magnetic field of the electrons acting on the nuclei (the mean value of the electron field determines the Knight shift in NMR [10]) can provide the necessary energy, leading to depolarization of the total nuclear spin, even in a relatively strong magnetic field. Calculations show that the nuclear dipole-dipole interaction weakly mixes the wave functions of different nuclear spin projection states, of order B_L/B. Transitions between these mixed states are induced by the hyperfine magnetic field of the electrons acting on the nucleus during the exciton lifetime. The dark exciton plays the main role in this process because $\tau_d \gg \tau_b$. This leads to a nuclear spin depolarization with a rate calculated in second order perturbation theory to be $T_{e-dip}^{-1} = 0.06\tau_d(\delta_s/\hbar)^2(B_L/B)^2N^{-1}$. Increasing of external field eliminates the role of leakage of nuclear spin. The polarization rate (Overhauser effect) and leakage rate becomes comparable when $T_e = T_{e-dip}$, i.e. at $B = \sqrt{\tilde{\xi}}B_L$. Parameter $\sqrt{\tilde{\xi}} \approx (\delta_0\sqrt{\tau_d\tau_b}/\hbar)$ is much greater than 1 in the experimental conditions. The steady state value of a mean nuclear spin

$$\langle I_z\rangle = \frac{I(I+1)}{S(S+1)}\langle S_z^d\rangle\frac{B^2}{B^2+\tilde{\xi}B_L^2}.$$

Here I, S are the nuclear and electron spins. A good agreement with experiment takes place when polarization of dark excitons $\langle S_z^d\rangle = 0.2$ and $\sqrt{\tau_d\tau_b} = 3.5$ ns.

Thus, the nuclear spin polarization tracking the electron spin polarization of the dark exciton does not depend on external magnetic field except in the strongly depolarized region around zero applied field with a Lorentzian lineshape with width that is two orders of magnitude greater than in bulk GaAs.

Acknowledgements

This work was supported by DARPA/SPINS, ONR (Grant Number N00014-00-1-4076, 4059 ONRIFO LTR40769) U.S. Civilian Research & Development Foundation for the Independent States of the Former Soviet Union (CRDF), Award No. RP1-2252, and the Russian Foundation for Basic Research, Award No. 00-02-16991.

References

[1] G. P. Flinn et al. *Semicond. Sci. Technol.* **5**, 533 (1990).

[2] V. K. Kalevich, V. L. Korenev and O. M. Fedorova, *Pis'ma Zh. Eksp. Teor. Fiz.* **52**, 964 (1990).
[3] V. K. Kalevich and V. L. Korenev, *JETP Lett.* **56**, 253 (1992).
[4] E. I. Ivchenko and G. E. Pikus, *Superlattices and Other Heterostructures, Symmetry and Optical Phenomena* Springer-Verlag, Berlin, 1995.
[5] D. Gammon et al. *Phys. Rev. Lett.* **76**, 3005 (1996).
[6] S. W. Brown et al., *Phys. Rev B* **54**, R17 339 (1996).
[7] F. Meier and B. P. Zakharchenya (eds.), *Optical Orientation* North Holland, NY, 1984.
[8] Al. L. Efros, *Phys. Rev. B* **46**, 7448 (1992).
[9] D. Gammon et al., *Science* **273**, 87 (1996).
[10] A. Abragam, *The Principles of Nuclear Magnetism* Clarendon Press, Oxford, 1961.

9th Int. Symp. "Nanostructures: Physics and Technology"
St Petersburg, Russia, June 18–22, 2001

Injection of spin-polarized carriers from a ZnMnSe/CdSe semimagnetic superlattice into a non-magnetic ZnCdSe quantum well

Ya. V. Terent'ev†, A. A. Toropov†, S. V. Sorokin†, A. V. Lebedev†,
S. V. Ivanov†, P. S. Kop'ev†, I. Buyanova‡, W. M. Chen‡ and B. Monemar‡
† Ioffe Physico-Technical Institute, St Petersburg, Russia
‡ Department of Physics and Measurement Technology, University of Linköping, S-581 83 Linköping, Sweden

Abstract. We report on magneto-optical studies of spin injection from a ZnMnSe/CdSe semimagnetic short-period superlattice (SL) to a non-magnetic ZnCdSe quantum well (QW). The carriers are photo-generated in the semimagnetic SL, spin polarized via the effect of giant Zeeman splitting and then injected into the non-magnetic QW through a tunneling mechanism. Near 25% injection efficiency has been demonstrated at the magnetic field of 0.8 T and low temperature (1.8 K).

Recently there has been a growing interest in semiconductor devices based on precise manipulation of an electron spin rather than on controlling an electron charge [1]. Among the proposed device ideas are spin memory devices, spin transistors and spin quantum computers. For all such devices spin-polarized electron injection in semiconductor heterostructures is a necessary requirement. Until recently, the most successful realizations of the injection of spin-polarized electrons have implied the use of diluted magnetic semiconductors (DMS) [2–4]. Both II–VI semimagnetic semiconductors [2, 3] and III–V ferromagnetic semiconductors [4] were used to demonstrate efficient spin injection into a non-magnetic III–V semiconductor structure.

In this work we study the injection process of spin-polarized carriers from a ZnMnSe/CdSe semimagnetic short-period superlattice (SL) to a ZnCdSe/ZnSe non-magnetic quantum well (QW). The samples studied here are a modification of the structures containing a ZnSe/CdSe SL (with sub-monolayer (ML) CdSe insertions) and an attached ZnCdSe QW, whose transport and optical properties are known in detail [5]. Incorporation of a small amount of Mn in the SL barriers makes possible almost complete spin polarization of the miniband electrons and holes by an external magnetic field via the effect of giant Zeeman splitting [6] and allows magneto-optical investigations of the spin-polarized carrier injection into the non-magnetic QW.

Two samples studied in this work were grown by molecular beam epitaxy pseudomorphically on (001) GaAs substrates. They consist of a ten-period $Zn_{0.96}Mn_{0.04}Se$ (4nm)/CdSe (0.8 ML) DMS superlattice and an attached 7 nm thick $Zn_{0.75}Cd_{0.25}Se$ single QW (SQW) (the schematic drawing of the essential sample region is shown in Fig. 1). The first SL barrier adjoining the SQW is free of Mn, to avoid overlapping of the electron and hole wave functions in the non-magnetic QW with the DMS regions. The two samples differ in the thickness of the first ZnSe barrier. In sample A its thickness is enhanced a factor two as compared with other SL barriers (up to 8 nm). In sample B all SL barriers are 4 nm thick. The "SL+SQW" region is surrounded by thick $Zn_{0.93}S_{0.07}Se$ claddings lattice-matched to GaAs. Photoluminescence (PL) of the samples was measured in an external magnetic field up to 5 T in Faraday geometry at 1.8 K. Different linearly polarized lines of a cw Ar^+ laser

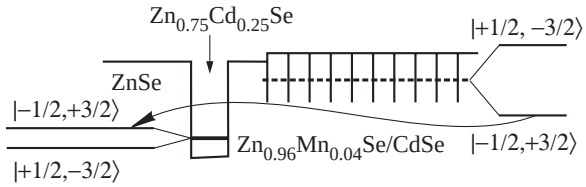

Fig. 1. Schematic drawing of the intrinsic region of the sample and a scheme of SQW and SL excitonic levels in a magnetic field.

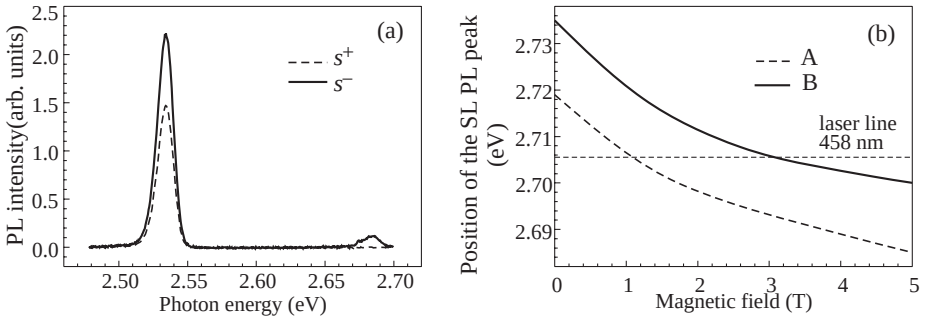

Fig. 2. (a) σ^+ and σ^- PL spectra measured in sample A at 5 T under 458 nm excitation. (b) Energy of the SL PL peak versus magnetic field for samples A (dashed curve) and B (solid curve).

were used for the PL excitation. The PL circular polarization was analyzed using a 1/4 plate followed by a linear polarizer.

Figure 2(a) shows the spectra of σ^+ and σ^- circular polarized PL measured at 5 T in sample A excited by a 458 nm laser line, i.e. above the fundamental band edge of the SL. There are two emission bands visible, attributed to the emission of localized heavy-hole excitons in the SL (2.685 eV) and the SQW (2.534 eV). The SL peak is almost completely σ^+ polarized, starting from small magnetic fields less than 1 T. Figure 2(b) demonstrates the SL PL peak energy versus magnetic field for both samples. The curves are identical, besides a small energy offset ($\sim$ 15 meV) which is due to a small difference in the nominal thickness of the CdSe layers between the samples. Both the PL shift and polarization are typical for the effect of giant Zeeman splitting of excitons, conventionally observed in Zn(Cd)MnSe based heterostructures [6].

For the SQW emission band, the magnetic-field-induced shift is negligibly small, which is expected for the non-magnetic QW. The dominant effect of the magnetic field is an increase in the PL circular polarization, the sign and the degree of polarization both depending on the wavelength of the exciting light. The polarization degree at the peak maximum versus magnetic field is plotted in Figs. 3(a) and (b) for samples A and B, respectively. The different curves correspond to excitation at 351 nm, 458 nm or 474 nm.

The excitation wavelength 474 nm corresponds to a selective excitation of the SQW, because the photon energy is below the SL band edge. The respective curves (dotted ones in the Figs. 3(a) and (b)) are practically the same for the two samples. The SQW PL in this case is weakly σ^- polarized (less than 10% at 5 T), with the polarization degree depending linearly on the magnetic field. This behavior is in good agreement with recent magneto-absorption measurements of ZnCdSe/ZnSe QWs [7], indicating a positive sign of the excitonic g-factor $g_{ex} = g_h - g_e$, where g_h and g_e are electron and hole g-factors. In this case, the lowest excitonic state in a magnetic field is $|+1/2, -3/2\rangle$, which is active in σ^- polarization. In $|s, m\rangle$ the notation $s(m)$ denotes the projection of the electron spin

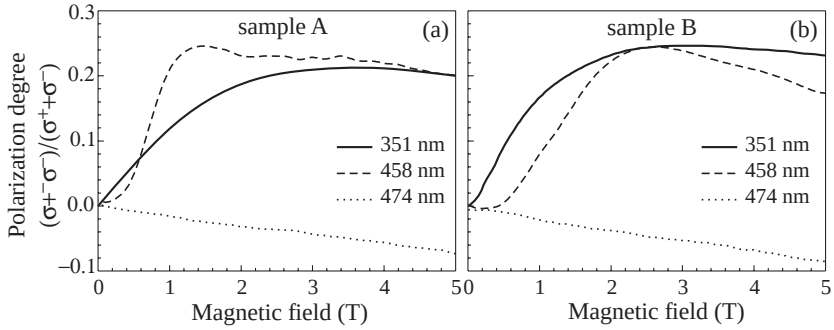

Fig. 3. Degree of circular polarization at the maximum of the SQW PL peak versus magnetic field for samples A (a) and B (b). Different curves correspond to various excitation wavelengths as indicated on the plot.

(hole angular momentum) on the z axis. The scheme of the spin structure of optically active SQW excitons in a magnetic field is shown in Fig. 1.

For the excitation above the SL band edge (351 nm and 458 nm) the SQW PL polarization changes its sign to σ^+. Also the circular polarization degree is noticeably larger in this case, reaching 40% (dashed curve in Fig. 3(a) near 0.8 T). This observation is indicative of efficient injection of spin-polarized electrons and holes from the DMS SL into the non-magnetic QW. Indeed, the lowest exciton in the DMS SL in a magnetic field is $|-1/2, +3/2\rangle$ (see the schematic drawing in Fig. 1). Being injected in the SQW, the $|-1/2\rangle$ electrons and $|+3/2\rangle$ holes contribute to population of the $|-1/2, +3/2\rangle$ excitons in the SQW, which results in the inverted population of the QW excitons and in enhancement of the σ^+ polarized PL. Therefore, the degree of σ^+ polarization of the SQW PL can serve as a measure of the spin injection efficiency.

For the non-resonant excitation (351 nm) the dependence of the polarization degree on magnetic field (solid curves in Figs. 3(a) and (b)) is mainly determined by two competitive factors. Firstly, at relatively small magnetic fields the σ^+ polarization increases due to the increase in the population of the $|-1/2, +3/2\rangle$ excitons in the DMS SL. At larger fields, the increase in the σ^+ polarization saturates due to the saturation behavior of the Brillouin function describing magnetization in DMS [6]. In this region, the dominant factor is an increase in the intrinsic σ^- polarization natural for a non-magnetic ZnCdSe/ZnSe QW. For the resonant excitation close to the SL exciton (458 nm), the degree of circular polarization of the SQW PL peak depends on magnetic field in a more complicated manner. As shown in Fig. 2(b), the SL exciton crosses the excitation energy at magnetic fields near 1 T for sample A and 3 T for sample B. The crossings manifest themselves in a resonant enhancement of the degree of circular polarization of the SQW PL in the vicinity of these fields (see dashed curves in Figs 3(a) and (b)). Note that for sample A the resonance is narrower and better pronounced than that for sample B, which results from larger steepness of the curves in Fig. 2(b) at 1 T and smaller contribution from the intrinsic σ^- polarization of QW excitons at this small magnetic field.

In conclusion, we have reported on a realization of efficient injection of photo-excited carriers, spin-polarized by an external magnetic field, from a DMS ZnMnSe/CdSe SL into a non-magnetic ZnCdSe SQW. A spin injection efficiency of at least 25% has been estimated by monitoring the degree of circular polarization of the QW excitonic PL.

Acknowledgements

This work was supported in part by Russian Foundation for Basic Research, Volkswagen-Stiftung, INTAS grant No 97-31907 and the Royal Swedish Academy of Sciences.

References

[1] G. A. Prinz, *Science* **282**, 1660 (1998).
[2] R. Fiederling, M. Keim, G. Reuscher, W. Ossau, G. Schmidt, A. Waag and L. W. Molenkamp, *Nature* **402**, 787 (1999).
[3] B. T. Jonker, Y. D. Park, B. R. Bennett, H. D. Cheong, G. Kioseoglou and A. Petrou, *Phys. Rev. B* **62**, 8180 (2000).
[4] Y. Ohno, D. K. Young, F. Matsukura, H. Ohno and D. D. Awschalom, *Nature* **402**, 790 (1999).
[5] A. A. Toropov, T. V. Shubina, S. V. Sorokin, A. Lebedev, R. N. Kyutt, S. V. Ivanov, M. Karlsteen, M. Willander, G. R. Pozina, J. P. Bergman and B. Monemar, *Phys. Rev. B* **59**, 2510 (1999).
[6] J. K. Furdyna and J. Kossut, *Diluted Magnetic Semiconductors*, Vol. 25 of Semiconductors and Semimetals (Academic, New York, 1988).
[7] J. Puls, V. V. Rossin, F. Henneberger and R. Zimmermann, *Phys. Rev. B* **54**, 4974 (1996).

9th Int. Symp. "Nanostructures: Physics and Technology"
St Petersburg, Russia, June 18–22, 2001

Spin dynamics of excitons in GaAs/AlGaAs superlattices in a magnetic field

Yu. K. Dolgikh†, S. A. Eliseev†, *I. Ya. Gerlovin*†, V. V. Ovsyankin†,
Yu. P. Efimov‡, I. V. Ignatev‡, I. E. Kozin‡, V. V. Petrov‡ and Y. Masumoto§
† Vavilov State Optical Institute, St Petersburg, Russia
‡ Institute of Physics, St Petersburg State University, Russia
§ Institute of Physics, University of Tsukuba, 305-8571, Japan

Abstract. Kinetics of resonance luminescence of GaAs/AlGaAs-superlattices in circular and linear polarizations is studied in a magnetic field of up to 5 T. Quantum beats of the luminescence are detected and their nature is identified. The energy and phase relaxation rates of excitonic spins are determined from the experimental data.

The spin relaxation times of electrons and holes in the GaAs-based high-quality heterostructures may amount to as much as hundreds of picosecond or even units of nanosecond [1–3]. At the same time, the spin relaxation rate of electron-hole pairs (excitons) couples by the Coulomb interaction appear to be essentially higher. Even under favorable conditions (low temperatures and low excitation power densities), the appropriate relaxation times do not exceed several tens of picoseconds. In the literature, several relaxation channels were discussed: independent electron or hole spin flips [4], relaxation of the electron magnetic moment as a whole [5], and reversible dephasing associated with inhomogeneous broadening of the excitonic fine structure [6]. Still, the predominant mechanism of the excitonic spin relaxation remains so far obscure.

In this note, we present results of experiments on dynamics of polarized resonance luminescence of HH-excitons in the GaAs/AlGaAs superlattices. The measurements were made both in linear and circular polarizations in an external magnetic field parallel to the structure growth axis. A joint analysis of the data thus obtained has allowed us to identify mechanisms of the energy and phase relaxation of magnetic moments and to evaluate role of each of them in dynamics of the polarized luminescence.

1. Experimental data

We studied a heterostructure with 50 periods of the superlattice with the GaAs and $Ga_{0.56}Al_{0.44}As$ layers 30 and 38 Å thick, respectively. The exciton linewidth in the steady-state luminescence spectrum at 4.2 K was 6 meV, with the Stokes shift between maxima of the luminescence and absorption lines being around 5 meV. The luminescence was excited by a tunable Ti-sapphire laser with the pulsewidth $3 \div 5$ ps. The luminescence kinetics was detected in real time using a Sinchroscan streak-camera. Spectral and time resolution of the detection system was 0.5 meV and 5 ps, respectively. The measurements were performed in conditions when spectra and kinetics of the photoluminescence did not depend on the pump power density. The magnetic field up to 5 T was produced by a superconducting solenoid immersed in liquid helium.

The luminescence was excited near the peak of the exciton absorption line. The luminescence was detected at the wavelength slightly shifted (by around 2 meV) toward long

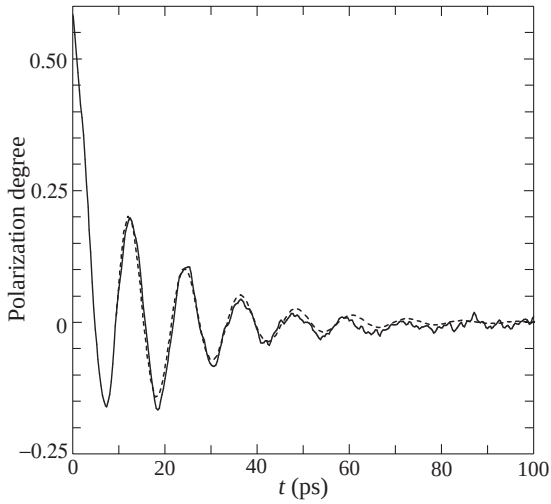

Fig. 1. The dynamics of linear polarization degree in longitudinal magnetic field $B = 5$ T. Full curve is experiment; dashed curve is theoretical fit.

wavelengths with respect to the excitation wavelength. Such a detuning, as has been established previously [7], does not noticeably change the luminescence polarization degree and, at the same time, allows one to completely eliminate the stray laser light.

The experiments have shown that, in the magnetic field parallel to the structure growth axis z (longitudinal field), the luminescence pulses detected in two orthogonal linear polarizations show well pronounced oscillations. Figure 1 shows dynamics of the degree of polarization measured in these conditions. Degree of polarization was defined in a conventional way by the formulae $p = (I_1 - I_2)/(I_1 + I_2)$, where I_1 and I_2 are the PL intensities in two orthogonal polarizations. The degree of polarization is seen to oscillate symmetrically with respect to horizontal axis, with the oscillation amplitude decaying in time. Fitting the

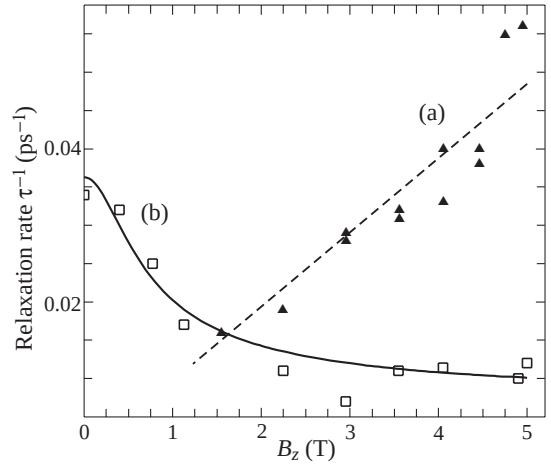

Fig. 2. Field dependence of relaxation rates: (a) the rate of oscillations damping in linear polarization; (b) the rate of circular polarization degree decay. Points—experimental data; curves is the guide for eye.

experimental curve by the function: $p(t) = p_0 \exp(-t/\tau_\pi \times \cos(\omega_\pi t + \varphi)$ allowed us to determine, from the experimental data, the oscillation frequency ω_π and the decay time τ_π. The measurements made at different values of the magnetic field strength B have shown that the oscillation frequency ω_π in magnetic fields up to 5 T is a linear function of B. It has been found also that the decay rate τ_π^{-1} increases with the field strength (curve *a* in Fig. 2).

Dynamics of the circularly polarized luminescence in longitudinal magnetic field appears to be essentially different. The degree of circular polarization p_σ does not show oscillations and decays monotonically in time. A considerable portion of the decay curve p_σ(t) can be approximated by an exponential function with the decay time τ_σ. It is important that the relaxation rate of the degree of circular polarization τ_σ^{-1} in the field $B = 5$ T appears to be smaller by a factor of 5 than the relaxation rate of the beats in linear polarization τ_π^{-1}. Moreover, as seen from Fig. 2, these quantities depend differently on the magnetic field strength.

2. Analysis of the results

The oscillations detected experimentally are related to quantum beats between Zeeman sublevels of the excitonic fine structure. As is known [8], the HH-exciton states in the GaAs-based structures are four-fold degenerate in total angular momentum. Exchange interaction between the electron and hole splits this quartet into two doublets – optically active (J_z = 1) and optically inactive ($J_z = 2$). The magnetic field, directed along the growth axis, splits the optically active doublet into the components $J_z = +1$ and $J_z = -1$, with transitions to these component corresponding to the right- and left-hand oscillators. Circularly polarized light excites only one component, and observation of the luminescence in orthogonal polarization becomes possible only after energy relaxation of the excitonic angular moment, characterized by the time constant T_1. It is this time that determines the decay rate of the degree of circular polarization of the luminescence, i.e., $\tau_\sigma^{-1} = T_1^{-1}$. The linearly polarized excitation creates coherent superposition of the states $J_z = +1$ and $J_z = -1$, which gives rise to beats in the degree of linear polarization of the emission (Fig. 1). The oscillation frequency is determined by the magnitude of the splitting, while the decay of the beats is related to decay of the coherence. The decay constant, in this case, is given by the relationship [4]: $\tau_\pi^{-1} = (2T_1)^{-1} + T_2^{-1}$, where T_2 is the dephasing time of the excitonic fine structure states. Comparison of the quantities τ_σ^{-1} and τ_π^{-1} makes it possible to determine independently the values of the energy and phase relaxation rates in the system under study. As is seen from Fig. 2 (curve *b*), the relaxation rate of the circular polarization in the fields above $B = 1$ T practically does not depend on the field strength and makes up 1×10^{10} s^{-1}. It is this value that should be ascribed to the energy relaxation rate between sublevels of the optically active excitonic state, split by the magnetic field. Behavior of the coherence decay rates (curve *a* in Fig. 2) appears to be essentially different, i. e. the quantity τ_π^{-1} increases with the field, reaching 5.4×10^{10} s^{-1} at $B = 5$ T. It follows from the difference between behavior of the quantities τ_π^{-1} and τ_σ^{-1} that the main reason for decay of the beats in linear polarization is the phase (rather than the energy) relaxation, characterized by the time T_2. The linear dependence of τ_π^{-1} on the field strength indicates that decay of the beats is associated with inhomogeneous spread of the excitonic g-factor, giving rise to corresponding spread of the splittings and, as a result, to spreading the phases of elementary emitters (the so-called reversible phase relaxation [9]).

A significant increase of τ_σ^{-1} in the fields below $B = 1$ T is likely to be caused by local anisotropy of the structures under study in the planes of heterolayers. This anisotropy arises

due to inhomogeneities in interfaces [3] and, for this reason, the value of the splitting and orientation of the oscillators in the layer plane can be random. In this case, any polarized excitation will create a coherent superposition of the split states, which will decay due to the reversible phase relaxation related to variations of the splitting. It is believed that this process is responsible for depolarization of the luminescence in the absence of magnetic field. The external magnetic field, parallel to the growth axis, suppresses the splitting caused by the in-plane anisotropy. This eliminates conditions needed for the reversible phase relaxation and, as a result, the quantity τ_σ^{-1} decreases.

3. Conclusion

In summary, the studies of kinetics of resonance photoluminescence of the GaAs/AlGaAs superlattice in external magnetic field has allowed us to obtain fundamentally new information about intrinsic dynamics of the exciton angular moment. We have determined separately the energy and phase relaxation rates between components of the optically active doublet. The energy relaxation rate is established to be independent of the external magnetic field strength within the range $1 \div 5$ T. It is concluded, from dependence of the phase relaxation rate on the magnetic field strength, that the relaxation is reversible and is therefore related to inhomogeneous spread of the excitonic g-factor. It is suggested that the main reason for depolarization of the resonance excitonic luminescence, in the absence of magnetic field, is also the reversible phase relaxation of excitonic fine structure states. Mechanism of the relaxation is related to statistical spread of local splittings of the optically active doublet, caused by inhomogeneous strains in the plane of the heterostructure.

Acknowledgments

The work is supported by the Russian Foundation for Basic Research.

References

[1] A. P. Heberle, W. W. Ruhle and K. Ploog, *Phys. Rev. Lett.* **72**, 3887, (1994).
[2] X. Marie, T. Amand, P. Le Jeune, M. Paillard, P. Renucci, L. E. Golub, V. D. Dymnikov and E. L. Ivchenko, *Phys. Rev. B* **60**, 5811 (1999).
[3] C. Gourdon and P. Lavallard, *Phys. Rev. B* **46**, 4644 (1992).
[4] M. Z. Maialle, E. A. de Andrada e Silva and L. J. Sham, *Phys. Rev. B* **47**, 15776 (1993).
[5] P. Le Jeune, X. Marie, T. Amand, F. Romstad, F. Perez, J. Barrau and M. Brouseau, *Phys. Rev. B* **58**, 4853, (1998).
[6] Yu. K. Dolgikh, S. A. Eliseev, I. Ya. Gerlovin, V. V. Ovsyankin, Yu. P. Efimov, I. V. Ignatev, I. E. Kozin, V. V. Petrov, V. Pantukhin and Y. Masumoto, *Nanostructures: Physics and Technology*, Ioffe Institute, St Petersburg, 1999, p 412.
[7] Yu. K. Dolgikh, S. A. Eliseev, I. Ya. Gerlovin, V. V. Ovsyankin, Yu. P. Efimov, I. V. Ignatev, I. E. Kozin, V. V. Petrov and Y. Masumoto, *The Physics of Semiconductors* (Proc. 25th Int. Conf. Phys. Semicond. (ICPS25), September 17–22, 2000, Osaka, Japan), 2001, in press.
[8] E. L. Ivchenko, *Pure Appl. Chem.* **67**, 463 (1995).
[9] J. Shah, *Ulrafast Spectroscopy of Semiconductors and Semiconductor Nanostructures* (Springer-Verlag, Heidelberg), 1996.

9th Int. Symp. "Nanostructures: Physics and Technology"
St Petersburg, Russia, June 18–22, 2001

Spin quantum beats in InP quantum dots in a magnetic field

I. A. Yugova†, V. G. Davydov‡, I. Ya. Gerlovin‡, I. V. Ignatiev†,
I. E. Kozin†, M. Sugisaki§ and Y. Masumoto¶

† Institute of Physics, St Petersburg State University,
St Petersburg 198904, Russia
‡ Vavilov State Optical Institute, St Petersburg, 190034, Russia
¶ Institute of Physics, University of Tsukuba, Tsukuba 305–8571, Japan
§ University of Toronto, Toronto, Ontario, Canada M5S 3E3

Abstract. In this paper, we studied quantum beats observed in kinetics of photoluminescence of a single layer of InP self-assembled quantum dots in a magnetic field. The reason for the quantum beats is shown to be Zeeman splitting of the exciton radiative level. Studies of behavior of the quantum beats versus the magnetic field magnitude and orientation and versus polarization of the exciting and detected light, have allowed us to identify fine structure of radiative level of the electron-hole pairs and to evaluate g-factors of electrons and holes.

Spin quantum beats is a phenomenon intensively studied in structures with quantum wells, whereas just a few observations of the spin quantum beats in quantum-dot structures is now available in the literature [1, 2]. The reason why the beats are absent in quantum dots, at present, becomes evident. The point is that quantum dots, as a rule, contain excess charge carriers (are charged), and, as a result, fine structure of the energy levels becomes much more complicated [2, 3, 4]. In this paper, we show that discharging quantum dots by means of external electric field gives rise to intense quantum beats in kinetics of photoluminescence (PL) of quantum dots in a magnetic field. Studies of behavior of the beats versus the magnetic field magnitude and orientation and versus polarization of the exciting and detected light have allowed us to identify fine structure of radiative level of electron-hole pairs and to evaluate g-factors of electrons and holes.

We studied a structure with a single layer of the InP quantum dots. A detailed description of the structure is given in [5]. The luminescence was excited by 3 ps pulses of a Ti:sapphire laser, 40 meV above the PL band maximum. The PL kinetics was measured with a time resolution of 6 ps using a 0.25 m subtractive-dispersion double monochromator and a streak-camera. The measurements were made in a cryostat with a superconducting solenoid, in magnetic fields from 1 to 7 T. The design of the cryostat allowed us to excite the sample and to detect its emission only along and across the magnetic field direction (the Faraday and Voigt configurations, respectively). To change the angle ϑ between the growth axis of the sample z and direction of the magnetic field B, we rotated the sample around vertical axis.

It has been established that the quantum beats can be observed only in the presence of electric bias $U_{bias} < -0.3$ V applied to the sample. Mote that the frequency of the beats proved to be independent of the voltage U_{bias}. The beats could be observed at Stokes shifts from 5 to 50 meV, with the form of the beats being virtually independent of the shift value. This is the main difference between these quantum beats and those observed in two-dimensional structures [6].

We have studied PL kinetics at linear and circular polarization of excitation, with co- and cross-polarizations of the detected PL. It was found that the amplitude of the beats is the greatest in circular co-polarization of the PL. It is noteworthy that in none of the experiments have been observed antiphase oscillations in the co- and cross-polarized luminescence, which are typical for quantum beats on Zeeman sublevels [7].

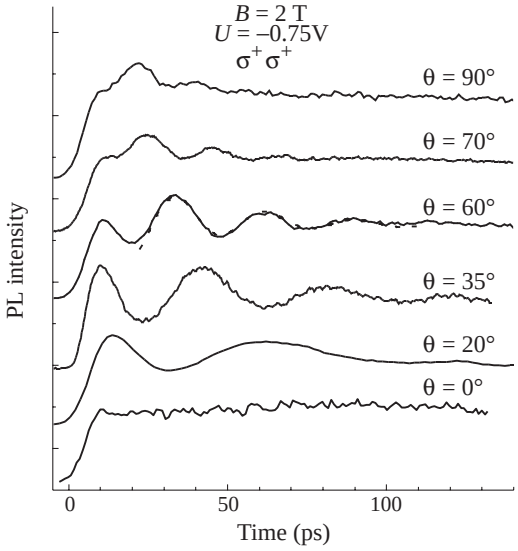

Fig. 1. PL kinetics in the magnetic field $B = 2$ T at different angles ϑ between the magnetic field and growth axis of the structure (solid lines). The dashed line shows fitting the oscillations in one kinetics by formula (1). Polarizations of the PL excitation and detection are σ^+. The PL Stokes shift — $\Delta E = 45$ meV, electric bias — $U_{bias} = -0.75$ V.

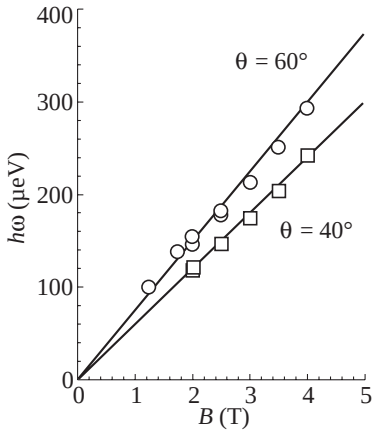

Fig. 2. Dependence of the beat frequency (in energy units) on the magnetic field at different ϑ. Solid lines — calculations by formulas (2) and (3).

Figure 1 shows kinetics of circularly polarized luminescence in the field $B = 2$ T at different ϑ. Intense beats are seen to be observed within the range of angles $\vartheta = 20-70^\circ$, the frequency of the beats being decreased with decreasing ϑ. These beats can be well described by the function

$$y = C \cdot \exp(-t/\tau)\cos(\omega t), \tag{1}$$

where the decay time τ and the beat frequency ω are the fitting parameters.

For the angle $\vartheta = 0^\circ$ no oscillations are observed at any magnetic field and any light polarization. Dependence of the oscillation frequency ω on magnetic field, measured at two values of the angle ϑ is shown in Fig. 2. As is seen from the figure, the experimental points well fit straight lines coming out of the coordinate origin.

We suggest that the oscillations observed are related to quantum beats between the fine-structure states of electron-hole pairs coherently excited by laser pulses via higher-energy states. To quantitatively describe the fine splitting, we used the spin-Hamiltonian of electron-hole pair in a magnetic field similar to that given in [8]. This Hamiltonian contains 6 free parameters - 2 components of the exchange splitting, two components of the electronic g-factor, and two components of the hole g-factor (assuming axial symmetry of a

quantum dot). Analysis of the above experimental data allowed us to significantly simplify the Hamiltonian. Since, as follows from Fig. 3, no deviation from linear dependence of the splitting is observed in the fields $B > 1$ T, the exchange splitting can be neglected. The magnetic field $B \parallel z$ splits the state of the electron-hole pair into 4 components, two of them being optically active. This splitting is proportional to the difference between z-components of the electron and hole g-factors: $\delta E \sim (g_{e,z} - g_{h,z})$. It follows from the aforementioned absence of antiphase oscillations at the angle $\vartheta = 0^\circ$ in any magnetic field that splitting of the radiative doublet, in such a field, is small, i.e., $g_{e,z} \approx g_{h,z}$. In addition, we suppose, for simplicity, that the electron g-factor tensor is spherical, i.e., $g_{e,x} = g_{e,x}$. In the framework of the these approximations, the spin-Hamiltonian depends on two free parameters only ($g_{e,z}$ and $g_{h,x}$), and the values of the fine-structure state energies can be calculated analytically:

$$E_{1,2,3,4} = \pm\frac{1}{\sqrt{2}}\mu B g_{e,z}\left\{\cos^2(\vartheta) + \frac{1}{2}(g_{e,z}^2 + g_{h,x}^2)\sin^2(\vartheta)\right. \qquad (2)$$
$$\left. \pm\left[(\cos^2(\vartheta) + g_{e,z}^2\sin^2(\vartheta))\cdot(\cos^2(\vartheta) + g_{h,x}^2\sin^2(\vartheta))\right]^{1/2}\right\}^{1/2}$$

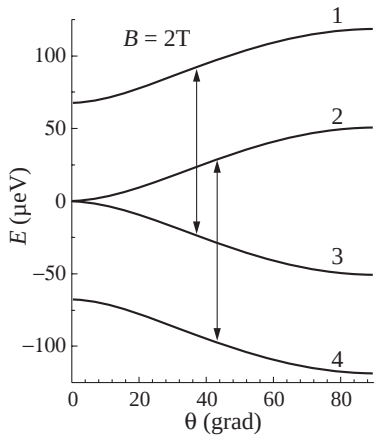

Fig. 3. Splitting of the electron-hole pair fine structure in a magnetic field at different ϑ. The states mixed by the magnetic field responsible for quantum beats in circular co-polarizations are bridged by arrows.

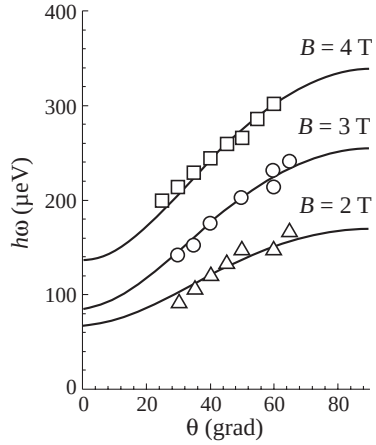

Fig. 4. Dependence of the beat frequency (in energy units) on the angle ϑ in different magnetic fields. Solid lines — calculations by formulas (2) and (3).

Figure 3 shows variation of the energy levels with the angle ϑ for the magnetic field $B = 2$ T, plotted using experimental values of the parameters (see below). At the angle $\vartheta = 0^\circ$, the optically active state is not split, and transitions into the split states are forbidden by the selection rules. Thus, no quantum beats can be observed in these conditions. At finite angles ϑ, the magnetic field mixes all the split states, and possibility to observe the beats is determined by the degree of their mixing. In the conditions of the experiment, the beats were mainly observed at a single frequency. A satisfactory agreements between calculated curves and experimental data proved to be possible under assumption that the mixed states are those bridged by arrows in Fig. 3.

Figure 4 shows dependence of the beat frequency (in energy units) on the angle ϑ in different magnetic fields. As is seen, the experimental dependences well agree with the calculated curves

$$\Delta E = E_1 - E_3, \tag{3}$$

where E_i are calculated by formula (2). The theoretical curves are plotted for the fitting parameters $g_{e,z} = g_{e,x} = g_{h,z} = 0.6$ and $g_{h,x} = 1.5$. The same parameters were used to calculate dependences of the beat frequencies on magnetic field (solid curves in Fig. 3).

In summary, the proposed model can describe fairly well behavior of the quantum beat frequencies in a magnetic field. To describe amplitudes of the quantum beats, a more detailed analysis is needed, which will make it possible to refine the model.

References

[1] V. K. Kalevich, M. N. Tkachuk, P. Le Jeune, X. Marie and T. Amand, *Solid State Phys.* (Russia) **41**, 871 (1999).

[2] I. E. Kozin, V. G. Davydov, A. V. Fedorov, I. V. Ignatiev, H. W. Ren, M. Sugisaki, S. Sugou and Y. Masumoto, *Proc. 25th Int. Conf. on the Physics of Semiconductors (ICPS25)*, Osaka, Iapan, September 17-22, 2000.

[3] M. Bayer, A. Kuther, A. Forchel, A. Gorbunov, V. B. Timofeev, F. Schafer, J. P. Reithmaier, T. L. Rienecke and S. N. Walck, *Phys. Rev. Lett.* **82**, 1748 (1999).

[4] F. Findeis, M. Bayer, A. Zrenner, M. Bichler, G. Abstraiter, U. Hohenester and E. Molinari, *Phys. Rev. Lett. submitted*.

[5] H.-W. Ren, M. Sugisaki, S. Sugou, K. Nishi, A. Gomyo and Y. Masumoto, *Jpn. J. Appl. Phys.* Part 1, **38**, 2438 (1999).

[6] T. Amand, X. Marie, P. Le. Jeune, M. Brousseau, D. Robart,J. Barrau and R. Planel, *Phys. Rew. Lett.* **78**, 1355 (1997).

[7] R. E. Worsley, N. J. Traynor, T. Grevatt and R. T. Harley, *Phys. Rew. Lett.* **76**, 3224 (1996).

[8] M. Bayer, O. Stern, A. Kuther and A. Forchel, *Phys. Rew. B* **61**, 7273 (2000).

9th Int. Symp. "Nanostructures: Physics and Technology"
St Petersburg, Russia, June 18–22, 2001

Spin quantum beats of hot trion in quantum dots

I. E. Kozin†, V. G. Davydov‡, I. V. Ignatiev†, A. Kavokin§,
K. Kavokin¶, M. Sugisaki◇ and Y. Masumoto‖

† Institute of Physics, St Petersburg State University, 198904 St Peterburg, Russia
‡ Vavilov State Optical Institute, 199034 St Petersburg, Russia
§ LASMEA-CNRS, Universite Blaise Pascal, 63177 Aubiere, France
¶ Ioffe Physico-Technical Institute, St Petersburg, Russia
◇ University of Toronto, Toronto, Canada
‖ Institute of Physics, University of Tsukuba, 305-8571 Tsukuba, Japan

Abstract. Spins of resident holes in charged quantum dots (QD's) act as local magnets inducing Zeeman splitting of excitons trapped into dots. This has been evidenced by observation of quantum beats in linearly polarized time-resolved photoluminescence of a biased array of self-assembled InP QD's. A theory is developed that considers the exchange interaction within the positively charged exciton (trion) states formed in the QD.

Electronic and optical properties of zero-dimensional quantum objects are extremely sensitive to the presence of single charge carriers in the system [1–3]. If a neutral quantum dot (QD) is an analog of an atom, a charged quantum dot is an analog of an ion. Peculiarities of singly charged QD's have become a subject of particular attention during recent couple of years, in connection with the problem of quantum computing [4].

Here we report a new spin-related effect in a charged QD. We have observed spin quantum beats (QB's) in linearly polarized photoluminescence (PL) of an array of InP QD's under linearly polarized excitation, while circular polarization of PL under circular-polarized excitation has shown almost no modulation. Such kind of beats is a signature of splitting between exciton resonance energies in σ^+ and σ^- polarizations. In neutral dots, this would have been possible only in a magnetic fields (Zeeman splitting). In our case, such a Zeeman-like splitting is observed in the absence of the external magnetic field. We attribute this unexpected behavior to a peculiar spin structure of the three-particle complex, or trion, formed in the positively charged QD on the exciton creation.

We have studied heterostructures with a single layer of InP self-assembled QD's embedded between $Ga_{0.5}In_{0.5}P$ barrier layers grown by the gas source molecular beam epitaxy. The average base diameter of the QD's was about 40 nm with a height of about 5 nm. The samples were provided with a semi-transparent Shottky contact on the top surface and with an ohmic contact on the back one. The total thickness of undoped layers was about 0.5 μm. The sample has been illuminated at normal incidence. The PL was excited quasiresonantly, i.e., within the PL band of the QD's, by 3 ps pulses of a mode-locked Ti:sapphire laser. The PL kinetics was measured with a time resolution of 6 ps using a 0.25 m subtractive dispersion double monochromator and a streak-camera. The measurements were done at 5 K.

We can summarize our experimental results as follows. Under certain conditions, namely, at applied bias around some value $U_{\rm opt}$ and under linearly polarized excitation, PL kinetics of the QD's exhibits pronounced oscillations both in *co*- and *cross*-polarizations (i.e., in polarizations which are identical or orthogonal to that of the incident light, re-

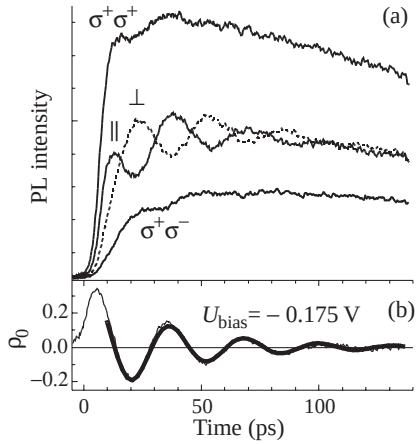

Fig. 1. (a) PL kinetics in the circular co- ($\sigma^+\sigma^+$) and cross- ($\sigma^+\sigma^-$) polarizations, and also in the linear co- ($\|$) and cross- ($\perp$) polarizations (indicated against each curve). (b) Degree of linear polarization ρ_l (noisy curve) and the fit (thick gray curve) by equation described in the text.

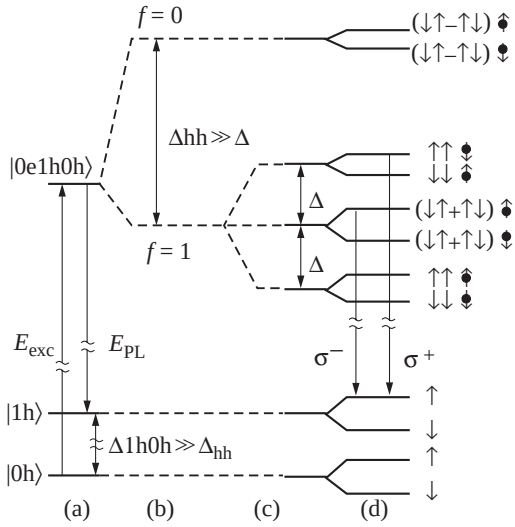

Fig. 2. Energy structure of the hot trion. Small arrows ↑ and ♦ indicates the hole and electron spins, respectively. See further details in the text.

spectively). These oscillations have opposite phases in co- and cross-polarizations thus giving a clear picture of the QB's. When exciting with a circularly polarized light (σ^+) and detecting either in σ^+ or σ^- circular polarizations, we do not observe any beats. The examples of the PL kinetics are shown in Fig. 1. The degree of linear polarization of the PL, $\rho_l = (I_\| - I_\perp)/(I_\| + I_\perp)$, where $I_\|$ and $I_\perp$ are, respectively, the PL intensities in the co- and cross-polarizations, can be well fitted by the equation $\rho_l(t) = \rho_0 \cos(\omega t) \exp(-t/\tau)$ as shown in Fig. 1(b). The period of the QB's $T = 2\pi/\omega$ is of 30–35 ps, which corresponds to a Zeeman splitting of about 120 μeV. The decay time of the QB's $\tau \approx 30$ ps which coincides, within the experimental error, with the PL rise time at negative bias $U < U_{\text{opt}}$.

The quantum beats are observed at a Stokes shift $\Delta E < 30$ meV. The beat amplitude is the greatest at $\Delta E = 15$ meV, being strongly dependent on the applied voltage U. For instance, at a small deviation of $U - U_{\text{opt}} = \pm 0.15$ V, the beat amplitude drops by a factor of 2. A shift of the excitation energy from short-wavelength to long-wavelength edge of the PL band of the QD's gives rise to insignificant increase of the beat amplitude and to moderate increase of the beat period (from 30 to 50 ps).

To describe the quantum beats, we will consider the following model. Quantum dots contain excess (resident) holes. Their number is controlled by the applied voltage. At $U = U_{\text{opt}}$, one quantum dot contains, in average, exactly one resident hole in its ground state $|0h\rangle$, see Fig. 2(a). Optical excitation created an electron-hole pair in the quantum dot. Note that the electron, in this case, is created in its ground state $|0e\rangle$, and the hole in the excited state $|1h\rangle$. As a result, the quantum dot passes into the state $|0e1h0h\rangle$, which is a hot trion state. The luminescence is caused by recombination of the electron with the resident hole, until the hot hole relaxes into the ground state.

Until the holes are on different energy levels, they may have parallel or antiparallel spins. The spin structure of the hot trion is governed by exchange interactions of the three particles. The holes, being identical particles, interact with each other much stronger than each of them with the electron. The exchange interaction of holes can be recast in the form similar to that of electrons by adopting the pseudospin formalism [5]:

$$\hat{H}_{hh}^{ex} = \Delta_{hh}\left(\vec{j}_1 \cdot \vec{j}_2\right), \tag{1}$$

where the pseudospin $j = 1/2$ has the basic states $\langle 1/2, -1/2|$ and $\langle 1/2, +1/2|$. This interaction gives rise to the singlet-triplet splitting in two levels with the values $f = 0$ and $f = 1$ of the total pseudospin of the two holes ($\vec{f} = \vec{j}_1 + \vec{j}_2$) as shown in Fig. 2(b). The value of the singlet-triplet splitting Δ_{hh} has been estimated as 3.5 meV for similar QD's by a comparison of model calculations with the experimental single-QD PL spectra [3].

The exchange interaction between an electron and a hole is known to form two spin doublets. The splitting between these doublets, Δ_0, is of the order of 0.1 meV [6, 7]. Since $\Delta_{hh} \gg \Delta_0$, one can consider the exchange interaction of two holes and one electron as interaction of the electron spin $\vec{s}$ with total pseudospin of the two holes $\vec{f}$:

$$\hat{H}_{ehh}^{ex} = 2\tilde{\Delta}_0 f_z s_z + \tilde{\Delta}_1(f_x s_x - f_y s_y) + \tilde{\Delta}_2(f_x s_x + f_y s_y). \tag{2}$$

In what follows, we neglect the two last terms in Eq. (2), since they are insignificant for QB's in linear polarizations. The corresponding energy spectrum of the hot trion comprises four Kramers doublets as shown in Fig. 2(c). Since the energy separation between the $f = 0$ and $f = 1$ level groups is greater than the exciting pulse bandwidth, we can consider them separately. The $f = 0$ doublet can evidently yield no beats. For this reason, the analysis below will be concentrated on the $f = 1$ group of levels. In this group, there are the following doublets (in the $|f_z\rangle|s_z\rangle$ notation): $|\pm 1\rangle|\pm 1/2\rangle$ (radiative), $|0\rangle|\pm 1/2\rangle$ (radiative), and $|\pm 1\rangle|\mp 1/2\rangle$ (non-radiative), see Fig. 2(d). The splitting between these doublets is equal to $\tilde{\Delta}_0$.

Circularly polarized light creates, in the pseudospin notation $|j_z\rangle|s_z\rangle$, the following electron-hole pairs:

$$\sigma^- \longrightarrow |+1/2\rangle|+1/2\rangle \qquad \sigma^+ \longrightarrow |-1/2\rangle|-1/2\rangle \tag{3}$$

Depending on the initial spin state of the resident hole, this results in excitation of different trion states. If the resident hole has $j_z = +1/2$,

$$\sigma^- \longrightarrow |+1\rangle|+1/2\rangle \exp(it\tilde{\Delta}_0/\hbar) \qquad \sigma^+ \longrightarrow |0\rangle|+1/2\rangle \tag{4}$$

If $j_z = -1/2$,

$$\sigma^+ \longrightarrow |-1\rangle|-1/2\rangle \exp(it\tilde{\Delta}_0/\hbar) \qquad \sigma^- \longrightarrow |0\rangle|-1/2\rangle \tag{5}$$

Here t is the time interval after excitation; the energy level of $f_z = 0$ doublet is chosen for zero energy. Radiative transitions from these states give rise to QB's in the PL of QD's if both of these states are excited coherently by the linearly polarized light. Using Eqs. (4) and (5), one can easily derive expressions for the degree of linear polarization of the PL under excitation by linearly polarized light $1/\sqrt{2}\left(\sigma^+ + \sigma^- \exp(2i\varphi)\right)$, where the angle φ determines the polarization plane). To do this, one should average intensities of the polarized light components over the spin states of the resident holes in the ensemble of

QD's. Assuming that spins of resident holes are not polarized, we come to the following expression for the degree of linear polarization of PL under linearly polarized excitation:

$$\rho_l(t) \approx 4/5 \cdot \cos\left((\tilde{\Delta}_0/\hbar) \cdot t\right). \quad (6)$$

Note that Eq. (6) is obtained assuming resonant excitation of the $f = 1$ sextet. However, due to inhomogeneous broadening in the QD ensemble, other levels (for instance, the $f = 0$ doublet), bearing no memory of linear polarization, can also be excited in a fraction of dots. This should result in lower value of the PL polarization than it is predicted by Eq. (6). Actually, the beat amplitude of around 0.2 is observed.

The photogenerated hole relaxes to the ground state for around 30 ps. Spins of the two holes, in this case, can be only antiparallel, with their total spin being equal to zero. This is why the fine energy structure of the cold trion is trivial and consists of an electron spin doublet. In this case, no beats can be observed in the absence of magnetic field. For this reason, in the framework of the above model, the beat decay rate coincides with the rate of the hot hole relaxation to its ground state. The luminescence decay time is evidently much larger and lies in the range of several hundreds of ps.

In conclusion, QB's in the PL kinetics of biased heterostructures with InP QD's are studied. The QB's arise due to coherent excitation of spin components of the radiative level. A Zeeman-like spin splitting is shown to be caused by presence of a resident hole inside the QD. The applied electric field controls the charging/discharging of the QD's. A model of the energy structure of hot trion is developed, which explains the main features of the observed QB's.

References

[1] R. J. Warburton *et al.*, *Phys. Rev. Lett.*, **79**, 5282 (1997).
[2] M. Bayer *et al.*, *Phys. Rev. B*, **60**, R8481 (1999).
[3] E.Dekel *et al.*, *Phys.Rev. B*, **61**, 11009 (2000).
[4] A. Imamoğlu, *Phys. Rev. Lett.*, **83**, 4204 (1999).
[5] E. L. Ivchenko and G. E. Pikus, *Superlattices and Other Heterostructures*, (Springer Verlag, Berlin, 1995)
[6] R. I. Dzhioev *et al.*, *Pis'ma Zh. Exp. Teor. Fiz.*, **65**, 766 (1997) [*JETP Lett.*, **65**, 804 (1997)]
[7] M. Bayer *et al.*, *Phys. Rev. Lett*, **82**, 1748 (1999)

9th Int. Symp. "Nanostructures: Physics and Technology"
St Petersburg, Russia, June 18–22, 2001

Quantum computation with FQHE quasiparticles

D. V. Averin and V. J. Goldman
Department of Physics and Astronomy, SUNY, Stony Brook, NY 11794, USA

Abstract. We propose an approach to implementing anyonic quantum computation in systems of antidots in the two-dimensional electron liquid in the FQHE regime. The approach is based on the adiabatic transfer of FQHE quasiparticles in the antidot systems, and uses their fractional statistics to perform quantum logic. Advantages of our scheme over other semiconductor-based proposals of quantum computation are the energy gap in the FQHE liquid that suppresses decoherence, and the topological nature of quasiparticle statistics that makes it possible to entangle two quasiparticles without their direct dynamic interaction.

Introduction

"Topological" quantum computation with anyons has been suggested as a way of implementing intrinsically fault-tolerant quantum computation [1–4]. Intertwining of anyons, quasiparticles of two-dimensional electron system (2DES) with non-trivial exchange statistics, induces unitary transformations of the system wavefunction that depend only on the topological order of the underlying 2DES. These transformations can be used to perform quantum logic, the topological nature of which is expected to make it more robust against environmental decoherence.

The aim of this work is to propose specific and experimentally feasible approach for implementation of basic elements of the anyonic quantum computation. The approach is based on adiabatic transport of the Fractional Quantum Hall Effect (FQHE) quasiparticles in systems of quantum antidots. An antidot is a small hole in the 2DES produced by electron depletion, which localizes FQHE quasiparticles at its boundary due to combined action of the magnetic field and the electric field created in the depleted region. If the antidot is sufficiently small, the energy spectrum of the antidot-bound quasiparticle states is discrete, with finite excitation energy Δ. When Δ is larger than temperature T, modulation of external gate voltage can be used to attract quasiparticles one by one to the antidot [5, 6]. In this regime, adiabatic transport of individual quasiparticles in the multi-antidot systems can be used to perform quantum logic, in close analogy to adiabatic transport of individual Cooper pairs in systems of small superconducting islands in the Coulomb blockade regime [7]. In what follows, we describe a specific design of such logic gates and discuss their parameters.

1. FQHE qubit and logic gates

In analogy to Cooper-pair qubits [7–9], information in the FQHE qubits can be encoded by the position of a quasiparticle in the system of two antidots. In this case, the FQHE qubit (Fig. 1) is the double-antidot system gate-voltage tuned near the resonance, where the energy difference ε between the quasiparticle states localized at the two antidots is small, $\varepsilon \ll \Delta$. At energies smaller than Δ, dynamics of such double-antidot system is equivalent to the dynamics of a common two-state system (qubit). The states localized at

the two antidots are the $|0\rangle$ and $|1\rangle$ states of the computational basis of this qubit. The gate electrodes of the structure can be designed to control separately the energy difference ε and the tunnel coupling Ω of the resonant quasiparticle states. In the existing experiments [5, 6] demonstrating transport of individual quasiparticles, the gate voltages were applied through a combination of a backgate and front gates etched into the 2DES. Both types of gates are not optimal for the antidot operation as qubit. The global backgate can not address selectively individual antidots, while the etched-in front gates create edges which support low-energy excitations and thus introduce decoherence in the antidot dynamics. An antidot structure optimized for qubit operation should use front gates that do not deplete 2DES, and therefore do not create edges. With such gates, application of the time-dependent gate voltages to individual antidots, and to the 2DES region between the antidots, should make it possible to vary the qubit parameters ε and Ω in a wide range, and as a result, to perform arbitrary single-qubit transformations.

Fig. 1. Schematic structure (a) and energy profile (b) of the double-antidot FQHE qubit. Solid (dashed) lines (in (b), horizontal lines) indicate the edges of the incompressible electron liquid when the quasiparticle is localized at the right (left) antidot. Displacement of the electron liquid is quantized due to quantization of the single-particle states circling the antidots.

The most natural approach to construction of two-qubit gates with the FQHE qubits is to use fractional statistics [10, 11] of the FQHE quasiparticles. Due to this statistics, intertwining of the two quasiparticle trajectories in the course of time-evolution of the two qubits realizes controlled-phase transformation. Precise result of this operation depends on the nature of the FQHE state. In this work, we discuss the most basic and robust Laughlin state with the filling factor $\nu = 1/3$, when the quasiparticles have abelian statistics and intertwining of trajectories leads to multiplication of the state wavefunction by the phase factor $e^{\pm 2\pi i/3}$. The sign of the phase depends on the direction of magnetic field and direction of rotation of one quasiparticle trajectory around another.

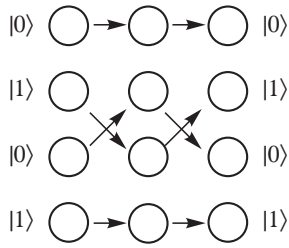

Fig. 2. Antidot implementation of the two-qubit controlled-phase gate. The states $|0\rangle$ and $|1\rangle$ are the computational basis states of the two qubits. The arrows show the quasiparticle transfer processes during the gate operation.

Possible structure of the controlled-phase gate is shown in Fig. 2. The columns of four antidots contains two qubits, and arrows denote trajectory of quasiparticle transfer through the system. The transfer leads to transformation of the quantum state of two qubits

and its shift from the gate input (left column in Fig. 2) to the output (right column). The quasiparticle transfer can be achieved by the standard adiabatic level-crossing dynamics. If a pair of antidots is coupled by the tunnel amplitude Ω, gate-voltage induced variation of the energy difference ε through the value $\varepsilon = 0$ (slow on the time scale Ω^{-1}) leads to the transfer of a quasiparticle between these antidots. Correct operation of the controlled-phase gate in Fig. 2 requires that the gate voltage pulses applied to the antidots are timed so that the state of the upper qubit is propagated at first halfway through the gate, then the state of the lower qubit is propagated through the whole gate, and finally the state of the upper qubit is transferred to the output. In this case, if the quasiparticle of the upper qubit is in the state $|1\rangle$, trajectories of the quasiparticle propagation in the lower qubit encircle this quasiparticle, and the two states of the lower qubit acquire additional phase difference $\pm 2\pi/3$, conditioned on the state of the upper qubit. We take the direction of magnetic field to be such that the state $|1\rangle$ of the lower qubit acquires a positive extra phase $2\pi/3$. Assuming that parameters of the driving pulses are adjusted in such a way that dynamic phases accumulated by the qubit states are the multiple integers of 2π, the evolution matrix P of the gate can be written as

$$P = \mathrm{diag}\,[1, 1, 1, e^{2\pi i/3}] \tag{1}$$

in the basis of the four gate states $|00\rangle$, $|01\rangle$, $|10\rangle$, $|11\rangle$. Controlled-phase gate (1) combined with the possibility of performing an arbitrary singe-qubit transformation is sufficient for universal quantum computation [12]. For instance, a combination of the two gates (1) with single-qubit gates can reproduce the usual controlled-NOT gate.

2. Estimates and discussion

The basic set of conditions necessary for correct operation of the FQHE qubits and gates described above can be summarized as $T \ll \varepsilon$, $\Omega \ll \Delta$. The antidot excitation energy Δ is estimated as $\Delta \simeq \hbar v/r$, where r is the antidot radius and $v \simeq 10^4 \div 10^5$ m/s [13] is the velocity of quasiparticle motion around the antidot. This means that at temperatures $T \simeq 0.1$ K the radius r should be smaller than 100 nm. Since the tunnel coupling Ω decreases rapidly with the distance d between the antidots, $\Omega \propto \exp\{-eBd^2/12\hbar\}$ [14], the fact that it should remain at least larger than T means that the distance between the tunnel-coupled antidots should not exceed few magnetic lengths $l = (eB/\hbar)^{1/2}$, where $l \simeq 10$ nm for typical values of the magnetic field B. Although these requirements on the radius r and antidot spacing d can in principle be satisfied with the present-day fabrication technology, they present a formidable challenge. It should be noted that these requirements are not specific to our FQHE scheme, but characterize all semiconductor solid-state qubits based directly on the quantum dynamics of individual quasiparticles, and not collective degrees of freedom (as in the case of superconductors). On the other hand, there are two advantages of the FQHE approach. First is the energy gap of the FQHE liquid that suppresses quasiparticle excitations and associated qubit decoherence in the bulk of the 2DES. The decoherence mechanisms for the FQHE qubits are localized at the 2DES edges and in the gate electrodes, and to a large extent can be controlled through the system layout. The second advantage is the topological nature of statistical phase that allows to entangle qubits without their direct dynamic interaction. This should lead to a much simpler design of the FQHE quantum logic circuit in comparison, e.g., to the superconducting qubits, where control of the qubit-qubit interaction presents a difficult problem.

Acknowledgements

This work was supported by ARDA and ARO.

References

[1] A. Yu. Kitaev, quant-ph/9707021.
[2] J. Preskill, in: *Introduction to quantum computation and information*, Eds. H.-K. Lo, S. Papesku, and T. Spiller, (World Scientific, 1998), p. 213.
[3] S. Lloyd, quant-ph/0004010.
[4] M. H. Freedman, A. Yu. Kitaev, M. J. Larsen and Z. Wang, quant-ph/0101025.
[5] V. J. Goldman and B. Su, *Science* **267**, 1010 (1995).
[6] I. J. Maasilta and V. J. Goldman, *Phys. Rev. Lett.* **84**, 1776 (2000).
[7] D. V. Averin, *Solid State Commun.* **105**, 657 (1998).
[8] Yu. Makhlin, G. Schön, and A. Shnirman, *Nature* **398**, 305 (1999).
[9] Y. Nakamura, Yu. A. Pashkin, and J. S. Tsai, *Nature* **398**, 786 (1999).
[10] B. I. Halperin, *Phys. Rev. Lett.* **52**, 1583 (1984).
[11] D. Arovas, J. R. Schrieffer, and F. Wilczek, *Phys. Rev. Lett.* **53**, 722 (1984).
[12] A. Barenco *et al. Phys. Rev. A* **52**, 1583 (1995).
[13] I. J. Maasilta and V. J. Goldman, *Phys. Rev. B* **57**, R4273 (1998).
[14] A. Auerbach, *Phys. Rev. Lett.* **80**, 817 (1998).

9th Int. Symp. "Nanostructures: Physics and Technology"
St Petersburg, Russia, June 18–22, 2001

Silicon-based NMR quantum computer using single electron

A. A. Larionov, *L. E. Fedichkin* and K. A. Valiev
Institute of Physics and Technology RAS,
34, Nakhimovsky pr., Moscow, 117218, Russia

Abstract. A new NMR quantum computer scheme based on semiconductor nanostructure is proposed. Energy spectrum of the spin-qubit system was obtained. Methods of single- and two-qubit gates realization are discussed. This variant of quantum computer is more simple to control and more coherent.

One of the most promising ideas for the real quantum computer construction is creating artificial multispin systems in semiconductor nanostructures with the help of individual addressing to any qubit. For the last time a lot of theoretical suggestions, i.e. [1, 2] of such idea were discussed. Unfortunately, there are many experimental difficulties for modern nanotechnology to create even quantum computer prototype. We are speculating a new semiconductor quantum computer variant, which looks more realistic to construct.

In the considering approach it is suggested to use silicon-based structure, where donor atoms of stable phosphorus isotope ^{31}P are implanted into the spinfree silicon isotope ^{28}Si. Donor atoms replace silicon ones in knots of crystal lattice. Every donor atom with nuclear spin in semiconductor structure is supposed to be placed regularly with adequate accuracy, when metallic gates must control the number of electrons in such quantum dots and their interaction with the nucleus of the donor atom. Consider the cell of this quantum computer consisting of two qubits. With the help of changing of the electric potential on the metallic gates one can control the electron density near the nucleus. It is possible to leave only one valent electron in the considering cell, when other electrons must be displaced from this area. This electron will interact with its "own" nucleus, as well as with the other. That is why the Hamiltonian of the system is:

$$\hat{H} = -2\mu_B \vec{B}\hat{\vec{S}} - g_N \mu_N \vec{B}\left(\hat{\vec{I}}_a + \hat{\vec{I}}_b\right) + A_a\left(\hat{\vec{I}}_a\hat{\vec{S}}\right) + A_b\left(\hat{\vec{I}}_b\hat{\vec{S}}\right) \tag{1}$$

when $\mu_B = 9.27 \cdot 10^{-24}\ J/T$ — Bohr magneton, $\mu_N = 5.05 \cdot 10^{-27}\ J/T$ — nuclear magneton, $g_N = 2.26$ — Lande's factor for ^{31}P, $\vec{B}$ — the magnetic field, $\hat{\vec{S}}$ — electron spin operator, $\hat{\vec{I}}_a$ and $\hat{\vec{I}}_b$ — spin operators for nuclei a and b, A_a and A_b — hyperfine interaction constants, depending on gate potentials. We choose eigen states of the Hamiltonian (1) in the strong magnetic field to be the basis states. Designating spin projections of the electron and the nuclei by arrows up ($\uparrow$) and down ($\downarrow$), we have (the first arrow concerns the electron, the second — nucleus a, the third - nucleus b):

$$\begin{array}{ll} |1\rangle = |\uparrow\uparrow\uparrow\rangle & |5\rangle = |\downarrow\uparrow\uparrow\rangle \\ |2\rangle = |\uparrow\uparrow\downarrow\rangle & |6\rangle = |\downarrow\uparrow\downarrow\rangle \\ |3\rangle = |\uparrow\downarrow\uparrow\rangle & |7\rangle = |\downarrow\downarrow\uparrow\rangle \\ |4\rangle = |\uparrow\downarrow\downarrow\rangle & |8\rangle = |\downarrow\downarrow\downarrow\rangle \end{array} \tag{2}$$

Table 1. CNOT gate scheme realization.

Operation	The state of the qubit A	The state of the qubit B	The electron state
—	Ψ_A	Ψ_B	$\|0\rangle$
SWAP operation between A qubit and the electron	$\|0\rangle$	Ψ_B	Ψ_A
Adiabatic transfer of the electron from nucleus A to nucleus B	—	—	—
CNOT operation between the electron and qubit B	$\|0\rangle$	Ψ_B	CNOT$\|\Psi_A, \Psi_B\rangle$
Adiabatic transfer of the electron from nucleus B to nucleus A	—	—	—
SWAP operation between the electron and A qubit	CNOT$\|\Psi_A, \Psi_B\rangle$	Ψ_B	$\|0\rangle$

Symmetric matrix 8×8, corresponding to the matrix of eigen states of Hamiltonian (1), in the considered basis, is

$$\begin{pmatrix}
\mu_B B - g_N \mu_N B + \frac{A_a + A_b}{4} & 0 & 0 & 0 & 0 & 0 & 0 & 0 \\
0 & -\mu_B B + \frac{A_a - A_b}{4} & 0 & 0 & A_b/2 & 0 & 0 & 0 \\
0 & 0 & -\mu_B B + \frac{-A_a + A_b}{4} & 0 & A_a/2 & 0 & 0 & 0 \\
0 & 0 & 0 & -\mu_B B + g_N \mu_N B - \frac{A_a + A_b}{4} & 0 & A_a/2 & A_b/2 & 0 \\
0 & A_b/2 & A_a/2 & 0 & \mu_B B - g_N \mu_N B + \frac{A_a + A_b}{4} & 0 & 0 & 0 \\
0 & 0 & 0 & A_a/2 & 0 & \mu_B B + \frac{A_a - A_b}{4} & 0 & 0 \\
0 & 0 & 0 & A_b/2 & 0 & 0 & \mu_B B + \frac{-A_a + A_b}{4} & 0 \\
0 & 0 & 0 & 0 & 0 & 0 & 0 & \mu_B B + g_N \mu_N B - \frac{A_a + A_b}{4}
\end{pmatrix}.$$

It is worth of noting that using only one electron to be the connection between two nuclei significantly decreases decoherence processes in quantum computer due to electron-

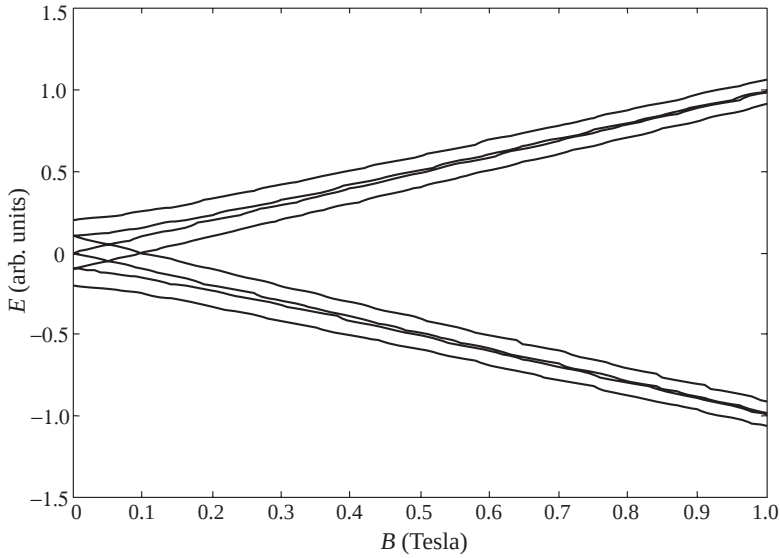

Fig. 1. Energy spectrum of the system, described by the Hamiltonian (1).

phonon interaction. Also, owing to other valent electrons absence metallic gates do not influence them (including other donors' electrons), that is why considered scheme is more simple to control. Quantum single-qubit operations (for example, NOT) are made with the help of radio-frequency pulses with resonant frequency. As concerns two-qubit operations (for example, CNOT), their realization is shown in Table 1.

One of the most important problems in quantum computing is the problem of the final state measurement. Unfortunately, the absence of the energy level anticrossing effect (Fig. 1) prevent using it to measure the final state, as it was made in [3, 4]. We suppose recent suggestion [5] to be the promising to solve this problem. A "turnstyle" can detect a current of electrons with definite polarization. This scheme can be used not only for single spin state measurements, but for spin system state measurement as well. When one wants to measure any qubit's state, SWAP operation between that nucleus spin-qubit and the electron must be made. After that electron spin state measurement (measurement of the spin polarization) completes the measurement process. Finally, we propose a novel qubit based on NMR of donor nuclei in semiconductor nanostructures. It is more coherent and more simple to control compared to proposal of Kane [1].

Acknowledgments

This work has been supported in part by Russian Ministry of Industry, Science and Technologies within framework of program "Advanced Technologies".

References

[1] Kane B. E. *Nature* **393**, 133 (1998).
[2] Reina J. H., Quiroga L., Johnson N. F. *Phys. Rev. B* **62** R2267 (2000).
[3] Larionov A. A., Fedichkin L. E., Kokin A. A., Valiev K. A. *Nanotechnology* **11** 392 (2000).
[4] Valiev K. A., Kokin A. A., Larionov A. A., Fedichkin L. E. *Russian Microelectronics* **29** 285 (2000).
[5] Molotkov S. N., Nazin S. S. *Pisma ZhETF* **70**, 141 (1999).

9th Int. Symp. "Nanostructures: Physics and Technology"
St Petersburg, Russia, June 18–22, 2001

Possible experiment on quantum Bayes theorem

Alexander N. Korotkov
Dept. of Electrical Engineering, University of California, Riverside, CA 92521 and Nuclear Physics Institute, Moscow State University, Moscow 119899

Abstract. We propose a solid-state experiment to study the process of continuous quantum measurement of a qubit state. The experiment would verify that the evolution of a qubit during the measurement is governed by the information obtained from the detector (Quantum Bayes Theorem). In particular, it can show that an individual qubit remains coherent during the measurement, in contrast to decoherence for the ensemble of qubits. The experiment can be carried out using quantum dots, single-electron transistors, or SQUIDs.

The problem of quantum measurement (wavefunction collapse) remains controversial for over seventy years. The interest to the problem is renewed nowadays because of its direct relation to quantum computing [1] and also because the progress in experimental techniques makes it now possible to resolve some of the controversial issues, which were discussed earlier only from the philosophical or mathematical points of view. One of such issues is the continuous measurement of a quantum system.

The success of the theory describing interaction of a quantum object with environment [2] has lead to an opinion common nowadays that the collapse postulate is a needless part of the quantum mechanics and can be derived from the Schrödinger equation tracing out the detector degrees of freedom. Then the measurement process is described by gradual decoherence of the measured object. Since the procedure requires ensemble averaging, the "modern philosophy" of quantum mechanics says that only ensemble-averaged quantities make sense while the discussion of the evolution of an individual quantum system is meaningless. This claim sharply contradicts, however, the point of view of "old" textbooks. Moreover, the modern approach cannot actually reproduce the "orthodox" collapse postulate, but only its ensemble-averaged version. The controversy has acquired a practical aspect since in the proposed solid-state quantum computers the qubit measurement is necessarily continuous (not instantaneous).

Recently developed Bayesian formalism [3] (for earlier somewhat similar theories see, e.g. [4]) reconciles the modern and orthodox approaches and allows us to describe the continuous measurement of an *individual* qubit. It shows that if the detector is good enough (basically, its sensitivity should be quantum-limited), then the qubit remains coherent (in a pure state) during the process of measurement, while the gradual decoherence claimed by the modern approach is just a result of averaging over the ensemble of measurement results. The Bayesian formalism can be applied for the realization of continuous quantum feedback control of a qubit and qubit purification, that is impossible using the ensemble-averaged formalism.

Since the issue remains controversial, it is important to show experimentally that the individual qubit stays coherent during measurement, in contrast to the claim of the modern approach. This paper describes such an experiment which can be realized at the present-day level of technology (for discussion of more direct experiments which, however, are too difficult for realization, see Ref. [3]).

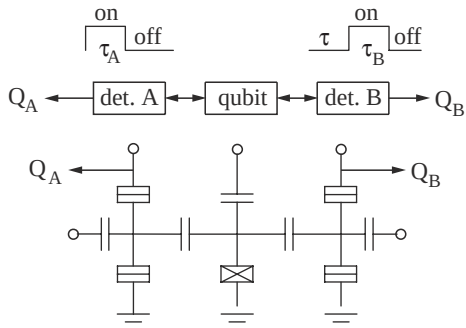

Fig. 1. Schematic of two-detector correlation experiment using Cooper-pair box and two single-electron transistors.

Within the Bayesian formalism the evolution of the density matrix ρ of the measured qubit (two-level system with the tunneling strength H and energy asymmetry ε) is described by equations

$$\dot{\rho}_{11} = -2H\,\mathrm{Im}\rho_{12} + (2\Delta I/S)\,\rho_{11}\rho_{22}[I(t) - I_0], \tag{1}$$

$$\dot{\rho}_{12} = \imath\varepsilon\rho_{12} + \imath H(\rho_{11} - \rho_{22}) - (\Delta I/S)\,(\rho_{11} - \rho_{22})[I(t) - I_0]\,\rho_{12} - \gamma\,\rho_{12}, \tag{2}$$

where $I(t)$ is the continuous detector output (we assume current), $\Delta I = I_1 - I_2$ is the difference between two average currents corresponding to qubit states $|1\rangle$ and $|2\rangle$, $I_0 \equiv (I_1 + I_2)/2 \gg |\Delta I|$, S is the output detector noise, and γ is the decoherence rate due to detector nonideality (for example, $\gamma = 0$ for quantum point contact), while the ensemble-averaged decoherence is $\Gamma = \gamma + (\Delta I)^2/4S$ (the detector ideality can be characterized by the parameter $\eta \equiv 1 - \gamma/\Gamma$).

The idea of the experiment is to use two detectors (A and B) connected to the same qubit (Fig. 1). The detectors are switched on for short periods of time by two shifted in time voltage pulses (one for each detector) with durations τ_A and τ_B, supplied from the outside. The output signal from the detector A is the total charge $Q_A = \int_0^{\tau_A} I_A(t)\,dt$ passed during the measurement period. Similarly, the output from the detector B is $Q_B = \int_\tau^{\tau+\tau_B} I_B(t)\,dt$, where τ is the time shift between pulses. If the measurement by the detector A changes the qubit density matrix, it will affect the result of measurement B. Repeating the experiment many times (with the same initial qubit state) we can obtain the probability distribution $P(Q_A, Q_B|\tau)$ of different outcomes, which contains the information about the effect of the quantum measurement on the qubit density matrix.

Figure 1 shows the realization of the experiment using single-electron transistors as detectors. Qubit is realized by the Cooper-pair box so that the electric charge of the central island can be in coherent combination of two discrete charge states. Another similar setup is two quantum point contacts measuring the charge state of a double-quantum-dot qubit. One more setup is the 3-SQUID experiment in which the qubit is realized by one SQUID while two other SQUIDs are in the detecting regime.

The ensemble-averaged formalism implies the absence of correlations between $\rho(t)$ and $I(t)$, so the average result of the second measurement $\overline{Q}_B(Q_A,\tau) \equiv \int Q_B\,P(Q_A, Q_B|\tau)\,dQ_B$ should not depend on Q_A. The Bayesian formalism (1)-(2) makes the different prediction: $\overline{Q}_B$ does depend on Q_A.

For simplicity let us assume symmetric qubit, $\varepsilon = 0$, which is initially in the ground state, $\rho_{11} = \rho_{22} = \rho_{12} = 0.5$, and also assume relatively strong coupling between the qubit and detectors, $(\Delta I_A)^2/HS_A \gg 1$, $(\Delta I_B)^2/HS_B \gg 1$ (subscripts A and B correspond to two detectors), so that we can neglect the qubit evolution due to finite H during the measurement periods τ_A and τ_B, which are assumed to be on the order of $S_{A,B}/(\Delta I_{A,B})^2$. Then from Eqs. (1)-(2) it follows that the first measurement only "partially" localizes the qubit state and after obtaining the result Q_A from the first measurement the qubit density matrix is

$$\rho_{11}(\tau_A) - \rho_{22}(\tau_A) = \tanh\left[\left[(Q_A - \tau_A I_{2A})^2 - (Q_A - \tau_A I_{1A})^2\right]/2S_A\tau_A\right], \quad (3)$$

$$\rho_{12}(\tau_A) = [\rho_{11}(\tau_A)\,\rho_{22}(\tau_A)]^{1/2}\exp(-\gamma_A\tau_A)\,. \quad (4)$$

Here Eq. (3) is the direct consequence of the Bayes formula, so this result can be called "Quantum Bayes Theorem" [5]. The qubit performs the free evolution during the time $\tau - \tau_A$ between measurements (here we neglect $\tau_A \ll \tau$) and the average result of the second measurement $\overline{Q}_B = \tau_B(I_{2B} + \rho_{11}(\tau)\Delta I_B)$ depends on Q_A in the following way (Fig. 2a):

$$\delta_B = (H/\Omega)\tanh\left[\left[(Q_A - \tau_A I_{2A})^2 - (Q_A - \tau_A I_{1A})^2\right]/2S_A\tau_A\right] \times \cos[\Omega\tau - \arcsin(\gamma_f/4H)]\exp(-\gamma_f\tau/2)\,, \quad (5)$$

where $\delta_B \equiv (\overline{Q}_B - \tau_B I_{0B})/\tau_B\Delta I_B$, γ_f is the dephasing with both detectors switched off, and $\Omega = (4H^2 - \gamma_f^2/4)^{1/2}$ is the frequency of quantum oscillations. Notice that δ_B changes sign together with the sign of $Q_A - \tau_A I_{0A}$, while the phase of oscillations is a piece-constant function of Q_A.

The dependence becomes quite different if the $\pi/2$ pulse is applied to the qubit immediately after the first measurement, that multiplies $\rho_{12}(\tau_A)$ given by Eq. (4) by the imaginary unit. In this case (Fig. 2b) $\delta_B = A\sin(\Omega\tau + \arcsin z/A)\exp(-\gamma_f\tau/2)$, where $A = [(z^2 + y^2 - yz\gamma_f/2H)/(1 - \gamma_f^2/16H^2)]^{1/2}$, while $z = \rho_{11}(\tau_A) - 1/2$ and $y = \mathrm{Im}\rho_{12}(\tau_A + 0) = \mathrm{Re}\rho_{12}(\tau_A - 0)$ are given by Eqs. (3) and (4). This expression considerably simplifies for weak dephasing, $\gamma_A\tau_A \ll 1$ and $\gamma_f \ll H$, when

$$\delta_B = \frac{1}{2}\sin[\Omega\tau + \arcsin(2\rho_{11}(\tau_A) - 1)]\exp(-\frac{\gamma_f\tau}{2}). \quad (6)$$

In contrast to Eq. (5), now the phase of oscillations of $\delta_B(\tau)$ depends on the result Q_A of the first measurement, while the amplitude is maximum possible and independent of Q_A. This fact is very important since it *proves* that after the first measurement (by an ideal detector) the qubit remains in the pure state for *any* result Q_A. This state depends on Q_A and is not one of the localized states as somebody could naively expect.

In a realistic experimental situation the assumption of strong coupling with detectors may be inapplicable. In this case the full probability distribution $P(Q_A, Q_B|\tau)$ as well as the dependence $\overline{Q}_B(Q_A, \tau)$ should be calculated numerically using Eqs. (1)–(2). The results of these calculations for $(\Delta I_A)^2/HS_A = (\Delta I_B)^2/HS_B = 1$ are shown in Figs. 2c and 2d. Weak coupling as well as the nonideality of the detectors decrease the correlation between the results of two measurements, however, for moderate values of the coupling and nonideality the correlation is still significant.

Experimental demonstration of the correlation and agreement with the results of the Bayesian formalism would prove the validity of this formalism and therefore confirm its

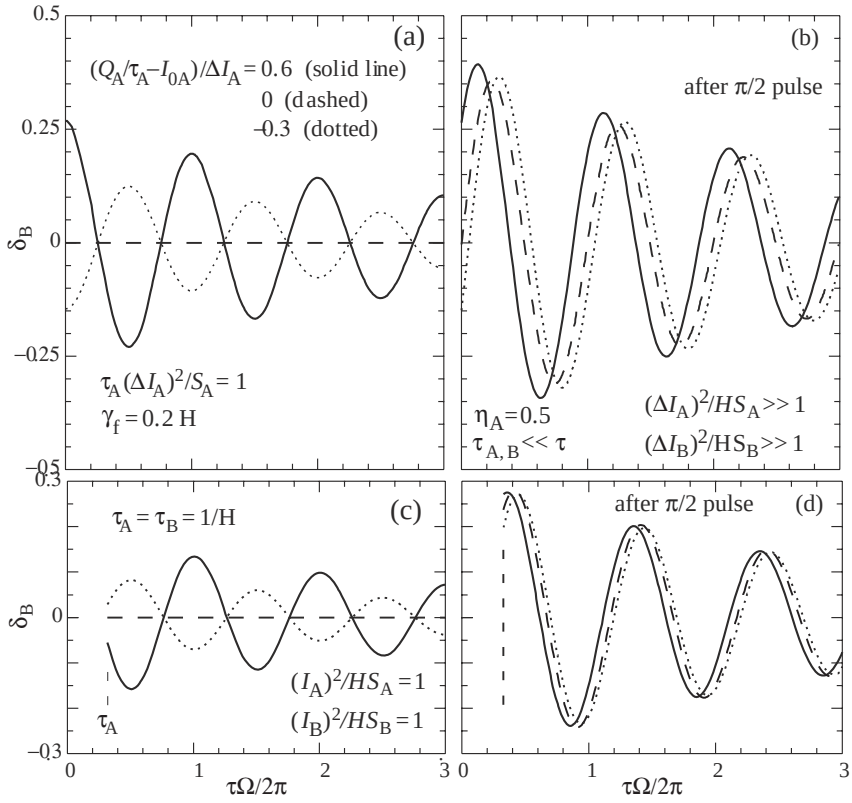

Fig. 2. The normalized average result δ_B of the second measurement for several selected results Q_A of the first measurement, as a function of the time τ between measurements. Panels (a)–(b) are for strong coupling and panels (c)–(d) for moderate coupling between the qubit and detectors.

other predictions. In particular, it would open the way to the qubit purification using continuous quantum feedback control.

References

[1] C. Bennett, *Phys. Today* **48 (10)**, 24 (1995).
[2] A. O. Caldeira and A. J. Leggett, *Ann. Phys.* (N.Y.) **149**, 374 (1983).
[3] A. N. Korotkov, *Phys. Rev. B* **60**, 5737 (1999); *Physica B* **280**, 412 (2000); cond-mat/0003225; cond-mat/0008003; cond-mat/0008461.
[4] H. J. Carmichael, *An Open System Approach to Quantum Optics* (Springer, Berlin, 1993); M. B. Mensky, *Phys. Usp.* **41**, 923 (1998); H. M. Wiseman and G. J. Milburn, *Phys. Rev. A* **47**, 1652 (1993).
[5] C. W. Gardiner, *Quantum noise* (Springer, Berlin, 1991), Ch. 2.2.

9th Int. Symp. "Nanostructures: Physics and Technology"
St Petersburg, Russia, June 18–22, 2001

Effect of Coulomb interaction on GaAs quantum computer performance

L. Fedichkin and M. Yanchenko
Institute of Physics and Technology RAS,
34, Nakhimovsky pr., Moscow, 117218, Russia

Abstract. Interaction between the quantum bits strongly limits quantum computer performance while using large quantum registers. We investigated influence of such interaction for recently proposed quantum computer based on GaAs quantum dots with built-in barrier. Our results show that such interaction could greatly reduce computational fidelity.

Introduction

There has been a tremendous progress in quantum computation theory since the pioneering work by R. Feynman [1]. One of the most important reasons why the experimental realization of practically useful large scale quantum computer is not attained until now is attitude of quantum computers (compared to classical ones) to various types of errors. Hopefully there are known quantum error correction procedures, which help to correct errors which occurred simultaneously in single quantum bit (qubit) or in few qubits due to interaction with environment or imprecise implementation of local gates.

In 1998 J. Gea-Banacloche [2] revealed the significance of another source of errors: internal interaction in quantum computer between neighbour qubits. The interaction serves to entangle qubits if necessary, so it should be switched on every time while implementing two-qubit gate and be switched off otherwise. But the accuracy of switcher amplitude could not be generally higher than several orders of magnitude. We should also control moments of switching off/on with such accuracy. Therefore there is weak unavoidable interaction between qubits any time. J. Gea-Banacloche [2] noted that even such a weak interaction leads to errors which could completely destroy quantum computer performance in large scale quantum registers. These errors differ from common few-qubit errors since they originate from internal qubit-qubit interaction rather than from influence of noisy environment. They conserve coherence of quantum computer but spreads over whole quantum register and make initially unentangled blocks of qubits to entangle each other. In 1999 it was pointed out by the same author [3] that common error correction methods do not solve the problem since these procedures imply that the probability of whole quantum register to be entangled due to errors during time of performing one of basic gates (we will denote this time as τ) is negligible.

1. Errors due to qubit-qubit interaction

As it was shown in [3] the interaction between neighbour qubits i and j frequently leads to Hamiltonian which in the basis $\{|00\rangle, |01\rangle, |10\rangle, |11\rangle\}$ will have a matrix like the following

$$H_{ij} = \begin{pmatrix} a^2 & 0 & 0 & 0 \\ 0 & ab & 0 & 0 \\ 0 & 0 & ab & 0 \\ 0 & 0 & 0 & b^2 \end{pmatrix}. \qquad (1)$$

The inequality $a \neq b$ results in nonadditive interaction energy. It is convenient to split interaction Hamiltonian into additive H_A and nonadditive parts H_N, where

$$H_A = \begin{pmatrix} a^2 & 0 & 0 & 0 \\ 0 & \frac{a^2+b^2}{2} & 0 & 0 \\ 0 & 0 & \frac{a^2+b^2}{2} & 0 \\ 0 & 0 & 0 & b^2 \end{pmatrix}, \tag{2}$$

$$H_N = \hbar\delta\omega \begin{pmatrix} 0 & 0 & 0 & 0 \\ 0 & 1 & 0 & 0 \\ 0 & 0 & 1 & 0 \\ 0 & 0 & 0 & 0 \end{pmatrix}, \tag{3}$$

where

$$\delta\omega = \frac{(a-b)^2}{2\hbar}. \tag{4}$$

The dimensionless parameter δ ($\delta = \tau\delta\omega$) can be used to evaluate entanglement during one computing step. The action of H_A does not entangle qubits. Moreover, by going to an interaction picture with state $|0\rangle$ having additional energy $a^2/2$ and state $|1\rangle$ having additional energy $b^2/2$ additive part can be effectively removed. The numerical value of factor $\delta\omega$ in H_N depends on qubits being used. In some cases non-additive part can contain also off-diagonal terms, whose influence on computation performance are similar to diagonal terms.

Fidelity F of quantum computer is

$$F = |\langle\Psi_{\text{ideal}}|\Psi_{\text{out}}\rangle|^2, \tag{5}$$

where $|\Psi_{\text{ideal}}\rangle$ is a result of ideal quantum computer, $|\Psi_{\text{out}}\rangle$ is a result of quantum computer being compared with the ideal one. For the calculation we use algorithm designed to add two n-bit numbers [4]. The computer consists of three registers, a, b, and c, of n, $n+1$, and n bits, respectively; and of $P = 2(4n-1)$ gates (CNOT and Toffoli gates). Computer action is the transfer $|a, b, c\rangle \rightarrow |a, a+b, c\rangle$, where $|c\rangle$ is zero ancilla register. The fidelity depends on the numbers being added. So we average the fidelity over b, using a in the fully entangled state:

$$F_{av} \equiv \frac{1}{2^n}\sum_{b=0}^{2^n-1} F(b). \tag{6}$$

Dependence of average fidelity versus scaled interaction strength $\sigma = \frac{1}{2}P\delta\sqrt{3n}$ is shown in Fig. 1.

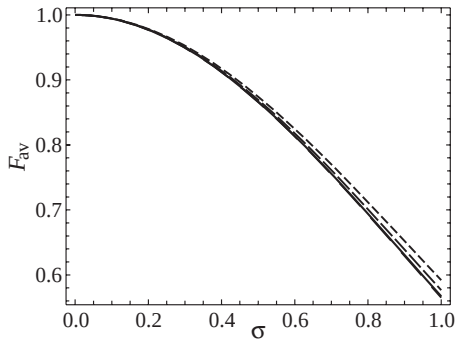

Fig. 1. Average fidelity versus scaled interaction strength. Case of dipole-dipole interaction. Solid curve, $n = 2$; short dashed curve, $n = 3$; dashed curve, $n = 4$; long dashed curve, $n = 5$.

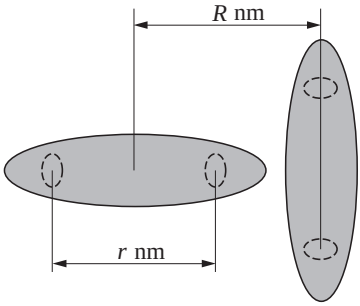

Fig. 2. GaAs quantum dot two-qubit structure.

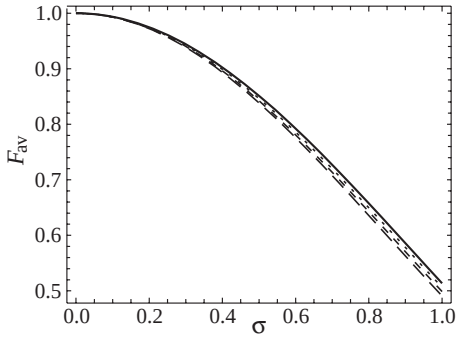

Fig. 3. Average fidelity versus scaled interaction strength. GaAs quantum dot quantum computer. Solid curve, $n = 2$; short dashed curve, $n = 3$; dashed curve, $n = 4$; long dashed curve, $n = 5$.

We investigated influence of Coulomb qubit-qubit interaction on performance of GaAs quantum dot quantum computer proposed in [5]. The geometry of the structure is shown in Fig. 2.

Parameter δ of the structure for such interaction goes from depends on geometrical parameters and the material (GaAs) of the structure. For calculation we used following parameters: $r = 10-14$ nm (the distance between minima of the qubit-forming potential), $R = 20-50$ nm (the distance between qubits), $\kappa = 12.85$ (dielectric permittivity in GaAs). CNOT gate operation time $\tau = 1-100$ ns [5].

Dependence of average fidelity versus scaled interaction strength with such interaction hamiltonian is shown in Fig. 3.

2. Conclusions

Operation of GaAs quantum computer performing adder algorithm was simulated in presence of Coulomb qubit-qubit interaction. Our simulation shows that in a large-scale quantum register ($n > 100$) qubit-qubit interaction could completely destroy quantum computer performance. Consequently use of multi-qubit error avoiding procedures in large-scale quantum computers with interacting qubits like firstly proposed algorithm [6] is obligatory to maintain steady operation.

Acknowledgments

This work has been supported in part by Russian Ministry of Industry, Science and Technologies within framework of program “Advanced Technologies”.

References

[1] Feynman R. P. *Int. J. Theor. Phys.* **21** 467 (1982).
[2] Gea-Banacloche J. *Phys. Rev. A* **57** R1 (1998).
[3] Gea-Banacloche J. *Phys. Rev. A* **60** 185 (1999).
[4] Vedral V., Barenco A. and Ekert A. *Phys. Rev. A* **54** 147 (1996).
[5] Fedichkin L., Yanchenko M. and Valiev K. *Nanotechnology* **11** 387 (2000).
[6] Fedichkin L. *Quantum Computers & Computing* **1** 84 (2000).

9th Int. Symp. "Nanostructures: Physics and Technology"
St Petersburg, Russia, June 18–22, 2001

Birefringent nanostructured silicon: new promising material for linear and nonlinear optics

D. Kovalev†, *V. Yu. Timoshenko*‡, L. Golovan‡, E. Gross†, N. Künzner†, G. Polisski†, J. Diener†, L. Kuznetsova‡, D. A. Sidorov-Biryukov‡, A. B. Fedotov‡, A. M. Zheltikov‡, P. K. Kashkarov‡ and F. Koch†

† Technical University Munich, Physics Department E16, 85748 Garching, Germany
‡ Moscow State M. V. Lomonosov University, Physics Department and International Laser Center, 119899 Moscow Russia

Abstract. Porous Si layers produced by anisotropic electrochemical etching of bulk Si exhibit strong in-plane birefringence which depends on the sizes of Si nanocrystals, spacing between them and dielectric properties of their surrounding media. Second harmonic generation experiments have revealed phase matching conditions for wave interaction in the layers. Furthermore, they can serve as a phase-matching matrix for optically nonlinear substance incorporated in their pores. This finding can significantly expand the choice of nonlinear optical media since their anomalous dispersion is not strictly required for phase matching conditions.

Introduction

Crystalline silicon has indirect band gap and highly isotropic cubic lattice structure what limits its optical applications. Most of research efforts to eliminate its properties were devoted to porous modification of Si (PSi) produced by its electrochemical etching [1, 2]. The absence of a large volume fraction of Si results in a reduced value of the refractive index (n) of PSi. PSi prepared on (100) Si substrates is demonstrated to be in-plane optically isotropic due to the equivalence of [010] and [001]crystallographic directions [2].

To achieve in-plane uniaxial dielectric anisotropy we have employed the electrochemical etching of (110) Si wafers. Because of the selective crystallographic pore propagation in equivalent [010] and [$1\bar{0}0$] directions tilted to the (110) surface [3] the projection of those on the (110) plane ([$1\bar{1}0$] direction) would result in an uniaxial surface symmetry with a dielectric constant $\varepsilon_{[1\bar{1}0]}$ being different from $\varepsilon_{[001]}$. Bulk Si is not anisotropic crystal but its porous modification becomes intrinsically uniaxial for this plane due to anisotropic dielectric nanostructuring. Since nanocrystals retain the diamond-like crystalline structure and their sizes (1–50 nm, depending on wafer doping and etching parameters used) [4] are much smaller than the wavelength of light, PSi still can be considered as a continuous optical medium. Therefore the effective medium approximation[5] can be applied to analyze the optical properties of PSi.

1. Experimental

PSi layers were prepared from (110) oriented, boron doped Si substrates with typical resistivity of $0.001-4\,\Omega\cdot$cm. The electrochemical etching was done in ethanoic hydrofluoric solution. The porosities of the layers were in the range from 50 to 70%. Free-standing PSi films were investigated by Fourier transform infrared (FTIR) spectroscopy. Optical transmittance of linearly polarized light was also measured to evaluate birefringence values in visible and near IR spectral regions.

The experimental set-up for second harmonic generation (SHG) consists of a picosecond Nd:YAG master oscillator with passive mode locking and amplification cascades. The second-harmonic signal was detected with a photomultiplier. The $\lambda/2$ plate was used to rotate polarization of fundamental wave. For details see [6].

2. Results and discussions

The clear evidence of the birefringence in anisotropically etched PSi layers comes from FTIR spectra measured for unpolarized light. Inset in Fig. 1 shows a typical reflectance spectrum at normal incidence. The spectrum exhibits interference fringes modulated by beats. The beats arise from the existence of two principal in-plane directions with different refractive indices and their difference (the birefringence) Δn is estimated to be about 0.18 while the mean refractive index n_m is 1.65 in the spectral range of 2–20 μm. We found that the birefringence level of PSi is mostly sensitive to the doping level of Si substrate and dielectric surrounding of Si nanocrystals. Figure 1 gives the values of Δn for three sets of the samples prepared on Si substrates having different doping levels and, therefore, different mean sizes of Si nanostructures (measured by TEM). Solid lines in Fig. 1 are fits according to the effective media approximation [5] for anisotropically spaced Si nanocrystals. A good agreement between the measurements and calculations shows that an increase of Δn for short wavelength arises mainly from the dielectric function dispersion of bulk Si.

The large birefringence of anisotropically etched PSi allows us to reach the phase matching conditions for nonlinear optical wave interaction. We consider both types of SHG in negative crystal (*ooe* and *oee*) with synchronism conditions $n_{1o} = n_{2e}$ and $(n_{1o} + n_{1e})/2 = n_{2e}$, correspondingly. For normal incidence of the fundamental radiation at 1.06 μm phase mismatch is less for the second type of interaction (*oee*). For the first-type synchronism the angle is of 54% with the optical axis. However, in this case the angle inside the material between the normal and synchronism direction is 36°, what is higher than the angle of the internal reflection. Thus, in air synchronism is not achieved in PSi film

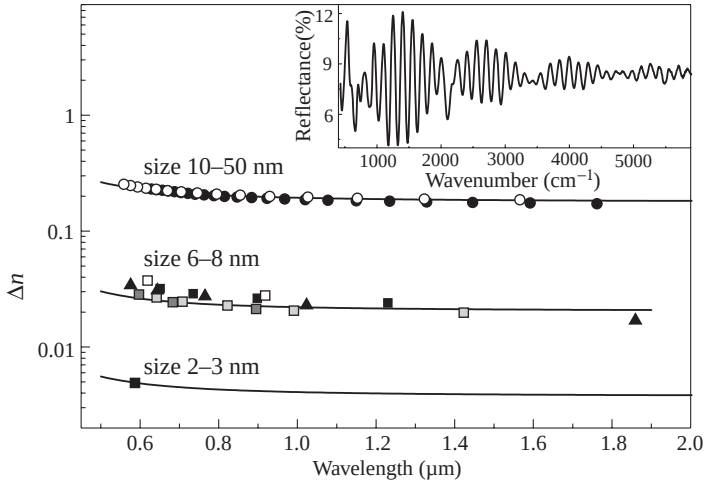

Fig. 1. Spectral dependence of the birefringence of PSi prepared on the substrates of p-Si (2–3 nm size of nanostructures), p^+-Si (6–8 nm size of nanostructures) and p^{++}-Si (10–50 nm size of nanostructures). Solid lines are fits according to the effective medium approximation. Inset: an example of the FTIR reflectance spectrum of PSi prepared on p^{++}-Si substrate.

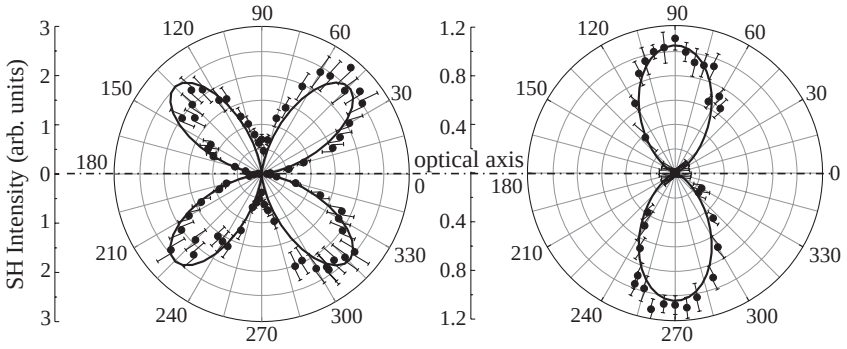

Fig. 2. Polarization dependences of the SH in PSi prepared on the p^{++}-Si substrate. The SHG experiments are performed in air at normal incidence of the fundamental radiation (a) and for incidence at 60° (b). Solid lines are theoretical fits.

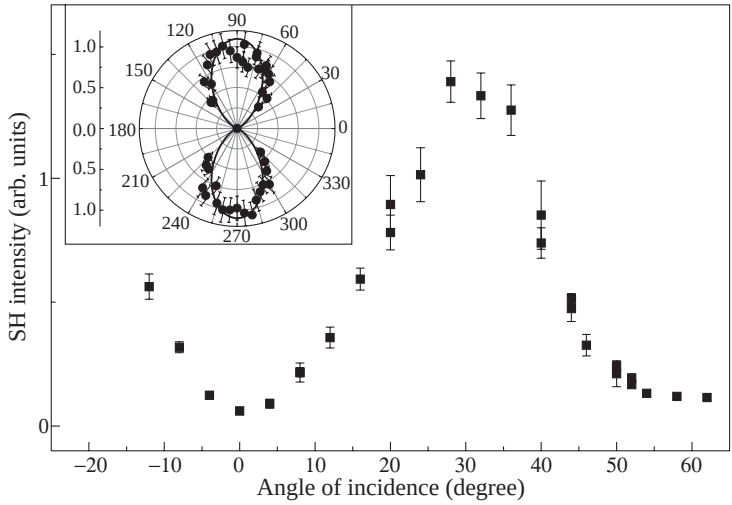

Fig. 3. Dependence of the SH in PSi (20 μm thick) on the angle of incidence. The pores of PSi are filled with glycerol. Inset: polarization dependence of the SH for normal incidence.

because its birefringence is too strong. The situation is changed when pores are filled with a dielectric media having a certain dielectric constant what reduces optical anisotropy. For example, according the effective media approximation the filling of the layer with glycerol ($n_g = 1.45$) gives the phase matching for *ooe* interaction at the angle of incidence of 31°.

Figure 2 shows dependences of the SH intensity for PSi on polarization of the pumping radiation. The SH is polarized along the optical axis of the PSi layer. If the pumping radiation falls normally to the surface the polarization dependence is two-fold (*oee* interaction), whereas for incidence at 60° it is one-fold (*ooe* interaction). The SH in the PSi layers filled with glycerol exhibits one-fold polarization dependence (inset in Fig. 3) independently on the angle of incidence. In fact, the filling of the pores with glycerol decreases anisotropy and, as a result, makes *ooe* interaction more effective even at normal incidence. The SHG in the layer filled with glycerol reaches the maximum for incidence at 30° (Fig. 3) what is in excellent agreement with our calculation for the phase matching condition. SHG in PSi is likely to be caused by bulk quadrupole nonlinearity because the elementary cells of

Si nanocrystals are rather centrosymmetrical [7]. The birefringence of PSi does not result in occurrence of effective dipole second-order susceptibility. The fact that maximal SHG efficiency in PSi with glycerol is observed at the expected angle of synchronism indicates that the phase matching can be achieved. This seems to be very promising for nonlinear optical applications since porous Si layers can play a role of a phase matching matrix for nonlinear media incorporated into its pores.

Acknowledgements

This work was partially supported by CRDF project RP2-2275 and the Russian Foundation for Basic Research (project No. 00-02-1756).

References

[1] A. G. Cullis, L. T. Canham and P. D. J. Calcott, *J. Appl. Phys.* **82**, 909 (1997).
[2] D. Kovalev et al. *phys. stat. sol. (b)* **215**, 871 (1999).
[3] S. F. Chuang, S. D. Collins, and R. L. Smith, *Appl. Phys. Lett.* **55**, 675 (1989).
[4] A. G. Cullis and L. T. Canham, *Nature (London)* **353**, 335 (1991).
[5] D. A. G. Bruggeman, *Annalen der Physik* **24**, 636 (1935).
[6] L. A. Golovan et al. *JETP Lett.* **69**, 300 (1999).
[7] L. A. Golovan et al. *Techn. Phys. Lett.* **20**, 334 (1994).

9th Int. Symp. "Nanostructures: Physics and Technology"
St Petersburg, Russia, June 18–22, 2001

Efficient photoluminescence upconversion in porous Si

N. Künzner†, J. Diener†, D. Kovalev†, G. Polisski†, F. Koch†,
Al. L. Efros‡ and M. Rosen‡

† Technische Universität München, Physik Department E16
D-85747 Garching, Germany
‡ Nanostructure Optics Section, Naval Research Laboratory
Washington, DC 20375, USA

Abstract. We report on a new phenomenon specific for a system of spatially interconnected nanocrystal assemblies: efficient low temperature photoluminescence (PL) upconversion at resonant optical excitation of porous Si. The upconverted photoluminescence (anti-Stokes PL) is observed at intensities as low as $0.1\,\mathrm{W/cm^2}$ and its intensity is as large as that of the Stokes PL band. The confirmation of the essence of connectivity between nanocrystals comes from the same type of studies performed on systems containing Si nanocrystals surrounded by a thick SiO_2 shell where the anti-Stokes PL is completely absent for any excitation energy and intensity used while the properties of the Stokes PL are very similar to those of porous Si.

The nonlinear optical response of nanocrystal assemblies has been clearly observed in single CdSe and InAs nanocrystals [1, 2]. The occupation of one nanocrystal with two electron-hole (e-h) pairs leads to Auger photo-luminescence damping, Auger autoionization and Auger quenching of the PL in the ionized crystal. In porous silicon, an assembly of silicon nanocrystals, the lifetime of e-h pairs is on the order of microseconds to milliseconds and therefore a double occupation of one nanocrystal with e-h pairs leading to strong nonlinear effects can be achieved at very low excitation intensity [3].

We observed efficient low temperature anti-Stokes PL at resonant excitation of a broad porous Si PL band. Figure 1 shows typical low temperature resonant PL spectra for a naturally oxidized and a hydrogen passivated porous Si sample, excited on the low energy side of the nonresonant emission band.

The samples were prepared from (100)-oriented p-type c-Si with resistivities $4-6\,\Omega$cm by anodic etching in a HF solution in the dark. The strongly oxidized Si nanocrystals were prepared either by oxidation of macroporous Si at 1000 °C or by Si ion implantation in a SiO_2 layer and subsequent annealing. For the excitation of the resonant and nonresonant PL a He-Cd and Ti:Sapphire laser were used. The PL was detected with a Si charge-coupled device or a fast photomultiplier. In order to suppress stray light from the exciting chopped CW laser the entrance slit of the monochromator was blocked by a mechanical shutter when the laser beam illuminated the sample. The Stokes PL consists of a set of peaks assigned to transisions involving no phonon, 1TA-, 2TA-, 1TO-, TO+TA- and 2TO-momentum-conserving phonons in the absorption-emission cycle [4]. The intense upconverted emission grows progressively relative to the Stokes PL with decreasing excitation energy and the efficiency of the anti-Stokes PL reaches that of the Stokes PL at the lowest excitation energy used. Different mechanisms are possible to provide the additional energy for the anti-Stokes PL. The energy gain from a phonon bath can be excluded since in this case the intensity of the anti-Stokes PL grows with increasing temperature in contrast to the observed temperature dependence. Also the thermal energy available from the phonon

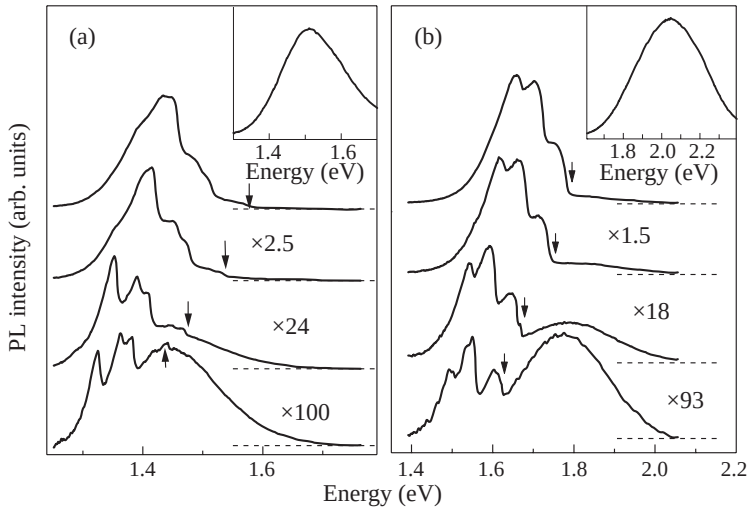

Fig. 1. Resonantly excited PL spectra of two porous silicon samples having different average nanocrystal sizes. (a) Naturally oxidized. (b) Hydrogen passivated. Excitation energies are indicated by arrows, $T = 4.2$ K, $I_{\rm exc} = 1\,{\rm W/cm^2}$.

bath at experimental temperatures ∼4 K is much too small to explain the spectral extension of the anti-Stokes spectra of up to a few hundreds of meV (see Fig. 1). Therefore the additional energy can only come from the absorption of a second photon or from the nonradiative Auger recombination of a second e-h pair. A simultaneous absorption of two exciting photons involving extremely short-lived virtual states is impossible because it would require much higher excitation intensities on the order of $\mathrm{MW/cm^2}-\mathrm{GW/cm^2}$ than those used in the experiments (down to $0.1\,\mathrm{W/cm^2}$).

The source of the anti-Stokes PL can be identified by comparing the lifetimes of the Stokes and anti-Stokes PL. The conventional Stokes PL lifetime of porous Si in thermal equilibrium depends on the temperature and is determined by the short-lived spin-singlet and the long-lived spin-triplet luminescing exciton state [5]. The lifetime of the anti-Stokes luminescence exactly follows the behavior of the Stokes PL lifetimes (Fig. 2) suggesting

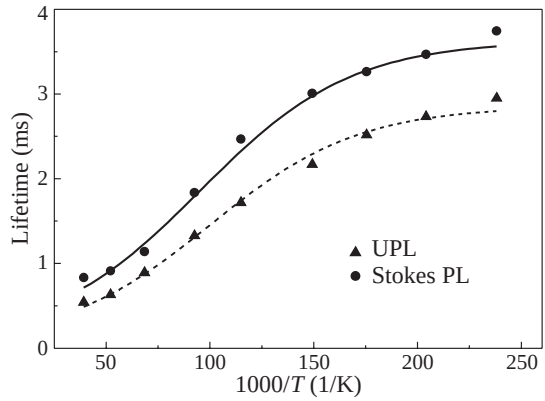

Fig. 2. The temperature dependence of the Stokes PL (circles) and anti-Stokes PL (triangles) lifetime.

that the excitons confined in Si nanocrystals are the source of both Stokes and anti-Stokes PL.

As can be seen in Fig. 3 the experiments show a linear dependence of the anti-Stokes PL on the excitation intensity (below the Auger PL quenching limit) and can be explained by a two-step absorption process with a saturation of a long-lived intermediate state giving rise to the anti-Stokes PL. The long decay time of these states allows them to be occupied even at very low excitation intensities. This long-lived state behaves like a spatially separated e-h pair state with the electron and the hole existing in neighboring nanocrystals. The overlap of wavefunctions of electron and hole localised in neighboring nanocrystals is weak and thus results in an enhanced decay time for the spatially separated state. The optical excitation of a second e-h pair in the larger of these nanocrystals occupied by an electron or hole, having the smaller bandgap leads to a nonradiative Auger process followed by the injection of a carrier into the smaller nanocrystal having larger bandgap with subsequent emission of anti-Stokes PL. The role of the charge separation can be studied by using nanocrystals

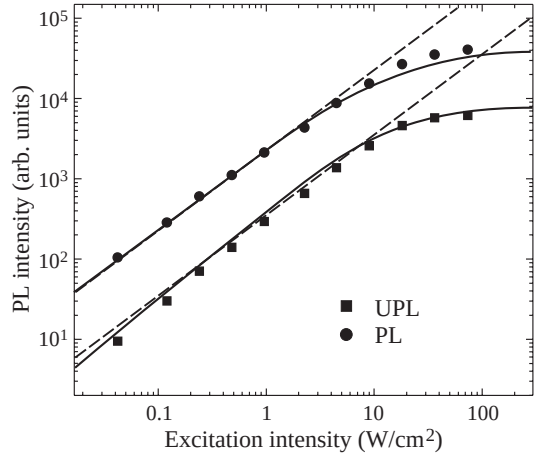

Fig. 3. Excitation intensity dependence of the PL measured at the 2TO peak energy position (circles) and anti-Stokes PL ($E_{\text{det}} = 1.5$ eV, squares). $T = 4.2$ K, $E_{\text{exc}} = 1.483$ eV.

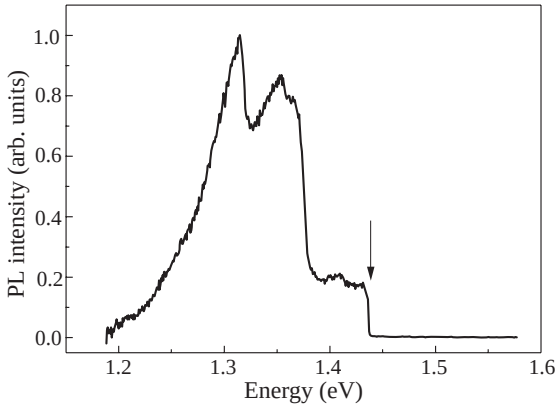

Fig. 4. Resonantly excited PL from Si nanocrystals having a thick oxide shell, $T = 4.2$ K, $I_{\text{exc}} = 1\,\text{W/cm}^2$. The excitation energy is shown by the arrow.

isolated by high potential barriers. For Si nanocrystals surrounded by a thick SiO_2 shell which prevents any carrier transfer between the crystallites the anti-Stokes PL is completely absent for all excitation energies used (Fig. 4).

This implies that the carrier transfer between nanocrystals plays an important role for the anti-Stokes PL. The existence of long-lived spatially separated charges is crucial for the model of the anti-Stokes PL. One has to assume lifetimes of the intermediate long-lived state to be on the order of seconds. Experimental evidence for such states comes from the observation of an extremely long-lived component of the PL after CW illumination of a porous Si sample immersed in superfluid He by a high energy Ar^+ laser beam. This illumination creates spatially separated e-h pairs which recombine slowly after switching off the excitation source (in a seconds time domain).

References

[1] M. Nirmal, B. O. Dabboussi, M. G. Bawendi, J. J. Macklin, J. K. Trautmann, T. D. Harris and L. E. Brus, *Nature* (London) **383**, 802 (1996).
[2] S. Empedocles, D. J. Norris and M. G. Bawendi, *Phys. Rev. Lett.* **77**, 3873 (1996).
[3] D. Kovalev, B. Averboukh, M. Ben-Chorin and F. Koch, *Phys. Rev. Lett.* **77**, 2089 (1996).
[4] D. Kovalev, H. Heckler, M. Ben-Chorin, G. Polisski, M. Schwartzkopff and F. Koch, *Phys. Rev. Lett.* **81**, 2803 (1998).
[5] P. D. J. Calcott, K. J. Nash, L. T. Canham, M. J. Kane and D. Brumhead, *J. Phys. Condens. Matter* **5**, L91 (1993).

9th Int. Symp. "Nanostructures: Physics and Technology"
St Petersburg, Russia, June 18–22, 2001

Noise properties of iron-filled carbon nanotubes

S. Roumiantsev[a]†, R. Vajtai‡, N. Pala†, B. Q. Wei‡, M. S. Shur†,
L. B. Kish§ and P. M. Ajayan‡
† Department of Electrical, Computer and Systems Engineering,
Rensselaer Polytechnic Institute, Troy, New York 12180-3590, U.S.A.
‡ Department of Materials Science and Engineering,
Rensselaer Polytechnic Institute, Troy, New York 12180-3590, U.S.A.
§ Department of Materials Science, The Ångström Laboratory,
Uppsala University, P.O.B. 534, S-75121, Uppsala, Sweden
[a] Ioffe Physico-Technical Institute, St Petersburg, Russia

Abstract. Extraordinary mechanical and electronic properties of carbon nanotubes have attracted great interest. In this talk we describe electrical and noise properties of iron-filled multi-walled nanotubes. Our results show that these nanotubes have unusual current dependence of noise and exhibit a much smaller noise than single-walled nanotubes.

Introduction

Carbon nanotubes have many unique properties that attracted the attention of microelectronics and nanotechnology communities. For example, the mechanical strength and thermal conductivity are higher than these values for diamond and boron nitride [1, 2]. Also, different types of nanotubes (single-walled tubes with varied chirality, multi-walled tubes) have different properties ranging from metallic to semiconducting behavior [1], and exhibiting different effects, such as ballistic electron transport [3] and Aharonov–Bohm oscillations [4].

Filling nanotubes with metals and semiconductors[5], inducing defects in their structure [6], producing "Y" shape tubes [7] or "decorating" them with functional groups covalently attached to their walls cause further variations of their widely varied electronic properties. These modified tubes might be used for building simple devices in individual nanotubes [8].

Low frequency noise analysis is an effective tool for device and material characterization. In many cases, noise is more sensitive to existing disorder, nonlinear behavior or contact problems in the device than dc measurements. Moreover, $1/f$ noise can be used as a diagnostic tool for quality and reliability assessment of electronic devices [9, 10].

On the other hand, the level of the low frequency noise is one of the most important characteristics of electronic devices, which determines whether the devices are suitable for practical microwave and optical systems [11]. So far, the results of the noise measurements on nanotubes are only available for single-walled nanotubes [12]. In this paper, we will present the results of the $1/f$ noise measurements for multi-walled, partially iron-filled nanotubes and demonstrate that these nanotubes have unusual current dependence of noise and exhibit a much smaller noise than single-walled nanotubes.

1. Experimental details

Carbon nanotubes used in our measurements were produced by chemical vapor deposition from xylene and ferrocene [13]. We applied a mixture of the two precursors resulting

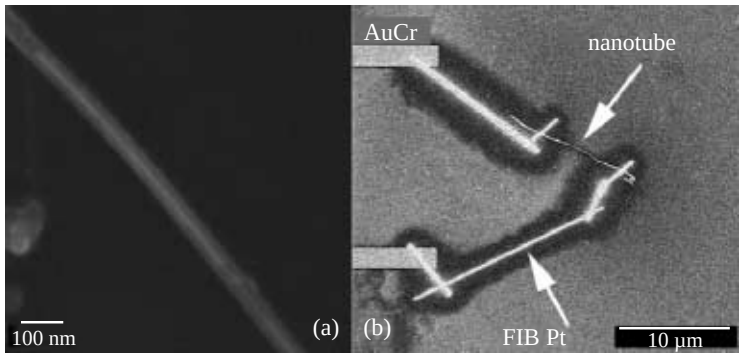

Fig. 1. (a) FE-SEM micrograph of a multi-walled nanotube filled partially with iron, (b) FE-SEM micrograph of the nanotube with FIB interconnects.

1:10 Fe/C atomic ratio in the reaction zone and near entire iron cores in growth nanotubes. As can be seen from Fig. 1(a), the nanotubes were only partially filled with iron. In order to perform dc and noise measurements on individual tubes, the samples were prepared as follows. First, the silicon wafer was thermally oxidized (resulting in 300 nm thick SiO_2 layer) and a metal (Au/Cr) electrode pattern was prepared using conventional lithography technique. In the next step the nanotubes were sprayed onto the SiO_2 surface as a low-density nanotube film, in which most of the tubes were separated from each other. Individual tubes with optimal location and shape were selected by FE-SEM microscopy. Focused Ion Beam (FIB) technique was used in order to deposit platinum interconnections and make contacts to the nanotubes (see Fig. 1(b)). The time and current of FIB preparation was minimized to avoid excessive ion irradiation of nanotubes and substrate.

The low frequency noise was measured in two contacts configuration in the frequency range from 1 Hz to 3 kHz at room temperature. The voltage fluctuations S_V from 2 kΩ resistor connected in series with the structures under test were measured by SR 770 Network Analyzer.

2. Results and discussion

Current voltage measurements showed that nanotubes had ohmic behavior under the dc bias from −4 to 4 V with resistance of ∼20 to 60 kΩ.

The noise spectra of the short circuit current fluctuations had the form $S_I \sim 1/f^\beta$ where β is close to unity. This $1/f$-like spectrum is very common for many semiconductor devices and materials and was also recently observed in single-walled nanotubes [12].

However, the current dependence of noise was quite different from that reported in [12] and from what is typical for linear metal and semiconductor resistors. In contrast to typical dependence of the spectral noise density $S_I \sim I^2$ (I is the current), we found $S_I \sim I^\alpha$ with $\alpha < 2$ (from 1 to 1.5 for different samples). This behavior indicates a current dependence in the number, amplitude or rate of elementary fluctuators or in the coupling strength if the effect is a cooperative (nonlinear) one. This unusual (for a linear region of the I–V characteristic) dependence might indicate that the noise could be generated by a small non-linear contact resistance at the points of the contacts of FIB metal to the nanotube. If in the contact resistor, the number of elementary fluctuators is proportional to the current (like in silicon diodes), a similar $S_I \sim I$ dependence can be expected [14].

In order to estimate role of the interconnects we also measured the noise of the test structure consisted from a simple FIB stripe. We found the conventional $S_I \sim I^2$ behavior

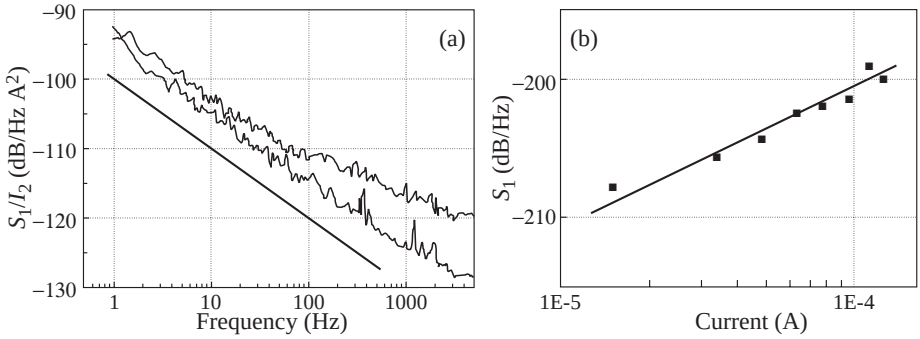

Fig. 2. Frequency (a) and current (b) dependencies of spectral noise density of current fluctuations for iron-filled multi-walled nanotubes. The applied dc voltage was 1 V and 4 V for the upper and lower spectrum, respectively, in part (a), and the frequency was 200 Hz for values displayed in part (b).

for the test structure.

At current $I = 10^{-5}-10^{-4}$ A the relative spectral noise density of current fluctuations in iron-filled multi-walled nanotubes was much smaller than that reported in Ref. [12].

Acknowledgements

This work at Rensselaer was partially supported under the DARPA Molecular Level Printing Program (Grant # N66001-98-1-8917). R. Vajtai's work is supported by the North Atlantic Treaty Organization (NATO) under a Grant awarded in 2000, (No. 0075178). L. B. Kish's work is supported by NFR, Sweden.

References

[1] R. Saito, G. Dresselhaus and M. S. Dresselhaus, *Physical Properties of Carbon Nanotubes* (Imperial College Press, London, 1998).
[2] P. M. Ajayan and T. W. Ebbesen, *Rep. Prog. Phys.* **60**, 1025 (1997).
[3] C. T. White and T. N. Todorov, *Nature* **393**, 240 (1998).
[4] A. Bachtold, et al. *Nature* **397**, 673 (1999).
[5] P. M. Ajayan and I. S. Iijima, *Nature* **361**, 333 (1993).
[6] B. Q. Wei, et al. under publication
[7] C. Papadopoulos, A. Rakitin, J. Li, A. S. Vedeneev and J. M. Xu, *Phys. Rev. Lett.* **85**, 3476 (2000).
[8] C. W. Zhou, J. Kong, E. Yenilmez and H.J. Dai, *Science* **290**, 1552 (2000).
[9] F. Otten, L. B. Kish, C.-G. Granqvist, L. K. J. Vandamme, R. Vajtai, F. E. Kruis and H. Fissan, *Appl. Phys. Lett.* **77**, 3421 (2000).
[10] C. Pennetta, L. B. Kiss, Z. Gingl and L. Reggiani, *J. Nanoparticle Res.* **2**, 97 (2000).
[11] M. J. Buckingham, *Noise in electronic devices and systems*, 1983.
[12] P. G. Collins, M. S. Fuhrer and A. Zettl, *Appl. Phys. Lett.* **76**, 894 (2000).
[13] B. Q. Wei, Z. J. Zhang, G. Ramanath and P. M. Ajayan, *Appl. Phys. Lett.* **77**, 2985 (2000).
[14] L. B. Kiss and T. G. M. Kleinpenning, *Physica B.* **145**, 185 (1987).

9th Int. Symp. "Nanostructures: Physics and Technology"
St Petersburg, Russia, June 18–22, 2001

Suppression of the Jahn–Teller effect in nanoparticles: AgCl nanocrystals embedded in KCl matrix

P. G. Baranov, N. G. Romanov, V. S. Vikhnin and V. A. Khramtsov
Ioffe Physico-Technical Institute, St Petersburg, Russia

Abstract. A strong decrease in the g-factor anisotropy was revealed by optically detected magnetic resonance for self-trapped Jahn–Teller holes (both isolated and forming self-trapped excitons) in AgCl nanocrystals embedded into the KCl crystal lattice. This implies a considerable suppression of the Jahn–Teller (J–T) effect in nanoparticles. A rather general mechanism of the suppression of the Jahn–Teller effect in nanocrystals is developed, taking into account the additional deformation field appearing because of the strong vibronic interaction at the interface.

Introduction

In the last decade, nanostructures have been successfully fabricated using self-organization effects common to strained heterosystems [1]. Fabrication of new structures and devices based on anisotropic nanoparticles is of great interest since anisotropic particles can exhibit novel and enhanced properties, compared with those of isotropic spherical particles. Semiconductor nanocrystals have been mainly studied for II–VI semiconductors dispersed in a vitreous matrix [2]. However, nanocrystals can show a common orientation only in a crystalline matrix, as recently demonstrated for CuCl and AgCl nanocrystals embedded in an alkali halide matrix [3–7].

It is well known that the electronic, as well as atomic, structure is considerably changed as the size increases from clusters to small particles and, finally, to a bulk material, through which manifold interesting properties are developed. In this respect, KCl:AgCl seems to be a very promising system for studying these effects. It has long been known that silver ions Ag^+ substitute for alkali ions in silver doped alkali halide crystals. Ultra-violet (UV) light or x-ray irradiation can produce a number of different silver-related point defects. On the other hand, silver halide nanometre- and micrometre-size crystals, i.e. nanocrystals and microcrystals, can be formed in growth of KCl single crystals heavily doped with AgCl, as recently reported in [5–7]. KCl and AgCl have the same face-centred cubic lattice with the lattice constants 0.629 nm and 0.555 nm, respectively. The energy gap are 8.7 eV for KCl and 3.26 eV for AgCl. Thus, AgCl crystals embedded in KCl can be considered as an array of self-organized microcrystals and nanocrystals (quantum dots) in a strained KCl:AgCl heterosystem.

The effects of confinement on shallow centres with Bohr radius comparable with the particle size are well known (see [1–2] for references). The influence of the nanoparticle size on deep level centres and local effects in solids is of fundamental importance, being, however, much less studied to our knowledge. The Jahn–Teller (J–T) effect is one of the basic local effects in solids, rather sensitive to internal fields and variations of the electron–phonon interaction. STH and STE in bulk AgCl are classical J–T systems well studied in bulk AgCl by various radiospectroscopic techniques. Therefore, investigation of AgCl nano- and microcrystal systems embedded in a crystalline matrix seems to be very interesting.

1. Results and discussion

The KCl:AgCl crystals were grown by the Stockbarger method. The silver concentration in the melt was 2%. ODMR at a frequency of 35 GHz and temperature of 1.6 K was detected from the luminescence excited by the UV light of an arc deuterium lamp with appropriate light filters. The microwave power in the cavity of an ODMR spectrometer was modulated at a sound frequency, and the microwave-induced changes in the luminescence intensity were detected using a lock-in detector. The samples (#1, #2 and #3) were cleaved from different parts of the grown crystal and represented transparent single crystals without visible inclusions.

In the present study two types of ODMR spectra have been observed in heavily doped KCl:AgCl which belong the following centres, presented in Table 1:

(i) The STH, STE and SEC in oriented AgCl microcrystals which have the parameters close to those for the bulk AgCl .

(ii) The anisotropic centres with $S = 1/2$ and $S = 1$ ascribed to STH and STE in AgCl nanocrystals and having the parameters which are essentially different from those of bulk AgCl. Similar $S = 1$ centres were ascribed in [6] to STE in AgCl nanocrystals with $L < 10$ nm.

In the 35 GHz ODMR spectra of sample #1 and bulk AgCl the lines of STH, STE and SEC are well resolved due to strong anisotropy of g-factors and relatively large fine structure splitting D. For the ODMR of $S = 1/2$ and $S = 1$ centres in samples #2 and #3 both the anisotropy of g-factors and the parameter D are considerably reduced. Nevertheless we were able to discriminate between the signals of the $S = 1$ and $S = 1/2$ centres since the relative intensities of the ODMR spectra depend on the microwave power and the chopping frequency. The angular variations of ODMR in sample #2 for the rotation in the (110) plane are shown in Fig. 1. Full and dashed lines show the ODMR spectra recorded with the chopping frequencies 80 Hz and 800 Hz, respectively. At higher chopping frequency the signals of the doublet spectrum are more pronounced. The $S = 1/2$ centres dominated in the ODMR spectrum of sample #3.

Observation of bulk-like ODMR in KCl:AgCl can be considered as the direct confirmation of the formation of AgCl microcrystals (apparently of micron size) in KCl matrix. These microcrystals have practically the same properties as bulk AgCl and maintain the orientation of the host KCl lattice. The misorientation of the AgCl microcrystals as estimated from the ODMR spectra is below 5°. Thus ODMR was used as a fingerprint of the embedded AgCl crystals and a confirmation of their high crystallographic quality.

Table 1. Parameters of STH, STE and SEC in bulk AgCl crystals and AgCl micro- and nanocrystals embedded in KCl matrix

		Centre						
		STH		STE			SEC	
Crystal		$g_\parallel$	$g_\perp$	$g_\parallel$	$g_\perp$	D (MHz)	g	Refs.
Bulk AgCl		2.147	2.040	2.0216	1.968	−710	1.881	[8]
AgCl	micro-crystals	2.147	2.040	2.020	1.966	−710	1.88–1.90	this work
embedded	nano-	—	—	1.992	1.964	−335	—	[6]
in KCl	crystals	2.016	1.974	1.992	1.965	−335	∼1.96	this work

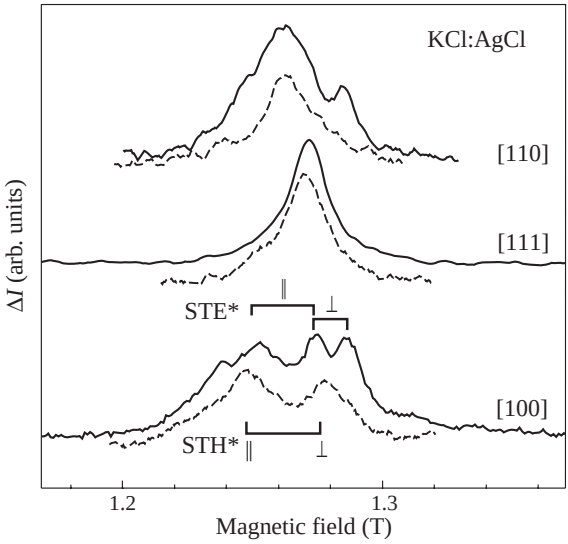

Fig. 1. ODMR in KCl:AgCl sample #2 recorded with microwave chopping frequency $f_{chop} =$ 80 Hz (full curves) and $f_{chop} = 800$ Hz (broken curves) for the three principal orientations in the (110) plane. The position of the ODMR lines for self-trapped excitons and self-trapped holes in AgCl nanocrystals are marked by STE* and STH*. Symbols ∥ and ⊥ denote the centres with the Jahn–Teller axis parallel and perpendicular to the magnetic field, respectively. $T = 1.6$ K; $\nu = 35.2$ GHz; $P_{\text{microwaves}} = 300$ mW.

Although the arguments in favour of the assignment of the ODMR spectra in samples #2 and #3 to AgCl nanocrystals seems to be rather convincing one can not totally exclude that they may be connected to point defects in KCl. Our analysis of the EPR and ODMR spectra showed that the obtained ODMR spectra do not correspond to EPR of any known point defect or STE in KCl.

There exist a direct link between the g-factors of STE and those of STH and SEC. $\overleftrightarrow{g}_{\text{STE}} = (\overleftrightarrow{g}_{\text{STH}} + \overleftrightarrow{g}_{e})/2$. This strictly holds for bulk AgCl crystals and AgCl microcrystals (see Table 1). It is natural to suppose that the same is valid for the AgCl nanocrystals. It is seen from Table 1 that g-factors for STH and STE in AgCl nanocrystals satisfy this equation within the experimental error if we suppose that g-factor of SEC remains isotropic in the nanocrystals. In addition, this allows to estimate the g-factor of SEC in AgCl nanocrystals as ca. 1.96 which is much larger than in bulk AgCl. We emphasise that the existence of correlation between g-factors of the $S = 1/2$ and $S = 1$ centres strongly supports their identification as STH and STE in AgCl nanocrystals.

Thus, in AgCl nanocrystals with the size down to 10 nm both the doublet and the triplet ODMR spectra ascribed to STH and STE in nanocrystals were found with the parameters essentially different from STH and STE in bulk AgCl (see Table 1). In bulk AgCl crystals the difference $g_{\parallel} - g_{\perp}$ is 0.107 for STH and 0.054 for STE. In AgCl nanocrystals the respective values are 0.042 and 0.027, i.e. about two times smaller.

The anisotropy of g-factor of the ^2E J–T state of STH in the cubic environment is determined by the effective Zeeman interaction and is described by introducing the appropriate electron operators $\widehat{U}_{\theta}$ and $\widehat{U}_{\varphi}$ in the basis of the ^2E state [9].

The average value of the g-factor tends to the isotropic contribution g_1 with a decrease of the strength of the J–T effect because $\langle \widehat{U}_{\theta} \rangle \to 0$ and $\langle \widehat{U}_{\varphi} \rangle \to 0$. Thus the observed

pronounced decrease of the g-factor anisotropy of STH in AgCl nanocrystals implies a considerable suppression of the J–T effect.

We consider a change in the energies of electron and hole states at the nanocrystal interface as a main mechanism governing the JTE in nanocrystals. It should be noted that the energy gap jump of $\sim$ 5 eV from KCl to AgCl occurs at a distance of about 3 Å. This results in a large vibronic coupling constant at the interface. The vibronic coupling at the interface brings about weakening or suppression of the pseudo Jahn–Teller effect in sufficiently small-sized nanocrystals. This results in a decrease or suppression of the anisotropy in the EPR (ODMR) spectra of STH; i.e., the difference $g_{\parallel} - g_{\perp}$ decreases. Since the STE is formed through electron capture by the STH, the anisotropy of the STE g tensor should also decrease or be suppressed. Estimates show that the considered mechanism can account for the reduction of the J–T effect of STH for $L < 10$ nm, which seems to be reasonable for the system under study. The details of the proposed mechanism can be found in [10, 11].

It should be noted that the proposed mechanism of the formation of the internal nanostructure strain field due to the interface vibronic effect is rather general and can be actual for a set of nanostructures and thin films.

Acknowledgements

This work was supported in part by the Russian Foundation for Basic Research (grant 00-02-16950) and the Russian program 'Physics of Solid State Nanostructures' (grant 99-3012).

References

[1] D. Bimberg, M. Grundmann and N. N. Ledentsov, *Quantum Dot Heterostructures* (John Wiley & Sons Ltd) 1999.
[2] U. Woggon, *Semiconductor Quantum Dots*, Springer Tracts in Modern Physics (Berlin: Springer) 1997, p. 136.
[3] D. Fröhlich, M. Haselhoff, K. Reimann and T. Itoh, *Solid State Commun.* **94**, 189 (1995).
[4] M. Haselhoff and H.-J. Weber, *Phys. Rev.* **B 58**, 5052 (1998).
[5] H. Stolz, H. Vogelsang and W. von der Osten, *Handbook of Optical Properties: Optics of Small Particles, Interfaces, and Surfaces* vol. II (Boca Raton, FL: CRC Press, 1997) p. 31.
[6] H. Vogelsang, O. Husberg, U. Khler, W. von der Osten and A. P. Marchetti, *Phys. Rev.* **B 61**, 1847 (2000).
[7] N. G. Romanov, R. A. Babunts, A. G. Badalyan, V. A. Khramtsov and P. G. Baranov, *Proc. 8th Int. Symp. Nanostructures: Physics and Technology*, St Petersburg 2000, p. 308.
[8] W. Hayes, I. B. Owen and P. J. Walker, *J. Phys. C: Solid State Phys.* **10**, 1751 (1977); A. P. Marchetti and D. S. Tinti, *Phys. Rev*. **B24**, 7361 (1981).
[9] A. Abraham and B. Bleaney, *Electron Paramagnetic Resonance of Transition Ions* (Clarendon, Oxford, 1970; Mir, Moscow, 1973), Vol. 2, p. 249.
[10] P. G. Baranov, V. S. Vikhnin, N. G. Romanov and V. A. Khramtsov, *JETP Lett.* **72**, 329 (2000).
[11] P. G. Baranov, N. G. Romanov, V. A. Khramtsov and V. S. Vikhnin, *Phys.-Cond. Matter 2001*, in press.

9th Int. Symp. "Nanostructures: Physics and Technology"
St Petersburg, Russia, June 18–22, 2001

Silicon nanoclusters embedded in SiO_2 studied by Raman scattering

F. J. Espinoza-Beltrán†, L. L. Díaz-Flores†, J. Morales-Hernández‡,
J. M. Yáñez-Limón†, F. Rodríguez-Melgarejo†, Y. V. Vorobiev†
and J. González-Hernández†

† CINVESTAV-IPN, Unidad Querétaro. Lib. Norponiente no. 2000,
Fracc. Real de Juriquilla, 76230 Querétaro, Qro., México,
‡ Programa de Posgrado en Ingeniería, Facultad de Ingeniería,
UAQ, Querétaro, Qro., México

Abstract. Low concentration of nanometric sized particles produced by a ball milling procedure were introduced into SiO_2 matrix by the sol-gel method. SiO_2 sol-gel formulations with high water-TEOS ratios were prepared. Samples with high silanol concentration was obtained for high temperatures as was proven by FTIR spectroscopy measurements. Raman scattering measurements showed evidence of a photo-oxidation effect of Si nanoparticles embedded into a SiO_2 matrix. Si particle sizes measured by Raman scattering were in the range from 7 to 14 nm.

1. Introduction

Si nanoparticles embedded into a SiO_2 matrix has been a goal for several researchers in the last years. The main interest to obtain these systems is the study of the light emission properties of Si when it is in a nano-sized structure. Among the different procedures used to obtain these systems are implanting Si atoms into SiO_2 matrix [1], reactive RF magnetron sputtering [2], Low Pressure Chemical Vapor Deposition (LPCVD) [3]. L. Zhang *et al* reported an interesting procedure to obtain Si nanoparticles into a sol-gel SiO_2 matrix, introducing Si particles from porous Si [4]. However, the materials obtained are instable, so that the initial light emission decreases with time and disappears. In this work we are introducing Si particles into SiO_2 by using a sol-gel solution with high water-TEOS ratio. It was introduced a milling process [5] by using a low energy ball mill, with the goal of study the effect of dispersion on the retention of water into the SiO_2 matrix. During the gelation process, the partially oxidized Si particles are covered by the SiO_2 material. The samples were studied by infrared and Raman scattering measurements.

2. Experimental

Preparation of small particles of Si: By using a high energy ball mill, granular silicon was milled to reduce its grain size. The weight ratio balls/silicon was of 2:1. The milling process was achieved in typical time of 30 min. 1.0 g of this milled powder was incorporated into an acidified solution of ethanol, HNO_3 and water, and reposed by 24 hours. The precipitated powder was separated from the mixture by a decanting process. This suspension was used to prepared the precursor formulations of SiO_2 with Si. Preparation of suspensions for SiO_2 matrix with Si particles the sol-gel solution precursor of the SiO_2 was prepared mixing during 15 minutes, by using a magnetic stirrer, the suspension with silicon particles and TEOS (tetraethyl-orthosilicate) in a molar ratio of 4:1. After this process, it was added water in a molar ration respect to TEOS of 17:1. The suspension was milled in a low

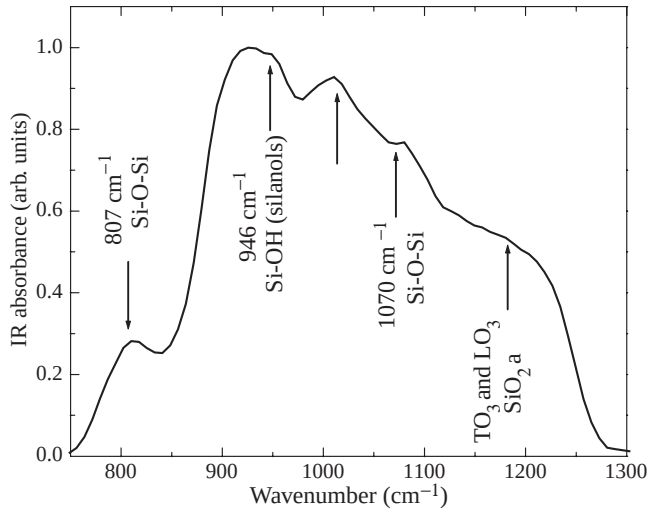

Fig. 1. IR spectrum for the SiO_2:Si sample, for the range from 750 to 1300 cm^{-1}, for a SiO_2-Si milled suspension after a thermal annealing at 500°C by 1.0 h.

energy ball mill. Dried samples were thermal annealed at 500°C of temperature. The experimental techniques used to analyze the samples were infrared spectroscopy (NICOLET mod. AVATAR 360-FTIR) in the diffuse reflectance mode and Micro-Raman (DILOR). For micro-Raman measurements the samples were exposed to two light intensities (20 and 5 mW by using a filter), and sequential periods of time. The laser light was focused to 1.0 μm^2 of area.

In Figure 1 there is shown an IR spectrum, in the range from 750 to 1300 cm^{-1}, of the SiO_2:Si sample. Five broad bands can be observed from this figure. These bands can be identified as vibrational modes of SiO_2 [6] and Si-OH (silanol) [7]: bending mode O-Si-O $\sim$819 cm^{-1} (δ), stretching mode Si-O $\sim$1070 cm^{-1}, stretching Si-OH $\sim$930 cm^{-1}, and TO and LO modes of O-Si-O $\sim$1100$-$1250 cm^{-1} [8, 9]. An additional band is observed for about 1030 cm^{-1}, this band has been attributed for structural order in the amorphous SiO_2 [10]. The position of these modes are signed in the figure by vertical arrows.

Powder samples were exposed to light bath for several periods of time, by using a 632 nm He-Ne laser (5–20 mW output power focused on 1.0 μm^2 of area) during the Raman Measurements. Figure 2 shows the Raman spectra for the sample for two case: (a) changing the focus distance from 0 to 10 μm in steps of 2.5 μm and, (b) measuring after exposition to variable laser light intensity and exposition time. Curves signed as A, B, C, and D, respectively, correspond to sample exposition of 6 (A), 9 (B), 12 (C) and 15(D) min with light intensity of 5 (A), 5 (B), 20 (C) and 20 (D) mW, respectively. The continuous line corresponds to the best fitting of the experimental data to a model [11] that considers spherical Si grains (see in figure). After 6 min of light exposition there is a shift of the peak for about 3 cm^{-1} that can be attributed to an temperature increase of the Si grains.

3. Discussion and Conclusions

Raman spectra for several light exposition times and variable effective power, of the SiO_2:Si sample showed an interesting effect of reduction of effective Si grain size. This sample has

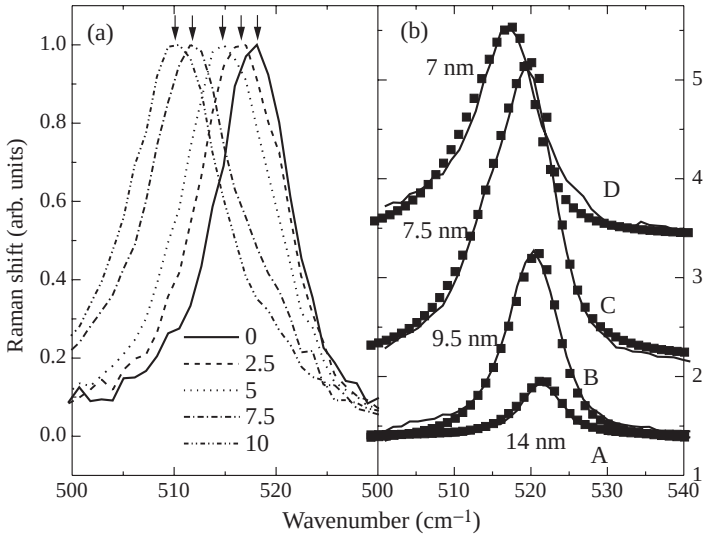

Fig. 2. Raman scattering spectra for the sample thermally annealed at 500°C: (a) changing laser focus distance (i.e. effective power) and, (b) measured after exposition to sample exposed during 6, 9, 12 and 15 min to a light intensity of 5 (A), 5 (B), 20 (C) and 20 (D) mW, respectively.

a high concentration of silanol bonds, even around the Si grains. So that the light bath can produce a chemical reaction that reduces the Si grain size. Also, the heating due light bath can produce intensive mechanical stresses on the silicon grains, so that the Raman peak shifts to lower values with the power intensity. The grain size reduction could be produced by a photo-chemical process like photo-oxidation of Si-Si bonds by the presence of Si-OH bonds. The small Si grains with sizes about 10 nm are irregular shapes with a great quantity of (-OH) ions linked to their surface. The weaker Si-Si bonds on the grain surface could easily be oxidized as effect of the light bath producing an effective reduction of the Si grain size. This mechanism is limited by the concentration of weak surface Si-Si bonds.

Nanometric sized particles produced by ball milling were introduced into SiO_2 matrix by the sol-gel method. SiO_2 matrix with high silanol concentration can be produced by a ball milling procedure of the sol-gel solution. The Si-OH concentration in this matrix can be kept for high temperatures as was proven by FT-IR spectroscopy measurements. Raman scattering measurements showed a reduction of Si grain size due light exposition which can be an evidence of a photo-chemistry process, or also to the presence of intensive stresses on the Si nanoparticles embedded into a SiO_2 matrix with high silanol concentration.

Acknowledgements

The authors thank Ing. Rivelino Flores Farías and Q. en A. Martin Adelaido Hernández Landaverde for their technical assistance. This work was partially supported by a CONCYTEQ (Consejo de Ciencia y Tecnología del Estado de Querétaro) and CONACyT from México.

References

[1] L. Rebohle, J. von Borany, R. Grötzschel, A. Markwitz, B. Schmidt, I. E. Tyschenko, W. Skorupa, H. Fröb, and K. Leo, *Phys. Stat. Sol. (a)* **165**, 31 (1998).

[2] H. Seifarth, R. Grötzschel, A. Markwitz, W. Matz, P. Nitzsche and L. Rebohle, *Thin Solid Films* **330**, 202 (1998).
[3] A. G. Nassiopoulou, V. Ioannou-Sougleridis, P. Photopoulos, A. Travlos, V. Tsakiri and D. Papadimitriou, *Phys. Stat. Sol. (a)* **165**, 79 (1998).
[4] L. Zhang, J. L. Coffer and T. W. Zerda, *J. Sol-Gel Sci. and Technol.*, **11**, 267 (1998).
[5] L. L. Díaz-Flores, J. J. Pérez-Bueno, F. J. Espinoza-Beltrán, J. F. Pérez-Robles, R. Ramírez-Bon, Y. V. Vorobiev and J. González-Hernández, *Microelectronic Engineering*, **51-52**, 659-666 (2000).
[6] K. Kim, *Phys. Rev.* **B 57**, 13072 (1998).
[7] J. A. Theil, D. V. Tsu, M. W. Watkins, S. S. Kim and G. Lucovsky, *J. Vac. Sci. Technol.* **A 83**, 1374 (1990).
[8] J. F. Pérez-Robles, L. A. García-Cerda, F. J. Espinoza-Beltrán, M. Yánez-Limón, J. González-Hernández, Y. V. Vorobiev, J. R. Parga-Torres, F. Ruíz and J. Méndez-Nonell. *Phys. Stat. Sol. (a)* **172**, 49 (1999).
[9] J. F. Pérez-Robles, S. Jiménez-Sandoval, J. González-Hernández, Y. V. Vorobiev, J. R. Parga-Torres and M. A. Hernández-Landaverde. *Rev. Mex. Fís.* **45**, 150 (1999).
[10] I. W. Boyd, *Appl. Phys. Lett.* **51(6)**, 418 (1987).
[11] I. H. Campbell and P. M. Fauchet, *Solid State Commun.* **58**, 739 (1981).

9th Int. Symp. "Nanostructures: Physics and Technology"
St Petersburg, Russia, June 18–22, 2001

Penetration of a magnetic field in a regular indium wireframe

R. V. Parfeniev†, *D. V. Shamshur*†, A. V. Chernyaev†,
A. V. Fokin† and S. G. Romanov†‡
† Ioffe Physico-Technical Institute, St Petersburg, Russia
‡ Institute of Materials Science and Department of Electrical Engineering,
University of Wuppertal, 42097 Wuppertal, Germany

Introduction

Studies of superconductors in confined geometries of various types are known since mid 60s [1] when the free space in a porous glass was used to restrain the size of metal grains. In contrast with granular superconductors prepared by e.g. co-evaporation with dielectric, where at least 60% filling fraction is mandatory to complete the percolation path, in porous dielectrics the volume fraction of metal can be made less than 10% with a dc conductivity of a metal type.

Opal is one example of a crystalline porous template — a face centred cubic (FCC) package of identical silica spheres [2] with empty interstitials, which are available for infilling with a superconductor. The important feature of thus formed ensemble of nanograins is the replacement of unstable intergrain point contacts of granular superconductors with continuous bridges connecting adjacent nanoparticles. In the opal-based nanocomposites the size and spacing of nanostructures are identical throughout the array within 5–10% deviation.

Early experiments made on In nanograins embedded in opal have shown the very unusual behaviour of the critical current and magnetoresistance [3, 4]. Here we discuss the alteration of critical parameters of the In-opal nanocomposite with the progressively reduced filling fraction of In from 26% to 8%.

1. Experimental results and discussion

Opals in use consist of silica spheres with diameter $D = 234$ nm. In accord with the void geometry there are alternated O-grains with characteristic size $d_O = 0.41D$ connected each with T-grains of $d_T = 0.23D$ via bridges of minimum diameter $d_b = 0.15D$. The upper limit of the grain volume fraction in the FCC lattice of hard spheres is 26%. An amorphous silica was deposited on the inner surface of opal voids thus reducing the free volume down to 13%. Further reduction of porosity was achieved by coating opal voids with 34 monolayers of TiO_2 (O34-sample). The set of O47-samples was prepared by coating the opal with TiO_2 — from 0 (O47.1) to 27 monolayers (O47.2) and to 54 monolayers (O47.3). Effectively, diameters of voids were, approximately, as $d_O = 95$ (90; 80; 60) nm, $d_T = 55$ (50; 40; 30) nm and $d_b = 35$ (30; 25; 20) nm for the O47.1, O47.2, O47.3 and O34 samples, respectively, as defined from the optical Bragg diffraction.

In Fig. 1 the $R(T)$ curves for investigated samples are shown in the vicinity of the superconducting transition. The critical temperatures of superconducting (SC) transition T_c exceed sufficiently $T_c = 3.41$ K of the bulk indium. The increase of the above the bulk value correlates with the reduction of the volume fraction occupied by the In network in the opal. Assuming that the superconductivity nucleates at the narrowest part of the superconductor, the onsets of the resistance drop correspond the SC fluctuations in intergrain bridges. The "average" diameter of the In wireframe can be figured out with the empirical expression $T_c = 3.41 + 5.1/d$ [d in nm] [4]. The value $d = 18$ nm for O34 gives the estimate of

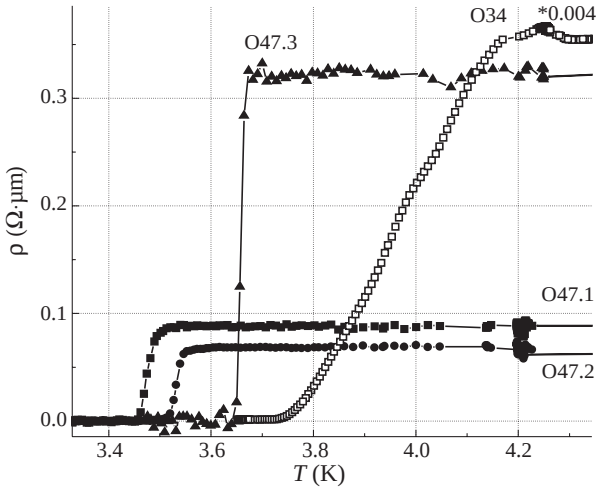

Fig. 1. Temperature dependencies of resistivity at low temperature for O47.1, O47.2, O47.3 and O34 samples (the values of resistivity for O34 sample are divided by 100).

the cross-size of the metal inclusion at the point where the SC spreads throughout the In wireframe as a whole, moreover this result is consistent with SEM data.

Resistivity curves in the temperature range from 300 K to Helium 4 temperatures are shown in Fig. 2 for all studied samples. The overall tendency is the decrease of the temperature-related change in the resistance with the decrease of the wireframe volume fraction, that is likely due to limiting the mean free path of electrons by scattering on grain boundaries rather than on phonons. $H_0(T)$ dependences were extracted from magnetoresistance curves, which are shown in the Fig. 3. The critical magnetic field H_0 is defined as the transition from the SC to the resistive state. Note that the $H_0 = 10$ kOe at $T = 1.57$ K exceeds by 35 times the critical field for the bulk In (280 Oe at $T = 0$ K). The SC transition for O34 sample is spread broadly over a field and shows a kink at approximately the midpoint of the transition. Accordingly, critical magnetic fields indicated as H_1 and H_2 (characteristic fields for derivative $\mathrm{d}R/\mathrm{d}H$ maxima) are shown in Fig. 3 for O34-sample. $H_0(T)$ curves follow the quadratic law, which is typical for type II superconductors. In particular, the expression $H_c(T) = H_c(0)(1 - (T/T_c)^2)$ for interconnected superconducting grains, whose size is less than the coherence length and/or the penetration depth, describes well the observed behaviour. From $R(T)$ curves the mean free path and then the coherence length were determined, which values show that the magnetic field penetrates freely through the In-opal nanocomposite. In this case magnetic vortices in the In grain network are effectively circulating supercurrents, which maintain the integrity of the flux quanta in encircled loops. Moreover, the effective diameter of these loops can exceed considerably the size of the minimum lattice-defined loop of $d_{\min} = 98$ nm. With the increase of the external field the effective loop area decreases and approaches $d_{\min}$. Apparently, this field defines the onset of the resistive state H_0. Because the FCC lattice contains loops, which are differently oriented with regard to the external magnetic field, the loops of smaller projected areas withstand the larger fields without switching to the normal state. Due to this effect the spread of the resistive state in $R(H)$ curves is very large. The fine structure of $R(H)$ curves observed in well-ordered samples can be due to the preferential orientation of the loops in the lattice, which refer to the projection of certain lattice planes on the field direction.

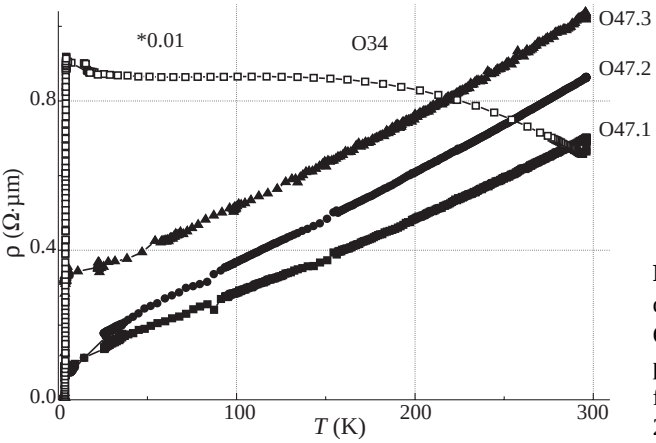

Fig. 2. Temperature dependencies of resistivity for O47.1, O47.2, O47.3 and O34 samples (the values of resistivity for O34 sample are divided by 250).

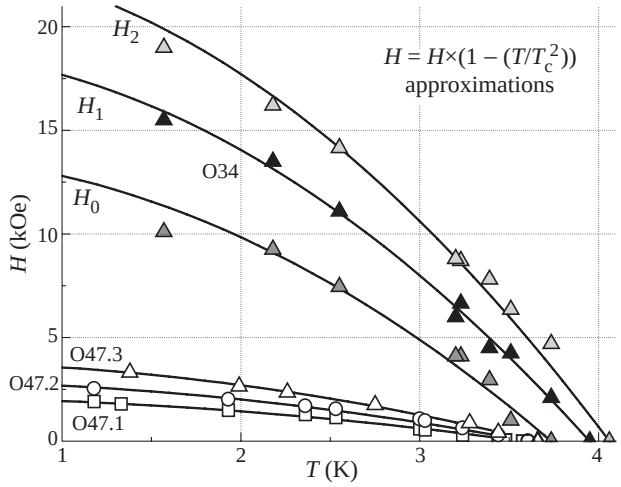

Fig. 3. Temperature dependencies of characteristic magnetic fields: H_0 (determined at the beginning of the resistive state at given T) for O47.1, O47.2, O47.3 and O34 samples; H_1 and H_2 (fields of $\mathrm{d}R/\mathrm{d}H$ maxima) for O34 sample. Solid lines are the $H(T) = H(0)(1-(T/T_c)^2)$ approximations.

2. Conclusions

The type II like superconducting transition has been observed in the in the regular lattice of interconnected In grains in the opal template. Effectively, this material is nanosize wire mesh made from type I superconductor. With the decrease of the cross-section of In component in the metal-dielectric nanocomposite the increase of the critical magnetic field was observed. The observed relation between the critical field and the effective thickness of In nanostructures correlates with the observed flattening of the $R(T)$ dependence.

Acknowledgements

This work was supported in part by RFBR grant 99-02-18156.

References

[1] J. H. P. Watson, *J. Appl. Phys.* **37**, 516 (1966); N. K. Hinley and J. H. P. Watson, *Phys. Rev. B* **183**, 525 (1969); J. H. P. Watson, *Phys. Rev. B* **2**, 1282 (1970).
[2] V. G. Balakirev et al., *Crystallogr. Rep.* **38**, 348 (1993).
[3] M. J. Graf et al., *Phys. Rev. B* **45**, 3133 (1992).
[4] D. V. Shamshur et al., *Proc. Nanostructures: Physics and Technology* 2000 p. 311; S. G. Romanov and D. V. Shamshur, *Phys. Solid State* **42**, 594 (2000).

9th Int. Symp. "Nanostructures: Physics and Technology"
St Petersburg, Russia, June 18–22, 2001

IR absorption spectra of liquid crystals confined in the channels of macroporous silicon

T. S. Perova†, J. K. Vij†, E. V. Astrova‡, A. G. Tkachenko‡ and O. A. Usov‡
† Department of Electronic and Electrical Engineering, University of Dublin, Trinity College, Dublin-2, Ireland
‡ Ioffe Physico-Technical Institute, St Petersburg, Russia

Abstract. Macroporous silicon, possessing a regular triangular pattern of air or liquid crystal (LC) encapsulated pores, was studied by FTIR spectroscopy. It was found that rod-like ferroelectric LC molecules are oriented along the pore axis and discotic LC columns are perpendicular to it. Strong intensity enhancement of the low-frequency vibrational bands was detected for both LC's infiltrated in the matrix of porous silicon and were assigned to the photonic confinement effects.

1. Introduction

Porous systems such as artificial opals, porous semiconductors, etc. have recently attracted a great attention. Of a special interest are regular porous structures, which can form photonic band gap of different dimensions. The idea to infiltrate porous systems with liquid crystals (LC) in order to control the position of their photonic band gap due to the change of the LC refractive index was suggested in [1, 2]. Today only first steps in the study of infiltration process and LC behavior in confined geometry of macroporous silicon have been done in [3]. In this paper we applied infrared spectroscopy to investigate the alignment of liquid crystal molecules of different shape in the macroporous silicon matrix.

2. Experimental

Macroporous silicon (ma-PS) under this study (Fig. 1(a)) is a material with a system of a regular cylindrical pores of 3–4.5 μm diameter and 200–250 μm depth, arranged in triangular lattice of 12 μm period. The pores were etched in HF solution under the back side illumination [4]. Two different types of liquid crystal materials were used in this study (see Fig. 1(b)): the commercial ferroelectric liquid crystal (FLC) mixture SCE-8 and the triphenylene based discotic liquid crystal (DLC) H7T-NO_2. The liquid crystals were infiltrated by capillary effect at temperature approximately 10°C above the transition temperature to the isotropic phase.

Fourier transform infrared (FTIR) measurements were performed with the help of Digilab FTS60A spectrometer in the wavenumber range of 450–4000 cm^{-1}. The alignment of LCs in porous silicon matrix was deduced from the comparison of the relative intensities and the position of different vibrational bands for the bulk liquid crystals and for that infiltrated into the pores. For this purpose a number of liquid crystalline cells with different type of alignment (homeotropic and planar) have been prepared. The relative intensities were compared for a number of vibrational bands with transition dipole moment oriented (i) along or perpendicular to the long molecular axis for rod-like molecules of the ferroelectric LC and (ii) parallel or perpendicular to the core for disk-shaped molecules in the case of the discotic LC. Porous matrix filled with LC had a fixed position with the respect to the incident light: normal to the wafer surface, i.e. along the pore axis.

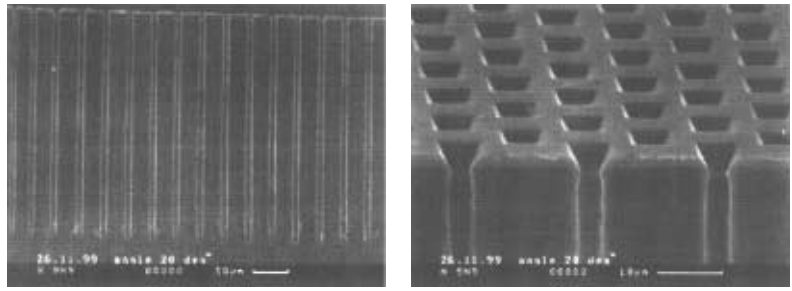

(a)

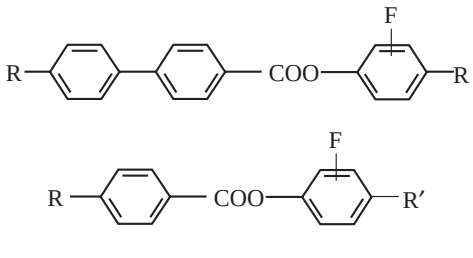

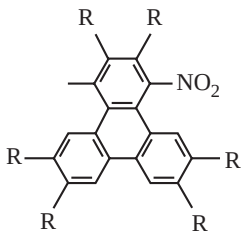

(b)

SCE8 H7T-NO_2

SmC* – 59 °C – SmA – 79 °C – N* – 100 °C – I Cr. – –5 °C – D – 134 °C – I

Fig. 1. Materials properties. (A) SEM image of macroporous silicon matrix (side view (a) and top view (b)), used to infiltrate with the liquid crystals; (B) Structure formulas and the phase sequences of ferroelectric liquid crystalline mixture SCE8 and the tryphenylene based discotic liquid crystal H7T-NO_2 (R = OC5H11).

3. Results and discussion

Figures 2(a,b) show the vibrational bands of discotic liquid crystal for homeotropic and planar alignment of molecules in liquid crystalline cell and in the porous matrix. It should be noted that the alignment of discotic liquid crystals is usually considered with the respect to the column axis, which is in general perpendicular to the core plane. The alignment of DLC is planar with respect to the substrate plane (or homeotropic with respect to the pore surface) (see Fig. 3). The most convincing result of this comparison is shown by behavior of the alkyl chain vibrations. In particular, as one can see from Fig. 2(a), the relative intensities of CH_3 symmetric (at $\sim$2871 cm^{-1}) and asymmetric (at $\sim$2959 cm^{-1}) stretching vibrations are different from the corresponding CH_2 stretching vibrations (at 2861 and 2934 cm^{-1}) for planar and homeotropic alignment of DLC cells. The spectrum of H7T-NO_2 in ma-PS is similar to that for the planar alignment of DLC cell in the same frequency range. Another argument is given in Fig. 2(b), where range the frequency 650–800 cm^{-1} is shown. Here the CH_2 rocking vibration shows up at 724 cm^{-1} for H7T-NO_2 in porous matrix and in ZnSe cell with planar alignment while for ZnSe cell with homeotropic alignment the position of this band is at $\sim$733 cm^{-1}. This shows that the alkyl chain is in all trans configurations for the planar alignment of DLC molecules [5]. The intensities ratio ($R = A^{\parallel}/A^{\perp}$) obtained for C–C aromatic stretching vibration at 1510 cm^{-1} (parallel to the core) and C-H aromatic out of plane vibrations at 824 cm^{-1} equal 16 for the planar cell, 8 for the homeotropic cell and 1.2 for ma-PS. Finally from all aforementioned data it is obvious that the behavior of H7T-NO_2 in ma-PS is exactly coincide with that for the

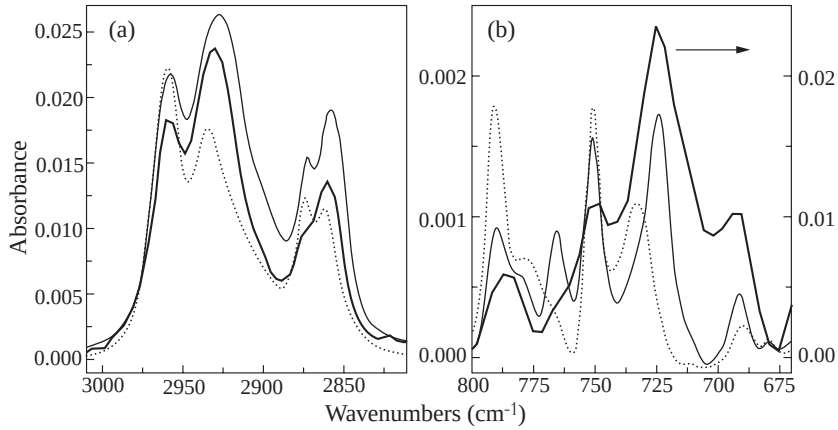

Fig. 2. FTIR spectra of H7T-NO_2 discotic liquid crystal infiltrated into porous silicon (heavy solid line) and contained in ZnSe cells with planar (thin solid line) and homeotropic (dashed line) alignment. (Note the different scale for the heavy line at plot (b) and that the absorbance for DLC cells reduced for planar cell by factor 50 and for homeotropic cell by factor 45 for convenience of presentation).

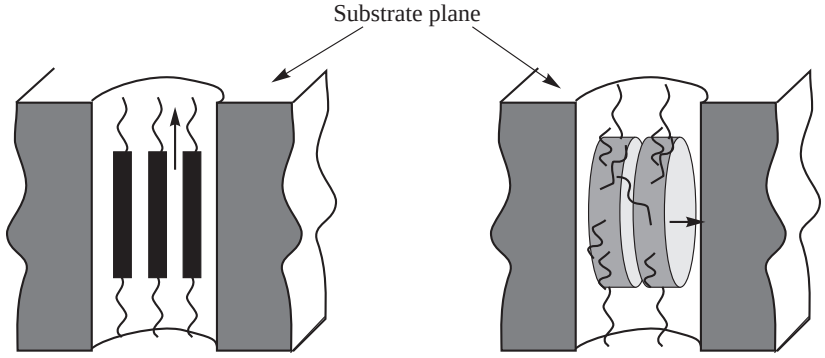

Fig. 3. Orientation of discotic (a) and ferroelectric (b) liquid crystal molecules in macroporous silicon matrix.

planar alignment of DLC cell. This is in accordance with the conclusions on the higher stability of homeotropic alignment for discotic liquid crystals [5].

IR spectra of SCE-8 infiltrated into porous silicon matrix show that the relative intensities of parallel and perpendicular bands in this case are close to that observed for the bulk LC cell with homeotropic alignment. This mean that the alignment of ferroelectric liquid crystal in confined porous silicon matrix is homeotropic with respect to the substrate's plane. This result coincides with the alignment obtained for nematic LC in macro and microporous silicon [6]. One could predict this kind of orientation if consider the alignment of rod-like molecules with respect to the surface of the pores. The alignment is planar with the respect to the pore surface. This type of alignment is typically observed for rod-like molecules on different untreated surfaces, including crystalline silicon substrate [7]. Only a special surface treatment or coating of the substrate surface by a surfactant may provide a homeotropic alignment of LC's formed of rod-like molecules.

In course of these investigation we found strong intensity enhancement of the low-

frequency vibrational bands (in 600–900 cm^{-1} region) for both types of liquid crystals (note the different scale for this region shown in Fig. 2(b)). This becomes in particular noticeable from a comparison of the intensities ratio shown above for parallel and perpendicular bands. As was already mentioned these intensities ratio appears much smaller than even obtained for both LC cells with homeotropic alignment. Moreover this enhancement is observed for all vibrational bands (parallel and perpendicular ones) show up for the wave lengths comparable with the lattice constant of the photonic crystal (12 μm). This enables us to consider the effect as being due to the light localization in the hole core of the structure as it takes place in the fibers with photonic band gap cladding [8]. Similar effects of absorbtion enhancement has been observed by Alieva et al. [9] for the species in the microcavity of 1D photonic structure.

4. Conclusion

We found that channel walls affect the orientation of LC molecules so that the column axis of discotic LC is perpendicular to them, and the long side of the rod-like moleculas of feroelectric LC is aligned along the channel walls. We observed the effect of photonic medium influence on the vibration properties of the LC molecules inside the matrix of macroporous silicon and suppose it to be related to Purcel type confinement effect.

References

[1] K. Bush and S. John, *Phys. Rev. Lett.* **83**, 967 (1999).
[2] M. Thonissen, M. Marso, R. Arens-Fisher, D. Hunkel, M. Kruger, V. Ganse, H. Luth and W. Theiss, *J. Porous Materials* **7**, 205 (2000).
[3] S. V. Leonard, J. P. Mondia, H. M. van Driel, O. Toader, S. John, K.Busch, A. Birner, O. Gosele, and V. Lehmann, *Phys. Rev. B* **61**, R2389 (2000).
[4] V. Lehmann and H. Foll, *J. Electrochem. Soc.* **137**, 653 (1990).
[5] T. S. Perova, J. K. Vij and A. Kocot, *Adv. Chem. Phys.* **113**, 341 (2000);
A. Kocot, J. K. Vij and T. S. Perova, ibid 203.
[6] M. V. Wolkin, S. Chan and P. M. Fauchet, *Proc. Int. Conf. on Porous Silicon*, Madrid, Spain, March, O-58, 2000.
[7] A. A. Sonin, *The Surface Physics of Liquid Crystals* (Gordon & Breach Science Publishers) Amsterdam, 1995, pp. 7–11.
[8] A. M. Zheltikov, *Usp. Fiz. Nauk* **170** (11), 1203–1214 (2000).
[9] E. V. Alieva, L. A. Kuzik, G. Mattei, J. E. Petrov and V. A. Yakovlev, *Phys. Stat. Solidi (a)* **175**, 115 (1999).

9th Int. Symp. "Nanostructures: Physics and Technology"
St Petersburg, Russia, June 18–22, 2001

Zn_2SiO_4:Mn^{2+} nano-particles grown in porous silicon

N. Taghavinia†, G. Lerondel†, H. Makino†, A. Yamamoto‡, T. Yao†, Y. Kawazoe† and T. Goto‡

† Institute for Materials Research, Tohoku University, Sendai 980-8577
‡ Department of Physics, Tohoku University, Sendai 980-8578, Japan

Abstract. We have succeeded to grow nano-crystalline $Zn_2SiO_4 : Mn^{2+}$ particles by chemical impregnation of porous silicon layers and heat treatment. Two different classes of samples have been obtained: green luminescent samples at 525 nm and yellow luminescent ones at 575 nm. We identify the green luminescence as the conventional luminescence of the alpha phase of $Zn_2SiO_4 : Mn^{2+}$, however the yellow luminescence comes from the beta phase of $Zn_2SiO_4 : Mn^{2+}$. XRD peaks of the yellow luminescent samples show wide and weak peaks, indicating smaller particles, compared to green luminescent particles. We discuss about the conditions which result in either green or yellow luminescent samples.

Introduction

Porous materials have been frequently used as a host to grow nano-structures. Porous silicon, having nanometer sized holes and with the ease of its formation is a good choice in this respect. The holes in the porous silicon layers allow impregnation of the layer with chemicals to grow other phases inside the layer or modify the properties of the layer. Impregnation of porous silicon with various dyes [1] is an example. On the other hand, $Zn_2SiO_4 : Mn^{2+}$ is an important phosphor which is particularly used in plasma displays. Its powder form is usually synthesized by solid state reaction of the starting powders. It luminesces at green peaking at about 525 nm.

Here we report a new method to grow $Zn_2SiO_4 : Mn^{2+}$ nano-particles into an oxidized porous silicon layer. This is a new concept in the impregnation of porous silicon, i.e. the growth of highly luminescent phosphor particles inside the porous layer. This involves the reaction of silicon walls with the impregnating chemicals, leading to a new phase inside the pores. This is also a new concept in phosphor applications, i.e. phsophor nano-particles embedded into a porous layer. In the following sections we report the details of experiment and results.

1. Experimental

Porous silicon layers were formed by the conventional electrochemical method. For most of the experiments, p^+ type wafers were processed using 17.5 percent HF solution and 80 mA/cm^2 current density. This leads to meso-porous layers with 70 percent porosity and almost 10 nm pore size. The typical thickness of layers is 15 nm. Porous silicon samples were impregnated by immersing them into $Zn(NO_3)_2 + x\ Mn(NO_3)_2$ solution for almost one hour. x is in the range of a few percent. Samples were then dried and put into the furnace for slow ramp heating up to 400°C followed by high temperature firing at 1050°C. This leads to the formation of Mn doped zinc silicate crystallites in a transparent matrix of oxidized porous silicon.

2. Results and discussion

With some variation in the details of the above conditions, both green and yellow luminescent samples can be obtained. These conditions are discussed later. Figure 1 shows the PL spectra for green and yellow luminescence at room temperature. The green luminescence is the conventional green of $Zn_2SiO_4 : Mn^{2+}$ phosphor, occurring at about 525 nm. The yellow luminescence peaks at 575 nm, with a peak width of 54 nm compared to 38 nm in case of the green peak. The peaks are featureless, even at low temperature. Decreasing the temperature down to 10 K makes the peaks narrower, but the intensity does not increase more than 20 percent in both cases. For green samples, the peak intensity is up to 40 percent of the commercial $Zn_2SiO_4 : Mn^{2+}$ phosphor, while this ratio is about 15 percent for yellow luminescence (by comparing the peak heights without instrument sensitivity correction).

The PLE of both green and yellow are quite similar, with some blue shift in case of yellow one. This demonstrates that the origin of both luminescence is the Mn activator. More insight about the difference between green and yellow luminescent samples can be obtained by the XRD data. Figure 2 shows the XRD patterns for both kinds of samples. The pattern for the green sample corresponds exactly to the rhombohedral phase of Zn_2SiO_4, also known as $\alpha - Zn_2SiO_4$. There is no additional peak, indicating that no ZnO, MnO_x or crystalline SiO_2 is present. The relatively large size of particles explains the almost sharp diffraction peaks. From the peak width the size estimated to be about 200 nm. The XRD pattern for the yellow sample consists of weak and broad peaks, at positions different

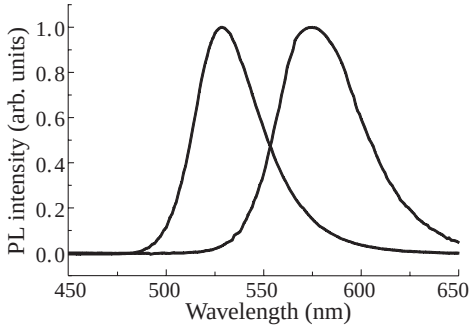

Fig. 1. Normalized PL intensity for green and yellow luminescent samples.

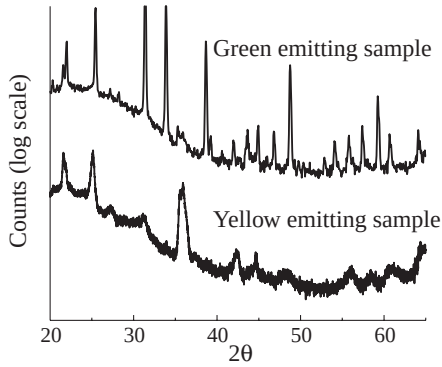

Fig. 2. The XRD patterns of green and yellow luminescent samples. The green sample shows the peaks of $\alpha - Zn_2SiO_4$, while the yellow one resembles the β phase.

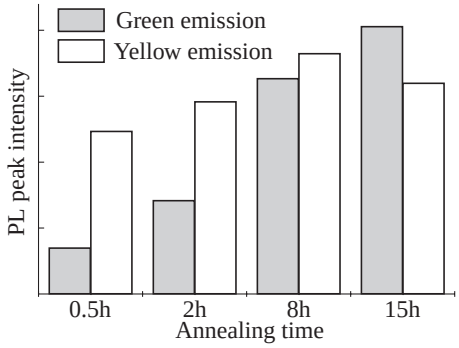

Fig. 3. Intensity of PL peaks of green and yellow luminescence for different annealing time at 1050°C.

from the rhombohedral Zn_2SiO_4. The pattern resembles that of $\beta - Zn_2SiO_4$, as reported by Taylor [2]. Like in case of the green sample, the pattern represents only one phase, demonstrating that the layer comprises $\beta - Zn_2SiO_4$ particles embedded in an amorphous oxidized porous body. The size of the particles, calculated from the width of the diffraction peaks is typically 30 nm.

We found various conditions in which the yellow luminescence appears. An important factor is the period and temperature of annealing. Basically, shorter annealing time and lower temperature leads to yellow luminescence. Figure 3 shows the PL intensity of green and yellow peaks as the annealing time is increased. The annealing temperature is 1050°C. After 30 min annealing, the sample emits both yellow and green, with yellow peak being almost four times stronger than green. With increasing the annealing time, green/yellow ratio increases and after 15 h green is more intense than yellow. This effect suggests that the yellow emission comes from smaller particles and as the particle size increases with annealing time, more particles transform to green emission phase. XRD results also confirm that the size of yellow luminescent particles are smaller than green luminescent particles. This is supported by the fact that if we start with nano-porous silicon, instead of meso-porous one, with the same growth conditions, it usually leads to yellow luminescence. In nano-porous silicon the size of pores are about 3–4 nm and that makes the diffusion process and subsequently particle growth slower, leaving more of small yellow emitting particles.

References

[1] P. Li, Q. Li, Y. Ma and R. Fang, *J. Appl. Phys.* **80**, 490 (1996).
[2] H. F. W. Taylor, *Am. Minral.* **47**, 932 (1962).

9th Int. Symp. “Nanostructures: Physics and Technology”
St Petersburg, Russia, June 18–22, 2001

Field effect in thin granulated metal films

D. A. Zakheim, I. V. Rozhansky, I. P. Smirnova and S. A. Gurevich
Ioffe Physico-Technical Institute, St Petersburg, Russia

Abstract. In this work we analyze the field effect in granulated metal films and propose the current-switching device utilizing this effect. It is shown as a result of numerical modeling that efficient current modulation can be achieved in thin granulated films if the charging energy of metallic granules is at least several times higher than the thermal energy kT.

1. Introduction

Last time considerable effort has been made to develop single-electron transistor (SET) in which the current path between source and drain is controlled by the charge state of the central metallic island having extremely low capacity. Due to Coulomb blockade the current through SET can be modulated by the gate electrode potential. Successful operation of SET made by conventional technique is possible at temperatures below 1 K because of limitations of lithography resolution [1]. The extension of operating temperature range requires the implementation of sophisticated technologies [2] based on manipulation with ultra-small metallic granules. These particles are fabricated by nanoparticle source, selected and then placed precisely in the source-drain gap. However in this approach the parameters of SET are critically dependent on island size and position which can hardly be controlled with desired accuracy.

The proposed way to avoid this critical dependence is to use the structures containing large number of metallic granules statistically distributed in the gap. In this case the characteristics of inter-granular tunnel junctions are averaged over the volume and, under certain conditions, the performance of the whole system is independent on individual grain positions. The current in such granulated film can still be controlled by external electric field due to modulation of charge distribution. In this work we consider the possibility of efficient current modulation in thin granulated films incorporated in the gap of current switch device shown schematically in Fig. 1. This consideration is based on the newly developed Monte-Carlo model of granulated film conductivity.

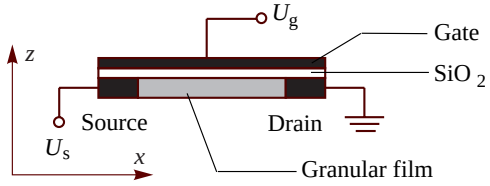

Fig. 1. Schematic diagram of current switching device.

2. Monte-Carlo model

In the model the granulated film is represented by the set of metallic balls randomly distributed in the given volume. At each step the system state is characterized by the electric charge of each ball expressed in terms of unit charge. For a given state the probabilities of electron tunneling from one ball to another are calculated taking into account the Coulomb

interaction of charged balls and the presence of the external electric field. One tunneling event is realized according to its relative probability by means of Monte-Carlo technique and this procedure is repeated many times. The macroscopic electric current could be calculated as time averaged number of electron hops across the selected cross-section. Since the number of granules involved in calculations was limited (to about 250 balls), the results were also averaged over different realizations to avoid the mesoscopic current fluctuations originating from the randomness of granules distribution.

This model has been tested by calculating the I–V curves and temperature dependencies of granular films conductivity and comparing the results with experimental data obtained on composite Cu:SiO_2 films [3].

3. Discussion

Simulating the behavior of the structure shown in Fig. 1 the potential distribution was first calculated by solving the 2-dimensional Poisson equation with given potentials at the electrodes. Then the obtained solution was used as an external potential in calculation of source-drain current according to the procedure described above. In calculations the parameters of granulated film were taken similar to those of composite Cu:SiO_2 films studied in our previous works [4]: granules diameter is 3 nm, the volume fraction of metal is 25% and the dielectric constant of the media is equal to 4. The thickness of SiO_2 layer isolating the gate from the film was taken to be 5 nm and the distance between source and drain — 30 nm.

It was found that the main effect of the gate is the generation of the excess charges at the granules adjacent to the gate if the gate potential is about or higher than the single-electron charging energy of granules (which is about 50 meV with regard to screening effects). Figure 2 shows the average charge distribution in 12 nm thick film simulated at gate voltage +1 V. As it seen from the figure, the field penetration depth, i.e. the area where the averaged charge density deviates from zero, is rather small (about 2–3 nm). In the rest part of the film the concentrations of negative and positive charges are controlled by the temperature and are equal to each other. This is the layer carrying excess charge which is responsible for the conductivity modulation, while the conductivity of the rest

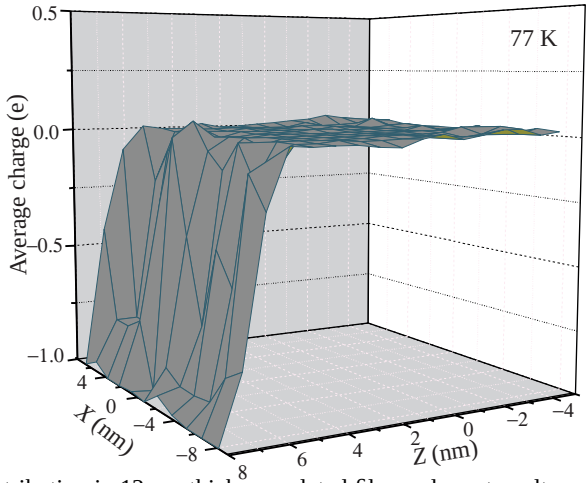

Fig. 2. Charge distribution in 12 nm thick granulated film under gate voltage +1 V ($z = 8$ nm is the film top interface).

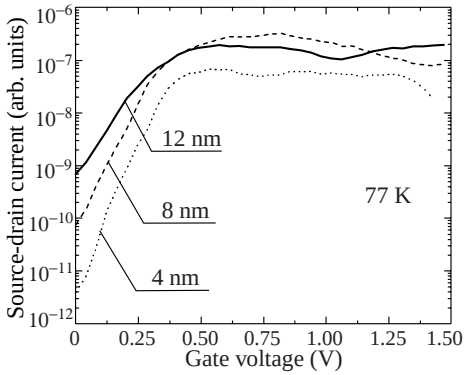

Fig. 3. Modulation characteristics for granulated films having different thickness. $U_{\text{source-drain}} = 0.014$ V.

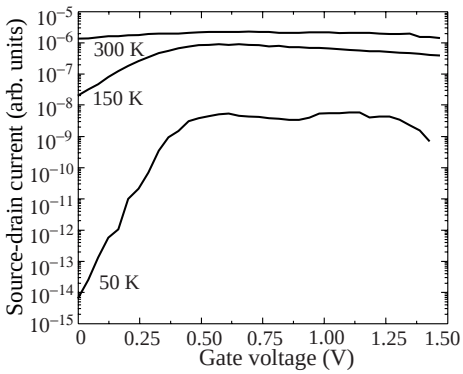

Fig. 4. Modulation characteristics for 4 nm thick granulated films at different temperatures. $U_{\text{source-drain}} = 0.01$ V.

part is unaffected by gate potential. This means that the efficiency of current modulation is highest in case of extremely thin films. This is illustrated in Fig. 3, where the modulation characteristics are shown for films having different thickness.

The other important parameter influencing the efficiency of current modulation is the temperature. The higher the temperature is, the more charges exist in the film in the absence of gate potential and the higher is initial conductivity. At the same time the upper limit of conductivity (reached at high gate voltage) is roughly defined by the granules concentration and does not depend on temperature. The dependence of modulation characteristics on temperature is shown in Fig. 4. This dependence manifests that the efficient modulation can be achieved if the charging energy of granules is at least several times higher than the thermal energy kT.

4. Summary

We have proposed the field-effect current switching device based on granulated metal film. The origin of current modulation is shown to be the charge generation in thin layer adjacent to the gate. The dependencies of the current modulation depth on film thickness and temperature were analyzed. The current modulation depth may amount to as much as four orders of magnitude at 77 K in the 5 nm thick films with charging energy of granules about 50 meV. The route to increase the operation temperature is to find the granulated structures in which the charging energy is higher. One of the promising candidates could be the structures recently fabricated by laser ablation technique [5].

References

[1] K. K. Likharev, *IEEE Trans.Magn.* **23**(2), 1142 (1987).
[2] T. Junno, S.-B. Carlsson, H. Xu, L. Montelius, L. Samuelson, *Appl. Phys. Lett.* **72**, 548 (1998).
[3] D. A. Zakheim, I. V. Rozhansky, I. P. Smirnova, S. A. Gurevich, *JETP* **91**, 553 (2000).
[4] S. A. Gurevich, T. A. Zarajskaya, S. G. Konnikov, V. M. Mikushkin et al., *Phys. Solid State* **39**, 1691 (1997).
[5] V. M. Kozhevin, D. A. Yavsin, V. M. Kouznetsov, V. M. Busov et al., *J. Vac. Sci. Technol. B* **18** (3) 1402 (2000).

9th Int. Symp. "Nanostructures: Physics and Technology"
St Petersburg, Russia, June 18–22, 2001

Nanostructure effects in Si-MOSFETs

M. Willander, M. Y. A. Yousif and O. Nur

Physical Electronics and Photonics, Microtechnology Centre at Chalmers (MC2), Physics Department, Chalmers University of Technology and Göteborg University, S-412 96 Göteborg, Sweden

Abstract. In this article we present a summary of the most important critical issues in nano-scaled field-effect transistors. The controversial issue of alloy scattering and the phenomenon of velocity overshoot which are important in the nano-scale regime are reviewed and discussed. The emerging $Si_{1-x}Ge_x$ technology contribution to improve scaled Si MOSFETs is presented. Achievements and problems associated with channel engineering and alternative gate electrodes and high-κ dielectric materials are also addressed. Finally, during the presentation we will discuss our results on filtering out hot carriers using channel engineering. We will also discuss our results on scaling down the MOS transistor to a single electron tunneling MOS transistor made in Si and with properties like room temperature Coloumb oscillations.

1. Introduction

The relentless scaling of Si MOSFET devices, which has offered outstanding improvement in performance seems to have reached an end. The gate oxide thickness is now in the direct tunneling regime <3 nm, which calls for other materials with higher dielectric constant to replace SiO_2, the substrate doping concentration $\sim 1 \times 10^{18}\,\mathrm{cm}^{-3}$ is also in the limit of source/drain-substrate p-n junction leakage current. Control of doping concentration and doping profile for source/drain still poses a challenge. Shallow S/D extensions alone is not enough; the surface impurity concentration should be as high as to achieve the desired improvement in the overall device characteristics. When low doping concentration is used, ultra shallow junctions can be achieved but this degrades the current drivability. In the nanometer regime, special techniques have been adopted to fabricate 40-nm gate length n-MOSFET with 10 nm depth source/drain junctions [1].

For a 14-nm gate length transistor, two gates separated by thick SiO_2 were used with the upper gate requiring 7 V to form the channel [2]. It is well known that, in such a regime, MOSFET devices suffer from significant fluctuations in the threshold voltage and in the output characteristics together with other various issues [3]. In order to suppress such effects and to explore the ultimate CMOS limit of about 25-nm gate length, a double-gate MOSFET device structure, is proposed and demonstrated experimentally [4]. However, the fabrication of such devices is by no means simple and requires more stringent methods; both gates have to be self-aligned to the source and drain. On the other hand, though it appears now that conventional Si technology is hard to beat, the emerging SiGe technology is expected to boost the performance of Si-based devices beyond that of Si. At least the Ge material, due to its favorable electrical properties, would probably be in every Si chip in future generations [5–9]. The $Si_{1-x}Ge_x$ alloys started to attract researchers' attention since more than sixty years ago [10]. Numerous scientific research papers are published where different $Si_{1-x}Ge_x$ alloy based devices were demonstrated and studied, see e.g. [11–21] and references there in.

2. Transport issues

2.1. Velocity overshoot

When the channel length of the MOSFET device is scaled down to 100 nm and below, the carrier transport along the channel can be considered as quasi-ballistic transport and, depending on the scattering events in the channel, the effect of velocity overshoot can be observed. For conventional Si MOSFETs, the overshoot phenomenon has been predicted theoretically in the 70s [22, 23] and observed experimentally in the mid 80s at different temperatures, namely 300 K, 77 K and 4.2 K [24, 25]. Velocity overshoot is important for increasing the transconductance and thus the speed of the device.

For strained Si or strained SiGe MOSFET devices, investigation of velocity overshoot has so far been mostly theoretical calculations and computer simulations. These simulations, though some of them approximate, provide useful information and predict the anticipated trend of carrier transport in the velocity overshoot regime [26–28]. Velocity overshoot has been predicted to occur closer to the source end and more pronounced in strained Si and strained SiGe channel MOSFETs than in conventional Si devices [26].

2.2. Alloy scattering

The significance of alloy scattering in the $Si_{1-x}Ge_x$ material system still remains a subject of debate. This controversy has both experimental and theoretical grounds. First of all it is important to have a well-defined theoretical formulation to evaluate the alloy scattering potential U_{al} because being a fitting parameter appears to be the origin of the debate. Different researchers chose different values and the spread of these values is large, e.g., $U_{al} = 0.2$ eV [29], 0.27 eV [30], 0.3 eV [31], 0.6 eV [32–34], 0.9 eV [35], and 2.0 eV [36]. It is worth mentioning that the value of 0.3 eV used in [31] is equivalent to that of 0.6 eV quoted in [32] and [33] and the factor of 2 is due to a difference in the volume of the primitive cell. The alloy scattering rate is known to be proportional to $x(1-x)(U_{al})^2$, where x is an alloy concentration. Therefore, one would expect that the contribution of alloy scattering is maximum at $x = 0.5$ and could be underestimated for small values of U_{al} or overestimated for larger values.

If we assume that alloy scattering is the only dominant mechanism at low temperatures then it would be easy to obtain a good estimate for the alloy potential and the case is reversed if any other scattering mechanism such as interface roughness and/or interface impurities is present. Recalling the dependence of the alloy scattering rate on the alloy concentration given above, it is experimentally observed that a strained $Si_{0.7}Ge_{0.3}$ grown on Si at 500 °C showed a significantly lower mobility due to interface roughness compared to the case when grown at 450 °C [37]. Also they obtained a higher mobility in $Si_{0.5}Ge_{0.5}$ strained layers on Si, which may rule out the significance of alloy scattering, in contrast to recent claims.

Beside the difficulty in extracting the alloy potential, in the presence of other scattering mechanisms, by fitting theoretical calculations to experimental data, experiment is normally for Hall mobility μ_H, which is related to the drift mobility μ_d via the relation $\mu_d = \mu_H/r_H$. The Hall factor r_H is a complicated function of the magnetic field and the scattering mechanism in the structures. Note that in thin quantum wells or inversion layers, typically less than 10 nm thick, the carriers can be considered as a two-dimensional hole/electron gas and quantum Hall effects can be observed [38]. Although the Hall factor r_H can, generally, have values between 1–2, it has also been observed experimentally to have values much lower than 1, depending on the Ge content and the doping concentration [39].

3. Channel engineering issues

The low mobility results in a low transconductance and hence the need for a wider PMOSFET transistor. Early suggestion of using $Si_{1-x}Ge_x$ technology in field effect devices was implemented during the 80s [40]. This pioneering work where a silicide Schottky gate was used in a MODFET structure was not successful due to the large leakage current at temperatures higher than liquid nitrogen. The use of buried strained- $Si_{1-x}Ge_x$ in a MOS structure as the main conducting channel was then left as the best alternative provided that strong inversion in the buried channel occurs before that in the surface low mobility Si channel [41, 42]. Beside being a solution to overcome the low hole mobility, the valence band alignment in the $Si/Si_{1-x}Ge_x$ heterojunction creates a quantum well (QW) channel that offers confinement away from the Si/SiO_2 interface [43]. The use of a single $Si/Si_{1-x}Ge_x$ QW for the PMOS transistors, although resulted in performance improvement, has still not offered the expected gain.

Improvement of the single QW PMOSFET performance can be achieved by using a modulation doped heterostructure. Here a single or double delta-doped layer is inserted either above and/or below the QW channel. Very high record hole mobility in excess of $19.000\,cm^2/V\,s$ at 7 K was reported for a single modulation doped QW structure [44]. A similar study intended to compare normal and inverted modulation doped QW structures showed that the mobility is higher for a normal modulation doped QW when compared to an inverted structure having the same inner physical parameters [45]. On the other hand, double modulation doped QW structure is expected to be advantageous for conductivity due to the confinement at both edges of the QW however, the result of Hall mobilities indicates a reduced mobility when compared to single modulation-doped structures [46]. The preceding discussion indicates that the design of the QW plays an important role in the performance of the PMOS QW based transistor. Theoretical investigation of the confined carrier concentrations in single QW $Si/Si_{1-x}Ge_x$ PMOSFET has indicated that at strong inversion most of the carriers accumulate at the heterointerface [47]. This accumulation is expected to be one of the most limiting factors in degrading the mobility. There have been many reports that dealt with different Ge profile in the QW, these include trapezoidal [48], and different triangular Ge profiles [49, 50]. Here, grading the Ge profile is advantageous in creating a wide QW. Carrier concentration investigation indicates that the carrier concentration is following the high Ge grading profile. Most recently, adding to the existing different QW based PMOSFET, we have proposed and investigated the feasibility of different designs of a double retrograde $Si/Si_{1-x}Ge_x$ QW structures [51–53].

Figure 1 shows the calculated valence band profile and the hole distribution. As it is clear, and in contrast to other single QW profiles, the peak of the carriers lies at the center of the main conducting channel. It is important to mention that recent studies indicates that interface roughness might be more dominating than other scattering mechanisms that contributes to mobility degradation [33]. Note that high quality interface will reduce the low-frequency noise and this is particularly important for microwave applications [54]. The retrograde structure also offers more engineering possibilities for further performance improvement. For example, the cap layer can be made ultrathin (1 nm or less) to suppress its inversion and keep the rather good quality of SiO_2/Si interface.

Figure 2 shows the reduction trends in the threshold voltage as the channel length is reduced. The drain-induced barrier lowering (DIBL) at a channel length of about $0.217\,\mu m$ is only 77 mV/V for 2.5 V operation, indicating a potentially acceptable short-channel behavior for this retrograde DQW device. In addition, for this structure, it should come as no surprise that hot-carrier degradation and loss of the inversion charge in the nanometer-

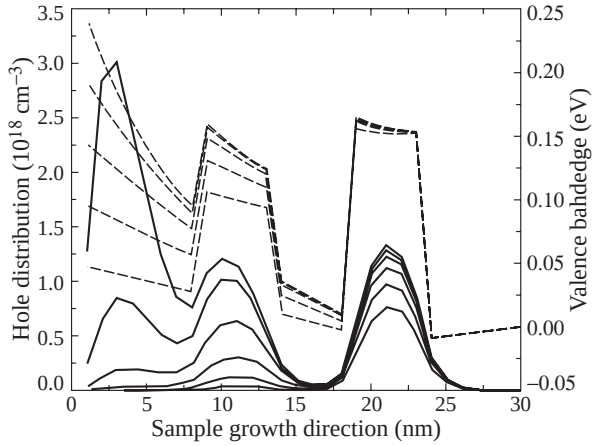

Fig. 1. Calculated valence band profile (dotted lines) and the 2D hole distribution profile (solid lines) along the sample growth direction as a function of gate voltage for the retrograde DQW structure.

scale devices will be improved because carriers have to travel longer distances to reach oxide interface.

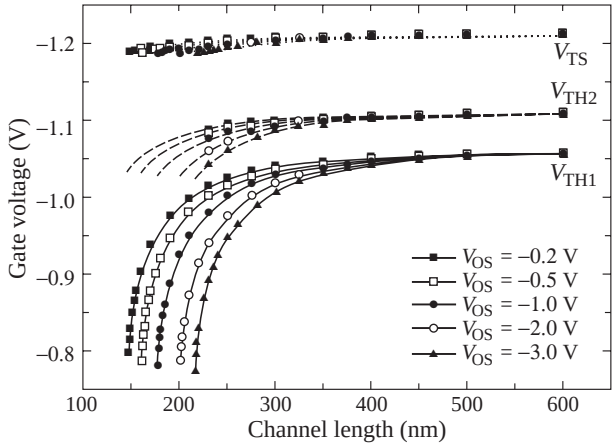

Fig. 2. The threshold voltage dependence on the channel length and drain voltage for the SiGe retrograde DQW shown in Fig. 2, but with a cap of 2 nm.

For engineering the channel for better electron confinement, a tensile strained Si is used as the main conducting channel. This is beneficial over the QW PMOS in the fact that alloy scattering effect is minimal. However, the growth of tensile strained Si is technologically not easy. The growth of relaxed $Si_{1-x}Ge_x$ virtual substrates for the growth of tensile strained Si is of global interest nowadays. These virtual substrates must contain low density of threading dislocations to be accepted electrically. There has been mainly three contending routes to engineer the growth of relaxed $Si_{1-x}Ge_x$ or relaxed pure Ge virtual substrates; (i) post processing of strained $Si_{1-x}Ge_x$ [55], (ii) use of an intermediate strain relieving compositionally linear and/or stepwise $Si_{1-x}Ge_x$ graded buffer layer [56, 57] and (iii) direct Ge epitaxy or surface mediated growth [58, 59]. Both Molecular Beam Epitaxy (MBE) and

different Chemical Vapor Expitaxial reactors have been used for the hetero-epitaxy of these virtual substrates. Recently, chemical mechanical polishing at intermediate growth levels is introduced to achieve higher surface quality and has shown remarkable improvement of the final relaxed Ge virtual substrate layer [60]. Although with today's technology, relatively thin very high quality 100% relaxed Ge buffer layers containing low threading dislocation densities have been achieved, still more research needs to be carried out in order to improve the surface morphology, which suffers roughness and undulations [61]. Finally, we will present new results from extraction of hot carriers in the channel. The hot carriers are filtered drown to the substrate by different engineering techniques [82, 83]. The goal of this technique is to reduce power consumption in CMOS circuits by using the heat generated from the carrier relaxation, to charge up the battery. The influence of this technique on circuit properties will also be discussed [84].

Examples of alternative metal gate electrodes are: damascene metals W/TiN or Al/TiN, Copper, Cu [67] and Tantalum, Ta [68]. Such metal gates can indeed be used to eliminate gate depletion. This, however, yields a buried-channel device, which suffers from more short-channel effects than the surface-channel device, but with better channel mobility [69].

One of the promising candidates among gate materials that is completely compatible with standard CMOS processing and suitable in dual N^+/P^+ gate technology is the p-type poly-$Si_{1-x}Ge_x$ gate [70–72]. This material has been shown to benefit from improved resistivity, tunable work function, and reduced gate depletion and boron penetration, compared to P^+ poly-Si [73–75]. The tunable work function of the poly-SiGe gate can be used to adjust the threshold voltage, while engineering the channel profile can be used to control short channel effects [76]. Figure 3 shows the dependence of the gate work function on the Ge content. It is worth mentioning here that the feasibility of a pure Ge ($x = 1$) gate has also been studied within an industrial 0.18-μm CMOS process with well controlled short-channel effects and reduced gate depletion [77].

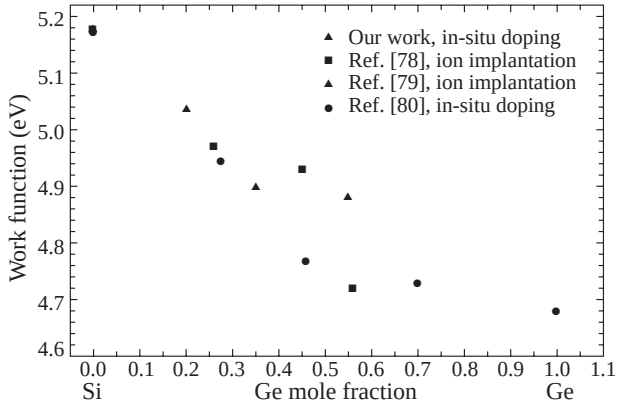

Fig. 3. The work function of B-doped P^+ poly-SiGe gate material as a function of Ge content.

4. New concept: The single electron transistor

The physical scaling consequences mentioned above, in addition to the power dissipation problem in a giga bite scale integrated Si chip have lead to the need of new engineered devices. The single electron transistor (SET) which uses the Coulomb blockade oscillation

was suggested as a possible candidate [81]. Randomly arranged metal islands were used when single electron transistor phenomena was first discovered in 1951 [85]. The first SET, where the number of electrons could be controlled by an external gate was demonstrated in 1987 [86]. However an isolated metal island has to be less than 5 nm in size to output a room to temperature Coulomb blockade oscillations. Silicon nano-crystals have shown to provide room temperature operation of the SET. Semiconductor SETs were first demonstrated in 1989 [87, 88]. During the talk we will present our results on e.g. room temperature Coloumb oscillations in Si based SETs [89, 90].

5. Conclusions and future perspectives

The general trend in most of today's Si-based MOSFETs research is to introduce new exotic methods to suit, in part, metal and/or mid-gap gate materials, high-κ dielectrics, and double gate technology, in order to explore the ultimate limit of these devices. Although this may offer an improved performance for some time, it also poses more processing complications. Without such complexities, the chance for the emerging SiGe technology to be in the main stream and to boost Si-based devices would be greater than ever in the very near future. Even, if we are to resort to low-temperature CMOS technology, where the performance is better by a factor of about two, the chance would still be bigger for SiGe. However, some more research is to be carried out for both n- and p-channel SiGe based MOSFETs. For the p-channel devices, more experimental work in the appealing issue of optimized carrier confinement is needed and a more accurate systematic study for the parameters of alloy and deformation potentials is indispensable. In addition, virtual substrate morphology and surface properties for the n-channel devices need to be improved.

References

[1] M. Ono, M. Saito, T. Yoshitomi, C. Fiegna, T. Ohguro and H. Iwai, *IEEE Trans. Electron Devic.* **42**, 1822 (1995).
[2] H. Kawaura, T. Sakamoto, T. Baba, Y. Ochiai, J. Fujita, S. Matsui and J. Sone, *IEEE Trans. Electron Devic.* **47** 856 (2000).
[3] Y. Taur, D. A. Buchanan, Wei Chen, D. J. Frank, K. E. Ismail, S-H. Lo, G. A. Sai-Halasz, R. G. Viswanathan, H-J. C. Wann, S. J. Wind and H-S. Wong, *IEEE Proc.* **85** 486 (1997).
[4] H.-S. P. Wong, K. K. Chan, and Y. Taur, *IEEE IEDM* p 427, 1997.
[5] S. C. Jain, *Germanium-Silicon Strained Layers and Heterostructures* Academic Press, Boston, 1994.
[6] S. Subbanna, V. P. Kesan, M. J. Tejwani, P. J. Restle, D. J. Mis, S. S. Iyer, *IEEE Symp. VLSI Technology* p 103, 1991.
[7] D. L. Harame, J. M. C. Stork, G. L. Patton, S. S. Iyer, B. S. Meyerson, G. J. Scilla, E. F. Crabbe, and E. Ganin, *IEEE IEDM* p 889, 1988.
[8] U. Konig, *IEE Colloquium on Advances in Semiconductor Devices* pp 6/1-6/6, 1998.
[9] M. Yang, C.-L. Chang, M. Carrol, and J. C. Strum, *IEEE Electron Dev. Lett.* **20**, 301 (1999).
[10] H. Stohr and W. Klemm, *Z. anorgu. U. allgem. Chem.* **241**, 305 (1939).
[11] C. K. Maiti, L. K. Bera, and S. Chattopadhyay, *Semicond. Sci. Techol.* **13**, 1225 (1998).
[12] Y. H. Xie, *Material Sci. Eng.* **25**, (1999).
[13] E. Kasper and J.C. Bean, eds, *Silicon-Molecular Beam Epitaxy* Vol. 1 and 2, CRC Press, 1988.
[14] M.I. Alonso and E. Bauser, *J. Appl. Phys.* **62** 4445 (1987).
[15] B.S. Meyerson, *Appl. Phys. Lett.* **48** 797 (1986).
[16] D. W. Greve and M. Racanelli, *J. Vac. Sci. Technology* **B8**, 511 (1990).
[17] J.F. Gibbons, C.M. Gronet and K.E. Williams, *Appl. Phys. Lett.* **47**, 721 (1985).
[18] W.B. de Boer and D.J. Meyer, *Appl. Phys. Lett.* **58**, 1286, (1991).

[19] H. Hirayama, T. Tatsumi, A. Ogura and N. Aizaki, *Appl. Phys. Lett.* **51**, 2213 (1987).
[20] D. Fathy, O.W. Holland and C.W. White, *Appl. Phys. Lett.* **51**, 1337 (1987).
[21] Van Opdorp, *Si-Ge Isotype Heterojunctions*, Philips Research Reports, Suppl. No. 10, 1969.
[22] G. Ruch, *IEEE Trans. Electron. Devic.* **ED-19**, 652 (1972).
[23] S. Huang and P. H. Ladbrooke, *J. Appl. Phys.* **48**, 4791 (1977).
[24] G. Shahidi, D. A. Antoniadis and H. I. Smith, *IEEE Electron Device Lett.* **9**, 94 (1988).
[25] .Y. Chou, D. A. Antoniadis and H. I. Smith, *IEEE Electron Device Lett.* **EDL-6**, 665 (1985).
[26] G. O'Neill and D. A. Antoniadis, *IEEE Trans. Electron Devices* **43**, 911 (1996).
[27] M. Bufler and B. Meinerzhagen, *IEEE Sixth Int. Workshop on Computational Electronics* p. 242, 1998.
[28] Y. P. Zhao, J. R. Watling, S. Kaya, A. Asenov and J. R. Barker, *Mater. Sci. Eng.* **B72**, 180 (2000).
[29] J. M. Hinckley and J. Singh, *Phys. Rev. B* **41**, 2912 (1990).
[30] T. Manku, J. M. McGregor, A. Nathan, D. J. Roulston, J.-P. Noel and D. C. Houghton, *IEEE Trans. Electron. Devices* **40**, 1990 (1993).
[31] B. Laikhtman and R. A. Kiel, *Phys. Rev. B* **47**, 10515 (1993).
[32] V. Venkataraman, C. W. Liu and J. C. Sturm, *Appl. Phys. Lett.* **63**, 2795 (1993).
[33] M. J. Kearney and A. I. Horrell, *Semicond. Sci. Technol.* **13**, 174 (1998).
[34] S. H. Li, J. M. Hinckley, J. Singh and P. K. Bhattacharya, *Appl. Phys. Lett.* **63**, 1393 (1993).
[35] M. V. Fischetti and S. E. Laux, *J. Appl. Phys.* **80**, 2234 (1996).
[36] P. J. Briggs, A. B. Walker and D. C. Herbert, *Semicond. Sci. Technol.* **13**, 692 (1998).
[37] K. Goto, J. Murota, T. Maeda, R. Schuetz, K. Aizawa, R. Kircher, K. Yokoo and S. Ono, *Jpn. J. Appl. Phys.* **32**, 438 (1993).
[38] K. V. Klitzing, G. Dorda and M. Pepper, *Phys. Rev. Lett.* **45**, 494 (1980).
[39] K. B. Joelsson, Y. Fu, W.-X. Ni, G. V. Hansson, *J. Appl. Phys.* **81**, 1264 (1997).
[40] T. P. Pearsall, J. C. Bean, R. People and A. T. Fiory, *Proc. 1st Int. Symp. Silicon Molecular Beam Epitaxy* J.. C. Bean (ed) Pennington NJ, Electrochemical society, p. 400, 1985.
[41] Nyak, J. C. S. Woo, J. S. Parker and K. L. Wang, *IEEE Electron Device Lett.* **12**, 154 (1991).
[42] M. Garone, V. Venkataraman, J. C. Sturm, *IEEE Electron Device Lett.* **13**, 56 (1991).
[43] Wang, S. G. Thomas, M.O.Tanner, *J. Mater. Res. Mater. Electron.* **6**, 311 (1995).
[44] E. Basaran, R. A. Kubiak, T. E. Whall and E. H. C. Parker, *Appl. Phys. Lett.* **64**, 3470 (1994).
[45] T. Mishima, C. W. Fredriksz, G. F. Walle, D. J. Gravestiejn, R. A. Heuvel and A. A. Gorkum, *Appl. Phys. Lett.* **57**, 2567 (1990).
[46] Venkataraman, P. V. Schwartz and C. J. Sturm, *Appl. Phys.* **59**, 2871 (1991).
[47] J. B. Kuo, M. C. Tang and J. H. Sim, *Solid-State Electron.* **36**, 1349 (1993).
[48] S. V. Vandebroek, E. F. Crabbe, B. S. Meyrson, D. L. Harame, P. J. Restle, J. M. C. Stork and J. B. Johnson, *IEEE Trans. Electron Devices* **41**, 90 (1994).
[49] S. Voinigescu and C. A. T. Salama, *Can. J. Phys.* **70**, 975 (1992).
[50] S. Voinigescu, C. A. T. Salama, T. J.-P. Noel and T. I. Kamins, *IEEE IEDM-94* p 369, 1994.
[51] M. Y. A. Yousif, O. Nur, O. Chretien, Y. Fu and M. Willander, *Solid State Electron.* **42**, 956 (1998).
[52] O. Chretien, M. Y. A. Yousif, O. Nur, C. J. Patel and M. Willander, *Semicond. Sci. Technol.* **13**, 999 (1998).
[53] M. Y. A. Yousif, O. Chretien, O. Nur and M. Willander, *Solid-State Electron.* **43**, 969 (1999).
[54] S. J. Mathew, et al., *IEEE Electron Device Lett.* **20**, 173 (1999).
[55] M. O. Tanner, M. A. Chu, K. L. Wang, M. Meshkinpour and M. S. Goorsky, *J. Crys. Growth* **157**, 121 (1995).
[56] E. A. Fitzgerald, Y-H. Xie, M. Green, D. Brasen, A. R. Kortan, J. Michael and B. E. Weir, *Appl. Phys. Lett.* **59**, 811 (1991).
[57] S. B. Samavedam and E. A. Fitzgerald, *J. Appl. Phys.* **81**, 3108 (1997).
[58] A. Sakai, T. Tatsumi and K. Aoyama, *Appl. Phys. Lett.* **71**, 3510 (1997).
[59] H.-C. Luan, D. R. Lim, K. K. Lee, K. M. Chen, J. G. Sandland, K. Wada and L. C. Kimerling, *Appl. Phys. Lett.* **75**, 2909 (1999).

[60] M. T. Currie, S. B. Samavedam, T. A. Langdo, C. W. Leitz and E. A. Fitzgerald, *Appl. Phys. Lett.* **72**, 1718 (1998).
[61] O. Nur, M. Karlsteen, U. Södervall, M. Willander, C. J. Patel, C. Hernandez, Y. Campidell, D. Bensahel and R. N. Kyutt, *Semicond. Sci. Technol.* **15**, L1 (2000).
[62] C. Chaneliere, S. Four, J. L. Autran, R. A. B. Devine and N. B. Sandler, *J. Appl. Phys.* **83**, 4823 (1998).
[63] A. Yagishita, et. al., *IEEE Trans. Electron. Dev.* **47**, 1028 (2000).
[64] S. A. Campbell, et. al., *IEEE Trans. Electron. Dev.* **44**, 104 (1997).
[65] C. Hobbs, et. al., *IEEE Symp. VLSI Tech. Dig.* p 133, 1999.
[66] Wen-Jie Qi, et. al., *IEEE IEDM Tech. Dig.* p 145, 1999.
[67] Y. Ma, D. R. Evans, T. Nguyen, Y. Ono and S. T. Hsu, *IEEE Electron. Dev. Lett.* **20**, 254 (1999).
[68] T. Ushiki, et. al., *IEEE Trans. Electron. Dev.* **44**, 1467 (1997).
[69] G. J. Hu and R. H. Bruce, *IEEE Trans. Electron. Dev.* **ED-32**, 584 (1985).
[70] T. J. King, J. R. Pfiester, J. D. Shott, J. P. McVittie and K. C. Saraswat, *IEEE IEDM Tech. Dig.* p 253, 1990.
[71] N. Kistler and J. Woo, *IEEE IEDM Tech. Dig.*, p 727, 1993.
[72] C. Salm, D. T. van Veen, J. Holleman and P. H. Woerlee, *Proc. European Solid-State Device Research Conf. ESSDERC'95*, p 131, 1995.
[73] W. C. Lee, T. J. King, C. Hu, *IEEE Electron. Dev. Lett.* **20**, 9 (1999).
[74] W. C. Lee, B. Watson, T. J. King, C. Hu, *IEEE Electron. Dev. Lett.* **20**, 232 (1999).
[75] M. Y. A. Yousif, M. Friesel, M. Willander, P. Lundgren, and M. Caymax, *Solid-State Electron.* **44**, 1425 (2000).
[76] Y. V. Ponomarev, P. A. Stolk, C. Salm, J. Schmitz, and P. H. Woerlee, *IEEE Trans. Electron. Dev.* **47**, 848 (2000).
[77] J. Alieu, et. al., *IEEE Symp. VLSI Tech. Dig.* p 192, 1998.
[78] T. J. King, J. P. McVittie, K. C. Saraswat and J. R. Pfiester, *IEEE Trans Electron Devic.* **44**, 228 (1994).
[79] P. Bouillon, T. Skotnicki, S. Bodnar, C. Morin, J. L. Regolini, P. Gouagout and P. Dollfus, *Proc. Euro. Solid-State Dev. Research Conf. ESSDERC'96* p 473, 1996.
[80] P.-E. Hellberg, S. L. Zhang and C. S. Petersson, *IEEE Electron Device Lett.* **18**, 456 (1997).
[81] H. Ahmed, *J. Vac. Sci. Technol. B* **15**, 2101 (1997).
[82] Y. Fu, and M. Willander. (To be published).
[83] I. Choquet and M. Willander. (To be published).
[84] J. Vincent, K. Jeppson, S. Bengtsson, H. Petterson, M. Karlsteen and M. Willander, *Swedish Foundation for Strategic Research; Conf. On Integrated Circuit Design*, May 2001.
[85] C. J. Gorber, *Physica* **15**, 777 (1951).
[86] T. A. Fulton and G. D. Dolan, *Phys. Rev. Lett.* **59**, 109 (1987).
[87] U. Meirav et al, *Phys. Rev. B* **40**, 5871 (1989).
[88] J. H. F. Scott-Thomas, et al, *Phys. Rev. Lett.* **62**, 582 (1999).
[89] Y. Fu, M. Willander, A. Dutta and S. Oda, *Superlatt. Microstruct.* **28**, 177 (2000).
[90] Y. Fu, M. Willander, A. Dutta and S. Oda, *Superlatt. Microstruct.* **28**, 189 (2000).

9th Int. Symp. "Nanostructures: Physics and Technology"
St Petersburg, Russia, June 18–22, 2001

Room-temperature operation of GaInAs/InP based ballistic rectifiers at frequencies up to 50 GHz

I. Shorubalko, P. Omling, L. Samuelson, W. Seifert, A. M. Song and H. Zirath†
Department of Solid State Physics and Nanometer Structure Consortium,
Lund University, Box 118, S-221 00 Lund, Sweden
†Department of Microwave Technology, Chalmers University of Technology, S-412 96 Göteborg, Sweden

Abstract. Ballistic rectifiers are realized in high-mobility GaInAs/InP quantum well materials using electron beam lithography and wet chemical etching. The devices are made small enough to function even at room temperature. Furthermore, we demonstrate that the devices operate at frequencies at least up to 50 GHz.

Introduction

Recently, a novel semiconductor ballistic rectifier fabricated from a GaAs/AlGaAs heterostructure was demonstrated [1]. In contrast to conventional semiconductor rectifiers, such as diodes, the ballistic rectifier consists of neither a p-n junction nor a barrier structure. The idea behind this ballistic rectifier is the guidance of electrons by a symmetry-breaking scatterer in the ballistic electron transport regime, where electrons are only scattered from designed geometrical boundaries and not from defects. This new working principle allows for very high working speed and also does not give any voltage or current threshold. Recently, it has been shown that the ballistic rectifiers can be realized in high-mobility GaInAs/InP quantum well materials [2], which gives higher efficiency and higher operation temperature of the devices. In this work, we demonstrate that the devices not only function at room temperature, but also operate up to at least 50 GHz.

1. Fabrication

The material used in this work is a modulation-doped $Ga_{0.25}In_{0.75}As$/InP heterostructure (details in ref. [3]) in which electrons are confined into a two-dimensional electron gas (2DEG) in a 9 nm thick quantum well, located 40 nm below the surface. The GaInAs/InP system is used because it has been proved to have less surface damage after etching, and therefore weaker electrical depletion around structures and higher room-temperature electron mobility than a GaAs/AlGaAs heterostructure. The 2DEG has the following parameters extracted from the Hall measurements at room temperature: carrier density 4.5×10^{11} cm^{-2} and mobility 12000 cm^2/Vs. Thus, the elastic mean-free-path of the electrons is 130 nm at room temperature. Using electron beam lithography and wet chemical etching (details in ref. [4]), a triangular area is etched away in a cross junction on conventional Hall-bars and also on specially designed layouts for high-frequency measurements. The scanning electron micrograph of the central part of the device is shown in Fig. 1. The antidot has an upper sidelength of 250 nm and height 230 nm. The lithographical width of the source (S) and drain (D) channels is 100 nm, and the upper (U) and lower (L) channels 500 nm.

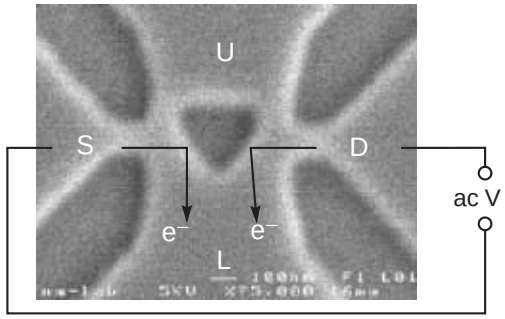

Fig. 1. Scanning electron micrograph of the middle part of the device. The etched triangular antidot scatters most of the electrons out of S and D downwards, independent of the direction of the applied SD voltage, as illustrated by the arrows

2. Results and discussion

Since the elastic mean-free-path of the electrons in our sample is comparable to the size of the central part of the device at room temperature, we expect that the electron transport will be, at least partially, ballistic in the device. Thus, the electron scattering from the triangular boundaries, as shown by the physical picture in Fig. 1, will largely determine the transport properties. If a finite voltage is applied to S and D, the applied field will enhance the electron transmission along the arrows shown in Fig.1 while the electron transmission along the reverse direction is less affected. This results in an accumulation of electrons in the L channel and therefore a negative potential at L. Indeed, our devices show this behavior. The average (dc) voltage between L and U as a function of applied (ac) SD voltage is measured at different temperatures, and the result is presented in the inset of Fig. 2. Smaller output at higher temperatures is expected since the elastic mean-free-path decreases when the temperature increases. Even there is no pronounced output from the device at low SD voltages at room temperature in inset of Fig. 2, the main curve in Fig. 2 plotted in a large SD voltage range shows that the device indeed works at room temperature. This proves that the transport of at least some electrons is still ballistic in the device. The quadratic dependency of the LU voltage, shown by the quadratic fit (solid line) on the SD voltage is expected from ref. [5].

The parasitic capacitance between electrical contacts is very low for this type of devices (the contacts are located on the sides instead of the surface and substrate, as for vertical devices). Also the working principle of this device does not rely on any minority carrier diffusion and no barrier structure is used along the current direction at all. Therefore we can expect that the ballistic rectifier should function at very high frequencies. Room-temperature operation of the ballistic rectifiers makes it much easier to perform high-frequency experiments than measurements in a cryostat. Figure 3 shows the average device output (measured by a DC multimeter) versus the power of the high-frequency SD signal (reading from the signal source) of another device at room temperature. The frequency of the SD signal is fixed at 50 GHz. As we can see, the output of the device is approximately linearly dependent on the 50 GHz signal power, which agrees with the quadratic dependency on applied voltage shown in Fig. 2. Also, we should point out that due to impedance mismatch between the signal source and the device, only a small fraction of the power from the signal source is actually absorbed by the device at 50 GHz. Therefore, the real sensitivity of the device is higher than that shown in Fig. 3. Although it is not possible for us to test the devices at frequencies higher than 50 GHz, from the working principle we

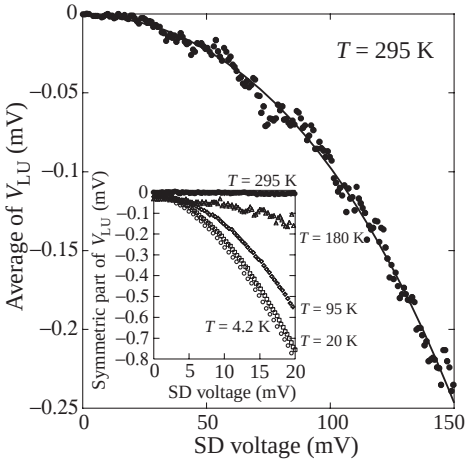

Fig. 2. DC output as a function of SD voltage at room temperature: dots are experimental data and solid line is a quadratic fit. The inset shows the result at lower temperatures.

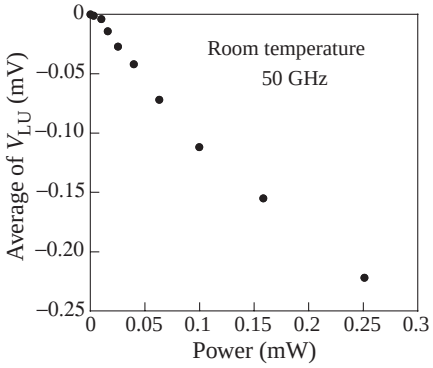

Fig. 3. DC output versus the power of the 50 GHz signal, which is applied to the devices via coplanar probes.

can expect them to work at much higher frequencies, possibly up to THz regime.

3. Conclusions

In this work we have shown that the ballistic rectification effect can be realized at room temperature in high-mobility InGaAs/InP quantum well materials. This is one of the very few types of electronic nano-devices which have been shown to have room-temperature operations so far. We have also demonstrated operations of the ballistic rectifiers at 50 GHz, which makes them very promising for practical applications.

Acknowledgements

We acknowledge the technical help of I. Maximov. This work was supported by the Swedish Natural Science Research Council, Swedish Research Council for Engineering Science, the Swedish Foundation for Strategic Research, as well as from the European Commission through LTR research project Q-SWITCH.

References

[1] A. M. Song, A. Lorke, A. Kriele, J. P. Kotthaus, W. Wegscheider and M. Bichler, *Phys. Rev. Lett.* **80**, 3831 (1998).

[2] I. Shorubalko, I. Maximov, P. Omling, L. Samuelson, W. Seifert, A. M. Song and H. Q. Xu, *Proc. of 25-th Internat. Conference on Physics of Semiconductors (Osaka 2000)*, published in January 2001.

[3] P. Ramvall, N. Carlsson, P. Omling, L. Samuelson, W. Seifert, M. Stolze and Q. Wang, *Appl. Phys. Lett.* **68**, 1111 (1996).

[4] I. Maximov, Q. Wang, M. Graczyk, P. Omling, L. Samuelson, W. Seifert, I. Shorubalko, K. Hieke, S. Lourdudoss and E. R. Messmer, *Proc. of 11th Int. Conf. on InP and Related Materials* (Institute of Electrical and Electronics Engineers, Davos, Switzerland 1999) p. 237.

[5] A. M. Song, *Phys. Rev. B* **59**, 9806 (1999).

9th Int. Symp. "Nanostructures: Physics and Technology"
St Petersburg, Russia, June 18–22, 2001

New quantum dot transistor

V. G. Mokerov, Yu. V. Fedorov, L. E. Velikovski and M. Yu. Scherbakova
Center of Micro- and Nanoelectronics of IRE RAS
101999, Moscow, Russia, GSP-3, 11, Mokchovaya str.

Abstract. Modulation doped N-AlGaAs/GaAs/InAs/GaAs/InAs/GaAs-heterostructures with InAs-quantum dots in device channel have been grown and investigated. Their photoluminescence spectra and electrical transport properties both in low and high electric fields were studied. Using these structures, modulation doped FET's have been fabricated and analyzed. It was demonstrated that the quantum dot FET's present the new type of the hot electron devices, promising for high speed applications.

Introduction

Recently it has become possible to fabricate laterally defined nanostructures, such as quantum dots (QD's). Properties of zero-dimensional electrons confined in such structures attract a great interest both in physics and device applications. The most promising nanometer (nm)-scale QD-structures are formed by the Stranski–Krastanow mode of the heteroepitaxial growth in which a material is deposited on a lattice mismatched substrate beyond some critical thickness to form very small dot structures ($\sim$20 nm) [1–3]. Although much work has been done on the structural and optical properties of QD's, relatively little is known on the influence of the dot-induced potentials on transport of electrons flowing in the neighborhood of dots, particularly, in very high electric field, and on the operation of the real QD-modulation doped field effect transistors (QD-MODFET's). In this work, we study the optical and electrical transport properties of the two dimensional (2D) electrons in the modulation doped N-AlGaAs/GaAs-heterostructures with the InAs-dots embedded in the GaAs-channel, and analyze the characteristics of QD-MODFET's fabricated on their basis. It was shown that mobility μ_{2D} and concentration n_{2D} of electrons are strongly influenced by the presence of QD's. The high field I–V-characteristics (I–V–C's) of MODFET's exhibit the contributions both from mobile 2D-electrons and the electrons localized in QD's. QD-devices demonstrate the new type of the hot electron transistors which can be promising for high speed applications.

1. MBE growth of QD MODFET-structures

The of QD-MODFET-structures (S1) studied here have been grown by molecular beam epitaxy (MBE) on (100)-semi insulating GaAs-substrates. Figure 1 shows schematically their cross sections. First we grew a 0.5-μm-thick undoped GaAs-buffer layer and two very thin InAs-layers, separated by the undoped GaAs spacer layer. Thickness of each InAs layer was 1.07 nm and thickness of the GaAs spacer layer was 5.6 nm. Two layers of QD's with respective size and density were formed. Then, after growth of the second GaAs-spacer layer with thickness of 5.6 nm, the 10 nm-thick undoped $Al_{0.2}Ga_{0.8}As$ spacer layer, a 2.5×10^{12} cm^{-2} Si δ-doped layer and a 35 nm-thick undoped $Al_{0.2}Ga_{0.8}As$ barrier layer were grown. The QD-MODFET-structures were completed by the 6 nm-thick undoped GaAs layer and the 40 nm-thick 3×10^{18} cm^{-3} Si-doped GaAs contact layer. Figure 2

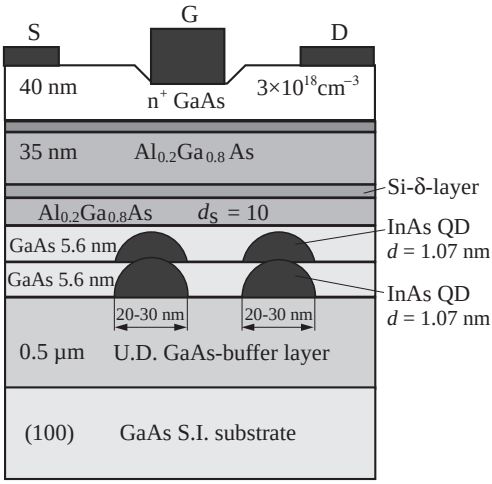

Fig. 1. Cross section of QD-MODFET structure.

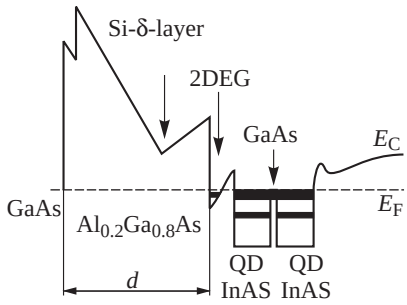

Fig. 2. Band diagram of QD-MODFET structure.

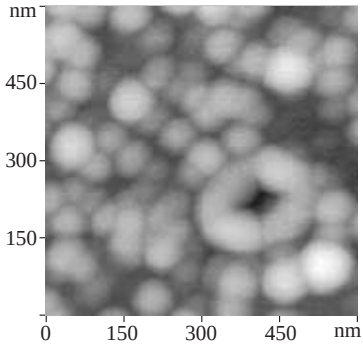

Fig. 3. AFM-photograph of sample S1.

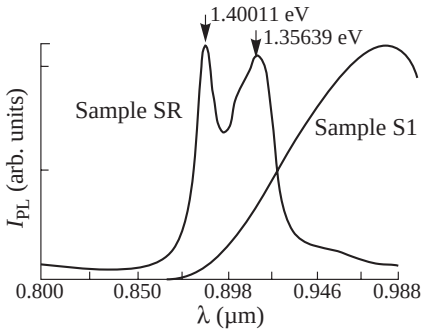

Fig. 4. PL-spectra of samples S1, SR.

depicts the energy diagram of the above QD-MODFET-structures. As a reference sample (SR), we also grew the pseudomorphic-MODFET-structure without QD's with the same average $In_{0.17}Ga_{0.83}As$ composition of the 12 nm-thick channel layer.

2. Optical and low field electrical properties of QD-MODFET-structures

Figure 3 shows AFM-photograph of the sample S1, in a case of which the MBE-growth was completed immediately after growing the second InAs layer. According to this figure, the average size of QD's and their areal density are ∼40 nm and 3×10^{10} cm^{-2}, respectively.

In Fig. 4 PL-spectra of the different samples, measured at 77 K, are presented. Two PL peaks in the sample RS, typical of the modulation doped quantum wells [4], correspond to the optical transitions between the two populated electron subbands and the hole subbands. On the other hand, the broad PL-bands in samples S1 correspond to the InAs-QD's. In Table 1 the results of the Hall effect measurements of electron mobility μ_{2D} and electron concentration n_{2D} of samples S1 and SR are presented. As seen, the insertion of QD's into the device channel results in the reduction of μ_e and the essential reduction of n_{2D} in sample S1. In the latter case, obviously, the trap of majority of electrons by QD's takes place. The low values of electron mobilities in sample S1 as compared with sample SR, are

Table 1. Results of the Hall effect measurements of μ_{2D} and n_{2D}.

Samples	μ_{2D} (cm^2/V s)		n_{2D} (cm^{-2})	
	77 K	300 K	77 K	300 K
SR	10108	4500	8.2×10^{11}	9×10^{11}
S1	3000	2852	1×10^{11}	6×10^{10}

the direct indication, that insertion of InAs-QD's gives rise the specific random potentials, which scatter 2D-electrons very effectively. The charges of electrons trapped by QD's and the effects of strain around each QD can be responsible for these potentials.

3. High field electric transport in QD-MODFET-structures

Because the essential part of electrons in samples S1 are trapped by QD's, they can not participate in the low field electric transport. However, their contributions can be displayed at high electric fields. For such experiments, special MODFET's with a the 2 μm-drain-to-source spacing, without gate and with different widths of the ohmic contacts have been fabricated. Their I–V–C's are shown in Fig. 5. As seen from this figure, in contrast to "standard" FET's, they have the anomalous "two-step" shape (instead of the conventional curve with "saturation"). When the distance between the sample surface and the channel is reduced by means of etching, the first current step is reduced or even completely disappeared, and I–V–C becomes of the threshold type, due to presence of second step only. The two current steps are explained by the contributions from two types of electron states: the mobile 2D-electrons (as in "standard" FET) responsible for the first step, and the electrons localized in QD's. The second ones, responsible for the second step, give the contribution only at the high electric field F, above some threshold value, as a result of the field induced electron emission from QD's. The reduction of the current at the first step, after the additional surface etching (the surface field induced depletion) supports our interpretation of this part of I–V–C.

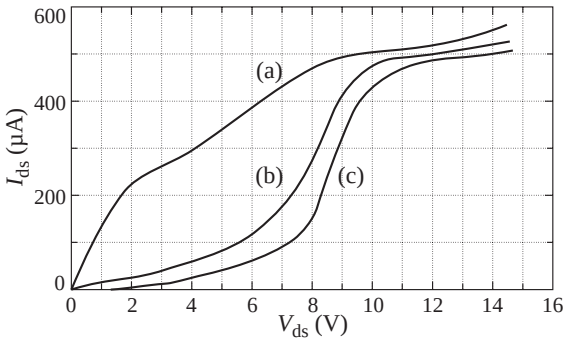

Fig. 5. I–V-characteristics of QD-MODFET structures: (a)—before etching, (b) and (c)—after additional surface etching.

4. QD-MODFET

Using the structures S1, MODFET's with gate length of 0.4 μm have been fabricated. The I–V–C's of these QD-MODFET's are shown in Fig. 6. As seen from this figure applying even the zero-bias to the gate leads to the essential shift of the second current step to the lower voltages as compared with the "ungated" devices. This effect can be explained by

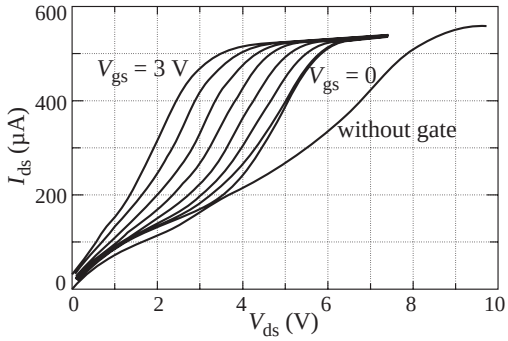

Fig. 6. I–V-characteristics of QD-MODFET structures for different values of V_g (step is -0.5 V).

the redistribution and increasing the peak value of electric field in the device channel under influence of gate voltage U_G. As seen from Fig. 6, the saturation current I_{dss} for the second step practically does not depend on the gate bias U_G. However, its threshold voltage U_{th} is very effectively influenced by negative values of U_G. This result is principally different from the behaviour of the "classical" FET, for which only the electron density and, respectively, I_{dss} are influenced by U_G. These results show, that in a case of QD-MODFET's, the concentration of electrons participated in the current flow, becomes independent on U_G, but threshold voltage U_{th}, for initiation of the electron emission from QD's, is reduced, when U_G becomes more negative. This reduction of U_{th} is explained by increasing the effective electric field in the d_{GD}-spacing. The threshold field, which is determined by the energy of electron states in QD's, can be evaluated from the I–V–C's of the "ungated" MODFET: $E_{th} = 4\,\mathrm{V}\,\mu\mathrm{m}^{-1}$. Proceeding from the effect of electron emission from QD's, we have evaluated the depth of the energy levels EQD in QD's: $E_{\mathrm{QD}} = eE_{th}d_{\mathrm{QD}} = 160$ meV, where $d_{\mathrm{QD}} = 40$ nm is the lateral size of QD's. The important result of this study is the finding of the sufficiently high value of the transconductance $g_m \cong 500$ mS/mm at the very small expected effective device capacitance.

5. Conclusion

New QD-MODFET has been demonstrated. Operation of the QD-MODFET is principally different from that of conventional ("classical") FET, in which U_G carries out the function of the modulation of the thickness of the conducting channel. On the other hand, in QD-MODFET, at small electric fields, we have not free electrons in device channel, because they are localized in QD's. At high electric field FDS in QD-MODFET, U_G-potential controls the electron emission from QD's, resulting in a new shape of I–V–C's. The operation of such a transistor reminds that of the vacuum triod, where, the gate electrod, similar to the grid electrod in vacuum triod, controls the electron emission from their source-QD's.

References

[1] D. Leonard, K. Pond and P. M. Petroff, *Phys. Rev.* **B50** 11687–92 (1994).
[2] J. M. Moison, F. Houzay et al, *Appl. Phys. Lett.* **64** 196–8 (1994).
[3] G. S. Solomon et al, *Appl. Phys. Lett.* **66** 3161–3 (1995).
[4] J. Pozela, V. Jucine, A. Namajinas, K. Pozela, V. G. Mokerov et al, *J. Appl. Phys.* **32** 5564–7 (1997).

9th Int. Symp. "Nanostructures: Physics and Technology"
St Petersburg, Russia, June 18–22, 2001

Fabrication and non-linear measurements of a GaInAs/InP electron waveguide T-branch switch

I. Maximov, R. Lewén†, L. Samuelson, I. Shorubalko, L. Thylén† and H. Xu
Department of Solid State Physics and Nanometer Structure Consortium,
Lund University, Box 118, S-221 00 Lund, Sweden
† Royal Institute of Technology, Department of Electronics
Laboratory of Photonics and Microwave Engineering Electrum 229,
Isafjordsgatan 22 S-164 40, Kista, Stockholm, Sweden

Devices based on electron waveguide phenomena attracted considerable interest during the last several years. Because of high velocity of electrons in the waveguides, these devices seem to be very promising for high speed electronics. Besides, they potentally allow extremely low power dissipation. The complicating factor, however, is a large impedance (13 kOhm for a single mode operation) of the electron waveguide devices, thus restricting their switching speed. Even though the potential for extreme speed (more than 100 GHz) operation might be limited, there is a need for investigation of high frequency limitations of such structures.

Here we present fabrication technology as well as DC and high-frequency (HF) characterization of an electron waveguide based GaInAs/InP T-branch switch (TBS). The TBS-device is formed by 3 reservoirs separated by three quantum point contacts (QPC); each of the QPCs is connected to a three port terminal device, Fig. 1. The device is fabricated using a high mobility 2DEG GaInAs/InP structure with a pseudomorphic $Ga_{0.25}In_{0.75}As$ QW

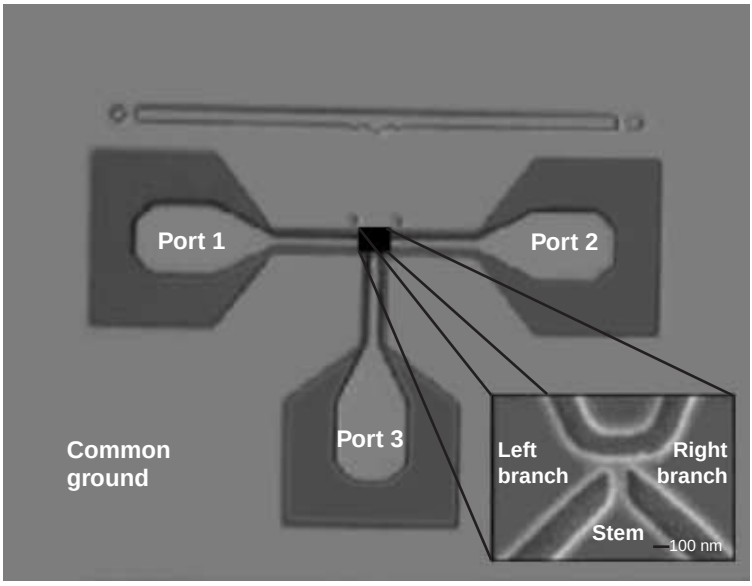

Fig. 1. Microwave pad design with SEM image of T-branch structure. HF-pads are optimized to have a parasitic signal crosstalk of less than −50 dB for frequency of up to 7 GHz.

positioned 40 nm below the InP cap layer. The 2DEG mobility and electron concentration in the GaInAs QW are 450 000 cm^2/Vs and 6-8$\times 10^{11}$ cm^{-2} at 0.3 K, respectively. High-resolution electron beam lithography operating at 35 kV was used to pattern ZEP520A7 positive tone resist to form a mask for wet etching. After a post development baking of the resist [1], a non-selective HBr-based etchant was used to define the TBS-device. Etching was performed down to InP substrate (about 80 nm in depth) in order to prevent parasitic leakage current from the active device area. Geometrical width of the waveguides in the device was about 150 nm, no epitaxial regrowth was applied.

The T-branch switch was fabricated on a coplanar microwave pad layout optimized for HF-measurement, Fig. 1. Pad-to-pad capacitance is 0.4 and 0.7 fF from port 1 to 2 and from port 1 to 3, respectively, which gives a required isolation of 50 dB (due to the high

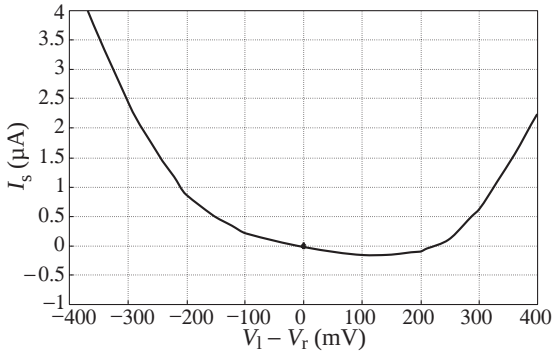

Fig. 2. Room temperature dependence of the stem current versus voltage difference between left and right branch ($V_l - V_r$). The stem is connected to ground ($V_s = 0$).

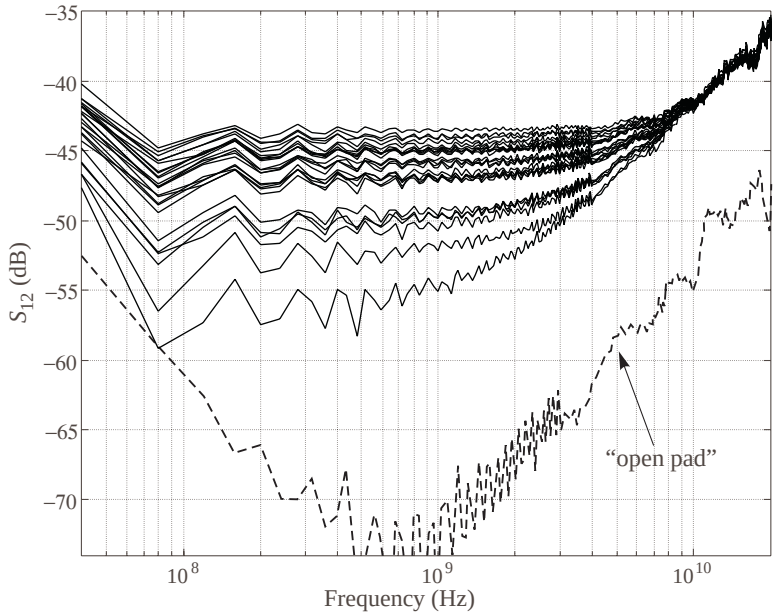

Fig. 3. Scattering parameter S_{12} measured at different biases (upper group of curves) on TBS-device at room temperature. "Open pad" measurement without T-branch device is also shown.

impedance nature of EWG structures) up to approximately 7 GHz.

According to theory [2] and previously made measurements on Y-branch structure [3], [4], the TBS-device can be used as a rectifier with voltages V_l and V_r applied to the left and the right branch in a push-pull mode ($V_l = -V_r$). Under these conditions, the stem voltage V_s is always negative and depends approximately quadratic at small V_l and V_r. This non-linearity originates from the ballistic electron transport between the reservoirs. Electron mean free path at 300 K is about 200 nm, which equals or slightly larger than the distance between the QPCs. Figure 2 shows the room temperature measurements of the stem current as a function of voltage difference on branches $V_l - V_r$. We demonstrated that this non-linearity effect could be used as a frequency mixer. The measured signal power spectrum of the TBS-device corresponds well to the expected quasi-DC response with an applied signal frequency of up to 300 MHz and second harmonic of 600 MHz. Signal transmission from the right branch to the left branch (parameter S_{12}) was measured as a function of DC bias of ports 1 and 2 for different frequencies. The stem electrode was connected to ground via a 50-Ohm resistor. The S_{12} scattering parameter indicates a clear non-linear (DC dependent) behavior up to about 3 GHz, above this frequency the signal is limited by a parasitic capacitance leakage between the ports, see Fig. 3. Prior to HF-measurement of the TBS-device, both “open pad” and “through” structures without the device were characterized for calibration purposes. All the HF-measurements were performed at room temperature using 50-Ohm loads.

Acknowledgements

This work was supported by the European Commission through long-term research project Q-SWITCH (30960). Technical help in microwave pad layout from M. Graczyk is greatly appreciated.

References

[1] I. Maximov, A. L. Bogdanov and L. Montelius, *J. Vac. Sci. Technol. B* **15**, 2921 (1997).
[2] H. Q. Xu, *submitted for publication*
[3] K. Hieke and M. Ulfward, *Phys. Rev. B* **62**, 16727 (2000).
[4] L. Worschech, H. Q. Xu, A. Forchel and L. Samuelson, *submitted for publication*

9th Int. Symp. "Nanostructures: Physics and Technology"
St Petersburg, Russia, June 18–22, 2001

New quantum wire field effect transistor

V. Larkin†, P. A. Houston†, G. Hill†, *S. Morozov*‡, D. Ivanov‡,
I. Larkin†, J. J. Jefferson† and Yu. Dubrovskii‡
† Dept. of Electronic and Electrical Engineering, University of Sheffield, UK
‡ Institute of Microelectronics Technology RAS, Chernogolovka, Russia

Abstract. We present field effect transistor with stand-alone quantum wire channel based on V-groove GaAs/AlGaAs heterostructure grown metal organic chemical-vapour-deposition.

Electron transport in one-dimensional (1D) systems has been extensively studied both experimentally and theoretically. The most striking feature of 1D transport is revealed in the ballistic limit, where the conductance is quantized in units of $G_0 = 2e^2/h$. This quantization has been observed in two-dimensional electron gas (2DEG) systems further confined to 1D by means of an electrostatic potential in a point contact geometry. In these structures, the 1D electron channels are adiabatically connected to the 2D electron reservoirs. However, other structures, which use "rigid" confinement potential (e.g., etched stripe structures [1], over-grown constrictions [2], and T-shaped cleaved-edge overgrown wires [3]), all show ballistic quantized conductance that significantly deviates from the G_0 values.

In this work we demonstrate field effect transistor fabricated on V-groove GaAs/$Al_xGa_{1-x}As$ heterostructure produced by metal-organic-chemical-vapour-deposition (MOCVD). This technique produces very long QWR's in heterostructures with hard wall confinement and large mini band separation. To provide electrons to sidewalls and QWR selectively doped AlGaAs layers were grown on both sides of thin epi-layer of undoped

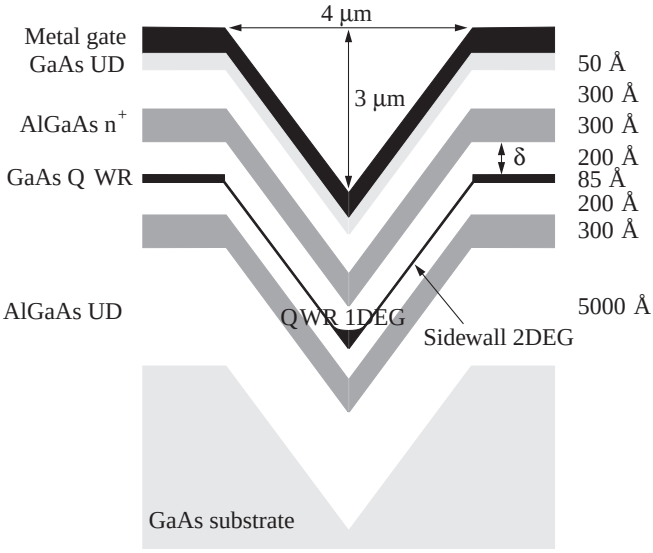

Fig. 1. Schematic cross-sectional picture of a QWR heterostructure.

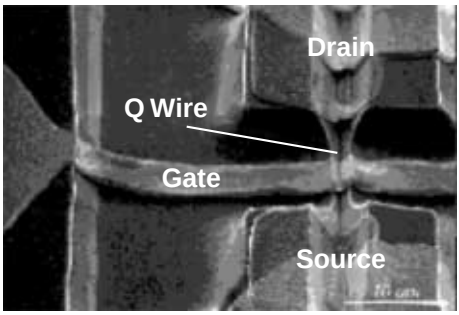

Fig. 2. SEM image of the device.

Fig. 3. Cross-sectional TEM images of a QWR heterostructure.

GaAs separated by 20 nm spacers (Fig. 1). To ensure good leads to QWR we fabricated AgGe ohmic contacts to 2DEG. 4 μm top Schottky gate was placed across the channel to control electron density (Fig. 2). The TEM image (Fig. 3) shows that for 8.5 nm GaAs layer in planar part the size of the QW in the sidewalls is less than 4 nm at the top of the V-groove. The transverse dimensions of the QWR are 18 nm by 75 nm.

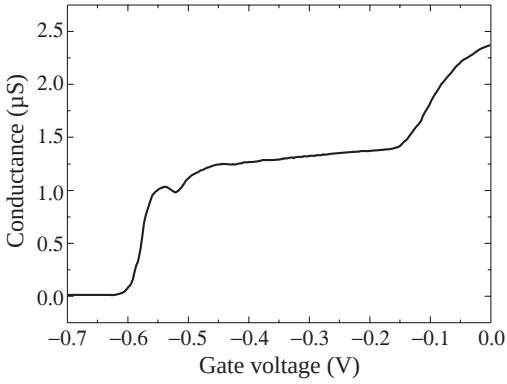

Fig. 4. Conductance vs gate voltage at 4.2 K.

The magneto-conductance measurements were performed on two different type of devices: one with planar two-dimensional electron gas (2DEG) and another with etched planar 2DEG. Both devices have cut-off gate voltage $\sim$0.5 V. The typical conductance of the second type device versus gate voltage at 4.2 K is shown in Fig. 4. By studies of the conductance in magnetic field of different orientation it have been shown that above the cut-off gate voltage the transport is determined by short one dimensional channels connected by tunnel junctions.

References

[1] S. Tarucha, T. Honda and T. Saku, *Solid State Commun.* **94**, 413 (1995); Y. Takagaki, K. Gamo, S. Namba, S. Takaoka and K. Murase, *Appl. Phys. Lett.* **57**, 2916 (1990).

[2] P. Ramvall, N. Carlsson, I. Maximov, P. Omling, L. Samuelson, W. Seifert, S. Lourdudoss and Q. Wang, *Appl. Phys. Lett.* **71**, 918 (1997).

[3] A. Yacoby, H. L. Stormer, N. S. Wingreen, L. N. Pfeiffer, K. W. Baldwin and K. W. West, *Phys. Rev. Lett.* **77**, 4612 (1996).

9th Int. Symp. "Nanostructures: Physics and Technology"
St Petersburg, Russia, June 18–22, 2001

Dynamical nature of peculiarities of RTD static V–I characteristic

E. A. Poltoratsky and G. S. Rychkov
Scientific Researeh Institute of Physical Problems, 103460 Moscow, Russia

Significant achievements in the way of creating nanostructures and studying physical phenomena in these ones are generally acknowledged by now. However the transition to creating nanoelements with definite functional properties goes forward slowly. One of the reason of such situation is the necessity to take into account the dynamic processes running in nanoelements [1].

An example, when the static characteristics are a consequence of dynamic behaviour nanoelements, is a bistable state of resonant tunneling diodes (RTD). This state shows that in the field of negative differential resistance (NDR) at the same bias voltage through the diode the current can have one value, or another [2]. And, as the function from a bias voltage, this phenomenon carries the brightly expressed hysteresis character. Except for hysteresis section there is also horizontal section in area NDR, which can be bent upwards or fall downwards. Usually this section is called "plateau" and connects to a generation of oscillations. Carried out by a number of the authors the numerical modeling of the behaviour of resonant-tunneling structure has shown a presence of current oscillations inside structure [2]. And the frequency of oscillations had very high values ($\sim$2.4 THz). The internal oscillations are connected with a presence of "plateau". As to hysteresis loops, the question remained open, as the authors of work [2] connected it to redistribution of a charge between the emitter and quantum well only.

It is natural, that the oscillations are connected to presence of an inductive element inside resonant-tunnel structure. Such element is the part of the emitter directly contiguous to the barrier (see Fig. 1). In view of an inductive element the authors of the considered works have given the equivalent circuit of RTD, submitted in Fig. 2(a). However, they could not use it for an explanation of anomalies in I–V characteristic as such circuit can not generate oscillation at all.

In [2] dynamic equations describing oscillation in resonant-tunneling structure are received also. The equations describe occurrence of small fluctuations that correspond to birth at dynamic system of a limiting cycle from the critical point in its some small area determined by some small parameter. The offered dynamic model describes occurrence of "soft" generation and by virtue of small amplitudes of oscillations explains the presence of "plateau" in I–V characteristic of resonant-tunneling structures only qualitatively. We offer the equivalent circuit of RTD, enabling to investigate dynamic processes more widely and to give an interpretation of "plateau" and hysteresis loops from the uniform point of view, namely from the point of view of oscillatory process, which in area "plateau" has the character of a "soft" mode of oscillations, and in area hysteresis loops — "rigid" mode.

The equivalent circuit, considered by us, is submitted in a Fig. 2(b). As a matter of fact it differs by one, but very important detail. A current source $i_0(v)$ is shunted by the capacity C, which reflects a presence of a quantum well containing a charge. The addition of this capacity, even as much as very small, causes the oscillations of high frequency in an internal contour formed by elements L, C and $i_0(v)$, which are shunted by capacity C_0.

For analysis of the limiting cycles the analytical and topological criteria allowing to estimate the number of limit cycles, their characteristics and their uniqueness are developed.

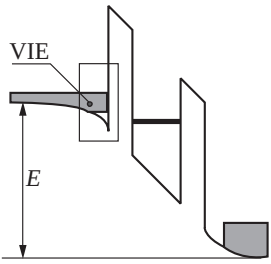

Fig. 1. Schematic band-edge diagram of the RTD under bias with virtual inductive element (VIE) marked by the frame.

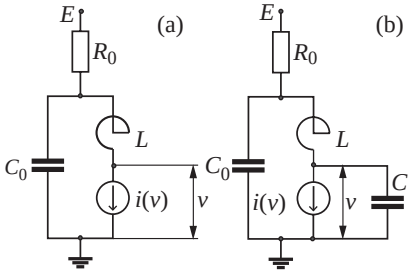

Fig. 2. (a) BJ model [2] of RTD equivalent-circuit; (b) proposed equivalent-circuit.

Here we shall present the simplified criterion of existence of limit cycles for the certain dynamic system, corresponding to the resonant-tunneling structure.

Let oscillatory system is described by the differential equations

$$\frac{\mathrm{d}i}{\mathrm{d}t} = a(E - v), \qquad \frac{\mathrm{d}i}{\mathrm{d}t} = i - i_0(v),$$

where a is constant, $i_0(v)$ is I–V static characteristic of oscillatory system, and E is bias voltage. Let $i_0^*(v) = i_0(2E - v)$. If the curves $i_0(v)$ and $i^*(v)$ are intersected in n points $(v_1, i_l) \ldots (v_n, i_n)$ for $v < E$, then the system has n limit cycles, and the voltage amplitude of k limit cycle v_{0k} satisfies to an inequality:

$$E - v_k < v_{0k} < E - v_{k+1}, \qquad 1 \le k \le n, \qquad v_{n+1} = -\infty.$$

If $i_0'(E) > 0$, the odd limit cycles will be unstable, and even — steady.
If $i_0'(E) < 0$, on the contrary.

More accurate formulation of criteria of limiting cycles presence and absence for considered and more complex dynamic systems can be found in [3].

Now on the basis of the presented criterion we shall carry out the analysis of resonant-tunneling structure, with an equivalent circuit submitted in Fig. 2(b). For simplicity we shall consider, that $R_0 = 0$. To give the problem a definite form, let us take the $i(v)$ in form represented in Fig. 3(a). Using criterion and assuming that "time-averaged" current of stable limit cycle equal $(I_p + I_v)/2$, we receive "time-averaged" I–V characteristic represented in Fig. 3(b).

We have I–V characteristic, which is obtained at external measurement. So the experimentally measured static I–V characteristic, exhibiting a plateaulike behavior and double hysteresis, have the dynamic nature:"soft" and "rigid" generation. Let's consider more in detail, that occurs at first at increasing of a bias voltage, and then at its decreasing. When the voltage increases, the dynamic system has only one steady critical point. At achievement of a point **a** the steady critical point turns in unstable and system goes to the stable dynamic state (to the stable limit cycle S_1 (see Fig. 4(a)), where there are the oscillation (so-called "soft" generation). Externally it corresponds to the transition from a point **a** in a point **b** (see Fig. 3(b)). At the further increase of a voltage the mode of "soft" generation is kept, until the point **g** will not be achieved. The further increase of a voltage results in birth from the critical point **O** unstable limit cycle S_2 and transition the system from "soft" mode of generation to "rigid" (see Fig. 4(b). The "rigid" mode is characterized by presence of two steady condition: one static state is represented by a steady critical point **O**, and second — dynamic, represented by steady oscillation (steady limit cycle S_1). As at increase of a bias

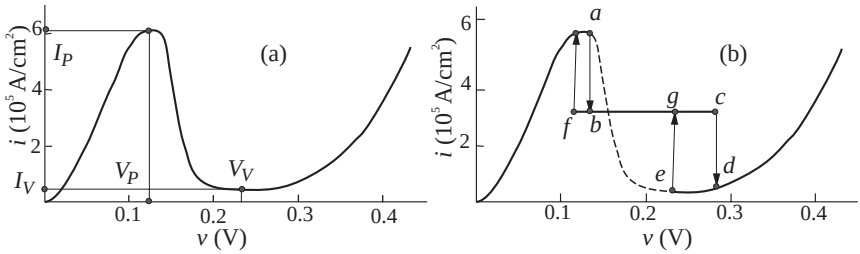

Fig. 3. (a) $i_0(v)$–I–V characteristic used for analyzing of RTD dynamical properties; (b) "time averaged" I–V characteristics of RTD, exhibiting plateaulike behavior and double hysteresis.

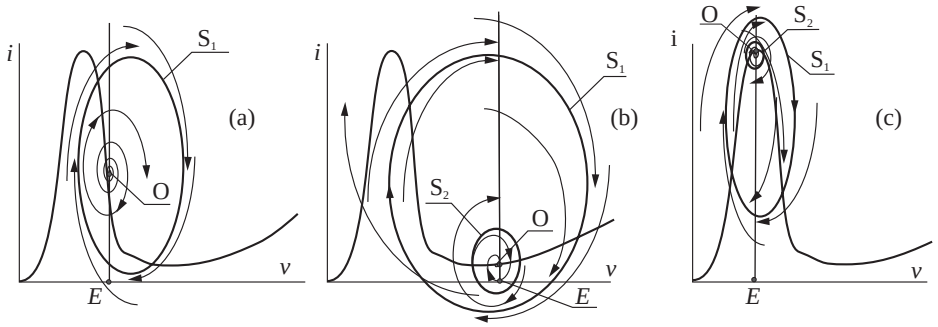

Fig. 4. Phase portraits of dynamical system shown in fig.2(b) for the cases: (a) "plateau"; (b) large "hysteresis" loop; c) small "hysteresis" loop.

voltage the system was in an oscillatory mode, it will continue to keep this state though the system can be transferred in a steady static state. The system will be in "rigid" mode of excitation of oscillations, while the point **c** will not be achieved. At this moment in phase space of system a steady limiting cycle S_1 is merged with unstable S_2 and the system will have only one steady critical point **O**. The system passes in a steady static state, which is represented by transition from a point **c** in **d** (Fig. 3(b)). Now at decrease of a bias voltage the system will be in a steady static state **O**, though it has also steady dynamic state **S** (Fig. 4(b)). It will proceed, while bias voltage will not be lowered up to the point **e**. Here the unstable limit cycle S_2 merges with the critical point **O**, which turns to the unstable critical point. The system passes in a "soft" mode of generation, which proceeds while the point **e** will not be achieved yet. At the further decrease of bias voltage the system will go on a section **bf**, that corresponds to a presence of the system in an excitation state, though it has also the steady static state **O**. Excitation is represented by the steady limit cycle S_1 (Fig. 4(c)). At last, at achievement of a point **f** the system passes in a unique static steady state **O**.

This work was supported in part by the Russian–Ukraine programme "Nanophysics and Nanoelectronics".

References

[1] E. A. Poltoratsky and G. S. Richkov, *Int. Symp. "Nanostructures: physics and technology*, Abstracts of invited lectures and contributed papers. St. Petersburg. 1994. p. 292-294.

[2] F. A. Buot, P. Zhao, H. L. Cui, D. L. Woolard, K. L. Jensen and C. M. Krowne, *Phys. Rev. B* **61**, 5644-5665 (2000).

[3] G. S. Rychkov, *Dynamic systems in micro- and nanoelectronic*, the degree of Ph.D., Moscow, 1994.

9th Int. Symp. "Nanostructures: Physics and Technology"
St Petersburg, Russia, June 18–22, 2001

Unmonotonous variation of oscillation threshold with in-plane magnetic field in resonant-tunneling diode

V. G. Popov, Yu. V. Dubrovskii, S. V. Dubonos,
L. Eaves†, M. Henini† and G. Hill‡
Institute of Problem of Microelectronics Technology RAS,
Chernogolovka 142432, Russia
† University of Nottingham, NG72 RD Nottingham, United Kingdom
‡ Department of Electronic and Electrical Engineering, University of Sheffield,
Mappin Street, Sheffield S1 3JD, United Kingdom

Abstract. Current oscillations in the negative differential conductance region of resonant tunneling diodes with different lateral pattern and size versus perpendicular to the tunneling current magnetic field have been studied. It is revealed that the value of the critical negative differential conductance or oscillations threshold, that is the value of conductance when the oscillations in measurement circuit are arisen, unmonotonically depends on magnetic field. The relation of the observed dependence with inhomogeneous distribution of the tunneling current is discussed.

Current instabilities have been investigated in semiconductor devices for over 50 years [1]. Inhomogeneous instabilities such as domains and filaments have attracted much attention and have been revealed in a wide range of the devices. As far as we know, a resonant tunneling diode (RTD) becomes experimentally investigated for the presence of the *inhomogeneous instabilities* very recently [2]. By inhomogeneous, we mean instabilities or charge inhomogeneties in the plane of the barrier and quantum well. Some theoretical works have already predicted this kind of instability in the RTD [3–7]. In particularly it was shown that increasing of the lateral size of the diode above some critical value leads to a significant inhomogeneous current distribution along the RTD structure when the diode is biased in the negative differential conductance (NDC) region.

A local probe technique has already been successfully exploited in Gunn diodes to determine the inhomogeneous current distribution [8]. However, for the RTD, this technique is not applicable, not only because of the relative small lateral size of the predicted current inhomogeneities but also because of inaccessibility of a local external probe to the barrier and quantum well region of the diode where the inhomogeneity is expected to occur. Another way to test for an inhomogeneous current distribution is to compare experimental data with those calculated from widely used RTD models derived on the assumption of a homogeneous current distribution along the tunnel junction. Features that cannot be explained by these models can then be searched for experimentally as evidence of current inhomogeneity.

In this work we present studies of the current oscillations excited in measurement circuit when RTD is biased to the negative differential conductance region in magnetic field parallel to the barriers focusing on the variation of the oscillation threshold conductance with magnetic field. The oscillations appear when negative differential conductance exceed some critical value — threshold conductance. In the approximation of homogeneous current distribution the threshold conductance is related with other measurement circuit parameters by stability condition. The in-plane magnetic field strongly effects and change

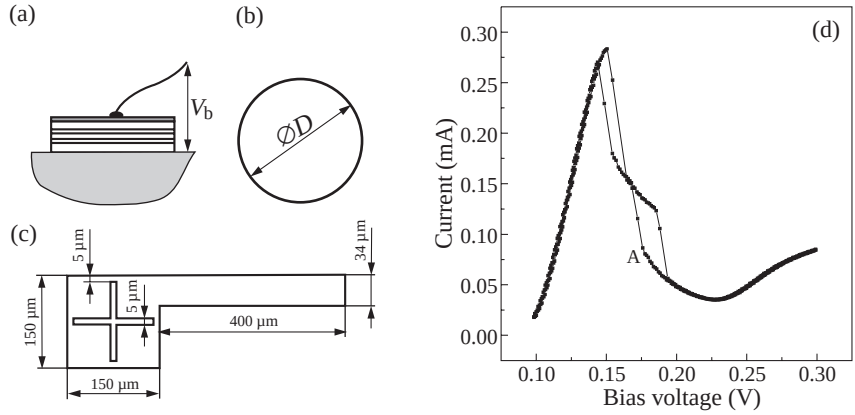

Fig. 1. (a) Resonant tunneling diode with ohmic metallization and applied bias voltage. (b) Circular mesa structure. The diameter D of the structure is equal to 200 μm for sample *A* and 400 μm for sample *B*. (c) Mesa structure of stripe-like sample *C*. (d) Current-voltage characteristic of the RTD measured with dc voltmeters. The point A is a transition point between stable current region and unstable current region at backward sweep of bias voltage. The threshold conductance is a differential conductance at point A.

dc current-voltage characteristic (I–V curve) of the RTD [9, 10]. It changes mainly differential conductance and remains other internal parameters of the diode almost unchanged. Evidently one could expect that threshold conductance measured without changing in the external circuit should remains almost the same at different magnetic fields. Contrary to this expectation we have found remarkable dependence of the threshold conductance on magnetic field.

The resonant tunneling diodes were fabricated from double barrier heterostructure grown on n^+ GaAs substrate. The heterostructure consisted of 11.8 nm wide QW sandwiched between two $Al_{0.4}Ga_{0.6}As$ 8.3 nm thick barriers. Undoped 30 nm spacer layers separated the barrier/well region from the n-doped contact layers. The diodes had different lateral sizes and forms of the mesa structure made by conventional wet etching (see Fig. 1(a)). Sample *A* had circular mesa of 200 μm diameter (see Fig. 1(b)). Sample B had circular mesa of 400 μm diameter. Sample *C* had mesa of stripe-like form and the area of the sample was equal the area of a square with 300 μm side (see Fig. 1(c)).

The I–V curves were measured with dc voltmeters. Since the dc voltmeter measures an average value of real voltage sudden appearance of nonlinear voltage oscillations cause an appearance of current steps and jumps in the NDC region (see Fig. 1(d)). The oscillations excitation was controlled by measurements with high sensitive oscilloscope. The oscillations were observed inside the voltage range of current step and they were absent out of this range.

Thus when the voltage is swept from stable region of the I–V curve to unstable one the differential conductance at point of the stable-unstable transition is equal to threshold conductance which could be determined from the data. So measuring the dc I–V curves at different magnetic fields one can get the dependence of the threshold conductance on magnetic field. In this work we have investigated stable-unstable transition in NDC region near current minimum (see Fig. 1(d), point A) for reverse bias sweep direction. Near the current peak the differential conductance changes very quickly with voltage therefore this

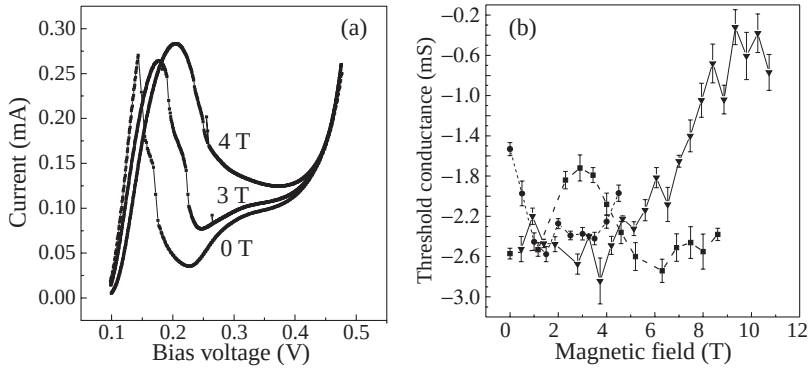

Fig. 2. (a) Current–voltage characteristics of the RTD at different in-plane magnetic fields. (b) Threshold conductance versus in-plane magnetic field. Circles with dotted line correspond to data measured on sample A. Squares with dash line correspond to sample B. Triangles with solid line correspond to sample C. Lines is used only as viewguide.

region is not convenient for the measurements. The I–V curves are shown in Fig. 2(a) at different in-plane magnetic fields. The in-plane magnetic field causes the broadening of the resonant peak and shifts it to higher voltages [9, 10]. The dependences of the threshold conductance on magnetic field are plotted in Fig. 2b for different samples.

As it was mentioned above the magnetic field effects only parameters of the RTD while other parameters of the measurement circuit remain the same. Furthermore in magnetic field the differential conductance changes more drastically then other parameters of the RTD, e.g. differential capacitance. From Fig. 2(b) one can see that threshold conductance is constant $\sigma_T \approx -2.5$ mS in the magnetic field range from 1 T to 2 T for all samples. In addition the σ_T has the same values for samples A and C from 1 T to 5 T. It is worth to note that capacitance of the sample C is twice larger than that of the sample A, which is four times less of capacitance of the sample B. The same relations should be valid for contact resistances of the samples. This is very surprising that the values of the threshold conductance are so closed for such different samples. It can be so when the σ_T is determined mainly by the external circuit parameters, which doesn't depend upon the magnetic field, and one should observe no dependence upon the magnetic field and no significant difference between different samples. On the other hand if we suppose inhomogeneous lateral current distribution the effective area of the samples will be determined by lateral size of the inhomogeneity that may be the same for the samples with different lateral sizes. The inhomogeneous current distribution should be very sensitive to the in-plane magnetic field and thus one should expect nontrivial dependence upon the magnetic field.

In summary, we have investigated the current oscillations in the NDC region of the RTD in the in-plane magnetic field. The samples of different size and form have been investigated. We have measured the differential conductance at transition point from stable current region to the region where the oscillations are exited. The threshold conductance is found to have a peak in its dependence on magnetic field. The peak positions and threshold conductance differ for the samples of different size. However the value of threshold conductance out of the peaks are the same for all samples. The observed features cannot be explain assuming homogeneous lateral current distribution in the NDC region of resonant tunneling diodes.

Acknowledgements

We are grateful to A. Levin and V. A. Volkov for helpful discussions. The work was supported by the INTAS (97-11475), RFBR (01-02-17844, 01-02-97020), Ministry of Science (PSSN-97-1057), and EPSRC (UK).

References

[1] M. P. Shaw, V. V. Mitin, E. Scholl, H. L. Grubin, *The Physics of Instabilities in Solid State Electron Devices.* (New York 1992), Plenum Press, 1992.
[2] V. G. Popov, Yu. V. Dubrovskii, L. Eaves, J. C. Maan, K. L. Wang, *Abstract of 8th International Symposium on Nanostructures: Physics and Technology*, St.-Petersburg, Russia, 2000, p. 347.
[3] A. Wacker, E. Scholl,*J. Appl. Phys.* **78**, 1 (1995).
[4] M. N. Feiginov, S. A. Mikhailov, V. A. Volkov, *Phys. Low-Dim. Struct.* **9**, 1,(1994).
[5] M. N. Feiginov and V. A. Volkov, *Abstracts of the 24th International Conference on the Physics of Semiconductors*, Jerusalem, Israel, Tu-P101 (1998).
[6] M. N. Feiginov, V. A. Volkov, *Pis'ma v Zh. Eksp. Teor. Fiz.* **68**, 633 (1998).
[7] M. N. Feiginov, *Ph. D. Thesis*, IRE RAS, Russia (1999).
[8] J. B. Gunn, *Plasma Effects in Solids* (Paris 1964), p 199.
[9] R. A. Davies, D. J. Newson, T. G. Powell, M. J. Kelly, and H. W. Myron, *Semicond. Sci. Technol.* **2**, 61 (1987).
[10] M. L. Leadbeater, L. Eaves, P. E. Simmonds, G. A. Toombs, F. W. Sheard, P. A. Claxton, G. Hill, and M. A. Pate, *Solid State Electron.* **31**, 707 (1988).

9th Int. Symp. "Nanostructures: Physics and Technology"
St Petersburg, Russia, June 18–22, 2001

New class of magnetoresistance oscillations: interaction of a two-dimensional electron gas with leaky interface phonons

A. L. Efros†, M. A. Zudov†, I. V. Ponomarev†, R. R. Du†,
J. A. Simmons‡ and J. L. Reno‡
† Department of Physics, University of Utah, USA
‡ Sandia National Laboratories, Albuquerque, NM USA

Abstract. We report on a new class of magnetoresistance oscillations observed in a high-mobility two-dimensional electron gas (2DEG) in GaAs-$Al_xGa_{1-x}As$ heterostructures. Appearing in a weak magnetic field ($B < 0.3$ T) and only in a narrow temperature range (2 K $< T <$ 9 K), these oscillations are periodic in $1/B$ with a frequency proportional to the electron Fermi wave vector, k_F. We interpret the effect as a magnetophonon resonance of the 2DEG with thermally excited leaky interface-acoustic phonons. Calculations show a few branches of such modes existing on the GaAs-$Al_xGa_{1-x}As$ interface, and their velocities are in quantitative agreement with the observation. We show that electrons mostly interact with the phonons carrying a wave vector $q = 2k_F$.

There are several classes of transverse magnetoresistance (MR) oscillations known to exist in a two-dimensional homogeneous electron gas (2DEG). The most common of these are the Shubnikov–de Haas oscillations (SdH), which arise from a magnetic field B-induced modulation of the density of states at the Fermi level E_F. They become more pronounced with decreasing temperature T. The magnetophonon resonance (MPR) [1, 2] is a source of another class of oscillations resulting from the absorption of bulk longitudinal optical phonons. These resonances appear under the condition $\omega_{LO} = l\omega_c$, where ω_{LO} and $\omega_c = eB/mc$ are the optical phonon and cyclotron frequencies respectively, l is an integer, and m is the effective mass of the carriers. These oscillations are only seen at relatively high $T \sim 100-180$ K [2]. Both SdH and MPR are periodic in $1/B$, but the SdH frequency (reciprocal period) scales with electron density as n_e, whereas MPR is n_e-independent.

In this paper, we report on a new class of MR oscillations observed in a high-mobility 2DEG in GaAs-$Al_xGa_{1-x}As$ heterostructures. Unrelated to either of the above origins, these novel oscillations are still periodic in $1/B$, but they appear *only* in a narrow temperature range (2 K $< T <$ 9 K), and their frequency scales with $\sqrt{n_e}$. We interpret the data in terms of a magnetophonon resonance mediated by thermally excited *leaky interface-acoustic phonon* (LIP) modes. In principle, the surface modes might provide a good explanation as well, but in our case 2DEG is located so far from the surface ($\sim$0.5 μm) that no such interaction is possible.

The leaky interface modes have been studied for a few decades in connection with the Earth's crust [3]. The term "leaky" shows that the waves propagate at a small angle with the interface, so that the energy radiates towards the outside media. At some specific parameters these waves may not be leaky [4], but for the interface under study all of them are leaky. Despite the fact that LIP is commonly presented in layered material systems [5], it has so far not been considered on the GaAs-$Al_xGa_{1-x}As$ interface. Due to radiation of energy, the frequency and velocity of leaky waves are complex: $u = \omega/q = u_R - iu_I$ with $u_I \ll u_R$.

The novel oscillations can be explained by a simple momentum selection rule which is derived later in the paper. It says that at high Landau levels (LLs) the electrons interact predominantly with the interface phonons carrying a wave vector $q = 2k_F$, where k_F is the Fermi wave vector of the 2DEG at zero B field. The condition for resonant absorption or emission of an interface phonon is then given by

$$2k_F u_R = l\omega_c, \qquad l = 1, 2, 3, \ldots \tag{1}$$

We claim that Eq. (1) determines the values of B for the *maxima* in these new MR oscillations. It shows that the oscillations are periodic in $1/B$ with a frequency $f = 2k_F umc/e$. Evidently, the bulk phonons can not account for the resonance, since their frequency depends on q_z, while the selection rule includes lateral momentum only.

Our primary samples are lithographically defined Hall bars cleaved from modulation-doped GaAs-$Al_{0.3}Ga_{0.7}As$ heterostructures of high-mobility $\mu \approx 3\times10^6$ cm^2/Vs. The wafers are grown by MBE on the (001) GaAs substrate. At low T, the density of the 2DEG, n_e (in units of 10^{11} cm^{-2} throughout the text), can be tuned by a combination of LED illumination and the NiCr front gate potential. The experiments were performed in a variable-temperature ^{4}He cryostat equipped with a superconducting magnet, employing a standard low-frequency lock-in technique for resistance measurement.

In Fig. 1 we show the normalized low-field magnetoresistivity $\rho_{xx}(B)/\rho_{xx}(0)$ measured at $T = 4$ K, for the electron density $n_e = 2.05$, 2.27 and 2.55, respectively. In addition to the damped SdH commonly seen in a 2DEG at this T, the traces reveal new oscillations that appear only at $B < 0.3$ T. The amplitude of the oscillations is about 2–3% in these traces.

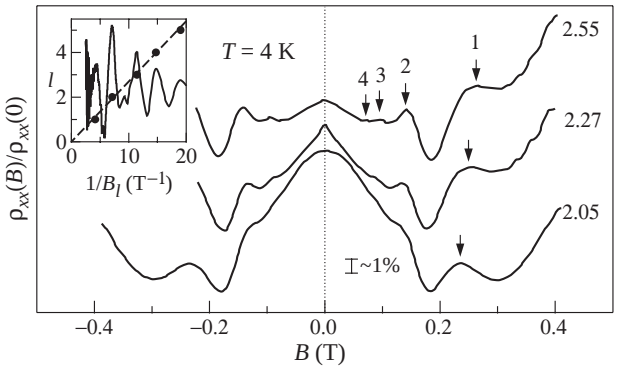

Fig. 1. $\rho_{xx}(B)/\rho_{xx}(0)$ traces (shifted vertically for clarity) are shown for three densities n_e of 2.05, 2.27 and 2.55 $\times$ 10^{11} cm^{-2}, respectively; arrows indicate the maxima for $l = 1, 2, 3, 4$ and the shift of the primary ($l = 1$) peak with increasing n_e; Inset shows that the oscillations are periodic in $1/B$.

Three aspects of the observation should be highlighted. First, the oscillations are roughly periodic in inverse magnetic field, $1/B$. The arrows next to the traces indicate the $\rho_{xx}(B_l)$ *maxima* (indexed as $l = 1, 2, 3, 4$) in this oscillatory structure. In the inset we plot the order of the oscillations, l (and $-d^2\rho_{xx}/dB^2$), vs. $1/B$ for $n_e = 2.55$ and observe a linear dependence. Such periodic oscillations have been seen for all n_e (from ~ 1.5 to 3) studied. Second, with increasing n_e the features shift orderly towards the higher B. Finally, the

oscillatory structure is accompanied by a negative MR background, apparently in the same B range where the oscillations take place.

In the following we shall focus on the analysis of the oscillatory structure, in particular, their dependence on the n_e and T. To further quantify our results, we have performed fast Fourier transform (FFT) on the resistance data. Surprisingly, such analysis has uncovered two frequencies, marked by A and B. The peak A corresponds to the main period, conforming to a simple fit in Fig. 1. The peak B is somewhat weaker, and occurs at $f_B \approx 1.5 f_A$. The shift of the doublet with increasing n_e is marked by three arrows for the main peaks. The FFT data have revealed a striking linear relation between the frequencies of oscillations and the electron Fermi wave vector. We plot f^2 of the FFT peaks against the electron density, n_e, which has been varied from 1.47 to 2.95 in the same specimen. Since $k_F = \sqrt{2\pi n_e}$, the observed linearity indicates that $f \propto k_F$.

Such a linear dependence distinguishes the new oscillations from SdH, as $f_{SdH} \propto k_F^2$, and is exactly what one expects from the phonon resonance scenario proposed here. As such, the oscillatory structure must be viewed as resulting from the resonance of the 2DEG with two branches of the interface modes. Using Eq. (1) and a single known material parameter, the GaAs band electron mass $m \approx 0.068 m_e$, we fit the data (solid line in the inset) and deduce a velocity for the slow (fast) mode $u_A \approx 2.9$ km/s ($u_B \approx 4.4$ km/s). Within the experimental error of 10% the data from several specimen collapse on the same lines, indicating that new oscillations are generic in high-mobility 2DEG in GaAs-$Al_xGa_{1-x}As$ heterostructures.

The T-dependence of the oscillations is consistent with a *thermally excited* phonon-scattering model. In our samples $\rho_{xx}(0)$ grows linearly with T, indicating that acoustic-phonon scattering dominates the electron mobility in this temperature range [6, 7]. Considering the interface phonon modes of interest here, we rely on the value of the slow mode $u_A = 2.9$ km/s to estimate a characteristic temperature, T_c, from $k_B T_c = \hbar u_A (2k_F)$. The value of $T_c \approx 5$ K can qualitatively account for the temperature dependence of the main features of the oscillations. While the SdH gradually diminishes as T increases, the oscillations are best developed at $T \approx 3-7$ K and are strongly damped at both higher and lower T. At $T \ll T_c$ the number of interface phonons carrying $q = 2k_F$ becomes small and therefore the amplitudes diminish. At high T the smearing of the LLs prevails and the oscillations disappear as well.

We now turn to the details of the theoretical explanation of the novel oscillations. We have performed the calculations [8] of LIP modes for the GaAs-$Al_{0.3}Ga_{0.7}As$ interface on the basal (001) plane. In anisotropic case the speed of LIPs depends on an angle between q and the [100] direction. Using the elastic moduli of the bulk lattices[9] we found series of modes with weak anisotropy and a small imaginary part of the velocity ($u_I/u_R < 0.03$). We have studied the modes within the interval of velocities 2.4–6.0 km/s. Two close groups of modes have been found within the interval of 3–3.5 km/s and that of 4.2–4.5 km/s, respectively. These modes may be responsible for two periods of oscillations which have been observed. The frequencies of the other modes found are too high to be detected in our experiment. Note that different modes may interact with electrons with a different strength.

To calculate the transverse conductivity due to the scattering of the 2DEG by the LIPs, we employ a 2D analog of the formula, first derived by Titeica.

$$\sigma_{xx} = \frac{4\pi e^2}{A m^2 k_B T \omega_c^2} \sum_{n,n'} \sum_{k_y,k_y'} \sum_{q_x,q_y} |I_{nn'}(q\lambda)|^2 \, q_y^2 \, |C(q)|^2 \times N_l f_n (1 - f_{n'}) \delta_{k_y - k_y' + q_y} \delta(\omega_c (n' - n) - qu). \quad (2)$$

Here A is the area, $N_l = (\exp(\hbar\omega/k_{\mathrm{B}}T) - 1)^{-1}$, $f_n = (\exp((E_n - \mu)/k_{\mathrm{B}}T) + 1)^{-1}$, $\lambda = \sqrt{\hbar c/eB}$ is the magnetic length, and $|C(q)|^2 \equiv v(q)/A$ is the square modulus of the 2DEG-LIP interaction, which has a power law dependence on q. This formula can be interpreted in the following way. A 2D electron in a magnetic field has a wave function which is a product of a plane wave in the y direction and an oscillatory wave function, centered at the position $x_0 = -c\hbar k_y/eB$: $\Psi = \exp(ik_y y)\phi_n(x - x_0)$, where n is the LL index. A transverse conductivity appears because an electron transfers wave vector $q_y = k'_y - k_y$ to a scatterer. This is equivalent to a jump in the x-direction at a distance $\Delta x_0 = c\hbar q_y/eB$. In Eq. (2) this physics is applied to electron-interface phonon scattering.

The theory proves selection rule $q = 2k_{\mathrm{F}}$ and provides an interpretation of the rule.

References

[1] V. L. Gurevich and Yu. A. Firsov, *Sov. Phys. JETP* **13**, 137 (1961).

[2] D. C. Tsui, Th. Englert, A. Y. Cho and A. C. Gossard, *Phys. Rev. Lett.* **44**, 341 (1980).

[3] see, *e.g.*, A. A. Maradudin, in *Surface Phonons*, ed. by W. Kress and F. W. de Wette (Springer-Verlag, Berlin, 1991) and references therein.

[4] R. Stoneley, *Proc. R. Soc. (London)* **A 106**, 416 (1924).

[5] *e.g.*, the leaky interface-acoustic modes on the N_3Si_4-GaAs (001) interface have been observed in Brillouin spectroscopy, P. Zinin, *et al.*, *Phys. Rev. B* **60**, 2844 (1999).

[6] E. E. Mendez, P. J. Price and M. Heiblum, *Appl. Phys. Lett.* **45**, 294 (1984).

[7] H. L. Stormer, *et al.*, *Phys. Rev. B* **41**, 1278 (1990).

[8] I. V. Ponomarev and A. L. Efros, *Phys. Rev. B* April 15 (2001).

[9] S. H. Simon, *Phys. Rev. B* **54**, 13 878 (1996).

9th Int. Symp. "Nanostructures: Physics and Technology"
St Petersburg, Russia, June 18–22, 2001

Chaos in nodal points and streamlines in ballistic electron transport through quantum dots

K.-F. Berggren†, K. N. Pichugin‡§, A. F. Sadreev‡
and A. A. Starikov†‡¶

† Department of Physics and Measurement Technology, Linköping University, S-581 83 Linköping, Sweden
‡ Kirensky Institute of Physics, 660036, Krasnoyarsk, Russia
§ Institute of Physics, Academy of Sciences, Cukrovarnická, 10, 16000 Prague
¶ Krasnoyarsk State University, Krasnoyarsk, Russia

Abstract. We trace signatures of quantum chaos in the distribution of nodal points and streamlines for coherent electron transport through different types of quantum dots (chaotical and regular). We have calculated normalized distribution functions for the nearest distances between nodal points and found that this distribution may be used as a new signature of quantum chaos for electron transport in open systems. All irregular billiards shows the same characteristic distribution function. These signatures of quantum chaos are well reproduced using well-known approaches of chaotic wave functions with the same characteristic distribution function. We have also investigated the quantum flows, and have found some remarkable properties of them.

Introduction

The field of quantum chaos has received much attention, due to the increase of the investigations of low-dimensional systems. The nature of quantum chaos in a specific system is traditionally inferred from its classical counterpart. Hence one may ask if quantum chaos is to be understood solely as a phenomenon that emerges in the classical limit, or if there are some intrinsically quantum phenomena, which can contribute to irregular behavior in the quantum domain. In the present work this problem is discussed in relation with ballistic quantum transport through regular and irregular electron billiards.

The eigenstates in closed irregular billiards have revealed the characteristic complex patterns of nodal lines [1]. Here we investigate the evolution of these patterns when opening the billiard and introducing a current through it. In order to clarify how the pertrubing leads reduce the symmetry and how a regular billiard may eventually turn into a chaotic one, we follow the evolution of the patterns with increasing energy.

For such an open system the wave function ψ is now a scattering state with both real and imaginary parts, each of which gives rise to separate sets of nodal lines ($Re[\psi] = 0$ or $Im[\psi] = 0$). Nodal points, i.e., the points at which these two sets of nodal lines intersect because $Re[\psi] = Im[\psi] = 0$, and their spatial distribution will play a crucual role for the characteristics of the flow in the system. The vicinity of a nodal point constitutes a forbidden area for quantum streamlines (Bohm trajectories) contributing to the net transport from source to drain [2, 3]. In our case the most important property of the nodal points of ψ is a formation of quantum vortices in the current probability flow which gives rise to the phenomenon that the quantum streamlines passing from source to drain can not skirt around the nodal points.

1. Theoretical model and calculation

For this study we use model of quantum billiard with two attached semi-infinite leads. Electrons are confined by hard wall boundaries. The interior potential is set equal to zero. We believe that principal results are not sensitive to the particular choice of boundaries. Using the dimensionless variables $x \to x/d$, $y \to y/d$ and the energy $\epsilon = 2m^* d^2 E/\hbar^2$, where d is the width of the leads, we map the Schrödinger equation for electron of a mass m^* onto a square lattice labeled (k, l) and with cell size a_0.

$$\left[4 - \left(\frac{d}{a_0}\right)^2 \epsilon\right] \psi_{k,l} - \psi_{k+1,l} - \psi_{k-1,l} - \psi_{k,l+1} - \psi_{k,l-1} = 0. \tag{1}$$

Typical grid sizes are between 200×400 and 600×1200 for rectangular stadium. Number of open transport channels was selected in a range form 1 to 20.

For introducing streamlines we use alternative interpretation of quantum mechanics. Writing the wave function in terms of a norm and a phase

$$\psi = \sqrt{\rho} \exp(iS/\hbar) \tag{2}$$

the time independent Schrödinger equation can be decomposed as follows [2, 3]

$$\begin{aligned} E &= \tfrac{1}{2} m v^2 + V + V_{QM} \\ \nabla \rho \mathbf{v} &= 0\,, \end{aligned} \tag{3}$$

where

$$\mathbf{v} = \nabla S/m. \tag{4}$$

Streamlines (Bohm trajectories) depends on the solution of time-dependent equations

$$\dot{x} = v_x, \dot{y} = v_y. \tag{5}$$

The nodal points were obtained as intersection of nodal lines of real and imaginary parts of wave function (lines where these parts change a sign). We propose that an appropriate signature of quantum chaos in open cavities may be formulated in the following way. The distribution of distances for the nearest neighbours of the nodal points are expected to be distinctly different for nominally regular and irregular billiards. The distribution of the distances for nearest neighbours was found in the following way. For i-th nodal point (x_i, y_i) the distance to the nearest neighbour r_i was evaluated. This was done for each channel for a given energy of incoming electron. Finally histograms for r_i was averaged over different numbers (51, 101 or more) of energy values in narrow energy interval, with a few conductance fluctuations. Then the distribution was normalized. We have also used a similar procedure for averaging over the positions of incoming leads.

In order to check our introduced signature of quantum chaos we have calculated the same distributions for a complex combination states in the nominally closed billiards (6) and also for Berry-type wave functions (7).

$$\psi(x, y) = \textstyle\sum_{mn} a_{mn} \psi_{mn}(x, y) \tag{6}$$

$$\psi(x, y) = \textstyle\sum_j a_j \exp(i\mathbf{k}_j \cdot \mathbf{r} + \phi_j), \tag{7}$$

where $\psi_{mn}(x, y)$ are discrete eigenstates of closed cavity, a_{mn}, a_j, ϕ_j are uniformly distributed coefficients and $\mathbf{k}_j$ are wave vectors of a given energy shell.

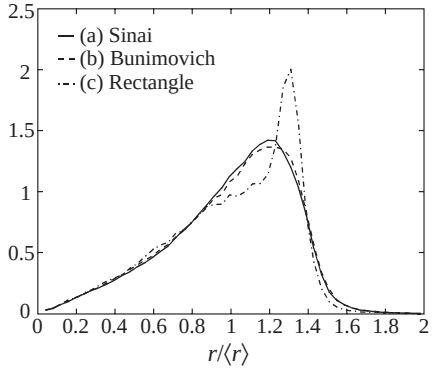

Fig. 1. Distributions of nearest distances for an electron transport through Sinai billiard $\epsilon = 50$ (a), Bunimovich stadium $\epsilon = 79$ (b), and rectangle with $\epsilon = 51$ (c), averaging by energy, size of grid is 840×400.

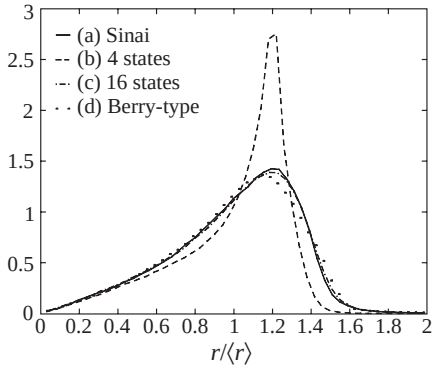

Fig. 2. Distributions for Sinai billiard (a), 4 mixed states in rectangular billiard (b), 12 mixed states (c) and Berry-type wave function (d).

2. Results and discussion

We have calculated normalized distribution functions for the nearest distances between nodal points. Our typical statistic is a few millions distances between nodal points. We have found that this distribution has a characteristic form for all types of open billiards except for rectangular ones (Fig. 1). We suggest that this form is universal one and may be used as a new signature of quantum chaos for an electron transport in the open systems. The universal distribution function is shown to be insensitive to the way of averaging (over positions of leads or over a narrow energy interval with a few conductance fluctuations). An integrable rectangular billiard yields a nonuniversal distribution for the nearest neighbour separations with a central peak corresponding to partial order of the nodal points (Fig. 1). The distributions for mixed states in the closed rectangle and for Berry-type wave function shown in Fig. 2 in comparision with our universal form for irregular cavities. Obviously, that distributions for this well-known approaches of chaotic wave functions are closed to our universal form. It confirm that our universal form can be used as the new signature of quantum chaos for an electron transport through quantum dots. Comparison of the distributions for the closed rectangle with different number of states and the distributions for regular and irregular dots let us to assert following statement. The difference between the distributions for different cavities are related to the number of eigenstates "effectively involved" into the electron transport because of symmetry.

Examples of streamlines are given in Fig. 3 and Fig. 4. We have found an effect of "channeling" of streamlines in the case of a regular cavity. This effect can be explained by partial order of nodal points. But in the same time patterns of quantum flows for irregular billiards are very complex and disordered.

Acknowledgments

This work has been partially supported by the Russian Foundation for Basic Research (RFBR Grant 97-02-16305) and the Royal Swedish Academy of Sciences.

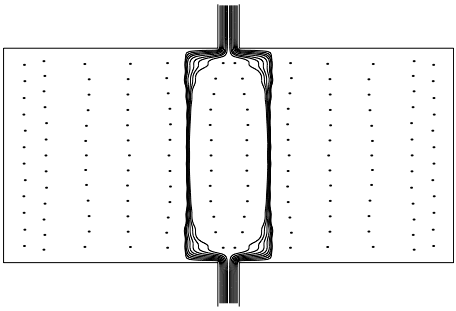

Fig. 3. Nodal lines and vortices positions for a rectangle in the tunneling regime at resonance energy $\epsilon \sim 19.2727$. The dimensions of the rectangle are $10d$ times $21d$ where d is the width of the channel. The tunneling situation is achieved by introducing appropriate barriers at the entrance and exit leads. The particle is injected through the upper lead.

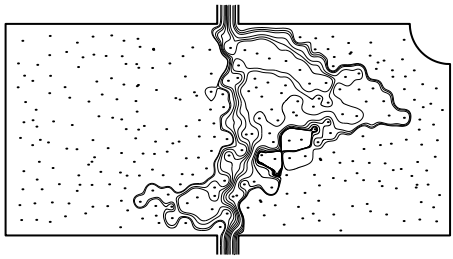

Fig. 4. Streamlines and positions of vor1tices for a Sinai billiard at an energy 20.79 (one open channel). The radius of the semicircular region is $2d$ where d is the width of the leads.

References

[1] S. W. McDonald and A. N. Kaufmann, *Phys. Rev. Lett.* **42**, 1189 (1979); *Phys. Rev. A* **37**, 3067 (1988).
[2] J. O. Hirschfelder, C. J. Goebel and L. W. Bruch, *J. Chem. Phys.* **61**, 5456 (1974).
[3] J. O. Hirschfelder, *J. Chem. Phys.* **67**, 5477 (1977).
[4] K.-F. Berggren, K. N. Pichugin, A. F. Sadreev and A. A. Starikov, *JETP Lett.* **70**, 403 (1999) [Pis'ma v ZhETF **70**, 398 (1999)].

9th Int. Symp. "Nanostructures: Physics and Technology"
St Petersburg, Russia, June 18–22, 2001

Large increase of electron mobility in a modulation-doped AlGaAs/GaAs/AlGaAs quantum well with an inserted thin AlAs barrier

K. Požela, *J. Požela* and V. Jucienė
Semiconductor Physics Institute, 2600 Vilnius, Lithuania

Abstract. The electron(polar optical (PO) phonon scattering mechanisms which determine the electron mobility in a $Al_{0.25}Ga_{0.75}As/GaAs/Al_{0.25}Ga_{0.75}As$ quantum well (QW) with an inserted thin AlAs barrier are considered. It is shown that the decrease of the second subband electron scattering by PO-phonon emission is responsible for the large increase of the mobility in the QW with the inserted barrier.

Introduction

There are many attempts to reduce electron(phonon scattering in modulation-doped quantum wells (QW) by confining polar optical (PO) phonons in a QW [1, 2]. It was shown that a thin barrier inserted into the QW reduces strongly electron scattering by confined phonons. But simultaneously the increase of electron scattering by interface phonons compensates this reduction. The competition of these scattering mechanisms determines the total electron scattering by PO phonons. In this paper the separate contribution to electron mobility of definite type intra- and intersubband electron transitions with absorption or emission of PO phonons is considered. The scattering mechanisms which are responsible for the increase of the mobility in a $Al_{0.25}Ga_{0.75}As/GaAs/Al_{0.25}Ga_{0.75}As$ QW with an inserted thin (1 nm) AlAs barrier are considered.

1. Confined electron–PO-phonon scattering rate and electron mobility

The transition frequencies $W^{a,e}_{ifv}$ of electrons, confined in a QW, from an initial state in subband i to any final state in subband f by emission (absorption) of v-mode PO-phonons are calculated by using the dielectric continuum model [3–6]. The nonelastic electron–PO-phonon scattering with a large change of scattered electron energy requires to take into account the different occupation of electrons in the initial and final states. Taking into account the electron state occupation, the electron–PO-phonon scattering rate is written as

$$W^{a,e}_{ifv} = \sum_v \int_{E_i}^{\infty} W^{a,e}_{ifv}(E) \frac{1 - f(E \pm \hbar\omega_v)}{1 - f(E)} \left[\int_{E_i}^{\infty} f(E) \mathrm{d}\, E \right]^{-1} \tag{1}$$

where E_i is the subband i bottom energy, $\hbar\omega_v$ is the phonon energy, and $f(E)$ is the electron Fermi–Dirac distribution function. The plus sign is for phonon absorption and the minus one is for phonon emission.

In this paper the estimation of a separate contribution of various type electron–PO-phonon scattering to electron mobility is done assuming the inverse mean frequency of electron transitions by PO-phonon absorption (emission) as a momentum relaxation time

$$\tau_{if} = \frac{1}{W_{if}}. \tag{2}$$

This relaxation time approximation gives only a crude estimation of the mobility limited by PO-phonon scattering, but it is expected that this approximation is sufficient for estimation the relative contribution to electron mobility of various electron scattering mechanisms by various phonon modes. Note that the values of mobility calculated within the used relaxation time approximation in the GaAs QW are near to the values observed experimentally.

In this approximation, the i-subband electron mobility is

$$\mu_i = \frac{e}{m}\left[\sum_f \left(W_{if}^e + W_{if}^a\right)\right]^{-1} \tag{3}$$

and the total electron mobility in the QW is

$$\mu = \frac{1}{n_s}\sum_i \mu_i n_i \tag{4}$$

where n_s and n_i is the sheet electron concentrations in the QW and in subband i, respectively.

2. The dependence of electron subband mobility on sheet electron concentration

The calculated intra- and intersubband electron–PO-phonon scattering rates as functions of sheet electron concentration n_s in the $Al_{0.25}Ga_{0.75}As/GaAs/Al_{0.25}Ga_{0.75}As$ QW of width $L = 20$ nm are presented in Fig. 1(a).

The significant enhancement of the intra- and intersubband scattering rates by PO-phonon absorption with increasing n_s is observed in lower subbands (W_{11}^a, W_{12}^a, W_{22}^a). The enhancement takes place in the subbands with degenerate electron gas. This is largest in the lowest (first) electron subband (W_{11}^a), where electron gas is most degenerated (see Fig. 1(a)).

The scattering rates by phonon emission from the upper subband to the lower one (W_{31}^e, W_{32}^e, W_{21}^e) opposite decrease with electron gas degeneration in the lower subband.

The increase of scattering rates by phonon absorption (W_{11}^a and W_{12}^a) is responsible for the strong decrease of electron mobilities with increasing n_s in the lowest (first) electron subband, μ_1, as it is shown in Fig. 1(b). The second subband mobility μ_2 increases due to decreasing second subband electron scattering by phonon emission when n_s changes in the range of $(5-15) \times 10^{15}\,\mathrm{m}^{-2}$. At $n_s > 15 \times 10^{15}\,\mathrm{m}^{-2}$, μ_2 decreases very fast because of the strong increase of electron scattering rates by phonon absorption, W_{22}^a, W_{21}^a, W_{23}^a.

As a result, the decrease of QW conductivity (μn_s) with increasing n_s takes place. This is shown in Fig. 1(b). When $n_s > 3 \times 10^{16}\,\mathrm{m}^{-2}$, the contribution of the third subband electrons to the enhancement of the mobility due to the decrease of W_{31}^e, W_{32}^e gives the enhancement of the total QW conductivity in spite of decreasing the first and second subband mobilities.

3. The QW with an inserted barrier

A thin (1 nm) AlAs barrier inserted into the QW center changes the electron subband energies and divides PO phonon spectra into two independent branches located at both sides of the barrier [2].

The electron subband energies are divided into two pairs. The lower energy subband pair (first and second subbands) are occupied by electrons, and the upper subband occupation is negligible at $L < 30$ nm. The lower subband electron scattering by phonons determines the QW conductivity and electron mobility.

Figure 2(a) shows the dependence of scattering rates in the lower subbands of the QW with a barrier on the sheet electron concentration n_s. Because the phonon emission between

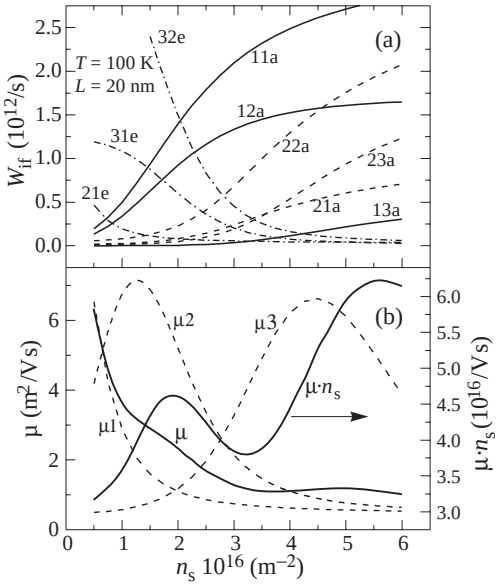

Fig. 1. The electron–PO-phonon scattering rates W_{if} with electron transitions from the initial state in subband i to the final one in subband f by phonon emission and absorption (labeled by ife and ifa, respectively) (a) and the electron mobilities in subbands $i = 1, 2, 3$ (labeled by μ_1, μ_2, μ_3), the total mobility μ and conductivity (μn_s) (b) as functions of sheet electron concentration n_s in the QW of width $L = 20$ nm.

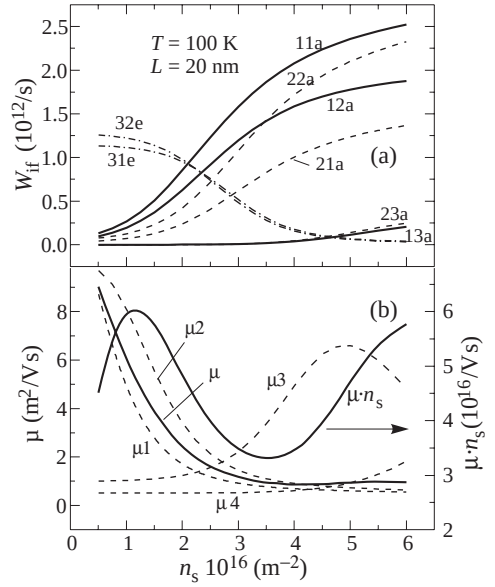

Fig. 2. The electron–PO-phonon scattering rates W_{if} (a) and the subband and total electron mobilities (b) as functions of sheet electron concentration n_s in the QW of width $L = 20$ nm. Notations are as in Fig. 1.

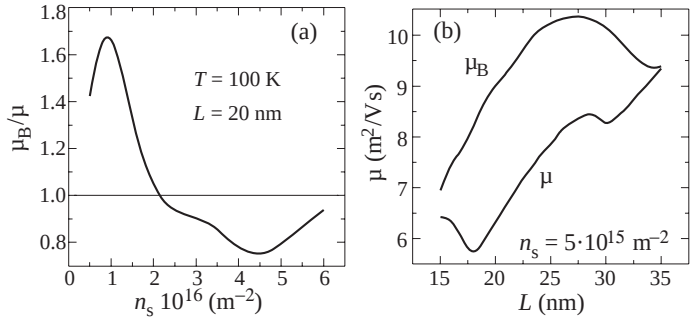

Fig. 3. The comparison of the mobilities in the QW with the inserted barrier, μ_B, and without the barrier, μ, as functions of sheet electron concentration n_s (a) and of QW width L (b).

the closely placed first and second subband levels is not permitted, the electron scattering with phonon absorption determines the mobility of first and second subband electrons. The scattering rates by phonon absorption (W^a_{11}, W^a_{22}, W^a_{12}, W^a_{21}) remain the predominant mechanism in a wide range of doping level ($5 \times 10^{15} < n_s < 6 \times 10^{16}\,\mathrm{m}^{-2}$).

It is seen from Figs. 1(a) and 2(a) that the W^a_{11} and W^e_{21} in the QW with an inserted barrier are less than these scattering rates in the QW without a barrier. The decrease of the W^a_{11} for the strong reduction of the scattering rate by the confined phonons when the barrier is inserted into the QW is responsible [3]. As a result, the first subband mobility is larger in the case when the barrier is inserted into the QW. For the enhancement of the total electron mobility in the QW with the inserted barrier, the decrease of the W^e_{21} and, consequently, the increase of the second subband mobility is responsible (see Fig. 2(b)).

Figure 3 shows the mobilities in the QW with the barrier and without it.

Conclusions

The electron–PO-phonon scattering mechanisms which are responsible for the dependence of electron mobility in the QW with and without barriers on the doping level are determined. It is shown that:

1. The increase of the scattering by PO-phonon absorption is responsible for the decrease of QW conductivity with increasing the sheet electron concentration.

2. The insertion of a thin AlAs barrier into the $Al_{0.25}Ga_{0.75}As/GaAs/Al_{0.25}Ga_{0.75}As$ QW center closes with each other the first and second subband levels and decreases the scattering rates of the second subband electrons by PO-phonon emission (W^e_{21}). As a result, the electron mobility in the QW with the inserted barrier exceeds that in the QW without the barrier at $n_s < 2 \times 10^{16}\,\mathrm{m}^{-2}$. At $n_s = 5 \times 10^{15}\,\mathrm{m}^{-2}$ the increase of the mobility in the QW with the barrier takes place in the interval of $15 < L < 35$ nm.

References

[1] J. Požela, K. Požela and V. Jucienė, *FTP* **34**, 1053 (2000).
[2] J. Požela, V. Jucienė, A. Namajunas and K. Požela, *Physica E* **5** 108 (1999).
[3] J. Požela, V. Jucienė and K. Požela, *Semicond. Sci. Technol.* 10 1555 (1995).
[4] N. Mori and T. Ando, *Phys. Rev. B* **40**, 6175 (1989).
[5] H. Rücker, E. Molinary and P. Lugli, *Phys. Rev. B* **45** 6747 (1992).
[6] I. Lee, S. M. Goodnick, M. Gulia, E. Molinary and P. Lugli, *Phys. Rev. B* **51** 7046 (1995).

9th Int. Symp. "Nanostructures: Physics and Technology"
St Petersburg, Russia, June 18–22, 2001

Analog of the Gunn effect in heterostructure with two tunnel-coupled quantum well

P. I. Biryulin†, A. A. Gorbatsevich† and Yu. V. Kopaev‡
† Moscow State Institute of Electronic Technology,
103498, K-498, MIET, Moscow, Russia
‡ P. N. Lebedev Physical Institute, Russian Academy of Science,
117924, Leninsky prospect, 53, Moscow, Russia

Abstract. Electron transport in heterostructure with two tunnel-coupled quantum well has been numerically investigated under condition of strong non-one-dimensionality of electric field in the structure. It is shown for the first time an ability of the effect in such heterostructures, which is similar to the Gunn effect in bulk semiconductor. The effect is conditioned by the electron tunneling transition between quantum wells with different mobility and is characterized by formation of the strong field domain and the negative differential conductivity region on current-voltage characteristic.

Introduction

Heterostructures with tunnel-coupled quantum wells (HS with TC QW) are a convenient object for investigation of quantum effects in macroscopic system which can be simply registered from changing conductivity of the system. Such structures can be also interesting for the fast electronics because the conductivity changing of HS with TC QW occurs at the electron tunneling transition on short distance. In [1–6] some devices and conductivity models of HS with TC QW were suggested and numerical calculations were executed in the external electric and magnetic field. These results have limited applicability for the calculations of real HS because of their one-dimensionality. 2D or 3D numerical calculations of HS with TC QW have not been done and this fact has conditioned the setting of the task. Since HS with TC QW have macroscopic size and have equivalent characteristics in the plane of QWs it permits to apply 2D calculations.

1. Studied heterostructure

Figure 1 shows physical structure of studied HS. Sheet electron concentration in QW1 is stabilized by donors in the lower barrier. The bottom of QW2 shifts with respect to that of QW1 as the gate is biased. The doping level is selected so that only two first subbands are filled. The mobility μ_{QW2} has been varied in the range 100–1000 $\mathrm{cm}^2/(\mathrm{Vs})$ at calculations. This mobility is conditioned by scattering on roughness of heterointerface and it is proportional to six degree of the QW width [7]. The mobility in the QW1 is supposed to be equal to electron mobility in 200 Å GaAs QW at 77 K. All calculations are executed for this temperature. If the gate voltage differs from the value corresponding to anticrossing of the first and second quantum levels, the wave functions of the different subbands are localized each in their own QW and the conductivity is implemented mainly by carriers in the QW1. At $V_{gs} \sim -0.7\,\mathrm{V}$ the anticrossing of the first and second subbands takes place and the wave function of each state is situated into both QWs simultaneously.

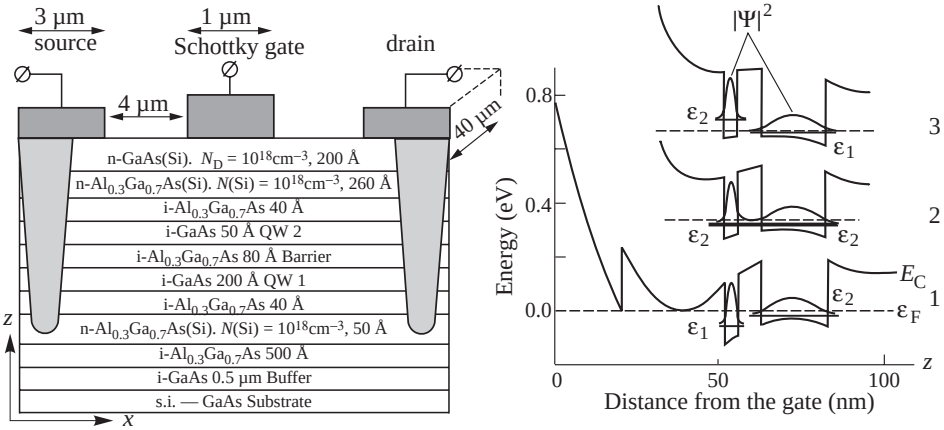

Fig. 1. Structure, topology of contacts and band diagram under the gate at different gate bias, $V_{ds} = 0$ V; (1) 0 V, (2) -0.7 V, (3) -0.9 V.

As consequence, the electrons from both subbands in both QWs scatter on roughness in the QW2. The total mobility and conductivity of the TC QW are decreased.

2. Conductivity model and calculation method

The tunnel connection between QWs can be strong diminished by scattering of the 2D momentum. At character mobility in QWs 10^3-10^4 cm^2/(Vs) the broadening of the states in QWs is $\hbar/\tau \sim 10-1$ meV. This value is comparable with intervalley tunnel matrix element T in TC QW. $T \sim 0.5-5$ meV for the GaAs/$Al_{0.3}Ga_{0.7}As$ system at barrier thickness 50–100 Å. The expression for lateral conductivity of two tunnel-coupled quantum wells taking into account momentum scattering was obtained in [5] with effective mobility:

$$\mu_{eff} = 2\mu \frac{1 + \alpha^2 4\mu^2(\Delta\varepsilon^2 + 4T^2)}{(1-\mu_S^2) + \alpha^2 4\mu^2(\Delta\varepsilon^2(1-\mu_S^2) + 4T^2)}. \qquad (1)$$

Here μ_1 and μ_2 are mobilities in the separately taken QW1 and QW2 without interaction; $1/\mu = 1/\mu_1 + 1/\mu_2$, $\mu_s = (\mu_1 - \mu_2)/(\mu_1 + \mu_2)$, $\alpha = m^*/e\hbar$, $n = n_1 + n_2$ is the total concentration in both QWs, $\Delta\varepsilon$ energy difference between 1st and 2nd subbands in the absence of tunneling, it is controlled by external field and equals zero at anticrossing. Because of the potential along QWs changes weakly on electron wavelength we solve numerically 1D Schrödinger equation in different TC QW cross-sections along the structure for finding $\Delta\varepsilon$ and T. In the whole HS the 2D Poison equation and discontinuity equation for electron current is solved numerically. The expression (1) is used as mobility model into TC QW. Diffusion coefficient is determined from Einstein relation. In the whole heterostructure except TC QW, we use mobility model for fonon and impurity scattering. The iteration procedure is used for solving Schrödinger equation consistently with DDM equations.

3. Calculations results

The calculated concentration and mobility in the TC QW, lateral current in the whole HS are presented in Fig. 2. Because of strong broadening of the levels the strongest mobility

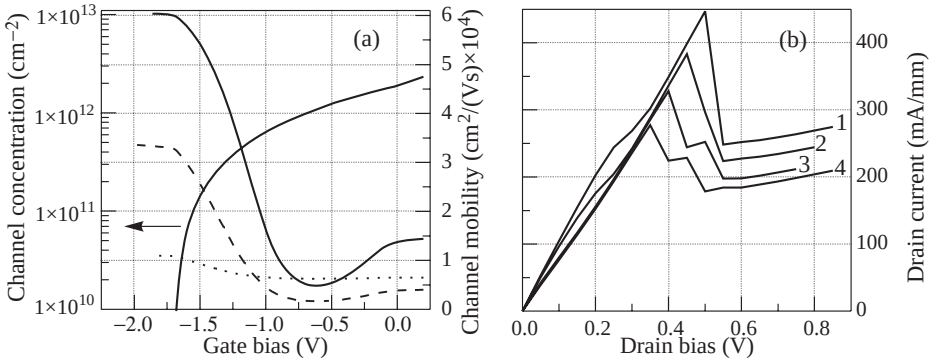

Fig. 2. (a) Dependence of mobility and concentration in TC QW on the gate bias and initial mobility in QW2. Solid line $\mu_{QW2} = 700$ cm^2/(Vs), dashed line 500 cm^2/(Vs), dotted line 100 cm^2/(Vs). $\mu_{QW1} = 7 \cdot 10^4$ cm^2/(Vs), $V_{ds} = 0$. (b) Dependence of the drain current on the drain voltage at different gate bias: (1) 0 V, (2) -0.1 V, (3) -0.3 V, (4) -0.4 V. $\mu_{QW2} = 700$ cm^2/(Vs).

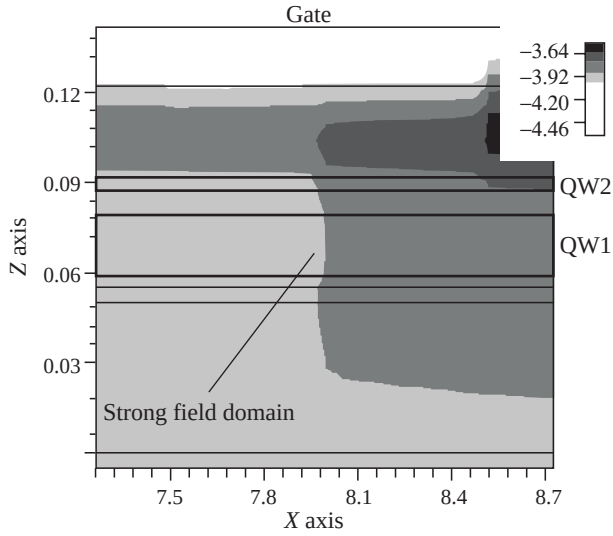

Fig. 3. 2D distribution of potential in the whole heterostructure. $V_{ds} = 0.56$ V, $V_{gs} = 0$.

variation is realized not at minimum of μ_{QW2}. On the $I_{ds}-V_{ds}$ curves the negative differential resistance appears when drain-source voltage produces lateral electric field compared with transverse. The drain-source voltage drops stronger along the QW1 than the QW2 because the potential of QW2 is fixed by the gate. Therefore the energy levels gradient along the gate is different and the anticrossing takes place in some point under the gate at $V_{ds} = 0.52$ V that leads to strong decrease of mobility and charge accumulation near this point. The electric field is increased locally, the carrier velocity starts to saturate and results in further decreasing of mobility and charge accumulation. As a result, the strong field domain is formed under the gate (Fig. 3) and the lateral current is decreased. The condition of the domain formation is the sufficient decreasing of mobility at anticrossing. $I_{ds}-V_{ds}$ characteristics calculated for $\mu_{QW1} = 8000$ cm^2/(Vs), do not posses the negative differential resistance region. In fact, this effect is the analog of the Gunn effect in bulk

semiconductor but in our case the effect is conditioned by interwell transfer of electrons. The calculation results don't differ practically for monotonic and nonmonotonic saturation velocity models (μ_{eff} is set as low field mobility in these models in TC QW, the nonmonotonic model describes the usual Gunn effectin in GaAs). It indicates prevalence of interwell transfer over intervalley. The effect is stable to variation of the structure parameters so it is not numerical.

Acknowledgements

The authors gratefully acknowledge useful discussions with V. V. Kapaev, I. V. Tokatly and V. T. Trofimov. The work was supported by Russian Federal Programs "Integration".

References

[1] H. Sakaki, *Jap. J. Appl. Phys.* **21**(6), L381 (1982).
[2] A. A. Gorbatsevich, V. V. Kapaev, Yu. V. Kopaev and V. Ya. Kremlev, *Phys. Low-Dim. Struct.* **4/5**, 57 (1994).
[3] V. L. Borblik, Z. S. Gribnikov, B. P. Markevich, *Fiz. Tekhn. Poluprov.* **25**, 1302 (1991).
[4] V. I. Belyavsky, Yu. V. Kopaev, Yu. A. Pomerantsev, *Phys. Low-Dim. Struct.* **1/2**, 1 (1997).
[5] F. T. Vasko and O. E. Raichev. *Zh. Exp. Teor. Fiz.* **107**, 951 (1995).
[6] P. Owen and M. Pepper, *Appl. Phys. Lett.* **62**, 1274 (1993).
[7] H. Sakaki, T. Noda, K. Hirakawa, M. Tanaka, T. Matsusue, *Appl. Phys. Lett.* **51**, 1934 (1987).
[8] P. I. Birjulin, N. A. Volchkov, S. P. Grishechkina, Yu. V. Kopaev, S. S. Shmelev, *Semicond. Sci. Technol.* **12**(4), 427 (1997).

9th Int. Symp. "Nanostructures: Physics and Technology"
St Petersburg, Russia, June 18–22, 2001

Transition from several to one conductor channel induced by intersubband scattering in 2D weak localization

N. S. Averkiev†, L. E. Golub†‡, *S. A. Tarasenko*† and M. Willander‡
† Ioffe Physico-Technical Institute, St Petersburg, Russia
‡ Physical Electronics and Photonics, Department of Physics, Chalmers University of Technology and Göteborg University, S-412 96, Göteborg, Sweden

Abstract. The theory of weak localization is presented for quasi-2D systems where several subbands of size quantization are occupied. The weak-localization correction to conductivity is shown to depend strongly on the level concentration ratio and intersubband scattering intensity. Specifically, at the comparable level occupations and equal relaxation times, the conductivity correction of the m-subband system decreases in m times when transiting from the isolated levels to the high-intensive intersubband scattering case.

A weak localization phenomenon is known to be an interference of waves propagating along the same paths in opposite directions [1]. Processes of phase and spin relaxation or magnetic field destroy the interference and therefore can make observable the weak localization effect. The brightest manifestation of the phenomenon is the anomalous behavior of resistance in classically weak magnetic fields, $\omega_c\tau \ll 1$. Here ω_c is the cyclotron frequency, and τ is the momentum relaxation time. Since the magnetic field destroys the coherence at distances comparable to magnetic length, l_B, this effect takes place when l_B is simultaneously equal to characteristic kinetic lengths.

In very low magnetic fields, the coherence is destructed at long trajectories, when the mean free path, l, is much less than l_B. This is so-called *diffusion* regime of weak localization, and the corresponding characteristic size is the dephasing length, l^φ. In higher fields, when $l_B \sim l$, short trajectories passing through several scatterers contribute to weak localization. This regime is called *non-diffusion*.

The anomalous magnetoresistance was widely investigated both theoretically and experimentally in bulk semiconductors and metals, thin films and ultra-quantum two-dimensional (2D) structures. A comparison of theory and experimental data in both diffusion and non-diffusion regimes allowed to determine the kinetic parameters such as times and lengths of elastic relaxation and dephasing.

Recently the magnetotransport investigations have been devoted to more complicated, so-called quasi-2D systems which are between three-dimensional and ultra-quantum two-dimensional ones. These structures are tunnel-coupled quantum wells, multivalley 2D semiconductors and quantum wells with two or several occupied levels of size quantization. Intersubband scattering taking place in these systems leads to effective averaging of the kinetic parameters corresponding to different levels and therefore can affect magnetotransport [2].

Quasi-2D systems are very attractive objects for study of weak localization because even rare intersubband transitions affect it strongly. Usually the intersubband scattering time, τ_{ij} $(i \neq j)$, exceeds enough the total momentum relaxation times in subbands, τ_i, therefore an influence of intersubband transitions on classical magnetotransport is insignificant. In opposite, the dependence of weak-localization correction to conductivity on magnetic field,

$\Delta\sigma(B)$, in the diffusion regime and its value in zero field, $\Delta\sigma(0)$, are determined by the dephasing time τ_i^{φ} exceeding τ_i. Therefore at τ_{ij} long with respect to τ_i but comparable to τ_i^{φ} intersubband scattering affects weak-localization correction strongly.

The aim of this communication is to present the theory of weak localization for multi-level 2D systems. We calculate the conductivity correction $\Delta\sigma(B)$ in the whole range of classically weak magnetic fields. To concentrate on the effect of intersubband transitions, scattering is assumed to be isotropic and a spin relaxation is neglected. Note, that $\Delta\sigma(B)$ in the frame of diffusion approximation was obtained in Ref. [3]

The main weak localization corrections to the conductivity appear in the first order in the parameter $(k_F l)^{-1}$ with respect to classical conductivity, where k_F is the Fermi wave vector. The corresponding expression has the form

$$\Delta\sigma = \Delta\sigma^{(a)} + \Delta\sigma^{(b)} , \tag{1}$$

where the terms are given by

$$\Delta\sigma^{(a)} = -\frac{e^2}{\pi^2\hbar}\sum_i \frac{l_i^2}{l_B^2}\tau_i \sum_{N=0}^{\infty} P_i(N)\,\mathcal{C}_{ii}^{(3)}(N) , \tag{2}$$

$$\Delta\sigma^{(b)} = \frac{e^2}{\pi^2\hbar}\sum_{ij} \frac{l_i l_j}{l_B^2}\frac{\tau_i\tau_j}{\tau_{ij}} \sum_{N=0}^{\infty} Q_i(N)Q_j(N)\frac{1}{2}\left[\mathcal{C}_{ij}^{(2)}(N) + \mathcal{C}_{ji}^{(2)}(N+1)\right] .$$

Here τ_{ij} $(i \neq j)$ and τ_{ii} are inter- and intrasubband scattering times, l_i and l_i^{φ} are the mean free path and the dephasing length in the i-th subband, e is the electron charge, $P_i(N)$ and $Q_i(N)$ are defined by

$$P_i(N) = \frac{l_B}{l_i}\int_0^{\infty} dx \exp\left[-x\frac{l_B}{l_i}\left(1+\frac{l_i}{l_i^{\varphi}}\right) - \frac{x^2}{2}\right] L_N(x^2) , \tag{3}$$

$$Q_i(N) = \frac{l_B}{l_i}\frac{1}{\sqrt{N+1}}\int_0^{\infty} dx\, x \exp\left[-x\frac{l_B}{l_i}\left(1+\frac{l_i}{l_i^{\varphi}}\right) - \frac{x^2}{2}\right] L_N^1(x^2) ,$$

with L_N and L_N^1 being the Laguerre polinomials. The Cooperons $\mathcal{C}^{(2)}$ and $\mathcal{C}^{(3)}$ are determined from the following system of linear equations

$$\sum_k \left(\delta_{ik} - \frac{\tau_k}{\tau_{ik}}P_k(N)\right)\mathcal{C}_{kj}^{(2)}(N) = \sum_k \frac{\tau_k}{\tau_{ik}\tau_{kj}}P_k(N) , \tag{4}$$

$$\mathcal{C}_{ij}^{(3)}(N) = \mathcal{C}_{ij}^{(2)}(N) - \sum_k \frac{\tau_k}{\tau_{ik}\tau_{kj}}P_k(N) .$$

The expressions (2) describe the weak-localization correction to conductivity in the whole range of classically weak magnetic field.

Figure 1 presents the dependence of $\Delta\sigma$ on magnetic field for the system with two size-quantized levels at various intersubband scattering rates and different level occupations. We assume here that the total relaxation times in the subbands coincide, $\tau_1 = \tau_2$, and the dephasing times are also identical and equal to $10\tau_1$. The solid, dashed and dotted curves

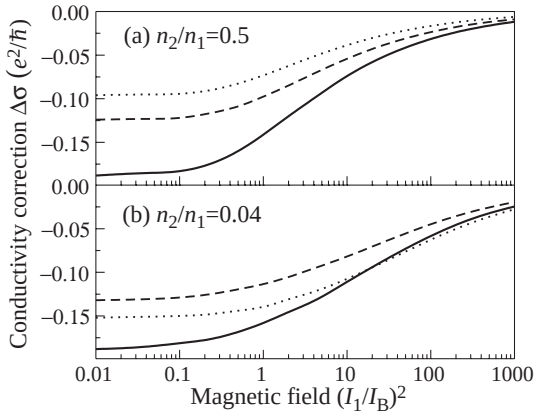

Fig. 1. The dependence of weak localization correction to the conductivity at different level occupations and various intersubband scattering times, $\tau_1/\tau_{12} = 0$ (solid curves), $\tau_1/\tau_{12} = 0.5$ (dashed curves), and $\tau_1/\tau_{12} = 0.1$ (dotted ones).

correspond to the cases of isolated levels, $\tau_{12} \gg \tau_1^{\varphi} \gg \tau_1$, relatively rare intersubband transitions, $\tau_{12} \sim \tau_1^{\varphi} \gg \tau_1$, and intensive intersubband scattering, $\tau_{12} \sim \tau_1 \ll \tau_1^{\varphi}$, respectively.

At the comparable level concentrations (Fig. 1a), $l_1 \sim l_2$, intersubband scattering decreases the absolute value of the conductivity correction, $|\Delta\sigma|$, with respect to the isolated level case (solid curve). Rare intersubband transitions (dashed curve) change $|\Delta\sigma|$ rather in low magnetic fields corresponding to the diffusion regime. The reason is that weak intersubband scattering acts as an additional dephasing and therefore leads to reduction of the effective dephasing time that determines the behavior of $\Delta\sigma$ in the diffusion regime. Frequent intersubband transitions (dotted curve) decrease $|\Delta\sigma|$ in the whole range of classically weak magnetic fields.

Moreover, one can say the increasing of the intersubband scattering intensity causes the transition from two-level into one-level system. Indeed, in the absence of intersubband scattering, two independent levels exist. In the case of intensive intersubband scattering, $\tau_{12} \sim \tau_1$, the level division does not take place. There is only one subband effectively with average kinetic parameters. Since the total and dephasing subband times are chosen to be identical respectively, $\tau_1 = \tau_2$, $\tau_1^{\varphi} = \tau_2^{\varphi}$, the average parameters of the 'effective subband' coincide with those of separate subbands at the comparable level occupations, $n_1 \approx n_2$. The one-level weak localization correction to conductivity is independent of the level occupation. Therefore at $n_1 \approx n_2$ the magnitude of $|\Delta\sigma|$ for intensive intersubband scattering is approximately half as much as for isolated subband system. This difference for a factor of 2 can be seen between solid and dotted curves in Fig. 1(a).

In the case of different level concentrations (Fig. 1(b)) the quantum conductivity correction depends on the intersubband scattering intensity in complicated manner. However at arbitrary concentration ratio, rare intersubband transitions do decrease $|\Delta\sigma|$ in the diffusion regime because, as mentioned above, the role of weak intersubband scattering is restricted to an additional dephasing.

In conclusion, the theory of weak localization has been presented for multilevel 2D systems.

Acknowledgements

This work is supported by the Russian Foundation for Basic Research: 00-02-17011 and 00-02-16894, and by the Russian State Programme "Physics of Solid State Nanostructures".

References

[1] B. L. Altschuler, A. G. Aronov, D. E. Khmelnitskii and A. I. Larkin, *Quantum Theory of Solids*, ed. by I. M. Lifshits, MIR Publishers, Moscow (1983).

[2] N. S. Averkiev, L. E. Golub, S. A. Tarasenko and M. Willander, *Proc. of 25th Int. Conf. Phys. Semicond.*, Springer-Verlag (2001).

[3] N. S. Averkiev, L. E. Golub and G. E. Pikus, *Fiz. Techn. Poluprov.* **32**, 1219 (1998) [*Semiconductors* **32**, 1087 (1998)].

9th Int. Symp. "Nanostructures: Physics and Technology"
St Petersburg, Russia, June 18–22, 2001

Disordered quasi-2D semiconductor structures: percolation, non-coherent mesoscopics, and conductance quantization

B. A. Aronzon[1], D. A. Bakaushin[2], N. K. Chumakov[1], A. B. Davydov[1] and *A. S. Vedeneev*[2]

[1] RSC "Kurchatov Institute", Moscow, Russia

[2] Institute of Radioengineering & Electronics RAS, Fryazino, Moscow distr. Russia

The electron transport properties of disordered (or condensed) quasi-2D semiconductor structures (in our case, the disorder is caused by the Coulomb-like chaotic potential relief induced by a statistic ensemble of built-in charges) are of the interest due to the fundamental problems open up-to-now. The ones actually imply the basic understanding of the metal-to-insulator transition regularities affected by both the system dimension and the disorder parameters. As the next, they entail the practical interest to the "quantum" FET-like systems with the conductance determined by the value of e^2/h at reliable conditions, say at temperatures much exceeding the 4.2 K.

Characteristic peculiarities of the electron transport previously observed in the structures with the strong fluctuation potential [1–3] are discussed in the report.

The objects for our consideration were the FET-like structures (i.e. the GaAs-based HEMTs or MESFETs both with a bulk or a delta-doping and the sub-micron gate-length, the Si-MOS FETs, etc.) presently used as the nano-electronic active elements. As we have shown, the built-in charge (the ionized impurity with the concentration $\sim 10^{18}$ cm^{-3}, i.e. $>10^{12}$ cm^{-2} induces the fluctuation potential (FP), strong enough (up to $\sim$100 meV) to change the electron transport properties of these structures even at temperatures $T \sim 300$ K.

Meanwhile, main experiments we have performed using the Si-MNOS (Si-SiO_2-Si_3N_4-Me) structures with the inversion n-channel as the model-object. The tunneling-thin SiO_2 layer ($\sim$3 nm) allows setting the built-in charge concentration (the negative charge on electron traps at the SiO_2–Si_3N_4 interface, i.e. the FP sources) in the frame of $10^{10}-10^{13}$ cm^{-2} by means of the electron injection from Si at strong electric-field (at the gate voltage $V_g > 30$ V). This way one can actually change the sample properties in a broad region by setting different built-in charge realization, which controls the energy and space scales of the FP.

The results under our consideration, thus obtained for the Si-MNOS structures [1–3], i.e. dependence of the Hall-effect and the conductance G vs. the gate voltage V_g and the temperature T (in the range 4.2–300 K) are as follows:

— the threshold behavior of the Hall-effect voltage (at the constant drain voltage, $\sim$10 mV, and low magnetic fields, $<$1 T) vs V_g, where the threshold of the Hall-effect disappearance corresponds to the finite value of the quasi-2D channel conductivity, $\sim e^2/h$;

— observation of the quasi-2D channel electrical non-homogeneity effected by the V_g decreasing; estimation of the non-homogeneity space scale, L_c, to be up to $\sim$10 mm or more, followed by the conclusion that practical FETs could naturally show both the percolation and the mesoscopic properties (we mean the non-coherent mesoscopics);

— observation of the plateau region on the conductance G vs V_g curves at the characteristic value of the $G \sim e^2/h$ just in the case of FETs with the gate length $L_g < L_c$; the plateau has been commonly observed regardless to the temperature (4.2–300 K), the built-in charge concentration ($10^{12}-10^{13}$ cm^{-2}), their nature (impurities, ions, or traps) and sign (regarding to the charge carriers in the quasi-2D channel, i.e. electrons or holes), the substrate material (Si or GaAs), the gate length (0.3 - 10 mm), and the gate length to the width relation (1/10–1/1000); the effect causes the dG/dV_g vs G maximum at the argument value $\sim e^2/h$;

— observation of the quasi-activation behavior of the G vs T dependence with different values of the pre-exponent, $\sim e^2/h$ at high temperatures and more then the order less at intermediate temperatures; observation of the power-like low, $G \propto \text{const} + T^2$, in the low-temperature region.

The experimental results are discussed in frames of the percolation theory taking into account the quantum behavior of the resistive elements (the latter controls the percolation cluster conductance, see [4]) and the macroscopic scale of electron puddles (the walls of the FP), both determine the micrometer-long correlation scale of the percolation cluster in our case.

Other word, as we assume, the gate voltage reducing (i.e. reducing of the FP electron screening) leads to the system transformation: initially (high gate voltage) quasi-2D system thus transformed into the percolation system. In the latter case, the electron transport is performed by transition of electrons from a wall (the electron puddle) to the neighboring one through the FP passes. Thus connected puddles form the percolation net, and this net properties are controlled by both the FP sources and electron screening.

So, the discussed transition to the percolating net should lead to disappearance of the Hall effect at some characteristic value of the structure conductivity. In our case, the conductance threshold value $\sim e^2/h$ obviously shows that we deal with the quantum-scale system regardless to their macroscopic scales.

So, considering the G vs V_g and T peculiarities in the short-gate FETs ($L_g < L_c$) assumes a situation when the electron transport is carried out along a number of percolation paths and is controlled for the each path by the most resistive element, the only one saddle-point constriction of the FP. In contrast to [4], we consider the transport through the constriction taking into account not a step-like but a smooth energy dependence of the tunneling probability determined by the saddle curvatures [5]. Using both the experimental data and results of our computer simulation (in frames of the Landauer–Buttiker formalism) we have estimated the energy parameters, $h\omega_x$ and $h\omega_y$, characterizing the saddle curvatures along the electron transport and in the perpendicular direction respectively. At $G \sim e^2/h$ the parameters have been found to be of the same order, $h\omega_x \sim h\omega_y \sim 100$ meV, in accordance with results of the FP simulation in frames of statistical model. The estimations show a possibility of the conductance quantization at relatively high temperatures, $T \ll h\omega_y/2$ [5].

The electron effective state density, N_{ss}, and dependence of the $h\omega_x$ vs the Fermi energy have been also analyzed. As we have found out, the state density doesn't have any noticeable energy dependence and $N_{ss} \sim 2m/ph^2$, while the parameter $h\omega_x$ rapidly drops from ~100 meV down to ~1 meV with the Fermi energy decreasing. The latter means that reducing of the FP screening leads to the saddle transformation into the narrow and long ballistic channel and thus determines the conductance behavior vs the gate voltage and temperature.

Acknowledgement

The work has been supported by the grants of the RFBR (No 98-02-16747, 99-02-16955) and Physics of Solid Nanostructures (No 97-1081, 99-1123).

References

[1] B. A. Aronzon, E. Z. Meilikhov, D. A. Bakaushin, A. S. Vedeneev and V. V. Rylkov, *JETP-Lett.* **66**, 668 (1997).
[2] B. A. Aronzon, D. A. Bakaushin, A. S. Vedeneev, V. V. Rylkov and V. E. Sizov, *Semiconductors* **31**, 1261 (1997).
[3] B. A. Aronzon, D. A. Bakaushin, A. S. Vedeneev, A. B. Davydov, E. Z. Meilikhov and N. K. Chumakov, *Semiconductors* **35**, 448 (2001).
[4] Y. Meir, *Phys. Rev. Lett.* **83**, 3506 (1999).
[5] M. Buttiker, *Phys. Rev. B* **41**, 7906 (1990).

9th Int. Symp. "Nanostructures: Physics and Technology"
St Petersburg, Russia, June 18–22, 2001

Edge states and their transport in a quantum wire exposed to a non-homogeneous magnetic field

S. M. Badalyan† and F. M. Peeters‡
† Department of Radiophysics, Yerevan State University, 375049 Yerevan, Armenia
‡ Department of Physics, University of Antwerp (UIA), B-2610 Antwerpen, Belgium

Abstract. Edge states and their transport in a quantum wire exposed to a perpendicular non-homogeneous magnetic field are investigated. Systems are studied where the magnetic field exhibits a discontinuous jump in the transverse direction. The energy spectra and wave functions of these systems, the corresponding group velocities along the interface and the particle average positions normal to the interface are calculated. The resistance of the quantum wire is obtained both in the ballistic and in the diffusive regimes as a function of the Fermi energy and of the homogeneous background magnetic field.

Introduction

Investigations of semiconductor nanosystems is frequently connected with the use of magnetic fields. In the last several years a complex situation of nanosystems in a non-uniform magnetic field has attracted considerable interest [1]. Different experimental groups have succeeded in realizing such systems [2] by depositing patterned gates of superconducting or ferromagnetic materials on top of the heterostructure. An alternative approach to produce non-homogeneous magnetic fields is by varying the *topography* of an electron gas [3].

We investigate the magnetic edge states and their transport properties (in the ballistic and diffusive regimes) in nanosystems exposed to a normal inhomogeneous magnetic field. Structures are studied where the magnetic field changes its sign, strength, and both sign and strength at the magnetic interface. Such a system was recently realized experimentally [4] by depositing a ferromagnetic stripe on top of the electron gas and by applying a background magnetic field normal to the electron gas. Varying the background field results in all the above situations.

1. Approach

Consider a one-dimensional electron channel along the y-direction formed by the parabolic confining potential $V(x)$ and exposed to a normal non-homogeneous magnetic field $B_z(x) = B_1$ and $B_z(x) = -B_2$ respectively on the left and the right hand side of the magnetic interface at $x = 0$. This system is placed in a homogeneous background magnetic field $B_z(x) = B_b$. In any finite region along the x-direction where the magnetic field is uniform, the system is described by the single particle Hamiltonian $H = (\vec{p} + e/c\vec{A})^2/2m^* + V(x)$ where m^* is the particle effective mass, $V(x) = m^*\omega_0^2 x^2/2$, ω_0 is the confining potential strength. We choose for the vector potential the Landau gauge $\vec{A} = (0, Bx, 0)$ and Schrödinger equation can be separated with the ansatz $\Psi(x, y) = e^{iky}\psi(x)$, where ψ is an eigenstate of the one-dimensional problem $(d^2/dx^2 + \nu + 1/2 - (x - X(k))^2/4)\psi(x - X(k)) = 0$. Here we introduce the following notations: $\nu + 1/2 = (\varepsilon - \hbar^2 k^2/2m_B)/\hbar\omega^*$ is the particle transverse energy in units of $\omega^* = \sqrt{\omega_B^2 + \omega_0^2}$, ω_B is the cyclotron frequency,

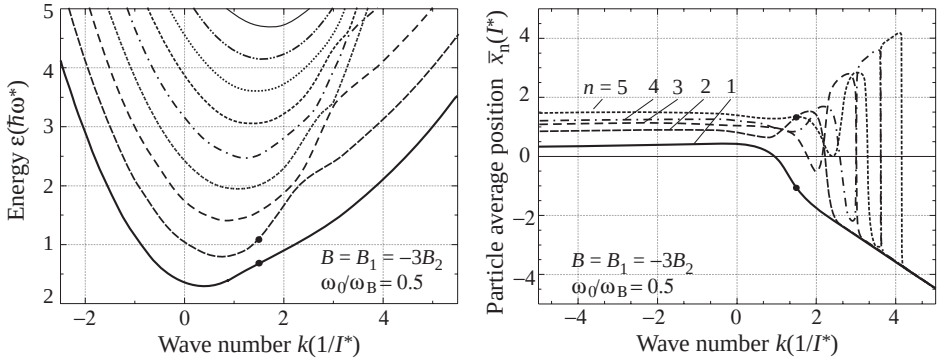

Fig. 1. The energy spectrum for the 8 lowest bands (left figure) and the particle average position corresponding to the 5 lowest energy bands (rigt figure).

ε and k are the energy and the momentum. The coordinate of the center of orbital rotation is $X(k) = kl^*\omega_B/\omega^*$ in units of the length scale $l^* = \sqrt{\hbar/(m^*\omega^*)}$. In the longitudinal direction the electron acquires a new field dependent mass $m_B = m^*\omega^{*2}/\omega_0^2$. The solutions of the above equation are the parabolic cylindrical functions $D_\nu(x)$.

In the non-homogeneous magnetic field case ν, X are different on the left and right hand side of the magnetic interface and we construct the wave function as $\psi_{\nu_1,\nu_2}(x, X_1, X_2) = D_{\nu_1}(\sqrt{2}(X_1(k) - x))$, if $x < 0$ and $\psi_{\nu_1,\nu_2}(x, X_1, X_2) = D_{\nu_2}(\sqrt{2}(x - X_2(k)))$, if $x > 0$. Indices 1, 2 refer to the values of quantities for which $\omega^* = \sqrt{\omega_B^2 + \omega_0^2}$ is taken with $B = B_1$, B_2, respectively. Matching of this wave function and its derivative at $x = 0$ leads to the dispersion equation $d\ln(D_{\nu_1}(x - X_1(k))/dx|_{x=-0} = d\ln(D_{\nu_2}(-x + X_2(k))/dx|_{x=+0}$. By solving this equation we obtain the energy and wave functions of the magnetic edge states, which are the solution of the one-dimensional problem with the effective potential $V_{eff}(x,k) = m\omega_1^{*2}(x - X_1(k))^2/2 + \hbar^2k^2/2m_{B_1}$, if $x < 0$ and $V_{eff}(x,k) = m\omega_2^{*2}(x - X_2(k))^2/2 + \hbar^2k^2/2m_{B_2}$, if $x > 0$. The shape of $V_{eff}(x,k)$ depends strongly on the sign of k and on the magnetic field profile.

2. Spectrum

For brevity here we restrict ourselves by consideration only asymmetric system: $B_1 \neq B_2$, $sign(B_1/B_2) = -1$. In this case $V_{eff}(x,k)$ exhibits a pronounced asymmetry both as a function of k and x. For negative values of k, $V_{eff}(x,k)$ is a triangular-like asymmetric well with a minimum of $\hbar^2k^2/2m^*$ at $x = 0$. For positive values of k, $V_{eff}(x,k)$ is a double well with different minima $\hbar^2k^2/2m_{B_1}$ and $\hbar^2k^2/2m_{B_2}$ at the positions $x = +X_1(k)$ and $x = -X_2(k)$, respectively. The triangular like barrier between the wells has again the height $\hbar^2k^2/2m^*$ at $x = 0$. Thus the confining potential together with the non-homogeneous magnetic field induces three effective masses (m^* for negative and m_{B_1}, m_{B_2} for positive values of k) in the system. The spectrum consists of alternating symmetrical and anti-symmetrical terms and is described by a discrete quantum number $n = 0, 1, 2, ...$ and the momentum k along the wire (Fig. 1). For negative values of k, the spectrum corresponds to snake orbits with free-like motion and with mass m^* along the y-direction. These states are effectively localized in the vicinity of the magnetic interface in the region where the magnetic field is smaller. The group velocity is approximately linear and the particle average

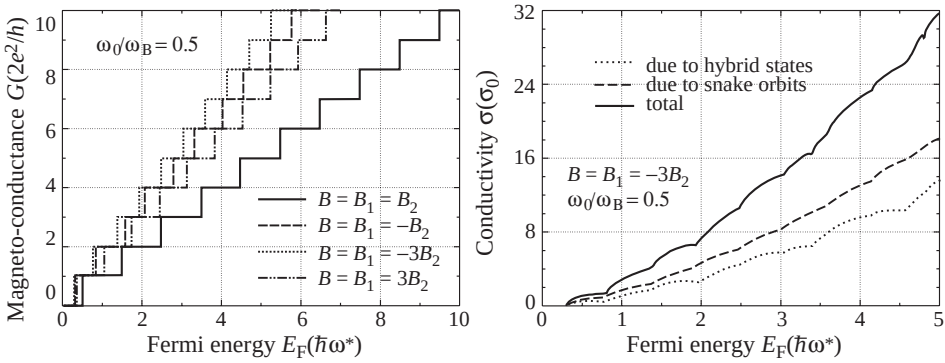

Fig. 2. The Fermi energy dependence of the conductance in the ballistic regime (left figure) and of the conductivity, in units of $\sigma_0 = e^2\tau/(\pi m^* l^*)$, in the diffusive regime (right figure).

position $\overline{x}_n$ is approximately independent of the wave number (Fig. 1). For positive k the spectrum characterizes the hybrid states. For some positive value of k the group velocity v_n and the particle average position $\overline{x}_n$ start to oscillate as a function of the wave number and the particle tunnels periodically from the left to the right side of the quantum wire and vice versa. At $k \to +\infty$ all states tend to be localized in the region where the magnetic field is large and the well of the effective potential is lower.

3. Transport

We calculate the zero temperature two terminal magneto-conductance for a perfect conductor using the Büttiker formula [5]. From Fig. 2 it is seen that the conductance, in the ballistic regime for different magnetic field profiles, exhibits stepwise variations as a function of the Fermi energy. For a given energy and confining potential strength, the conductance in the non-homogeneous magnetic field is nearly twice that for the homogeneous field case. The conductance decreases when going from the profile $B_1 = -3B_2$ to the profiles $B_1 = -B_2$, and $B_1 = +3B_2$.

The conductivity in the diffusive regime is calculated in the relaxation time approximation. We obtain $\sigma_{1D} = 2e^2/h\ \tau(E_F) \sum_n |v_n(k)|_{\varepsilon=E_F}$ in the zero temperature limit, τ is the momentum relaxation time. For the profiles $B_1 = -3B_2$ (see Fig. 2) and $B_1 = +3B_2$ the conductivity due to states with negative velocities (dashed curves) is larger than that due to states with positive velocities (dotted curves). In the case when the magnetic field changes its sign, the states with negative velocities are the snake states, which are always faster than the states with positive velocities which are related to the hybrid states. In the case of $B_1 = +3B_2$ all the states are hybrid states, however, the contribution to the conductivity of the states with negative velocities is larger because these states have the small mass m_B, and large velocity v_n. For both $v_n > 0$ and $v_n < 0$ parts, the conductivity has an oscillating structure as a function of the Fermi energy which is due to a divergence of the density of states at the bottom of the $\varepsilon_n(k)$ band. However, the contributions due to states with $v_n > 0$ exhibit an additional structure related to the oscillations of the group velocity as a function of k. This structure is more pronounced in the case of $B_1 = -3B_2$, the conductivity has additional distinct minima that reflect the tunneling effect discussed above.

The magneto-resistance in the ballistic regime exhibits stepwise variations as a function of the background magnetic field B_b. In the diffusive regime the resistance exhibits small

peaks as a function of B_b that are associated with the magnetic depopulation effect and that are on top of a positive magneto-resistance background, which increases with B_b.

4. Summary

We developed a theory for the non-homogeneous magnetic field induced edge states and their transport in a quantum wire. We calculated rigorously the spectrum of these systems, the corresponding group velocities along the magnetic interface and the particle average position normal to the magnetic interface. Exploiting these results, we calculated the conductance and the conductivity of the quantum wire in the ballistic and diffusive regimes.

Acknowledgment

This work was partially supported by the Flemish Science Foundation (FWO-Vl), the IUAP-IV (Belgium), and the CRDF grant No 375100.

References

[1] F. M. Peeters and J. De Boeck, in *Handbook of Nanostructured Materials and Technology*, ed. N. S. Nalwa, Vol. 3 (Academic Press, N. Y., 1999), p. 345.

[2] P. D. Ye, D. Weiss, R. R. Gerhardts, M. Seeger, K. von Klitzing, K. Eberl and H. Nickel, *Phys. Rev. Lett.* **74**, 3013 (1995);
S. Izawa, S. Katsumoto, A. Endo, and Y. Iye, *J. Phys. Soc. Jpn.* **64**, 706 (1995);
H. A. Carmona, A. K. Geim, A. Nogaret, P. C. Main, T. J. Foster, M. Henini, S. P. Beaumont and M. E. Blamire, *Phys. Rev. Lett.* **74**, 3009 (1995).

[3] C. L. Foden, M. L. Leadbeater, J. H. Burroughes and M. Pepper, *J. Phys.: Cond. Matt.* **6**, L127 (1994).

[4] S. J. A. Nogaret, Bending and M. Henini, *Phys. Rev. Lett.* **84**, 2231 (2000).

[5] M. Büttiker, *Phys. Rev. B* **38**, 9375 (1988).

9th Int. Symp. "Nanostructures: Physics and Technology"
St Petersburg, Russia, June 18–22, 2001

Nonlinear transport in superlattices under quantizing magnetic fields

P. Kleinert† and V. V. Bryksin‡
† Paul-Drude-Institut für Festkörperelektronik,
Hausvogteiplatz 5-7, 10117 Berlin, Germany
‡ Ioffe Physico-Technical Institute, St Petersburg, Russia

Abstract. The transport in semiconductor superlattices subject to quantizing electric and magnetic fields is studied based on the double-time Green function method. Our rigorous quantum-mechanical approach, which goes beyond the Kadanoff–Baym ansatz, reveals the hopping nature of the high-field transport in narrow-miniband superlattices. In both, the electric- and magnetic-field dependence of the current, gaps appear.

1. Introduction

Coherent carrier dynamics has been studied in semiconductor superlattices (SLs). The application of a strong dc electric field parallel to the SL axis leads to a reduction of the electron coherence. The electric-field induced reduction of the electron coherence in a SL is due to Bloch oscillations of electrons confined to a region of the order of Δ/eE (E is the electric field and Δ the miniband width). A different approach to Bloch oscillations is the formation of Wannier–Stark ladder states replacing the miniband energy spectrum, which is well defined in an unbiased SL. Nonlinear carrier transport along the SL axis is only possible via inelastic scattering.

When a strong magnetic field is applied parallel to the SL axis, the in-plane free electron motion quantizes into Landau levels. Consequently, the energy spectrum becomes completely discrete due to both WS and Landau quantization. The application of strong electric and magnetic fields creates a so-called quantum-box SL (QBSL), the characteristic properties of which are tunable by varying the electric and magnetic field.

From a theoretical point of view, the complete field-induced quantization of the electronic eigenstates poses some interesting problems related to the importance of lifetime broadening. Without any scattering, there is neither a collisional broadening of the energy spectrum nor carrier transport described by the nonequilibrium distribution function. To account for lifetime broadening, scattering has to be treated beyond perturbation theory. What is so fascinating about the quantum transport in QBSLs is the strong correlation between the particle spectrum and the statistical properties of the system. In the strongly biased nonequilibrium system, in which the field-dependent eigenstates are completely discrete, many-particle effects drastically change both the energy spectrum and the carrier statistics. The retroaction of the collisional broadening on the carrier statistics is accounted for by a specific, explicit time dependence of the distribution function. This so-called double-time nature of the problem emerges just beyond the Kadanoff–Baym (KB) ansatz [1] or the hitherto published density-matrix approaches (see, e.g., Ref. [2]). The nonlinear quantum transport in QBSLs provides an interesting example, for which the consideration of the double-time nature of the problem is inevitable.

2. Theoretical model

Our calculation of the SL current density is based on the double-time Kadanoff–Baym–Keldysh nonequilibrium Green function technique. The derivation of a general expression for the current density starts from the Dyson equation and takes into account the symmetry of a system subject both to electric and magnetic fields. In the related Wigner representation, the Dyson equation simplifies considerably. It is assumed that the nondegenerate electron gas remains essentially within the lowest miniband and that the lifetime broadening results mainly from elastic scattering on impurities. Inelastic scattering on polar-optical phonons has to be accounted for in the determination of the nonequilibrium distribution function. It is essential for our calculation that we go beyond the quasiclassical approach and do not rely on the Kadanoff–Baym ansatz. Our final result for the current density

$$j_z = en_s \frac{2\pi}{\hbar^2 V} \mid M \mid^2 \sum\nolimits_{l=-\infty}^{\infty} l F_l\left(\frac{\Delta}{\hbar\Omega}\right) \int_{-\infty}^{\infty} \frac{d\omega}{2\pi} \widetilde{f_0^>}(\omega)\, \widetilde{f_0^>}(\omega + l\Omega - \omega_0) \times [(N_0+1) f(\omega) - N_0 f(\omega + l\Omega - \omega_0)] \tag{1}$$

allows a clear physical interpretation within the hopping transport picture, in which the hopping length ld (d is the SL period), the hopping probability $F_l(\Delta/\hbar\Omega)$ ($\Omega = eEd/\hbar$ is the Bloch frequency), and the electric- and magnetic-field-dependent combined density-of-states (DOS) $\widetilde{f_0^>}(\omega)\widetilde{f_0^>}(\omega + l\Omega - \omega_0)$ appear. The carrier transport proceeds by phonon-induced tunneling transitions governed by the distribution function $f(\omega)$, which is the solution of a new integral equation obtained beyond the KB ansatz. In Eq. (1), n_s denotes the sheet density, N_0 the Bose–Einstein distribution function for polar-optical phonons, and M the energy-independent electron-phonon coupling constant. $f(\omega)$ accounts for a possible non-Markovian behavior of the hopping transport. However, in the sequential tunneling limit ($\Delta \to 0$), when the thermalization time is much shorter than a characteristic hopping time, we obtain

$$f(\omega) = A \exp\left(-\frac{\hbar\omega}{k_B T}\right), \tag{2}$$

where the constant A is calculated from the normalization condition

$$\int_{-\infty}^{\infty} \frac{d\omega}{2\pi} \widetilde{f_0^>}(\omega) f(\omega) = 1. \tag{3}$$

The lateral distribution function is calculated within the simple, self-consistent Born approximation. The Laplace transformed analytical solution has the form

$$\widetilde{f_0^>}(s) = \sum\nolimits_n \left[\frac{i\omega_n - s}{2u} + \sqrt{\frac{a^2}{2\pi l_B^2 u} + \left(\frac{i\omega_n - s}{2u}\right)^2}\right], \tag{4}$$

where $\omega_n = \omega_c(n + 1/2)$ and $l_B^2 = \hbar/m\omega_c$, with ω_c denoting the cyclotron frequency. u refers to the dimensionless strength of the impurity scattering and a to the lattice constant of the SL layers. The hopping probability is given by

$$F_l\left(\frac{\Delta}{\hbar\Omega}\right) = \frac{1}{\pi} \int_0^{\pi} dx\, J_l^2\left(\frac{\Delta}{\hbar\Omega} \sin x\right). \tag{5}$$

With the approximations in Eqs. (2) and (4), we recognize that the simple model has not been chosen to give an accurate representation of real systems. Here, it is rather our intent to use a sufficiently simple model for extensive calculations to demonstrate qualitative features resulting from the double-time nature of the problem.

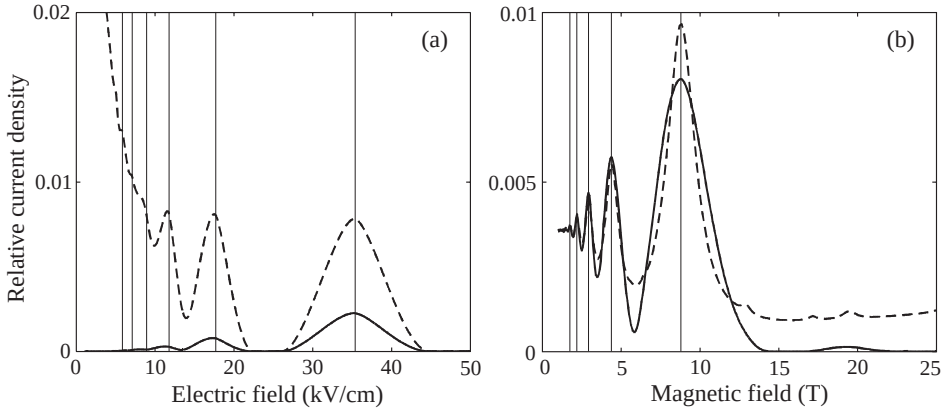

Fig. 1. (a) The electric field dependence of the relative current density j_z/j_0 ($j_0 = 2\pi e n \omega_0 \Gamma/\hbar^2 a^2$ with $|M|^2 = \omega_0^2 \Gamma$) for $\alpha = \Delta/\hbar\omega_0 = 0.5$ (solid line) and $\alpha = 1$ (dashed line). The positions of electro-phonon resonances occurring at $l\Omega = \omega_0$ are marked by thin vertical lines. Parameters used in the calculation are $B = 15$ Tesla, $\beta = \hbar\omega_0/k_B T = 1$, and $u = 0.02$. (b) The magnetic field dependence of the relative current density j_z/j_0 for $\alpha = \Delta/\hbar\omega_0 = 0.5$, $\beta = \hbar\omega_0/k_B T = 5$, $u = 0.02$, and $E = 50$ kV/cm (solid line). Combined cyclotron-Stark-phonon resonances occurring at $n\omega_c = \Omega - \omega_0$ are marked by thin vertical lines. The dashed line (multiplied by 23) has been calculated within the density-matrix approach [2] by using a phenomenological damping parameter of $\delta = 0.05$.

3. Numerical results and discussion

Numerical results for the relative current density at high electric and magnetic fields calculated from Eqs. (1) to (5) are shown in Fig. 1. Two interesting properties appear in the electric-field dependence of the current density as displayed in Fig. 1(a) for $\alpha = \Delta/\hbar\omega_0 = 0.5$ and 1 by the solid and dashed lines, respectively. Electro-phonon resonances are marked by vertical lines. Firstly, real current gaps occur as long as scattering on acoustical phonons and the Coulomb interaction are not taken into account. This is a consequence of the fact that the DOS bands, which exhibit sharp edges, do not overlap. Secondly, at low and intermediate field strengths, a crossover occurs from the quasiclassical field dependence ($\sim 1/E$) for wide minibands to an activated, hopping-like dependence for narrow minibands. These two features of the current-voltage characteristics are not reproduced by the density-matrix approach [2].

In Fig. 1(b), the magnetic field dependence of the relative current density is depicted. Positions of combined cyclotron-Stark-phonon resonances at $n\omega_c = \Omega - \omega_0$ are marked by vertical lines. Again real current gaps occur at about 16 and 23 T for this particular electric field. As shown by the dashed line, this result is not reproduced by our former density-matrix approach [2]. The magnetic field dependence of the current density depends sensitively on the electric field strength.

References

[1] V. V. Bryksin and P. Kleinert, *J. Phys. A: Math. Gen.* **33**, 233 (2000).
[2] V. V. Bryksin and P. Kleinert, *Physica B* **269**, 163 (1999).

9th Int. Symp. "Nanostructures: Physics and Technology"
St Petersburg, Russia, June 18–22, 2001

Persistent photoconductivity in p-type $Al_{0.5}Ga_{0.5}As/GaAs/Al_{0.5}Ga_{0.5}As$ heterostructures

W. Kraak†, N. Ya. Minina‡, *A. M. Savin*‡, A. A. Ilyevsky‡
and I. V. Berman§

† Institute of Physics, Humboldt University, D-10115 Berlin, Germany
‡ Faculty of Physics, Moscow State University, 119899 Moscow, Russia
§ Physics Department, San Jose State University, San Jose, California, USA

Abstract. Illumination of a double $p - Al_{0.5}Ga_{0.5}As/GaAs/Al_{0.5}Ga_{0.5}As$ heterostructure by a red light emitting diode results in a negative photoconductivity that, after the diode is switched off, slowly relaxes to a positive persistent photoconductivity, characterised by about 1.5 increase of a two-dimensional hole concentration. This metastable state may be explained in a framework of the model in which deep electron traps are supposed to be located above the Fermi level on the inverted heterointerface.

Introduction

In recent years a great interest in the study of GaAs/AlAs (GaAs/AlGaAs) superlattices has been connected with a striking difference in the electronic properties of normal "AlAs on GaAs" and inverted "GaAs on AlAs" interfaces. We study how the presence of an inverted heterointerface influences photoconductivity in these structures. Previously it was observed that the illumination of a single p-type $GaAs/Al_{0.5}Ga_{0.5}As$ heterostructure doped with Be by a red light emitting diode (LED) at liquid helium temperature results in a negative photoconductivity (NPC) that, after the light is switched off, slowly relaxes to the initial resistivity in dark [1]. In the present work we report on the effect of a red LED illumination on a conductivity of uniaxially compressed p-type double heterostructure $Al_{0.5}Ga_{0.5}As/GaAs/Al_{0.5}Ga_{0.5}As$, that differs from the structure in Reference 1 by the presence of the inverted heterointerface.

1. Experiment

At the beginning we repeated the results of Ref. [1] on the similar single $GaAs/Al_{0.5}Ga_{0.5}As$ heterojunction, that was grown by molecular beam epitaxy (MBE) in [001] direction with the normal sequence of AlGaAs on GaAs and modulation doped with Be (Fig. 1). The samples were prepared by photolithography in a Hall bar configuration with current being along [110] direction. At the temperature of experiment $T = 1.5\,\mathrm{K}$ the hole density is $N = 2.8 * 10^{15}\,\mathrm{m}^{-2}$. The characteristic LED photon energy is 1.9 eV. Our results are in a good agreement with ones from Ref. [1].

The double p-type $Al_{0.5}Ga_{0.5}As/GaAs/Al_{0.5}Ga_{0.5}As$ heterostructure was grown under the similar conditions as the single one and modulation doped with Be in $Al_{0.5}Ga_{0.5}As$. The process of the sample preparation and experimental details were not changed. Illumination of the samples with the red LED also caused the NPC effect. However in this case, when the LED was switched off, the non-exponential transient process led to the positive persistent photoconductivity (PPC) characterised by higher values of carrier density and mobility in

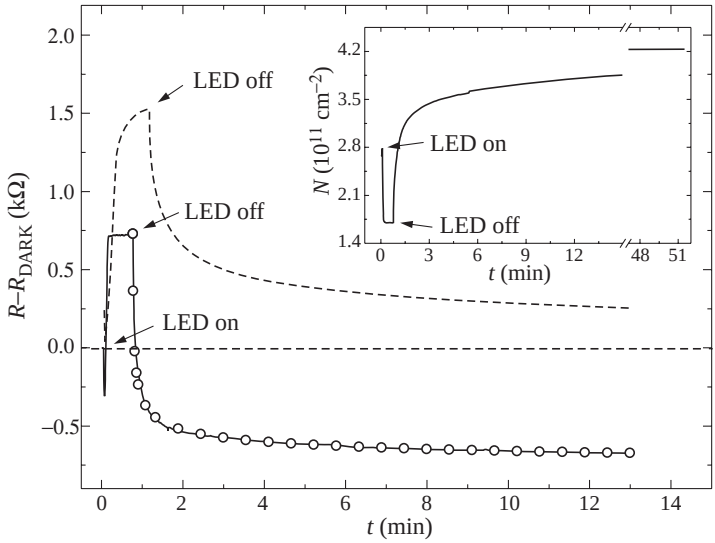

Fig. 1. NPC and PPC effects in single p − $GaAs/Al_{0.5}Ga_{0.5}As$ (dashed line) and double p − $Al_{0.5}Ga_{0.5}As/GaAs/Al_{0.5}Ga_{0.5}As$ (solid line) heterostructures. Open circles are the result of fitting according to Ref. [1]. The $N(t)$ dependence in p−$Al_{0.5}Ga_{0.5}As/GaAs/Al_{0.5}Ga_{0.5}As$ is represented in the insert.

comparison with the initial state in dark (Fig. 1). The initial state in dark could be restored by warming the sample up to room temperature and slow cooling it to 1.5 K.

The carrier concentration was controlled by the Hall effect and quantum transport measurements: Shubnikov–de Haas (SdH) oscillations and quantum Hall (QH) effect. The numerical values of carrier concentration in dark and in PPC state, calculated from the Hall effect and the frequency of SdH oscillations, are the same within the experimental error about 2%. These data in connection with the fact, that SdH oscillations and QH plateaus in Fig. 2 are not distorted after illumination, ensure that the observed PPC is not connected with the parallel conductivity described in Ref. [2]. In the PPC state we consider the value after 1 hour after the LED was switched off.

The transient process between NPC and PPC states is not exponential and may be well fitted by the logarithmic law like it was done in Ref. [1].

2. Discussion

The direct energy gap E_g in $Al_{0.5}Ga_{0.5}As$ is 2.14 eV at $T = 4.2$ K and it is larger than the red LED photon energy 1.9 eV. Therefore the direct band to band transitions under illumination are not possible. Following the conception of the NPC effect developed in Ref. [1], we have to suppose the presence of deep donor-like states located a bit below the Fermi level (FL) in the spacer just near the heterointerface. Being below the FL these states are neutral. Under illumination electrons photogenerated from these states to the conduction band are swept by the junction electric field into the quantum well (QW) and recombine with 2D holes, causing the reduction of their density. In the single heterojunction investigated in Ref. [1], as well as in the present work, the decay process to the initial state in dark is connected with a tunneling of holes from the positively charged exited donor like states back to the QW.

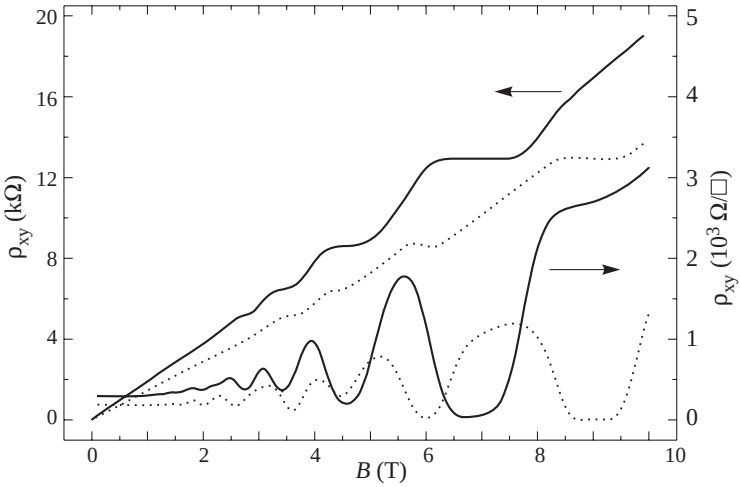

Fig. 2. SdH oscillation and QH efect in p − $Al_{0.5}Ga_{0.5}As/GaAs/Al_{0.5}Ga_{0.5}As$ dark (solid lines) and PPC (dashed lines) states.

The PPC effect in the double heterostructure is characterised by a considerable increase of the 2D hole concentration compared with one in dark. Since the p − $Al_{0.5}Ga_{0.5}As/GaAs/Al_{0.5}Ga_{0.5}As$ structure differs from p − $GaAs/Al_{0.5}Ga_{0.5}As$ by the presence of the second inverted heterointererface, the excess of 2D holes may be explained if we assume that during the transient process some amount of electrons is captured by deep electron traps located on this interface above the FL. It was recently established by deep-level transient spectroscopy that a series of four well defined deep levels is characteristic of inverted $GaAs/Al_xGa_{1-x}As$ interface grown by conventional MBE technique. These levels originate from intrinsic defects which are associated with arsenic vacancies and antisites acting like electron traps [3]. So the observed PPC effect is most probably associated with them.

The results are especially important for laser diodes because the observed PPC effect in AlGaAs/GaAs/AlGaAs let us suppose that electron traps at inverted heterointerfaces of quantum wells may be a source of nonradiative recombination processes.

Acknowledgements

This work has been supported by grant 00-15-96784 from the Russian Foundation for Basic Research.

References

[1] M. J. Chou, D. C. Tsui and G. Weimann, *Appl. Phys. Lett.*, **47**, 609 (1985).
[2] R. M. Kusters, T. J. B. M. Janssen, C. J. G. M. Langerak, J. Singleton, J. A. A. J. Perenboom, G. A. C. Jones, D. A. Ritchie and J. E. F. Frost, *Semicond. Sci. Technol.*, **7**, 961 (1992)
[3] P. Krispin, R. Hey and H. Kostial, *J. Appl. Phys.*, **77**, 11 (1995)

9th Int. Symp. "Nanostructures: Physics and Technology"
St Petersburg, Russia, June 18–22, 2001

Normal-to-plane magnetoresistance of single crystalline refractory metal nanostructures

G. M. Mikhailov†, I. V. Malikov†, A. V. Chernykh†, L. A. Fomin†, P. Joyez‡, H. Pothier‡, D. Esteve‡ and E. Olsson§
† IMT RAS, 142432 Chernogolovka, Russia
‡ SPEC-CEA Saclay, France
§ Angstrom Laboratory, Uppsala University, Sweden

Abstract. We have performed normal-to-plane magnetotransport measurements in single crystalline (100) W and Mo nanostructures down to 1.5 K. Fabricated nanostructures possess large mean free path due to their bulk crystalline perfection and low surface roughness. Under these conditions electrons scatter only on the boundaries of nanostructures and may travel long distance without scattering. We found that in this regime the normal-to-plane magnetoresistance of planar metallic nanostructures exhibit specific for ballistic transport attributes such as transverse magnetic focusing, suppression of Hall resistance (quenching Hall effect) and negative bend resistance at moderate magnetic fields.

Introduction

Investigation of novel planar heteroepitaxial metallic structures (thin films and nanostructures) attract much attention as they demonstrate new properties. Because of high crystalline quality and low roughness of their interface conducting electrons may travel long distance without scattering in these structures. Both ballistic and waveguiding properties become apparent. Electron momentum dissipation is driven by electron scattering on the irregularities of the boundaries. In this regime the electron current is mainly formed by grazing electron flow. Normal-to-plane magnetic field modifies their trajectories and the edge states (skipping orbits) are formed. In the following, we present for the first time the results of magnetoresistance investigation of refractory metal single crystalline planar nanostructures under conditions, when electron mean free path is comparable or superior the structure dimensions.

1. Experimental set-up and characterizations

Fabrication of the structures has been performed using pulse laser epitaxy of refractory metals, namely Mo (100) and W(100), on r-plane sapphire. Grown films possess high crystalline quality and low interface roughness. In Figure 1(a) we present transmission electron microscope image of Mo (100) thin foil that demonstrate atomic layers of substrate and metallic film. As electron scattering is driven by boundaries irregularities, we have been investigated the film morphology using scanning atomic force microscope (P47-Solver-NT-MDT). Root mean square (r.m.s.) of roughness amplitude has been found from larger than one by one micrometer topography scan. It equals 0.216 and 0.14 nm for Mo film surface and substrate, respectively. To characterize scattering properties of the rough surface the power spectrum of surface fluctuation and mean scattering wave vector have been building up. They are shown in Fig. 1(b) and (c). As can be seen in the latter, both

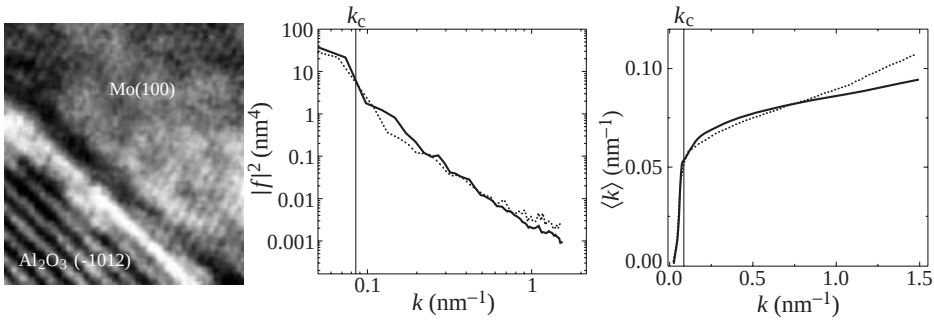

Fig. 1. Transmission electron microscope image of thin foil of Mo(100) films (a), power spectrum (b) and mean transfer wave vector (c) for surface fluctuation of Mo(100) surface (solid line) and substrate (dotted line).

small ($< k_c/k_F$) and large ($\gg k_c/k_F$) angle electron scattering contributes to electron momentum dissipation, where correlating wave vector is equaled to $k_c \approx 0.085$ nm^{-1} both for Mo film and substrate surfaces and k_F is Fermi wave vector. These well-characterized single crystalline films have been used for fabrication of single crystalline nanostructures with the help of subtractive electron lithography, Al nanomask developing and low energy ion milling. The resistance was measured by conventional ac techniques at 4.2 K, with an applied magnetic field up to 8 T directed perpendicular to the sample plane. The effective mean free path (EMFP) of electrons, estimated from the bridge-resistance ratio at $T = 295$ and 4.2 K, is found to be dependent on the film thickness. At low temperature, it is approximately an order of magnitude larger the film thickness. The mean cyclotron radius is estimated as $r_L = 3\,(\mathrm{T}\mu\mathrm{m})/\mathrm{B(T)}$.

1.1. Transverse magnetic focusing

To perform focusing experiment we fabricated planar Mo (100) structure that depicted in Fig. 2 (left) together with electric set-up. Semi-plane of 200 nm thickness is connected to the potential (3, 4) and current leads (1 or 2) in one side. Counterpart current lead

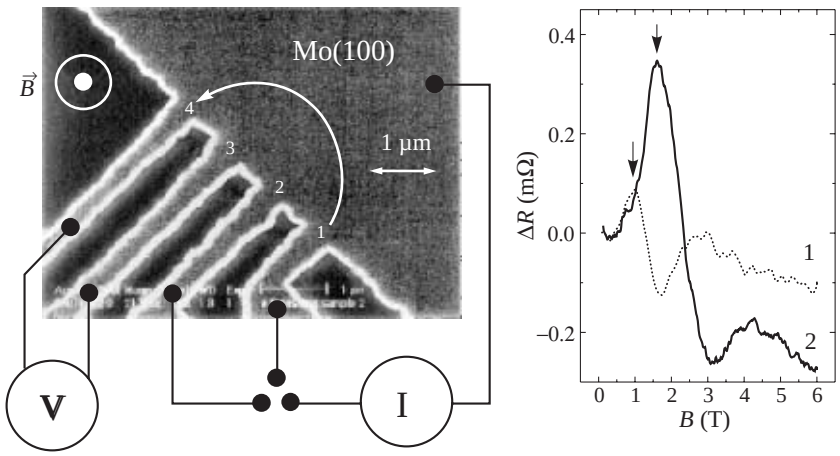

Fig. 2. The Mo (100) structure and electric set-up (left) and antisymmetric magnetoresistance for the lead 1 (dotted curve) or the lead 2 (solid curve) as an injecting electrode.

(schematically shown) is attached to the opposite side of the semi-plane. The current lead (1 or 2) serves as an injecting electrode, while potential leads 4 or 3 as an accepting electrode. Considering further isotropic electron spectrum for simplicity, we show in Fig. 2 an electron trajectory bended by applied magnetic field that close the injecting electrode 1 and accepting electrode 4 (positive lead of potentiometer), the cyclotron radius being twice smaller than the inter-electrode distance. By increasing of magnetic field we scan electron focusing point toward the injecting electrode. At some its meaning the bended electron trajectory points the lead 3 (negative lead of potentiometer). As the result we found in antisymmetric magnetoresistance ($\Delta R = R(B) - R(-B)$) positive and negative peaks, respectively (dotted curve in Fig. 2, right). For the lead 2 as an injecting electrode we found the same dependence but extended toward higher magnetic field in about two times (solid curve). Amplitude of the positive peaks, indicated by vertical arrows in the figure, increases as the inter-electrode distance decrease. Estimation by exponential dependence decay gives damping length 1.4 μm. It is comparable the inter-electrode distance and slightly smaller than transport length (EMFP). The latter is explained by significant influence of large angle electron scattering as found from the data of Fig. 1(c). Estimation of the cyclotron radios gives 1.4 (Tμm)/B(T), which is two times smaller than mean radius and corresponds to the smallest horde of Electron Jack valley of molybdenum.

1.2. Hall and bend resistances

We investigated cross type W (100) nanostructures of 300 nm width and 90 nm thick. Schematic drawing is shown in Fig. 3 (left). The scale parameters for the resistance and the magnetic field are defined as $R_0 = 90\,\mathrm{m}\Omega$ and $B_0 = 10$ T. Hall resistance has been measured using 1,3 connections as potential leads and 2, 4 — as current leads. It shows (Fig. 3 (right), curve (1)) quasi-linear dependence at B/B_0 larger than 0.2, indicated by vertical arrow B_b. Under lowering magnetic field it decreases faster (quenching) approximately as B in power 3 and near $B_a/B_0 = 0.025$ twice crossing zero. These two characteristic points are related to the following cyclotron radii $R_b = 5$ w and $R_a = 40$ w, respectively. Corresponding electron trajectories (a and b) are shown in the schematic drawing. Electrons may scatter by the corner of the cross and pass to the negative potential (3), as shown for trajectory a. It may cause the change of the sign of the Hall resistance at low magnetic field (point Ba in the left drawing). Electron trajectory b possesses the skip smaller (under

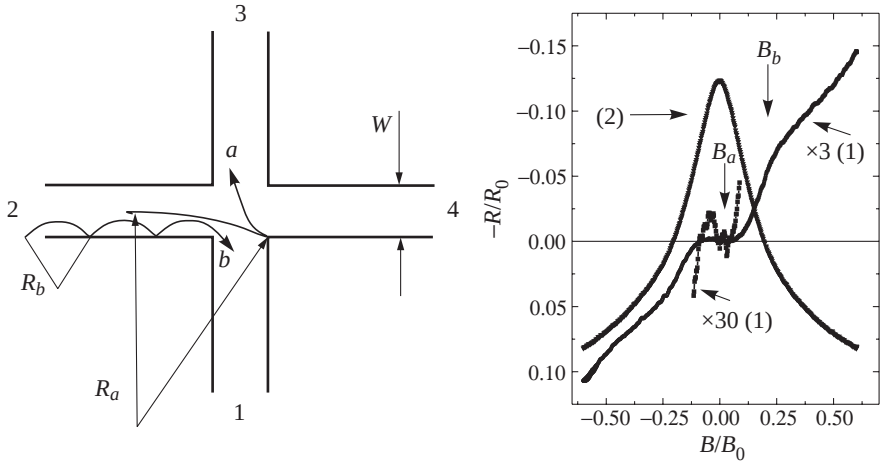

Fig. 3. Schematic drawing (left) and Hall (1) and bend (2) magnetoresistances (right).

magnetic field increase) than the lead width, while it does not at lower magnetic field. It changes a dependence of transmission probability of electrons to pass straight (from 2 to 4) or turn to the right (from 2 to 1) as a function of magnetic field. If electron flow is collimated at $B < B_b$ the Hall resistance is quenched. For the bend resistance measurements we used 1, 2 connections as a current leads and 4, 3 as a potential. Bend magnetoresistance is negative at low magnetic field and cross zero near the point B_b. For this reason, we explain its suppression by b type electron trajectory — skipping orbit, which suppress forward transmission probability under magnetic field increase.

Conclusion

We found that the normal-to-plane magnetoresistance of planar metallic single crystalline nanostructures exhibit specific for ballistic transport attributes such as transverse magnetic focusing, suppression of Hall resistance (quenching Hall effect) and negative bend resistance at moderate magnetic fields.

Acknowledgements

The work was supported by Physics of solid state nanostructures program (grant 99-1126), RFBR (grant 00-02-16601) and INTAS (grant 99-193).

9th Int. Symp. "Nanostructures: Physics and Technology"
St Petersburg, Russia, June 18–22, 2001

Dynamic susceptibility of 1D conductors: the short-range electron correlation effect

V. A. Sablikov and Yasha Gindikin
Institute of Radio Engineering and Electronics RAS,
Moscow district, Fryazino, 141120, Russia

Abstract. The dynamic density response and susceptibility of interacting electrons in 1D conductors is investigated taking into account the electron correlations reflecting the short-range order in a Luttinger liquid. We have shown that a narrow band of strong absorption appears in the dissipative susceptibility spectrum near to the wave vector $2k_F$ due to the short-range correlations, in addition to the commonly known δ-peak coming from the long-wave fluctuations. The adsorption band shape depends on the electron-electron interaction potential. This band is found to contribute dominantly to the dissipative conductance determined via the power absorbed in 1D conductor under local excitation.

Introduction

The electron-electron interaction in 1D conductors gives rise to the strongly correlated Luttinger liquid [1]. In this state the correlation function decreases slowly with distance showing the existence of short-range order. The electron density excitations are characterized by the existence of two components. One of them is a long-wavelength (LW) fluctuation coming from compression and extention of the Luttinger liquid. It caused mainly by the forward scattering processes. The other component arises due to backward scattering of electrons. It is represents the electron density oscillations on the scale of inter-electron distance. This component is similar to the charge-density waves (CDW) in Pierls conductors. The LW density component, as well as its contribution to transport properties, is well investigated in the literature. The CDW component was explored only in the connection with the pinning of a Luttinger liquid by impurities. It is obvious, that since short-range electron correlations contribute to the density, they must also contribute to transport even if there is no impurity.

In the present paper we investigate the dynamic density response and susceptibility of interacting electrons in 1D conductors taking into account the CDW component of the electron density. We have found that the short-range electron correlations produce a narrow band of strong absorption near to the wave vector $2k_F$, in addition to the commonly known δ-peak coming from the LW fluctuations. The band shape depends strongly on the electron-electron interaction potential. We have considered a scheme of experiment where the 1D conductor is subjected to the local external potential and the dissipated power is measured. Our calculations show that the contribution of CDWs to the absorbed power dominates over that of the LW density in the low-frequency regime.

1. The electron density

The collective motion of electrons is described by the bosonic phase $\Phi(x,t)$ which is connected with the electron density $\rho(x,t)$. The standard expression, which relates the

CDW density to Φ, was recently shown [2] to contradict to the requirement of the total particle number conservation. The correct expression of the density operator via Φ was proposed in Ref. [2]

$$\rho(x,t) = -\frac{1}{\pi}\partial_x \left[\Phi - \frac{1}{2}\sin\left(2k_F x - 2\Phi\right) \right], \tag{1}$$

where k_F is the Fermi wave vector. The first term describes the LW excitations that are smooth on the k_F scale. The second (oscillating) term relates to CDWs. The oscillations reflect the real physical picture of the excitations in a Luttinger liquid. In addition to the elastic waves, which are due to the LW density, the electrons are undergone the back scattering by neighboring particles. The interferences of the right- and left-moving electrons results in the density oscillations with the characteristic scale of $2k_F$. The oscillating density is also disturbed by an external potential and corresponding fluctuations propagate along the conductor contributing to the susceptibility, the current response and dissipated energy.

2. The dynamic susceptibility

The density response function $\chi(x,t)$ and the dynamic susceptibility are calculated using the bosonization technique and the Kubo formula.

The response function $\chi_1(x,t)$, which is due to LW density, represents the compression and extension waves in the Luttinger liquid moving from the excitation point. These waves are of the simplest form in the case of short-range interaction. They propagate with a constant velocity v renormalized by the interaction ($v = v_F/g$, with g being the interaction parameter). In the Coulomb interaction case, the charge waves propagate with dispersion. The velocity increases with the time as $(\ln t)^{1/2}$ which results in smoothing of the fronts and in the density oscillations.

The susceptibility $\chi_1(q,\omega)$ caused by the LW density has the pole at $\omega = qv(q)$ (with q being the wave vector, ω the frequency). It corresponds to the well-known plasmon pole.

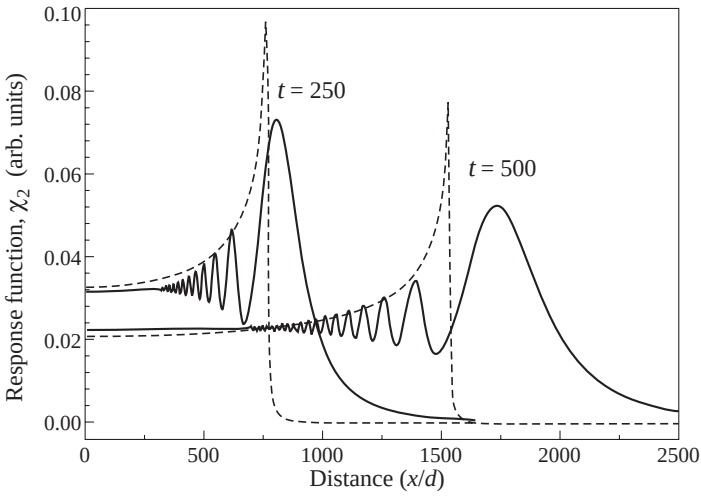

Fig. 1. The envelope of the CDW response function $\chi_2(x,t)$ for two moments of time (t is normalized to d/v_F, d being the wire diameter). Solid lines present the Coulomb interaction case, dashed lines correspond to the short-range interaction with the effective interaction parameter $g_{eff} = 0.326$.

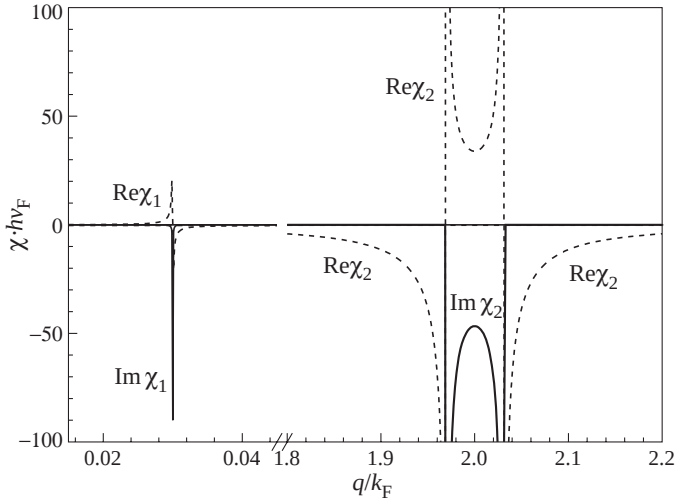

Fig. 2. The real and imaginary parts of the susceptibilities caused by the LW (χ_1) and CDW (χ_2) density components. The calculations are for $g = 0.3$ and $\hbar\omega = 0.1\varepsilon_F$.

The response function $\chi_2(x, t)$ coming from the CDW density describes the density oscillations rapidly varying in space with the wave vector $2k_F$ and modulated by the envelope that has a form of a propagating front. This is illustrated by Fig. 1 where the envelope is shown for two moment of time. The solid lines show the Coulomb interaction case. The dashed lines correspond to the short-range interaction with the effective interaction parameter g. In the latter case the front propagates with the constant velocity $v = v_F/g$ and the amtlitude decreases with the time as t^{-2g}.

The spectrum of the CDW susceptibility $\chi_2(q, \omega)$ is characterized by the presence of a narrow band of strong absorption near $q = 2k_F$. It is shown in Fig. 2. The band edges are determined by the dispersion of bosons in Luttinger liquid, $\omega = \omega(q)$. The edges are positioned at $q = 2k_F \pm q_\omega$ where q_ω is the wave vector of bosons at the frequency ω. The imaginary part of the susceptibility $\mathrm{Im}\chi_2$ as a function of q is determined by the electron-electron interaction potential. $\mathrm{Im}\chi_2(q, \omega)$ is connected with dynamic correlations of interacting electrons and coincides practically with the dynamic form-factor. In the short-interaction case, $q_\omega = \omega/v$ and the singularities of $\mathrm{Im}\chi_2$ at the band edges have the form: $\mathrm{Im}\chi_2 \propto \left|(2k_F \pm \omega/v)^2 - q^2\right|^{(g-1)}$. If electrons interact via the Coulomb law, the correlations are strongly changed [3] which results in corresponding change of the absorption band. The real part of the susceptibility $\mathrm{Re}\chi_2$ does not equal to zero in the whole region of q and ω. It has also the singularities at the band edges. In the long-wavelength limit, $\mathrm{Re}\chi$ varies as $\mathrm{Re}\chi \sim q^2$ in the whole frequency range showing that the CDWs do not contribute to the screening.

3. The dissipated power

The imaginary part of the susceptibility determines the conductivity. Since the CDW density contributes significantly to the susceptibility, a strong effect in the conductivity can also be expected. To show this we consider the situation where the 1D conductor without leads is locally disturbed by the electric potential of the conducting probe. The conductivity is determined by the power dissipated in the sample. It consists of two parts P_1 and P_2 that correspond to the LW and CDW components of the electron density. The dissipated

power due to the LW density is estimated as $P_1 \propto (\omega^2/g)|\varphi_{\omega/v}|^2$, where $\varphi_{\omega/v}$ is the Fourier harmonic of the external potential at the wave vector ω/v. The power caused by the CDW density depends much strongly on the interaction potential and on the frequency. Thus, for the short-range interaction

$$P_2 = \frac{e^2}{h} \frac{\Gamma(\frac{1}{2})}{4^g \Gamma(g)\Gamma(g+\frac{1}{2})} \left(\frac{\omega}{v k_F}\right)^{2g} k_F^2 \left|\varphi_{2k_F}\right|^2 . \tag{2}$$

It is of interest that the ratio of the above powers $P_2/P_1 \sim \omega^{2g-2}$ increases when the frequency is decreased. Hence in the low frequency regime, the dissipative conductance is determined mainly by the CDWs rather than the LW density as it is commonly believed.

Acknowledgements

This work was supported by RFBR-Moscow Region grant No 01-02-97017, Program "Physics of solid state nanostructures" grant No 97-1054 and Program "Surface atomic structures" grant No 5.3.99.

References

[1] J. Voit, *Rep. Prog. Phys.* **58**, 977 (1995).
[2] V. A. Sablikov and Ya. Gindikin, *Phys. Rev. B* **61**, 12766 (2000).
[3] H. J. Schulz, *Phys. Rev. Lett.* **71**, 1864 (1993).

9th Int. Symp. "Nanostructures: Physics and Technology"
St Petersburg, Russia, June 18–22, 2001

On the conduction mechanism in granular materials

I. P. Zvyagin† and R. Keiper‡
† Faculty of Physics, Moscow State University, 119899 Moscow, Russia
‡ Institute of Physics, Humboldt University Berlin, 10115 Berlin, Germany

Abstract. We discuss the effect of virtual intermediate localized states on inter-grain tunneling that controls conduction in granular conductors on the insulating side of the metal–insulator transition. It is shown that intermediate states can substantially increase inter-grain tunneling transition probabilities and give rise to the conductivity temperature dependence of the form $\ln\sigma \sim -(T_0/T)^x$, where $x \approx 0.4$, and to a large enhancement of the conductivity.

Introduction

Granular conductors are finely divided mixtures of a conducting and nonconducting phases; granular metals with characteristic grain sizes in the nanometer range are most commonly studied. It has been established a long time ago that on the insulating side of the metal-insulator transition, the conductivity of many of these materials in a wide temperature range is small and is well described by

$$\sigma \sim \exp\{-(T_0/T)\}^x, \tag{1}$$

where T_0 is a parameter and the exponent is $x < 1$ (usually $x \approx 0.5$) (see [1–3]). Such behavior was observed in cermets, discontinuous metal films, granular Fe-SiO_2 films, heavily doped and organic semiconductors and other materials.

Numerous theories were proposed to explain the dependence (1). Practically all theories agree that the conduction mechanism in granular metals in the dielectric regime is activated tunneling (hopping) between grains with disorder in grain size and inter-grain separation. If hopping is restricted to near neighbors only [4–6], the conductivity temperature dependence (1) can be obtained if there exists some special structural correlation between the grain size d and inter-grain separation w, e.g., $w/d = const$ [4]. The analysis of Adkins [7] showed that there is no clear correlation between d and w; the implication is that variable-range hopping must be taking place. For an almost constant density of states, the standard argument gives the Mott law with $x = 1/4$ at low temperatures. Assuming for granular metals the quadratic Coulomb gap at the Fermi level [8], one obtains Eq. (1) corresponding to the Efros–Shklovskii law [9] often observed in doped semiconductors at low temperatures.

It was noted however that there are substantial difficulties in explaining the available experimental data by using the Coulomb gap model. The data for different types of granular metal systems were analyzed in [3] using this model. The estimated hop distance appeared to be too small for variable-range hopping to be effective. Moreover, fitting of magnitude of the measured conductivity required much lower values of α than those expected on the basis of the known electronic structure of the materials. In [8], the authors have attempted to improve the theory replacing the wave function decay parameter α by the effective parameter $\alpha_m \approx \alpha w/(w+d)$, where w is the average thickness of the insulating layer between adjoining grains and d is the grain diameter. This *ad hoc* assumption was not consistently justified but even with the use of this assumption, the explanation of

the observed temperature variation of the conductivity still appears to be difficult [3, 7]. Moreover, under typical experimental conditions the Coulomb gap effects are not expected to be important for granular metals. Indeed, the interaction is appreciably reduced by screening, the estimated hop distances are not large and the temperatures at which the dependence (1) is observed are too high. Accordingly, in what follows we do not consider inter-site correlations that produce the Coulomb gap. We discuss a different approach to the theory of conduction in granular metals related to the role of intermediate virtual states.

1. Effect of virtual states on distant-neighbor transition rates

In accordance with the standard approach, we assume that the conduction mechanism is inelastic tunneling (hopping) between states localized at different grains. The intergrain transition probabilities depend on the overlap of wave functions of different grains and hence on the edge-to-edge separation between the grains; for near grains it can be much smaller than the grain size. So we have a system with hopping sites of extended size; an example of such systems is a superlattice with intentional disorder. It was shown [10, 11] that when calculating distant-site transition rates, important contributions to transition rates can come from transitions involving intermediate virtual states. In what follows we demonstrate that virtual states also play an important role for distant-neighbor transitions in granular conductors.

For phonon-assisted single-electron transitions, the matrix element for phonon-assisted transitions between a given grain and a grain lying in the n th coordination sphere is expressed as a sum over different paths involving $n-1$ virtual intermediate states ($n-1$ steps corresponding to coherent tunneling and one step with phonon absorption or emission). In analogy with [11] it can be shown that the contribution of direct inelastic tunneling between distant initial and final grains can be neglected compared to the process involving virtual states; the ratio of the corresponding contributions to the transition rate is of the order of $(\Delta E/t_0)^{2(n-1)} \exp\{-2\alpha_0(w_{ab} - n\bar{w})\}$, ΔE is a characteristic energy difference of the levels of neighboring grains, t_0 is the preexponential factor in the transfer integral, w_{ab} is the edge-to-edge separation between the initial and final grains and $\bar{w}$ is the average separation between the near grains. For large grains and narrow inter-grain barriers, we have $w_{ab} >> n\bar{w}$ and this ratio is small due to the exponential gain in tunneling distance.

2. Percolation arguments

As in the standard hopping theory, the conductivity problem can be reduced to finding the resistance of the equivalent random network, where the sites correspond to grains and the conductances connecting sites i and j can be written as $G_{ij} = G_0 \exp(-2\alpha S_{ij} - E_{ij}/kT)$, where G_0 is the preexponential factor that only weakly (nonexponentially) depends on inter-site separations and grain energy levels, S_{ij} is the total tunneling distance, $S_{ij} = n\bar{w}$, $E_{ij} = |E_i - \mu| + |E_j - \mu| + |E_i - E_j|$ and E_i are effective one-particle energy levels introduced in a way similar to that used in the theory of multivalent defects in semiconductors [12]. Here the difference from the standard expression for inter-grain conductance is that due to large grain size, for distant grains i and j we have $S_{ij} < w_{ij}$.

If the scatter in transition rates is large, then we can apply the standard percolative arguments. We say that for some fixed $G = G_0 \exp(-\eta)$, any two sites i and j are bonded if $G_{ij} > G$, i.e., if $2\alpha S_{ij} + E_{ij}/kT < \eta$. The critical value of η corresponding to the percolation threshold can be estimated by the bonding criterion [13] stating that the threshold corresponds to the condition that the average number of bonds per site $\bar{\nu}$ attains some critical value ν_c.

To estimate the number of bonds, we must know the distribution of energy levels E_i of localized states in the energy domain near the Fermi level taking account of both confinement and Coulomb interaction effects. Due to weak overlap of localized wave functions of different grains, to a good approximation we can assume that the level positions for different sites are uncorrelated (see [14]).

The one-electron energy spectrum can be exactly calculated for an ideal spherical quantum dot in the absence of intra-site correlations [16]. Both the average interlevel distance and the average level degeneracy increase with energy; random fluctuations in grain shape as well as variations of work function for different crystallographic faces lift the level degeneracy [15, 14]. If the characteristic level splitting is larger than the level spacing for a spherical dot at the Fermi level, then in the relevant energy range the level distribution is practically uniform, and the effective density of states (per grain) for conductivity $\bar{\rho_0}$ is practically constant in the region of interest near the Fermi level. In this case the average number of bonds per site is easily evaluated.

In the continuous limit, for distant coordination spheres, we have for the average number of bonds per site $\nu = \int d\varepsilon \mathbf{dR} \rho_0 \theta\,(\eta - 2\alpha n(R)\bar{s} - \varepsilon/kT)$, where $\mathbf{R}$ is the position vector of the final grain, $\rho_0 = (r/v_0)\bar{\rho_0}$, r is the volume fraction of metal, v_0 is the average grain volume and $n(R)$ is the number of the coordination sphere. Due to large grain size, in granular metals there is strong correlation in spatial positions of the grains preserving a short-range order in the spatial arrangement of grains. So to find the function $n(R)$ of the dependence of the radius R_n of the n th coordination sphere on n, we can use a model of regular close packed structures. For a regular close packings of spheres (f.c.c. and b.c.c. structures), the variation of R_n versus n th is quite well approximated by $R_n \approx d \cdot n^{\beta}$, where $\beta \approx 0.5$. Using this, we can evaluate the integral in the expression for ν; then by the bonding criterion, we obtain for the conductivity Eq. (1), where $x = 1/(1+3\beta)$ and

$$T_0 = (B/k)\frac{(2\alpha\bar{s})^{3\beta}}{\rho_0 d^3}. \tag{2}$$

Here $B = 15\nu_c/16\pi$ is a constant; setting $\nu_c = 1.5$ (see [9]), we obtain $B \approx 0.45$.

3. Discussion

For $\beta = 0.5$ we have $x = 0.4$, i.e. we obtain the conductivity variation of the form (1) that is close to that usually observed experimentally.

By Eq. (2), we can estimate the values of material parameters. The data for a Ni-SiO_2 film with $r = 0.24$ produced by cosputtering [1] can be approximated by Eq. (1) with $T_0 = 6 \cdot 10^4$ K. The value of $\bar{\rho}$ is related to the characteristic interlevel spacing $\Delta = 1/\bar{\rho}$. Taking $\Delta = 50$ meV [14], from (2) we derive $2\alpha\bar{s} = 5$. For the estimated barrier width $\bar{s} = 0,7$ nm, we have the decay length of about 3 Å, which is reasonable.

Thus virtual states give rise to a substantial increase in inter-grain transition probabilities and to a temperature dependence of the conductivity of the form (1), where $x \approx 0.4$. It should be noted that this dependence is obtained for a model of variable-range hopping in the absence of Coulomb gap effects and with no appreciable energy disorder.

Acknowledgements

We thank Prof. M. Pollak for numerous fruitful discussions. The work was supported by the Russian Foundation for Basic Research (grant 00-02-16676), the program "Universities of Russia" and the Russian Ministry of Education.

References

[1] B. Abeles, P. Sheng, M. D. Coutts and Y. Arie, *Adv. Phys.* **24**, 406 (1975).
[2] P. Sheng *Phil. Mag.* **B65**, 357 (1992).
[3] C. J. Adkins, in: *Hopping and Related Phenomena. Proc. 6th Int. Conf.*, ed. O. Millo and Z. Ovadyahu, Jerusalem: Racah Inst. Phys., The Hebrew Univ., 1995,p.245.
[4] P. Sheng, B. Abeles and Y. Arie, *Phys. Rev. Lett.* **31**, 44 (1973).
[5] C. J. Šimanek, *Solid St. Commun.* **40**, 1021 (1981).
[6] E. Z. Meilikhov, *JETP*, **115**, 1484 (1999).
[7] C. J. Adkins, *J. Phys.: Condensed Matter* **1**, 1253 (1989).
[8] O. Entin-Wohlman, Y. Gefen and Y. Shapira, *J. Phys. C* **16**, 1161 (1983).
[9] B .I. Shklovskii and A. L. Efros, *Electronic Properties of Doped Semiconductors*, Berlin, Springer, 1984.
[10] I. P. Zvyagin, in: *Proc. 7th Int. Symp. "Nanostructures: Physics and Technology", St. Petersburg, 14-18 June, 1999*, p.287.
[11] I. P. Zvyagin, *JETP Letters* **69**, 932 (1999).
[12] V. L. Bonch-Bruevich and S. G. Kalashnikov, *Physics of Semiconductors*, Moscow: Nauka, 1990.
[13] V. L. Bonch-Bruevich, I. P. Zvyagin, R. Keiper, A. G. Mironov, R. Enderlein and B. Esser, *Electronic Theory of Disordered Semiconductors*, Moscow: Nauka, 1982.
[14] E. Cuevas, M. Ortuno and J. Ruiz, *Phys. Rev. Lett.* **71**, 1871 (1993).
[15] M. Pollak and C. J. Adkins, *Phil. Mag.* **B65**, 855 (1992).
[16] R. L. Liboff, *Phys. Rev. B* **43**, 5765 (1991).

9th Int. Symp. "Nanostructures: Physics and Technology"
St Petersburg, Russia, June 18–22, 2001

One- and two-colour superradiant lasing in magnetized quantum-well heterostructures

A. A. Belyanin†‡, V. V. Kocharovsky†‡, Vl. V. Kocharovsky† and *D. S. Pestov*†
† Institute of Applied Physics, 603600 Nizhny Novgorod, Russia
‡ Texas A&M University, College Station, Texas 77843, USA

Abstract. We study generation of femtosecond superradiance pulses due to collective recombination of electron-hole (*eh*) pairs in quantum wells placed in a strong magnetic field oriented perpendicular to the growth plane. Such a superradiant laser can work under the conditions of continuous pumping and at room temperature due to complete quantization of particle motion, maximum possible spectral density of states, high volume density of cyclotron quantum dots, and partial suppression of the intraband scattering. It is shown that two-colour superradiant generation is possible at frequencies resonant to frequencies of the neighbouring interband transitions defined by *e*, *h* Landau levels.

1. Introduction. Cyclotron quantum dots

As is known [1, 2], superradiant coherent recombination of *eh* pairs in semiconductors can occur faster than the processes of nonradiative recombination and intraband scattering of carriers. This provides possibility to obtain femtosecond pulses in lasers based on both standard optoelectronic materials, such as GaAs, and materials with low efficiency of radiative recombination, e.g., wide-gap and even indirect-gap semiconductors. Ideal candidate for an active medium of a superradiant semiconductor laser is a multilayer heterostructure of cyclotron quantum dots created when a quantizing magnetic field $B \sim 10 \div 50$ T is imposed on the multiple quantum-well (QW) structure perpendicular to the growth plane [3, 4].

We will have in mind AlGaAs/GaAs QW structure under the conditions when an electron gyrofrequency satisfies the inequality $\omega_{Be} > \{1/T_2, 1/T_2^*\}$, where $1/T_2, 1/T_2^* < 10$ meV are homogeneous and inhomogeneous broadening of the Landau levels. Note that if the cyclotron energy $\hbar\omega_{Be}$ exceeds the energy of the optical phonon, one can expect suppression of the intraband relaxation, i.e. $1/T_2$.

Maxwell–Bloch equations describing interaction of *eh* pairs with radiation have the following form (in the semiclassical and rotating-wave approximations for slowly varying amplitudes of the electric field $E(t)$ and polarization $P(t)$) [1, 2]

$$\mathrm{d}E/\mathrm{d}t + E/T_E = 2\pi i \Omega\Gamma\, P/\mu^2\,, \tag{1}$$

$$\mathrm{d}P/\mathrm{d}t + [1/T_2 + i\,(\omega_0 - \Omega)]\,P = -i d^2\,\Delta N_l\,E/(2\hbar)\,, \tag{2}$$

$$\mathrm{d}\Delta N_l/\mathrm{d}t + (\Delta N_l - \Delta N_l^{\mathrm{p}})/T_1 = \mathrm{Im}(E^* P)/(2\hbar)\,. \tag{3}$$

Here Ω, Γ,and μ are the frequency, optical confinement factor, and refraction index for a given cavity mode. For a moment we neglect inhomogeneous broadening and consider only the transitions at frequency ω_0 between *e*, *h* Landau levels with the same number l and given transverse quasimomentum k_n. The time T_E of the field decay in a cavity of length L due to radiative losses only is equal to $4\mu L/|c\ln(R_1 R_2)|$, where c is the velocity of light in vacuum, $R_{1,2}$ are the reflection coefficients on the cavity facets. In the above equations

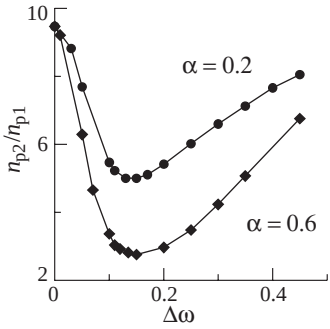

Fig. 1. First-to-second threshold ratio vs. a sublevel splitting $\Delta\omega$ (in units $\omega_c(2N_0)/2$).

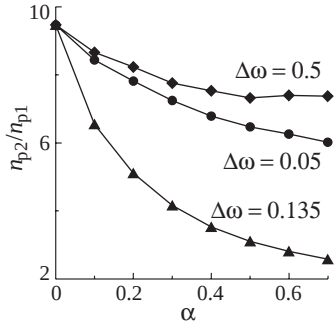

Fig. 2. First-to-second threshold ratio vs. an exponent α.

we introduced the volume density of inversion $\Delta N_l(t)$ for a given interband transition with dipole moment d. The quantity $\Delta N_l^{\rm p}$ is its equilibrium value supported by pumping (in the absence of generation). The relaxation time of inversion $T_1 \geq T_2$. Inversion is achieved when the density N of all pairs in QWs exceeds the value $N_l = \omega_{Be} m_e k_n\,(2l+1)/(4\pi^2\hbar)$.

2. One-colour superradiance and inhomogeneous broadening

One-colour superradiance (SR) of femtosecond pulses in a magnetized QW structure at resonance $\Omega \simeq \omega_0$ is realized most easily when [4, 5] $1/T_E \leq \omega_c/2 \leq \omega_{Be}$ and the SR growth rate of the corresponding initial-value problem reaches its maximum value of the order of half the so-called cooperative frequency of eh pairs:

$$\omega_c = [4\pi d^2 \Gamma\, \Delta N_l\, \omega_0/(\hbar\mu^2)]^{1/2}; \quad \Delta N_l \leq 2\,\Delta N_{l=0} \leq 4N_0 = \omega_{Be} m_e k_n/(\pi^2\hbar). \quad (4)$$

Analysis of stability of the steady state of Eqs. (1)–(3) shows [2, 5, 6] that for the appearance of pulsation regime leading to SR the inequalities $\omega_c^2\,(\Delta N_l^{\rm p}) > 36/(T_2 T_E)$ and $1/T_E > 1/T_1 + 1/T_2$ have to be satisfied. This means that the pumping should exceed some (second) threshold value and low-Q laser cavity must be used. The required cavity length is linearly proportional to the relaxation time of polarization and for $T_2 = 0.2$ pc is of order 10–20 μm. The required magnetic field is inversely proportional to Γ, so that for $\Gamma = 0.2$ it is about 50 T and decreases as $1/T_2^2$.

Inhomogeneous broadening of the Landau levels can lead to substantial changes of the generation thresholds. Typically it increases the threshold of stationary generation (the first threshold), but it can also decrease the second threshold [6, 7].

To simplify the problem, we will assume that inhomogeneous broadening is defined by discrete fluctuations of a thickness of a QW or barrier that are multiple of the atomic monolayer thickness. In such a discrete model, the neighbouring spectral components (sublevels) of a working transition are separated by some value $\Delta\omega$ which is usually of order several meV. We assume also the simplest distribution of the total pumping $\Delta N_l^{\rm p}$ between different spectral components j, $\Delta N_j^{\rm p}$, namely a geometric progression law with an exponent $\alpha < 1$: $\Delta N_j^{\rm p}/\Delta N_0^{\rm p} = \alpha^{|j|}$.

Qualitative analysis and numerical simulations show that SR pulses under the inhomogeneous broadening have generally larger duration, lower power and repetition rate as compared to SR pulses generated under the condition of homogeneous broadening. The

numerical results for the first $n_{p1} = \Delta N_{p1}/(2N_0)$ and second $n_{p2} = \Delta N_{p2}/(4N_0)$ generation thresholds on the interband transition between ground e, h Landau states are shown in Figs. 1, 2 for typical values of the relaxation times $T_1 = 10T_2 = 30T_E = 180/\omega_c(2N_0)$ in the case of three sublevels. At a given pumping, the first threshold rises monotonously when $\Delta\omega$ or α increases. The second threshold which indicates the onset of SR gets substantially lower with increasing inhomogeneous broadening (growing $\Delta\omega$ and α), if the latter is not higher than homogeneous broadening, i.e., if $\Delta\omega < 1/T_2$ for $\alpha \sim 1/2$. For larger inhomogeneous broadening, when $1/T_2 > \Delta\omega > 1/T_E$ and $\alpha \sim 1/2$, the second threshold begins growing with increasing sublevel splitting $\Delta\omega$ due to the weakening of interaction between different spectral components of polarization, because a dephasing timescale is defined by $1/\Delta\omega$ and not equal to T_2. Therefore, the minimum of the ratio of thresholds n_{p2}/n_{p1} is achieved when $\Delta\omega \sim 1/T_2$ and $\alpha \to 1$ (see Figs. 1, 2).

3. Two-colour superradiance for adjacent interband Landau transitions

Standard injection or optical pumping of a multilayer heterostructure with magnetized QWs creates carriers with energies considerably higher than the energies of the lower levels of dimensional quantization and Landau sublevels of the lower dimensional quantization level. In this case the intraband scattering provides a cascade pumping of neighbouring

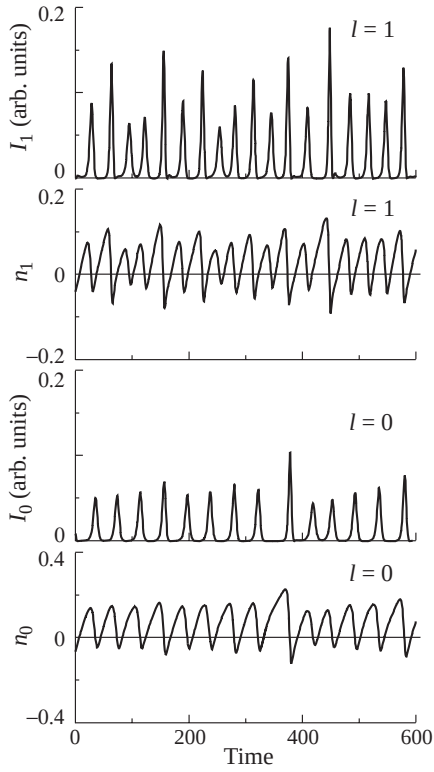

Fig. 3. Two-colour superradiance: radiation intensity, I, and inversion, n, normalized to unity, vs normalized time, $\tau = 0.5t\omega_c(2N_0)$ for the ground, $l = 0$, and first, $l = 1$, Landau levels at $n_p \equiv \Delta N_1^p/(4N_0) = 1.55$ and $T_1 = 7.5T_{01} = 10T_2 = 30T_E = 180/\omega_c(2N_0) = 9000/\omega_0 = 9450/\omega_1$.

recombination transitions which can lead, in principle, to a simultaneous generation of corresponding resonant modes.

We have analyzed SR generation of two modes resonant to the two transitions between pairs of neighbouring Landau levels [7] (e.g., between the first and second e, h Landau levels). The rate of intraband relaxation from the upper to lower level was characterized by a phenomenological time of nonradiative cyclotron transition T_{01}. Using known expressions for the first and second threshold in the case of an isolated transition [6], we obtain analytical estimates of the threshold pumping in a given 4-level system (see [7]). In fact, each threshold for a system of two incoherently connected transitions corresponds to a minimal pumping required to drive one subsystem out of equilibrium while the state of other subsystem is fixed.

Numerical analysis of corresponding Maxwell–Bloch equations demonstrates the possibility of two-colour SR under continuous pumping. This regime is conserved under substantial variation of the system and pumping parameters (when they are changed by at least tens of per cent). The most important condition for coexistence of SR on the neighbouring recombination transitions is a proximity of non-stationary lasing thresholds for corresponding laser modes and approximate equality of their gain coefficients. An example of two-colour SR is shown in Fig. 3. In this regime the pulse sequences generated on the adjacent recombination transitions can be essentially different (with respect to the repetition rate, power, and duration). However, in any case each pulse is accompanied by changing the inversion sign on the corresponding transition which is unusual for a standard lasing.

4. Summary

In conclusion, our study of threshold conditions and dynamics of femtosecond SR generation in semiconductor QW lasers placed in a quantizing magnetic field shows that a system of cyclotron quantum dots is rather promising for the creation of superradiant laser. In particular, we found that inhomogeneous broadening, until it does not exceed homogeneous one, leads to considerable lowering of a SR threshold. Finally, we demonstrated possibility of two-colour SR under a constant cascade pumping of e, h Landau levels and calculated corresponding thresholds.

References

[1] A. A. Belyanin, V. V. Kocharovsky and Vl. V. Kocharovsky, *Quant. Semiclass. Optics* **9**, 1 (1997).
[2] A. A. Belyanin, V. V. Kocharovsky and Vl. V. Kocharovsky, *Bull. Rus. Acad. Sci. Physics* **62**, 305 (1998); *Quant. Semiclass. Optics* **10**, L13 (1998).
[3] L. V. Butov and V. D. Kulakovskii, *Phys. Rev. B* **44**, 10680 (1991).
[4] A. A. Belyanin, V. V. Kocharovsky and Vl. V. Kocharovsky, *Bull. Rus. Acad. Sci. Physics* **64**, 205 (2000).
[5] A. A. Belyanin, V. V. Kocharovsky, Vl. V. Kocharovsky and D. S. Pestov, *J. Universal Computer Sci. Appl.*, in press (2001).
[6] Y. I. Khanin, *Principles of Laser Dynamics*, Elsevier, Amsterdam, 1995.
[7] A. A. Belyanin, V. V. Kocharovsky, Vl. V. Kocharovsky and D. S. Pestov, *Radiophys. Quantum Electron.* **44**, n. 1-2 (2001).

9th Int. Symp. "Nanostructures: Physics and Technology"
St Petersburg, Russia, June 18–22, 2001

A comparative study of QD and nitrogen-based 1.3 μm VCSELs

A. P. Vasil'ev, N. A. Maleev, A. Yu. Egorov, A. E. Zhukov, A. R. Kovsh, I. L. Krestnikov, V. M. Ustinov, N. N. Ledentsov and Zh. I. Alferov
Ioffe Physico-Technical Institute, St Petersburg, Russia

Abstract. We study two types of GaAs-based heterostructures (InAs/InGaAs quantum dots and InGaAsN quantum wells) designed for 1.3 μm vertical-cavity surface-emitting lasers (VCSELs) and compare different device designs. A correlation between properties of the active region and parameters of the optical microcavity required for lasing was found and investigated. The comparative analysis of the vertical-cavity surface-emitting lasers with either InAs/InGaAs quantum dots or InGaAsN quantum wells active region operating in continuous wave regime at room temperature was done. Optimization of the optical microcavity provides the internal round-trip optical loss less than 0.05%.

Introduction

Development of high-quality surface emitters for 1.3 μm wavelength range can open way for wide use of optical fiber communications in the local area networks and potentially significantly increase the market of optoelectronic devices [1]. Have been in the last years several GaAs-based materials grown by molecular beam epitaxy (MBE) proposed as promising candidates for 1.3 μm emitters. Among them InGaAsN quantum well (QW) and InGaAs quantum dots (QD) structures.

The main issues of the design of InGaAsN/GaAs VCSELs related with degradation of the optical properties at the relatively large amount of nitrogen. As a result the optical gain of 1.3 μm emitting structures is sufficiently less than one for standard 0.98 μm InGaAs QW structures [2]. Therefore, careful optimisation of the microcavity design and device construction is necessary for laser realization.

As for 1.3 μm QD structures the basic problem is a relatively low optical gain of the ground-state transition [3]. Because the thickness of VCSEL microcavity is typically a few l, which is much less than the usual stripe length of an edge-emitting laser, the output loss in VCSEL can significantly exceed the saturated gain of the QD active region.

In this contribution we study two types of MBE-grown GaAs-based heterostructures (InAs/InGaAs QD and InGaAsN QW) designed for 1.3 μm VCSELs and compare different device designs.

Devices design

Figure 1 shows optical gain curves for InGaAsN QW and InAs/InGaAs QD structures estimated from experimental results on Jth for broad-area edge-emitting lasers of various length [2,3]. InGaAsN structure demonstrates much high gain as compare to QD structure. Therefore proper design of the optical microcavity is a especially critical point for QD VCSELs. Assuming the maximum QD gain of 12 cm^{-1}[3], the minimum reflectivity of DBR is estimated to be 0.9994–0.9998 depending on the internal loss. In the standard VCSEL design the main contribution fo internal loss is associated with light absorption in

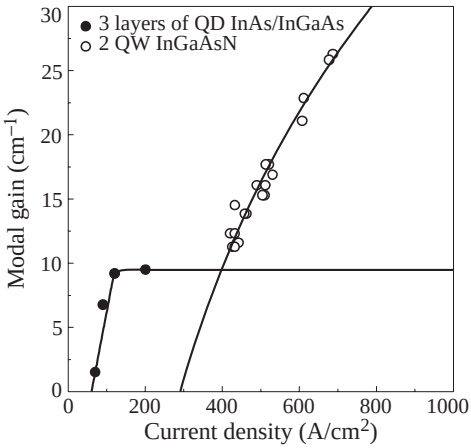

Fig. 1. Dependence of modal optical gain on current density for laser diodes with active region based on three planes of InAs/InGaAs QDs (● ● ●) and double InGaAsN QWs (○ ○ ○).

doped distributed Bragg reflectors (DBRs). To overcome the above issues we use top and bottom AlGaO/GaAs DBRs and double current apertures in combination with intracavity contacts.

This approach provides low optical loss and suitable to realize small-size VCSELs with low threshold current as it was previously demonstrated by the first realization of QD VCSEL emitting near 1 μm [4]. For InGaAsN VCSEL we used undoped AlGaAs/GaAs mirrors and single selectively oxidized AlGaO current aperture. Structures with AlGaO/GaAs DBRs provides relatively short effective cavity length and redistribution of the optical field intensity which leads to larger confinement factor.

Experimental results

A schematic cross-sectional diagrams of a fabricated 1.3 μm VCSELa are given in Fig. 2. The InGaAsN VCSEL active region contains two InGaAsN/GaAs QW separated by GaAs spacers. The QD VCSEL active region consists of three planar sheets of InAs islands formed by a 2.5 monolayer-thick InAs deposition with a 5 nm-thick $In_{0.15}Ga_{0.85}As$ quantum well overgrowth layer and two 25 nm-thick GaAs barrier/separation layers [5]. The devices have approximately square current apertures (8×8 μm).

The devices were tested in pulsed and continuous wave regimes at 25–70°C on a temperature controlled probe station. The emission wavelength is in the 1280–1305 nm range depending on the particular position on the wafers. The room temperature pulsed light power-current (L-I) and current-voltage (I–V) characteristics of a typical InGaAsN QW and InAs-InGaAs QD VCSELs are shown in Fig. 2. The curves are for an experimental structures emitting at 1285 nm (InGaAsN QW VCSEL) and 1300 nm (QD VCSEL). The threshold currents are 1.8 mA for QD VCSEL and 3.5 mA for InGaAsN QW VCSEL. The CW output power as high as 650 μW at drive current of 2.8 mA was observed for InAs/InGaAs QD VCSEL under continuous wave mode at 25°C. InGaAsN VCSEL demonstrates even higher CW output power ($>$ 1 mW) and lasing up to 65°C.

The main difference between two fabricated devices is seems to be external quantum efficiency. In the case of QD VCSEL it is higher than 40% while for InGaAsN VCSEL less

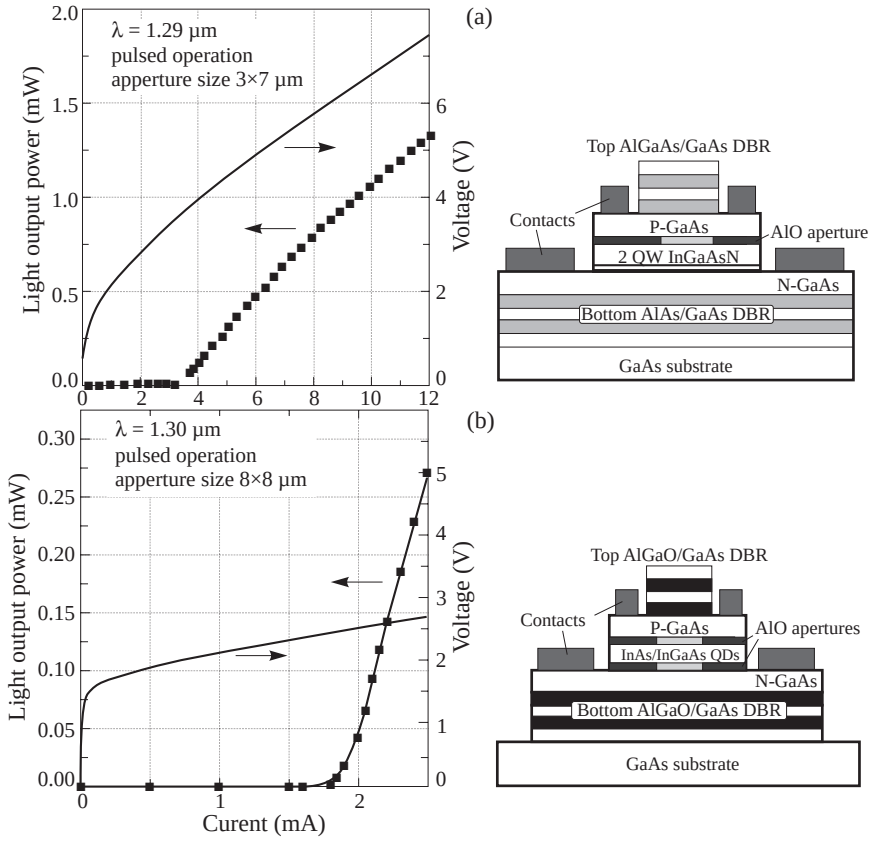

Fig. 2. Schematic representation and lasing characteristics of VCSELs with active region based on double InGaAsN QWs (a) and based on three layers of InAs/InGaAs QDs (b).

than 10%. It is impossible to explain so large difference based on active material properties only. Explanation for this phenomenon may be founded from detail analysis of the structure design and device characteristics. We estimated the maximum possible values for internal optical loss for both cases and concluded that QD VCSELs demonstrates sufficiently low round trip loss ($< 0.05\%$). This value is well comparable with the best results published for any type of VCSELs.

Conclusion

Successful realization of long-wavelength InAs/InGaAs QD and InGaAsN QW VCSELs demonstrate significant potential of GaAs-based lasers for application in optical communication systems. In the case of InGaAsN VCSELs, the main attantion showld be paij to optimization of microcavity design. As for QD VCSELs, further work showld be focused on devices with an increased number of the QD planes in the active region grown with reduced spacer thickness. This will allow us to improve the maximum QD gain that would result in long-wavelength ground-state lasing at lower Q cavities (VCSEL) with higher external differential efficiency.

Acknowledgements

This work was supported by the Russian Foundation for Basic Research, NanOp and CRDF (grant RE1-2221).

References

[1] *Vertical-Cavity Surface-Emitting Lasers*, Ed. C. W. Wilmsen, H. Temkin and L. A. Coldren, Cambridge Univ. Press, 1999.

[2] A. Yu. Egorov, D. Bernklau, D. Livshits, V. Ustinov, Zh. I. Alferov and H. Riechert, *Electron. Lett.* **35**, 1643 (1999).

[3] A. E. Zhukov, A. R. Kovsh, V. M. Ustinov, Yu. M. Shernyakov, S. S. Mikhrin, N. A. Maleev, E. Yu. Kondrat'eva, D. A. Lifshits, M. V. Maximov, B. V. Volovik, D. A. Bedarev, Yu. G. Musikhin, N. N. Ledentsov, P. S. Kop'ev, Zh. I. Alferov and D. Bimberg, *IEEE. Photon. Lett.* **11**, 1345 (1999).

[4] J. A. Lott, N. N. Ledentsov, V. M. Ustinov, A. Yu. Egorov, A. E. Zhukov, P. S. Kop'ev, Zh. I. Alferov and D. Bimberg, *Electron. Lett.* **33**, 1150 (1997).

[5] J. A. Lott, N. N. Ledentsov, V. M. Ustinov, N. A. Maleev, A. E. Zhukov, A. R. Kovsh, M. V. Maximov, B. V. Volovik, Zh. I. Alferov and D. Bimberg, *Electron. Lett.* **36**, 1384 (2000).

9th Int. Symp. "Nanostructures: Physics and Technology"
St Petersburg, Russia, June 18–22, 2001

Kinetic processes in unipolar semiconductor lasers on asymmetric quantum wells

V. V. Kapaev†, Yu. V. Kopaev† and *N. V. Kornyakov*‡
† P. N. Lebedev Physical Institute, RAS, 117924 Moscow, Russia
‡ Institute of Microelectronics, RAS, 150051 Yaroslavl, Russia

Abstract. Kinetic processes in an unipolar semiconductor laser on asymmetric quantum wells are described. An active element of the semiconductor laser structure, first tuned up from a quantum-mechanical point of view, is now optimized with taking into account generation-recombination processes to achieve a maximum of the population inversion. The value of the population inversion is calculated as well as subband electron concentrations. Some ways for an advancement of the laser parameters is proposed.

1. Unipolar semiconductor laser on asymmetric quantum wells

Unipolar semiconductor laser on asymmetric quantum wells (SLAW) was proposed a short time ago in [1]. The peculiarities of the proposed design are strongly asymmetric barriers surrounding a double-well laser active element. This causes a transformation of the electronic state dimensionality for the lower working subband at a small momentum and allows to suppress intersubband electron transitions to this subband. So the population inversion in this system can be easily realized.

The laser active element comprises two quantum wells h_1 and h_2 separated by a tunnel barrier b_1 (see Fig. 1). This double-well structure forms three size-quantized subbands with adjusted distances between them. The lowest subband ε_1 is a reservoir of electrons. Near the equilibrium this reservoir is filled in with electrons up to a desired concentration. The optical phonon energy (E_{LO}) above the reservoir, a bottom laser subband (BLS) ε_2 is located. This allows electrons to leave the BLS as quickly as possible. Above the BLS, at the distance that is sufficient for the optical pumping of electrons from the reservoir, there is a top laser subband (TLS) ε_3.

This part of the active element is typical of the unipolar semiconductor laser. New elements are strongly asymmetric barriers U_0 and U_1 ($U_0 \gg U_1$) surrounding the double-well

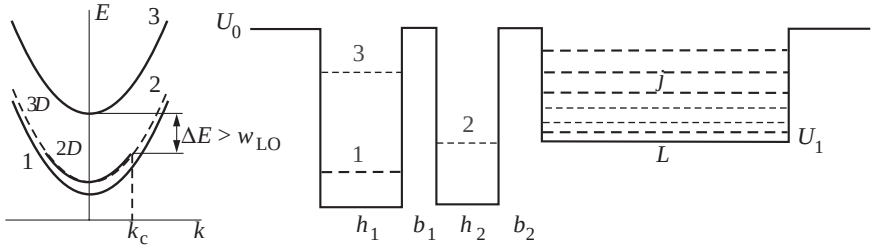

Fig. 1. Energy spectrum for the three active laser subbands and the schematic band diagram of the unipolar semiconductor laser.

structure. The barrier height U_1 is chosen to be close down to the ε_2 subband minimum in order to destroy the 2D-dimensionality of the BLS above the small quasi-momentum k_c value. In such a way a phonon relaxation time τ_{32} for the intersubband electron transitions from the TLS ε_3 to the BLS ε_2 can be increased appreciably comparad to the τ_{21} relaxation time from the BLS to the reservoir: $\tau_{32} \gg \tau_{21}$. The last strength inequality is a indispensable condition for the population inversion. The highest value for the population inversion is

$$I_{\max} = \tau_{32}/\tau_{21}. \tag{1}$$

Unfortunately, a finite width L of the lower binding barrier U_1 causes an existence of size-quantized quasi-3D states, which are localized beyond the double-well structure, but can serve as intermediate states on the path of electrons from the TLS to the BLS. So we have to take into account quasi-continuous states during the SLAW structure optimization.

The active element of the SLAW has been previously optimized in [2] from a quantum-mechanical point of view. This tuning was made in the assumption of the optical pumping that allows to simplify the laser structure since neither transport nor cooling of the carriers in the injector region are required. The main requirement is the largest value of a parameter

$$\eta = (\varepsilon_3 - \varepsilon_2)^3 (Z_{31} Z_{32})^2 \tag{2}$$

(where Z_{ij} are the radiative dipole matrix elements), which defines the ratio of the gain in the system to the loss [3]. For example, an adjustment of the barrier thickness b_1 allows to increase the value of the η parameter two times. Next the lifetime of electrons in the TLS was maximized. For example, changes of the width L of the lower binding barrier produce abrupt modulations of the electron lifetimes in the TLS because of a resonant nature of the intersubband transitions.

This investigation gives us a rough bottom estimation for the population inversion, i.e. shows the worst case, and allows to get the next parameters of the SLAW: GaAs/$Al_xGa_{1-x}As$ structure with molar fractions of aluminium $x = 0.35$ in the higher barrier U_0 and $x = 0.09$ in the lower barrier U_1. The widths of the quantum wells in the active region h_1=82 Å and $h_2 = 51$ Å were chosen to obtain an energy gap between the ε_3 and ε_2 subbands of about 120 meV for the pumping with a CO_2 laser and ε_2 and ε_1 separation close to the LO phonon energy $\hbar\omega_{\mathrm{LO}} \approx 36$ meV.

However, to obtain the exact value of the population inversion we must study a BLS population that depends on a rate of electron transitions (also from the quasi-continuous states) to this subband.

2. Population inversion in laser on asymmetric quantum wells

The quasi-continuous states are mostly placed exactly between the TLS and BLS. So a situation seems to be desperate. Nevertheless, a feature of this thoroughly designed structure is just the finite width L of the lower binding barrier. That is why electrons have got only a few intermediate states on their path from the TLS to BLS.

The predominated channel for the nonradiative electron energy dissipation in SLAW is the optical phonon emanation. Due to the fixed energy of the optical phonon, the quasi-continuous states, which are located below the TLS at the distance less than the $\hbar\omega_{\mathrm{LO}}$, are inaccessible. Similarly, the BLS is inaccessible from the states which are located nearer than the $\hbar\omega_{\mathrm{LO}}$ above this state. Thus, only a narrow band $(\varepsilon_3 - \varepsilon_2) - 2\hbar\omega_{\mathrm{LO}} \sim 15$ meV contains the dangerous intermediate states. It is very important that the width of the *dangerous band* is smaller than the optical phonon energy. So any transitions between

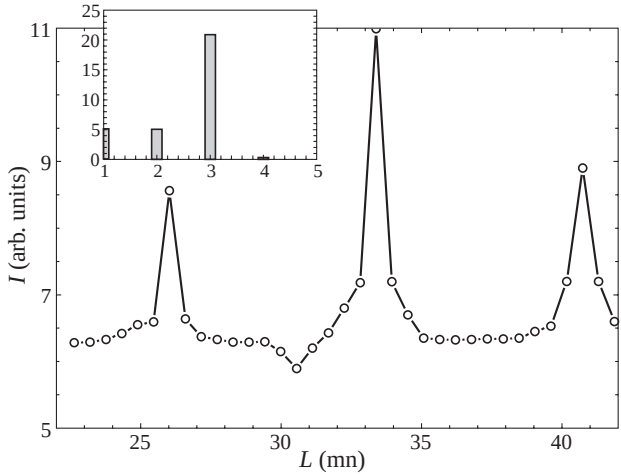

Fig. 2. The I population inversion value as a function of the L width of the lower binding barrier for the unipolar semiconductor laser. The inset shows the arbitrary population of the quasi-continuous states by the $L = 33.4$ nm.

the quasi-continuous states inside the dangerous band are impossible and one can consider these states non-interacting.

In fact, there exist following channels for the electron transitions from the TLS to BLS. First, an electron can leap down to the BLS directly. This process is characterized by the τ_{32} relaxation time. In any cases this time must be as large as possible in order to increase the $I_{\max}$ value. Another possibility is the electron transition to a j quasi-continuous state with the τ_{3j} relaxation time. Afterward, there are three ways.

(a) If the host subband hold its minimum in the dangerous band then an electron can go down to the bottom and wait for the transition to the BLS during the τ_{j2} time. Only the one subband usually fulfil this condition and this subband can be removed from dangerous band with the appropriate choice of the SLAW structure.

(b) If the host subband hold its minimum outside the dangerous band then an electron can slowly go down through this band due to the intraband relaxation. On this path electron can perform an interband transition to the BLS with the τ_{j2} time.

(c) Finally, an electron just can leave the dangerous band due to either the intraband relaxation after the τ_0 time or the interband transition to the another i quasi-continuous states during the τ_{ji} time. In the both cases there exist only the way to the reservoir.

These facts form the backgrounds of our phenomenological model. This model has an analytical solution and gives us the next expression for the population inversion:

$$I = I_{\max}\Big(1 + \sum_{j\in L} \frac{\tau_{32}}{\tau_{3j}} \frac{\tau_j}{\tau_{j2}}\Big)^{-1}, \qquad \tau_j^{-1} = \tau_{j2}^{-1} + \tau_0^{-1} + \sum_{i\in L} \tau_{ji}^{-1}. \tag{3}$$

It is evident from the (3) that the highest value of the population inversion is the $I_{\max}$ as before in the (1). The destructive effect of the each j quasi-continuous state depends on the ratio of the τ_j electron lifetime in the dangerous band to the τ_{j2} transition time to the BLS. Thus, to decrease the influence of the quasi-continuous states to the population

inversion value we have to accelerate first of all the electron departure from the dangerous band.

Results of numerical calculation the population inversion value for the case of the fast intraband electron relaxation is shown in Fig. 1.

Acknowledgements

This work was supported in part by the Russian Foundation for Basic Research, Russian Programme 'Physics of Solid State Nanostructures' and the Federal Programme 'Integration'.

References

[1] V. F. Elesin, A. V. Tsukanov, V. V. Kapaev and Yu. V. Kopaev, *JETP Lett.* **66**, 742 (1997).
[2] Yu. A. Aleshchenko, V. V. Kapaev, Yu. V. Kopaev and N. V. Kornyakov, *Nanotechnology* **11**, 206 (2000).
[3] O. Gauthier-Lafaye, S. Sauvage, P. Boucard, F. H. Julien, F. Glotin, R. Prazeres, J.-M. Ortega, V. Thierry-Mieg and R. Planel, *J. Appl. Phys.* **83**, 2920 (1998).

9th Int. Symp. "Nanostructures: Physics and Technology"
St Petersburg, Russia, June 18–22, 2001

Quantum-well curved-grating DBR laser structure

G. S. Sokolovskii†, E. U. Rafailov‡, A. G. Deryagin†, V. I. Kuchinskii†,
D. J. L. Birkin‡ and W. Sibbett‡
† Ioffe Physico-Technical Institute, St Petersburg, Russia
‡ School of Physics and Astronomy, University of St Andrews,
North Haugh, St. Andrews, Fife KY16 9SS UK

Abstract. Theoretical investigation of the separate confinement single/multi quantum-well DBR laser with "curved-groove" diffraction gratings (c-DBR) is presented. Our calculations show that the proposed laser design provides both spectral selectivity of conventional DBR resonator and output beam focusing in the plane of p-n-junction. A comparison of the c-DBR and the c-DFB laser designs is also presented.

Recent advances in the technology of optoelectronic devices based on nano-sized heterostructures are opening up interesting avenues for research and enabling a wide range of new applications for laser diodes, notably in fields such as telecommunications and photomedicine. However, for most of these applications high-power single-frequency laser diodes with spatially controllable emission are required.

One approach to addressing this objective involving the design of a distributed feedback laser with a "curved-groove" diffraction grating (c-DFB) has already been introduced [1]. The use of a curved grating enables the combination of the high-power of a broad stripe device and spectral control provided by a diffraction grating together with output beam focusing in the plane of p-n-junction [2]. The main disadvantage of the distributed feedback structures is the requirement of subsequent regrowth of the grating structure within the pumping area. This additional technological process usually causes an increase in the internal losses and affects dramatically the yield of useful devices.

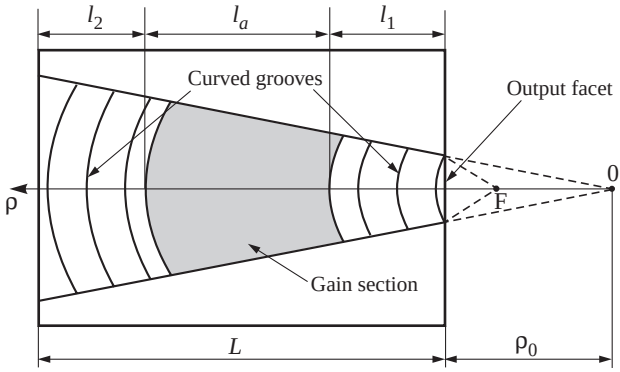

Fig. 1. A simplified schematic of the c-DBR laser.

To simplify the fabrication process required to produce the curved-grating laser diode a new type device is proposed. In this paper we describe a novel type of distributed Bragg reflector laser having a "curved-groove" diffraction grating (c-DBR). Figure 1 is a simplified schematic of such a c-DBR laser. This device also has the advantage of decreased internal

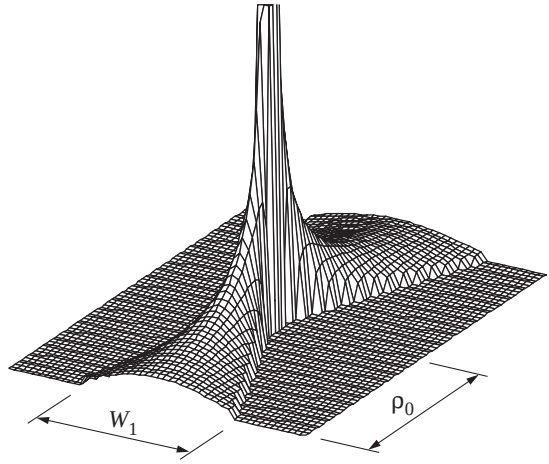

Fig. 2. The modelled performance of the c-DBR laser.

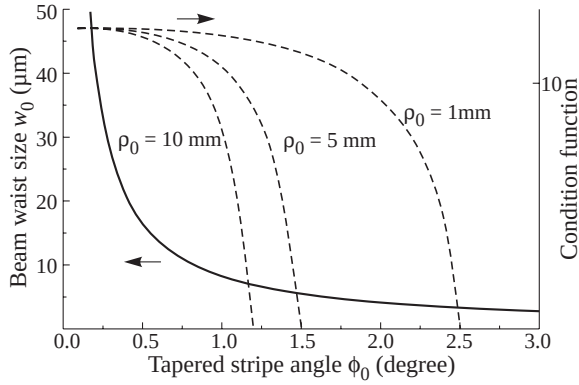

Fig. 3. Beam waist size w_0 versus the angular aperture ϕ_0 of the c-DBR laser in quasi-paraxial approximation (solid line). This quasi-paraxial condition is satisfied when the condition function (dashed line) is positive.

losses due to the replacement of the curved grating from the pumping area to the passive edge regions.

A diffraction grating with curved-grooves can be designed to concentrate the output emission to the focus determined by the curvature of the grating. Figure 2 shows the calculated far-field distribution in the plane of p-n-junction of a c-DBR laser for a single transverse mode operation. Laser beam focusing in the direction orthogonal to the plane of the p-n-junction can be obtained by the cylindrical lens mounted on the laser heat-sink. A comparison of the c-DBR and the c-DFB laser designs shows that the c-DBR laser offers the practical advantages of (i) simplified technology compared to c-DFB and (ii) improved "flexibility" of the design. This thus permits the laser to have beam properties that are compatible with different applications: In particular, the beam waist size external to the facet is significantly smaller than the emission aperture and the beam can be focused at a controllable distance from the exit facet without additional optics. A short focal length

is for example suitable for efficient optical coupling to a single-mode fibre or long focal length for pumping of gain or nonlinear crystals.

In summary, we have proposed a novel construction for a DBR laser having a “curved-groove” diffraction grating. The theoretical analysis shows that a laser with this novel construction can combine both the high-power of a broad stripe device and the spectral control provided by a diffraction grating together with exploitable beam focusing in the plane of p-n-junction.

References

[1] G. S. Sokolovskii, E. U. Rafailov, D. J. L. Birkin and W. Sibbett, *J. Opt. Quantum Electron.* **31**, 215 (1999).

[2] G. S. Sokolovskii, E. U. Rafailov, D. J. L. Birkin and W. Sibbett, *IEEE J. Quantum Electron.* **36**, 1412 (2000).

9th Int. Symp. "Nanostructures: Physics and Technology"
St Petersburg, Russia, June 18–22, 2001

Enhanced probabilities of phonon-assisted optical transitions in semiconductor quantum dots

J. T. Devreese[1]
Theoretische Fysica van de Vaste Stof, Universiteit Antwerpen (UIA&RUCA)
c/o Universiteitsplein 1, B-2610 Antwerpen, Belgium
Technische Universiteit Eindhoven, P.O. Box 513, 5600 MB Eindhoven,
The Netherlands

Abstract. A theory of phonon-assisted optical transitions in semiconductor quantum dots is developed which takes into account non-adiabaticity of the exciton-phonon system. The role of non-adiabaticity is shown to be of paramount importance in spherical quantum dots, where the lowest one-exciton state can be degenerate or quasi-degenerate. In quantum dots of lower symmetry, the effects of non-adiabaticity reveal themselves mainly due to the phonon-induced mixing of states, which belong to different energy levels. Our approach is applied to explain the optical spectra of several quantum-dot structures: ensembles of spherical CdSe, $CdSe_xS_{1-x}$ and PbS quantum dots, self-assembled InAs/GaAs and CdSe/ZnSe quantum dots, brick-shaped InAs/GaAs quantum dots.

Introduction

The interest in the optical properties of quantum dots is continuously growing because of the great prospects of these structures for optoelectronic applications. Numerous experiments, e. g., recent measurements [1–5] of photoluminescence of self-assembled InAs/GaAs quantum dots reveal a remarkably high probability of the phonon-assisted transitions. Attempts to interpret some of these experiments on the basis of the adiabatic theory meet considerable difficulties. Thus, for spherical CdSe quantum dots, the Huang-Rhys parameter S takes values, which appear to be significantly (by one or two orders of magnitude) smaller than the so-called experimental values of the Huang-Rhys parameter, $S_{\rm exp}$, derived from the ratio of the measured intensities of the phonon satellites. In the framework of the adiabatic approach, various mechanisms, which ensure separation of the electron and hole pair in space [3, 6, 7], are commonly considered as a possible origin for the increased Huang-Rhys parameter. We show that the proposed non-adiabatic treatment of phonon-assisted optical transitions can provide an explanation for the remarkably high intensities of phonon satellites observed in the photoluminescence and Raman spectra of various quantum-dot structures.

1. Photoluminescence spectra of quantum dots

The adiabatic approach [8, 9] supposes that (i) both the initial and final state for a quantum transition are non-degenerate, (ii) energy differences between the electron (exciton) states are much larger than the phonon energies. We have revealed, that these conditions are often violated for optical transitions in quantum dots. In other words, we emphasize, that the exciton-phonon system in a quantum dot can be essentially *non-adiabatic*. There can

[1] In collaboration with V. M. Fomin, V. N. Gladilin, E. P. Pokatilov, S. N. Klimin, and S. N. Balaban

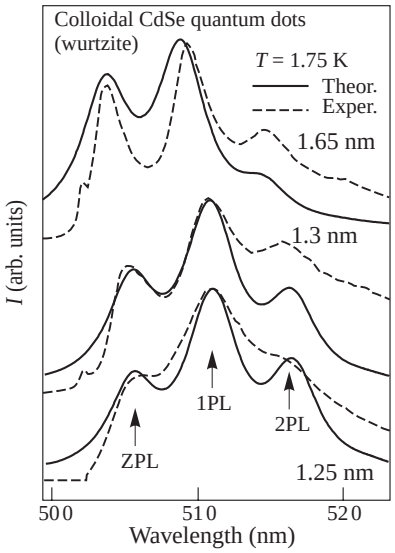

Fig. 1. Fluorescence spectra of spherical CdSe quantum dots with wurtzite structure at various average radii $\langle R \rangle$. Dashed curves represent the experimental data [11]. Solid curves are calculated within non-adiabatic approach (see Ref. [12]).

be two cases: the interaction of an exciton in a degenerate state with phonons results in *internal non-adiabaticity* (the proper Jahn–Teller effect), while the existence of exciton levels separated by an energy comparable with the LO-phonon energy leads to *external non-adiabaticity* (the pseudo Jahn–Teller effect) [10].

In Figure 1, we show the photoluminescence spectra of spherical CdSe quantum dots with various average radii. For the measured K-phonon-peak intensities, I_K, the ratios I_1/I_0 and $2I_2/I_1$ obviously differ from each other. In other words, the observed phonon-peak intensities obey a serial low, which significantly deviates from the Franck–Condon progression. Solid curves in Fig. 1 represent the photoluminescence spectra calculated within the non-adiabatic approach developed in Ref. [12]. As seen from Fig. 1, taking into consideration the effects of non-adiabaticity provides an adequate description of the observed phonon-peak intensities as well as their dependence on the size of quantum dots.

As shown in Ref. [12], the photoluminescence spectra of quantum dots can be strongly affected by the processes of phonon emission in the course of absorption of the exciting radiation. In Ref. [13] we have calculated the optical spectra of brick-shaped InAs/GaAs quantum dots created by AFM-mediated local anodic oxidation. For ensembles of those quantum dots with relatively narrow size distributions, the aforementioned processes appear to provide a dominant contribution to the intensities of phonon satellites in the spectra of resonant photoluminescence.

Figure 2 illustrates the crucial role of the non-adiabaticity effects on the phonon-assisted light absorption by InAs/GaAs self-assembled quantum dots. We have modeled the quantum-dot structure by an InAs cylinder of height h and radius R embedded into GaAs. The absorption spectrum is calculated taking into account the four lowest energy levels of an electron-hole pair. The results shown in Fig. 2 imply that, due to the effects of non-adiabaticity, a significant enhancement of phonon-satellites intensities must occur also in photoluminescence spectra of self-assembled quantum dots.

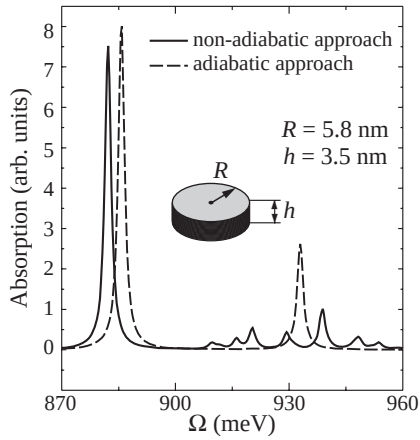

Fig. 2. The absorption spectra of a cylindrical InAs quantum dot calculated within the adiabatic and non-adiabatic approaches.

The triplet structure of the first phonon replica, recently observed in the photoluminescence spectra of self-assembled CdSe/ZnSe quantum dots structures [14], is interpreted [15] in terms of resonant relaxation of excitons with participation of optical phonons. The optical-phonon modes specific to these nanostructures are: (i) CdSe-like modes confined to the quantum dot, (ii) spatially extended CdSe-like and ZnSe-like modes. In Figure 3, our theoretical results for the phonon-assisted photoluminescence spectra are shown for two ensembles of cylindrical CdSe quantum dots. Within each ensemble, the quantum dots have a fixed height h and various diameters d. Three most pronounced peaks, which belong to the first phonon replica in the measured photoluminescence spectra of CdSe quantum dots [14], can be attributed to spatially extended ZnSe-like phonon modes, to localized CdSe-like modes and to spatially extended CdSe-like modes (in order of increasing detec-

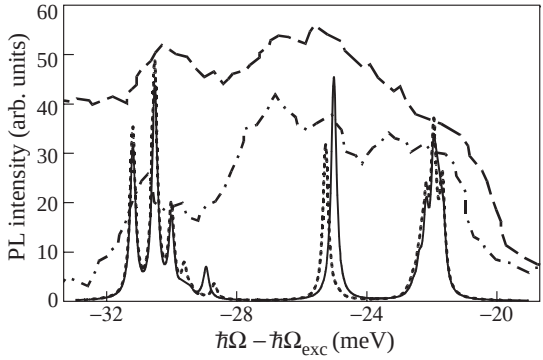

Fig. 3. Photoluminescence spectra [15] of CdSe quantum dots with height $h = 2$ nm (solid curve) and $h = 1.8$ nm (dotted curve) on a 2ML remnant layer, as calculated within the present theory, compared to the experimental data for a CdSe quantum dot structure formed by thermally activated surface reorganization of an initially uniform 3 ML CdSe film (after Lowisch *et al.* [14]). The dashed and dash-dot curves correspond to the excitation energies $\hbar\Omega_{\rm exc} = 2.495$ eV and $\hbar\Omega_{\rm exc} = 2.465$ eV, respectively. For clarity, the experimental spectra have been shifted along the ordinate.

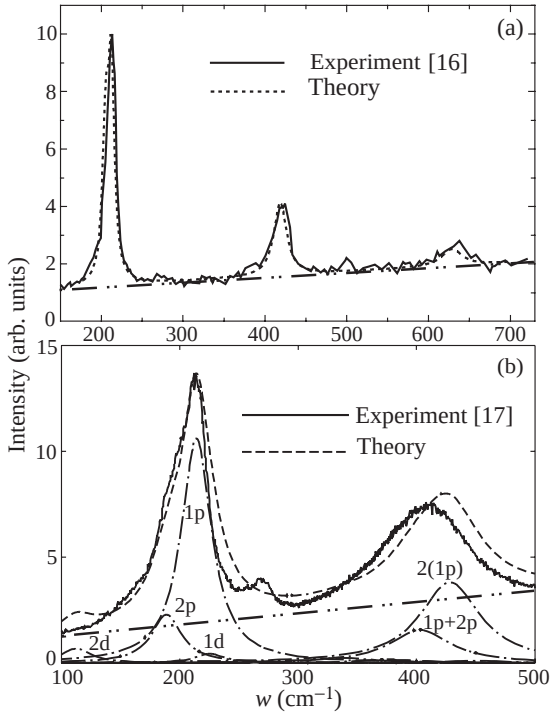

Fig. 4. Resonant Raman scattering spectra of an ensemble of CdSe quantum dots with average radius 2 nm (panel *a*) and of PbS quantum dots with average radius 1.5 nm (panel *b*). The dash-dot-dot curves show the luminescence background. The dash-dot curves in panel *b* indicate contributions of phonon modes (classified in analogy with electron states in a hydrogen atom) into the Raman spectrum.

tion energy $\hbar\Omega$). The calculated positions and the relative heights of the peaks induced by spatially extended ZnSe- and CdSe-like phonon modes are in a fair agreement with the experimental data [14]. The experimental peaks, which can be related to localized phonons, are characterized by a rather large frequency spread when compared with the theoretically calculated peaks. This may be due to inhomogeneous strain distribution as well as to fluctuations of the chemical composition in the experimental samples.

2. Raman scattering in quantum dots

Since the electron-phonon coupling constant α in the quantum dots under consideration is relatively small ($\alpha < 1$), the K-phonon Raman scattering intensity, corresponding to a definite combinatorial frequency $\sum_{j=1}^{K} \omega_{\nu_j}$, can be analyzed to the lowest (K-th) order in α. The scattering intensity is then expressed through a squared modulus of the scattering amplitude:

$$F_K^{(\pm)}(\nu_1, \ldots, \nu_K) = \sum\nolimits_{\mu_0,\ldots,\mu_K} \frac{d^I_{\mu_0}\left(d^S_{\mu_K}\right)^*}{\tilde{\omega}_{\mu_0} - \Omega_I + i\tilde{\Gamma}_{\mu_0}}$$

$$\times \prod\nolimits_{j=1}^{K} \langle \mu_j | \hat{\beta}_{\nu_j} | \mu_{j-1} \rangle \left[\tilde{\omega}_{\mu_j} - \Omega_I \pm \sum_{k=1}^{j} \left(\omega_{\nu_k} \pm i\Gamma_{\nu_k} \right) + i\tilde{\Gamma}_{\mu_j} \right]^{-1}.$$

Here $\tilde{\omega}_\mu$ is the transition frequency and $d_\mu^{I(S)} \equiv \langle\mu|\hat{d}^{I(S)}|0\rangle$ is the dipole matrix element for a transition from the exciton vacuum to the eigenstate $|\mu\rangle$ of the exciton Hamiltonian, $\tilde{\Gamma}_\mu$ is the inverse lifetime of an exciton in the state $|\mu\rangle$, Γ_ν is the inverse lifetime of a phonon of the mode ν. The exciton-phonon interaction amplitude, $\hat{\beta}_\nu = \hat{\gamma}_\nu(\mathbf{r}_e) - \hat{\gamma}_\nu(\mathbf{r}_h)$, is determined by the amplitudes of the electron-phonon and hole-phonon interaction. $\mathbf{r}_e$ and $\mathbf{r}_h$ are the coordinates of an electron and of a hole, respectively. It is worth noting, that the above equation is not based on the adiabatic approximation and takes into account both the Jahn–Teller and pseudo-Jahn–Teller effects. The calculated by us Raman spectra for CdSe and PbS quantum dots (see Fig. 4) show an excellent agreement with experimental results [16, 17].

The effects of non-adiabaticity result in selection rules for the Raman scattering, which differ essentially from those derived within the adiabatic approximation. Owing to a considerable LO-phonon dispersion in the bulk material, Raman peaks are easily identified. The main contribution into both fundamental and overtone bands is due to $1p$- and $2p$-phonons, while the adiabatic approach would imply a domination of peaks corresponding to s-phonons.

Acknowledgements

This work has been supported by the I.U.A.P., GOA BOF UA 2000, F.W.O.-V. projects Nos. G.0287.95, 9.0193.97, G.02774.01.N and the W.O.G. WO.025.99N (Belgium).

References

[1] L. R. Wilson, D. J. Mowbray, M. S. Skolnick, M. Morifuji, M. J. Steer, I. A. Larkin and M. Hopkinson, *Phys. Rev. B* **57**, R2073 (1998).
[2] A. Garcia-Cristobal, A. W. E. Minnaert, V. M. Fomin, J. T. Devreese, A. Yu. Silov, J. E. M. Haverkort and J. H. Wolter, *Phys. Stat. Sol. (b)* **215**, 331 (1999).
[3] R. Heitz, I. Mukhametzhanov, O. Stier, A. Madhukar and D. Bimberg, *Phys. Rev. Letters* **83**, 4654 (1999).
[4] M. Bissiri, G. Baldassarri Höger von Högersthal, A. S. Bhatti, M. Capizzi, A. Frova, P. Frigeri and S. Franchi, *Phys. Rev. B* **62**, 4642 (2000).
[5] M. Bissiri, M. Capizzi, V. M. Fomin, V. N. Gladilin and J. T. Devreese, *International Conference on Semiconductor Quantum Dots (QD 2000), München, July 31-August 3, 2000*, Abstract Book, p. 189.
[6] S. Nomura and T. Kobayashi, *Phys. Rev. B* **45**, 1305 (1992).
[7] P. W. Fry, I. E. Itskevich, D. J. Mowbray, M. S. Skolnick, J. J. Finley, J. A. Barker, E. P. O'Reilly, L. R. Wilson, I. A. Larkin, P. A. Maksym, M. Al-Knafaji, J. P. R. David, A. G. Cullis, G. Hill and J. C. Clark, *Phys. Rev. Lett.* **84**, 733 (2000).
[8] S. I. Pekar, *Zh. Eksp. Teor. Fiz.* **20**, 267 (1950).
[9] K. Huang and A. Rhys, *Proc. R. Soc. London, Ser. A* **204**, 406 (1950).
[10] I. B. Bersuker and V. Z. Polinger, *Vibronic Interactions in Molecules and Crystals*, Springer, Berlin, 1989.
[11] M. Nirmal, C. B. Murray, D. J. Norris and M. G. Bawendi, *Z. Phys. D* **26**, 361 (1993).
[12] V. M. Fomin, V. N. Gladilin, J. T. Devreese, E. P. Pokatilov, S. N. Balaban and S. N. Klimin, *Phys. Rev. B* **57**, 2415 (1998).
[13] V. M. Fomin, V. N. Gladilin, S. N. Klimin. J. T. Devreese, P. M. Koenraad and J. H. Wolter, *Phys. Rev. B* **61**, R2436 (2000).
[14] M. Lowisch, M. Rabe, F. Kreller and F. Henneberger, *Appl. Phys. Lett.* **74**, 2489 (1999).
[15] V. M. Fomin, S. N. Klimin, V. N. Gladilin and J. T. Devreese, *J. Lumin.* **87-89**, 330 (2000).
[16] M. C. Klein, F. Hache, D. Ricard and C. Flytzanis, *Phys. Rev. B* **42**, 11123 (1990).
[17] T. D. Krauss and F. W. Wise, *Phys. Rev. B* **55**, 9860 (1997).

9th Int. Symp. "Nanostructures: Physics and Technology"
St Petersburg, Russia, June 18–22, 2001

Fine structure of excitons and e–h pairs in GaAs/AlAs superlattices at the X-Γ crossover

N. G. Romanov and P. G. Baranov
Ioffe Physico-Technical Institute, St Petersburg, Russia

Abstract. Optically detected magnetic resonance (ODMR) and level anticrossing spectroscopy was applied to study g-factors and exchange splitting of localized excitonsand e–h pairs at the $X_z-\Gamma$ crossover of the conduction band states in a GaAs/AlAs superlattice with a composition gradient. In the transition region we clearly observed disappearance of type II excitons and appearance of type I excitons. In addition, "intermediate" type-II-like and type-I-like excitons were found by ODMR and LAC. Besides ODMR of excitons with a definite fine structure splitting ODMR ascribed to separately localized electrons and holes with a distribution of exchange splittings was detected.

Introduction

In GaAs/AlAs superlattices (SL) both type II and type I band alignment can be obtained. When a GaAs quantum well (QW) thickness is greater than 36 Å, the lowest-energy subbands of the conduction and valence bands are Γ states in the QW (type-I SL). Below a GaAs thickness of Å and provided that the AlAs thickness is not too small the electron and hole wavefunctions are derived from X states in AlAs and Γ states in GaAs and the SL is of type II. The quantum confinement makes the X valley in AlAs split into two states, i.e., X_z along the growth direction [001] and X_{xy} perpendicular to it. Owing to the competition between confinement and strain effects, the lowest electron state is X_z for AlAs thickness below 70 Å or X_{xy} otherwise. Optical transitions are direct in type I systems. In type II SL the optical transitions are indirect and therefore forbidden. For recombination that creates a heavy hole (HH) with Xz electrons the transitions become weakly allowed due to the $\Gamma-X$ coupling (pseudodirect type II SL).

Type II GaAs/AlAs SL's were widely studied by optically detected magnetic resonance (ODMR) which made it possible to measure directly electron and hole g-factors and exciton exchange splitting [1, 2], to determine the order of the conduction band valleys X_z and X_{xy} from the anisotropy of the electron g-factor [3], and also to use these results for a local diagnostics of SL's [4]. Early ODMR studies of the type II-type I transition [5, 6] were mainly focused on the extreme cases of type II and type I recombination. In these works level-anticrossing (LAC) spectroscopy of type I systems was developed [5–7]. In the present communication we apply ODMR and LAC for a study of the $X-\Gamma$ crossover in GaAs/AlAs SL with a smooth transition from pseudodirect type II to type I SL.

1. Results and discussion

Several MBE-grown GaAs/AlAs SL's were studied but the most important results were obtained on a SL (E913) grown with the spatial gradient of the GaAs/AlAs composition in the SL plane along the sample length: from 20.8 Å/12.2 Å to 22.8 Å/11.2 Å. A smooth transition from a pseudodirect type-II SL ($x = 0$) to type-I SL ($x = 23$ mm) has been evidenced in this sample by the time-resolved luminescence measurements [8] and by

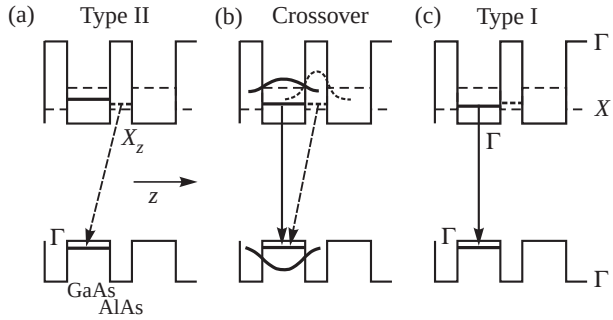

Fig. 1. The valence and conduction band structure together with the recombination transitions for the type II (a), type I (c) and crossover (b) regions of the investigated GaAs/AlAs superlattice with a composition gradient. Narrow lines show energy of Γ(solid lines) and X (dashed lines) states in the bulk materials, thick lines correspond to the superlattice states. In (b), the calculated probability densities of the wavefunctions of electrons and holes in each quantum state are also shown. The axis z is the growth direction.

ODMR and LAC spectroscopy [5–7]. A simplified diagram of the valence and conduction band structure calculated within the envelope wave function approximation using the ECA4 program [9] is shown in Fig. 1 together with the recombination transitions. The energy difference between the X_z and Γ states decreases and reverse its sign, i.e. a $X-\Gamma$ crossover occurs with the change of the GaAs/AlAs composition along the sample. Figure 2 shows the experimental dependences of circularly polarised luminescence on the magnetic field measured at different positions of the excitation spot on the sample with 35 GHz microwaves applied. Luminescence was excited far above the bandgap and detected within the zero-

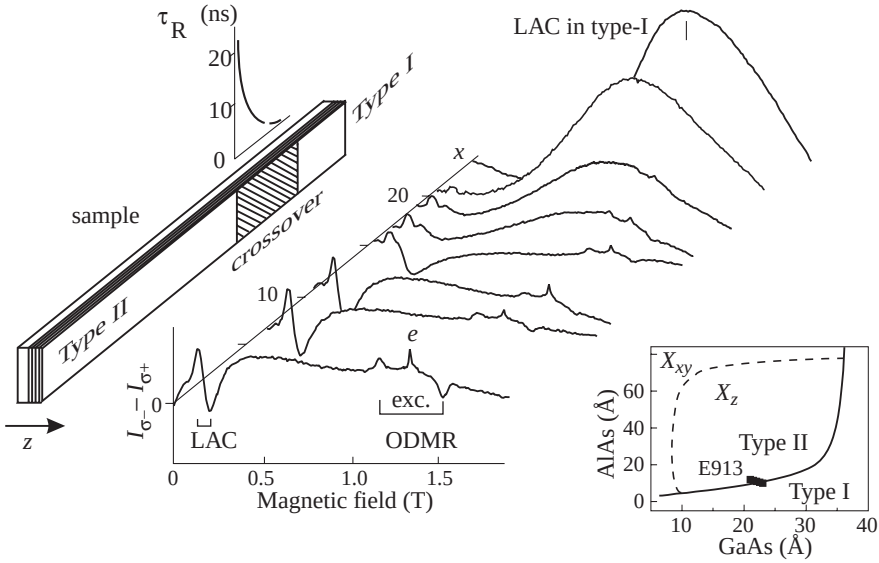

Fig. 2. 35 GHz ODMR and LAC measured as variations of the circular polarization of luminescence at different positions of the excitation spot on the GaAs/AlAs SL (sample E913) with a smooth transition from type II to type I. Inset shows the position of the investigated sample in the map displaying the boundary between type II and type I SL. $T = 1.6$ K. $B \parallel [001]$.

phonon luminescence line. The location of the sample E913 in the map displaying the boundary between type II and type I SL is shown in the insert.

In Fig. 2 resonance signals at 1–1.5 T are due to the microwave-induced EPR transitions between the exciton levels and those of the electrons in e–h pairs. In many cases ODMR of holes was also observed with smaller intensity because for holes the EPR transitions are forbidden and relaxation is much faster. One can see that ODMR disappears in the crossover region ($x = 15{-}20$ mm) where τ_R decreases from the μs range down to 0.3 ns. In addition to the ODMR, resonance signals produced by the state mixing at anticrossing of optically allowed and forbidden exciton levels are seen in Fig. 2. LAC's do not depend on microwaves and can be observed even for very short lifetimes.

The experimental spectra in a wider field range are shown in Fig. 3. At the type II side of the sample one kind of excitons is observed both by ODMR and LAC. For type I side only LAC can be detected for excitons with about an order of magnitude higher exchange splitting Δ [5–7]. Since the $X{-}\Gamma$ mixing is proportional to $1/(E_X - E_\Gamma)^2$ it strongly increases in the transition region and new type-II-like and type-I-like excitons appear with the parameters different from the type II and type I excitons ((1) and (2) in Fig. 3).

For type-II-like excitons ODMR is not is detected because of shorter τ_R and the lines of LAC are broadened.

The isotropic exchange splitting $\Delta = 21\,\mu$eV, i.e. larger than $\Delta = 13.3\,\mu$eV for type II excitons in this region, $g_{h\parallel} = 2.4$, $g_e = 1.8$. For type-I-like excitons the parameters $\Delta = 140\,\mu$eV, $g_{h\parallel} = 2.4$, $g_e = 1.05$ are close to $\Delta = 170\,\mu$eV, $g_{h\parallel} = 2.4$, $g_e = 0.9$ for

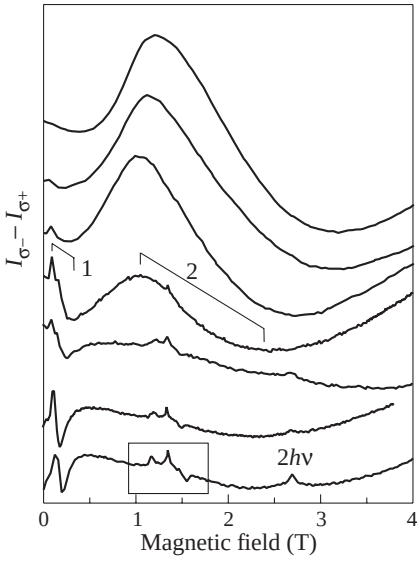

Fig. 3. Disappearance of the characteristic ODMR and LAC of HH–X_z type II excitons and appearance of LAC of HH–Γ type I excitons at the $X{-}\Gamma$ crossover. (1) and (2) mark the positions of the type-II-like and type-I-like excitons. The spectra were taken at $x = 0$, 8, 15, 17, 19, 21, and 23 mm in SL E913 (from bottom to top).

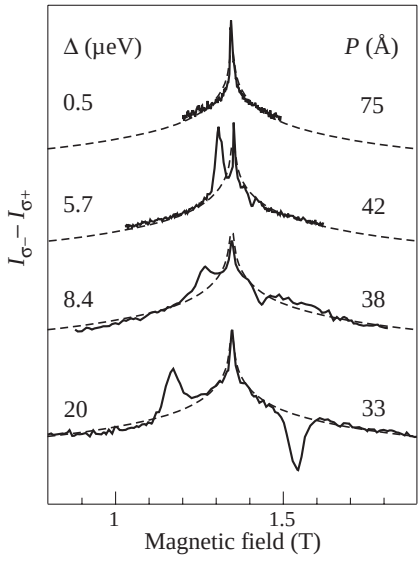

Fig. 4. Coexistence of ODMR originating from type II excitons with a definite exchange splitting D and ODMR of e–h pairs with a distribution of interpair separations in different type II GaAs/AlAs SL's with a period P. The dashed line is calculated for a random distribution of e and h localized in the SL plane. $\nu = 35$ GHz. $B \parallel [001]$.

type I excitons at $x = 23$ mm. At the crossover recombination is determined by an interplay of the recombination rates and probability for the electron to be at the X_z or Γ level. The HH–Γ recombination is faster, therefore coexistence of type-II-like and type-I-like excitons is possible only for X_z below Γ.

Besides the exciton ODMR (" exc." in Fig. 2), broad ODMR signals are seen in Fig. 2 and 3 with $g = 1.88$ corresponding the X_z electrons in AlAs. This ODMR in E913 is shown in the bottom of Fig. 4 in which ODMR recorded in other SL's with different periods P is represented. It is seen that the splitting between the exciton ODMR lines strongly depends on the SL period whereas the shape of the broad ODMR signal does not vary and is period independent in the first approximation. For some SL's we observed similar ODMR of holes. For excitons the splitting of the ODMR lines is proportional to Δ which has a definite value for each SL [3, 7]. Observation of the same shape of the broad electron signal by multiquantum ODMR (the effective frequencies 35, 70, 105 GHz) proves that the broadening is determined by a spreading of the zero-field (i.e. exchange) splittings rather than the g-factors. This implies an existence of e–h recombination of the electrons in AlAs and holes in GaAs which may be localized by the interface roughness potential. Dashed line in Fig. 4 shows the result of calculations for a random distribution of thermalised e–h pairs in the SL plane. For the excitons which are localised as a whole the e–h separation is mainly determined by the SL period. In the $X_z - \Gamma$ transition region ODMR of electrons is seen even after the disappearance of the type-II excitons probably due to longer e–h recombination times.

Acknowledgements

We are indebted to P. Lavallard, C. Gourdon, and R. Planel for supplying some samples and fruitful discussions. This work was supported in part by the Russian Foundation for Basic Research (grant 00-02-16950) and the PSSN program (grant 99-3012).

References

[1] H. W. van Kesteren, E. C. Cosman, W. A. J. A. van der Pool and C. T. Foxon, *Phys. Rev.* **B41**, 5283 (1990).
[2] P. G. Baranov, I. V. Mashkov, N. G. Romanov, P. Lavallard and R. Planel, *Solid State Commun.* **87**, 649 (1993)
[3] H. W. van Kesteren, E. C. Cosman, P. Dawson, K. M. Moore and C. T. Foxon, *Phys. Rev.* **B39**, 13 426 (1989).
[4] P. G. Baranov, N. G. Romanov and I. V. Mashkov, *Phys Solid State.* **37,** 1648 (1995).
[5] N. G. Romanov, I. V. Mashkov, P. G. Baranov, P. Lavallard and R. Planel, *JETP Lett.* **57**, 802 (1993).
[6] N. G. Romanov, P. G. Baranov, I. V. Mashkov, P. Lavallard and R. Planel, *Solid State Electron.* **37**, 911 (1994).
[7] P. G. Baranov and N. G. Romanov, *The Physics of Semiconductors* ed. J. Lockwood (World Scientific, 1994) v. 2, p. 1400
[8] C. Gourdon and P. Lavallard, *Phys. Rev.* **B 46**, 4644 (1992).
[9] R. Teissier, *Thèse de Doctorat*, Université Paris VI (1992).

9th Int. Symp. "Nanostructures: Physics and Technology"
St Petersburg, Russia, June 18–22, 2001

Localized excitons in random and partly phase separated solid solutions: evidence of fractal structure of islands

A. Reznitsky‡, A. Klochikhin†,‡, L. Tenishev‡, *S. Permogorov*‡, S. Sorokin‡, S. Ivanov‡, W. Lundin‡, A. Usikov‡, E. Kurtz§, H. Kalt§ and C. Klingshirn§
‡ Ioffe Physico-Technical Institute, St Petersburg, Russia
† Petersburg Institute of Nuclear Physics, Russian Academy of Sciences, Gatchina, 188350, St Petersburg, Russia,
§ Institut für Angewandte Physik, Universität Karlsruhe, 76128 Karlsruhe, Germany

Abstract. Temperature dependence of photoluminescence (PL) spectra of MBE grown ZnSe/CdSe/ZnSe QWs with 0.3–1.5 ML nominal CdSe thicknesses as well as MOCVD grown double heterostructures (DHS) GaN/InGaN/GaN with In content in the range 0.004–0.06 within the temperature interval 2–300 K has been studied. Much in common has been found in the PL band temperature behavior for both systems. Depending on the concentration of the solid solution, the PL band maximum position $\epsilon_{\max}^{PL}(T)$ follows either "normal" or "anomalous" (known as "S-shape") dependence. We consider both dependences in detail and argue that anomalous behavior is caused by the fractal-like structure of the islands.

1. Experimental details and results

We have studied PL and excitation of PL (PLE) spectra of two systems: (i) single quantum wells formed by either MEE cycled deposition of CdSe (by 0.3 ML per cycle) in ZnSe matrices with the following number of cycles: 1, 2, 5, 8 and 10, or MBE grown ZnSe/CdSe/ZnSe QW with nominal CdSe content of 1.5 ML; and (ii) MOCVD grown GaN/InGaN/GaN double heterostructures with a well width and an In content ranging between 50–100 nm and 0.004 and 0.06, respectively (for more growth details see [1, 2]). The 441.6 nm or 325 nm He-Cd laser excitation were used for ZnCdSe and InGaN PL spectra, respectively. PLE spectra were excited by the second monochromator with a Xe-lamp. For both systems we have found that in the small composition range the PL spectra posses a fine structure, attributed to the exciton localization by clusters of 2 or 3 atoms of the narrow band component. It has been shown that the number of such clusters obeys the random distribution statistics [3, 4]. For Cd content in ZnCdSe more than $5 \cdot 0.3$ ML (which corresponds to $c = 0.15$ in the ZnCdSe QW [5]) as well as for In content exceeding ≈ 0.02 in InGaN solid solutions the PL fine structure is smoothed away and Stokes shifts between PL and PLE spectra is larger than that expected for the random statistics. Thus we can conclude that for more concentrated solid solutions the process of phase separation (or islands formation) starts to develop for the growth conditions used. In Figs. 1 and 2 temperature dependences of PL band maximum position $\epsilon_{\max}^{\mathrm{PL}}(T)$ of ZnCdSe and InGaN solid solutions, diluted (Figs. 1(a), 2(a)) and concentrated (Figs. 1(b,c) and 2(b,c)), respectively, are shown by symbols.

As it is seen in Figs. 1 and 2, for diluted solid solutions the maximum of PL band $\epsilon_{\max}^{\mathrm{PL}}(T)$ follows the temperature dependence which we shall call as "normal" for the reasons explained below: at the temperature increase $\epsilon_{\max}^{\mathrm{PL}}(T)$ shifts toward high energies and then tends to the band gap temperature dependence. At the increase of the narrow gap component

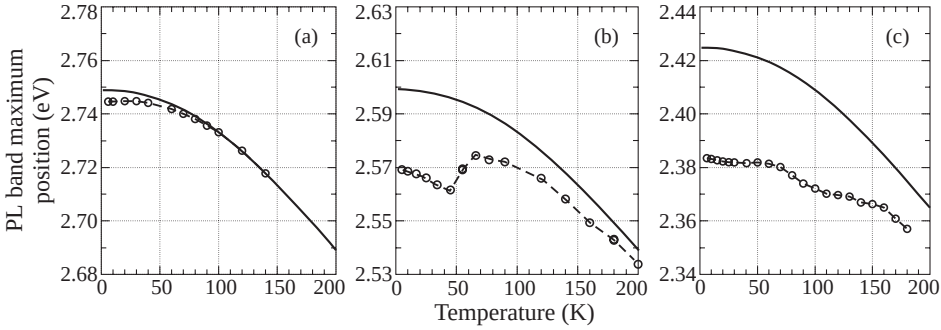

Fig. 1. PL band maximum versus the temperature (symbols) of ZnCdSe QWs with nominal Cd thicknesses 0.6 ML (a), 1.5 ML (b) and 2.4 ML (c). Solid lines — temperature dependence of corresponding PLE maximum.

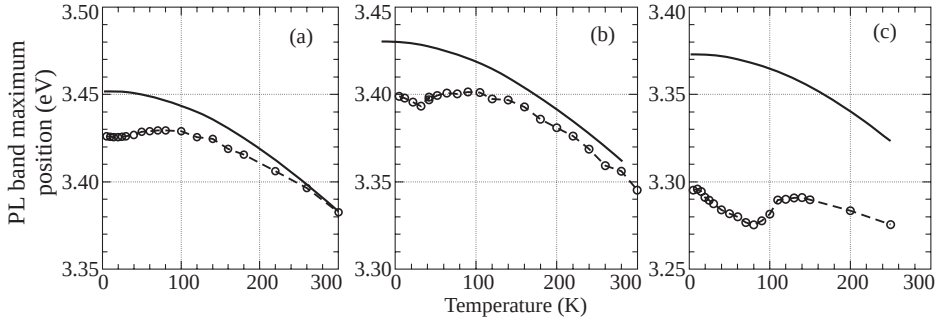

Fig. 2. Similar to that in Fig. 1 but for GaN/InGaN/GaN DHS with In content 0.005 (a), 0.02 (b) and 0.03 (c).

content, when the formation of nanoislands can be expected, the dependence of $\epsilon_{\max}^{\mathrm{PL}}(T)$ becomes "anomalous" (Figs. 1(b,c) and 2(b,c)): as the temperature raises, it shows either minor red shift, which is often wave-like modulated, or exhibits the distinct "S-shape" dependence with the pronounced red shift followed by blue shift and, afterwards, by the red shift again. Similar behavior was found also for more concentrated ZnCdSe QWs [6] and InGaN [7] solid solutions.

2. Discussion

2.1. Band gap temperature dependence

The band gap temperature dependence $E_g(T)$ results from the electron and hole interaction with lattice vibrations [8]. We have found that the dependence $E_g(T)$ for both ZnSe and GaN bulk materials can be well fitted by the sum of two terms proportional to the phonon occupation numbers: the first one with Debye temperature Θ_D of the host lattice and the second with $\Theta_{eff} \approx 0.2\Theta_D$, corresponding to the interaction with optical and acoustical phonons, respectively. In Figs 1 and 2 the obtained dependences for free exciton transitions of ZnSe ($\Theta_D = 340$ K [9]) and GaN ($\Theta_D = 570$ K [10]), shifted to fit the position of corresponding PLE maximum, are shown by solid lines. (For the solid solutions at low concentration the difference between Debye temperature of a wide-gap compound and that

of the solid solutions can be neglected). It is worth to note that the difference in the electron-phonon interaction of localized and free excitons can result in some difference in the thermal shift for localized excitons and in $E_g(T)$, but usually this difference is negligible.

2.2. Normal and anomalous temperature dependence of localized exciton PL band

Temperature shift of the localized exciton PL band maximum $\epsilon_{\max}^{\mathrm{PL}}(T)$ is determined by two causes: band gap dependence $E_g(T)$ and population of the excited states of super-clusters, which at low temperature relaxes nonradiatively to the ground states [4]. The latter factor leads to the blue shift of the PL band maximum until it reaches the position of the absorption band maximum. Then $\epsilon_{\max}^{\mathrm{PL}}(T)$ should follow $E_g(T)$ dependence. Such expected behavior completely agrees with the experimental behavior in the diluted solid solutions (see Figs. 1(a), 2(a)) and we regard this as a normal for random solutions. For more concentrated solutions, when the initial stage of phase separation takes place, the dependence $\epsilon_{\max}^{\mathrm{PL}}(T)$ essentially differs from the normal behavior.

2.3. Metastable electronic states of the island as a cause of anomalous dependence

The red shift of the PL maximum at low temperature indicates that an appreciable part of the radiative states of excitons in nanoislands are metastable rather than the ground ones and can relax to deeper ground states at the temperature increase, provided that at the lowest temperature the rate of nonradiative decay of these states is insufficient for the process to occur. One of the possible scenario of metastable state occurrence is formation of an archipelago consisting of a few slightly overlapping islands. The number of such archipelagos should be large enough to produce a pronounced effect on PL. For the statistical reasons a sufficient number of archipelagos can not arise occasionally as a result of random space distribution of islands due to small concentration of islands. Therefore, the complex archipelago-like islands should be an intrinsic feature of the island structure.

2.4. Diffusion-Limited Aggregations as an origin of metastable states

Some preliminary experiments indicate that thermal annealing of InGaN samples after the growth processes [11] or increasing a growth interruption time before the cap layer deposition in ZnSe/CdSe/ZnSe system [12] affects drastically the number and the composition of islands. These facts give evidence of an important role of the diffusion processes in island formation. Processes of diffusion limited aggregation lead to a complex shape of aggregates with disordered fractal properties ([13]). One of the important features of such aggregates is a multibranch structure with the common center. The most part of atoms are in branches, which are well isolated from each other by distances comparable with the size of branches. This assumption explains the observed PL band temperature dependence. Indeed, every branch of the aggregate can be treated as a separate island which is weakly connected with the others through center part of the fractal. Energy levels of the different branches are randomly distributed over some energy interval due to the random branch configuration. Localization of the exciton by different branches appears to have a comparable probability and the subsequent energy relaxation takes place if an occupied state is not the lowest one.

3. Summary

We have studied temperature dependences of the PL band maximum both in random and inhomogeneous solid solutions with partial phase separation. The arguments has been suggested that the anomalous temperature dependence reflects the fractal form of the islands caused by diffusion limited aggregation.

Acknowledgments

This work was partly supported by Deutsche Forschungsgemeinschaft, INTAS (97-31907), Program “Physics of Solid State Nanostructures” and Russian Foundation for Basic Research.

References

[1] S. Sorokin *et. al., J.Cryst.Growth* **201/202**, 461 (1999).
[2] W. V. Lundin *et.al., phys.stat.sol.(a)* **176**, 379 (1999) .
[3] A. Klochikhin, A. Reznitsky *et. al.*, this volume, p. 554
[4] A. Klochikhin, A. Reznitsky, S. Permogorov *et.al., Phys. Rev. B* **59**, 12947 (1999).
[5] N. Peranio, *et.al., Phys. Rev. B* **61**, 16015 (2000).
[6] S. Wachter *et.al., to be published in phys.stat.sol. (b)* **224** (2001).
[7] A. V. Sakharov *et.al., phys.stat.sol.(b)* **216**, 435 (1999).
[8] L. Vina, S. Logothetidis and M. Cardona, *Phys. Rev. B* **30**, 1979 (1984).
[9] *Landolt-Boernstein: Numerical Data* New Series, **22** (Springer, Berlin, 1989).
[10] J. C. Nipko *et.al., Appl. Phys. Lett.* **73**, 34 (1998).
[11] A. V. Sakharov *et.al., Proc.8-th Intern.Symp. “Nanostructures: Physics and Technology, St. Petersburg, Russia*, p. 216 (2000).
[12] E. Kurtz *et.al., J. Cryst. Growth* **214/215**, 712 (2000).
[13] *Fractals in Physics* ed. L. Pietronero and E. Tesatti, North Holland, 1986

9th Int. Symp. "Nanostructures: Physics and Technology"
St Petersburg, Russia, June 18–22, 2001

Effect of additional illumination on the kinetics of exciton complex formation in the quantum wells of undoped GaAs/AlGaAs structures

N. N. Sibeldin, *M. L. Skorikov* and V. A. Tsvetkov
P. N. Lebedev Physical Institute, Russian Academy of Sciences,
Moscow, Russia

Abstract. Low-temperature ($T = 2$ K) photoluminescence (PL) and photoluminescence excitation (PLE) spectra of GaAs/AlGaAs ($x = 0.05$) structures with shallow quantum wells (QW) and the effect of additional illumination by He–Ne laser radiation on these spectra were investigated. It was found that the PLE spectra exhibit a number of broad bands in the above-barrier energy region; these bands alternate "in opposite phases" in the spectra of free excitons and excitonic complexes (trions) (i.e., an increase in the exciton luminescence intensity is accompanied by a decrease in the luminescence intensity of the complexes). In the case where the photon energy of the Ti-sapphire laser is tuned to excite the QW states, additional illumination results in the shift of the equilibrium in the exciton–trion system towards an increase in the concentration of the latter species. On the other hand, upon excitation into certain barrier states with energy both below and above the barrier band gap, additional illumination shifts the equilibrium in the opposite direction.

Charged three-particle excitonic complexes (trions) in low-dimensional semiconductor structures were actively investigated in the recent years. In particular, it was demonstrated that, in GaAs/AlGaAs structures without intentional doping, negatively or positively charged localized trions can be formed due to the preferential capture of electrons or holes into the quantum wells (QWs), as well as due to the presence of residual impurities in the barrier layers [1–4].

It is of substantial interest to follow the variation of the "molecular composition" of the excitonic system as the photon energy of the exciting radiation is continuously tuned in the range including the band gap of the barrier layers, i.e., under the transition from the excitation into the QWs to the above-barrier excitation. This can be carried out for GaAs/AlGaAs structures with low Al content in the barrier layers.

The structure under study contains two shallow tunneling-isolated GaAs QWs of width 4 and 3 nm, separated by a 60-nm-wide $Al_{0.05}Ga_{0.95}As$ barrier and confined from both sides by 100-nm $Al_{0.05}Ga_{0.95}As$ layers. The band gap in the barrier layers $E_{gb} \simeq 1.6$ eV, and the tuning range of a Ti-sapphire laser (in our case, 1.49–1.77 eV) is sufficient to perform the measurements discussed above. In addition, these structures has a relatively simple energy spectrum (there is just one single-particle quantum-confinement level for each kind of quasiparticles in each QW [5]), which makes data analysis and interpretation more straightforward.

The photoluminescence (PL) spectrum of the narrow QW of the structure under the He–Ne laser excitation (photon energy 1.959 eV) is shown in Fig. 2 (inset, upper curve). The spectrum consists of two lines, the higher-energy one being related to the recombination radiation of the free heavy-hole excitons (FE) and the lower-energy one, to the recombination radiation of the excitonic complexes (EC). The EC and FE PL excitation (PLE) spectra for this QW (recorded with the monochromator output slit fixed at the corresponding PL lines) are shown by solid lines in Figs. 1 and 2, respectively. The shape of the PLE spectra

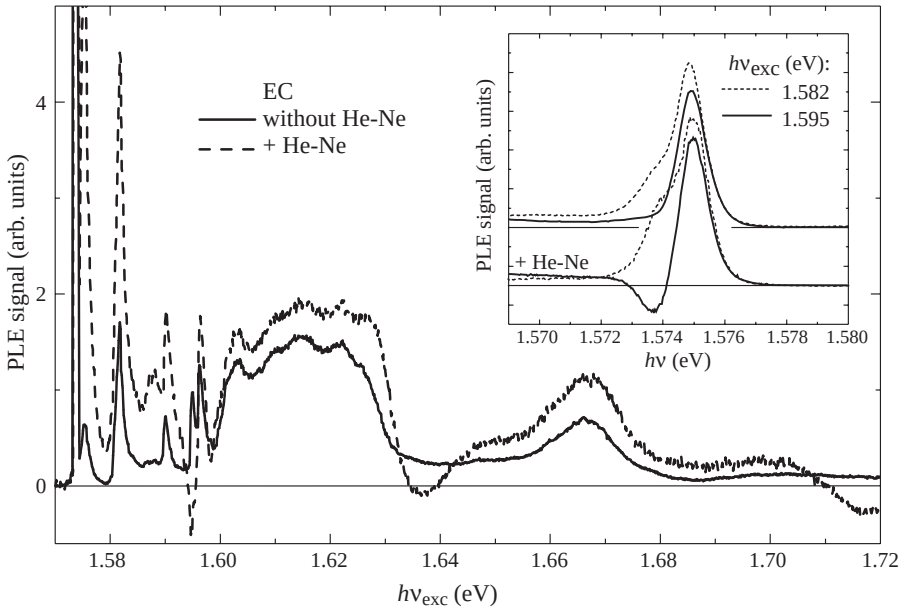

Fig. 1. Excitation spectra of the excitonic complex PL without and with additional illumination by a He-Ne laser. Inset: PL spectra for two excitation photon energies without (upper part) and with (lower part) additional illimination by a He–Ne laser.

of the free excitons and the complexes differ considerably when the photon energy exceeds the barrier band gap E_{gb}: there are broad bands whose position do not coincide in the FE and EC spectra; moreover, the maxima and minima in both curves alternate "in opposite phases", i.e., an increase in the excitonic complex PL intensity is accompanied by a decrease in the PL intensity of the free excitons. Thus, the shape of the QW PL spectrum depends significantly on the photon energy of exciting radiation.

It seems likely that the variation of the luminescence intensity related to the free excitons and excitonic complexes with the energy of exciting photons in the above-barrier spectral region is due to the dependence of the efficiency of the photoexcited charge carrier capture into the QW on their initial energy. The concentration n_T of the excitonic complexes depends on the density n of the electron (or hole) gas and the exciton concentration n_{ex} in the QW ($n_T \sim n_{ex} \cdot n$). Therefore, the efficiency of the excitonic complex formation should increase when the nonequilibrium charge carriers of one sign are preferentially captured into the QW. The energy width of the bands in the EC PLE spectrum (Fig. 1) gives an indication of the charge carrier energy region where such a situation does take place. Under these conditions, the density of the exciton gas in the QW should decrease due to exciton binding into trions.

The density of electron (hole) gas and even the type of the conduction in the QW can be changed by an additional illumination of the sample by the radiation with the photon energy exceeding the band gap in the barrier layers [2, 3]. The effect of the additional illumination of the sample by the He–Ne laser radiation on the PLE spectra of the EC and FE in the narrow QW is shown in Figs. 1 and 2, respectively. When the QW states are excited (the Ti-sapphire laser photon energy $h\nu_{exc} < 1.592$ eV), additional illumination results in an increase of the EC luminescence intensity (Fig. 1), which is accompanied by a decrease

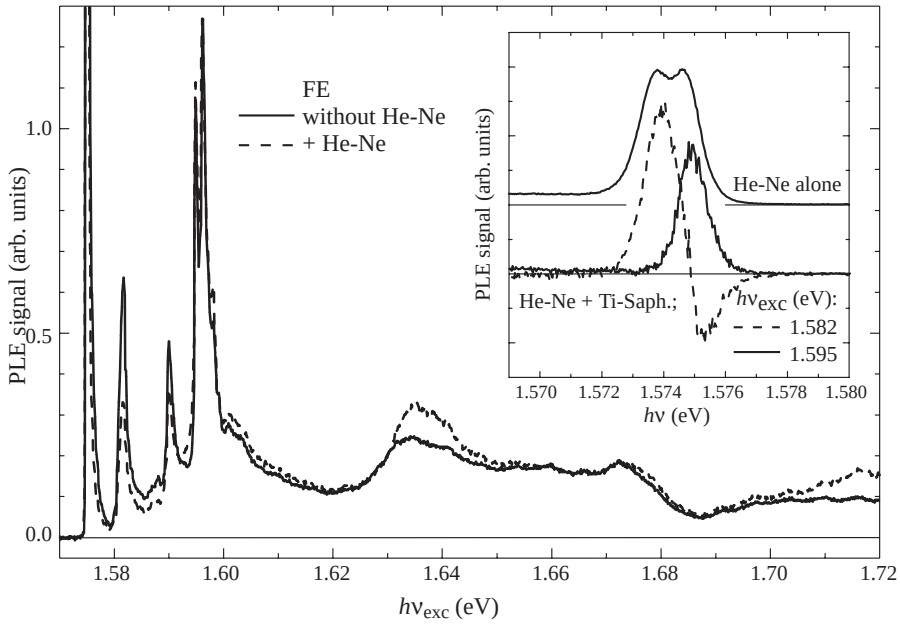

Fig. 2. Excitation spectra of the free exciton PL without and with additional illumination by a He–Ne laser. Inset shows the PL spectra: upper part, lumunescence excited by a He–Ne laser; lower part, differential spectra (see the text) for two excitation photon energies.

of the intensity of the FE luminescence (Fig. 2). A more complicated picture is observed when we excite the above-barrier states or the states with the energies slightly below but close to $E_{\rm gb}$ responsible for the triplet in the PLE spectra at $h\nu_{\rm exc} \simeq 1.592{-}1.599$ eV. While the additional illumination leads to an increase in the intensity of the free-exciton PL in the whole range of excitation photon energies $h\nu_{\rm exc} > 1.592$ eV, the intensity of the PL of excitonic complexes can either increase or decrease. Moreover, at certain values of the excitation photon energy (e.g., $h\nu_{\rm exc} \simeq 1.595$, 1.636 eV etc.) the phase of the photodetector signal changes in such a way that negative signal appears at the output of the lock-in amplifier (Fig. 1). Note that the energy difference between the values of $h\nu_{\rm exc}$ corresponding to the regions of negative signal in the PLE spectra under additional illumination (Fig. 1) is of the order of the optical phonon energy in the barrier layers.

The influence of additional illumination on the radiative recombination processes in the QW, seen in the PLE spectra, is also reflected very clearly in the PL spectra. The PL spectra obtained, like the PLE spectra in Figs. 1 and 2, under the excitation by modulated Ti-sapphire laser radiation and the additional stationary illumination by a He–Ne laser are shown in the inset to Fig. 1. In the case of resonance excitation into the QW light-hole exciton states ($h\nu_{\rm exc} = 1.582$ eV), He–Ne illumination results in enhanced EC luminescence intensity because of an increase in the trion concentration, which takes place due to the binding of the excitons created by the excitation radiation with the nonequlibrium charge carriers in the QW originating from the additional illumination. In the case of excitation into the states corresponding to the low-energy component of the triplet ($h\nu_{\rm exc} = 1.595$ eV), charge carriers of opposite signs are created in the QW by the excitation and the additional-illumination radiation, which leads to a decrease in the stationary concentration of the charge carriers and, thus, of the trions. This brings about the appearance of the negative

signal in the PL and PLE spectra (Fig. 1). Such a behavior of the electron–hole system is also reflected in a something different way in the differential (with respect to the additional illumination intensity) PL spectra recorded under the conditions of stationary excitation by a Ti-sapphire laser and modulated additional illumination (Fig. 2, inset). In this case, the changes in the PL spectra related to the additional illumination are recorded.

The PL and PLE spectra of the wide QW of the structure exhibit similar behavior to that of the narrow QW.

Acknowledgements

We are grateful to B. Etienne, I. P. Kazakov and V. I. Tsekhosh for growing the structures and to N. V. Zamkovets and B. D. Kopylovskii for technical assistance.

This study was supported by the projects of the Russian Foundation for Basic Research (no. 99-02-16367), the Program in Support of the Scientific Schools (no. 00-15-96568), and the Russian Research Programs “Physics of the Solid-State Nanostructures” (no. 97-1050) and “Fundamental Spectroscopy” (no. 08.02.73).

References

[1] J. L. Osborne, A. J. Shields, M. Pepper et al., *Phys. Rev. B* **53**, 13002 (1996).
[2] O. V. Volkov, V. E. Zhitomirskii, I. V. Kukushkin et al, *Pis’ma Zh. Eksp. Teor. Fiz.* **66**, 730 (1997).
[3] O. V. Volkov, V. E. Zhitomirskii, I. V. Kukushkin et al., *Pis’ma Zh. Eksp. Teor. Fiz.* **67**, 707 (1998).
[4] V. B. Timofeev, A. V. Larionov, M. Grassi Alessi et al., *Phys. Rev. B* **60**, 8897 (1999).
[5] E. A. Muljarov, N. N. Sibel’din, M. L. Skorikov et al., *Pis’ma Zh. Eksp. Teor. Fiz.* **70**, 613 (1999).

9th Int. Symp. "Nanostructures: Physics and Technology"
St Petersburg, Russia, June 18–22, 2001

Determination of the minimum island size for full exciton localization due to thickness fluctuations in $Zn_{1-x}Cd_xSe$ quantum wells

P. Diaz-Arencibia and I. Hernandez-Calderon
Physics Department, CINVESTAV, Apdo. Postal 14-740, 07000 Mexico, D.F. Mexico

Abstract. Atomic layer fluctuations of the thickness of quantum wells (QWs) are one of the causes of exciton localization. Here, we present the results of the determination of the minimum lateral dimensions of islands formed by thickness fluctuations in $Zn_{1-x}Cd_xSe$ QWs which produce full exciton localization. We have calculated the localization energy of excitons in the frame of the factorized-envelope approximation. We found that the excitons are well localized in the islands of the QW when their dimensions are larger than ∼15 times the exciton Bohr radius. This result allows us to evaluate the quality of the QW structure and interpret the photoluminescence characteristics of QWs.

Introduction

In ideal QW structures the interfaces are flat planes, free of imperfections. However, in real QWs the interfaces present structural and chemical defects that result in potential fluctuations which alter the motion of the particles within the QW. In high quality QWs these defects result in flat, large area regions of constant thickness, these large regions (that we will call terraces) present differences in thickness of one or two monomolecular layers (ML, 1 ML $= a/2$, where a is the lattice constant). Then, for the case of a high quality QW structure with average thickness $Na/2$, where N is the number of ML, it is normally expected the existence of terraces $(N \pm 1)a/2$ and $(N \pm 2)a/2$ thick and in such a way that QW thickness fluctuations will give place to exciton localization [1]. Since the 1s energy of the exciton localized in an $(N + 1)$-terrace will be lower than the 1s energy of an exciton localized at an N-terrace, at low temperatures and low excitation levels the $(N + 1)$-QWs will be the most populated; $U \equiv E_{1s}(N) - E_{1s}(N + 1)$ is the barrier height that localizes the exciton inside the $(N + 1)$-QW; $E_{1s}(N)$ is the energy of the free 1s exciton in the N-monolayer thick QW. As the temperature raises, the assistance of acoustical phonons makes possible the migration of excitons to the N-terraces. For this process to occur the exciton must overcome the localization energy $\Delta E \leq U$. ΔE may be lower than U when the QW has regions with reduced lateral dimensions L_x, L_y in such a way that confinement effects caused by the comparable spatial extensions of the $(N + 1)$-thick *island* and the wavefunction of the exciton result in the raising of the ground state of the 1s exciton and then a lowering of the localization energy. In other words, additional quantization in the x and y directions (z is perpendicular to the QW plane) reduces the energy that the exciton needs to migrate to the N-thick terrace. Many of the phenomena related to exciton localization and phonon assisted migration can be observed when studying the photoluminescence (PL) vs. temperature characteristics of high quality QWs. The analysis requires a clear identification of the different excitonic emission mechanisms which may be present in the QW PL spectrum [2]. Bound excitons (BX) [3] and biexcitons (BB) [4, 5] have been assigned to optical transitions in the PL spectra of $Zn_{1-x}Cd_xSe$ QWs. In previous papers we have analyzed in detail the mechanisms of exciton localization and exciton migration

as a function of temperature for the case of two structurally different $Zn_{1-x}Cd_xSe$ QWs grown by molecular beam epitaxy (MBE) with different barrier materials [2, 6, 7]. Based on those studies we have made estimates of the relative total area of islands with different thickness, but that analysis does not give information about the area of individual islands [2]. In the following we will present a calculation of the minimum size (L_x, L_y) of an $(N + 1)$ island that is necessary to produce *full* localization of excitons, that is, when $\Delta E \approx U = E_{1s}(N) - E_{1s}(N + 1)$.

1. Theory

The minimum size of an $(N + 1)$-island with full exciton localization can be estimated calculating the 1s energy of the exciton as a function of their lateral dimensions. The $(N + 1)$-island is assumed to be laterally surrounded by a N thick QW and is formed in one of the interfaces while the opposite interface is completely flat. The islands are assumed to have a rectangular shape $L_x \times L_y$ and the energy of the barrier that localizes the exciton in the $(N + 1)$-island is U. The calculations are made using the factorized-envelope approximation described by Gupalov, Ivchenko and Kavokin [8] and references therein. In the case of very large islands or islands with square shape, the 1s state is doubly degenerated, however, the islands will generally be asymmetric, breaking this degeneracy. Then, the ground state of the localized exciton will be denoted by $E_{1s}^{xy}(N + 1)$. We solve the Schrödinger equation for the in-plane envelope function of the exciton $F(X, Y)$, which describes the localization of the 1s exciton as a whole within the island, where X and Y are the components of the in-plane exciton center of mass radius vector $R_\parallel \equiv (X, Y)$ of the localized exciton at the island. If we represent $F(X, Y)$ as a product of separate functions $F_X(X)$ and $F_Y(Y)$, the Schrödinger equation is decomposed in a set of two coupled Hartree equations:

$$\begin{cases} \left[-\frac{\hbar}{2M}\frac{\partial^2}{\partial X^2} - U P_Y \theta\left(\frac{L_x}{2} - |X|\right)\right] \cdot F_X(X) = -\varepsilon_X F_X(X) \\ \left[-\frac{\hbar}{2M}\frac{\partial^2}{\partial Y^2} - U P_X \theta\left(\frac{L_y}{2} - |Y|\right)\right] \cdot F_Y(Y) = -\varepsilon_Y F_Y(Y) \end{cases} \tag{1}$$

Here θ is the step function; $\theta(s \geq 0) = 1, \theta(s < 0) = 0$. The energies ε_X and ε_Y determine the localization energy $\Delta E = \varepsilon_X + \varepsilon_Y - U \cdot P_X \cdot P_Y$; where P_X and P_Y are the coupling factors of Eqs. (1) and are just the particle probability density inside the island:

$$P_X = \int_{-L_x/2}^{L_x/2} F_X^2(X)\mathrm{d}X \quad \text{and} \quad P_Y = \int_{-L_y/2}^{L_y/2} F_Y^2(Y)\mathrm{d}Y \tag{2}$$

$P_X, P_Y < 1$ since the functions $F_X(X)$ and $F_Y(Y)$ extend beyond the potential barriers of the island. The localization energy can be also written as $\Delta E = E_{1s}(N) - E_{1s}^{xy}(N + 1)$. The boundary conditions demand that the envelope functions $F_X(X)$, $F_Y(Y)$ and their derivatives in the directions perpendicular to the sides of the rectangle are continuous on the perimeter of the island.

2. Results and discussion

Calculations were made for two structurally different $Zn_{1-x}Cd_xSe$ QWs [2, 6, 7]. The parameters used in calculation are listed in Table 1.

The results are shown in Fig. 1, the exciton localization energy ΔE is plotted as a function of the dimensions of the island. Each curve represents an island with constant L_y

Table 1. Parameters used in calculations; $M_w = m_e^w + m_{hh}^w$ and $M_B = m_e^B + m_{hh}^B$.

Sample	x	L_w (Å)	E_g (eV)	M_w/m_0	M_B/m_0	U (meV)
A-809	0.69	40	2.028	0.582	0.63	11.7
C-161	0.26	50	2.482	0.612	0.63	8.8

and varying L_x, in terms of integer multiples of the exciton Bohr radius a_B. As can be seen, the localization energy ΔE of the fundamental state $E_{1s}^{x,y}$ approaches U when the dimensions of the sides L_x and L_y of the rectangular island are of the order or larger than 15 times the exciton Bohr radius, i.e, larger than ∼600 Å. This means that the minimum area of the $(N+1)$ island for a full exciton localization is of the order of $3.08 \times 10^{-3}\ \mu\text{m}^2$ and $4.36 \times 10^{-3}\ \mu\text{m}^2$ for samples A-809 and C161, respectively. When one of the sides of the rectangle is less than $15a_B$ the exciton localization energy is less than U. This means that the exciton is not fully localized in the island. The presence of small $(N+1)$-islands (L_x, $L_y < 15a_B$) will lead to contributions in the emission spectrum of the QW at intermediate energies compared to those corresponding to the N-QW and $(N+1)$-islands with L_x, $L_y > 15a_B$. The excitation energy ΔE that the exciton needs to migrate at higher temperatures is then also less than U. The conclusion is that it is necessary for the islands to present dimensions in L_x and L_y much larger than the Bohr radius in order to achieve full localization of excitons. Then, as a consequence, a careful examination of the PL spectrum of a QW can give substantial information about its structural quality, the energy of the emission peaks and their spectral width are directly related to the abundance and size of the islands produced by thickness fluctuations of the QW. Moreover, the PL bands could be not symmetric. Broadening of the PL spectra at the high energy side of the $(N+1)$-QW

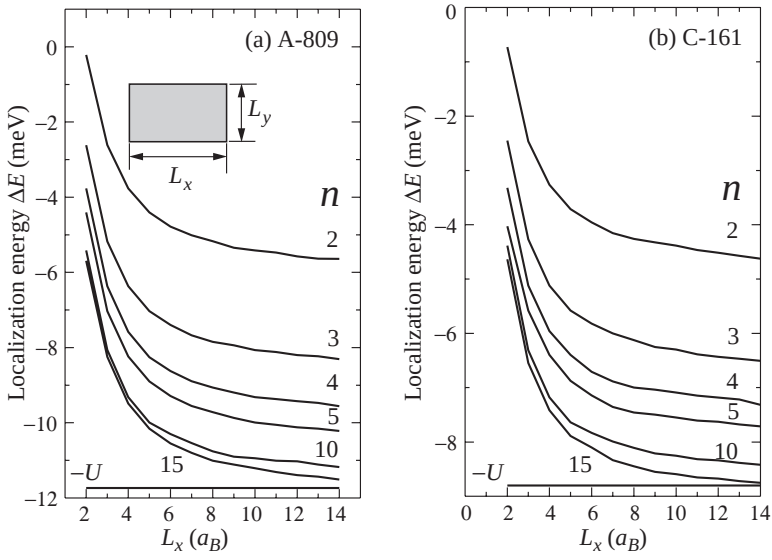

Fig. 1. Localization energy of the fundamental state of excitons localized at $(N+1)$ and $(N+2)$-islands for samples A-809 and C-161, respectively. (a) Sample A-809 $N+1 = 14$, $U = 11.7$ meV. (b) Sample C-161, $N+2 = 19$, $U = 8.8$ meV.

and in the low energy side of the N-QW may appear due to inhomogeneous broadening caused by the size distribution of the $(N+1)$-islands. Examination under this criteria of the PL spectra of the emission of QWs A-809 and C161 allows us to conclude that the main emission peaks correspond to islands with full localization, therefore having lateral dimensions of at least 15 times the Bohr radius of the exciton. The fact that two (symmetric) gaussian lines fit very well the PL emission suggests that those QWs are formed by large terraces, as expected in high quality QWs.

In summary, in the frame of the factorized-envelope approximation we have obtained the localization energy of excitons in II–VI QWs as a function of the lateral dimensions of a $(N+1)$-island within a N-QW. We found that for a full exciton localization ($\Delta E \sim U$) the lateral sizes of the island (L_x, L_y) must be larger than $\sim$15 times the exciton Bohr radius, i.e, L_x, $L_y \gg a_B$. This analysis helps to the interpretation of the excitonic features in the PL spectra and brings information useful to the evaluation of the structural properties of QWs.

References

[1] D. S. Citrin, *Phys. Rev. B* **47**, 3832 (1993).
[2] P. Diaz-Arencibia, I. Hernandez-Calderon, L. M. Hernandez-Ramirez and M. C. Tamargo, *Microelectronics J.* **31**, 443 (2000).
[3] See for example: H. J. Lozykowsky and V. K. Shastri, *J. Appl. Phys* **69**, 3235 (1991): L. Aigouy, B. Gil, O. Briot, T. Cloitre, N. Briot, R. L. Aulombard and M. Averous, *J. Electron. Mat.* **25**, 183 (1996).
[4] Y. Yamada, T. Mishina, Y. Masumoto, Y. Kawakami, S. Yamaguchi, K. Ichino, S. Fujita and T. Taguchi, *Superlatt. & Microstruct.* **15**, 33 (1994).
[5] L. Wang and J. H. Simmons, *Appl. Phys. Lett.* **67**, 1450 (1995).
[6] P. Diaz-Arencibia, I. Hernandez-Calderon, L. M. Hernandez-Ramirez and M. C. Tamargo, *J. Vac. Sci. Technol. B* **18**, 1526 (2000).
[7] P. Diaz-Arencibia, I. Hernandez-Calderon, L. M. Hernandez-Ramirez and M. C. Tamargo, *Phys. Stat. Sol. (b)* **220**, 27 (2000).
[8] S. V. Gupalov, E. L. Ivchenko and A. V. Kavokin, *J. Exp. Theor. Phys.* **86**, 388 (1998).

9th Int. Symp. "Nanostructures: Physics and Technology"
St Petersburg, Russia, June 18–22, 2001

Vertical motional narrowing of exciton-polaritons in GaN based multiple quantum wells

Alexey Kavokin and Guillaume Malpuech
Laboratoire des Sciences et Materiaux pour l'Electronique, et d'Automatique, UMR 6602 du CNRS, Universite Blaise Pascal - Clermont-Ferrand II, 63177 Aubiere Cedex, France

Abstract. Numerical simulation of time-resolved light reflection from GaN/AlGaN single and multi-quantum wells (MQWs) revealed a pronounced vertical motional narrowing effect. This effect consists in reduction of the inhomogeneous broadening of the exciton peaks and increase of the decay-time of the time-resolved reflection due to the averaging of the vertical disorder in the structure by extended exciton–polariton modes. The theory predicts pronounced oscillations in the time-resolved reflection of MQWs resulting from the interference of exciton–polariton modes in the structure.

Random potential fluctuations strongly affect the confined exciton states in GaN/AlGaN and GaN/InGaN quantum wells (QWs) thus reducing the advantages of these structures for opto-electronics applications [1, 2]. The disorder arises mainly due to random polarization fields [3, 4] and is manifested by a huge Stokes-shift and inhomogeneous broadening of the exciton lines. Recently, it has been shown experimentally [5] and theoretically [6] that the radiative coupling between excitons confined in different QWs in multiple quantum well (MQW) structures may reduce effectively the disorder effect on the exciton. This effect known as the vertical motional narrowing (VMN) effect manifests itself in the increase of the decay-time of the time-resolved reflection signal from MQWs as a function of the number of wells. It results from the averaging of the disorder potential in a MQW structure by extended exciton–polariton modes that occupy the entire structure.

Four parameters govern the VMN, namely, the exciton radiative recombination rate, Γ_0, the exciton inhomogeneous broadening, Δ, the spacing between wells, d, and the number of the wells, N. The parameter $\eta\Delta$ is in the range of 10 meV for the best quality MQW structures based on nitrides available now [1, 2]. The exciton oscillator strength in nitrides is an order of magnitude larger than in GaAs, so that $\eta\Gamma_0$ achieves 0.4 meV in GaN/AlGaN QWs [7]. The coincidence of the strong disorder and huge exciton oscillator strength makes us to expect an extremely pronounced VMN effect in nitride-based MQWs.

In this paper we examine theoretically the time-resolved response of GaN/AlGaN MQWs. We show that, except for Bragg-arranged MQWs, the VMN effect governs the excitonic decay rate in these structures.

According to the semi-classical model [8], the exciton inhomogeneous broadening can be accounted for by averaging of the non-local dielectric susceptibility with a continuous distribution function of the exciton resonance frequency (chosen to be a Gaussian function for simplicity):

$$\tilde{\chi}(\omega,\gamma) = \frac{\eta}{\sqrt{\pi}\Delta}\int \chi(\omega,\nu,\gamma)\exp\left[-eta^2\left(\frac{\nu-\omega_0}{\Delta}\right)^2\right]\mathrm{d}\nu \qquad (1)$$

where ω_0 is the central frequency of the exciton distribution, $\chi(\omega, \nu, \gamma)$ is the dielectric susceptibility of the single free exciton state with the resonance frequency ν and homogeneous broadening γ.

Solving the Maxwell equations within the non-local dielectric response theory [8], one can find the amplitude reflection coefficient for light incident on a single quantum well (SQW) characterized by the response function (1) in form:

$$r_{\mathrm{QW}} = -\frac{\sqrt{\pi}\Gamma_0 w(z)}{\Delta + \sqrt{\pi}\Gamma_0 w(z)} \tag{2}$$

where $w(z) = \mathrm{e}^{-z^2} erfc(-iz)$, $z = (\omega - \omega_0 + i\gamma)/\Delta$, and $erfc(z)$ is the complementary error function. The frequency-dependent reflection amplitude of the whole structure $r(\omega)$ can be expressed in terms of r_{QW} using the transfer matrix method. The time-resolved reflection of the MQW system is a Fourier transform of $r(\omega)$ convoluted with the spectral function of the incident pulse [9]:

$$r(t) = \int_{-\infty}^{\infty} \frac{d\omega}{2\pi} r(\omega) g(\omega) \mathrm{e}^{-i\omega t}. \tag{3}$$

In the numerical calculations, for all the QWs under consideration we have taken $\eta\gamma = 0.1$ meV, $d = 70$ nm, $\eta\omega_0 = 3.6$ eV. We will consider either "disordered" QW structures with $\eta\Delta = 5$ meV, for GaN/AlGaN QWs [1] or "homogeneous" QWs with $\Delta = 0$ (for the reference). The value of 5 meV for the inhomogeneous broadening should hopefully be achieved by future optimization of material quality.

Figure 1 shows the time-resolved reflection spectra of a disordered SQW (a), of disordered MQWs containing 10 wells (b), 50 wells (c), 100 wells (d), and of a homogeneous SQW (e). Comparing the curves (a) and (e) in Fig. 1, one can see that the exciton inhomogeneous broadening induces a dramatic decrease of the decay time of the time-resolved reflection. This reflects appearance of additional channels of energy relaxation for excitons as the disorder increases in the structure [8]. Note the strong decrease of the exciton decay time with increase of the number of QWs in the structure. This is a manifestation of the VMN effect, which is visibly stronger than one observed experimentally in the GaAs/AlGaAs MQWs [5]. Note also pronounced oscillations in the spectra of MQWs and a disordered SQW (Fig. 1(a-d)). These oscillations have been widely discussed during recent years [5, 6, 8–10]. Basically, they arise both from the interference of different exciton–polariton modes and the interference within each single exciton–polariton mode due to the inhomogeneous broadening.

In the rest of this paper we report an analytical theory aimed to express the decay time of the coherent optical response of MQWs and the period of oscillations via the structure parameters and excitonic characteristics. We adopt the effective dielectric media (EDM) approximation [11] which describes the MQW structure as a homogeneous layer containing a single inhomogeneously broadened exciton resonance. This approximation is valid if excited states and A, B, C, bands are ignored, if $\Gamma_0 \ll \gamma$ and if one can find an integer n such as:

$$kd - n\pi \ll 1 \tag{4}$$

where k is the wave vector of light in the media at the exciton resonance frequency. The formalism allowing to calculate the time-resolved response of a semiconductor film containing an inhomogeneously broadened exciton resonance has been developed in Ref. [10].

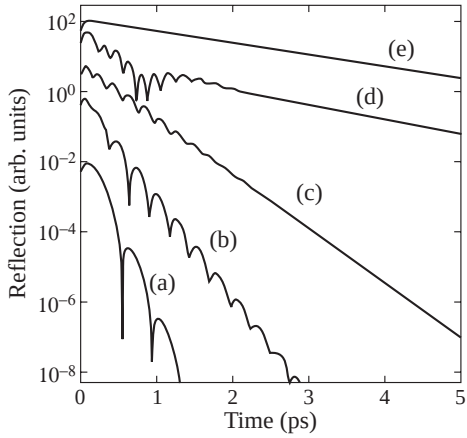

Fig. 1. Time-resolved reflection of GaN/AlGaN quantum well structures: (a) SQW with $\eta\Delta = 5$ meV; (b) MQW, $N = 10$, $\eta\Delta = 5$ meV; (c) MQW, $N = 50$, $\eta\Delta = 5$ meV; (d) MQW, $N = 100$, $\eta\Delta = 5$ meV; (e) SQW with $\eta\Delta = 0$ meV.

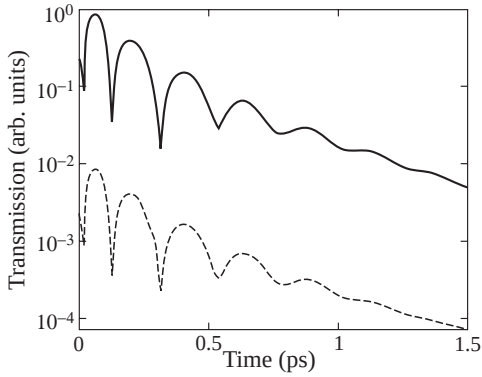

Fig. 2. Time-resolved transmission of light through the GaN/AlGaN MQW structure containing 50 QWs (solid) and through the thin film of a bulk semiconductor characterized by an effective dielectric susceptibility according to the EDM approximation (dashed).

To describe the MQWs one should substitute in that formalism the thickness of the film by Nd and the exciton longitudinal-transverse splitting $\omega_{\rm LT}$ by $2\Gamma_0/kd$ [11].

Figure 2 shows the time-resolved transmission of the structure (c) calculated within the EDM approximation (dashed line) in comparison with the exact calculation (solid line). Note, that the criterion (4) is satisfied for this structure, with $n = 1$. An excellent agreement between the exact and approximate calculations allows us to apply the steepest descent method presented in Ref. [10] to find the decay time τ and the period of oscillations T in the time-resolved reflection of the MQWs. Using Eq. (27) from Ref. [10] one can obtain

$$T(t) = \frac{\pi\sqrt{t}}{\sqrt{N\Gamma_0}[1 + (3\Delta^2 t/4N\Gamma_0)]}. \tag{5}$$

In order to find a compact analytical formula for the decay time τ one has to extend substantially the formalism of Ref. [10] and the EDM approximation. Let us remind that the spectrum of exciton–polariton eigen-modes in a MQW structure consists of a few super-

radiant modes having a huge oscillator strength and of many dark modes having a very small oscillator strength. If the condition (4) is satisfied, i.e. either for short-period MQWs or for quasi-Bragg-arranged MQWs, there is only one super-radiant mode with an extremely short decay-time. At the pico-second time-scale the exciton radiative decay is governed by the dark modes, which form two bands similar to the bulk exciton–polariton bands. That is why the EDM approximation works so well for this kind of MQWs.

In the limit $\Delta \ll N\Gamma_0$ one can assume the sum of the oscillator strengths of the exciton–polariton modes to be independent of Δ. Thus, the oscillator strength of the dark modes can be estimated as a total oscillator strength (proportional to $N\Gamma_0$) minus the oscillator strength of the super-radiant mode, which decreases with increase of Δ. Within this hypothesis and with use of the Eq. (A6) from Ref. [10] one can find the decay rate of the time-resolved optical response of a MQW structure as

$$\frac{1}{2\tau} = \gamma + \frac{\Delta^2}{2[N\Gamma_0 - (\Delta^2/2N\Gamma_0)]}. \tag{6}$$

In conclusion, we have shown that the vertical motional narrowing effect is of great importance for the coherent optical spectra of the GaN/AlGaN MQWs. The approximate analytical expressions for the decay rate and period of oscillations of the time-resolved reflection and transmission spectra of MQWs have been derived.

Acknowledgement

The work has been supported by the European Commission in the framework of a contract HPRN-CT-1999-00132.

References

[1] N. Grandjean, J. Massies and M. Leroux, *Appl. Phys. Lett.* **74**, 2361, (1999).
[2] B. Gil, et al, *Phys. Rev. B* **59**, 10246 (1999).
[3] F. Bernardini, V. Fiorentini and D. Vanderbilt, *Phys. Rev. Lett.* **79**, 3958 (1997).
[4] F. Della Sala et al, *Appl. Phys. Lett.* **74**, 2002 (1998).
[5] J. J. Baumberg et al, *Phys. Rev. Lett.* **80**, 3567 (1998).
[6] A. V. Kavokin and J. J. Baumberg, *Phys. Rev. B* **57**, R12 697 (1998).
[7] P. Lefebvre et al, *Phys. Rev. B* **57**, R9447 (1998).
[8] L. C. Andreani et al, *Phys. Rev. B* **57**, 4670 (1998).
[9] A. V. Kavokin et al, *Phys. Rev B* **60**, 13 298 (1999).
[10] G. Malpuech, A. Kavokin and G. Panzarini, *Phys. Rev B* **60**, 16 788 (1999).
[11] E. L. Ivchenko, *Sov. Phys. Solid State* **33**, 1344 (1991).
[12] E. L. Ivchenko et al., *Phys. Solid State* **16**, 17 (1994);
Y. Merle d'Aubigne et al., *Phys. Rev. B* **54**, 14 003 (1996).

9th Int. Symp. "Nanostructures: Physics and Technology"
St Petersburg, Russia, June 18–22, 2001

Exciton localization by clusters in diluted bulk InGaN and two-dimensional ZnCdSe solid solutions

A. Klochikhin†,‡, A. Reznitsky‡, L. Tenishev‡, S. Permogorov‡, W. Lundin‡, A. Usikov‡, S. Sorokin‡, S. Ivanov‡, M. Schmidt§, H. Kalt§ and C. Klingshirn§

† St Petersburg Institute of Nuclear Physics, Russian Academy of Sciences, Gatchina, 188350, St Petersburg, Russia,
‡ Ioffe Physico-Technical Institute, St Petersburg, Russia
§ Institut für Angewandte Physik, Universität Karlsruhe, 76128 Karlsruhe, Germany

Abstract. The photoluminescence (PL) bands of MOCVD grown double heterostructures (DHS) GaN/InGaN/GaN with In content in the range 0.4–2% as well as MEE grown ZnSe/CdSe/ZnSe QWs with 0.3–1.5 ML CdSe nominal thicknesses show a fine structure which can be attributed to small In or Cd clusters, respectively, occurring in cation sublattices at random filling of the lattice sites. This fine structure is smoothed away at further concentration increase in both systems. At the lowest concentration the exciton motion in these systems has a character of 3D and 2D percolation over the "impurity" bands formed by clusters of size $s = 2$ in both cases. We have found that similarity of InGaN and ZnCdSe PL-band shapes despite the different dimensionality of objects (3D DHS and 2D QWs) is due to a different perturbation strength produced by In and Cd, respectively.

Introduction

Solid solution grown from constituents with highly mismatched lattices can be considered as "ideal" or random alloy, at best, at low concentration only. On the other hand, the conventional treatment of disorder effect on the electron states in a solid solution assumes usually its random character. In the low concentration limit the random distribution of the diluted atoms can be described by clusters of relatively small size [1]. As a result, the localization of exciton occurs due to perturbation of the potential relief by randomly distributed clusters. The shape of the density of states (DOS) of localized states is very sensitive to the size and number of clusters which are responsible for the localization. For 3D systems the low concentration limit is most interesting in cases when the perturbation strength of diluted atoms is large enough for exciton localization by the clusters of small size. In these cases the cluster structure of DOS can be directly observed in the luminescence spectra [2].

2D exciton states which can be realized in QWs formed by solid solution are much more sensitive to the disorder and, therefore, a relatively weak perturbation can be sufficient for the cluster localization of exciton. Here two important problems are encountered: (i) what is the minimum concentration of the diluted atoms necessary to form a QW, and (ii) how to distinguish the mobile and localized excitons in the case when the fluctuations can not be considered as a small correction.

We have studied PL and excitation of PL (PLE) spectra of two systems: (i) MOCVD grown GaN/InGaN/GaN double heterostructures (DHs) with a well width of 100 nm and an In content from 0.4% to 2%, and (ii) single QWs formed by a MEE cycled deposition of CdSe (by 0.3 ML per cycle) in ZnSe matrices with the number of cycles 1, 2 and 5

(for more growth details see [3, 4], respectively). The 441.6 nm or 325 nm He-Cd laser lines were used to excite PL spectra of ZnCdSe and InGaN systems, respectively. PLE spectra were excited by a second monochromator with Xe-lamp. For both systems we have found that in the composition range under investigation the PL spectra posses a fine structure, which can be attributed to exciton localization by clusters of 2 or 3 atoms of the narrow gap component. The number of such clusters obeys the random distribution statistics. For In content exceeding ≈ 0.02 in InGaN solid solutions as well as for Cd content in ZnCdSe more than $5 \cdot 0.3$ ML this fine structure in the PL spectra is smoothed out and the Stokes shifts between PL and PLE spectra becomes larger than that expected for the random statistics [5].

1. Cluster structure of InGaN luminescence band in the limit of low In concentration

The luminescence spectra of InGaN epilayers in Figs. 1(a,b) show a structure which becomes less pronounced with the In content increase and disappears completely already at 2% of In (Fig. 1(c)). Due to this structure the PL in Figs. 1(a,b) differs considerably from the usual structureless spectra of concentrated solid solutions with the Urbach tails of localized states.

1. To account for the observed structure of PL bands we have assumed a random distribution of In atoms over the cation sublattice. Neglecting the difference between the sublattice geometry of hexagonal InGaN and that of a fcc lattice we have used the percolation theory for fcc lattice to find the number of clusters of different size. Using the approach described in [1] we have calculated the exciton density of states (DOS) (curves 1), spectral density of states (SDOS) (curves 2), and SDOS of radiative states (curves 3 in Fig. 1). The cluster structure can appear at low concentrations if the perturbation strength produced by substituting atoms is large enough and the localized states split off for the clusters which size does not exceed $s = 3$. The number of space configurations of clusters of larger size increases rapidly [6] and a dependence of the localization energy on the cluster configuration suppresses appearance of resolved luminescence structure for such clusters. The model fit of experimental data presented in Fig. 1 shows that the structure of PL spectra of InGaN solid solution can be assigned to clusters with $s = 2, 3$.

2. The following characteristics of an InGaN solid solution were obtained as a result of calculations.

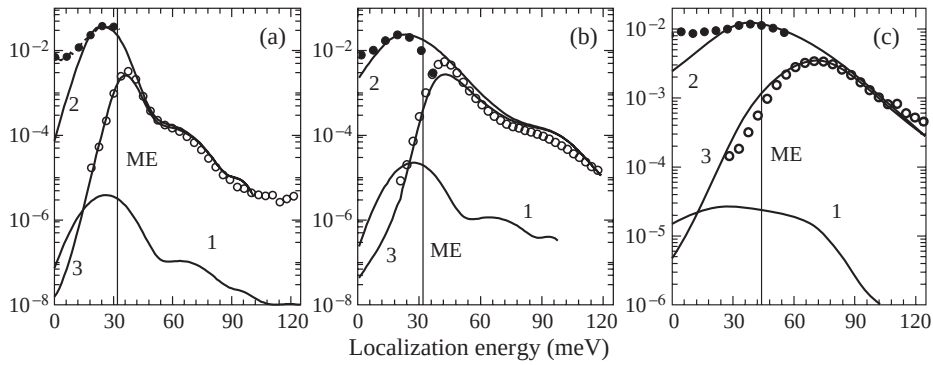

Fig. 1. PL (open circles) and PLE (solid circles) spectra of GaN/InGaN/GaN DHS with In content 0.4% (a), 1% (b) and 2% (c) (symbols). Solid lines are the calculated DOS (1), spectral DOS (SDOS) (2), and SDOS of radiative states (3). Vertical lines ME mark the mobility edge positions.

a) The potential well depth created for exciton by single In atom in GaN lattice is about $\Delta \approx 400$ meV.
b) The ratio of the potential amplitude Δ to the critical perturbation which splitts off the localized state with zeroth localization energy is close to unity ($\Delta / E_{cr} \approx 0.9$) which means the strong scattering regime already for a single In atoms.
c) The bowing parameter for composition dependence of the band gap is large and equal to ≈ 3 eV.
d) For the studied compositions the percolation threshold (ME) is situated in the energy range where the clusters of two In atoms are responsible for the DOS and moves toward the deeper localization energies with the increase in In concentration.

2. Cluster structure of PL spectra of QWs formed by ZnCdSe solid solution at small Cd concentrations

1. The PL and PLE spectra of QWs with nominal Cd thickness of 1, 2, and 5 cycles by 0.3 ML are shown in Figs. 2(a,b,c), respectively. For these samples we estimated the average Cd content in broadened QWs as 2.5, 5 and 12.5% which is in good agreement with the data of [7]. The PL spectra of the first two samples show a structure which can be attributed to the clusters with $s = 2$ and 3. This structure disappears with the Cd content increase and at 12.5% Cd it is not observable. The calculations performed have allowed us to estimate also the potential amplitude of Cd in the ZnSe matrix as $\Delta \approx 150$ meV and the ratio $\Delta / E_{cr} \approx 0.3$ (E_{cr} is a characteristics of the 3D ZnCdSe solid solution). The obtained small values of Δ / E_{cr} and Δ explain why the 3D Urbach tail is not detected experimentally in this solid solution [8]. Hence, the observed properties of PL spectra of QWs are due entirely to the 2D character of exciton states in this system.

2. Taking into account that the QW width amounts about 10 ML [7], we have used in calculations of the number of clusters also the 3D statistics for the fcc lattice. The results can be formulated as follows:
(a) The fine structure of PL band is concerned with the clusters of size $s = 2$ and 3.
(b) The mobility edge position occurs in the energy range of the $s = 2, 3$ DOS maxima. Therefore, as in the previous InGaN case the exciton motion has a character of percolation over an "impurity band" formed by these clusters.
(c) The position of the mobility edge in the QW formed by 0.3 ML of Cd is close to barrier exciton SDOS maximum while the SDOS of the 2D excitons corresponds to the localized

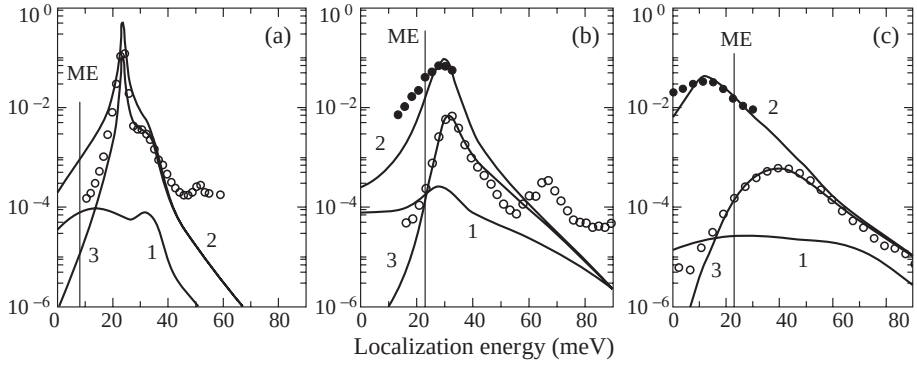

Fig. 2. Similar to that in Fig. 1 but for ZnCdSe QWs with nominal CdSe thicknesses 0.3 ML (a), $2 \cdot 0.3$ ML (b) and $5 \cdot 0.3$ ML (c).

exciton states. So we can conclude that the concentration of Cd in 0.3 ML QW is close to the critical one at which the QW is just formed.

Summary

We have found a fine structure of PL spectra of diluted bulk InGaN and 2D ZnCdSe solid solutions and have attributed it to the DOS structure caused by statistical clusters consisting of 2 or 3 atoms of narrow gap component. The perturbation potentials of In in GaN and Cd in ZnSe are estimated. It is shown that a single In atom in GaN produces a perturbation which is almost sufficient for the splitting off the localized state in 3D case, while the perturbation of Cd atom in ZnSe matrix gives a localized state only in the systems of reduced dimensionalities.

Acknowledgments

This work was partly supported by Deutsche Forschungsgemeinschaft, INTAS (97-31907), Program “Physics of Solid State Nanostructures” and Russian Foundation for Basic Research.

References

[1] A. Klochikhin, A. Reznitsky *et.al., Phys. Rev. B* **59**, 12947 (1999).
[2] S. Permogorov, A. Reznitsky *et.al., J. Luminescence* **59**, 12947 (1999).
[3] W. V. Lundin *et.al., phys. stat. sol. (a)* **176**, 379 (1999) .
[4] S. Sorokin *et.al., J. Cryst. Growth* **201/202**, 461 (1999).
[5] A. Klochikhin, A. Reznitsky *et. al.*, this volume, p. 538
[6] M. F. Sykes *et al. J. Phys. A.: Math. Gen.* **9**, 1705 (1976).
[7] N. Peranio, *et.al., Phys. Rev. B* **61**, 16015 (2000).
[8] S. Permogorov *et. al. Phys. Solid State* **37**, 1350 (1995).

9th Int. Symp. "Nanostructures: Physics and Technology"
St Petersburg, Russia, June 18–22, 2001

The formation of the charged exciton complexes in self-assembled InAs single quantum dots

E. S. Moskalenko†‡, K. F. Karlsson‡, P. O. Holtz‡, B. Monemar‡,
W. V. Schoenfeld§, J. M. Garcia§ and P. M. Petroff§
† Ioffe Physico-Technical Institute, St Petersburg, Russia
‡ Department of Physics and Measurement Technology, Linköping University, S-581 83 Linköping, Sweden
§ Materials Department, University of California, Santa Babara, California 93106

Abstract. We study the low-temperature photoluminescence (PL) of the self-assembled InAs single quantum dots (QDs) using conventional μ-PL setup to detect PL from an individual QD. We demonstrate, that at certain experimental conditions, what concerns the laser excitation energy, the laser power and the sample temperature, several novel lines appear in the PL spectra. The lines, redshifted relative to the exciton PL line, are interpreted in terms of charged exciton complexes.

Introduction

Multiparticle effects in quantum dots (QDs), which were studied both theoretically [1, 3] and experimentally [2–5], determine the performance of a number of optoelectronic devices, for example QD lasers and single-electron transistors, which in turn are considerably affected by the charge, stored in the QD [6]. This highlights the outstanding role of multiparticle complexes with non-equal number of electrons e and holes h which were spectroscopically examined on large ensembles of QDs [2, 3] as well as in single QDs [4, 5]. In the latter type of studies, the effect of inhomogeneity is avoided but is still associated with some disadvantages: The supplying of extra electrons into the QD from the doped layers [4] is based on the use of an external electric field, which in turn affects the entire spectrum of the QD. Feeding the QD with the extra charges from the impurity atoms positioned in a close vicinity of a QD [5] makes the transfer of excess carriers into QD random and hardly controlled.

In the present contribution we propose a new method to create charged excitons in QDs. This is based on the possibility to monitor the photogenerated carrier diffusivity by means of tuning the laser excitation energy ($h\nu$) and changing the crystal temperature (T). As a result, under certain experimental conditions, we can detect the appearance of two new lines in photoluminescence (PL), redshifted relative to the fundamental single exciton line. These novel lines are interpreted in terms of charged exciton complexes.

1. Samples and experimental setup

The sample studied consists of one layer of InAs self-assembled QDs between two 100 nm wide GaAs barriers (the MBE growth procedure used is described in detail elsewhere [7]). The QDs formed are lens shaped with a lateral size of 35 nm and a height of 10 nm. Typical interdot distance is 10 μm, which allows the use of a conventional micro-PL setup (described in detail in Ref. [8]) in order to spatially resolve individual dots. The laser beam could be focused on the sample surface with a spot size down to 2 μm, to excite and study

the PL from a single QD. The cw light of a Ti-Sp laser was used for the photoexcitation. The sample temperature was maintained in the range 4 K $\leq T \leq$ 40 K.

Four single quantum dots located at different spatial positions of the sample were examined in this study. All of them revealed an analogous behavior and for consistency, we present the results taken from only one single quantum dot to demonstrate a typical behavior of the QDs.

2. Experimental results and discussion

Figure 1 shows PL spectra measured at $T = 4$ K on a selected single QD taken for a wide range of excitation powers, P_{ex}, and excitation energies, $h\nu$. At lowest P_{ex} and $h\nu = 1.684$ eV (Fig. 1(a)), the spectrum consists of a single line, X. With increasing P_{ex}, two groups of lines appear in the spectra: One is redshifted relatively the X line (by 3–7 meV), while the other (marked as X_{pp}) appears blueshifted by a 30 meV. At highest P_{ex}, the intensity for the first group of lines tends to saturate and even decrease, while the intensity of the second one progressively increases. These observations imply that the first (second) group of lines originates from the ground (first excited) state of the QD. For another excitation energy $h\nu = 1.536$ eV (Fig. 1(b)), a qualitatively similar behavior for the PL spectra was revealed at high P_{ex}, while the spectrum taken at lowest P_{ex} differs markedly from the corresponding one in Fig. 1(a). Two new lines, marked as X^- and X^{--}, appear in this spectrum.

We will below propose an explanation for these dramatic changes obtained at lowest P_{ex} initiated by the tuning of $h\nu$. We first note that as this difference occurs at lowest P_{ex}, we can exclude the occupation with more than one exciton ($e - h$ pair) in the QD as an explanation. Second, the appearance of X^- and X^{--} when changing $h\nu$ can not be explained in terms of impurity related transitions, because these would be observed at any $h\nu$ [5]. Instead, we exploit a model which predicts a dependence of the photogenerated free carrier diffusivity on $h\nu$. Indeed, carriers being excited in the GaAs barriers (Fig. 1(a) and (b)) can release their kinetic energy either via fast emission of LO phonons (with energy $\hbar\omega_{\mathrm{LO}}$), or by an emission of a cascade of acoustic phonons, which takes much longer time.

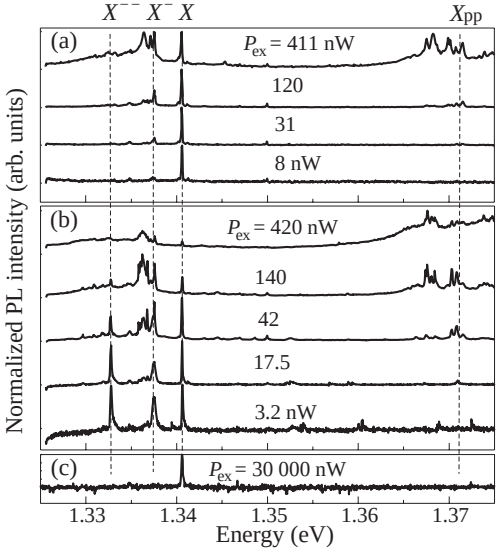

Fig. 1. Normalized PL spectra of an individual QD taken at $T = 4$ K, for a number of P_{ex} at different pump-photon energies:
(a) $h\nu = 1.684$ eV,
(b) $h\nu = 1.536$ eV
and (c) $h\nu = 1.433$ eV.

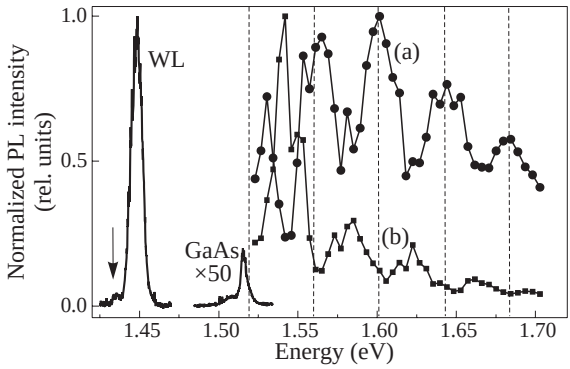

Fig. 2. The normalized peak PL intensities of (a) X and (b) X^{--} lines as a function of $h\nu$, taken at $T = 4$ K and $P_{ex} = 10$ nW. The normalized PL spectrum of the wetting layer (WL) and of the GaAs barrier is also shown for the same values of T and P_{ex} at $h\nu = 1.536$ eV.

As a result we expect that carriers, for which the kinetic energy fits with an integer number of $\hbar\omega_{\mathrm{LO}}$, become motionless at the band edge shortly after generation, while for any other kinetic energy, a much longer time for carriers is expected to cool down. Consequently this carrier is able to move a much longer distance in the crystal. Eventually, the latter case results in a higher diffusivity, which in turn increases the probability for this carrier to pass in the close vicinity of a QD and to become captured by the dot.

We consider the electrons as more likely candidates for such a process, since electrons in GaAs are seven times lighter than the holes. Thus we explain the appearance of the two new lines X^{-} (X^{--}) at a certain $h\nu$ as a recombination of complexes consisting of a single exciton and one (two) extra electron(s) captured to the QD to form negatively charged excitons. This assignment is supported by the prediction [1] that only electrons can be bound to the exciton in lens shaped QDs, as well as by the comparison of the binding energies for X^{-} (X^{--}) derived from experiment as the differences in the PL energy positions between X and X^{-} (X^{-} and X^{--}) lines as 3.1 meV (4.7 meV) with calculated ones of 2.6 meV (4.9 meV) using simple perturbation theory [3]. If one excites only immobile carriers, e.g. by excitation resonant with the localized states of the WL (as marked by an arrow in Fig. 2), no lines except X are expected in the PL spectrum. This is in full agreement with our experiment (Fig. 1(c)).

As follows from our model, the electron diffusivity should be modulated with $h\nu$, and accordingly, the amplitudes of the neutral and charged exciton lines should oscillate. In fact such a behavior is nicely demonstrated in Fig. 2, where the amplitudes of the line X (Fig. 2(a)) and X^{--} (Fig. 2(b)) are shown as a function of $h\nu$. They oscillate in counterphase as expected with a characteristic period of 41.4 meV (shown by the vertical dotted lines) which fits well with the calculated energy difference of $h\nu$ changing the electron part of the kinetic energy by the LO phonon energy.

An alternative way to increase the electron diffusivity, and hence to initiate the appearance (or enhance the intensity) of the charged exciton lines is to increase the sample temperature. The results are shown in Fig. 3, for three characteristic $h\nu$. For the excitation energy $h\nu$, which gives rise only to the X line at lowest T (Fig. 3(a)), the increase of T evidently redistributes the PL intensity in favour of X^{-} and X^{--} lines. For excitation energies $h\nu$ at which the three lines are of comparable intensities at low T (Fig. 3(b)), the X line evidently disappears at highest T and the spectrum is instead dominated by the X^{--} line. In the case of excitation of solely localized carriers at $h\nu = 1.433$ eV (at the arrow in

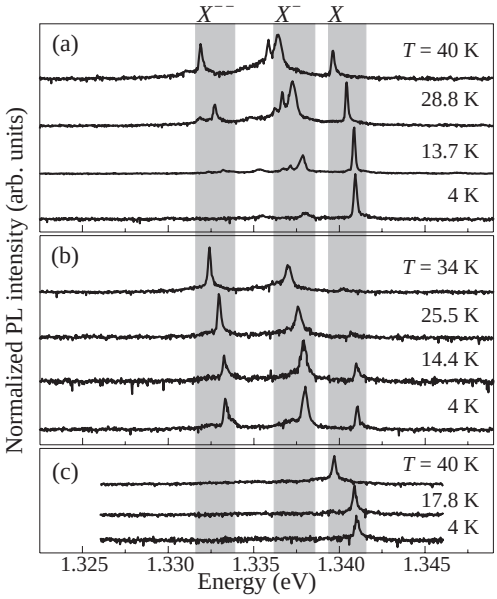

Fig. 3. Normalized PL spectra of a selected QD taken for a number of T and different excitation energies: (a) $h\nu = 1.686$ eV and $P_{ex} = 5$ nW, (b) $h\nu = 1.557$ eV and $P_{ex} = 5$ nW and (c) $h\nu = 1.433$ eV and $P_{ex} = 30000$ nW.

Fig. 2), no diffusion of carriers is expected and in the PL spectra only a small redshift of X is observed at higher temperatures (Fig. 3(c)) due to the band gap shrinkage (the same as in Fig. 3(a) and (b)). This result (Fig. 3(c)) confirms that the temperature effect on the PL spectra is due to an increased photogenerated carrier diffusivity and not due to an activation of localized electrons (for example electrons localized at impurities in the close vicinity of the QD).

Thus, the present study demonstrates a new method to create charged excitons by changing the effective carrier diffusivity by means of an altered excitation energy and/or sample temperature.

Acknowledgements

One of us (E.S.M.) gratefully acknowledges financial support of Svenska Institutet within the Visby Programme.

References

[1] Ph. Lelong and G. Bastard, *Solid State Commun.* **98**, 819 (1996).
[2] K. H. Schmidt et al., *Phys. Rev. B* **54** 11346 (1996).
[3] R. J. Warburton, B. T. Miller, C. S. Durr et al., *Phys. Rev. B* **58** 16221 (1998).
[4] M. Baier, F. Findeis, A. Zrenner, M. Bichler and G. Abstreiter, *Abstracts of the 25th International Conference on Physics of Semiconductors,* Osaka, Japan, 207 (2000).
[5] A. Hartmann, Y. Ducommun, E. Kapon et al., *Phys. Rev. Lett.***84** 5648 (2000).
[6] D. Bimberg, M. Grundmann and N. N. Ledentsov, *Quantum Dot Heterostructures*, (John Willey and Sons,1999, England);
[7] J. M. Garsia et al., *Appl. Phys. Lett.* **71** 2014 (1997).
[8] E. S. Moskalenko, K. F. Karlsson, P. O. Holtz et al., *submitted to PRB* (2001).

9th Int. Symp. "Nanostructures: Physics and Technology"
St Petersburg, Russia, June 18–22, 2001

Linearly-polarized optical transitions at type-II interfaces in the tight-binding approach

M. O. Nestoklon and E. L. Ivchenko
Ioffe Physico-Technical Institute, St Petersburg, Russia

Abstract. The sp^3 tight-binding method has been applied to calculate the in-plane anisotropy of optical matrix elements for indirect electron-hole radiative recombination at a type-II interface. It has been shown that, in type-II heterostructures with large band off-sets, the linear polarization of the photoluminescence vary in a wide range, including values ∼100%, as a function of the tight-binding parameters characterizing the interface cations and anions. The behaviour of electron and hole quantum-confined states near the interface and their overlap has been analyzed as well.

Recently it has been demonstrated that, in type II zinc-blende-lattice multi-layered heterostructures grown along the [001] principal axis, the interfaces can induce a remarkable in-plane anisotropy. The anisotropy arises due to tetrahedral orientation of chemical bonds lying in the (110) and $(1\bar{1}0)$ planes. As a result the vertical photoluminescence (PL) is linearly polarized with the polarization reaching high values up to 80% in BeTe/ZnSe [1] and 21% in CdS/ZnSe [2].

In type II CA/C′A′ systems with large conduction- and valence-band offsets (∼2 eV and ∼1 eV for the BeTe/ZnSe pair) the penetration depth for an electron into the CA layer and for a hole into the C′A′ layer has the order of the lattice constant. Therefore in such a system the wavefunctions of an electron and a hole participating in the spatially indirect radiative recombination overlap remarkably only over few atomic planes. In this case the validity for the conventional envelope function approximation is questionable and one must instead use pseudopotential or tight-binding models.

We have applied the empiric tight-binding model sp^3 in the nearest-neighbor approximation, see [3], in order to find electron states quantum-confined within a C′A′ layer and hole states confined in a CA layer. For a (001)-grown structure, the carrier wave function in the state with the zero in-plane wave vector may be written as

$$\psi = \sum_{n,\alpha} C_n^{\alpha} \phi_{n\alpha}\,(x, y, z - z_n)\ , \tag{1}$$

where z is the growth direction [001], $z_n = na_0/4$, a_0 is the lattice constant, the integer n enumerates anion (for even $n = 2l$) and cation (for odd $n = 2l - 1$) atomic planes, $\phi_{n\alpha}$ are the planar atomic orbitals, and we take into consideration the orbitals $\alpha = s$, $p_{x'}$, $p_{y'}$, p_z. Hereafter we use the coordinate system with $x \parallel [100]$, $y \parallel [010]$ and $x' \parallel [1\bar{1}0]$, $y' \parallel [110]$.

For the C′A′ material we used the tight-binding parameters close to those presented for ZnSe by Vogl et al. [3]. The parameters for another material, CA, and for the interface atoms are indicated in caption to Fig. 1. Most of them coincide with those of C′A′ and only a few are different, in order to get the band gap $E_g(CA) = 4.3$ eV and the band off-sets

$$E_c(CA) - E_c(C'A') = 2.5\,\text{eV} \quad \text{and} \quad E_v(CA) - E_v(C'A') = 0.9\,\text{eV},$$

respectively for the conduction and valence bands.

The optical matrix elements for the emission of photons polarized along $x' \parallel [1\bar{1}0]$ and $y' \parallel [110]$ axes are calculated in the framework of the theory briefly outlined in [1] and given by

$$M_\alpha = i\frac{a_0 m_0}{4\hbar} \sum_{l=0,\pm 1\ldots} V_l^\alpha \,,$$

$$\begin{aligned} V_l^{x'} &= V_{sa,pc} C_{2l}^s C_{2l-1}^{x'} + V_{pa,sc} C_{2l-1}^s C_{2l}^{x'} \,, \\ V_l^{y'} &= V_{sa,pc} C_{2l}^s C_{2l+1}^{y'} + V_{pa,sc} C_{2l+1}^s C_{2l}^{y'} \,. \end{aligned} \tag{2}$$

Here M_α is the interband matrix element of the momentum operator $\hat{p}_\alpha$ for $\alpha = x'$ and y', $V_l^{x'}$ is the contribution to $M_{x'}$ from interatomic transitions between the anion plane $2l$ and cation plane $2l-1$, $V_l^{y'}$ is that for the pair of planes $2l$ and $2l+1$, $V_{sa,pc}$ and $V_{pa,sc}$ are the anion-cation transfer tight-binding parameters, C_n^s is the s-orbital coefficient in the expansion (1) for the lowest quantum-confined electron state in the conduction band, C_n^α is the similar p_α-orbital coefficient for the lowest quantum-confined heavy-hole state in the valence band. We exploit the theory by Lew Yan Voon and Ram-Mohan [4] where the intrasite contribution to the optical matrix elements is ignored and the interatomic transitions between the planes $2l$, $2l-1$ and $2l$, $2l+1$ are coupled with photons polarized respectively along $[1\bar{1}0]$ and $[110]$.

Fig. 1 illustrates the calculation of the polarization degree, P_{lin}, defined as the ratio $(I_{1\bar{1}0} - I_{110})/(I_{1\bar{1}0} + I_{110})$, where $I_{110}, I_{1\bar{1}0}$ are the intensities of the PL components polarized along the corresponding axes. In the figure we present results for the interface

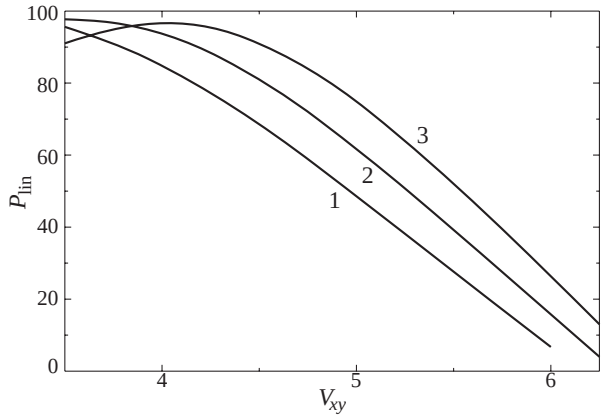

Fig. 1. The degree of PL in-plane linear polarization calculated as a function of the tight-binding transfer parameter V_{xy} for the C′A chemical bond at the (001) interface between the binar compositional materials CA and C′A′. The other parameters used are as follows: the diagonal energies $E_{sa} = -11.2$ eV, $E_{sc} = 2.8$ eV, $E_{pa} = 2.0$ eV, $E_{pc} = 8.8$ eV in CA and $E'_{sa} = -11.8$ eV, $E'_{sc} = 0.02$ eV, $E'_{pa} = 1.5$ eV, $E'_{pc} = 6.0$ eV in $C'A'$; the interatomic transfer matrix elements $V_{ss} = -6.2$ eV , $V_{xx} = 3$ eV, $V_{sa,pc} = 3.5$ eV and $V_{pa,sc} = 6.3$ eV are chosen to be the same in CA, C′A′ and at the interface bonds, $V_{xy} = 6$ eV in CA, C′A′ and arbitrary at the interface. As for the diagonal energies $\tilde{E}_{sa}$, $\tilde{E}_{sc}$ and $\tilde{E}_{pa}$ at the interface atoms C′ and A, the average values $(E_{sa} + E'_{sa})/2$ etc. are taken. Curves 1, 2 and 3 are obtained respectively for $\tilde{E}_{pc} = 6.4$ eV, 7.4 eV and 8.4 eV.

C′A assuming the interfacial bonds to lie in the (110) plane containing the $[1\bar{1}0]$ and [001] axes. For the CA′ interface the results are similar but in this case the polarization is directed along [110]. Thus, the polarization follows the direction of the interface chemical bonds as predicted in [1]. Note that the parameter V_{xy} for the interface cations and anions can remarkably differ from its value in the bulk semiconductor C′A and is considered as an indipendent variable. We see that, provided all other parameters are fixed, values of P_{lin} increase with decreasing V_{xy} from 6 eV to 4 eV and exceed 80% for $V_{xy} < 4.2$. The polarization is almost insensitive to the electron and hole confinement energies within a wide energy range. However we remind that here we consider only the electron and hole states with $k_x = k_y = 0$.

To demonstrate the behaviour of the electron and hole wave functions near the interface, we presented in Table 1 values of C_n^α for n between -4 and 4 assuming the C′ and A interface planes correspond to $n = -1$ and $n = 0$ respectively. One can see that the conduction-band coefficients C_{2l}^s at anions or C_{2l-1}^s at cations rapidly decrease with increasing l whereas the valence-band coefficients decay the C′A′ material.

For completeness we presented in Fig. 2 the dependence $V^{x'}$ and $V^{y'}$ upon l. As predicted in [1] the maximum contribution to $M_{x'}$ is given by the pair of the interface planes A′ and C and the main contribution to M_α comes from V_l^α with $|l| \leq 3$. The maximum contributions to $M_{x'}$ and $M_{y'}$ come from the planes -1, 0 and 0, $+1$. According to Eq. (2), the ratio of these particular contributions is mainly given by

$$\eta = \frac{C_{-1}^s C_0^{x'}}{C_1^s C_0^{y'}} .$$

From Table 1 calculated for $V_{xy}(C'A) = 5$ eV, $E_{pc} = 7.4$ eV we have $\eta = 2.2$ and $(\eta^2 - 1)/(\eta^2 + 1) = 0.65$ which is close to $M_{x'}/M_{y'} = 2.06$ resulting in $P_{lin} = 62\%$.

We thank A. V. Platonov and A. A. Toropov for useful discussions and acknowledge partial financial support by INTAS under the grant 99-00015 and the Russian Foundation for Fundamental Research (the grant 00-02-16997).

References

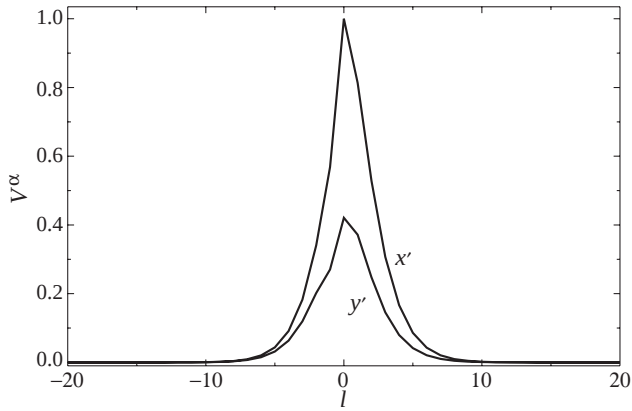

Fig. 2. Contribution of particular pairs of planes, $(2l, 2l-1)$ and $(2l, 2l+1)$, to the optical matrix elements, respectively in the x' and y' polarization.

Table 1. The unnormalized coefficients of the expansion (1) near the interface for the set of tight-binding parameters presented in caption to Fig. 1 and for $V_{xy}(C'A) = 5$ eV, $\tilde{E}_{pc} = 7.4$ eV.

Atom	A'	C'	A'	C'	A	C	A	C	A
n	-4	-3	-2	-1	0	1	2	3	4
C^s	-0.26	0.50	-0.17	0.27	-0.08	0.13	-0.04	0.06	-0.02
$C^{x'}$	0.05	-0.08	0.11	-0.2	0.36	-0.31	0.66	-0.41	0.95
$C^{y'}$	0.04	-0.01	0.10	-0.02	0.34	-0.07	0.64	-0.19	0.93

[1] A. V. Platonov, V. P. Kochereshko, E. L. Ivchenko, G. V. Mikhailov, D. R. Yakovlev, M. Keim, W. Ossau, A. Waag and G. Landwehr, *Phys. Rev. Lett.* **83**, 3546 (1999).
[2] M. Schmidt, M. Grün, S. Petillon, E. Kurtz and C. Klingshirn, *Appl. Phys. Lett.* **77**, 85 (2000).
[3] P. Vogl, H. P. Hjalmarson and J. D. Dow, *J. Phys. Chem.* **44**, 365–378 (1983).
[4] L. C. Lew Yan Voon and L. R. Ram-Mohan, *Phys. Rev. Lett.* **47**, 15500 (1993).

9th Int. Symp. "Nanostructures: Physics and Technology"
St Petersburg, Russia, June 18–22, 2001

Singlet and triplet states of X^+ and X^- trions in a 2D quantum well

R. A. Sergeev and R. A. Suris
Ioffe Physico-Technical Institute, St Petersburg, Russia

Abstract. A new simple variational wave function with a few variational parameters for 2D X^+ and X^- trions has been suggested. The function gives accurate results for the singlet and triplet state energies of X^+ and X^- trions in the whole range of electron-to-hole mass ratio. The mass ratio range where the triplet state exists has been found, and the behavior of the triplet state energy has been examined near the critical mass ratio.

Introduction

Three particle electron-hole complexes (trions) in bulk semiconductors were considered by Lampert in 1958 [1]. A trion is an analog of the ion H^- that was firstly considered by Bethe [2]. However, the experimental investigation of trions in bulk semiconductors is made difficult by their small binding energy.

Recently interest in experiment and theory of trions has quickened due to considerable progress in heterostructure synthesis. The theoretical calculations performed in the 1980s [3–6] predicted a substantial (up to tenfold) increase of trion binding energy in quantum well heterostructures as against bulk trions. This made possible experimental studies which were firstly performed by K. Kheng et al. [7].

In recent years the trion energies versus the effective mass ratio were intensively studied in a two-dimensional case or in a single quantum well [8–14]. Nevertheless, only a singlet state of trions in a zero magnetic field was considered. In 1958 Lampert [1] predicted the existence of triplet state for the complex consisting of two heavy carriers (holes) and one light particle (electron) for a large hole-to-electron mass ratio when the trion is an analog of molecule H_2^+. He pointed out that it would be of interest to fix the mass ratio region where the complex exists. However, the triplet state of trion in a zero magnetic field is not completely studied up to now. Some calculations of trion triplet state were performed only for the 3D case [15–17].

In this paper we consider singlet and triplet states of 2D trion in the whole range of mass ratio. Using simple variational calculations, we find the mass ratio region where the triplet trion exists.

1. Singlet state

For singlet state variational calculations, the following symmetric coordinate trial function was used:

$$\psi_s(\vec{r_1}, \vec{r_2}) = (\exp(-ar_1 - br_2) + \exp(-ar_2 - br_1)) \frac{1 + cR}{1 + d(R - R_0)^2} \exp(-sR), \quad (1)$$

where $\vec{r_1}$ and $\vec{r_2}$ are the 2D vectors from hole (for simplicity the terms of X^- are used) to electrons, $R = |\vec{r_1} - \vec{r_2}|$ is the distance between two electrons, a, b, c, d, R_0, and s are the variational parameters. The parameters a and b are the reciprocal radii of two electron

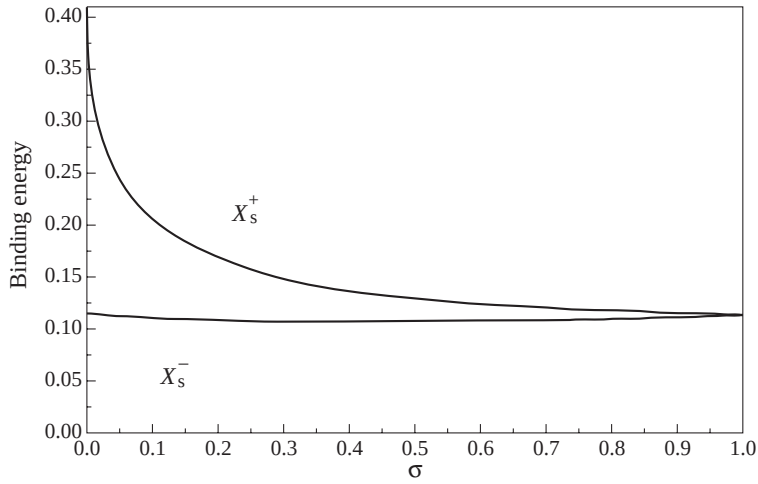

Fig. 1. Singlet state binding energies of 2D X^- and X^+ trions versus $\sigma = m_e^*/m_h^*$. The energy is measured in 2D exciton binding energy units.

orbits. The parameter c corresponds to the polarization of electron-hole pair by the third charged particle. The parameter d takes into account longitudinal oscillations of two equal particles near the equilibrium distance R_0. These two parameters are essentially important for the calculation of trion energy in the mass ratio region near the molecule H_2^+-like trion. The parameter s is used to correct the trion wave function at large distances. Reasonable results can be obtained even without the use of the latter parameter. A detailed discussion of the variational function is presented in [18].

The singlet state energy versus the electron-to-hole mass ratio, $\sigma = m_e^*/m_h^*$, is shown in Fig. 1. It should be noted that as expected, the energy behaves as square root of σ at $\sigma \to 0$.

We would like to stress that we obtained the binding energy dependence for whole domain of the electron-to-hole mass ratio (Fig. 1) using the same trial wavefunction with only 6 parameters. Actually, the limit $\sigma \to 0$ is difficult for consideration due to delta-like shape of the wavefunction on $R - R_0$ for two heavy particles. It is why the calculations in [5] were limited with $\sigma > 0.1$. A sophisticated variational technique for the charge exciton energy calculations was developed in [13]. The technique gives very precise results in the whole mass ratio domain. However, in contrast to our rather simple calculations, the trial wavefunction shape in [13] depends on the mass ratio and the number of variational parameters increases with decrease of the mass ratio.

In spite of a rather small number of the variational parameters used, our results are in good agreement with results of more sophisticated calculations [5, 8, 10, 13].

2. Triplet state

We take the triplet state trial function as an antisymmetrized singlet state function (1):

$$\psi_t(\vec{r}_1, \vec{r}_2) = \left[\exp(-ar_1 - br_2) + \exp(-ar_2 - br_1)\right] \frac{R\exp(-sR)}{1 + d(R - R_0)^2} \exp(i\theta_R), \quad (2)$$

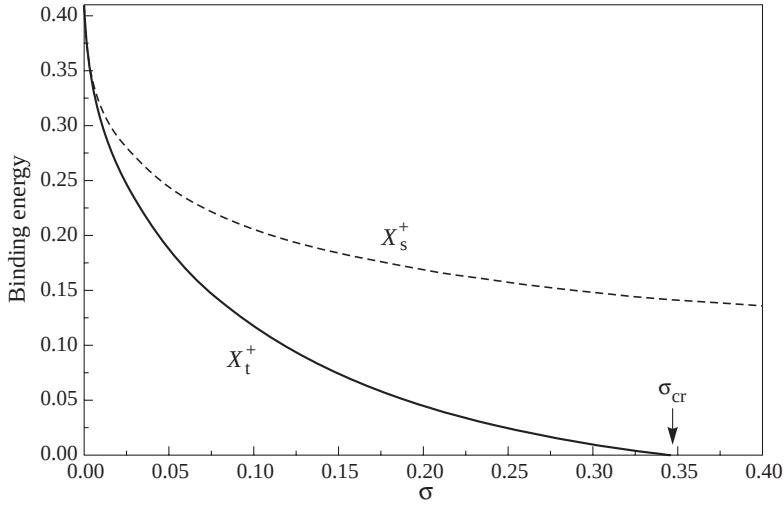

Fig. 2. The binding energy of 2D triplet X^+ trion (solid) versus $\sigma = m_e^*/m_h^*$ (in 2D exciton binding energies). The dashed curve is the singlet state X^+ binding energy.

where θ_R is the angle between the vector $\vec{R}$ and a certain direction given beforehand. The factor $\exp(i\theta_R)$ describes the antisymmetry of triplet state wave function and corresponds to the whole trion momentum $l = 1$.

Figure 2 shows the triplet state binding energy of X^+ trion versus the mass ratio. For reference, the singlet energy dependence is also plotted.

As was found from variational calculations, the triplet state vanishes, transforming into a resonant state at the critical mass ratio $\sigma_{cr} \approx 0.35$. The variational method gives the energy value that cannot be lower than its exact value. Therefore, the critical value of mass ratio provided by this method cannot exceed its exact value.

Let the triplet state binding energy of trion versus $\sigma - \sigma_{cr}$ be found near the critical value of mass ratio. We notice that this problem is analogous to the problem on vanishing the bound state of a particle with the momentum $l = 1$ in a 2D potential. In this case we have

$$E\ ln\left(\frac{E_{eff}}{E}\right) = -A(\sigma - \sigma_{cr}), \tag{3}$$

where E is the binding energy of trion triplet state in relation to the decomposition to an exciton and a free particle. The positive parameters E_{eff} and A can be evaluated from the variational calculations:

$$E_{eff} \approx 2.70; \qquad A \approx 1.17. \tag{4}$$

3. Conclusion

Simple variational wave functions with a few variational parameters are suggested to calculate with a good accuracy the singlet and triplet state energies of 2D X^+ and X^- trions in the whole range of electron-to-hole effective mass ratio. In a zero magnetic field, the trion triplet state is found to exist in a considerable mass ratio area close to the H_2^+-like trion. The critical value of electron-to-hole mass ratio is found to be more than 0.35.

Acknowledgments

This work was supported by the Russian Foundation for Basic Research, Grants 99-02-16796, 00-02-04020NNIO_a, and by the Federal Program on Support of Leading Scientific Schools, Grant 00-15-96812.

References

[1] M. A. Lampert, *Phys. Rev. Lett.* **1**, 12, 450 (1958).
[2] H. A. Bethe, *Z. Phys.* **57**, 815 (1929).
[3] B. Stebe and C. Comte, *Phys. Rev. B* **15**, 8, 3967 (1977).
[4] R. Schilling and D. C. Mattis, *Phys. Rev. Lett.* **49**, 11, 808 (1982).
[5] B. Stebe and A. Ainane, *Superlatt. Microstruct.* **5**, 4, 545 (1989).
[6] Z. Chen and C. D. Lin, *Phys. Rev. A* **42**, 1, 18 (1990).
[7] K. Kheng, R. T. Cox, Y. M. d'Aubigne, F. Bassani, K. Saminadayar and S. Tatarenko, *Phys. Rev. Lett.* **71**, 11, 1752 (1993).
[8] A. Thilagam, *Phys. Rev. B* **55**, 12, 7804 (1996).
[9] B. Stebe, G. Munschy, L. Stauffer, F. Dujardin and J. Murat, *Phys. Rev. B* **56**, 19, 12454 (1997).
[10] J. Usukura, Y. Suzuki and K. Varga *Phys. Rev. B* **59**, 9, 5652 (1999).
[11] W. Y. Ruan, K. S. Chan, H. P. Ho, R. Q. Zhang and E. Y. B. Pun, *Phys. Rev. B* **60**, 8, 5714 (1999).
[12] B. Stebe, A. Moradi and F. Dujardin, *Phys. Rev. B* **61**, 11, 7231 (2000).
[13] A. Esser, E. Runge and R. Zimmermann *Phys. Rev. B* **62**, 12, 8232 (2000).
[14] C. Riva, F. M. Peeters, K. Varga, *Phys. Status Solidi A* **178**, 1, 513 (2000).
[15] A. P. Mills, Jr. *Rhys. Rev. A* **24**, 6, 3242 (1981).
[16] A. K. Bhatia, R. J. Drachman, *Rhys. Rev. A* **28**, 4, 2523 (1983).
[17] A. K. Bhatia and R. J. Drachman, *Rhys. Rev. A* **35**, 10, 4051 (1987).
[18] R. A. Sergeev and R. A. Suris, to be published in *Phys. Solid State* **43**, 4 (2001), [translated from *Fiz. Tverd. Tela* **43**, 4, 714 (2001)].

9th Int. Symp. "Nanostructures: Physics and Technology"
St Petersburg, Russia, June 18–22, 2001

Resonant exciton-phonon spectra in ZnCdSe/ZnSe single QW: Raman scattering and hot luminescence; extended and localized excitons

V. V. Travnikov†, V. H. Kaibyshev†, M. Rabe‡ and F. Henneberger‡
† Ioffe Physico-Technical Institute, St Petersburg, Russia
‡ Humboldt University, Berlin, Germany

Introduction

Exciton–phonon spectra at resonant photoexcitation of ZnCdSe layers have been investigated in a number of works [1, 2, 3] earlier. However, the interpretation of their formation mechanisms had rather conflicting character. Part of authors considered that the observed lines go through Raman scattering mechanism and the others treated them as luminescence lines. The nature of exciton and phonon states which are involved in the process of REP formation have been treated differently also.

In the presented paper we have investigated in detail fine structure and intensity of resonant exciton–phonon (REP) spectra in ZnCdSe/ZnSe QW structures as function of tunable laser energy at 8 K. We have found that in REP spectra two types of lines are presented simultaneously. The most intensive REP component correspond to Raman scattering through extended exciton states. Other less intensive REP components correspond to hot luminescence of localized excitons. Analysis of phonon modes which can be involved in formation of REP spectra in our strain QW structures has been carried out.

Experimental

The investigated samples consisted from single 5 nm ZnCdSe quantum well (Cd mole fraction $\sim$ 13%) which was sandwiched between 20 nm (cap) and 25 nm (buffer) ZnSe layers. Emission spectra have been measured at $T \sim 8$ K at photo-excitation by a tunable dye laser. Typical resonant emission spectra, taken on one of the samples, for different excitation energies E_{ex} in the energy region of the ZnCdSe ground (heavy-hole) exciton resonance (the position of this resonance is shown by the arrow E_{1hh}) state are shown in Fig. 1. The most characteristic feature of these spectra is the presence of strong lines at the energy positions $E_{emi} = E_{ex} - \omega_i$, where ω_i is the characteristic phonon energy. Besides these resonant exciton–phonon (REP) lines a rather intensive photoluminescence (PL) band corresponding to the luminescence of ground exciton state E_{1hh} is observed (see spectrum 3 in Fig. 1).

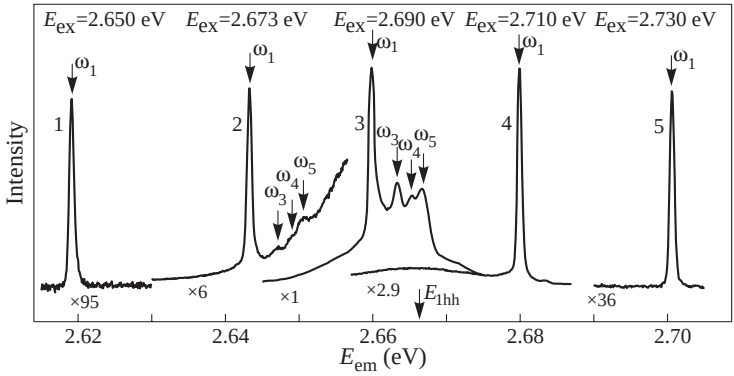

Fig. 1. Emission spectra of the QWW sample at different excitation energies ($T = 8$ K).

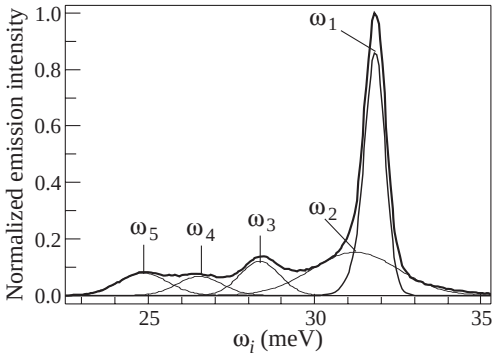

Fig. 2. Decomposition of one of the observed spectra.

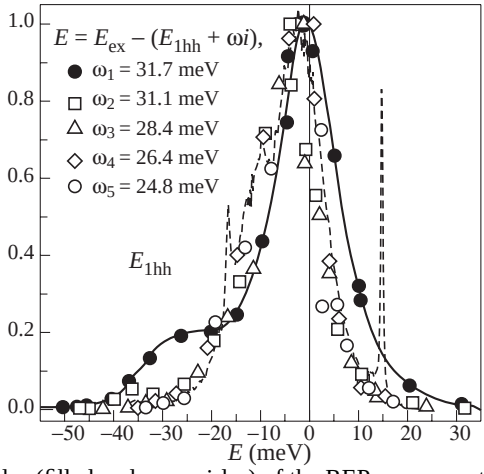

Fig. 3. Resonance profiles (filled and open cirles) of the REP components. The dashed line is the PL spectrum. The solid line is a guide for eye only.

The intensity of the $\omega_3 - \omega_5$ REP lines correlates with the intensity of the PL background under these lines. The lines are observed only in the energy regions where the PL background has noticeable intensity (spectra 2, 3, 4 in Fig. 1). At excitation far from the resonance (spectra 1, 5) where the PL background intensity is negligible there are only the ω_1 lines in the observed spectra. By the subtraction of the PL background from a spectrum we have obtained spectra which correspond to "pure" resonant exciton phonon optical transitions. After that we have decomposed with high accuracy these spectra into five components (Fig. 2) and have measured the resonance profiles (emission intensity versus laser energy) for all obtained REP components. The resonance profiles of all components are characterized by pronounced outgoing resonance (resonance enhancement for emitted (scattered) light). As far as the energy of participating phonons are different the energy position of maxima of the resonance profiles are shifted relatively each other. Therefore to have possibility to compare the character of the obtained resonance profiles we have presented in Fig. 3 the intensities of the REP components as a function of the energy $E = E_{emi} - E_{1hh} = E_{ex} - (\omega_i + E_{1hh})$ (where $E_{1hh} = 2.667$ eV). Figure 3 clearly shows, that the resonance profiles for the $\omega_2 - \omega_5$ components (open signs) in the limits of experimental accuracy are practically the same but they are quite different from the ω_1 resonance profile (solid circles).

The horizontal axis in Fig. 3 corresponds to the energy of final (emitting) photon states relative to the resonant energy E_{1hh}. Luminescence spectra also can be presented as a function of the energy E_{em} of emitting states relative to the energy E_{1hh} ($E = E_{em} - E_{1hh}$). As a result we have possibility to compare the efficiency of the REP processes with efficiency of luminescence for the terminal (final) states with the same energy. Dashed line in Fig. 3 corresponds to luminescence intensity as a function of the energy $E = E_{em} - E_{1hh}$ for the PL spectrum which was obtained at the excitation energy 2.712 eV (sharp lines in the spectrum correspond to Raman scattering).

Besides the emission spectra we have investigated the excitation spectra of the investigated emission. Properties of these spectra also have been used for suggested interpretation.

Analysis and discussion

The resonance profile for the ω_1 component has characteristic shape with the pronounced outgoing resonance ($E_{ex} = E_{1hh} + h1$) and the incoming resonance ($E_{ex} = E_{1hh}$) as a shoulder. Such shape is a characteristic for resonant Raman scattering through free exciton states with simultaneous participation of elastic scattering on defects or impurities [4, 5, 6] and it was observed earlier at investigation of RRS in bulk semiconductors [4, 5] and in QW structures [6]. If the Raman scattering would involve only phonons alone the incoming and the outgoing resonance would have the same intensity [6] in contrast to our results. In our case the outgoing resonance is the dominant feature of the ω_1 resonance profile. It indicates to an participation of additional elastic scattering events in the Raman process [6]. In QW structures such elastic process can be connected with scattering on roughness [6]. At excitation above the exciton resonance the elastic processes lead to the scattering through the real exciton states. Participation of real exciton states with large density of states increases essentially the intensity of resonant Raman scattering [6, 7] and it is this that leads to the dominant outgoing resonance. Taking into account the shape of the ω_1 resonance profile and the fact that the ω_1 line is observed in all parts of the investigated energy region we suppose that in our case the ω_1 line correspond to resonant Raman scattering on optical phonons through free exciton state.

In real QW structures the free exciton motion is restricted by processes of exciton localization at disorder potential fluctuations (mainly fluctuation of concentration and fluctuation of QW width). Excitons with kinetic energies exceeding the amplitude of the potential fluctuations are extended states and can be considered as free particles with "good" k_{xy} wave vectors in the QW(xy) plane. Evidently it are these extended exciton states that are mainly responsible for the ω_1 line.

Figure 3 shows that the resonance profiles of the $\omega_2 - \omega_5$ components are in the limits of experimental error coincident with the distribution of emission intensity in the PL spectrum. It is well known that at low temperature photoluminescence correspond to emission of localized excitons [8]. Coincidence of the resonance profiles of the $\omega_2 - \omega_5$ lines with the shape of PL band indicates that the formation mechanism of the $\omega_2 - \omega_5$ REP components is similar to mechanism of localized exciton luminescence formation. Such coincidence is evidently connected with the fact that the shape of both PL band and the resonance profile is determined basically by the energy spectrum of density of localized exciton states which are distributed mainly in the region of the "virtual" exciton band bottoms.

The phonon spectrum of our ZnCdSe/ZnSe structure can be changed in respect to bulk ZnSe values due to several causes: phonon confinement, composition and strain effects. In contrast to previous works we have estimated the influence of all these causes on the phonon energies in our structures. Our estimates shown that it is possible to neglect the

influence of confinement at discussion of phonon spectra in our structures. At the same time the influence of composition and strain is rather noticeable. In a mixed ZnCdSe crystal two additional phonon modes are appeared in the restrahl band region in comparison with pure initial crystals [9]. Due to the difference in lattice constants both ZnCdSe and ZnSe thin layers in our structures are lattice-matched to the GaAs substrate. As a result both layers are biaxially strained by the substrate. The biaxial strain leads to shift and splitting of the energy of optical phonons [10]. As a result the structure of phonon modes with k_{xy} wave vectors in a strained ZnCdSe layer are determined by six characteristic optical phonon energies in the centre of the Brillouin zone, all these energies are being in the restrahl band region.

Analysis and comparison of the estimated characteristic phonon energies with energies of the $\omega_2 - \omega_5$ components in the hot luminescence spectra shown that they can be connected with interaction of localized excitons with phonons which are characteristic for strained ZnCdSe solid solution and wave vectors of those not far from the centre of the Brillouin zone ($k \sim 1/a_B$, where a_B is the exciton Bohr radius). Nevertheless it is not possible to exclude some influences of density of phonon states on the shape of REP spectra [1].

The energy of the Raman (ω_1) component in our spectra is rather close to and between the estimated values of LO values both in ZnCdSe and ZnSe strained layers. In our structure the thickness of ZnSe barrier regions is much larger than the thickness of ZnCdSe well. As a result, Raman scattering in the ZnSe regions could give some contribution to the observed spectra. However, scattering on ZnSe phonons hardly gives any input in the ω_1 line formation because difference between the energy of the observed ω_1 Raman component and the estimated energies of ZnSe LO phonons is larger than our experimental accuracy. Moreover, the intensity of the ω_1 line resonantly increases by more than two orders in the energy region of ZnCdSe exciton states. This resonance enhancement evidences that the Raman process is connected with ZnCdSe QW slab.

The ω_1 Raman process goes through k_{xy} extended exciton states. Due to wave vector conservation law the ω_1 phonon also must correspond to k_{xy} component. However the difference between the ω_1 energy and the energy of the k_{xy} component is larger than our experimental accuracy. At the same time the ω_1 energy is close to position which is characteristic for interface optical phonon. If our estimations are correct it can mean that Raman scattering goes through interface optical phonons.

We gratefully acknowledge the financial support of the NATO Science Program, the Russian Foundation for Basic Research and the Deutsche Forschungsgemeinschaft

References

[1] S. Permogorov, et.al. *Proc. of the 23rd Int. Conf. on the Phys. of Semiconductors*, Berlin,1996, ed. by M. Scheffler and R. Zimmermann, p. 2015.
[2] I. Reshina, et.al. *Solid St. Commun.* **112**, 351 (1999).
[3] M. Lowish et al., *Phys. Rev. B* **54**, R11074 (1996).
[4] A. A. Klochikhin and A. G. Plyukhin, *JETP Lett.* **21**, 267 (1975).
[5] S. Permogorov and V. Travnikov, *Phys. Stat. Sol. (b)* **78**, 389 (1976).
[6] A. J. Shields, et al., *Phys. Rev. B* **46**, 6990 (1992).
[7] A. A. Gogolin and E. I. Rashba, *Sol. St. Commun.* **19**, 1177 (1976).
[8] E. Runger, A. Schlzgen, F. Henneberger and R. Zimmermann, *Phys. Stat. Sol. (b)* **188**, 547 (1995).
[9] R. G. Alonso, et al., *Phys. Rev. B* **40**, 3720 (1989).
[10] F. Cerdeira et al., *Phys. Rev. B* **5**, 580 (1972).

9th Int. Symp. "Nanostructures: Physics and Technology"
St Petersburg, Russia, June 18–22, 2001

Excitons and exciton oscillator strengths in two-dimensional superlattices

M. M. Voronov and E. L. Ivchenko
Ioffe Physico-Technical Institute, St Petersburg, Russia

Abstract. We have calculated excitonic Bloch states in a quantum well with a two-dimensional (2D) periodic potential. For the potential parameters used the two lowest states can be well described in the tight-binding approach while the higher states represent free excitons affected by the periodic potential. The redistribution of oscillator strengths for bound-like and free-like excitons with varying the period has been also analyzed.

The resonant optical reflection from a lateral array of quantum dots was calculated in [1] for particular limiting cases, namely, for short-period structures or in the constant-field approximation. Analytical results for arbitrary relation between the lateral period a and the light wavelength as well as between the exciton radiative and nonradiative damping rates have been presented recently in [2]. The theories [1, 2] are derived neglecting the overlap of the exciton envelope functions excited at different dots. In the present work we extend the theory allowing an exciton to tunnel coherently from one potential minimum to another.

We consider a quantum well (QW) with a periodic two-dimensional (2D) potential $V(x, y) = V(x + a, y) = V(x, y + a)$ acting at an exciton as at a single particle and making no effect on the exciton internal state, i.e. x, y are the in-plane coordinates of the exciton center-of-mass. For simplicity, we assume the potential $V(x, y)$ to have the point symmetry of a quadrate: $V(x, y) = V(\pm x, \pm y) = V(y, x)$. Due to the potential $V(x, y)$ the exciton energy spectrum is transformed from the parabolic dispersion $E_{exc}(k_x, k_y) = \hbar^2(k_x^2 + k_y^2)/(2M)$ in an ideal QW with $V \equiv 0$ into a series of 2D minibranches (M is the exciton in-plane translational effective mass).

Under normal incidence of the light only the Γ_1 excitonic states with $k_x = k_y = 0$ are excited. We enumerate these states by the index ν. The corresponding envelope functions, $\psi^\nu(x, y)$, of the exciton translational motion are periodic and invariant under all quadratic symmetry operations. They can be expanded in the Fourier series

$$\psi^\nu(x, y) = \frac{1}{a} \sum_{lm} c_{lm} \exp\left[i \frac{2\pi}{a}(lx + my)\right], \tag{1}$$

where l, m are integers $0, \pm 1...$ We choose the normalization condition $\int_{\Omega_0} |\psi|^2 \, dxdy = 1$, where Ω_0 is the unit cell, say the area $-a/2 < x, y < a/2$. Thus, the expansion coefficients c_{lm} satisfy the condition $\sum_{lm} |c_{lm}|^2 = 1$, whence

$$\sum_{lm} c_{lm}^{(\nu)*} c_{lm}^{(\nu')} = \delta_{\nu\nu'} \, . \tag{2}$$

Let us consider a pair of integers l, m as a two-component vector and denote the star of the vector (l, m) as β. The star contains the vectors $(\pm l, \pm m)$ and $(\pm m, \pm l)$. For $l \neq m \neq 0$ the star consists of eight vectors, otherwise it has four different vectors (if

$l = m \neq 0$ or $l = 0, m \neq 0$ or $l \neq 0, m = 0$) and one vector in the particular case $l = m = 0$. Note that, for the Γ_1 states, the coefficients c_{lm} in Eq. (1) with l, m belonging to the same star coincide: $c_{l,m} \equiv c_\beta$. In the method of plane waves defined by Eq. (1) the Schrödinger equation reads

$$\left[\frac{\hbar^2}{2M}\left(\frac{2\pi}{a}\right)^2 \beta^2 - E\right] c_\beta + \sum_{\beta'} c_{\beta'} \sum_{(l',m')\in\beta'} V_{lm,l'm'} = 0\,, \tag{3}$$

$$V_{lm,l'm'} = \frac{1}{a^2}\int_{\Omega_0} V(x,y)\,\cos\left\{\frac{2\pi}{a}[(l'-l)x + (m'-m)y]\right\} dxdy\,,$$

where $\beta^2 = l^2 + m^2$, E is the energy referred to the bottom of the exciton band in an ideal QW. Now we define the lateral potential as a periodic array of disks, namely,

$$V(x,y) = \sum_{lm} v(x - la, y - ma)\,, \tag{4}$$

$$v(x,y) \equiv v(\rho) = \begin{cases} -v_0\,, & \text{if} \quad \rho \leq R \\ 0\,, & \text{if} \quad \rho > R\,, \end{cases}$$

where $\rho = \sqrt{x^2 + y^2}$. Then one has

$$V_{lm,l'm'} = -v_0 \frac{R}{a} \frac{J_1\left(2\pi\sqrt{(l'-l)^2 + (m'-m)^2}\, R/a\right)}{\sqrt{(l'-l)^2 + (m'-m)^2}}\,, \tag{5}$$

where $J_1(t)$ is the Bessel function.

For the sake of convenience we introduce the dimensionless variables

$$\varepsilon = \frac{E}{E_0}\,,\ u_0 = \frac{v_0}{E_0}\,,\ \mu = \frac{R}{a}\,, \quad \text{where} \quad E_0 = \frac{\hbar^2}{2M}\left(\frac{2\pi}{R}\right)^2\,, \tag{6}$$

and the coefficients

$$C_\beta = \sqrt{n_\beta} c_\beta\,, \tag{7}$$

where n_β is the number of vectors in the star β. Then we can rewrite Eq. (3) in the dimensionless form as

$$(\mu^2\beta^2 - \varepsilon) C_\beta - u_0 \sum_{\beta'} U_{\beta\beta'} C_{\beta'} = 0\,, \tag{8}$$

$$U_{\beta\beta'} = -\frac{1}{v_0\sqrt{n_\beta n_{\beta'}}} \sum_{\substack{(l,m)\,\in\,\beta \\ (l',m')\,\in\,\beta'}} V_{lm,l'm'}\,.$$

The oscillator strength for the exciton ν is proportional to

$$f_\nu = \left[\frac{1}{a}\int_{\Omega_0} \psi^\nu(x,y) dxdy\right]^2 = \left[C_{0,0}^{(\nu)}\right]^2 = \left[c_{0,0}^{(\nu)}\right]^2\,. \tag{9}$$

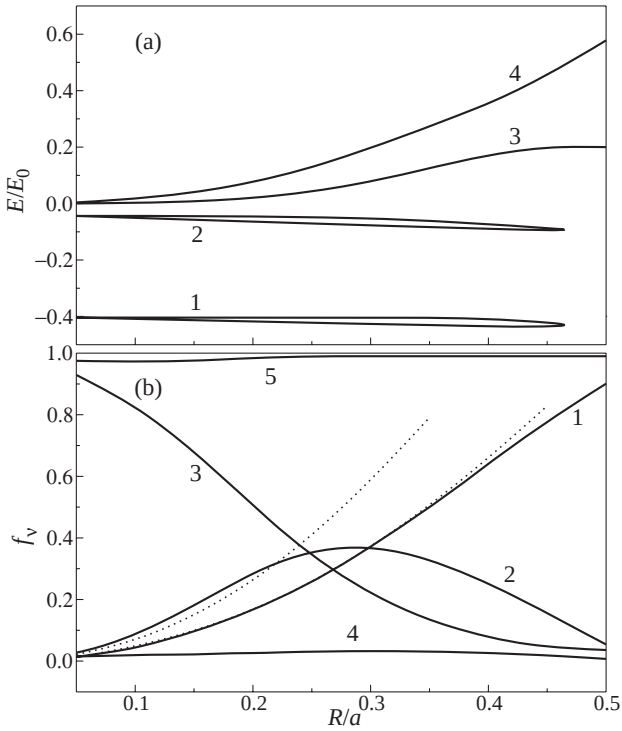

Fig. 1. The energy E_ν (a) and the oscillator strength f_ν (b) of the exciton in a 2D superlattice as a function of the ratio R/a. The calculation is performed for $u_0 = v_0/E_0 = 0.5$; a value of R is being kept fixed while the lateral period a is a variable. The index ν enumerates the exciton Bloch states with $k_x = k_y = 0$; curve 5 in (b) represents the sum of f_ν over the four lowest energy states. Dotted curves are obtained by using the tight-binding approximation, see Eq. (10).

The sum of oscillator strengths is conserved because according to (2) one has $\sum_\nu f_\nu = 1$.

Figures 1 and 2 represent calculations of E_ν and f_ν ($\nu = 1 - 4$) performed for values $u_0 = 0.5$ and $u_0 = 1$. The sum of f_ν over $\nu = 1 - 4$ is represented by curves 5 in Figs. 1b and 2b. Since this sum is close to 1 in the whole range of R/a from 0 up to 0.5, we conclude that the oscillator strengths for excitons with $\nu > 4$ is negligible.

For large enough periods, the exciton states $\nu = 1, 2$ with negative values of E can be approximated by the tight-binding functions

$$\psi^\nu(x, y) = \sum_{lm} \varphi_\nu(x - la, y - ma) ,$$

where $\varphi_\nu(x, y)$ are the normalized excitonic functions localized at a single potential $v(\rho)$ and characterized by the uniaxial symmetry. In the tight-binding approximation the oscillator strength is given by

$$f_\nu = \frac{1}{a^2} \left(\int \varphi_\nu(x, y) dx dy \right)^2 . \qquad (10)$$

Dotted curves in Figs. 1b and 2b are calculated by using Eq. (10). Another important result obtained is that for large a, i.e. for small ratios R/a, the oscillator strength for the exciton $\nu = 3$ is prevailing or, in other words, the state $\nu = 3$ is close to the free exciton state in

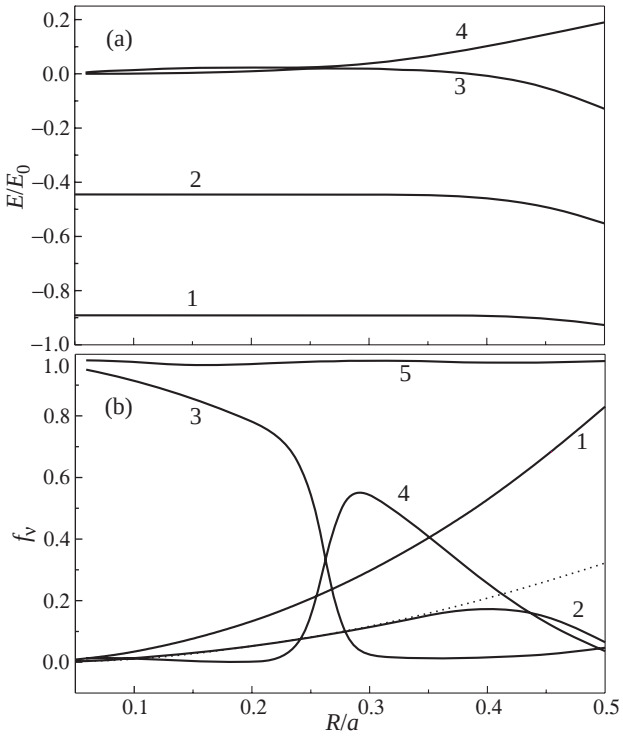

Fig. 2. The same as Fig. 1 but for $u_0 = 1$.

an ideal QW which is described by Eq. (1) with $c_{0,0} = 1$, $c_{lm} = 0$ if $l \neq 0, m \neq 0$ and, therefore, $f = 1$. With increasing R/a the oscillator strength is redistributed in favour of the bound-like states $\nu = 1$ and $\nu = 2$. This redistribution can be used for a qualitative analysis of "stealing oscillator strength" from neutral excitons X to charged excitons X^- mentioned by Kheng et al. [3] (as far as we ignore that the electrons filling the conduction band are not distributed periodically in the interface plane).

The states 3 and 4 in Fig. 2 clearly demonstrate the effect of anticrossing near the point $R/a = 0.25$. In this region the oscillator strengths f_3 and f_4 are linear functions of R/a with the sum $f_3 + f_4$ being constant, at the point $R/a \approx 0.26$ they become equal and the energy difference $E_4 - E_3$ exhibits a minimum, all these properties being fingerprints of the anticrossing effect.

Acknowledgements

The work is supported by Russian Ministry of Science, the program "Physics of Nanostructures".

References

[1] E. L. Ivchenko and A. V. Kavokin, *Fiz. Tverd. Tela* **34**, 1815 (1992) [*Sov. Phys. Solid State* **34**, 968 (1992)].

[2] E.L. Ivchenko, Y. Fu and M. Willander, *Fiz. Tverd. Tela* **42**, 1707 (2000) [*Phys. Solid State* **42**, 1756 (2000)].

[3] K. Kheng et al., *Phys. Rev. Lett.* **71**, 1752 (1993).

9th Int. Symp. "Nanostructures: Physics and Technology"
St Petersburg, Russia, June 18–22, 2001

Nonlinear absorption of surface acoustic waves by composite fermions

J. Bergli† and Y. M. Galperin†‡
† Department of Physics, University of Oslo,
PO Box 1048 Blindern, N-0316 Oslo, Norway
‡ Ioffe Physico-Technical Institute, St Petersburg, Russia

Abstract. Absorption of surface acoustic waves by a two-dimensional electron gas in a perpendicular magnetic field is considered. The structure of such system at the filling factor ν close to 1/2 can be understood as a gas of *composite fermions*. It is shown that the absorption at $\nu = 1/2$ can be strongly nonlinear, while small deviation form 1/2 will restore the linear absorption. Study of nonlinear absorption allows one to determine the force acting upon the composite fermions from the acoustic wave at turning points of their trajectories.

Introduction

Two-dimensional electron gases (2DEG) have been intensely studied in the last years. One of the experimental techniques used to investigate the properties of this system its interaction with a surface acoustic wave (SAW). We will consider the 2DEG in the fractional quantum Hall regime where a strong magnetic field is applied normal to the plane of the 2DEG. As well known, close to the half filling of the lowest Landau level the system will exhibit a metallic phase. This phase can be described in terms of a new type of quasiparticles, called composite fermions. The theory of composite fermions, as formulated in the language of Chern–Simons field theory in [1], has successfully explained the acoustic properties of the electron gas [2]. So far, however, greatest attention, both experimentally and theoretically, has been given to the linear response regime, which is appropriate for low intensity acoustic waves. From the study of ultrasonic absorption by electrons in metals it is known [3] that very interesting nonlinear effects can be observed. It is therefore natural to study nonlinear effects in the context of SAW absorption by the composite fermion metallic state. In particular are we interested in the fact that when nonlinear absorption occurs in a metal, a weak external magnetic field will restore the linear absorption [4].

First we need to understand how the acoustic wave interacts with the electron gas. Two mechanisms are usually considered, the deformational and the piezoelectric interactions. In typical experimental sets the deformational interaction can be neglected, and we consider only the piezoelectric field of the wave. Letting the x-axis point in the direction of sound propagation this is then given by $\mathbf{E}(x,t) = \mathbf{E}_0 \sin\xi = -\nabla\Phi$ with $\Phi = \Phi_0 \cos\xi$. Here Ω is the SAW frequency, and $\xi = qx - \omega t$ is the wave coordinate; $\mathbf{E}_0 \parallel \mathbf{q} \parallel \hat{\mathbf{x}}$. By Φ we mean the screened electrostatic potential.

The sensitivity to external magnetic fields was explained in the following way. If the wavelength $2\pi/q$ of the acoustic wave is much smaller than the electron mean free path ℓ, the electrons will traverse many periods of the wave before being scattered. If the electron moves in such a way that the component of its velocity in the direction in which the acoustic wave is propagating, it will experience a rapidly oscillating force. Consequently, the interaction between this electron and the acoustic wave will be weak. Since the electron (Fermi) velocity is much larger than the sound velocity, this will be the case for most of

the electrons. Only a small group, called the resonant group, will have their velocities in the sound propagation direction matched to the sound velocity, and thus interact strongly with the wave. The linear absorption, which is obtained in the limit of an acoustic wave of small (infinitesimal) amplitude, is determined by these resonant electrons. Consider a finite amplitude wave. Some of the resonant electrons will then be trapped in the valleys of the potential of the acoustic wave, see Fig. 1(a). The trapped electrons, moving in complete

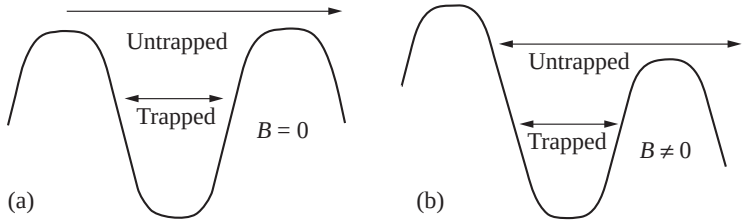

Fig. 1. On the trapping of resonant electrons in the absence (a) and in the presence (b) of an external magnetic field B.

synchrony with the wave, will not contribute to the absorption, and the absorption decreases. This leads to a amplitude dependent absorption coefficient, *i.e.* to nonlinear absorption. Consider now the effect of an externally applied magnetic field. The electrons will feel an extra force which will act to remove the electrons from the trapped group, see Fig. 1(b). Thus, we expect the linear absorption to be restored by the application of a magnetic field. The important point is that the magnetic force needed to restore the linear absorption gives a direct measure of the trapping force from the acoustic wave. That is, from the strength of the field needed to restore linear absorption we can infer the strength of the force from the acoustic wave on the electrons.

Theory of nonlinear acoustic absorption

Let us recall the main facts of the Chern-Simons theory for the composite fermions [1]. The Chern–Simons transformation mapping the electron system to an equivalent system of composite fermions can be described as attaching an even number of fictitious flux quanta of Chern–Simons magnetic field to each electron. In the mean field approximation the composite fermions will experience an effective field $B_0^* = B - m\phi_0 n_0$, where B is the external field, m is the number of attached flux quanta, $\phi_0 = h/e$ is the flux quantum and n_0 is the electron density. If $m = 2$, the effective field will vanish if the Landau level filling factor $\nu = 1/2$. The perturbation by the acoustic wave will induce a density modulation in the electron gas, $n = n_0 + \delta n$. This will lead to an oscillating component of the Chern–Simons magnetic field, so that the total effective field will be $B^* = B_0^* + b^{\rm ac}$ with $b^{\rm ac} = -2\phi_0 \delta n$. In addition, the motion of the electrons will drag with it the attached flux, and by Faraday law induce a Chern–Simons electric field, $\mathbf{e}^{\rm ac} = (2\phi_0/e)\,[\hat{\mathbf{z}} \times \mathbf{j}]$. The y-component of this field is found from the x-component of the current, which can be related to the density modulation by the equation for conservation of charge. Assuming the density modulation to be harmonic, $\delta n = (\delta n)_0 \cos\xi$, we get $e_y^{\rm ac} = 2\phi_0 v_s \delta n$. We will later see that this assumption is justified. As explained in [5] can we combine the x-component of $\mathbf{e}^{\rm ac}$ with the piezoelectric field of the acoustic wave. The corresponding total potential will be denoted Ψ. The main objective of this work is to determine the trapping of the electrons by the combined action of these fields, which are not present in the previously

studied electron problem.

Now we use the Boltzmann equation to calculate the nonequilibrium distribution function, f, of composite fermions, from which the absorption can be found. The Hamiltonian is

$$H = (\mathbf{P} + e\mathbf{A})^2/2m - e\Psi, \tag{1}$$

where $\mathbf{P}$ is the canonical momentum (the kinematic momentum is $\mathbf{p} = \mathbf{P} + e\mathbf{A}$), $\mathbf{A}$ is the vector potential. The vector potential consists of two parts. One emerges from the static external effective magnetic field B^*, and one from the AC Chern–Simons field that is created by the SAW-induced density modulation. the magnetic field is then $b^{\mathrm{ac}} = 2\phi_0 \left[n_0 - (2\pi\hbar)^{-2} \int d^2P\, f\right]$.

It is convenient to split the distribution function as $f = f_0(H) + f_1$ where f_0 is the Fermi function. Then the Boltzmann equation for f_1 is

$$\partial f_1/\partial t + \nabla_{\mathbf{P}} H \nabla_{\mathbf{r}} f_1 - \nabla_{\mathbf{r}} H \nabla_{\mathbf{P}} f_1 + f_1/\tau = -(\partial H/\partial t)(\partial f_0/\partial H). \tag{2}$$

Here we use the relaxation time approximation $-f_1/\tau$ for the collision operator which significantly simplifies the calculations. It should be noted that the Hamiltonian (1) is written in terms of the AC Chern–Simons magnetic field b^{ac}. The latter must be expressed through the density modulation as an integral over the distribution function. The Boltzmann equation (2) is then in reality a complicated integro-differential equation for the non-equilibrium distribution function. It is easy to show, however, that the main contribution to the density modulation comes from the equilibrium part $f_0(H)$, so that in calculating f_1 we can approximate the density modulation with $\delta n^{(0)}$ coming from $f_0(H)$. Indeed, using the fact that in all the region of acoustic amplitudes $e\Psi \ll \epsilon_{\mathrm{F}}$, where ϵ_{F} is the Fermi energy, we can then expand $f_0(H)$ around the point $H = p^2/2m$. The lowest-order term, $\delta n^{(0)}$, is estimated as

$$\delta n^{(0)} = -e\Psi(2\pi\hbar)^{-2} \int d^2p\, (\partial f_0/\partial H)\,\big|_{H=p^2/2m} = ge\Psi \tag{3}$$

Here $g = m/2\pi\hbar^2$ is the density of states per spin (as usual, we assume the 2DEG to be fully spin-polarized). Then we can solve Eq. (2) for f_1 with the assumption that $\delta n = \delta n^{(0)}$, and come back to show that the non-equilibrium correction coming from f_1 is small compared to $\delta n^{(0)}$. This will then justify our assumption of a harmonic density perturbation.

Solving the Boltzmann equation (2) by the method of characteristics we find the distribution function from which we calculate the absorption using the expression

$$P = \int \frac{d^2p}{(2\pi\hbar)^2} \langle \dot{H} f \rangle, \tag{4}$$

where $\langle \cdots \rangle$ denotes average over the period of the acoustic wave. For the case $\nu = 1/2$, $B^* = 0$ we find, after rather tedious calculations, the result

$$P = C(e\Pi_0/2\pi)^2\, (v_s/v_{\mathrm{F}})\, g\omega a\,, \tag{5}$$

where $C \sim 1$ is some numerical factor that can be found from numerical integration. Here $\Pi_0 = \Psi_0\sqrt{1+\alpha^2}$, $\alpha = 2mv_{\mathrm{F}}/q\hbar$ and $a = (\omega_0\tau)^{-1}$. $\omega_0 = q\sqrt{e\Pi_0/m}$ is the typical oscillation frequency of the trapped electrons in the potential of the acoustic wave. Since each scattering event rotates the particle momentum and leads to its escape from the

resonant group, nonlinear behavior exists only if $\omega_0\tau \gg 1$, or $a \ll 1$ Thus a is the main parameter responsible for nonlinear behavior. The above result (5) is the first term in an expansion in powers of a. We see that the absorption decreases when there is pronounced nonlinear behavior.

By studying the solution of (2) in the presence of a nonzero effective magnetic field we find that as expected the absorption is restored to the value of the linear absorption. The field necessary for this is $B^* \geq B_c = q\Pi_0/v_F$.

Discussion

We can now see how the various fields contribute in the trapping of the composite fermions. For electrons we would have Φ_0 appearing in place of Π_0 in the expression for B_c. In the present case we can show using our solution of the Boltzmann equation that in the limit of strong nonlinearity, $a \ll 1$, $\Psi_0 = \Phi_0$. That is, the effect of the x-component of the Chern–Simons field vanishes. In that case we have $\Pi_0 = \Phi_0\sqrt{1+\alpha^2}$, the factor $\sqrt{1+\alpha^2}$ describing the trapping effect of the oscillating Chern–Simons magnetic field b^{ac}. Inserting reasonable values, $m = 10^{-30}$ kg, $v_F = 10^5$ m/s, $v_s = 3\cdot10^3$ m/s and $\Omega/2\pi = 3\cdot10^9$ GHz, we get $\alpha \approx 50$. We see that the effect of the Chern–Simons field is to considerably enhance the efficiency of the acoustic wave in trapping composite fermions, and consequently that the effective magnetic field necessary to restore linear absorption will be correspondingly larger. Consequently, a way to check the above concept is first to reach nonlinear behavior at $B = B_{1/2}$, then restore the linear behavior by changing magnetic field by a quantity $\geq B_c$, without changing the SAW intensity.

References

[1] B. Halperin, P. A. Lee and N. Read, *Phys. Rev. B* **47**, 7312 (1993).
[2] R. L. Willett *et al. Phys. Rev. Lett.* **65**, 112 (1990);
A. D. Mirlin and P. Wölfle, *Phys. Rev. Lett.* **78**, 3717 (1997).
[3] Y. M. Galperin, V. D. Kagan and V .I. Kozub, *Zh. Eksp. Teor. Fiz.* **62**, 1521 (1972) [*Sov. Phys. JETP* **35** 798 (1972)];
V. D. Fil', V. I. Denisenko and P. A. Bezuglyi, *Fiz. Nizk. Temp.* **1**, 1217 (1975) [*Sov. J. Low Temp. Phys.* **1** 584 (1975)].
[4] Y. M. Galperin, V. L. Gurevich and V. I. Kozub, *Usp. Fiz. Nauk* **128**, 133 (1979) [*Sov. Phys. Uspekhi* **22** 352 (1979)].
[5] J. Bergli and Y. M. Galperin, cond-mat/9911234, 2000.

9th Int. Symp. "Nanostructures: Physics and Technology"
St Petersburg, Russia, June 18–22, 2001

δ-layer quenched high-frequency conductivity in GaAs/AlGaAs heterostructures: Acoustical studies

I. L. Drichko†, A. M. Diakonov†, Yu. M. Galperin†*, A. V. Patsekin†,
I. Yu. Smirnov† and A. I. Toropov‡
† Ioffe Physico-Technical Institute, St Petersburg, Russia
* Department of Physics, University of Oslo,
PO Box 1048 Blindern, 0316 Oslo, Norway
‡ Semiconductors Physics Institute of SD of RAS,
630090 Novosibirsk, Russia

Abstract. Electron density and high-frequency (hf) hopping conductivity of two-dimensional electron gas (2DEG) in SI δ-doped GaAs/AlGaAs heterostructures are studied by acoustic methods. In the quantum Hall regime at small filling factors both quantities appear dependent on the cooling procedure, characterized by an initial temperature T_0 of a fast cooling to 4.2 K by immersing into liquid He. These facts are interpreted assuming that T_0 is the freezing temperature for the conductivity of the δ-layer which supplies electrons to 2D channel.

Introduction

Acoustical studies of heterostructures in the quantum Hall regime allow one to determine their high-frequency conductivity, $\sigma_{xx}(\omega)$, as a function of magnetic field. At large half-integer filling factors, when the electron states at the Fermi level are extended, $\sigma_{xx}(\omega)$ does not differ from that measured in a conventional direct-current experiment, $\sigma_{xx}^{dc} \equiv \sigma_{xx}(0)$ [1]. However, the difference is enormous at small filling factors, or near the middle points of developed Hall's plateaus where σ_{xx}^{dc} is extremely small while both real and imaginary parts of $\sigma_{xx}(\omega) \equiv \sigma_1(\omega) - i\sigma_2(\omega)$ are noticeable [2]. They can be determined from simultaneous measurements of attenuation and velocity of a surface acoustic wave (SAW) propagating along the interface and interacting with 2DEG. The experiment [2] evidenced that $\sigma_2 \gg \sigma_1$. This fact, along with the observed temperature and frequency dependences of σ_1 and σ_2, lead to a conclusion that the conductance is due to electron hopping between two local minima of a random impurity potential spaced by a distance smaller that the average correlation length of the latter, see [3]. Another important feature of δ-doped GaAs/AlGaAs heterostructures is that near the centers of the Hall plateaus the 2D channel appears to be considerably shunted by a Si δ-layer which supplying the carriers to the channel [4].

Our previous experiments with different samples have shown that near the Hall plateaus centers both the SAW attenuation, Γ, and the velocity variation, $\Delta V/V$, are poorly reproducible. Namely, the values of σ_{xx} measured in different experiments may vary by several times. At the same time, the quantities measured either in low magnetic fields, or at half-integer filling factors do not differ by more than 20%. We believe that the lack of reproducibility is due to different cooling procedures from room temperature to 4.2 K. In the present work we study this phenomenon systematically.

Experimental results and discussion

We have measured the attenuation coefficient, Γ, and variation of the sound velocity, $\Delta V/V$, of a SAW as function of magnetic field $H \leq 7$ T in a GaAs/AlGaAs heterostructure with the sheet density $n_s \approx 1.4 \times 10^{11}\,\mathrm{cm}^{-2}$. The measurement were performed for SAW frequencies, 30 and 150 MHz, at two temperatures, 4.2 and 1.5 K. The details of the experimental method, as well as the way to extract $\sigma_{xx}(\omega)$ from measured quantities, are presented in [1, 2, 4]. The cooling process was carefully checked and controlled.

The magnetic field dependences of σ_1 and σ_2 at the frequency 30 MHz are shown in Fig. 1(a) (the raw data for Γ and $\Delta V/V$ are presented in the inset). Acoustic methods at low temperatures require placing the sample in a evacuated chamber, since a cooling liquid causes an extensive SAW absorption. To achieve cooling of a sample attached to a cold finger down to 1.5–4.2 K one needs (after pumping) to fill the chamber with an exchange gas (He^4 at a pressure 0.1 mm Hg). The chamber itself is surrounded with liquid He^4 which can also be pumped to lower the boiling point. Besides, the superconducting solenoid is usually cooled with liquid N_2 before the liquid He^4 being poured into the cryostat.

Fast cooling of a sample is actually accomplished when in the chamber there is the exchange gas and the chamber itself is immersed in the liquid helium. To vary the cooling procedure the sample was pre-cooled to a certain temperature, T_0, with the aid of cool He^4. After the sample chamber was quickly immersed into the liquid helium. This pre-cool temperature, T_0, was measured with a carbon resistor.

Magnetic field dependences of σ_1 in the region 2–4 T for different T_0 are presented in Fig. 1(b). The minima of the curves correspond to the filling factor $\nu = 2$. It follows that the variation of the cooling procedure influences both the minimum position and the minimal value, $\sigma_{\min}$, of σ_1.

The dependence of $\sigma_{\min}$ on the pre-cool temperature T_0 is shown in Fig. 2(a). It follows

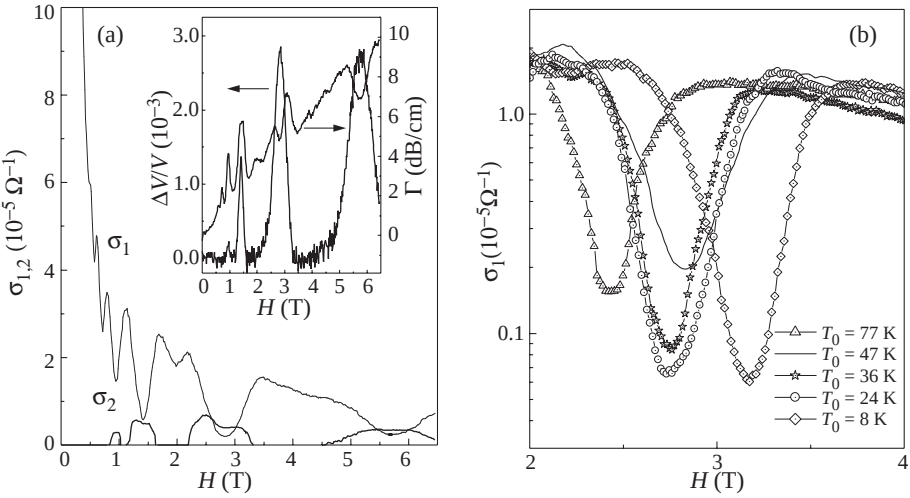

Fig. 1. (a) Dependences of the hf-conductivity components σ_1 and σ_2 on the magnetic field H. $T = 1.5$ K, $f = 30$ MHz. Inset: magnetic field dependences of the SAW attenuation, Γ, and of the relative velocity change $\Delta V/V$, $T = 1.5$ K, $f = 30$ MHz. (b) Magnetic field dependences of σ_1 for $H = 2{-}4$ T and different initial temperatures, T_0. $T = 1.5$ K, $f = 30$ MHz.

that $\sigma_{\min}$ is an increasing function of T_0. The effective 2DEG density determined from the equation $\nu = 2$ for the minimum position is shown in Fig. 2(b). It is a *decreasing* function of T_0. The results for $\nu = 1$ are similar to those mentioned above.

For the case of $T_0 = 77$ K, time dependences of $\Gamma(H)$ and $\Delta V(H)/V$ have also been monitored. After the sample has been cooled, the measurements were performed every second hour during 28 hours. No changes in both quantities were observed. However, this cooling process proved to be quite reversible. If one takes a sample previously cooled to 4.2 K from, say, $T_0 = 8$ K, heats it back to 24 K, and then cools it again to 4.2 K, one obtains the same experimental values of Γ and $\Delta V/V$ as they were at 4.2 K in the preceding cooling cycle.

We believe that the aforementioned results are consistent with our previous conclusion [4] regarding an important role of hf-conductance through δ-layer in the situation when the electron states in the 2D-channel are localized.

To explain qualitatively the observed behavior let us analyze δ-layer contribution to σ_1. Since the electron density in the 2D-channel is about 10 times smaller than the impurity density in the δ-layer, to the lowest approximation one can consider the latter as being isolated from the channel. Because of the same reason, at low temperatures, the electron Fermi level in the δ-layer is located above the density-of-states maximum. Thermal ionization of some impurities leads to its shift *downwards*, i. e. to the region of *larger* density of states. Now, let us assume that the initial electron energy distribution at $T = T_0$ is *quenched* due to electron trapping and does not change during subsequent cooling. Then we immediately arrive at the conclusion that the Fermi-level density of states, and consequently σ_1, are *increasing* functions of T_0. The observed decrease in the 2D-channel density with increase of T_0 can be also explained as caused by an additional thermally-induced electron trapping in the δ-layer which is also quenched at $T \leq T_0$. Thus the above assumptions are consistent with Figs. 2(a) and 2(b).

We have employed the method [4] to extract the "hopping" contribution of the 2D-channel. It appears almost independent of T_0 and equal to $(2.7 \pm 0.6) \times 10^{-8}\,\Omega^{-1}$. The electron localization length calculated from this value is $\xi = 2.6 \times 10^{-6}$ cm which is slightly greater than the magnetic length 1.6×10^{-6} cm for $H \approx 2.8$ T. Note that σ_1 at

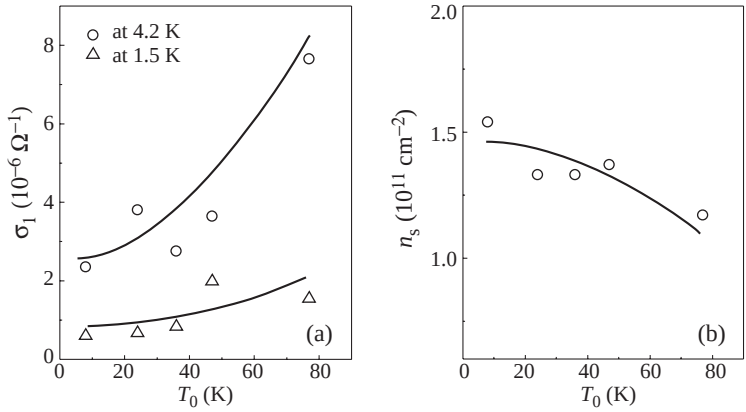

Fig. 2. The experimental dependencies of real part of hf-conductivity σ_1 (a) and sheet density (b) on T_0 at filling factor $\nu = 2$ at $T = 1.5$ K and 4.2 K. $f = 30$ MHz.

half-integer filling factors, within the experimental error appears to be independent of the cooling procedure.

Conclusion

We conclude that hf-conductance of δ-doped GaAs/AlGaAs heterostructures is sensitive to the cooling procedure, and a proper control of the latter is important.

Acknowledgments

The work is supported by RFBR 01-02-17891 and MNRF 97-1043 grants.

References

[1] I. L. Drichko, A. M. D'yakonov, A. M. Kreshchuk, T. A. Polyanskaya, I. G. Savel'ev, I. Yu. Smirnov and A. V. Suslov, *FTP* **31**, 451 (1997) [Semiconductors 31, 384 (1997)].
[2] I. L. Drichko, A. M. D'yakonov, V. D. Kagan, I. Yu. Smirnov and A. I. Toropov, *Proc. of 24th ICPS*, Jerusalem, on CD-ROM (1998).
[3] A. L. Efros, *Zh. Eksp. Teor. Fiz.* **89**, 1834 (1985) [JETP **89**, 1057 (1985)].
[4] I. L. Drichko, A. M. Diakonov, I. Yu. Smirnov, Yu. M. Galperin and A. I. Toropov, *Phys. Rev. B* **62**, 7470 (2000).

9th Int. Symp. "Nanostructures: Physics and Technology"
St Petersburg, Russia, June 18–22, 2001

Dilation of the giant vortex state in a mesoscopic superconducting loop

S. Pedersen, G. R. Kofod, J. C. Hollingbery, C. B. Sørensen and P. E. Lindelof
The Niels Bohr Institute, University of Copenhagen,
Universitetsparken 5, DK-2100 Copenhagen, Denmark

Abstract. We have experimentally investigated the magnetisation of a mesoscopic aluminum loop at temperatures well below the superconducting transition temperature T_c. The flux quantisation of the superconducting loop was investigated by a μ-Hall magnetometer in magnetic intensities between ± 100 Gauss. The magnetic intensity periodicity observed in the magnetisation measurements corresponds to integer values of the superconducting flux quantum $\Phi_0 = h/2e$. A closer inspection of the periodicity however reveal a systematic variation of the magnetic intensity periodicity. These variations we interpret as a consequence of a giant vortex state nucleating on either the inner or the outer side of the loop.

The measurement described in this paper were performed on a micron sized superconducting aluminium loop placed on top a μ-Hall magnetometer. The μ-Hall magnetometer was etched out of a GaAs/$Ga_{0.7}Al_{0.3}As$ heterostructure. The mobility and electron density of the two-dimensional electron gas was $\mu = 42\,\mathrm{T}^{-1}$ and $n = 1.9 \times 10^{15}\,\mathrm{m}^{-2}$. A symmetrical $4\,\mu\mathrm{m} \times 4\,\mu\mathrm{m}$ Hall geometry was defined by standard e-beam lithography on top of the heterostructure. In a later processing step a lift-off mask was defined on top of the μ-Hall probe by e-beam lithography. After deposition of a $t = 90$ nm thick layer of aluminium and lift-off the sample looked as presented in Fig. 1.

The mean radius of the aluminium loop was $R = 2.16\,\mu\mathrm{m}$ and the average wire width w was 316 ± 40 nm.

By using the expression

$$n\Phi_0 = n\frac{h}{2e} = \Delta(\mu_0 H)\pi R^2, \tag{1}$$

where $A = \pi R^2$ is the area of the loop given by its mean radius R, it is found that a single flux jumps ($n = 1$) corresponds to a magnetic intensity periodicity given by $\Delta(\mu_0 H) = 1.412$ Gauss.

The samples was immersed in a ^{3}He cryostat equipped with a superconducting soleniode driven by a DC current supply. The relation between the Hall voltage V_H and the magnetic intensity H perpendicular to the μ-Hall magnetometer is given by the classical Hall effect

$$V_H = -\frac{I}{ne}\mu_0(H + \alpha M), \tag{2}$$

were I is the DC current through the μ-Hall magnetometer and α is a dimensionless number of the order of unity, which corresponds to the ratio between the sensitive area of the μ-Hall probe and the area of the object which is the source to the magnetisation M. In our case we find that α typically was in the range between $0.3 \ldots 0.4$.

By using standard AC lock-in techniques where the driving current I was modulated the Hall voltage V_H was measured as a function of magnetic intensity $\mu_0 H$.

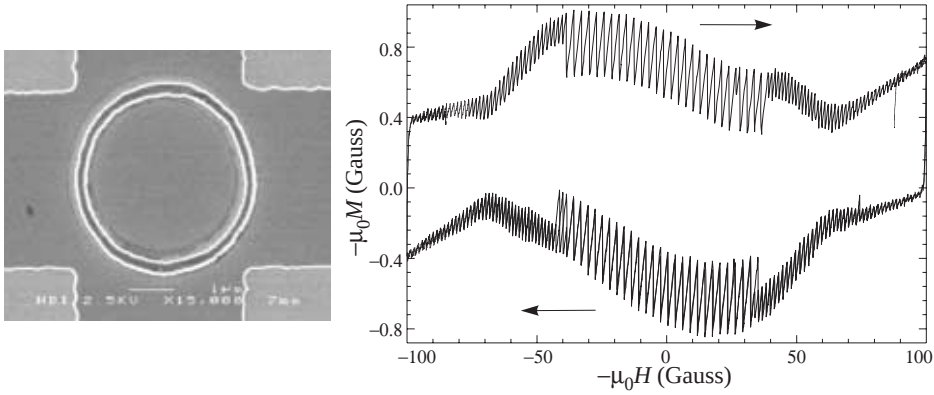

Fig. 1. Left: Scanning electron microscope image of a μ-Hall probe and aluminium loop. Right: Measured magnetisation $\mu_0 M$ detected by the μ-Hall probe as a function of magnetic intensity $\mu_0 H$. The curve displays distinct jumps corresponding to the abrupt changes in magnetisation of the superconducting loop when the system changes state. The measurements were performed at $T = 0.36$ K.

In Fig. 1 is displayed the measured local magnetsation $\mu_0 M$ detected by the μ-Hall probe as a function of magnetic intensity $\mu_0 H$. The curve displays a series of distinct jumps corresponding to the abrupt changes in magnetisation of the superconducting loop. The difference in magnetic intensity between two successive flux jumps is approximately given by $\Delta(\mu_0 H) = 1.4$ Gauss or $\Delta(\mu_0 H) = 2.8$ Gauss which corresponds to either single or double flux jumps ($n = 1$ or $n = 2$).

Large flux jumps ($n > 1$) or flux avalanches, occur whenever the system is trapped in a metastable state. It was generally observed that these flux avalanches become more pronounced with decreasing temperature, at low magnetic intensities and for wide loops.

The energy barrier causing the metastability of the eigenstates of the loop, are due to either the Beam-Livingston surface barrier or the volume barrier, or even an interplay of both [1, 3, 4].

In Fig. 2 the magnetic intensity difference between successive jumps $\Delta(\mu_0 H)$ in units of the 1.412 Gauss (corresponding to a single superconducting flux quantum), has been plotted as a function of magnetic intensity. It is seen that the magnetic intensity difference between the observed jumps is, to a high accuracy, given as integer values of 1.412 Gauss. At absolute magnetic intensities lower than 40 Gauss double flux jumps dominates, whereas at higher absolute magnetic intensities only single flux jumps are observed. The curve presents both an up sweep and a down sweep - indicated by the arrows.

For the graphs presented in Fig. 2 it is seen that a small systematic variation of the value of the flux jumps occur when the magnetic intensity is changed. This variation appear in the sense, that as the magnetic intensity is increased (decreased) the size of the flux jumps decreases (increases). Thus these deviations are depended, on not only the size of the magnetic intensity but also, on which direction the magnetic intensity was sweeped during measurements.

In the right part of Fig. 2 we use Eq. (1) to calculated the effective radius R of the superconducting loop and plot this radius as a function of magnetic intensity. The horizontal lines represents the mean inner R_i and outer radius R_o determined from the SEM picture. It is seen that as the magnetic intensity is changed from negative to positive values, the effective radius, as defined from the flux quantization condition of the loop, changes from

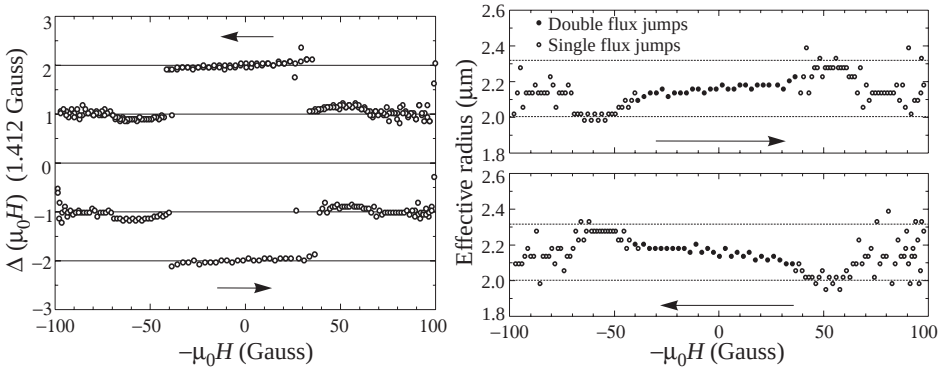

Fig. 2. Right: Effective radius R calculated by using Eq. (1). The filled (open) dots corresponds to single flux jumps $n = 1$ (double flux jumps $n = 2$). Left: The magnetic intensity difference $\Delta(\mu_0 H)$ between two successive jumps in magnetisation. Given in units of 1.412 Gauss corresponding to a single flux quantum $\Phi_0 = h/2e$. The positive (negative) flux values corresponds to the case where $\mu_0 H$ was decreased (increased) during the measurements. Arrows indicate sweep direction.

inner to outer radius and vice versa.

In a superconducting loop at low magnetic intensities, it is expected that the appropriate effective radius is given by the geometrical mean between outer and inner radius $R = \sqrt{R_i R_o}$ [5]. This is in good agreement with the observed behavior around zero magnetic intensity.

However in the regime of high magnetic intensities the concept of surface superconductivity becomes important and a giant vortex state will occur. In this regime two degenerate current carrying situations are possible — the giant vortex state can either circulate the loop clockwise or anti-clockwise. In the case of a positive magnetic intensity, and a clockwise (anti-clockwise) circulating current the giant vortex state will nucleate at the outer (inner) edge of the loop. On the other hand if the magnetic intensity is negative the giant vortex state will nucleate at the inner (outer) radius of the loop [6].

The width of the giant vortex state is approximately given by the magnetic length $l_H = \sqrt{\hbar/eH}$ [2]. Hence any variation of the effective radius should take place over a magntic field range given by the condition that the width of the loop width of the loop and the magnetic length is comparable; $w = l_H$. Such an estimate gives a characteristic magnetic intensity of 34 Gauss in good agreement with the presented data in Fig. 2.

Since the orientation of the current in the loop is determined by the sweep direction (Lenz' law), a decreasing (increasing) magnetic intensity will give rise to a anti-clockwise (clockwise) circulation. Hence as the magnetic intensity is sweeped from e.g. a high positive value to a high negative value the effective radius of the loop will change from inner to outer radius and vice versa.

The important dimensionless parameter for comparison the presented results with the theoretical results in[7, 8, 9]; are given by the ratio $x = R_i/R_o$ between outer and inner radius. In our case corresponding to $x = 0.86$.

Both theoretical groups find that at large x values (corresponding to a loop consisting of a one-dimensional wire) no or little variation of the effective radius should be observed. Whereas at small x values (corresponding to a disc) a fast decrease of the effective radius occur as the magnetic intensity increases. In the intermediate regime $x = 0.5$, a rather smooth transition between average and outer radius should take place when the magnetic

intensity increases.

In the presented measurement $x = 0.75$, we indeed observe that the effective radius vary smoothly between inner and outer radius. This behavior looks similar to the one predicted for loops with $x = 0.5$, however not similar to the one predicted expected for $x = 0.75$. However we do not find this discrepancy sever due to the following reasons: The calculations by Bruyndoncx et al. [9] were done using a linearized first Ginzburg–Landau equation, hence these results are only valid close to the phase transition, viz. $R_o/\xi_o < 1$. In the work by Peeters et al. [7, 8] the full set of non-linear Ginzburg–Landau equations were solved self-consistently, but under the assumption that $R_o/\xi_o = 4$ and 2. Neither of these conditions were fulfilled in our experiments, were we estimate $R_o/\xi_o \approx 20$, it is furthermore seen by comparing the results of Peeters et al. that calculations with larger values of R_o/ξ_0 properly would give rise to a better agreement.

References

[1] P. Singha Deo, V. A. Schweigert and F. M. Peeters, *Phys. Rev. B* **59** 6039 (1999).
[2] R. Benoist and W. Zwerger, *Z. Phys. B* **103** 377-381 (1997).
[3] C. P. Bean and J. D. Livingston, *Phys. Rev. Lett.* **12**, 14 (1964).
[4] X. Zhang and J. C. Price, *Phys. Rev. B* **55** 3128 (1997).
[5] R. M. Arutunian and G. F. Zharkov, *Journal of Low Temp. Phys.* **52** 409 (1983).
[6] M. Tinkham, *Introduction to superconductivity*, (McGraw-Hill 1975).
[7] F. M. Peeters, V. A. Schweigert, B. J. Baelus and P. S. Deo, cond-mat/9910172 to appear in Physica C (Proceedings Conf. on Vortex Matter, Crete (September 1999)
[8] B. J. Baelus, F. M. Peeters and V. A. Schweigert, cond-mat/9910030.
[9] V. Bruyndoncx, L. Van Look, M. Verschuere and V. V. Moshchalkov, *Phys. Rev. B* **60** 10468 (1999).

9th Int. Symp. "Nanostructures: Physics and Technology"
St Petersburg, Russia, June 18–22, 2001

Manifestation of the upper Hubbard band in conductivity of 2D p-GaAs-AlGaAs structures

N. V. Agrinskaya, Yu. L. Ivanov, V. M. Ustinov and D. A. Poloskin
Ioffe Physico-Technical Institute, St Petersburg, Russia

A significant increase to studies of conductivity in 2D structures in recent years was mostly related to experimental observation of metallic-type conductivity in Si MOSFETs and GaAs/AlGaAs heterostructures [1, 2]. Since the scaling theory of localization predicts a dielectric behavior at $T \to 0$ for any 2D structure such an observation was of principal importance. Although a lot of possible explanations of this behavior was suggested (see e.g. [3, 4]) until now no unique mechanism capable to explain all experimental features was evidenced. An attempt to attack this problem was in particular undertaken in our paper [5] where we assumed that the behavior observed is dominated by a contribution of the upper Hubbard band corresponding to the bandtail of localized states. However an absence of independent information concerning the localized states in the 2D structures mentioned above does not allow a direct comparison of theoretical predictions with experimental data.

Correspondingly, a possibility to study transport in the upper Hubbard band in some model system with a clear picture of localized states is to our opinion of undoubted interest. One expects that for 3D case an observation of the contribution of the upper Hubbard band is a complicated task since according to theoretical calculations the energy of doubly occupied shallow impurity state of donor (D^-) or acceptor (A^+) type is too small ($E_- = 0.055E_0$, where E_0 is the binding energy of the isolated impurity); correspondingly, the conductivity over the upper Hubbard band was considered to be unimportant with respect to the contribution of the standard conductivity band. Note that according to our previous studies the signiture of the upper Hubbard band can be traced in hopping magnetoresistance of different semiconducting materials while the extracted values of the corresponding Hubbard energy have appeared to be much less than theoretical estimates.

An encouraging situation in this concern corresponds to 2D systems with selective doping where the concentration of electrons in a well can be varied in a controlled way and, cosequently, one can control a relation between single-occupied and doubly-occupied localized states. Then, in the narrow enough wells (when the spatial scale of the site wave function becomes to be comparable to the well width) the energies E_- and E_0 are enhanced. It is expected that such an enhancement of the binding energy is more pronounced for D^- state because of the larger value of localization radius. Thus a situation is possible when the energy of D^- state is already lowered while the energy of D_0 state is not changed significantly which leads to a decrease of the Hubbard energy. This latter fact improves the possibilities to study the contribution of the D-band.

We have chosen the system GaAs/AlGaAs with the well width $d \sim 15$ nm which was doped by acceptor impurity Be having a localization radius (2 nm) much smaller than d. By a selective doping of the well regions and the barrier regions we have reached a situation when the upper Hubbard band has been occupied in the equilibrium, the conductivity being over its states. The experiments have shown that the binding energy of A^+ state increases significantly for the wells with $d = 15$ nm with respect to the bulk case. We have estimated

the radius of this state independently from an analysis of temperature behavior of hopping conductivity.

1. Experiment

The structures to be studied were MBE-grown on semiinsulating substrates GaAs(100) with a help of Riber 32P equipment supplied by solid sourses Ga, Al, As and Be. The growth took place in As-enreached conditions at the substrate temperature 580 °C, the growth rate being 10 nm/min. The structures contain 10 quantum wells with a width 15 nm separated by barriers AlGaAs with a thickness 15 nm. The confining layers AlGaAs were deposited before the first well and after the last one. The growth was finished by a deposition of the covering GaAs layer with a thickness 20 nm. In the both samples studied the middle region of the well (with a thickness 5 nm) was doped; in one of the samples (293) the barriers were undoped while in another sample (213) the middle region of the barriers with a width 5 nm was doped. Thus the widths of the undoped spacer layers from both sides of the barrier. We used Be as p-type dopant with a concentration 10^17 atoms/cm^3; the hole concentration measured at $T = 300$ K was equal to $8 \cdot 10^16\,\mathrm{cm}^{-3}$ and $10^{17}\,\mathrm{cm}^{-3}$ for sample 293 and 213 correspondently. The contacts were made by cintering in of sputtered Au containing 3% of Zn during 2 min at temperature 150 °C.

In Fig. 1 we showed temperature behavior of Hall coefficient for the two samples. The temperature region 50–300 K corresponds to ionization of acceptors into the valence band. The fact that the carrier transport takes place in the valence band is evidenced by rather high values of mobility — (300–500) cm^2 V/s at 300 K — and by its temperature behavior $\mu \sim T^{-3/2}$. At low temperatures the activation law of Hall coefficient is observed; at higher temperatures the slop is decreased which can be related to devastation of impurities. In particular, for the sample 293 exhibiting some compensation degree (rather probable in a view of a presence of background impurities and interface states) at low temperatures there exists a region with a slope E_a while at higher temperatures a region with a slope $E_a/2$ is exhibited. The ionization energies estimated from the slopes mentioned above appear to

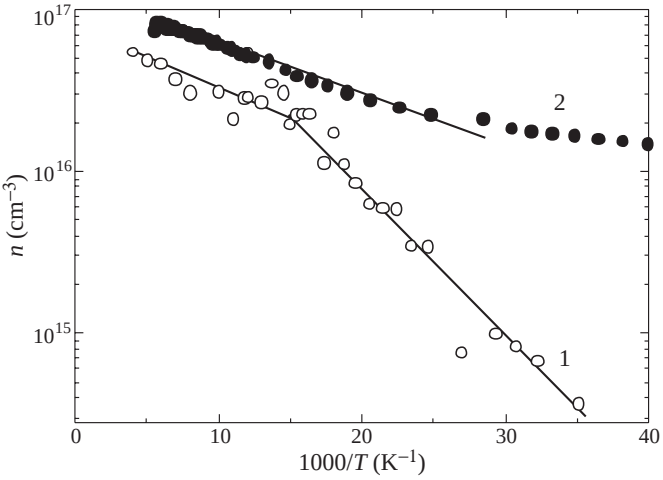

Fig. 1. Temperature behavior of carrier concentrations for the two samples calculated from Hall coeficient: 1—sample 293, 2—sample 213. The carrier concentrations were calculated as averaged over the volume with an account of the sample thickness 150 nm

be different for the two samples and are equal to 7 meV and 21 meV, respectively.

At temperatures lower than 50 K (up to 1.7 K) the temperature behavior of conductivity evidences its hopping character (Fig. 2). The slopes of $\sigma(T)$ in terms of $T^{-1/3}$ are different for the two samples.

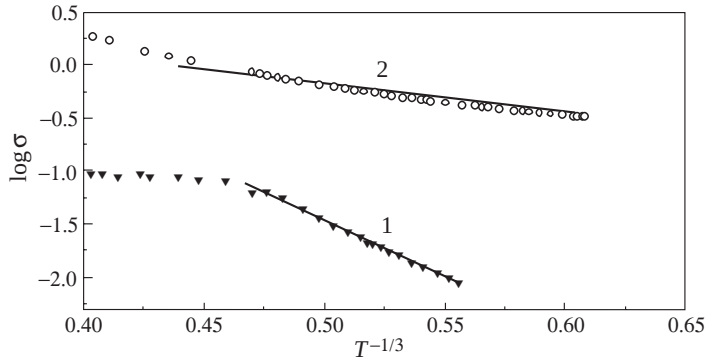

Fig. 2. Temperature behavior of conductivity for the two samples: 1—sample 293, 2—sample 213.

2. Discussion

According to the data published until now, the position of Be level in GaAs corresponds to 27 meV. Our experiment shows for the sample 293 (only GaAs layers are doped) the activation energy 20 meV. The discrepance can be ascribed to a finite width of the impurity band W which for weakly compensated sample according to theoretical prediction is

$$W = \frac{e^2}{\kappa} N^{1/3}$$

where κ is the dielectric constant, N is the impurity concentration. This estimate gives for $N = 10^{17}\,\mathrm{cm}^{-3}$ $W = 10$ meV that is the value of $W/2$ is in agreement with the difference between the ionization energy observed and the energy of the bare level. For the sample 213 (both GaAs layers and the barrier regions are doped) much lower ionization energy (7 meV) is observed. In this case the additional holes occupy the second charge state A^+ of the acceptors in GaAs layers. According to the theoretical estimates the ionization energy of the A^+ state is $0.05E_0$. The observed value is by a factor of 5 higher which we ascribe to the 2D character of the structure. Indeed, while the ground state radius a_0 is equal to 30 Å (which is much less than the well width) the radius of A^+ state is expected to be much larger ($\sim 4a_0$) and is of the order of the well width. This factor leads to a lowering of the A^+ energy and to a decrease of the Hubbard energy (by definition being a difference between energies of A_0 and A^+ centers). The indepenndent estimate of A_0 and A^+ centers radii can be obtained on the base of the analysis of low temperature conductivity corresponding to variable range hopping. Since the hopping length al low temperatures definitely exceeds the well width, we deal with 2D hopping described by the law

$$\sigma = \sigma_0 \exp\left(-\frac{T_0}{T}\right)^{1/3}$$

where T_0 is the parameter related to the density of states at the Fermi level and the localization radius:

$$T_0 = C(N_F a^2)^{-1}$$

($C = 13.8$ being a numerical coefficient). In Fig. 2 we depicted the low temperature behavior of conductivity for the two samples in terms of $T^{-1/3}$. As it is seen, the behavior corresponds to straight lines while the slopes allow to extract the values of T_0 — 103 K (sample 293) and $1.5 \cdot 10^3$ K (sample 213). If one supposes that the densities of states at the Fermi level are equal for 293 and 213 samples the square root of the ratio of these parameters gives the ratio of the radia corresponding to the two samples . The ratio of the radia of A_0 and A^+ states found in such a way is equal to 4, that is the radius of A^+ center is equal to 12 nm which is comparable with the size of the structure. Thus the experiments evidenced that the A^+ binding energy is significantly (by a factor of 5) enhanced for the wells with a width 15 nm with respect to the bulk case which is related to the fact that the radius of A^+ state is comparable to the well width.

Acknowledgements

We are grateful to A. E. Zhukov for the participation of the structures growth and to V. I. Kozub for discussions. The paper was supported by RFFI (Grants 00-02-16992 and 98-02-18403).

References

[1] S. V. Kravchenko, G. V. Kravchenko, J. E. Furneaux, V. M. Pudalov and M. D'Lorio, *Phys. Rev. B* **50**, 8039, (1994).
[2] D. Simmonian et al., *Phys. Rev. Lett.* **79**, 2304, (1997)
[3] A. Perez-Garrido, M. Ortuno, E. Cuevas, J. Ruiz and M. Pollak, *Phys. Rev. B* **55**, R8630, (1997).
[4] B. L. Alsthuler and D. l. Maslov, *Phys. Rev. Lett.* **82**, 145, (1999).
[5] V. I. Kozub , N. V. Agrinskaya, S. I. Khondaker and I. Shlimak Cond-mat. 9911450 1999.
[6] O. D. Dubon, W. Walukiewicz, J. W. Beeman and E. E. Haller, *Phys. Rev. Lett.* **78**, 3519, (1997).
[7] N. V. Agrinskaya, V. I. Kozub and T. A. Polyanskaya *Phys. Stat. Sol.(b)* **218**, 159, (2000).

9th Int. Symp. "Nanostructures: Physics and Technology"
St Petersburg, Russia, June 18–22, 2001

Simulation approach to weak localization in inhomogeneous two-dimensional systems

A. V. Germanenko, G. M. Minkov and O. E. Rut
Institute of Physics and Applied Mathematics, Ural State University
620083 Ekaterinburg, Russia

Abstract. A weak localization effect has been studied in macroscopically inhomogeneous 2D system. It is shown, that although the real phase breaking length tends to infinity when the temperature tends to zero, such a system can reveal a saturated behavior of the temperature dependence of that parameter, which is obtained from the standard analysis of the negative magnetoresistance and usually identified by experimenters with the phase braking length.

In recent years, interest to the problem of weak localization is reappeared. One of the reason is that the new experimental results have been obtained. Among them is the saturation of the temperature dependence of the phase breaking length [1]. It causes a storm discussion in the literature (see, e.g., [2] and references therein) and stimulate a new flux of the papers concerning the weak localization.

In order to determine the phase breaking time, a standard fitting procedure is used in most cases: experimental magnetic field dependencies of negative magnetoresistance are fitted to the well-known Hikami expression, the phase breaking length l_φ is used as fitting parameter.

Another approach to the negative magnetoresistance examination is based on analysis of statistics of closed paths [3]. Here, we develop this method and present the results of numerical studies of the negative magnetoresistace due to weak localization in macroscopically inhomogeneous systems. One of possible reasons of the low-temperature saturation of $l_\varphi(T)$ dependence is offered.

1. Main idea

We suppose that an inhomogeneous 2D system consists of a number of puddles which are connected one with other by means of channels (Fig. 1(a)). The transport over puddles and channels is diffusive, i.e. their dimensions are much greater than the mean free path of electrons. In this case a quasi-classical treatment to the problem can be applied. In order to simplify the problem, we believe that the conductance of puddles is much greater than the conductance of channels. Such type of inhomogeneity can be due to inhomogeneous distribution of compensating impurity, for example. It is clear that in this approximation the conductance of 2D system is determined by the conductance of channels, and the interference quantum correction to the conductivity of the system is mainly determined by the closed paths, which starting points lie within the channels. So, if we obtain the area distribution function of the closed paths, which start within the channels, we can calculate the magnetic field dependence of magnetoresistance in such a system.

2. Simulation details

The model inhomogeneous 2D system consists of a number of identical elements connected in series-parallel. Each element includes the channel and parts of puddles. We present the results obtained for two cases: the puddles are connected via long and narrow channels (Fig. 1(b)); and the channels are short and wide (Fig. 1(c)). In simulation, the element is represented as a lattice, the scatterers are placed in a part of lattice sites with the use of a random number generator. A particle starts from some random point within the channel, moves with a constant velocity along straight lines, which happen to be terminated by collisions with the scatterers. After collision it changes the motion direction. If the particle collides with the wells of element, it is reflected specularly. If the particle escapes the channel (shadowed in Fig. 1(c)), it can return back with some probability less than unity (we use the value 0.3). Thereby we specify the kind of inhomogeneity: within the channel the Fermi momentum is less than that in the puddles, that may result from fluctuation of the energy of conduction band bottom. If the particle passes near the starting point at the distance less than $d/2$ (where d is a prescribed value, which is small enough), the path is perceived as being closed. Its length and enclosed algebraic area are calculated and kept in memory. The particle walks over the element until it riches one of the opened ends of the element. As this happens we believe that the particle has left to infinity and will not return. A new start point is chosen and all is repeated.

The parameters used in simulation procedure are following: for the case of long channel, the length and width are equal to 17000 and 400, respectively; for short channel, they are 300 and 2900. The dimensions of each half-puddle are 3000×3000 for both cases. For control, we will present the results obtained for comparably large system with dimensions $10^4 \times 10^4$, which is near-equivalent to the classical infinite 2D system. The density of scatterers fed into simulation gave the mean free path about 40 for all three cases.

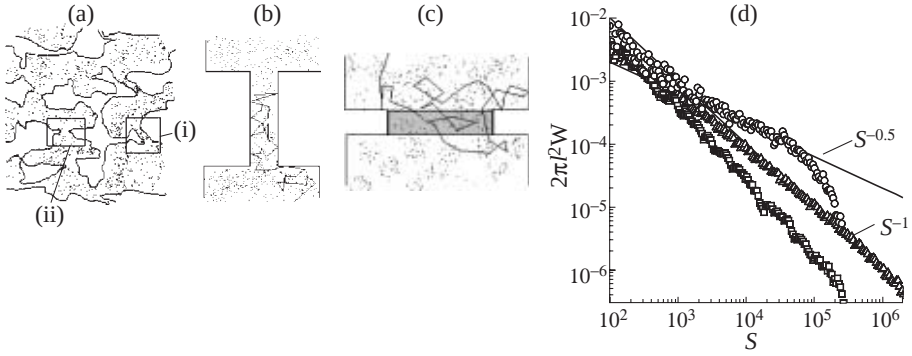

Fig. 1. (a) Sketch of inhomogeneous 2D system. The key parts determining the conductance are enclosed in rectangles. The long and short channels are labeled as (i) and (ii), respectively. Non-conducting areas are white. Points represent scatterers. (b), (c) The simulation models of long and short channels, respectively. Polygonal lines show particle trajectories. The opened ends of shadowed area in (c) work as diode (see text for details). (d) The area distribution function of closed paths. Symbols are the simulation results for the case of long (○), short (□) channels, and for large (control) 2D system (△).

3. Results and discussion

The area distribution functions W, weighted by factor $2\pi l^2$, are shown in Fig. 1(d). As is seen the data obtained for control system and depicted by triangles reveal the behavior which is very close to the well known result of diffusion theory: $2\pi l^2 W = S^{-1}$.

The area dependence of $2\pi l^2 W$ is much complicated for long channels. When S varies within the range $1 \times 10^3 - 5 \times 10^4$, it is close to $S^{-0.5}$-law. Just the same behavior is theoretically predicted for diffusive motion over infinitely long, narrow strip. A particular interest is drastic decrease of the area distribution function evident for $S > 10^5$. The origin is that the particle, moving over long trajectories, escapes the channel through its ends and carries on its motion mainly over the puddles. After escaping it cannot easily enter back, because the width of channel is much less than the puddle's dimensions.

As for short channels, the $2\pi l^2 W$-versus-S plot shows the power behavior close to $W \propto S^{-1.2}$ in whole range of S. This results from the fact that the ratio of the channel's length to the mean free path is not very large as in previous case. Therefore, not only long, but short closed trajectories spread over puddles. Since the channel/puddle borders work as diodes, this leads to more rapid decreasing of $W(S)$ as compared with S^{-1}-law.

The negative magnetoresistance due to magnetic field suppression of the interference quantum correction to the conductivity has been calculated according to [3] and for some l/l_φ value is shown in Fig. 2(a) by symbols. The solid curves in this figure are the results of fitting to the Hikami expression. Namely such a procedure is usually used by experimenters to determine the value of l_φ in real samples. As is seen the Hikami formula well describes the simulation data excepting may be the long channel case.

Figure 2(b) shows the most important result of the paper: how the fitting parameter γ depends on the value of l/l_φ fed into the simulation. As is clearly seen the control 2D system exhibits very clear behavior: as it must the fitting procedure gives the value of γ which is equal to l/l_φ used in simulation. Some inconsistency evident for smallest l/l_φ-value is the result of finiteness of the model system.

For other cases, the fitting procedure gives nearly true value of l/l_φ when $l/l_\varphi >$

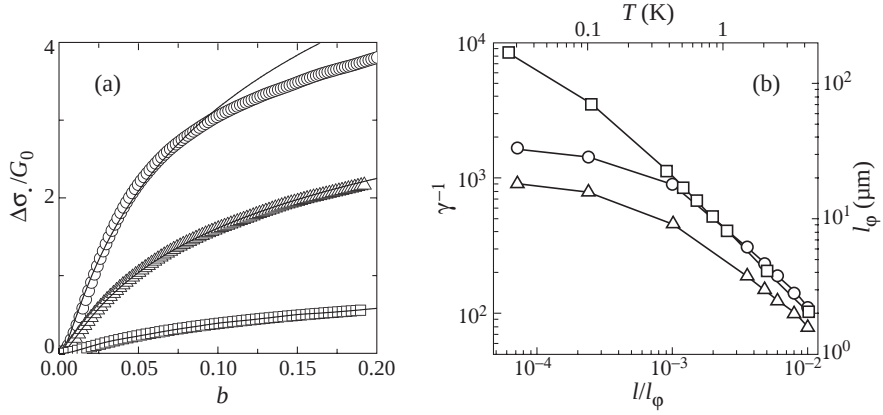

Fig. 2. (a) The magnetic field dependence of interference quantum correction to the conductivity calculated for $l/l_\varphi = 3.5 \times 10^{-3}$. Designations are the same as in Fig. 1(d). Curves are the best fit to the Hikami formula, carried out for low magnetic field $b \leq 0.1$. (b) The fitting parameter γ as function of l to l_φ ratio fed into simulation. Top and right axis give the scale in absolute unites for the 2D system with $n = 1.5 \times 10^{12}$ cm $^{-2}$.

$(2-3)\times 10^{-3}$. For lower values of l/l_φ, the γ-versus-l/l_φ plot shows saturation with l/l_φ decreasing. On the assumption of $l_\varphi \propto T^{-1}$ Figure 2(b) shows the temperature dependencies of the "phase breaking length" as it could be found from the standard fitting procedure of negative magnetoresistance to the Hikami expression. In order to specify the scales in Fig. 2(b), let us assume the lattice constant in the simulation to be equal to 5 Å. In this case our model provides an example of 2D system with local density of scatterers 1.5×10^{12} cm^{-2}, mean free path $l = 200$ Å. Then, Fig. 2(b) shows the temperature dependence of the "phase breaking length" for such sample within the temperature range from 25 mK to 4.2 K. Thus, although the real phase breaking length l_φ decreases linearly with decrease of temperature, the value obtained from the fitting procedure is saturated.

4. Conclusion

We have numerically studied the statistics of closed paths and the negative magnetoresistance in macroscopically inhomogeneous 2D systems. It has been shown that such systems can exhibit saturated behavior of the temperature dependence of the "phase breaking length", if it is obtained from the standard fitting procedure of experimental magnetic field dependence of the negative magnetoresistance to the Hikami expression. This fitting parameter can have nothing in common with the real value of phase breaking length at low temperatures.

Acknowledgments

This work was supported in part by the RFBR through Grants No. 00-02-16215 and No. 01-02-17003, the Program *University of Russia* through Grants No. 990409 and No. 990425, and the CRDF through Award No. REC-005.

References

[1] P. Mohanty, E. M. Q. Jarivala and R. A. Webb, *Phys. Rev. Lett.* **78**, 3366 (1997); P. Mohanty and R. A. Webb, *Phys. Rev. B* **55**, 13452 (1997); C. Prasad, D. K. Ferry, A. Shailos, *et al*, *Phys. Rev. B* **62**, 15356 (2000).

[2] I. L. Aleiner, B. L. Altshuler and M. E. Gershenson. *Waves in Random Media* **9**, 201 (1999).

[3] G. M. Minkov, A. V. Germanenko, O. E. Rut *et al*, *Phys. Rev. B* **61**, 13164 (2000); **61**, 13172 (2000); **62**, 17089 (2000).

9th Int. Symp. "Nanostructures: Physics and Technology"
St Petersburg, Russia, June 18–22, 2001

The role of doped layers in dephasing of 2D electrons in quantum well structures

G. M. Minkov†, A. V. Germanenko†, O. E. Rut†, B. N. Zvonkov‡, E. A. Uskova‡ and A. A. Birukov‡

† Institute of Physics and Applied Mathematics, Ural State University, 620083 Ekaterinburg, Russia
‡ Physical-Technical Research Institute, University of Nizhni Novgorod, 603600 Nizhni Novgorod, Russia

Abstract. The temperature and gate voltage dependencies of the phase breaking time is studied experimentally in the structures with quantum well based on GaAs/InGaAs. There is shown that arising of the states at the Fermi energy in the doped layers (Sn δ layer in our case) leads to significant decreasing of the phase breaking time and to weakness its temperature dependence.

The inelastic of the electron-electron interaction is the main phase breaking mechanism in low dimensional structures at low temperature. This mechanism predicts divergence of phase breaking time (τ_φ) with decreasing temperature. But unexpected saturation of τ_φ at low temperatures was revealed in recent years in one and two dimensional structures [1, 2]. It is one of reason of the particular interest to the possible additional dephasing mechanisms in such structures.

The analysis of the low field negative magnetoresistance, resulting from destruction of the interference correction to the conductivity, is the main method of determination of the phase breaking time. We report the results of detailed studying of the negative magnetoresistance in gated structures based on GaAs/InGaAs. The heterostructures investigated consist of 0.5 μm-thik undoped GaAs epilayer, a Sn δ-layer, a 60 Å spacer of undoped GaAs, a 80 Å $In_{0.2}Ga_{0.8}As$ well, a 60 Å spacer of undoped GaAs, a Sn δ-layer, and a 3000 Å cap layer of undoped GaAs. The samples were mesa etched into standard Hall bridges and Al gate was thermally evaporated over the cap layer. The gate voltage dependencies of the electron density, conductivity and Hall mobility are presented in Fig. 1 for one of the structures. The low field magnetoresistance for some voltage are shown in Fig. 2. The magnetic field dependencies of $\Delta\sigma(B)$ at $B < 1 - 0.5B_{tr}$, where $B_{tr} = \hbar c/2el^2$, l is mean free path, are well described by the standard Hikami expression [3]:

$$\Delta\sigma(b) = \alpha G_0 \left[\psi\left(\frac{1}{2} + \frac{\tau_p}{\tau_\varphi}\frac{1}{b}\right) - \psi\left(\frac{1}{2} + \frac{1}{b}\right) - \ln\frac{\tau_p}{\tau_\varphi} \right], \qquad (1)$$

where $G_0 = e^2/(2\pi^2\hbar)$, b is magnetic field measured in units of B_{tr}, τ_p is momentum relaxation time, and $\alpha = 1$ in the diffusion approximation. In [4] we showed that (1) well describes $\Delta\sigma(B)$ beyond the diffusion approximation also, but with $\alpha < 1$. Thus, one can determine α and τ_φ as fitting parameters, comparing the experimental $\Delta\sigma(B)$ dependence with (1). Note that values of α and τ_φ determined by this way depend on fitting magnetic field range and in Fig. 3 the conductivity dependencies of τ_φ as determined from the different fitting range are presented.

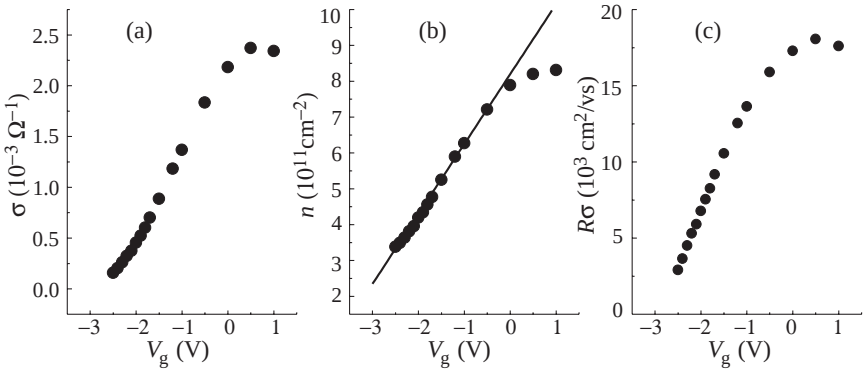

Fig. 1. The gate voltage dependencies of the conductivity (a), electron density (b), and Hall mobility (c) at $T = 4.2$ K. The straight line in (b) is the theoretical total density of the electrons.

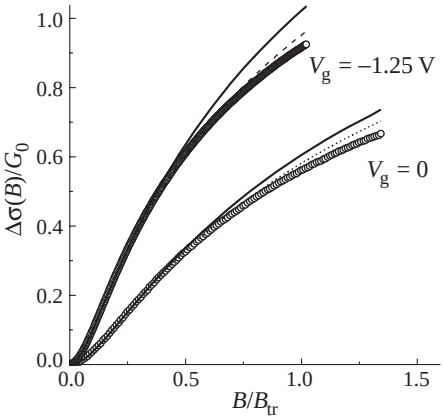

Fig. 2. Negative magnitoresistance at $T = 4.2$ K for two gate voltages. Curves are the theoretical dependencies according to (1) with parameters obtained by the fitting in magnetic field range $0 - 0.25B_{tr}$ (solid curves) and $0 - 0.5B_{tr}$ (dotted curves).

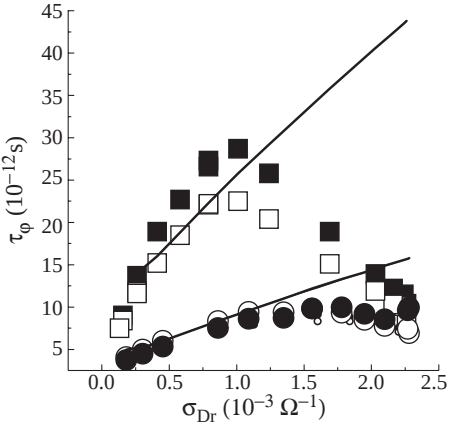

Fig. 3. Conductivity dependencies of τ_φ obtained by the fitting in magnetic field range $0-0.25B_{tr}$ (open symbols) and $0-0.5B_{tr}$ (solid symbols) for $T = 4.2$ K (circles) and $T = 1.5$ K (squares). Curves are the theoretical dependencies given by (2).

When inelasticity of electron-electron interaction is main phase breaking mechanism, τ_φ depends on conductivity and temperature only and for 2D case

$$\tau_\varphi = \frac{\hbar}{kT}\frac{\sigma}{2\pi G_0}\frac{1}{\ln\left(\frac{\sigma}{2\pi G_0}\right)}. \qquad (2)$$

As is seen from Fig. 3 the conductivity dependence of τ_φ is close to the theoretical one when σ varies in the range $(0.2-1.2) \times 10^{-3}\,\Omega^{-1}$, but significant deviation is evident for larger σ. The temperature dependencies of τ_φ are presented in Fig. 4 for some gate voltage and one can see that τ_φ deviates from $1/T$ dependence just for $\sigma > 1 \times 10^{-3}\,\Omega^{-1}$.

To interpret these temperature and conductivity dependencies of τ_φ let us analyze the variation of density of electron in quantum well n (exactly this value is determined from the Hall effect and Shubnikov–de Haas oscillation) with gate voltage (see Fig. 1). The

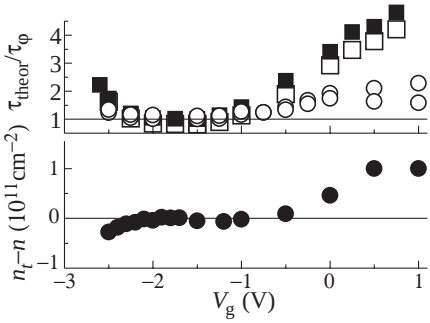

Fig. 4. Gate voltage dependencies of the ratio $\tau_{theor}/\tau_\varphi$ (a) for $T = 4.2$ K (circles) and $T = 1.5$ K (squares). The difference between the total electron density and density of 2D electron in the quantum well as function of V_g (b).

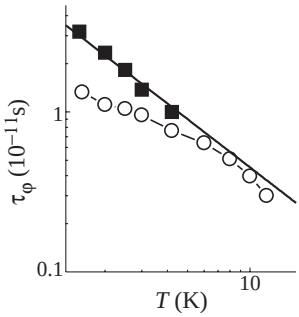

Fig. 5. Temperature dependencies of τ_φ at $V_g = -1.8$ V (squares) and $V_g = +0.5$ V (circles). The line is the $1/T$ dependence.

variation of the total electron density n_t with V_g has to be described by the simple expression $n_t(V_g) = n(0) + Vg\,C/e$, where C is the gate–2D channel capacity per centimeter squared (straight line in Fig. 1(a)). One can see that in the range of V_g from -1 to -3 V the experimental data are close to this dependence, but at $V_g > -1$ V the electron density in the quantum well is less, than the total density of the electrons n_t. It means that at $V_g > -1$ V the fraction of the electrons $(n_t - n)$ occupies the states in δ-layers. From Fig. 4, where the gate voltage dependence of $(n_t - n)$ and ratio $\tau_\varphi/\tau_{theor}$ are presented, one can see that $\tau_\varphi/\tau_{theor}$ deviates from unity when the electrons arise in δ-layers. Thus, appearance of the states in δ-layer at the Fermi energy, and, consequently, the arising of the tunneling of the electrons between quantum well and δ-layer leads to decreasing τ_φ. This interdependence is clear when the phase breaking time of an electron in δ-layer is significantly shorter than that in quantum well. The phase breaking mechanisms in the doped layers, where electrons occupy the states in the tail of density states, are the subject of additional study, but it seems no wonder that dephasing in this layers occurs faster than in quantum well.

In conclusion, the δ- or modulation doped layers are arranged in heterostructures to create the carriers in quantum well or near the hetero-junction. When the states at the Fermi energy appear in the doped layers, the tunneling of the carriers between quantum well and doped layers arises. This process can lead to significant decreasing of the phase breaking time of the carriers in quantum well.

Acknowledgment

This work was supported in part by the RFBR through Grants No. 00-02-16215 and No. 01-02-17003, the Program *University of Russia* through Grants No. 990409 and No. 990425, and the CRDF through Award No. REC-005.

References

[1] P. Mohanty, E. M. Jarivala and A. Webb, *Phys. Rev. Lett.* **78**, 3366 (1997).
[2] W. Poirier, D. Mailly and M. Sanquer, cond-mat/9706287
[3] S. Hikami, A. Larkin, Y. Nagaoka, *Prog. Theor. Phys.* **63**, 67 (1980).
[4] G. M. Minkov, A. V. Germanenko, A. V. Larionova, S. A. Negashev and I. V. Gornyi, *Phys. Rev. B* **61**, 13164 (2000)

9th Int. Symp. "Nanostructures: Physics and Technology"
St Petersburg, Russia, June 18–22, 2001

Challenges in nanoelectronics

Raphael Tsu
University of North Carolina at Charlotte, Charlotte, NC 28223, USA

Abstract. The size of electronic devices has been decreasing to nanometer size regime which requires quantum mechanics to understand its operation and optimization. Many features associated with quantum effects are not all desirable from the engineering point of view: the charging of a nano-capacitor runs into Coulomb blockade; the dielectric constants of nanoparticles is much reduced; the binding energy of the shallow dopants in a nanoscale quantum dots becomes many times of kBT resulting in intrinsic behavior regardless of doping density; etc. There are other serious problems preventing the implementation of redundancy and robustness which are so essential to the electronic devices, for example, inadvertent defects cannot be avoided; contacts and input/output have to be sufficiently small resulting in pushing beyond the frontier of lithography. This article aims to discuss some of the fundamental points still requiring better understanding, and what lies ahead in future nanoelectronics.

Introduction

Professor Kroemer at the Nobel lectures during the APS March Meeting said that: "You notice the old figures of heterostructures that I showed with rounded profiles without scales, it is because I did not know how sharp are the band-edge offsets, nor how large are the offsets". This sentence points to the relative roles of understanding versus technological advances. We all agree that ideas and understandings are crucial to new technologies, however it is the steadfast advancement of technology that brought mankind to what we have today. Traditionally, machines help us to tilt and rearrange our land for farming and control of our habitat, but now, computers are extending our brain. We are expanding our reach as well as accelerating our control of nature. In what follows some are fundamental physics and engineering details while others are based on my personal assessment. For example, only devices like detectors may be operated at low temperatures whereas memory devices should not be operated at low temperatures, and the steady march toward ever decreasing size of integrated circuits (ICs) is based on ever refinement of nano-lithography. Another point is that quantum wells (QW) are far more likely to be incorporated into ICs than quantum dots (QD) because contacts for QW is planar while it is necessary to use quantum wires for QD.

Tunneling time in a quantum well

Several approaches [1, 2] were used: (a) solving the time dependent Schroedinger equation with prescribed initial conditions, and (b) specifying a wave-packet and calculating the time it takes to traverse the double barrier structure [2]. Results show that the tunneling time of a Gaussian packet from the time-dependent solution is very close to the phase-delay time $\tau = \mathrm{d}\phi/d\omega$, where $\phi = kd + \theta$, is the total phase shift, with θ being the phase of the transmission coefficient, and d, the length of the double barrier (DB) structure. Resonance is produced by a wave bouncing back and forth for a number of cycles determined by the quality factor of the resonant system.

The tunneling time given by the time for a Gaussian wave-packet traverses the structure using the time dependent Schrödinger equation gives essentially the same result [3]. Since the thesis [2] is not readily available, several salient features of this work are highlighted here. First, the Green's function for the one dimensional equation for the double barrier (DB) structure is obtained. Excitation functions are chosen for various cases: specifying a spatial distribution at $t = 0$, or specifying a time function (usually a pulse at a given energy between $t = 0$ to T) at a given location such as $x = 0$, or $x =$ center of the well, etc. Laplace transform is then used. The inverse transforms give the desired results. If one wants to calculate the charge inside the well at any given time for a particular distribution, it would be necessary to multiply $Q(t)$ for the charge by $n(\omega) - n'(\omega)$ and integrate over all ω, with n and n' given by the distribution functions on the inside and transmitted side of the DB respectively. $Q(t)$ confined within the system is obtained as a function of time by integrating $|\psi(t)|^2$ over both the well and the barrier regions.

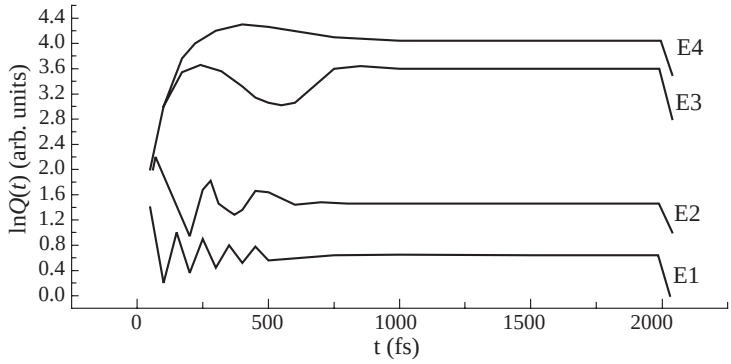

Fig. 1.

Figure 1 shows the charge inside the quantum well for an incident wave at energy E and duration 2 ps. The top curve E4 is at $E = 0.068$ eV, the energy at resonance for a DB structure of barrier width 2.5 nm and GaAs well width of 6nm, and a barrier height of 0.3 eV. Note that at energies away from the resonance, (E3, E2 and E1=0.079, 0.05 and 0.03 eV), oscillation of $Q(t)$ is very strong during the build-up time, while it is more monotonic at resonance. However, the decay is always monotonic. Instead of specifying the initial condition at the left side of the DB structure, we have also studied the build-up time and decay time for an excitation $\exp(-i\omega t)$ at a point within the well and calculate the steady state wave-packet. To our surprise, as the point of excitation moves towards the center of the well from the edge of the barrier, the resonance behavior gradually disappears. The details of those cases are not quite the same. Precise results do depend on the form of the excitation. Although in all cases tunneling does slow down near resonance. The delay time at resonance calculated from $\tau d_0/(hk/2m^*)\,(E/\Delta E)$ with E and ΔE being the energy and linewidth is so close to the solution for Gaussian packet. Although tunneling time slows down near resonance, at the first resonance, it is still less than one quarter of a ps, and 25 fs near the second resonance. An ideal resonant tunneling device is very fast.

Coulomb blockade and quantum of conductance G_0

Conductance for a device, in this case a QD, connected to two leads at very low temperature exhibits equally spaced steps of $G_0 = e^2/h$ versus voltage [4]. The discrete steps originate from the discrete nature of the electronic charge. The applied voltage needs to increase in

steps of e/C to overcome the Coulomb potential of the charging of a capacity C, known as Coulomb Blockade [5, 6]. Typically for a QD of dimension 2 nm $\times$ 2 nm, the electrostatic energy is $\sim$10 mV so that discrete steps in conductance may be observed at low temperatures. It is important to note that C is not a constant because each additional charge introduced into the dot, the additional electron interacts with the electrons already present in a complicated manner to be discussed in the next section. There is another far more important point to be stressed here, i.e. all the work thus far involves adding an additional electron to the dot as a time independent before and after description. To understand device performance such as the charging speed, it is necessary to employ the time-dependent Schrödinger equation. Oscillations again will occur, as the tunneling case presented, for G_0, $2G_0$, etc. The physics is same as the charging of a capacitor where oscillation depends on the length of the transmission line used in bringing in the charge.

Capacitance of a nanoscale sphere

A classical capacitor stores charges, and the electrostatic energy is the only energy stored. However, electrons have kinetic energy as standing waves confined inside a quantum well or quantum dot. We have calculated the quantum mechanical capacitance of a small sphere from the definition $E_2 - E_1 = e^2/2C_{\text{eff}}$, where E_1 and E_2 are the one- and two-electron ground state of the quantum dot [7]. The effective capacitance may also be defined in terms of $E_3 - E_2$ and so on. Since the added electron needs to interact with two electrons present in the dot, the effective capacitance will not be a constant with respect to the number of electrons already present in the dot. Quantum mechanically, it is somewhat similar to the difference between the He atom and hydrogen atom, only that the calculation is quite complex because it is necessary to include the electron-electron interaction together with the induced image-charge and their interactions. We were surprised that even the classical electrostatic calculation of the capacitance taking into account all the interactions of electron-electron and their images, have not been calculated [7]. These interactions lowers the total energy of the systems inside a capacitor, resulting in a deviation from the classical capacitance. The quantum mechanical calculation includes the kinetic energy, thus drastically reduce the capacitance at nanoscale regime.

Since we assumed that the coherence length of the electron wave function is only 12 nm, it is expected that C_{eff} at 12 nm approaches the 'classical' value (including all the e-e interactions), $\sim 10^{-18}$ to 10^{-19} F, we found that at 6 nm and 3 nm, C_{eff} is only one-half and one-third as large as the classical values, respectively. Likharev used a constant value for the capacitance in his Hamiltonian because the size of the quantum dot is quite large in his case [6]. The kinetic energy of an electron is inversely proportional to the square of the dimension of confinement, which grows faster than the Coulomb energies. Consequently, C_{eff} decreases when the ground state energies dominates over the electrostatic energies. Not only that this C_{eff} should be used in nanoscale modeling, it should be possible to tailor-made capacitor in a nano-composite.

Dielectric constant and doping of a nanoscale silicon particle

Reduction of the static dielectric constant becomes significant as the size of the quantum confined systems, such as quantum dots and wires, approaches the nanometric range. A reduced static dielectric constant increases Coulomb interaction energy in quantum confined structures. The increase of the exciton binding energy significantly modifies the optical properties, and the increase of the shallow impurity binding energy may profoundly alter the transport, i.e., resulting in an intrinsic conduction even with doping. The dielectric constant

$\varepsilon(a)$ was first derived using a modified Penn model taking into account the eigenstates of a sphere instead of the usual free electron energy-momentum relation [8–10]. The size-dependent $\varepsilon(a)$ is given by [10]

$$\varepsilon(a) = 1 + (\varepsilon_B - 1)/[1 + (\Delta E/E_g)^2] \quad \text{and} \quad \Delta E = \pi E_F/(k_F a),$$

where E_F and k_F are the energy and k vector at the Fermi level with the total number of the valence electrons, and E_g is taken as 4 eV, the center of the ε_2 versus energy for silicon. For a 1 nm QD, $\varepsilon(a)$ is reduced to half the value. The formula is easily applicable to a number of situation in nanoscale modeling. For example, the binding energy of dopants of a nanodot [11], estimating the breakdown voltage of ultra-thin oxide, and in Coulomb blockade. The dielectric mismatch between the media results in induced charges at the interface. We found that these induced effects are as important as the dielectric constant effect. There are many such induced terms: in addition to the direct Coulomb term, there are the self-polarization between the electron and its image; the term between the electron and the induced polarization of the donor. Since both the self-polarization and induced-polarization terms depend on $\varepsilon_1 - \varepsilon_2$, with 1 and 2 for the nanoparticle and the matrix respectively, the binding energy can be strongly affected by the sign of $\varepsilon_1 - \varepsilon_2$. For vacuum, at a radius of 2 nm, the binding energy is 0.8 eV resulting in no extrinsic conduction at room temperature. Immersing in water, the binding energy is reduced to 0.1 eV, allowing some extrinsic conduction at room temperature. Since doping is essential to the operation of semiconductor devices, and the trend of ever reducing the device size, the mechanism of extrinsic conduction governed by the size forms an important issue in modeling.

Tunneling via nanoscale silicon particles

Nicollian and I reasoned that if we could make the particles small enough, confinement would increase the energy separation to values allowing resonant tunneling at room temperature. A diode structure was fabricated with nanoparticles of silicon, $\sim$4–8 nm, embedded in an oxide matrix [12, 13]. Sharp conductance peaks were observed at reverse bias between 10–11 V. Resonant tunneling diode, RTD gives current peaks whenever the energy of the incident electron coincides with the eigenstates of the quantum system [14]. Using a metal contact having a large Fermi energy, current steps instead of peaks should result at resonant. We found that the conductance peaks appear near 10–11 V reverse bias, and steps appear above 20 volts bias, with a pronounced hysteresis shift of $\sim$7 mV [15, 3]. The details are quite complicated. Some salient features are summarized below:

1. The linewidth of the conductance peaks $\sim k_B T$.

2. The QD energies are much greater than the Coulomb energy for the size under consideration. Therefore we observed two groups of closely spaced current steps separated by the separation of the E_1 and E_2 quantum states of the dot [16, 17].

3. With large metal contacts, conductance is proportional to the density of states, giving rise to conductance peaks for 3D and steps for 1D structures. (We think that some of the particles are coupled to form 1D structures.)

4. Hysteresis is present in most cases particularly noticeable at higher bias, but not always.

5. We observed oscillation in time due to negative resistance resulted from e-h pair production by hot electrons injected into the substrate [17, 18].

6. What we have learned is that devices with large contact covering many QDs is unlikely to play a role in future devices. Significant progress in nanostructure devices must wait for the improvement in lithography allowing contacting a single QD. Although we thought about a multifunctional device, but not really seriously! See Ref. [18] for a summary of this work.

A new type of superlattice: semiconductor-atomic superlattice (SAS)

Conventional superlattices are formed with repeating a basic period consisting of a heterojunction between two materials [19]. A new type of superlattice are formed by replacing the heterojunction between adjacent semiconductors with semiconductor layers separated by adsorbed species such as oxygen atoms; and CO, molecules, etc. [20, 21]. This new type of superlattice, SAS, semiconductor-atomic-superlattice, fabricated epitaxially, enriches the present class of heterojunction superlattices and quantum wells for quantum devices. The Si growth beyond the adsorbed monolayer of oxygen is epitaxial with fairly low defect density. At present, such a structure shows stable electroluminescence and insulating behavior, useful for optoelectronic and SOI (silicon-on-insulator) applications. SAS may form the basis of future all silicon 'superchip' with both electrons and photons. Without a strong optical transition, silicon has not played a role in optoelectronic technologies such as injection lasers and light emitting diodes. Superlattices and related quantum wells have been developed into the mainstream of research and development in semiconductor physics and devices primarily with III–V and II–VI compound semiconductors. Silicon dioxide with a barrier height of 3.2 eV in the conduction band of silicon is amorphous, preventing the building of a quantum well structure on top of the a-SiO_2 barrier. Several years ago, it was proposed that the oxides of one or two monolayers might allow the continuation of epitaxy [23]. Our growth beyond a barrier structure consisting of 1 or 2 nm of silicon sandwiched between adjacent layers of adsorbed oxygen up to 50 Langmuirs of exposure for each layer is epitaxial and low in stacking faults as determined in high resolution X-TEM. We have presented high resolution TEM in both cross-section and plane-view [22]. The measured barrier height is $\sim$0.5 eV [24]. Using an assumption that in the SAS structure, the amount of electron transfer from the Si to O is only half as much as SiO_2, the maximum barrier height is estimated at 1.5 eV instead of 3.2 eV [25]. Following the observation of visible luminescence in nanoscale silicon particles [26], we have observed stable electroluminescence in the visible spectrum of a 9-period SAS structures [27]. With partially transparent Au electrode, the emitted light is green. The spectrum extends well into the blue region of the visible spectrum. The defect density is below 10^9 cm^2. We have lowered the defects by almost two orders of magnitude during the past couple of years. Thus we are optimistic that further reduction should be possible. Note that the defect density in Si/a–SiO_2 interface is generally much higher.

We have also fabricated a 9-period Si/O superlattice for possible replacement of SOI (silicon-on-insulator). Preliminary results show the structure is epitaxial with insulating behavior. With similarly doped silicon, a decrease in current of five orders of magnitude at the same applied voltage of several volts has been observed.

What we have demonstrated is that silicon can grow epitaxially beyond adsorbed atomic or molecular species, resulting in a new kind of superlattice. We want to emphasize that it is important to have the silicon layer having at least several atomic layers. Otherwise, the

structure becomes similar to the ALE, atomic layer epitaxy, which is entirely different from the SAS. In SAS, the adsorbed oxygen monolayers are constrained by the Si surfaces on both sides, whereas, in ALE, there is nothing to prevent silicon and oxygen atoms forming a specific crystalline structure, or an alloy structure. It is the constraint imposed by the silicon surfaces that gives rise to the superlattice structure, exhibiting the physical characteristics reported here. As we have shown that SAS, or SMS (M for molecular) indeed constitutes a new type of superlattice. It is hopeful that the reported EL and PL can allow applications in optoelectronic devices, and the reported epitaxially grown SOI can replace the present SOI for quantum devices, such as 3D ICs.

To Summarize, 1D quantum confinement will dominate future devices because of the planar nature of the contacts for input/output. Any 3D nanostructures will have to wait for further improvement in nano-lithography.

Acknowledgments

This work has been supported by ARO and ONR, as well as BMDO and DARPA through NanoDynamics. In particular, almost all the postdoctoral supports came from NanoDynamics.

References

[1] R. Tsu and F. Zypman, *Surf. Sci.* **228**, 418 (1990).
[2] Subrata Sen, *MS Thesis*, unpublished, A&T State Univ. 1989.
[3] R. Tsu, *Int. J. High Speed Electron. Syst.* **9**, 145 (1998).
[4] R. Landauer, *Phil. Mag.* **21**, 863 (1970).
[5] M. A. Reed, J. H. Randall, R. J. Aggarwal, R. J. Matyi, T. M. Moore and A. E. Wetsel, *Phys. Rev. Lett.* **60**, 535 (1988).
[6] K. K. Likarev, *Granular Nanoelectronics*, ed. by D. Ferry (Plenum, New York, 1991).
[7] D. Babic, R. Tsu and R. F. Greene, *Phys Rev. B* **45**, 14150 (1992).
[8] R. Tsu, L. Ioriatti, J. F. Harvey, H. Shen and R. Lux, *Mat. Res. Soc. Symp. Soc. Proc.* **283**, 437 (1993).
[9] R. Tsu, *Physica B* **189**, 235 (1993).
[10] R. Tsu, D. Babic and L. Ioriatti, *J. Appl. Phys.* **82**, 1 (1997).
[11] R. Tsu and D. Babic, *Appl Phys. Lett.* **64**, 1806 (1994).
[12] Q. Y. Ye, R. Tsu and E. H. Nicollian, *Phys. Rev. B* **44** 1806 (1991).
[13] E. H. Nicollain and R. Tsu, *J. Appl. Phys.* **74**, 4020 (1993).
[14] R. Tsu and L. Esaki, *Appl. Phys. Lett.* **22**, 562 (1973).
[15] Xiao-Lei Li, *MS thesis*, Department of Elect. Engr. UNC-Charlotte, 1993.
[16] R. Tsu, X. L. Li, and E. H. Nicollian, *Appl. Phys. Lett.* **65**, 842 (1994).
[17] D. W. Boeringer and R. Tsu, *Phys. Rev. B* **51**, 13 337 (1995).
[18] R. Tsu, *Appl. Phys. A* **71**, 391 (2000).
[19] L. Esaki and R. Tsu, *IBM J. Res. Develop*. **14**, 61 (1970).
[20] R. Tsu, A. Filios, C. Lofgren, K. Dovidenko and C. G. Wang, *Electrochem Solid State Lett.* **1** (2) 80 (1998).
[21] R. Tsu, Q. Zhang and A. Filios, *SPIE* **3290**, 246 (1997).
[22] R. Tsu, K. Dovidenko and C. Lofgren, *ECS Proc.* **99-22**, 294–301 (1999).
[23] R. Tsu, *Nature* **364** 19 (1993).
[24] J. Ding and R. Tsu, *Appl. Phys. Lett.* **71**, 2124 (1997).
[25] R. Tsu, *ECS Proc.* **98-19**, 3 (1999).
[26] Z. H. Lu, D. J. Lockwood and J. M. Barlbeau, *Nature* **378**, 825 (1995).
[27] R. Tsu, *Phys. Stat. Sol. (a)* **180**, 333 (2000).

Author Index